The Eurasia Proceedings of Science, Technology, Engineering & Mathematics

EPSTEM

VOLUME 32 ICONTES CONFERENCE

ISSN: 2602-3199
ISBN: 978-625-6959-56-9
IConTES 2024: 8th International Conference on Technology, Engineering and Science
November 14-17, 2024 Antalya, Turkey
Edited by: Prof.Dr. Mehmet Ozaslan - Gaziantep University, Turkey

IConTES 2024

8th International Conference on Technology, Engineering and Science (IConTES)

Proceedings Book

Editor

Mehmet Ozaslan
Gaziantep University, Turkey

ISBN: 978-625-6959-56-9

Published by the ISRES Publishing

Address: Askan Mah. Akinbey Sok. No: 5-A/Konya/Turkey

Web: www.isres.org

Contact: isrespublishing@gmail.com

https://www.2024.icontes.net

Dates: November 14-17, 2024

Location: Antalya, Turkey

ISSN: 2602-3199

About Editor

Prof Dr. Mehmet Ozaslan
Department of Biology, Gaziantep University, Turkey
Website: mehmetozaslan.com
E-mail: ozaslanmd@gantep.edu.tr

Language Editor

Lecturer Ceren Dogan
School of Foreign Languages, Necmettin Erbakan University, Turkey
Email: cerendogan@erbakan.edu.tr

ISSN: 2602-3199

The Eurasia Proceedings of Science, Technology, Engineering & Mathematics (EPSTEM)
ISSN: 2602-3199

Editorial Policies

ISRES Publishing follows the steps below in the procedings book publishing process.
In the first stage, the papers sent to the conferences organized by ISRES are subject to editorial oversight. In the second stage, the papers that pass the first step are reviewed by at least two international field experts in the conference committee in terms of suitability for the content and subject area. In the third stage, it is reviewed by at least one member of the organizing committee for the suitability of references. In the fourth step, the language editor reviews the language for clarity.

Review Process

Abstracts and full-text reports uploaded to the conference system undergo a review procedure. Abstracts will be evaluated on the basis of abstracts/proposals. The conference system allows the full text to be sent if the abstract is accepted. Participants must wait for the evaluation results after uploading their article abstracts to the conference system. If their abstracts are accepted, they can upload their full texts to the conference system. The full texts are then sent to at least two reviewers for review. The conference has a double-blind peer-review process. Any paper submitted for the conference is reviewed by at least two international reviewers with expertise in the relevant subject area. Based on the reviewers' comments, papers are accepted, rejected or accepted with revision. If the comments are not addressed well in the improved paper, then the paper is sent back to the authors to make further revisions. The accepted papers are formatted by the conference for publication in the proceedings.

Aims & Scope

In the 21st century, developments in science and technology have led to significant changes in the field of engineering. Creativity and design skills are at the center of studies in the field of engineering today. The main focus of this conference is original studies in the field of engineering. In addition, technology and basic science studies that are directly or indirectly related to engineering are also accepted at the conference.

The aim of the conference is to bring together researchers and administrators from different countries, and to discuss theoretical and practical issues in all fields of Engineering.

The Eurasia Proceedings of Science, Technology, Engineering & Mathematics (EPSTEM)
ISSN: 2602-3199

Articles: 1- 71

CONTENTS

The Eurasia Proceedings of Science, Technology, Engineering & Mathematics (EPSTEM)
ISSN: 2602-3199

The Eurasia Proceedings of Science, Technology, Engineering & Mathematics (EPSTEM)
ISSN: 2602-3199

The Eurasia Proceedings of Science, Technology, Engineering & Mathematics (EPSTEM), 2024

Volume 32, Pages 1-11

IConTES 2024: International Conference on Technology, Engineering and Science

Fresh and Hardened Properties of Self-Compacting Concrete Reinforced with Recycled Steel Fibers from Mechanical Parts Turning Waste

Sabria Malika Mansour
M'Hamed Bougara University of Boumerdes

Youcef Ghernouti
M'Hamed Bougara University of Boumerdes

Bahia Rabehi
M'Hamed Bougara University of Boumerdes

Abstract: The main reason for using fibers is to control cracking of concrete members due to plastic shrinkage and drying of concrete and to delay crack propagation. The use of fibers such as steel fibers improves the flexural strength and ductility of concrete. The main objective of this work is to study the effects of adding fibers resulting from the turning operation of mechanical parts on the behavior of self-compacting concrete. Fresh properties such as slump flow, passing ability and segregation rate and hardened properties such as compressive strength and flexural strength were analyzed. The obtained results have shown that all produced self-compacting concretes are homogeneous, stable and their mobility in confined environment is ensured. Furthermore, incorporation of fibers in the self-compacting concretes allowed to increase its flexural strength, also to have a gain of ductility witch can avoid sudden failure of the specimens. In conclusion, the turning waste can offer a new source of fiber supply and can replace steel fibers.

Keywords: Self-compacting concrete, Turning waste, Steel fibers, Compressive strength, Flexural strength

Introduction

The objective of making concrete more resistant in flexion and tension still attracts the attention of numerous research. The approach most mentioned in the literature to overcome this weakness in tensile behavior consists of the addition of steel fibers in the concrete formulation. The latter play a reinforcing role, which compensates the fragility of concrete by stitching micro cracking and macro cracking. Thus, the fibers have the capacity to control the opening of cracks, acting as energy absorbers (Mansour, 2021; Mansour, 2020; Haddadou et al.2021). The fibers used in the making of concrete are steel fibers. Despite the appreciable improvements obtained in terms of the mechanical behavior of concrete, the incorporation of fibers into concrete remains problematic from the point of view of workability and homogeneous distribution of fibers. To remedy these problems, the association of fibers with self-compacting concrete (SCC) seems promising. The absence of vibration of these materials avoids a heterogeneous distribution of fibers in the matrix (Haddadou et al., 2021).

In this work, recycled steel fibers obtained from waste of the turning operation carried out on mechanical parts were used to reinforce self-compacting concrete. It is demonstrated that utilizing recycled steel fibers RSF for producing High-Performance fiber reinforced concrete has a potential effect in producing some structures with lower price, higher mechanical performance, and more ecological beneficial impact (Mansour, 2021). Using RSF in concrete efficiently reduces the brittle behavior of concrete, and improves the durability of concrete by arresting crack propagation and limiting the crack width of concrete using bridging action (Ahmad et al., 2023; Alabduljabbar et al., 2019; Ali et al., 2020b; Geng et al., 2021). The main objective of this work is to investigate

- Selection and peer-review under responsibility of the Organizing Committee of the Conference

the effects of using recycled steel fibers on the behavior of self-compacting concrete. Three self-compacting concrete mixtures SCCs introducing 0%, 0.5%, and 1% RSF content in terms of volume were analyzed in the fresh state to estimate fresh properties such as spreading, L-box passing ability and resistance to segregation. The hardened phase was related to the evaluation of compressive and flexural strength of the developed SCCs in 7, 14 and 28 days of maturing. In addition, to determine in the hardened state the mechanical properties such as compressive strength and flexural strength. The self-compacting concretes are control SCC concrete and two SCC concretes containing 0.5% and 1% of recycled fibers.

Experimental Program

Materials

The SCC concrete mixtures investigated in this study were prepared with Portland cement (PC) CPJ-CEM II/B 42.5 according with NA 442, EN 197-1 and NF P 15-301/94 standard. Its physical-mechanical properties are given in Table 1. A 0/3 natural sand from Oued Souf was used. The coarse aggregates are crushed from natural limestone rock in two granular classes (3/8 and 8/15). The characteristics of aggregates are given in Table 2. As addition, the limestone fillers rich in CaO were used (Table 1). The particle size analysis of aggregates is shown in figure 1 and the chemical composition of cement and limestone fillers is presented in Table 3.

Table 1. Physical-mechanical properties of cement and limestone fillers

Properties	Cement	Limestone fillers
Specific density(g/cm^3)	3.01	2.66
Blaine specific area(cm^2/g^{-1})	3170	4020
Compressive strength(MPa)	48	-
Flexural strength(MPa)	7	-

Table 2. Physical properties of aggregates

Aggregates	S0-3 mm	G3-8 Mm	G8-15 Mm
Absolute density	2.67	2.71	2,70
Water content	2.49	0.6	0.1
Sand equivalent	79	-	-
Fineness modulus	3.9	-	-
Los Angeles coefficient	-	27	26
Micro Deval coefficient	-	17	16
Water Absorption (%)	2.65	0.97	0.14
Porosity (%)	5.59	1.85	0.40

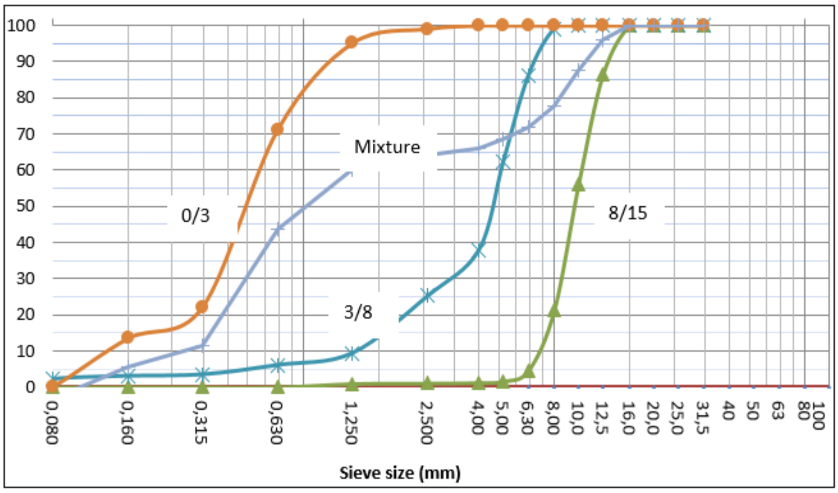

Figure 1. Particle size analysis of aggregates: percentage passing as function as sieve size

Limestone fillers were obtained by extensive grinding of limestone. It is a product with a high limestone content, rich in lime with a CaO content greater than 51%. It is shown that the dominant constituent of Portland cement PC and limestone is CaO.

Table 3. Chemical compositions of cement, limestone fillers

Oxides (%)	SiO_2	Al_2O_3	Fe_2O_3	CaO	MgO	SO_3	Na_2O+ K_2O	LOI	[SiO_2+Al_2O_3+ Fe_2O_3]	Σ
Portland Cement	15.80	4.15	2.31	61.90	2.39	2.80	0.75	9.59	22.26	96.81
Limestone	4.83	1.04	0.37	51.73	0.46	0.08	0.22	41.17	6.24	99.9

The used steel fibers were obtained from waste of the turning operation of mechanical parts. Their technical characteristics are illustrated in Figure 2 and given in Table 4.

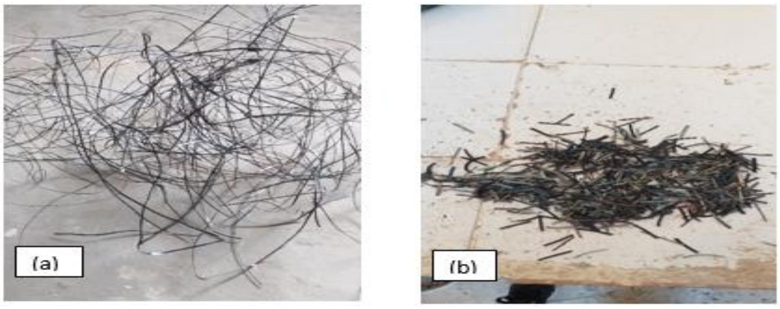

Figure 2. (a) Waste of the turning operation- (b) Waste fibers

Table 4. Technical characteristics of the fibers

Characteristics	Nature	Length	Width	Tensile strength	Young's modulus
Value	Steel	25mm	2mm	227MPa	55678MPa

As superplasticiser (SP), a third generation super water-reducing superplasticizer based on modified polycarboxylates was used at a dosage of 1.7% of cement weight. Its specific gravity is 1.06 and solid content is 25%.

Mix Proportions of Self-Compacting Concretes

Based on the Japanese method (Okamura & Ozawa, 1994), the self-compacting concrete SCC was formulated. Three formulations were elaborated with a water-to binder ratio W/B = 0.38, gravel to sand ratio G/S = 0.9 and a dosage of superplasticizer of 1.7% of cement weight. The dosage of superplasticizer is defined as the admixture saturation point. One (01) reference SCCR concrete without fibers and two (02) SCCs containing 0.5% and 1% of steel fibers respectively were elaborated. The proportions of self-compacting concretes are given in Table 5.

Table 5. Mix proportion of reinforced self-compacting concretes (kg.m-^{3})

SCC/Constituent	SCCR	SCC0.5%	SCC1%
Cement	430	430	430
Limestone Fillers	43	43	43
Sand	924	924	924
Coarse aggregate G3/8	276	276	276
Coarse aggregate G8/15	559	559	559
Water	175	175	175
Superplasticizer	8	8	8
Fibers	-	39	78

Specimen Preparation and Testing

After mixing, the apparent density of fresh SCC concretes was measured according to the standard (NF EN 12350-6, 2012). In addition, workability tests were applied to determine fresh properties, which must be in accordance with Specification and Guidelines for SCC prepared by (EFNARC, 2005, European Federation of National Trade Associations). The tests are Abram cone to determine slump flow diameter according to standard (EN 12350 – 8, 2010), L-box to define the filling rate according to standard (EN 12350 – 10, 2010) as well as sieve stability to characterize the resistance to segregation according to standard (EN 12350–11, 2010).

After, for each SCC concrete, three cubic specimens 150x150x150 mm and three prismatic specimens 70 × 70 × 280 mm were prepared according to European Standard (EN 12390-2, 2012). After 24 h, specimens were cured in water at a temperature of 20 ± 2°C until testing. After 24 h, specimens were cured in water at a temperature of 20 ± 2°C until testing. Finally, destructive tests have been made on cubic specimens to determine compressive strength in accordance with standard (EN, 2012) and on prism specimens to determine flexural strength in accordance with standard (EN 12390-5, 2012) at 7d, 14d and 28 days.

Results

Properties of Fresh SCC Concretes

Bulk Density

Bulk density measurement determines the density performance of the composition of fresh self-compacting concrete and makes it possible to verify the validity of the theoretical formulation. The results are given in Table 6 and illustrated on Figure 3.

Table 6. Workability properties of fresh SCC concretes

SCC/property	Slump flow diameter (cm)	L-Box ratio	Sieve stability (%)	Bulk density (kg.m^{-3})
SSCR	72	0.86	12.4	2341
SCC0.5%	68	0.83	9.2	2338
SCC1%	65	0.81	7.3	2332

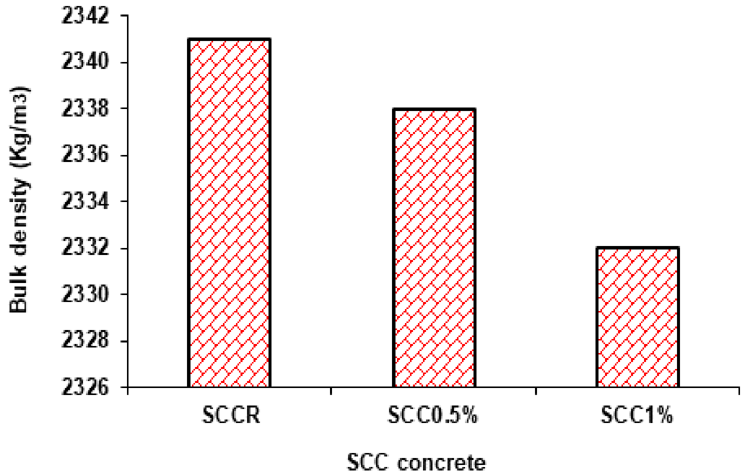

Figure 3. Bulk density of fresh reinforced SCC concretes

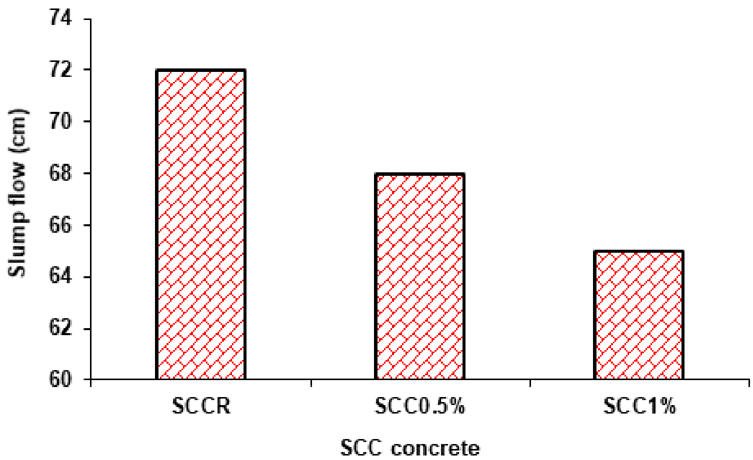

Figure 4. Slump flow diameter of reinforced SCC concretes

Workability Properties

The fluidity and mobility of SCC in an unconfined environment are characterized by measuring the slump flow diameter (Abrams cone) generally fixed in the range 550 cm to 80 cm. Moreover, the mobility of the SCC in confined environment is characterized by the passing rate (H1/H2) (L-Box) which must be greater than 0.8. The sieve stability test allows to assess the risk of segregation must be less than 15% of the global weight. Table 6 shows all results of workability tests on fresh concretes. Results of the tests are illustrated in Figure 4, 5 and Figure 6.

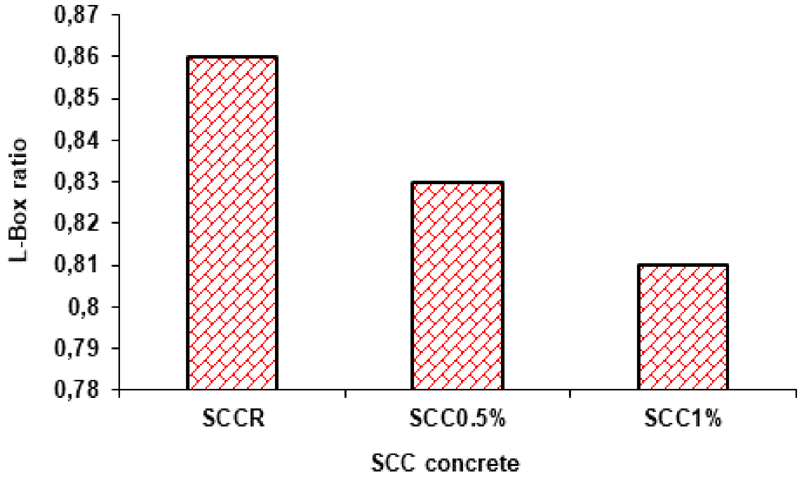

Figure 5. L-Box ratio/ passing ability of SCC Concretes

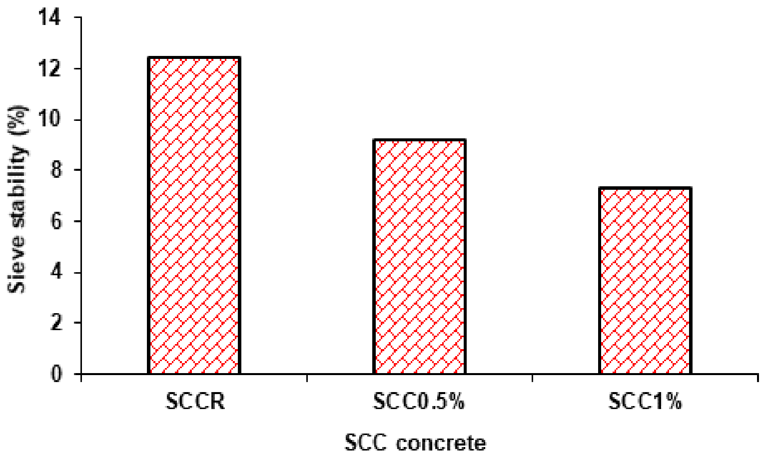

Figure 6. Sieve stability /Segregation rate of SCC concretes

Mechanical Properties of Hardened SCC Concretes

Compressive Strength

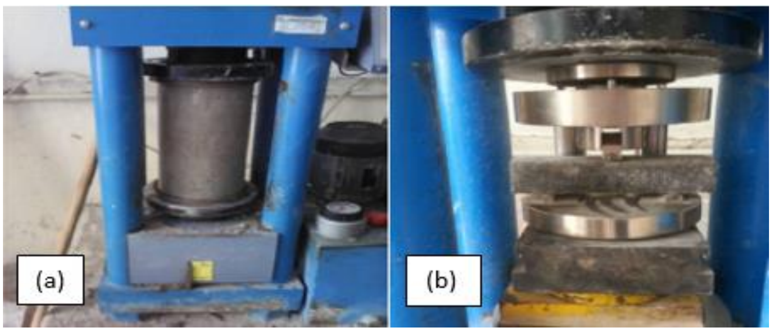

Figure 7. Test on hardened SCCs: (a) - Compression test, (b)- Flexural test

Compressive strength of SCC concretes with and without fibers were determined at 7, 14 and 28 days. The compression tests were carried out with 3000 KN hydraulic compressive testing machine on 150 × 150 × 150 mm^3 cubes. (Figure 7). Results are illustrated in Figure 8 and 9.

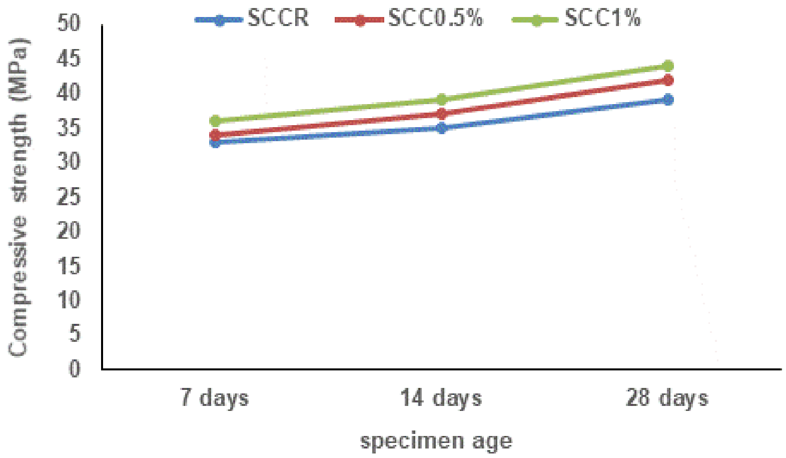

Figure 8. Compressive strength evolution of reinforced SCC concretes as function as age

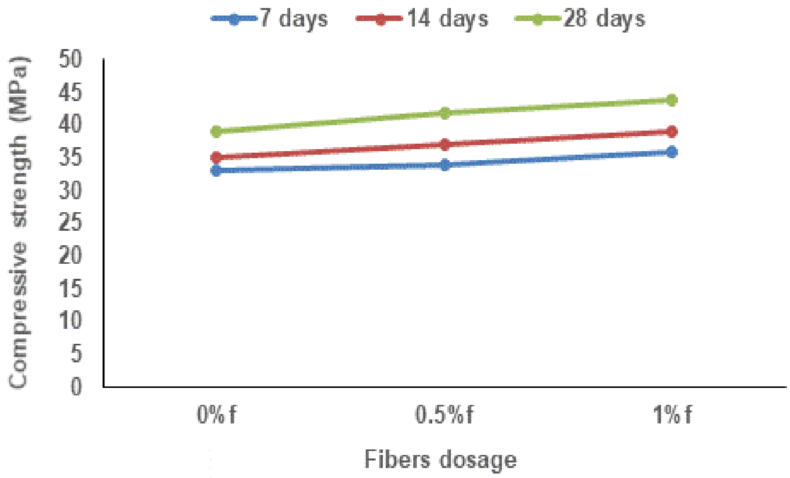

Figure 9. Compressive strength of reinforced SCC concretes as function as fibers dosage

The flexural strength was measured on 70 x70x280 mm^3 prismatic specimens at 7, 14 and 28 days old applying a three-point bending test, (Figure 7). Test results are reported in Figure 10 and 11.

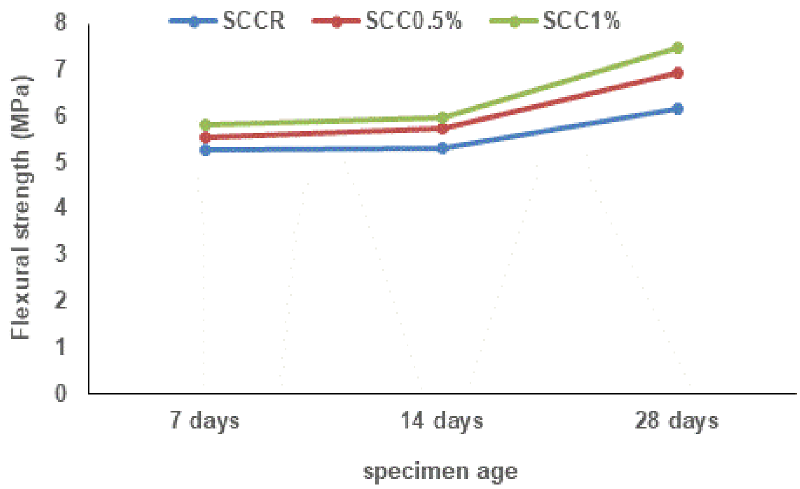

Figure 10. Flexural strength evolution of reinforced SCC concretes as function as age

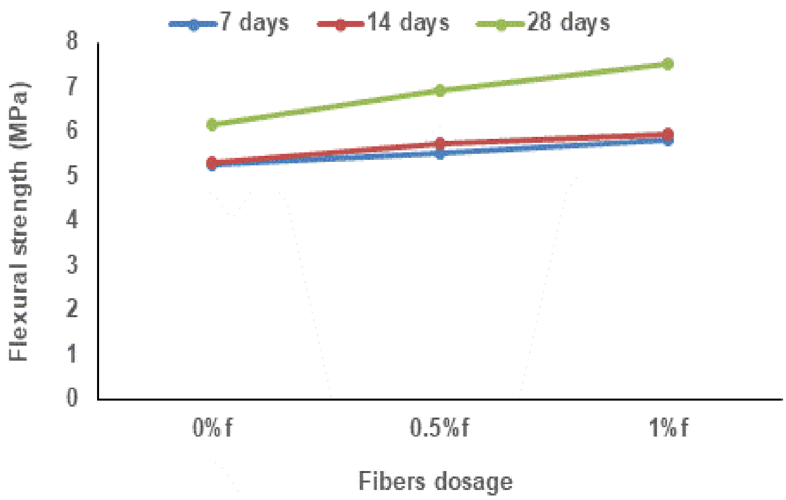

Figure 11. Flexural strength of reinforced SCC concretes as function as fibers dosage

A relationship between compressive strength and its flexural strength at 7, 14 and 28 days was obtained with a correlation coefficient R^2 of 0.9073 for all specimens (Figure 12). The analyses show an excellent linear relationship expressed by equation (1):

$$f_f = 4.7726 \text{ x } f_c + 9.0307 \qquad (1)$$

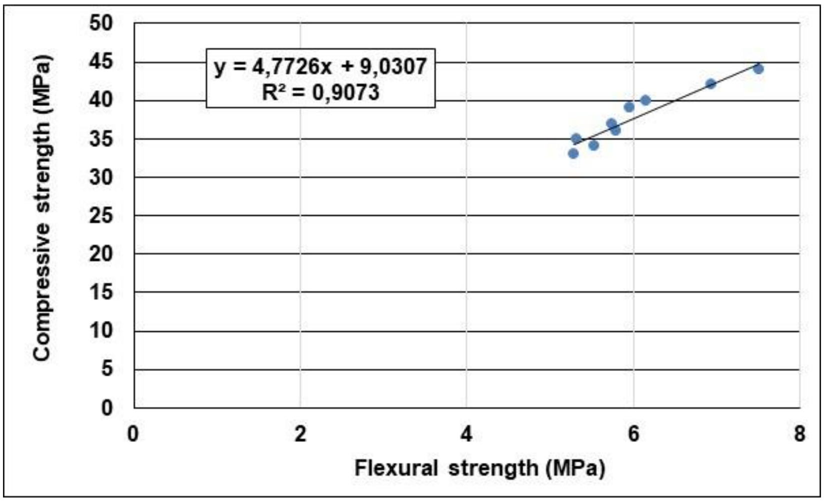

Figure 12. Relationship between flexural and compressive and flexural strength of SCC

Discussion

Properties of Fresh SCC Concretes

Bulk Density

Measurement of fresh bulk density determines the volume yield of the composition of fresh self-compacting concrete and makes it possible to verify the validity of the theoretical formulation. The results illustrated in Figure 3 showed that the bulk density values of the fiber-reinforced SCCs were practically the same compared to that of the control SCC without fibers. This is due to the weight of the fibers, which is considered low compared to the weight of the aggregates.

Workability Properties

To classify a concrete as self-compacting, the requirements for filling and passing ability as well as segregation resistance must follow the limitations specified by EFNARC. Indeed, the obtained results correspond to the criteria of the recommendations of EFNARC. The fresh properties are in the range of 65-72 cm for the slump flow, 0.81- 0.86 for the L-box ratio and 7.3% - 12.4% for the sieve stability. All concrete mixtures are considered as Self- compacting concretes (SCC).

The results of Figure 4 show that all SCC concretes have slump flow values located within the SCC range (60cm- 80cm). The coarse aggregates and fibers were distributed uniformly and no concentration of the latter could appear in the center of concretes. They were homogeneous. Nevertheless, a reduction of the slump flow values of fibered SCCs compared to the control concrete was marked. In addition, increasing the fiber dosage from 0.5% to 1% reduced spreading and therefore reduced flow capacity. This is due to the presence of fibers, which slightly slowed down the movement of SCC during its spreading due to its thickening. The reduction of slump flow is 5.6% for SCC0, 5% and 10% for SCC1%.

The SCC Mixes can be classified as SF1 slump flow class concrete except for SCC containing 1% of fibers, which is classified as SF2. The SF1 class is suitable for unarmed or weakly armed structures or for lining tunnels, piles and certain deep foundations. The SF2 class is suitable for ordinary applications such as walls and columns (Madandoust & Mousavi, 2012).

Moreover, for all SCC concretes, L-Bx ratio (the filling rate) was greater than 0.8 (Figure 5). This avoided the risk of blocking of concretes between the reinforcement and therefore their mobility in a confined environment was ensured. Indeed, results showed that All SCCs mixtures can be classified as PL2 (passing ability ≥ 0.80 with 3 rebars) regarding the NF EN 206-9 consistency classification (Badogiannis et al., 2005). These SCCs mixes are suitable for placing into formwork with more closely spaced and denser reinforcement (Liu, 2009). The greatest value of filling capacity recorded was at the level of the control SCC composition. This decreased slightly with the incorporation of fiber. As the fiber dosage increased from 0.5% to 1%, the filling capacity decreased. This means that the fibers have slightly weakened the flow through more or less dense reinforcement. This reduction is not significant because the fibers used are very short and fine. The reduction of L-Box is 3.5% for SCC0,5% and 6% for SCC1%. The results are consistent with what can be expected from self-compacting concrete. However, the most important in this test is that the tested concrete flows through the reinforcement correctly, which is directly related to workability.

The sieve stability test made it possible to calculate a segregation rate and to deduce whether the tested concrete has satisfactory stability or not. The results (Figure 6) of the sieve stability tests used to measure the ability of self-compacting concrete to resist static segregation show acceptable rates values for all compositions according to the EFNARC recommendations. Indeed, the segregation rates obtained are all less than 15% indicating satisfactory stability for all SCCs according to the acceptability criteria of a formulation of an SCC. None of the SCCs developed presented a risk of static segregation. According to the NF EN 206-9 standard (Afnor & EN, 206-9, 2010), all fiber SCCs mixtures under investigation can be categorized as sieve segregation class 2 (SR2) since all values of the segregation rate are less than 15% of the sample weight. In addition, the rate of fibered SCCs containing fibers did not exceed that of the control SCC. An improvement in stability was marked with the incorporation of fibers. It clearly appears that the high rate value recorded was at the level of the composition of the control SCC. The latter decreased with the incorporation of fiber. The lower the segregation rate, the greater the resistance to segregation, the more stable the SCC. When the fiber dosage increased, the resistance to segregation increased. Fiber SCCs are homogeneous and more stable than reference SCC. The good adhesion between cement paste and fibers explains this advantageous behavior. Compared to the segregation rate of the control SCC, the reduction is 26% for SCC0.5% and 41% for SCC1%.

In conclusion, results of the tests on the SCCs in the fresh state showed that since the slump flow of the tested concretes are greater than 60 cm, their passing rate in the L-box is greater than 80%, the segregation rate is less than 15 %, are stable, homogeneous and present no risk of segregation according to EFNARC criteria. It seems that 0.5% of fibers is the optimum rate for good fresh properties of SCC.

Properties of Hardened SCC Concretes

Compressive Strength

Figure 8 shows the evolution of compressive strength of SCCs with age. It is clearly shown that the compressive strength of all SCCs increased with age from 7d, 14d to 28d. Compared to the 7-day strength, the increase is 6%

at 14 days and 12% at 28 days for control SCC. It is 9% at 14 days and 15% at 28 days for SCC0.5%. It is 8% at 14 days and 14% at 28 days for SCC1%. Figure 9 shows that the compressive strengths of the fibered SCCs (SSC0.5% and SCC1%) exceed that of the control SCCR at all maturities. Indeed, compared to SCCR control, a slight increase of compressive strength was obtained. It is of the order of 3% and 9% at 7 days, 5% and 11% at 14 days and 28 days for SSC0.5% and SCC1% concretes respectively. The best formulation of fibered SCC concrete is that containing 1% of fibers from mechanical parts turning waste.

Flexural Strength

The results of the bending tests carried out on the different SCCs at 7, 14 and 28 days are ullustrated in Figure 10 and 11. It is clearly shown in Figure 10 that the strengths of all SCCs increased according to the age. Compared to the 7-day strength, the increase is 0.8% at 14 days and 16% at 28 days for control SCC. It is 4% at 14 days and 25% at 28 days for SCC0.5%. It is 3% at 14 days and 29% at 28 days for SCC1%. Moreover, Figure 11 shows the effect of fibers on the flexural strength. Indeed, the flexural strengths of the SCCs containing the fibers exceed those of the control SCCR without fibers at all ages. In addition, as the fiber dosage increases, the strength increases. SCC1% fibered with 1% presents a strength greater than that of SCC0.5% fibered with 0.5% as well as that the control SCCR. Compared to the SCCR strength, a gain of around 5% and 10% at 7 days, 8% and 12% at 14 days, 13% and 22% at 28 days was obtained for SCC0.5% and SCC1% respectively. The higher gain is that of SCC containing 1% filming waste fibers. This increase in flexural strength is attributed to the good adhesion between the fibers and the cement matrix as well as the strength of the used fibers. A relationship between compressive and flexural strength was obtained with a correlation coefficient R^2 for all specimens of 0.9073 (Figure 7). Analyses show a good linear relationship expressed by equation (1):

$$f_c = 4.7726 x f_f^{\,2} + 9.0307 \qquad (1)$$

Breaking Mode

Case of Control SCCR Concrete

According to Figure 12, the failure of the control SCC concrete is considered fragile, when the strength limit is reached, we observed a sudden rupture of the specimen which breaks and divides into two parts, this is explained by the low strength of SCCR alone to the tensile forces developed in the tense zone of the flexed element.

Figure12. Fragile failure at mid-span of the control SCCR specimen

Case of Fiberized SCC

The mode of failure observed on the fiber-reinforced concrete specimens is different to that of the control SCC (Figure 13). There are appearance of micro cracks and a major crack in the body of the SCC without it dividing into two parts. This is the ductile failure mode due to the presence of fibers, whose role is to sew the micro cracks and stop the rapid development of the opening of the master crack. Finally, we can say that the fibers work to increase the flexural strength and their presence is a barrier, which counteracts and resists external pressures.

Figure 13. Fragile failure at mid-span of fiberized SCC specimen

Conclusion

According to the results obtained in this work on using recycled steel fibers obtained from waste of the turning operation in SCCs self-compacting concretes, the following conclusions could be drawn:

- The Japanese method made it possible to provide a better SCC concrete composition whose properties in the fresh and hardened state are satisfactory.
- From a workability point of view, results of the tests on all concretes with and without fibers showed that the fresh properties are in the range of 65-72 cm for the slump flow, 0.81- 0.86 greater than 80% for the passing ability in L-box and 7.3% - 12.4% less than 15 % for the segregation rate from sieve stability. All concrete mixtures were considered as Self- compacting concretes (SCCs). These concretes are stable, homogeneous and present no risk of segregation according to EFNARC criteria. It seems that 0.5% of fibers is the optimum rate for good fresh properties of SCC.
- The incorporation of fibers into the SCC made it possible to increase its compressive strength by a maximum of 14% at 28 days and its flexural strength by 22% with 1% fibers. The latter made it possible to gain plasticity, delay cracking, reduce the width of the cracks and avoid sudden rupture of the specimens.
- Good linear relationship was obtained between the compressive strength and flexural strength with a correlation coefficient R^2 of 0.9073 for all specimens.
- Concerning breaking mode, the failure of the control SCC concrete is considered fragile, when the strength limit is reached, we observed a sudden rupture of the specimen, which breaks and divides into two parts. The mode of failure observed on the fiber-reinforced concrete specimens is different to that of the control SCC. There are appearance of micro cracks and a major crack in the body of the SCC without it dividing into two parts. This is the ductile failure mode due to the presence of fibers, whose role is to sew the micro cracks and stop the rapid development of the opening of the master crack.
- The possibility of using recycled steel fibers obtained from waste of the turning operation in self-compacting concretes SCCs allow to contribute in a fairly humble way to the valorization of the latter at low cost, to the national economy and can also mitigate environmental problems. In conclusion, the turning waste offers a new source of fiber supply and can replace steel fibers.

Scientific Ethics Declaration

The authors declare that the scientific ethical and legal responsibility of this article published in EPSTEM Journal belongs to the authors.

Acknowledgements or Notes

* This article was presented as an oral presentation at the International Conference on Technology, Engineering and Science (www.icontes.net) held in Antalya/Turkey on November 14-17, 2024.

References

Afnor. (Ed.). (2010.) *NF EN 206-9 : Béton – partie 9 : Règles complémentaires pour le béton auto – plaçant* (p.28). Paris, France : Afnor.

Ahmad, J., Zhou, Z., & Deifalla, A. F. (2023). Steel fiber reinforced self-compacting concrete: A comprehensive review. *International Journal of Concrete Structures and Materials*, *17*(1), 51.

Alabduljabbar, H., Alyousef, R., Alrshoudi, F., Alaskar, A., & Fathi, A., & Mohamed, A. M. (2019). Mechanical effect of steel fiber on the cement replacement materials of self-compacting concrete. *Fibers*, *7*(4), 36.

Ali, I. F., Abdulridha, A. A., & Abbas, S. A. (2020b). Behavior and strength properties of steel fiber reinforced self-compacting concrete columns. *Journal of Engineering Science and Technology*, *15*(5), 3204–3217.

Badogiannis, E., Kakali, G., Dimopoulou, G., Chaniotakis, E., & Tsivilisa, S. (2005). Metakaolin as a main cement constituent. Exploitation of poor Greek kaolins. *Cement and Concrete Composites*, *27*(2), 197–203.

EFNARC. (2005). *European guidelines for self-compacting concrete: specification, production and use, self-compacting concrete.* Retrieved from https://www.theconcreteinitiative.eu.pdf

Geng, H., Ding, X., Hao, Du., Shi, J., Li, C., & Li, X. (2022). Application of self-compacting steel fiber reinforced concrete for pervious frames used for river revetment. *Applied Sciences*, *12(*20), 10457.

Haddadou, N., Boulkhiout, M., Mansour, S.M., Chaid, R., & Ghernouti, Y. (2021). The effect of steel fiber size on the properties of fresh and hardened self-compacting concrete incorporating marble powder. *SSP Journal*, 16(1), 23-34.

Liu, M. (2009). *Wider application of additions in self-compacting concrete*. (Doctoral dissertation, University College London, UK).

Madandoust, R., & Mousavi, S.Y. (2012). Fresh and hardened properties of self-compacting concrete containing metakaolin. *Construction and Building Materials*, *35*, 752–760.

Mansour, S. M. (2020). Physical-mechanical properties of steel fiber- reinforced self-compacting concrete containing natural perlite addition. *International Journal of Microstructure and Materials Properties*, *15*(2).

Mansour, S. M. (2021). New generation of fiber self-compacting concrete based on pyrophyllite. *Emerging Materials Research*, *10*(2), 1-12.

Mansour, S. M. (2021). Use of natural pyrophyllite as cement substitution in ultra performance polypropylene fiber concrete. *International Journal of Engineering Research in Africa*, *56*, 123-135.

NF EN 12350-10. (2010). *Essai pour béton frais – partie 10 : Béton autoplaçant – Essai à la boite en L.* Paris, France : Afnor.

NF EN 12350-11. (2010). *Essai pour béton frais – partie 11 : Eton autoplaçant – Essai de stabilité au tamis.* Paris, France: Afnor.

NF EN 12350-6. (2012). *Essais pour béton frais – Partie 6 : Masse volumique*. Paris, France: Afnor.

NF EN 12350-8. (2010). *Essai pour béton frais – Partie 8 : Béton autoplaçant – Essai d'étalement au cône d'Abrams*. Paris, France: Afnor.

NF EN 12390-2. (2012). *Essais pour béton durci – partie 2 : Confection et conservation des éprouvettes pour essais de résistance*. Paris, France: Afnor.

NF EN 12390-3. (2012). *Essais pour béton durci – partie 3 : Résistance à la compression des éprouvettes*. Paris, France: Afnor.

NF EN 12390-5. (2012). *Essais pour béton durci – partie 5 : Résistance à la flexion sur éprouvettes*. Paris, France: Afnor.

Okamura, H., & Ozawa, K. (1994). Self- compacting high performance concrete in Japan. *International Workshop on High Performance Concrete*, 31–44.

Author Information

Sabria Malika Mansour
M'Hamed Bougara University
Avenue de l'Indépendance, 35 000 Boumerdès – Algeria
Contact e-mail: *s.mansour@univ-boumerdes.dz*

Youcef Ghernouti
M'Hamed Bougara University
Avenue de l'Indépendance, 35 000 Boumerdès – Algeria

Bahia Rabehi
M'Hamed Bougara University
Avenue de l'Indépendance, 35 000 Boumerdès – Algeria

To cite this article:

Mansour, S.M., Ghernouti, Y., & Rabehi, B., (2024). Fresh and hardened properties of self-compacting concrete reinforced with recycled steel fibers from mechanical parts turning waste. *The Eurasia Proceedings of Science, Technology, Engineering & Mathematics (EPSTEM)*, *32*, 1-11.

The Eurasia Proceedings of Science, Technology, Engineering & Mathematics (EPSTEM)
ISSN: 2602-3199

The Eurasia Proceedings of Science, Technology, Engineering & Mathematics (EPSTEM), 2024

Volume 32, Pages 12-18

IConTES 2024: International Conference on Technology, Engineering and Science

Electrical Innovations in Electrocoagulation: Designing and Testing Prototypes for Sustainable Water Treatment

Latroch Maamar
Hassiba Benbouali University of Chlef

Aissa Bokhtachte Aicha
Hassiba Benbouali University of Chlef

Badni Nadia
Hassiba Benbouali University of Chlef

Abstract: Electrocoagulation is emerging as a sustainable solution for water treatment, despite higher energy consumption compared to traditional biological methods. Its advantages include shorter treatment times and the absence of chemical additives. Particularly suitable for arid regions facing water scarcity, this method promotes water conservation and reuse. Our research highlights an innovative prototype featuring an electrical generator designed to optimize the coagulation process and enhance overall treatment efficiency. Through comprehensive experimental testing, we demonstrate the reliability and effectiveness of this system for treating industrial wastewater, paving the way for broader adoption in industries committed to sustainability and responsible water resource management.

Keywords: Electrocoagulation, Water treatment, Prototype design, Chemical-free treatment, Industrial water reuse

Introduction

Electrocoagulation is a water treatment method that uses electrical currents to generate ions from metal electrodes, such as aluminum or iron, which neutralize and remove contaminants like heavy metals, oils, and suspended particles. It is recognized for its cost efficiency, environmental benefits, and adaptability, making it suitable for industrial wastewater, sewage, and drinking water treatment (Mollah, 2001; Vasudevan, 2014; Kobya, 2003).

Recent advancements have demonstrated its effectiveness against emerging pollutants like microplastics and pharmaceuticals, while innovations in electrode materials aim to enhance contaminant removal and reduce energy consumption (Rajala et al., 2020). Studies also highlight the potential of low-voltage systems to maintain efficiency while lowering energy use, a critical factor for sustainable, large-scale applications (Karimifard & Moghaddam, 2018; Xie et al., 2021). Additionally, adaptive power supply systems have proven beneficial in industrial applications, such as textile wastewater treatment (Chen, 2004; Kobya et al., 2018).

Efficient power systems allow immediate reuse of treated water, conserving resources and supporting operational efficiency. These systems also reduce energy costs while meeting water quality standards, making them valuable in industrial settings (Karimifard & Moghaddam, 2018; Xie, Zhang, & Ji, 2021). This paper examines the power supply system in electrocoagulation plants, detailing the system's design, implementation, and experimental results to optimize energy use and treatment efficiency.

- Selection and peer-review under responsibility of the Organizing Committee of the Conference

Overview of the Electrocoagulation Plant

This section provides an overview of the critical components and operational principles of an electrocoagulation plant, a wastewater treatment technology that removes contaminants by applying electrical currents to metal electrodes, typically aluminum or iron. The electrocoagulation system's key components include the reaction chamber, where the treatment process takes place. The chamber's design—specifically its dimensions and hydraulic retention time—plays a pivotal role in treatment efficiency, as optimized flow patterns promote effective interactions between pollutants and charged ions (Xie et al., 2021). Furthermore, the selection and arrangement of electrode materials are vital, as they directly influence ion release and pollutant removal efficiency. Proper spacing and sufficient electrode surface area are essential to enhancing electrochemical reactions while minimizing energy consumption (Karimifard & Moghaddam, 2018).

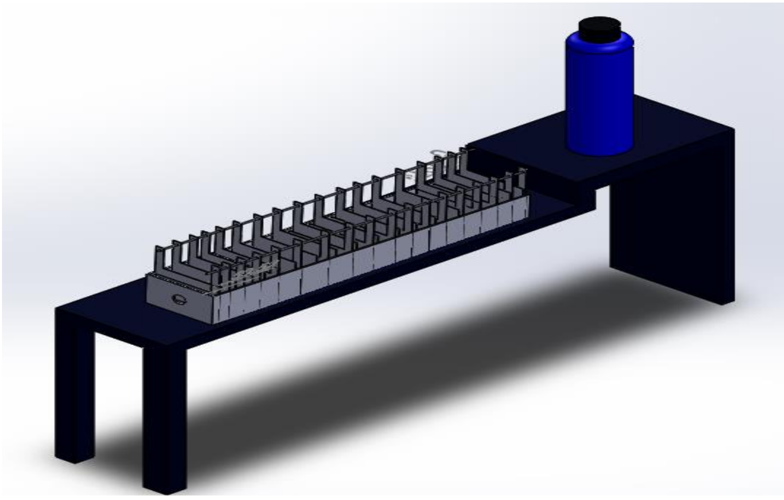
Figure 1. Water treatment using electrocoagulation process.

Generator Location in the Process, Chambers` Design

Figure 1 illustrates the key chambers and functions of the electrocoagulation plant in our prototype. The central reaction chamber treats unsuitable water through electrocoagulation, where a stack of 14 iron electrodes (7 anodes and 7 cathodes), each measuring 18 cm x 30 cm with a 2 mm thickness, is powered by a high-current supply. These electrodes, arranged with a 2 cm spacing in a single-phase parallel configuration, ensure uniform current distribution, reduced resistance, and energy-efficient operation.

Following the reaction chamber, a sludge removal chamber uses a conveyor belt with scrapers to collect floating sludge, directing it to a hopper for further treatment and preventing interference with sedimentation. The final sedimentation chamber separates clean water from heavier solids, which settle at the bottom and are directed to a basin with specialized filters. Filtered water is either pumped back for reuse or further disinfected via ozonation or chlorination before distribution or safe discharge into the environment. The prototype's design optimizes pollutant removal while minimizing energy consumption and ensuring water quality for reuse or environmental release.

Design of Power Supply for Electrocoagulation Water Treatment

The power supply is a critical component of the electrocoagulation (EC) system, requiring customization to meet the specific operational requirements of the electrocoagulation process. Below, we outline the key considerations and design features essential for creating an efficient power supply for electrocoagulation water treatment.

Voltage and Current Requirements

The electrocoagulation process relies on a specific voltage and current to create the electric field between electrodes. An adjustable voltage supply, typically ranging from 10 to 100 volts, is essential to optimize coagulation based on water quality and contaminants. Additionally, a constant current mode ensures operational stability and prevents electrode overheating, enhancing system efficiency and durability.

Power Supply Type

Electrocoagulation systems typically use DC power supplies, with some advanced designs employing pulsed power to enhance floc formation and reduce electrode fouling (Khan, 2016). An efficient control system is crucial for optimizing power supply parameters. Modern setups often feature microcontroller integration for real-time monitoring and adjustments of voltage, current, and temperature. User-friendly interfaces further enable operators to manage settings, monitor performance, and receive alerts for potential issues.

Safety Features

Safety is a critical consideration in the design of power supplies for electrocoagulation systems. To ensure reliability and protection, several key features should be incorporated. First, overcurrent protection is essential; the inclusion of circuit breakers or fuses can safeguard the system against excessive current, thereby preventing potential damage. Second, effective temperature monitoring is vital; thermal sensors can automatically shut down the power supply when critical temperature thresholds are exceeded, thus averting overheating incidents. Furthermore, galvanic isolation plays a crucial role in protecting human operators by preventing direct electrical connections. This can be achieved through the use of isolation devices such as transformers and optoisolators, which enhance safety by shielding equipment from voltage spikes and ensuring stable control signals. Typically, switching power supplies are employed to convert alternating current (AC) into direct current (DC) efficiently, thereby contributing to a reliable and secure operational environment for electrocoagulation systems.

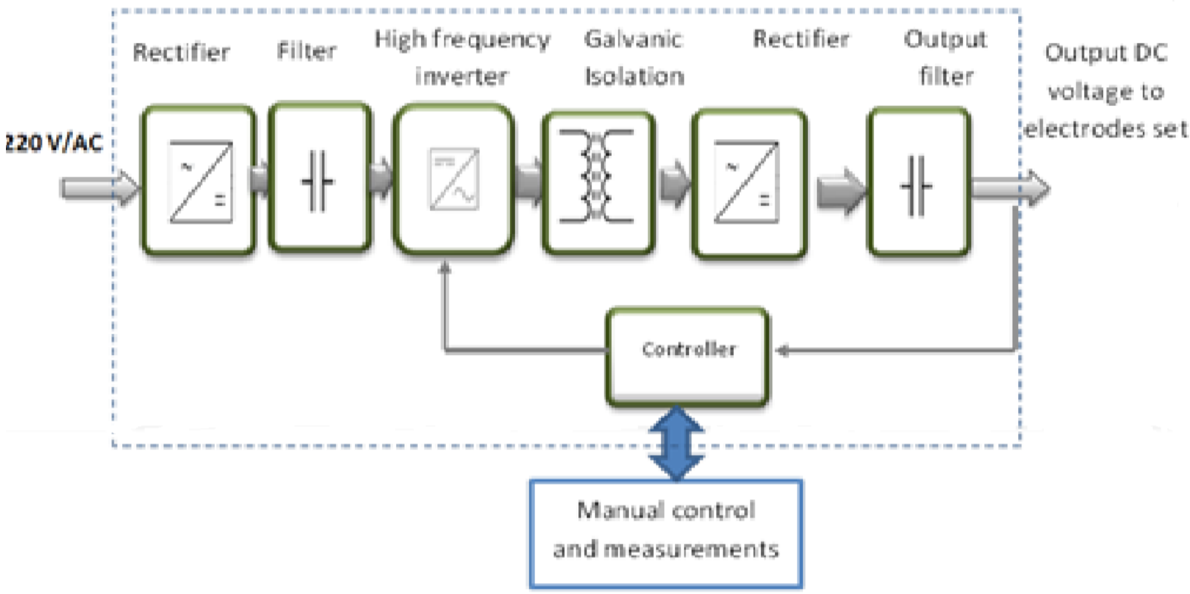

Figure 2. Main stages of the generator used in the electrocoagulation process

Figure 2 provides a detailed overview of the key stages involved in the power supply system discussed in this paper. At the initial stage, a rectifier is installed to convert the incoming alternating current (AC) into direct current (DC). Following the rectification process, a filter is employed to smooth out the DC output, significantly reducing voltage fluctuations and enhancing electromagnetic compatibility. This smoothing effect is crucial for maintaining stable operation in sensitive electronic systems and minimizing electromagnetic interference.

The next critical stage involves an inverter, which takes the smoothed DC output and converts it into high-frequency AC voltage. This conversion is achieved through pulse-width modulation (PWM), a technique that enables precise control over the output voltage level. The PWM signal is generated by a feedback controller, which plays a pivotal role in monitoring system performance. This controller continuously collects data on the output voltage and the current flowing to the electrodes, comparing these measurements to the desired values. By doing so, the controller regulates the power output, ensuring compliance with the optimal electrocoagulation requirements that have been established through prior studies. Once the high-frequency AC voltage is generated, it is transformed to a lower voltage level using a galvanic transformer. This step is vital not only for ensuring the output is suitable for further processing but also for enhancing safety. The transformer provides isolation on the output side, protecting users from electrical hazards while working with the system. Subsequently, the output rectifier converts the transformed AC voltage back into DC. This rectified output is then passed through an output filter, which further smooth and stabilizes the voltage and current. The filtered DC is then delivered to the electrodes that are submerged in the water to be treated. This final stage is crucial, as it allows for the effective electrocoagulation process to take place, utilizing the regulated DC current and voltage to achieve the desired treatment outcomes. Through these meticulously designed stages, the power supply system ensures reliable and efficient operation tailored to the specific requirements of electrocoagulation. (Smith, 2023).

In the following section, we will present the prototype developed as part of this study. This section will include a detailed description of the prototype's design and key features, highlighting its capabilities to meet the requirements of the electrocoagulation process. Additionally, we will discuss the results obtained from testing the prototype, including performance metrics, efficiency analyses, and any challenges encountered during the testing phase. This comprehensive examination will provide insights into how effectively the prototype meets the intended objectives and will lay the groundwork for further exploration and potential improvements in future work.

Prototype and Test Results

Implementation of the DC Generator

The switching power supply has been designed as a full bridge, following the schematic illustrated below. This design choice is based on the specific requirements outlined in our specifications.

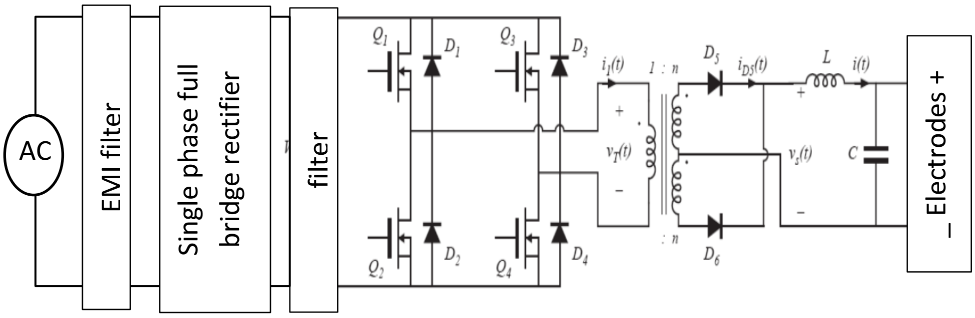

Figure 3. Switched-mode power supply (SMPS) specifically adapted for real-time electrocoagulation in water treatment applications used in the present prototype design.

Figure 3 shows the schematic of a switched-mode power supply (SMPS) specifically adapted for real-time electrocoagulation in large scale water treatment applications. The schematic begins with an EMI filter, designed to reduce electromagnetic interference, ensuring compliance with EMC standards critical in online systems. Next, a single-phase full-bridge rectifier converts the incoming AC to pulsating DC using four diodes configured in a bridge arrangement.

Following the rectifier, a DC filter smooths this pulsating DC through a capacitor, resulting in a stable DC voltage. This stable DC is then input to a high-frequency inverter, where it is rapidly switched using MOSFETS, producing a high-frequency AC waveform. This high-frequency switching enables the use of a more compact high-frequency transformer, which provides both galvanic isolation for user protection and the ability to adjust the voltage up or down as required for the electrocoagulation process.

On the secondary side of the transformer, a half-bridge rectifier converts the high-frequency AC back into DC using two fast diodes. Finally, a DC output filter, comprising capacitors and inductors, smooths the rectified signal to ensure a stable DC output for the electrocoagulation electrodes. Each stage in Figure 3 is essential for achieving efficient AC-to-DC conversion, delivering clean, stable power required for real-time electrocoagulation water treatment. The design of the power supply for electrocoagulation water treatment is critical to the effectiveness and efficiency of the process. As water treatment needs evolve, continued advancements in power supply technology will play a significant role in optimizing electrocoagulation processes for sustainable water management. The following specifications are required for sizing the generator operating in continuous conduction mode (CCM):

- Input Voltage Range: $\mathrm{Vemin} = 180\ \mathrm{V}, \mathrm{Vemax} = 265\ \mathrm{V}$,
- Nominal Output Voltage Range: $\mathrm{Vsmin} = 6.2$, $\mathrm{Vemax} = 26\ \mathrm{V}$.
- Output Current Adjustment Range: $\mathrm{Ismin} = 0\ \mathrm{A}, \mathrm{I\ smax} = 200\ \mathrm{A}$;
- Switching Frequency: $\mathrm{f} = 50$ KHz.

Figure 3 shows the experimental setup of the power supply, installed to test the prototype under real operating conditions. This setup allows us to monitor input voltage stability, output regulation, and efficiency at different load levels, verifying the power supply's performance and readiness for full-scale application. In this paper, the current power supply operates in open-loop control for the electrocoagulation treatment; only the desired current can be regulated in closed-loop control.

Test and Result

Experimental Procedure and Performance Evaluation of the Electrocoagulation System

Figure 4. Final prototype including the generator

Figure 4 shows the final prototype used in the experimental tests. Testing and verifying the performance of the electrocoagulation system is essential to assess the efficiency and reliability of the integrated generator. This section describes the tests conducted to validate the system's functionality. Three specific tests were performed:

Electrocoagulation Test of Methylene Blue

The first test focused on the electrocoagulation of methylene blue using varying current values. Methylene blue was chosen as a model substance to assess the process's effectiveness, with the goal of determining the optimal current value for efficient coagulation. Key parameters such as methylene blue decolorization, coagulation time, and flocculation efficiency were evaluated to identify the most effective current setting in this specific context. Three trials were conducted under different conditions to assess the process's performance. The results for each trial are presented in the following figures 5.

The electrocoagulation wastewater treatment experiment, focusing on the removal of methyl blue dye, demonstrated promising results at a fixed water flow rate of 2 L/min from the inlet to the outlet. Across the tested samples at varying current levels of 5A, 10A, and 15A, an improvement in dye removal efficiency was observed with increasing current. The most significant enhancement occurred when increasing the current from 5A to 10A, indicating effective coagulation and flocculation processes at this level. However, the transition from 10A to 15A yielded only marginal improvements in dye removal efficiency, suggesting a potential point of diminishing returns at higher currents.

While the overall treatment performance continued to improve, raising the current to 15A resulted in a noticeable increase in water temperature. This thermal effect may impact the stability of the treatment process and the potential degradation of organic compounds. Additionally, the electrolysis process intensified with higher current, as evidenced by the increased formation of bubbles. This enhanced gas evolution can contribute to better mixing and stirring of the wastewater, potentially improving the coagulation process.

In summary, the electrocoagulation method shows effective potential for treating wastewater containing methyl blue dye, particularly at lower currents and under a fixed flow rate of 2 L/min. However, careful consideration must be given to operational parameters, as increasing current may lead to thermal concerns and diminishing returns in treatment efficiency beyond a certain point. Future studies should focus on optimizing current settings and flow rates to balance treatment effectiveness with operational efficiency and safety.

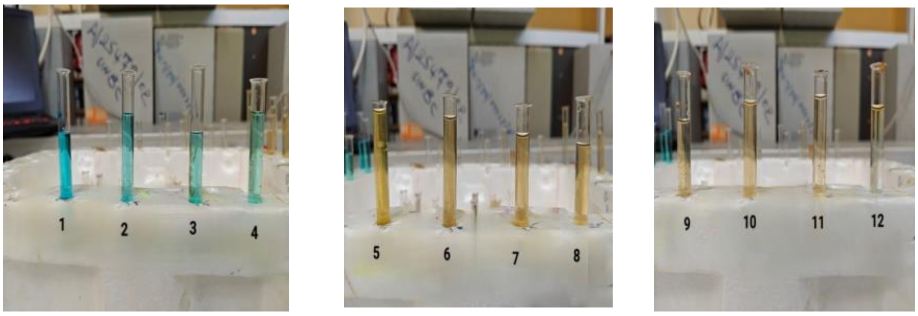

(a) (b) (c)

Figure 5. Electrocoagulation Treatment of Methylene Blue Solution at Varying Current Levels with a Fixed Flow Rate of 2 L/min

Note: a) Post treatment with supplying current I=5A b) Post treatment with supplying current I=10A c) Post treatment with supplying current I=15A

Conclusion

This paper explores the development and testing of a generator prototype aimed at supporting large-scale electrocoagulation for sustainable water treatment. The study highlights how electrical innovations can provide the power needed to enhance contaminant removal efficiency, showing promise for scaling electrocoagulation systems. The results emphasize the importance of design improvements in achieving both scalability and effectiveness in water treatment technologies. The findings suggest that electrical advancements can overcome limitations of traditional electrocoagulation, particularly for larger or more complex wastewater treatments. However, further research is needed to optimize the prototype under varying wastewater compositions and operational conditions for broader real-world applications.

In conclusion, this study demonstrates that scalable electrical innovations can play a critical role in advancing sustainable water treatment technologies, offering a strong foundation for future developments in improving global water quality and wastewater management.

References

Alimi, O. S. (2018). Challenges and perspectives on the development of electrocoagulation for sustainable wastewater treatment. *Journal of Cleaner Production, 172,* 2557-2575.

Cao, S., Wang, S., Zhao, Y., Wang, L., Ma, Y., Schäffer, A., & Ji, R. (2020). Fate of bisphenol S (BPS) and characterization of non-extractable residues in soil: Insights into persistence of BPS. *Environment International*, *143*, 105908.

Chen, G. (2004). Electrochemical technologies in wastewater treatment. *Separation and Purification Technology, 38*(1), 11-41.

Karimifard, S., & Moghaddam, M. R. A. (2018). Application of response surface methodology in physicochemical removal of contaminants by electrocoagulation: A review. *Chemical Engineering Research and Design, 123,* 1-19.

Khan, M. I. (2016). Design considerations for electrocoagulation systems. *Water Research, 104,* 1-12.

Kobya, M., Can, O. T., & Bayramoglu, M. (2003). Treatment of textile wastewaters by electrocoagulation using iron and aluminum electrodes. *Journal of Hazardous Materials, 100*(1-3), 163–178.

Kobya, M., Ulu, F., & Gebologlu, U. (2018). Treatment of textile wastewater by electrocoagulation enhanced with chemical oxidation processes. *Environmental Technology, 39*(22), 2887-2895.

Mollah, M. Y. A., Schennach, R., Parga, J. R., & Cocke, D. L. (2001). Electrocoagulation (EC)—science and applications. *Journal of Hazardous Materials, 84*(1), 29-41.

Smith, J., & Doe, A. (2023). Optimizing power supply systems for electrocoagulation applications. *Journal of Environnemental Engineering, 45*(3), 123-135.

Vasudevan, S. (2014). Prospective of electrocoagulation process in wastewater treatment: A review. *Environmental Science: Water Research & Technology, 1*(1), 58-67.

Xie, Y., Zhang, C., & Ji, L. (2021). Effect of electrical current and electrode material on sludge formation in electrocoagulation. *Environmental Science and Pollution Research, 28*(16), 19971–19980.

Author Information

Latroch Maamar
Hassiba Benbouali University of Chlef,
(LGEER) laboratoy
BP 151 Hai Essalam 02000 Chlef, Algeria
Contact e-mail: *m.latroch@univ-chlef.dz*

Aissa Bokhtachte Aicha
Hassiba Benbouali University of Chlef,
(LGEER) laboratoy
BP 151 Hai Essalam 02000 Chlef, Algeria.

Badni Nadia
Hassiba Benbouali University of Chlef,
CRAPC research center Bousmail.
BP 151 Hai Essalam 02000 Chlef, Algeria

To cite this article:

Maamar, L., Aicha, A. B., & Nadia,.B. (2024). Electrical innovations in electrocoagulation: Designing and testing prototypes for sustainable water treatment. *The Eurasia Proceedings of Science, Technology, Engineering & Mathematics (EPSTEM), 32*, 12-18.

The Eurasia Proceedings of Science, Technology, Engineering & Mathematics (EPSTEM)
ISSN: 2602-3199

The Eurasia Proceedings of Science, Technology, Engineering & Mathematics (EPSTEM), 2024

Volume 32, Pages 19-24

IConTES 2024: International Conference on Technology, Engineering and Science

Computer Modeling and Study of the Influence of Pre-Heat Treatment and Radial-Shear Rolling on the Evolution of the Structure of 5KHV2S Steel

Andrey Tolkushkin
Rudny Industrial University

Pavel Tsyba
Rudny Industrial University

Andrey Marukov
Rudny Industrial University

Abdrakhman Naizabekov
Innovative University of Eurasia

Yevgeniy Panin
Karaganda Industrial University

Alexandr Arbuz
AEO Nazarbayev University

Abstract: An increase in the properties of various metals and alloys can be achieved by refining their microstructure using intensive plastic deformation and/or various heat treatment modes. Currently, a few studies have been conducted to identify the effect of radial shear rolling on the evolution of the microstructure and changes in the mechanical properties of bars made of various ferrous and non-ferrous metals and alloys. This paper is devoted to the study of the influence of various modes of pre-heat treatment of 5KHV2S steel on the evolution of its microstructure during subsequent radial-shear rolling using computer modeling in the DEFORM software package. The conducted studies have shown that under the selected modes of pre-heat treatment, although the initial grain size increased, the subsequent radial-shear rolling allowed the sludge to obtain a gradient fine-grained structure in 5KHV2S steel.

Keywords: Computer modeling, Pre-heat treatment, Radial shear rolling, Microstructure, Grain size

Introduction

It has long been proven that the development and application in practice of new methods for controlling the structural and phase state of traditional structural metal materials, even without changing their chemical composition, can improve their mechanical and functional properties. One of the main ways to increase the level of properties of various metals and alloys by refining their microstructure is severe plastic deformation, implemented during various methods of metal forming (Naizabekov et al., 2005; Puspasari et al., 2024; Volokitin et al., 2021; Grabovetskaya et al., 2022; Sidelnikov et al., 2024; Lezhnev et al., 2017), and heat treatment (both preliminary and final). Combining these two technologies into a single technological scheme should make it possible to intensify the process of grain refinement of the structure (Naizabekov et al., 2024).

The technology of radial shear rolling has been successfully applied for more than 25 years. Many scientific papers have proved that this method of deformation is one of the main methods of gradient modification of long products made of ferrous and non-ferrous metals and alloys. Only a small part of the papers (Gamin et al., 2020; Mishin et al., 2020; Akopyan et al., 2022; Patrin et al., 2020) is devoted to the study of the effect of radial-shear rolling on the evolution of the microstructure and changes in the properties of various ferrous and non-ferrous metals and alloys. However, there are not so many works devoted to the direct study of the effect of radial-shear rolling on changes in the structure and properties of tool alloy steels. The aim of this work is computer modeling and study of the influence of various modes of pre-heat treatment of 5KHV2S steel on the evolution of its microstructure during subsequent radial-shear rolling.

Method

To perform computer modeling of the processes of pre-heat treatment (PHT) and subsequent radial-shear rolling (RSR) of samples made of 5KHV2S steel, it was decided to use the cellular automata mechanism [13] version 2.0, implemented in the Deform v. 13 system. This mechanism allows not only modeling grain size changes, but also predicting its shape during deformation or heat treatment. Since after preliminary heat treatment steel 5KHV2S will be subjected to several passes at the radial shear rolling mill RSP 10-30 of Karaganda Industrial University, a rod of circular cross-section with a diameter of 30 mm and a length of 150 mm was set as the initial blank. For 5KHV2S steel, the following PHT modes were selected:

- heating up to 880°C, exposure time for 35 minutes, cooling with a furnace (annealing № 1);
- heating up to 880°C, exposure time 35 minutes, air cooling (annealing № 2).

To create a model of microstructure evolution during pre-heat treatment, only static recrystallization should be used. The key parameters of the cellular automata algorithm are input of model constants, whose values depend on the nature of the material. For most steels, the suitable values of the Cellular Automata 2.0 model constants are considered in (Azarbarmas, 2020; Kugler et al., 2004). Table 1 shows the values of these constants.

Table 1. Constants of the Cellular Automata 2.0 model

Material	G, N/^{m2}	b, m	γ, J/^{m2}	δD_{0b}, м^{m3}/ s	Q_b, kJ/mol	$A1_1$	n_1	Q_{def}, kJ/mol
Steel	4,21×10-1^{-10}	2,56×10-10^{-10}	0,625	7,5,5×10-1^{-15}	110	2,0,0×10^{44}	7,6,6	275

Results and Discussion

The essence of calculating the evolution of the microstructure by this method is reduced to using a ready-made, calculated model. At the selected points, calculation windows with a certain resolution are set, in which both the grain size and shape change is observed. Considering that the initial grain size was set to 55.0 microns, it was decided to choose a square window with a face size of 200 microns, so that it would be possible to track the full sizes of several grains before and after the PHT.

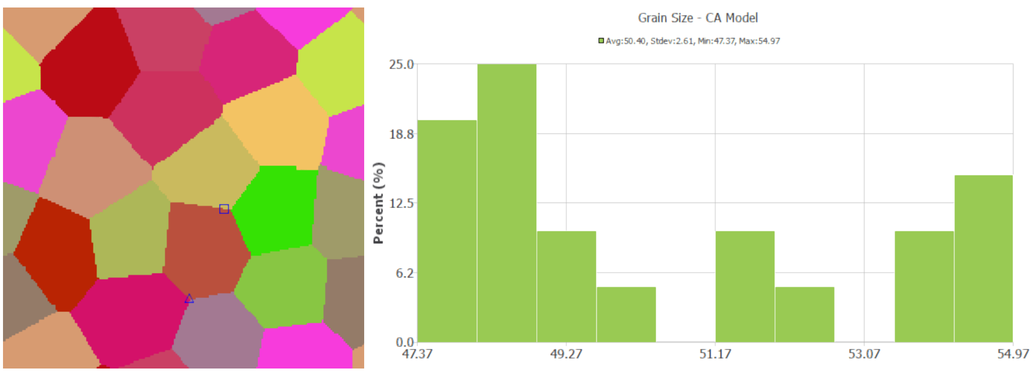

Figure 1. Initial structure

After two different PHT tests, the following results were obtained (Figure 2).

a)
b)
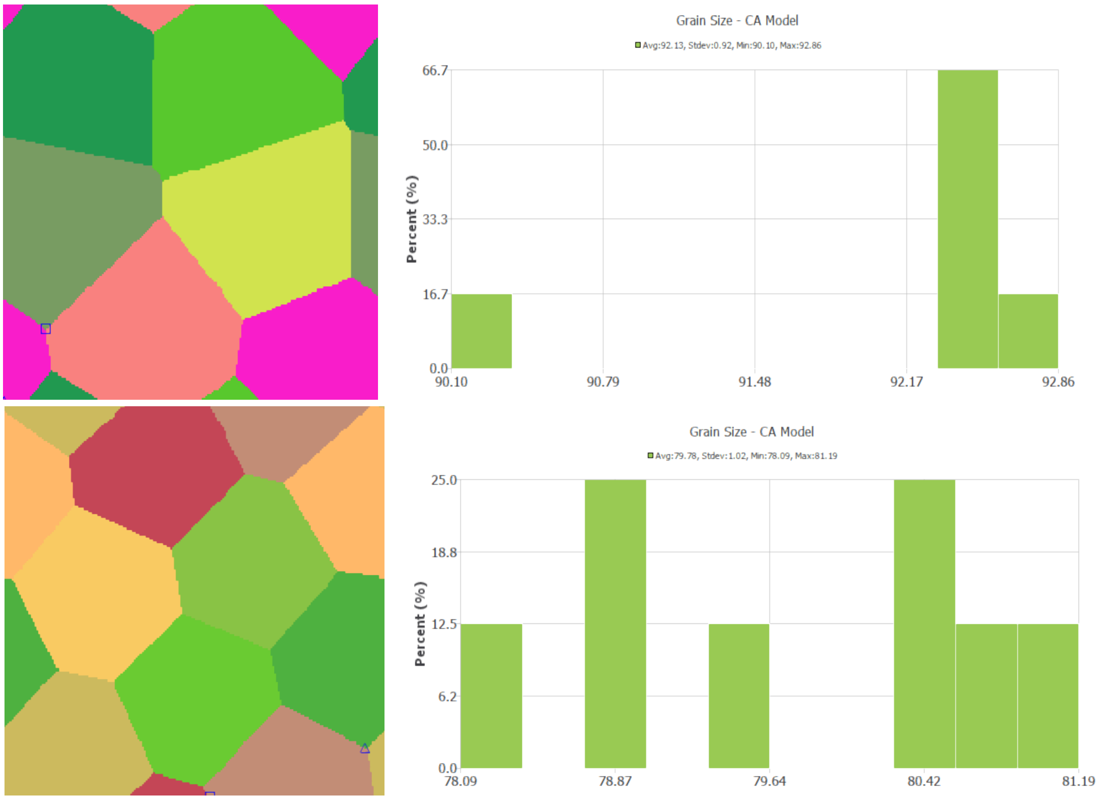

Figure 2. Structure of 5KHV2S steel after various technical tests:
a - after annealing № 1 b - after annealing № 2

After annealing № 1, the initial grain size of 5.0 microns increased to about 92 microns, while after annealing № 2, the initial grain size increased to about 80 microns. Based on the results obtained, it can be concluded that the most effective mode of PHT of the two selected ones is annealing № 2, which is heating to 880°C, holding for 35 minutes and then cooling in air.

When modeling the process of radial-shear rolling at the RSR 10-30 mill and studying the evolution of the structure, as already noted above, a billet with a diameter of 3.0 mm and a length of 150 mm was adopted. The deformation cycle consisted of 6 passes with a compression of 3 mm in each pass. The structure was studied after 3 passes, when the diameter of the resulting bar was 2.1 mm, and after all 6 passes, i.e., when the bar diameter was 12 mm. The structure obtained earlier after annealing № 2 was chosen as the initial state of the billet, since this mode allowed us to obtain a finer-grained initial structure. The roll rotation speed of 100 rpm was chosen as the speed characteristic. As a temperature characteristic, the heating temperature of the billet before rolling was chosen to be 1000°C.

It was decided to consider the microstructure in the longitudinal direction, since this approach gives a complete picture of the change in grain shape over the entire cross-section of the billet during radial shear rolling. To study the structure, two points were considered: in the axial zone and in the surface zone (at 3 mm from the surface). This is since experiments have repeatedly proved the presence of a gradient distribution of grain size and a significant difference in their shape along the diameter of the billet after the RSR. Figures 3-4 show the results of modeling the microstructure of 5KHV2S steel after 3 and 6 passes of RSR.

After annealing № 2 and three RSR passes, the average grain size was approximately 40 microns in the transverse direction and 57 microns in the longitudinal direction. In this case, in the transverse direction, the grain shape is close to equiaxial, and in the longitudinal direction, the grains are stretched in the rolling direction.

After annealing № 2 and six RSR passes, the average grain size was approximately 10 microns in the transverse direction and 35 microns in the longitudinal direction. In the transverse direction, the grains retain an equiaxial shape, and in the longitudinal direction, the grains are strongly elongated in the rolling direction.

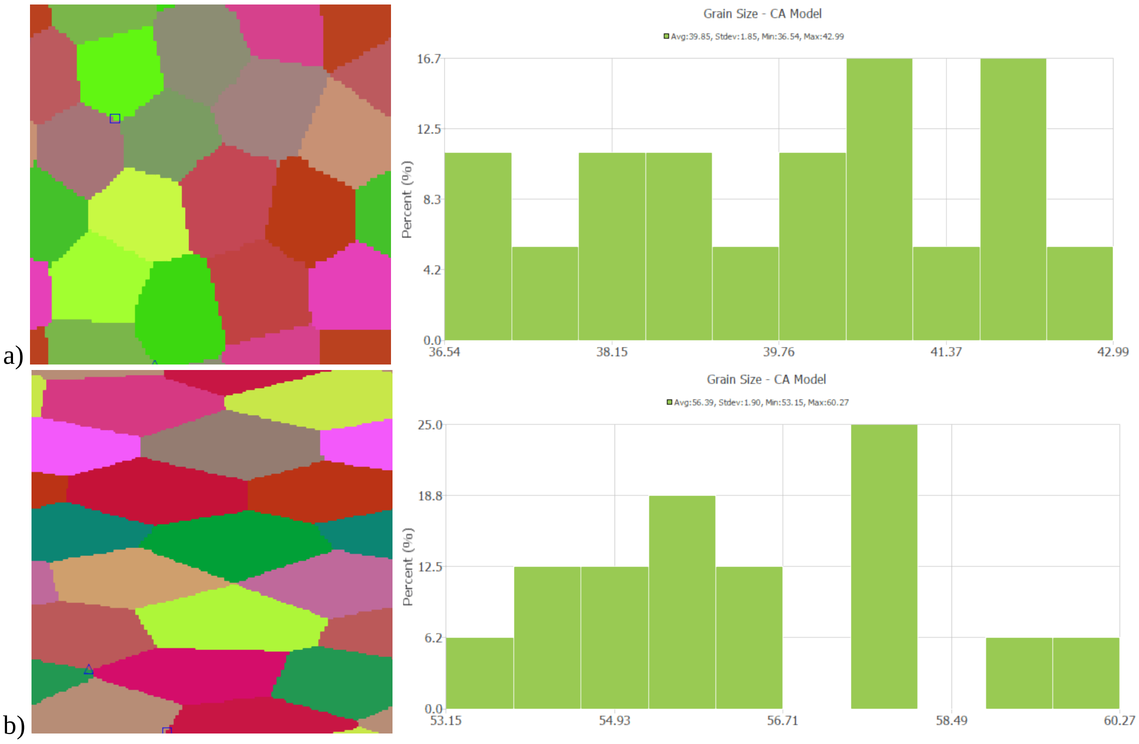

Figure 3. Structure of 5KHV2S steel after 3 RSR cycles
a – surface; b – center

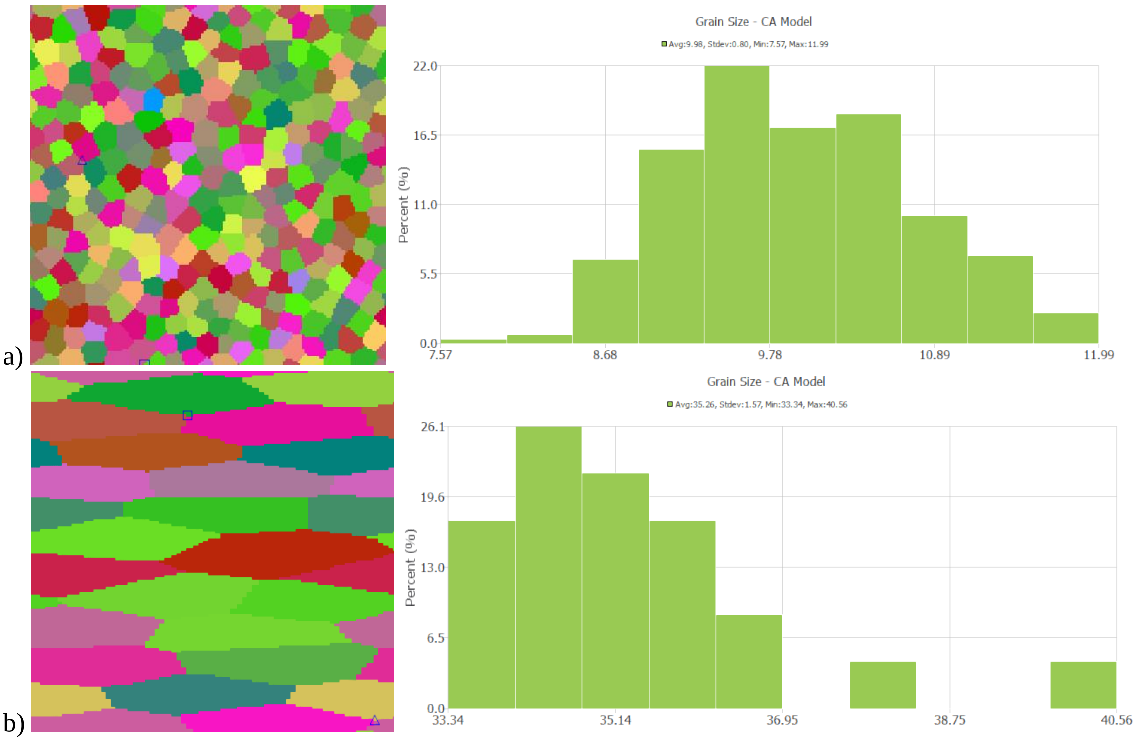

Figure 4. Structure of 5KHV2S steel after 6 RSR cycles
a – surface; b – center

Conclusion

The computer simulation of thermomechanical processing, including pre-heat treatment and subsequent radial shear rolling, of 5KHV2S steel showed that although PHT leads to the initial grain growth, the subsequent deformation of billets made of this steel in a radial shear rolling mill allows them to obtain a gradient fine-grained structure. The role of pre-heat treatment of 5KHV2C steel in practice - is in our case not to refine the initial grain size of the structure, but to remove internal stresses, and eliminate other defects in the steel, which during further pressure processing, in particular, during radial shear rolling, will allow deforming the initial billets with large compressions (50% or more) without destroying them and get metal products in the form of bars with a given level of properties.

Scientific Ethics Declaration

The authors declare that the scientific ethical and legal responsibility of this article published in EPSTEM Journal belongs to the authors.

Acknowledgements

* This article was presented as a poster presentation at the International Conference on Technology, Engineering and Science (www.icontes.net) held in Antalya/Turkey on November 14-17, 2024.

* This research was funded by the Science Committee of the Ministry of Science and Higher Education of the Republic of Kazakhstan (Grant № AP14869135).

References

Akopyan, T. K., Gamin, Y. V., Galkin, S. P., Prosviryakov, A. S., Aleshchenko, A. S., Noshin, M. A., Koshmin, A. N., & Fomin, A. V. (2020). Radial-shear rolling of high-strength aluminum alloys: Finite element simulation and analysis of microstructure and mechanical properties. *Materials Science and Engineering A, 768*, 139424.

Azarbarmas, M. (2020). Modeling the dynamic recrystallization by using cellular automaton: The current status, challenges and future prospects. *Iranian Journal of Materials Science and Engineering, 17*, 103.

Gamin, Y. V., Korotitskiy, A. V., Kin, T. Y., Galkin, S. P. Kostin, S. A., & Tikhomirov, E. O. (2022). Development of temperature-rate modes of hot deformation of the Co–28Cr–6Mo alloy based on processing maps. *Steel in Translation, 52*, 1027-1036.

Gamin, Y. V., Koshmin, A. N., Dolbachev, A. P., Galkin, S. P., Aleschenko, A. S., & Kadach, M. V. (2020). Studying the influence of radial-shear rolling on thermal deformation conditions of A1050 processing. *Russ. Journals of Non-Ferrous Metals, 61*, 646–657.

Grabovetskaya, G. P., Mishin, I. P., Naydenkin, E. V., Zabudchenko, O. V., & Stepanova, E. N. (2022). Mechanical properties and creep of VT22 alloy after radial-shear rolling and subsequent aging. *AIP Conf. Proceedings, 2509*, 020078.

Kugler G., & Turk R. (2004). Modeling the dynamic recrystallization under multi-stage hot deformation. *Acta Materialia, 52*, 4659-4668.

Lezhnev, S., Naizabekov, A., Volokitin, A., Volokitina, I., Panin, E., & Knapinski, M. (2017). Development and research of combined process of "equal channel angular pressing – drawing". *Journal of Chemical Technology and Metallurgy, 52*, 172-179.

Mishin, I. P., Naydenkin, E. V., Ratochka, I. V., Lykova, O. N., Vinokurov, V. A., & Manisheva A. I. (2020). Effect of radial shear rolling and aging on the structure and mechanical properties of titanium alloy VT35, *AIP Conference Proceedings, 2310*, 020206.

Naizabekov, A. B., Ashkeev, Zh. A., Toleuova, A. R., & Lezhnev S. N. (2005). Billet deformation in uniform-channel stepped die. *Steel in Translation, 35*(2), 37-39.

Naizabekov, A., Lezhnev, S., Volokitina, I., Panin, E., Tolkushkin, A., Belsky, S., & Pishchov, M. (2024). Investigation of the effect of combined thermomechanical processing on the brass microstructure evolution and the microhardness change. *Metalurgija, 63*, 283-286.

Patrin, P. V., Karpov, B. V., Aleshchenko, A. S., & Galkin, S. P. (2020). Capability process assessment of radial-displacement rolling of heat-resistant alloy HN73MBTYU. *Steel Translation, 50*(1), 42-45.

Puspasari, V., Astawa, I. N. G. P., Herbirowo, S., & Mabruri, E. (2024). Mechanical properties and microstructure of Al–Mg (5052) alloy processed by equal-channel angular pressing (ECAP) with variation of ECAP routes and heat treatment. *Izvestiya Ferrous Metallurgy, 67*(1), 37-46.

Sidelnikov, S. B., Lopatina, E. S. Konstantinov, I. L., Voroshilov, D. S., Mansurov, Yu., Bersenev, A. S., & Durnopyanov, A. V. (2024). Technology for the producing calibrated bars made of aluminum alloy 6082 prepared using ingotless rolling-pressing. *Metallurgist, 67*(3), 1293-1301.

Volokitin, A. V., Volokitina, I. E., Panin, E. A., Naizabekov, A. B., & Lezhnev, S. N. (2021). Strain state and microstructure evolution of AISI-316 austenitic stainless steel during high-pressure torsion (HPT) process in the new stamp design. *Metalurgija, 60*(3-4), 325-328.

Author Information

Andrey Tolkushkin
Rudny Industrial University
38 50 let Oktyabrya str., Rudny, Kazakhstan
Contact e-mail*: mrgugimon@gmail.com*

Pavel Tsyba
Rudny Industrial University
38 50 let Oktyabrya str., Rudny, Kazakhstan

Andrey Marukov
Rudny Industrial University
38 50 let Oktyabrya str., Rudny, Kazakhstan

Abdrakhman Naizabekov
Innovative University of Eurasia
Lomova 45 str., Pavlodar, Kazakhstan

Yevgeniy Panin
Karaganda Industrial University
Republic 30, Temirtau, Kazakhstan

Alexandr Arbuz
AEO Nazarbayev University
Kabanbai batyr, 53, Astana, Kazakhstan

To cite this article:

Tolkushkin, A., Tsyba, P., Marukov, A., Naizabekov, A., Panin, Y, & Arbuz, A. (2024). Computer modeling and study of the influence of pre-heat treatment and radial-shear rolling on the evolution of the structure of 5KHV2S steel. *The Eurasia Proceedings of Science, Technology, Engineering & Mathematics (EPSTEM), 32,* 19-24.

The Eurasia Proceedings of Science, Technology, Engineering & Mathematics (EPSTEM)
ISSN: 2602-3199

The Eurasia Proceedings of Science, Technology, Engineering & Mathematics (EPSTEM), 2024

Volume 32, Pages 25-29

IConTES 2024: International Conference on Technology, Engineering and Science

OCDMA Based Satellite to Underwater VLC Transmissions for Oceanic Monitoring

Kandouci Chahinaz
Djillali Liabes University

Bouziani Merahi
Djillali Liabes University

Abstract: Recently, optical wireless communication has emerged as a promising alternative to radio frequency communication across various domains such as atmospheric, deep space, and underwater transmissions. Specifically, the technology of satellite-to-underwater communication holds immense potential for applications in commercial, naval, scientific, and engineering sectors owing to its attributes including high data rates, robust security, extensive reach, and cost-effectiveness. This study delves into the performance assessment of an oceanic monitoring system aimed at bridging the gap between underwater and terrestrial environments. To ensure continuous real-time monitoring and widespread coverage, the communication infrastructure is augmented by a satellite link. The evaluation focuses on a direct detection Optical Code Division Multiple Access (OCDMA) system operating within an underwater wireless optical channel (UWOC). Various performance metrics are scrutinized through analytical analyses, with simulations conducted by manipulating key parameters such as range, transmitted power, user count, and inclination angle. The investigation also accounts for different modulation techniques tailored to distinct water types classified according to the Jerlov classification system. The obtained results reveal a substantial correlation between Bit Error Rate (BER) performance and both the water type and the receiver's positioning.

Keywords: Optical Code Division Multiple Access (OCDMA), Visible Light Communication (VLC), Under Water Optical Wireless Communication (UWOC), 5g networks.

Introduction

Oceanic Light Detection and Ranging **(O-LiDAR)** represents a significant remote sensing apparatus utilized for the assessment of near-coastal water depth and the exploration of optical attributes within aquatic environments (Kandouci , 2022). The proliferation of LiDAR commercialization has spurred heightened global inquiry into the theoretical underpinnings governing the transmission properties of LiDAR in underwater settings.

Currently, ground-to-space and ground-toaircraft communications rely on microwave technology. Eventually, aircraft-to-aircraft links will be OWC. Inter-aircraft optical wireless communication systems can transmit data at speeds of several Gbps over long distances of many kilometers. A satellite-to-ground communication system has been developed utilizing OWC technology (Kumari, 2024). Even though OWC technology has many merits, it also has several disadvantages, including scintillation loss (being sensitive to temperature variations caused by the Earth's heat rise), geometric loss, the attenuation of beam-spreading power, absorption loss (photons absorbed by water molecules or CO2), atmospheric attenuation, and scattering loss (Kumari, 2024). In addition, the ground–underwater communication system can support the development of services like deep-sea mining, high-definition video transmission, and offshore exploration through underwater wireless optical communication (UWOC). It is, therefore, possible to generate high-speed as well as long-distance OWC transmission by using satellite–ground–underwater integrated systems (Kannan, 2024). Currently, ground-to-

- Selection and peer-review under responsibility of the Organizing Committee of the Conference

space and ground-toaircraft communications rely on microwave technology. Eventually, aircraft-to-aircraft links will be OWC. Inter-aircraft optical wireless communication systems can transmit data at speeds of several Gbps over long distances of many kilometers. A satellite-to-ground communication system has been developed utilizing OWC technology (Mitra, 2006). Even though OWC technology has many merits, it also has several disadvantages, including scintillation loss (being sensitive to temperature variations caused by the Earth's heat rise), geometric loss, the attenuation of beam-spreading power, absorption loss (photons absorbed by water molecules or CO_2), atmospheric attenuation, and scattering loss (Kandouci, 2022) In addition, the ground–underwater communication system can support the development of services like deep-sea mining, high-definition video transmission, and offshore exploration through underwater wireless optical communication (UWOC). It is, therefore, possible to generate high-speed as well as long-distance OWC transmission by using satellite–ground–underwater integrated systems (Mitra, 2006).

Method

Jerlov Water Types

In optical oceanography, Jerlov categorized waters into oceanic and coastal types based on their chlorophyll concentration. The latter directly affects the water's particles sizes and consequently the scattering and absorption effects on any light beam propagation underwater (Kandouci , 2022). Another important parameter to take into consideration is the attenuation co-efficient c(λ) (see table 1) . In UWOC it depends on the operating transmission wavelength. It's also defined as the sum of absorption and scattering coefficient respectively represented by a(λ) and b(λ):

$$c(\lambda) = a(\lambda) + b(\lambda) \tag{1}$$

Table. 1. Ideal transmission wavelength for different water types

Jerlov water type	$a(m^{-1})$	$b(m^{-1})$	$c(m^{-1})$
Clear water	0.053	0.003	0.056
Clear ocean	0.069	0.08	0.15
Coastal ocean	0.088	0.216	0.305
Turbid harbor	0.295	1.875	2.17

In order to overcome those drawbacks, we propose to translate the benefits of Optical Code Division Multiple Acces (OCDMA, more traditionally implemented in optical fibers systems) in UWOC systems by using two dimensional wavelength hopping / time spreading (WH/TS) codes to generate and detect the O-Lidar impulsions (Kandouci , 2022)

OCDMA Codes

The choice of optical codes and their parameters involves trade-offs. Increasing the code length or number of wavelengths can improve interference management and support for more users, but this may also increase system complexity and hardware requirements. In this paper, two dimensional time spreading / wavelength hopping optical code division multiple access codes (2D - WH/TS OCDMA) are chosen for their correlation properties necessary to generate the desired Lidar pulses. Wavelength-hopping/ Time-spreading codes are generated either by using mathematical approach or by the extension of existing one dimensional codes.

The cross-correlation function in the context of 2D wavelength-hopping time-spreading (WH/TS) OCDMA codes is a key measure of how much interference is present between different users' codes. It indicates the degree of overlap between the codes of different users and is critical for evaluating the multiple-access interference (MAI) in an OCDMA system.

Autocorrelation of a WH/TS code x(t) is defined in equation 2:

$$Z_{x,x} = \sum_{m=1}^{R}\left(\sum_{n=1}^{L_T} x_{m,n} x_{m,(n+1)\ mod\ L_T}\right) \tag{2}$$

With:

N is the number of codes;

R is the number of rows;

L_T is the number of columns;

Our codes satisfies$Z_{x,x}$ = W.

The cross correlation between two W/T codes x(t) and y(t) is defined as follows in equation 3

$$Z_{x,y} = \sum_{m=1}^{R}\left(\sum_{n=1}^{L_T} x_{m,n}x_{m,(n+1)modL_T}\right) \tag{3}$$

In our case

$$Z_{x,y} = \begin{cases} 1 \ for \ (Z_{C_{i,k},C_{i+1,k}}) \\ \quad 1 \end{cases}$$

The cross-correlation functions directly impacts the system's bit error rate (BER) and capacity. Lower cross-correlation values reduce the chance of code collision, allowing more users to share the same channel without excessive interference, which improves system scalability and reliability , thus allowing the sending of the impulsions for monitoring without any overlap.

Results and Discussion

The consists of a demultiplexer (composed of a reconfigurable selection filter) to separate the components of the three wavelengths, $\lambda_1, \lambda_3, \lambda_9$), of the spectral signature. Each component is then sent to an optical delay line and finally recombined by a multiplexer. A delay time T_D was introduced between the different wavelengths of each user's code. It can be calculated as in equation (4).

$$T_D = p \times \frac{T_b}{s} \tag{4}$$

Where p is the position of the slot ;$T_b$is the bit time and s is the number of slots

This impulsions coding is illustrated in figure 1.

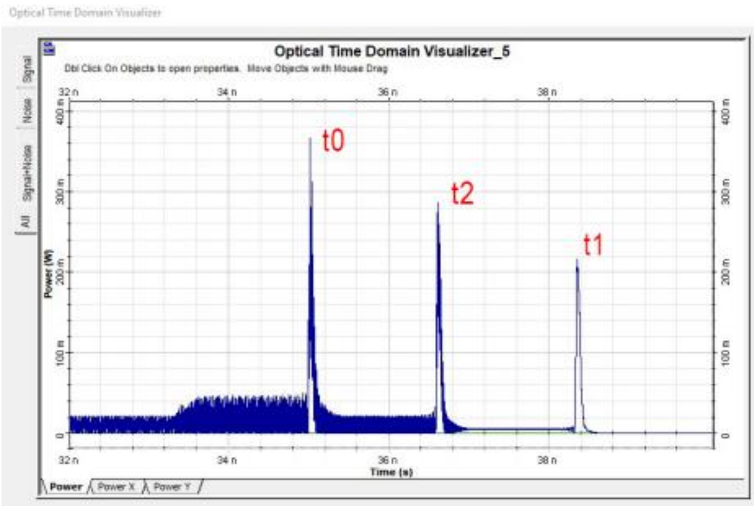

Figure 1. LiDAR impulsion's

At the receiver , each wavelength is firstly detected then delayed through delay lines. The time delay at the reception (T_R) is calculated as follow in equation (5).

$$T_R = (s - 1 - p) \times \frac{T_b}{s} \tag{5}$$

The transmission and reception delays will be the same for all codes, but in a different order and with different wavelengths to be transmitted. According to previous calculations, the three pulses should all have been received at the same instant. However, there is a slight offset due to dispersion effects. Figure 2shows the delayed wavelengths, which are then recombined at the decoder level (Mux).

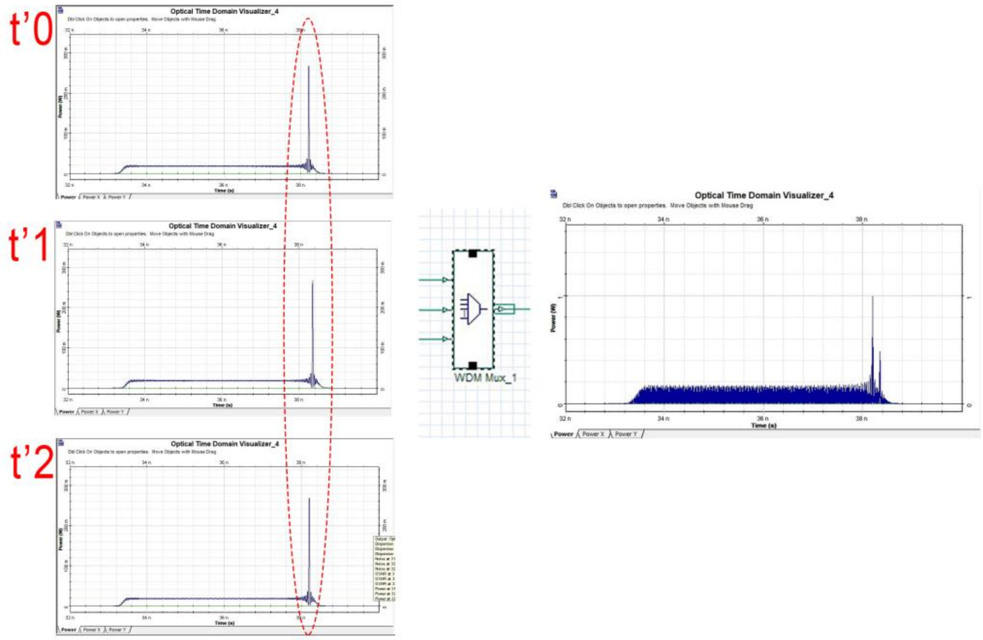

Figure 2. Impulsion's detection

The component library in the OptiSystem software uses the "BER Analyzer" block to compare the received signal with the transmitted data and then displays the expected values for various parameters (decision threshold, decision instant) and evaluation criteria (Q-factor, bit error rate (BER), eye diagram opening) to assess system performance (Figure 3).

Analysis

Max. Q Factor	15.3067
Min. BER	3.39016e-053
Eye Height	0.0269003
Threshold	0.0229518
Decision Inst.	0.572163

Figure 3. Performance analysis

Figure 4 shows an eye diagram as a function of bit time. The two main characteristics of this graph are the vertical opening of the eye (which indicates the system's noise immunity) and the decision time.

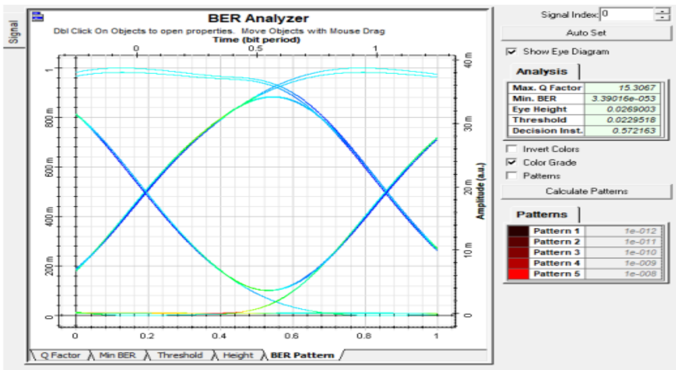

Figure 4. Performance results

Conclusion

The application of O-LiDAR technology in environmental monitoring has demonstrated significant potential in enhancing the accuracy and efficiency of data collection. Its ability to provide high-resolution, three-dimensional spatial information allows for detailed analysis of various environmental parameters, from vegetation structure to topographical changes. The results of our study underscore the value of O-LiDAR in supporting sustainable environmental management practices, offering a powerful tool for researchers and policymakers to better understand and mitigate the impacts of environmental changes

Scientific Ethics Declaration

The authors declare that the scientific ethical and legal responsibility of this article published in EPSTEM Journal belongs to the authors.

Acknowledgements or Notes

* This article was presented as an oral presentation at the International Conference on Technology, Engineering and Science (www.icontes.net) held in Antalya/Turkey on November 14-17, 2024.

References

Kandouci, C. (2022). Performances enhancement of underwater wireless optical communications (UWOC) using pulse position modulation. *Journal of Optical Communications*, *43*(2), 289-294.

Kandouci, C. (2022). Investigation of Jervol water types properties effects on underwater optical wireless OCDMA system performances for different modulation techniques. *Optical and Quantum Electronics, 54* , 3.

Kannan, A. B. (2024). Experimental demonstration and performance analysis of free space and underwater optical wireless communication systems. *Wireless Personal Communications*, *134*(12) , 69–93.

Kumari, M., & Satyendra, K. M. (2024). High-efficiency 4 × 4 × 10 Gbps orbital angular momentum modes ıncorporated into satellite–ground–underwater optical wireless system under diverse turbulences. *Photonics*, *11*(4), 355.

Mitra, A. C. J. (2006). Lidar detection of underwater objects using a neuro-SVM-based architecture. *IEEE Transactions on Neural Networks 17*(3) , 717-731.

Author Information

Kandouci Chahinaz
Telecommunications and Digital Signal Processing Laboratory, Faculty of Electrical Engineering
Djillali Liabes University , 22000 Sidi Bel Abbes, Algeria
Contact e-mail: chahinazkandouci@gmail.com

Bouziani Merahi
Telecommunications and Digital Signal Processing Laboratory, Faculty of Electrical Engineering
Djillali Liabes University , 22000 Sidi Bel Abbes, Algeria

To cite this article:

Chahinaz, K. & Merahi, B. (2024). OCDMA based satellite to underwater VLC transmissions for oceanic monitoring. *The Eurasia Proceedings of Science, Technology, Engineering & Mathematics (EPSTEM), 32,* 25-29

The Eurasia Proceedings of Science, Technology,
Engineering & Mathematics (EPSTEM)
ISSN: 2602-3199

The Eurasia Proceedings of Science, Technology, Engineering & Mathematics (EPSTEM), 2024

Volume 32, Pages 30-40

IConTES 2024: International Conference on Technology, Engineering and Science

Development and Characterization of Stabilized Earth Blocks Based on Recycled Sediment and Lightweight Aggregates

Bahia Rabehi
University M'Hamed Bougara of Boumerdes

Youcef Ghernouti
University M'Hamed Bougara of Boumerdes

Sabria Malika Mansour
University M'Hamed Bougara of Boumerdes

Khaled Boumchedda
University M'Hamed Bougara of Boumerdes

Abstract: The main objective of this experimental study is the development of eco-materials based on recycled material by recovery of dam sediment, and the incorporation of lightweight aggregates in order to improve the physical, mechanical and thermal properties of the stabilized earth blocks (SEB) used in construction. The development of stabilized earth blocks is carried out using different amounts of stabilizers (cement, lime) and different dosages of lightweight aggregates in substitution of dam sediment (10, 20, 40 and 50%). An experimental campaign was directed to test the physical, mechanical and thermal characteristics of the blocks produced. The obtained results show that the blocks made from 50% lightweight aggregates and 10% stabilizer (cement) have the best performances. Adding lightweight aggregates to the block composition improves shrinkage. Using a higher percentage of lightweight aggregates and combined to a fixed quantity of binder leads to better stability of the earth blocks by reducing weight loss and increasing durability.

Keywords: Earth block, Recycled sediment, Strength, Thermal conductivity, Lightweight aggregates

Introduction

Stabilized earth blocks (SET) are considere an interesting option for durable, comfortable and economical construction. Although criticized for its sensitivity to water and lack of durability, this material has many advantages when used appropriately, such as low energy consumption during its production, its aesthetic qualities and its thermal inertia. The use of stabilizers such as cement or lime and other materials such as fibers in stabilizing the earth in general is a fairly well known field thanks to significant research work, which has made it possible to understand the mechanisms of reactions between the earth and these stabilizers, and their effects on the properties of the earth.The compaction and/or incorporation of granulates or fibers can affect the mechanical and/or thermal performances due to their physico-mechanical effects in the earthen matrix. However, this approach does not necessarily guarantee the earthen material to resist in contact with liquid water (Bruno et al., 2017). Furthermore, the recycling and recovery of waste and by-products in the field of construction can also contribute to solving the ecological and environmental problems linked to the rejection of these materials, which offers interesting perspectives for sustainable and economical construction.

Masuka et al. (2018) used coal fly ash, lime, and wood aggregates for the production of earth blocks. The authors reported comparable or even higher dry compressive strength than cement stabilized blocks, but

- Selection and peer-review under responsibility of the Organizing Committee of the Conference

deplored the necessity of little (4%) cement content for better-wet strength. Hakimi et al. (1998) studies the thermo-physical properties of the earth, stabilized with cement contents ranging from 0 to 10% (0%, 4%, 5%, 5%, 8%, and 10%).The obtained results reveals that the thermal parameters evolved considerably with the water content for raw earth, (0% cement) and cement. Ouedraogo et al. (2015) carried out an experimental study on the mechanical and thermophysical characteristics of compressed earth blocks, stabilized using paper (cellulose) and/or cement. The results indicated a significant improvement in the properties of the earth blocks following stabilization, and the incorporation of paper into the earth-cement mixture had a less pronounced impact on the mechanical strengths. However, this addition made it possible to achieve even higher performances than those observed with raw earth. Gueffaf, et al. (2020) conducted a study to assess the feasibility of recycling dam sediments for the manufacture of stabilized blocks. For elaborated samples, different percentages of cement and lime were chose respectively (0, 6, 8, 10 and 15%), (0, 5, 8 and 10%). The results showed that blocks made from dam sediments could have an improved compressive strength of 172% at 15% cement and 85% at 10% lime. The thermal conductivity is also improve, with a value of 1.06 W/m.k at 15% cement and 0.73 W/m.k at 10% lime.

Several work has been carried out on improving the thermal properties of earth blocks by incorporating lightweight aggregates such as in the work of Layachi et al. (2023) which examines the impact of the incorporation of expanded polystyrene (EPS) on the thermal, mechanical and environmental properties of lightweight earth blocks (LWB). The blocks were manufacture with different percentages of EPS (from 0% to 65%) and were subject to extensive characterization, including thermal properties such as conductivity, diffusivity and heat capacity, mechanical properties such as flexure and compression, as well as environmental life cycle assessment. The results indicate a significant improvement in thermal insulation with the increase in the percentage of EPS, although this is accompanying by a reduction in mechanical resistance. The addition of EPS also improved the ductility of LWBs. Environmentally, the use of LWBs with 65% EPS showed a notable reduction in the energy required and CO_2 emissions compared to conventional walls, thus highlighting that the incorporation of EPS in LWBs presents a strategic promising for increasing the energy efficiency of buildings. The objective of this work is the optimization of the formulation of eco-materials based on recycled dam sediment, lightweight aggregates and stabilizer in order to improve the physical, mechanical, thermal properties and the durability of earth blocks.

Material Used

Sediment

The sediment used in this experimental work comes from the KEDDARA dam located in BOUMERDES city, 8 km south of BOUDOUAOU and 35km east from Algiers the capital with a capacity of 142,391 Hm^3 is supplied by contributions from the Keddara Oueds.

Figure 1. Keddara dam: Sampling sites

Chemical Composition

The chemical analysis of the kaddara sediment was carried out by X-ray fluorescence according to standard NF P 15-467 (Table 1). Sediment is essentially formed of oxides of silicon SiO2 and aluminum Al_2O_3 that are the majority oxides, an acceptable content of Fe_2O_3 of CaO, K2O and MgO, this material is also made up of TiO2, Na_2O, SO_3, MnO and P_2O_5 with a small amount. The SiO_2/Al_2O_3 mass ratio of our sediment is 2.92.

Table 1. Chemical composition of sediment

Constituant	SiO2	Al2O3	Fe2O3	CaO	K2O	MgO	TiO2	Na2O	SO3	MnO	P2O5
% Massique	58.5	20.0	7.46	5.85	3.91	2.05	0.852	0.638	0.343	0.149	0.122

Mineralogical Analysis

The mineralogical analysis of the sediment was carried out by X-ray diffraction, which gives us an idea of the main crystalline minerals by the existence of the characterizing lines.

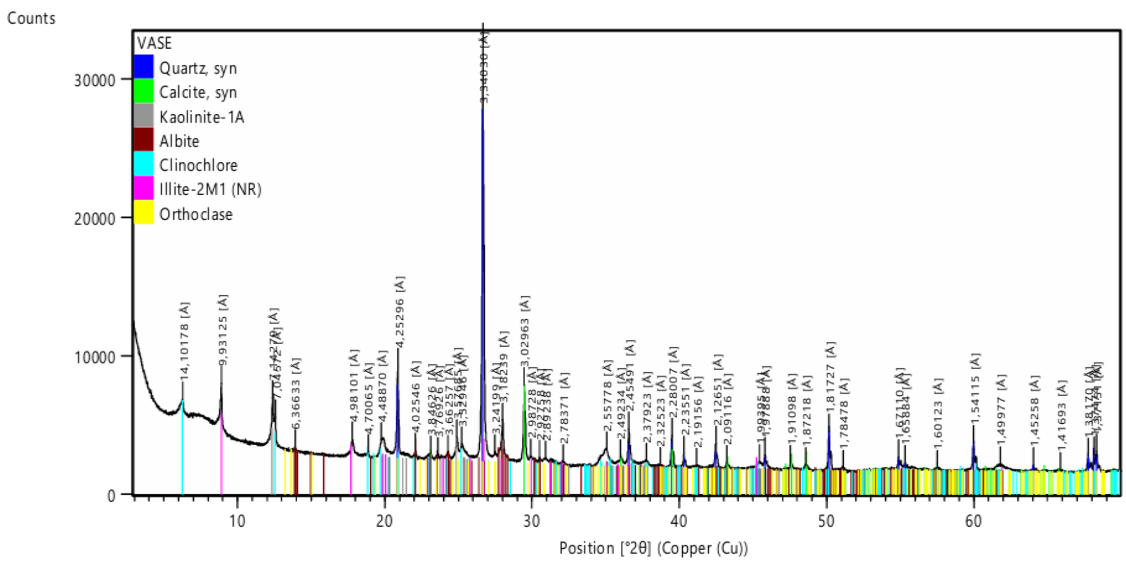

Figure 2. Mineralogical analysis of the sediment used

The Figure 2 indicates the presence of Quartz (SiO2) with significant peaks, followed by calcite ($CaCO_3$) and a good proportion of Alumina (AL_2O_3) represented as Kaolinite (AL_2O_3 $2SiO_2$ $2H_2O$) and illite, clinochlore, albite (NaAl Si_3O_8) and orthoclase are in low proportions.

Liquidity Limit

The test is carried out by the falling cone method and plasticity limit: NF EN ISO 17892-12 (June 2018). The obtained results are shows in Table 2. The obtained results in table 2 shows that the limits of plasticity are acceptable but sediment contain too many fines particles for compressed earth blocks (XP P 13-901 standard).

Table 2. Liquidity and plasticity limit

Material	W_L (%)	W_P (%)	I_P (%)
Sediment	42	23	19

Lightweight Aggregate

Lightweight aggregate used in this work is sand with a low density compared to traditional aggregates. It is made from expanded clay. The Granulometric analysis of Lightweight sand is realized according to EN 933-1 standard and indicates that is classified as 0/3. Technical sheet of Lightweight sand are presented in table 3.

Table 3. Technical sheet of lightweight sand

Testing and standards	Results
Bulk density EN 1097-3	1074 Kg/m^3
real density EN 1097-6	1730 Kg/m^3
Fine content EN 933-1	2.06%
Sand equivalent NF EN 933-8	94
Fineness modulus EN 12620	3.22
Water absorption (5') EN 1097-6	8,24%
Water absorption (30') EN 1097-6	10,96%
Water absorption (24 h) EN 1097-6	15,00%

Cement

In this work we used a Portland cement composed CEM II / B-L 42.5 N according to the NF EN 197-1 standard. Technical characteristics of cement are presented in Table 4.

Table 4. Technical characteristics of cement

Testing	Results
Loss on ignition (%) (NA5042)	10.0±2
Sulphate content (SO3) (%)	2.5±0.5
Magnesium oxide content MgO (%)	1.7±0.5
Chloride content (NA5042) (%)	0.02-0.05
C3S (%)	60±3
C3A (%)	7.5±1
Normal Consistency (%)	26.5±2.0
Fineness according to the Blaine method (cm2/g) (NA231)	3700-5200
Shrinkage at 28 days (µm/m)	<1000
Expansion (mm)	≤3.0
Start of setting (min)	150±30
End of setting (min)	230±50
Compressive strength 28 days (MPa)	≥42.5

Lime

Lime used is air lime; it is a white powder with a maximum grain size of 90 µm, having a high CaO content (greater than 73%). It has a specific density of $2g/cm^3$.

Earth Block Production Process

After treatment and driying of the sediments, it was crushed and finally passed through a 5 mm sieve to eliminate the large lumps. According to (Mahdad et al, 2018).The compaction of the blocks was achieved by using a hydraulic semi automatic press with a compaction pressure of 7 MPa and the dimensions of the tested blocks are 295 mm of length, 140 mm of width and 90 mm of height. Two binders and different dosages of lightweight sand were used cement with different contents: 0%, 2.5%, 5%, 7.5% and 10% and lime of percentages:0%, 5%, and 10%. Lightweight sand is introduced in blocks at differents dosages 10%, 20%, 40% and 50%. The required testing age for sediment/cement blocks is 28 days when 90 days are necessary for sediment /lime (Rigassi, 1995). The earth blocks sample production process is represented in Figure 3.

Results and Discussions

Several tests were carried out on the stabilized earth blocks. The production of more than 200 stabilized earth blocks allowed us to obtain results that are more representative and to present several observations. Experimental tests carried out on earth blocks allow the evaluation of different characteristics and performances of the blocks. For all tests, the following designations are adopted:
S: sediment, C: cement, L: lime, LS: lightweight sand

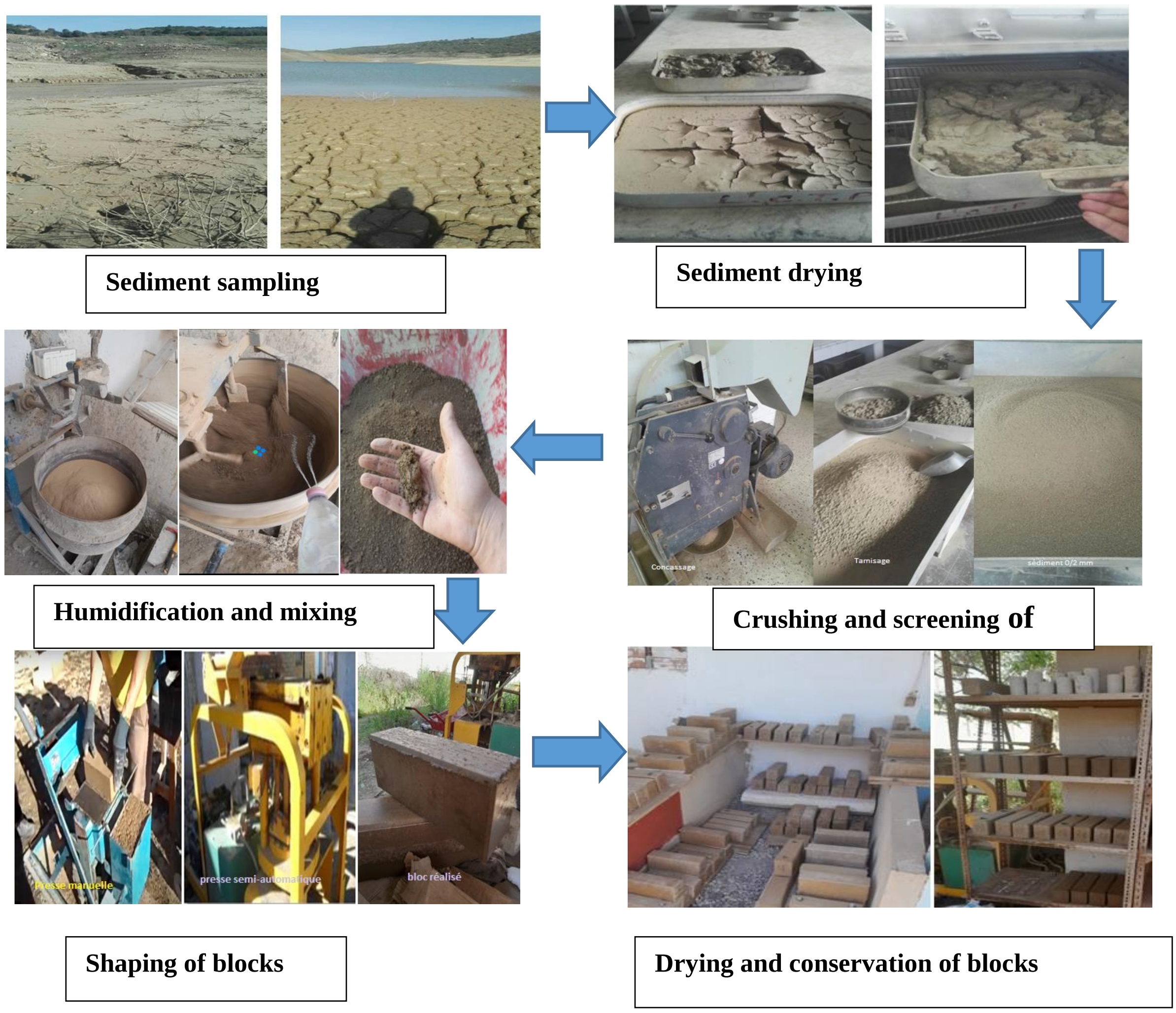

Figure 3. Earth blocks sample production process

Shrinkage Test

The drying shrinkage test of earth blocks according to standards XP P13-901. The results of the shrinkage tests carried out on the earth blocks prepared using sediment and stabilizers with different dosages of lightweight sand are illustrate in Figures 4 and 5.

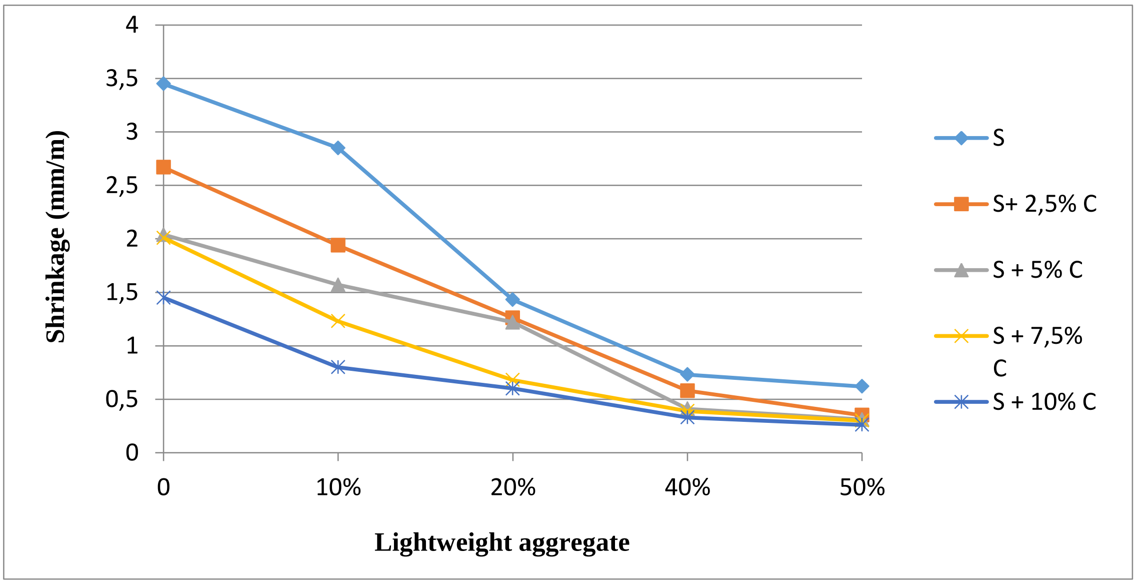

Figure 4. Shrinkage test for blocks based on Cement

The results show that the shrinkage decreases with the increase in the percentage of lightweight sand. The blocks of stabilized earth made by sediment with 40% and 50% light sand stabilized by cement 7.5% and 10% presenting less shrinkage compared to the blocks stabilized earth by sediment only and sediment with 10% and 20% light sand stabilized by cement 2.5% and 5%. The blocks stabilized with 40% and 50% of light sand, stabilized by lime at 5% and 10%, exhibited less shrinkage compared to the blocks stabilized by sediment only and sediment with 10% and 20% of light sand stabilized by lime 5% and 10%. The addition of lightweight sand to the composition of the stabilized earth blocks seems to improve their shrinkage properties. In addition, stabilization with lime or cement seems to reinforce this positive effect.

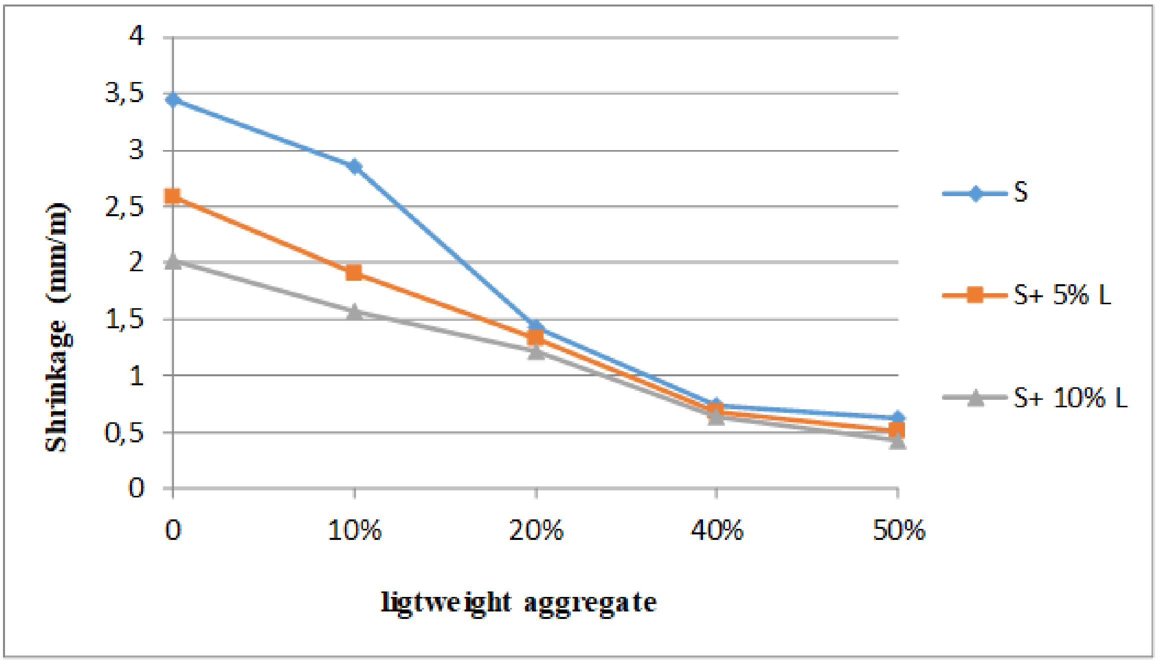

Figure 5. Shrinkage test for blocks based on lime

Water Absorption Test

The water absorption test consists in determining the water content absorbed by capillarity in compressed earth block. Before being immersed, the sample was weighted with an accuracy of 2g; then the lower face of the sample was immersed in a water bath to a depth of 5 mm and left for 10 min according to STANDARD XP

P13-901. The results of water absorption in the partial immersion test for blocks with different dosages of lightweight sand and stabilizer (cement, lime) are show in Figure 6.

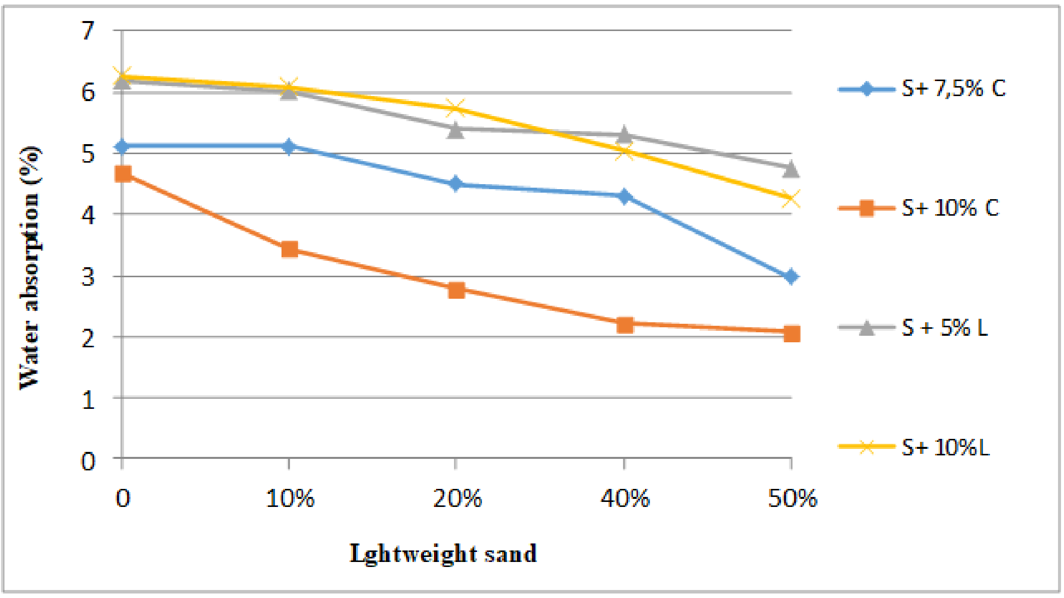

Figure 6. Absorption test for blocks based on cement, lime and lightweight sand

According to the results, a decrease in absorption is observed when the percentage of light sand increases. The stabilized blocks made with 40% and 50% light sand, stabilized with 10% cement, have a lower absorption compared to the stabilized earth blocks with 10% and 20% light sand, stabilized at 5% and 10% with lime, as well as at 7.5% with cement. Increasing the percentage of light sand seems to improve the resistance to water absorption of the stabilized blocks. Stabilizing the earth blocks by adding and increasing the dosage of light sand significantly reduces the water absorption rate.

Wetting-Drying Test

The wetting/drying durability test was also conducted in the laboratory. According to ASTM D559-57 standard, the procedure consists of immersing the blocks in water for 5 hours and then putting them in an oven at a temperature of 71°C for 42 hours. Then, the samples were brushed to remove the soil fragment affected by wetting and drying cycle. This procedure is repeated six times. Obtained results are represents in figures 7 and 8.

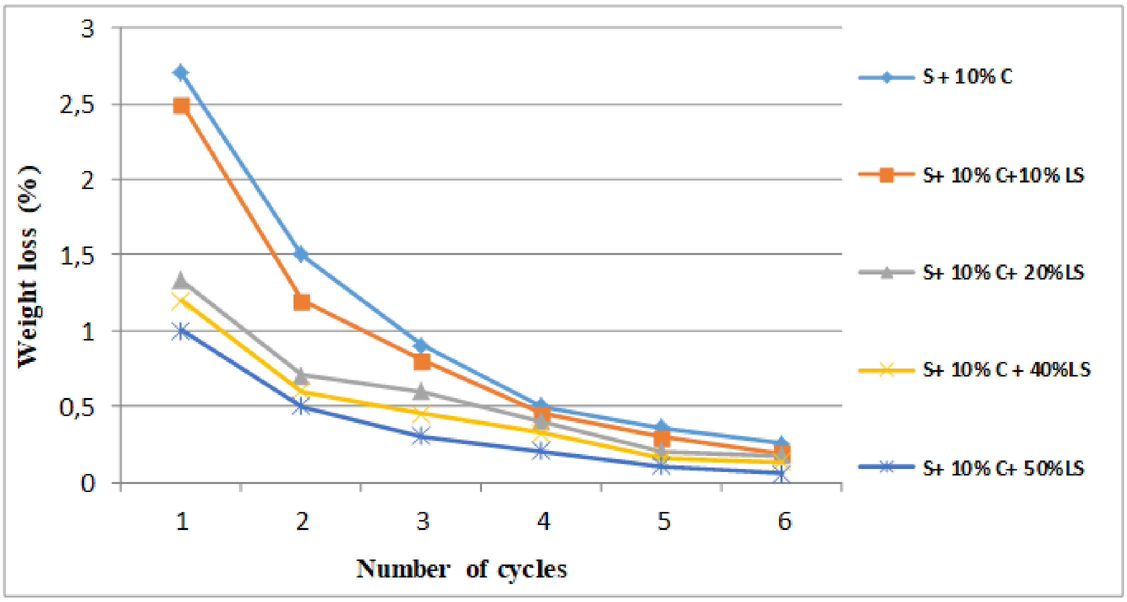

Figure 7. Wetting-drying test after 6 cycles for blocks based on lightweight sand and 10% cement

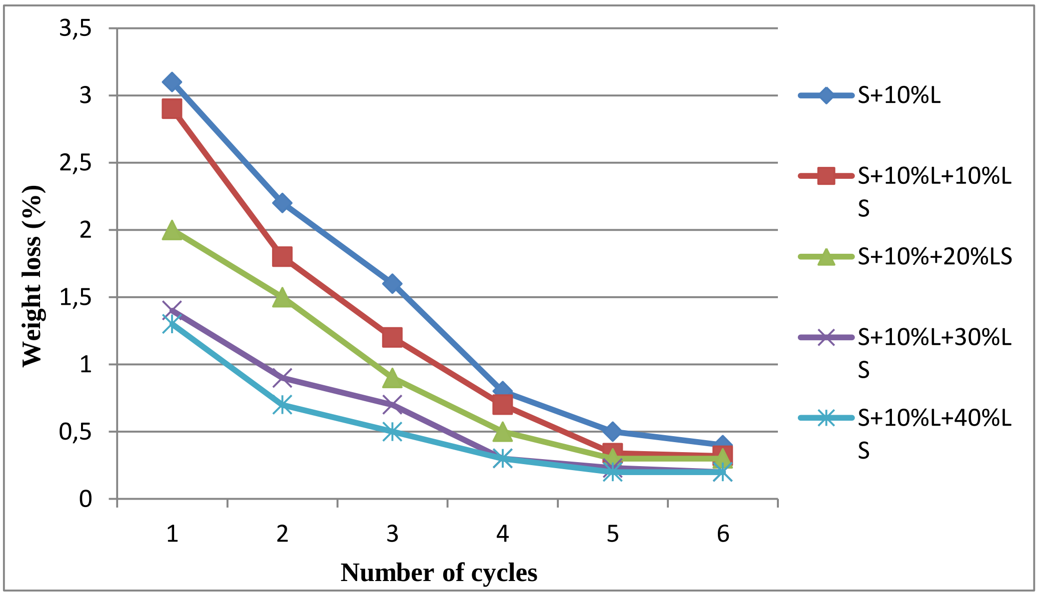

Figure 8. Wetting-drying test after 6 cycles for blocks based on lightweight sand and 10% lime

According to the results, a correlation is observed between the percentage of light sand used in the manufacture of stabilized blocks and the weight loss manifested. More precisely, an increase in the percentage of light sand seems to lead to a decrease in weight loss. This suggests that the use of a higher percentage of lightweight sand in combination with a fixed amount of lime can lead to a better stability of the earth blocks and therefore to a decrease in weight loss.

Compressive Strength Test

The compression test was carried out according to the XP P13-901 standard. Three samples were tested for each variant in order to evaluate the compressive strength of the stabilized earth block with a regular load speed of approximately 1.5 mm/min. An increase in the dosage of lightweight sand for blocks stabilized with cement or those with lime appears to lead percentage of lightweight sand, to an increase in the mechanical strength of the blocks. This can be explaining by the properties of lightweight sand, such as its particle size and density. The larger particles of lightweight sand and its hardness can help to strengthen the structure of the blocks and increase their mechanical strength.

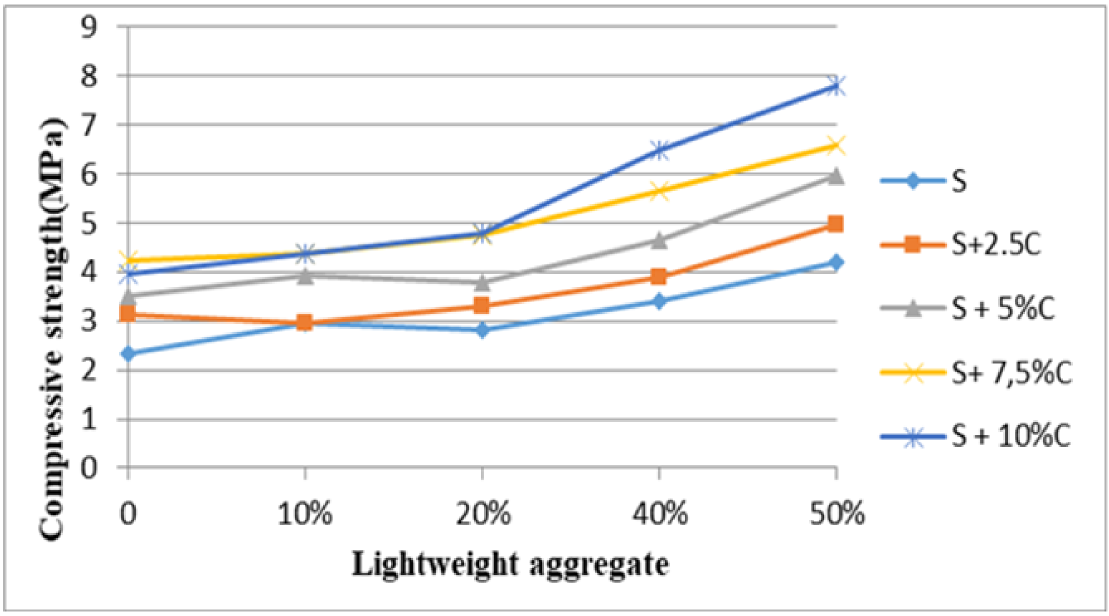

Figure 9. Compressive strength of stabilized blocks based on lightweight sand and cement

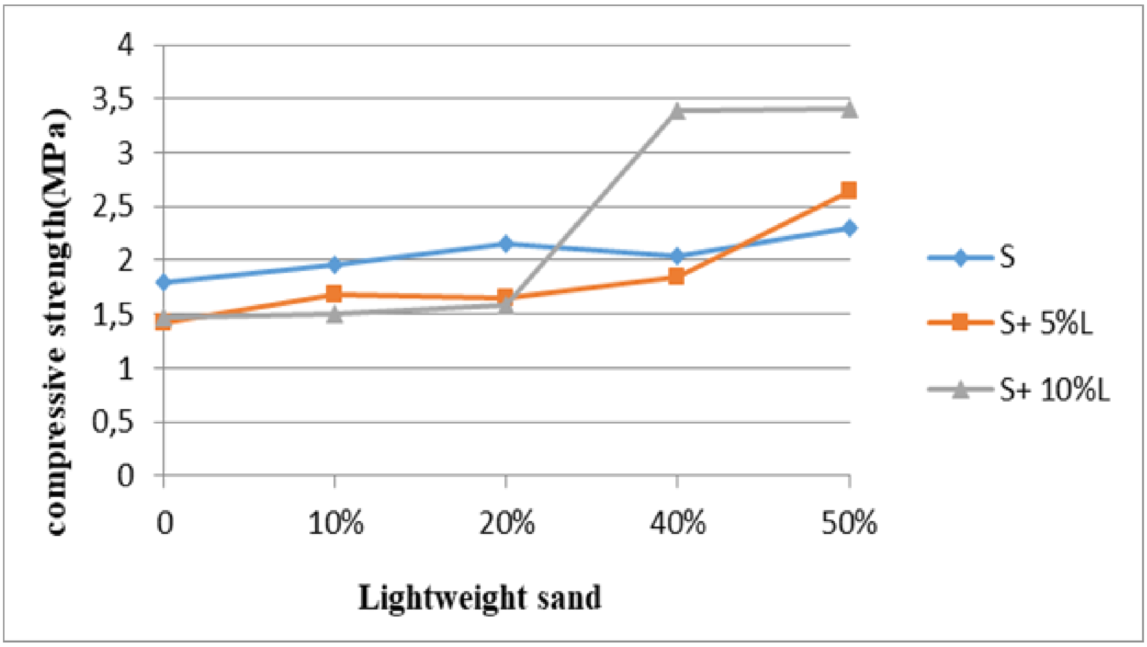

Figure 10. Compressive strength of stabilized blocks based on lightweight sand and lime

Bulk Density Test

The use of lightweight sand in the manufacture of stabilized earth blocks (SEB) can result a decrease in the density of the blocks. This reduction depends on the percentage of lightweight sand used in the mix. Using 50%, lightweight sand in the manufacture of blocks can result in a weight reduction of 5.05% compared to the blocks made with sediment only. A lower density means a lower weight per unit volume, which makes them easier to handle and transport to the construction site. The results of bulk density test are indicating in figure 11.

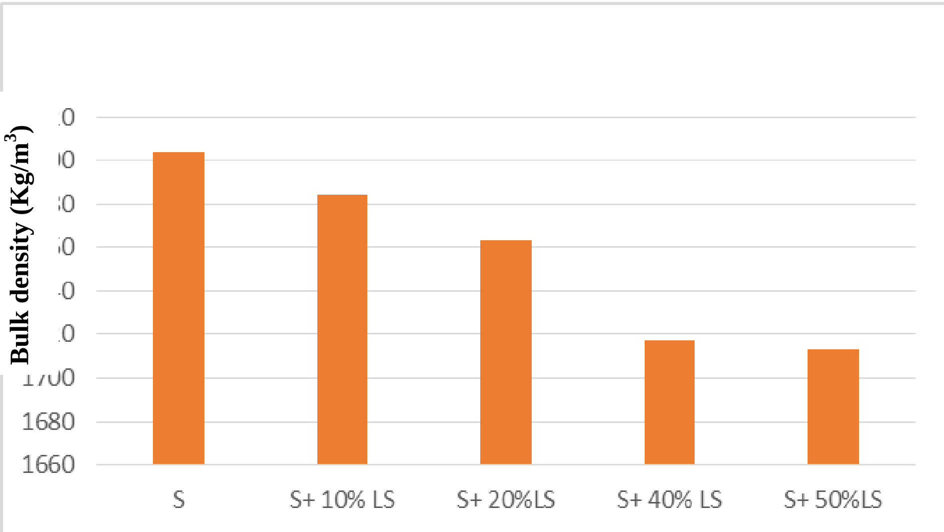

Figure 11. Bulk density of stabilized blocks with lightweight sand

Thermal Conductivity

Thermal conductivity is measured according to standard NF EN 993-15 using a CT-Meter, which operates on the hot wire principle. The results show that thermal conductivity decreases with increasing percentage of light sand. Lightweight sand is characterized by a porous structure, which can reduce the transmission of heat through the material. The pores present in lightweight sand can trap air or other gases, which are poor conductors of heat. Thus, the more lightweight sand there is in the material, the more pores there are and the less efficiently heat can propagate through the material.

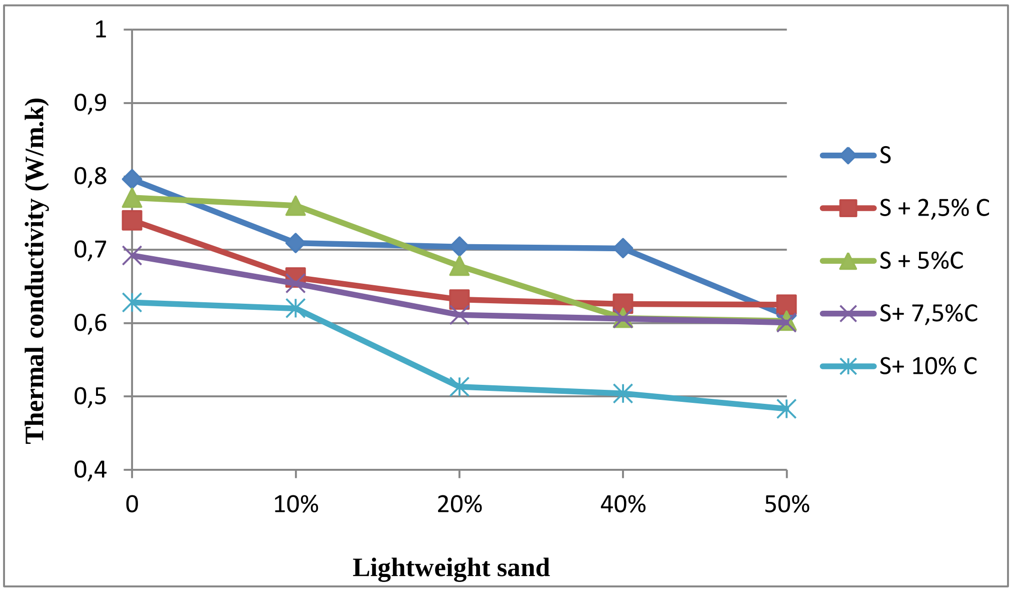

Figure 12. Results of thermal conductivity tests of blocks based on cement

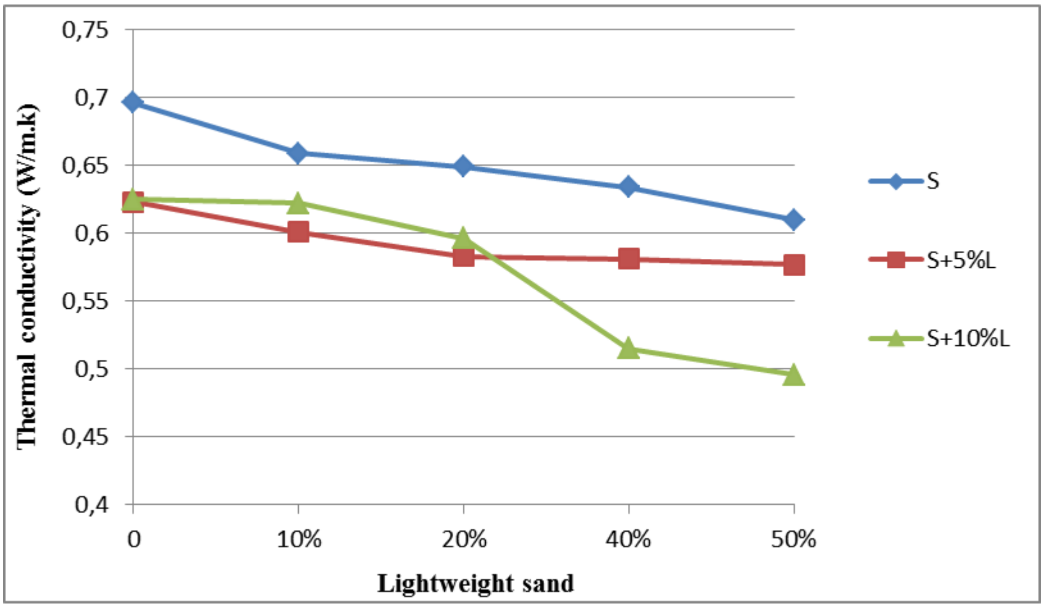

Figure 13. Results of thermal conductivity tests of stabilized blocks based on lime

Conclusion

From all the obtained results, it can be conclude:

- The use of lightweight sand in the composition of the blocks improves the shrinkage properties higher percentage of lightweight sand in combination with a fixed amount of lime or cement can lead to a better stability of the blocks and a decrease in weight loss. This is confirmed by the results obtained, the stabilized earth blocks made by sediment with 40% and 50% light sand stabilized by cement (7.5% and 10%) and stabilized by lime (5% and 10%) presenting less shrinkage.
- The blocks made with a higher percentage of light sand present a lower water absorption. This results in a decrease in weight loss and an increase in their durability. The samples made with 40% and 50% lightweight sand stabilized with 10% cement and 10% lime show good stability.

- Improved thermal insulation: The porous characteristics of lightweight sand allow reducing the heat transmission through the blocks. By increasing the percentage of lightweight sand, the thermal insulation of the blocks can be optimized. The tested stabilized blocks exhibit good thermal insulation with a thermal conductivity of 0.643 W/m.k for stabilized blocks with 10% cement 50% light sand and 0.496 W/m.k for blocks stabilized with 10% lime and 50% light sand.

The use of dam sediments, lightweight aggregates and stabilizers such as lime or cement in the manufacture of stabilized earth blocks allows obtaining blocks with good shrinkage properties, low water absorption, better stability, improved thermal insulation and increased mechanical strength. This offers interesting prospects for sustainable and ecological construction.

Scientific Ethics Declaration

The authors declare that the scientific ethical and legal responsibility of this article published in EPSTEM Journal belongs to the authors.

References

Bruno, A. W., Gallipoli, D., Perlot, C., & Mendes, J. (2017). Effect of stabilisation on mechanical properties, moisture buffering and water durability of hypercompacted earth. *Construction and Building Materials*, *149*, 733-740.

Gueffaf, N., Rabehi, B., & Boumchedda, K. (2020). Recycling dam sediments for the elaboration of stabilized blocks. *International Journal of Engineering Research in Africa*, *50*, 131-144.

Hakimi, A., Ouissi, H., El Kortbi, M., & Yamani, N. (1998). 'Un test d'humidification-séchage pour les blocs de terre comprim6e et stabilisé au ciment'. *Materials and Structures, 31*, 20-26

Layachi S., Izemmoure, O., Dakhia, A., Taalla, B., Atiki, E., Almeasar, K.S., Layachi, M., & Guettala, A. (2023). Effect of incorporating Expanded polystyrene beads on thermophysical, mechanical properties and life cycle analysis of lightweight earth blocks'. *Construction and Building Materials*, *375*, 130948.

Mahdad, M., Benidir, A., & Brara, A. (2018).'Hydro-mechanical properties and durability of earth blocks: influence of different stabilisers and compaction levels. *Sustainable Building Technology and Urban Development*, *9*(3), 183.

Masuka, S., Gwenzi, W., & Rukuni, T. (2018). Development, engineering properties and potential applications of unfired earth bricks reinforced by coal fly ash, lime and wood aggregates. *Journal of Building Engineering*, *18*, 312-320.

Ouedraogo, E., Coulibaly, O., Ouedraogo, A., & Messan, A. (2015). Mechanical and thermophysical properties of cement and/or paper (cellulose) stabilized compressed clay bricks. *Journal of Materials and Engineering Structures «JMES»*, *2*(2), 68-76.

Rigassi, V. (1995). '*Compressed earth blocks' CRATerre-EAG'*. Vieweg.

Author Information

Bahia Rabehi
University M'Hamed Bougara of Boumerdes
Independence avenue, 35000 Boumerdes-Algeria
Contact e-mail: *b.rabehi@univ-boulerdes.dz*

Youcef Ghernouti
University M'Hamed Bougara of Boumerdes
Independence avenue, 35000 Boumerdes-Algeria

Sabria Malika Mansour
University M'Hamed Bougara of Boumerdes- Algeria
Independence avenue, 35000 Boumerdes-Algeria

Khaled Boumchedda
University M'Hamed Bougara of Boumerdes- Algeria
Independence avenue, 35000 Boumerdes-Algeria

To cite this article:

Rahebi, B., Ghernouti, Y., Mansour, S. M. & Boumchedda, K. (2024). Development and characterization of stabilized earth blocks based on recycled sediment and lightweight aggregates. *The Eurasia Proceedings of Science, Technology, Engineering & Mathematics (EPSTEM), 32,* 30-40.

The Eurasia Proceedings of Science, Technology, Engineering & Mathematics (EPSTEM)
ISSN: 2602-3199

The Eurasia Proceedings of Science, Technology, Engineering & Mathematics (EPSTEM), 2024

Volume 32, Pages 41-52

IConTES 2024: International Conference on Technology, Engineering and Science

ANSYS Creep Modeling in a Beam with a 45° of Opening Crack

Ghouilem Kamel
University Mouloud Mammeri of Tizi – Ouzou

Atlaoui Djamal
University Mouloud Mammeri of Tizi – Ouzou

Mehaddene Rachid
University Mouloud Mammeri of Tizi – Ouzou

Merakeb Seddik
University Mouloud Mammeri of Tizi – Ouzou

Abstract: The main of this study is yo presents a prediction of creep behavior beam with opening crack at 45° subjected to a constant load during 12hours (720mn) and describe a procedure for modeling the primary creep law using ANSYS ® software. The procedure modeling of creep behavior consist to applied the finite element method (FEM) based on a model called (Modified Time hardening model) using the computer code ANSYS 17.1. This paper illustrates a new approach of study crack and creep behavior by the FEM in the elements structural. Crack analysis is typically accomplished using either the energy criterion or the stress-intensity-factor criterion. For the energy criterion, the energy required for a unit extension of the crack (the energy-release rate) characterizes the fracture toughness. For the stress-intensity-factor criterion, the critical value of the amplitude of the stress and deformation fields characterizes the fracture toughness. ANSYS ® 17.1 software has been used to perform the numerical calculation in this paper. The main objective of this study is to determine the distribution of stresses, creep strains as well as the mechanical behavior around crack. Results show that creep strain rate, and the resulting axial stresses will gradually increase at the spring line of the final lining.

Keywords: ANSYS, Creep, Finite element model, Crack, Time hardening model

Introduction

Crack growth and fracture is a problem that can be seen both in nature, and in man-made structures. Where the common cause of the propagation is the presence of tensile or shear stress within the material (Bjorheim, 2019). To solve the crack mechanics problems, a fracture analysis is a combination of stress analysis and fracture mechanics parameter calculation. The stress analysis is a standard linear elastic or nonlinear elastic plastic analysis. Because high stress gradients exist in the region around the crack tip, the finite element modeling of a component containing a crack requires special attention in that region. The stresses near a crack tip in linear elastic fracture mechanics can be described by the following equation given in (Anderson 2005):

$$\sigma_{ij} = \left(\frac{k}{\sqrt{r}}\right) f_{ij}(\theta) + \sum_{m=0}^{\infty} A_m r^{\frac{m}{2}} g_{ij}^{m}(\theta) \tag{1}$$

Where: σi is the Stress tensor, r is Distance from crack tip, θis the angle in relation to crack plane, k is the Constant and fij is the dimensionless function of θ in the leading term. This formula can be found in Anderson (2005) and this solution is exact according to Tada et al. (2000). The tensile fracture of the plain concrete is as a rule regarded brittle, because concrete does not have the yield behavior, which is very typical for metals. Its tensile stress-strain constitutive law is nearly linear up to the critical point, but after that, it starts to descend. In spite of that, the concrete still has considerable toughness. The reason is the formation of the fracture process zone and the phenomenon called strain localization. Because of this long damage zone, the methods of the linear elastic fracture mechanics (LEFM) can not be directly applied for concrete.

$$K_I = \sigma cos^2(\beta)\sqrt{\pi a} \tag{2}$$

$$K_{II} = \sigma sin(\beta)\cos(\beta)\sqrt{\pi a} \tag{3}$$

Where: σ is the remote stress, β is the angle of the slanted crack and ais a half crack length. Figure.2 illustrate the concrete beam crack test produced in the LGEA laboratory

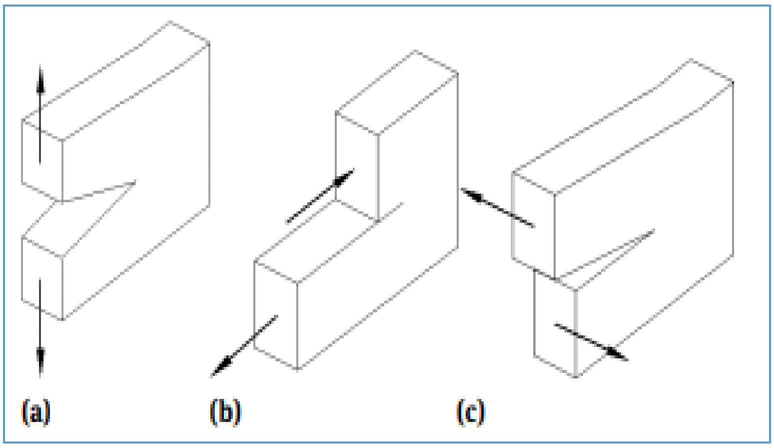

Figure 1.Three modes of fracture, (a) mode I - opening, (b) mode II - in plane shear, (c) mode III - out-of-plane shear (DTD Handbook 2005)

Figure 2. Beam crack test at 45°

It was pointed out by (Petersson 1981), that the application of LEFM to concrete is closely related to the dimensions of the structure into consideration. He has shown that, when the structural size increases, the material becomes more and more "brittle", i.e. the final collapse can only be described by means of fracture mechanics. As the structural size decreases, the final collapse mode is approaching "plastic" type and can be described by some of the plasticity models. That fact was the reason for the unsuccessful early applications of LEFM to concrete. This dependency is called size effect and is very well described in the book of (Bazant,1998). Of course, there is an intermediate case of the structural sizes where the material behaviour is considered as "quasi-brittle". The theory of fracture mechanics, applicable to quasi-brittle materials has taken a definite form in the last decade. The size of the concrete element (in most cases we use the height of the beam D, as a characteristic size) is closely related to its behavior and the mode of fracture, see figure 1 above , where three typical failure modes are shown, depending on the size of the concrete beam.

Creep involves time dependent deformation under constant compressive stress and temperature level. In materials science, creep is the tendency of a solid material to move slowly or deform permanently under the influence of stresses. the yield strength of the material. Creep is more severe in materials that are subjected to heat for long periodsand near their melting point. Creep always increases with temperature. In general, the creep equation is following:

$$\dot{\varepsilon}_{cr} = \frac{C\sigma^{m}}{d^{n}} e^{-\frac{Q}{KT}} \tag{4}$$

Where, $\dot{\varepsilon}_{cr}$ is the creep strain rate, C are a constant dependent on the material and the particular creep mechanism, m and n are exponents dependent on the creep mechanism, Q is the activation energy of the creep mechanism, σ is the applied stress, d is the grain size of the material, k is Boltzmann's constant, and T is the absolute temperature

Finite Element Modeling of Crack region

Stress and deformation fields around the crack tip generally have high gradients. The precise nature of these fields depends on the material, geometry, and other factors. To capture the rapidly varying stress and deformation fields, use a refined mesh in the region around the crack tip (ANSYS 2016). For linear elastic problems, the displacements near the crack tip (or crack front) vary as

$\sqrt{r}$ where r is the distance from the crack tip. The stresses and strains are singular at the crack tip, varying as

$1/\sqrt{r}$ to produce this singularity in stresses and strains, the crack tip mesh should have certain characteristics:

- The crack faces should be coincident.

- The elements around the crack tip shown in Figure 3, Should be quadratic, with the mid side nodes placed at the quarter points. (Such elements are called singular elements)

The recommended element type for a 2-D fracture model is PLANE183, the 8-node quadratic solid. The first row of elements around the crack tip should be singular, as illustrated (figure 4). The PREP7 preprocessor's KSCON command which assigns element division sizes around a key point is particularly useful in a crack model. It automatically generates singular elements around the specified key point. Other fields on the command allow you to control the radius of the first row of elements, the number of elements in the circumferential direction, and more. Figure 3 shows a fracture model generated with the help of KSCON.

The use of singularity elements was adopted for FEM, because it was found to reduce the required refinement near the crack tip, also when the interaction integral is applied. An illustration of how the mesh is user defined near the crack tip, is shown in Figure 4. RRAT is here 0,5, as it can be seen that the CTSize is twice as large as CTSize*RRAT. Figure 5 shows how the refined region near the crack tip, when 4 rows of elements are used, and RRAT is set to 0,5. The rows of elements are numbered 1, 2, 3 and 4, and these are also the rows of elements that the interaction integral will be performed along. Thus, contour number 1 is the interaction integral performed along the 1st row of elements, contour number 2 would be the interaction integral performed along the 2nd row of elements

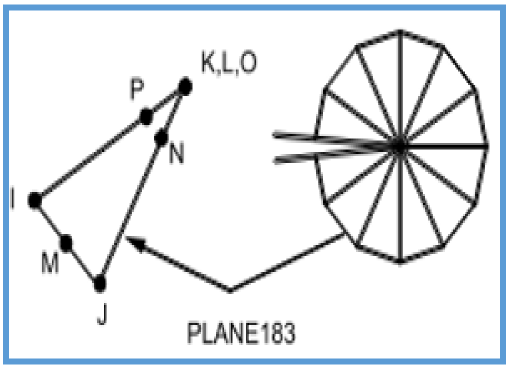

Figure 3. Singular finite element on ANSYS [5]

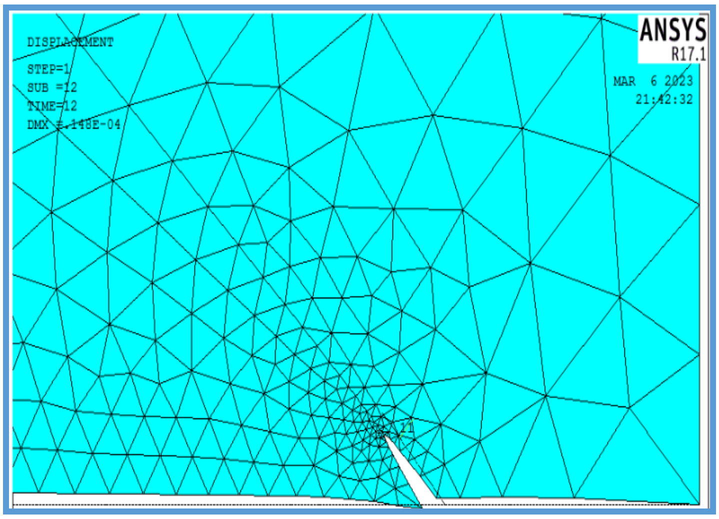

Figure 4. 2-D FEM crack modeling

The topic of the paper is to modeling the fracture mechanics, where the behavior of linear elastic fracture mechanics (LEFM) is taking into account. The general theory of LEFM, criteria and models for simulate the crack opening depending of time due to static loading is described. The finite element program Mechanical APDL 17.1, called ANSYS, is used to programme APDL code that simulate the crack of a 2D structure subjected for a load case. In order to conduct the APDL code user-friendly it is implemented in the ANSYS user interface menu GUI, by the user interface design language (UIDL).

Linear Fracture Mechanics Parameter Calculation

The fracture mechanics parameters describe either the energy-release rate or the amplitude of the stress and deformation fields ahead of the crack tip. The following parameters are widely used in fracture mechanics analysis:

- Stress-intensity factor
- Energy-release rate
- J-Integral

The stress intensity factor and energy-release rate are limited to linear elastic fracture mechanics. The J-Integral is applicable to both linear elastic and nonlinear elastic-plastic materials.

Stress-Intensity Factor

To evaluate stress distribution a stress intensity factor (SIF) is defined. The stress intensity factors represent the magnitude of the stresses around the tip of the singular point. The stress intensity factor (SIF) is considered to be the main parameter of the linear fracture mechanics. George Irwin formulates three different fracture modes (deformation) at the crack tip – opening, sliding and tearing shown at Figure 1. When it comes to determining the stress intensity factors (SIF) analytically, there are some closed form solutions. Where the required parameters to calculate the SIF are the geometry of the crack and the remote loading. SIF for the slanted through thickness crack in an infinite plate are given by:

$$\sigma_{ij} = -\frac{K}{\sqrt{r}} f_{ij}(\theta) \tag{5}$$

$$\varepsilon_{ij} = -\frac{K}{\sqrt{r}} g_{ij}(\theta) \tag{6}$$

Where K is the stress-intensity factor, r and θ arecoordinates of a polar coordinate system. These equations apply to any of the three fracture modes. For a Mode I crack, the stress field is given as:

$$\sigma_x = \frac{K_I}{\sqrt{2\pi r}}\cos(\frac{\theta}{2})\left(1 - \sin\left(\frac{\theta}{2}\right)\sin(\frac{3\theta}{2})\right) \tag{7}$$

$$\sigma_y = \frac{K_I}{\sqrt{2\pi r}}\cos(\frac{\theta}{2})\left(1 + \sin\left(\frac{\theta}{2}\right)\sin(\frac{3\theta}{2})\right) \tag{8}$$

$$\sigma_{xy} = \frac{K_I}{\sqrt{2\pi r}}\cos\left(\frac{\theta}{2}\right)\sin\left(\frac{\theta}{2}\right)\cos(\frac{3\theta}{2}) \tag{9}$$

Energy-Release Rate

The energy-release rate is based on the energy criterion for fracture proposed by Griffith and further development by Irwin. In this approach, the crack growth occurs when the energy available for crack growth is sufficient to overcome the resistance of the material (Anderson,2005).The energy-release rate G is defined in elastic materials as the rate of change of potential energy released from a structure when a crack opens. For example, the following Figure. 5 shown a crack of length 2a in a large elastic body with modulus E subject to a tensile stress (σ).

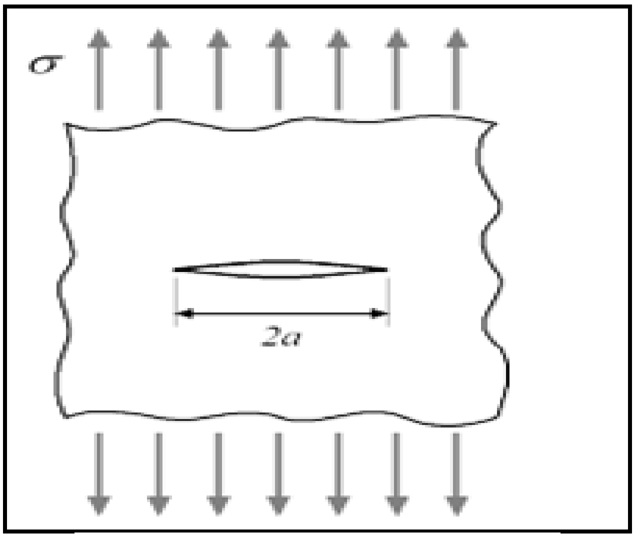

Figure 5. 2-D large plate with a 2a long crack

The energy-release rate is given by:

$$G = \frac{\pi\sigma^2 a}{E} \tag{10}$$

J- Integral

J-Integral is one of the most widely accepted parameters for elastic-plastic fracture mechanics. The J-Integral is defined as follows (Rice,1968):

$$J = \lim_{\Gamma\to 0}\int_{\Gamma_0}\left[(w+T)\delta_{ij} - \sigma_{ij}\frac{\partial U_j}{\partial X_i}\right]n_i\,d\Gamma \tag{11}$$

Where W is the strain energy density, T is the kinematic energy density, σij represents the stresses, U is the displacement vector, and Γ is the contour over which the integration is carried out.For a crack in a linear elastic material, the J-integral represents the energy-release rate. Also, the amplitudes of the crack-tip stress and deformation fields are characterized by the J-integral for a crack in a nonlinear elastic material.

Elastic Plastic Fracture Mechanics

Fracture/crack growth is a phenomenon in which two surfaces are separated from each other, or material is progressively damaged under external loading. The material in front of a propagating crack will be highly strained and all the points of the curve will be represented. Three different zones can be separated around the crack tip.

- The linear elastic zone: in this crack zone the stress is so low that the material behaves in a linear elastic way.
- The plastic zone: in this zone the stress – strain relation is non linear and the stress increases or at least remains constant as the strain increases
- The fracture zone: in this zone the stress decreases as the strain increases

The following parameter C*-integral characterizes the crack tip conditions in homogenous materials undergoing a secondary (steady-state) creep deformation (Riedel, 1980, Riedel, 1981) is widely used in fracture mechanics analysis:

$$C^* = \int_A \left[\sigma_{ij}\frac{\partial \dot{U}_j}{\partial X_i} - \dot{w}\,\delta_{ij}\right]\frac{\partial q}{\partial X_i}\,\mathrm{dA} \tag{12}$$

Where σij is the stress tensor, $\dot{U}_j$ is the displacement rate vector, $\dot{w}$ is the strain energy rate density, δ_{ij} is the Kronecker delta, X_i is the coordinate axis, and q is the crack-extension vector.

Modeling Creep Behavior

Creep is a rate dependent material nonlinearity in which the material continues to deform under a constant load ANSYS (2016). Creep is highly time dependent and it displays its effects over a long time. Creep has 3 stages: Primary, Secondary, and Tertiary creep as depicted in Fig 6. Descriptively, these stages areassociated with transient, steady state, and accelerating creep, respectively Betten(2002).The three phases of creep are described as follows:

- First Stage: It is considered by the work-hardening behavior of the material. It makes the material more difficult to deform under strain.
- Second Stage: Creep in this stage is steady state. In this stage, there is a balance work-hardening and thermal-softening which causes a constant and steady creep. (minimum creep rate)
- Third Stage: In this stage, creep accelerates due to the accumulating damage which will cause rupture at the end of the stage.

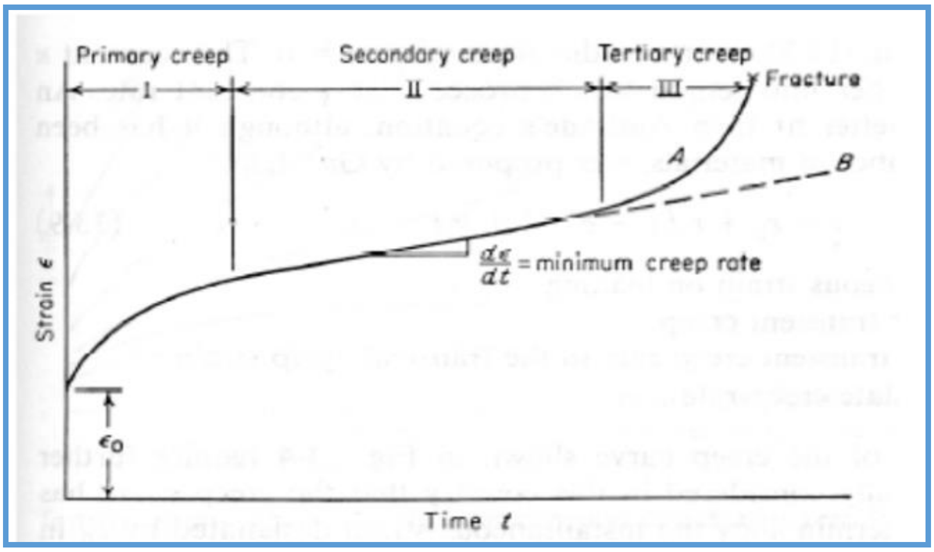

Figure 6. Creep curve typic under moderate load (1) and intense loading (2)
(Dieter, 1988; Ashby a& Jones, 1991)

Strain as a function of time due to constant stress over an extended period for a viscoelastic material. In the initial stage, or primary creep, the strain rate is relatively high, but slows with increasing time. This is due to work hardening. The strain rate eventually reaches a minimum and becomes near constant. This is due to the balance between work hardening and annealing (thermal softening). This stage is known as secondary or steady-state creep. This stage is the most understood. The characterized "creep strain rate" typically refers to the rate in this secondary stage. Stress dependence of this rate depends on the creep mechanism. In tertiary creep, the strain rate exponentially increases with stress because of necking phenomena.

General Creep Equation

The general creep equation is described as follows. $\dot{\varepsilon}_{cr}$ follows an Arrhenius type Law.

$$\dot{\varepsilon}_{cr} = \frac{C\sigma^{m}}{d^{b}} e^{-\frac{Q}{kT}} \tag{13}$$

Where $\dot{\varepsilon}_{cr}$ is the creep strain, C is a constant dependent on the material and the particular creep mechanism, m and b are exponents dependent on the creep mechanism, Q(J/mol) is the activation energy of the creep mechanism, σ is the applied stress, d is the grain size of the material, k(8.314 J/mol.K) is Boltzmann's constant, and T(Kelvin)is the absolute temperature.

At high stresses (relative to the shear modulus), creep is controlled by the movement of dislocations. For dislocation creep, Q = Q(self-diffusion), m = 4-6, and b = 0. Therefore, dislocation creep has a strong dependence on the applied stress and no grain size dependence In the Nabarro-Herring creep, atoms diffuse through the lattice causing grains to elongate along the stress axis; k is related to the diffusion coefficient of atoms through the lattice, Q = Q(self-diffusion), m = 1, and b = 2. This type of creep called (diffusion creep). Creep can be formulated as a function of several equations such as:

Primary Creep Equations

Traditionally, the transient creep observed in the primary creep stage is accounted for using Andrade's law for primary creep of the form Eq. (14).

$$\varepsilon_{cr} = \varepsilon_0 + At^{1/q} \tag{14}$$

Where: ε_0 is instantaneous creep, $At^{1/q}$ is a coefficient, and q is a unitless exponent. The constant q has been experimentally observed to be 3 for most materials (Andrade, 1910; Dvorkin,1994). A number of authors have attempted to disprove the uniformity of this constant with limited success (Nabarro, 1997). A more advantageous formulation for primary creep is based around a power law of the simple form Eq. (15):

$$\varepsilon_{cr} = A\sigma^{n}t^{m} \tag{15}$$

When stress is assumed to be constant, a primary creep time-hardening strain rate equation can be developed of the form Eq. (16):

$$\dot{\varepsilon}_{cr} = Am\sigma^{n}t^{m-1} \tag{16}$$

Where:σ (MPa) is the applied stress and A (MPa –nhr -m), n, and m are temperature-dependent primary creep constants (Pantelakis, 1983).

Secondary Creep Equations

The classical approach to modeling the secondary creep behavior for materials is the Norton power law Eq. (17) for secondary creep (Norton, 1929)

$$\dot{\varepsilon}_{cr} = A\sigma_{eq}^{n} \tag{17}$$

Where:A and n are the secondary creep constants, and σ_{eq} is an equivalent stress. ANSYS software give us a multitude formulation of secondary creep such as:

- Generalized Garofalo (Secandary stage):

$$\dot{\varepsilon}_{cr} = \{C_1 \sigma^{C_2}[(C_3+1)\varepsilon_{cr}]^{C_3}\}^{1/(C_3+1)} e^{(-C_4/T)} \tag{18}$$

- Time Hardening (primary +secondary models):

$$\dot{\varepsilon}_{cr} = \frac{C_1 \sigma^{C_2} t^{(C_3+1)} e^{-\frac{C_4}{T}}}{C_3+1} + C_5 \sigma^{C_6} t e^{(-C_7/T)/} \tag{19}$$

Finite Element Modeling of Creep

The Finite Element Analysis (FEA) method is a powerful computational technique for approximate solutions. ANSYS is engineering software, worldwide used by researchers for simulation. It develops general purpose of finite element analysis. To create the finite element model in ANSYS there are multiple tasks that have to be completed for the model to run properly. Models can be created using command prompt line input or the Graphical User Interface (GUI).

- The first step is to modeling the finite element structure by choosing an appropriate item to the type of analysis to be performed. As part of this work, we limited ourselves to address the problem in two-dimensional finite element used the element (PLANE 183) see Figs.7-8 bellow. In this model, the number of elements structural is approximately 177 elements.
- The 2nd step is divided into three, namely:

- Step pre-processor: who is to introduce the geometry of the problem, material properties and Boundary conditions.
- While in the solution phase, we choose the type of analysis that must be performed.
- Finally, the results of the completed solution are observed in the post-processing step.

In order to modeling the creep behavior, we have introduced the model equation called (***Modified Time hardening model***) see Eq. (20) bellow. It is considered that the material is isotropic, and the basic solution method used is that of Newton-Raphson

$$\varepsilon_{cr} = C_1 \sigma^{C_2} t^{C_3} e^{(-C_4/T)} \tag{20}$$

With: ε_{cr}: Creep strain, σ : Equivalent stress, t: Time at end of sub – steps, C1, C2, C3, C4 : Creep parameters : C1 = 41.10-8 1/s, C2 = 1.48, C3 = -0.63, C4= Q/K=0, T : Temperature in Kelvin

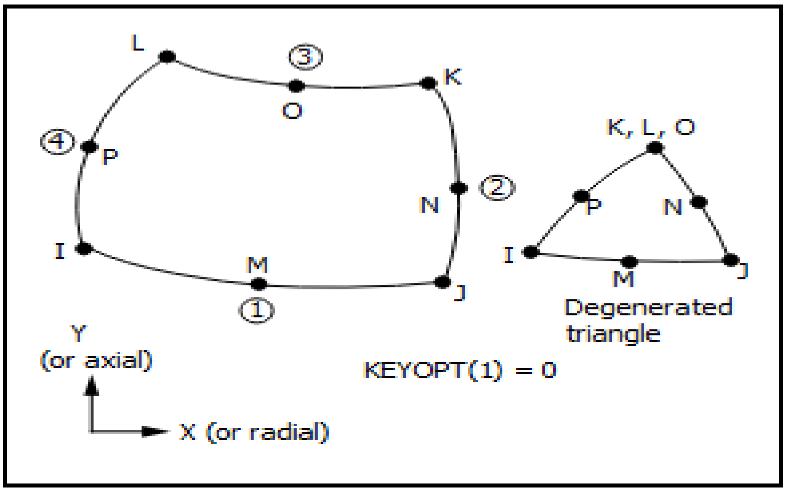

Figure. 7. PLANE 183 Geometry (ANSYS technology guide 2016)

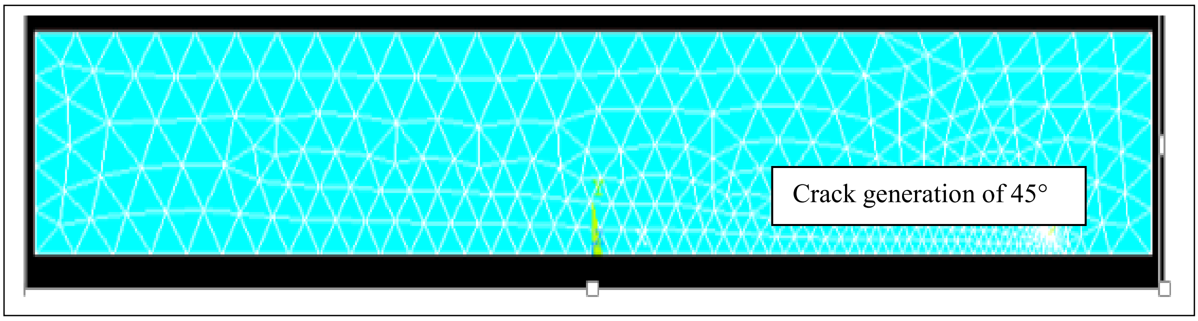

Figure 8. Beam cross section modeling

Results and Discussion

In order to conduct time-dependent numerical modeling, the finite element code ANSYS occurs the different results shown in the following figures. This Item illustrate a time-dependent behaviour of beam with crack opening subjected to a constant load. The following Figures 9, Figure 10, Figure 11, illustrate the stress contour plot, (σ_{xx}), (σ_{yy}) and the shear stress (τ_{xy}) of mode I obtained according to the equation 1 above and simulation resluts during 12 hours of constant loading.

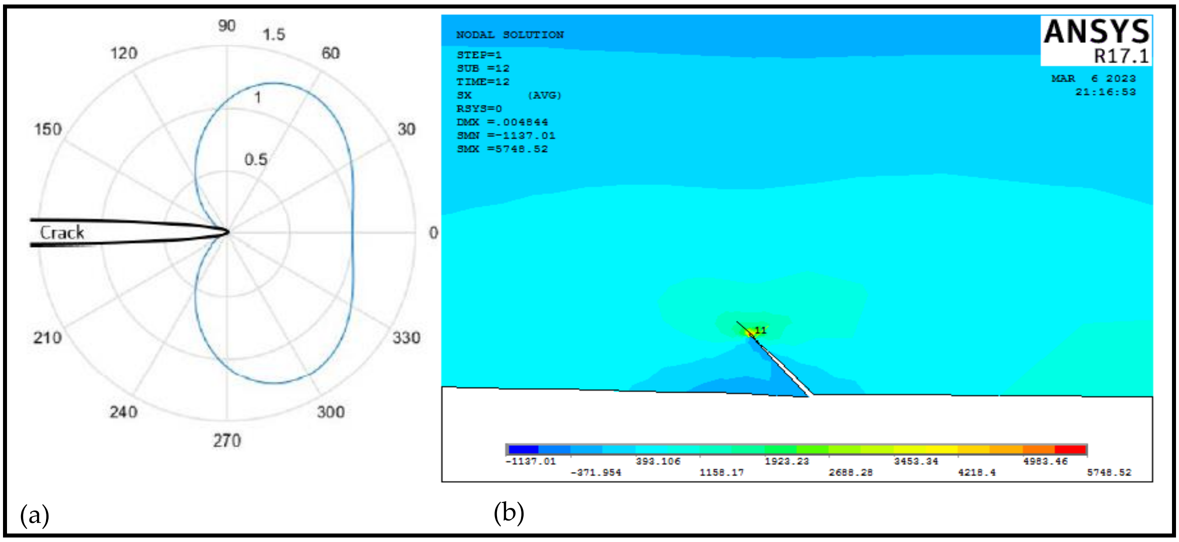

Figure 9. Contour plot of σ_{xx} stress components from Eq. 1 (a) and numericals results simulation of mode I

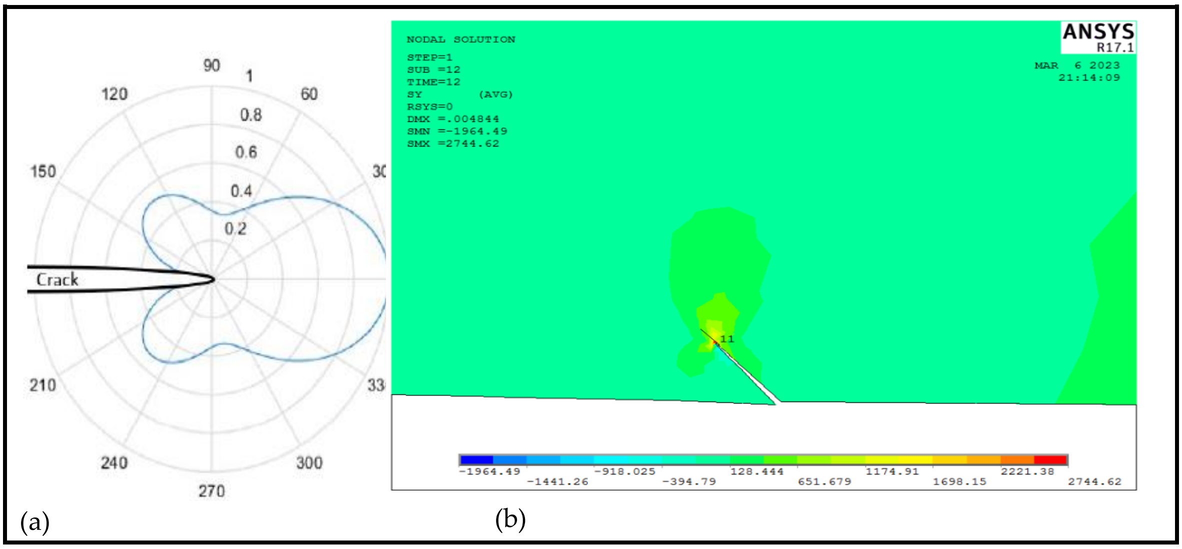

Figure 10. Contour plot of σ_{yy} stress components from Eq. 1 (a) and numericals results simulation of mode II

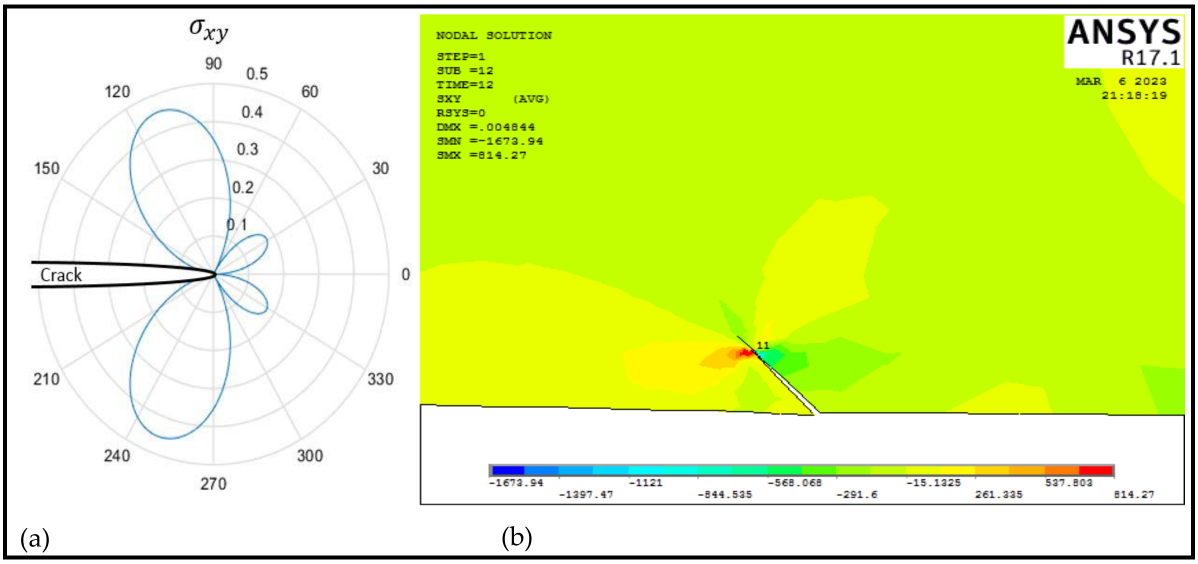

Figure 11. Contour plot of τ_{xy} Shear stress components from Eq. 1 and numericals results simulation of mode I

The following Figure 12 and Figure 13 illustrates the contour plot Creep Strain $(\varepsilon_X^{cr}, \varepsilon_Y^{cr})$ respectively obtained by the implemation of the creep equation 5 above, in the programme ansys softwar. Figure 14 illustrate the creep curve under different loading values of stress, such us 10 MPa; 25 MPa and 75 MPa respectively after 720mn (12hours).

According the figure, we can say than the creep strain curves are characterized by three steeps namely:

- 1st steep: t= 0 days: we note an initial strain (ε_0),
- 2nd steep: 0 days < t < 240 min : The Creep strain increase rapidly
- 3rd steep: 240 min < t < 720 min: The Creep strain increase slightly

From these results of creep curves obtained, we can be seen that the creep strains rate reaches 30% after 250 min. At 720min from loading, these deformations reach 6 times the initial strain. In terms of results of the creep behaviour simulation, the curves obtained according to the time hardening model correlate approximately with the experimental creep curve illustrated in figure 4 above. The difficulties encountered in the experimental test is how to determine the stress intensity factors in order to be able to compare them with the numerical results. The mains of these papers are to cite the creep behaviour and crack opening modelling with ANSYS softwar. Creep curves strain and shear creep curves numerical results of the different load values are show's in the above figures. In terms of perspective, we intend to compare the numerical results to the experimental results.

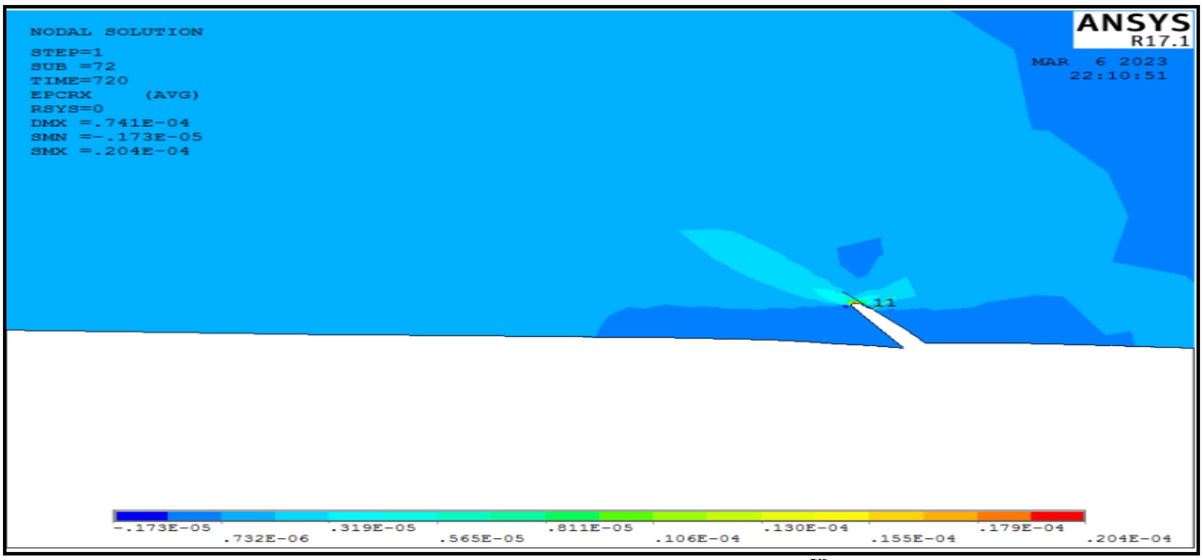

Figure 12. Contour plot of creep strain ε_x^{cr}

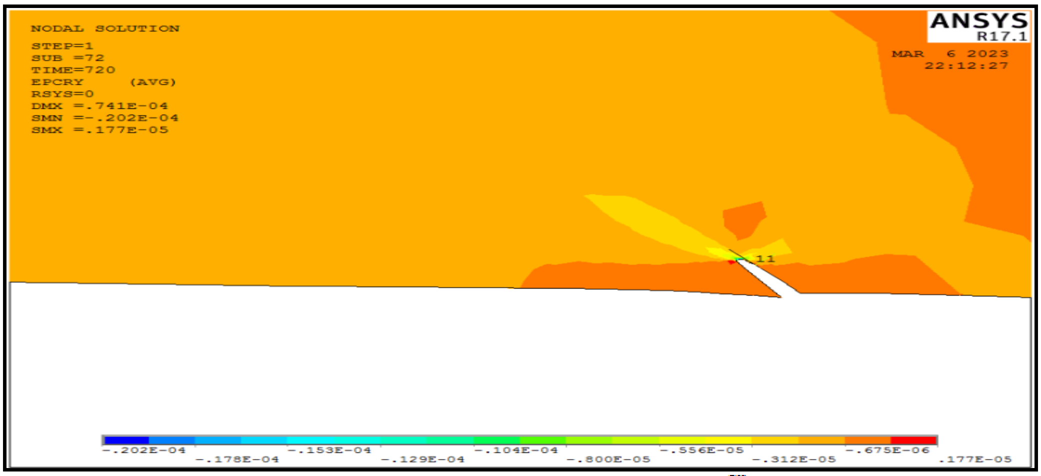

Figure 13. Contour plot of creep strain ε_Y^{cr}

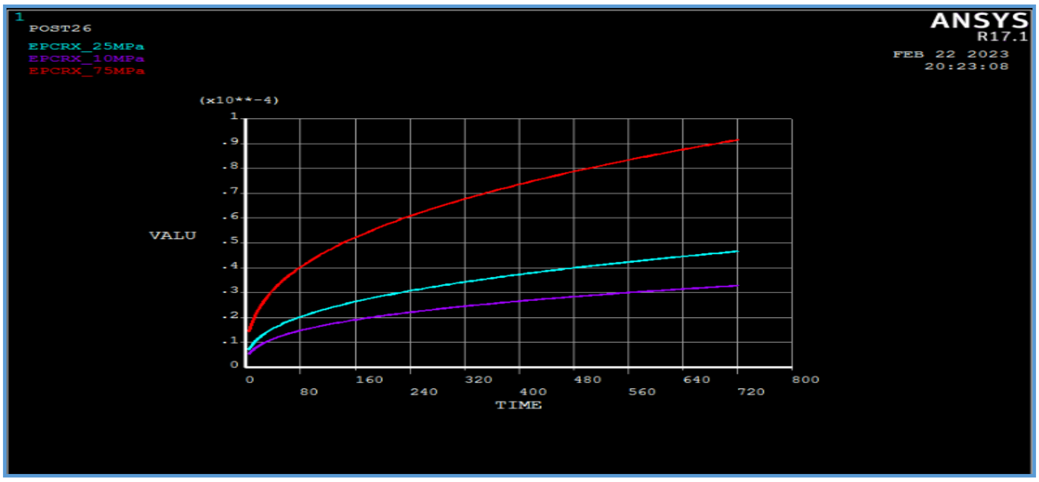

Figure 14. Creep curve (ε_{cr}) under different constant load after 720mn

Conclusion

A fracture analysis is a combination of stress analysis and fracture mechanics para calculation. The stress analysis is a standard linear elastic or nonlinear elastic plastic analysis. The work presented in this paper is a part of a research program, aimed at developing a model fracture mechanical suitable for analysing the micro and macro – fracture in the reinforced concrete beam and similar materials. In terms of conclusion, the creep behavior simulation, and the creep curves obtained according to the time hardening model correlate approximately with the experimental creep curve illustrated in figure 4 above. The difficulties encountered in the experimental test are how to determine the stress intensity factors in order to be able to compare them with the numerical results. The mains of these papers are to cite the creep behaviour and crack opening modelling with ANSYS software. Creep curves strain and shear creep curves numerical results of the different load values are show's in the above figures. in terms of perspective, we intend to compare the numerical results to the experimental results. The difficulties encountered in the experimental test is how to determine the stress intensity factors in order to be able to compare them with the numerical results. The mains of these papers are to cite the creep behaviour and crack opening modelling with ANSYS softwar. Creep curves strain and shear creep curves numerical results of the different load values are show's in the above figures. In terms of perspective, we intend to compare the numerical results to the experimental results.

Scientific Ethics Declaration

The authors declare that the scientific ethical and legal responsibility of this article published in EPSTEM Journal belongs to the authors.

Notes

This article was presented as a poster presentation at the International Conference on Technology, Engineering and Science (www.icontes.net) held in Antalya/Turkey on November 14-17, 2024.

References

Afgrow. (2015). *Handbook DTD*. Retrieved from http://www.afgrow.net

Anderson, T. L., *Fracture mechanics: fundamentals and applications* (2nd ed.). Boca Raton: CRC Press.

Andrade, E. N. D. C. (1910). On the viscous flow in metals, and allied phenomena. *Proceedings of the Royal Society of London. Series A, Containing Papers of a Mathematical and Physical Character*, *84*(567), 1-12.

ANSYS Technology Guide. (2016). ANSYS release 17.1 documentation. Retrieved from https://www.ansys.com

Ashby, M. F., Jones, D. R. H., & Bréchet, Y. (1996). *Matériaux: Propriétés et applications*. Dunod.

Bazant, Z. P., & Planas, J. (2019). *Fracture and size effect in concrete and other quasibrittle materials*. Routledge.

Betten, J. (2002). *Creep mechanics*. Newyork, NY: Springer.

Bjørheim, F. (2019). *Practical comparison of crack meshing in ANSYS mechanical APDL 19.2* (Master's thesis, University of Stavanger, Norway).

Dieter, G.E. (1988). *Mechanical metallurgy.* McGraw-Hill Book Company.

Dvorkin, J., Nur, A., & Yin, H. (1994). Effective properties of cemented granular materials. *Mechanics of Materials*, *18*(4), 351-366.

Nabarro, F. R. N. (1997). Thermal activation and Andrade creep. *Philosophical Magazine Letters*, *75*(4), 227-233.

Norton, F.H. (1929). *"The creep of steel at high temperatures.* McGraw-Hill: London.

Pantelakis, S. (1983). *Kriechverhalten metallischer werkstoffe bei zeitveranderlicher spannung* (Doctoral dissertation, RWTH Aachen University).

Petersson, P. E. (1981). *Crack growth and development of fracture zones in plain concrete and similar materials.* Retrieved from https://lucris.lub.lu.se/ws/portalfiles/portal/4631196/1607139.pdf

Rice, J.R. (1968). A path independent integral and the approximateanalysis of strain concentration by notched and cracks. *Journalof Applied Mathematics, 35*(2), 379-386.

Riedel, H. (1980). Tensile cracks in creeping solids." *Fracture Mechanics: Twelfth Conference American Society for Testing and Material (ASTM),* 112-130.

Riedel, H. (1981). Creep deformation at crack tips in elastic-viscoplastic solids. *Journal of the Mechanics and Physics of Solids*, *29*(1), 35-49.

Tada, H., Paris, P. C., & Irwin, G. R. (2000). *The stress analysis of cracks handbook (3rd ed.).* New York, N.Y, London: ASME Press Professional Engineering Publishing

Author Information

Kamel Ghouilem
University Mouloud MAMMERI of Tizi - Ouzou
Ummto, BP 17 RP, Tizi-Ouzou 15000, Algeria
E-mail: kamel.ghouilem@ummto.dz

Atlaoui Djamal
University Mouloud MAMMERI of Tizi - Ouzou
Ummto, BP 17 RP, Tizi-Ouzou 15000, Algeria

Mehaddene Rachid
University Mouloud MAMMERI of Tizi - Ouzou
Ummto, BP 17 RP, Tizi-Ouzou 15000, Algeria

Merakeb Seddik
University Mouloud MAMMERI of Tizi - Ouzou
Ummto, BP 17 RP, Tizi-Ouzou 15000, Algeria

To cite this article:

Ghouilem, K. Djamal A, Rachid, M., & Seddik, M. (2024). ANSYS creep modeling in a beam with 45° of opening crack. *The Eurasia Proceedings of Science, Technology, Engineering & Mathematics (EPSTEM), 32,* 41-52.

The Eurasia Proceedings of Science, Technology, Engineering & Mathematics (EPSTEM)
ISSN: 2602-3199

The Eurasia Proceedings of Science, Technology, Engineering & Mathematics (EPSTEM), 2024

Volume 32, Pages 53-65

IConTES 2024: International Conference on Technology, Engineering and Science

Comparative Analysis of Three Converters Providing Power to a Discharge Lamp-electronic Ballast System Designed for Water Sterilization

Aicha Aissa-Bokhtache
Hassiba Benbouali University of Chlef

Maamar Latroch
Hassiba Benbouali University of Chlef

Nadia Badni
Scientific and Technical Research Center in Physico-Chemical Analysis of Tipaza

Alla Eddine Toubal-Maamar
M'hamed Bougara University of Boumerdes

Lemya Djafer
Hassiba Benbouali University of Chlef

Amina Merini
Hassiba Benbouali University of Chlef

Abstract: Water, an essential resource, has faced a continuous decline in quality over the years. Addressing this concern is crucial, and UV-C technology emerges as a fitting solution, meeting both quality treatment and environmental preservation needs. The UV bactericidal concept involves generating ultraviolet rays in a treatment chamber containing water. Ensuring a reliable power supply to low-pressure mercury-argon discharge lamps is imperative for the efficacy of UV-C disinfection. This research aims to identify the most optimal power source. To achieve this, the discharge lamp-electronic ballast system will be energized by three different converter types. The first utilizes a conventional converter with a half-bridge rectifier and inverter, employing PWM control. The second employs a 4-cell serial multicell converter, adopting a direct control strategy. The third relies on a single-phase matrix converter. Therefore, modern converters utilizing semiconductor-based switches with high switching frequencies (above 50 kHz for MOSFETs) have been used in this study.

Keywords: Electronic ballast, Half-bridge inverter, Multi-cell converter

Introduction

To obtain disinfected water, there are two main types of processes in the literature, chemical processes which use oxidants such as chlorine, generating trihalomethanes which are considered carcinogenic and physical processes which use Ultraviolet radiation. Decontamination by UV-c has a germicidal or germistatic affect without generating harmful chemical effluents for the environment, hence its undeniable advantage. It is an economical process that respects the environment. In this work, we set ourselves the goal of supplying the system of low pressure mercury-argon discharge lamp-electronic ballast in the best conditions (current source which generates a current at high frequency (50 kHz) and the most possible sinusoidal (low THD)) in order to generate the maximum UV radiation at 253.7 nm with high germicidal power.

It seems that for discharge lamps, by increasing the supply frequency, the electrodes wear out more slowly and the life of the lamp increases. In this context, modern converters have been used consisting of switches based on semiconductor components with a high switching frequency (for MOSFETs the frequency is greater than 50 kHz). To choose the right converter for this type of application, we powered our discharge lamp-electronic ballast system with 3 different power supplies using a classic converter, a multi-cell converter and a matrix converter.

Our first system consists of an input filter (low pass), a rectifier, and a half-bridge inverter. The PWM control strategy was used. The second system is based on a serial multicell converter which implements floating capacitors whose voltages must be controlled. For this, the direct control strategy has been adopted. This new topology facilitates series connection, by ensuring a balancing of the voltages at the terminals of the switches in static mode (Aissa-Bokhtache et al., 2016; Aissa-Bokhtache et al., 2015; Aissa-Bokhtache et al., 2017). Finally we used a matrix converter, the latter allows the direct conversion of the frequency without having recourse to the continuous intermediate circuit which characterizes the conventional converters, as well as the elimination of the passive elements of storage of energy which strongly influence the intermediate circuit continuous, without forgetting that the symmetry of the matrix allows the flow of power in both directions (Costache, 2000; De Oro et al., 2014). These switching cells with fully controllable bidirectional switches provide it with frequency advantages. In order to obtain the desired amplitude and frequency, the PWM control strategy was used.

Description and Modeling of the Discharge Lamp-Electronic Ballast System

In this section, the description and modeling of the proposed discharge lamp-electronic ballast system are presented.

System Overview

Discharge lamps are devices where electrical, thermal and chemical phenomena are involved, which give rise to a complex system that is very difficult to model. The lamp power supply must be able to initiate the discharge and then control the electronic avalanche once triggered. Knowing the electrical characteristics of the load to be powered makes it possible to size the power supply for such a system. It is therefore important to establish a more detailed specification which will define the characteristics of our load.

So the supply of our system, discharge lamp-electronic ballast, must be made by a high frequency current source because the maximum UV radiation is obtained at high frequencies, (after calculation, the frequency used is 50 kHz) and with an effective arcing current of 0.65A (Aissa-Bokhtache et al., 2016). This arc current varies according to the temperature of the basin in which the lamp is immersed as well as the arc power. The maximum emission of UV radiation is achieved with a wave of 253.7 nm which is between 35 °C and 45 °C for the cold spot temperature (42 °C) (Aissa-Bokhtache et al., 2023). Figure 1 illustrates the reactor designed for water treatment using UV radiation.

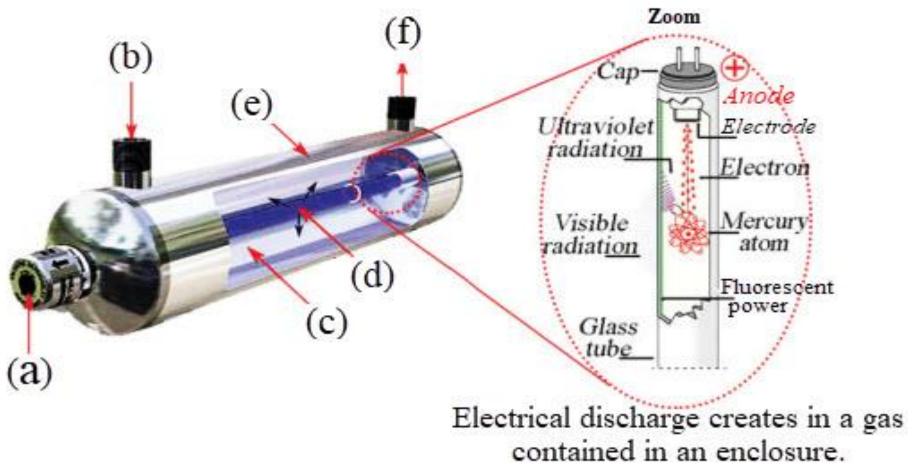

Figure 1. Reactor for water treatment by UV radiation, (a) End cap, (b) Water inlet to deal, (c) Chamber disinfection, (d) Ultraviolet rays, (e) Stainless steel chamber, (f) Disinfect water.

Model of the Electric Circuit of the Discharge Lamp

Our lamp model is represented by resistor "R_{arc}" depending of a lamp arc power and temperature and an "r_f" resistor for each cathode filament as shown in Figure 2.

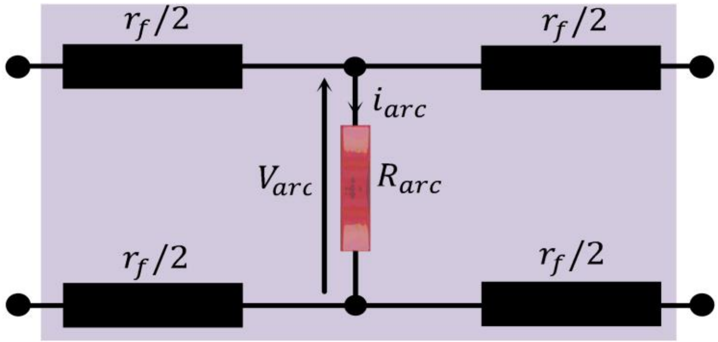

Figure 2. Model of the electric circuit of the gas-discharge lamp

Figure 3 summarizes the system studied: Discharge lamp-electronic ballast powered by a converter.

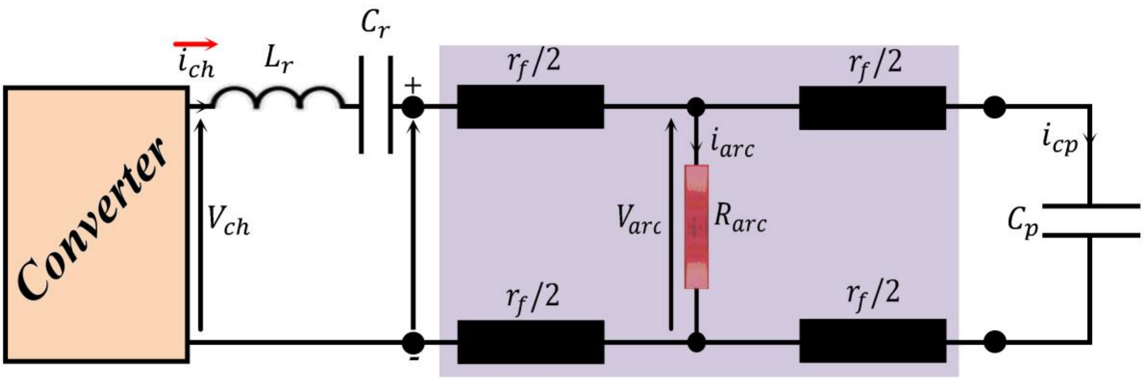

Figure 3. Equivalent circuit of electronic ballast-discharge lamp with converter

Characteristics of the Discharge Lamp

The lamp used in the simulation is a real discharge lamp described in references (Aissa Bokhtache et al., 2023), the main characteristics of the discharge lamp-electronic ballast are given in (Table1) below:

Table 1. Characteristics of the discharge lamp-electronic ballast assembly

Variables	Symbol	Values
Capacitance	C_r	*147 nF/ 250 V*
Capacitance	C_P	*8.2 nF/ 600 V*
Inductance	L_r	*1.08 mH*
Power	P_{Lamp}	*65 W*
Frequency	f	*50 KHz*
Resistance	R_{arc}	*170.769 Ω*
Resistance	r_f	*5 Ω*
Length	L_{tube}	*150 cm*
Current	I_{arcrms}	*0.65 A*

The consideration of R_{arc} and r_f allows us to better describe the behavior of our discharge lamp. The modeling allowed us to obtain the following transfer function, qualified as complete:

$$\frac{I_{arc}}{V_{ch}} = \frac{r_f C_r C_p S^2 + C_r S}{\left(R_{arc}+r_f\right) L_r C_r C_p S^3 + \left[\left(2R_{arc}+r_f\right) L_r C_r C_p + L_r C_r\right] S^2 + \left(R_{arc}+r_f\right)\left(C_r + C_p\right) S + 1} \quad (1)$$

With : r_f: filament resistor, R_{arc}: arc resistance, Z_{cp} : starter impedance, i_{arc}: arc current, V_{arc} :arc voltage, i_r: load current, i_{cp}: starter current, V_{lamp} :lamp voltage, L_r , C_r: resonant circuit parameters, C_p: starter capacitor. We propose to power our discharge lamp-electronic Ballast system by 3 converters to finally choose the best power supply which is in fact a current source generating a sinusoidal current with the lowest possible THD and a high frequency of 50kHz.

Method

The proposed discharge lamp-electronic ballast system is tested using three different converters, each regulating the arc current through a PI controller. Initially, the system is powered by a conventional converter. Next, it is powered by a multicell converter. Finally, the system is powered using a matrix converter.

Power Supply of the System by a Conventional Converter

Figure 4 depicts the system with a conventional converter. Characteristics of the conventional converter (Aissa Bokhtache et al., 2023) are: $C_{F1} = C_{F2} = 47\mu F$/ 250 V, L_f = 8.2 nF/ 600 V, and C_f = 220 nF / 630 V.

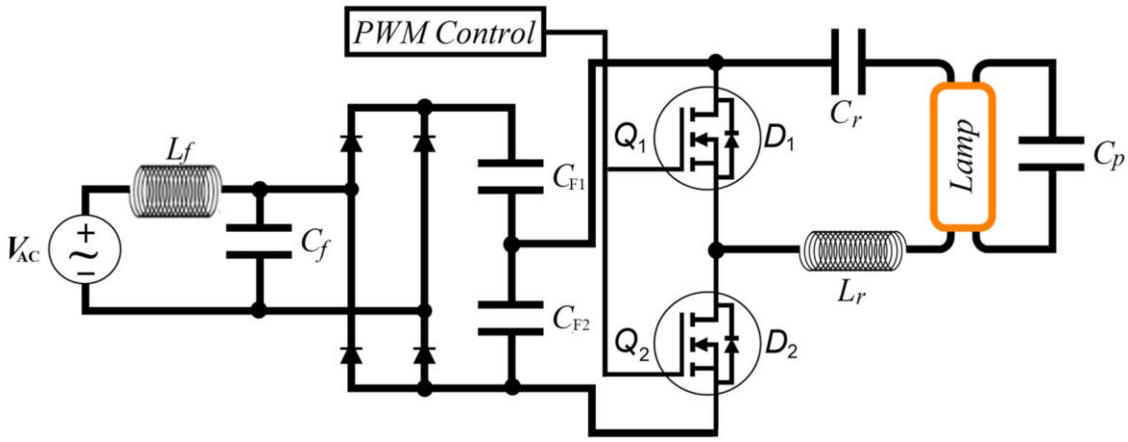

Figure 4. Electronic ballast structure using a conventional converter

Figure 5 depicts the voltage and the arc current of the discharge lamp. The voltage and the arc current of the discharge lamp are modulated at a frequency of 50 kHz and are contained in an envelope which oscillates at 1 kHz with a modulation rate (maximum value / value minimum) equal to approximately 5 and that the effective value of the arcing current of the lamp oscillates at the frequency of the envelope of the supply current which is evaluated at 1kHz. The THDs of the arc voltage and arc current of our discharge lamp are equal to 6.51% and 10.41%, respectively (as shown in Figure 6). A direct consequence of this ripple in the rms current value is a decrease in the mean time between system failures, as well as deterioration in lamp efficiency and effectiveness in germicidal treatment.

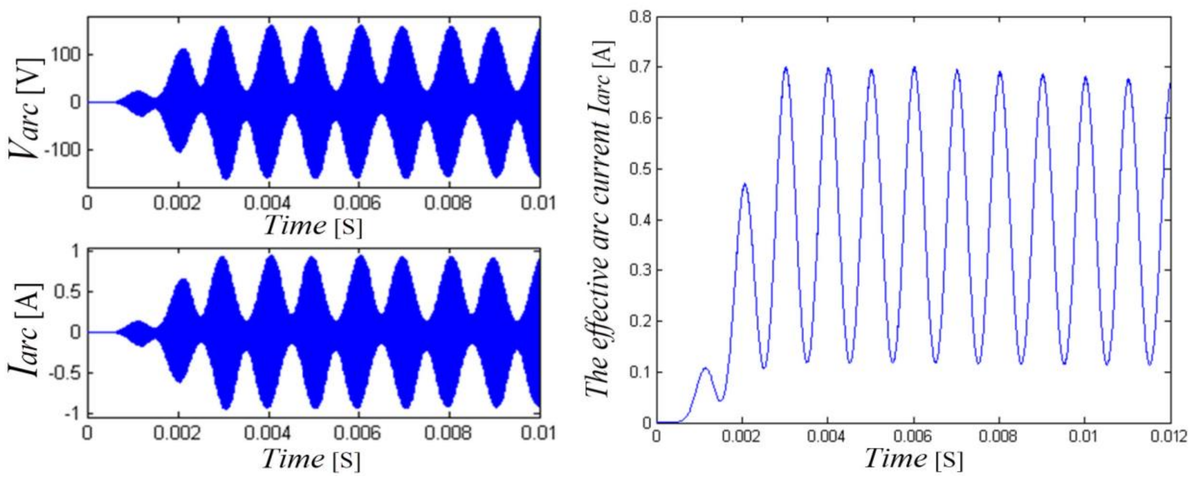

Figure 5. Representation of currents and arc voltage of the discharge lamp

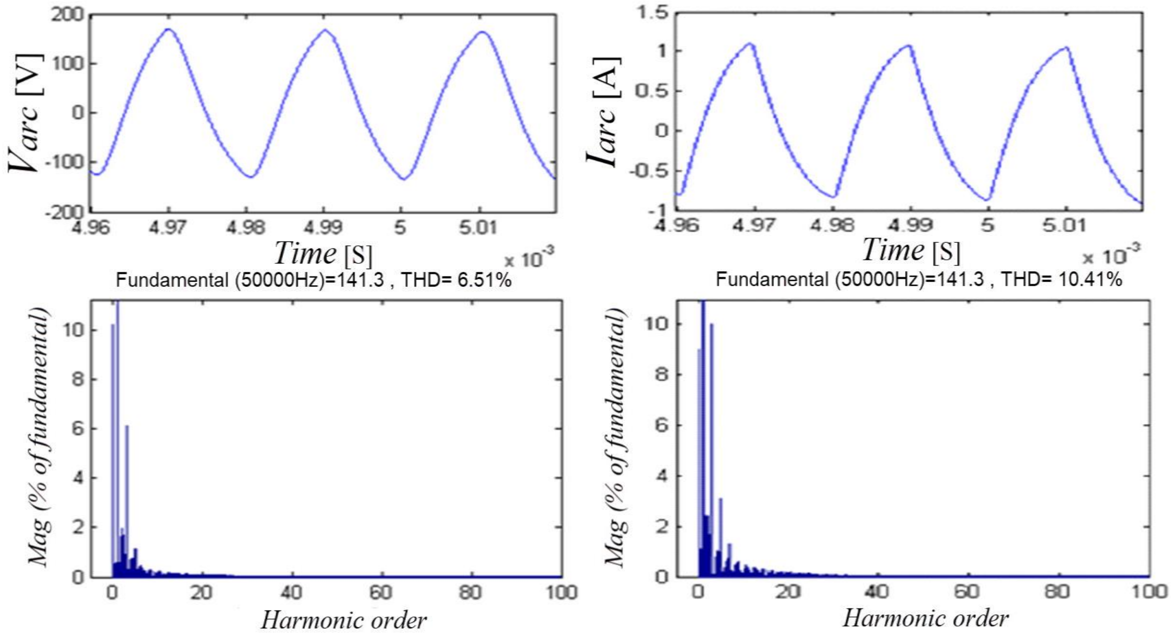

Figure 6. Distortion rate of discharge lamp arc voltage and current

These poor performances of the open-loop system lead us to consider a closed-loop system with PI regulator of the arc current (Aissa- Bokhtache et al., 2016). The block diagram of the system with PI controller is illustrated in Figure 7.

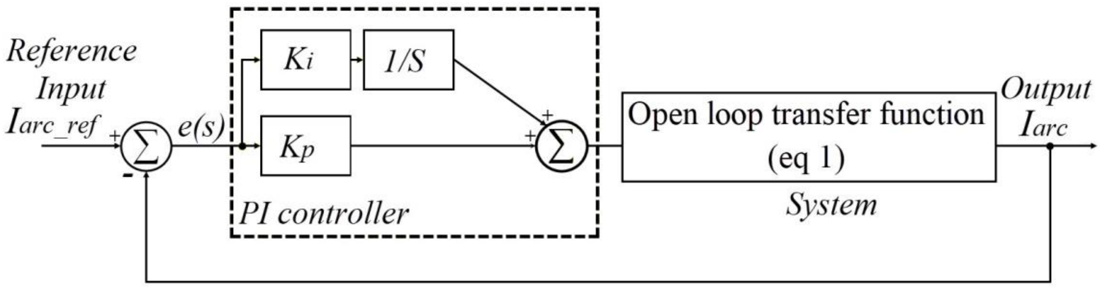

Figure 7. Closed-loop control system with PI controller

The transfer function C(S) of the proportional-integral controller is given by:

$$C(S) = K_p + \frac{K_i}{S} \tag{2}$$

Where: K_p, and K_i are the controller gains calculated using pole placement method, K_p = 0.0081 and K_i = 0.0091. The closed-loop transfer function (TFCL) of the system can be calculated by:

$$TFCL(S) = \frac{C(S).G(S)}{1 + C(S).G(S)} \tag{3}$$

Where: $G(s)$ is the open-loop transfer function of the system.

Figure 8 depicts the voltage and the arc current of the discharge lamp in closed-loop control system with PI controller. The figure clearly shows the improvements made to the waveforms compared with those of the open-loop simulation (Figure 5). Indeed the introduction of the PI in the closed loop eliminated the oscillations of the envelopes, one notes that after the transitory mode, the amplitudes become constant and the system is more stable.

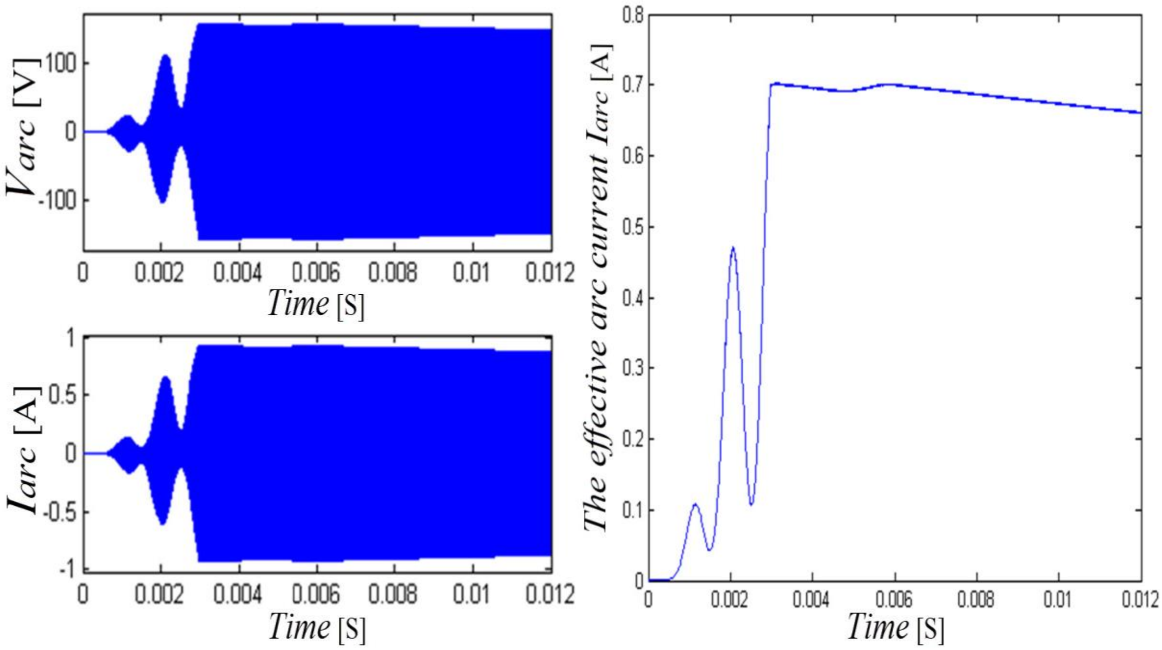

Figure 8. Closed-loop control system with PI controller

Power Supply of the System by a Multicell Converter

Figure 9 depicts the system with a multicell converter. It is an inverter assembly with multiple cells of a switching type cell (with a capacitive midpoint). This structure is composed of (P = 4) switching cells, separated from each other by P-1= 3 floating capacitors. The five voltage levels obtained by this inverter give it frequency advantages and allow it to obtain a good current source, of high quality both in terms of waveform and frequency response (Aissa-Bokhtache et al., 2020; Aissa-Bokhtache et al., 2021; Aimé et al., 2004). Characteristics of the Midpoint Series Four Cell Inverter (Aissa-Bokhtache et al.,2023) are:
E = 800 V, $C_1 = C_2 = C_3 = 5$ nF, $f_{dec} = 3{,}2$ MHz, $f_{mod} = 50$ KHz.

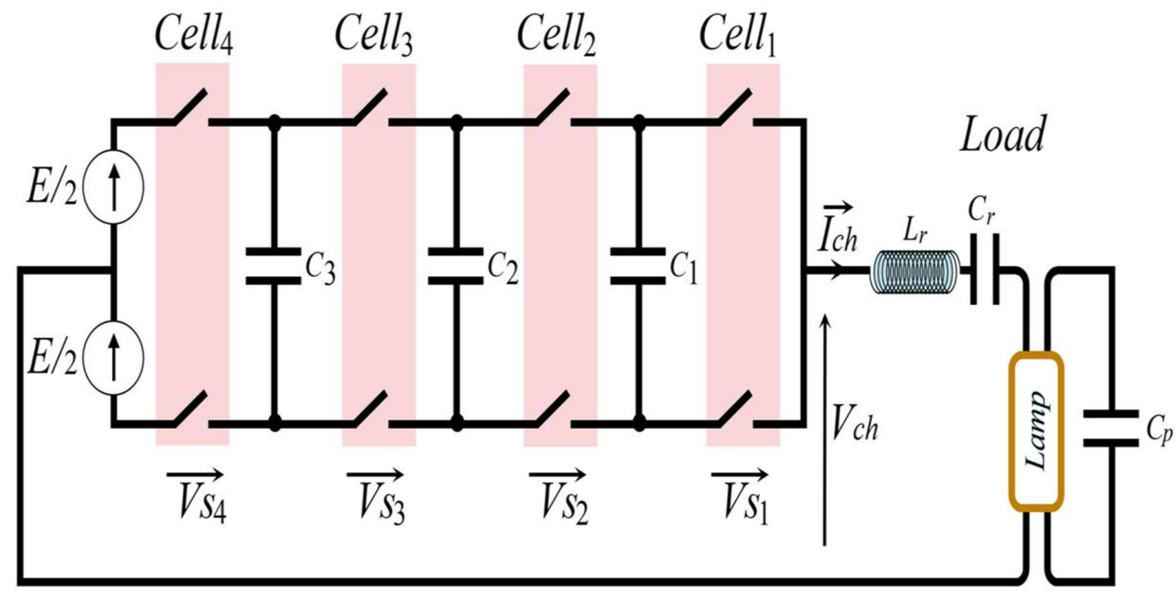

Figure 9. Voltage Source Midpoint Series Four Cell Inverter

The instantaneous modeling of the converter gives us the following system of equations:

$$
\begin{cases}
\dfrac{dV_{C_1}}{dt} = \dfrac{1}{C_1}\left(u_2 - u_1\right) I_{LOAD} \\
\dfrac{dV_{C_2}}{dt} = \dfrac{1}{C_2}\left(u_3 - u_2\right) I_{LOAD} \\
\dfrac{dV_{C_3}}{dt} = \dfrac{1}{C_3}\left(u_4 - u_3\right) I_{LOAD} \\
V_{LOAD} = \left(\left(u_1 - u_2\right) V_{C_1} + \left(u_2 - u_3\right) V_{C_2} + \left(u_3 - u_4\right) V_{C_3} + u_4 E - \dfrac{E}{2} \right)
\end{cases} \tag{4}
$$

We use the direct command to control the switches. Direct control aims to maintain the voltages across the floating capacitors at their desired reference values, both in static and dynamic conditions. Also, it ensures that the output voltage of the converter meets the required discrete level. To achieve this, the control algorithm considers two key factors:

1- Knowledge of the required discrete voltage level: The control algorithm takes into account the specific voltage level needed at the converter's output. The output voltage can have (p + 1) possible values, with each level ideally having a predetermined amplitude.

$$V_j = j \times \frac{E}{p}, \qquad j = 0,1,2,.......p \tag{5}$$

2- Knowledge of the state of the floating capacitors' voltages relative to their equilibrium values: The control algorithm also considers the voltages across the floating capacitors and their relationship to the desired equilibrium state. Each floating capacitor can be in one of three states:

- ✓ Equilibrium state: Capacitor's voltage level falls within an allowable range around its equilibrium value.
- ✓ State of higher imbalance: The capacitor's voltage level exceeds the allowable range.
- ✓ State of lower imbalance: The capacitor's voltage level falls below the allowable range.

Table 2 gives the theoretical output voltage V_{ch}, charging or discharging capacitors (C_1, C_2, C_3) according to the control of the switches (u_1, u_2, u_3, u_4) and the direction of the current (+*I*, -*I*).

Table 2. Output voltage level with corresponding conducting switches

Output voltage V_{ch}					Switch control				Balancing capacitors						Nº
									C_1		C_2		C_3		
-E/2	-E/4	0	E/4	E/2	U_1	U_2	U_3	U_4	+*I*	-*I*	+*I*	-*I*	+*I*	-*I*	
×					0	0	0	0	0	0	0	0	0	0	1
	×				0	0	0	1	0	0	0	0	+	-	2
	×				0	0	1	0	0	0	+	-	-	+	3
		×			0	0	1	1	0	0	+	-	0	0	4
	×				0	1	0	0	+	-	-	+	0	0	5
		×			0	1	0	1	+	-	-	+	+	-	6
		×			0	1	1	0	+	-	0	0	-	+	7
			×		0	1	1	1	+	-	0	0	0	0	8
	×				1	0	0	0	-	+	0	0	0	0	9
		×			1	0	0	1	-	+	0	0	+	-	10
		×			1	0	1	0	-	+	+	-	-	+	11
			×		1	0	1	1	-	+	+	-	0	0	12
		×			1	1	0	0	0	0	-	+	0	0	13
			×		1	1	0	1	0	0	-	+	+	-	14
			×		1	1	1	0	0	0	0	0	-	+	15
				×	1	1	1	1	0	0	0	0	0	0	16

Table 2 illustrates that the converter is capable of generating five distinct voltage levels. However, to achieve better accuracy in controlling discharge lamps, it is advantageous to generate seventeen voltage values. This can be accomplished by employing four voltage levels during a single switching period, allowing for more precise control. Figure 10 depicts the schematic representation of the voltages to be generated; the top portion shows the voltages that can be generated using the five basic levels, while the bottom portion displays the voltage thresholds necessary for controlling the switches.

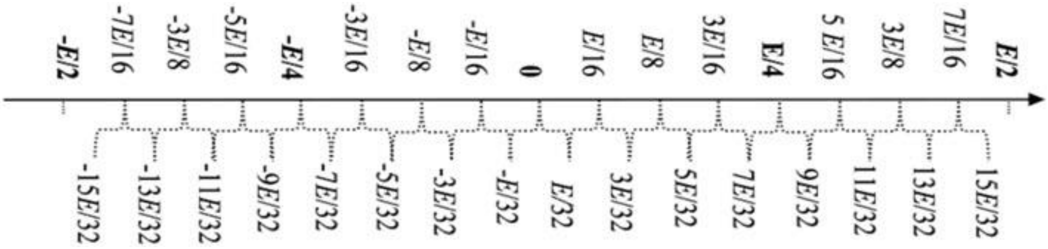

Figure 10. Schematic representation of the voltages to be generated

In the following figures we present the simulation results concerning a series multicell inverter formed by four midpoint cells, supplying the discharge lamp. Figure 11 depicts the curves of discharge lamp Arc voltage and current. RMS Arc current and flying capacitors voltages are shown in Figure 12.

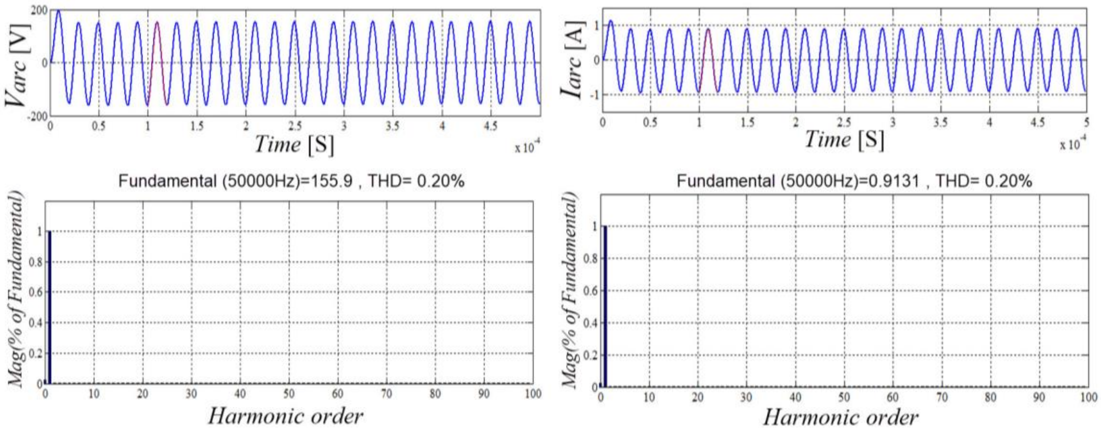

Figure 11. Discharge lamp arc voltage and current

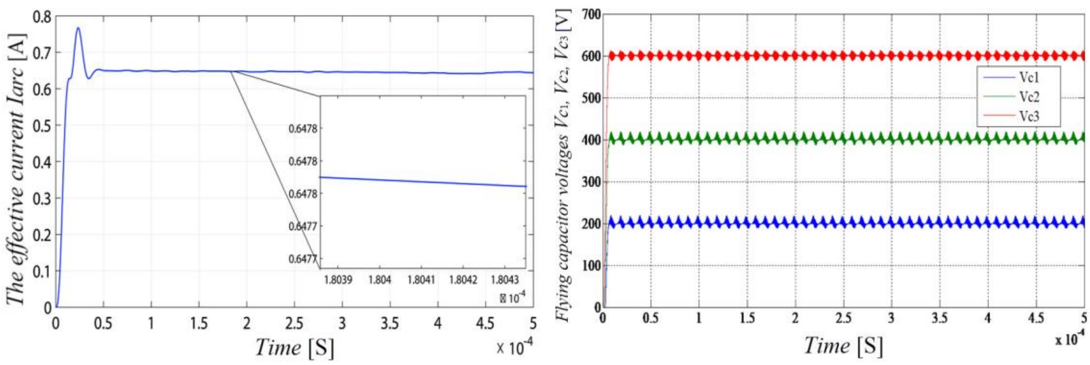

Figure 12. (a) RMS arc current, (b) Flying capacitor voltages

According to Figure 11, the waveforms of the arc voltage and current are sinusoidal, their frequencies are identical to the frequency of the modulating (50kHz) with a harmonic distortion rate of 0.20% for both. This means that the arc voltage and arc current are in phase. This means that the discharge lamp behaves like a simple resistor in arc mode. We also note in Figure 12(a) that the effective value of the arc current has actually reached the desired value which is 0.65A after 40 µs with an accuracy of 0.001A. According to the Figure 12(b), voltages at the terminals of the floating capacitors stabilizes at the values (k×E/P) corresponding to Vc_1 = 200V, Vc_2 = 400 V, and Vc_3 = 600 V, at the instant (20 µs). the effective arcing current stabilizes at 0.65 A (desired value) after 60 µs.

The introduction of a classic PI in the closed loop of the system has significantly improved the THDs, as shown in the following Figures. Figure13 depicts the lamp Arc voltage and current and their Harmonic spectrum with PI regulator. Figure 14 depicts the RMS arc current of the lamp with a PI regulator.

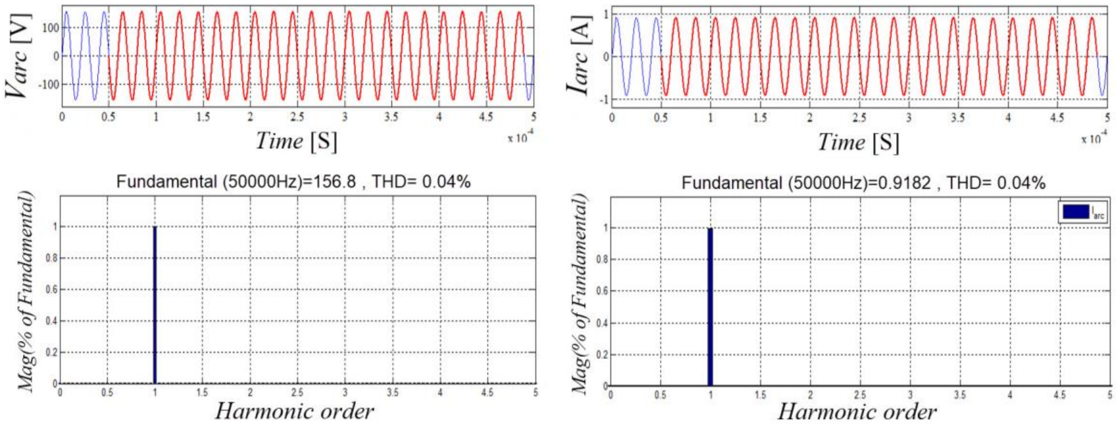

Figure 13. Lamp Arc voltage and current and their Harmonic spectrum with PI regulator

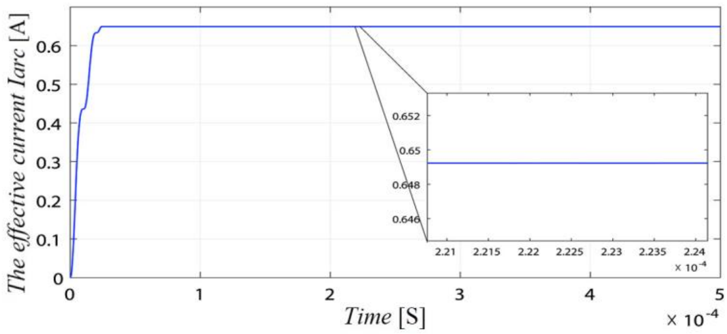

Figure 14. RMS arc current of the lamp with a PI regulator

We note that the arc current perfectly follows the sinusoidal reference that we imposed on our lamp (the frequency = 50 KHz), in Figure 13, with response time of 27 µs to reach 0.65 A depicted in effective value curve in Figure 14. We also notice a considerable improvement on the THD level which is 0.04% compared to the simulation on open loop which is 0.20%.

Power Supply of the System by a Matrix Converter

Figure 15 depicts the system with a Matrix converter. This converter is characterized by a matrix topology of four switches (matrix [2x2]), (Toumi et al., 2013), such that the two input phases of the network are interconnected to the two output phases of the converter by means of bidirectional power switches (Zuckerberger et al., 1997; Friedli et al., 2012).

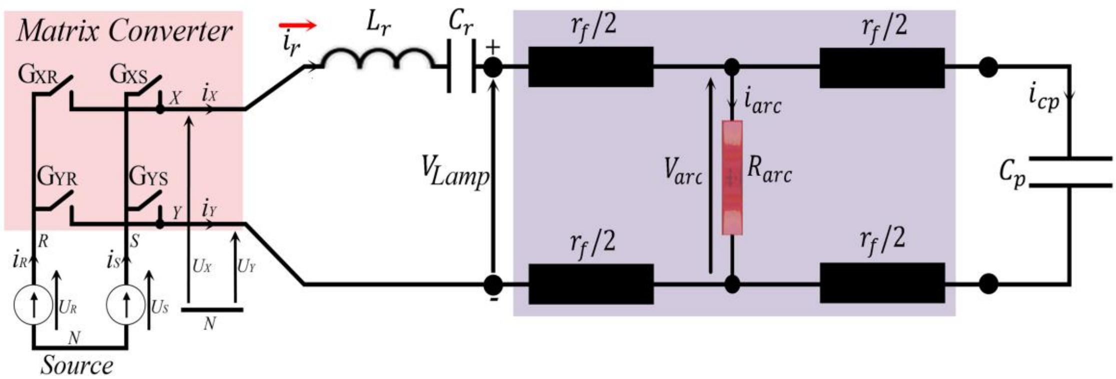

Figure 15. Discharge lamp-electronic ballast system powered by a matrix converter

Figure16 shows the lamp arc current and voltage waveforms and their THDs. Note that the arc voltage and current envelopes oscillate at a frequency of 100 Hz. Curves show that the arc current and voltage oscillate at the desired frequency which is 50 kHz with a distortion rate of 1.98% for the arc current and the arc voltage. Also, we note that the current and the voltage are totally in phase with the same THD. This is explained by the fact that the electric arc of the lamp is characterized by a resistance R_{arc}. The voltage and current waveforms are perfectly sinusoidal in steady state operation.

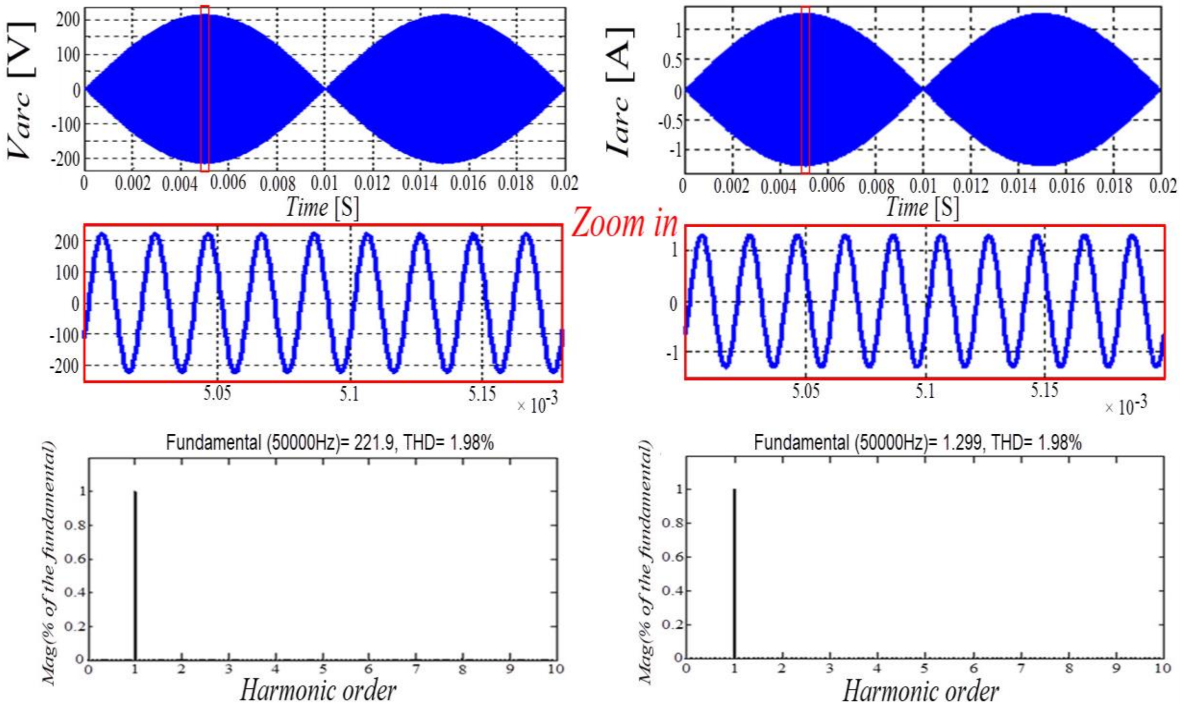

Figure 16. Waveforms of arc current and voltage of the lamp and their harmonic spectrum in open-loop

Figure 17 depicts the RMS arc current in open-loop case, when the system is powered by a matrix converter. The curve shows that the effective arc current is stabilized at 0.65A (the desired value) after a transient state of about 0.0195 Seconds.

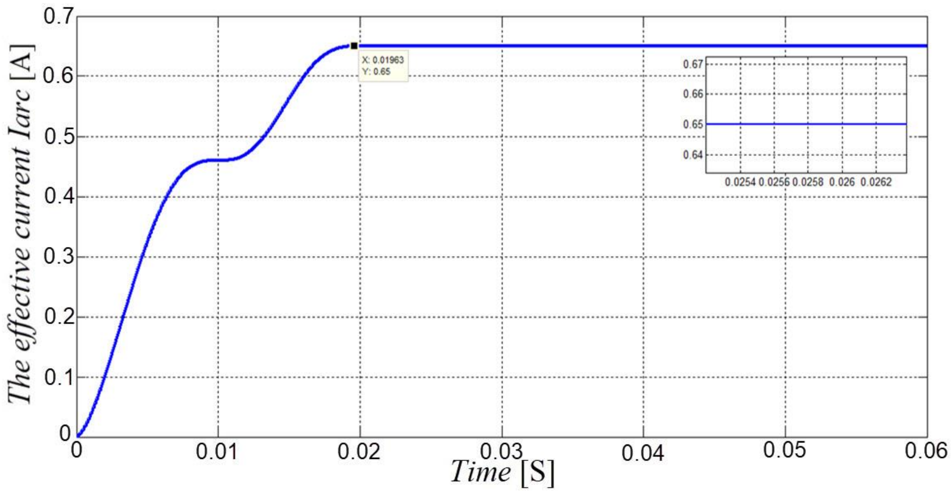

Figure 17. RMS arc current in open-loop

As the previous two cases using the conventional and the multicell converters, we impose arc current regulation using matrix converter with a reference of 0.65A. The difference will be transformed into the switching frequency of the switches. We use the pole placement method to calculate the gains of the classical PI controller. The calculated K_P and K_I values are: $K_P = 5.345\times10^{20}$ and $K_I = 3.095\times10^{24}$. Figure 18 illustrates the waveforms of arc current and voltage of the lamp and their harmonic spectrum in closed-loop case.

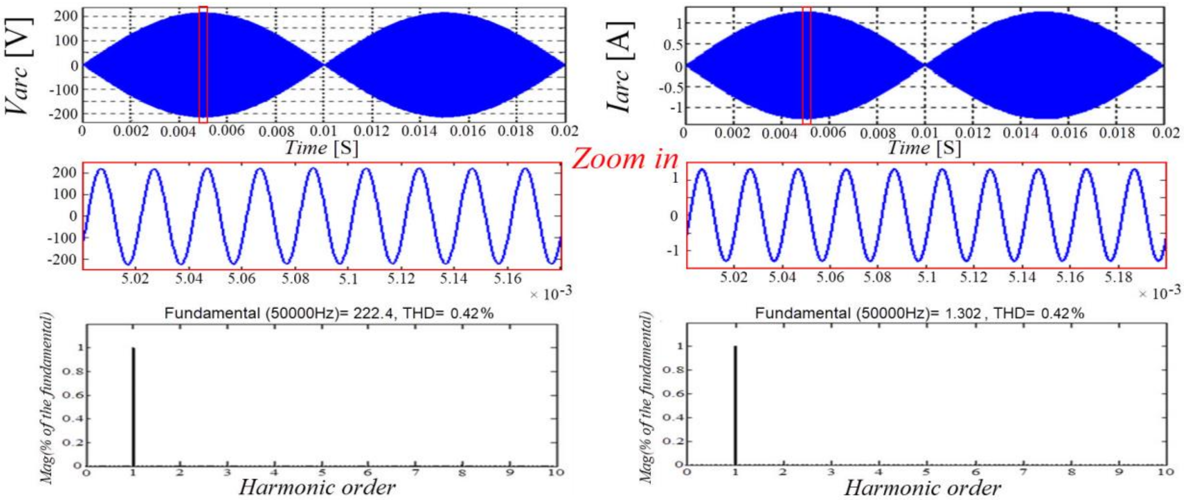

Figure 18. Waveforms of arc current and voltage of the lamp and their harmonic spectrum in closed-loop

We can see from the Figure 18 that the arc current and the arc voltage are totally in phase with the same THD. The voltage and current waveforms are perfectly sinusoidal in steady state with a frequency of 50 kHz. The THD is improved (0.42% with introduction of the PI in the regulation loop against 1.98% in open-loop). Figure 19 shows the RMS arc current in closed-loop case, when the system is powered by a matrix converter. The effective arc current is stabilized at 0.65A (the desired value) after a transient state of about 0.01 Seconds.

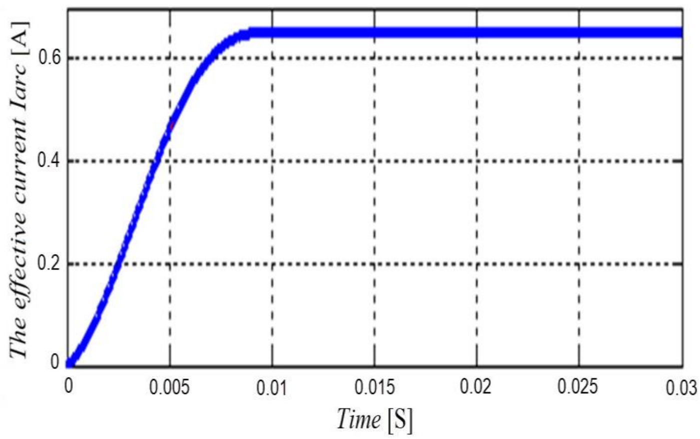

Figure 19. RMS arc current in closed-loop

Results Comparison

To clearly illustrate the advantages of the converter topologies discussed, a comparative analysis has been conducted between the conventional converter, multi-cell converter, and matrix converter, as summarized in Table 3. The key parameters evaluated for comparison include transient response (in milliseconds) and total harmonic distortion (THD). From Table 3, we observe that the results obtained using the series multicellular converter are the best, as it behaves like a good current source, delivering a sinusoidal current at its output (with almost zero THD), without ripples even in open-loop.

Table 3. Comparison between the results of the three converters

Type of converter		Waveforms	THDs (%)	Transient regime (ms)
Classic	Open-loop	*arc* current ripple with 1 kHz	10.41	2.5
Converter	Closed-loop	Eliminates of *Iarc RMS* oscillations	5.59	3
Multi-cell	Open-loop	Sinusoidal signal without envelope	0.20	0.043
Converter	Closed-loop	Waveform improvement	0.04	0.025
Matrix	Open-loop	Envelope of 100 Hz	1.98	19.5
Converter	Closed-loop	Envelope of 100 Hz	0.42	9.5

Conclusion

The objective of this study was to develop the most optimal current source for powering the discharge lamp-electronic ballast system used in water purification. The serial multicell converter functions as an efficient current source, delivering a sinusoidal current with nearly zero THD and no ripple, even in open-loop operation. It operates at a frequency of 50 kHz with an RMS value of 0.65 A, generating maximum UV radiation at 253.7 nm. This ensures optimal power delivery to the system, resulting in an effective germicidal action.

Scientific Ethics Declaration

The authors declare that the scientific ethical and legal responsibility of this article published in EPSTEM Journal belongs to the authors.

Acknowledgements or Notes

* This article was presented as an poster presentation at the International Conference on Technology, Engineering and Science (www.icontes.net) held in Antalya/Turkey on November 14-17, 2024.

References

Aimé, M., Gateau, G., & Fadel, M. (2004). Commande des convertisseurs multi cellulaires série à fréquence fixe en mode courant : Control of serial multi-cellular converters at fixed frequency in current mode. *CIFA'04, Douz, (Tunisie)*, 22–24.

Aissa-Bokhtache, A., Zegaoui, A., Kellal, M., Boucherit, M.S., Belmadani, B., & Aillerie, M. (2016). Optimization based on fuzzy logic control of discharge lamp-electronic ballast system for water purification. *Electric Power Components and Systems*, *44*, 1981–1990.

Aissa-Bokhtache, A., Zegaoui, A., Belmadani, B., & Boucherit, M.S. (2015). Water purification by a lamp discharge-electronic ballast system using a full bridge inverter. *Energy Procedia*, *74*, 446–452.

Aissa-Bokhtache, A., Zegaoui, A., Aillerie, M., Djahbar, A., Allouache, H., Hemici, K., Kessassia, F.Z, & Bouchrit, M. S. (2017). Power supply improvements for ballasts-low pressure mercury/argon discharge lamp for water purification. *AIP Conference Proceedings 1814*, 020059, doi: 10.1063/1.4976278.

Aissa-Bokhtache, A., Zegaouia, A., Taleb, R., & Aillerie, M. (2021). Control of an electronic ballast-discharge lamp system supplied by a multicellular converter dedicated to water purification. *Desalination and Water Treatment, 228*, 176–186.

Aissa - Bokhtache, A., Zegaoui, A., Taleb, R., & Aillerie, M. (2020). Super twisting sliding mode control algorithm of a discharge lamp for water sterilization. *Kansai University Reports*, *62*(4), 1731- 1741.

Aissa - Bokhtachte, A., Latroch, M., Toualbia, A., Djafer, L., & Benallou, M. (2023). Modern control of a power supply based on a matrix converter for water disinfection by UVC radiation. *The Eurasia Proceedings of Science, Technology Engineering & Mathematics (EPSTEM), 26*, 733-740.

Aissa- Bokhtache, A., Latroch, M., Toualbia, A., Toubal Maamar, A. E., & Boucherit, M. S. (2023). Optimization of a power supply using 3 types of converters of a discharge lamp-electronic ballast system for water purification. *Proceedings of 2nd International Conference on Electronics, Energy and Measurement (IC2EM)*, 1-6.

Amet, L., Ghanes, M., & Barbot, J.P. (2011). Direct control based on sliding mode techniques for multicell serial chopper. *Proceedings of the 2011 American Control Conference (ACC),* 751–756.

Costache, M. C., Damelincourt, J.J., & Zissis, G. (2000). Optimisation of an ultraviolet source working in a consumer water reactor. *UVX 2000 Colloque Sur Les Sources Cohérentes et incohérentes UV, VUV, et X – Applications et Développements Récents*, *87*(5), 65–66.

De Oro, L. A., Melo, G. de A., & Canesin, C. A. (2014). UV dose investigation for imersed lamp purifier for electronic ballast UV lamps design. *IEEE 16th International Power Electronics and Motion Control Conference and Exposition (PEMC),* 893-900.

Friedli, T., & Kolar, J. W. (2012). Milestones in matrix converter research. *IEEJ Journal of Industry Applications*, *1*(1), 2-14.

Holmes, D. G., & Lipo, T. A., (1992). Implementation of a controlled rectifier using ac-ac matrix converter theory. *IEEE Transactions on Power Electronics*, *7*(1), 240-250.

Toumi, A., Chhun, L., Bhosle, S., Zissis, G., Maussion, P., & Hirsch, J. (2013). Acoustic resonance characterization and numerical model including acoustic streaming in an HPS lamp. *IEEE Industry Applications Society Annual Meeting, 49*, 1154–1160.

Zuckerberger, A., Weinstock, D., & Alexandrovitz, A. (1997). Single-phase matrix converter. *IEE Proceedings - Electric Power Applications, 144*(4), 235-240.

Author Information

Aicha Aissa -Bokhtache
Laboratoire Génie Electrique et Energies Renouvelables (LGEER), Electrical Engineering Department, Hassiba Benbouali University of Chlef
BP. 151, Hai Essalam, 02000 Chlef, Algeria
Contact e-mail: *ahcial71@gmail.com*
a.aissabokhtache@univ-chlef.dz

Maamar Latroch
Laboratoire Génie Electrique et Energies Renouvelables (LGEER), Electrical Engineering Department, Hassiba Benbouali University of Chlef
BP. 151, Hai Essalam, 02000 Chlef, Algeria

Nadia Badni
Center of Scientific and Technical Research in Physico-chemical Analysis of Tipaza (CRAPC),
BP. 384, Ex-Pasna Industrial Zone, Bou-Ismail PO Box 42004, Tipaza, Algeria.

Alla Eddine Toubal-Maamar
Department of Electrical Systems Engineering, Faculty of Technology, University of M'hamed Bougara of Boumerdes
Frantz Fanon city, 35000 Boumerdes, Algeria

Lemya Djafer
Laboratoire Génie Electrique et Energies Renouvelables (LGEER), Electrical Engineering Department, Hassiba Benbouali University of Chlef
BP. 151, Hai Essalam, 02000 Chlef, Algeria

Amina Merini
Laboratoire Génie Electrique et Energies Renouvelables (LGEER), Electrical Engineering Department, Hassiba Benbouali University of Chlef
BP. 151, Hai Essalam, 02000 Chlef, Algeria

To cite this article:

Aissa-Bokhtache, A., Latroch, M., Badni, N., Toubal-Maamar, A.E., Djafer, L., & Merini, A. (2024). Comparative analysis of three converters providing power to a discharge lamp-electronic ballast system designed for water sterilization. *The Eurasia Proceedings of Science, Technology, Engineering & Mathematics (EPSTEM), 32*, 53-65.

The Eurasia Proceedings of Science, Technology, Engineering & Mathematics (EPSTEM)
ISSN: 2602-3199

The Eurasia Proceedings of Science, Technology, Engineering & Mathematics (EPSTEM), 2024

Volume 32, Pages 66-79

IConTES 2024: International Conference on Technology, Engineering and Science

Effect of Preliminary Nitric Chemical Treatment on Corrosion Behavior of 316 Stainless Steel in Chloride Solution Contain Glucose

Djedjiga Ben-Abdesselam
Mouloud Mammeri University of Tizi-Ouzou

Nacer Zazi
Mouloud Mammeri University of Tizi-Ouzou

Youcef Hadj-Ali
Mouloud Mammeri University of Tizi-Ouzou

Fatah Hellal
Ecole Nationale Polytechnique

Jean Paul Chopart
University of Reims Champagne-Ardenne

Mărioara Abrudeanu
University of Pitesti

Denis Negrea
Regional Center of Research & Development for Materials

Abstract: The aim of this study is to analyze the impact of a preliminary nitric acid chemical treatment on the corrosion of 316 stainless steel particularly used in implant applications, in a 0.9% chloride solution containing glucose. The steel 316 study has a variety of distinct phases and inclusions. Chemical nitric acid treatment for three days at 22°C changes the open circuit potential in the chloride solution, containing one, two or four grams per liter of glucose, after one hour and eight days of immersion at 37°C. The results show that the open circuit potential is higher when the solution contains two or four grams of glucose per liter after one hour and eight days of immersion at 37°C. In contrast, the corrosion potential of chemically treated samples increases when immersed in a chloride solution containing two, or four grams of glucose per liter, while their resistance to polarization decreases after one hour of immersion. However, after eight days of immersion in sodium chloride solution, chemically treated samples have lower corrosion potentials for different glucose concentrations compared to untreated samples, and the polarization resistance decreases only for those immersed in chloride solutions containing two or four grams of glucose per liter. In addition, untreated samples show an increase in their polarization resistance and corrosion potential with the increase in glucose concentration after one week of immersion. A significant morphological difference in corrosion is observed between chemically treated and untreated samples when immersed in a chloride solution. In addition, the rate of pitting formation decreases for untreated samples after one week of corrosion; this may be explained by the passivation of untreated 316 steel after one week of free corrosion in the sodium chloride solution.

Keywords: Corrosion resistance, Corrosion morphology, Implants, Glucose, Nitric chemical treatment.

Introduction

Austenite stainless steels are distinguished by their exceptional properties. This has greatly expanded their applications. Notably, 316 SS and 316L SSL found extensive use as body implants (Bouaziz & Zanoun, 2011; Kannan et al., 2005; Varmaziar et al., 2022), due to their ability to develop a thin protective oxide layer spontaneously during air exposure, commonly referred to as the "passive layer". Although these materials are initially protected, following implantation they are instantly exposed to hostile bodily fluids. This can cause degradation over time, primarily from localized corrosion in physiological conditions, and may even result in in vitro failures. Consequently, even though passive film has benefits, it is clear that it cannot ensure long-term protection during implantation. Several studies have concentrated on ways to increase the corrosion resistance and operating life of stainless steels in order to address this difficulty(Ahmad et al., 2009; Bouaziz & Zanoun, 2011; Kannan et al., 2005; Noh et al., 2000a; Shalash & Nasher, 2010; Varmaziar et al., 2022).

Numerous researchers have delved into the impact of surface treatments—be they mechanical, chemical, or electrochemical—on enhancing the corrosion resistance of stainless steels. (Kannan et al., 2005; Noh et al., 2000b). An electrochemical study conducted by G. Hulquist and C. Leygraf (Hultquist & Leygraf, 1980) revealed that nitric acid passivation treatment fosters the development of chromium oxide Cr-O and chromium hydroxide Cr-OH bonds within the protective passive film. These bonds serve to prevent the rupture of the passive layer. Moreover, nitric acid passivation enhances the chromium content within the passive film. Consequently, this treatment enhances resistance against both crevice and pitting corrosion (Hultquist & Leygraf, 1980; Noh et al., 2000b). Many researchers consider nitric acid passivation treatment to be the most effective approach to strengthening corrosion resistance in aggressive environments (Hultquist & Leygraf, 1980; Kannan et al., 2005; Noh et al., 2000b).

Other research highlights not only the impact of surface treatments on corrosion resistance but also the effect of glucose addition at varying concentrations in the physiological solution. In a study by Alam-Eldein et al. (Alam-Eldein et al., 2018), the objective was to evaluate the impact of glycemic control on the stability of implant-attached mandibular prostheses. After three years of follow-up, it appeared that glucose control had an impact on the survival of implants supporting mandibular prostheses in type II diabetic patients. Zeng et al. (Zeng et al., 2015) found that the corrosion rate of pure Mg in the saline solution increased in proportion to the glucose concentration. However, in Hank's solution, they found a noticeable improvement in the corrosion resistance of pure magnesium with an increase in glucose content. These observations highlight the impact of glucose on the corrosion behavior of implants in physiological solutions.

The normal concentration of glucose in the blood of a non-diabetic person on an empty stomach is generally between 70 and 120 mg/dl (Wimmer et al., 2019). In contrast, a person is diagnosed with diabetes when his fasting blood sugar exceeds 120 mg/dl (Maheshwari et al., 2012). In this study, three glucose concentrations were used: 100 mg/dl (representing a non-diabetic person), 200 mg/dl (corresponding to a diabetic person), and 400 mg/dl (simulating hyperglycemia) in order to assess the impact of glucose on 316 steels used as implants in non-diabetic people and those with the disease.

Experimental Methods

Materials and Procedures

The material selected for this study is austenitic stainless steel AISI 316, which is in the form of 2 mm thick sheets and has been subjected to heat treatment in the factory. This material consists mainly of 16.65% chromium (Cr) and 10.43% nickel (Ni), with a molybdenum content (Mo) greater than 2.19%. The latter is recognized for its ability to significantly improve the pitting corrosion resistance and stress corrosion of stainless steels (Bond et al., 1973; Brunet et al., 1967; Colombié et al., 1973; Steinemann, 1968; Sumita et al., 2004). The detailed chemical composition of this steel is presented in Table 1. The chemical analysis was performed using optical emission spectrometry (OES). For scanning electron and optical microscopic analyses, 1 cm² samples were cut with a guillotine and prepared according to the standard metallographic procedure. First, they were polished with sandpaper ranging from 400 to 4000 grains. Then the samples were cleaned with distilled water and finally air-dried. To characterize the structure and phases constituting our steel, we performed an analysis by X-ray diffraction (XRD). The identification of the phases present in our material was carried out using the software "HighScore plus".

We opted for the use of the Aqua Regia solution, consisting of 20 ml of nitric acid (HNO_3) and 60 ml of hydrochloric acid (HCl), to achieve a chemical attack on 316 stainless steel containing 2.19% molybdenum. This approach allowed us to analyze and observe its microstructure with precision. For surface treatment, the samples were immersed for 3 days in nitric acid [HNO_3], followed by a thorough rinsing with distilled water. All surface treatments were performed at room temperature.

Table 1. Chemical composition of AISI 316 stainless steel.

Elements (wt %)	AISI 316	Elements (wt %)	AISI 316	Elements (wt %)	AISI 316
C	0.049	Cu	0.12	Bi	0.009
Si	0.63	Nb	0.016	Ca	0.0006
Mn	0.95	Ti	0.006	Ce	0.012
P	0.007	V	0.066	Sb	<0.002
S	0.004	W	<0.007	Se	<0.001
Cr	16.65	Pb	<0.002	Te	0.005
Mo	2.19	Sn	0.017	Ta	0.057
Ni	10.43	Mg	0.012	B	0.0004
Al	0.003	As	0.013	Zn	0.002
Co	0.31	Zr	0.004	La	0.001
				Fe	68.4

Electrochemical studies were conducted using physiological solutions composed of 0.9% NaCl, to which different glucose concentrations were added (one, two, and four grams per liter). These experiments were conducted at a temperature of 37°C. The specific characteristics of the samples used are listed in Table 2.

Table 2. Sample types used for different electrochemical tests.

Sample characteristics	Without treatment	With treatment	Immersion time in the physiological solution	With 1g/l of glucose	With 2g/l of glucose	With 4g/l of glucose
1	x		1 hour	x		
2	x		1 hour		x	
3	x		1 hour			x
4		x	1 hour	x		
5		x	1 hour		x	
6		x	1 hour			x
7	x		8 days	x		
8	x		8 days		x	
9	x		8 days			x
10		x	8 days	x		
11		x	8 days		x	
12		x	8 days			x

Corrosion Behavior

Corrosion measurements were performed in a 0.9% NaCl solution with the addition of various glucose concentrations (one, two, and four grams/liter), maintained at a temperature of 37°C in an aerated environment. The electrochemical studies were conducted in a four-electrode cell, and the test environment remained stable throughout the duration of the evaluations. This medium was selected for its suitability for the study of corrosion due to the presence of corrosion activators, including chloride ions (Hache, 1956) and simulating a physiological solution (Chaouki et al., 2005; Eschler et al., 2001; Hanawa, 2002; Lorsbach & Schmitz, 2018). The working electrode consisted of an AISI 316 (WE) stainless steel substrate associated with an Ag/AgCl (RE) reference electrode, while two graphite electrodes were used as counter-electrodes (CE). The open-circuit potential measurements (E_{OCP}) were performed with an Ag/AgCl reference electrode. The potentiodynamic polarization tests covered a range from -1500 mV to 1500 mV, with an acquisition rate of 60 mV/min. The current-potential curves were obtained after 1 hour and 8 days of immersion. The open-circuit potential and current-to-potential curves were recorded using an AUTOLAB potentiostat/galvanostat. The corrosion potential (Ecorr) and the polarization resistance (Rp) were determined from the obtained curves.

Results and Discussions

After subjecting the surface of 316 stainless steel, which contains a molybdenum content greater than 2.19% by weight, to a chemical attack in an Aqua Regia solution, we performed a scanning electron microscope analysis (see Figure 1). This observation revealed the presence of multiple distinct phases in our steel.

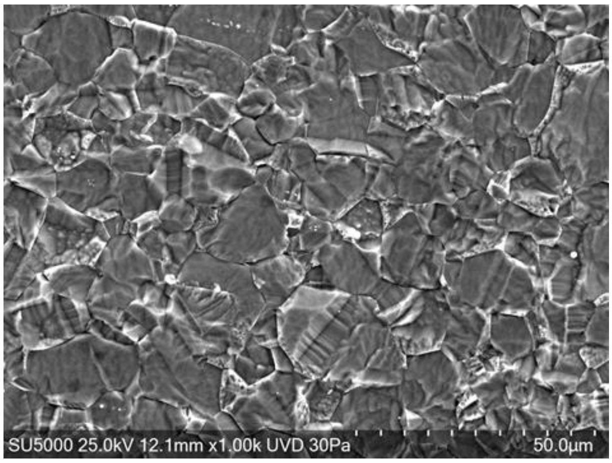

Figure 1. Scanning electron microscopic observation of 316 steel containing 2.19% molybdenum.

The results of the X-ray diffraction confirmed the previous observations, revealing the presence of several phases and highlighting the presence of austenitic and ferritic phases in the steel 316 studied. The peaks corresponding to austenite and ferrite are illustrated in Figure 2. The appearance of the ferritic phase on the diffractogram is attributed to the content of chromium (16.65%) and molybdenum (2.19%) in alloy 316, thus promoting the formation of this ferritic phase (Cunat, 2000; Leger, 1993; Sumita et al., 2004). The austenite content in the alloy is 73.3%, while the ferrite content is 18.1%, and the other phases represent 8.6% of the total composition, which classifies this steel as an austenitic type.

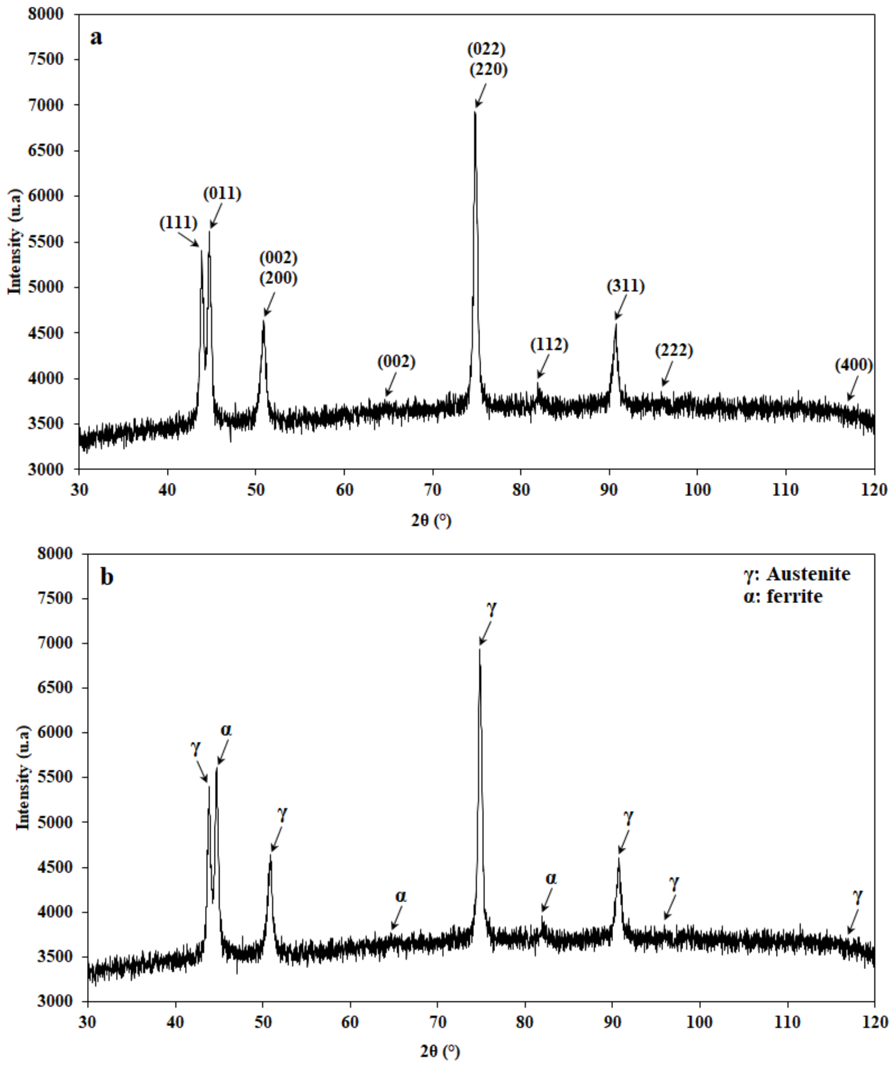

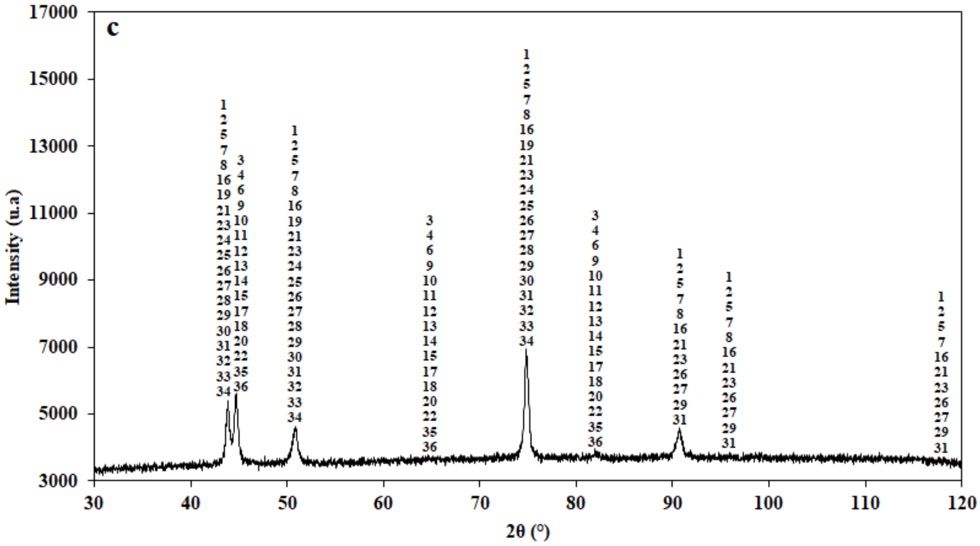

Figure 2. X-ray diffraction of austenitic stainless steel 316, **a-** Diffraction planes, **b-** Picks of austenitic phase and ferritic phase, **c-** All Thirty-six phases in the alloy.

Table 3. Thirty-six phases present in 316 stainless steel containing 2.19 % Mo.

Phase number	Chemical formula	Diffraction angle 2θ (°)	Diffraction plans (hkl)	PGCD
1	$C_{0.06}Cr_{0.29}FeNi_{0.16}$	43.583, 50.792, 74.699, 90.697, 95.968, 118.161.	(111), (002), (220), (311), (222), (400).	ICDD 00-033-0397.
2	$Nb_{0.1}Ni_{0.9}$	43.698, 50.901, 74.852, 90.899, 96.202, 118.514.	(111), (200), (220), (311), (222), (400).	ICDD 03-065-9420.
3	$Fe_{1.8}V_{0.2}$	44.484, 64.729, 81.932.	(011), (002), (122).	ICSD 98-063-4038
4	$Ce_{0.0045}Fe_{0.9955}$	44.696, 65.059, 82.384.	(011), (002), (112).	ICSD 98-010-2148.
5	$B_2Fe_3Ni_3$	43.507, 50.674, 74.487, 90.416, 95.671, 117.716.	(111), (200), (220), (311), (222), (400).	ICDD 03-065-8674.
6	$Fe_{0.984}W_{0.016}$	44.696, 65.059, 82.384.	(011), (002), (112).	ICSD 98-010-3696.
7	$C_{0.05}Fe_{0.95}$	43.473, 50.674, 74.679, 90.676, 95.944, 117.716.	(111), (200), (220), (311), (222), (400).	ICDD 00-023-0298.
8	$Fe_{0.64}Ni_{0.36}$	43.605, 50.795, 74.679, 90.633, 95.907.	(111), (200), (220), (311), (222).	ICDD 00-047-1405.
9	$Fe_{0.82}$ $B_{0.18}$	44.779, 65.186, 82.559.	(011), (002), (112).	COD 96-151-1092.
10	$Fe_{1,98}Ta_{0,02}$	44.631, 64.957, 82.244.	(011), (002), (112).	ICSD 98-063-3793.
11	$Fe_{1.95}Ti_{0.05}$	44,581, 64,881, 82,140.	(011), (002), (112).	ICSD 98-063-3933.
12	$Fe_{0.991}Sn_{0.006}Zr_{0.003}$	44.647, 64.982, 82.279.	(011), (002), (112).	ICSD 98-016-8654.
13	$Fe_{1.8}Si_{0.2}$	44.779, 65.186, 82.559.	(011), (002), (112).	ICSD 98-063-3527.
14	$Al_{0.5}Cr_{0.5}Fe_1$	44.614, 64.931, 82.201.	(011), (002), (112).	ICSD 98-005-7655.
15	$Fe_{0.96}Ni_{0.03}Sb_{0.01}$	44.631, 64.957, 82.244.	(011), (002), (112).	ICSD 98-010-3570.
16	Fe_3Ni_2	43.530, 50.705, 74.535, 90.479, 95.742, 117.822.	(111), (200), (220), (311), (222), (400).	ICDD 03-065-5131.
17	$Fe_{2.00}$	44.680, 65,033, 82,349.	(011), (002), (112).	COD 96-900-

				6589.
18	$Cu_{0.3}Fe_{1.7}$	44.435, 64.653, 81.828.	(011), (002), (112).	ICSD 98-062-7297.
19	$Fe_{4.00}$	43.724, 50.932, 74.901.	(111), (002), (022).	COD 96-901-4592.
20	$Cr_{0.7}Fe_{0.3}$	44.581, 64.881, 82.140.	(011), (002), (112).	ICSD 98-010-2754.
21	$Al_{0.34}Co_{0.41}Cr_{0.21}W_{0,04}$	43.473, 50.674, 74.679, 89.934, 95.578, 117.716.	(111), (200), (220), (311), (222), (400).	ICDD 00-050-1290.
22	$Cr_{0.2}Fe_{0.8}$	44.680, 65.033, 82.349.	(011), (002), (112).	ICSD 98-010-2752.
23	$Cr_{1.7}Fe_{6.6}Mo_{0.1}Ni_{1.2}Si_{0.2}$	43.473, 50.674, 74.679, 89.934, 95.578, 117.716.	(111), (200), (220), (311), (222), (400).	ICDD 00-050-1293.
24	$Al_{0.05}Cr_{0.3}Ni_{0.65}$	43.943, 51.192, 75.320.	(111), (002), (022).	ICSD 98-010-7768.
25	$Cr_{0.23}Mn_{0.08}Ni_{0.69}$	43.749, 50.962, 74.950.	(111), (002), (022).	ICSD 98-010-8339.
26	$Al_{0.5}CNi_3Ti_{0.5}$	43.473, 50.644, 74.610, 90.676, 96.190, 118.353.	(111), (200), (220), (311), (222),(400).	ICDD 00-019-0035.
27	$Cu_{3.8}Ni$	43.473, 50.765, 74.748, 90.569, 95.944, 118.140.	(111), (200), (220), (311), (222), (400).	ICDD 00-009-0205.
28	$Cr_{0.4}Ni_{0.6}$	43.775, 50.993, 74.999.	(111), (002), (022).	ICSD 98-010-2821.
29	$Ni_{17}W_3$	43.680, 50.880, 74.818, 90.854, 96.153, 118.439.	(111), (200), (220), (311), (222), (400).	ICDD 03-065-4828.
30	Ni_4Zn_1	43.904, 51.146, 75.246.	(111), (002), (022).	ICSD 98-064-7139.
31	$Ni_{9.1}Sb_{0.9}$	43.608, 50.795, 74.682, 90.673, 95.953, 118.140.	(111), (200), (220), (311), (222), (400).	ICDD 03-065-4321.
32	$Ni_{0.92}Ta_{0.08}$	43.711, 50.917, 74.877.	(111), (002), (022).	ICSD 98-010-5393.
33	$Fe_{2.6}Mn_{1.2}Ni_{0.2}$	43.736, 50,947, 74.926.	(111), (002), (022).	ICSD 98-063-2501.
34	Ni_3Si	43.724, 50.932, 74.901.	(111), (002), (022),	ICSD 98-064-6580.
35	$Fe_{0.96}P_{0.04}$	44,729, 65,110, 82.454.	(011), (002), (112).	ICSD 98-010-8462.
36	$As_{0.2}Fe_{1.8}$	44.370, 64.553, 81.690.	(011), (002), (112).	ICSD 98-061-0476.

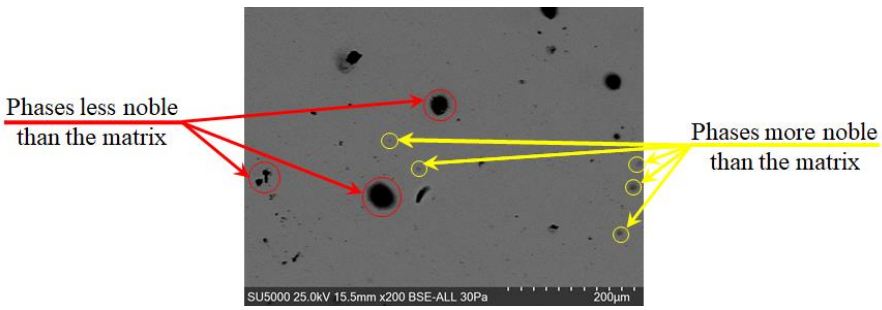

Figure 3. Scanning electron microscopic observation of 316 steel containing 2.19% molybdenum, after treatment in 65 wt% nitric acid.

After immersion of the surface of 316 stainless steel in a 65% nitric acid solution by weight for a period of 3 days, a scanning electron microscope analysis was performed (see Figure 3). This observation showed more pronounced corrosion in the less noble phases than the matrix, those with a lower corrosion potential than the matrix (austenite). On the other hand, phases with a higher potential than the matrix were relatively spared. These findings confirm the conclusions drawn from X-ray diffraction (XRD) analyses; our steel 316 is composed of several distinct phases.

After chemical treatment with nitric acid over a period of three days, electrochemical studies were conducted in physiological solutions of 0.9% NaCl aerated, to which different glucose concentrations (one, two, and four grams per liter) were added. These experiments were conducted at a constant temperature of 37°C. Figure 4 illustrates the variation of the open circuit potential (OCP) during one hour of immersion in a physiological solution of 0.9 % NaCl for austenitic stainless steel under different experimental conditions, namely (a) without treatment and (b) after nitric acid treatment. The results show that the corrosion potentials of nitric acid-treated samples are higher than those of untreated samples, which is consistent with previous research (Barbosa, 1983; Kannan et al., 2005; Noh et al., 2000b; Salvago & Fumagalli, 1994). At the time of immersion, the corrosion potential of sample 3 is highest, measured at approximately E = 0.092 V; this value decreases continuously to reach E = -0.069 V after one hour of immersion. In contrast, the corrosion potential of sample 2 is initially less noble than that of sample 3, measured at E = -0.015 V. However, it increases to E = 0.125 V after 360 seconds, then decreases to E = -0.154 V after 410 seconds, to finally increase again and reach a higher potential, measured at E = 0.042 V after one hour of immersion. Samples with the addition of one gram of glucose (1 and 4) have the lowest corrosion potentials, whether treated or not. Samples 2 and 5 have the highest corrosion potentials after one hour of immersion in the sodium chloride solution. It appears that the concentration of two grams of glucose in the saline solution has an optimal effect on the corrosion potential after one hour of exposure.

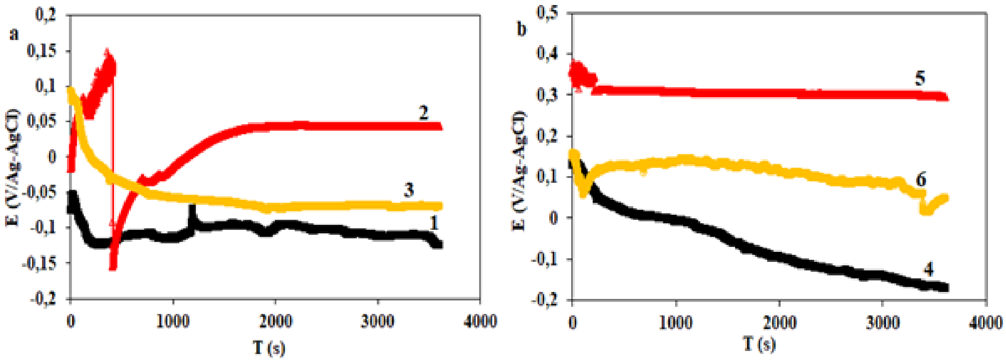

Figure 4. The open circuit potential (OCP) of austenitic steel 316 from samples, ■ samples 1 and 4 (one gram of glucose), ▲ samples 2 and 5 (two grams of glucose), ● samples 3 and 6 (four grams of glucose), in the physiological solution of 0.9% NaCl for one hour, (a) without treatment (b) after treatment.

In order to evaluate the effect of chemical treatment with nitric acid as well as the impact of glucose addition at different concentrations on the corrosion morphology of 316 stainless steel after one hour of immersion in a physiological solution of 0.9 % NaCl, the samples were examined using an optical microscope. The results of these observations are presented in Figure 5. Samples 1, 2, and 3, represented by (a), (b), and (c), respectively, were tested without treatment, while samples 4, 5, and 6, represented by (a'), (b'), and (c'), respectively, were subjected to chemical treatment.

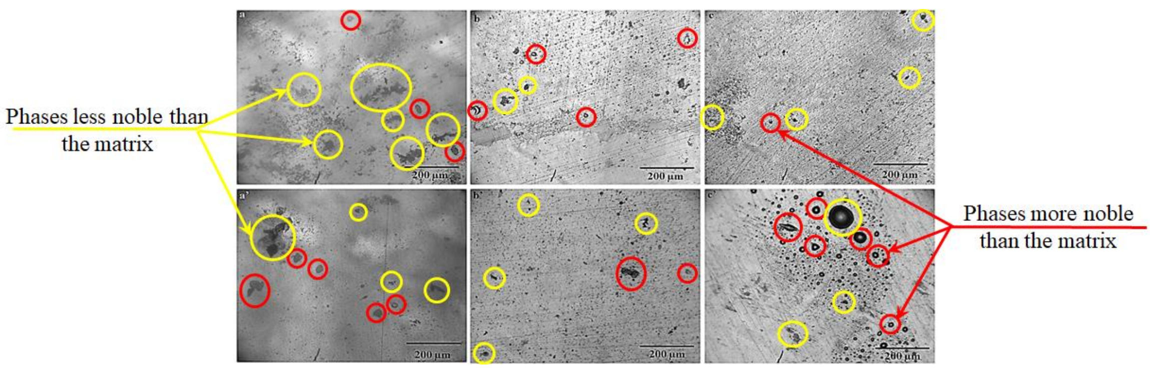

Figure 5. Corrosion morphology of austenitic steel 316, for different experimental conditions, samples 1, 2 and 3, represented by (a), (b) and (c) respectively, were tested without treatment. Samples 4, 5 and 6, represented by (a'), (b') and (c') respectively, were subjected to chemical treatment.

Localized corrosion was observed on all samples but was more pronounced on untreated samples. This can be explained by the passivation of the samples treated with nitric acid and the increase in chromium concentration in the passive film after surface treatment, as reported in references (Barbosa, 1983; Hultquist & Leygraf, 1980; Noh et al., 2000b). In addition, we observed that the corrosion rate decreases with an increase in glucose concentration. We found that some particles are completely corroded. In this case, these are less noble than the matrix (austenite). However, other particles remained intact; only their contours were corroded. These particles are more noble than the matrix.

In order to study the effect of nitric acid chemical treatment and the impact of glucose addition at different concentrations on polarization resistance and corrosion potential, we performed polarization tests in a 0.9% NaCl solution with the addition of one, two, and four grams/liter of glucose. These experiments were conducted at a constant temperature of 37°C. Figure 6 shows the polarization curves of 316 stainless steel, while Table 3 lists the values of corrosion potential and polarization resistance calculated from the polarization curves.

Figure 6 (a and a') show the polarization curves (i=f(E)) and their magnification effect, while (b and b') show the polarization curves (log (i)=f(E)) after one hour of corrosion (OCP) in the physiological solution 0,9% NaCl at different glucose concentrations. Figure 6 (a and b) without surface treatment; however, (a' and b') with nitric acid treatment. From these curves and the data in Table 3, we observed that the corrosion potentials of samples without treatment (1, 2, and 3) are very close compared to those of samples treated chemically (4, 5, and 6). In addition, the corrosion potentials of samples 5 and 6 are higher than those of samples without treatment 2 and 3, indicating that the addition of glucose (two and four grams) has an optimal effect on the corrosion potential (Ecorr) after chemical treatment with nitric acid. In contrast, samples 1 and 4 have the lowest potentials, confirming the results in Figure 4. However, the polarization resistance of chemically unprocessed samples is higher than that of treated samples (4, 5, and 6), and the polarization resistance decrease with surface treatment.

Table 4. Polarization resistance and corrosion potential of AISI 316 steel, after one hour of free corrosion (OCP), without and with nitric acid treatment.

Samples	Corrosion time	Rp (Ω cm^2)	Ecorr (v)
1	1 hour	7446	-0,3123
2	1 hour	19228	-0,2929
3	1 hour	10228	-0,3028
4	1 hour	2330	-0,4261
5	1 hour	7324	-0,0886
6	1 hour	8514	-0,1515

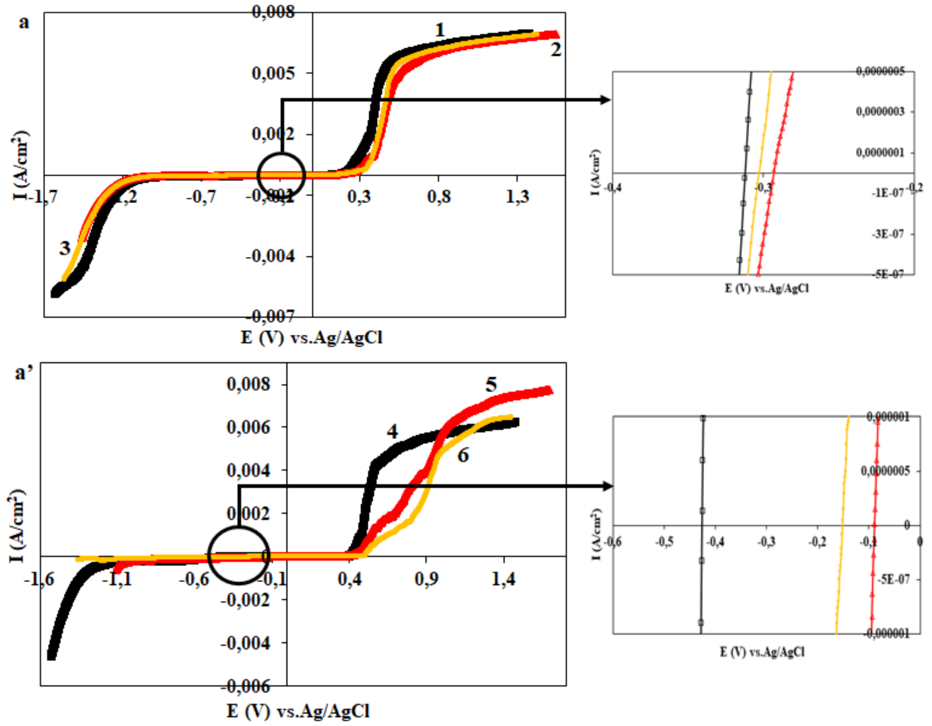

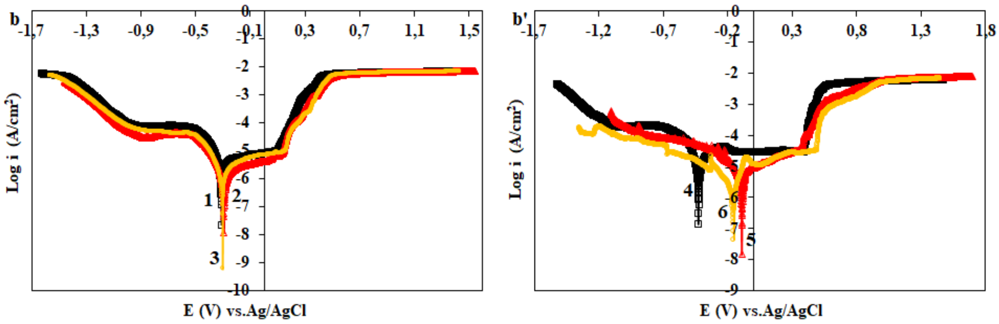

Figure 6. Polarization curves of austenitic steel 316, (a and a') shows the polarization curves (i=f(E)) and their magnification effect, (b and b') shows the polarization curves (log(i)=f(E)) after one hour of free corrosion (OCP) in physiological solution at different glucose concentrations, (a and b) without surface treatment, (a' and b') with nitric acid treatment.

Microscopic observations were made after each polarization test in a physiological solution after one hour of immersion. The results of these observations are presented in Figure 7. Samples 1, 2, and 3, noted respectively (a), (b), and (c), were tested without treatment, while samples 4, 5, and 6, noted (a'), (b'), and (c'), were subjected to pre-treatment.

Localized corrosion was observed on all samples but was more pronounced on untreated samples. This can be explained by the passivation of the samples by nitric acid (HNO_3) and the increase of the chromium concentration in the passive film after surface treatment, as indicated in references (Barbosa, 1983; Hultquist & Leygraf, 1980; Noh et al., 2000b). In particular, we noted that the corrosion rate decreases with an increase in glucose concentration, especially for samples that have undergone chemical treatment (HNO_3). We also observed that some particles are completely corroded, these are less noble than the matrix (austenite). On the other hand, other particles remained intact, only their contours having been corroded, the latter are more noble than the matrix.

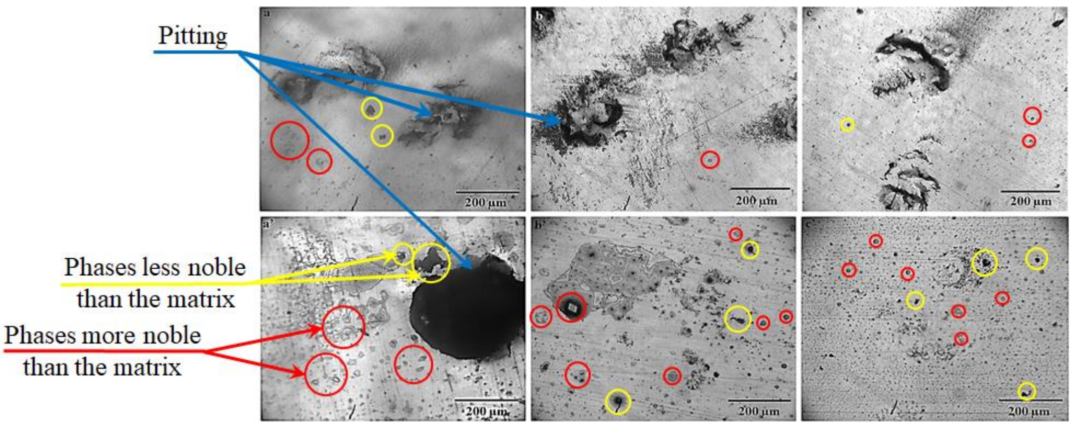

Figure 7. Corrosion morphology of austenitic steel 316 after each polarization test, after one week of corrosion, for different experimental conditions, samples without treatment 1, 2, and 3, designated by (a), (b), and (c) respectively. Samples with chemical treatment 4, 5, and 6, designated by (a'), (b'), and (c') respectively.

Figure 8 (a and b) show the evolution of the open circuit potential (OCP) during one week of immersion in a physiological solution for austenitic stainless steel under different experimental conditions, namely (a) without treatment and (b) after treatment with nitric acid. Contrary to the results observed after one hour of OCP and after one week, the potentials of samples not treated with nitric acid are higher than those of the treated samples, which means that the samples are passivated in the physiological solution of 0.9% NaCl in the presence of glucose. We noted that the potentials of the samples (8 and 9), subjected to the addition of two and four grams of glucose without treatment, are similar and nobler than those of sample 7, and similarly, for acid-treated samples (11 and 12), their potentials are close to and superior to those of sample 10. After eight days of corrosion, the potential is measured at approximately E = 0.64 V for sample 8 and E = 0.208 V for sample 9. It is virtually identical for samples with treatment (11 and 12), measured at approximately E = 0.064 V. Samples with the addition of one gram of glucose (7 and 10) have the lowest potentials, whether treated or not. It is obvious that the concentration of two and four grams of glucose in the saline solution exerts an optimal effect on the potential one week of immersion for the treated samples or not.

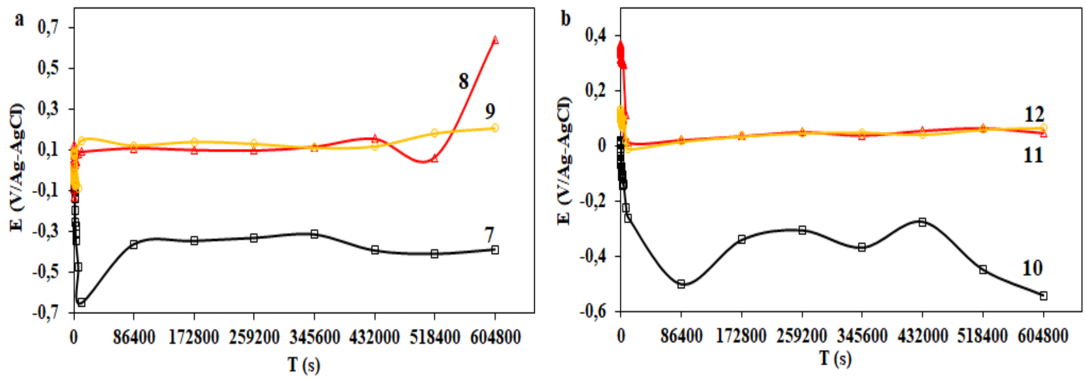

Figure 8. The open-circuit potential (OCP) of austenitic steel 316 from samples, ■ samples 7 and 10 (one gram of glucose), ▲ samples 8 and 11 (two grams of glucose), ● samples 9 and 12 (four grams of glucose), in the physiological solution of 0.9% NaCl for one week, (a) without treatment (b) after treatment.

In order to see the effect of nitric acid chemical treatment and the influence of glucose addition at different concentrations on 316 stainless steel corrosion morphology after one week of immersion in a physiological solution of 0.9% NaCl, we made microscopic optical observations. The results of these observations are shown in Figure 9. Samples 7, 8, and 9, represented by (a), (b), and (c) respectively, were tested without treatment, while samples 10, 11, and 12, represented by (a'), (b'), and (c') respectively, were subjected to chemical treatment. We found localized corrosion on all samples, but this corrosion is more pronounced on untreated samples. This can be explained by the passivation of the samples after 8 days of corrosion and the increase in chromium concentration in the passive film after surface treatment. Also, we found that the rate of corrosion decreases with an increase in glucose concentration, especially for samples treated with HNO_3 acid (a', b', and c'). Some particles were completely corroded, corresponding to the less noble particles than the matrix (austenite). On the other hand, other particles remained intact; only their contours were corroded, these particles are more noble than the matrix.

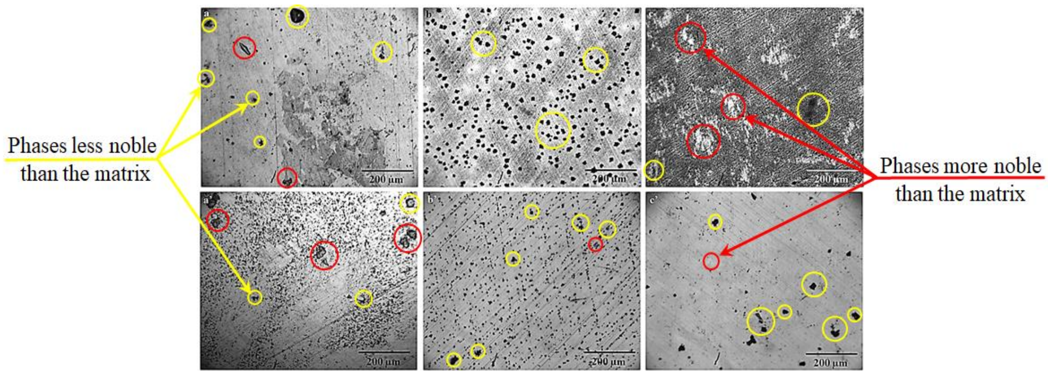

Figure 9. Corrosion morphology of austenitic steel 316, for different experimental conditions, untreated samples 7, 8 and 9, represented by (a), (b) and (c) respectively. Samples with chemical treatment 10, 11 and 12, represented by (a'), (b') and (c') respectively.

After one week of corrosion exposure (OCP), polarization tests were performed in a 0.9% NaCl solution with the addition of one, two, and four grams of glucose per liter. The polarization curves for 316 stainless steel are shown in Figure 10, while Table 4 summarizes the values of corrosion potential and polarization resistance calculated from these curves.

The polarization curves (i=f(E)) are illustrated in Figure 10 (a and a'), with their lope effect, while (b and b') show the polarization curves (log (i)=f(E)) after one week of corrosion exposure (OCP) in the physiological solution of 0.9% NaCl at different glucose concentrations. The samples in Figure 10 (a and b) are without surface treatment, while (a' and b') have been treated with nitric acid. Based on these curves and the data in Table 4, we found that the corrosion potentials of untreated samples (7, 8, and 9) are higher than those of chemically treated samples (10, 11, and 12). This phenomenon can be explained by the passivation of untreated samples after 8 days of corrosion in the solution saline. In addition, the polarization resistance and corrosion potentials of untreated samples increase with the increase in glucose concentration in the physiological solution. The polarization resistance values are respectively Rp = 2509 Ω/cm^2, Rp = 4022 Ω/cm^2, and Rp = 4598 Ω/cm^2, so the corrosion potentials are measured at about E = -0.3586 V, E = -0.2712 V, and E = -0.2301 V for one, two, and four grams of glucose per liter, respectively. These results indicate that the addition of two and four grams of glucose per liter has an optimal effect on polarization resistance and corrosion potential (Ecorr) after one week of corrosion. However, for chemically treated samples, Sample 11 has the highest corrosion potential, thus confirming the previous results (Figure 6 (a')). The nitric acid treatment and the addition of two grams of glucose to the solution of saline have a significant effect on the corrosion potential of stainless steel. In addition, the polarization resistance of chemically untreated samples (7, 8, and 9) is higher than that of treated samples (10, 11, and 12), indicating a decrease in polarization resistance with surface treatment.

Table 5. Polarization resistance and corrosion potential of AISI 316 steel, after one week of free corrosion (OCP), without and with nitric acid treatment.

Samples	Corrosion time	Rp (Ω cm^2)	Ecorr (v)
7	8 days	2509	-0.3586
8	8 days	4022	-0.2712
9	8 days	4598	-0.2301
10	8 days	75895	-0.6257
11	8 days	3489	-0.2748
12	8 day	2018	-0.4845

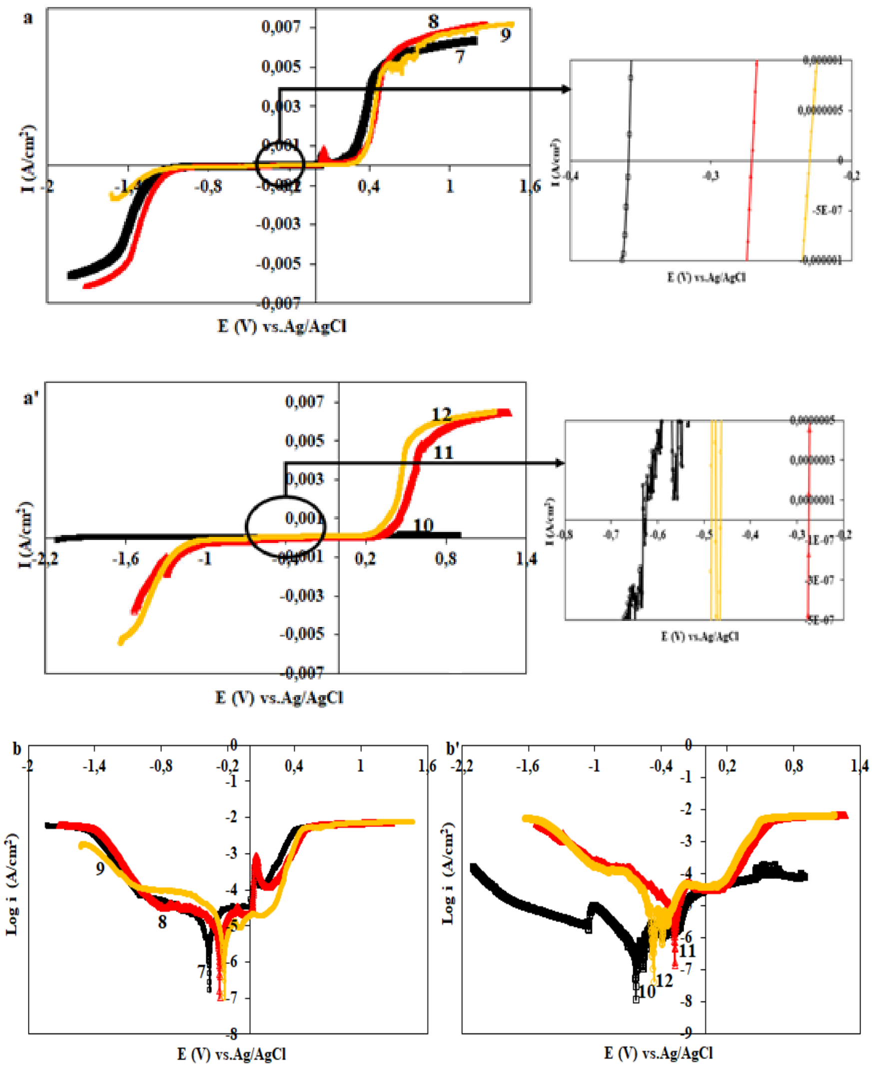

Figure 10. Polarization curves of austenitic steel 316, (a and a') shows the polarization curves (i=f(E)) and their magnification effect, (b and b') shows the polarization curves (log(i)=f(E)) after one week of free corrosion (OCP) in physiological solution at different glucose concentrations, (a and b) without surface treatment, (a' and b') with nitric acid treatment.

In order to evaluate the impact of HNO_3 nitric acid chemical treatment as well as the influence of glucose addition at different concentrations on the corrosion morphology of 316 stainless steel, microscopic observations were made after each polarization test in a physiological solution after one week of corrosion. The results of these observations are presented in Figure 11. Samples 7, 8, and 9, designated by (a), (b), and (c), respectively, were tested without treatment, while samples 10, 11, and 12, designated by (a'), (b') and (c'), were subjected to pre-treatment.

Localized corrosion was observed on all the samples; however, it is more pronounced on the treated samples. This fact can be explained by the passivation of the untreated samples after 8 days of free corrosion in the saline solution. In particular, we noticed that the corrosion rate decreased with the increase in glucose concentration, especially for untreated samples (glucose improves the passivation of austenitic steels, 316). We also found that some particles are completely corroded, corresponding to less noble particles than the matrix (austenite). On the other hand, other particles remained intact, only their contours having been corroded, these particles are more noble than the matrix.

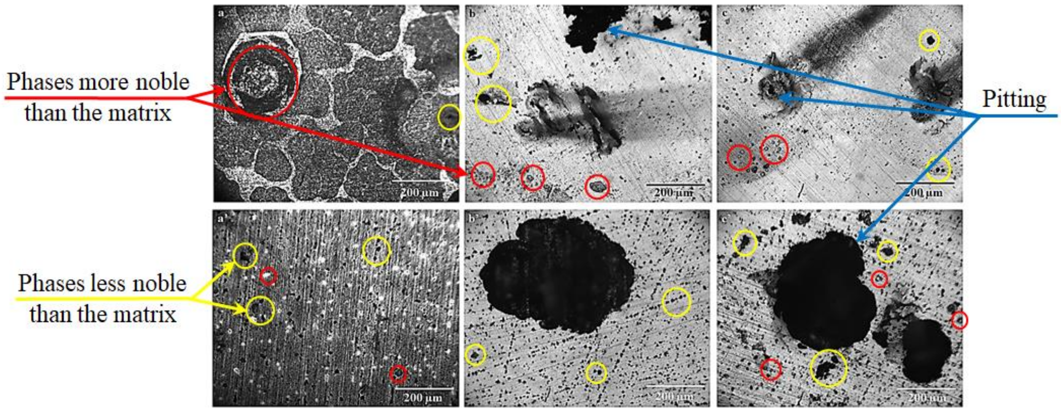

Figure 11. Corrosion morphology of austenitic steel 316 after each polarization test, after one week of corrosion, for different experimental conditions, samples without treatment 1, 2 and 3, designated by (a), (b) and (c) respectively. Samples with chemical treatment 4, 5 and 6, designated by (a'), (b') and (c') respectively.

Conclusion

The study examines the corrosion resistance of stainless steel 316 exposed to a 0.9% NaCl solution with different glucose concentrations following surface treatment with nitric acid. Through various analyses, including microscopic examination, X-ray diffraction, and electrochemical tests, several important conclusions are drawn:

Initially, the AISI 316 has a variety of distinct phases and inclusions. The corrosion potential increases after one hour of corrosion, while the polarization resistance decreases for treated samples. The impact of corrosion on AISI 316 is particularly marked, especially with the addition of 2 grams of glucose in the solution, while the pitting rate decreases for treated samples after one hour of corrosion. In addition, untreated samples show a significant increase in potential after one week of corrosion. The addition of glucose optimizes the polarization resistance and corrosion potential; the samples passivate in the NaCl solution in the presence of glucose. The corrosion behavior of AISI 316 is significantly influenced, especially with the addition of 2 grams of glucose to the solution after treatment with HNO_3 acid. In addition, the polarization resistance and corrosion potentials of untreated samples increase with increasing glucose concentrations, while the pitting rate decreases for these samples.

Scientific Ethics Declaration

The authors declare that the scientific ethical and legal responsibility of this article published in EPSTEM Journal belongs to the authors.

Acknowledgements or Notes

* This article was presented as an poster presentation at the International Conference on Technology, Engineering and Science (www.icontes.net) held in Antalya/Turkey on November 14-17, 2024.

References

Ahmad, A., Yahya, Z., Mohd Daud, N. A. Q., & Daud, M. (2009). The effects of addition of Zn, Sn, Mg, Cu, Fe, and Si on the morphology and corrosion behaviour of aluminium alloys in seawater. *2009 3rd International Conference on Energy and Environment (ICEE)*, 117–123.

Alam-Eldein, A. M., Mostafa, T. M. N., & Mabrouk, E. A. (2018). Effect of glycemic control on ımplants assisted mandibular overdentures. *Egyptian Dental Journal*, *64*(1), 635–644.

Barbosa, M. A. (1983). The pitting resistance of AISI 316 stainless steel passivated in diluted nitric acid. *Corrosion Science*, *23*(12), 1293–1305.

Bond, A. P., Dundas, H. J., Schmidt, W., & Wol, M. (1973). Etude de la résistance à la corrosion d'aciersinoxydables en vue de leur utilisationen distribution d'eau chaude. *Revue de Métallurgie*, *70*(1), 33–42.

Bouaziz, S. A., & Zanoun, A. (2011). Comportement électrochimique de l'acier X2CrNiMo17-12-2 (AISI 316L) boruré utilisé comme implant. *Matériaux & Techniques*, *99*(7), 717–724.

Brunet, S., Coriou, H., Grall, L., Mahieu, C., & Pelras, M. (1967). Influence de divers facteurs sur la corrosion sous contrainte d'aciers inoxydables austenitiques dans les milieux chlorures. *Desalination*, *3*(1), 118–124.

Chaouki, H., Chtaini, A., & Bouadili, A. E. (2005). Resıstance a la corrosıon des allıages utılıses comme ımplants en mılıeu bıologıque. *Scientific Study & Research*, 35-42

Colombié, M., Condylis, A., Desestret, A., Grand, R., & Mayoud, R. (1973). Les aciers ferritiques inoxydables ductiles à haute teneur en chrome. Nouveaux matériaux résistant à la corrosion par piqûre, par crevasse et à la corrosion sous tension. *Revue de Métallurgie*, *70*(12), 949–962.

Cunat, P.J. (2000). Aciers inoxydables—Critères de choix et structure. *Étude et Propriétés Des Métaux,1*, 4540.

Eschler, P.-Y., Reclaru, L., & Blatter, A. (2001). Relargage du nickel et corrosion par piqûres des aciers inoxydables. Influence de la direction de laminage. *Journée d'étude SSC, Société Suisse de chronométrie, Neuchatel,* 11-16

Hache, A. (1956). Contribution à l'étude de la corrosion de l'acier en solutions salines. *Revue de Métallurgie*, *53*(1), 76–80.

Hanawa, T. (2002). Evaluation techniques of metallic biomaterials in vitro. *Science and Technology of Advanced Materials*, *3*(4), 289–295.

Hultquist, G., & Leygraf, C. (1980). Surface composition of a type 316 stainless steel related to ınitiation of crevice corrosion. *Corrosion*, *36*(3), 126–129.

Kannan, S., Balamurugan, A., & Rajeswari, S. (2005). Electrochemical characterization of hydroxyapatite coatings on HNO3 passivated 316L SS for implant applications. *Electrochimica Acta*, *50*(10), 2065–2072.

Leger, M. T. (1993). Aciers moulés inoxydables martensitiques, propriétés d'emploi et de mise en œuvre. *Revue de Métallurgie*, *90*(10), 1357–1356.

Lorsbach, B., & Schmitz, E. (2018). Influence of test parameters of potentiodynamic current density measurements on the determination of the pitting corrosion resistance of austenitic stainless steels. *Materials and Corrosion*, *69*(1), 37–43.

Maheshwari, V., Rangaiah, G. P., & Samavedham, L. (2012). A Novel multi-objective optimization based experimental design and its application for physiological model of type 1 diabetes. *IFAC Proceedings Volumes*, *45*(15), 638–643.

Noh, J. S., Laycock, N. J., Gao, W., & Wells, D. B. (2000a). Effects of nitric acid passivation on the pitting resistance of 316 stainless steel. *Corrosion Science*, *42*(12), 2069–2084

Noh, J. S., Laycock, N. J., Gao, W., & Wells, D. B. (2000b). Effects of nitric acid passivation on the pitting resistance of 316 stainless steel. *Corrosion Science*, *42*(12), 2069–2084.

Salvago, G., & Fumagalli, G. (1994). The distribution of stainless steel breakdown potentials: The effect of surface finishing degree and HNO3 treatment. *Corrosion Science*, *36*(4), 733–742.

Shalash, L. B. T., & Nasher, L. S. H. (2010). Study the effect of magnetic field on the corrosion of steel in sodium chloride solution (NaCl). *Misan Journal of Academic Studies*, *9*, 30–38.

Steinemann, S. (1968). Résistance à la corrosion par piqûres de l'acier inoxydable au chrome-nickel-molybdène élaboré normalement à haute fréquence et refondu sous laitier électroconducteur (ESR). *Revue de Métallurgie*, *65*(10), 651–658.

Sumita, M., Hanawa, T., & Teoh, S. H. (2004). Development of nitrogen-containing nickel-free austenitic stainless steels for metallic biomaterials—Review. *Materials Science and Engineering: C*, *24*(6–8), 753–760.

Varmaziar, S., Atapour, M., & Hedberg, Y. S. (2022). Corrosion and metal release characterization of stainless steel 316L weld zones in whey protein solution. *Npj Materials Degradation*, *6*(1), 19.

Wimmer, R. A., Leopoldi, A., Aichinger, M., Wick, N., Hantusch, B., Novatchkova, M., Taubenschmid, J., Hämmerle, M., Esk, C., Bagley, J. A., Lindenhofer, D., Chen, G., Boehm, M., Agu, C. A., Yang, F., Fu, B., Zuber, J., Knoblich, J. A., Kerjaschki, D., & Penninger, J. M. (2019). Human blood vessel organoids as a model of diabetic vasculopathy. *Nature*, *565*(7740), 505-510.

Zeng, R.-C., Li, X.T., Li, S. Q., Zhang, F., & Han, E.-H. (2015). In vitro degradation of pure Mg in response to glucose. *Scientific Reports*, *5*(1), 13026.

Author Information

Djedjiga Ben Abdesselam
Mouloud Mammeri University of Tizi-Ouzou Faculty of Construction Engineering Department of Mechanical Engineering Laboratory of Structural Mechanics and Energy (LMSE) B.P.17 RP Tizi-Ouzou, Algeria.
Contact e-mail: djedjiga.benabdesselam@ummto.dz

Nacer Zazi
Mouloud Mammeri University of Tizi-Ouzou Faculty of Construction Engineering Department of Mechanical Engineering Laboratory of Structural Mechanics and Energy (LMSE) B.P.17 RP Tizi-Ouzou, Algeria.

Fatah Hellal
Ecole Nationale Polytechnique, Department of Metallurgy, LSGM, BP 182, 16051, El Harrach, Algiers, Alegria.

Youcef Hadj Ali
Mouloud Mammeri University of Tizi-Ouzou Faculty of Construction Engineering Department of Mechanical Engineering Laboratory of Structural Mechanics and Energy (LMSE) B.P.17 RP Tizi-Ouzou, Algeria.

Jean Paul Chopart
MATIM Laboratory, University of Reims Champagne-Ardenne, 51687 Reims, France.

Mărioara Abrudeanu
Interdisciplinary Doctoral School, University of Pitesti, Str. Targu din Vale Nr. 1, 110040 Pitesti, Romania.

Denis Negrea
Interdisciplinary Doctoral School, University of Pitesti, Str. Targu din Vale Nr. 1, 110040 Pitesti, Romania.

To cite this article:

Ben-Abdesselam, D. & Zazi, N. Hadj-Ali, Y.,. Hellal, F. Chopart, J.P. Abrudeanu, M., & Negrea, D. (2024). Effect of preliminary nitric chemical treatment on corrosion behavior of 316 stainless steel in chloride solution contain glucose. *The Eurasia Proceedings of Science, Technology, Engineering & Mathematics (EPSTEM), 32, 66*-79.

The Eurasia Proceedings of Science, Technology, Engineering & Mathematics (EPSTEM)
ISSN: 2602-3199

The Eurasia Proceedings of Science, Technology, Engineering & Mathematics (EPSTEM), 2024

Volume 32, Pages 80-85

IConTES 2024: International Conference on Technology, Engineering and Science

Effect of Crystallite Size on Magnetic Properties of Nanostructured FeAlTiBZr Alloy

Abderrahmane Younes
Research Center in Industrial Technologies (CRTI)

Nadia Metidji
UDES/Centre de Développement des Energies Renouvelables (CDER) Bou Ismail

Nacer Dilmi
Center for Development of Advanced Technologies

Rachid Amraoui
Research Center in Industrial Technologies (CRTI)

Abderahim Abada
University of Blida

Abstract: This study investigates the influence of crystallite size (D) on two key magnetic parameters, saturation magnetization (MS) and coercivity (HC), in nanostructured FeAlTiBZr alloy. The fabrication of this nanostructured material involved a mechanical grinding process. Structural, morphological, and magnetic properties of the nanostructured FeAlTiBZr alloy at various production stages were thoroughly examined using advanced characterization techniques, including Scanning Electron Microscopy (SEM), Energy Dispersive Spectroscopy (EDS), X-ray Diffraction (XRD), and Vibrating Sample Magnetometer (VSM). The crystallite size decreased from 38 to 26 nm, while the lattice strain increased from 0.17933% to 0.25194%. This shift in lattice parameters, from 0.2867 to 0.2876, can be attributed to the milling time effect. Additionally, the morphology of particles underwent changes, with particle size increasing over the milling period. However, the magnetic properties exhibited a contrasting trend: coercivity, saturation magnetization, remanence magnetization, and squareness decreased from 55.78 Oe, 77.35 emu/g, 3.08 emu/g, and 0.039 to 42.83 Oe, 66.39 emu/g, 2.04 emu/g, and 0.030, respectively.

Keywords: Nanostructured FeAlTiBZr alloy, Magnetic properties, Structural and morphology

Introduction

In recent years, the development of nanostructured materials has garnered significant attention due to their unique properties and potential applications in various fields, including electronics, energy storage, and magnetic devices. Among these materials, nanostructured FeAlTiBZr alloy holds particular promise for its intriguing magnetic properties and structural characteristics (Xu et al., 2019; Ji et al., 2011; Zhang et al., 2016,; Kuchibhatla et al., 2007; Gao et al., 2013). This study delves into the effects of crystallite size (D) on two fundamental magnetic parameters, saturation magnetization (Ms) and coercivity (Hc), in nanostructured FeAlTiBZr alloy. Fabricated through a mechanical grinding process, this alloy offers a compelling avenue for exploring the intricate interplay between structural, morphological, and magnetic properties at the nanoscale. Utilizing advanced characterization techniques such as Scanning Electron Microscopy (SEM), Energy Dispersive Spectroscopy (EDS), X-ray Diffraction (XRD), and Vibrating Sample Magnetometer (VSM), this research meticulously investigates the evolution of the nanostructured FeAlTiBZr alloy throughout different production stages. Key focus is placed on elucidating changes in crystallite size, lattice strain, morphology, and magnetic behavior as influenced by milling time.

The findings presented herein shed light on the complex relationship between crystallite size and magnetic properties in nanostructured materials, offering valuable insights into the design and optimization of magnetic devices. Moreover, this study underscores the significance of structural and morphological characterization in tailoring the properties of nanostructured alloys for diverse applications.

Method

The synthesis process employed a PM 400 ball mill with two WC jars, operated at 280 rpm. Nanostructured FeAlTiBZr was synthesized by blending elemental powders of Fe, Al, Ti, B, and Zr at a mass ratio of 1:12. The raw materials exhibited mean particle sizes of 62 µm, 55 µm, 51 µm, 43 µm, and 58 µm for Fe, Al, Ti, B, and Zr, respectively, with purities of 99.7%, 99.1%, 99.3%, 98.8%, and 98.9%, respectively.

Morphological changes were examined using SEM microscopy equipped with EDS spectroscopy. X-ray diffraction analysis, performed with an XPERT PRO instrument using Co Kα radiation (wavelength λ = 1.7902 Å) in the 2θ range from 0° to 120°, facilitated the identification of different phases during milling and determination of structural parameters. The magnetic properties, influenced by milling time, were evaluated utilizing a Micro Sense EV9 vibrating sample magnetometer.

Results and Discussion

Structural Analysis

In Figure 1, the progress of XRD patterns for nanostructured FeAlTiBZr alloys milled for various periods is depicted. Each sample exhibits distinct diffraction peaks, accompanied by observable broadening and intensity fluctuations, indicative of particle size reduction and strain accumulation throughout the milling process. Upon detailed analysis of alloys milled for different durations, notable transformations emerge. The diffraction peaks exhibit increased broadness and reduced relative intensity, hinting at phenomena extending beyond conventional grain refinement and lattice strain.

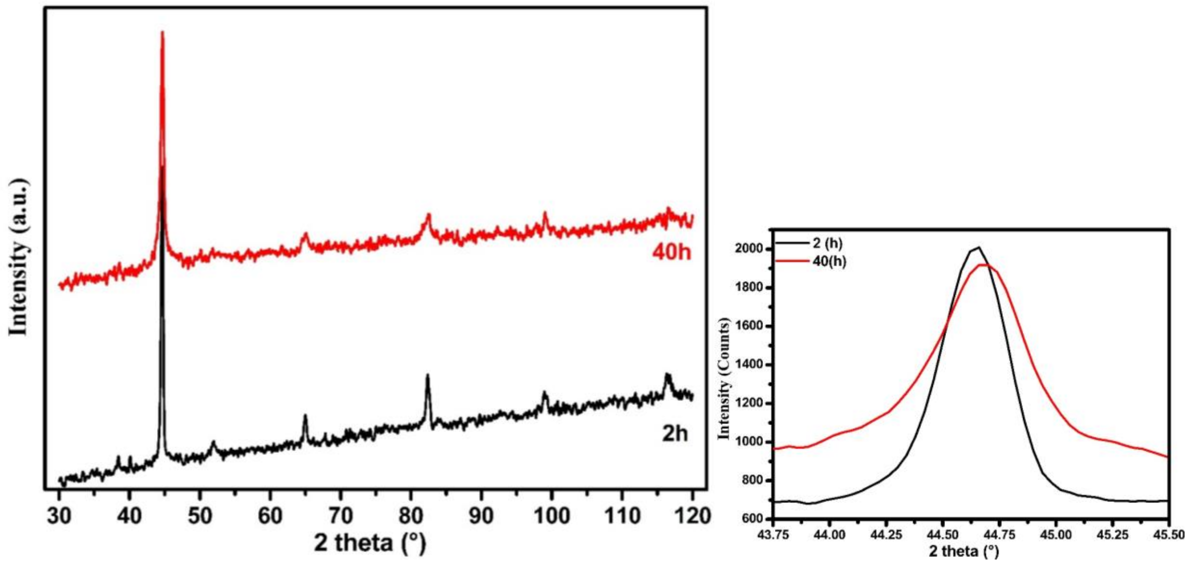

Figure 1. XRD patterns of nanostructured FeAlTiBZr alloy milled with different times

Table 1 presents the dynamic changes in structural parameters, including crystallite size, lattice strain, and lattice parameters, observed in nanostructured FeAlTiBZr throughout the milling process. The data indicates a significant reduction in crystallite size, from an initial value of 38 nm to 26 nm, concomitant with an increase in lattice strain, rising from 0.17933% to 0.25194%. These alterations are primarily attributed to the milling time effect, where prolonged mechanical milling leads to enhanced dislocation densities and lattice defects, thereby contributing to strain accumulation and crystallite refinement. Furthermore, a discernible shift in lattice parameters is evident, transitioning from 0.2867 to 0.2876, indicative of lattice distortion induced by mechanical deformation during milling. This phenomenon underscores the intricate interplay between processing parameters and resultant structural modifications in nanostructured alloys (Metidji et al., 2023; Metidji et al., 2020; Metidji et al., 2022)

Table 1. Structural parameters of nanostructured FeAlTiBZr alloy milled with different times

Milling time (h)	Crystallite size (nm)	FWHM (°)	lattice strain (%)	lattice parameters (nm)
2h	38	0.25	0.17933	0.2867
40h	26	0.269	0.25194	0.2876

Morphology

Figure 2 depicts the scanning electron microscope (SEM) analysis of nanostructured FeAlTiBZr alloy subjected to varying grinding durations. Initially, at 2 hours of grinding, the Fe, Al, Ti, B, and Zr particles exhibit a coarse or agglomerated state, resulting in irregularly shaped particles and clusters. However, with prolonged grinding durations extending up to 40 hours, the mechanical forces exerted by the grinding tool, including the grinding balls, induce continuous deformation and fragmentation of the particles.

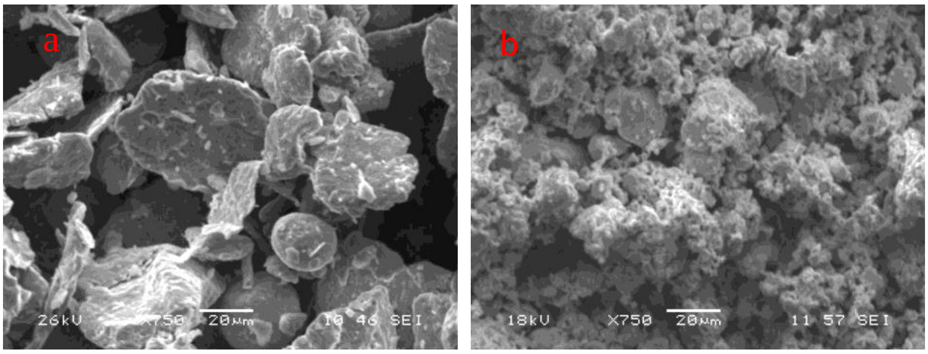

Figure 2. SEM examination of nanostructured FeAlTiBZr alloy milled with different times

This mechanical action leads to a progressive reduction in particle size and alters their morphology. Specifically, the nanostructured alloy particles undergo a transformation towards smaller and more regular shapes compared to their initial state. This phenomenon arises from the cumulative effect of particle fracture and refinement mechanisms such as cold welding and grain boundary rearrangement induced by prolonged mechanical milling. The resulting nanostructured morphology holds implications for the material's properties and performance in various applications (Peng et al., 2019; Fan et al., 2020; Pereira et al., 2007; Shen et al., 2023).

Magnetic Investigation

The hysteresis analysis of the nanostructured FeAlTiBZr alloy was conducted by a Vibrating Sample Magnetometer (VSM) apparatus, employing an applied magnetic field ranging from -17 kOe to 17 kOe, as illustrated in Figure 3. It was observed that all samples exhibit ferromagnetic behavior, characterized by narrow hysteresis loops, indicative of the formation of soft magnetic materials. Notably, the nanostructured FeAlTiBZr alloy achieves full saturation at a magnetic field of 17 kOe.

The magnetic properties of the nanostructured FeAlTiBZr alloy, influenced by milling duration, are subject to various factors such as particle size, shape, chemical composition, milling conditions, and the presence of impurities (Metidji et al., 2020). Previous studies have established correlations between observed magnetic behavior and structural defects, underscoring the pivotal role of prolonged milling times in phase transformation processes. Interestingly, despite the milling-induced alterations in other structural parameters, such as lattice strain and morphology, the crystallite size of the milled samples undergoes only marginal changes throughout the milling process (Jirásková et al., 2018). This observation suggests a nuanced interplay between milling-induced structural modifications and resultant magnetic properties, warranting further investigation into the underlying mechanisms governing the magnetic behavior of nanostructured alloys (Hsieh et al., 2011).

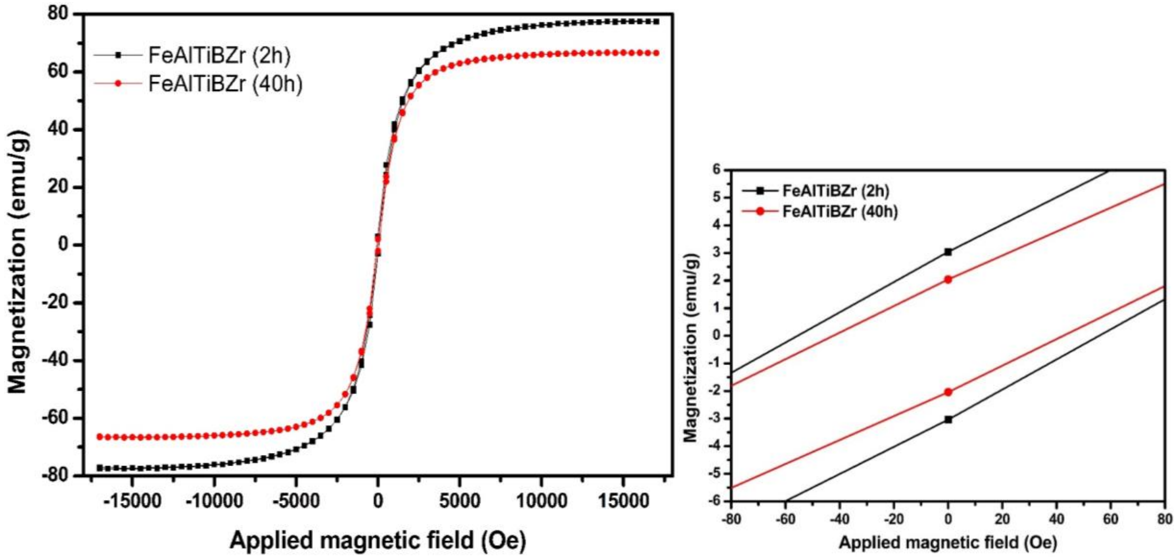

Figure 3**.** Hysteresis loops of nanostructured FeAlTiBZr alloy milled with different times

Table 2 presents the evolution of coercivity (Hc), saturation magnetization (Ms), remanence magnetization (Mr), and the ratio of remanence magnetization to saturation magnetization (Mr/Ms) over various milling durations. Coercivity (Hc) exhibits a consistent decrease over time, correlating with the reduction in average crystallite size. This relationship highlights the important influence of particle size variations on Hc. As particle size diminishes, the heightened surface-to-volume ratio increases surface reactivity, facilitating the formation of crystallographic defects such as dislocations and vacancies. These defects serve to effectively pin magnetic domain walls, thereby augmenting the coercivity of the nanostructured alloy (Rico et al., 2012; Meng et al., 2017).

Table 1. Magnetic parameters of nanostructured FeAlTiBZr alloy milled with different times

Milling time (h)	Hc (Oe)	Ms (emu/g)	Mr (emu/g)	Mr/Ms
2	55.78	77.35	3.08	0.039
40	42.83	66.39	2.04	0.030

The notable increase in both saturation magnetization (Ms), remanence magnetization (Mr), and the ratio Mr/Ms observed in the nanostructured FeAlTiBZr alloy during milling is closely tied to profound alterations in the magnetic domain structure. This phenomenon is further compounded by the heightened magnetic anisotropy resulting from concurrent processes of particle size reduction and defect formation (Strothers et al. 1991 and Strothers et al. 2023).

Conclusion

In conclusion, this study provides a comprehensive analysis of the structural and magnetic properties of nanostructured FeAlTiBZr alloy synthesized through mechanical milling. Through systematic investigation, it was observed that milling duration plays a crucial role in shaping the structural characteristics and magnetic behavior of the alloy. Notably, the reduction in crystallite size and increase in lattice strain during milling signify the progressive refinement and deformation of the alloy particles.

Furthermore, the observed trends in coercivity (Hc), saturation magnetization (Ms), and remanence magnetization (Mr) underscore the intricate interplay between particle size, defect formation, and magnetic domain structure. The decrease in Hc alongside the simultaneous rise in Ms, Mr, and the Mr/Ms ratio suggest a transition towards soft magnetic behavior, facilitated by the enhanced magnetic anisotropy resulting from particle size reduction and defect-induced pinning effects. These findings shed light on the fundamental mechanisms governing the magnetic properties of nanostructured alloys and hold significant implications for the design and optimization of magnetic materials for various technological applications. Future research endeavors may focus on further elucidating the underlying mechanisms driving the observed phenomena and exploring novel processing techniques to tailor the properties of nanostructured alloys for specific applications.

Recommendations

Future research should refine milling parameters and explore alloy composition adjustments to enhance control over magnetic properties. Advanced characterization and modeling would provide deeper insights; while environmental stability and application-specific testing, particularly for high-frequency devices, will help, confirm practical utility. Alternative synthesis methods and scalability assessments will also support transitioning FeAlTiBZr alloys from lab to industrial applications.

Scientific Ethics Declaration

The authors declare that the scientific ethical and legal responsibility of this article published in EPSTEM Journal belongs to the authors.

Acknowledgements or Notes

* This article was presented as a poster presentation at the International Conference on Technology, Engineering and Science (www.icontes.net) held in Antalya/Turkey on November 14-17, 2024.

References

Fan, J. T., Zhang, M. D., Zhang, L. J., Fu, L. M., Yu, P. F., Liaw, P. K., & Li, G. (2020). A new multi-component alloy with a nanostructured morphology and superior mechanical behavior. *Materials Science and Engineering: A, 771*, 138616.

Gao, M. R., Xu, Y. F., Jiang, J., & Yu, S. H. (2013). Nanostructured metal chalcogenides: synthesis, modification, and applications in energy conversion and storage devices. *Chemical Society Reviews, 42*(7), 2986-3017.

Hsieh, C. C., Jian, M. Y., Chang, H. W., Zhao, X. G., & Chang, W. C. (2011). Magnetic properties and high frequency characteristics of sputtered FeAl and FeAlB. *Journal of Physics: Conference Series*, *266*(1), 012031.

Ji, L., Lin, Z., Alcoutlabi, M., & Zhang, X. (2011). Recent developments in nanostructured anode materials for rechargeable lithium-ion batteries. *Energy & Environmental Science, 4*(8), 2682-2699.

Jirásková, Y., Pizurova, N., Titov, A., Janickovic, D., & Friak, M. (2018). Phase separation in Fe-Ti-Al alloy–structural, magnetic, and Mössbauer study. *Journal of Magnetism and Magnetic Materials, 468*, 91-99.

Kuchibhatla, S. V., Karakoti, A. S., Bera, D., & Seal, S. (2007). One dimensional nanostructured materials. *Progress in Materials Science, 52*(5), 699-913.

Metidji, N., & Younes, A.(2022). Effects of boron, nickel and molybdenum content on the microstructure, mechanical behaviour and wear properties of FeAl alloy made by vacuum arc melting. *Transactions of the Indian Institute of Metals, 75*(10), 2691–2699.

Metidji, N., Bacha, N.E., Younes, A.,& Saidi, D. (2020). The effect of Ti addition on microstructure and magnetic properties of nanocrystalline FeAl40 alloy powders prepared by mechanical alloying. *Powder Metallurgy and Metal Ceramics, 59*(3-4), 160–170

Metidji, N., Younes, A., Allou, D., & Dilmi, N. (2023). Effect of zirconium on the corrosion behavior of FeAl40Ti3B intermetallic compounds for use in solar water heaters. *Journal of Applied Electrochemistry, 54*(6),1-11.

Peng, J., Moszner, F., Rechmann, J., Vogel, D., Palm, M., & Rohwerder, M. (2019). Influence of Al content and pre-oxidation on the aqueous corrosion resistance of binary Fe-Al alloys in sulphuric acid. *Corrosion Science, 149*, 123-132.

Pereira, R. D., Passamani, E. C., Larica, C., Freitas, J. C. C., & Takeuchi, A. Y. (2007). Nanostructured FeZrCuB alloys prepared by mechanosynthesis. *Journal of Applied Physics, 102*(3).

Rico, M. M., Alcázar, G. P., & Greneche, J. M. (2014). Effect of boron in Fe 70 Al 30 nanostructured alloys produced by mechanical alloying. *LACAME 2012: Proceedings of the 13th Latin American Conference on the Applications of the Mössbauer Effect, (LACAME 2012)* (pp. 307-315). Netherlands: Springer.

Shen, G., Xiang, Z., Ma, X., Huang, J., Li, J., Wang, B., & Chen, Z. (2023). Microstructures and mechanical properties of a nanostructured Al-Zn-Mg-Cu-Zr-Sc alloy under natural aging. *Materials, 16*(12), 4346.

Xu, C., Anusuyadevi, P. R., Aymonier, C., Luque, R., & Marre, S. (2019). Nanostructured materials for photocatalysis. *Chemical Society Reviews, 48*(14), 3868-3902.

Zhang, J., Liu, X., Neri, G., & Pinna, N. (2016). Nanostructured materials for room-temperature gas sensors. *Advanced Materials, 28*(5), 795-831.

Author Information

Abderrahmane Younes
Research Centre in Industrial Technologies (CRTI)
P.OBox 64, Cheraga 16014 Algiers, Algeria
Contact e-mail: *younesabdo11@gmail.com*

Nadia Metidji
UDES/Centre de Développement des Energies Renouvelables, CDER Bou Ismail, 42415, Tipaza, Algeria

Nacer Dilmi
Center for Development of Advanced Technologies, 20 Aout 1956, Baba Hassan, Algiers, Algeria

Rachid Amraoui
Research Center in Industrial Technologies (CRTI)
P.OBox 64, Cheraga 16014 Algiers, Algeria

Abderahim Abada
Laboratory of Aeronautic Science, Aeronautic Institute, University of Blida 1
BP 270 road Soumâa -Blida-, Algeria

To cite this article:

Younes, A., Metidji, N., Dilmi, N., Amraoui, R., & Abada, A. (2024). Effect of crystallite size on magnetic properties of nanostructured FeAlTiBZr alloy. *The Eurasia Proceedings of Science, Technology, Engineering & Mathematics (EPSTEM), 32,* 80-85.

The Eurasia Proceedings of Science, Technology, Engineering & Mathematics (EPSTEM)
ISSN: 2602-3199

The Eurasia Proceedings of Science, Technology, Engineering & Mathematics (EPSTEM), 2024

Volume 32, Pages 86-92

IConTES 2024: International Conference on Technology, Engineering and Science

The Effect of Rehabilitation on the Vulnerability Evolution of an RC Water Tank throughout Its Lifecycle

Amar Aliche
Mouloud Mammeri University

Hocine Hammoum
Mouloud Mammeri University

Karima Bouzelha
Mouloud Mammeri University

Ourdia Ider
Mouloud Mammeri University

Abstract: In the field of civil engineering, reinforced concrete (RC) storage tanks are considered as important infrastructure that play a key role in the daily life of citizens, given their role of supply and storage of drinking water. These structures undergo regular monitoring and inspections as part of preventive maintenance programs to ensure their proper functioning and safety, as they are exposed to degradation and ageing due to natural hazards such as earthquakes, wind, and unfavorable weather. Expensive rehabilitation actions are often necessary to extend their lifecycle.In this context, a predictive model of vulnerability index evolution is developed, using a combined finite element approach with exponential extrapolation. This numerical model can predict the vulnerability evolution at any time in the lifecycle of the RC tank, following rehabilitation actions. This predictive model is successfully tested on a real case of RC storage tank located in the Tizi-Ouzou region (Algeria), and demonstrated its efficacy.

Keywords: Vulnerability, Concrete tanks, Rehabilitation, Predictive model, Lifecycle.

Introduction

In Algeria, drinking water reservoir infrastructures comprise approximately 40,000 tanks, the majority of which are constructed with reinforced concrete (Hammoum et al., 2012). These infrastructures, considered as specialized structures, hold a crucial position within civil engineering constructions. Their essential role in daily life gives them significant socio-economic importance. Owing to this, they are highly sensitive to public opinion. The closure of these tanks for maintenance or repair often causes negative reactions from consumers. In response to growing societal demand for water, the managers of these infrastructures must address numerous challenges, such as the ageing of the materials and structures, the increased risk of extreme climatic events, and the necessity to maintain or even improve service levels.

The assessment of the condition and behavior of these ageing storage structures, while taking into account these constraints, is therefore essential to ensure their continuous operation. The study of the degradation and ageing of these structures has been the focus of numerous research efforts. Several experts have developed methods and techniques for diagnosis, risk analysis (vulnerability), and the development of action and maintenance plans: Curt (2007) and Peyras (2002) have worked on dams, Serre (2009) on flood protection levees, while Hammoum (2011), Mathieu (2003), and Aliche (2016, 2017) have focused on storage tanks.

As part of this research, and in order to better manage rehabilitation interventions, which are often costly and complex, and to prioritize the structures to be rehabilitated, a novel approach is proposed, aiming at determining the impact of rehabilitation and maintenance actions on the vulnerability evolution of a reinforced concrete reservoir throughout its life cycle. Our approach is based on the predictive model developed by Aliche et al. (2017), assuming that the progression of ageing is known up to the time of intervention, a post-rehabilitation vulnerability model is proposed. The present case study yielded satisfactory results.

Methodology for Evaluation of the Vulnerability Index 'Iv'

The vulnerability index 'Iv' of a reinforced concrete storage tank at time (t) is obtained based on the method proposed by Hammoum (2011, 2012), involving thirteen (13) influential parameters: environmental, structural, and functional, as defined in Table 1.

Table 1. List of analysis parameters

Analysis type	N°	Definition of the parameters
Environmental Analysis	1	Tank location
	2	Seismic zone
	3	Soil type
	4	Snow zone
	5	Wind zone
Structural Analysis	6	Structure type
	7	Foundation type
	8	Sealing walls
	9	Sealing Cover
	10	Apparent defects
Functional Analysis	11	Tank role
	12	Tank importance
	13	Maintenance frequency

Each of these thirteen parameters will be assigned an elementary grading 'Nei'. The chosen grading principle corresponds to the criteria for amplifying grades based on vulnerability increasing risk. To each grade is assigned a weighting coefficient 'Pi'. Both the elementary grades Nei and weighting coefficient Pi for each parameter range from 1 to 4: where 1 corresponds to the ideal situation, while 4 to the critical situation. The partial grade of a parameter is then obtained through the product (Nei × Pi), and the vulnerability index 'Iv' is then expressed as the sum of the partial grades of the various parameters, as given by equation (1).

$$Iv = \sum_{i=1}^{13} N_{ei} \cdot P_i = N_e + N_s + N_f \tag{1}$$

Considering all the analysis criteria listed above, a classification scale for reservoirs, classifying vulnerability into four levels is adopted (Table 2).

Table 2. Classification of Reservoirs Based on their 'Iv'.

Vulnerability level	Green	Orange 1	Orange 2	Red
Vulnerability index IV	13 - 49	49 - 87	87 - 136	136– 196

The application of the vulnerability index method to the reservoir stock in the Tizi-Ouzou province has highlighted an evolution of the vulnerability index (Iv) throughout the life cycle of the tanks.

The methodology presented has been successfully tested on a real scale with a stock of 30 circular reinforced concrete tanks assessed in the Tizi-Ouzou province (northern Algeria). This region is classified as an area of moderate seismicity (Zone IIa) according to the Algerian Seismic Regulation (RPA99/2003). According to the Snow and Wind Regulation, the region is classified as Snow Zone A and Wind Zone I. The vulnerability index 'Iv' is determined for each tank based on the technical sheets were developed and completed during the assessment. Table 3 provides an example of an evaluation of the vulnerability index 'Iv' for the Touaresse tanks located in the centre of the Draa Ben Kheda district in the Tizi-Ouzou province.

Table 3. Evaluation of the Vulnerability Index 'Iv' of a tank.

Analysis	Elementary parameter	Scoring Criteria	N_{ei}	Weighting parameter	Scoring Criteria	Pi	$N_{ei}.P_i$
Environmental	Tank location	mountain	1.00	Hydraulic parameter	Center northern band	3.00	3.00
	Seismic zone	Zone IIa	2.00	Implantation site	Urban area	4.00	8.00
	Soil type	Loose soil	3.00	Site Effect	Risk of sliding	4.00	12.00
	Snow zone	Zone A	4.00	Roofing form	Vault	1.00	4.00
	Wind zone	Zone I	2.00	Height Land category Topographic site Surface state	Ph = 0,75, Pc = 0,50, Pt = 0,75, Ps = 0,75.	2.75	5.50
Structural	Type of tank	On ground	3.00	Material	Reinforced concrete	3.00	9.00
	Foundation type	General raft	2.00	Settlement state	No apparent	1.00	2.00
	Sealing walls	Classe B	2.00	Seal State	Moderately satisfactory	3.00	6.00
	Cover Type	Sealing by coating	2.00	Seal State	Anough satisfactory	2.00	4.00
	Gravity index	Level 3	3.00	Age of the tank	49 years	4.00	12.00
Functional	Tank role	Distribution	2.00	Accessibility to the tank	By paved road	1.00	2.00
	Importance of tank	For buildings (Group 1B)	3.00	Capacity of the tank	Capacity : 1000 m^3	2.00	6.00
	Maintenance frequency	Annual	4.00			4.00	4.00
					Vulnerability Index I_V		**77.50**

At the scale of the stock and for each tank, the vulnerability index was calculated on the day of the assessment, while the vulnerability index was simulated on the day of commissioning. The results of these calculations are illustrated in Table 5.

Predictive Model Iv(t)

Table 4. Evolution of the variation in the vulnerability index of a typical reservoir over time

N°	Location	Year of commissioning	Year of expertise	Whole domain	Elements	subdomains	Age of the tank (ti)	I_{vo}	I_{vi}	ΔI_{vi}
01	Taghanimth	2014	2014	**0 < t < 49**	1	Ω^1	0	47.50	47.50	00.00
02	Sidi-Namane (SR2)	2012	2014				2	53.50	54.50	01.00
03	Mouldiouane Zone	2010	2014				4	49.50	51.50	02.00
04	Megdoule 1	2008	2014		2	Ω^2	6	54.00	56.50	02.50
05	Taksebt	2000	2010				10	43.00	48.50	05.50
06	Sidi-Namane (SR1)	1999	2014				15	53.50	59.50	06.00
07	Behalil 1	1996	2014		3	Ω^3	18	46.00	53.00	07.00
08	Kaf Laagab	1988	2014				26	56.00	65.00	09.00
09	Tighilt Tiguerfiouine	1985	2014				29	56.00	66.00	10.00
10	Herrouka 2	1984	2014		4	Ω^4	30	46.00	56.50	10.50
11	Touares 2	1980	2014				34	61.00	72.00	11.00
12	Taghanimth	1972	2010				38	47.50	60.50	13.00
13	Mekla Chef-Lieu (SR2)	1975	2014		5	Ω^5	39	50.50	64.00	13.50
14	Herrouka 1	1972	2014				42	48.50	63.50	15.00
15	Touares 1	1965	2014				49	60.50	77.50	17.00

In a professional context, it would be impractical to wait several decades to obtain a series of data for each assessed tank. To address this constraint, an alternative approach is suggested, based on the analysis of the thirteen parameters common to several tanks of different ages, in order to identify a typical tank that is the subject of study (Table 4) (Aliche et al., 2017).

The evolution of the vulnerability index of a typical tank over time, within a known domain, has resulted in the following mathematical model (Aliche et al., 2017):

$$I_v(t) = I_{v0}+\Delta I_v(t) \quad (2)$$

This evolution is illustrated in the case of the Touares tank, located in the Draa Ben Khedda district (Tizi-Ouzou, Algeria).

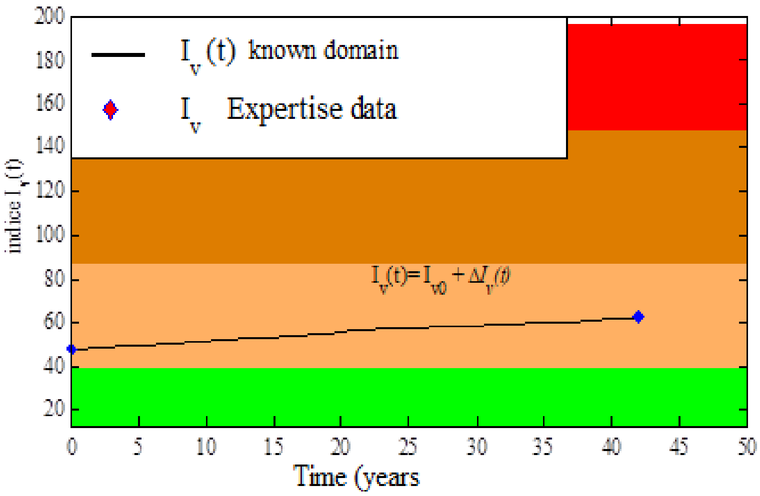

Figure 1. Evolution of the vulnerability index of the Touares tank

To assess the evolution of the ageing of a tank in an unknown domain, the extrapolation of the observed data into the future using an exponential model is performed, as shown in (Aliche et al., 2016):

$$I_v(t) = I_{v49} + \Delta I_{v39}\ e^{0.0231*(t\text{-}39)} \qquad \text{Pour } t\ > 49 \quad (3)$$

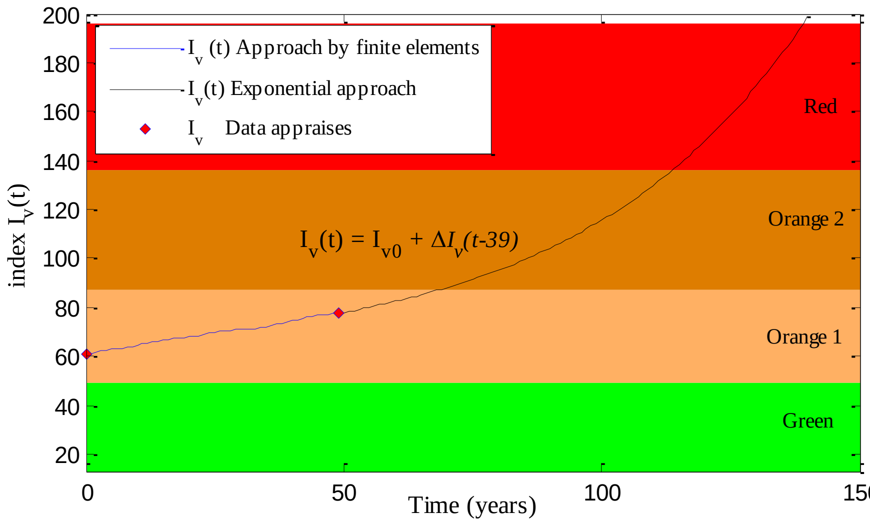

Figure 2. Evolution of the index $I_V(t)$ through the different levels of vulnerability of the Touares tank

Figure 2 illustrates the evolution of index Iv(t) of the Touares tank, showing the different levels of vulnerability that it may reach during its life cycle, based on the developed model. It can be observed that at commissioning, the tank was at level orange 1; it reaches level orange 2 at 68 years and then level red at the age of 114 years, where it should be taken out of service or, at least, immediately placed under usage restrictions. It will reach the extreme level of ruin at the age of 139 years.

Impact of Maintenance on the Evolution of the Vulnerability Index

The Reinforced concrete water storage tanks, like all civil engineering structures, age and deteriorate over their life cycle; this is why these structures enter a new era that requires maintenance actions. One can mention two main maintenance strategies (3): corrective maintenance and preventive maintenance (Figure 3). The choice of one strategy over the other varies depending on the element considered, as well as the type of structure and the operational and monitoring policy (Cremona, 2011).

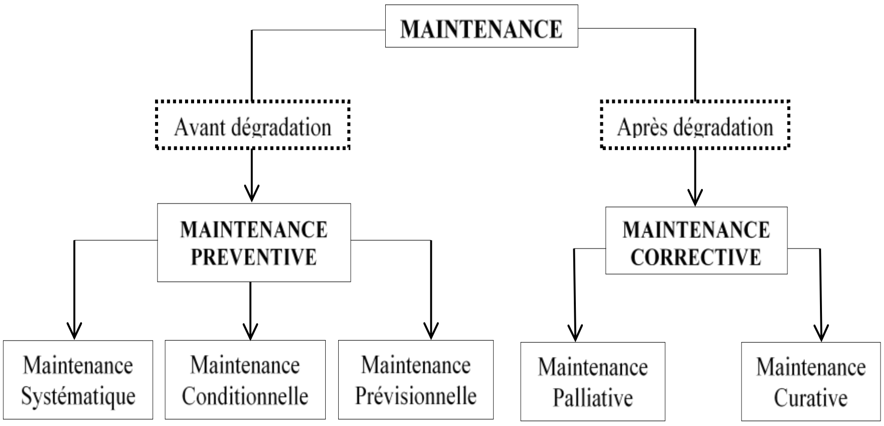

Figure 3. Maintenance strategies (Zwingelstein, 1996)

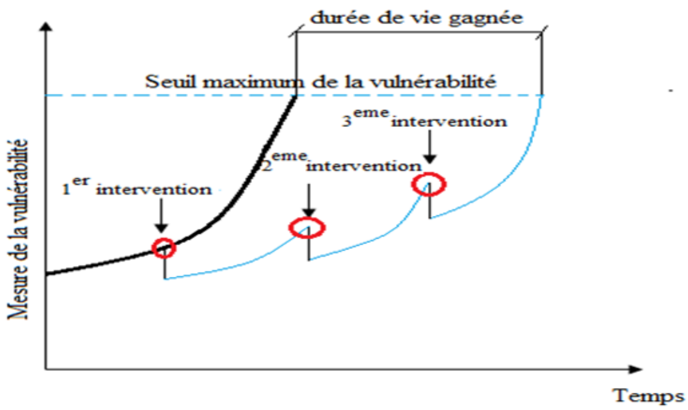

Figure 4. Impact of maintenance on the evolution of vulnerability in the life cycle of the structure (Cremona, 2011)

In real-life scenarios, it is recommended that the manager organizes frequent maintenance and reinforcement actions for the improved ageing behavior of these structures. Figure 4 shows the effect of certain maintenance actions on the evolution of the vulnerability index Iv(t). These actions theoretically allow the vulnerability state of the structure to be returned to a previous condition, which, in most cases, lies between the initial vulnerability state and the state prior to intervention. The effect of this action on the life cycle of the structure is represented by the gained life span referred to as 'time gained,' as illustrated in Figure 4 (Zwingelstein et al, 1996).

Presentation of the Model: Rehabilitation Actions

In order to introduce a 'Rehabilitation Actions' module into the model developed in the previous section, the impact assessment of one or more rehabilitation actions on the evolution of the vulnerability index, during the life cycle of tanks from the assessed stock was performed. These actions should be undertaken while the vulnerability index of the structure is at the 'moderately vulnerable' level, which is, within the limits of the end of the orange 1 range and the beginning of the orange 2 range. The idea is to enhance the performance of the structure and prevent it from entering the advanced vulnerability zone, (the red range), where it would be taken out of service.

To highlight the impact of the rehabilitation action, the example of the Touares tank discussed in the previous section will be revisited. Let us assume that the first rehabilitation action is carried out on this tank at the boundary between the orange 1 and orange 2 domains, addressing its structural and functional parameters. This first rehabilitation action will reduce the index of the structure from Iv = 87 to Iv_R = 72.50 (Figure 5).

Thus, the evolution law of the vulnerability index of the structure at a time ($t > t_R$) after rehabilitation becomes:

$$I_v^R(t) = I_{v0} + \Delta I_{v0}^R e^{0.231(t - t_R)} \tag{4}$$

With:

$$\Delta I_{v0}^R = I_v^R(t_R) - I_{v0} \tag{5}$$

$I_v^R(t_R)$ Denotes the vulnerability index of the structure after rehabilitation at age t_R.

After this first rehabilitation action, the red vulnerability level is reached at the age of 151 instead of 114 years, which corresponds to a lifespan gain of 37 years. If a second rehabilitation action was to be carried out at the age of t_{R2} = 105 years, corresponding to the boundary of the orange 2 domain, the vulnerability index of the structure would decrease from 87 to 76, and the red vulnerability level would be reached at the age of 174 years, representing a second lifespan gain of 23 years. With these two rehabilitation actions, the tank will gain a lifespan of 60 years (Figure 6).

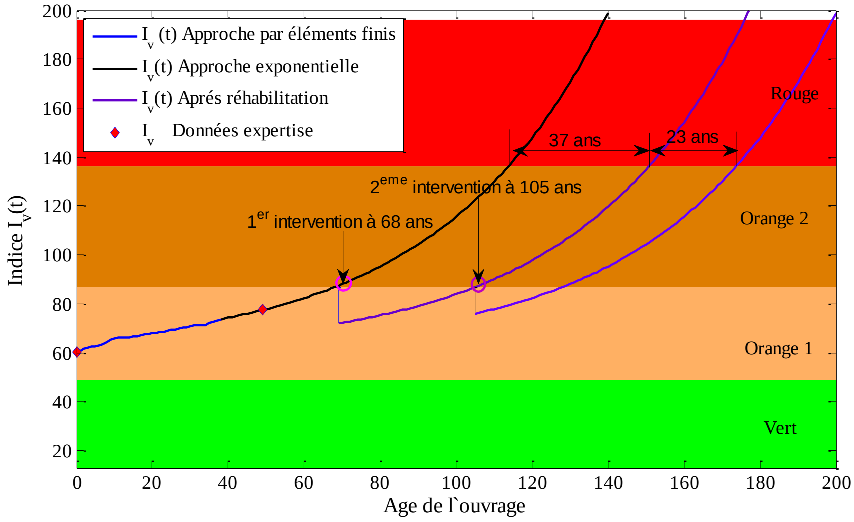

Figure 5. Evaluation of the index I_V after the rehabilitation action

Conclusion

In this research, a model for the vulnerability evolution of ageing concrete tanks, incorporating the concept of rehabilitation is proposed. The developed relationships allow for a simplified and rapid assessment of vulnerability related to the ageing of tanks at any point in their life cycle. For managers, this model provides insight into the lifespan that a structure can gain after a rehabilitation action, facilitating the establishment of a priority intervention plan within their rehabilitation or repair program, thus optimizing the management of the infrastructure stock and allowing for proactive planning of financial investments, particularly in the case of significant budget constraints. Furthermore, for engineers in design offices, these relationships can be used from the design phase of the structure, enabling the simulation of the vulnerability index during its operation and predicting the frequency of monitoring.

Scientific Ethics Declaration

The authors declare that the scientific ethical and legal responsibility of this article published in EPSTEM Journal belongs to the authors.

Acknowledgements or Notes

* This article was presented as a poster presentation at the International Conference on Technology, Engineering and Science (www.icontes.net) held in Antalya/Turkey on November 14-17, 2024.

References

Aliche, A. (2016). *Contribution to the analysis of the evolution of vulnerability in concrete reservoirs throughout their life cycle*. (Doctoral dissertation). Mouloud Mammeri University of Tizi-Ouzou, Algeria.

Aliche, A., Hammoum, H., Bouzelha, K., & Hannachi, N. E. (2017). Development and validation of predictive model to describe the growth of concrete water tank vulnerability with time. *Periodica Polytechnica Civil Engineering*, *61*(2), 244-255.

Cremona, C. (2011). *Structural performance: Probability-based assessment.* Hoboken, USA: John Wiley & Sons.,

DTR/B-C 2–48. (2003). National seismic code for building design and construction (R.P.A 99/ version 2003).

Hammoum, H., Bouzelha, K., Hannachi, N., & Serre, D. (2011). Vulnerability assessment of the concrete tanks storage at natural hazards. *Proceeding Concrete Solutions 2011*, 45-53

Hammoum, H., Bouzelha, K., Hannachi, N.E., & Serre, D. (2012). Vulnerability assessment of the concrete tanks storage at natural hazards. Grantham, V. Mechtcherine, U. Schnech (Eds.). In *Concrete solution*. London: Taylor and Francis Group CRC Press.

Mathieu, G. (2003). Méthodologie d'évaluation des ouvrages hydrauliques en béton appliquée un patrimoine. *Annales du BTP*, *5*(6), 39-61.

Peyras, L., Royet, P., & Boissier, D. (2002). Development of a scenario-based DSS for dam ageing diagnosis. *Journal of Decision Systems*, *11*, 445–458.

Serre, D., Peyras, L., Curt, C., Boissier, D., & Diab, Y. (2007). Evaluation des ouvrages hydrauliques de génie civil. *Canadian Geotechnical Journal*, *44*(11), 1298-1313.

Serre, D., Peyras, L., Maurel, P., Tourment, R., & Diab, Y. (2009). A spatial decision support system aiding levee managers in their repair and maintenance planning. *Journal of Decision Systems*, *18(*3), 347-373.

Zwingelstein, G. (1996). *La maintenance basée sur la fiabilité, guide pratique d'application de la RCM* Paris: Hermès.

Author Information

Aliche Amar
Mouloud Mammeri University
Civil Engineering Department, Mouloud Mammeri University, 15 000 Tizi-Ouzou, Algeria
Contact e-mail: *amar.aliche@ummto.dz*

Hammoum Hocine
Mouloud Mammeri University
Civil Engineering Department, Mouloud Mammeri University, 15 000 Tizi-Ouzou, Algeria

Bouzelha Karima
Mouloud Mammeri University
Civil Engineering Department, Mouloud Mammeri University, 15 000 Tizi-Ouzou, Algeria

Ider Ourdia
Mouloud Mammeri University
Civil Engineering Department, Mouloud Mammeri University, 15 000 Tizi-Ouzou, Algeria

To cite this article:

Aliche, A,. Hammoum, H., Bouzelha, K., & Ider, O. (2024). The effect of rehabilitation on the vulnerability evolution of an RC water tank throughout its lifecycle. *The Eurasia Proceedings of Science, Technology, Engineering & Mathematics (EPSTEM), 32,* 86-92.

The Eurasia Proceedings of Science, Technology, Engineering & Mathematics (EPSTEM)
ISSN: 2602-3199

The Eurasia Proceedings of Science, Technology, Engineering & Mathematics (EPSTEM), 2024

Volume 32, Pages 93-100

IConTES 2024: International Conference on Technology, Engineering and Science

Enhancing Analysis of Cross-Ply Laminated Composite Plates: A Simplified Approach for Flexural and Stability Evaluation

Abdelmoumen Anis Bousahla
University of Sidi Bel Abbés

Hichem Bellifa
University of Sidi Bel Abbés

Abdeldjabbar Tounsi
University of Sidi Bel Abbés

Lakhdar Khelifa
University of Rélizane

Abstract: In this article, we examine cross-ply laminated composite plates using a simple sinusoidal shear deformation model to analyze their flexural and stability behaviors. Our model, which contains only four unknown variables, offers a more concise alternative to first-order shear deformation theories (FSDT) or other higher-order models. By integrating undetermined integral terms into the in-plane kinematics, we accurately capture the influence of shear deformation. Our proposed theory ensures adherence to the conditions of zero shear stress at the bottom and top faces of the plates, without resorting to the shear correction coefficient. The equations of motion stem from our formulation using the principle of virtual work in its dynamic version. The an analytical solution is obtained through double trigonometric series proposed by Navier. We then compare the stresses, displacements and natural frequencies, forces calculated using our method with other published data, thereby demonstrating a good level of agreement between the results.

Keywords: Shear deformation, Flexural, Navier, Cross-ply laminates, Laminated plates.

Introduction

Composite materials are increasingly utilized across various engineering sectors due to their remarkable attributes, such as high strength, stiffness, lightweight nature, exceptional thermal properties, corrosion resistance, prolonged fatigue life, and resilience to wear. The accurate assessment of their structural behavior, including both free vibration and bending, is paramount.

In thicker structures, the influence of transverse shear strain becomes more pronounced compared to thinner counterparts, necessitating advanced plate models capable of accurately predicting both free vibration and bending characteristics. Classical plate theory (CPT), pioneered by Kirchhoff (1850). Proves inadequate for thick structures as it neglects transverse shear deformation. Similarly, first-order shear deformation theory (FSDT), proposed by Mindlin (1951). Lacks in meeting zero stress conditions at plate surfaces and necessitates the use of shear correction factors.

To overcome these shortcomings, several higher-order shear deformation theories have been proposed. In recent years, novel plate models, characterized by minimal variables, have emerged. For instance introduced a two variable model tailored for the dynamic study of orthotropic plates, later extending its application to account for

- Selection and peer-review under responsibility of the Organizing Committee of the Conference

thermo-mechanical effects in functionally graded plates. (Shimpi & Patel,2006). Another notable development involves models incorporating undetermined integral terms to simplify governing equations, aiming to enhance the accuracy of both free vibration and bending analyses of composite plates without relying on shear correction coefficients.

In this study, we evaluate the effectiveness of a refined four-variable shear deformation theory in analyzing the free vibration and bending behavior of composite plates. The model integrates undetermined integral terms into its kinematic description to accommodate shear deformation effects, ensuring zero shear stress at plate surfaces. By deriving equations of motion through the virtual work principle and obtaining analytical solutions via a double trigonometric series method, we compare our findings with exact elasticity solutions reported by Pagano (1970). For free vibration analysis, for dynamic analysis, and for stability analysis of laminated composite plates (Noor,1973, 1975). This comparative analysis provides insights into the efficacy of our proposed model in accurately predicting both the free vibration and bending characteristics of composite plates.

Theoretical Formulation

Consider a rectangular plate with sides of lengths *aa* and *bb*, a uniform thickness *hh*, and an origin at point *oo* as illustrated in Fig. 1. The plate is composed of *nn* homogeneous layers, perfectly bonded together, and each layer is made of linearly elastic, orthotropic material. This plate occupies the region defined by these dimensions. $0 \leq x \leq a$, $0 \leq y \leq b$, $-h/2 \leq z \leq h/2$ in Cartesian coordinate system. A transverse load q(x, y) is applied on the upper surface of the plate.

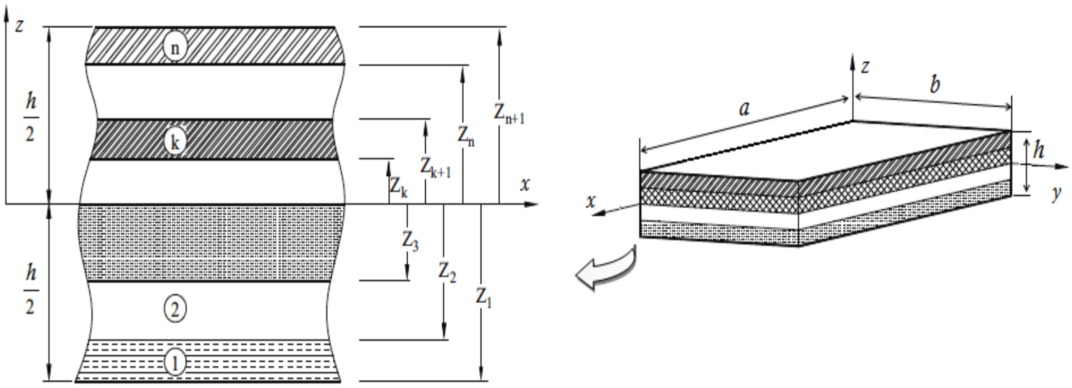

Figure 1. Rectangular plate

Kinematics and Strains

In the unified shear-deformable plate theory, the displacement field at a point in the laminated plate is expressed as (Bakhadda et al., 2018).

$$\begin{aligned} u(x,y,z) &= u_0(x,y) - z\frac{\partial w_0}{\partial x} + f(z)\varphi_x(x,y) \\ v(x,y,z) &= v_0(x,y) - z\frac{\partial w_0}{\partial y} + f(z)\varphi_y(x,y) \\ w(x,y,z) &= w_0(x,y) \end{aligned} \tag{1}$$

a shape function determining the changes in the transverse shear strain and the stress distribution along the thickness of the plate and is defined as (Touratier,1991).

$$f(z) = \left(\frac{h}{\pi}\right)\sin\left(\frac{\pi z}{h}\right) \tag{2}$$

The strains associated with the present theory are obtained using strain-displacement relationship from theory of elasticity.

$$\begin{Bmatrix} \varepsilon_x \\ \varepsilon_y \\ \gamma_{xy} \end{Bmatrix} = \begin{Bmatrix} \dfrac{\partial u}{\partial x} \\ \dfrac{\partial v}{\partial y} \\ \dfrac{\partial u}{\partial y} + \dfrac{\partial v}{\partial x} \end{Bmatrix} = \begin{Bmatrix} \varepsilon_x^0 \\ \varepsilon_y^0 \\ \gamma_{xy}^0 \end{Bmatrix} + z \begin{Bmatrix} \varepsilon_x^1 \\ \varepsilon_y^1 \\ \gamma_{xy}^1 \end{Bmatrix} + f(z) \begin{Bmatrix} \varepsilon_x^2 \\ \varepsilon_y^2 \\ \gamma_{xy}^2 \end{Bmatrix} \tag{3a}$$

$$\begin{Bmatrix} \gamma_{yz} \\ \gamma_{xz} \end{Bmatrix} = \begin{Bmatrix} \dfrac{\partial v}{\partial z} + \dfrac{\partial w}{\partial y} \\ \dfrac{\partial u}{\partial z} + \dfrac{\partial w}{\partial x} \end{Bmatrix} = g(z) \begin{Bmatrix} \gamma_{yz}^0 \\ \gamma_{xz}^0 \end{Bmatrix} \tag{3b}$$

Constitutive Relations

Given that the laminate consists of multiple orthotropic layers, the stress-strain relations for the layer of the laminated plate in the material coordinate system are expressed as:

$$\begin{Bmatrix} \sigma_x \\ \sigma_y \\ \tau_{xy} \\ \tau_{yz} \\ \tau_{xz} \end{Bmatrix}^{(k)} = \begin{bmatrix} \overline{Q}_{11} & \overline{Q}_{12} & \overline{Q}_{16} & 0 & 0 \\ \overline{Q}_{12} & \overline{Q}_{22} & \overline{Q}_{26} & 0 & 0 \\ \overline{Q}_{16} & \overline{Q}_{26} & \overline{Q}_{66} & 0 & 0 \\ 0 & 0 & 0 & \overline{Q}_{44} & 0 \\ 0 & 0 & 0 & 0 & \overline{Q}_{55} \end{bmatrix}^{(k)} \begin{Bmatrix} \varepsilon_x \\ \varepsilon_y \\ \gamma_{xy} \\ \gamma_{yz} \\ \gamma_{xz} \end{Bmatrix}^{(k)} \tag{4}$$

the plane stress-reduced stiffness coefficients defined in terms of the engineering constants in the material axes of the layer:

$$Q_{11} = \frac{E_{11}}{1-\nu_{12}\nu_{21}}, Q_{22} = \frac{E_{22}}{1-\nu_{12}\nu_{21}}, Q_{12} = \frac{\nu_{12}E_{11}}{1-\nu_{12}\nu_{21}}, \tag{5a}$$

$$Q_{66} = G_{12}, Q_{44} = G_{23}, \quad Q_{44} = G_{23}, Q_{55} = G_{13} \tag{5b}$$

Equations of Motion

The governing equations and boundary conditions of the present higher order shear deformation theory are derived using principle of virtual work. The principle of virtual work is applied in the following analytical form (Bourada et al., 2019).

$$\int_{-h/2}^{h/2} \int_A \left(\sigma_x \delta\varepsilon_x + \sigma_y \delta\varepsilon_y + \tau_{xy} \delta\gamma_{xy} + \tau_{yz} \delta\gamma_{yz} + \tau_{xz} \delta\gamma_{xz} \right) dAdz + \int_{-h/2}^{h/2} \int_A \rho \left(\frac{\partial^2 u}{\partial t^2} \delta u + \frac{\partial^2 v}{\partial t^2} \delta v + \frac{\partial^2 w}{\partial t^2} \delta w \right) dAdz$$
$$- \int_A q(x,y) \delta w dA - \int_A \left(N_x^0 \frac{\partial^2 w}{\partial x^2} + N_y^0 \frac{\partial^2 w}{\partial y^2} + 2N_{xy}^0 \frac{\partial^2 w}{\partial x \partial y} \right) \delta w dA = 0 \tag{6}$$

where A is the area of the top surface of the plate, ρ is the density of material, $q(x, y)$ and N_x^0, N_y^0, N_{xy}^0 are transverse and in-plane applied loads, respectively. The symbol δ denotes the variational operator. Substituting expressions for stresses and virtual strains into the principle of virtual work and integrating Eq. (6) by parts and collecting the coefficients of δu_0, δv_0, δw_0 and $\delta\theta$ the following equations of motion of the plate are obtained in terms of stress resultants, Cartesian coordinate system and the stress resultants $(N_x,\ N_y,\ N_{xy})$, $(M_x^b,\ M_y^b,\ M_{xy}^b)$, $(M_x^s,\ M_y^s,\ M_{xy}^s)$ and $(S_{xz}^s,\ S_{yz}^s)$ are defined as:

$$
\begin{aligned}
\left(N_x, N_y, N_{xy}\right) &= \sum_{k=1}^{n} \int_{z_k}^{z_{k+1}} \left(\sigma_x, \sigma_y, \tau_{xy}\right) dz, \\
\left(M_x^b, M_y^b, M_{xy}^b\right) &= \sum_{k=1}^{n} \int_{z_k}^{z_{k+1}} \left(\sigma_x, \sigma_y, \tau_{xy}\right) z dz, \\
\left(M_x^s, M_y^s, M_{xy}^s\right) &= \sum_{k=1}^{n} \int_{z_k}^{z_{k+1}} \left(\sigma_x, \sigma_y, \tau_{xy}\right) f(z) dz, \\
\left(Q_{xz}^s, Q_{yz}^s\right) &= \sum_{k=1}^{n} \int_{z_k}^{z_{k+1}} \left(\tau_{xz}, \tau_{yz}\right) g(z) dz
\end{aligned} \tag{7}
$$

and the inertia constants I_i $(i = 0, 2, 3, 4, 5)$ are defined by the following equations:

$$
\left(I_0, I_1, I_2, I_3, I_4, I_5\right) = \sum_{k=1}^{n} \int_{z_k}^{z_{k+1}} \rho^{(k)} \left(1, z, z^2, f(z), z\ f(z), [f(z)]^2\right) dz \tag{8}
$$

Analytical Solution for Laminated Composite Plates

The Navier approach is employed to determine the analytical solutions for the free vibration analysis of simply supported laminated rectangular plates. The following simply supported boundary conditions at all four edges are given by:

$$
u_0 = w_0 = N_y = M_y^b = M_y^s = \theta = 0 \quad \text{on edges } (y = 0, b) \tag{9a}
$$

$$
v_0 = w_0 = N_x = M_x^b = M_x^s = \theta = 0 \quad \text{on edges } (x = 0, a) \tag{9b}
$$

The displacement variables which automatically satisfy the above boundary conditions can be expressed in the following Fourier series:

$$
\begin{Bmatrix} u_0 \\ v_0 \\ w_0 \\ \theta \end{Bmatrix} = \sum_{m=1}^{\infty} \sum_{n=1}^{\infty} \begin{Bmatrix} U_{mn} \cos(\alpha\ x) \sin(\beta\ y)\ e^{i\omega t} \\ V_{mn} \sin(\alpha\ x) \cos(\beta\ y)\ e^{i\omega t} \\ W_{mn} \sin(\alpha\ x) \sin(\beta\ y)\ e^{i\omega t} \\ \Phi_{mn} \sin(\alpha\ x) \sin(\beta\ y)\ e^{i\omega t} \end{Bmatrix} \tag{10}
$$

where U_{mn}, V_{mn}, W_{mn} and Φ_{mn} are the unknown Fourier coefficients to be determined for each (m, n) value, as well as the parameters α and β are defined as:

$$
\alpha = m\pi / a,\ \beta = n\pi / b \tag{11}
$$

The transverse load $q(x, y)$ is expanded in the double-Fourier sine series as:

$$
q(x, y) = \sum_{m=1}^{\infty} \sum_{n=1}^{\infty} q_{mn} \sin(\alpha\ x) \cos(\beta\ y) \tag{12}
$$

where $q_{mn} = q_0$ for sinusoidally distributed load $m = 1, n = 1$ and q_0 is the maximum intensity of distributed load at the centre of plate. Substituting the solution form from Eq. (10) and the transverse load from Eq. (7) into the equations results in the following matrix representation.

$$\begin{bmatrix} K_{11} & K_{12} & K_{13} & K_{14} \\ K_{12} & K_{22} & K_{23} & K_{24} \\ K_{13} & K_{23} & K_{33}+N_{33} & K_{34} \\ K_{14} & K_{24} & K_{34} & K_{44} \end{bmatrix} - \omega^2 \begin{bmatrix} M_{11} & M_{12} & M_{13} & M_{14} \\ M_{12} & M_{22} & M_{23} & M_{24} \\ M_{13} & M_{23} & M_{33} & M_{34} \\ M_{14} & M_{24} & M_{34} & M_{44} \end{bmatrix} \begin{Bmatrix} U_{mn} \\ V_{mn} \\ W_{mn} \\ \Phi_{mn} \end{Bmatrix} = \begin{Bmatrix} 0 \\ 0 \\ q_{mn} \\ 0 \end{Bmatrix} \tag{13}$$

Discussion of Numerical Results

Bending Analysis of Laminated Composite Plates

The bending analysis of simply supported anti-symmetric laminated composite square plates under sinusoidally distributed load is conducted using the following material properties.

$$E_{11} = 25E_{22}\,,\; G_{12} = G_{13} = 0.5E_{22}\,,\; G_{23} = 0.2E_{22}\,,\; \nu_{12} = 0.25\,,\; \nu_{21} = \frac{E_{22}}{E_{11}}\nu_{12} \tag{14}$$

The displacements and stresses are presented in the following non-dimensional form.

$$\bar{u}\left(0,\frac{b}{2},-\frac{h}{2}\right) = \frac{uE_2h^2}{q_0a^3}\,,\; \bar{w}\left(\frac{a}{2},\frac{b}{2},0\right) = \frac{100wh^3E_2}{q_0a^4}\,,\; \bar{\sigma}_x = \frac{h^2}{q_0a^2}\sigma_x\left(\frac{a}{2},\frac{b}{2},-\frac{h}{2}\right),$$
$$\bar{\sigma}_y = \frac{h^2}{q_0a^2}\sigma_y\left(\frac{a}{2},\frac{b}{2},-\frac{h}{2}\right),\; \bar{\tau}_{xy} = \frac{h^2}{q_0a^2}\tau_{xy}\left(0,0,-\frac{h}{2}\right),$$
$$\bar{\tau}_{xz} = \frac{h}{q_0a}\tau_{xz}\left(0,\frac{b}{2},0\right),\bar{\tau}_{yz} = \frac{h}{q_0a}\tau_{yz}\left(\frac{a}{2},0,0\right) \tag{15}$$

Table 1. Comparison of non-dimensional displacements and stresses for the two layered (0°/90°) laminated composite square plate subjected to sinusoidally distributed load.

a/h	Theory	$\bar{u}$	$\bar{w}$	$\bar{\sigma}_x$	$\bar{\sigma}_y$	$\bar{\tau}_{xy}$	$\bar{\tau}_{xz}$	$\bar{\tau}_{yz}$
4	Present	0.0114	1.9766	0.9143	0.0889	0.0577	0.1274	0.1274
	Sayyad et al. (2016)	0.0114	1.9793	0.9154	0.0890	0.0578	0.0660	0.1276
	Sayyad and Ghugal (2014a)	0.0111	1.9424	0.9062	0.0964	0.0562	0.1270	0.1270
	Reddy (1984)	0.0114	2.0256	0.9172	0.0932	0.0713	0.1270	0.1270
	Mindlin (1951)	0.0088	1.9682	0.7157	0.0843	0.0525	0.0910	0.0910
	Kirchhoff (1850)	0.0088	1.0636	0.7157	0.0843	0.0525	—	—
	Pagano (1970)	—	2.0670	0.8410	0.1090	0.0591	0.1200	0.1350
10	Present	0.0093	1.2132	0.7483	0.0851	0.0533	0.1304	0.1304
	Sayyad et al. (2016)	0.0093	1.2135	0.7484	0.0851	0.0534	0.1270	0.1306
	Sayyad and Ghugal (2014a)	0.0092	1.2089	0.7471	0.0876	0.0530	0.1300	0.1300
	Reddy (1984)	0.0095	1.2479	0.7652	0.0889	0.0680	0.1310	0.1310
	Mindlin (1951)	0.0088	1.2083	0.7157	0.0843	0.0525	0.0910	0.0910
	Kirchhoff (1850)	0.0088	1.0636	0.7157	0.0843	0.0525	—	—
	Pagano (1970)	—	1.2250	0.7302	0.0886	0.0535	0.1210	0.1250

In this numerical illustration, we showcase the efficacy of the current theory in analyzing the bending behavior of simply supported two-layered (0°/90°) anti-symmetric laminated composite square plates under sinusoidally distributed loads. We compare and discuss the non-dimensional displacement and stresses computed using our model with those obtained from classical plate theory (CPT) by Kirchhoff (1850), first-order shear deformation theory (FSDT) by Mindlin (1951), higher-order shear deformation theory (HSDT) by Reddy (1984), sinusoidal shear and normal deformation theory (SSNDT) by Sayyad and Ghugal (2014), and the exact elasticity solution provided by Pagano (1970). The non-dimensional results are tabulated in Table 1. It is observed that the in-plane displacement computed using our theory exhibits good agreement with results from other models. Specifically, the in-plane displacement is maximized in the 90° layer and minimized in the 0° layer (see Figure

2). While our proposed model slightly underestimates the transverse displacement for an aspect ratio of 4, it aligns well with exact solutions and other higher-order models for an aspect ratio of 10.

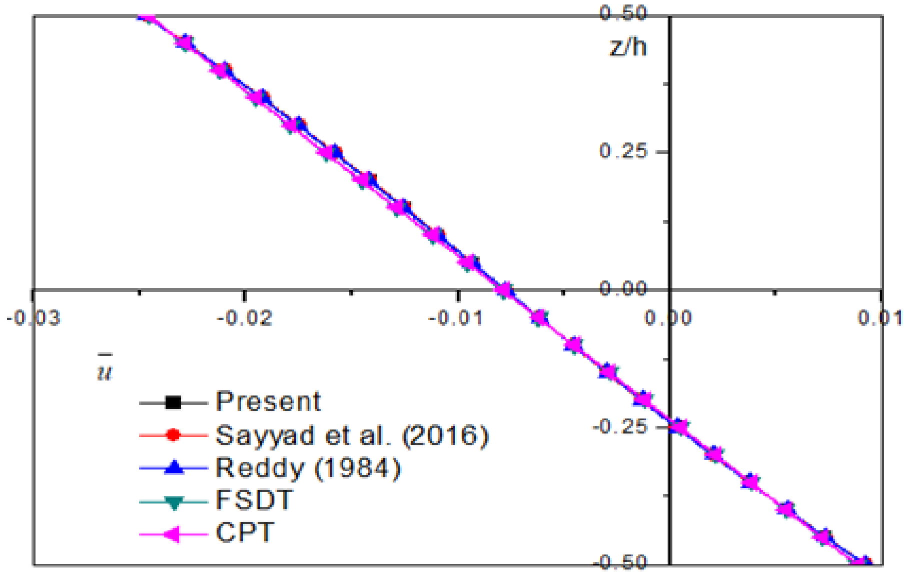

Figure 2. Through thickness distribution of in-plane displacement ($\bar{u}$) for two layered (0°/90°) laminated composite plate subjected to sinusoidally distributed load (*b/a*=1, *a/h*= 10)

Free Vibration Analysis of Laminated Composite Plates

For this study, the material properties given by Eq. (14) are employed. Natural frequencies are presented in the following non-dimensional form:

$$\bar{\omega} = \omega\sqrt{\rho h^2 / E_{22}} \tag{16}$$

Table. 2. Comparison of non-dimensional natural frequencies of simply supported square laminated composite plates (*a/h*= 10)

Lay-up	Theory	E_{11}/E_{22} 10	20	30	40
0/90	Present	0.27988	0.31355	0.34130	0.36499
	Sayyad et al. (2016)	0.27987	0.31354	0.34128	0.36498
	FSDT	0.27757	0.30824	0.33284	0.35353
	CPT	0.30968	0.35422	0.39335	0.42884
0/90/0	Present	0.34309	0.40641	0.44510	0.47165
	Sayyad et al. (2016)	0.34261	0.40623	0.44502	0.47162
	FSDT	0.32739	0.37110	0.39540	0.41158
	CPT	0.42599	0.55793	0.66419	0.75565
0/90/0/90	Present	0.3281	0.3852	0.4211	0.44658
	Sayyad et al. (2016)	0.3422	0.4055	0.4441	0.4706
	FSDT	0.3319	0.3826	0.4130	0.4341
	CPT	0.4260	0.5579	0.6642	0.7556
0/90/0/90/0	Present	0.3434	0.4066	0.4451	0.4718
	Sayyad et al. (2016)	0.3430	0.4063	0.4449	0.4715
	FSDT	0.3368	0.3930	0.4271	0.4506
	CPT	0.4259	0.5579	0.6641	0.7556

In Table 1, non-dimensional natural frequencies of simply supported square laminated composite plates for different modular ratios (E_{11}/E_{22}) are given and compared with those predicted SSNDT of (Sayyad et al.,2016). FSDT of (Mindlin,1951). CPT of (Kirchhoff,1850). Table 2 demonstrates that the proposed model accurately predicts the natural frequencies of laminated composite plates. In contrast, the CPT tends to overestimate these frequencies because it neglects the influence of transverse shear deformation. Additionally, it is observed that the natural frequencies of laminated composite plates increase as the modular ratios increase. (E_{11} / E_{22}).

Fig. 3 illustrates the variation of the natural frequency for simply supported square laminated composite plates with respect to the a/h ratio, based on the current refined sinusoidal shear deformation theory. It can be observed that the natural frequency decreases with increasing the ratio. This decrease is attributed to the plate becoming thinner as the a/h ratio increases. In other words, an increase in the a/h ratio corresponds to a decrease in the relative thickness of the plate, leading to a reduction in its stiffness and, consequently, its natural vibration frequency. This observation underscores the importance of considering not only material properties but also geometric dimensions when designing and analyzing laminated composite plates to ensure their desired vibrational performance.

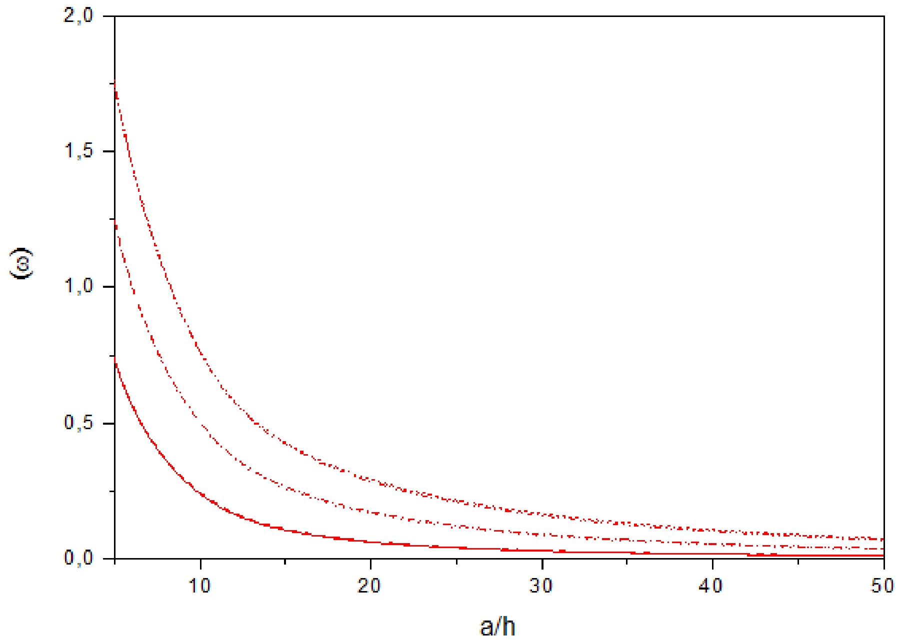

Figure 3. Variation of the natural frequency for the simply supported square laminated composite plates with respect to the a/h ratio

Conclusions

In this study, we have utilized a refined theory of sinusoidal shear deformation to analyze both the free vibrations and bending behavior of laminated composite plates. The simplicity of this theory, with only four unknowns compared to five in first-order shear deformation theory and other higher-order theories, significantly reduces computational complexity. Moreover, our theory effectively addresses the tensile conditions on the upper and lower surfaces of the plates without requiring a shear correction factor. This not only enhances efficiency but also improves accuracy in predicting the natural frequencies and bending responses of laminated composite plates. Numerical results demonstrate that our proposed theory closely aligns with experimental solutions reported in the literature, providing reliable predictions of both free vibration behavior and bending characteristics. Accurately predicting these aspects is vital for designing and analyzing composite structures where dynamic performance and bending integrity are paramount. In conclusion, our refined approach offers a more efficient and precise method for comprehensively analyzing the dynamic and bending characteristics of laminated composite plates, thus contributing to improved structural design and performance evaluation.

Scientific Ethics Declaration

The authors declare that the scientific ethical and legal responsibility of this article published in EPSTEM Journal belongs to the authors.

Acknowledgements or Notes

* This article was presented as a poster presentation at the International Conference on Technology, Engineering and Science (www.icontes.net) held in Antalya/Turkey on November 14-17, 2024.

References

Bakhadda, B., Bachir Bouiadjra, M., Bourada, F., Bousahla, A.A., Tounsi, A., & Mahmoud, S.R. (2018). Dynamic and bending analysis of carbon nanotube-reinforced composite plates with elastic foundation. *Wind and Structures*, *27*(5), 311-324.

Bourada, F., Bousahla, A.A., Bourada, M., Azzaz, A., Zinata, A., & Tounsi, A. (2019). Dynamic investigation of porous functionally graded beam using a sinusoidal shear deformation theory. *Wind and Structures*, *28*(1), 19-30.

Kirchhoff, G. (1850). Uber die uchwingungen einer kriesformigen elastischen scheibe. *Annalen der Physik, 81*, 58-264.

Kolahchi, R., & Cheraghbak, A. (2017). Agglomeration effects on the dynamic buckling of viscoelastic microplates reinforced with SWCNTs using Bolotin method. *Nonlinear Dynamics*, *90*(1), 479–492.

Kolahchi, R., Safari, M., & Esmailpour, M. (2016b). Dynamic stability analysis of temperature-dependent functionally graded CNT-reinforced visco-plates resting on orthotropic elastomeric medium. *Composite Structures*, *150*, 255–265.

Mindlin, R.D. (1951). Influence of rotary inertia and shear on flexural motions of isotropic, elastic plates. *Journal of Applied Mechanics ASME*, *18*(1), 31-38.

Noor, A.K. (1973). Free vibrations of multilayered composite plates. *AIAA Journal*, *11*(7), 1038-1039.

Noor, A.K. (1975). Stability of multilayered composite plates. *Fibre Science and Technology, 8*(2), 81-89.

Pagano, N.J. (1970). Exact solutions for bidirectional composites and sandwich plates. *Journal of Composite Materials*, *4*, 20-34.

Reddy, J.N. (1984). A simple higher-order theory for laminated composite plates. *Journal of Applied Mechanics*, *51*, 745-752.

Sayyad, A.S., &Ghugal, Y.M. (2014b). On the buckling ofisotropic, transversely isotropic and laminated composite rectangular plates. *International Journal of Structural Stability and Dynamics*, *14*, 1-32.

Sayyad, A.S., Shinde, B.M., & Ghugal, Y.M. (2016). Bending, vibration & buckling of laminated composite plates using a simple four variable plate theory. *Latin American Journal of Solids and Structures*, *13*(3), 516-535.

Shimpi, R.P., & Patel, H.G. (2006). A two variable refined plate theory for orthotropic plate analysis. *International Journal Solids and Structures*, *43*, 6783–6799.

Touratier, M. (1991). An efficient standard plate theory. *International Journal of Engineering Sciences*, *29*(8), 901–916.

Author Information

Abdelmoumen Anis Bousahla
Laboratoire des Matériaux et Hydrologie, Faculty of Technology, University of Sidi Bel Abbés, Algeria
Contact e-mail: bousahla.anis@gmail.com

Hichem Bellifa
Faculty of Technology, University of Sidi Bel Abbés, Algeria

Abdeldjabbar Tounsi
Laboratoire des Matériaux et Hydrologie, Faculty of Technology, University of Sidi Bel Abbés, Algeria

Lakhdar Khelifa
Faculty of Science and Technology, University of Rélizane, Relizane, Algeria

To cite this article:

Bousahla, A. A., Bellifa, H., Tounsi, A., & Khelifa, L. (2024). Enhancing analysis of cross-ply laminated composite plates: A simplified approach for flexural and stability evaluation. *The Eurasia Proceedings of Science, Technology, Engineering & Mathematics (EPSTEM), 32,* 93-100.

The Eurasia Proceedings of Science, Technology, Engineering & Mathematics (EPSTEM)
ISSN: 2602-3199

The Eurasia Proceedings of Science, Technology, Engineering & Mathematics (EPSTEM), 2024

Volume 32, Pages 101-105

IConTES 2024: International Conference on Technology, Engineering and Science

Research of Combined Copper Processing Technology Including Heat Treatment and Radial-Shear Rolling

Vladislav Pishchikov
Rudny Industrial University

Sergey Kuzmin
Rudny Industrial University

Valeriy Chigirinsky
Rudny Industrial University

Andrey Marukov
Rudny Industrial University

Abdrakhman Naizabekov
Innovative University of Eurasia

Irina Volokitina
Karaganda Industrial University

Abstract: This paper is devoted to the study of the influence of a combined technology, including both pre-heat treatment and deformation on a radial-shear rolling mill, on changes in the mechanical properties of M1 grade copper. The conducted studies have shown that after preliminary heat treatment, namely quenching at a temperature 500°C, and subsequent deformation of billets at temperatures of 20 and 200°C on a radial-shear rolling mill, an increase in the strength properties of copper is observed with a decrease in its plastic properties within the normal range. Also, according to the results of the conducted studies, it was found that the cross-section of the obtained copper bars shows a spread of microhardness values, which fully correlates with the data on the formation of areas with different microstructures after radial shear rolling in this cross-section.

Keywords: Combined technology, Pre-heat treatment, Radial shear rolling, Copper, Mechanical properties, Microhardness

Introduction

Currently, three-roll radial-shear rolling mills are widely used in the production of solid rolled bars of circular cross-section made of non-ferrous and ferrous metals and alloys. The main feature of the radial-shear rolling process is the ability to control the scheme of the stress-strain state of metal in a sufficiently wide range, which ensures the production of high-quality round rolled products with the necessary structure and a given level of mechanical properties. Currently, there are many scientific papers devoted to the study of the influence of radial-shear rolling on the evolution of microstructure and changes in the mechanical properties of not only various ferrous and non-ferrous metals, but also modern composite materials. Here are some of these scientific papers Gamin et al. (2021), Lezhnev et al. (2021), Arbuz et al. (2023), Akopyan et al. (2018), Gamin et al. (2023), Sheremet'ev et al. (2019), Lezhnev et al. (2023), Naizabekov et al.(2020). The authors of these works proved that using radial shear rolling, it is possible to produce high-quality bars of different sizes in diameter from various materials that will have a gradient ultra-fine-grained structure and a given level of mechanical properties.

It has also long been proven that heat treatment can also achieve additional grain refinement in various materials, if the correct modes of its implementation are chosen, which also has a positive effect on the properties of metal products subjected to heat treatment. Including in several scientific works, it was proved that combining into a single technological process pre-heat treatment in different modes and different methods of metal forming allows achieving better results in refining the initial grain of various materials (Lezhnev et al., 2014).

Based on the analysis of the above works, as well as several other works in this area of research, we have previously conducted studies of the effect of combined processing technology for M1 grade copper, including pre-heat treatment, namely quenching from a temperature of 500C and radial-shear rolling at temperatures of 20°C and 200°C, on evolution of the structure of this material. The results of these studies are given in Naizabekov et al. (2023). However, we did not study the effect of the combined technology considered in this paper on the change in the mechanical properties of M1 grade copper. Therefore, the purpose of this work is to study the combined technology of processing M1 grade copper, including heat treatment and radial-shear rolling, for changing the mechanical properties of this material.

Method

To achieve this goal, we conducted a physical experiment. As initial blanks, copper (M1 grade copper) blanks with a diameter of 25 mm and a length of 150 mm were taken. Which, based on the results previously obtained in Naizabekov et al. (2023), were subjected to preliminary heat treatment, namely, quenching from a temperature of 500C. Further, these billets were deformed on a radial shear rolling mill RSP 10-30 at two temperatures: 20 and 2000C. The blanks were deformed to a diameter of 16 mm and 12 mm with an absolute compression step of 3.0 mm in diameter when deformed to a diameter of 16 mm and 2.0 mm when deformed to a diameter of 12 mm (i.e. ∅25→∅22→∅19→∅16→∅14→∅12 mm) according to the standard deformation scheme, shown in Figure 1.

To determine the mechanical characteristics of the obtained M1 grade copper bars after preliminary heat treatment and multi-transition deformation at a radial-shear rolling mill, it was decided to conduct tensile tests and measure the microhardness distribution over the cross-section of the bars.

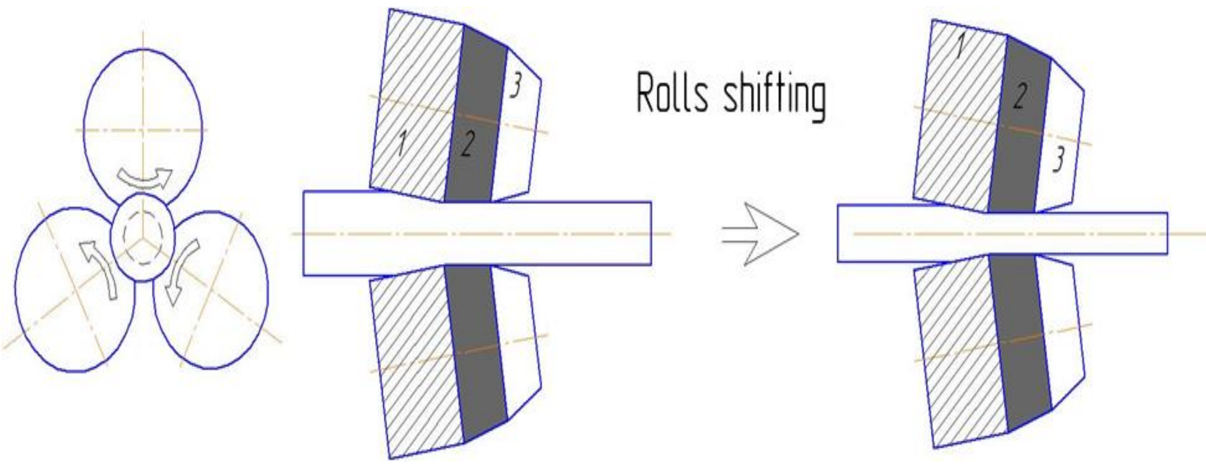

Figure 1. Scheme of billet deformation at the RSR 10-30 mill

To perform tear tests, test samples were cut from all deformed bars (both up to a diameter of 16 mm and 12 mm) on a high-precision automated cutting machine GTQ-5000 in the form of strips with dimensions h×b×l=0.3×3×30 mm. These strips were cut in the longitudinal direction of the bar from the surface, intermediate and the central zone. Similar samples were also prepared to determine the mechanical properties of M1 grade copper after preliminary heat treatment. The prepared samples were tested on a two-column digital tensile testing machine with a force of 1000 kN from Qingdao Guangyue Rubber Machinery Manufacturing Co., Ltd (China). At the same time, the tests for each material were duplicated three times to avoid errors.

Results and Discussion

Based on the obtained and statistically processed data of tensile tests, the average value of mechanical properties was determined and the corresponding graphs of the dependence of the ultimate strength σ b and the relative elongation δ on the type of processing were plotted (Figure 2). Analysis of the results of mechanical tests shown on the graphs of the dependence of the ultimate strength σ b and the relative elongation δ on the type of processing (Figure 2) showed that in the process of radial-shear rolling, the strength properties of M1 grade copper previously subjected to heat treatment according to the selected mode increase, both in the surface and in the intermediate and central regions of the deformed bar, and the value of the relative elongation, which characterizes the plastic properties of these materials, on the contrary, decreases. Moreover, the greater the compression, the greater these changes.

In addition, the graphs shown in Figure 2 show that the deformation temperature directly affects the change in mechanical properties. Thus, at the deformation temperature at the RSR mill equal to 200°C there is a smaller increase in the tensile strength and, accordingly, a smaller drop in the relative elongation for M1 grade copper compared to its deformation at a temperature of 20°C.

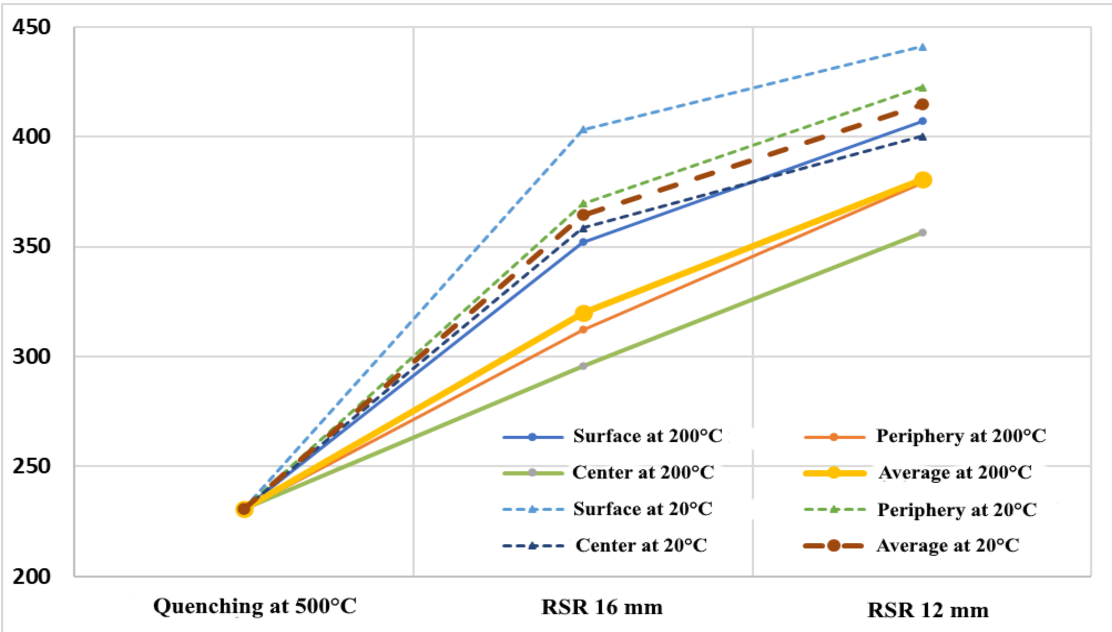

a)

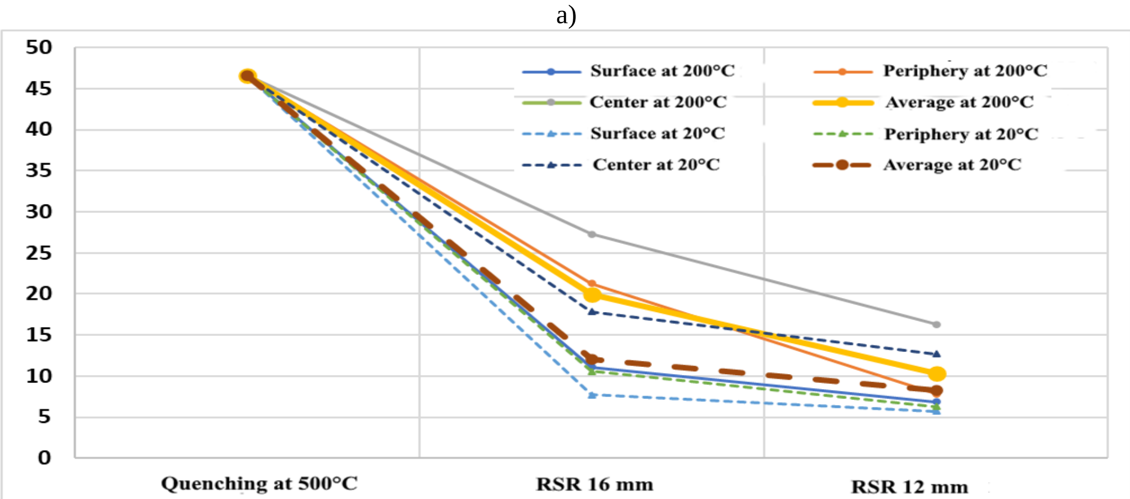

b)

Figure 2. Mechanical properties of M1 grade copper: A-ultimate strength σ; b - relative elongation δ

Also, from the graphs shown in Figure 2, the highest values of tensile strength and the lowest values of relative elongation are observed in the surface layers of the workpiece. Conversely, the highest values of relative elongation and the lowest values of ultimate strength are observed in the central layers of the workpiece. This is fully consistent with the previously reported results of studying the evolution of the microstructure of M1 grade copper during their deformation in a radial-shear rolling mill, which showed that a gradient structure is formed in these materials along the bar cross-section during the RSP process (Naizabekov et al., 2023). Also, from the obtained results of studying the mechanical characteristics of M1 grade copper, at the first stage of deformation, i.e. up to a diameter of 16 mm, the values of mechanical properties (strength and plastic) in the intermediate region are closer to the values of the same mechanical properties in the central zone of the deformable bar. With further deformation of these bars, the values of mechanical properties in the intermediate region become closer to the values of the same mechanical properties in the surface region of the deformable bar. This is also fully consistent with the results of the study of the evolution of the microstructure of various materials, which are also given in the works Gamin et al. (2021) Lezhnev et al. (2021) Arbuz et al. (2023) Akopyan et al. (2018) Gamin et al. (2023) Sheremet’ev et al. (2019) Lezhnev et al. (2023) Naizabekov et al. (2020). Namely, with the fact that during radial-shear rolling, with increasing compression, the number of elongated grains in the intermediate zone decreases and at the same time they become misoriented. A further increase in compression leads to the fact that the surface zone of deformable bars, as it were, absorbs the intermediate zone and an equiaxially fine-grained structure is formed in it, while preserving a small number of misoriented elongated grains.

To clarify the gradient of changes in the mechanical properties of M1 grade copper and compare it with the established features of the evolution of the microstructure gradient over the cross-section of the sample as it is modified by radial-shear rolling, microhardness distribution over the cross-section of 20°C to diameters of 16 and 12 mm was studied. Microhardness measurements were carried out on a microhardness meter "Micromet-II" with a load of 50 g according to GOST 9450-76. Analysis of the obtained results of microhardness studies over the cross-section of a copper bar showed that in general, they are consistent with the studies of microstructure evolution previously conducted in Naizabekov et al. (2023). So, in both cases (i.e., in a bar with a diameter of 16 mm, and in a bar with a diameter of 12 mm), a gradient distribution of microhardness over the cross-section of the bar is observed. The maximum values of microhardness for copper subjected to RSR are observed in the surface layers, and the minimum values are observed in the central zone, respectively. Thus, the maximum microhardness value in the surface layer of a bar with a diameter of 16 mm reached 940 MPa, and a diameter of 12 mm-1240 MPa (at the initial microhardness value of 545 MPa, i.e. after quenching from a temperature of 500°C). In the central layer of M1 grade copper deformed at the RSP mill, the average microhardness value was in a bar with a diameter of 16 mm – 765 MPa, and in a diameter of 12 mm-960 MPa.

Conclusion

Studies of the mechanical properties of M1 grade copper have shown that in the process of radial-shear rolling, the cross-section-averaged strength properties of these materials previously subjected to heat treatment under the selected modes increase, while the plastic ones, on the contrary, fall. Thus, for M1 grade copper, the cross-section-averaged value of the tensile strength after radial shear rolling at 200 ° C to a diameter of 12 mm increased by 65% compared to the value of this indicator after quenching at 500°C, and after RSR at a temperature of 20°C the same diameter by 80%. The average value of the relative elongation, which characterizes plastic properties, in a bar decreased by 78% after RSR to a diameter of 12 mm at a deformation temperature of 200°C and by 83% after RSR at a deformation temperature of 20C. The reduction of the plastic characteristic, namely the relative elongation, for M1 grade copper during radial shear rolling is within the normal range for this material subjected to severe plastic deformation during the implementation of various pressure processing methods. Microhardness studies have shown that the cross-section spread of microhardness values is observed in the copper bars obtained by the RSR, which is completely correlated with the data on the formation of areas with different microstructures in the cross-section of the bars after radial shear rolling.

Scientific Ethics Declaration

The authors declare that the scientific ethical and legal responsibility of this article published in EPSTEM Journal belongs to the authors.

Acknowledgements

* This article was presented as a poster presentation at the International Conference on Technology, Engineering and Science (www.icontes.net) held in Antalya/Turkey on November 14-17, 2024.

* This research was funded by the Science Committee of the Ministry of Science and Higher Education of the Republic of Kazakhstan (Grant № AP14869128).

References

Akopyan, T., Aleshchenko, A. S., Belov, N. A., & Galkin, S. P. (2018). Effect of radial-shear rolling on the formation of structure and mechanical properties of Al–Ni and Al–Ca aluminum-matrix composite alloys of eutectic type. *Physics of Metals and Metallography, 119*, 241-250.

Arbuz, A., Kawalek, A., Panichkin, A., Ozhmegov, K., Popov, F., & Lutchenko, N. (2023). Using the radial shear rolling method for fast and deep processing technology of a steel ingot cast structure. *Materials, 16*(24), 7547.

Gamin, Y. V., Galkin, S. P., Romantsev, B. A., Koshmin, A. N., Goncharuk, A. V., & Kadach, M. V. (2021). Influence of radial-shear rolling conditions on the metal consumption rate and properties of d16 aluminum alloy rods. *Metallurgist, 65*, 650-659.

Gamin, Y. V., Korotitskiy, A. V., Kin, T. Y., Galkin, S. P. Kostin, S. A., & Tikhomirov, E. O. (2022). Development of temperature-rate modes of hot deformation of the Co–28Cr–6Mo alloy based on processing maps. *Steel in Translation, 52*(11), 1027-1036.

Lezhnev, S. N., Naizabekov, A. B., Panin, E. A., Volokitina, I. E., & Arbuz, A. S. (2021). Graded microstructure preparation in austenitic stainless steel during radial-shear rolling. *Metallurgist, 64*(2), 1150-1159.

Lezhnev, S., Naizabekov, A., Pishchikov, V., Panin, E., & Arbuz, A. (2023). Investigation of the efficiency of reversible radial-shear rolling to obtain a gradient ultrafine-grained structure in 5KHV2S steel. *The Eurasia Proceedings of Science, Technology, Engineering and Mathematics (EPSTEM), 26*, 672-676.

Lezhnev, S., Volokitina, I., & Koinov, T. (2014). Research of influence equal channel angular pressing on the microstructure of copper. *Journal of Chemical Technology and Metallurgy, 49*(6), 621-630.

Naizabekov, A. B., Lezhnev, S. N., & Arbuz, A. S. (2020). The effect of radial-shear rolling on the microstructure and mechanical properties of technical titanium. *Solid State Phenomena, 299*(27), 565-570.

Naizabekov, A. B., Volokitina, I. E., Panin, E. A., & Volokitin, A. V. (2023). Studies of the effect of preliminary heat treatment on the evolution of copper microstructure during deformation. *Collection of Scientific Papers of the International Scientific and Practical Conference "Advanced Engineering Technologies", 292*-296.

Sheremet’ev, V. A., Kudryashova, A. A., Dinh, X. T., Galkin, S. P., Prokoshkin, S. D., & Brailovskii, V. (2019). Advanced technology for preparing bar from medical grade Ti-Zr-Nb superelastic alloy based on combination of radial-shear rolling and rotary forging. *Metallurgist, 63*(3), 51-61.

Author Information

Vladislav Pishchikov
Rudny Industrial University
38 50 let Oktyabrya str., Rudny, Kazakhstan

Sergey Kuzmin
Rudny Industrial University
38 50 let Oktyabrya str., Rudny, Kazakhstan

Valeriy Chigirinsky
Rudny Industrial University
38 50 let Oktyabrya str., Rudny, Kazakhstan

Andrey Marukov
Rudny Industrial University
38 50 let Oktyabrya str., Rudny, Kazakhstan

Abdrakhman Naizabekov
Innovative University of Eurasia
Lomova 45 str., Pavlodar, Kazakhstan
Contact e-mail: naizabekov57@mail.ru

Irina Volokitina
Karaganda Industrial University
Republic 30, Temirtau, Kazakhstan

To cite this article:

Pishchikov, V., Kuzmin, S., Chigirinsky, V., Marukov, A., Naizabekov, A., & Volokitina, I. (2024). Research of combined copper processing technology including heat treatment and radial-shear rolling. *The Eurasia Proceedings of Science, Technology, Engineering & Mathematics (EPSTEM), 32,* 101-105.

The Eurasia Proceedings of Science, Technology, Engineering & Mathematics (EPSTEM)
ISSN: 2602-3199

The Eurasia Proceedings of Science, Technology, Engineering & Mathematics (EPSTEM), 2024

Volume 32, Pages 106-115

IConTES 2024: International Conference on Technology, Engineering and Science

Micro-Jet Control of Flow in NACA 4412 Wing

Hocine Tebbiche
Mouloud Mammeri University of Tizi-Ouzou

Mohammed Saîd Boutoudj
Mouloud Mammeri University of Tizi-Ouzou

Abstract: The separation and coherent structures resulting from the fluid detachment and the presence of marginal wing vortices lead to a decline in aerodynamic performance, noise generation, and vibrations. To address these issues, boundary layer control through blowing via micro-jets proves to be a highly effective solution, as it allows for a significant input of momentum near the wall. An experimental study, based on continuous tangential blowing through a series of micro-orifices, was conducted in a wind tunnel to analyze the effect on the flow over the upper surface of a NACA 4412 wing. Force measurements were taken for various velocities and angles of incidence. Wall and wake pressure measurements also carried out. The results obtained indicate that the blowing effect depends on the location of the blowing orifices and the ejected air flow rate. The analysis of drag and pressure mappings in the wake reveals that blowing near the wingtip generally leads to the generation of a more intense trailing vortex, causing the production of parasitic drag. Furthermore, lift results show a maximum relative gain of 37% at a Reynolds number of 1.6×10^5, accompanied by a 2-degree delay in stall.

Keywords: NACA 4412 wing, Boundary layer, Drag and lift, Pressure coefficient, Blowing

Introduction

In the flow around a wing, the separation of the boundary layer (Schlichting et al., 1979), and the presence of tip vortices result in energy dissipation and the generation of vibrations and noise. Boundary layer control techniques (Gad-el-Hak, 2001). Make it possible to decrease, or even eliminate, the separated region, thus reducing energy consumption and, consequently, lowering greenhouse gas emissions.

Solutions for control have been proposed in previous studies to reduce drag (Manolesos et al., 2015) increase lift (Satar et al., 2024) and mitigate the wake vortex area (Haverkamp et al., 2005). The winglet-wing configuration is the simplest among non-planar wings. Other suggestions include box wings or closed wings (Kroo, 2001). However, all non-planar wings suffer from structural complexity and increased weight (Jupp, 2001). Various leading-edge devices have also been considered for noise reduction (Slooff, 2002). And alleviating the wake vortex issue (Coustols et al., 2003)

The main drawback of most of the aforementioned leading-edge devices is that they are fixed on the wing and can only be optimized for a single flight condition, thus being less effective during the rest of the flight. In contrast, the use of an active means of flow control ensures optimal aircraft performance across the entire flight envelope. Active control can be implemented using movable parts, such as flaps, but this could lead to structural issues. That's why a number of researchers have focused on the blowing strategy. Numerous experimental studies are currently dedicated to investigating this control strategy (Bourgois, 2006; Roumeas, 2006; Chen et al., 2024). Favier et al., 2005 conducted a study on controlling the onset of separation on the upper surface of an ONERA D-type airfoil using blowing through a series of micro-jets inclined at 90° to the chord. A slight increase in lift is recorded with this configuration; which leaves us with fairly broad paths of exploration in order to define new trends in optimization.

In this paper, we present an experimental study aimed at improving the aerodynamic characteristics of a NACA 4412 wing with a 5° sweep angle, a mid-chord length of 140 mm, and a span of 200 mm. The active control strategy employed in this study is continuous blowing through micro-jets. Micro-holes with a diameter of 0.6 mm are linearly arranged on the wing upper surface, at 10% from the leading edge. Unlike conventional control strategies, blowing through the micro-jets allows for a much deeper penetration of the jet into the flow and results in air consumption savings.

The experimental study is divided into two main components. The first part focuses on the wind tunnel investigation of the airfoil and the NACA 4412 wing's behavior concerning separation, assessed through the measurement of aerodynamic forces and uncontrolled flow pressure measurements. The second part addresses the effect of varying the blowing rate, wing angles of attack, and the upstream free-stream velocity, while keeping a focus on the control efficiency regarding the aerodynamic stall phenomenon.

Experimental Device

Wind Tunnel and Acquisition Chain

All experiments were conducted in a Deltalab™ type wind tunnel. The maximum measurable velocity exceeds 40 m/s. The turbulence level is set by a grid at the inlet with a size of 5×5 mm^2. The test section length and cross-sectional area are 100 cm and 30×30 cm^2, respectively (Figure 1). Lift and drag forces were measured using an aerodynamic balance connected to a data acquisition system. Each conducted test was repeated three times, and the average was considered. The acquisition time was set to 60 s with a frequency of 500 Hz.

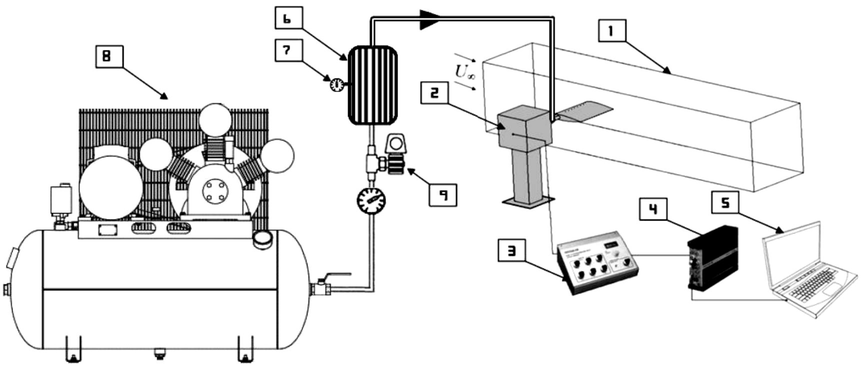

Figure 1. Sketch showing the wind tunnel and blowing device (1: Test tunnel, 2: Aerodynamic balance, 3: Stress indicator, 4: Converter, 5: Acquisition and processing of data on computer, 6: Stilling chamber, 7: Pressure gauge , 8: Air compressor, 9: Valve)

Wind Tunnel And Acquisition Chain

NACA 4412 Airfoil

Figure 2. NACA 4412 airfoil (1: static pressure taps).

The aerodynamic profile used in the experiments is a cambered NACA 4412 airfoil with a chord length of 150mm, a span of 200mm, a maximum camber of 4% of the chord, and a maximum thickness of 12%, as indicated in its designation. Two endplates were used to minimize the 3D end effects on the airfoil. They were constructed from steel sheets and measured 200mm × 50mm, with a radius of 25mm. These dimensions were chosen in consideration of the wind tunnel test section dimensions to minimize aerodynamic blockage effects. The airfoil is equipped with fourteen pressure taps arranged along its mid-chord line (Figure 2).

NACA 4412 Wing

The model created is a wing with a 5° sweep angle, built using a NACA 4412 airfoil, featuring a mid-chord length of 140 mm and a span of 200 mm (Figure 3). It is equipped with 10 micro-holes of 0.6 mm diameter evenly arranged at 10% of the leading edge. The micro-holes, employed for blowing, are oriented at a 45° angle relative to the wing's chord (Figure 4).

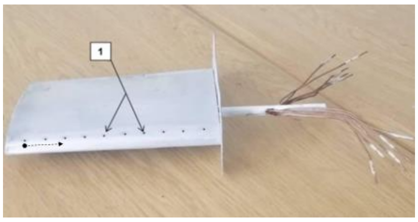

Figure 3. NACA 4412 wing (1: blowing holes).
The numbering direction of the blowing orifices is indicated by the dashed arrow (from 1 to 10).

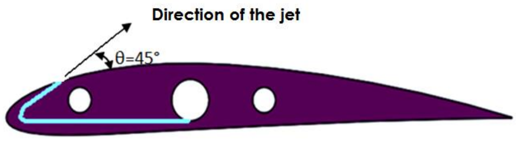

Figure 4. Sectional view showing the position of the blowing orifices on the model.
The arrow indicates the jet direction as well as the tilting angle θ of the blowing nozzles.

Blowing Device

To achieve flow control around the NACA 4412 wing, the blowing device primarily consists of an air compressor, a stilling chamber, and a flow control valve. The Schneider-type compressor compresses air, achieving a maximum relative pressure of 16 bar. Compressed air flows through a valve used to regulate pressure in the generating state, then it is directed into the stilling chamber designed to minimize turbulence caused by the compressor. It is then conveyed to a ramp constructed from a copper tube with a diameter D=14mm, onto which capillary tubes are implanted, each having an outlet section with a diameter d=0.6mm. The ten capillary tubes are connected to the blowing orifices of the wing.

Our blowing configuration can be likened to a convergent nozzle, where the nozzle throat corresponds to the cylindrical opening of the capillary tubes used for blowing. To better characterize the flow at the blowing orifices, it is essential to establish a relationship between the air pressures measured in the generating state and in the immediate vicinity of the micro-orifices, and the ejected air flow. The latter is determined by the following equation:

$$Q_j = S_j \sqrt{\frac{2k}{(k-1)} \frac{P_t}{\nu_t} \left(\left(\frac{P}{P_t} \right)^{2/k} - \left(\frac{P}{P_t} \right)^{(k+1)/k} \right)} \tag{1}$$

With: k: Adiabatic constant, P_t: Total pressure in the generating state, ν_t: Specific volume at the generating state. The jet velocity V_j is determined from the flow rate using the following expression:

$$V_j = \frac{\nu Q_j}{S_j} \tag{2}$$

Blowing through micro-jets is performed in eight distinct modes based on the number of open orifices and the blowing pressure in the generating state. Table 1 illustrates the eight jet modes.

Table 1. Various blowing modes tested in a wind tunnel. With (1: opened hole and 0: closed hole).

	Hole number									
Mode	**1**	**2**	**3**	**4**	**5**	**6**	**7**	**8**	**9**	**10**
a	*1*	*1*	*1*	*1*	*1*	*1*	*1*	*1*	*1*	*1*
b	*1*	*1*	*1*	*1*	*1*	*0*	*0*	*0*	*0*	*0*
c	*0*	*0*	*0*	*0*	*0*	*1*	*1*	*1*	*1*	*1*
d	*1*	*1*	*0*	*0*	*1*	*1*	*0*	*0*	*1*	*1*
e	*0*	*0*	*1*	*1*	*0*	*0*	*1*	*1*	*0*	*0*
f	*1*	*0*	*1*	*0*	*1*	*0*	*1*	*0*	*1*	*0*
g	*0*	*1*	*0*	*1*	*0*	*1*	*0*	*1*	*0*	*1*
h	*0*	*1*	*1*	*1*	*0*	*1*	*1*	*1*	*1*	*0*

Aerodynamic Coefficients

The lift and drag coefficients are measured using the aerodynamic balance connected to the airfoil. These aerodynamic coefficients are commonly defined as follows:

$$C_{D,L} = \frac{F_{x,y}}{\frac{1}{2}\rho U_\infty^2 S_\infty} \tag{3}$$

With: $F_{x,y}$: Aerodynamic lift and drag forces, ρ : Air density, S_∞ : Wing area, U_∞: Free-stream velocity.

Results and Discussion

In this section, the results of the experiments conducted with the two models (airfoil and NACA 4412 wing) are presented. Measurements were taken over an angle of attack range from 0° to 25°, for two flow Reynolds numbers: Re=1.6×10^5 and Re=2.5×10^5.

Uncontrolled Flow

Aerodynamic Forces in the Case of the Airfoil and NACA 4412 Wing

Measurements of aerodynamic forces are conducted for various attack angles using an aerodynamic balance (see Figure 1). The curves of lift and drag coefficients as a function of attack angle (uncorrected for the blockage effect) are depicted in Figures 5.a and 5.b for two Reynolds numbers.

In the case of the NACA 4412 airfoil, it can be observed from these figures that the stall angles are 16° and 18°, respectively, for Re=1.6×10^5 and Re=2.5×10^5. Beyond these angles, there is a noticeable increase in drag values due to aerodynamic stall. As for the flow around the 5° sweep wing, both lift and drag forces are lower compared to the airfoil case. The lift curves exhibit a non-linear trend at low attack angles, indicating the presence of the wingtip vortex that disrupts the pressure distribution around the wing. Stall occurs in this case at 17° and 18°, respectively, for Re=1.6×10^5 and Re=2.5×10^5.

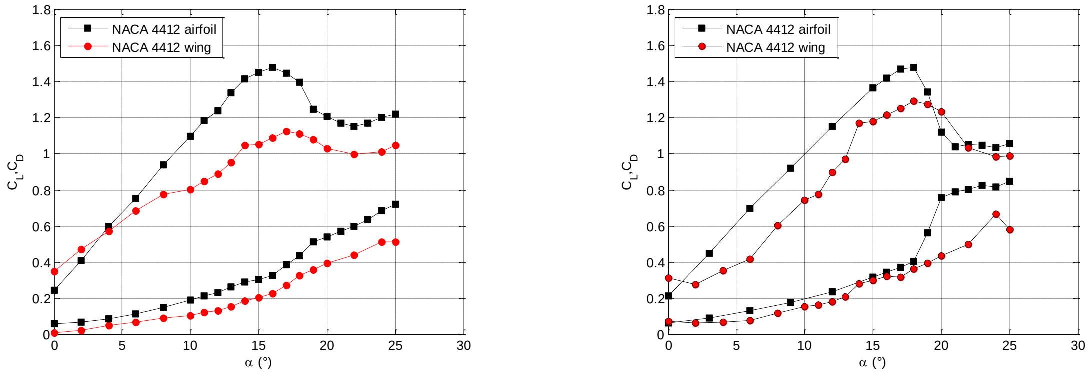

a) Re=1.6×10^5. b) Re=2.5× 10^5.

Figure 5. Evolution of lift and drag coefficients as a function of attack angle, uncontrolled case.

Pressure Field around the NACA 4412 Airfoil

The flow properties around the uncontrolled NACA 4412 airfoil are initially studied, and the corresponding distributions of the static pressure coefficient are determined. Figures 6.a-b show the distributions of the static pressure coefficient around the NACA 4412 airfoil for angles of attack ranging from [0°-25°] and two flow Reynolds numbers [1.6×10^5; 2.5×10^5]. Since the NACA 4412 is a cambered airfoil, at zero angle of attack, the static pressure on the airfoil is asymmetric, resulting in the existence of lift force (Figures 45.a-b). There are regions of accelerated flow on the airfoil that reach the highest depressions, corresponding to the maximum thickness of the airfoil at zero incidence. The maximum pressure occurs at the stagnation point where the velocity is zero.

As the airfoil attack angle is increased to around 18°, the adverse pressure gradient imposed on the boundary layers becomes so significant that flow separation occurs. A recirculation flow region over almost the entire upper surface of the airfoil is formed. Consequently, lift decreases significantly, and drag increases sharply. For a further increase in the attack angle, the stagnation point moves significantly toward the trailing edge on the lower surface. The recirculation flow region becomes dominant, covering the entire upper surface; the air flow is completely separated from the airfoil surface. This leads to a further reduction in lift force and a substantial increase in drag force. This situation is characterized by the formation of an almost constant C_P plateau (see Figure 5, α=25°).

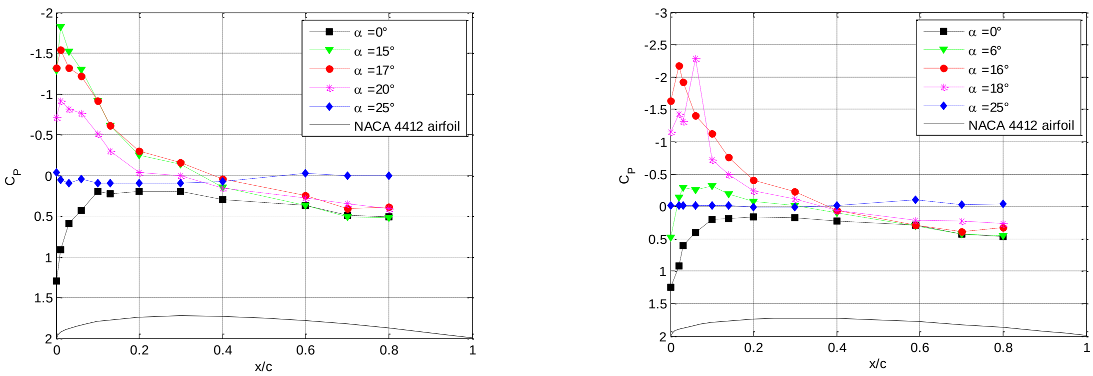

a) Re=1.6×10^5. b) Re=2.5× 10^5.

Figure 6. Evolution of the pressure coefficient at various attack angles of the airfoil, without control.

Controlled Flow

The action of the micro-jet on a wing allows for a remarkable influence on aerodynamic coefficients. However, to optimize this type of blowing system, it is necessary to study the influence of certain parameters, either adjustable by the user or imposed by the technology of the blowing device used. Indeed, the influence of varying the blowing rate, wing incidences, and the free-stream velocity upstream has been analyzed during the test series conducted in the laboratory. Other geometric parameters such as diameter, spacing, position relative to the chord of the holes, and their tilt angle are kept constant. However, the control efficiency may change by varying these geometric parameters, making the optimization study of control efficiency appear somewhat simplified.

Aerodynamic Forces of the Controlled Boundary Layer by Blowing in the Case of the NACA 4412 Wing

a. Effect of tangential blowing on control efficiency

The control is achieved through continuous jets via a series of 0.6 mm diameter orifices located on the upper surface of the NACA 4412 wing (Figure 3). The micro-orifices are positioned at 10% from the leading edge. Figure 7, presented as a histogram, illustrates the lift gains obtained for all blowing modes (Table 2) tested in the wind tunnel at a Reynolds number of 1.6×10^5. It is evident from these results that a more significant lift improvement is recorded for mode (a) and at a pressure Pr=2.0 bar, corresponding to full blowing.

Considering the results in Figure 7, it is apparent that for mode (b), no lift gain is recorded. This can be explained by the fact that the position of the blowing orifices (blowing on the left half of the wing) for this mode is not conducive to boundary layer reattachment to the wall. Instead, it acts on reducing the cross-sectional area of the wake, directly influencing induced drag (Refer to the following section), which is a consequence of limiting the wing's aspect ratio (transition from two-dimensional to three-dimensional aerodynamics).

Delays in stall, ranging from 1 to 2 degrees, are also observed in some blowing modes such as mode (b), (e), (f), and (g). Moreover, blowing control on this type of wing did not result in any reduction in drag. On the contrary, parasitic drag is observed for almost all blowing modes, except for mode (b), where a maximum drag reduction of 70% was measured at an incidence of 10 degrees.

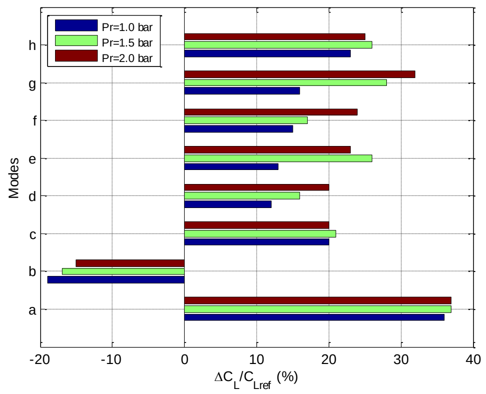

Figure 7. Lift gains obtained for different blowing modes, Re=1.6×10^5.

b. Effect of Blowing Rate

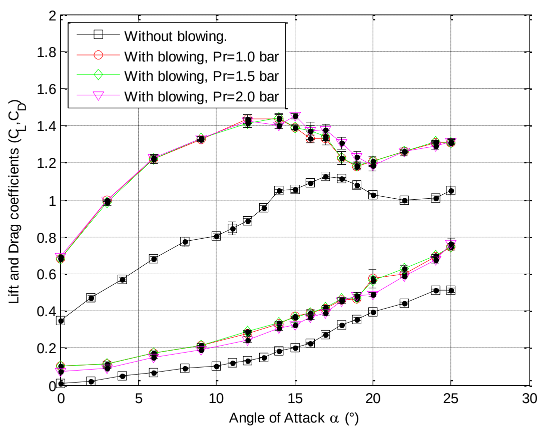

Figure 8. Evolution of the lift and drag coefficients as a function of attack angle, with and without control. Re=1.6×10^5, mode (a).

Significant improvements in the lift coefficient and a delay in stall are observed with control (Figure 7). The increase in the lift coefficient is closely related to the increase in the blowing rate. In the absence of blowing, the profile stalls at 16° for Re=1.6×10^5. The effect of control begins even at low angles of attack; a gradual increase in lift is observed, noticeable for all angles of attack before stall. Comparing the control curves, it is evident that they are relatively close for all attack angles ; there is a saturation of the lift coefficient, and the control effect is limited by the sonic blockage phenomenon at the blowing holes.

It is also interesting to analyze the effect of control on the drag coefficient. The trends of the C_D coefficient shown in Figure 8 indicate that the drag of the controlled case evolves roughly in the same manner, exhibiting a parasitic increase.

c. Effect of Reynolds number on aerodynamic coefficients

Figures 8 and 9 show the overlay of lift and drag coefficients curves for the reference case and with control using the micro-holes. For both Reynolds numbers studied, an improvement in lift is observed. At a Reynolds number of 2.5×10^5, the control effect on the lift coefficient is slightly less effective than in the case with Re=1.6×10^5. Specifically, a 37% lift gain is recorded for flow at 1.6×10^5, and only a 4% relative lift increase is observed for the second case (Re=2.5×10^5) compared to C_{Lmax}, with a 2° delay in stall. The analysis of drag reveals a greater production of parasitic drag in flows with low Reynolds numbers at high angles of attack.

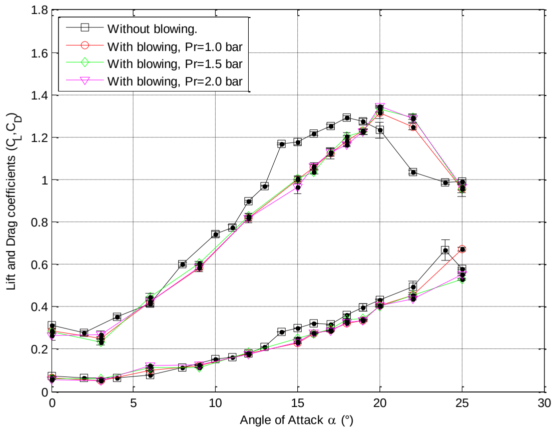

Figure 9. Evolution of the lift and drag coefficients as a function of attack angle, with and without control. Re=2.5×10^5, mode (a).

Pressure Coefficient around the NACA 4412 Wing with and without Flow Control

The results depicted in the figures below are analyzed based on the averaged mappings of static pressure loss Cp. Energy losses associated with pressure drag significantly contribute to the development of total aerodynamic drag. Pressure measurements are conducted using a wake rake positioned 250 mm downstream from the wing's leading edge. This rake consists of fifteen capillary tubes spaced 10 mm apart and oriented in the flow direction. The wake is scanned with a regular 10 mm step along the y-axis, forming a measurement plane of 15×12 cm². Total pressures are measured using a differential manometer. The evolving pressure shown therein clearly indicates the wake's depression.

Vortex shedding occurs wherever a lifting surface ends in a fluid. The flow around the NACA 4412 wing generates lift by producing low static pressures above the wing and comparatively higher pressures below. This pressure difference between the upper and lower wing surfaces accelerates the fluid around the wingtip, creating a marginal vortex. This is clearly discernible in the Cp iso-value maps for the uncontrolled case (Figure 10).

When blowing occurs near the wing surface, despite the significant improvements in lift recorded, the previously observed drag measurement indicates a tendency to increase. This is supported by the calculation of the average Cp value for the uncontrolled case (Cp_{moy}=0.59, See Figure 10) and the controlled case (Cp_{moy}=0.63, See Figure 11). The increase in drag is directly related to the locally created depression by blowing at the upper surface, which remains insufficient to reattach the fluid streamlines on the wing.

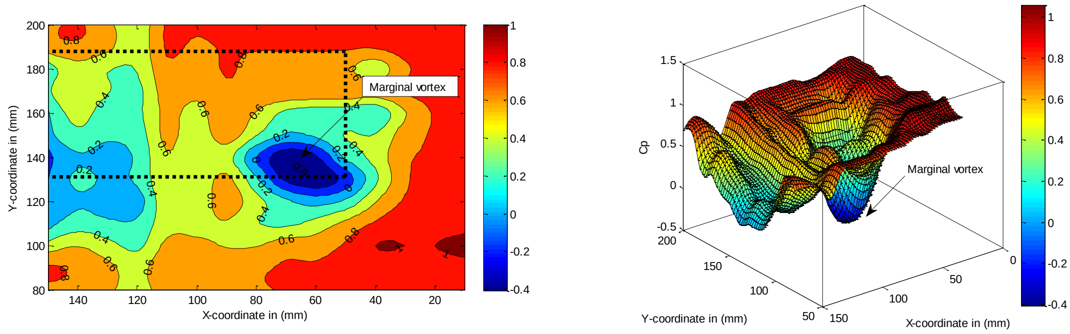

a) Isovalue contours of the pressure coefficient. b) Three-dimensional pressure coefficient.

Figure 10. Static pressure coefficient recorded at Z/c=1.67, Re=1.6×10^5, α=15°. The dashed lines represent the wing contour.

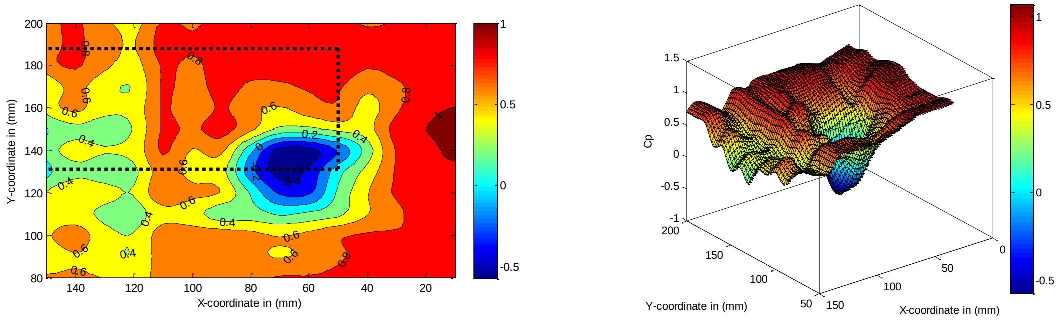

a) Isovalue contours of the pressure coefficient. b) Three-dimensional pressure coefficient.

Figure 11. Static pressure coefficient recorded at Z/c=1.67, Re=1.6×10^5, α=15°, mode (a), Pr=2.0 bar. The dashed lines represent the wing contour.

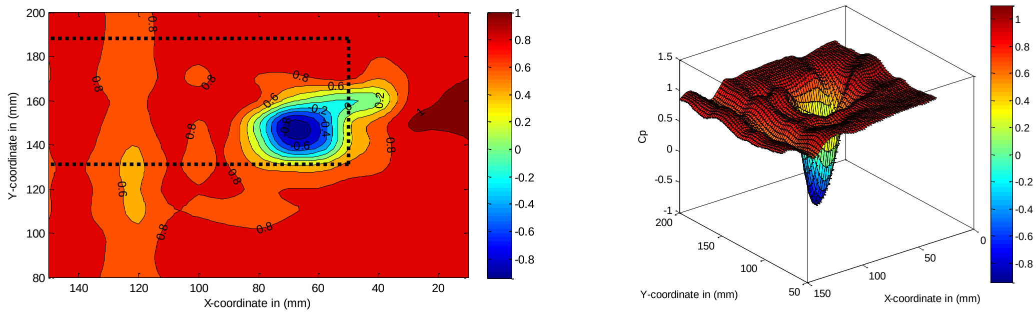

a) Isovalue contours of the pressure coefficient. b) Three-dimensional pressure coefficient.

Figure 12. Static pressure coefficient recorded at Z/c=1.67, Re=1.6×10^5, α=17°, without control. The dashed lines represent the wing contour.

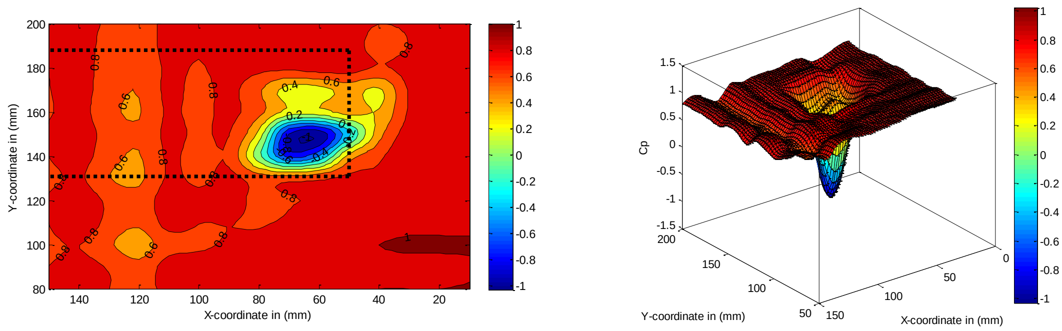

a) Isovalue contours of the pressure coefficient. b) Three-dimensional pressure coefficient.

Figure 13. Static pressure coefficient recorded at Z/c=1.67, Re=2.5×10^5, α=17°, mode (a), Pr=2.0 bar, with control. The dashed lines represent the wing contour.

Similarly, for flow at a high Reynolds number (Re=2.5×10^5), an increase in the average Cp value from the uncontrolled case (Cp=0.77, see Figure 12) to the controlled case (Cp=0.79, see Figure 13) is observed. However, the intensity of the vortex is much more pronounced in this case compared to the results at Re=1.6×10^5. The performance of the control necessarily degrades in 3D (in the case of a wing) due to the presence of highly energetic longitudinal vortex structures. Nevertheless, the results presented here still serve as an interesting foundation for the exploration of three-dimensional solutions. In this regard, the topology of the wake flow must be analyzed to identify the control mechanisms and the origins of drag reduction.

Conclusion

The results of this present study emphasize the importance of blowing through the micro-orifices. In the case of the NACA 4412 wing, the effects of controlling the blowing rate at Reynolds numbers ranging from (1.6×10^5 – 2.5×10^5) and different angles of attack are evaluated. When the stagnation pressure is varied and analyzed over the range of (1.0 – 2.0 bar), the following results were obtained:

- Although the steady blowing was only performed at 10% of the chord, the results indicate that an increase in blowing pressure enhances the aerodynamic coefficients. Indeed, a very noticeable increase in maximum lift of about 37% is achieved when Pt=2.0 bar, and at a Reynolds number equal to 1.6×10^5. These lift gains depend on the Reynolds number of the flow. Additionally, a significant reduction in drag of approximately 20% is observed for a specific blowing mode (b).

- A delay in stall of about two degrees is achieved.

- To achieve a real improvement in aerodynamic performance, it appears necessary to apply an optimization approach to the position of the micro-holes, the inclination angle, as well as their diameter. These parameters influence the coherent flow structures and can delay or even eliminate boundary layer separation.

Scientific Ethics Declaration

The authors declare that the scientific ethical and legal responsibility of this article published in EPSTEM Journal belongs to the authors.

Acknowledgements or Notes

* This article was presented as a poster presentation at the International Conference on Technology, Engineering and Science (www.icontes.net) held in Antalya/Turkey on November 14-17, 2024.

References

Bourgois, S. (2006). *Etude Expérimentale du Décollement Sur profils d'aile : Analyse et contrôle* (Doctoral dissertation). Université de Poitiers. Retrieved from https://tel.archives-ouvertes.fr/tel-00308715

Chen, Y., Avital, E., Willams, J., Santra, S., & Seifert, A. (2024). Effects of leading-edge blowing control and reduced frequency on airfoil aerodynamic performances. *Journal of Fluids Engineering*, *146*(10),1-56.

Coustols, E., Stumpf, E., Jacquin, L., Moens, F., Vollmers, H., & Gerz, T. (2003). "Minimised wake": A collaborative research programme on aircraft wake vortices. *41st Aerospace Sciences Meeting and Exhibit*.

Favier, J., Bourgois, S., Sommier, E., Tensi, J., & Kourta, A. (2005). Contrôle fluidique du décollement sur un profil d'aile. *In 17ème Congrès Français de Mécanique*.

Gad-el-Hak, M. (2001). Flow control. The future. *Journal of Aircraft, 38*(3), 402–418.

Haverkamp, S., Neuwerth, G., & Jacob, D. (2005). Active and passive vortex wake mitigation using control surfaces. *Aerospace Science and Technology*, *9*(1), 5-18.

Jupp, J. (2001). Wing aerodynamics and the science of compromise. *The Aeronautical Journal*, *105*(1053), 633–641.

Kroo, I. (2001). Drag due to lift: concepts for prediction and reduction. *Annual Rev: Fluid Mechanics, 33*(1), 587–617.

Manolesos, M., & Voutsinas, S. G. (2016). Experimental study of drag-reduction devices on a flatback airfoil. *AIAA Journal*, *54*(11), 3382-3396.

Roumeas, M. (2006). *Contribution à l'analyse et au contrôle des sillages de corps épais par aspiration ou soufflage continu* (Doctoral dissertation). Institut National Polytechnique de Toulouse. Retrieved from https://oatao.univ-toulouse.fr/7493/1/roumeas.pdf

Satar, M. H. A., Razak, N. A., Abdullah, M. S., & Ismal, F. (2024). A comprehensive comparison of passive flow controls on the wind turbine blade lift and drag performances. A CFD approach. *European Journal of Mechanics-B/Fluids*, *108*, 119-133.

Schlichting, Hermann. (1979). *Boundary layer theory*. New York. NY: McGraw-Hill.

Sloof, J., de Wolf, W., van der Wal, H., & Masel&, J. (2002). Aerodynamic and aero-acoustic effects of flap tip fences. *40th AIAA Aerospace Sciences Meeting and Exhibit*.

Author Information

Hocine Tebbiche
Mouloud MAMMERI University of Tizi-Ouzou
15000, Tizi-Ouzou, Algeria
Contact e-mail: *hocine.tebbiche@ummto.dz*

Mohammed Saîd Boutoudj
Mouloud MAMMERI University of Tizi-Ouzou
15000, Tizi-Ouzou, Algeria

To cite this article:

Tebbiche, H. & Boutoudj, M.S. (2024). Micro-jet control of flow in NACA 4412 wing. *The Eurasia Proceedings of Science, Technology, Engineering & Mathematics (EPSTEM), 32,* 106-115.

The Eurasia Proceedings of Science, Technology, Engineering & Mathematics (EPSTEM)
ISSN: 2602-3199

The Eurasia Proceedings of Science, Technology, Engineering & Mathematics (EPSTEM), 2024

Volume 32, Pages 116-122

IConTES 2024: International Conference on Technology, Engineering and Science

Effects of Micro-Blowing and Vortex Generators on the Boundary Layer Separation Control of a NACA 0015 Airfoil

Mohammed Said Boutoudj
Mouloud Mammeri University of Tizi-Ouzou

Hocine Tebbiche
Mouloud Mammeri University of Tizi-Ouzou

Abstract: The flow on the upper surface of an airfoil is subject to an adverse pressure gradient when the incidence increases. This leads to boundary layer separation, causing losses in aerodynamic performance by decreasing lift and increasing drag. Various techniques, both passive and active, exist for boundary layer control to delay or eliminate fluid separation. Vortex generators (VGs) are simple use and among the most effective passive flow control solutions. They bring momentum from the external flow to the boundary layer, making it more resistant to separation. Active control methods, such as blowing through micro-holes, are also very effective but more challenging to implement. In the present work, a comparative experimental study of the flow control around a NACA 0015 airfoil is conducted in a subsonic wind tunnel using the two types of control strategies. The used VGs are the Lin's counter –rotating configuration. They are triangular shape, placed on the suction face at 10% of the airfoil chord. The active control solution proposed relates to a steady blowing carried out with an angle of 45° relative to chord line, through a series of micro-holes of 0.6 mm in diameter uniformly arranged also at 10% from the leading edge. An improvement in aerodynamic performance was achieved with both strategies, with a more significant increase of approximately 49% in lift and a reduction of about 69% in drag in the case of micro-blowing.

Keywords: NACA 0015 airfoil, Boundary layer, Vortex generators, Micro-blowing, Lift, Drag

Introduction

The flow on the upper surface airfoil is subject to an adverse pressure gradient when the incidence increases. This leads to the boundary layer separation which causes looses in the aerodynamic performances (lift decrease and drag increase). It is well known that the lift around an airfoil is rather created by the suction on the upper surface than the overpressure on the lower one. The flow control aims to delay or eliminate the fluid separation and its undesirable effects like vibrations and aerodynamic noise.

In the aircraft industries the flow control takes on capital importance for the reduction of the energy overconsumption and the aerodynamic noise. Moreover, during take-off or landing, the speed is low and the attack angle needs to be high for the lift enhancement. This situation is also encountered in wind turbine blades where the increase in the captured energy requires an increase in the incidence of the blades, particularly in the vicinity of the hub.

There are two types of boundary layer control (Gad-el-Hak, 2001). Active methods and passive ones. Active techniques require adding external energy to the boundary layer to make it more resistant to the separation. Methods such as suction, blowing (Huang et al., 2004). Or moving surfaces (Modi, 1997). Have been investigated in various applications. Active methods are however difficult to implement and they cause problems of congestion.

Unlike active techniques, passive methods do not require any external energy supply. They are therefore easier to use but still have appreciable effectiveness. Among existing passive techniques, vortex generators (VGs) have proven to be very effective in controlling the flow separation. VGs were first introduced by Taylor (1947). And have been since widely investigated in several configurations. They are placed on a surface subject to an adverse gradient pressure and can be rectangular, triangular or aero shaped form. VGs produce streamwise vortices which induce momentum transfer from the freestream to the region close to the wall, leading to the delay or suppression of the boundary layer separation. Vortex generators enhance the aerodynamic performances and the most efficiency are the Lin's ones V-shaped when their height is less than the boundary layer thickness (Rao et al., 1988).

The main use of the VG is in the field of military or civil aviation, and recently in wind turbines with the objective of increasing lift and decreasing drag. Enhancement of the airfoil aerodynamic performances by VGs constitute a preliminary solution to passive control over a wind blade, even the flow in the last case is more complex because of the rotation. Wind blades equipped with VGs on the suction surface could be a potential solution to improve aerodynamic efficiency of horizontal axis wind turbines by delaying stall, increasing lift and reducing drag. The influence of the VGs geometrical parameters such as height, inclination angle or even their location on their aerodynamic performance has been reported by several authors (Lin, 2002; Godard et al., 2006; Fouatih et al., 2016; Bouderbala, 2025).

The present work focuses on the control flow around a NACA 0015 airfoil by means of two strategies: passive method by VGs and active technique by blowing. Experimental measurements of the aerodynamics forces (lift and drag) as well as the wall pressure field around the airfoil were undertaken. The effectiveness of each strategy is then examined.

Descrition of the Experiments

Wind Tunnel and Measuring Equipments

The experiments were conducted in a Deltalab™ type wind tunnel. The maximum measurable velocity exceeds 40 m/s. The turbulence level is set by a grid at the inlet with a size of 5×5 mm^2. The test section length and cross-sectional area are 100 cm and 30×30 cm^2, respectively. Lift and drag forces were measured using an aerodynamic balance connected to a data acquisition system. Each conducted test was repeated three times, and the average was considered. The acquisition time was set to 60 s with a frequency of 500 Hz. The pressure was given by a manometer which allows simultanous measurement until 24 pressure taps. The freestream velocity was measured using a Pitot tube connected to a differential oil pressure gauge (Tebbiche et al., 2019).

The blowing system consists of an air compressor, a stilling chamber, and a flow control valve. The Schneider-type compressor compresses air, achieving a maximum relative pressure of 16 bar. Compressed air flows through a valve used to regulate pressure in the generating state, then it is directed into the stilling chamber designed to minimize turbulence caused by the compressor. It is then conveyed to a ramp constructed from a copper tube with a diameter D=14mm, onto which capillary tubes are implanted, each having an outlet section with a diameter d=0.6mm. The capillary tubes are connected to the blowing orifices of the airfoil. More details about the blowing installation are given in a previous work (Tebbiche et al., 2021).

Passive Vortex Generators

Passive control by VGs is a strategy that does not require any external energy to the flow. Their particularity is to bring the momentum from the external flow to the near-wall flow regions. VGs can be co-rotating or counter-rotating. The second category is known to be more efficient because it generates better mixing between the external flow and the boundary layer (Lin, 2002).

In the case of an aerodynamic profile, the implantation of VGs line on its upper face leads to delay or even eliminate the detachment. Vortex generators are placed upstream of the baseline separation and their geometrical parameters such as the height h, the spacing λ, the relative incidence angle β as well as their position according to the chord length affect the flow control efficiency. Among these parameters, the height and the relative incidence angle particcularly are linked to the circulation of the generated vorticies.

Initially, Taylor in its experimental investigation, using triangular Vortex Generators, evaluated the height to the boundary-layer thickness δ (Taylor, 1947). Rao et al. (1988) tested different VGs configurations; the idea was to reduce the height by submerging them in the boundary layer. They estimated that h reduced to about 0.6δ is more effective compared to the classical one. Lin (1999) tested two different micro-generators configurations co-rotating and counter-rotating. His conclusion was that the VGs taken on counter-rotating mode at the threshold height $h/\delta \approx 0.2$ allows a significant improvement in control. For $h/\delta > 0.2$, an increase in drag is considered not as significantly improving their performances. For values of $h/\delta < 0.2$, a consistent decrease in the VGs efficiency is thus remarked. As for the optimal incidence angle, several works tend to evaluate it between 10 and 20 degrees (Fouatih et al., 2016).

In this work, the studied vortex generators are counter rotating, triangular shape and placed normal to the surface at 10% of the airfoil chord. They were manufactured using a very thin sheet metal of 0.3mm glued on plastic ribbons which facilitates their positioning in the precise location along the chord-wise and spanwise of the airfoil. The dimensions of the triangular plates are given in the Table 1. The line VGs was constituted by six generators.

The considered profile is the NACA 0015; the chord c length is 150 *mm* and the depth is equal to 200 *mm*. The airfoil is equipped with guard plates to eliminate edge effects and 14 pressure taps on the suction face for the measurement of the pressure fields. The boundary layer thickness estimated at 0.19c using a 2D-RANS numerical approach is about 10 mm for a Reynolds number Re = 2.5 10^5 when the attack angle equals 13° (Tebbiche et al., 2019). Figure 1 shows the VGs and the airfoil.

Table 1. Geometrical characteristic of the tested VGs

H (mm)	*l (mm)*	*a* (mm)	λ (mm)	β (°)
5.5	14.3	7	13.5	15

H: height, *l*: length, *a*: space between the same VG, λ: distance between two passive devices, β: the relative incidence angle.

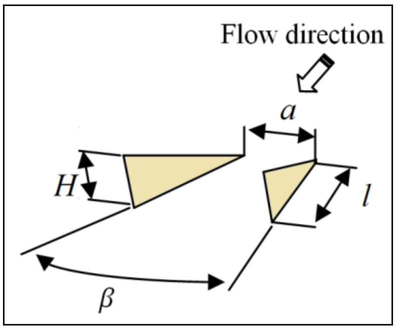

a)

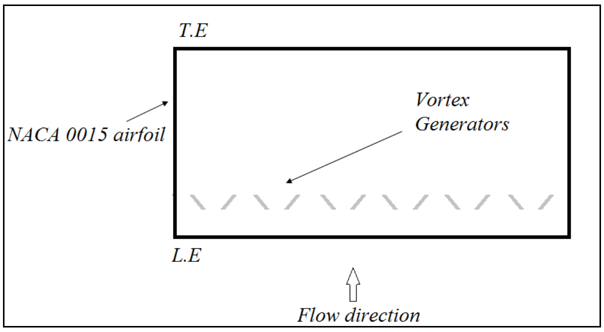

b)

Figure 1. a) Vortex generators. b) The line of VGs on the airfoil.

Active Control by Blowing

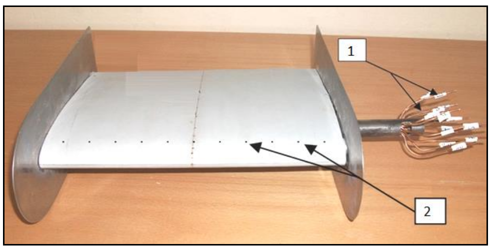

a)

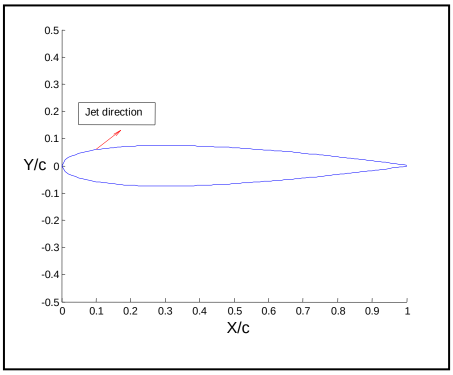

b)

Figure 2. a) Position of the blowing holes on the NACA 0015 airfoil. 1: Capillary air tubes, 2: Bowing Micro-holes, b) Jet direction

The active control strategy employed in this study is continuous blowing through micro-jets. Micro-holes with a diameter of 0.6 mm are linearly arranged on the wing upper surface at 10% from the leading edge. Unlike conventional control strategies, blowing through the micro-jets allows for a much deeper penetration of the jet into the flow and results in air consumption savings. The airfoil used in this case is identical to that described previously and used for the passive control. It is a NACA 0015 with a chord c = 150 *mm* and a depth equal to 200 *mm*. It is equipped with 10 micro-holes of 0.6 mm diameter evenly arranged at 10% of the leading edge. The micro-holes, employed for blowing, are oriented at a 45° angle relative to the wing's chord (Figure 2).

The blowing configuration can be likened to a convergent nozzle, where the nozzle throat corresponds to the cylindrical opening of the capillary tubes used for blowing. To better characterize the flow at the blowing orifices, it is essential to establish a relationship between the air pressures measured in the generating state and in the immediate vicinity of the micro-orifices, and the ejected air flow. The latter is determined by the following equation:

$$Q_j = S_j \sqrt{\frac{2k}{(k-1)} \frac{P_t}{v_t} \left(\left(\frac{P}{P_t} \right)^{2/k} - \left(\frac{P}{P_t} \right)^{(k+1)/k} \right)} \tag{1}$$

With: *k*: Adiabatic constant ($k = 1.2$), P_t: Total pressure in the generating state, : *P*: Static pressure at the outlet of the orifice, v_t : Specific volume at the generating state. The jet velocity V_j is determined from the flow rate using the following expression:

$$V_j = \frac{vQ_j}{S_j} \tag{2}$$

Aerodynamic Coefficients

The interaction between the fluid and an airfoil results in two forces, lift and drag, which are commonly given by the two respective aerodynamic coefficients:

$$C_L = \frac{F_y}{\frac{1}{2} \rho U_\infty^2 S} \tag{1}$$

and

$$C_d = \frac{F_x}{\frac{1}{2} \rho U_\infty^2 S} \tag{2}$$

F_y and F_x are respectively the lift and the drag, ρ is the volumic weight, S the surface airfoil and U_∞ the upstream velocity.

Results and Discussion

Uncontrolled Flow around NACA 0015 Airfoil

Pressure Coefficient Distribution

Figure 3 presents a typical example of the upper surface pressure distribution for a Reynolds number of 2.5×10^5. At low angles of attack, no clear evidence of a bubble is shown by the pressure distribution. When the incidence reaches 11 degrees, a bubble that is approximately 11% of the chord length appears very close to the leading edge. Between 11° and 15°, the bubble length decreases to about 7%. As the angle of attack increases, the pressure difference between the upper and lower surfaces also increases until leading edge laminar separation occurs, as shown at an angle of attack of 16°. Here, the measured pressure at the separation point is almost the same for all pressure taps along the profile. This is clearly evident through the appearance of a plateau in the upper surface pressure data.

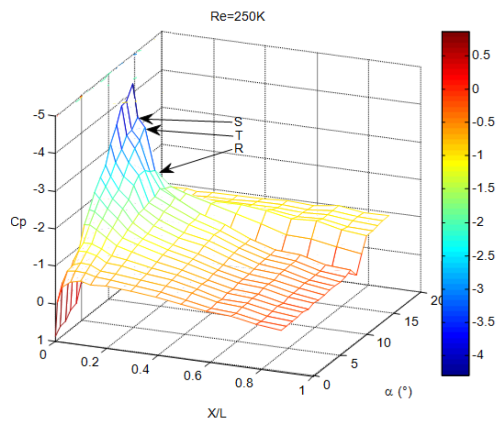

Figure 3. Cp coefficient vs X/L at various attack angles. **S**: Laminar separation, **T**: Transition, **R**: Reattachment.

Lift and Drag Coefficient Curves

The characteristics of the lift and drag coefficients for Reynolds numbers from 1.5×10^5 to 3×10^5 are presented in Figure 4. These curves are used as reference; the given results are not corrected as the main objective being the contribution of the control on the aerodynamic coefficients. The uncontrolled flow is characterized by a stall which occurs for an incidence around α= 15°. The sudden drop in lift is accompanied by a high production of the drag.

An increase in the maximum lift coefficient is observed as the Reynolds number increased. A variation in Reynolds number affects the slope of the lift curve, which is influenced by flow separation on the upper surface of the airfoil. It is well known that a decrease in Reynolds number extends the length of laminar separation bubbles on the upper surface and leads to complete flow separation at low angles of attack. Non-linear behavior is observed for the different Reynolds numbers tested. This non-linearity is related to the presence of flow separations on the upper surface of the airfoil at different angles of attack.

The non-linear phenomenon in the lift curve slope can be explained by two distinct phenomena that occur in low Reynolds number flows ($10^5 < Re < 10^6$). Between 0 and 8 degrees angle of attack, there is a separation bubble on the upper surface of the airfoil that moves from the trailing edge toward the leading edge, altering the transition point of the flow from laminar to turbulent. After approximately 8 degrees, a conventional separation bubble near the trailing edge forms as the angle of attack increases, eventually leading to complete separation on the upper surface of the airfoil, known as stall. Drag also increases at lower angles of attack as the Reynolds number raises, indicating an earlier onset of flow separation. After stall, the drag coefficient increases significantly as shown in figure 4b.

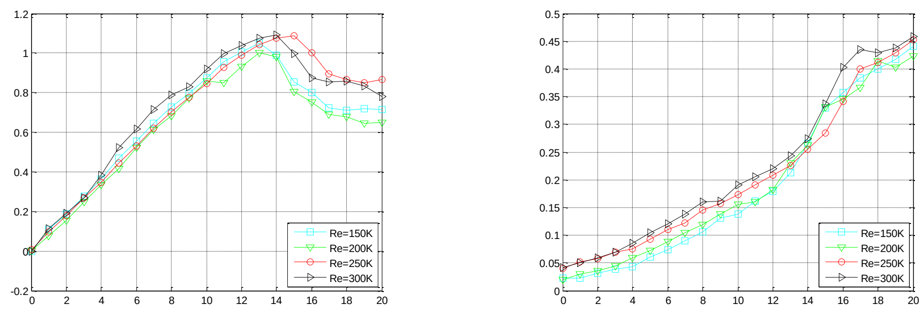

a) b)

Figure 4. Lift and drag coefficients versus angles of attack at various Reynolds numbers.
a) Lift coefficient, b) Drag coefficient

Controlled Flow

Passive Flow Control Using VGs

Figure 5 shows the C_L and C_d evolutions versus the incidence angle for both the reference case and the controlled flow. One can see in Figure 4a a delay in stall of two degrees and a lift enhancement between 14° and 17°. Figure 4b shows a decrease in drag from α= 10° which becomes more pronounced post stall. These variations result in an improvement of 52% for the ratio C_L/C_D .

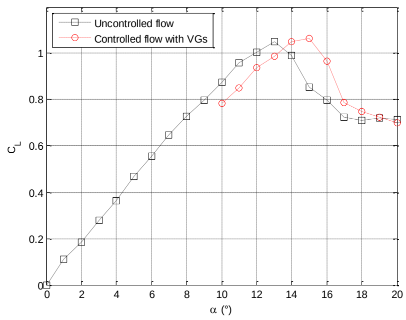

a)

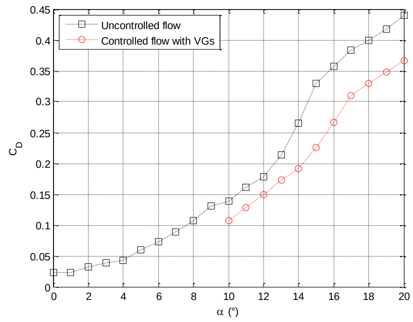

b)

Figure 5. Lift and drag coefficients versus angles of attack. With and without control using VGs, Re=1.5×10^5. a) Lift coefficient, b) Drag coefficient

Controlled Flow with Micro-Blowing

Figure 6 shows the C_L and C_D evolutions versus the incidence angle for both the reference case and the controlled flow by blowing. Three mass flow rates were considered: 0.75 g/s, 0.91 g/s and 1.06 g/s. Figure 6a shows a significant increase in the lift coefficient and a delay in stall of four degrees when the flow is controlled. The lift increase is linked to the blowing flow rate. Figure 6b shows a decrease in drag for the entire range of the incidences, from α= 0° to α= 20°. Furthermore, one can see an important gap between the reference case and the controlled flow when the incidence exceeds 12°. An improvement in aerodynamic performance was achieved with an increase of approximately 49% in lift, a reduction of about 69% in drag and an enhancement of 75% for the ratio C_L/C_D .

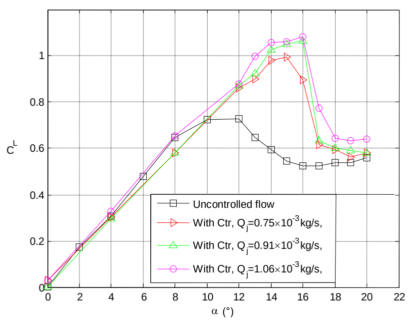

a)

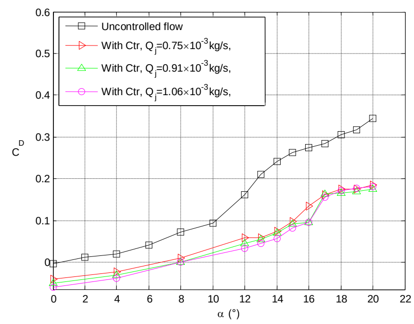

b)

Figure 6. Lift and drag coefficients versus angles of attack. With and without control using micro-blowing, Re=1.5×10^5, a) Lift coefficient, b) Drag coefficient.

Conclusion

This study presents a comparative analysis of flow control around a NACA 0015 airfoil conducted in a subsonic wind tunnel, utilizing both passive and active control strategies. The passive control strategy employed Lin's counter-rotating vortex generators (VGs) of triangular shape, positioned normal to the upper surface at 10% of the airfoil chord. The results demonstrated a delay in stall by two degrees and an improvement of 52% in the lift-to-drag ratio (C_L/C_D). The active control solution proposed relates to a steady blowing carried out with an angle of 45° relative to chord line, through a series of micro-holes of 0.6 mm in diameter uniformly arranged also at 10% from the leading edge. This approach yielded an even more significant delay in stall of four degrees and a substantial improvement of 75% in the C_L/C_D ratio, underscoring the effectiveness of active control methods. Overall, the findings indicate that both strategies enhance aerodynamic performance, each with distinct advantages and disadvantages. The passive control method using Lin's counter-rotating vortex generators (VGs) is straightforward and requires minimal maintenance, though its effectiveness is limited. In contrast, the active control method with steady blowing through micro-holes offers superior enhancements, such as greater stall delay and improved lift-to-drag ratio, but comes with increased complexity and energy consumption. Thus, while the active method provides significant benefits, the passive method serves as a more accessible alternative, highlighting the importance of context in selecting a flow control strategy.

Scientific Ethics Declaration

The authors declare that the scientific ethical and legal responsibility of this article published in EPSTEM Journal belongs to the authors

Acknowledgements or Notes

This article was presented as a poster presentation at the International Conference on Technology, Engineering and Science (www.icontes.net) held in Antalya/Turkey on November 14-17, 2024.

References

Bouderbala, F. (2025). Passive flow control around a NACA4415 airfoil by means of vortex generators. *International Journal of Fluid Mechanics Research*, *52*(1), 1-16.

Fouatih, O. M., Medale, M., Imine, O., & Imine, B. (2016). Design optimization of the aerodynamic passive flow control on NACA 4415 airfoil using vortex generators. *European Journal of Mechanics-B/Fluids*, *56*, 82-96.

Gad-el-Hak, M. (2001). Flow control: The future. *Journal of Aircraft*, *38*(3), 402–418.

Godard, G., & Stanislas, M. (2006). Control of a decelerating boundary layer. Part 1: Optimization of passive vortex generators. *Aerospace Science and Technology*, *10*(3), 181-191.

Huang, L., Huang, P. G., LeBeau, R. P., & Hauser, T. (2004). Numerical study of blowing and suction control mechanism on NACA0012 airfoil. *Journal of Aircraft*, *41*(5), 1005-1013.

Lin, J. C. (2002). Review of research on low-profile vortex generators to control boundary-layer separation. *Progress in Aerospace Sciences*, *38*(4-5), 389-420.

Lin, J. C. (1999). Control of turbulent boundary-layer separation using micro-vortex generators. *30th Fluid Dynamics Conference*, 3404.

Modi, V. J. (1997). Moving surface boundary-layer control, a review. *Journal of Fluids and Structures*, *11*(6), 627-663.

Rao, D., & Kariya, T. (1988). Boundary-layer submerged vortex generators for separation control-an exploratory study. *1st National Fluid Dynamics Conference*, 3546.

Taylor, H. D. (1947). The elimination of diffuser separation by vortex generators. *United Aircraft Corporation Research Department* ,103.

Tebbiche, H., & Boutoudj, M. S. (2021). Active flow control by micro-blowing and effects on aerodynamic performances. Ahmed body and NACA 0015 airfoil. *International Journal of Fluid Mechanics Research*, *48*(2).

Tebbiche, H., & Boutoudj, M. S. (2019). Turbulent flow control with vortex generators around a symmetrical airfoil at high attack angles. *Journal of the Serbian Society for Computational Mechanics*, *13*(2), 67-85.

Author Information

Mohammed Saîd Boutoudj
Laboratoire d'Energétique, Mécanique et Matériaux – LEMM,
Mouloud MAMMERI University of Tizi-Ouzou
15000, Tizi-Ouzou, Algeria
Contact e-mail: *mohammedsaid.boutoudj@ummto.dz*

Hocine Tebbiche
Laboratoire d'Energétique, Mécanique et Matériaux – LEMM
Mouloud MAMMERI University of Tizi-Ouzou
15000, Tizi-Ouzou, Algeria

To cite this article:

Boutoudj, M.S. & Tebbiche, H. (2024). Effects of micro-blowing and vortex generators on the boundary layer separation control of a NACA 0015 airfoil. *The Eurasia Proceedings of Science, Technology, Engineering & Mathematics (EPSTEM), 32*, 116-122.

The Eurasia Proceedings of Science, Technology, Engineering & Mathematics (EPSTEM)
ISSN: 2602-3199

The Eurasia Proceedings of Science, Technology, Engineering & Mathematics (EPSTEM), 2024

Volume 32, Pages 123-130

IConTES 2024: International Conference on Technology, Engineering and Science

Comprehensive Investigation of Structural, Electronic and Optical Properties of KBaP Using Density Functional Theory

Aidouni Ahmed Amine
University of Ahmed Draya, Adrar

Ould-Mohamed Mounir
University of Blida

Aissat Abdelkader
University of Ahmed Draya, Adrar

Belbachir Souheil
University Abdelhamid Bn Badis of Mostaganem

Abstract: In this study, we investigate the structural, mechanical, dynamical, electronic, thermodynamic, and optical properties of KBaP using density functional theory (DFT) within the plane-wave pseudopotential method as implemented in Quantum ESPRESSO. Our structural analysis reveals that the β-phase of the half-Heusler structure is the most stable, with an equilibrium lattice parameter of 7.36 Å. Mechanical and dynamical stability are confirmed through the calculation of elastic constants and phonon dispersion, respectively. Electronic properties show that KBaP is a direct bandgap semiconductor with a bandgap of 1.30 eV at the X-X point, suggesting potential applications in optoelectronic devices. Additionally, we explore the thermodynamic and optical properties, further demonstrating the potential of KBaP in energy-related applications. Our findings provide a comprehensive understanding of KBaP, establishing it as a promising material for future technological developments.

Keywords: Half Heusler alloys, Electronic properties, Optical properties, Phonon dispersion curves

Introduction

Heusler compounds, discovered by Friedrich Heusler in the early 20th century, are recognized for unique properties such as the ferromagnetism of Cu_2MnAl, despite comprising non-magnetic elements (Heusler, 1903). Over 1000 compounds exist, categorized as full-Heusler and half-Heusler based on valence electron count, with applications in solar cells and spintronics (Wederni et al., 2024; Felser & Hirohata, 2015; Hayashi et al., 2020; Tavares et al., 2023; Graf et al., 2016).

Full-Heusler (X_2YZ) and half-Heusler (XYZ) compounds crystallize in $L2_1$ (space group 225, Fm-3m) and C1b (space group 216, F-43m) structures, respectively, with the latter containing transition metals at X and Y sites and a main group element at Z (Felser & Hirohata, 2016). The electronic properties vary, with 8-valence electron systems acting as semiconductors and 18-electron systems exhibiting tunable band gaps (0 to 4 eV) based on electronegativity differences. These features have driven significant research in spintronics and topological insulators. Certain half-Heusler compounds, like KBaP, are underexplored. DFT studies report a lattice parameter of 7.65 Å (Gruhn, 2010) And 7.36 Å (Carrete et al., 2014). Suggesting a foundation for future research. (Zhang et al., 2012). Found an indirect band gap of 2.03 eV for KBaP using DFT and the GW approximation.

This study explores KBaP, a stable half-Heusler compound notable for its dynamic, mechanical, electronic, thermal, and optical properties. Despite previous research, many of its physical characteristics remain underexamined, necessitating a thorough investigation. Utilizing advanced techniques such as DFT (Hohenberg & Kohn, 1964; Kohn & Sham, 1965). And density functional perturbation theory (DFPT) (Baroni et al., 2001a). We analyzed its lattice, elastic, electronic, and optical properties, aiming to enhance understanding of KBaP and evaluate its potential for thermoelectric and optoelectronic applications.

Computational Methodology

This study employed first-principles calculations using density functional theory (DFT) and the pseudopotential plane-wave method in Quantum Espresso (QE) (Giannozzi et al., 2017; Giannozzi et al., 2020; Giannozzi et al., 2009). The Perdew–Burke–Ernzerhof (PBE) functional was used for exchange-correlation energy (Perdew et al., 1998) alongside norm-conserving pseudopotentials (Troullier & Martins, 1991). A kinetic energy cut-off of 70 Ry for wave functions and 700 Ry for charge density was applied with an 8 × 8 × 8 Monkhorst–Pack k-point grid (Monkhorst & Pack, 1976). Ionic positions and lattice parameters were optimized using the BFGS algorithm (Broyden, 1970). Phonon dispersion and density of states were computed using density functional perturbation theory (DFPT) (Baroni et al., 2001b). On a 4 × 4 × 4 q-point mesh. Elastic constants were derived using the thermo_pw code (Corso, 2016). And optical properties were calculated with time-dependent density functional theory (TDDFT) via the turbo_eels package (Motornyi et al., 2020; Timrov et al., 2015a; Timrov et al., 2015b).

Results and Discussion

Table 1. Structural, electronic and elastic properties

Structural and electronic properties		a (A)	B (GPa)	B'	E_g^d,Eg^i
	This study	7.36	25.05	4.02	1.30, 1.35
	Other	7.65[a] 7.36[b]			2.06[c], 2.03[c]
Elastic properties		C_{11}, $C_{12,}$ C_{44}	E(GPa)	G (GPa)	υ
	This study	48.13, 12 .19, 11.19	34.22	13.54	0.26

[a](Gruhn, 2010), [b](Carrete et al., 2014), [c](Zhang et al., 2012)

Structural Properties

Half-Heusler XYZ alloys exhibit a C1b structure, classified in space group F–43m (No.: 216), with three configurations for X, Y, and Z elements: type-α, type-β, and type-γ. In the type-α phase, X occupies 4c (0.25, 0.25, 0.25), Y is at 4a (0.0, 0.0, 0.0), and Z at 4b (0.5, 0.5, 0.5). For type-β, X is at 4a, Y at 4b, and Z at 4c, while type-γ positions reverse accordingly. Energy minimization revealed the type-β phase as the most stable for KBaP, based on the total energy vs. volume curve as shown in Figure 1. The structural parameters, summarized in Table 1, were derived from Murnaghan's equation of state (Murnaghan, 1944), and align with earlier theoretical studies.

Lattice Dynamical Properties

To assess the dynamical stability of KBaP in its β-phase, we generated the phonon dispersion spectrum along high-symmetry directions, as shown in Figure 2. The absence of imaginary modes at high-symmetry k-points confirms the material's dynamical stability. This analysis is novel for KBaP. The primitive cell consists of three atoms, resulting in nine vibrational branches: three acoustic and six optical modes. Figure 2 illustrates the phonon spectrum, revealing three distinct band groups. The acoustic-optical band gap is observed at 25 cm^{-1} at the L point, attributed to variations in atomic masses.

Elastic Structure

The analysis of elastic constants is crucial for evaluating the mechanical properties of materials, including stability and ductility. For cubic structures, three independent elastic constants C11, C12, and C44 are essential, with our calculated values summarized in Table 2. The Half-Heusler alloys meet the Born-Huang criteria for mechanical stability, and C12 being lower than C11 indicates stronger bonding in the 100 direction. Mechanical parameters like shear modulus (G), Young's modulus (E), and Poisson's ratio (ν) are estimated from these constants, with results compiled in Table 1. The B/G ratio, or Pugh's ratio, indicates ductility, as values above 1.75 suggest ductile behavior; our results show KBaP is ductile. Additionally, KBaP displays high rigidity, evident from its Young's modulus values.

The analysis of elastic constants is essential for understanding key mechanical properties such as stability, hardness, strength, stiffness, and whether materials are brittle or ductile. For cubic structures, only three independent elastic constants are relevant: C11, C12, and C44. The values we calculated for these constants, summarized in Table 2, show that the three studied Half-Heusler alloys satisfy the Born-Huang criteria for mechanical stability, specifically:

$(C_{11} + 2C_{12})/3 > 0$, $(C_{11} - C_{12})/2 > 0$, $C_{44} > 0$ and $C_{12} < B < C_{11}$ Additionally, the fact that C12 is lower than C11 implies that bonding strength is greater in the ⟨100⟩ direction than in the ⟨011⟩ direction.

Using the Voigt (V), Reuss (R), and averaged Hill approximations , we can estimate mechanical parameters such as bulk modulus B, shear modulus G, Young's modulus E, and Poisson's ratio ν from the results of the elastic constants using the following relations. (Reuss,1929;Hill, 1952).

$$B_V = B_R = \frac{C_{11} + 2C_{12}}{3} \tag{1}$$

$$B_H = \frac{B_V + B_R}{2} = \frac{C_{11} + 2C_{12}}{3} \tag{2}$$

$$G_V = \frac{C_{11} - C_{12} + 3C_{44}}{5} \tag{3}$$

$$G_R = \frac{5G_{44(}C_{11} - C_{12})}{4C_{44} + 3(C_{11} - C_{12})} \tag{4}$$

$$G_H = \frac{G_V + G_R}{2} \tag{5}$$

$$E_H = \frac{9BG}{3B + G} \tag{6}$$

$$\upsilon = \frac{3B - 2G}{6B - 2G} \tag{7}$$

The calculated mechanical parameters are presented in Table 1. The assessment of whether a material is brittle or ductile is typically conducted using the ratio of bulk modulus (B) to shear modulus (G), known as Pugh's ratio. According to this criterion, a B/G ratio greater than 1.75 indicates a ductile material, while a ratio below 1.75 suggests brittleness. As indicated in Table 1, all calculated B/G ratios for the compound exceed 1.75, confirming its ductile nature. Young's modulus (E), an important parameter in industrial applications, is defined as the ratio of stress to strain, which reflects the stiffness of the material; higher values of E are associated with increased stiffness. For the Half-Heusler alloy KBaP, the Young's modulus is particularly high, showcasing its significant rigidity.

Electronic Properties

The analysis of electronic band structures is essential for understanding the physical characteristics of solid material, which largely account for their optical and transport properties. Figure 3 illustrates the electronic structure along high-symmetry directions in k-space, with the Fermi level adjusted to zero. The maximum of the valence band and the minimum of the conduction band are located at the X point, indicating semiconductor behavior characterized by a direct bandgap. The bandgap energy value (Eg) for KBaP is approximately 1.30 eV. Table 1 summarizes the calculated band energie for this alloy alongside other computed values.

Optical Properties

In this section, we examine the optical properties of KBaP to evaluate its potential for use in optoelectronic devices. The optical parameters are derived from the complex dielectric function, $\epsilon(\omega)=\epsilon_1(\omega)+i\epsilon_2(\omega)$ (Pourghazi & Dadsetani, 2005) Where the imaginary part $\epsilon_2(\omega)$ represents light absorption, and the real part $\epsilon_1(\omega)$ describes the slowing down of light within the material. The dielectric function for the studied structures is illustrated in Figure 4.

At first glance, the dielectric functions of KBaP appear quite similar. From Figure 4(a), we observe that the static value of the real part $\epsilon_1(0)$ is approximately 5.75. The inverse relationship between the bandgap Eg and $\epsilon_1(0)$ supports the correlation described by the Penn model (Penn, 1962).

$$\epsilon_1(0)=\hbar\omega/Eg \tag{8}$$

The dielectric functions show a peak at 2.70 eV, located within the visible spectrum. Additionally, the real part $\epsilon 1$ becomes negative in the energy range of 4 to 11 eV, indicating metallic behavior within this energy range. The imaginary part ϵ_2, illustrated in Figure 4(b), exhibits a notable peak around 4.05 eV in the visible region, followed by a rapid decrease with small peaks also present in the UV range.

Other optical properties, including the refractive index n, extinction coefficient k, reflectivity R, and energy loss function L, can be derived from the real and imaginary parts of the dielectric function. The equations for these parameters are as follows:

$$n(\omega) = \frac{1}{\sqrt{2}}\left(\sqrt{\epsilon_1{}^2(\omega) + \epsilon_2{}^2(\omega)} + \epsilon_1(\omega)\right)^{\frac{1}{2}} \tag{9}$$

$$k(\omega) = \frac{1}{\sqrt{2}}\left(\sqrt{\epsilon_1{}^2(\omega) + \epsilon_2{}^2(\omega)} - \epsilon_1(\omega)\right)^{\frac{1}{2}} \tag{10}$$

$$R(\omega) = \frac{(n-1)^2+k^2}{(n+1)^2-k^2} \tag{11}$$

$$L(\omega) = \frac{\epsilon_2(\omega)}{\epsilon_1{}^2(\omega)+\epsilon_2{}^2(\omega)} \tag{12}$$

Figure 5(a) shows the refractive indices of the materials under investigation. $n(\omega)$ reaches a maximum in the visible region, with a maximum of 2.85 eV for KBaP. The zero-frequency refractive index n(0) is 2.40, confirming the relationship between the real part and the static refractive index $\sqrt{\epsilon_1(0)} = n(0)$.

Figure 5(b) presents the extinction coefficient as a function of photon energy. The extinction coefficient is notably low in the energy ranges below 0.85 eV and above 13.87 eV, indicating minimal light absorption, which is advantageous for the material's transparency in these energy ranges. The reflection coefficient $R(\omega)$ quantifies a material's ability to reflect electromagnetic radiation. The reflectivity graph of KBaP is shown in Figure 5(c), where the initial value is 0.17, reaching a peak at 4.20 eV, corresponding to the ultraviolet (UV) region of the alloy. Consequently, KBaP exhibit low reflectivity in the infrared and visible ranges while showing high reflectivity in the UV range, making them suitable for UV radiation protection.

The energy loss function $L(\omega)$ describes the energy lost by a fast electron traveling through a material. Figure 5(d) illustrates this energy loss function with peak values at 11.72 eV, associated with plasmon excitations. Additionally, the absorption coefficient $\alpha(\omega)$, a key parameter for understanding light interaction with a material, can be expressed as follows (Kocak et al., 2013; Kara-Zaitri et al., 2022):

$$\alpha(\omega) = \frac{2\omega}{c}\left(\frac{1}{\sqrt{2}}\sqrt{\epsilon_1{}^2(\omega) + \epsilon_2{}^2(\omega)} - \epsilon_1(\omega)\right)^{\frac{1}{2}} \tag{13}$$

c is the speed of light in a vacuum.

Figure 6 illustrates the absorption spectrum variation as a function of the wavelength for KBaP. The proposed structure's absorption spectrum spans from 41.5 to 1000 nm. The main absorption spectrum of the studied alloy is located in the UV range, with a maximum recorded at 173 nm. KBaP exhibits the highest absorption with a maximum absorption coefficient reaching 130×10^{-4} cm^{-1} at a wavelength of 173 nm. Additionally, the absorption coefficient approaches zero in the near-infrared range. This simulation allows for optimization of the material's absorption coefficient.

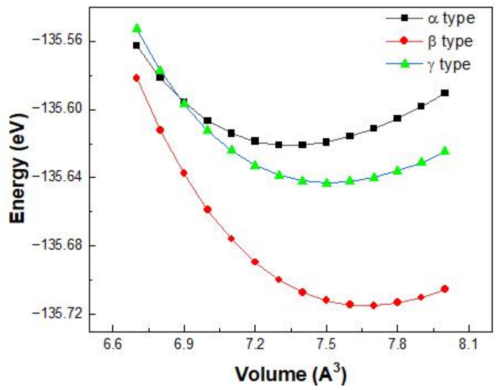

Figure 1. Energy vs Volume

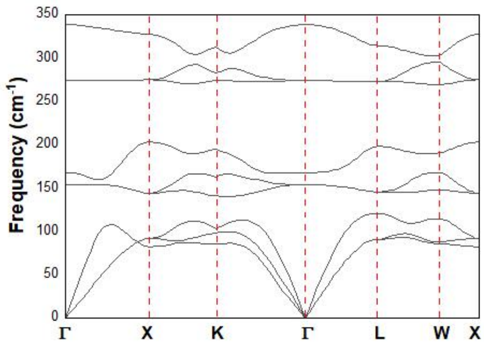

Figure 2. Phonon dispersion spectrum for KBaP

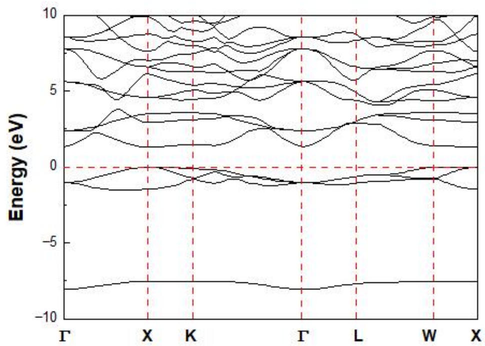

Figure 3. Band structure for KBaP

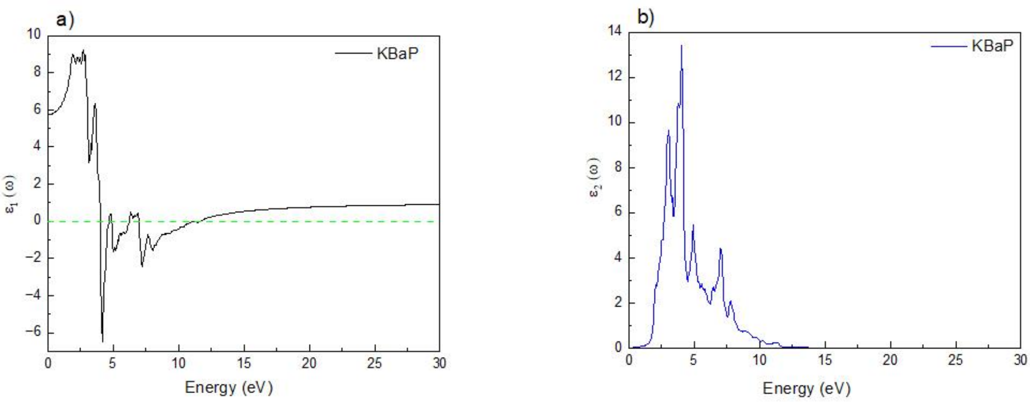

Figure 4. The dielectric function for KBaP

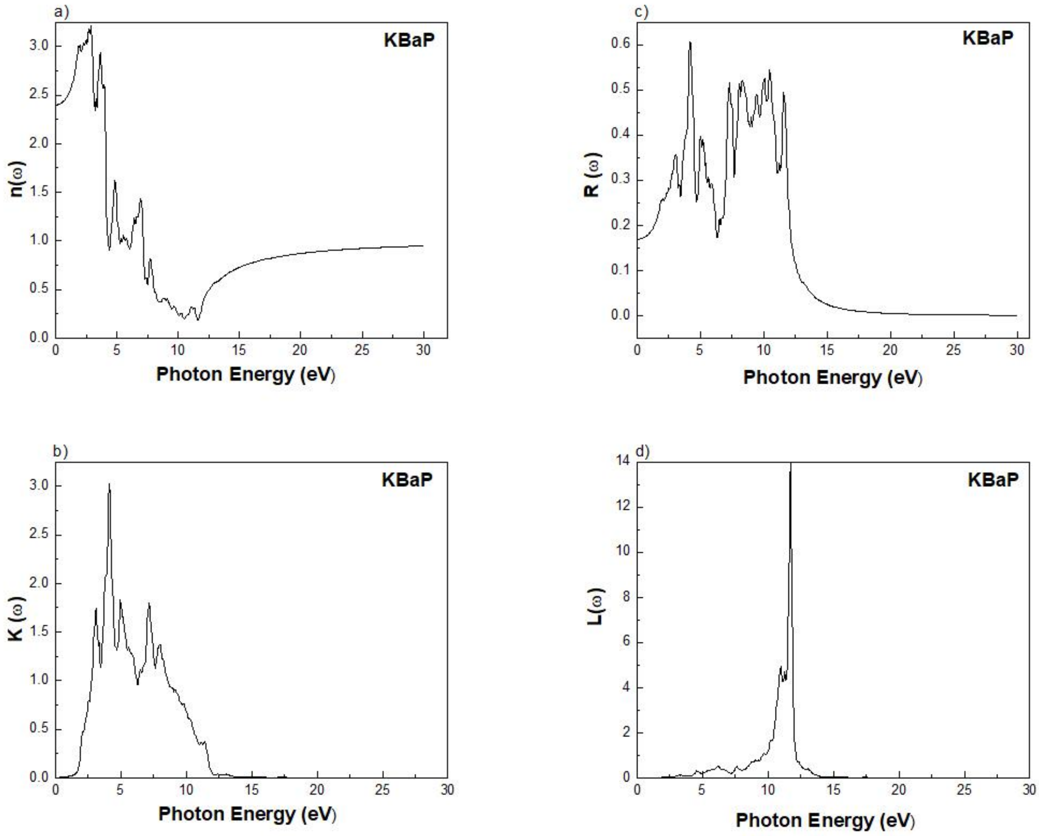

Figure 5. Optical properties for KBaP

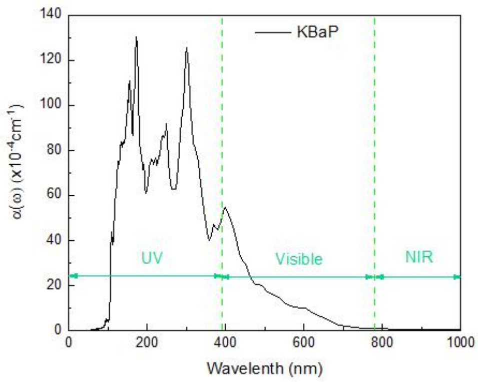

Figure 6. Absorption spectra for KBaP

Conclusion

In conclusion, this study offers a comprehensive analysis of the half-Heusler compound KBaP, providing new insights into its structural, mechanical, electronic, thermodynamic, and optical properties. Through the application of advanced computational techniques, including density functional theory (DFT) and density functional perturbation theory (DFPT), the stability of KBaP in its β-phase has been confirmed. The material exhibits promising characteristics, such as a direct bandgap of 1.30 eV, dynamic stability, and favorable elastic properties, making it a strong candidate for use in thermoelectric and optoelectronic applications. Additionally, the calculated optical properties, including the dielectric function and absorption spectra, further highlight the material's potential in ultraviolet radiation protection and other high-frequency applications. This work paves the way for future experimental studies and the exploration of KBaP's practical applications in advanced technological fields.

Scientific Ethics Declaration

The authors declares that the scientific ethical and legal responsibility of this article published in EPSTEM Journal belongs to the authors.

Acknowledgements or Notes

* This article was presented as a poster presentation at the International Conference on Technology, Engineering and Science (www.icontes.net) held in Antalya/Turkey on November 14-17, 2024.

References

Baroni, S., De Gironcoli, S., Dal Corso, A., & Giannozzi, P. (2001a). Phonons and related crystal properties from density-functional perturbation theory. *Reviews of Modern Physics*, *73*(2), 515–562.

Baroni, S., De Gironcoli, S., Dal Corso, A., & Giannozzi, P. (2001b). Phonons and related crystal properties from density-functional perturbation theory. *Reviews of Modern Physics*, *73*(2), 515–562.

Broyden, C. G. (1970). The convergence of a class of double-rank minimization algorithms 1. general considerations. *IMA Journal of Applied Mathematics*, *6*(1), 76–90.

Carrete, J., Li, W., Mingo, N., Wang, S., & Curtarolo, S. (2014). Finding unprecedentedly low-thermal-conductivity half-Heusler semiconductors via high-throughput materials modeling. *Physical Review X*, *4*(1), 011019.

Corso, A. D. (2016). Elastic constants of beryllium: A first-principles investigation. *Journal of Physics: Condensed Matter*, *28*(7), 075401.

Felser, C., & Hirohata, A. (2015). *Heusler alloys* (Vol. 222). Springer.

Felser, C., & Hirohata, A. (2016). *Heusler alloys: Properties, growth, applications* (Vol. 222). Springer.

Giannozzi, P., Andreussi, O., Brumme, T., Bunau, O., Nardelli, M. B., Calandra, M., Car, R., Cavazzoni, C., Ceresoli, D., & Cococcioni, M. (2017). Advanced capabilities for materials modelling with quantum espresso. *Journal of Physics: Condensed Matter*, *29*(46), 465901.

Giannozzi, P., Baroni, S., Bonini, N., Calandra, M., Car, R., Cavazzoni, C., Ceresoli, D., Chiarotti, G. L., Cococcioni, M., Dabo, I., Corso, A. D., Gironcoli, S. de, Fabris, S., Fratesi, G., Gebauer, R., Gerstmann, U., Gougoussis, C., Kokalj, A., Lazzeri, M., … & Wentzcovitch, R. M. (2009). Quantum espresso: A modular and open-source software project for quantum simulations of materials. *Journal of Physics: Condensed Matter*, *21*(39), 395502.

Giannozzi, P., Baseggio, O., Bonfà, P., Brunato, D., Car, R., Carnimeo, I., Cavazzoni, C., De Gironcoli, S., Delugas, P., & Ferrari Ruffino, F. (2020). Quantum espresso toward the exascale. *The Journal of Chemical Physics*, *152*(15), 154105.

Graf, T., Felser, C., & Parkin, S. S. P. (2016). Heusler compounds: Applications in spintronics. In Y. Xu, D. D. Awschalom, J. Nitta (Eds.), *Handbook of spintronics* (pp.335–364). Netherlands: Springer.

Gruhn, T. (2010). Comparative *ab initio* study of half-Heusler compounds for optoelectronic applications. *Physical Review B*, *82*(12), 125210.

Hayashi, K., Li, H., Eguchi, M., Nagashima, Y., & Miyazaki, Y. (2020). Magnetic full-Heusler compounds for thermoelectric applications. In *Magnetic materials and magnetic levitation* (Vol.65). IntechOpen

He, K., Ma, X., Chen, X., & Xue, Q. K. (2013). New materials. In M. Franz & L. Molenkamp (Eds.), *Contemporary Concepts of Condensed Matter Science* (Vol. 6, pp. 237–262). Elsevier.

Heusler, F. (1903). Uber magnetische manganlegierungen. In *Verhandlungen der Deutschen Physikalischen Gesellschaft.* (p.131). Friedr. Vieweg & Sohn.

Hill, R. (1952). The elastic behaviour of a crystalline aggregate. *Proceedings of the Physical Society Section A*, *65*(5), 349.

Hohenberg, P., & Kohn, W. (1964). Density functional theory (DFT). *Physical Review Journals*, *136*(1964), B864.

Kara-Zaitri, K., Bendaoudi, L., Ould-Mohamed, M., & Ouahrani, T. (2022). Stability and opto-electronic properties of low dimensional Ag2WS4 material, from ab initio calculations. *Materials Science in Semiconductor Processing*, *150*, 106938.

Kocak, B., Ciftci, Y. O., Colakoglu, K., Deligoz, E., & Tatar, A. (2013). Pressure depended elastic, vibration and optical properties of NbIrSn from first principles calculations. *Materials Science and Technology*, *29*(8), 925–930.

Kohn, W., & Sham, L. J. (1965). Self-Consistent equations including exchange and correlation effects. *Physical Review*, *140*(4A), A1133–A1138.

Monkhorst, H. J., & Pack, J. D. (1976). Special points for Brillouin-zone integrations. *Physical Review B*, *13*(12), 5188–5192.

Motornyi, O., Vast, N., Timrov, I., Baseggio, O., Baroni, S., & Dal - Corso, A. (2020). Electron energy loss spectroscopy of bulk gold with ultrasoft pseudopotentials and the Liouville-Lanczos method. *Physical Review B*, *102*(3), 035156.

Murnaghan, F. D. (1944). The compressibility of media under extreme pressures. *Proceedings of the National Academy of Sciences*, *30*(9), 244–247.

Penn, D. R. (1962). Wave-number-dependent dielectric function of semiconductors. *Physical Review*, *128*(5), 2093–2097.

Perdew, J. P., Burke, K., & Ernzerhof, M. (1998). Perdew, Burke, and Ernzerhof reply. *Physical Review Letters*, *80*(4), 891–891.

Pourghazi, A., & Dadsetani, M. (2005). Electronic and optical properties of BaTe, BaSe and BaS from first principles. *Physica B: Condensed Matter*, *370*(1–4), 35–45.

Reuss, Ajzj. (1929). Berechnung der fließgrenze von mischkristallen aufgrund der Konstanten des einkristalls. zeit. *Angewandante Mathematik und Mechanik*, *9*, 49–58.

Tavares, S., Yang, K., & Meyers, M. A. (2023). Heusler alloys: Past, properties, new alloys, and prospects. *Progress in Materials Science*, *132*, 101017.

Timrov, I., Vast, N., Gebauer, R., & Baroni, S. (2015a). Erratum: Electron energy loss and inelastic x-ray scattering cross sections from time-dependent density-functional perturbation theory. *Physical Review B*, *91*(13), 139901.

Timrov, I., Vast, N., Gebauer, R., & Baroni, S. (2015b). TurboEELS—A code for the simulation of the electron energy loss and inelastic x-ray scattering spectra using the Liouville–Lanczos approach to time-dependent density-functional perturbation theory. *Computer Physics Communications*, *196*, 460–469.

Troullier, N., & Martins, J. L. (1991). Efficient pseudopotentials for plane-wave calculations. *Physical Review B*, *43*(3), 1993–2006.

Wederni, A., Daza, J., Ben Mbarek, W., Saurina, J., Escoda, L., & Suñol, J.-J. (2024). Crystal structure and properties of Heusler alloys: a comprehensive review. *Metals*, *14*(6), 688.

Zhang, X., Yu, L., Zakutayev, A., & Zunger, A. (2012). Sorting stable versus unstable hypothetical compounds: the case of multi-functional abx half-Heusler filled tetrahedral structures. *Advanced Functional Materials*, *22*(7), 1425–1435.

Author Information

Aidouni Ahmed Amine
University of Ahmed Draya, Adrar, Algeria
VPR7+89M, National Road No. 06, Adrar, Algeria
Contact e-mail: *aa.aidouni@univ-adrar.edu.dz*

Ould-Mohamed Mounir
Name of Institution or University
BP 270 Blida 09000, Algeria

Aissat Abdelkader
University of Ahmed Draya, Adrar, Algeria
VPR7+89M, National Road No. 06, Adrar, Algeria

Belbachir Souheil
University Abdelhamid Bn Badis of Mostaganem, Algeria
National Road No. 11, Kharouba, Mostaganem 27000, Algeria

To cite this article:

Amine, A.A., & Mounir, O.M.., Abdelkader, A., & Souheil, B. (2024). Comprehensive investigation of structural, electronic and optical properties of KBaP using density functional theory. *The Eurasia Proceedings of Science, Technology, Engineering & Mathematics (EPSTEM), 32*, 123-130.

The Eurasia Proceedings of Science, Technology, Engineering & Mathematics (EPSTEM)
ISSN: 2602-3199

The Eurasia Proceedings of Science, Technology, Engineering & Mathematics (EPSTEM), 2024

Volume 32, Pages 131-136

IConTES 2024: International Conference on Technology, Engineering and Science

Transfer Function Method for EMC High-Frequency Modeling of Electrical Machines

Mohammed Hamza Bermaki
Djillali Liabès University of Sidi Bel-Abbes

Houcine Miloudi
Djillali Liabès University of Sidi Bel-Abbes

Mohamed Miloudi
Relizane University

Abdelkader Gourbi
ISTA, Oran University

Abdelber Bendaoud
Djillali Liabès University of Sidi Bel-Abbes

Abstract: Any electrical machine can be exposed to electromagnetic interference, or even be the source of it. Researchers are increasingly taking EMC problems in electrical machines seriously, because of the consequences they can have in terms of operation, efficiency and service life. High-frequency modelling of the winding impedance of electrical machines is becoming increasingly important in this context, as it can be a practical asset for engineers in predicting the EMC behaviour of any machine. Several models have been developed for different electrical machines. In this paper a method based on the principle of transfer functions has been used to model several electric motors for the two propagation modes: differential and common modes. The results obtained show the effectiveness of the proposed model in predicting the impedance of the windings of any motor for frequencies up to 10MHz.

Keywords: EMC, High frequency, Electrical machines, Differential mode, Commun mode.

Introduction

Nowadays, the use of electrical machines has become indispensable to human daily life. These machines cover the majority of mechanical and electrical energy needs in the industrial, commercial and residential sectors (Kudelina et al., 2021). However, these machines are often disruptive to the electromagnetic environment in which they are used (Moreno et al., 2024). This has prompted researchers to take an early interest in the electromagnetic compatibility (EMC) performance of these devices. Several studies have already revealed that most machines are either disruptors or victims of electromagnetic interference, whether conducted or radiated (Das Himadri Sekhar et al., 2024). It was therefore necessary to take EMC aspects into consideration right from the design stage of electrical machines, in order to guarantee higher performance, longer life and a healthier EMC environment (Mariscotti, & Sandrolini, 2021).

Since then, a number of studies have focused on the prediction of conducted electromagnetic disturbances generated by different types of machines, and in particular on the modeling of these disturbances to identify and minimize the sources of electromagnetic emissions likely to disturb neighboring equipment, in order to guarantee harmonious operation in sensitive environments. A HF modeling technique for induction motors based on neural networks was described by Xianzhe et al. (2024). An improved permanent magnet synchronous motor lumped parameter model was developed by Rahimi and Kanzi (2020) and Ruiz-Sarrió et al. (2021), used finite element approach to predicting the high-frequency behavior of rotating electrical machines. For developing a high-frequency model of the induction machine, an automated fitting process is suggested by Bruno and Monopoli (2022).

Using transfer functions to model electrical motors is an established technique in EMC analysis because it enables you to examine how the motor reacts to different inputs and disturbances, including electromagnetic interference (EMI). Several recent papers have already used this technique to establish predictive models of conducted disturbances generated by electrical machines for the study of CM and DM path currents, (Miloudi et al, 2022). Proposed an identification method in high frequency for induction motor has been proposed based on the transfer function and the same approach was then used by Bermaki et al. (2023). To propose a predictive model of the DM impedance of the universal motor (Mioudi et al., 2024). Propose and develop a new model based on transfer function for obtaining the High Frequency (HF) characteristics of a single-phase induction motor with capacitance-Start. In this paper, we have applied the transfer function modeling method to the asynchronous machine in order to analyze its effectiveness for EMC studies in CM and DM for frequencies up to 10 MHz.

Materials and Methods

Impedance Measurement of Electrical Machines in CM and DM

Impedance analysis of CM and DM electrical machines is essential for understanding their behavior in the face of electromagnetic disturbances, often in the context of EMC. This measurement is commonly performed using an impedance analyzer, a precise instrument for characterizing impedances in different configurations. In our case, before we can proceed with modeling any electrical machine, it's essential to measure its impedance as a function of frequency. This is done by connecting the machine directly to the impedance analyzer, as shown in Figure 1.

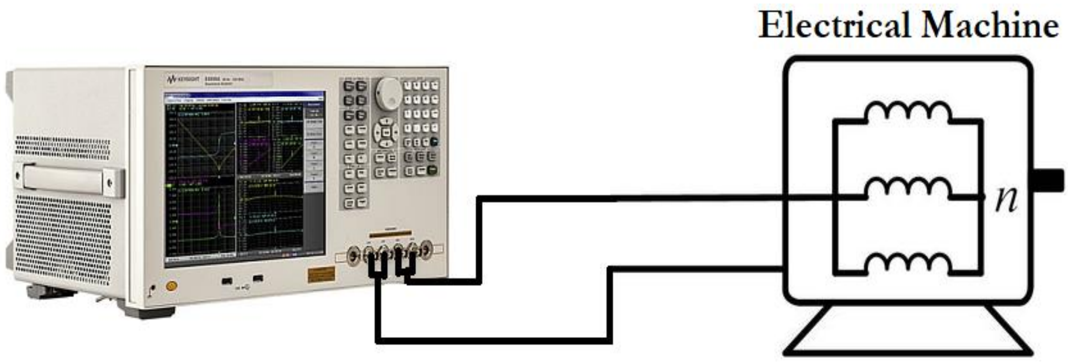

Figure 1. Impedance measurement of electrical machines

In CM, the current flows in both conductors in the same direction relative to machine ground. This type of measurement can be used to assess disturbances between the system and ground. both analyzer terminals are connected to the same point (e.g. phases) in relation to the machine frame. The current moves in opposing directions between the two conductors when in DM. This enables the analysis of disturbances between two specific points, as well as between phases or, in the case of a three-phase system, between phase and neutral. The two terminals of the impedance analyzer must therefore be connected between two points of interest on the electrical machine, e.g. between two phases or between phase and neutral.

Transfer Function Modeling Method

In situations where electromagnetic interference (EMI) might affect performance, modeling electrical machines for EMC and high-frequency behavior is essential. A strong framework for this analysis is provided by the transfer function approach in combination with impedance measurements and asymptotic Bode graphs. Using impedance measurements, the asymptotic Bode method offers an organized way to simulate the dynamic behavior of an electric motor. This procedure makes it possible to identify important dynamic features and create a prediction model that can be applied to simulation and control.

- From the plot of the impedance as a function of frequency of the electrical machine obtained with the impedance analyzer, the first thing to do is to identify the breakpoints representing the frequencies at which there is a significant variation in the slope of the impedance curve.
- The second step consists in extracting the initial gain as well as the poles and zeros. The initial gain is the impedance value at low frequency, before the first breakpoint. This gain can be noted K. Poles correspond to frequencies where impedance increases rapidly in response to an increasing frequency and zeros represents to frequencies where impedance decreases. For each breakpoint at frequency fc, If the slope increases: this is probably a zero. If the slope decreases: this is probably a pole.
- Using the gain K, poles and zeros, we can write the transfer function. If we have n zeros and m poles, the transfer function takes the following form:

$$Z\ (s) = K\ .\frac{(s - z_1)\ (s - z_2) \dots\ (s - z_3)}{(s - p_1)\ (s - p_2) \dots\ (s - p_3)}$$

where :

zi are zero frequencies,
pi are pole frequencies,
K is the initial gain.

- Finally, once the transfer function has been obtained, we can plot the curve of the predictive model of the electrical machine's impedance, and compare it with experimental measurements to assess its reliability. This can be done using analysis software such as MATLAB.

Results and Discussion

The transfer function modeling method described above was used to model the frequency behavior of the induction motor windings in CM. The motor used in this work has two windings, a main winding and an auxiliary winding, plus a starting capacitor. In the following, the results of impedance measurements for each winding and the proposed model will be presented.

Asynchronous Motor Behavior in CM

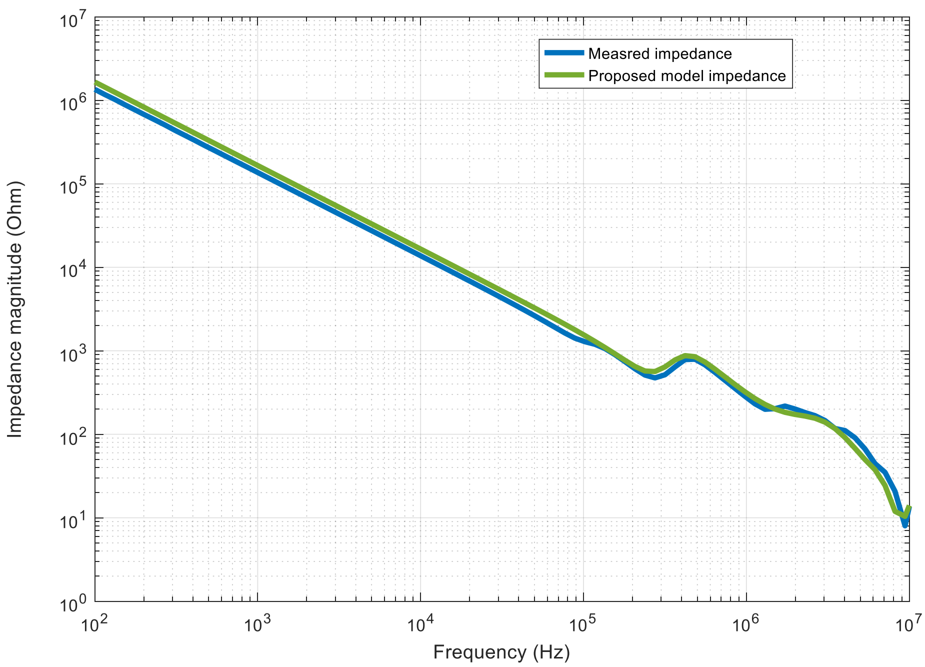

Figure 2. CM impedance measurement and simulation for main asynchronous motor winding

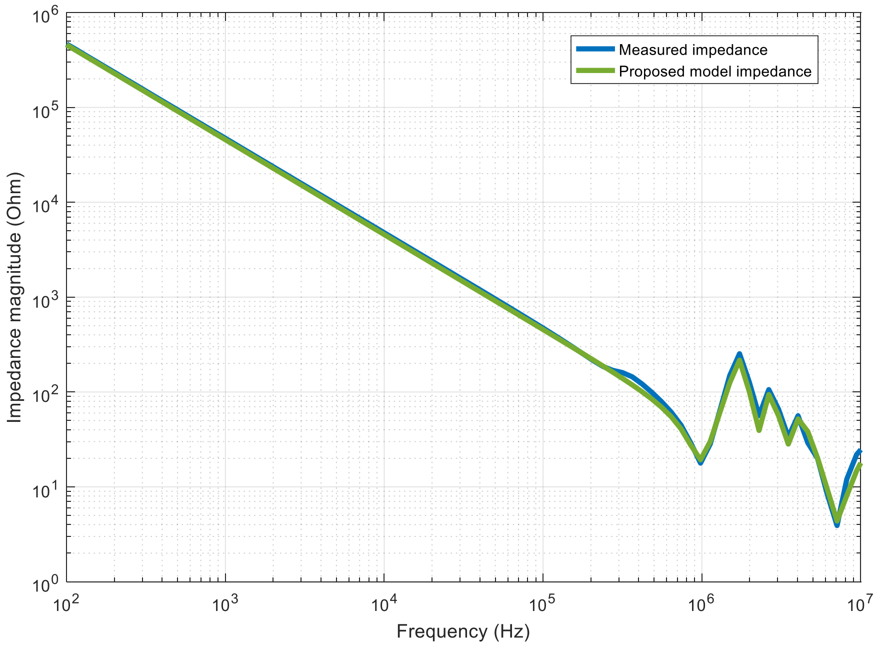

Figure 3. CM impedance measurement and simulation for auxiliary asynchronous motor winding

First, the two motor windings were studied independently. Figure 2 shows the measurement and simulation results obtained. We can clearly see that the CM impedance behaves capacitively over most of the frequency range considered. Figure 03 illustrates the behavior of the auxiliary winding in CM. In this case, capacitive behavior predominates for frequencies up to 1Mhz. Above this value, several resonances are observed.

After studying each winding separately, both were taken into consideration in order to analyze the behavior of the asynchronous motor as a whole in CM. Figure 4 shows the measurement and simulation results obtained from the variation in impedance of the asynchronous motor in CM. It can be seen that the behavior of the induction motor in CM is very similar to that of the auxiliary winding. This shows that the auxiliary winding has a greater influence on the machine's EMC performance.

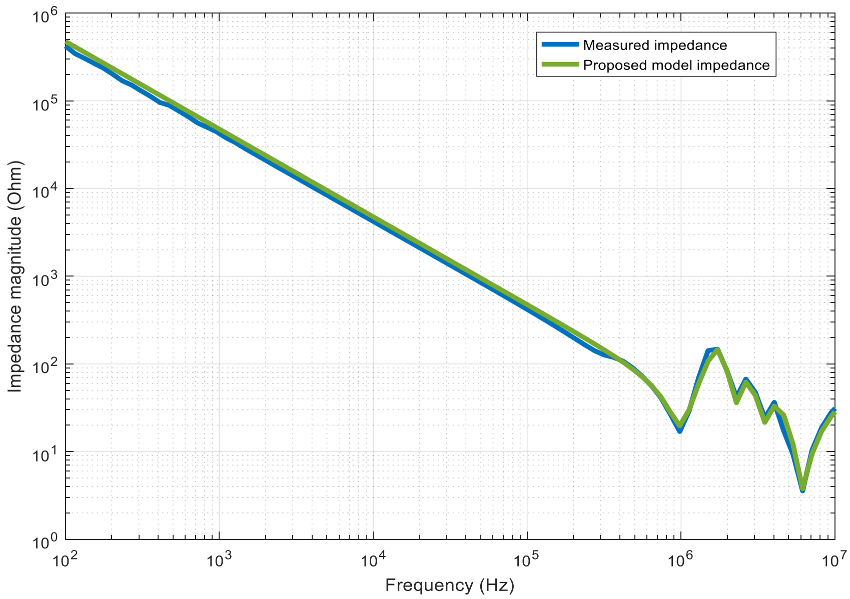

Figure 4. CM impedance measurement and simulation for asynchronous motor

The results obtained in Figures 2, 3 and 4 clearly show total alignment between the measurement curves obtained with the impedance analyzer and the simulation curves obtained with transfer function modeling for the entire frequency band between 100 Hz and 10 MHz. This confirms the reliability of this CM modeling method.

Asynchronous Motor Behavior in DM

Once the transfer function modeling of our electric machine had been validated in CM, we tested the same modeling method for the same machine, the asynchronous motor, but in DM.

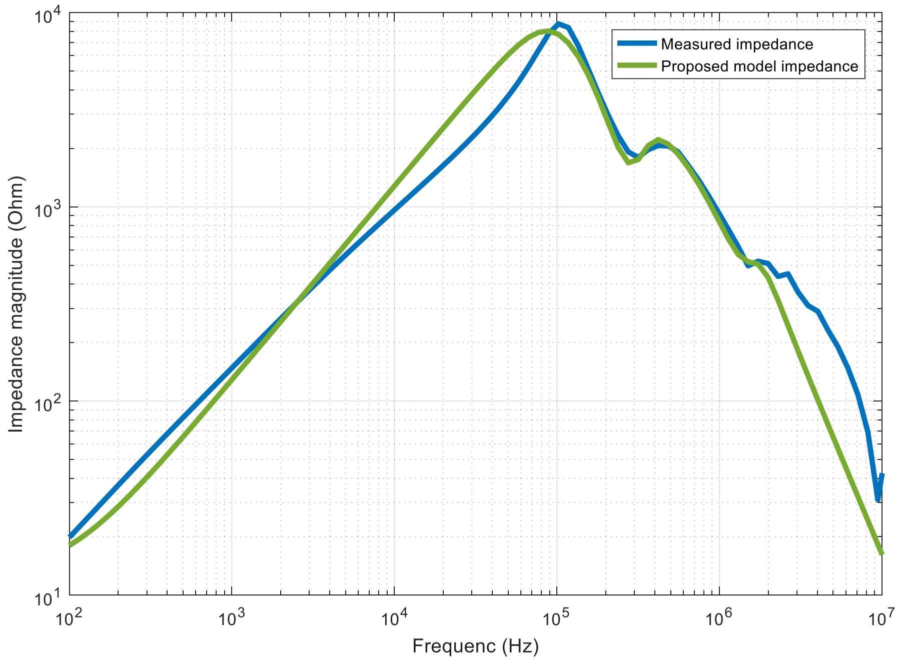

Figure 5. DM impedance measurement and simulation for asynchronous motor

The first observation we can make is that the impedance behavior of the DM machine is divided into two parts: an inductive behavior for frequencies below 100 KHz and a capacitive behavior for frequencies above this value. As for the reliability of the DM model, the measured impedance curve has the same shape as the impedance curve obtained by simulation. However, there are certain frequency ranges where the two curves are not aligned, with a fairly substantial gap between the two. This can be explained by the nature of the impedance of electrical machines, which is stable in CM and quite complex in DM. This calls for greater effort in determining the breakpoints, as the transfer function may be more complex, but will result in a more efficient predictive model.

Conclusion

In this paper, we present a method for modeling electrical machines used for EMC studies. This method is based on the principle of transfer functions and allows the impedance behavior of any electrical machine to be predicted for very high frequency ranges. This method has been applied to the asynchronous machine, and the results obtained have demonstrated the reliability of transfer function modeling, especially for the common mode. Differential mode modeling, however, requires some additional effort to improve the proposed model.

Scientific Ethics Declaration

The authors declare that the scientific ethical and legal responsibility of this article published in EPSTEM Journal belongs to the authors.

Acknowledgements or Notes

* This article was presented as an Poster presentation at the International Conference on Technology, Engineering and Science (www.icontes.net) held in Antalya/Turkey on November 14-17, 2024.

References

Bermaki, M. H., Miloudi, H., Miloudi, M., Gourbi, A., & Bendaoud, A. (2023). High-frequency differential mode modeling of universal motor's windings. *International Journal of Electrical and Electronics Research, 11*(4), 1057-1064.

Bruno, L., & Monopoli, V. G. (2022). A method for the parameter identification of an ac motor high-frequency model based on the exchange market algorithm. *International Symposium on Power Electronics, Electrical Drives, Automation and Motion (SPEEDAM)* (pp.288-293). IEEE.

Das, H. S., Mishra, S., Mahapatra, G. R., & Akitsu, T. (2023). Reviews on electromagnetic interference/compatibilities. in advances in. *Microwave Engineering* (pp.226-244). CRC Press.

Kudelina, K., Vaimann, T., Asad, B., Rassõlkin, A., Kallaste, A., & Demidova, G. (2021). Trends and challenges in intelligent condition monitoring of electrical machines using machine learning. *Applied Sciences, 11*(6), 2761.

Mariscotti, A., & Sandrolini, L. (2021). Review of models and measurement methods for compliance of electromagnetic emissions of electric machines and drives. *Acta Imeko, 10*(2), 162-173.

Miloudi, H., Miloudi, M., Ardjoun, S. A. E. M., Mahmoud, M. M., Telba, A. A., Denaï, M., ... & Ewias, A. M. (2024). Electromagnetic compatibility characterization of start-capacitor single-phase induction motor. *IEEE Access*.

Miloudi, H., Miloudi, M., Gourbi, A., Bermaki, M. H., Bendaoud, A., & Zeghoudi, A. (2022). A high-frequency modeling of AC motor in a frequency range from 40 Hz to 110 MHz. *Electrical Engineering and Electromechanics, (6),* 3-7.

Moreno, Y., Egea, A., Almandoz, G., Ugalde, G., Urdangarin, A., & Moreno, R. (2024). High-frequency modelling of electrical machines for EMC analysis. *Electronics, 13*(4), 787.

Rahimi, A., & Kanzi, K. (2020). High-frequency modelling of permanent magnet synchronous motor for conducted EMI studies. *IET Electric Power Applications, 14*(11), 2027-2036.

Ruiz-Sarrió, J. E., Chauvicourt, F., Gyselinck, J., & Martis, C. (2021). High-frequency modelling of electrical machine windings using numerical methods. *International Electric Machines & Drives Conference* (IEMDC) (pp.1-7). IEEE.

Wu, X., Zhao, Z., Jie, H., Sun, Q., & See, K. Y. (2024). improved neural network-based high-frequency behavioral modeling of induction motors. *IEEE Joint International Symposium on Electromagnetic Compatibility, Signal & Power Integrity: EMC Japan/Asia-Pacific International Symposium on Electromagnetic Compatibility (EMC Japan/APEMC Okinawa)* (pp.329-332). IEEE.

Author Information

Mohammed Hamza Bermaki
Djillali Liabès University
Sidi Bel-Abbes , Algeria
Contact e-mail: *bermaki.hamza@gmail.com*

Houcine Miloudi
Djillali Liabès University
Sidi Bel-Abbes , Algeria

Mohamed Miloudi
Relizane University
Relizane , Algeria

Abdelkader Gourbi
ISTA, Oran University
Oran, Algeria

Abdelber Bendaoud
Djillali Liabès University
Sidi Bel-Abbes , Algeria

To cite this article:

Bermaki M.H., Miloudi, H., Miloudi, M., Gourbi, A., & Bendaoud, A. (2024). Transfer function method for EMC high-frequency modeling of electrical machines. *The Eurasia Proceedings of Science, Technology, Engineering & Mathematics (EPSTEM), 32,* 131-136.

The Eurasia Proceedings of Science, Technology, Engineering & Mathematics (EPSTEM)
ISSN: 2602-3199

The Eurasia Proceedings of Science, Technology, Engineering & Mathematics (EPSTEM), 2024

Volume 32, Pages 137-141

IConTES 2024: International Conference on Technology, Engineering and Science

Studying the Microstructure Evolution by Various Methods in the Development of New Combined Deformation Processes

Yevgeniy Panin
Karaganda Industrial University

Gulzhainat Akhmetova
Karaganda Industrial University

Aibol Esbolat
Karaganda Industrial University

Abstract: When studying the microstructure, the key parameters for the researcher are the size and shape of metal grains after one or another mechanical or thermal treatment. When developing a new technological process, one of the main tasks is to predict and possibly control the microstructure, which ultimately will allow to obtain products with specified properties. The paper presents the results of finite element modeling of the microstructure evolution obtained during the development and research of new metal forming processes "rolling-ECAP" with vertical and horizontal rolls and "ECAP-Linex", which are combined schemes of two discrete deformation processes. JMAK and Cellular Automata methods were used to model the microstructure. It is shown that both methods give good convergence results. At the same time, the use of the Cellular Automata method gives an advantage over the JMAK method in obtaining data not only on changes in grain size, but also its shape – in the longitudinal direction, the grains receive a slight elongation due to the advance when metal is captured by rolls or chain conveyor elements.

Keywords: Finite element modeling, Microstructure evolution, JMAK, Cellular automata

Introduction

In recent years, there has been a tendency to develop so-called "combined" metal forming processes, which are a combination of two or more conventional deformation processes. The main feature of combined metal forming processes is that often, when they are implemented, the disadvantages of conventional metal forming processes that are included in the combined process are reduced or completely eliminated. Also, recently, more and more attention has been paid to energy-saving technologies based on the use of active friction forces for deformation. Based on the analysis of these processes, the following new concepts of combined processes were proposed:

1) the combined ECAP – Linex process for continuous pressing of non-ferrous metals and alloys, the key difference from the classic Linex process will be the possibility of deformation without significantly changing the initial dimensions of the workpiece. Here, the workpiece is fed to the device, where movable tape blocks capture the workpiece and push it through the channels of the fixed matrix. Each belt gripping unit is mounted on two pulleys, one of which is idle, and the other is driven by an electric motor. It is due to this that the tape gripping blocks are set in motion. The horizontal forming of the tape gripping blocks is created due to their movement along the workpiece and fixed locking blocks that perform a clamping role. To reduce the deformation force, grease is applied to the walls of the fixed die, while there is no lubricant supply to the moving parts in order to increase the gripping ability.

- Selection and peer-review under responsibility of the Organizing Committee of the Conference

2) the combined rolling-ECAP process with combined rolls. The usual "rolling-ECAP" deformation scheme with horizontal rolls, despite all its advantages, has one drawback. With multi-cycle deformation according to this scheme, the workpiece will be compressed several times in height, which as a result will lead to a significant change in the size and shape of the initial cross-section, which is often undesirable, and sometimes a negative factor. Therefore, this scheme has been improved by replacing the second pair of horizontal rolls with vertical rolls. Thus, after leaving the matrix, the workpiece will receive compression not in height, as before, but in width. As a result, the change in the shape and size of the cross section will not be as intense.

During investigation of new deformation process a comprehensive study using computer modeling by the finite element method is recommended to estimate the parameters of the deformation process. With this method, the researcher has much wider opportunities to study the parameters of the process. In particular, it becomes possible to study various parameters at any point of the workpiece and tool, analyze their values for exceeding permissible limits, which makes it possible to assess the possibility of various defects on the workpiece or the probability of failure of the deforming tool.

The purpose of this work was to study the evolution of the microstructure of the AD31 aluminum alloy during deformation by the ECAP-Linex method, described by Panin et al. (2023) and the combined rolling-ECAP method with vertical and horizontal rolls, described by Panin et al. (2024). The value of the channel junction angle in the matrix was chosen 140°. The rheological properties of aluminum alloy AD31 were taken from the Deform material database for the nearest analog (alloy 6063).

Method

The study of the evolution of the microstructure was also decided to be carried out at two points (in the center and on the surface). The most effective way in this case would be to model the microstructure using Cellular Automata (CA). The key feature of this algorithm is the ability to predict not only the grain size, but also their shape. A detailed description of the calculation mechanism using cellular automata is presented in Hesselbarth (1991). The initial average grain size is used as the initial data for the calculation in this algorithm. In addition, several model coefficients should be introduced, the values of which depend on the nature of the material being processed. The official documentation of the DEFORM system presents a number of coefficients of the CA model, including for aluminum alloys. The value of 20 μm was taken as the initial grain size in the calculation. To display the structure during the calculation, the parameters of the 50 x 50 μm window were set.

When calculating the rolling-ECAP process model with combined rolls, the JMAK model, described by Fanfoni et al. (1998) was used. To use this method, it is necessary to initially calculate a model with the specified parameters of the initial grain size. By default, the model assumes an even distribution of the initial grain size over the entire volume of the workpiece. The initial grain size of the aluminum alloy AD31 was assumed to be 100 μm. Taking into account the variation in the values of the heating temperature and the circumferential speed of the rolls, the following models were built:

1) with a workpiece heating temperature of 100°C and a circumferential speed of rolls of 60 rpm;
2) with a workpiece heating temperature of 100°C and a circumferential speed of rolls of 35 rpm;
3) with a workpiece heating temperature of 20°C and a circumferential speed of rolls of 60 rpm;
4) with a workpiece heating temperature of 20°C and a circumferential speed of rolls of 35 rpm.

Results and Discussion

Figure 1 shows the initial structure and after each deformation cycle of ECAP-Linex process in both studied zones. After carrying out one deformation cycle, it was found that the initial grain is crushed to 6-7 μm in both zones. However, a slight elongation of the grains in the longitudinal direction was recorded on the surface. This is the result of both the rolling stage (where, along with compression, the workpiece receives a significant level of elongation) and the pressing stage in the matrix, where the surface layers receive a certain level of extraction due to an increased level of adhesion to the conveyor links. In the second and third cycles, the workpiece received a lower compression level of 1.5 mm, which was quite sufficient, since initially a matrix with an increased channel junction angle and, as a result, with a reduced back pressure level was used. After the second deformation cycle, the structure is crushed to 2-3 μm in both zones. On the surface, the level of grain pulling becomes more noticeable. After the third deformation cycle, the structure is crushed to 1 micron in both zones, individual grains have a size of 0.8-0.9 μm. On the surface, the grains become strongly elongated.

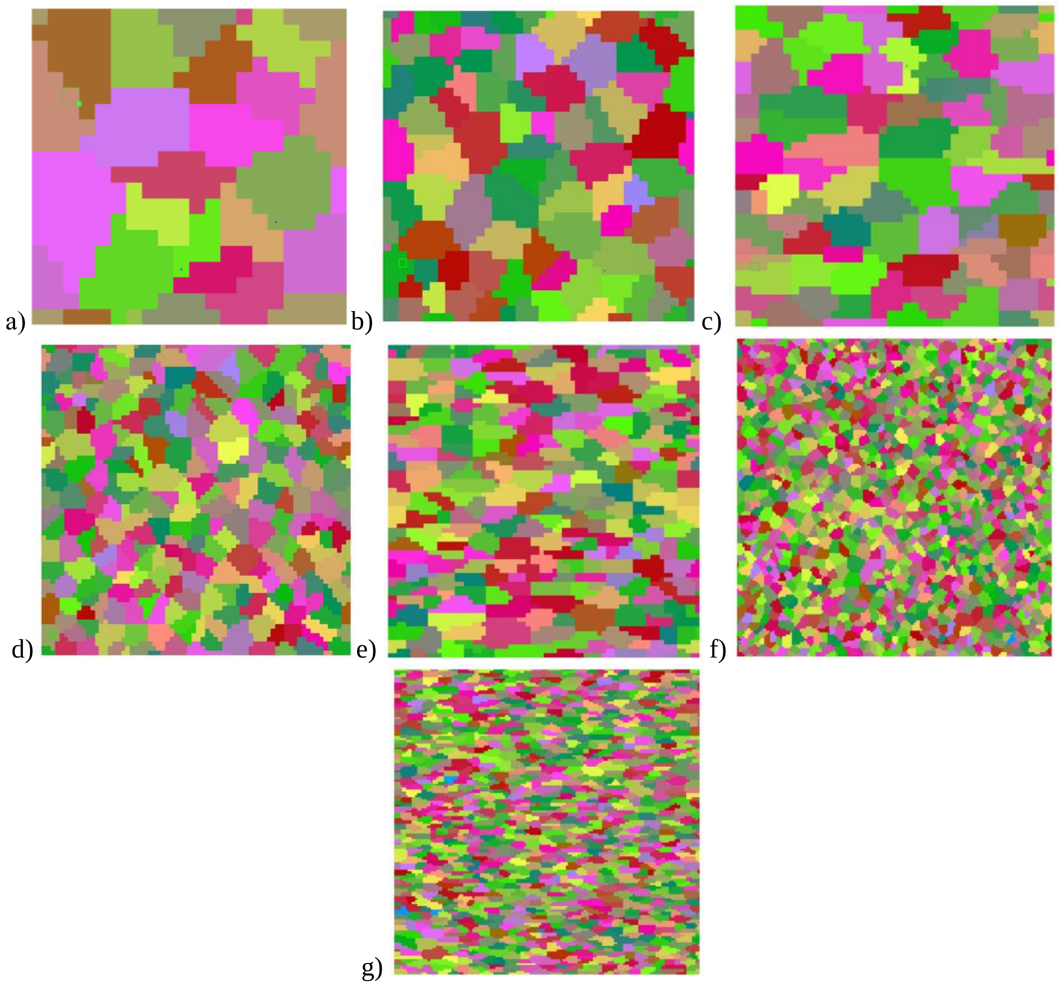

Figure 1. Structure in multi-pass modeling using the ECAP-Linex method: a – initial; b – 1st cycle, center; c – 1st cycle, surface; d – 2nd cycle, center; e – 2nd cycle, surface; f – 3rd cycle, center; g – 3rd cycle, surface

When analyzing the rolling-ECAP process model with the parameters "100°C / 60 rpm", it was revealed that after one deformation cycle, the initial grain size of 100 μm is refined to 40 μm (Figure 2). At the same time, it should be noted that modeling the microstructure in this way has one distinctive feature – the grain size distribution pattern over the volume of the workpiece is similar to the distribution pattern of equivalent deformation in inverse dependence, i.e. the higher the deformation level at a given point, the lower the grain size value. Accordingly, the minimum grain size of 40 microns is observed in the central zone after leaving the second pair of rolls. On the surface, the grain size is slightly higher, about 47 μm.

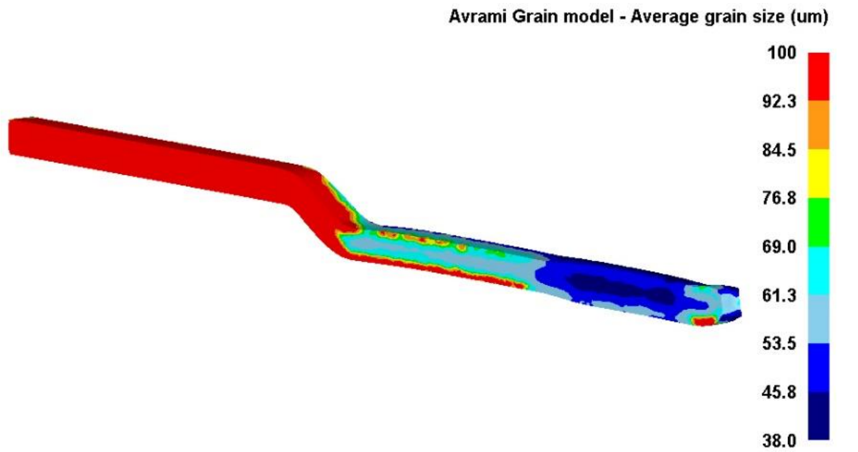

Figure 2. Microstructure evolution according to the JMAK method in the rolling-ECAP process model with parameters "100°C / 60 rpm"

After calculating the model with the parameters "100°C / 35 rpm", it was found that after one deformation cycle, the initial grain size of 100 μm is refined to 49 μm in the central zone and to 55 μm on the surface (Figure 3). After calculating the model with the parameters "20°C / 60 rpm", it was found that after one deformation cycle, the initial grain size of 100 μm is refined to 51 μm in the central zone and to 59 μm on the surface (Figure 4). After calculating the model with the parameters "20 °C / 35 rpm", it was found that after one deformation cycle, the initial grain size of 100 μm is refined to 53 μm in the central zone and to 63 μm on the surface (Figure 5).

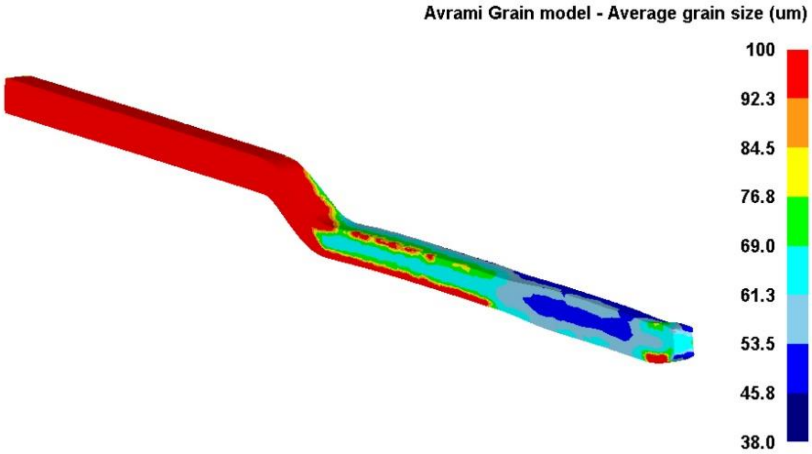

Figure 3. Microstructure evolution according to the JMAK method in the rolling-ECAP process model with parameters "100°C / 35 rpm"

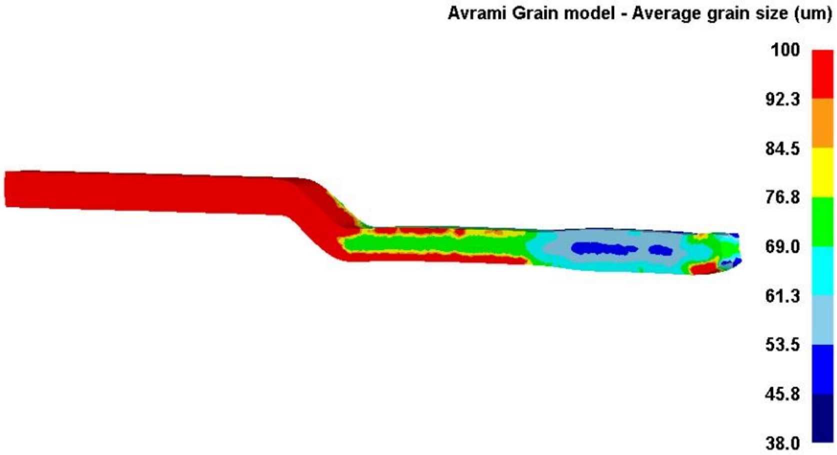

Figure 4. Microstructure evolution according to the JMAK method in the rolling-ECAP process model with parameters "20°C / 60 rpm"

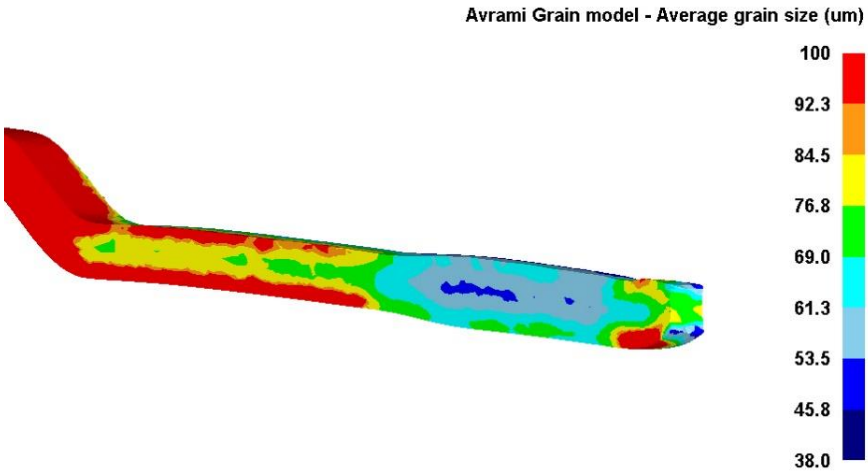

Figure 5. Microstructure evolution according to the JMAK method in the rolling-ECAP process model with parameters "20°C / 35 rpm"

Conclusion

In this section, finite element modeling of the evolution of the microstructure of the combined rolling-ECAP process with combined rolls and ECAP-Linex was carried out using JMAK and Cellular Automata methods. An analysis of the microstructure evolution of the rolling-ECAP process showed that the most optimal option is a model in which the workpiece was heated to 100 °The deformation was carried out at a circumferential speed of the first pair of rolls of 60 rpm. At the same time, options with a single temperature reduction to 20°C or a deformation rate of up to 35 rpm also give good results in grain grinding, only slightly inferior to the basic model in the intensity of grinding. As a result of multi-pass modeling, it was found that using the combined ECAP-Linex deformation method, it is possible to obtain an ultrafine-grained structure after at least three deformation cycles. The difference in the shape of the grains in the thickness of the workpiece indicates the gradient factor of the structure. At the same time, using the Cellular Automata method gives an advantage over the JMAK method and obtaining data not only on changes in grain size, but also its shape.

Scientific Ethics Declaration

The authors declare that the scientific ethical and legal responsibility of this article published in EPSTEM Journal belongs to the authors.

Acknowledgements

* This article was presented as a poster presentation at the International Conference on Technology, Engineering and Science (www.icontes.net) held in Antalya/Turkey on November 14-17, 2024.

* This research was funded by the Science Committee of the Ministry of Science and Higher Education of the Republic of Kazakhstan (Grant № AP13067723).

References

Fanfoni, M., & Tomellini, M. (1998). The Johnson-Mehl-Avrami-Kolmogorov model: A brief review. *Nuovo Cimento della Societa Italiana di Fisica D - Condensed Matter, Atomic, Molecular and Chemical Physics, Biophysics, 20*(7), 1171-1182.

Hesselbarth, H.W., & Gobel, I. R. (1991). Simulation of recrystallization by cellular automata. *Acta Metallurgica et Materialia, 39*(9), 2135-2143.

Panin, E., Volokitina, I., Volokitin, A., Naizabekov, A., Akhmetova, G., Lezhnev, S., Tolkushkin, A., & Esbolat, A., Yordanova R. (2023). Finite element modeling of ECAP-linex combined process of severe plastic deformation. *Modelling and Simulation in Engineering, 2023*, 1573884.

Panin, E., Volokitina, I., Volokitin, A., Naizabekov, A., Akhmetova, G., Lezhnev, S., Tolkushkin, A., & Esbolat A. (2024). FEM simulation of rolling-pressing process with horizontal and vertical rolls. *Tehnički Vjesnik, 31*(6), 1805-1814.

Author Information

Yevgeniy Panin
Karaganda Industrial University
Republic 30, Temirtau, Kazakhstan
Contact e-mail: *ye.panin@tttu.edu.kz*

Gulzhainat Akhmetova
Karaganda Industrial University
Republic 30, Temirtau, Kazakhstan

Aibol Esbolat
Karaganda Industrial University
Republic 30, Temirtau, Kazakhstan

To cite this article:

Panin, Y., Akhmetova, G., & Esbolat, A. (2024). Studying the microstructure evolution by various methods in the development of new combined deformation processes. *The Eurasia Proceedings of Science, Technology, Engineering & Mathematics (EPSTEM), 32*, 137-141.

The Eurasia Proceedings of Science, Technology, Engineering & Mathematics (EPSTEM)
ISSN: 2602-3199

The Eurasia Proceedings of Science, Technology, Engineering & Mathematics (EPSTEM), 2024

Volume 32, Pages 142-153

IConTES 2024: International Conference on Technology, Engineering and Science

Performance Evaluation of Radio Fingerprinting Localization

Smail Medjedoub
University of Bouira

Bilal Saoud
University of Bouira

Mourad Benziane
University of Bouira

Khaled Rouabah
University of M'sila

Abstract: This paper introduces a radio fingerprinting localization method for positioning unknown radio transmitters (URTs) based on received signal strength difference (RSSD). The method incorporates Kalman filter (KF) preprocessing, principal component analysis (PCA), similarity measures, and weighted k-nearest neighbors (WKNN). First, the Kalman filter is applied to the received signal strength (RSS) measurements to reduce noise. Next, PCA is used for dimensionality reduction and decorrelation by extracting the principal components from the RSSD data. In the final stage, the similarity between offline and online principal component databases is measured using various metrics, while WKNN estimates the transmitter's position by assigning weights to nearby reference points (RPs). Simulations are conducted to evaluate the impact of preprocessing, the number of PCA components, and the choice of similarity measures on localization performance. The results provide a comprehensive analysis of the trade-offs between these techniques, highlighting their effectiveness in different environments and conditions for fingerprinting-based WLAN localization.

Keywords: Fingerprinting, Localization, RSSD, PCA, WKNN

Introduction

Recent technological advancements in mobile networks, coupled with the increasing demand for security, have led to the diversification of techniques for locating wireless device users. Radio signals, which are integral to daily life, play a crucial role in communication systems, facilitating applications such as mobile searches, emergency communications, and public safety (Zhang et al., 2019). However, these systems remain susceptible to interference from unauthorized or illegal transmissions. Unlicensed radios and intentional jammers, collectively known as Unauthorized Radio Transmitters (URTs), pose significant threats by illegally occupying wireless communication channels. As a result, the accurate detection of URTs has become a prominent area of research, drawing considerable attention in recent years.

In this context, radio fingerprinting technology has gained widespread adoption, particularly for indoor localization. This technique involves creating a database of radio fingerprints unique to a specific environment. Most previous research on radio fingerprinting localization techniques uses RSS due to its availability in various environments and the fact that it does not require additional hardware. RSS measurements are collected during the offline phase, and once the system is deployed, real-time measurements from the online phase are compared to the offline data to determine the location of URT (Zafari et al., 2019).

The accuracy of fingerprint-based localization depends not only on the precision of RSS measurements but also on the effectiveness of the algorithm used to match real-time measurements with the offline RSS fingerprint database during the testing phase (Polak et al., 2021). However, even at the same location and within the same time interval, RSS values varied due to differences in the power output and antenna gain of the radio transmitters. RSSD-based fingerprint positioning techniques, which operate by calculating the difference in RSS among access points (APs), effectively eliminate the influence of radio emitter power and antenna gain (Zhang et al., 2023). Compared to traditional RSS methods, RSSD-based approaches offer greater stability in heterogeneous environments and enhance the ability to locate URTs.

In Guenther & Julian)2016), a study on Wi-Fi location fingerprinting in indoor environments explores the use of Wi-Fi signal strength for positioning. The study evaluates nine distance metrics—including Manhattan, Euclidean, Chebyshev, and Cosine distances—to determine the most effective metric for accurate positioning. In (Zhang et al., 2019). A new KNN-based geo-location method utilizing RSSD and virtual reference points is proposed to improve URT localization. (Le et al., 2021) . Present an indoor positioning method that enhances accuracy and reduces power consumption by utilizing RSS fingerprints. This approach involves selecting fixed APs in the offline phase, applying PCA, and employing kernel-based ridge regression. (Zhou et al., 2021). Propose a robust fingerprint localization method using an adaptive KNN approach that dynamically selects the optimal number of neighbors. Additionally, (Zhang et al., 2023). İnvestigate a method based on RSSD, PCA, and the Pearson correlation coefficient to enhance feature extraction and reduce redundancy and cross-correlation in fingerprint data.

In this paper, we evaluate URT localization performance in WLAN networks by analyzing both accuracy and computational complexity (running time) based on various simulation parameters. These include the application of the Kalman filter, the number of PCA components used for dimensionality reduction, the choice of K in the WKNN algorithm, and different similarity test metrics. Specifically, the RSS measurements are preprocessed using a Kalman filter to reduce noise. Subsequently, the RSSD is calculated, and PCA is employed for dimensionality reduction in the offline phase. In the online phase, we apply the Kalman filter again on the RSS of URT, calculate the RSSD, and project the online RSSD onto the PCA coefficients derived from the offline phase. Various similarity tests are utilized to evaluate the similarity between the reduced datasets. Based on the results of these similarity tests, RPs are selected, and the WKNN algorithm is applied to accurately estimate the position of the URT. The remainder of this paper is organized as follows: Section 2 provides an overview of radio fingerprinting localization. Section 3 describes the system model used in the study. Section 4 presents the results and discussion. Finally, Section 5 concludes the paper, summarizing key findings and potential directions for future work.

Fingerprint Localization

Radio fingerprinting localization is a widely adopted technique for indoor positioning due to its high accuracy and ability to manage the complexities of indoor signal propagation. Unlike other methods, it does not require line-of-sight measurements of APs, has low complexity, and is well-suited for complex environments (Subedi & Pyun, 2017). This makes it widely applicable for accurate indoor localization, even in environments with challenging signal conditions. fingerprinting localization, typically require an environmental survey to collect fingerprints or features of the environment, which enhances the system's positioning accuracy. In this work, RSSD of different APs, which are deployed for network services, is used as feature location. The method consists of two main phases as shown in Figure 1, the offline phase and the online phase (Abed & Abdel-Qader, 2019).

In the offline phase, the area of interest is divided into grid points, referred to as RPs, each identified by Cartesian coordinates (x_i, y_i). At each RP, RSSD measurements between pairs of APs are collected along with the (x_i, y_i)coordinates of each RP to build a comprehensive fingerprinting database. These fingerprinting represent the unique signal characteristics of the environment and are stored for future comparison in the localization process. During the online phase, real-time RSS values received from the URT are converted into RSSD measurements by various APs within the area of interest. These RSSD measurements are then compared to entries in the fingerprinting database to estimate the URT's location using a pattern matching algorithm. The localization process determines the closest match between the real-time RSSD values and the stored fingerprints to accurately estimate the URT's position. To further enhance accuracy, multiple similarity metrics can be applied to determine the optimal match, with the final location estimated through an average or weighted calculation of the closest reference points.

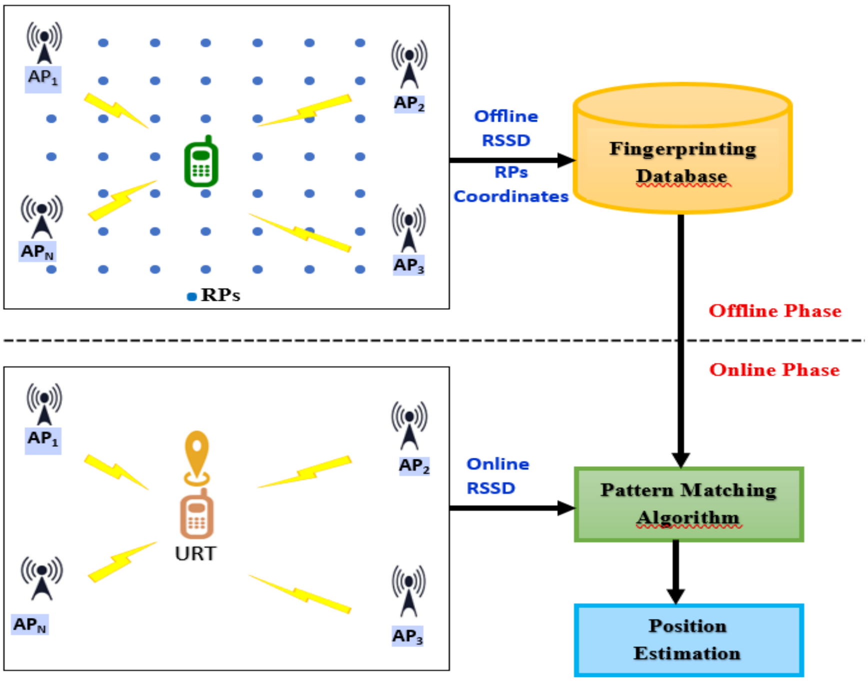

Figure 1. Radio fingerprinting localization method

System Model

In this section, we present the methodology employed by the proposed positioning system for estimating the location of a URT. The operational process of the RSSD-based PCA-WKNN fingerprinting positioning system consists of two primary phases: the offline database creation phase and the online positioning phase, as illustrated in Fig. 2.

During the offline phase, an appropriate grid distance is selected to partition the area into sub-positioning zones, with each vertex representing a RP. In our system, twelve APs are uniformly deployed. A known radio emitter is sequentially positioned at each RP, allowing for the collection of RSS measurements at each AP. Each RP corresponds to a unique set of location fingerprint vectors, capturing specific scene characteristics. Additionally, a Kalman filtering preprocessing step is employed to reduce noise in the RSS measurements, further improving the accuracy of the positioning system. The RP coordinates, along with the differences in observations from the APs, constitute the offline RSSD database. Notably, the RSSD values of adjacent calculations exhibit significant spatial and temporal correlation. To enhance computational efficiency in the online phase, we apply PCA on the offline database to extract the PCA coefficients, which are subsequently used to reduce dimensionality for both the offline and online databases.

In the online phase, real-time RSS from the URT is received by the APs. The same Kalman filtering preprocessing applied in the offline phase is utilized during this phase. Subsequently, the URT RSSD database is constructed through difference operations. Dimensionality reduction and decorrelation processing of the RSSD are performed using the previously computed PCA coefficients. The primary objective of the online positioning phase is to identify the most closely related reference point (RP) combinations. Similarity is evaluated by calculating various similarity metrics. The results are based on the WKNN algorithm, ultimately facilitating the selection of RP coordinates to estimate the URT's position.

RSSD Database Generation

In a positioning area with K RPs and N APs, the offline RSS fingerprint database, initially records RSS measurements from various APs, resulting in multidimensional features that characterize each RP. After applying Kalman filtering, the RSSD values are calculated, transforming the data into an RSSD fingerprint database, as depicted in Table 1 (Zhang et al., 2023).

Table 1. The offline RSSD fingerprint database.

Coordinates	RSSD sample			
(x_1, y_1)	$RSSD_{1,1-2}$	$RSSD_{1,2-3}$	...	$RSSD_{1,N-1}$
(x_2, y_2)	$RSSD_{2,1-2}$	$RSSD_{2,2-3}$	...	$RSSD_{2,N-1}$
(x_3, y_3)	$RSSD_{3,1-2}$	$RSSD_{3,2-3}$	...	$RSSD_{3,N-1}$
$\vdots$	$\vdots$	$\vdots$	$\vdots$	$\vdots$
(x_K, y_K)	$RSSD_{K,1-2}$	$RSSD_{K,2-3}$	...	$RSSD_{K,N-1}$

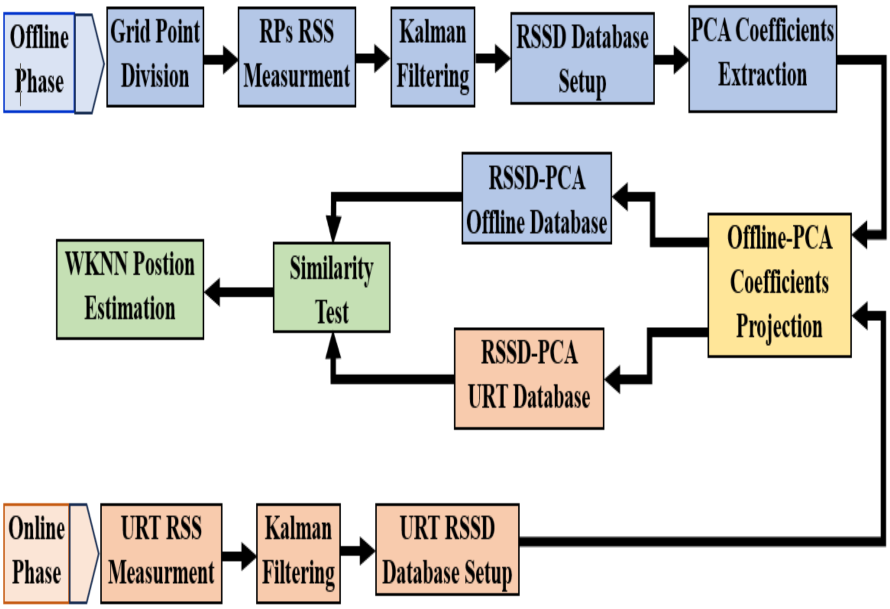

Figure 2. Flowchart of the studied scheme

PCA is used to reduce the feature space dimensions and eliminate correlation among original features without losing critical information. The offline RSSD sample matrix, denoted as $RSSD_{off}$ is structured as follow:

$$RSSD_{off} = \begin{pmatrix} RSSD_{1,1-2} & RSSD_{1,2-3} & \dots & RSSD_{1,N-1} \\ RSSD_{2,1-2} & RSSD_{2,2-3} & \dots & RSSD_{2,N-1} \\ \vdots & \vdots & \vdots & \vdots \\ RSSD_{K,1-2} & RSSD_{K,2-3} & \dots & RSSD_{K,N-1} \end{pmatrix} \tag{1}$$

Where $RSSD_{i,j}$ represents the RSSD value for the *i-th* RP and *j-th* AP. PCA coefficients (principal components) are extracted from $RSSD_{off}$. This process involves calculating the covariance matrix *C* of $RSSD_{off}$. Eigenvalue decomposition is then performed on *C*, yielding the matrix of eigenvectors, *P*. The eigenvectors are sorted in descending order according to their corresponding eigenvalues, with the top c eigenvectors selected as the c principal components. These selected eigenvectors are then combined to construct the projection matrix W (Jiang et al., 2021). Both the offline and online RSSD databases are then reduced by projecting onto the matrix W. The dimension reduction and RSSD decorrelation processing can be expressed as follows:

$$PRSSD_{off} = RSSD_{off}.W \tag{2}$$

Where $PRSSD_{off}$ is the reduced representation of the offline database. Similarly, during the online phase, the same matrix W is used to project the online RSSD data:

$$PRSSD_{on} = RSSD_{on}.W \tag{3}$$

Where $PRSSD_{on}$ is the reduced representation of the online database.

Similarity Testing

After dimensionality reduction, similarity between the reduced offline and online RSSD databases is evaluated using various similarity metrics. These metrics quantify the closeness of the reduced feature vectors to estimate the position accurately. Specifically, Euclidean distance, Manhattan distance, Chebychev distance, Cosine similarty and correlation are applied as similarity measures to compare the reduced representations. The description of each similarity test, as outlined in (Moghtadaiee & Dempster, 2015;Guenther & Julian, 2016). İs discussed in the following subsection.

Euclidean Distance

Euclidean distance quantifies the shortest distance between two points in a Cartesian coordinate system, effectively measuring the straight-line distance between two vectors.

$$d_e = \sqrt{\sum_{j=1}^{c}\left(PRSSD_{off,j} - PRSSD_{on,j}\right)^2} \tag{4}$$

where *c* is the number of principal components selected during PCA dimonsionality reuction.

Manhattan Distance

Manhattan distance, also known as city block distance, boxcar distance, or absolute value distance, is a commonly used metric for measuring similarity. This distance metric represents the distance between points on a grid-based.

$$d_m = \sum_{j=1}^{c}\left(PRSSD_{off,j} - PRSSD_{on,j}\right)^2 \tag{5}$$

Chebychev Distance

Chebychev distance, also known as the minimax metric or infinity norm. This distance calculation determines the maximum absolute difference between the corresponding elements of two vectors. It represents the greatest magnitude along any dimension of the vector space and is particularly useful in systems where calculation time is critical, as it can serve as an efficient alternative to other distance metrics. The Chebyshev distance is given by:

$$L_\infty = \max_c\left|PRSSD_{off,c} - PRSSD_{on,c}\right| \tag{6}$$

Cosine Distance

Cosine distance, d_{cos}, is a measure of similarity between two vectors rather than a traditional distance or dissimilarity metric. It calculates the angular separation between vectors, with values ranging from -1 to 1, where higher values indicate greater similarity between the vectors. By subtracting this similarity term from 1, the result can be interpreted as a vector distance. A higher cosine similarity value signifies a smaller angular separation, indicating that the two objects are more alike.

$$d_{cos} = 1 - \frac{\sum_{j=1}^{c} PRSSD_{off,j} \cdot PRSSD_{on,j}}{\left(\sum_{j=1}^{c} PRSSD_{off,j}{}^2 \cdot \sum_{j=1}^{c} PRSSD_{on,j}{}^2\right)^{1/2}} \tag{7}$$

Correlation Distance

Correlation distance measures the similarity between two vectors based on the linear relationship of their values. Unlike other distance metrics, correlation distance quantifies the degree to which one vector varies in relation to the other, with values ranging between -1 and 1. A value close to 1 indicates strong positive correlation (similar direction), 0 indicates no correlation, and -1 indicates strong negative correlation (opposite direction).

$$d_{cor} = \frac{\sum_{j=1}^{c}(PRSSD_{off,j} - \overline{PRSSD_{off}}).(PRSSD_{on,j} - \overline{PRSSD_{on}})}{\left(\sum_{j=1}^{c}(PRSSD_{off,j} - \overline{PRSSD_{off}})^2 . \sum_{j=1}^{c}(PRSSD_{on,j} - \overline{PRSSD_{on}})^2\right)^{1/2}} \quad (8)$$

Where $\overline{PRSSD_{off}}$ and $\overline{PRSSD_{on}}$ are the mean values of $PRSSD_{off}$ and $PRSSD_{on,}$, respectively.

For position estimation, the RP coordinates with the highest coefficients are selected. We use WKNN algorithm to obtain the estimated coordinate(x_{URT}, y_{URT}) of the URT, which is expressed by:

$$\begin{cases} x_{URT} = \frac{1}{K}\sum_{i=1}^{K} x_i \\ y_{URT} = \frac{1}{K}\sum_{i=1}^{K} y_i \end{cases}) \quad (9)$$

where (x_i, y_i) represents the coordinate of the *i-th* RP and *K* is the number of selected RPs

Results and Discussion

In this section, we present simulations that were conducted to assess the performance of a wireless localization system based on radio fingerprinting for URT positionning. The goal of these simulations is to evaluate the impact of different parameters and preprocessing techniques on localization accuracy and computational efficiency. The performance was analyzed under varying conditions, including the application of Kalman filter preprocessing, PCA components, similarity tests, and influnce of varying WKNN values. The simulation takes place in a 2D area of 100×100 meters. The environment consists of 12 fixed APs positioned throughout the area, which provide RSS measurements.The performance criteria used in these simulations include Localization error, defined as the distance between the estimated position of the URT and its true position. This error measures the system's accuracy. Running time which reflects the computational efficiency of the system under different configurations,

APs Distribution and URT Trajectory

The simulation area is divided into a grid of RPs spaced 0.5 meters apart. 12 fixed APs are positioned throughout the area, to ensure sufficient coverage, as shown in Figure 3. To simulate the movement of the URT, a series of key reference points was selected to form a path covering a significant part of the environment, dipected in Figure Y. The step size between trajectory points is set to 0.5 meters, allowing for detailed and precise simulation of the URT's motion

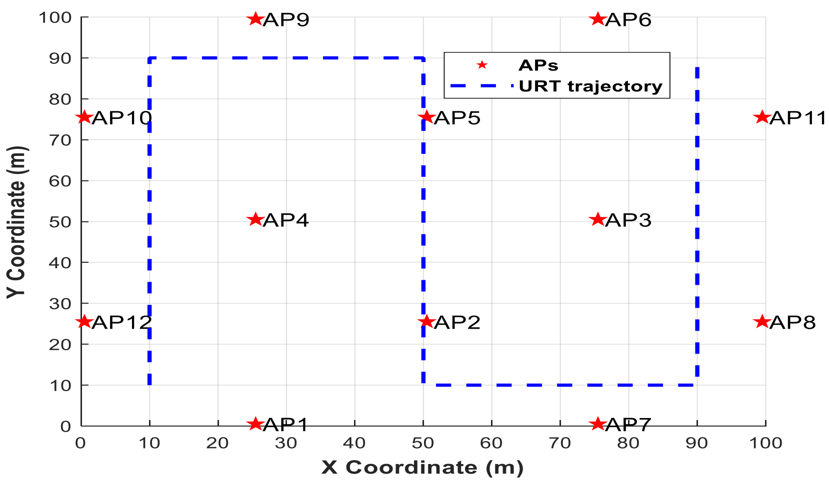

Figure 3. APs distribution and URT trajectory with 0.5m steps

RSS Modeling

To generate the RSS values in an indoor environment, a log-distance path loss model is used in (Zhang et al., 2019). This model is defined by the following equation:

$$P(d_{p,q}) = P(d_0) - 10.\alpha.log\frac{d_{p,q}}{d_0} + x_q$$

where:

- $P(d_{p,q})$ is the RSS at the q-th RP located at a distance $d_{p,q}$ p-th AP,
- $P(d_0)$ is the RSS at the reference distance d_0**,**
- d_0 is the reference distance,
- α is the path loss exponent,
- $d_{p,q}$ represents the distance between the p-th AP and the q-th RP,
- x_q is a Gaussian random noise following the distribution $N(0,\sigma^2)$,
- σ^2 represents the variance of the RSS measurement.

For our simulation, the following values for the model constants were used: $P(d_0)=10\ dB$, $d_0=1meter$, $\alpha=1.8$ and $\sigma^2=5.2\ dB$

Simulation Setup and Results

In the following subsections, we present the detailed results of various simulations. The process begins with the application of Kalman filter preprocessing on the RSS measurements. After preprocessing, we compute the RSSD by calculating the difference between the RSS values of different APs at the same RP. Next, we analyze the impact of PCA and various similarity tests on localization accuracy and computational complexity. Finally, the influence of different WKNN values on the performance of the radio fingerprinting localization system is evaluated, with a focus on both accuracy and efficiency.

Impact of Kalman Filter

In this simulation, we employ the Euclidean distance metric with 80 WKNN to estimate the position of URT. The objective is to compare the localization error under two scenarios: one without preprocessing and another where a Kalman filter is applied to RSS measurements during both the offline and online phases. The Kalman filter is utilized to reduce noise in the RSS data, aiming to enhance the localization accuracy.

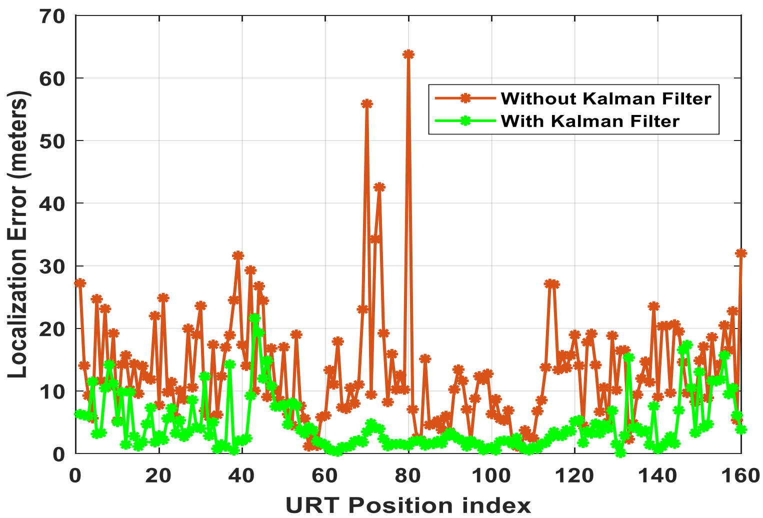

Figure 4. Localization error of URT.

The simulation results demonstrate that incorporating the Kalman filter leads to a significant reduction in localization error. The Kalman filter effectively smooths the RSS measurements, minimizing the impact of noise and fluctuations. Consequently, this improves the accuracy of matching real-time RSS data with the precomputed fingerprint database, yielding more precise location estimates. These findings underscore the importance of filtering techniques, such as the Kalman filter, in enhancing the reliability of indoor localization systems.

Impact of PCA Components

This simulation evaluates the effect of PCA on the accuracy and computational efficiency of fingerprinting-based localization. PCA is applied with varying numbers of components, ranging from 3 to 9, to assess its impact on localization error. PCA components 1 and 2 are excluded from the analysis due to their insignificant results, while components beyond 9 (i.e., 10 and 11) yield similar outcomes to those with 9 components, offering no further improvement.

The similarity between the online and offline RSSD databases is determined using correlation, while location estimation of the URT is achieved using 80 WKNN. A Kalman filter is also implemented in both the offline and online phases to reduce noise in the RSS measurements. Additionally, we compare these results with a scenario in which PCA is not applied, aiming to find an optimal balance between dimensionality reduction for improved computational speed and accurate localization performance.

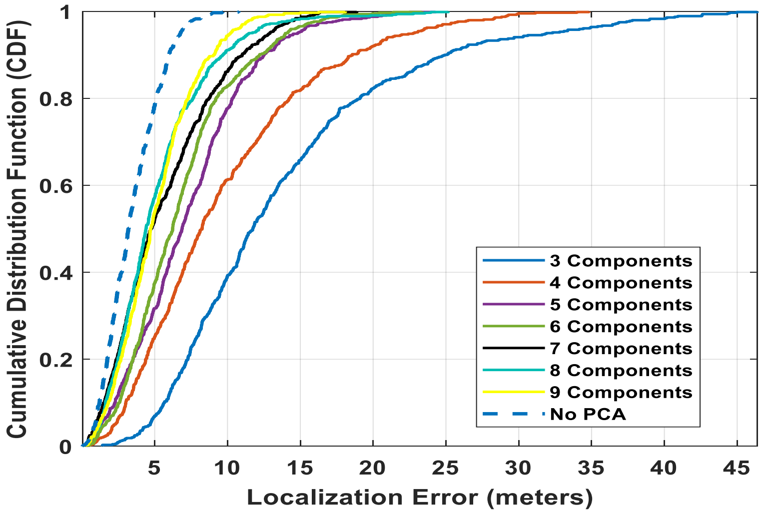

Figure 5. CDF of localization error for PCA components

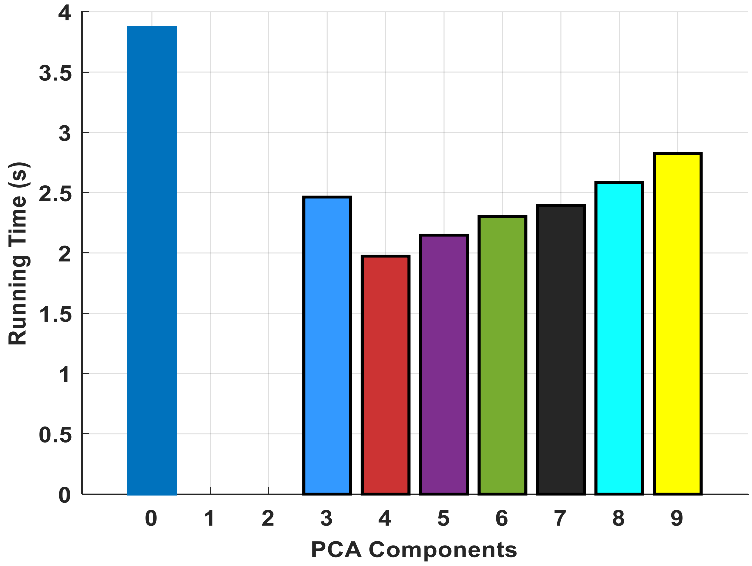

Figure 6. Runing time vs. PCA components (Including no PCA)

The simulation results, as illustrated in figures 5 and figure 6, reveal several important insights regarding the impact of PCA components on both localization accuracy and computational efficiency. Firstly, as the number of PCA components increases, the localization error decreases. This improvement occurs because higher numbers of PCA components retain more significant features from the original RSSD data, enhancing the system's ability to distinguish between different locations. However, beyond eight components, the localization accuracy shows minimal improvement, indicating that the additional components contribute marginally to error reduction. Secondly, the running time exhibits a positive correlation with the number of PCA components, reflecting the increased computational complexity required for higher-dimensional data. Notably, an anomaly is observed when using three PCA components, where the running time is unexpectedly higher. This irregularity could be attributed to inefficiencies in processing lower-dimensional data within the PCA framework. Lastly, performing localization without PCA yields a marginally lower localization error since no information is lost during dimensionality reduction. However, this comes at the cost of significantly longer running times, highlighting the computational inefficiency associated with handling high-dimensional data directly.

These findings underscore the trade-off between localization accuracy and computational cost. While using up to eight PCA components strikes a balance between minimizing error and maintaining efficient processing times, further increases in components offer diminishing returns in accuracy while imposing a heavier computational complexity.

Impact of Similarity Tests

In this simulation, we investigate the effectiveness of various similarity tests. Utilizing 8 PCA components, we apply an 80 WKNN algorithm alongside a Kalman filter for noise reduction in both the offline and online RSS databases. The aim is to compare the performance of different similarity metrics, including Euclidean, Manhattan, Chebyshev, Cosine, and Correlation, to determine their impact on localization accuracy and computational efficiency.

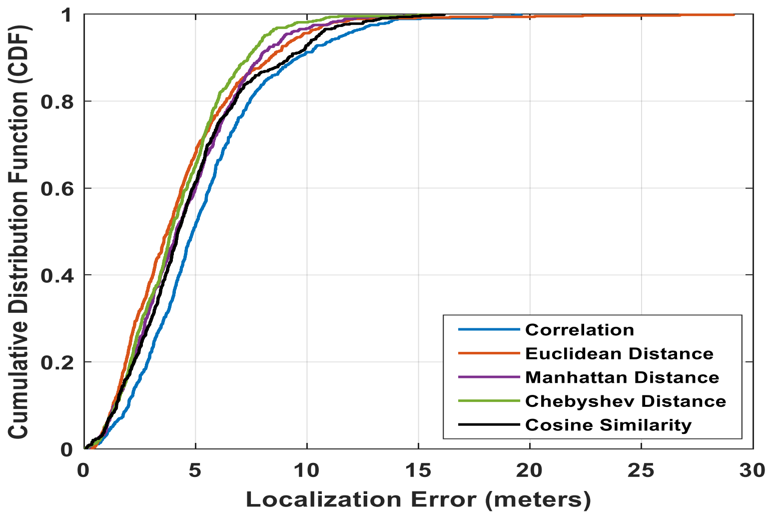

Figure 7. CDF of localization error for ifferent similarity measures

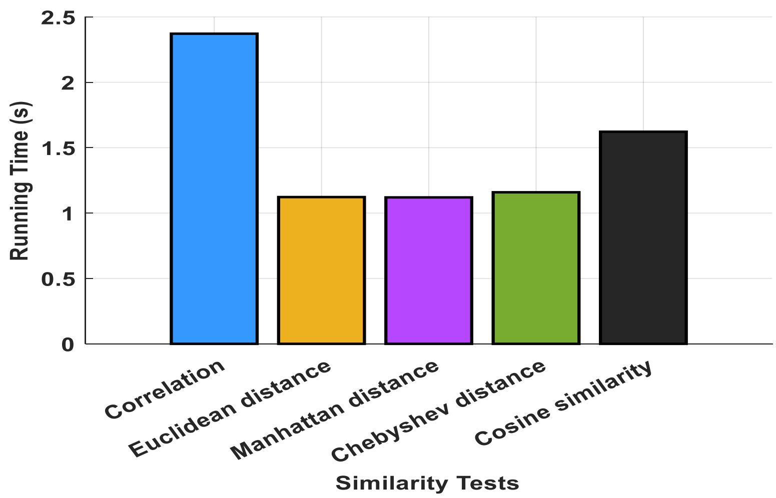

Figure 8. Running time vs similarity tests

The comparison between the different similarity measures—Euclidean, Manhattan, Chebyshev, Cosine, and Correlation—reveals several important findings related to both localization accuracy and computational efficiency. From the perspective of accuracy, the Euclidean and Chebyshev distance metrics provide the best performance, yielding the lowest localization error. Manhattan distance and Cosine similarity perform slightly worse but are still close in terms of accuracy to the best-performing metrics. The correlation-based similarity measure, however, exhibits the poorest accuracy, resulting in higher localization errors compared to the other methods. In terms of computational efficiency, Euclidean, Manhattan, and Chebyshev distances demonstrate the best performance with comparable running times, making them the most computationally efficient in this comparison. Cosine similarity incurs a higher computational cost, resulting in a longer running time. Correlation, while being the least accurate, also presents the highest running time, performing worse than Cosine in terms of speed.These results suggest that Euclidean and Chebyshev distances provide the best trade-off between accuracy and computational efficiency, making them ideal choices for practical fingerprinting localization applications. In contrast, correlation should be avoided due to both its lower accuracy and higher computational burden.

Impact of WKNN Values

In this simulation, the impact of varying WKNN values on localization error was evaluated using Euclidean distance as the similarity measure and applying a Kalman filter to RSS measurements during both the offline and online phases. By testing WKNN values ranging from 10 to 150, the goal was to determine the optimal number of neighbors that minimize localization error.

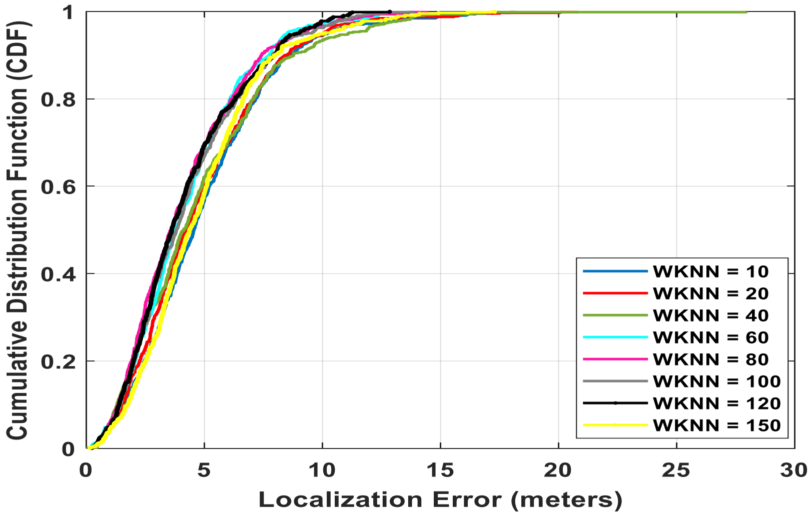

Figure 9. CDF of localization error for different WKNN values

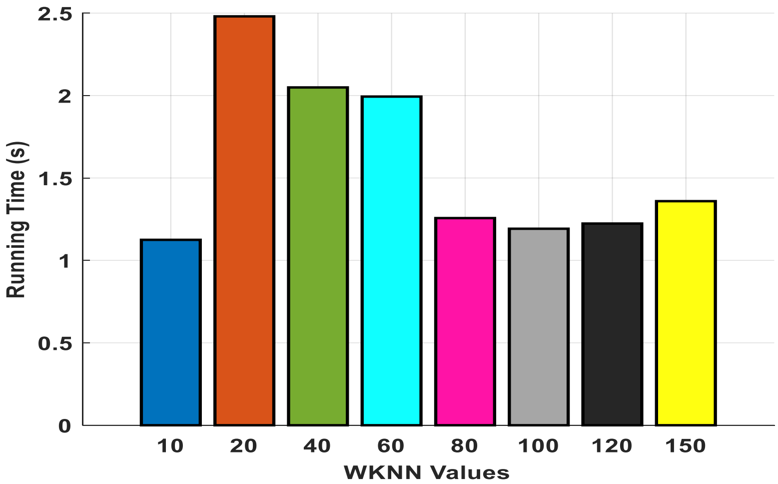

Figure 10. Running time vs. WKNN values

The results of the localization error analysis reveal an optimal range for WKNN values between 60 and 120, where localization accuracy is consistently high. Specifically, WKNN values of 60, 80, 100, and 120 show the best performance in terms of accuracy. In contrast, lower WKNN values (10, 20, 40) and the higher value of 150 exhibit slightly decreased accuracy, suggesting that an excessively small or large number of neighbors may negatively affect localization precision.

Regarding running time, there is a noticeable variation across different WKNN values. For WKNN = 10, the running time is 1.1248 seconds, which increases as WKNN grows, peaking at WKNN = 20 with 2.4803 seconds. Interestingly, after WKNN = 40 (2.0492 sec), the running time starts decreasing and stabilizes, with the best results found for WKNN = 80 (1.2566 sec) and WKNN = 100 (1.1921 sec). As WKNN increases further, there is a slight increase in running time, reaching 1.3593 seconds for WKNN = 150. The running time results suggest that a WKNN value between 60 and 120 strikes the best balance between high localization accuracy and computational efficiency. Values higher than 120 result in diminishing returns in terms of both accuracy and speed. These findings highlight the importance of selecting an appropriate WKNN value to ensure optimal localization performance in practical systems.

Conclusion

This study evaluates the performance of a radio fingerprinting localization system for localizing URTs in WLAN environments, employing a radio fingerprinting technique based on RSSD. It highlights the crucial role of Kalman filter preprocessing in reducing noise and enhancing localization accuracy. The analysis reveals that using up to eight PCA components achieves an optimal balance between accuracy and computational efficiency, while additional components offer diminishing returns. Among various similarity measures, Euclidean and Chebyshev distances demonstrated superior effectiveness in both accuracy and efficiency, whereas correlation performed poorly. Furthermore, an optimal WKNN range of 60 to 120 was identified, providing a balance between high localization accuracy and computational efficiency. These findings emphasize the importance of judiciously selecting preprocessing techniques, dimensionality reduction methods, similarity measures, and WKNN values to optimize localization performance in practical applications.

Scientific Ethics Declaration

The authors declare that the scientific ethical and legal responsibility of this article published in EPSTEM Journal belongs to the authors.

Acknowledgements or Notes

* This article was presented as an oral presentation at the International Conference on Technology, Engineering and Science (www.icontes.net) held in Antalya/Turkey on November 14-17, 2024.

* This research article is conducted as part of the academic research project PRFU - Projet de recherche formation universitaire intitulé: Transmission de l'information dans un environnement sans-fil: Propagation,

References

Abed, A., & Abdel-Qader, I. (2019). RSS-fingerprint dimensionality reduction for multiple service set identifier-based indoor positioning systems. *Applied Sciences*, *9*(15), 3137.

Guenther, R., & Julian, J. (2016). Comparison of different vector distance measure calculation variants for indoor location fingerprinting. In G. Georg & H. Haosheng (Eds.), *Proceedings of the 13th International Conference on Location-Based Services* (pp. 53–76).

Jiang, J. R., Subakti, H., & Liang, H. S. (2021). Fingerprint feature extraction for indoor localization. *Sensors, 21*(16), 5434.

Le, Y., Jin, S., Zhang, H., Shi, W., & Yao, H. (2021). Fingerprinting indoor positioning method based on kernel ridge regression with feature reduction. *Wireless Communications and Mobile Computing, 2021*(1), 1-12.

Moghtadaiee, V., & Dempster, A. G. (2015). Vector distance measure comparison in indoor location fingerprinting. *International Global Navigation Satellite Systems Society IGNSS Symposium*.

Polak, L., Rozum, S., Slanina, M., Bravenec, T., Fryza, T., & Pikrakis, A. (2021). Received signal strength fingerprinting-based indoor location estimation employing machine learning. *Sensors, 21*(13), 4605.

Subedi, S., & Pyun, J. Y. (2017). Practical fingerprinting localization for indoor positioning system by using beacons. *Journal of Sensors, 2017*(3), 1-16.

Zafari, F., Gkelias, A., & Leung, K. K. (2019). A survey of indoor localization systems and technologies. *IEEE Communications Surveys and Tutorials, 21*(3), 2568-2599.

Zhang, L., Du, T., & Jiang, C. (2019). Detection of an unknown radio transmitter using an enhanced K-nearest neighbor algorithm based on virtual reference point and RSSD information. *Eurasip Journal on Wireless Communications and Networking, 2019*(1), 71.

Zhang, L., Liu, K., Pan, Z., Pan, L., Gao, R., & Zhang, Q. (2023). An indoor unknown radio emitter positioning approach using improved RSSD location fingerprinting. *International Journal of Antennas and Propagation,*5462081.

Zhou, R., Yang, Y., & Chen, P. (2021). An RSS transform—based WKNN for indoor positioning. *Sensors, 21*(17), 5685.

Author Information

Smail Medjedoub
Department of Electrical Engineering, Sciences and Applied Sciences Faculty, University of Bouira, Bouira 1000, Algeria
Contact e-mail: *s.medjedoub@univ-bouira.dz*

Bilal Saoud
Department of Electrical Engineering, Sciences and Applied Sciences Faculty, University of Bouira, Bouira 1000, Algeria

Mourad Benziane
Department of Electrical Engineering, Sciences and Applied Sciences Faculty, University of Bouira, Bouira 1000, Algeria

Khaled Rouabah
Electronics Department.
University of Mohamed BOUDIAF.
Msila 28000, Algeria

To cite this article:

Medjedoub, S., Saoud, B., Benziane, M., & Rouabah,K. (2024). Performance evaluation of radio fingerpriniting localization. *The Eurasia Proceedings of Science, Technology, Engineering & Mathematics (EPSTEM), 32,* 142-153.

The Eurasia Proceedings of Science, Technology, Engineering & Mathematics (EPSTEM)
ISSN: 2602-3199

The Eurasia Proceedings of Science, Technology, Engineering & Mathematics (EPSTEM), 2024

Volume 32, Pages 154-159

IConTES 2024: International Conference on Technology, Engineering and Science

Evaluating Polyetheretherketone (PEEK) as a Superior Alternative to Titanium in Middle Ear Implants: A Finite Element Modeling Study

Omar Khatir
University of Sidi Bel Abbes

Abdelkader Benkhettou
University of Sidi Bel Abbes

Sidi Mohamed Fekih
University of Sidi Bel Abbes

Abderahmene Sahli
University of Sidi Bel Abbes

Ismail Boudjemaa
University of Sciences and Technology of Oran Mohamed Boudiaf

Abstract: This study presents a comprehensive finite element analysis (FEA) of hydroxyapatite (HA)-coated middle ear prostheses, evaluating the biocompatibility, mechanical integrity, and material suitability of polyetheretherketone (PEEK), titanium, and stainless steel in middle ear environments. Simulations assessed stress distribution, displacement behavior, and coating performance under auditory frequencies of 250–8000 Hz and an applied acoustic pressure of 90 dB. Results indicated that PEEK closely parallels titanium in stress tolerance and mechanical displacement, demonstrating reduced fabrication complexity and enhanced adaptability for HA coatings. This analysis supports PEEK as a practical and potentially superior alternative, offering insights into innovative material applications for middle ear prosthetic devices.

Keywords: Middel ear, Prosthesis, Ossicles, Vibration analysis, Finite-element method.

Introduction

Middle ear disorders, which can lead to substantial hearing loss, represent a significant global health concern, affecting millions of individuals and impacting quality of life. To address these conditions, total and partial ossicular replacement prostheses (TORPs and PORPs) are commonly utilized in surgical interventions, aiming to restore sound transmission by reconstructing damaged ossicular chains (Khatir et al.,2024). The success of these devices depends largely on their biocompatibility, durability, and capacity to integrate with surrounding tissue structures, all while withstanding the vibrational forces within the middle ear environment.

One key advancement in this field has been the integration of hydroxyapatite (HA) coatings on prosthetic devices. HA, a naturally occurring calcium phosphate that resembles human bone mineral, is widely valued for its biocompatibility and osseointegration properties. In middle ear implants, HA has shown potential in promoting stable interfaces with biological tissues (Jang et al., 2008., Holzer,1973). Which is crucial for effective and long-term sound transmission. Despite its benefits, HA's intrinsic brittleness and limited mechanical strength present challenges in the dynamic, load-bearing environment of the middle ear. These limitations have led to the development of HA coatings applied to stronger substrates, with titanium being the conventional choice due to its high strength-to-weight ratio, corrosion resistance, and bioinert nature (Benkhettou et al., 2024). However, while titanium remains a widely used material, its processing requirements, particularly for HA coating adhesion, involve complex and costly manufacturing techniques. These steps can limit the feasibility of customizing prosthetics to individual anatomical requirements. To address these constraints, polyetheretherketone (PEEK) has emerged as a promising alternative substrate for HA coatings. PEEK is a high-performance thermoplastic known for its bioinertness, durability, and mechanical properties comparable to human bone, including a lower modulus of elasticity than metals (Krupala et al., 1988), which can help in stress absorption. Additionally, PEEK's adaptability to various manufacturing methods, such as 3D printing, allows for greater flexibility in creating patient-specific prostheses, making it a potential substitute for titanium in middle ear applications (Yea et al., n.d., Sun et al., 2002).

Despite these advantages, there is a lack of comprehensive research on PEEK's mechanical behavior when coated with HA in middle ear prosthetic applications. Existing studies suggest that while PEEK may perform comparably to titanium under general load-bearing conditions, its performance in environments subject to auditory frequency vibrations has not been thoroughly assessed. Given this context, this study aims to evaluate the suitability of HA-coated PEEK in comparison with titanium and stainless steel by employing finite element modeling (FEM). This approach enables a precise simulation of stress distribution, displacement behavior, and coating integrity under physiological conditions. The hypothesis underlying this study is that HA-coated PEEK can achieve mechanical performance comparable to that of titanium, with additional advantages in manufacturing flexibility and customization potential. By analyzing the performance of these materials under middle ear-simulated loading conditions, this work seeks to advance the development of middle ear implants that better balance biocompatibility, mechanical resilience, and cost-effectiveness, potentially expanding access to effective auditory prosthetics.

Method

Model Design and Geometry

The prosthetic model was based on the 1004 238 TORP prosthesis from Kurz, Germany, chosen for its compatibility with standard middle ear reconstruction procedures. Using CAD software, the prosthesis was designed to replicate anatomically relevant dimensions, refined with reference to high-resolution CT scan data for precise 3D modeling. The geometry included critical components such as the tympanic membrane, ossicular chain, and cochlear interface, accurately rendered to reflect in-situ positioning (Figure 1).

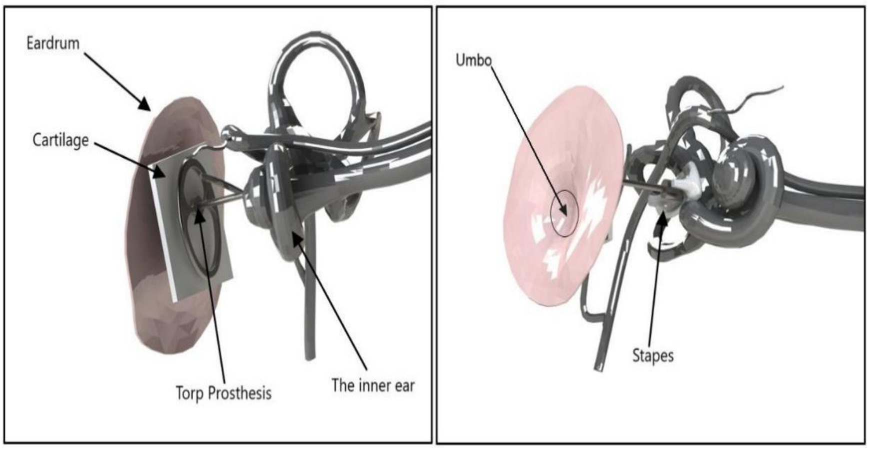

Figure 1. Illustration of middle ear prosthesis placement

Simulation Setup and Boundary Conditions

The FEM simulation integrated a tetrahedral mesh to ensure detailed resolution of the small-scale prosthetic model, with a convergence threshold set at 0.2 mm. Acoustic pressures ranging from 250–8000 Hz at 90 dB SPL were applied to simulate typical auditory stimulus impacts on the prosthesis. Boundary conditions accounted for physiological attachments, including the suspension and fixation points of the middle ear (figure 2), modeled as ligament-mimicking constraints to replicate the malleus and incus replacement.

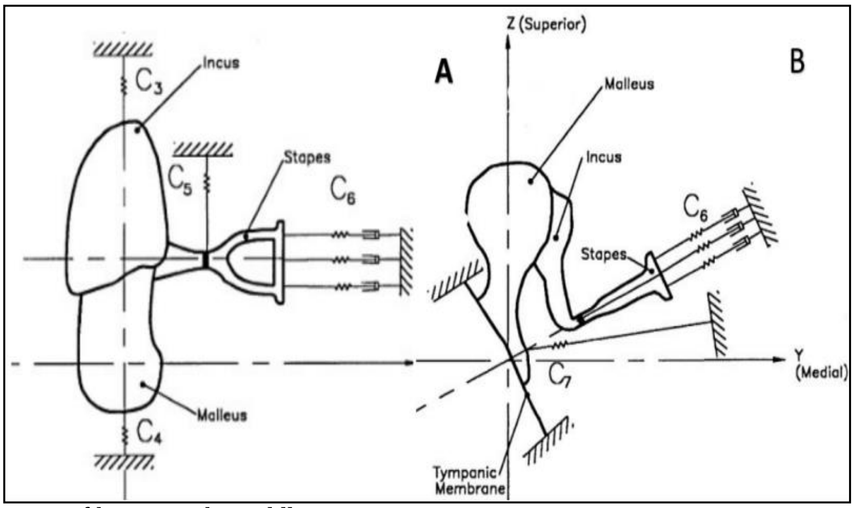

Figure 2. Schematic of human right middle ear structure. A, superior view B, an terior view. C1, C2, C3, C4, C5, and C7, attached ligaments and muscles; C6, cochlear fluid constraint(Gan et al., 2004).

Material Properties

Mechanical properties of the materials under study were assigned based on ASTM F67 standards for titanium, while values for PEEK and stainless steel were sourced from validated biomedical research. Young's modulus, Poisson's ratio, and density for each material are provided in Table 1, ensuring that simulated conditions reflect actual prosthetic performance. Each material's HA coating was uniformly set at 0.08 mm thickness, a parameter chosen for its proven efficacy in promoting osseointegration without compromising mechanical flexibility.

Table 1. Properties of the materials used in the middle ear FE model.

Material	Young's Modulus (MPa)	Poisson's Ratio	Density (kg/m3)
Titane pur (ASTM F67) Grade 2 [Laurent et al., 1988 ;Lee et al.,2006)	102.7× 103	0.37	4500
Stainless steel (Mohamed et al., 2024)	200× 103	0.3	8000
Hydroxyapatite ceramics (Shen et al., 2011)	155× 103	0.3	1200
PEEK (Niinomi,1988)	4.6× 103	0.38	2200

Performance Metrics

To evaluate each material's suitability, von Mises stress analysis and displacement behavior along the Z-axis were monitored across frequency bands. These metrics provided insights into material stability, stress endurance, and displacement fidelity in the middle ear. Comparative studies between HA-coated PEEK, titanium, and stainless steel highlighted performance distinctions, particularly in stress resistance and movement stability within the simulated auditory environment.

Results and Discussion

Stress and Displacement Analysis

Results demonstrated a pronounced difference in stress distribution across materials, with PEEK exhibiting the lowest average von Mises stress at 2.951E-09 MPa, signifying superior stress absorption compared to titanium (2.553E-07 MPa) and stainless steel (8.446E-07 MPa). The displacement analysis revealed that PEEK and titanium maintained comparable values, both displaying stability conducive to middle ear function. Stainless steel, however, showed elevated displacement, potentially limiting its applicability in finely tuned auditory prosthetics. The mechanical performance of HA-coated PEEK was especially noteworthy, as it maintained consistent stress distribution across simulated frequencies, suggesting effective load-sharing between the coating and substrate. Figures 3,4 and 5 depict the detailed stress contours and displacement vectors, illustrating how

PEEK's flexibility could contribute to more resilient prosthetic designs with minimized risk of material failure under physiological loads.

Hydroxyapatite Coating Efficacy

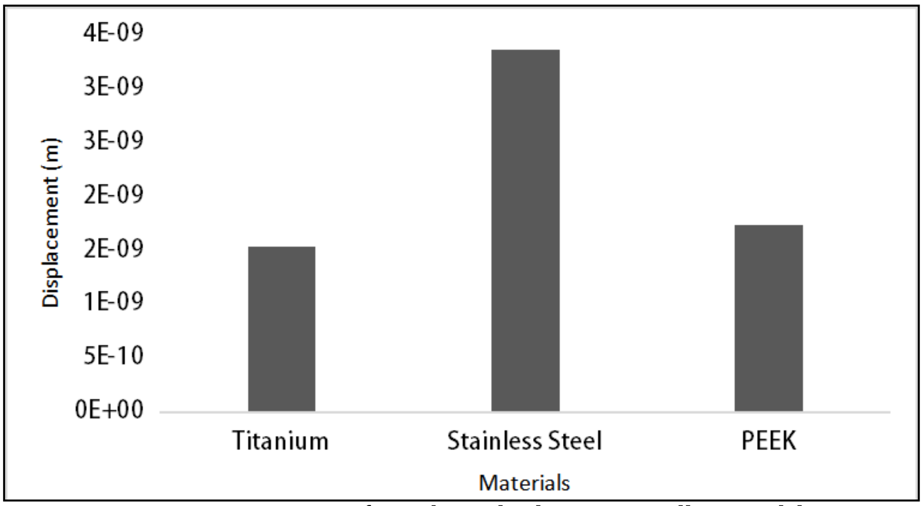

Figure 3. Comparison of prosthesis displacement in all FE models

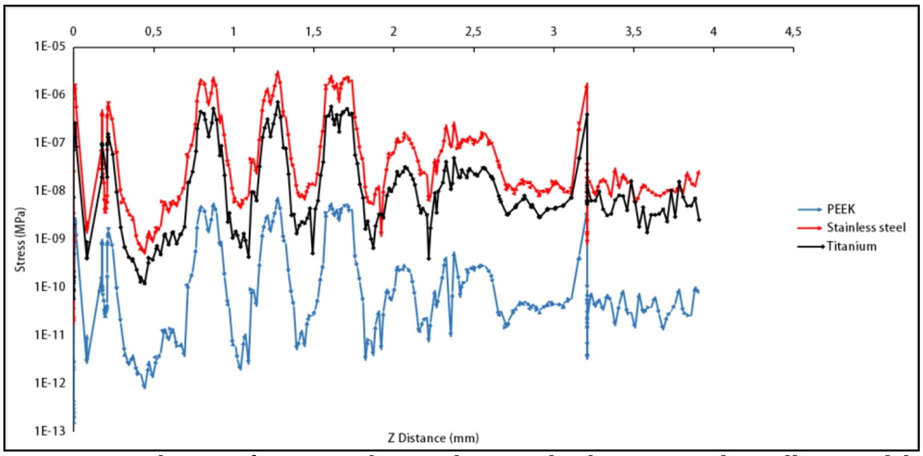

Figure 4 Distribution of stress on the prosthesis in the three materials in all FE models

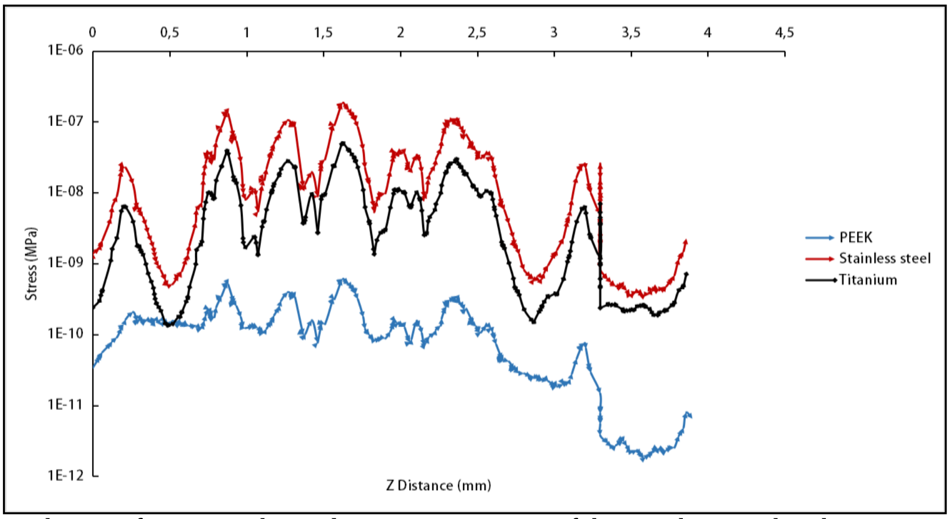

Figure 5. Distribution of Stress on the Hydroxyapatite Coating of the Prosthesis in the Three Materials in all FE models.

HA-coated PEEK displayed uniform stress across the coating layer, underscoring its compatibility with HA and potential for stable bio-integration. The coating maintained structural integrity without delamination, indicating that PEEK's surface properties favor coating adherence and durability. This contrasts with titanium and stainless steel, where higher stress concentration at the interface suggests potential wear over time. The simulations validate PEEK's functional compatibility with HA coatings in load-bearing, dynamic applications like the middle ear. Its lower modulus allows for slight conformability, enhancing interface stability and reducing potential for micro-movements that could disrupt the coating layer, thus extending prosthesis longevity.

Conclusion

The comparative FEM analysis establishes PEEK as a promising alternative to titanium for HA-coated middle ear prostheses. Its lower stress profile, adaptability to HA coating, and favorable displacement characteristics make it suitable for applications where mechanical stability and biocompatibility are critical. PEEK's manufacturing flexibility also supports customized, patient-specific implants through techniques like 3D printing, which could revolutionize middle ear prosthetic availability and functionality.

Future work should investigate the long-term bio-response of PEEK in vivo, with emphasis on HA coating adhesion and possible degradation over extended use. This research sets a foundation for developing more efficient, accessible, and effective middle ear prostheses, leveraging PEEK's mechanical and manufacturing advantages to address clinical needs in auditory restoration.

Scientific Ethics Declaration

The authors declare that the scientific ethical and legal responsibility of this article published in EPSTEM Journal belongs to the authors.

Acknowledgements or Notes

* This article was presented as a poster presentation at the International Conference on Technology, Engineering and Science (www.icontes.net) held in Antalya/Turkey on November 14-17, 2024.

References

Benkhettou, A., Khatir, O., Boudjemaa, Atef, H., I., Sahli, A., Bouiadjra, B. A. B., & Benbarek, S. (2024). Enhancing pressure ulcer prevention through optimized design of a multi-cellular foam mattress. *Mechanics of Advanced Materials and Structures*, 1–9.

Benkhettou, A., Khatir, O., Boudjemaa, I., Sahli, A., Bouiadjra, B. A. B., & Benbarek, S. (2024). Multi-objective optimization of prosthetic multi-cells foam liner. *Mechanics of Advanced Materials and Structures*, 1–9.

Boudjemaa, I., Khatir, O., Hamada, A., Benkhettou, A., Sahli, A., Abdoune, Y., & Ghali, D. (2024). Enhanced orthopedic implant design for transfemoral amputation incorporating a honeycomb structure technology. *Mechanics of Advanced Materials and Structures,* 1–7.

Gan, R. Z., Wood, M. W., & Dormer, K. J. (2004). Human middle ear transfer function measured by double laser interferometry system. *Otology & Neurotology, 25*(4),423-435.

Gan, R. Z., Feng, B., & Sun, Q. (2004). Three-dimensional finite element modeling of human ear for sound transmission. *Annals of Biomedical Engineering, 32,* 847-859.

Holzer, F. (1973). The fate of gelatin film in the middle ear. *Archives of Otolaryngology, 98*(5), 319-321.

Jang, C. H., Park, H., Cho, Y. B., & Choi, C. H. (2008). The effect of anti-adhesive packing agents in the middle ear of guinea pig. *International Journal of Pediatric Otorhinolaryngology, 72*(11), 1603-1608.

Khatir, O., Fekih, S. M., Sahli, A., Boudjemaa, I., Benkhettou, A., Salem, M., & Bouiadjra, B. B. (2024). Optimizing mechanical behavior of middle ear prosthesis using finite element method with material degradation FGM in three functions. *Mechanics of Advanced Materials and Structures,* 1–10.

Khatir, O., Fekih, S. M., Sahli, A., Boudjemaa, I., Benkhettou, (2024). Optimizing Torp middle ear prosthesis material performance using FGM material degradation approach . *Journal of the Serbian Society for Computational Mechanics, 18*(1), 94-109.

Khatir, O., Sidi Mohamed, F., Albedah, A., Hamada, A., Pawłowski, Ł., Sahli, A., …& Bouiadjra, B. B. (2024). Enhancing middle ear implants. Study of biocompatible materials with hydroxyapatite coating. *Mechanics of Advanced Materials and Structures,* 1–8.

Krupala, J. L., Gianoli, G. J., & Smith, R. A. (1998). The efficacy of hyaluronic acid foam as a middle ear packing agent in experimental tympanoplasty. *Otology & Neurotology*, *19*(5), 546-550.

Koike, T., Wada, H., & Kobayashi, T. (2002). Modeling of the human middle ear using the finite-element method. *The Journal of the Acoustical Society of America, 111*(3), 1306-1317

Laurent, C., Hellström, S., & Fellenius, E. (1988). Hyaluronan improves the healing of experimental tympanic membrane perforations. A comparison of preparations with different rheologic properties. *Archives of Otolaryngology–Head & Neck Surgery, 114*(12), 1435-1441.

Lee, C. F., Hsu, L. P., Chen, P. R., Chou, Y. F., Chen, J. H., & Liu, T. C. (2006). Biomechanical modeling and design optimization of cartilage myringoplasty using finite element analysis. *Audiology and Neurotology, 11*(6), 380-388.

Liening, D. A., McGath, J. H., & McKinney, L. (1995). Comparison of polydioxanone and silicone plastic in the prevention of adhesive otitis media in the Mongolian gerbil. *Otolaryngology—Head and Neck Surgery, 112*(2), 303-307.

Mohamed, F. S., Omar, K., Abderahmene, S., Ismail, B., & Abdelkader, B. (2024). Evaluation and comparison of the mechanical behaviors of a middle ear prosthesis using the finite element method. *Acta Mech. Slovaca, 28*(1), 38-44.

Niinomi, M. (1998). Mechanical properties of biomedical titanium alloys. *Materials Science and Engineering: A, 243*(1-2), 231-236.

Revesz, G. (1961). Use of lyophilized plasma substance in tympanoplasties. *Journal of Laryngology and Otology 7*, 77-80.

Shen, Y., Mei Teh, B., Friedland, P. L., Eikelboom, R. H., & Atlas, M. D. (2011). To pack or not to pack? A contemporary review of middle ear packing agents. *The Laryngoscope, 121*(5), 1040-1048.

Sun, Q., Gan, R. Z., Chang, K. H., & Dormer, K. J. (2002). Computer-integrated finite element modeling of human middle ear. *Biomechanics and Modeling in Mechanobiology, 1*, 109-122.

Yao, W., Li, B., Huang, X., Guo, C., Luo, X., Zhou, W., & Duan, M. (2012). Restoring hearing using total ossicular replacement prostheses–analysis of 3D finite element model. *Acta Oto-Laryngologica, 132*(2), 152-159.

Author Information

Omar Khatir
Department of Mechanical Engineering, Laboratory Mechanics Physics of Materials (LMPM), University of Sidi Bel Abbes, BP 89, cite Ben M'hidi, Sidi Bel Abbes, 22000, Algeria
Contact e-mail: *khatiromar8@gmail.com*

Benkhettou Abdekader
Department of Mechanical Engineering, Laboratory Mechanics Physics of Materials (LMPM), University of Sidi Bel Abbes, BP 89, cite Ben M'hidi, Sidi Bel Abbes, 22000, Algeria

Boudjemaa Ismail
Faculty of mechanical engineering,University of Sciences and Technology of Oran Mohamed Boudiaf (USTO-MB), El Mnaouer, BP1505, Bir El Djir 31000, Oran, Algeria.

Fekih Sidi Mohamed
Department of Mechanical Engineering, Laboratory Mechanics Physics of Materials (LMPM), University of Sidi Bel Abbes, BP 89, cite Ben M'hidi, Sidi Bel Abbes, 22000, Algeria

Sahli Abdrehmene
Department of Mechanical Engineering, Laboratory Mechanics Physics of Materials (LMPM), University of Sidi Bel Abbes, BP 89, cite Ben M'hidi, Sidi Bel Abbes, 22000, Algeria

To cite this article:

Khatir, O. Benkhettou, A., Fekih, S.M.., Sahli, A., & Boujemaa, I . (2024). Evaluating Polyetheretherketone (PEEK) as a superior alternative to titanium in middle ear implants: A finite element modeling study. *The Eurasia Proceedings of Science, Technology, Engineering & Mathematics (EPSTEM), 32,* 154-159.

The Eurasia Proceedings of Science, Technology, Engineering & Mathematics (EPSTEM)
ISSN: 2602-3199

The Eurasia Proceedings of Science, Technology, Engineering & Mathematics (EPSTEM), 2024

Volume 32, Pages 160-172

IConTES 2024: International Conference on Technology, Engineering and Science

Tailored Support for Weight Loss: A Personalized Smartphone Application for Weight Loss

Yara Oneissy
Lebanese German University

Melissa Waked
Lebanese German University

Ralph Al-Hassrouty
Lebanese German University

Marielle Mansour
Lebanese German University

Lama Bou-Farah
Lebanese German University

Abstract: Obesity and overweight are major public health concerns in Lebanon, affecting a large proportion of the population. Recent studies show that 39.9% of adult women (aged 18 and up) and 30.5% of adult men suffer from obesity. Lebanon's obesity prevalence is higher than the regional average of 10.3% for women and 7.5% for men, these alarming figures place Lebanon among the countries with the highest obesity rates in the MENA region. Faced with this concerning issue, a partnership between the biomedical engineering department and the nutrition department at the Lebanese German University resulted in the development of an innovative weight reduction application "NutriTrack". This research describes the creation of this application, concentrating on its usefulness in assisting users to lose weight in a healthy and sustainable manner in the setting of Lebanon. The app will harness the capabilities of digital technology to deliver nutritional advice, facilitate meal preparation and track functionalities which allows individuals to follow a suitable dietary plan. This user-friendly interface contains a vast database of recipes, dietary plans, nutritional information and advice provided by the nutrition department that will help individuals in choosing the suitable option tailored to their needs in alignment with their preferences and restrictions. Additionally, "NutriTrack" encourages users to adopt better dietary practices, supports greater nutrition management, and inspires them to choose healthier foods. Users of the program may increase their understanding of nutrition, which is one of its main advantages. The app will include instructional materials on a variety of nutrition-related subjects, including macronutrients, portion management, and designing well-balanced meal plans. Through engaging features like quizzes and informative articles, users can actively enhance their understanding of healthy eating principles and improve their overall nutritional knowledge. The overarching goal of the app is to drive positive health outcomes.

Keywords: Healthy lifestyle, Nutritrack, Dietary plan, Lifestyle improvement, Nutritional advice.

Introduction

Vigorous eating, practicing physical exercises, getting enough sleep and reducing stress are key points to obtaining a healthy weight. If Individuals do not manage their health lifestyle in an appropriate way, they risk

- Selection and peer-review under responsibility of the Organizing Committee of the Conference

becoming subject to serious diseases and health conditions. In order to obtain an optimal living, taking care of your body's needs is a must! A balanced diet plan that contains multiple nutrients plays an important role in managing your weight as well as following regular physical activities and getting sufficient sleep while making sure that the human body is getting rid of all the unnecessary stress (Johns Hopkins Medicine et al, 2024). A good diet is a foundation for health, well-being, optimal development and growth that offers defense against all types of malnourishment. Unhealthy diets are one of the biggest reasons behind illness, mostly for noncommunicable diseases including cancer, diabetes, and cardiovascular disease (World Health Organization, 2024).

In recent years, a mixture of technology and health management services have emerged seeking to control obesity. Most of them have taken the shape of mobile and web-based applications (Ghelani et al., 2020). "NutriTrack" was created out of purpose to revolutionize the way people approach a better lifestyle by allowing them to insert their personal information such as name, last name, age, gender, weight and height .By inputting such data users will be able to unlock a special diet that meets their requirements. One of the standouts features of the application is the availability of diverse recipes, meals, snacks and drinks options that makes it easier to find healthy yet delicious nutrients. An array of sports video links, routine exercises and tips are available! It is important to understand that physical activity is as important as following a healthy dietary plan when improving a lifestyle.

Motivation and Background

Since 1990, the global obesity rate has more than quadrupled, highlighting the need of having strategies and resources in place to assist unhealthy and obese individuals (World Health Organization, 2024). The purpose of this project is to design and build an application that promotes individuals to live better lifestyles. According to several research, as shown in (Figure 1.), the United States, China, and India have the highest rates of obesity in their populations. Obesity rates are on the rise, which is a concerning issue that must be addressed immediately. Obesity is a chronic complex disease defined by excessive fat deposits that can impair health. Obesity can lead to increased risk of type 2 diabetes and heart disease, it can affect bone health and reproduction, it increases the risk of certain cancers. (World Health Organization, 2024).

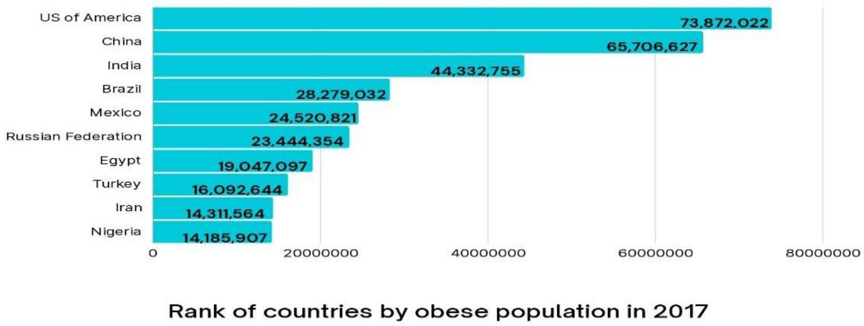

Figure 1. Rank of countries by obese population in 2017

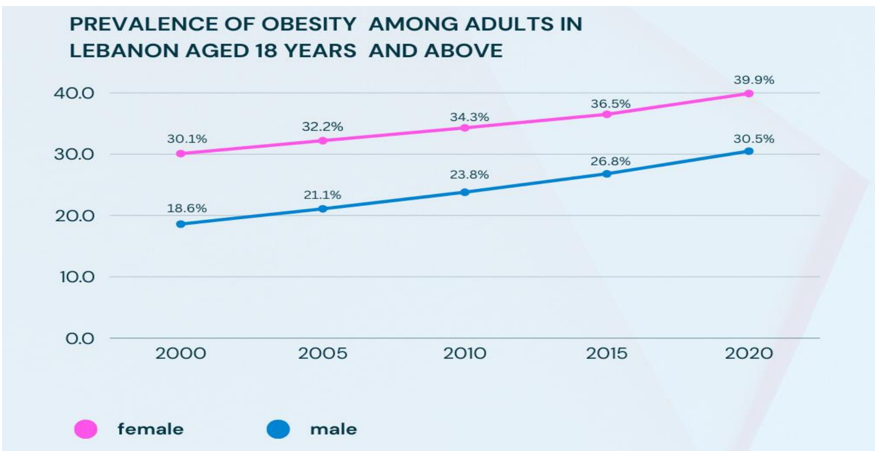

Figure 2. Prevalence of obesity among adults in Lebanon over the years

According to the World Health Organization (WHO), chronic illnesses account for approximately 40 million deaths annually, with 15 million occurring in individuals aged 30 to 69. Cardiovascular diseases, cancer, diabetes, and chronic respiratory illnesses collectively account for 82% of global fatalities. In Lebanon, chronic diseases represent 85% of total mortality, driven by risk factors such as tobacco use, physical inactivity, hazardous alcohol use, and poor diets. In 2014, over 1.9 billion individuals were classified as overweight globally, with Lebanon reporting a prevalence of obesity and overweight at 65.4% (27.4% obese, 38% overweight) (Bardus et al, 2018). Obesity and overweight are primarily caused by an energy imbalance between caloric intake and consumption. This imbalance is caused by global trends of greater availability and consumption of energy-dense foods high in sugar and saturated fats, as well as insufficient physical exercise as a result of the sedentary character of many kinds of labor, modes of transportation, and urbanization (Mansour et al,. 2019). All of these behavioral risk factors are avoidable, since they may be addressed by certain adjustments. We will talk about what made us want to do this study below.

Our main source of motivation is an intense desire for bettering people's lives and preventing obesity's negative impacts. Millions of people worldwide are influenced by the obesity pandemic. The data shown in (Figure 2.), was a powerful call to action for us because this concerning trend emphasizes the need for a comprehensive strategy to address the root causes of obesity and promote healthy lifestyles among the Lebanese people so we set out to design a system that would enable individuals to take charge of their diet and make sustainable behavioral changes. "NutriTrack" was developed to give people an accurate and customized approach to nutrition. We truly think that when it comes to addressing the many requirements and difficulties people have in controlling their weight and general health, one-size-fits-all strategies are unproductive. To combat this, "NutriTrack" creates customized meal plans based on the most recent research and technology, each of which is suited to the individual needs of the user. The urge to remove obstacles and enable everyone to have access to nutrition management has motivated us into creating "NutriTrack".

Literature Review

The World Health Organization defines obesity as an abnormal or excessive buildup of fat that creates a health concern (Bazán et al., 2018). Since obesity is a significant health issue it has now been regarded as a chronic and progressive disease, causing high morbidity and death rates due to associated multiple medical conditions, social issues, and low quality of life (Demir & Bektas, 2017). Scientific evidence is the base of nutritional guidelines in order to improve general health and avoid chronic illnesses. These principles give a broad assessment for users into making informed food decisions and maintaining a healthy diet. The following section describes major hypotheses referring to the design and operation of the NutriTrack application. According to the Health Belief Model, people are more likely willing to participate in practices that promote health if they feel they are at risk of developing a serious health condition and that the advantages of taking action exceed the costs (Haller et al., 2008). According to The Theory of Planned Behaviors, the most important predictor of a behavior is the individual's intention of executing it. NutriTrack believes that knowing consumers' attitudes toward healthy eating, the social obstacles they face, and their own capacity to modify their nutritional patterns is essential (Bosnjak et al., 2020). By addressing these aspects, the app can help users create and achieve their nutritional objectives. The rates of obesity continue to rise, demanding new and effective intervention measures to tackle the epidemic. In our effort to create a health management application for weight loss, we researched existing literature reviews and insights from two important studies. Study 1: "Use of technology-based ınterventions in the treatment of patients with Overweight and Obesity: A Systematic Review" (Rumbo-Rodríguez et al., 2020) and Study 2: "Understanding User Preferences in Nutrition Apps: A Qualitative Study" (Vasiloglou et al., 2021).

In recent years, technology has been viewed as a possible helper in weight management, providing new methods for people to embark on their health journey (Hinchliffe et al., 2022). The first study looks at the empirical data supporting the use of technology in promoting weight reduction in obese people. Obesity prevalence has increased dramatically from 1975 till 2014, with rates increasing from 3.2% to 10.8% among adult men and from 6.4% to 14.9% among adult women which requires immediate effective solutions. Forty-seven studies from reliable resources, such as PubMed, ScienceDirect, Cochrane Library, and MedLine, were carefully reviewed. The focus was on different innovations in technology, such as cell phones, mobile applications, and the Internet.

The results demonstrated that around 47% of these therapies resulted in considerable decreases in weight for patients. Furthermore, the study revealed that technology-enhanced weight loss programs for overweight or obese individuals appear to be more effective than traditional approaches in enhancing therapy through self-monitoring mechanisms, resulting in better weight reduction outcomes. However, the study did identify a key drawback that shows the ongoing challenge of effectively reducing obesity in modern culture, such as a lack of user interaction and individualized feedback (Rumbo-Rodríguez et al., 2020). In recent years, digital technologies, particularly mobile apps, have developed quickly. About 3.7 billion apps were downloaded in 2017, with about 325,000 being mobile health (mHealth) apps that were fitness and health-related (Bosnjak et al., 2020). The second study targets the understanding of user preferences in nutrition apps. Mobile apps lower medical expenses, boost public health information transmission, and improve patient-provider communication (Demir & Bektas, 2017). A multidisciplinary team developed and assembled the survey. Eighteen end users were part of a pilot test before it was released. Eventually, a 19-question survey was established and translated into one of the six languages: Greek, Italian, German, French, Spanish, and English. A total of 3587 people saw the survey. A total of 2382 participants, of which 79.4% were female and 19.9% were male, were analyzed. Roughly 50% of the individuals have previously utilized a nutrition application (Vasiloglou et al., 2021). The following graphs in (Figure 3.) & (Figure 4.), illustrates the poll results while highlighting the reasons that may prevent people from using the App as well as the factors that encourage them to use a nutrition application.

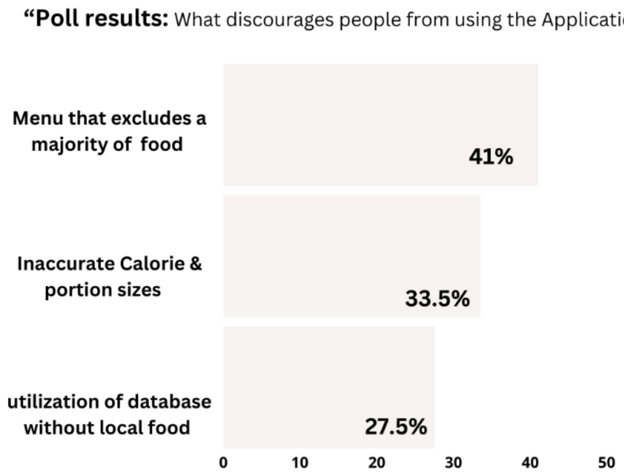

Figure 3. Poll Results of the factors preventing users from choosing an application

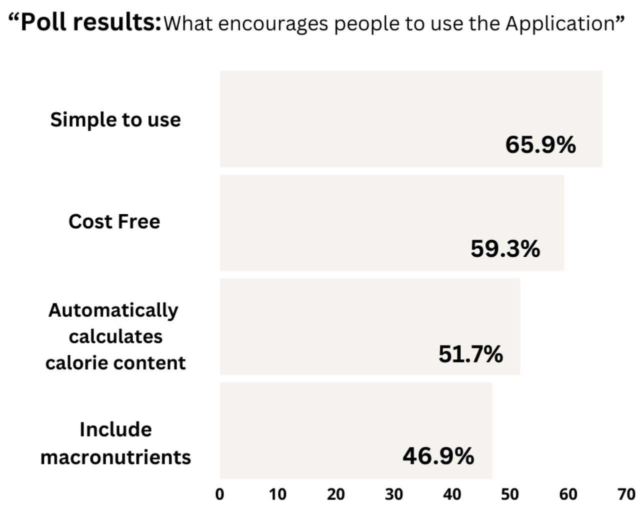

Figure 4. Poll Results of the factors encouraging users to choose the application

The study shows that users pick diet and nutrition applications that are simple to use, free, and accurately determine food's energy and nutrient content. Choosing a nutrition app can be challenging due to inadequate nutritional databases that exclude important foods, inaccurate calorie and nutrient estimates, and a lack of specific options and validation. Researchers from different kinds of fields need to comprehend the user's perspective to construct and develop applications that meet users' expectations and requests. By relying on insights from these studies, we were able to identify the critical points and step backs present in current platforms. NutriTrack was designed to address the barriers highlighted while enhancing each user's experience. Our App, allows users to receive tailored recommendations based on their preferences , follow a specialized dietary plan that includes the right amount of portion of food that their body should take , contact experts, browse multiple recipes mostly local ones, engage in quizzes and scroll through a vast section of physical activities without any financial barrier as it is cost free. In summary, we aim to fill the gaps noticed in existing studies by addressing these limitations in NutriTrack (Vasiloglou et al., 2021).

Methodology

Our research project seeks towards developing a nutritional program that encourages healthy food choices and helps users manage their well-being better. In order to achieve our objectives and for the development of "NutriTrack", we adopted a thorough strategy that included intensive study, questionnaires, and coordination with the Nutrition Department in gathering nutritional data and dietary guidelines. All of this data was incorporated into the app, providing users with accurate and dependable information.

To establish a solid foundation, quantitative methodologies were used to assess the prevalence of obesity and overweight, analyze user data and comments for tailored experiences and for rapid prototyping. A review of previous studies was undertaken to assess the prevalence of obesity and overweight. This review was eye-opening since it identified many danger factors that we felt the need to address when developing the App. Surveys and user analytics were used to collect information about users' interests and activities. This information was necessary to personalize the app's features and suggestions to the users' individual needs. A group of three people utilized the Jotform platform to prototype and create the App. This approach of development allowed the creation of a user-centered design process based on the fast adjustments possible in response to user feedback and analytical insights.

To supplement the quantitative data , qualitative methodologies were also employed to acquire deeper insights into user experiences and expert validation. We established a partnership with the nutrition branch in the Lebanese German University to advantage from their revel in and assets. The Biomedical technology crew performed several communication sessions with the head of the nutrition department RD Marielle Mansour, to gain beneficial facts on nutritional tendencies and practices. This partnership provided us with correct dietary facts, nutritional regimens, and recommendations that had been essential for the app's development. During App development, user feedback was requested to influence design and functionality. This engagement with people enabled the discovery of our weak points, which were then used to improve the overall user experience . NutriTrack's strong methodology, combining research, surveys, expert collaboration, and user feedback, ensures that it provides accurate, personalized and effective nutritional information to its users.

Design and Development

The design and development of the NutriTrack obesity management application occurred in two distinct phases. The initial phase focused on defining the application's scope through the collection of detailed food information, including meal composition and quantity. This relevant data was sourced from the Nutritional Department at the Lebanese German University, providing a robust dataset that includes nutritional information for essential food items such as vegetables, tubers, legumes, fruits, fish, and meats. These food components were categorized and structured to facilitate the creation of complete meals based on user-preferred recipes. During this phase, we prioritized user functionalities, enabling users to create personalized profiles and receive tailored meal plans with calorie and nutrient recommendations based on their individual data. Users can easily log the foods they consume and track their calorie intake. Additional features considered included meal planning, recipe management, and physical exercise capabilities, such as browsing and bookmarking healthy food ideas. Integrated fitness tracking, educational resources, and assistance were also designed to enhance the overall user experience.

The second phase involved selecting the appropriate platform and programming languages for the application. Typically, applications are designed for specific operating systems, such as iOS, Android, or Windows. In our case, we opted for a web-based application to maximize accessibility. This choice allows users to download data captured by the app and access it on various operating systems or through any internet-connected device, including those without smartphones. The app functions similarly to web pages, enabling users to access it via their mobile device's web browser. Since JotForm is a form-building platform we used 4 programming languages:

- HTML to arrange the layout and content of the app's many pages, including the personal information form, the sections displaying the computed **BMI (Body Mass Index = amount of body fat you have), BMR**

(Basal Metabolic Rate = number of calories required for basic functions at rest), BFP (Body Fat Percentage = measure of fitness level), and **TDEE (Total Daily Energy Expenditure)**, and the diet plan creation.

- Cascading customize Sheets (CSS) to customize the visual look of the app, such as the layout, colors, fonts, and other design aspects.
- JavaScript to construct the logic for calculating the **BMI, BMR, BFP,** and **TDEE**, as well as producing the diet plan depending on the user's preferences (for example, whether to include or exclude milk).
- JotForm API we linked the app with JotForm's functionality, such as handling form submissions, accessing form data, and perhaps automated diet plan production depending on user inputs.

To illustrate an example of this programming find below the flowchart in **(Figure 5.)**

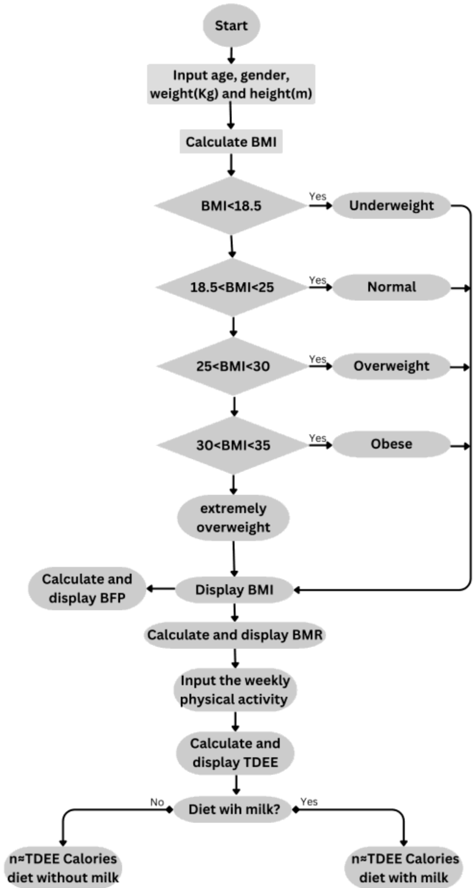

Figure 5. Flow diagram demonstrating the BMI, BMR, BFP and TDEE calculations to display a diet plan

For example, if we have a 30 year old male that weighs 85 kg and height 1.75 cm, the system will calculate the user's **BMI,** which is in the overweight range ($25 \leq$ BMI < 30). Based on this, the system classifies the person as overweight. The application then calculates and shows the user's **BFP** and **BMR.** Next, the user enters their weekly physical activity level, which the system utilizes to compute and show their **TDEE**. Later on, the user is asked if they wish to incorporate milk into their diet plan or not. If the user chooses not to include milk, the system generates a diet plan with the appropriate calorie intake based on the **TDEE.** If the user chooses to include milk, the system generates a diet plan with the appropriate calorie intake that accounts for the inclusion of milk.

The visual aesthetics of the app such as logo, templates of diet plans, recipe meals, snacks, detox juices … were designed using an online graphic design tool **[CANVA].** This ensured a professional and appealing look, enhancing user engagement and overall experience. Below, **(Figure 6.)** highlights key aspects of the app's design, including the logo, templates for diet plans, and the overall visual style. These elements work together to create a welcoming and motivating environment for users as they embark on their journey toward healthier eating habits.

Figure 6. Example highlighting key aspects of app's design

To further illustrate the personalized diet recommendation process, we will include several visual representations. **(Figure 7.)** & **(Figure 8.)** shows respectively how the app generates diet plans based on the user's TDEE and their preference regarding milk inclusivity and the diet displayed in the app, showing how it aligns with the calorie calculations detailed in **(Figure 5.).** The following will provide a clear example of how NutriTrack translates nutritional data into actionable meal plans for users.

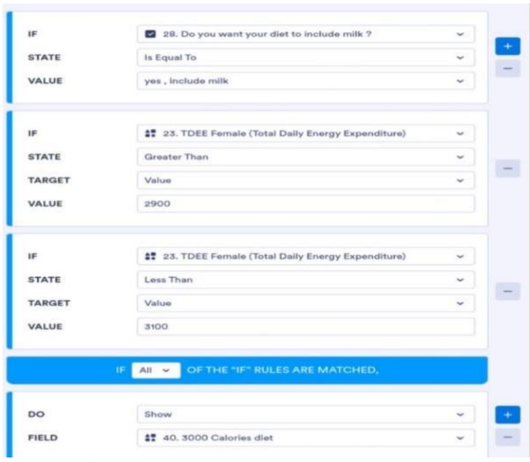

Figure 7. Personalized diet recommendation logic

Figure 8. Example of diet displayed in the app with caloric ınformation

Results

Developed over an 8-month period, NutriTrack offers users a comprehensive approach to support their weight loss journey. Users are able to report considerable changes in their diet quality and accomplish their desired weight reduction or maintenance while reporting higher levels of motivation, self-efficacy, and mental well-being as a result of continuously recording their progress and participating in a supportive health community.

The workout features set advances in physical strength, cardiovascular health, and flexibility. All interested users improve their exercise thanks to the training videos, progress monitoring, and social features that keeps them motivated and interested in their fitness routines also discovering new types of exercise they love while browsing the app's vast workout library. The app's simplicity and diversity of recipes help in keeping up to the tailored meal plans and nutritional guidelines.

NutriTrack automatically calculates essential health metrics such as **BMI, BMR, BFP, and TDEE**. These metrics are determined based on user inputs like height, weight, age, and activity level, enabling users to understand their current body type (underweight, normal, overweight, or obese) and make informed health choices. The following section outlines essential health metrics and their corresponding formulas, which serve as the foundation for assessing body composition and daily energy requirements.

Body Mass Index (BMI) is calculated using the metric formula:

$$BMI = \frac{weight\ (kg)}{height\ (m)^2}$$

BMI is used to estimate the **body fat percentage** using the formulas:

$$BFP(Male) = (1.20 \times BMI) + (0.23 \times Age) - 16.2$$

$$BFP(Female) = (1.20 \times BMI) + (0.23 \times Age) - 5.4$$

Basal Metabolic rate (BMR) is calculated using Mifflin Formula:

$$BMR\ (male) = 10 \times weight\ (in\ kg) + 6.25 \times height\ (in\ cm) - 5 \times age\ (in\ years) + 5$$

$$BMR\ (Female) = 10 \times weight\ (in\ kg) + 6.25 \times height\ (in\ cm) - 5 \times age\ (in\ years) - 161$$

Total daily energy expenditure (TDEE) is the daily calorie needs based on activity level and calculated using the formula:

$$TDEE(Male) = BMR(Male) \times Physical\ activity\ level$$

$$TDEE(Female) = BMR(Female) \times Physical\ activity\ level$$

The diet plan will be displayed according to the calculated TDEE. The app generates personalized diet plans that offer specific daily calorie targets, recommended food items, and portion sizes tailored to users' goals. Users can choose to include or exclude milk from their plans, accommodating personal preferences and dietary restrictions.

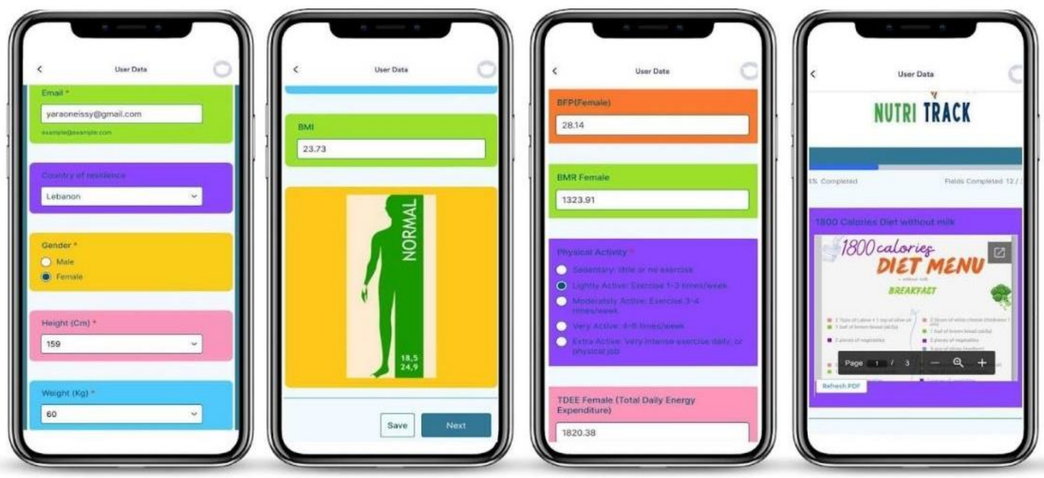

Figure 9. Screenshots on an iPhone device showing how app’s functionality and features

NutriTrack includes tools for logging food intake, helping users effectively monitor their dietary habits. Users can manually log all food and beverage intake, select meal type (breakfast, afternoon snack, etc.), estimate calorie content, and even take photos of their meals. After logging, food will be saved in a spreadsheet for easier tracking. This feature enhances logging accuracy and helps users remember portion sizes.

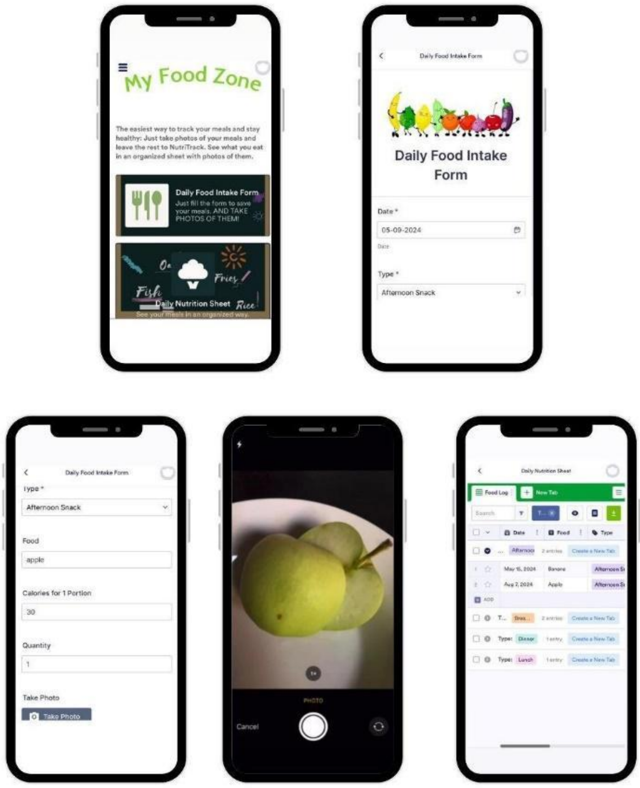

Figure 10. Screenshots taken on an iphone device showing the option of logging food ıntake

On the fitness side, users can log daily physical activities, including cardio and strength training exercises. For cardio, users can track duration, distance, intensity, and estimated calories burned. For strength training, they can record exercise names, sets, reps, weights used, and calories burned, providing a clear record of their fitness routines.

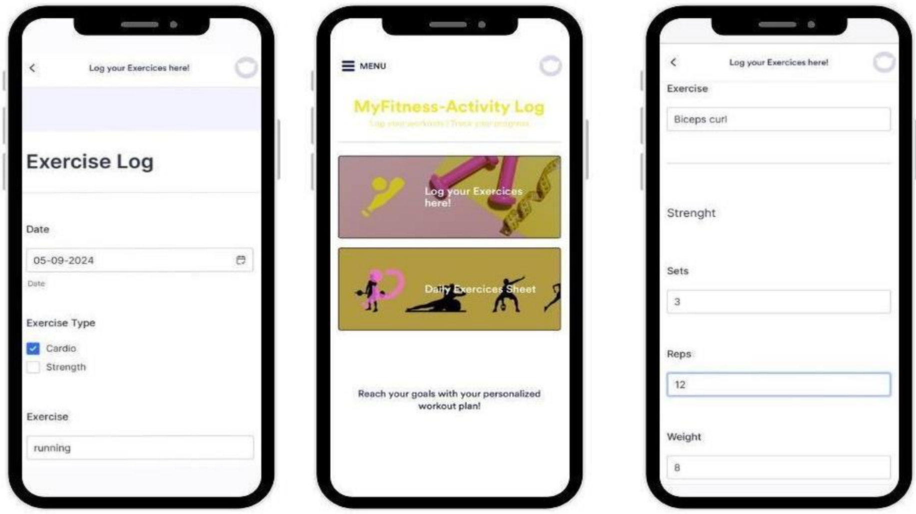

Figure 11. Screenshots taken on an iphone device showing the option for logging physical actvity exercises

The app features a curated collection of healthy meals, detox juices, and nutritious desserts. Each recipe includes detailed instructions and ingredient lists, ensuring users have the necessary information to replicate dishes at home. Recipes are developed by registered dietitians, guaranteeing a balance of macronutrients and essential micronutrients.

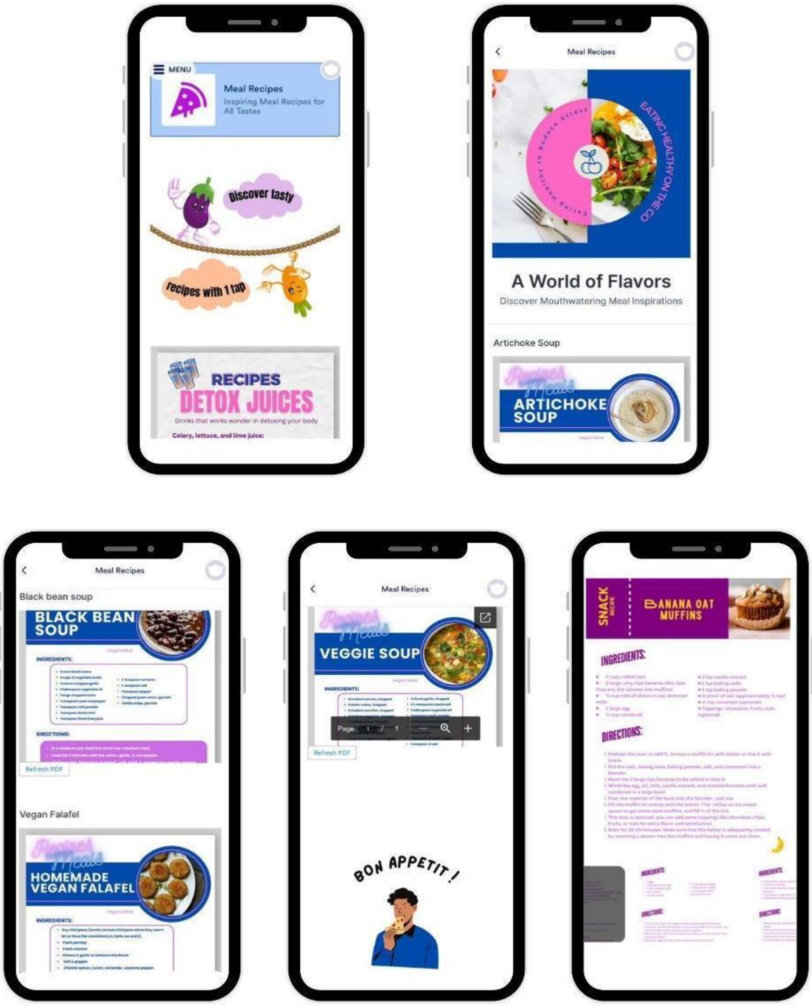

Figure 12. Screenshots taken on an iPhone device showing the vast recipe library of nutritrack

NutriTrack provides a variety of educational resources covering general nutrition recommendations. Users can explore topics such as macronutrients, portion control, and balanced diets. The Interactive quizzes feature helps in assessing users' nutrition knowledge, identifying areas where they may need more information.

Figure 13. Screenshots taken on an iPhone device showing the educational resources in the app

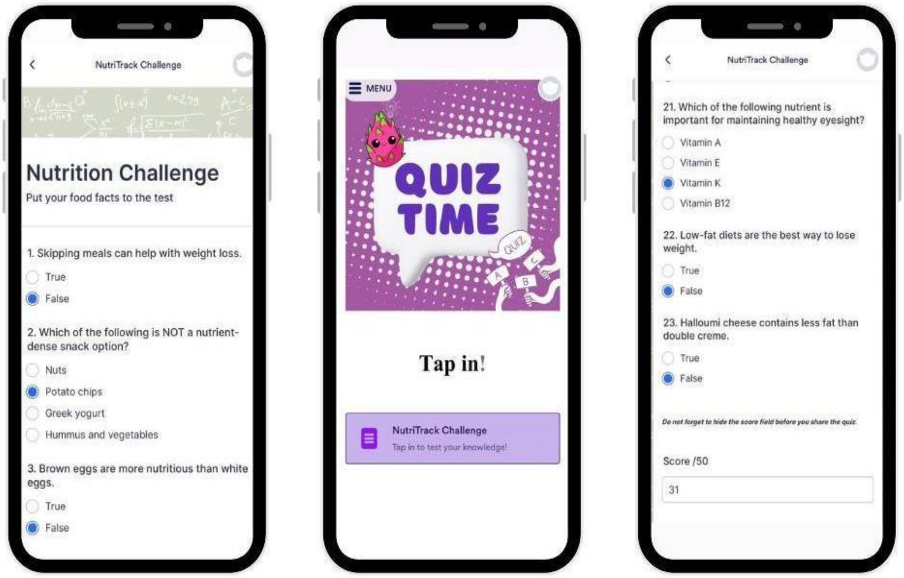

Figure 14. Screenshots taken on an iPhone device showing the quizz feature

The Expert Consultation feature allows users to communicate directly with qualified nutritionists for personalized guidance. Users can consult with registered dietitian Marielle Mansour to address specific dietary questions and concerns. Additionally, the option to schedule virtual consultations ensures users receive tailored advice and support.

The main advantages of this system are the following : Customized meal plans based on user preferences, dietary restrictions , Automatic calculation of key health metrics to assist users in their wellness journey , user-friendly design that makes it easy for users to navigate and simplifies meal/activity logging , access to a wide variety of healthy recipes that help users maintain variety in their diets , provides users with essential information on nutrition and portion control, direct connection to registered dietitian for personalized guidance and assistance and lastly as a web-based app, it can be accessed from any device or operating system, including iOS and Android, allowing users to monitor their health on-the-go.

However, this system has several limitations that will be addressed in future designs: The limitations we noticed such as the reliance on user’s input, diligence and honesty to accurately log food and health metrics. Many features require an internet connection, which restrict usability in offline situations. The majority of the recipes in the current recipe library and diet plans are from Lebanon which may not suit all users' varied dietary preferences. Some users may find the meal plans too inflexible or not fully aligned with their preferences. Like any app, there may be bugs or technical difficulties that could disrupt user experience.

Conclusion

In this paper, we have described the process of developing a nutrition application called NutriTrack that attempts to improve diet and physical exercise lifestyle patterns. The dietary app is a promising collaboration between our team and the Department of Nutrition. Using the department's knowledge of evidence-based dietary standards and meal planning, we created a complete app that offers users individualized diet plans, nutritious recipes, and tools for tracking their nutritional consumption. The software distinguishes itself from other calorie-counting applications on the market by allowing users to build unique meal plans and recipes based on their tastes, dietary limitations, and health objectives. Moving ahead, we believe it has the potential to dramatically change people's eating habits and make a significant difference in their lives. The team's application is a potential step forward in tackling Lebanon's alarming surge in adult obesity rates. The early user testing findings are encouraging, with 50% of trial participants reporting a smooth download and functioning of the software. By providing individualized nutrition and wellness features, the app encourages users to take an active role in managing their health and living better lifestyles. The high level of user involvement seen during the initial testing phase suggests that the app's features appeal to the target population which establishes a solid foundation for on-going growth**.** As the prevalence of obesity in Lebanon increases, it is critical to use technology solutions such as NutriTrack to offer individuals with the knowledge and assistance they need to make educated decisions about their nutrition and general well-being.

Moving forward, the team should prioritize increasing the app's user base, incorporating comprehensive data analytics to better understand user wants and preferences, and constantly upgrading content and features to ensure relevance and effectiveness. With a commitment to user-centric design and a focus on long-term habit change, the NutriTrack app has the potential to significantly improve the health and wellness of the Lebanese community.

Scientific Ethics Declaration

The authors declare that the scientific ethical and legal responsibility of this article published in EPSTEM Journal belongs to the authors.

Acknowledgements or Notes

* This article was presented as an oral presentation at the International Conference on Technology, Engineering and Science (www.icontes.net) held in Antalya/Turkey on November 14-17, 2024.

* We thank, RD Marielle Mansour, for providing us with the necessary datasets needed to create “NutriTrack”.

References

Bardus, M., Hamadeh, G., Hayek, B., & Kherfan, R. A. (2018). A self-directed mobile ıntervention (waznapp) to promote weight control among employees at a Lebanese University protocol for a feasibility pilot randomized controlled trial. *JMIR Research Protocols*, *7*(5), e133.

Bazán, M. J. A., Trujillo, M. I. J., Wärnberg, J., Fernández, S. D., De Andrés, A. L., & Farinós, N. P. (2018). Differences in the prevalence of diagnosis of overweight-obesity in Spanish children according to the diagnostic criteria set used. *Gaceta Sanitaria*, *32*(5), 477–480.

Bosnjak, M., Ajzen, I., & Schmidt, P. (2020). The theory of planned behavior. Selected recent advances and applications. *Europe’s Journal of Psychology*, *16*(3), 352–356.

Demir, D., & Bektas, M. (2017). The effect of childrens’ eating behaviors and parental feeding style on childhood obesity. *Eating Behaviors*, *26*, 137–142.

Eckel, R. H., & Krauss, R. M. (1998). American heart association call to action obesity as a major risk factor for coronary heart disease. *Circulation*, *97*(21), 2099–2100.

Ghelani, D. P., Moran, L. J., Johnson, C., Mousa, A., & Naderpoor, N. (2020). Mobile apps for weight management a review of the latest evidence to ınform practice. *Frontiers in Endocrinology*, *11*, 412.

Haller, D. M., Sanci, L. A., Sawyer, S. M., & Patton, G. (2008). Do young people’s ıllness beliefs affect healthcare? a systematic review. *Journal of Adolescent Health*, *42*(5), 436–449.

Hinchliffe, N., Capehorn, M. S., Bewick, M., & Feenie, J. (2022). The potential role of digital health in obesity care. *Advances in Therapy*, *39*(10), 4397–4412.

Mansour, M., Tamim, H., Nasreddine, L., Khoury, C. E., Hwalla, N., Chaaya, M., Farhat, A., & Sibai, A. M. (2019). Prevalence and associations of behavioural risk factors with blood lipids profile in Lebanese adults findings from WHO STEPwise NCD cross-sectional survey. *BMJ Open*, *9*(8), e026148.

Rumbo-Rodríguez, L., Sánchez-SanSegundo, M., Ruiz-Robledillo, N., Albaladejo-Blázquez, N., Ferrer-Cascales, R., & Zaragoza-Martí, A. (2020). Use of technology-based ınterventions in the treatment of patients with overweight and obesity a systematic review. *Nutrients*, *12*(12), 3634.

Johns Hopkin’s Medicine. (2024, June 20). *Tips to manage stress eating*. Retrieved from https//www.hopkinsmedicine.org

Vasiloglou, M. F., Christodoulidis, S., Reber, E., Stathopoulou, T., Lu, Y., Stanga, Z., & Mougiakakou, S. (2021). Perspectives and preferences of adult smartphone users regarding nutrition and diet apps web-based survey study. *JMIR Mhealth and Uhealth*, *9*(7), e27885.

Body fat percentage (2024, July 2). *In* Wikipedia. Retrieved from https//en.m.wikipedia.org/wiki/Body_fat_percentage

World Health Organization. (2024, March 1). One in eight people are now living with obesity. WHO. Retrieved from https//www.who.int/news/item/01-03-2024-one-in-eight-people-are now-living-with-obesity

World Health Organization. (2024a, March 1). *Obesity and overweight*. WHO. Retrieved from https//www.who.int/news-room/fact-sheets/detail/obesity-and-overweight

Author Information

Yara Oneissy
Lebanese German University
Biomedical Technologies Department, Main, Sahel Alma, Jounieh, Lebanon
Contact e-mail: *yara-n.anaissy@lgu.edu.lb*

Melissa Waked
Lebanese German University
Biomedical Technologies Department, Main, Sahel Alma, Jounieh, Lebanon

Ralph Al Hassrouty
Lebanese German University
Biomedical Technologies Department, Main, Sahel Alma, Jounieh, Lebanon

Marielle Mansour
Lebanese German University
Nutrition Department, Main, Sahel Alma, Jounieh, Lebanon

Lama Bou Farah
Lebanese German University
Biomedical Technologies Department, Main, Sahel Alma, Jounieh, Lebanon

To cite this article:

Oneissy, Y., Waked, M., Al Hassrouty, R., Mansour, M., & Bou Farah, L. (2024). Tailored support for weight loss: A personalized smartphone application for weight loss. *The Eurasia Proceedings of Science, Technology, Engineering & Mathematics (EPSTEM), 32,* 160-172.

The Eurasia Proceedings of Science, Technology, Engineering & Mathematics (EPSTEM), 2024

Volume 32, Pages 173-184

IConTES 2024: International Conference on Technology, Engineering and Science

Numerical Damage Prediction of Marine Structures Reinforced by Composite Patch with XFEM and CZM Methods

Harmel Mohammed Walid
Djilali Liabes University of Sidi-Bel-Abbes

Zouggar Kamel
Djilali Liabes University of Sidi-Bel-Abbes

Baghdadi Mohammed
Djilali Liabes University of Sidi-Bel-Abbes

Mhamdia Rachid
Djilali Liabes University of Sidi-Bel-Abbes

Abstract: The present work presents the numerical model of a marine steel with a hole repaired by a bonded composite patch. For modelling, Extended Finite Element Method (XFEM) technique is used in conjunction with the Cohesive Zone Model (CZM) to perform the damage analyses of different adhesives used in the repair of marine steels. The main objective of the study is to analyse the mechanical behaviour of the repair and compare different types of composite adhesives in order to optimize this kind of repair design. Numerical modelling is used in order to assess the stresses, strains, initiation, and propagation of damage in the repaired assembly. The mechanical performance test of the specimen proved that the mechanical performance of the repair is strongly dependent on the choice of the composite adhesive. Some adhesives possess better mechanical strength and a high resistance to damage compared to other kinds of adhesives. These results will provide important data in guiding the selection of materials for designing composite patch repairs on marine steel structures.

Keywords: Marine steel, Composite patch repair, Cohesive zone model, Adhesive damage.

Introduction

In general, the degradation of structures in extreme environments is a major problem in a number of fields, such as the maritime, the aeronautical and the civil engineering sectors (Karatzas, 2016). This can cause cracks and significant damage throughout the life of the structures. Due to its excellent mechanical properties, which provide good resistance to the harsh operating conditions, the majority of marine structures are made of steel. In spite of these advantages, steel remains particularly susceptible to the cumulative effects of corrosion and fatigue, which are exacerbated by prolonged exposure to the marine environment and which accelerate the propagation of cracks and increase the risk of structural failure (Feng et al., 2020; Abbas & Shafiee, 2020).

Many recent experimental studies have been instrumental in improving the reliability of this method to increase the strength and durability of damaged structures (Silva et al., 2023; Liu et al., 2022; Karatzas, Kotsidis, & Tsouvalis, 2015; Mishra, Lal, & Sutaria, 2023). Research by Madani et al. (2010) shows that patch repair can reduce the stress concentration around notches in a reinforced plate, with a lower total amount of strain. Furthermore, the use of CFRP patches was found to effectively limit crack propagation and extend the fatigue life of steel structures by Yu et al. (2014). However, according to Benyahia et al. (2015) the performance of the

- Selection and peer-review under responsibility of the Organizing Committee of the Conference

repair decreases with increasing soaking time. Li et al. (2019) found that the square shaped patch gave the best performance. Berrahou and Amari (2022) investigated different patch types and shapes for the repair of notched composite panels, identifying the boron/epoxy and solid configurations as the optimal options. (Riveros et al., 2022). Demonstrate that a basalt fiber patch (BFRP) significantly improves the service life of repaired structures.

Meanwhile, numerical simulations using FEM modelling software such as Abaqus and Ansys have been instrumental in the analysis and improvement of repair techniques (Kaddouri et al., 2020; Breitzman et al., 2009; Fekih et al., 2012; Iváñez & Braun, 2018; Zhang et al., 2018), investigated the stress distribution in the adhesive for different crack lengths. Their results effectively predicted failure in the adhesive. Moreover, the boron/epoxy circular patch was identified as the best solution for the repair of aluminium alloy marine structures by Sadek et al. (2018). In addition, Shivaie -Kojouri et al. (2023) carried out a comparative study between aged and non-aged composite patches, which highlighted the effect of ageing on the performance of the repair.

Advanced modelling techniques such as XFEM and CZM have been used to study repair damage with the development of numerical research (Talebi & Abedian, 2016; Talebi, Abedian, & Firooz, 2016; Bellali et al., 2021). In this context Bellali et al. (2020) have analysed crack propagation and adhesive debonding. They found that the damage varies depending on the interface strength and the effect of the notch in the repaired panel. Djebbar et al. (2021) have shown that the modelling techniques used correlate well with the experimental results, allowing the performance of the repair to be optimized.

The aim of this study is to evaluate the effectiveness of bonded composite patch repairs on notched marine steel structures subjected to tensile loading, by examining the mechanical behaviour of steel repaired with different types of structural adhesives. The tests are designed to ensure maximum reduction of stress concentrations around the notches and to extend the life of the repaired structure by determining how these adhesives affect the durability and strength of the repair under tensile loading.

Model Preview

Geometric Model and Mechanical Properties

The study is focused on a DH-36 marine-grade steel plate with a thickness of 2 mm, a length Hp=140 and a width Wp=40. The plate has a central circular hole with a radius of R=10 mm. This geometry was chosen to evaluate the performance of the repair technique using a composite patch. For the repair, a 1.5 mm thick composite patch was used. This part was bonded to the surface of the plate with a 0.2 mm thick layer of structural adhesive. The configuration and dimensions of the repaired area are detailed in Figure 1. Both the patch and the adhesive layer have the same dimensions.

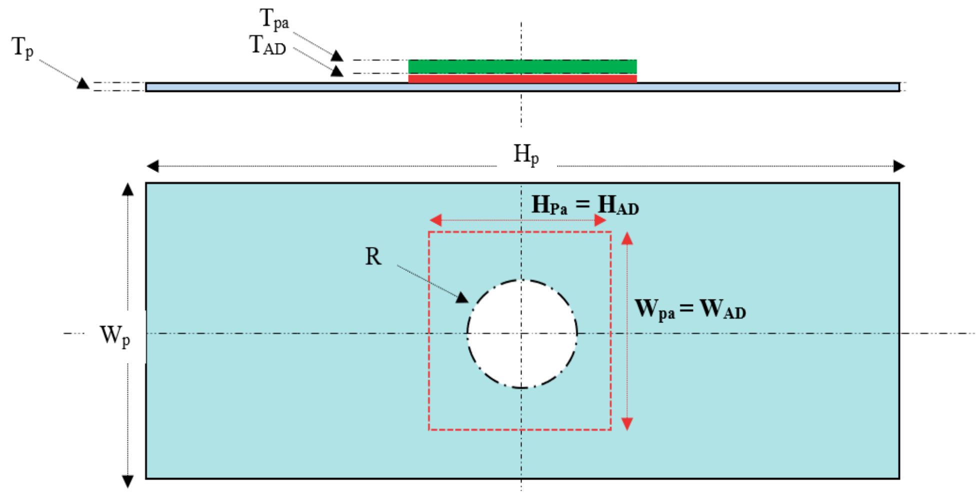

Figure 1. Geometric model presentation.

This study evaluates DH-36 steel, widely used in the marine industry for its excellent mechanical properties, particularly high strength and toughness. Its mechanical properties are detailed in Table 1. For the construction of marine structures exposed to harsh conditions such as high stress environments and dynamic loads, DH-36 steel is often preferred.

Table 1. Mechanical properties of Dh-36 steel (Gao & Zhang, 2010).

Dh-36 Steel	
Young's modulus E (MPa)	200000
Poisson's ratio, ν	0.3
Shear modulus G (MPa)	76000
Elongation at fracture	0.126
Yield strength	636
Tensile strength	352

Three types of adhesives were examined: Adekit A-140, Araldite AV-138, and Sikaforce 7752. These adhesives were selected for their distinct mechanical properties, enabling the assessment of their respective performance in reinforcement applications. The mechanical characteristics of each adhesive are summarized in Table 2.

Table 2. Mechanical properties of adhesives (Djebbar et al., 2022; Santos & Campilho, 2017).

Property	Adekit-A140	Araldite-AV138	Sikaforce-7752
Young's modulus E (GPa)	2.6	4.89	0.49
Poisson's ratio, ν	0.3	0.35	0.30
Shear modulus G (GPa)	1	1.56	0.19
Tensile strength, σ_f	35.9	39.45	11.48
Shear strength, τ_f	30.9	30.2	10.17
Thoughness in tension, G_{IC}	0.5	0.20	2.36
Thoughness in shear, G_{IIC}	2.41	0.38	5.41

A carbon fiber reinforced polymer (CFRP) composite patch is used as the reinforcing material. This patch consists of 8 layers of 0.1875mm thickness, the stacking sequence follows an alternating orientation: $[0°/90°]_4$ to ensure optimal distribution of longitudinal and transverse stress. Table 3 shows the mechanical properties of the CFRP patch. Figure2 shows the tensile curves of the various materials used in this study.

Table 3. Mechanical properties of CFRP patch (Djebbar et al., 2022).

Carbon/Epoxy patch	
E_1 (MPa)	216525
E2 (MPa)	9860.94
E3 (MPa)	9860.94
Nu_{12}	0.37
Nu_{13}	0.37
Nu_{23}	0.37
G_{12} (MPa)	5340
G_{13} (MPa)	5340
G_{23}(MPa)	4338

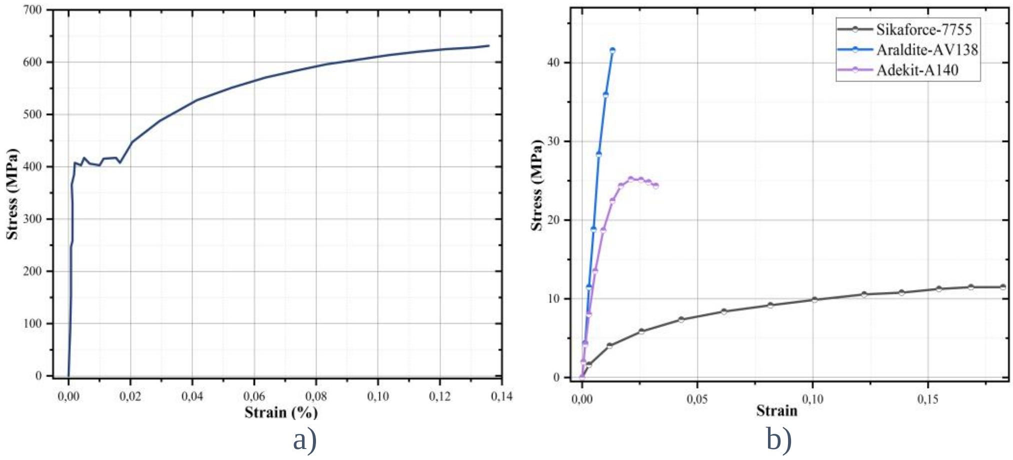

a) b)

Figure 2. a) Tensile test curve of Dh-36 steels, b) Stress strain curves of different adhesives used in this study (Gao & Zhang, 2010; Santos & Campilho, 2017).

Boundaray Conditions

In order to evaluate the performance of the repair process, the repaired DH-36 steel plate was subjected to a uniaxial tensile test (Figure 3). The test configuration is described below:

- *Zone A*: Fully constrained in all three displacement directions U_1, U_2 and U_3 (U_1=U_2=U_3=0 fixed along the x, y, and z axes), with free rotation around these axes (UR_1=UR_2=$UR_3 \neq 0$).
- *Zone B*: (opposite side): Partially constrained, with displacements blocked along U_2 and U_3 (U_2=U_3=0), but with free rotation around all three axes. Along the longitudinal axis $U_{1,}$ a displacement of 15 mm (U_1 =15mm) has been applied.

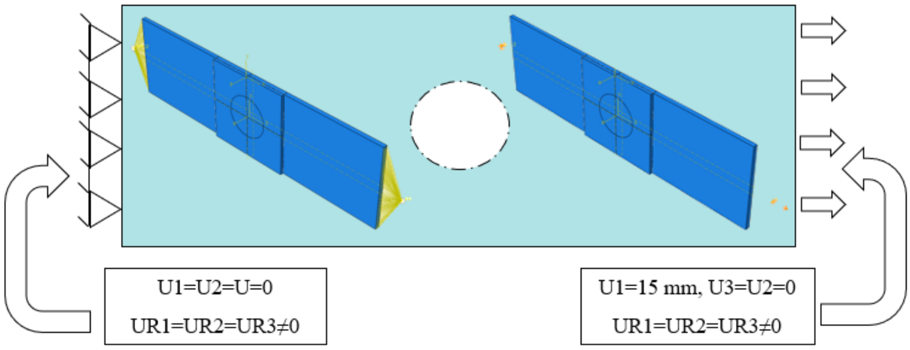

Figure 3. Boundary condition of present tensile test

Numerical Model

Finite element modelling was used to model and mesh the three components of this study (plate, adhesive and patch) in a three-dimensional model (**Hata! Başvuru kaynağı bulunamadı.**). where for the plate and patch, an element size of 1 mm was used, with C3D8R type elements. For the adhesive, COH3D8 cohesive elements of the same size were used. This was done to accurately capture the interactions between the plate, adhesive and the patch. The total number of elements used in the numerical model is shown in Table 3

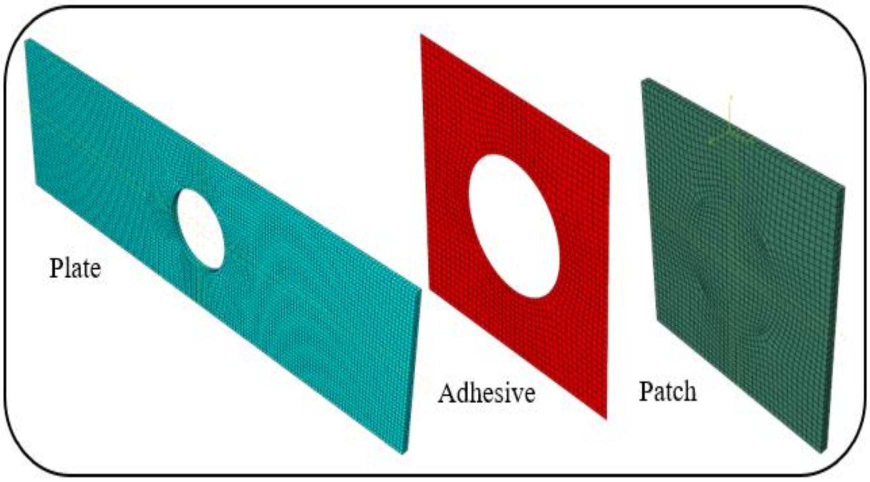

Figure 4. Numerical mesh presentation

Table 3. Numbers of mesh size elements.

Parts	Numbers of elements	Elements types
Plate	10696	C3D8R
Adhesive	1348	COH3D8
Patch	3488	C3D8R
Total number of elements	15532	

Method

In this present work, two numerical modelling approaches have been applied due to their importance in assessing damage in the plate, the adhesive and the patch. The extended finite element method (XFEM) is being applied to modelling the crack propagation in the plate, while the Cohesive Zone Method (CZM) provides the opportunity to simulate the cohesive behaviour of the adhesive used, and also simulate the deboning during the test. These two approaches together offer a thorough understanding of the damage mechanism.

Extended Finite Elements Modelling (XFEM)

This method makes the simulation more efficient as it is based on the concept of partitioning the finite element unit by using enrichment functions, which adds specific degrees of freedom to the nodes crossed by the crack or close to the crack tips, eliminating the need for re-meshing at each time unit and ensuring the fluidity of the crack propagation simulation. The XFEM method's mathematical formulation is given by the following equation:

$$U_{XFEM}(X) = \sum_{i\epsilon J} N_i(X)\, U_i + \sum_{i\epsilon J} N_i(X)\, H(X) a_i + \sum_{i\epsilon K} N_i(X)\, F(X) b_i \tag{1}$$

With, I represent the set of all mesh nodes, J and K are the nodes enriched by the Heaviside function $H(X)$ and the crack tip function $F(X)$.The nodal form functions $N_i(X)$ are employed to interpolate the standard displacements U_i and the enriched displacements a_i et b_i . The terms associated with $H(X)$ modelling the discontinuity in the elements traversed by the crack, while the terms linked to $F(X)$ capture the stress singularities near the crack tip.

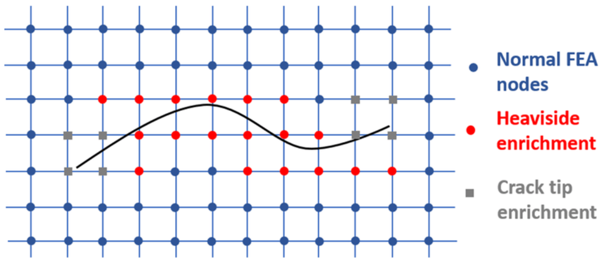

Figure 5. Enriched nodes in the XFEM (Gairola & Jayaganthan, 2021).

The discontinuity through the crack is modelled by the Heaviside function, given by the following equation (22*)*

$$H(X) = \begin{cases} 1 & if \quad x > 0 \\ -1 & if \quad x < 0 \end{cases} \tag{2}$$

This function makes it possible to model the discontinuity in the displacement field of the elements transverse to the crack without having to divide these elements. On the other hand, the improvement in accuracy at the crack point provided by the crack tip functions where stresses are highest. These functions, expressed in polar coordinates (r, θ), capture the singularities of the stress field near the crack tip and are defined by:

$$F_\alpha(r,\theta) = \left[\sqrt{r}\sin\left(\frac{\theta}{2}\right), \sqrt{r}\cos\left(\frac{\theta}{2}\right), \sqrt{r}\sin(\theta)\sin\left(\frac{\theta}{2}\right), \sqrt{r}\sin(\theta)\cos\left(\frac{\theta}{2}\right)\right] \tag{3}$$

Giving r as the distance to the crack and θ as the angle in polar coordinates. The initiation of crack propagation is controlled by the maximum principal stress criterion (MAXPS), which evaluates the maximum principal stress (MAXPS) in the enriched elements in ratio to the critical stress according to the relationship (4)

$$\left\{\frac{\sigma_{max}}{\sigma_{max_0}}\right\} = 1 \tag{4}$$

Once the stress exceeds the critical limit, crack initiation begins.

Cohesive Zone Modelling (CZM)

In present work, the numerical model is based on the evolution of damage between the adhesive surfaces of the plate and the patch by the linear traction-separation law, which gives the ability to track which deduce by the relationship (5)

$$\mathrm{T}(\delta) = K.\delta \qquad (5)$$

Where K is the stiffness matrix and δ represents the relative displacement of the contact surfaces, T is the nominal traction stress vector. In this way, we can also write

$$\mathrm{T} = \begin{Bmatrix} T_n \\ T_s \\ T_t \end{Bmatrix} = \begin{bmatrix} K_{nn} & K_{ns} & K_{nt} \\ K_{ns} & K_{ss} & K_{st} \\ K_{nt} & K_{st} & K_{tt} \end{bmatrix} . \begin{Bmatrix} \varepsilon_n \\ \varepsilon_s \\ \varepsilon_t \end{Bmatrix} \qquad (6)$$

The parameters K_{nn} and K_{ss} and K_{tt} are respectively the stress normal stiffness, the shear stiffness in the tangential direction 1, and the shear stiffness in the tangential direction 2 (Figure 6), and ε_n, ε_s and ε_t are the separations corresponding to the three directions.

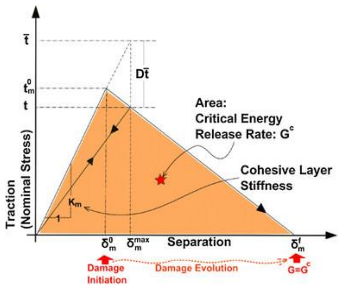

Figure 6. Linear traction-separation law for CZM (Haddad & Sepehrnoori, 2016).

The quadratic nominal stress criterion (QUADS) is chosen for damage initiation in our model, since this criterion assumes that damage begins when a quadratic interaction function involving the nominal strain ratios is represented by the following formula

$$\left(\frac{T_n}{T_n^0}\right)^2 + \left(\frac{T_s}{T_s^0}\right)^2 + \left(\frac{T_t}{T_t^0}\right)^2 = 1 \qquad (7)$$

T_n, Ts et T_t are the nominal stresses in normal (tension), shear 1 and shear 2 modes, and T_n^0 , T_s^0 et T_t^0 are the corresponding critical stresses. The damage evolution is modelled by the energy dissipation according to the Benzeggagh-Kenane criterion which takes into account the separation in the mixed modes (tension and shear) according to the following relationship (8)

$$G_{IC} + (G_{IiC} + G_{IC}).\left(\frac{G_s}{G_T}\right)^n = G_c \qquad (8)$$

where $G_s = G_{IiC} + G_{IC}$, $G_t = G_{IC} + G_s$ and η a characteristic material parameter, G_{IC} , G_{IIC} and G_{IIIC} represent the energy restitution rates for the modes I, II, et III

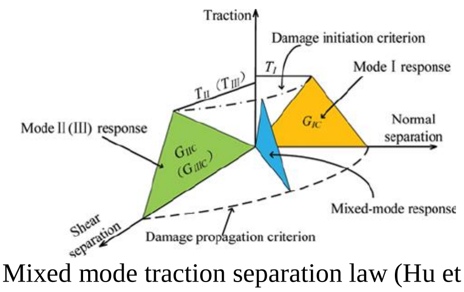

Figure 7. Mixed mode traction separation law (Hu et al., 2014).

Results and Discussion

Effect of Adhesively Bonded Patch

The results of the load-displacement curves for the repair using a patch are presented in Figure 8. The maximum recorded loads are 28 kN and 21 kN for the repaired and damaged plates, respectively. Consequently, there has been an improvement of 33% in strength compared to the notched plate. Moreover, a notable discrepancy in the post-peak load levels across the various tests is evident, wherein the repaired plate exhibits a gradual decrease, in contrast to the damaged one, which displays a precipitous reduction. This suggests that the repair enhances the ductility of the structure. The findings illustrate that the patch, bonded with structural adhesive in the damaged marine structure, plays a pivotal role in the load redistribution process.

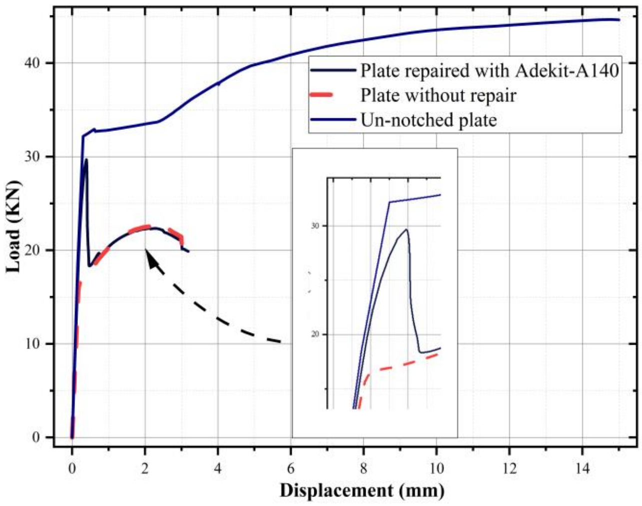

Figure 8. Load-displacement of repaired, notched and un-notched plate.

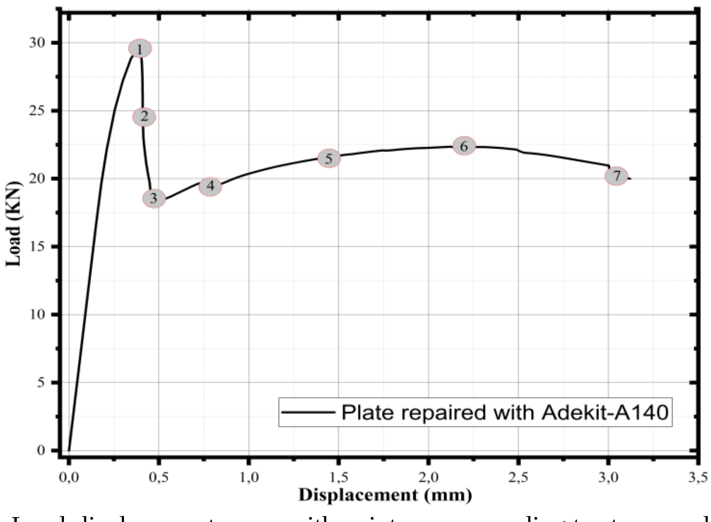

Figure 9. Load-displacement curve with points corresponding to stress analysis stages.

Stress Distribution Evaluation

It is essential to monitor the stress distribution in order to analyse the performance of the repair. Figure 9 shows the load-displacement curve, marked by numbered points corresponding to the detailed analysis frames of the von Mises σ_{mises} stresses in the plate and adhesive, as well as the S_{11} stresses in the loading direction presented in **Hata! Başvuru kaynağı bulunamadı.**. When the load reaches its maximum value of 28 kN, a significant stress concentration is recorded in the plate. The adhesive plays a key role in load transfer, with high stresses concentrated at its edges. The patch also shows high levels of stress, absorbing some of the load to lighten the plate and support the overall structure.

Table 4. Stress distribution in the plate, adhesive and patch.

Frame	Plate	Adhesive	Patch

(1)

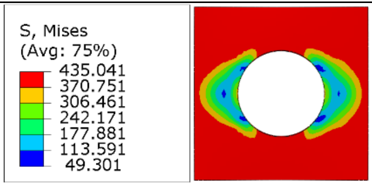

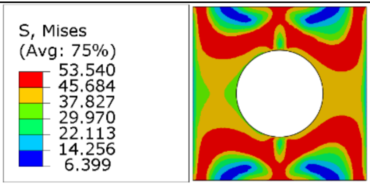

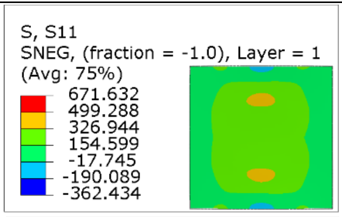

(2)

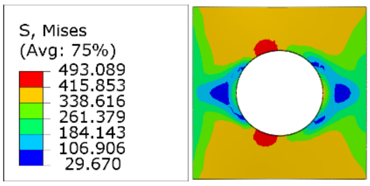

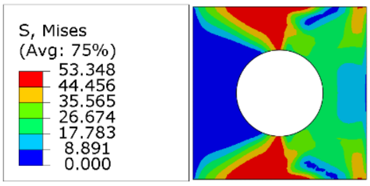

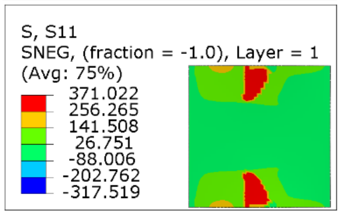

(3)

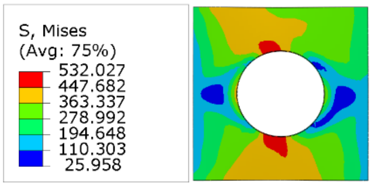

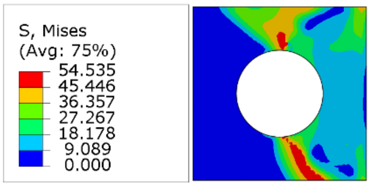

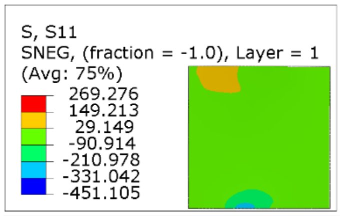

(4)

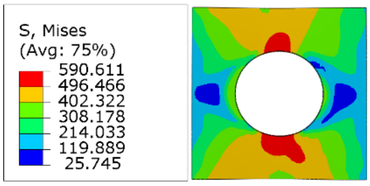

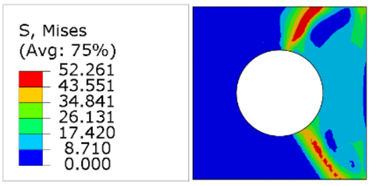

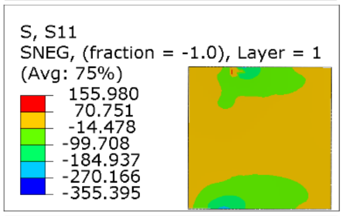

(5)

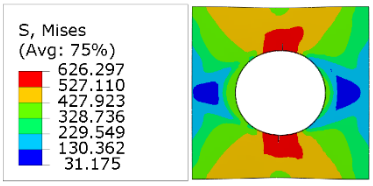

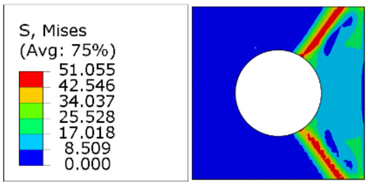

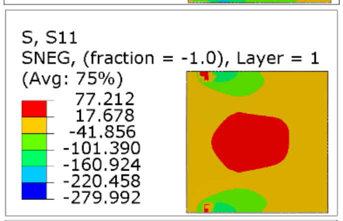

(6)

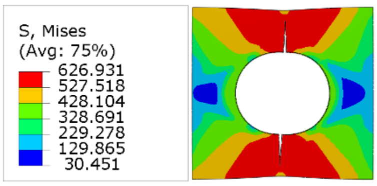

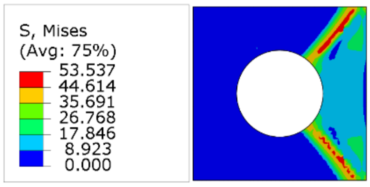

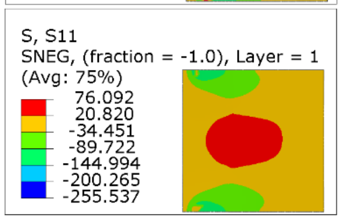

(7)

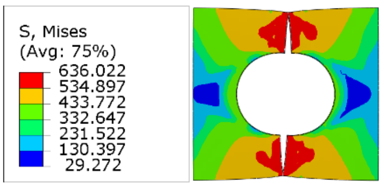

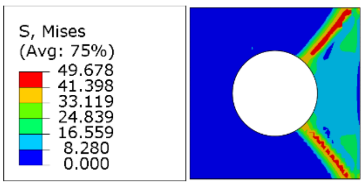

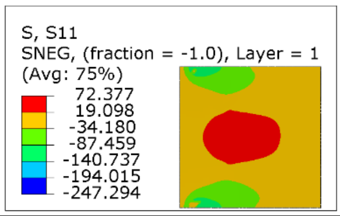

Subsequently, stresses increase rapidly in the plate, while the adhesive maintains a stable stress level around 52 MPa on average. However, signs of debonding begin to appear and progress quickly due to the high loads transferred from the plate. This debonding causes a gradual decrease in stress within the patch. As the process continues, a crack initiates in the plate and propagates rapidly as the adhesive debonding extends, leading to failure at a maximum stress level of 636 MPa in the plate. At the point of rupture, the patch reaches a stress level of 72 MPa, indicating a reduced contribution to structural support due to the diminished load absorption from the adhesive debonding.

Effect of Adhesives Natur

The effect of the strength of different adhesives was analysed by means of stress-strain curves, as illustrated in Figure 10. The results demonstrate that the Adekit-A140 repair exhibits the most favourable performance and strength with steel in terms of overall efficacy when compared to Araldite AV-138 and Sikaforce 7752. Moreover, the A140 initially exhibits rigid behaviour, followed by a decrease in charge before reaching a stable peak load of approximately 24 kN, ultimately leading to the failure of the plate. The data suggests that energy is transferred and that the material undergoes favourable ductile behaviour once the peak load is reached.

Moreover, the results for Araldite AV-138 also illustrate a noteworthy performance, with a maximum load of 25 kN. Nevertheless, a rapid decrease in charge is observed after the peak, indicating that the adhesive in question performs well in the initial loading phase but has more limited bond strength at the interface. In contrast, the Sikaforce 7752 adhesive manifests reduced strength in comparison to the other adhesives, reaching a maximum of 22 kN. Additionally, upon reaching the maximum load, the Sikaforce 7752 exhibits a more pronounced loss of load, suggesting a more brittle behaviour. Such observations could indicate that this adhesive has a reduced capacity to retain residual stresses after damage initiation at the patch-plate interface.

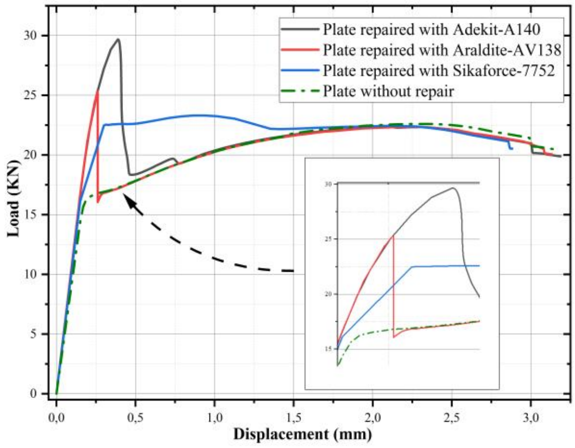

Figure 10. Load-displacement curve of different adhesives used.

Debonding Progression Views during Test

Table 5. Debonding progress views

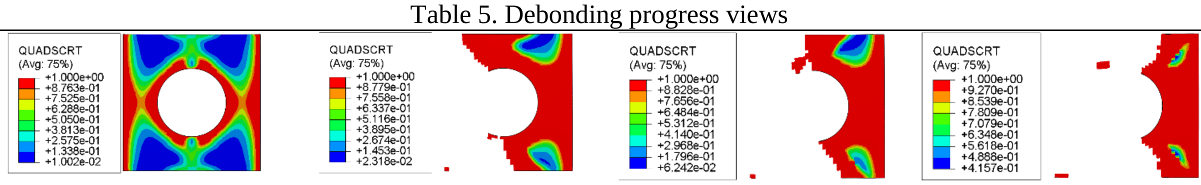

U_1= 0.25 mm	U_1= 0.50 mm	U_1= 0.76 mm	U_1= 3.18 mm

Plate repaired with Adekit-A140

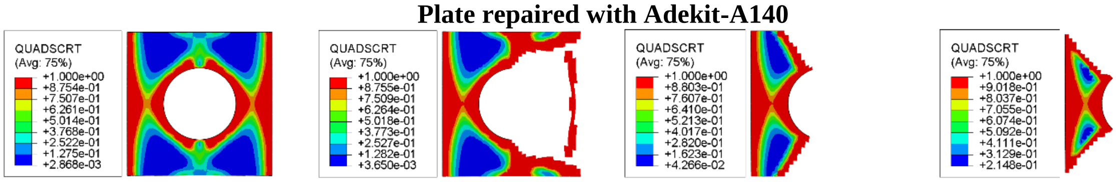

U_1= 0.25 mm	U_1= 0.26 mm	U_1= 0.50 mm	U_1= 3.13 mm

Plate repaired with Araldite-AV138

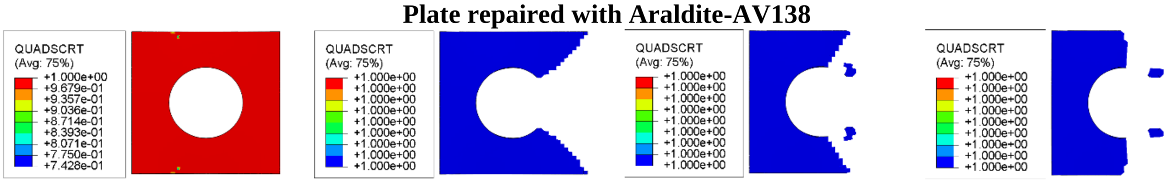

U_1 = 0.31 mm	U_1= 1.23 mm	U_1= 1.74 mm	U_1= 2.97 mm

Plate repaired with Sikaforce-7752

The monitoring of the delamination process in the repaired plate are presented in Table 5.. The analysis of delamination for the three adhesives (Adekit-A140, Araldite-AV138, and Sikaforce-7752) reveals a comparable damage progression, whereby delamination initiates and propagates at the edges of the patch as the longitudinal displacement U1 increases towards the notch.

For instance, for small displacements (U1 around =0.2 to 0.31mm), all adhesives demonstrate delamination zones that are limited to the opening. However, Sikaforce-7752 exhibits a slightly faster propagation rate. In contrast, at moderate displacements (U1 around 0.5 to 1.7 mm), all three adhesives display a notable progression in delamination. Moreover, at high displacements (U1=3mm), nearly the entire patch is delaminated, with extensive damage observed for all three adhesives. Although Sikaforce-7752 appears to delaminate more uniformly, the damage is nevertheless significant. Furthermore, the delamination progression observed in Adekit-A140 and Araldite-AV138 is relatively gradual, whereas Sikaforce-7752 demonstrates a more rapid initiation and propagation of damage.

Conclusion

This study presents a numerical analysis, using advanced finite element modelling techniques including the Extended Finite Element Method (XFEM) and Cohesive Zone Model (CZM) approaches, of the repair performance of damaged marine steel structures using bonded composite patch repair techniques.

- The results show that the type of adhesive plays a critical role in the repair performance of steel structures, directly influencing the evolution of the mechanical behaviour according to the specific properties of each adhesive.
- Adekit A-140 proved to be much more durable and stronger than those tested and provided better load retention.
- The debonding in each of the adhesives revealed the specific deboning phenomena of each type of adhesive, highlighting the importance of selecting a suitable adhesive to optimize the durability and effectiveness of the repair.

Scientific Ethics Declaration

The authors declare that the scientific ethical and legal responsibility of this article published in EPSTEM Journal belongs to the authors.

Acknowledgements or Notes

* This article was presented as a poster presentation at the International Conference on Technology, Engineering and Science (www.icontes.net) held in Antalya/Turkey on November 14-17, 2024.

References

Abbas, M., & Shafiee, M. (2020). An overview of maintenance management strategies for corroded steel structures in extreme marine environments. *Marine Structures, 71*, 102718.

Bellali, M. A., Mokhtari, M., Benzaama, H., Fekirini, H., Serier, B., & Madani, K. (2020). Using CZM and XFEM to predict the damage to aluminum notched plates reinforced with a composite patch. *Journal of Mechanics of Materials and Structures, 15*(2), 185-201.

Bellali, M. A., Serier, B., Mokhtari, M., Campilho, R. D. S. G., Lebon, F., & Fekirini, H. (2021). XFEM and CZM modeling to predict the repair damage by composite patch of aircraft structures. Debonding parameters. *Composite Structures, 266*, 113805.

Benyahia, F., Aminallah, L., Albedah, A., Bachir Bouiadjra, B., & Achour, T. (2015). Experimental and numerical analysis of bonded composite patch repair in aluminum alloy 7075 T6. *Materials & Design, 73*, 67-73.

Berrahou, M., & Amari, K. (2022). Experimental and numerical study on the efficiency of the repair of composite structures cracked and V-notched by different types and shapes of composite material patch. *Strojnícky Časopis - Journal of Mechanical Engineering, 72*(1), 1-14.

Breitzman, T. D., Iarve, E. V., Cook, B. M., Schoeppner, G. A., & Lipton, R. P. (2009). Optimization of a composite scarf repair patch under tensile loading. *Composites Part A: Applied Science and Manufacturing, 40*(12), 1921-1930.

Colak, Z., Ayan, Y., & Kahraman, N. (2020). Weld morphology and mechanical performance of marine structural steel welded underwater in a real marine environment. *The International Journal of Advanced Manufacturing Technology, 109*(1), 491-501.

Djebbar, S. C., Madani, K., El Ajrami, M., Houari, A., Kaddouri, N., Mokhtari, M., Feaugas, X., & Campilho, R. D. S. G. (2022). Substrate geometry effect on the strength of repaired plates: Combined XFEM and CZM approach. *International Journal of Adhesion and Adhesives*, *119*, 103252.

Fekih, S. M., Albedah, A., Benyahia, F., Belhouari, M., Bachir Bouiadjra, B., & Miloudi, A. (2012). Optimisation of the sizes of bonded composite repair in aircraft structures. *Materials & Design, 41*, 171-176.

Feng, L., He, J., Hu, L., Shi, H., Yu, C., Wang, S., & Yang, S. (2020). A parametric study on effects of pitting corrosion on steel plate's ultimate strength. *Applied Ocean Research, 95*, 102026.

Gairola, S., & Jayaganthan, R. (2021). XFEM simulation of tensile and fracture behavior of ultrafine-grained Al 6061 alloy. *Metals*, *11*(11), 1761.

Gao, X., & Zhang, G. (2010). A study on the effect of the stress state on ductile fracture. *International Journal of Damage Mechanics, 19(1)*, 75-94.

Grabovac, I., & Whittaker, D. (2009). Application of bonded composites in the repair of ships structures – A 15-year service experience. *Composites Part A: Applied Science and Manufacturing, 40*(9), 1381-1398.

Haddad, M., & Sepehrnoori, K. (2016). XFEM-based CZM for the simulation of 3D multiple-cluster hydraulic fracturing in quasi-brittle shale formations. *Rock Mechanics and Rock Engineering, 49*(12), 4731-4748.

Hu, P., Shi, Z. W., Wang, X. X., Li, W. D., Zhou, S. G., & Han, X. (2014). Strength degradation of adhesively bonded single-lap joints in a cyclic-temperature environment using a cohesive zone model. *Journal of Adhesion, 91*(8), 587-603.

Iváñez, I., & Braun, M. (2018). Numerical analysis of surface cracks repaired with single and double patches of composites. *Journal of Composite Materials, 52*(8), 1113-1120.

Kaddouri, N., Madani, K., Rezgani, L., Mokhtari, M., & Feaugas, X. (2020). Analysis of the effect of modifying the thickness of a damaged and repaired plate by composite patch on the j-integral; effect of bonding defects. *Journal of the Brazilian Society of Mechanical Sciences and Engineering, 42*(8), 426.

Karatzas, V. A. (2016). *Assessment and design of composite patch repairing in marine applications*. file:///C:/Users/pc/Downloads/PhD_Vasileios_Karatzas.pdf.

Karatzas, V. A., Kotsidis, E. A., & Tsouvalis, N. G. (2015). Experimental fatigue study of composite patch repaired steel plates with cracks. *Applied Composite Materials, 22*(5), 507-523.

Li, C., Zhao, Q., Yuan, J., Hou, Y., & Tie, Y. (2019). Simulation and experiment on the effect of patch shape on adhesive repair of composite structures. *Journal of Composite Materials, 53*(28-30), 4125-4135.

Liu, Z., Li, Z., Huang, C., & Jiang, X. (2022). An investigation on the fatigue performance of cracked steel plates reinforced with FRP and stop hole. *Mechanics of Advanced Materials and Structures, 29*(25), 3646-3657.

Madani, K., Touzain, S., Feaugas, X., Cohendouz, S., & Ratwani, M. (2010). Experimental and numerical study of repair techniques for panels with geometrical discontinuities. *Computational Materials Science, 48*(1), 83-93.

Marioli-Riga, Z., & Gdoutos, E. E. (2004). Composite patch repair methodology for damaged aircrafts structural components. In *2004 SEM Annual Conference*, 7-10.

Mishra, K., Lal, A., & Sutaria, B. M. (2023). Experimental investigation of repair of plate with edge and center crack by surface bounded composite patch. *International Journal of Steel Structures, 23*(2), 534-547.

Mohammadi, S., Yousefi, M., & Khazaei, M. (2021). A review on composite patch repairs and the most important parameters affecting its efficiency and durability. *Journal of Reinforced Plastics and Composites, 40*(1-2), 3-15.

Riveros, G., Hassan, E. M., Hudak, L., & Mahmoud, H. (2022). Basalt fibers for underwater fatigue repair of steel panels. *Journal of Structural Engineering, 148*(11), 04022184.

Sadek, K., Aour, B., Bachir Bouiadjra, B. A., Bouanani, M. F., & Khelil, F. (2018). Analysis of crack propagation by bonded composite for different patch shapes repairs in marine structures. A numerical analysis. *International Journal of Engineering Research in Africa, 35*, 175-184.

Santos, M. A. S., & Campilho, R. D. S. G. (2017). Mixed-mode fracture analysis of composite bonded joints considering adhesives of different ductility. *International Journal of Fracture, 207*(1), 55-71.

Shivaie- Kojouri, A., Safarabadi, M., & Parvas, D. (2023). A numerical comparison between aged and non-aged composite patches on repaired aluminum 7075-T6 plate. *Materials Chemistry and Mechanics, 1*(1),74-87.

Silva, D. L., Echer, L., Rojo Tanzi, B. N., Marczak, R. J., & Iturrioz, I. (2023). Experimental investigation of the structural performance of fiber-reinforced patches in the repair of locally damaged steel pipes. *Journal of the Brazilian Society of Mechanical Sciences and Engineering, 45*(8), 435.

Soutis, C., & Hu, F. Z. (1997). Design and performance of bonded patch repairs of composite structures. *Proceedings of the Institution of Mechanical Engineers, Part G: Journal of Aerospace Engineering, 211*(4), 263-271.

Talebi, B., & Abedian, A. (2016). Numerical modeling of adhesively bonded composite patch repair of cracked aluminum panels with concept of CZM and XFEM. *Proceedings of the Institution of Mechanical Engineers, Part G: Journal of Aerospace Engineering*, *230*(8), 1448-1466.

Talebi, B., Abedian, A., & Firooz, S. (2016). Optimization of composite patch repair for inclined crack on aluminum plate using genetic algorithm. *Archive, 231*(20).

Yu, Q. Q., Zhao, X. L., Al-Mahaidi, R., Xiao, Z. G., Chen, T., & Gu, X. L. (2014). Tests on cracked steel plates with different damage levels strengthened by CFRP laminates. *International Journal of Structural Stability and Dynamics*, *14*(06), 1450018.

Zhang, Y., Zhang, K., Zhao, H., Xin, J., & Duan, M. (2018). Stress analysis of adhesive in a cracked steel plate repaired with CFRP. *Journal of Constructional Steel Research*, *145*, 210-217.

Author Information

Harmel Mohammed Walid
Djilali Liabes University of Sidi-Bel-Abbes
BP 89, Sidi Bel Abbes 22000, Algeria
Contact e-mail: harmelwalid03*@gmail.com*

Zouggar Kamel
Djilali Liabes University of Sidi-Bel-Abbes
BP 89, Sidi Bel Abbes 22000, Algeria

Baghdadi Mohammed
Djilali Liabes University of Sidi-Bel-Abbes
BP 89, Sidi Bel Abbes 22000, Algeria

Mhamdia Rachid
Djilali Liabes University of Sidi-Bel-Abbes
BP 89, Sidi Bel Abbes 22000, Algeria

To cite this article:

Walid, H.,M., Kamel, Z., Mohammed, B. & Rachid, M. (2024). Numerical damage prediction of marine structures reinforced by composite patch with XFEM and CZM methods. *The Eurasia Proceedings of Science, Technology, Engineering & Mathematics (EPSTEM), 32,* 173-184.

The Eurasia Proceedings of Science, Technology, Engineering & Mathematics (EPSTEM)
ISSN: 2602-3199

The Eurasia Proceedings of Science, Technology, Engineering & Mathematics (EPSTEM), 2024

Volume 32, Pages 185-193

IConTES 2024: International Conference on Technology, Engineering and Science

Multidimensional Analysis of Potential Cost-to-Cost Risks of Climate Disruption for Energy-Focused Facilities Using Remote Sensing, Drone Photogrammetry, and GIS Methods

Muntaha Kassim Alzubade
University of Technology

Oyku Alkan
Graduated Istanbul Technical University

Abstract: One of the changing world climate disorders generally caused by human beings in the long term is abnormal precipitation or droughts. Abnormal rainfalls or droughts experienced in almost every season in Turkey and in the world continue to take a high share of this situation in power plants operating in the energy sector. One of the regions in Turkey affected by the sudden decrease and sudden suppression of rainfall in recent years is the Eastern Anatolia Region. This study was carried out to investigate possible environmental risk factors in a series of HEPP areas built side by side within the borders of Erzincan and Erzurum Provinces. In these power plants, uncontrolled floods caused by excessive rainfall, potential damage to structures such as transmission channels, pools and weirs, or malfunctions in main sections such as main buildings and regulators will be directly affected. Although these structures are built to withstand natural disasters such as earthquakes and excessive rainfall, it may not be foreseeable that climate disturbances will not pose a greater risk. This study was carried out using Geographic Information Systems (GIS)-based Multi-Criteria Decision Analysis (MCDA) by taking into account environmental risk factors such as precipitation risks and landslides that have affected in recent years by evaluating them together with land use. A digital terrain model and orthophoto images were created using drone photogrammetry over the approximately 15 km length and 50 meters wide area where the two power plants are located. An attempt was made to create a risk model with the parameters of land use, elevation, slope, aspect, precipitation, temperature and distance to the streams.

Keywords: Drone photogrammetry, Risk assessment, HEPP, Environmental threats, Remote sensing

Introduction

The increasing global demand for sustainable and renewable energy sources has highlighted the significance of evaluating potential environmental risks associated with energy-focused facilities. Among the renewable energy options, hydroelectric power plants (HEPPs) are pivotal for their contribution to reducing dependency on fossil fuels and supporting cleaner energy production. However, the environmental impacts and the risks posed by climate fluctuations remain critical challenges for energy infrastructure, especially in regions prone to erratic weather patterns. Turkey, a country with diverse topographical and climatic conditions, has experienced notable changes in precipitation and drought patterns in recent years. These alterations have had pronounced effects on energy facilities, particularly in areas such as the Eastern Anatolia Region. Facilities in these areas face challenges from unexpected extreme weather events, which can result in uncontrolled flooding and structural damage. The potential for severe rainfall and climate-induced disturbances to disrupt the operation of HEPPs necessitates comprehensive risk assessment methodologies.

Considering the critical need for efficiency of renewable energy and environmental protection through assessment of environmental sustainability, identification and reduction of potential risks, hydroelectric and solar power plants in Turkey are of utmost importance. Rising concerns about environmental pollution and energy security have increased interest in developing renewable and environmentally friendly energy sources such as wind, solar, hydroelectric, geothermal, hydrogen and biomass to replace fossil fuels (Ahmed, 2024). It is also important that the location selection of all power plants is evaluated with multidisciplinary engineering formation in areas where climatic effects will be minimized.

As decisions increase in complexity and importance, so does the need to formalise them using available information, and to document the rationale. Multi-criteria decision analysis (MCDA) is a decision-making approach that aims to structure complex decisions and evaluate multiple conflicting criteria (Greene et al., 2011). This approach allows decision makers to consider and balance multiple factors such as topography, LULC type, and ecological and social importance values when evaluating different land use options (Mohamadzadeh et al., 2020). It helps to determine environmentally sustainable land use strategies by ensuring that various factors such as elevation, stream structure, slope, geology, and meteorological data are taken into account in the decision-making process, also considering risk factors (Suab et al., 2024).

Geographic Information Systems (GIS) and remote sensing have become indispensable tools in spatial analysis and decision-making processes. GIS provides a robust platform for capturing, storing, analyzing, and visualizing spatial data, while remote sensing enhances data acquisition by enabling the collection of information from satellites, drones, and other aerial systems. These technologies play a critical role in various sectors, including urban planning, environmental management, disaster response, and agriculture.

In recent years, the integration of drones or Unmanned Aerial Vehicles (UAVs) in mapping has revolutionized the field by offering high-resolution, up-to-date imagery at relatively low cost and with significant flexibility. UAVs equipped with advanced sensors allow for detailed, accurate, and efficient data collection over specific areas, bridging gaps between traditional satellite imagery and ground surveys. This capability has expanded the scope of spatial data analysis, making it accessible for more targeted and dynamic projects.

Multi-Criteria Decision Analysis (MCDA) methods complement GIS and remote sensing by providing a systematic framework for evaluating multiple, often conflicting criteria. MCDA aids decision-makers by integrating qualitative and quantitative data to prioritize alternatives or make informed choices in complex scenarios. When combined with GIS, MCDA can be used to solve spatial decision problems, such as site selection, resource allocation, and risk assessment. This integrated approach ensures a comprehensive assessment that accounts for a wide array of spatial and non-spatial variables. By leveraging the combined power of GIS, UAV mapping, and MCDA methods, professionals can gain deeper insights into spatial phenomena and make data-driven decisions with higher precision and reliability.

The integration of Geographic Information Systems (GIS) with Multi-Criteria Decision Analysis (MCDA) represents a significant advancement in spatial decision-making processes. This combined approach leverages the spatial analysis capabilities of GIS and the structured decision-making processes of MCDA, facilitating complex evaluations across multiple criteria. The application of GIS-MCDA has been observed across various fields, such as environmental management, urban planning, and resource allocation (Feizizadeh et al., 2015). Highlight its role in conducting sensitivity and uncertainty analyses for economic vulnerability assessments, emphasizing the robustness that GIS-MCDA can provide in decision-making processes (Feizizadeh & Kamran, 2015).

A comprehensive review by Lokhande et al. (2017) outlines the methodological versatility of GIS integrated with MCDA in landfill site selection, showcasing how different MCDA techniques—such as Analytic Hierarchy Process (AHP) and Weighted Linear Combination (WLC)—can be employed to enhance spatial decisionmaking (Lokhande, 2017). Similarly Abdullah (2014) demonstrates the adaptability of GIS-MCDA for spatial distribution Modeling of settlements, providing insights into the compatibility between environmental elements and criteria (Abdullah, 2014).

The ecological applications of GIS-MCDA are exemplified by Kazemi and Akinci (2018) who used this combination for land use suitability analysis for rainfed farming, showcasing the ability of GIS-MCDA to assess spatial data holistically (Kazemi & Akinci, 2018). In a similar vein, Ozkan et al. (2020) ıntegrated hesitant fuzzy linguistic term sets with GIS-MCDA to evaluate landfill sites, which further confirms the method's applicability in addressing uncertain decision environments (Ozkan et al., 2020).

Cetinkaya et al. (2016) presented a GIS-based fuzzy MCDA approach for refugee camp site selection in southeastern Turkey, highlighting its strategic importance in humanitarian logistics The methodological framework involving fuzzy logic was expanded by Ustaoglu et al. (2021) who employed the TOPSIS method integrated into a GIS environment to optimize agricultural land suitability in peri-urban areas (Ustaoglu et al., 2021). Additionally, the work of Fernandes et al. (2021) on prioritizing water quality interventions demonstrated the effectiveness of GIS-MCDA in environmental monitoring, illustrating how contamination risk and intervention complexity can be analyzed using this hybrid approach (Fernandes et al., 2021).

This integration also extends to public safety and urban planning, as evidenced by Alemdar et al. (2020). Who explored pedestrian crossing evaluations using AHP and VIKOR in a GIS context (Alemdar et al., 2020). Finally, Kavurmaci (2016) applied the GIS-MCDA model for groundwater quality assessment in Aksaray, Turkey, showcasing the adaptability of such systems for hydrological studies (Kavurmaci, 2016).

This study was conducted to assess the environmental sustainability and efficiency of two adjacent Hydroelectric Power Plants (HEPP) between Erzincan and Erzurum Provinces, located in the north-eastern part of Turkey. This study aimed to perform MCDA using remote sensing, drone mapping and Geographic Information Systems for sustainable HEPP and Solar Energy Power Plant (SEPP) management in the Eastern Black Sea region of Turkey. Studies focuses on the environmental risk factors influencing two hydroelectric power plants in Erzincan Province, Turkey. Utilizing Geographic Information Systems (GIS)-based Multi-Criteria Decision Analysis (MCDA), combined with drone photogrammetry and remote sensing techniques (Alkan et al.,2023), the study aims to develop a risk model that accounts for critical factors such as land use, elevation, slope, precipitation, and distance to streams. This multidisciplinary approach offers a framework for assessing and mitigating environmental risks, ensuring sustainable operation and resilience of energy facilities.

Method

Study Area, Methodology and Data Collection

In the first phase of this study, the risks posed by a series of Hydroelectric Power Plants in Erzurum and Erzincan provinces, especially against unpredictable excessive rainfall, were investigated. The selected area spanned approximately 15 km in length and 50 meters in width around the two HEPP sites (Figure 1).

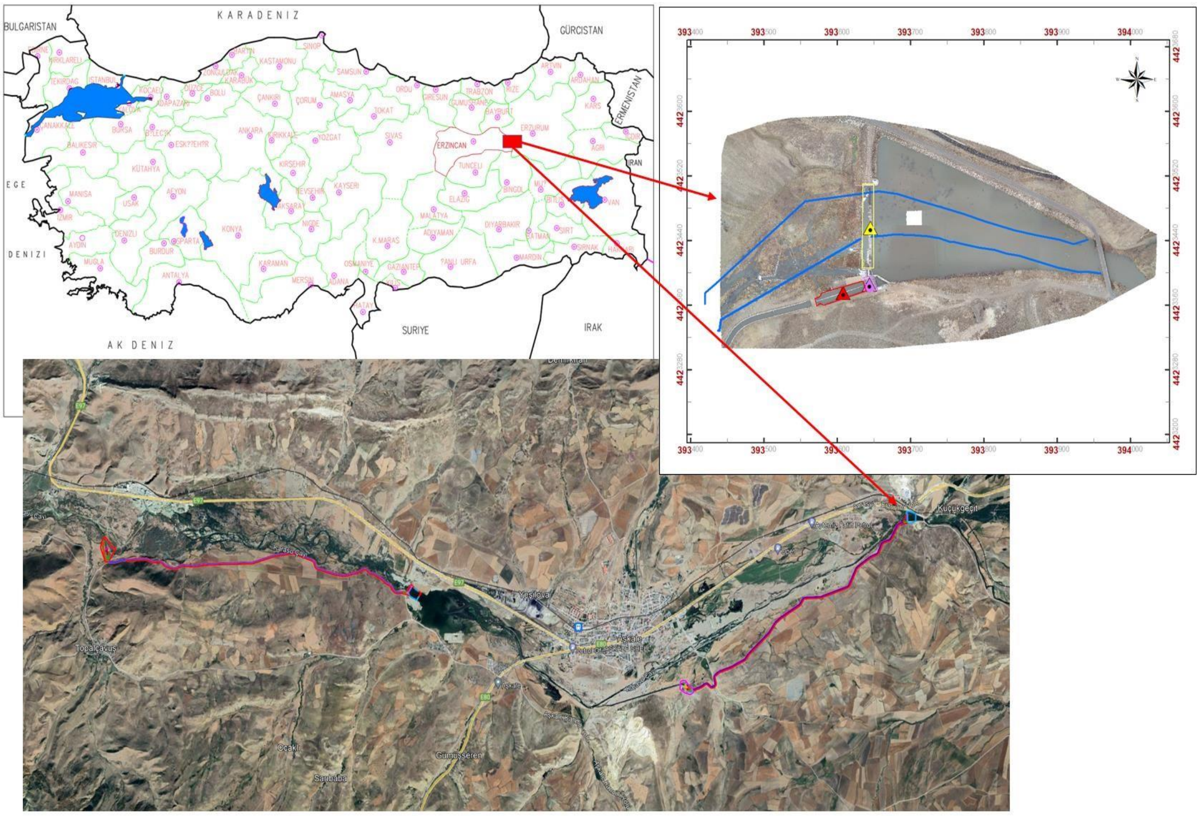

Figure 1. Location of the study area

The GIS-based multi-criteria decision analysis (MCDA) method approaches a correct decision analysis for each criterion. An analytic hierarchy process (AHP) is a well-known technique in the MCDA method due to its flexibility, simplicity, implementation in a GIS environment, and the ability of users to derive the weight of criteria on maps(Malczewski, 2007; Rauf et al., 2023). AHP is based on a pairwise comparison approach that compares criteria with each other according to their importance (Ishizakaand Nemery, 2013). To conduct a comprehensive environmental risk assessment of the two HEPPs in Erzincan Province, a combination of GIS-based MCDA, drone photogrammetry and remote sensing (Alzubade&Alkan,2022) was employed. The work steps were tried to be put into practice with the flow chart summarizing the work (Figure 2).

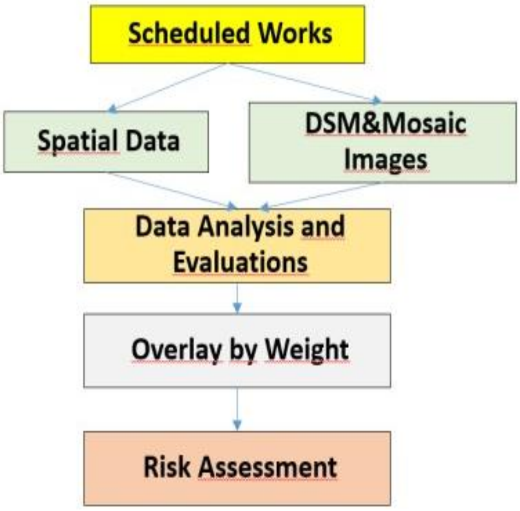

Figure 2. Flow chart of the work

With GPS module drone flights, firstly the images of the approximately 15 km long line including the power plant building-transmission channel-regulator area of the two power plants were obtained. By processing these images, mosaic images of the region were obtained and Digital Surface Model (DSM) and Digital Elevation Model (DEM) were created. Data collection involved capturing high-resolution orthophoto images using drone photogrammetry and integrating these images into a (DSM) and (DEM) (Figure 3).

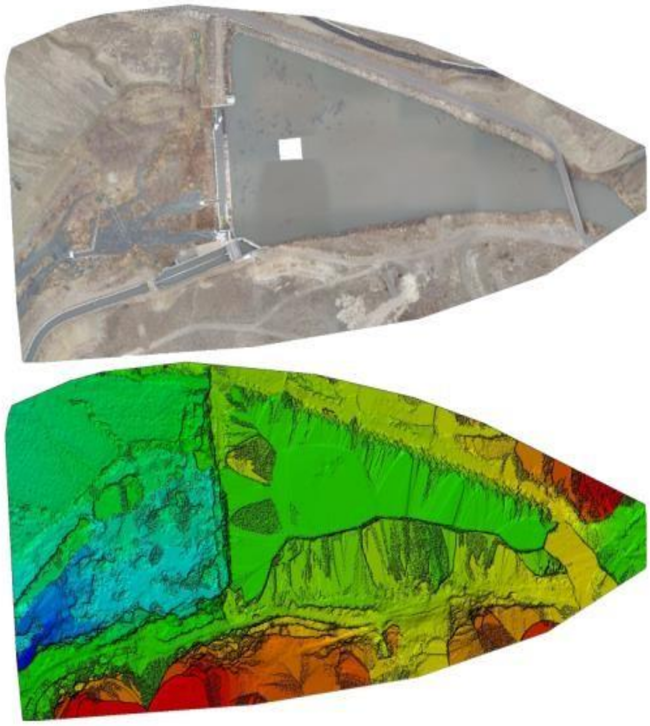
Figure 3. Digital Surface Model (DSM) and Digital Elevation Model (DEM) of the study area

MCDA Framework

MCDA was applied to include various environmental data into the risk model. Parameters affecting risk factors include land use and land cover (LULC) , elevation, slope, aspect, curvature, and distance to water bodies. The decision-making process was structured to evaluate the relative importance of each factor and its contribution to possible risks. GIS analyses were performed by Arcmap software and raster result data were obtained. The risk criteria that are predicted to affects the region were determined as a result of feasibility reports prepared before the construction phase of HEPPs, updated reports, and literature research and studies GIS-based weighted overlay analysis was applied. The weights and scores of the determined criteria were obtained with the help of these environment-specific reports and expert opinions (Table 1). Slope, aspect, distance to water bodies, land use capacity, land use status were accepted as natural criteria.

Table 1. Scores and weights for used criteria

Criteria	Subcriteria	Average Score	Average Weight
Slope	0%-5%	4	20%
	5%-10%	5	
	10%-25%	3	
	25%-40%	1	
	40%-100%	0	
Aspect	S	5	20%
	SE-SW	4	
	E-W	3	
	NE-NW	2	
	N	1	
Land Use	Agriculturel Zone1	1	20%
	Agriculturel Zone2	2	
	Limited Agr.Zone	3	
	Forest	0	
	Grassland	5	
Curvature	I	1	20%
	II	2	
	III	3	
	IV	4	
	V	5	
Hdrology (Distance to Waterbody)	0-20	5	20%
	20-50	4	
	50-70	3	
	70-100	2	
	100+	1	

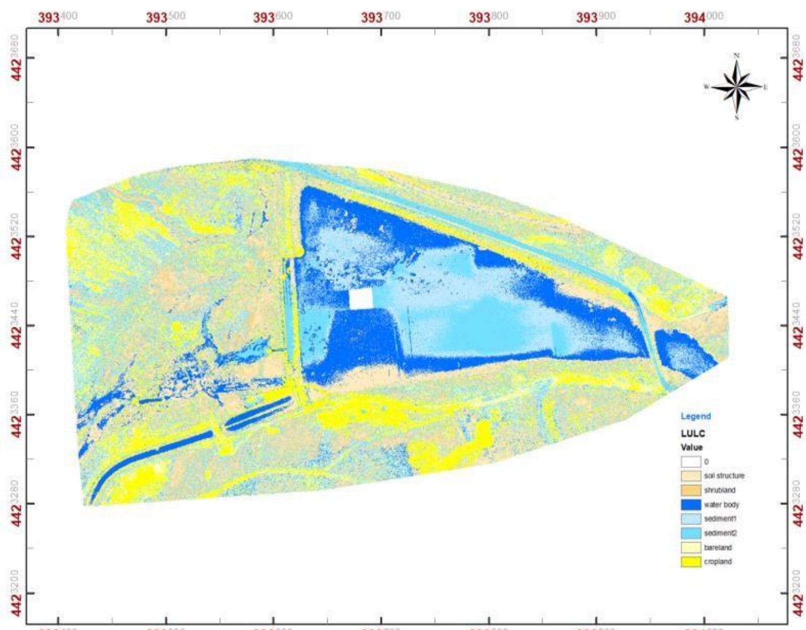

Figure 4. Land Use Land Cover (LULC) image

In the study area, the topography is dominated by the north, north-west and south-west, west orientation. The Karasu River, which HEPP's benefit from, extends in the east-west direction, but forms deep pits when directed south. In the south-west side, where the orientation is risky, the risk of flooding in an unexpectedly excessive rainfall is a negative factor. For Land Use Land Cover (LUCL) Analysis, supervised classification was performed for 7 classes by obtaining high-precision drone images as mosaics using remote sensing techniques (Alkan et al.,2022) with visible and infrared bands. Accuracy analysis was performed by sampling the land structure and usage around the area where the HEPP transmission channel, sedimentation basin and regulator are located. The classified result image in this study, where user accuracy is 87%, is shown in Figure 4. The other data to be used in the overlay analysis stages is the Digital Elevation Model created by processing drone images of the region (Figure 5)

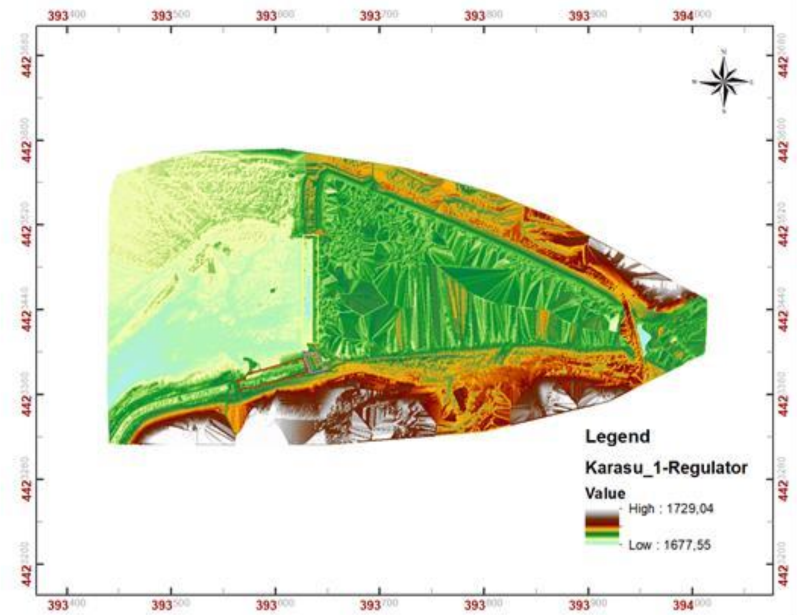

Figure5. DEM ımage of the study area

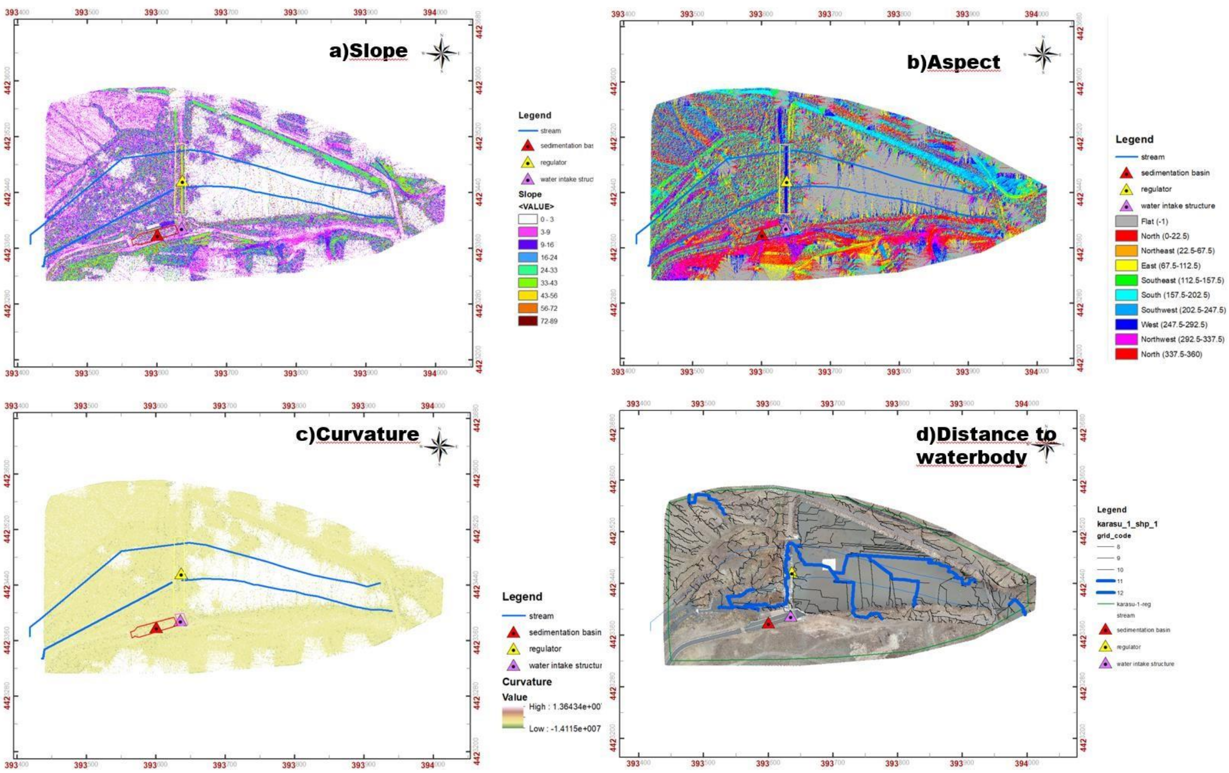

Figure 6. Criteria reclassified images of the study area

Aspect analysis was produced from the DEM image with all direction data and was also reclassified and included in the scoring. The regulator structure carrying risky. The slope in most of the study area is slightly above 3%. It has a slope range of 3% to 9%. The sections in the north and south directions have meadow areas with a slope of 24% and more. The main stream line passes parallel to the transmission channel, and the side branches are quite dense as a result of the analysis.The results of the analysis of Slope, Aspect, Curvature and proximity to the stream, which were studied in stages using the DEM, are shown in Figure 6.

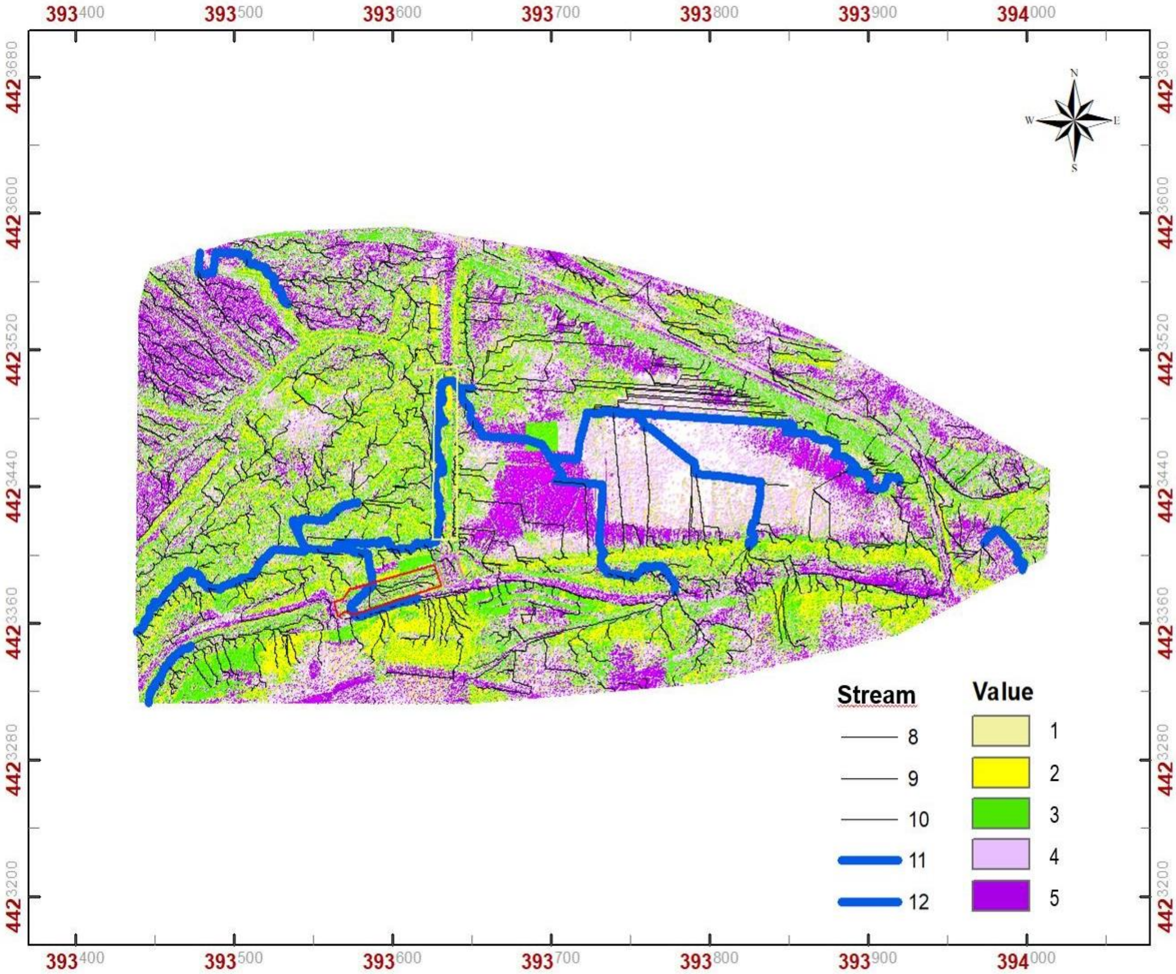

Figure 7. The resulted ımage produced by weighted overlay analysis

Conclusion

In this test study conducted for the Karasu 1 HEPP regulator area, which is the first stage of the application; the weighted overlap model determined according to the criteria explained in the methodology section shows that the risk of being affected by unexpected extraordinary rainfall in the Karasu 1 HEPP regulator area is focused on the southern part of the study area. Areas where the risk is relatively low but should be considered are scored with 4 and 5 points, average suitability areas are scored with 3 points, and areas with the least risk are scored as 1 and 2 (Figure 7).

According to the evaluated data and the climatic anomalies experienced in Turkey and the world in recent years, it can be predicted that the region is in very harsh climatic conditions and when it rains, the snow load at an ellipsoidal height exceeding 1700 meters should be added to the risk factor. In decision-making processes, it is possible to periodically monitor the region with very high-precision images made specifically for drones and to apply risk analyses to the entirety of the power stations. The multi-criteria decision-making method used in this study aims to draw attention to possible precipitation anomalies. The determined dynamics were evaluated with the data studied specifically for the regulator. Sub-criteria such as settlement, economy, geology were not added to the decision-making process, and the area was not expanded so that the main structures in the regulator were evaluated primarily specifically for the water intake structure. In the next stages of this study, it would be appropriate to include geological data and settlement areas in the decision-making process. In addition, meteorological data should be obtained on a monthly basis and this complex world climate process should be monitored.

Recommendations

When the study is evaluated in terms of its rich data, integrity of its methods and environmental quality It is anticipated that this planned work will be permanent in the long term. A different decision-making process can also be created by taking into account the interaction of these HEPPs in series equipped with power plant buildings, transmission structures and regulators.

Scientific Ethics Declaration

The authors declare that the scientific ethical and legal responsibility of this article published in EPSTEM Journal belongs to the authors.

Acknowledgements or Notes

* This article was presented as an oral presentation at the International Conference on Technology, Engineering and Science (www.icontes.net) held in Antalya/Turkey on November 14-17, 2024.

References

Abdullah, N. S. (2014). Suitability model based on GIS and MCDA for spatial distribution of settlements in different geographic environments. *1st Mediterranean InterDisiplinary Forum on Social Sciences and Humanities, 2*, 229.

Alemdar, K. D., Kaya, O., & Codur, M. Y. (2020). A GIS and microsimulation-based MCDA approach for evaluation of pedestrian crossings. *Accident Analysis & Prevention*, *148*, 105771.

Alkan, O., Al-Zubade, M.K., & Alkan, M.N. (2023) Assessing the effects of alluvial transport in the Kizilirmak river on dams with local, photogrammetric and remote sensing methods. *The Eurasia Proceedings of Science, Technology, Engineering and Mathematics, 26*, 217-224

Alkan, O., Al-Zubade, M.K., Alkan,M.N.(2022). Detection of the mineral presence and ıts effects on different tree species using drone photogrammetry and remote sensing methods, *The Eurasia Proceedings of Science, Technology, Engineering and Mathematics, 21*, 266-273

Al-Zubade, M. K. H. & Alkan, O. (2022). The role of drone photogrammetry, remote sensing and GIS methods in the detection of ore areas and their surroundings. *The Eurasia Proceedings of Science Technology Engineering and Mathematics, 21*, 380-387.

Cetinkaya, C., Ozceylan, E., Erbas, M., & Kabak, M. (2016). GIS-based fuzzy MCDA approach for siting refugee camp: A case study for Southeastern Turkey. *International Journal of Disaster Risk Reduction*, *18,* 218-231.

Feizizadeh, B., Kienberger, S., & Kamran, K. V. (2015). Sensitivity and uncertainty analysis approach for GIS-MCDA based economic vulnerability assessment. *Journal of Geographical Information Science*, *1,* 81-89..

Fernandes, A. C. P., Terêncio, D. P. S., Pacheco, F. A. L., & Fernandes, L. S. (2021). A combined GIS-MCDA approach to prioritize stream water quality interventions, based on the contamination risk and intervention complexity. *Science of the Total Environment*, *798*, 149322.

Kavurmaci, M. (2016). Evaluation of groundwater quality using a GIS-MCDA-based model: a case study in Aksaray, Turkey. *Environmental Earth Sciences*, *75*, 1-17.

Kazemi, H., & Akinci, H. (2018). A land use suitability model for rainfed farming by multi-criteria decision-making analysis (MCDA) and geographic information System (GIS). *Ecological Engineering*, *116*, 1-6.

Lokhande, T. I., Mane, S. J., & Mali, S. T. (2017). Landfill site selection using GIS and MCDA methods: a review. *International Journal of Engineering, Science and Technology*, *3*, 25-30.

Mirghaed, F. A., Mohammadzadeh, M., Salmanmahiny, A., and Mirkarimi, S. H. (2020). Decision scenarios using ecosystem services for land allocation optimization across Gharehsoo watershed in northern Iran. *Ecological Indicators*, *117*, 106645.

Ozkan, B., Sarıcicek, I., & Ozceylan, E. (2020). Evaluation of landfill sites using GIS-based MCDA with hesitant fuzzy linguistic term sets. *Environmental Science and Pollution Research*, *27*(34), 42908-42932.

Greene, R., Devillers, R., Luther, J. E., & Eddy, B. G. (2011). GIS-based multiple-criteria decision analysis. *Geography Compass*, *5*(6), 412-432.

Suab, S. A., Supe, H., Louw, A. S., Korom, A., Rakib, M. R. M., Wong, Y. B., ... & Avtar, R. (2024). Assessing Borneo's tropical forests and plantations: A multi-sensor remote sensing and geospatial MCDA approach to environmental sustainability. *Frontiers in Forests and Global Change*, *7*, 1337535.

Ustaoglu, E., Sisman, S., & Aydınoglu, A. C. (2021). Determining agricultural suitable and in peri-urban geography using GIS and Multi Criteria Decision Analysis (MCDA) techniques. *Ecological Modelling*, *455*, 109610.

Author Information

Muntaha Kassim Alzubade
University of Technology,
Baghdad, Iraq
Contact e-mail: *muntaha.k.alzubade@uotechnology.edu.iq*

Oyku Alkan
Graduated Istanbul Technical University
Istanbul, Turkiye

To cite this article:

Alzubade, M.K. & Alkan, O. (2024). Multidimensional analysis of potential cost-to-cost risks of climate disruption for energy-focused facilities using remote sensing, drone photogrammetry, and GIS methods *The Eurasia Proceedings of Science, Technology, Engineering & Mathematics (EPSTEM), 26,* 185-193.

The Eurasia Proceedings of Science, Technology, Engineering & Mathematics (EPSTEM)
ISSN: 2602-3199

The Eurasia Proceedings of Science, Technology, Engineering & Mathematics (EPSTEM), 2024

Volume 32, Pages 194-207

IConTES 2024: International Conference on Technology, Engineering and Science

SWOT Analysis of Quantum Computing in Accounting

Hamide Ozyurek
OSTIM Technical University

Abstract: This article aims to examine the potential and impact of quantum computing in the field of accounting, evaluating how this new technology can contribute to the sector. Specifically, it is important to investigate the balance between the advantages that can be gained in accounting processes and the challenges that may arise. To achieve this goal, a SWOT analysis method has been employed to systematically examine the strengths, weaknesses, opportunities, and threats of quantum computing in accounting. The existing literature and industry data form the foundation of this analysis, providing a more comprehensive evaluation. As a result, quantum computing offers significant strengths in the accounting field, such as high computational power, enhanced security, and automation capabilities. However, there are also weaknesses, including its current developmental stage, high costs, and the need for education. Additionally, while there are opportunities for new analytical methods and competitive advantages, threats such as technological uncertainties and increasing competition must also be considered. In this context, it is crucial for accounting professionals to be prepared for this new technology, as it holds critical importance for their future success. Thus, the effects of quantum computing on the accounting sector can be better understood, and its potential can be maximized.

Keywords: Quantum computing, Accounting, SWOT Analysis

Introduction

Quantum computing emerges as one of the most striking technological innovations of our time, with Quantum Internet being considered the future of computer science (Golec & Gill, 2024). Although the era of quantum computing has not yet arrived, it already represents a next-generation technology that promises exciting advancements (Wang et al., 2021). And has the potential to transform economic, industrial, academic, and social landscapes (Lekitsch et al., 2017). The rapid development of quantum computer technology is having significant and profound impacts on the information economy across various sectors, including cybersecurity, healthcare, finance, and logistics (Coccia & Roshani, 2024). By transcending traditional computing paradigms, quantum computers possess the capacity to solve complex problems more quickly and effectively (Liu, 2021; How and Cheah, 2023). For instance, the ability of quantum computers to process multiple states enables the analysis of large datasets to be completed in a shorter time frame compared to classical computers. The accounting and finance sector holds critical importance in leveraging the potential offered by quantum technology, as increased computational power, improvements in data security, and advantages in process automation present significant opportunities. Quantum computers can execute complex calculations such as financial reporting, derivative pricing, fraud detection (Herman et al., 2022). Risk analysis (e.g., evaluating a company's risk portfolio), and portfolio optimization (Hegade et al., 2022; Jabeur et al., 2024). Much more rapidly. While calculations conducted through traditional methods can be time-consuming and prone to errors, quantum algorithms optimize these processes, yielding more accurate and reliable results. By offering the potential to resolve various financial scenarios with suitable algorithms (Fontanela et al., 2021). Quantum computers provide immense savings in both time and memory for computational tasks, thereby enhancing the accuracy of calculations (Chang et al., 2023). Quantum cryptography, along with fault-tolerant quantum computers (Campbell, 2019). Has the potential to establish a new standard for the protection of accounting data, significantly reducing the risk of sensitive financial information leakage. Quantum computers facilitate the secure and efficient exchange of

- Selection and peer-review under responsibility of the Organizing Committee of the Conference

digital assets by eliminating the vulnerability of traditional cryptographic systems to quantum attacks, while also providing low processing costs and fast execution times, thus lowering overall expenses (Joshi et al., 2023). Accounting processes can be automated using quantum algorithms during data collection and reporting phases, enabling accounting professionals to focus on more strategic tasks while achieving significant cost reductions.

Moreover, quantum computers have the potential to optimize job scheduling problems in automatic storage and retrieval systems, minimizing costs associated with transport operations and empty trips (Windmann, 2024). Additionally, by increasing efficiency, they can enhance market-making investments, leading to higher profits (Bova et al., 2023). Quantum computers have the potential to significantly reduce costs by decreasing computation times for complex industrial processes from hundreds of hours to mere seconds, thereby enabling leaders to make better, real-time decisions (Villalba-Diez & Zheng, 2020). By enhancing big data analytics applications, they offer the potential to address existing challenges in the e-commerce sector, contributing significantly to the development of management strategies and decision-making processes (Zhuang, 2021). Additionally, quantum computers can positively impact cost structures by reducing the design and production costs of integrated circuits, thus enabling sustainable economic scaling (Loesch, 2009). The adoption of this technology involves not only potential opportunities but also certain challenges and uncertainties (Hellstem, 2021). For instance, factors such as difficulties in integrating with existing infrastructures, high costs, and a lack of knowledge regarding quantum technologies may limit the impact of quantum computing on accounting practices. This study aims to comprehensively evaluate the effects and potential of quantum computers on accounting. Specifically, the SWOT analysis method will be employed to establish a balance between the advantages provided by this new technology and the challenges that may be encountered. Thus, a framework will be presented to enable accounting professionals to maximize the opportunities brought by quantum computing and to develop strategic approaches against potential threats.

The Impact of Quantum Computing on Accounting Processes

Quantum computers emerge as an innovative technology that enhances information processing capacity through the use of quantum bits (qubits), distinguishing them from classical computers. Due to their ability to exist in multiple states simultaneously, qubits can perform complex calculations (Lazirko, 2024). At significantly higher speeds. This characteristic presents a revolutionary potential for quantum computers in processing large datasets, solving optimization problems, and simulating complex systems. Once integrated, it is believed that they could enhance the quality of life across various domains for humanity (Gill et al., 2024). Quantum computing has the potential to reshape business processes in the accounting sector by offering various innovations and opportunities. The high computational power and advanced data processing capabilities provided by quantum computers enable accounting operations to be performed more quickly and efficiently (Diep et al., 2017). This advancement allows firms to gain a competitive advantage. Quantum computing is transforming accounting processes. Traditional accounting methods often involve time-consuming and manual processes. With quantum computers, these processes can be automated and accelerated. For instance, data collection, analysis, and reporting stages can be executed more effectively using quantum algorithms. This transformation allows accounting professionals to focus more on strategic decision-making while also reducing costs. One of the most significant advantages provided by quantum computing is the rapid and effective analysis of large datasets. In the accounting field, this capability leads to substantial improvements in data analysis and reporting processes. As processes become more efficient, advanced data analysis and reporting can be facilitated. Quantum computers also offer the potential to enhance fraud detection processes by providing significant accuracy in data analysis and classification (Mitra & JV, 2021).

Method

SWOT Analysis

SWOT analysis stands out for its value in focusing on significant issues (Bull et al., 2016). It is used to systematically identify the strengths and weaknesses, opportunities, and threats of an organization or project (Rahmanta & Cahyo, 2024; Shinde et al., 2023). This method serves various purposes, such as helping organizations achieve their long-term goals, guiding the evaluation of alternative strategies, understanding the competitive environment, and ensuring more effective management of existing resources (Nilashi et al., 2023). SWOT analysis enables the exploration of strategic relationships between an idea, concept, technology (Brandas et al., 2015). Or asset and its internal and external environment (Mukamwi et al., 2023).

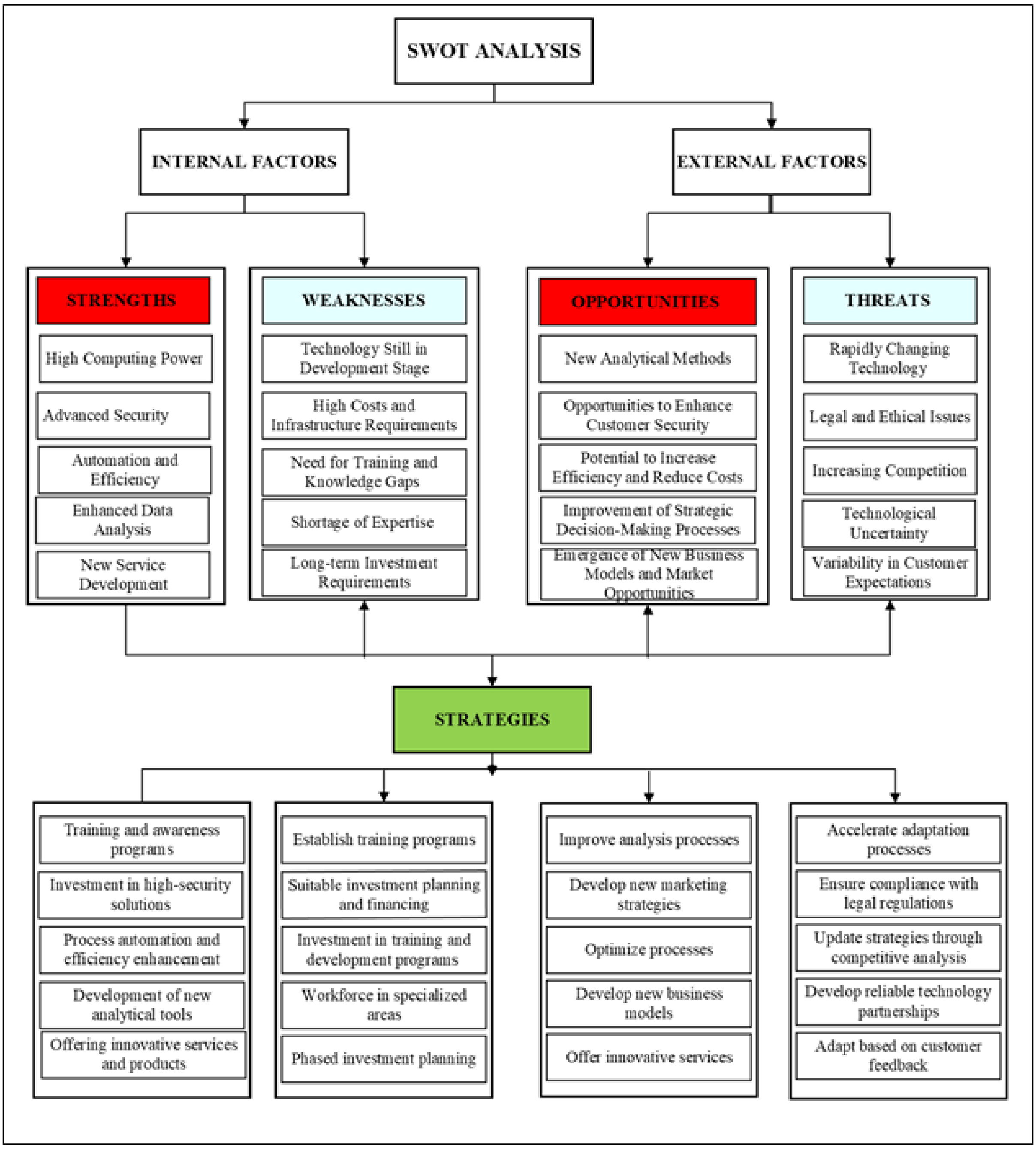

Figure 1. SWOT analysis of quantum computing in accounting

Strengths

Quantum computing has the potential to create significant transformation in the field of accounting through its notable strengths. Its high computational power allows for the rapid execution of complex financial analyses, while advanced security features enhance data protection and privacy, providing a reliable environment. Automation and increased efficiency facilitate the quicker and more accurate completion of routine accounting tasks, while advanced data analysis and predictive capabilities strengthen data-driven decision-making processes. These strengths help accounting firms develop innovative services and products, thereby enhancing their competitive advantages and fostering innovation within the industry. Consequently, the adoption of quantum technology stands out as one of the keys to future success in the field of accounting.

High Computational Power; The strategic importance of quantum computers, regarded as one of humanity's most advanced inventions, becomes particularly evident in industries that require complex simulation capabilities and high data processing speeds, such as cryptography (Kahyaoglu, 2023). Quantum computing provides solutions to complex problems in accounting and finance that exceed the computational power offered by traditional computers. Quantum computers utilize quantum bits (qubits), which can represent multiple states simultaneously, as opposed to the binary states (0 and 1) of classical bits (Demski et al., 2009). This capability significantly enhances parallel processing capacity, accelerating the processing and analysis of multidimensional datasets. The high performance of quantum computing, particularly in areas such as big data analysis and statistical modeling, enhances the effectiveness of accounting processes. For instance, complex operations such as Monte Carlo simulations, probability calculations, and risk analyses can be completed much more quickly using quantum algorithms compared to traditional methods. This allows accounting firms to achieve faster and more reliable results in financial reporting and auditing processes. Quantum computing offers new approaches in data mining and analytical applications. Quantum algorithms expedite the process of obtaining meaningful insights from large datasets, helping accounting professionals make more data-driven and accurate decisions. In this context, significant advantages are gained in areas such as increased accuracy in financial forecasting, optimization of investment strategies, and improvement in risk management. The high performance provided by quantum computing leads to noticeable enhancements in efficiency, speed, and accuracy in the accounting sector, thereby contributing to the competitive positioning of professionals and firms.

Innovation ;Quantum computing brings innovative solutions to the field of accounting. Notably, changes in data processing and analytical capabilities enhance accounting applications. The high computational power enables complex financial analyses and simulations to be conducted more rapidly and efficiently. This allows accounting professionals to provide deeper insights to their clients and supports strategic decision-making processes. New analytical methods developed through quantum algorithms facilitate the creation of more precise models in risk management and forecasting. Moreover, this technology leads to the emergence of new business opportunities and service models within the accounting sector. Early adoption offers the chance to leverage the advantages provided by technology, creating differentiation from other players in the industry. Quantum-enabled solutions not only enhance financial efficiency but also contribute to the development of innovative services that increase customer satisfaction and loyalty.

Enhanced Security; The cybersecurity risks and threats faced by accounting information systems necessitate the development of new measures against risks such as cybersecurity controls, assurances related to cybersecurity, and breaches (Cram et al., 2023). Quantum computing stands out for its potential to enhance data security in the accounting sector. This technology has the capacity to significantly reduce the vulnerabilities encountered by classical computer systems. The principles of quantum mechanics, which form the foundation of quantum computing, offer innovative methods to enhance security in information transmission. In particular, applications such as Quantum Key Distribution (QKD) emerge as a revolutionary approach to ensuring data privacy in communication processes. QKD facilitates secure key exchanges between two parties using quantum bits (qubits). This process relies on the principles of quantum entanglement and uncertainty, allowing the system to detect any attempts at intrusion instantaneously. Consequently, the risk of interference or leakage during data communication is significantly reduced. This advantage is especially critical for protecting financial data, customer information, and sensitive financial documents, thereby minimizing the risk of fraud and data theft.

Moreover, it enables the development of more secure alternatives to existing encryption methods. As quantum computers advance, the development of quantum-resistant cryptographic algorithms becomes increasingly important (Lazirko, 2023). Quantum encryption enhances accounting firms' capabilities to protect sensitive data by minimizing the risk of compromise associated with classical encryption systems. Particularly, these new encryption methods increase resilience against attempts by cybercriminals to capture data using classical encryption techniques. To detect rising cybersecurity risks through early warning mechanisms, it is essential to leverage quantum technology in practical applications of artificial intelligence and/or blockchain (Yi, 2022; Kahyaoglu, 2023). The security advantages provided by quantum technologies also positively contribute to regulatory and compliance requirements. The financial sector is subject to stringent data protection laws and standards. Quantum computing assists firms in complying with these requirements, enabling them to meet legal obligations and enhance customer trust.

Automation and Increased Efficiency; Quantum computing has the potential to enhance overall productivity in accounting processes by promoting automation. Traditional accounting practices are often burdened with time-consuming and repetitive tasks, which can pose significant strains on both human and financial resources. Quantum technologies enable the automation of such tasks, allowing accounting professionals to focus on more strategic and value-added activities. By increasing data processing speed and capacity, quantum computing facilitates the analysis of large datasets. This capability enables accounting firms to perform more complex calculations quickly and manage databases effectively. For instance, processes such as account reconciliation, invoice verification, and financial reporting can be executed more swiftly and with fewer errors, thanks to the high processing power provided by quantum algorithms. Consequently, the acceleration of these processes results in more effective resource utilization and a noticeable increase in overall efficiency. Quantum computing offers an innovative approach to accounting processes through algorithms developed for decision support systems and predictive tools. Quantum algorithms can be employed to solve complex optimization problems aimed at increasing efficiency. This application allows for more accurate forecasts in budgeting processes while simultaneously optimizing resource allocation. Automation reduces human errors and enhances the consistency of accounting processes.

Advanced Data Analysis and Predictive Capability; Quantum computing has the potential to fundamentally transform data analysis and forecasting processes in the field of accounting. This technology offers innovative and comprehensive analytical opportunities in accounting applications due to its high computational power and complex algorithms, enabling faster and more effective processing of large datasets (Schuld, 2019). Traditional accounting methods often rely on limited data processing capacities and classical algorithms, creating challenges in conducting complex financial analyses and reporting. Quantum computing provides significant advantages in processing and analyzing multidimensional datasets, allowing for the overcoming of such limitations. For instance, quantum algorithms enable the simulation of complex financial scenarios, improving the accuracy of predictions regarding future financial outcomes. This capability allows accounting professionals to make better-informed decisions and optimize strategic planning processes. Additionally, quantum computing facilitates the extraction of meaningful insights from large datasets through data mining applications. This process encompasses a wide range of data analyses, from analyzing customer behaviors to forecasting market trends. For example, accounting firms can use quantum-supported analytical methods to detect anomalies in financial data more swiftly and manage risk more effectively. In terms of predictive capabilities, quantum algorithms present substantial potential, especially when integrated with machine learning applications in the accounting domain. This integration allows for the analysis of historical data to identify future financial trends and potential risks. For instance, more accurate and timely forecasts can be made in critical areas such as sales forecasting, budgeting processes, and cash flow management.

New Service and Product Development; Quantum computing significantly expands opportunities for new service and product development within the accounting sector. While traditional accounting practices often rely on static and predetermined processes, quantum technologies offer dynamic and innovative solutions that have the potential to enhance competitive advantages in the industry. In this context, accounting firms can respond more quickly and effectively to customer needs by leveraging quantum computing technology. The high computational power and complex data analysis capabilities provided by quantum computing enable accounting firms to develop new service models. For instance, quantum-supported analytical tools allow for a deeper examination of customer data, facilitating the provision of customized financial consulting services. Such services can enhance customer satisfaction by developing tailored strategies that address individual client needs.

Moreover, quantum technologies go beyond mere automation in accounting processes, promoting the development of new products. For example, innovative products developed through quantum algorithms in risk management and forecasting allow firms to present more accurate and reliable financial reports. Additionally, quantum-based auditing tools improve the speed and effectiveness of financial transaction examinations, thereby enhancing the quality of audit processes. These innovative solutions enabled by quantum computing not only strengthen the market positions of accounting firms but also pave the way for new business opportunities. In particular, newly integrated services with quantum computing contribute to the development of innovative applications in the financial technology (FinTech) sector, thereby increasing competition within the industry.

Weaknesses

The adoption of quantum computing in the accounting sector faces several weaknesses and barriers. These weaknesses may adversely affect the effective implementation of the technology and the transformation processes within the industry.

Development Stage; Quantum computing is still considered an immature technology. This implies that on going research and development activities are necessary to realize its potential. In an environment where quantum computers and algorithms are effectively designed and implemented, many theoretical concepts remain untested in practice. For instance, there is no clear roadmap for how quantum algorithms can be applied in various accounting processes and how these processes can be optimized. At the current stage of development of quantum computing systems, technical challenges, particularly related to error rates and system stability, are also noteworthy. Interactions between quantum bits (qubits) can affect the system's capacity to produce accurate and reliable results, posing risks that may undermine the reliability of accounting applications. Therefore, the early-stage nature of quantum computing reduces the willingness of accounting firms to adopt this technology and creates uncertainty. Most existing research has concentrated on specific areas, indicating a need for broader studies to develop solutions tailored to accounting processes. Consequently, academic and industrial collaborations related to quantum computing are critical for advancing applications in the sector.

High Costs; The adoption of quantum computing in the accounting sector faces a significant weakness in the form of high costs. Quantum computers are considerably more expensive than classical computers, and this expense applies to both hardware and software components (Golec et al., 2024). The installation of quantum computing systems requires specialized infrastructure, advanced cooling systems, and complex engineering solutions, necessitating a substantial allocation of financial resources. These high initial costs represent a significant barrier, particularly for small and medium-sized accounting firms. Such firms typically operate with limited budgets, making the adoption of quantum technology potentially financially unsustainable. Consequently, their willingness to invest in quantum technology is restricted due to high costs. Additionally, the maintenance and updating requirements of quantum computing systems further contribute to rising costs. Given that quantum technologies are in a continually evolving field, ongoing investments are necessary to stay current. This situation imposes additional financial obligations on accounting firms as they strive to enhance existing systems and integrate new technologies. Beyond costs, the return on investment for such technologies remains uncertain. The potential benefits of quantum computing have not yet been fully demonstrated, creating ambiguities regarding the profitability of investments for firms. This uncertainty complicates the decision-making process for accounting professionals and managers considering this new technology.

Education; Quantum computing represents a field that requires significant training and expertise to be effectively implemented in the accounting sector. The complexity of quantum technology necessitates that accounting professionals develop in-depth knowledge and skills to utilize these new systems effectively. However, existing educational programs often do not adequately cover innovative developments in this area. This situation hinders professionals from grasping fundamental concepts related to quantum computing and acquiring practical skills. The need for education extends beyond the development of technical skills; it also encompasses the necessity to enhance knowledge regarding the integration of quantum technologies into accounting processes. For instance, training on concrete examples and applications of how quantum algorithms can be used in accounting practices is essential, as is raising awareness among professionals about ethical and security issues associated with quantum computing. The lack of knowledge in the field of quantum computing could also yield negative outcomes in terms of innovation and competitiveness within the sector. Educational deficiencies weaken firms' resolve to adopt this new technology and slow down the processes of innovative service and product development. In this context, it is critical for accounting professionals to have access to continuous education and development opportunities to understand and apply quantum technologies effectively.

Compliance Processes and Regulation; The integration of quantum computing into the accounting sector necessitates compliance with existing legal and regulatory frameworks, presenting a significant weakness that complicates the adoption of this technology. Accounting firms are required to adhere to data protection laws and financial reporting standards at both national and international levels. However, there is a notable lack of clear guidance on how quantum computing systems can be integrated into these regulations. Regulations concerning data privacy and security are critical factors that affect the use of quantum technologies. For instance, regulations related to the protection of personal data are essential considerations during the development and implementation of quantum computing systems. The data processing capabilities afforded by quantum computing may introduce new challenges in securely managing and processing such data. Consequently, accounting firms are subjected to additional obligations to ensure compliance with legal requirements while utilizing quantum technology and safeguarding customer security. Furthermore, the compliance processes for quantum computing systems are complex and require substantial training and expertise. Firms must possess not only the technical knowledge required by this new technology but also the capability to understand regulatory requirements and develop appropriate strategies for compliance. In this context, it is vital for professionals in the sector to have continuous access to up-to-date information to track regulations related to quantum computing and effectively manage compliance processes.

Technological Uncertainties; Quantum computing is not only a dynamic field but also carries significant uncertainties regarding its development. These uncertainties may negatively impact the process of adopting quantum technologies within the accounting sector. In particular, uncertainties surrounding the future evolution of quantum computing and the areas in which this technology will have the most significant impact complicate firms' strategic planning processes. The performance and availability of quantum computers remain unpredictable, which may influence accounting firms' decisions to invest in these technologies. Firms that decide to invest need clear information not only about the potential benefits of quantum computing but also regarding its possible limitations and challenges. However, existing literature and research do not provide definitive forecasts on when quantum technology will achieve its full potential. Keeping pace with the rapid developments in quantum computing can be a challenging process for accounting firms. The continuous evolution of the technology implies that firms must prepare themselves for these changes. Yet, uncertainties exist regarding how this preparation should be conducted and which strategies should be pursued. This situation may particularly hinder small and medium-sized firms from utilizing their resources effectively.

Opportunities

The opportunities presented by quantum computing in the accounting sector have the potential to accelerate transformation in this field. These opportunities are not limited to the optimization of existing processes but also lay the groundwork for the development of new business models and services. In an increasingly digital business environment, it is emphasized that accounting must provide a structure capable of reflecting potential loss and default risks based on advanced risk management tools. Given the complexity of economic factors, analyzing this complexity and converting it into accounting records necessitates the creation of a new business culture and professional standards (Kahyaoglu, 2023). The high computational power and innovative analytical methods offered by quantum technology present accounting firms with opportunities to enhance their competitiveness, respond more effectively to customer demands, and improve overall efficiency. In this context, the opportunities detailed below are crucial for accounting professionals and firms in their adoption of quantum computing technology.

New Analytical Methods; Quantum computing has the potential to introduce revolutionary new methods for data analysis in the accounting sector. Traditional computing systems face certain limitations when processing and analyzing large data sets, making it challenging to effectively evaluate complex financial data. Quantum algorithms enable more efficient and rapid results, particularly in the processing of high-dimensional data. For instance, quantum computing facilitates optimal management of costs and profits through algorithms designed to solve optimization problems. Such optimization allows firms to use their resources more efficiently and adjust their budgets with greater accuracy. Moreover, quantum computers can quickly simulate complex mathematical models to yield more accurate and rapid results in financial forecasting and valuation processes. When combined with machine learning and artificial intelligence applications, quantum computing enables deeper analysis of data. For example, learning from historical financial data to predict future market trends can provide accounting firms with significant advantages in strategic decision-making. In this context, quantum algorithms can enhance the analysis of customer behaviors, market fluctuations, and financial risks, thereby assisting firms in developing more effective strategies**.**

Competitive Advantage and Automation; Quantum computing assists accounting firms in achieving a distinct competitive advantage by enhancing their operational efficiency. The high computing power of quantum systems provides significant benefits, particularly in the processing and analysis of large data sets. Quantum computers possess the capacity to execute numerous operations in parallel, significantly accelerating the processes of data analysis and reporting. For instance, routine tasks such as the preparation of financial statements, tax calculations, and budgeting can be completed with reduced time and human resources due to quantum computing. This enables firms to redirect their resources towards more strategic areas. The automation capabilities afforded by quantum computing can also reduce human errors in accounting processes, thereby enhancing quality. Automation ensures that routine tasks are executed more quickly and accurately, allowing accounting professionals to dedicate their time to more complex and creative assignments. This not only increases overall efficiency but also positively impacts employee satisfaction. The competitive advantage derived from quantum technology extends beyond the improvement of internal processes; it also has the potential to enhance customer service. Rapid data analysis and more accurate reporting enable firms to provide better service to their clients. For example, offering customized reports and advisory services tailored to clients' specific needs can enhance customer loyalty.

Advanced Risk Management and Real-Time Auditing; While traditional computing methods have certain limitations in analyzing complex financial scenarios, quantum technology possesses the capacity to execute these processes more quickly and accurately. Quantum algorithms provide significant advantages in identifying and managing potential risks by establishing more effective relationships among multidimensional data sets and variables. For instance, simulating different market conditions and variables to assess the performance of an investment portfolio can be achieved in a more realistic and comprehensive manner with quantum computers.

This capability enables firms to better anticipate and manage risks, thereby contributing to the prevention of losses. The advanced analytical methods derived from quantum computing facilitate a more detailed analysis of various types of risks, including credit risk, market risk, and operational risk. Consequently, accounting firms can offer more reliable and comprehensive risk management services to their clients, enhancing customer satisfaction. For example, predicting potential adverse effects on a client's financial situation can be conducted with greater accuracy through quantum-assisted analytics.

The speed and precision afforded by quantum computing also enhance the ability to simulate emergency scenarios. Firms can leverage the simulation capabilities provided by quantum computers to strengthen their preparations for market fluctuations, economic crises, or other unexpected events. This improves both strategic decision-making processes and crisis management plans. Moreover, quantum computing enables real-time financial and operational audits through accounting records. Given that accounting systems process large volumes of information, the insights offered by quantum tools play a crucial role in determining whether external interventions have occurred. Particularly in the context of cybersecurity, the speed of digital tools necessitates the integration of quantum cybersecurity infrastructure and quantum cryptography to ensure economic stability and sustainability for financial institutions (Chan et al., 2018).

Innovative Service and Product Development; Quantum computing enables firms to transform their existing services and create entirely new types of offerings. Specifically, quantum algorithms and analytical methods can elevate accounting applications to previously unattainable levels. For instance, quantum-assisted data analysis tools allow firms to provide customized reports and services tailored to client needs. Personalized analyses and forecasts can help clients develop their business strategies more effectively. In this context, the rapid data processing capabilities offered by quantum technology enable accounting firms to respond to client demands more swiftly and to personalize their services. Quantum computing also presents opportunities for developing new products in areas such as financial modeling and risk analysis. For example, firms can use quantum-based simulations to evaluate complex financial scenarios more realistically, thereby facilitating the development of new investment vehicles or financial products.

Sectoral Innovation; Traditional accounting practices often rely on specific and static processes; however, quantum technology facilitates the adoption of more dynamic and flexible approaches. This transformation has the potential to reshape existing business models within the sector and create new opportunities. Quantum computing can not only enhance efficiency in accounting processes but also change the way business is conducted. For example, automated reporting, analysis, and data management processes reduce the need for human intervention, thereby decreasing error rates and allowing the workforce to focus on more strategic tasks. This shift can redefine the roles of employees in the sector, fostering a more innovative and creative work environment. Additionally, the new analytical capabilities offered by quantum technology enable accounting firms to expand their services into different domains. For instance, accounting firms may move beyond financial analysis to offer strategic consulting services to their clients.

Threats

Despite the significant opportunities presented by quantum computing in the accounting sector, it also brings various threats. These threats emerge as critical factors that must be considered during the adoption and integration of the technology.

Technological Uncertainties; The process of adopting and implementing quantum technology involves various uncertainties. As quantum technology is still in its maturation phase, the speed and direction of developments in this field create unpredictability for accounting firms. This uncertainty can negatively impact firms' strategic planning processes, as accounting professionals lack definitive information regarding the costs and benefits of quantum computing applications, making long-term investments more challenging. Moreover, the complexity of accounting applications and the regulatory requirements within the sector further complicate the integration of quantum technology. For instance, insufficient knowledge about how traditional accounting methods and processes will interact with quantum computing can increase the challenges firms may face when applying this technology. Additionally, there remains uncertainty regarding how specific standards and regulations within the accounting field will evolve during the development and implementation of quantum algorithms. This situation may delay the preparations required for accounting firms to adopt quantum technology. Furthermore, uncertainties also stem from the limited knowledge and experience related to quantum computing across the sector.

Increasing Competition; The advantages offered by quantum technology, particularly in areas such as data analysis, risk management, and processing speed, are becoming significant competitive factors for existing firms. However, the rapid adoption of these advantages is leading to the emergence of new players in the sector and efforts by current firms to enhance their competitiveness. The adoption of quantum technology by new entrants can significantly alter the competitive landscape. These new actors often gain a competitive edge over traditional accounting firms through more innovative and flexible business models. For example, the rapid data processing and analytical capabilities enabled by quantum computing allow these firms to respond to customer demands more swiftly and effectively. This situation may lead to challenges for existing accounting firms in maintaining their market share. The increase in competition among current accounting firms can also accelerate innovation processes. Firms may seek to differentiate themselves by leveraging the advantages of quantum computing to enhance their services and products. However, this could result in narrowing profit margins and increasing cost pressures. Moreover, intensified competition will require firms to continually invest in new technologies and exert greater effort to enhance customer satisfaction. The rise in competition may compel existing players in the sector to reassess their business strategies and develop innovative solutions, while simultaneously elevating customer expectations. Clients may begin to demand faster and more accurate services made possible by quantum technology, necessitating a more proactive approach by firms to strengthen customer relationships and ensure sustainable growth.

Education and Skills Gap; The adoption of quantum computing technology presents a significant education and skills gap in the accounting sector. Given that quantum technology relies on complex mathematical and computational principles, it has become crucial for current accounting professionals to possess adequate knowledge and skills in this area. However, the majority of existing accounting education programs do not offer a comprehensive curriculum on advanced technologies such as quantum computing. This shortfall may hinder the development of the skilled workforce that the industry requires. The lack of knowledge regarding quantum computing makes it challenging for accounting firms to implement this technology effectively. Professionals' unfamiliarity with quantum algorithms, data analysis techniques, and the innovative approaches brought by this technology could lead firms to lose their competitive advantage in the field. Moreover, educational deficiencies may impede the development of the strategic thinking skills necessary to capitalize on the opportunities presented by quantum technology. In this context, it is essential for accounting firms to organize training programs and seminars related to quantum technology, enabling their employees to enhance their competencies in this area. Universities and educational institutions can also facilitate professionals' adaptation to this technology by developing specialized courses and certification programs in quantum computing. This approach will equip both current employees and recent graduates with the ability to effectively leverage the potential offered by quantum computing.

Legal and Ethical Issues; While quantum computing presents innovative opportunities in the accounting sector, it also brings significant legal and ethical challenges that must be addressed during the implementation and adoption of this technology. The data processing and analytical capabilities offered by quantum technology provide substantial advantages, particularly in managing large datasets; however, these advantages may also introduce various risks related to data privacy and security. One of the primary concerns is the confidentiality and security of data obtained through quantum computing. The processing power of quantum computers may facilitate the breach of encryption systems, thereby posing greater challenges for accounting firms in safeguarding client information. Protecting customer data is not only a legal obligation within the accounting sector but also an ethical responsibility. Consequently, firms need to reassess their data protection strategies and develop security measures that comply with quantum technology. The ethical dimensions of services provided through quantum computing must also be considered. Questions regarding how firms utilize data acquired through quantum technology and whether such uses align with clients' best interests may lead to ethical debates within the industry. A lack of ethical standards could undermine customer trust and negatively impact firms' reputations. In this context, it is crucial for accounting firms to establish ethical guidelines related to quantum technology and ensure compliance with these standards. Additionally, legal regulations must be updated to reflect the implications of quantum computing.

The Future of Quantum Computing and Strategic Approaches

The future of quantum computing will bring significant changes in both technology and the business landscape. In the accounting sector, this transformation will manifest through increased efficiency, more accurate data analysis, and opportunities for innovation. In the coming years, the adoption of quantum computing is expected to enhance competitive advantages within the industry, enabling firms to offer more innovative services to their clients. In this context, accounting firms must develop strategic approaches in the field of quantum computing.

These strategies should focus on early adaptation to the technology, the development of necessary competencies, and the ability to respond to changes within the sector. Additionally, the integration of quantum solutions to optimize business processes should be considered. For firms to effectively capitalize on the opportunities presented by this new technology, it is critical that they enhance their knowledge of quantum computing and establish strategic partnerships.

Education and Knowledge Development; The effective adoption of quantum computing in the accounting sector is contingent upon strengthening education and knowledge development processes. In this context, it is critical to develop the knowledge and skills that sector professionals need to understand the complex nature of quantum computing technology. Educational and knowledge development strategies should encompass various aspects for both current employees and the next generation of accounting professionals. Those practicing accounting and auditing professionally, as well as those who wish to continue doing so in the future, must be prepared for a new learning process (Kahyaoglu, 2023).

Updating Educational Curricula; To cultivate competent individuals in the field of quantum computing, it is necessary to review existing educational curricula. Universities and educational institutions should offer specialized courses and programs focused on quantum computing, data analytics, and related technologies. These curricula should include both theoretical knowledge and practical training opportunities. For instance, students could gain practical experience by working on quantum algorithms.

Continuing Education and Professional Development; To achieve the necessary pace in practice, quantum approaches will be required. It is a reality that managers must consider in terms of corporate sustainability and cybersecurity (Kahyaoğlu S. B, 2023). In this context, the rapid development of quantum technology necessitates that accounting professionals engage in continuous education. Firms should organize regular seminars, workshops, and online training programs to support their employees in updating their knowledge. Such events will enable employees to keep abreast of the latest innovations in the sector while simultaneously enhancing their understanding of quantum computing. Gaining experience in quantum computing is a crucial component of the educational process. Firms can collaborate with universities to offer practical training programs and internship opportunities. Allowing students and recent graduates to experience quantum computing applications in a real work environment will reinforce their theoretical knowledge and help them better understand business processes in the sector. These opportunities will enhance the employability of graduates and contribute to the development of a competent workforce in the industry.

Mentorship and Consulting Programs; The involvement of professionals specialized in quantum computing in mentorship roles for other individuals and firms within the sector can significantly contribute to the knowledge development process. Mentorship programs facilitate the transfer of knowledge and experience from seasoned professionals to the next generation of accounting experts. Additionally, such programs positively impact individuals' career development while enhancing knowledge sharing within the industry.

Research and Development Support; Investing in research and development activities is essential for uncovering the potential of quantum computing in the field of accounting. Educational institutions and firms can support projects related to quantum technology, thereby developing new applications and solutions. Such support will promote knowledge development at both academic and industry levels, ensuring that the benefits of quantum computing reach a wider audience.

Integration Strategies; The integration of quantum computing into accounting processes is a critical step for enhancing competitive advantage within the sector. In this context, developing effective integration strategies will enable firms to derive maximum benefits from this new technology.

Review and Restructuring of Existing Systems; The integration process of quantum technology should begin with a comprehensive review of existing accounting systems. At this stage, firms must assess data flow, business processes, and system architecture to plan updates that align with quantum computing capabilities. The restructuring of these processes will facilitate the establishment of the necessary infrastructure for integrating quantum solutions. Specifically, improvements made in data management and analysis processes will maximize the computational advantages offered by quantum technology.

Establishing Pilot Projects and Test Environments; To evaluate the feasibility of quantum technology, firms should develop pilot projects and create test environments. Such projects help to understand how quantum computing applications perform under real-world conditions. The data obtained from pilot projects will enable firms to determine how they can implement this technology on a broader scale. Additionally, the challenges and successes encountered during this process will provide valuable feedback for future investments.

Collaboration and Partnership Development; Establishing collaborations and partnerships is a significant advantage for the integration of quantum computing. Firms can enhance their knowledge base and share best practices by collaborating with technology providers, universities, and research institutions. Such partnerships facilitate the development of innovative solutions and enable the effective application of quantum technology. Additionally, sharing information and exchanging experiences with other firms in the industry can help accelerate the integration process.

Education and Capacity Development; To develop the competencies required for the integration of quantum computing, firms should organize training programs for their employees. These training sessions will not only ensure that employees acquire knowledge in quantum computing and data analysis but also enhance their ability to effectively implement this technology. By offering continuous education and professional development opportunities, firms can keep their employees' knowledge and skills up to date, thereby enabling them to leverage the potential of quantum computing more effectively.

Strategic Investment and Resource Allocation; During the transition to quantum computing technology, it is essential for firms to make strategic investments and allocate resources effectively. A significant constraint in the current business landscape is the need for process owners to have access to appropriate tools and infrastructure capable of carrying out tasks from a quantum perspective (Roberts, 2019). These investments should encompass areas such as software and hardware upgrades, research and development activities, and training programs. As firms evaluate the opportunities presented by quantum technology, they must carefully analyze the costs and benefits that may arise during this process. This approach enables more informed resource allocation and supports long-term sustainable growth objectives.

Results and Discussion

We are still at the very beginning of quantum technology, and during this process, there is a need for "quantum corporate governance principles" to conduct the development process on a well-designed, controlled, secure, transparent, and ethical foundation (Kahyaoglu, 2023).

Suggestions for Future Research

Studies on the potential of quantum computing in the field of accounting are still in their early stages, presenting various research opportunities. Below are recommendations for future research:

Table 1. Recommendations for future research

Topics	Explanation
Application-Based Studies	Focusing on the integration of quantum algorithms into existing accounting software to understand how they operate in practice.
Development of Educational Models	Identifying training needs in quantum computing and developing effective training programs to enhance employee competencies.
Cross-Disciplinary Research	Bringing together experts from various disciplines such as computer science, finance, and law to evaluate the opportunities and challenges of quantum computing.
Examination of Ethical and Legal Frameworks	Conducting in-depth analyses of the ethical and legal dimensions of quantum computing applications, specifically regarding data security, privacy, and compliance.
Long-Term Impact Analyses	Assessing the long-term impacts of quantum computing on the accounting sector to understand its contribution to sustainable growth.
User Experience Studies	Examining the end-user experience of quantum computing applications to develop user-centric designs and increase adoption rates.

Conclusion

Quantum computing emerges as a technology with the potential to bring revolutionary changes to the accounting sector. Its high computational power, advanced data analysis capabilities, and security advantages enable quantum computers to transform accounting processes, making them more efficient and effective. This technology offers accounting professionals the ability to quickly analyze complex data sets and make strategic decisions, while also providing significant opportunities for cost reduction through process automation. However, there are several weaknesses and threats associated with the adoption of quantum computing. Challenges such as being in the developmental stage, high costs, and the need for training may hinder the sector's transition to quantum technology. Considering ethical and legal issues is critical for the effective implementation of quantum computing. In this context, various opportunities exist to fully evaluate the role of quantum computing in accounting. Education and knowledge development strategies will facilitate industry professionals' understanding and application of this new technology.

Additionally, application-based research and interdisciplinary collaborations are crucial for leveraging the opportunities presented by quantum computing. Future studies that thoroughly examine the impacts of quantum computing on accounting could accelerate the transformation within the sector. Research focused on applications, educational programs, and user experience evaluations will support the adoption and effective use of this technology. While quantum computing has significant transformative potential in the accounting field, its successful realization requires a systematic and strategic approach. Therefore, it is essential for all stakeholders to collaborate effectively to maximize the opportunities offered by quantum technology.

Scientific Ethics Declaration

The author declares that the scientific ethical and legal responsibility of this article published in EPSTEM Journal belongs to the author.

Acknowledgements or Notes

* This article was presented as an oral presentation at the International Conference on Technology, Engineering and Science (www.icontes.net) held in Antalya/Turkey on November 14-17, 2024.

References

Bova, F., Goldfarb, A., & Melko, R. G. (2023). Quantum economic advantage. *Management Science*, *69*(2), 1116-1126.

Brandas, C., Megan, O., & Didraga, O. (2015). Global perspectives on accounting information systems. mobile and cloud approach. *Procedia Economics and Finance*, *20*, 88-93.

Bull, J. W., Jobstvogt, N., Bohnke-Henrichs, A., Mascarenhas, A., Sitas, N., Baulcomb, C., ... & Koss, R. (2016). Strengths, weaknesses, opportunities and threats : A SWOT analysis of the ecosystem services framework. *Ecosystem Services*, *17*, 99-111.

Campbell Sr, R. (2019). Evaluation of post-quantum distributed ledger cryptography. *The Journal of the British Blockchain Association*, *2*(1).

Chan, D.Y., Chiu, V. & Vasarhelyi, M.A. (Eds.). (2018). *Continuous auditing. Theory and applicatıon. Bingly. emerald. (online).* Retrieved from https.//books.emeraldinsight.com

Chang, Y. J., Sie, M. F., Liao, S. W., & Chang, C. R. (2023). The prospects of quantum computing for quantitative finance and beyond. *IEEE Nanotechnology Magazine*, *17*(2), 31-37.

Coccia, M., & Roshani, S. (2024). Path-breaking directions in quantum computing technology. a patent analysis with multiple techniques. *Journal of the Knowledge Economy*, 1-34.

Cram, W. A., Wang, T., & Yuan, J. (2023). Cybersecurity research in accounting information systems. A review and framework. *Journal of Emerging Technologies in Accounting*, *20*(1), 15-38.

Demski, J. S., FitzGerald, S. A., Ijiri, Y., Ijiri, Y., & Lin, H. (2009). quantum ınformation and accounting ınformation: A revolutionary trend and the world of topology. *Journal of Accounting and Public Policy*, *28*(2), 133-147.

Diep, D. N., Giang, D. H., & Van Minh, N. (2017). Quantum Gauss-Jordan elimination and simulation of accounting principles on quantum computers. *International Journal of Theoretical Physics*, *56*, 1948-1960.

Fontanela, F., Jacquier, A., & Oumgari, M. (2021). A quantum algorithm for linear PDEs arising in finance. *SIAM Journal on Financial Mathematics*, *12*(4), SC98-SC114.

Gill, S. S., Cetinkaya, O., Marrone, S., Combarro, E. F., Claudino, D., Haunschild, D., ... & Ramamohanarao, K. (2024). Quantum computing. vision and challenges. *arXiv preprint arXiv*,2403.02240.

Golec, M., & Gill, S. S. (2024). Computing. looking back and moving forward. *arXiv preprint arXiv*, 2407.12558.

Golec, M., Hatay, E. S., Golec, M., Uyar, M., Golec, M., & Gill, S. S. (2024). Quantum cloud computing. Trends and challenges. *Journal of Economy and Technology*, *2*, 190-199.

Hegade, N. N., Chandarana, P., Paul, K., Chen, X., Albarrán-Arriagada, F., & Solano, E. (2022). Portfolio optimization with digitized counterdiabatic quantum algorithms. *Physical Review Research*, *4*(4), 043204.

Hellstem, G. (2021). Hybrid quantum network for classification of finance and MNIST data. In *2021 IEEE 18th International Conference on Software Architecture Companion (ICSA-C)* (pp.1-4). *IEEE.*

Herman, D., Googin, C., Liu, X., Galda, A., Safro, I., Sun, Y., ... & Alexeev, Y. (2022). A survey of quantum computing for finance. *arXiv preprint arXiv*,2201.02773.

How, M. L., & Cheah, S. M. (2023). Business renaissance. Opportunities and challenges at the dawn of the quantum computing era. *Businesses*, *3*(4), 585-605.

Jabeur, S. B., Gozgor, G., Rezgui, H., & Mohammed, K. S. (2024). Dynamic dependence between quantum computing stocks and bitcoin. Portfolio strategies for a new era of asset classes. *International Review of Financial Analysis*, *95*, 103478.

Joshi, S., Choudhury, A., & Minu, R. I. (2023). Quantum blockchain-enabled exchange protocol model for decentralized systems. *Quantum Information Processing*, *22*(11), 404.

Kahyaoglu, S. B. (2023). An evaluation of accounting and auditing framework within the quantum perspective. *Southern African Journal of Accountability and Auditing Research*, *25*(1), 1-5.

Lazirko, M. (2023). Quantum computing standards & accounting information systems. *arXiv preprint arXiv*,2311.11925.

Lazirko, M. (2024). The quantum dynamics of cost accounting. ınvestigating wıp via the time-ındependent schrodinger equation. *arXiv preprint arXiv*,2405.00047.

Lekitsch, B., Weidt, S., Fowler, A. G., Mølmer, K., Devitt, S. J., Wunderlich, C., & Hensinger, W. K. (2017). Blueprint for a microwave trapped ion quantum computer. *Science Advances*, *3*(2), e1601540.

Liu, D. (2021). Principles and characteristics of quantum computing. *Journal of Physics Conference Series*, *2014*(1), 012012.

Loesch, C. W. (2009). Beyond moore's law-beyond CMOS-post silicon. *Sponsors Of Idımt-2009*, 413.

Mitra, S., & JV, K. R. (2021). Experiments on fraud detection use case with QML and TDA mapper. In *2021 IEEE International Conference on Quantum Computing and Engineering (QCE)* (pp. 471-472). IEEE.

Mukamwi, M., Somorin, T., Soloha, R., & Dace, E. (2023). Databases for biomass and waste biorefinery–a mini-review and SWOT analysis. *Bioengineered*, *14*(1), 2286722.

Nilashi, M., Abumalloh, R. A., Mohd, S., Azhar, S. N. F. S., Samad, S., Thi, H. H., ... & Alghamdi, A. (2023). COVID-19 and sustainable development goals. A bibliometric analysis and SWOT analysis in Malaysian context. *Telematics and Informatics*, *76*, 101923.

Rahmanta, M. A., & Cahyo, N. (2024, July). Implementing biomass co-firing in Indonesia to achieve net zero emissions. a comprehensive review and SWOT analysis. *In 2024 International Seminar on Intelligent Technology and Its Applications (ISITIA)* (pp. 59-64). IEEE.

Roberts, J. (2019). *Quantum computers will soon outperform classical machines. (online).* European Commission. Retrieved from https://ec.europa.eu/research-and-innovation/en/horizon-magazine/quantum-computers-will-soon-outperform classical-machines

Schuld, M. (2019). Machine learning in quantum spaces. *Nature*, *567*(7747), 179-181.

Shinde, P. A., Abbas, Q., Chodankar, N. R., Ariga, K., Abdelkareem, M. A., & Olabi, A. G. (2023). Strengths, weaknesses, opportunities, and threats (SWOT) analysis of supercapacitors. A review. *Journal of Energy Chemistry*, *79*, 611-638.

Villalba-Diez, J., & Zheng, X. (2020). Quantum strategic organizational design. alignment in industry 4.0 complex-networked cyber-physical lean management systems. *Sensors*, *20*(20), 5856.

Wang, J., Shen, L., & Zhou, W. (2021). A bibliometric analysis of quantum computing literature. mapping and evidences from scopus. *Technology Analysis & Strategic Management*, *33*(11), 1347-1363.

Windmann, S. (2024). Quantum computer-aided job scheduling for storage and retrieval systems. *at-Automatisierungstechnik*, *72*(1), 15-21.

Yi, H. (2021). Secure social internet of things based on post-quantum blockchain. *IEEE transactions on Network Science and Engineering*, *9*(3), 950-957.

Zhuang, W. (2021). The ınfluence of big data analytics on e-commerce. case study of the US and China. *Wireless Communications and Mobile Computing*, *2021*(1), 2888673.

Author Information

Hamide Ozyurek
OSTIM Technical University
Ankara, Turkiye
Contact e-mail: *hamide.ozyurek@ostimteknik.edu.tr*

To cite this article:

Ozyurek, H. (2024). SWOT analysis of quantum computing in accounting. *The Eurasia Proceedings of Science, Technology, Engineering & Mathematics (EPSTEM), 32*, 194-207.

The Eurasia Proceedings of Science, Technology, Engineering & Mathematics (EPSTEM)
ISSN: 2602-3199

The Eurasia Proceedings of Science, Technology, Engineering & Mathematics (EPSTEM), 2024

Volume 32, Pages 208-229

IConTES 2024: International Conference on Technology, Engineering and Science

Machine Learning Approaches for Bank Customer Churn Analysis

Yasemin Bozkurt
Kutahya Dumlupinar University

Hasan Temurtas
Kutahya Dumlupinar University

Cigdem Bakir
Kutahya Dumlupinar University

Abstract: With the development of technology, rapid developments are experienced in the banking sector, as in many other sectors. However, with these developments, many problems arise, especially customer losses. Customer losses are a common problem not only in banks but also in many institutions such as insurance, production and logistics, etc. Customer churn is when people performing banking activities begin to abandon these services. It also causes financial and prestige loss for banks. It is possible to minimize or eliminate this problem by providing good service to customers. However, in order to achieve this, it is necessary to accurately analyze the trends that customers care about when providing banking services and the characteristics that cause customer loss. For these reasons, this study aims to estimate the probability of a bank customer leaving the bank from which he receives service. In this study, a data set containing customer data of a bank was used. The data set has various features that include customers' demographic information, financial situations, and interactions with the bank. Using common machine learning algorithms such as Logistic Regression, Decision Trees, Support Vector Machines (SVM), Gradient Boosting, K-Nearest Neighbors (KNN) and Multi-Layer Perceptron (MLP), the reasons for bank customers leaving were determined and the results were evaluated. Cross-validation method was used to evaluate the performance of each proposed machine learning algorithm. Additionally, hyperparameter optimization was used to increase the classification accuracy of the proposed methods. The best parameters were determined with the GridSearchCV hyperparameter optimization method. The performances of the proposed machine learning algorithms are compared. When the findings were evaluated, it was observed that the Gradient Boosting method achieved the highest accuracy rate.

Keywords: Machine learning, Gradient boosting, Gridsearchcv, Hyperparameter optimization

Introduction

In today's competitive banking environment, customer loyalty and customer relationship management are critical for financial institutions. Customer churn is a major concern for banks, and financial institutions are constantly developing strategies to understand and predict customer behavior in order to retain and grow their customer base (Amuda&Adeyemo, 2019). In this context, machine learning and data analytics techniques offer powerful tools for predicting and managing bank customer churn.

Imani and Arabnia conducted a study to predict customer losses in the telecommunications sector using SVM, RF (Random Forest), Decision Trees, ANN (Artificial Neural Networks), LightGBM, XGBoost and CatBoost methods (Imani&Arabnia, 2023). SMOTE technique was used for the unbalanced class problem and the success of the models used with different evaluation criteria such as F1, precision and recall was compared. When ROC analysis was performed, both XGBoost and CatBoost were more successful than other methods. As a result of

- Selection and peer-review under responsibility of the Organizing Committee of the Conference

Optuna hyperparameter optimization, CatBoost achieved 93% success. The success of the proposed models is increased with hybrid data sampling techniques. Approximately 91% F1 Score was obtained with the LightGBM gradient boosting technique. However, on larger and unbalanced data sets, the system can be further tested for success with deep learning methods such as Long Short Term Memory (LSTM). Additionally, the negative effects of missing predictions in the data on classification success can be reduced.

It is very risky for businesses to leave customers from the businesses they receive service from for different reasons. Customers who are not satisfied with the service do not recommend these businesses to other users. These problems cause great financial losses and loss of prestige of businesses. Determining customer losses is very important for businesses to minimize these problems. Khattak et al., have carried out studies to detect customer churn using combined deep learning models (BiLSTM-CNN) (Khattak etc., 2023). In this study, it is aimed to increase the accuracy in the detection process of customer losses with the combined deep learning model they proposed. Their proposed model provided approximately 81% accuracy, 66% precision, 65% F1-Score, and 64% recall. However, a two-class data set was used in this study. Analysis is needed for multi-class data sets. Additionally, studies can be carried out to select features and determine feature types.

Liu et al. (2024) used the Extreme Gradient Boosting Tree (XGBT) method to retain customers and determine customer churn in businesses. Hyperparameters and weights of XGBT trees are optimized with Bayes theorem. The XGBT method performed with Bayesian optimization is called BO-XGBT. By adjusting the class weights through the study conducted on real datasets, the computational cost was greatly reduced and the classification accuracy was increased. Additionally, the working time is more optimum than other methods. Thus, the problem of misclassification is reduced. In the study, the relationship between customer tendencies and the cost of retaining customers can be determined on different data sets. Therefore, it can be used in different areas such as credit fraud and fraud detection, apart from modeling customer loss prediction. Jajam et al. (2023) Arithmetic Optimization Algorithm (AOA) and Ensemble Deep Learning SBLSTM (Stacked Bidirectional Long Short-term Memory) –RNN (Rcurrent Neural Network)-IGSA (Improved Gravitational Search Optimization Algorithm) for customer churn prediction (CCP) and customer satisfaction. They proposed the model. The classification accuracy was increased by eliminating the IGSA optimization developed by hyperparameter tuning with the proposed AOA-SBLSTM-RNN model, and the results of both methods were compared. Three different health data were used to measure the success of these two proposed models. The results of the AOA-SBLSTM-RNN deep learning model were analyzed with different evaluation criteria and achieved 97.67% and 97.89% success in the 1st and 2nd dataset, respectively. In this study, customer turnover was estimated efficiently and effectively. Further analysis can be done with time series methods. Xiahou and Harada (2022) have developed methods based on K-Means and SVM method to determine e-commerce customer losses of B2C E-commerce organization, because in e-commerce organizations, preventing customer losses and retaining customers is very important, especially in determining and implementing marketing strategies. For this reason, in this study, the temporal characteristics of customers' e-commerce shopping were modeled with k-means and SVM. Additionally, the proposed models were compared with logistic regression. However, expanding the customer segmentation applied in this study can also strengthen customer relationships.

The use of artificial intelligence and machine learning methods in CCP (Customer Churn Prediction) systems has increased the performance of businesses. Faritha et al. (2022). proposed an artificial intelligence-based CCP model for early prediction of customer churn in the telecommunications industry.The model called AICCP (AI-based CCP)-TBM (Telecommunication Business Markets) identifies customers in the telecom sector. It aims to prevent customer losses in the Telecom sector by identifying subscribed and non-subscribed customers. In addition, the AICCP-TBM model Chaotic Salp Swarm Optimization-based Feature Selection (CSSO-FS) determined the best features in three datasets. The AICCP-TBM model they applied on these datasets achieved 97.25%, 97.5% and 94.33% success, respectively. The proposed model can be used for CCP systems in real-time cloud data on large datasets.

Sana et al. (2022) developed a model based on machine learning techniques (Naïve Bayes, Random forest, Gradient boosting, KNN, Feed Forward Neural Networks, Logistic Regression, Recurrent Neural Networks) for CCP to identify customers who are likely to leave in the telecommunications industry. For this model, they used various data transformation (Box-Cox, Log, Z-Score, Rank) and feature selection methods on CRM (Customer Relationship Management) data. Grid search method was applied to determine and optimize the most optimum and best hyperparameters through univariate feature selection. Research was conducted on the TCI data set with sensitivity, recall, AUC, F-Score evaluation criteria. CCP prediction was increased by 26.2% and 17% in terms of AUC and F-Score, respectively. The proposed model can be tested on other telecommunications data and larger data sets.

In our study, the use of various 6 different machine learning methods on a bank customer churn data set is examined. Our aim is to identify the factors affecting bank customer churn and to determine the most effective model to predict customer churn using these factors. In our study, hyperparameter optimization was used to increase the success of all machine learning methods. By performing GridSearchCV optimization hyperparameter fine-tuning, the classification success, i.e. accuracy, of all proposed machine learning methods has been increased. The best parameter values for all methods proposed in this study were determined and presented in the application section. The accuracy of the proposed models with different evaluation criteria was analyzed and the success of the proposed models was compared. This study can help banks improve their strategies for managing customer relationships and allow for more effective measures to protect their customer base.

Method

In this section, all methods used in the study are shown.

Logistic Regression

Logistic Regression is a widely used machine learning technique for classification problems. Its main purpose is to estimate the probability of the dependent variable (outcome) based on the independent variables (predictor). It is often used in binary classification problems, meaning that the outcome can be split between two categories (such as pass or fail). Logistic regression transforms a linear combination of input features into a probability value using the sigmoid function (De Caigny et al., 2018). This probability value expresses the probability of belonging to a particular class. The training process occurs by comparing the probabilities predicted by the model with the observed labels. The model uses the maximum likelihood method to learn the parameters that best fit the data (Table 1) (Jain et al., 2020).

Table 1. Logistic regression advantages and dezavantages

Advantages	**Disadvantages**
Simplicity: The simplicity of the model makes it easy to implement and interpret.	Sensitivity to outliers: Logistic regression may be less flexible in tolerating outliers than nonlinear models.
Good performance: Linear models can work effectively even on large data sets.	Multi-class classification: Logistic regression focuses on binary classification by default and cannot be directly extended for multi-class classification problems.
Good interpretability: Coefficients help us understand the impact on each feature.	Assumption of linear relationship between independent variables: Logistic regression is based on the assumption of a linear relationship between independent variables. If such a relationship does not exist, the model may give misleading results.

Decision Tree

Table 2. Decision tree advantages and dezavantages

Advantages	**Disadvantages**
Understandability: Decision trees can be easily interpreted by users because the rules they create are clear and understandable.	Tendency to Overfit: They tend to fit too much to the data set, which can trigger overfitting and decreased generalization performance.
Easy Applicability: They do not require complex data preprocessing and can easily work with categorical/numeric data.	Sensitivity: They can be sensitive to small data changes, which can affect the stability of the model.
Determining Variable Importance Level: They can be used to evaluate the importance of each attribute in classification.	Complexity: As the dataset complexity increases, the constructed tree becomes more complex, which can reduce the understandability of the model.

Decision trees are a machine learning technique that identifies patterns in data sets using a tree structure to solve a classification or regression problem (Nie et al., 2011). Essentially, a decision tree creates a tree structure that represents a set of decision rules. Each node tests a specific range of values of an attribute and is divided into different branches based on this test result. This process is used to assign data points to a particular class or estimate a value (Table 2) (Hoppner et al., 2020).

Support Vector Machines (SVM)

SVM is a powerful and popular classification method used in machine learning and data mining (Zhao et al., 2005). This method sets decision boundaries to classify data and tries to minimize classification error. SVM is a technique that is generally effective on high-dimensional datasets and is used to solve nonlinear classification problems. SVM is a supervised learning algorithm that finds the best separation line (hyperplane) to separate data into two classes. SVM uses support vectors to find this hyperplane. This hyperplane performs the classification process by maximizing the margin between two classes. Support vectors are the data points closest to the classification boundary, and these points play a critical role in the classification decision. While SVM directly determines a hyperplane for linear separable data, for non-linear separable data it transforms the data into a higher dimensional space using kernel functions and makes distinctions there (Table 3) (Xia &J in, 2008).

Table 3. SVM advantages and dezavantages

Advantages	**Disadvantages**
High Accuracy: SVM offers high accuracy rates, especially on large and complex data sets. By maximizing the margin between classes, the model better separates the data and minimizes classification errors.	Computational Cost: SVM has high computational cost when working on large datasets and high-dimensional data. Training time can be long, which can be a limiting factor in big data applications.
Generalization Ability: SVM is resistant to overfitting problems. Thanks to the margin maximization strategy, the model can also show high performance on new and unprecedented data.	Hyperparameter Tuning: The performance of SVM depends on careful tuning of various hyperparameters. This can make the process of optimizing the model complex and time-consuming.
Flexibility: Thanks to kernel functions, SVM can solve both linear and non-linear classification problems. This makes it possible for the model to adapt to different types of data sets.	Significance: SVM can be difficult to explain how the model works and how the decision boundaries are determined. This can reduce the transparency and understandability of the model.

Gradient Boosting Classifier

Table 4. Gradient boosting classifier advantages and dezavantages

Advantages	**Dezavantages**
High Accuracy: Gradient Boosting often achieves high accuracy rates because it corrects errors at each step and improves the overall performance of the model.	Precise Parameter Tuning: Careful tuning of hyperparameters is necessary to optimize the performance of the model. Incorrect adjustments may reduce the performance of the model.
Flexibility: Can be used for both regression and classification problems.	Computational Cost: Gradient Boosting is computationally intensive and can be time consuming because it creates many trees.
Overfitting Control: Overfitting can be controlled thanks to parameter settings. In particular, hyperparameters such as learning rate and tree depth can be optimized to increase the generalization ability of the model.	Error Propagation: If the model makes large errors initially, these errors can propagate to subsequent trees, negatively impacting overall performance.
Feature Importance: Gradient Boosting is powerful in evaluating feature importance, which helps understand which features are more critical to the model.	Complexity: It is more complex than some other ensemble methods (e.g. Bagging) and requires more detailed knowledge of hyperparameter settings.

Gradient Boosting is a machine learning ensemble method that aims to create a strong learner by sequentially combining multiple weak learners (usually decision trees). This method gradually improves the model's performance by trying to correct errors at each step. Gradient Boosting in turn performs an optimization process on the outputs of tree-based models and repeats this process to reduce errors at each stage, increasing the accuracy of the final model (Table 4) (Raeisi&Sajedi, 2020). Gradient Boosting focuses on fixing errors step by step. The process can be summarized as follows (Gregory, 2018):

1. Creating the Initial Model: The process usually begins with the creation of a simple model (for example, a decision tree).
2. Calculation of Errors: Differences (residuals) between the predictions of the initial model and the actual values are calculated.
3. Training New Models: These residuals are estimated with a new decision tree. The new tree learns from these mistakes in the best possible way.
4. Model Update: The new tree is added to the existing model and the model's predictions are updated.
5. Iteration: Steps 2-4 are repeated for a certain number of iterations (or until errors are sufficiently reduced).

K-Nearest Neighbors

K-Nearest Neighbors (KNN) is a simple but powerful classification and regression algorithm used in machine learning. Developed by Evelyn Fix and Joseph Hodges in 1951, KNN is known for working effectively especially on small and medium-sized data sets. KNN takes into account the labels or values of its nearest *k* neighbor to classify a particular data point or predict a value. Euclidean distance is usually used to determine neighbors, but other distance measurements can also be used (Table 5). The KNN algorithm works by storing training data in memory and refers to this training data when classifying or predicting a new data point. Its operation can be summarized as follows (Sjarif et al., 2019):

1. Parameter Selection: kkk value is determined. This indicates how many neighbors will be taken into account.
2. Distance Calculation: Distances between the new data point and all points in the training data set are calculated.
3. Determining Neighbors: The closest neighbor is selected.
4. Classification/Prediction:

- Classification: The class of the new data point is determined by looking at which neighbors' labels are most common.
- Regression: The value of the new data point is estimated by averaging the values of the neighbors.

Table 5. KNN classifier advantages and dezavantages

Advantages	**Dezavantages**
Simplicity: The KNN algorithm is quite simple and understandable. It does not require complex mathematical modeling.	Memory Usage: Memory usage can be a problem in large data sets as it needs to store the entire training data in memory.
No Training Period: There is no training phase; This is done by storing the training data in memory and therefore training time is negligible.	Computational Cost: In large data sets, classifying a new data point can take a lot of time. Since distance must be calculated with all training data, it is costly.
Adaptability: It can easily adapt to different data types and distributions.	Sensitivity to Records: Noisy and redundant data can negatively impact the performance of KNN.
Flexibility: It can be used in both classification and regression problems.	Attribute Scaling: Different scales of attributes in the data may affect distance calculations. Therefore, the data needs to be scaled beforehand.
Effective on Small Data Sets: KNN can provide very effective results on small and medium-sized data sets.	Complexity Parameter k: Choosing the appropriate k value is critical. While too small k value may cause overfitting, too large k value may lead to underfitting.

Multi-Layer Perceptron

Multi-Layer Perceptron (MLP) is the simplest and most widely used type of artificial neural networks, one of the basic building blocks of deep learning (Ismail et al., 2015). MLP is a feed-forward neural network model that contains multiple layers and multiple neurons (perceptrons) in each layer. MLP is an artificial neural network consisting of an input layer, one or more hidden layers, and an output layer. Each neuron takes inputs from the previous layer, weights those inputs, and calculates its output through an activation function. This process ensures the network's ability to learn and ensures the flow of information from inputs to outputs.

- Input Layer: This is the first layer that receives input data. Each neuron corresponds to an input feature.
- Hidden Layers: One or more layers located between the input layer and the output layer. These layers enable the network to learn complex relationships.
- Output Layer: It is the last layer and produces the final predictions or classifications of the network.

The working principle of MLP consists of two main steps: feedforward and backpropagation (Tang et al., 2020):

1. Feedforward: Input data is passed through the layers of the network and each neuron produces an output by weighting the inputs it receives and applying an activation function. This output is given as input to the next layer and the process continues until it reaches the output layer.
2. Backpropagation: The error between the model's predictions and the actual values is calculated. This error is propagated backwards to adjust the weights of the network. The goal is to minimize the error function, and this is accomplished using optimization algorithms such as gradient descent.

Commonly used activation functions in MLP are:

- Sigmoid: Compresses the output between 0 and 1, especially used in the output layer.
- ReLU (Rectified Linear Unit): If the input is positive, it leaves it as is, if it is negative, it resets it. It is widely used in deep networks.
- Tanh: Compresses the output between -1 and 1, reducing the gradient vanishing problem.

Multi-Layer Perceptron (MLP) is one of the cornerstones of artificial neural networks and forms the basis of deep learning models. It is capable of learning and modeling complex data relationships, thanks to feedforward and backpropagation processes between input, hidden and output layers. However, it has disadvantages such as high computational costs and hyperparameter tuning difficulties. Nevertheless, it has been used successfully in a wide range of applications due to its flexibility and generalization capacity.

Table 6. MLP classifier advantages and dezavantages

Advantages	**Dezavantages**
Flexibility and Power: MLP has the ability to learn and model complex data sets. In particular, its multi-layered structure can capture complex relationships in data sets.	Computational Costs: Training MLPs can be quite time-consuming and computationally intensive, especially for large data sets and networks with large numbers of layers and neurons.
Generalization Capacity: A sufficiently large and deep MLP can generalize data effectively and perform well on previously unseen data points.	Hyperparameter Tuning: The performance of MLPs depends on many hyperparameters such as number of layers, number of neurons, learning rate, and activation functions. Optimizing these hyperparameters can be complex and time-consuming.
Universal Approximation: Theoretically, a sufficiently large MLP can approximately model any continuous function with arbitrary accuracy.	Overfitting: A very large network may lose its ability to generalize by overfitting the training data. To avoid this situation, regularization methods and cross-validation techniques are used.

Experimental Study

The data set used in this study represents the customer base of a bank in Figure 1 (https://www.kaggle.com/datasets/saurabhbadole/bank-customer-churn-prediction-dataset/data). The data set includes various characteristics of customers, such as demographics (age, gender, geographic location), financial status (credit score, balance, estimated income), and interactions with bank products. It contains a total of 10,000 customers and 14 attribute columns. The data set is as follows (Figure 1): The data set contains the following columns:

1. RowNumber: Shows the row number that specifies the row for customers in the data set.
2. CustomerId: Shows the id number of the customers registered in the data set.

3. Surname: Shows the surname of the customers registered in the bank.
4. CreditScore: A numerical value that represents the customer's credit history. A high credit score generally indicates financial stability and credit availability.

	RowNumber	CustomerId	Surname	CreditScore	Geography	Gender	Age	Tenure	Balance	NumOfProducts	HasCrCard	IsActiveMember	EstimatedSalary	E
0	1	15634602	Hargrave	619	France	Female	42	2	0.00	1	1	1	101348.88	
1	2	15647311	Hill	608	Spain	Female	41	1	83807.86	1	0	1	112542.58	
2	3	15619304	Onio	502	France	Female	42	8	159660.80	3	1	0	113931.57	
3	4	15701354	Boni	699	France	Female	39	1	0.00	2	0	0	93826.63	
4	5	15737888	Mitchell	850	Spain	Female	43	2	125510.82	1	1	1	79084.10	
...	...	...	...	...	...	...	...	...	...	...	...	...	...	
9995	9996	15606229	Obijiaku	771	France	Male	39	5	0.00	2	1	0	96270.64	
9996	9997	15569892	Johnstone	516	France	Male	35	10	57369.61	1	1	1	101699.77	
9997	9998	15584532	Liu	709	France	Female	36	7	0.00	1	0	1	42085.58	
9998	9999	15682355	Sabbatini	772	Germany	Male	42	3	75075.31	2	1	0	92888.52	
9999	10000	15628319	Walker	792	France	Female	28	4	130142.79	1	1	0	38190.78	

10000 rows × 14 columns

Figure 1. Bank dataset analysis for customer churn prediction

5. Geography: The geographical region where the customer lives. This information can be used to analyze whether there are differences in bank abandonment rates or behavior of customers in different regions.
6. Gender: The gender of the customer. It can be used to examine the impact of gender on customer abandonment rates.
7. Age: A numerical value representing the customer's age. Age can be a significant factor in customer abandonment rates.
8. Tenure: A numerical value that expresses how long the customer has been in the bank. It can have a significant impact on customer loyalty.
9. Balance: The balance in the customer's bank account. This provides information about the customer's financial situation and may influence the abandonment decision.
10. NumOfProducts: Number of products purchased by the customer from the bank. It can indicate the customer's level of interaction with the bank.
11. HasCrCard: A binary variable indicating whether the customer has a credit card. This may reflect customer shopping habits and propensity to use bank products.
12 IsActiveMember: A binary variable indicating whether the customer is an active member. Active membership can indicate the customer's level of interaction with the bank.
13. EstimatedSalary: The customer's estimated annual salary. This provides additional information about the customer's financial situation.
14. Exited: A binary variable indicating whether the customer has left the bank. This represents the target variable in the data set and is the main focus to be analyzed.

The preprocessing steps performed on the data set are:

1. Examining and Filling in Missing Values: First, it was checked whether there were missing values in the data set. When missing values were detected, the missing values in the columns containing the missing values were filled in with an appropriate strategy. This is usually accomplished using the mean, median, or most frequent value.
2. Removal of Unnecessary Columns: Columns that were considered unnecessary for the analysis (such as Customer Identification Number and Customer Surname) were removed from the data set. These columns contain information that has no impact on the results of the analysis or is semantically unimportant.
3. Coding of Categorical Variables: Categorical variables were converted into numerical values for the modeling process. In this step, categorical variables such as geographic region and gender were converted to numerical values using methods such as label coding or one-hot coding.
4. Feature Scaling: Finally, numerical features were scaled to improve model performance. Scaling is usually done using Standardization or Normalization methods. In this way, the range of values between different features is balanced and the model works better.

These preprocessing steps make the dataset usable by machine learning models and increase the accuracy of the model. After the pre-processing steps, the final version of the data set is in Figure 2:

	CreditScore	Geography	Gender	Age	Tenure	Balance	NumOfProducts	HasCrCard	IsActiveMember	EstimatedSalary	Exited
0	-0.326221	0	0	0.293517	-1.041760	-1.225848	-0.911583	1	1	0.021886	1
1	-0.440036	2	0	0.198164	-1.387538	0.117350	-0.911583	0	1	0.216534	0
2	-1.536794	0	0	0.293517	1.032908	1.333053	2.527057	1	0	0.240687	1
3	0.501521	0	0	0.007457	-1.387538	-1.225848	0.807737	0	0	-0.108918	0
4	2.063884	2	0	0.388871	-1.041760	0.785728	-0.911583	1	1	-0.365276	0

Figure 2. Bank dataset pre-processing for customer churn prediction

Examining the distribution of data in the data set and the relationships between variables constituted one of the critical steps in the data analysis process. Understanding the distribution of the data helped to see the overall structure and characteristics of the data set, while understanding the relationships between variables guided the modeling process.

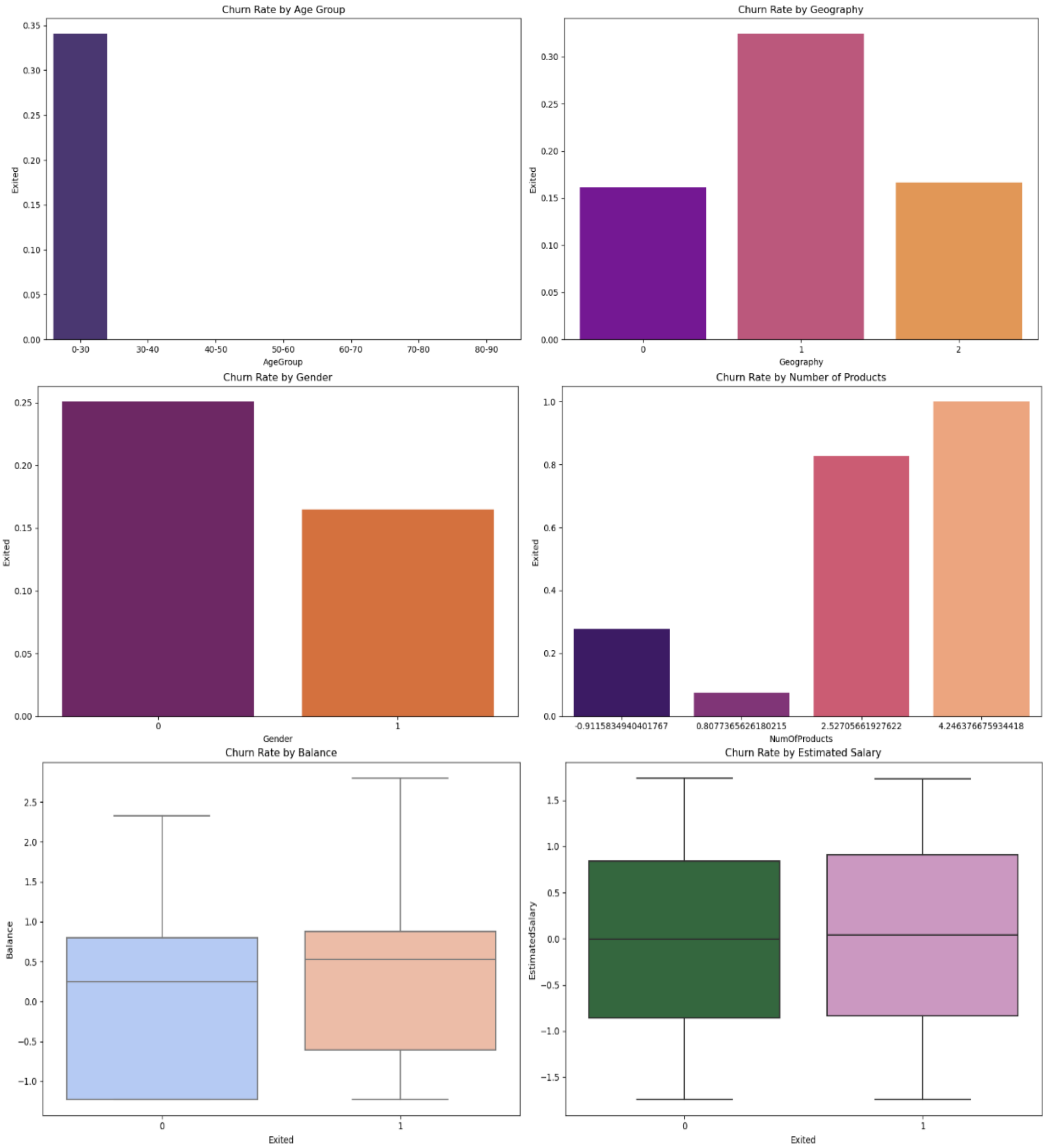

Figure 3. Bank dataset features for customer churn prediction

First, various graphical methods were used to understand the basic statistical properties of the data set. Histograms were created to examine the distribution of numerical variables. For example, the histogram showing the distribution of customer age revealed how the ages of customers were distributed and whether there were concentrations in certain age ranges. Histograms helped quickly understand the overall distribution of the data set by visualizing the frequencies of certain values in the data set.

Column charts were used to analyze the distribution of categorical variables in Figure 3. These charts show how many data points are in each category. For example, when analyzing the geographical distribution of customers, the number of customers in each geographic region was visualized. This analysis helped understand in which regions customers are concentrated and customer behavior in certain regions.

While analyzing the data set, a correlation matrix was used to better understand the relationships between variables and this matrix was displayed graphically. The correlation matrix measures the linear relationship between each pair of variables and usually takes values between -1 and 1. A value of -1 indicates a completely negative correlation between two variables; A value of 1 indicates a completely positive correlation. A value of 0 indicates that there is no linear relationship between the two variables. By visualizing this matrix, relationships between variables in the data set can be detected more easily and quickly.

A heatmap was used to graphically represent the correlation matrix. The heat map represents correlation values with color tones, so it can be quickly visually discerned which pairs of variables have strong or weak correlations. The color tones on the chart indicate positive correlations, generally with warmer (red) colors, and negative correlations with cooler (blue) colors. Increasing color intensity indicates increasing strength of the correlation.

Numerical variables of the data set were used to create the correlation matrix. In this way, the relationships between variables such as credit score, age, balance, number of products, credit card ownership status, active membership status and estimated salary were examined. Looking at the correlation matrix, it was found that some variables had high correlations with each other, while others showed low correlations. This information guided the study on which variables should be included in the model when establishing a logistic regression model.

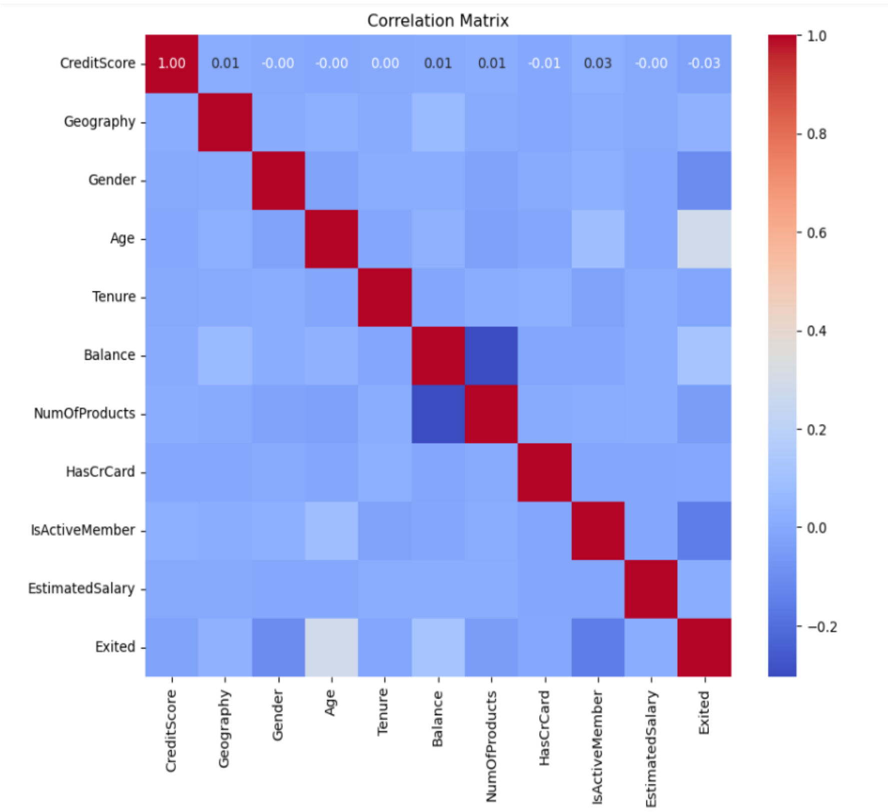

Figure 4. Correlation analysis for customer churn prediction

For example, a negative correlation has been observed between customer age and credit score (Figure 4). This may indicate that your credit score decreases with age. Similarly, a positive correlation was found between customer balance and estimated salary, which may indicate that as salary increases, bank balance also increases. This information from correlation analysis helped us understand the structure of our data set and make more informed decisions when building our logistic regression model.

By analyzing the distribution of data in the data set and the relationships between variables with these methods, the general structure of the data set was better understood. This understanding allowed more informed decisions to be made during the modeling process and provided important information in preparation for advanced analysis methods such as logistic regression model. Understanding the distribution and correlations of the data played a critical role in both the data cleaning and preprocessing steps and the model building and evaluation stages.

Logistic Regression

While applying the logistic regression model, various factors were taken into consideration to improve model performance. Among these, trying to get the best performance by trying different parameter combinations using GridSearchCV, making appropriate parameter adjustments to prevent problems such as overfitting and underfitting, reliably evaluating the performance of the model with the cross-validation method, selecting parameter values appropriately for the problem and data set, unbalanced classes. There are factors such as addressing and taking precautions if necessary. These factors are very important to increase the accuracy of the model and obtain reliable results.

As a result of the hyperparameter grid search, it was determined with which hyperparameters the best performance of the model was achieved. According to the hyperparameter grid search results for the Logistic Regression model, the hyperparameter combinations that achieved the best performance were determined. During this analysis process, different regularization forces (C), penalty norms (penalty) and optimization algorithms (solver) were evaluated in order to optimize the accuracy of the model. The grid search result graph visualizes the model's accuracy scores for each hyperparameter combination. Logistic Regression Hyperparameter Grid Search chart values and results of the data set are as shown in the chart below:

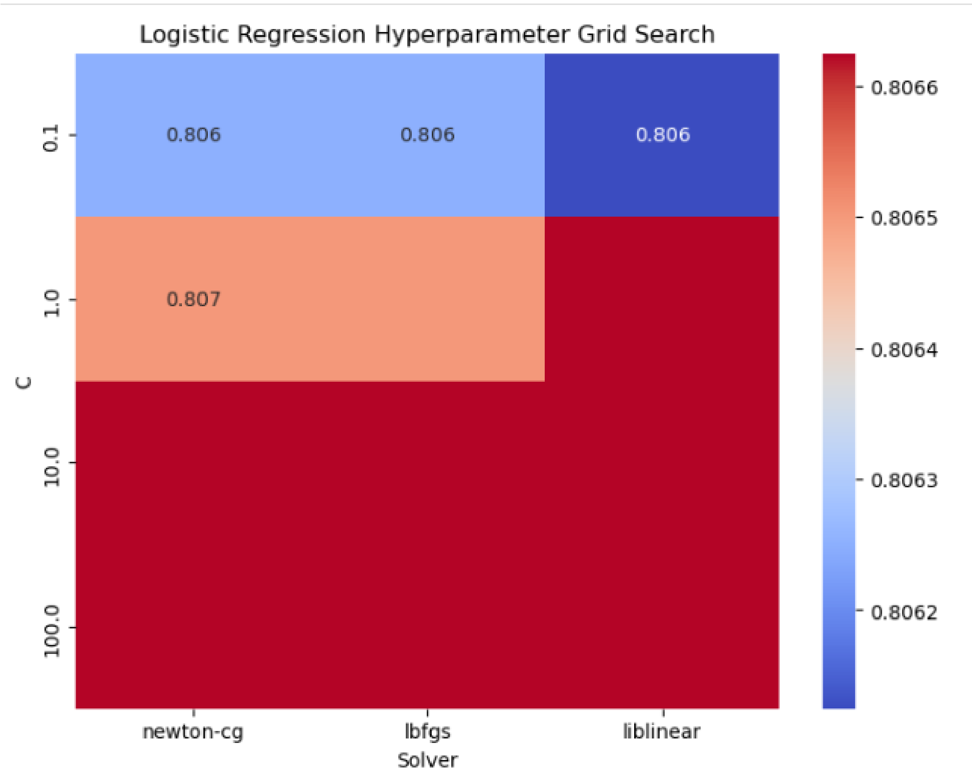

Figure 5. Logistic regression hyperparameters gridseacrh CV

Figure 5 shows that the highest accuracy scores are concentrated in certain combinations of hyperparameters. In particular, it has been observed that the combination where the 'C' value is '1' and the 'penalty' value is 'l2' has the highest accuracy. This finding shows that the model achieves its best performance with these hyperparameters. Another important finding is that the performance of the model increases significantly when 'liblinear' is used as the 'solver' parameter. This solver is known for performing well, especially on small datasets and low-dimensional data. The hyperparameter grid search plot reveals that the C value inversely determines the strength of regularization, with medium-sized C values (0.1, 1, 10) providing higher accuracy. It has been observed that extremely large or extremely small C values may negatively affect the performance of the model. Therefore, the C value must be chosen carefully. When looking at the penalty parameter, it is seen that the l2 norm generally provides higher accuracy. Different performances were observed between L1 (Lasso) and L2 (Ridge) norms, and it was understood that the L2 norm was more effective in terms of regularization. This shows that the l2 norm is more successful in reducing the overfitting problem of the model.

As a result of the hyperparameter grid search, it was determined with which hyperparameters we achieved the best performance of our model. In particular, it was determined that the model reached the highest accuracy when C value was used as 1, l2 as penalty and liblinear as solver. These combinations of hyperparameters can be used to optimize our model and obtain more reliable results. This process contributes to more effective and efficient use of the model in real-world applications. As a result, the best hyperparameter combinations for the Logistic Regression model were determined thanks to the hyperparameter grid search chart. These combinations can be used to increase the model's accuracy and optimize prediction performance. Retraining the model with the best hyperparameters will enable more accurate and reliable predictions.

Figure 6 showing the best hyperparameters of our Logistic Regression model and the accuracy values obtained with these hyperparameters is an important tool to evaluate the performance of the model. This graph visualizes the impact of different combinations of C (inverse regularization strength), Threshold (decision making threshold), Tol (tolerance) values on accuracy. First, the C value represents the regularization parameter of the logistic regression model. This value determines how complex or simple the model will be. Looking at the results in the graph, it can be seen that C varies between 0.6 and 0.7. In this range, it can be said that the model is optimized and performs well. The Threshold value determines how classification decisions are made in the logistic regression model. According to the data in the chart, the threshold value varies between 0.2 and 0.3. This value indicates how precise or flexible the model will classify. The Tol value is a tolerance value that determines when the model converges. According to the data in the chart, the tol value varies between 0.0 and 0.1. This value indicates how accurate the model is in the optimization process.

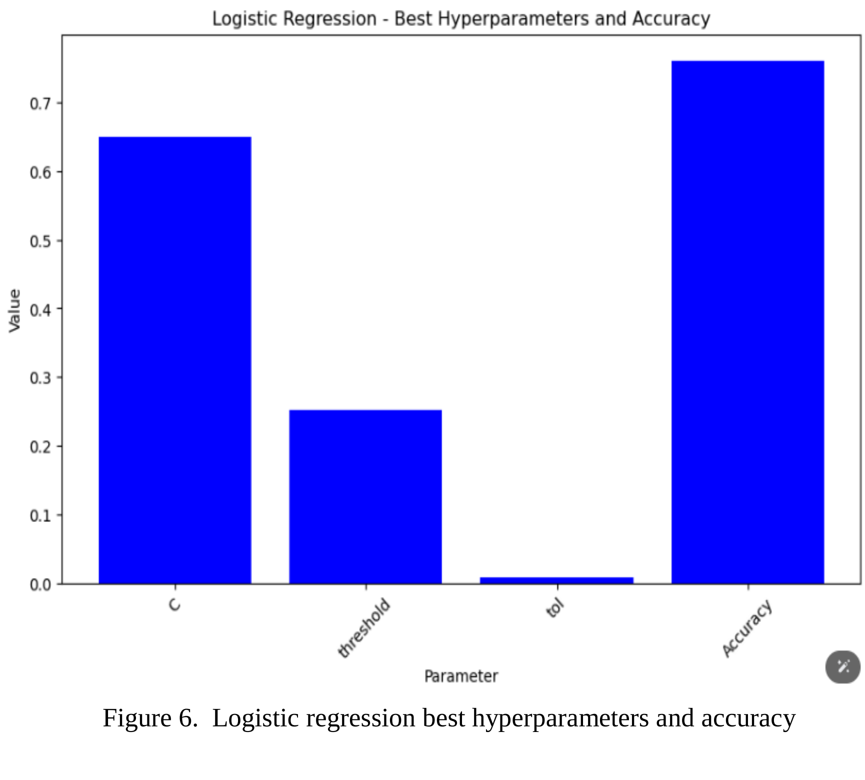

Figure 6. Logistic regression best hyperparameters and accuracy

Decision Tree

The optimized decision tree model is evaluated on the test data set and the results are visualized. Additionally, the performance and accuracy values of the decision tree model according to its parameters are examined comparatively. Decision Tree Hyperparameter Grid Search chart values and results for the data sets are as shown in Figure 7:

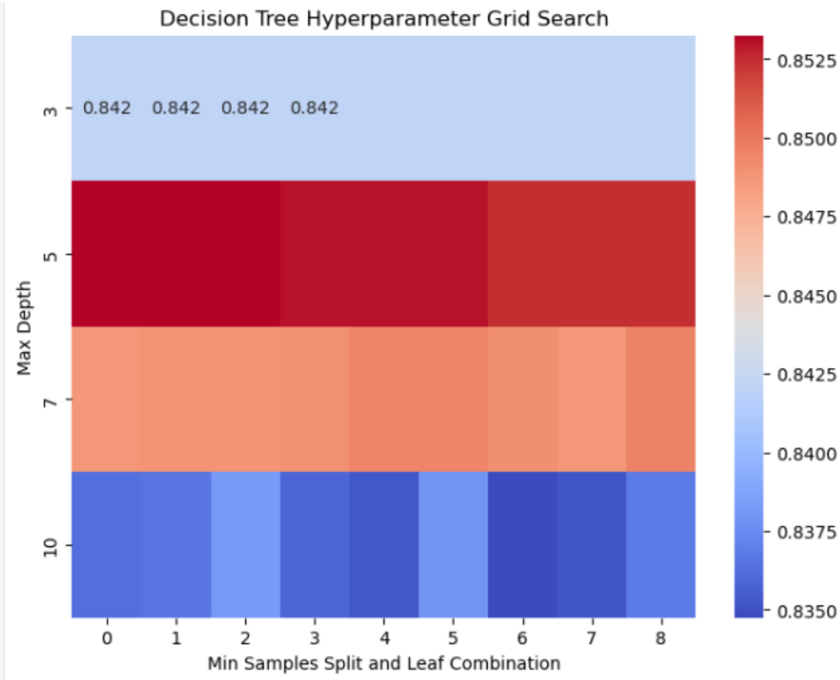

Figure 7. Decision tree hyperparameters GridSeacrh CV

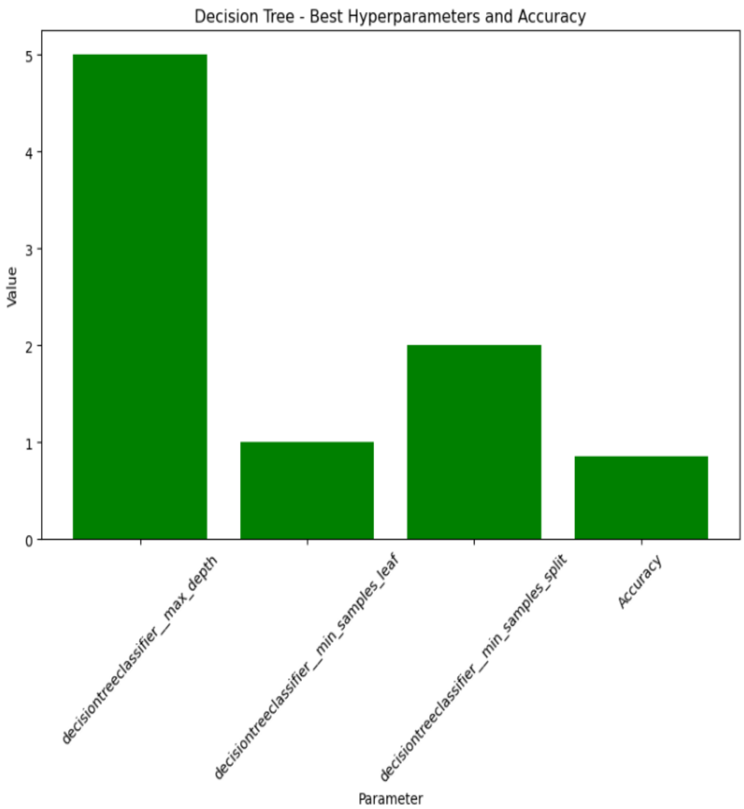

Figure 8. Decision tree hyperparameters and accuracy

- Max Depth: Determines the maximum depth of the tree. As tree depth increases, the model becomes more complex and can better fit the training data, but it can also become prone to overfitting. By choosing various depths such as 5, 10, 15, 20, 25, it was aimed to test the performance of the model at different complexity levels.
- Min Samples Split: Specifies the minimum number of samples required to split an internal node. If this value is low, the model may make more divisions and its complexity increases. By selecting values of 2, 5, 10, 15, 20, the effect of division operations on the model performance was examined.
- Min Samples Leaf: Determines the minimum number of samples that should be present in a leaf node. If this value is low, the model may make more divisions. By choosing values of 1, 2, 5, 10, 15, the effect of the minimum number of samples in leaf nodes was examined.
- Criterion: Determines the criterion to be used in divisions. There are two options, 'gini' and 'entropy'. Both criteria were selected and it was tested which criterion provided better performance.

If we interpret the Figure 8 in detail, the maximum depth values on the X axis vary as 5, 10, 15, 20 and 25. In general, a moderate maximum depth (for example, 10) performs better. The combined effect of min_samples_split and min_samples_leaf values on the y axis was examined. It is observed that the performance improves when these two parameters, which vary along the y-axis in the graph, take higher values.

The color tones in the graph visually present the performance of different hyperparameter combinations. Dark colors represent higher performance and light colors represent lower performance. This visual analysis helps determine which hyperparameter values should be selected to achieve the best performance. The best parameter combinations obtained as a result of Grid Search were used to increase the accuracy of the model. Optimal parameters provide better performance by balancing the complexity and generalization ability of the model. In conclusion, the Decision Tree Hyperparameter Grid Search chart shows how different parameter combinations affect model accuracy. By analyzing this graph, we can select the parameters where the model performs best and minimize the risk of overfitting. According to the graphical results obtained from the code, the accuracy of the model was maximized by selecting the optimum values of the max_depth and min_samples_split parameters.

Support Vector Machines (SVM)

The model is trained with the best hyperparameter values obtained after the Grid Search process, and its accuracy is measured on the test data set. This metric shows how well the model performs under the conditions where it achieves its best performance. The results obtained provide important information about the generalization ability and accuracy rate of the model. This analysis is a critical step to evaluate how well the model works with real-world data. The SVM model was created with StandardScaler using the 'make_pipeline' function. This ensures standardization of features across the dataset and helps the model perform better. GridSearchCV is trained to determine the best parameters of the model using the specified hyperparameter grid. 5-fold cross validation determined by the 'cv' parameter was used. Then, the best model was evaluated with the test data and the test accuracy score was calculated. This value indicates the generalization ability of the model. Finally, the accuracy scores of the hyperparameter combinations were visualized using a heat map. This heatmap shows the average accuracy scores obtained for different C and gamma values, using color coding.

Figure 9 shows the average accuracy scores obtained for different C and gamma values. Each cell corresponds to a specific combination of C and gamma values. The graph visualizes the accuracy scores of these combinations using color coding. Dense colors represent higher accuracy scores, while lighter colors represent lower accuracy scores. Therefore, it is possible to get an idea about which combinations of hyperparameters achieve the best performance. For example, when the C value is 1 and the gamma value is 'scale' (with a high accuracy score), the RBF kernel may be the best preferred configuration. However, the heat map must be taken into account to observe the interaction of different C and gamma values. For example, one can examine how accuracy scores change if gamma is 'scale' and 'auto' for a given C value. Such analyzes are important to understand which hyperparameters and their values of the model provide the best performance.

- When C Value is 1: The highest accuracy scores were obtained with the 'scale' gamma value. This combination allows the model to perform well on both training and testing data.
- When C Value is 10: Performance decreases slightly, which indicates that the model may be slightly overfitting.
- When C Value is 0.1: The accuracy score is lower, which indicates that the model is not complex enough and the accuracy rate decreases.

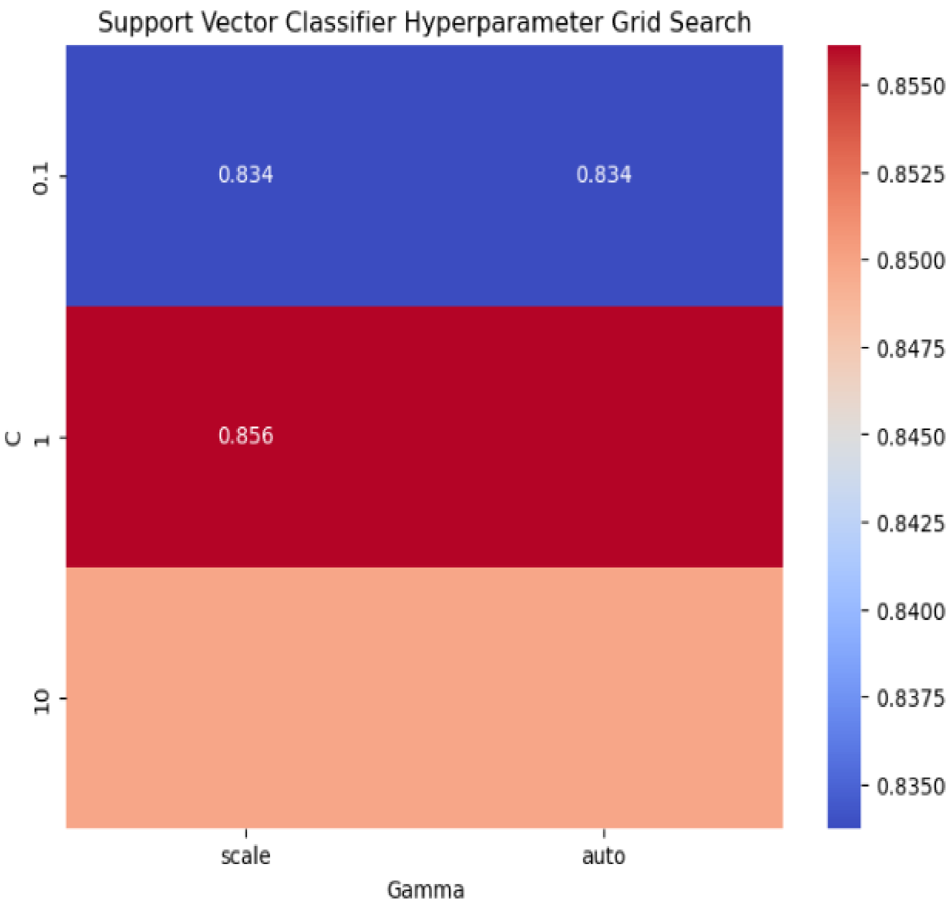

Figure 9. SVM hyperparameters GridSeacrh CV

When the 'C' value is selected as 1, the model performs well in balancing errors and correct classifications. When the 'Gamma' value is set to 'scale', this parameter is automatically scaled according to the characteristics of the data set. When 'rbf' (radial basis function) is selected as the 'kernel' type, the model can better learn complex relationships between classes. The best CV score was found to be 0.8561. This score expresses how well the model performs on the training data. This score, obtained by 5-fold cross-validation, also provides information about the generalization ability of the model.

The test accuracy score was found to be 85.75%. This score is the accuracy rate achieved by the model on test data. The model trained with the best parameters determined during training performed with an accuracy rate of 85.75% on the test data. This shows that the model can also perform well on real-world data.

Gradient Boosting Classifier

Gradient Boosting Classifier (GBC) was optimized using grid search method for various hyperparameters. In this analysis, the effects of three main hyperparameters such as learning rate, number of estimators and maximum depth were evaluated. In particular, a heatmap was created to visualize the effect of the learning rate and the number of trees on the performance of the model (Figure 10).

The best hyperparameters were determined as n_estimators (number of trees) 200, learning_rate (learning rate) 0.1 and max_depth (maximum depth) 3. This combination achieved the highest average accuracy score (0.869) during the cross-validation (CV) process. These parameters were determined as the combination that achieved the highest average accuracy score during the cross-validation (CV) process. The model trained with the best hyperparameters was also evaluated on the test data set and a result of 86.75% was obtained for test accuracy. This result demonstrates the performance of the model on real-world data and is consistent with the high accuracy score obtained during cross-validation. The graph showing the best parameters and accuracy value is as follows:

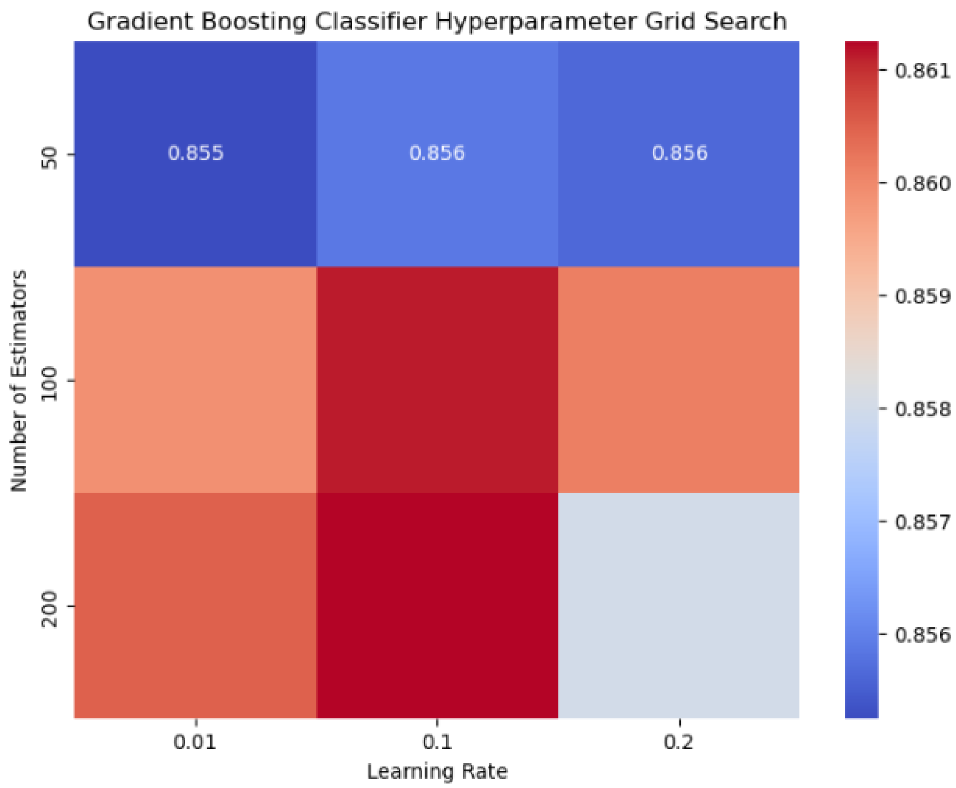

Figure 10. Gradient boosting classifier hyperparameters GridSeacrh CV

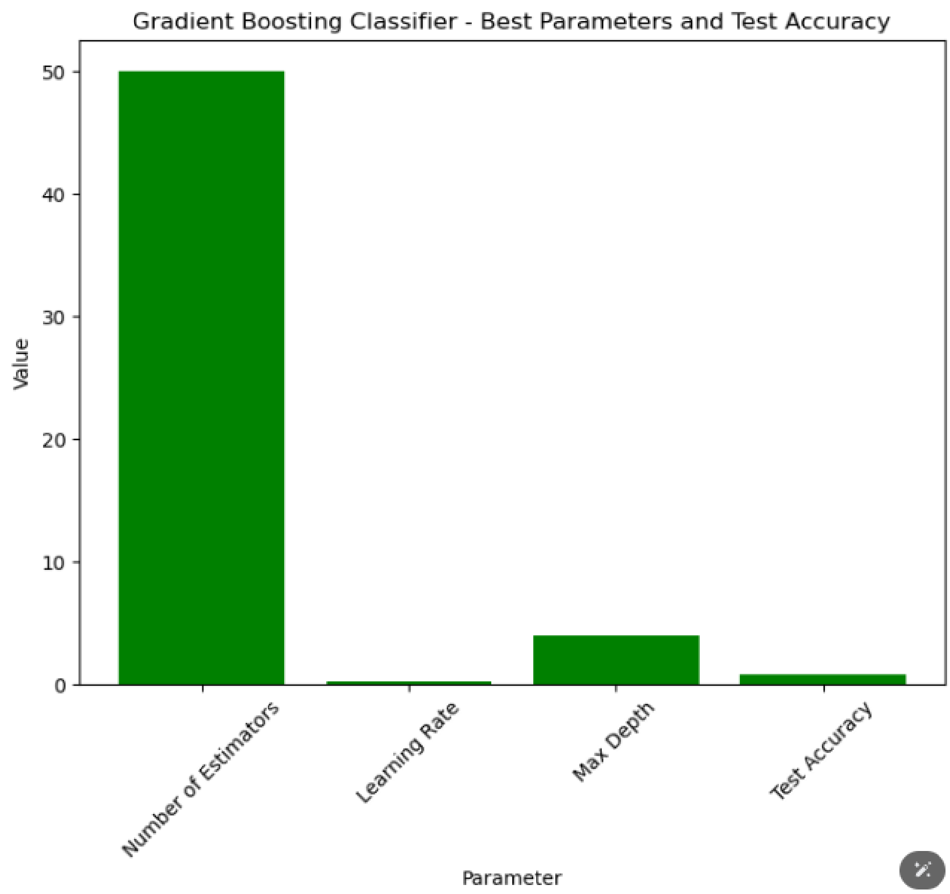

Figure 11. Gradient boosting classifier best parameters and test accuracy

Heatmap visualizes the average accuracy scores obtained during the grid search process, based on the learning rate and number of trees parameters. This visualization helps us understand how hyperparameter combinations affect model performance (Figure 11).

- Higher accuracy scores were obtained with a learning rate between 0.1 and 0.2.
- It has been observed that accuracy scores generally increase as the number of trees increases (from 50 to 200). This shows that more trees make the model more powerful and generalizing.

Learning Rate:

- 0.01: Low learning rate is generally associated with low accuracy scores. This causes the model to learn slowly and therefore not generalize well enough.
- 0.1: It is seen as the optimal learning rate. In this range, the model learns fast enough while also showing good generalization capacity.
- 0.2: Although high accuracy scores were obtained, it was observed that a learning rate of 0.2 could lead to overfitting in some cases.

Number of Trees:

- 50: Low number of trees is generally associated with low accuracy scores. This indicates that the model is not complex enough and fails to capture the complex structure of the data.
- 100 and 200: Higher tree numbers significantly increased the performance of the model. In particular, the highest accuracy scores were achieved with 200 trees.

Best Combination:

- n_estimators=200 and learning_rate=0.1: This combination represents the region on the heatmap where the highest accuracy scores were obtained. This indicates that these parameters are optimal and maximize the generalization ability of the model.

Heatmap analysis is an important tool in determining optimal hyperparameter combinations for the Gradient Boosting Classifier. This analysis shows which hyperparameters are more effective to maximize the performance of the model. The model, with a learning rate of 0.1 and number of trees of 200, achieved high accuracy scores on both cross-validation and the test data set, confirming that this combination gave the best results. These findings provide valuable information on how to optimize the Gradient Boosting Classifier model on a specific data set and serve as a guide for future work.

K-Nearest Neighbors

The K-Nearest Neighbors (KNN) algorithm is a method that attracts attention with its simplicity and flexibility in the field of machine learning. It can provide effective results especially on small and medium-sized data sets. However, it has disadvantages such as computational cost and memory usage in large data sets. With the selection of appropriate hyperparameters and correct scaling of the data, KNN can be used successfully in many application areas. Selection of the most appropriate algorithm for a particular problem should be made by taking into account the advantages and disadvantages of KNN. Here, a heatmap was created that visualizes the results of the Grid Search process performed to optimize the hyperparameter settings of the K-Nearest Neighbors (KNN) algorithm. This map is used to visualize how different combinations of hyperparameters affect the performance of the model .

Figure 12, the horizontal axis represents the weights hyperparameter, and the vertical axis represents the n_neighbors (number of neighbors) hyperparameter. Each cell shows the average cross-validation score for the corresponding hyperparameter combination. This value reflects how well the model performs with a particular combination of hyperparameters.

- Horizontal Axis: Weights

1. uniform: Gives equal weight to all neighbors.

2. distance: Gives neighbors weight inversely proportional to their distance; that is, closer neighbors are given more weight.

- Vertical Axis: Number of Neighbors

o 3, 5, 7: Specifies how many neighbors the model will take into account. Lower values may cause the model to be more complex and overfitting, while higher values may cause it to be simpler and more generalizing (underfitting).

- Color Scale and Scores

o Color scale represents average cross-validation scores. Darker colors (especially dark red) indicate lower validation scores, and lighter colors (toward yellow) indicate higher validation scores.

o The numerical value in each cell indicates the average cross-validation score obtained with the corresponding hyperparameter combination.

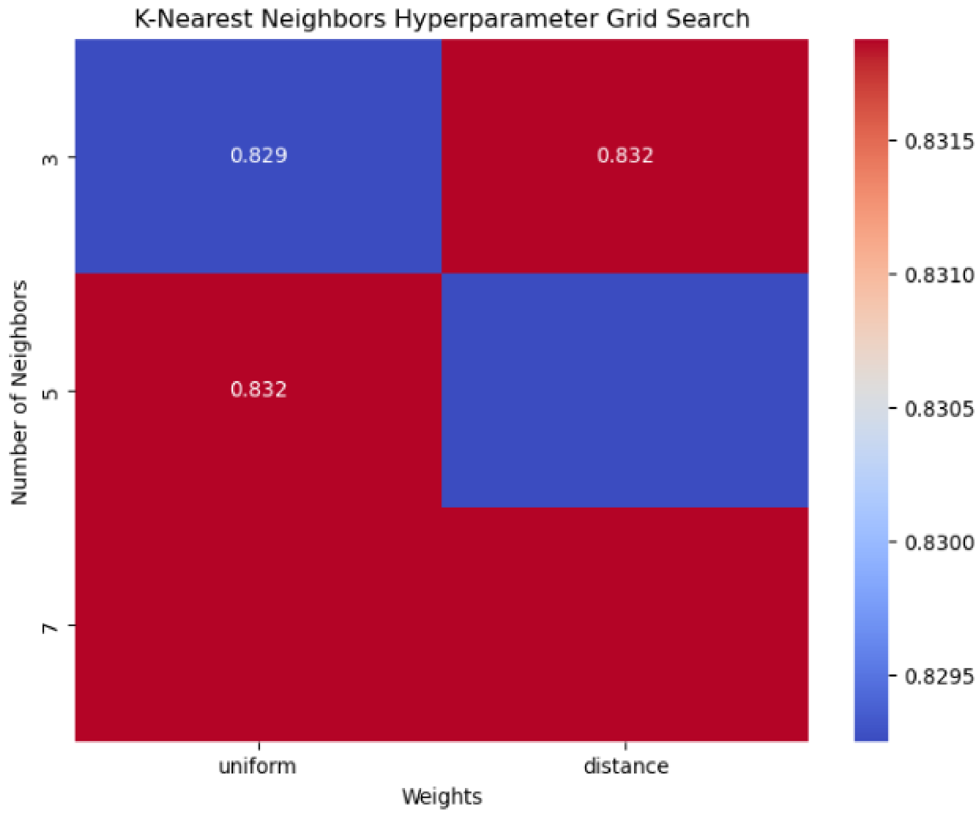

Figure 12. KNN hyperparameter GridSearchCV

In general, we can observe that the 'distance weighting method provides higher validation scores than the 'uniform' method. This suggests that giving more weight to closer neighbors can improve the performance of the model. When the number of neighbors was 5 or 7, higher validation scores were obtained, especially with the distance weighting method. This indicates that the number of neighbors must be carefully selected to achieve the optimal performance of the model. It is observed that the highest scores are obtained in combinations of n_neighbors = 5 or 7 and weights = distance. This indicates that the best combination of hyperparameters lies at these values.

This heatmap was used to visualize how the hyperparameters (number of neighbors and weighting method) of the K-Nearest Neighbors model affect the model performance. The best validation scores were obtained in combinations where the number of neighbors was 5 or 7 and the weighting method was distance. This analysis highlights the importance of choosing the right hyperparameters to improve the performance of the model. Such visualizations are a critical tool for optimizing the model and achieving the best results.

Multi-layer Perceptron

Grid search was used to optimize the hyperparameters of the MLP model. The determined hyperparameters are in Figure 13:

- hidden_layer_sizes: Number of neurons in the hidden layer (determined as 50 and 100).
- activation: Activation function (Only 'relu' is used in our study).
- solver: Optimization algorithm (Only 'man' is used in our study).
- alpha: L2 regularization parameter (set as 0.0001 in our study).
- learning_rate: Learning rate (specified as 'constant' in our study).

As a result of the grid search, it was seen that the best hyperparameters (hidden_layer_sizes: (100,), activation: 'relu', solver: 'adam', alpha: 0.0001, learning_rate: 'constant') were determined and the cross-validation (CV) score of the model was measured as 0.875. . The model obtained with these hyperparameters showed successful performance on the dataset. In addition, the Heatmap method enabled the effect of certain hyperparameter combinations to be easily seen on model performance. While creating the heatmap, cross-validation scores were calculated for each hyperparameter combination and the best combination was determined using these scores. This heatmap is created only for hidden_layer_sizes and activation hyperparameters. Other hyperparameters (solver, alpha, learning_rate) were kept constant. The heatmap's axes are as follows:

- On Y Axis: hidden_layer_sizes (Numbers of Neurons in the Hidden Layer)
- On X Axis: activation (Activation Function)

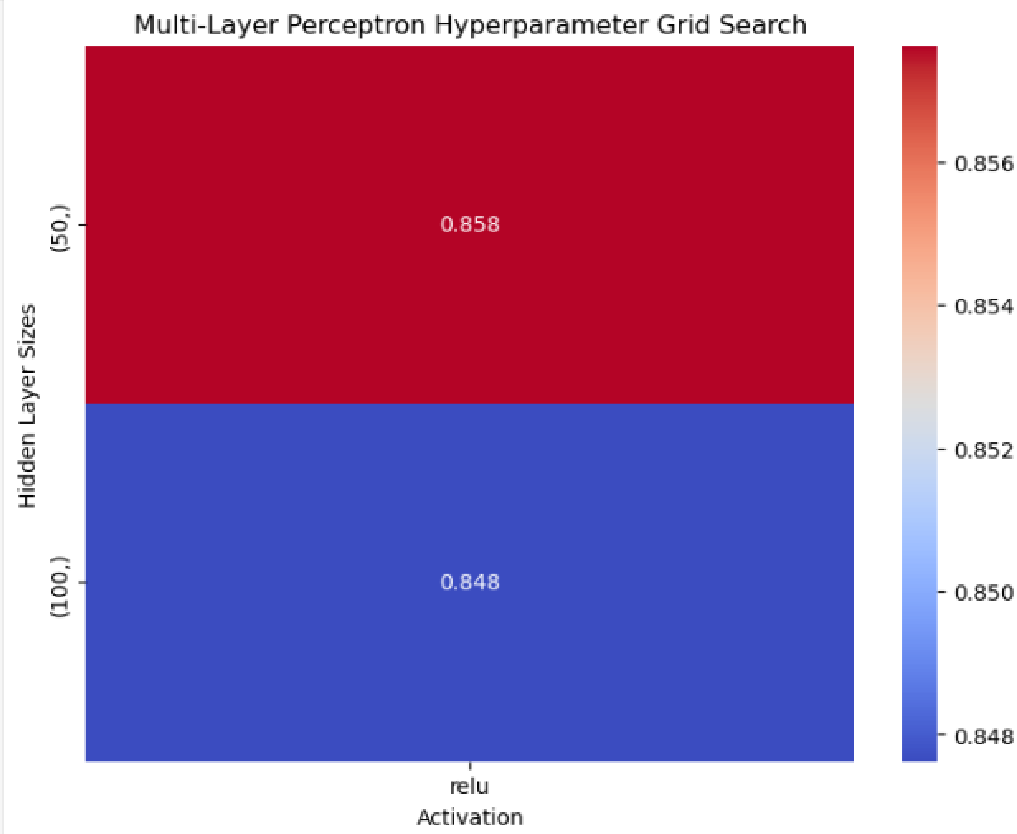

Figure 13. MLP hyperparameter GridSearchCV

However, since only the 'relu' activation function is used in this example, the X-axis represents a single value.

- Scores of hidden_layer_sizes and activation combinations: Average cross-validation scores were calculated for each combination and these scores were visualized through colors on the heatmap.

- Best hyperparameter combination: The cell representing the highest score in the heatmap shows the best hyperparameter combination. In this case, (100,) hidden_layer_sizes and 'relu' activation function worked best.

In this example, the grid search process used to determine the best hyperparameter combination of the MLP model and the results of this process are visualized with a heatmap. The obtained results clearly show how the MLP model can achieve higher performance with the correct hyperparameters. The power, flexibility, and generalization capacity of MLP make it an ideal choice for solving many machine learning problems. However, determining the correct hyperparameters is critical to maximize model performance, and visualization tools such as heatmap provide great convenience in this process.

Results and Discussion

The graph was created to compare the performances of different machine learning algorithms (Logistic Regression, Gradient Boosting Classifier, K-Nearest Neighbors, Multi-Layer Perceptron, Support Vector Classifier and Decision Tree Classifier) and the best parameters of these algorithms (Figure 14). Each bar represents a machine learning algorithm. The height of the bars indicates the accuracy score obtained by each algorithm on the test data set. A high bar indicates that the corresponding algorithm is performing better. Each line indicates the best parameter of the corresponding algorithm. For example, a dashed line represents the n_neighbors (number of neighbors for K-Nearest Neighbors) parameter for which the respective algorithm performs best. The dashed line visually indicates the value of the corresponding parameter. The x-axis represents each algorithm. The name of each algorithm is indicated in labels below the axis. The y-axis represents test accuracy. Accuracy is the ratio of correctly classified samples to the total number of samples. High accuracy indicates how well a model performs on the test data set. This graph is very useful for comparing the performance of different machine learning algorithms. To determine which algorithm performs better in which situations, attention should be paid to both test accuracy and best parameters. For example, one algorithm may achieve higher accuracy than others, but at a certain parameter setting this performance may decrease. This type of analysis can be extremely valuable for optimizing the performance of a machine learning application.

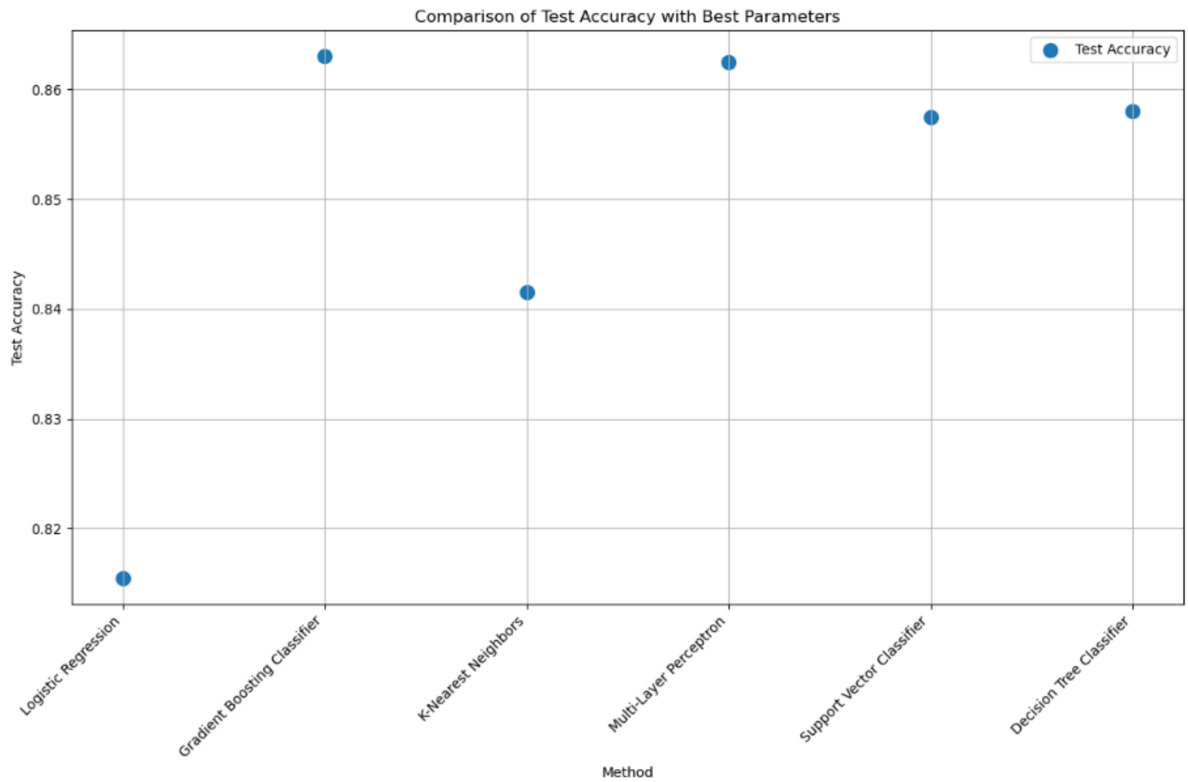

Figure 14. All proposed models test accuracy results for best parameters

Based on Figure 7, the performances of different machine learning methods were compared. The Gradient Boosting Classifier method stands out as the most effective method as it has the highest test accuracy compared to other methods. These results take into account the complexity of the dataset and nonlinear relationships and highlight the efficiency of the algorithm. Furthermore, these results are generally consistent with Cross-Validation (CV) scores, indicating that the models' overall CV performance is a good measure of predicting test accuracy. However, in some cases the CV score may not predict test accuracy well enough, so it is important to consider both metrics when choosing a model. As a result, the Gradient Boosting Classifier method provides the highest test accuracy by best capturing the features of our data set. Therefore, this method is more likely to perform better in real-world applications.

Table 7. All proposed models test accuracy for GridSearchCV

Method	Best Parameters	CV Score	Test Accuracy
Logistic Regression	C : 1 solver: liblinear	0.806625	0.8155
Decision Tree	max_depth: 5 min_samples_split: 2 min_samples_leaf: 1	0.853250	0.8580
Support Vector Classifier	C : 1 gamma: scale kernel: 'rbf'	0.856125	0.8575
Gradient Boosting Classifier	n_estimators: 50 learning_rate: 0.2 max_depth: 4	0.861125	0.8630
K-Nearest Neighbors	n_neighbors: 7 weights: uniform algorithm: auto	0.831875	0.8415
Multi-Layer Perceptron	hidden_layer_sizes:(100,) activation: relu solver: adam alpha: 0.0001 learning_rate: constant	0.853625	0.8625

As a result of the Grid Search study conducted for the data set, the hyperparameters that provide the best performance were determined. These hyperparameters; 'entropy' as the criterion, 10 as the maximum depth, 2 as the minimum number of sample divisions and 1 as the minimum number of leaf samples. The highest accuracy score obtained with this hyperparameter combination was recorded as 85.6%. This result demonstrates the classification success of the model on the dataset and confirms that the determined hyperparameters optimize the overall performance of the model.As a result, the Decision Tree - Best Hyperparameters and Accuracy chart obtained from the code reveals the parameter combinations where the model performs best. Optimizing max_depth and min_samples_split values increases both the accuracy and generalization ability of the model. Careful selection of these parameters maximizes the model's performance on training and test data, resulting in more reliable results.

Conclusion

This study focuses on predicting customer churn in the banking sector. Customer churn is a major concern for financial institutions, and estimating these losses and assessing their impacts are critical to financial sustainability and competitive advantage. In our study, a series of models were developed to predict customer churn using machine learning methods. These models include Logistic Regression, Decision Tree, Support Vector Classifier, Gradient Boosting Classifier, K-Nearest Neighbors and Multi-Layer Perceptron methods. Each of these methods has different features and advantages, and a variety of metrics have been used to evaluate their ability to predict customer churn.

The results obtained show that the Gradient Boosting Classifier method has the highest test accuracy compared to other methods. This suggests that the model's ability to predict customer churn is most effective when it takes into account the complexity of our data set and non-linear relationships. These findings encourage financial institutions to use machine learning models to predict customer churn and develop appropriate strategies. In addition to reducing customer churn, these models can also help financial institutions take preventive steps to increase customer satisfaction. However, this study has some limitations. The focus of our data set on a specific time period and a specific geographic region may limit the generalizability of the results. It should also be noted that the results obtained could be improved by collecting more data and using more complex modeling techniques. This study contributes to research on predicting customer churn in the banking industry, while also helping financial institutions better understand their strategies for maintaining and expanding their customer base. Future studies can further deepen knowledge in this area with broader data coverage and more comprehensive analysis.

Scientific Ethics Declaration

The authors declare that the scientific ethical and legal responsibility of this article published in EPSTEM Journal belongs to the authors.

Acknowledgements or Notes

* This article was presented as an oral presentation at the International Conference on Technology, Engineering and Science (www.icontes.net) held in Antalya/Turkey on November 14-17, 2024.

References

Amuda, K. A., & Adeyemo, A. B. (2019). Customers churn prediction in financial institution using artificial neural network. *arXiv preprint arXiv*:*1912*,11346.

De Caigny, A., Coussement, K., & De Bock, K. W. (2018). A new hybrid classification algorithm for customer churn prediction based on logistic regression and decision trees. *European Journal of Operational Research, 269*(2), 760-772.

Faritha Banu, J., Neelakandan, S., Geetha, B. T., Selvalakshmi, V., Umadevi, A., & Martinson, E. O. (2022). Artificial intelligence based customer churn prediction model for business markets. *Computational Intelligence and Neuroscience, 2022*(1), 1703696.

Gregory, B. (2018). Predicting customer churn: Extreme gradient boosting with temporal data. *arXiv preprint arXiv:1802*, 03396.

Höppner, S., Stripling, E., Baesens, B., vanden Broucke, S., & Verdonck, T. (2020). Profit driven decision trees for churn prediction. *European Journal of Operational Research, 284*(3), 920-933.

Imani, M., & Arabnia, H. R. (2023). Hyperparameter optimization and combined data sampling techniques in machine learning for customer churn prediction: a comparative analysis. *Technologies*, *11*(6), 167.

Ismail, M. R., Awang, M. K., Rahman, M. N. A., & Makhtar, M. (2015). A multi-layer perceptron approach for customer churn prediction. *International Journal of Multimedia and Ubiquitous Engineering, 10*(7), 213-222.

Jain, H., Khunteta, A., & Srivastava, S. (2020). Churn prediction in telecommunication using logistic regression and logit boost. *Procedia Computer Science, 167*, 101-112.

Jajam, N., Challa, N. P., Prasanna, K. S., & Ch, V. S. D. (2023). Arithmetic optimization with ensemble deep learning SBLSTM-RNN-IGSA model for customer churn prediction. *IEEE Access*.

Khattak, A., Mehak, Z., Ahmad, H., Asghar, M. U., Asghar, M. Z., & Khan, A. (2023). Customer churn prediction using composite deep learning technique. *Scientific Reports*, *13*(1), 17294.

Liu, Z., Jiang, P., De Bock, K. W., Wang, J., Zhang, L., & Niu, X. (2024). Extreme gradient boosting trees with efficient Bayesian optimization for profit-driven customer churn prediction. *Technological Forecasting and Social Change*, *198*, 122945.

Nie, G., Rowe, W., Zhang, L., Tian, Y., & Shi, Y. (2011). Credit card churn forecasting by logistic regression and decision tree. *Expert Systems with Applications, 38*(12), 15273-15285.

Raeisi, S., & Sajedi, H. (2020, October). E-commerce customer churn prediction by gradient boosted trees. In 2020 *10th International Conference on Computer and Knowledge Engineering (ICCKE)* (pp.55-59). IEEE.

Sana, J. K., Abedin, M. Z., Rahman, M. S., & Rahman, M. S. (2022). A novel customer churn prediction model for the telecommunication industry using data transformation methods and feature selection. *Plos one, 17*(12), e0278095.

Sjarif, N., Rusydi, M., Yusof, M., Hooi, D., Wong, T., Yaakob, S., ... & Osman, M. (2019). A customer Churn prediction using pearson correlation function and K nearest neighbor algorithm for telecommunication industry. *International Journal of Advance Soft Computing Applications, 11*(2).

Tang, Q., Xia, G., Zhang, X., & Long, F. (2020, March). A customer churn prediction model based on XGBoost and MLP. *In 2020 International Conference on Computer Engineering and Application (ICCEA)* (608-612). IEEE.

Xia, G. E., & Jin, W. D. (2008). Model of customer churn prediction on support vector machine. *Systems Engineering-Theory & Practice*, *28*(1), 71-77.

Xiahou, X., & Harada, Y. (2022). B2C E-commerce customer churn prediction based on K-means and SVM. *Journal of Theoretical and Applied Electronic Commerce Research*, *17*(2), 458-475.

Zhao, Y., Li, B., Li, X., Liu, W., & Ren, S. (2005). Customer churn prediction using improved one-class support vector machine. In *Advanced Data Mining and Applications*: *First International Conference, ADMA 2005* (Vol 1., pp. 300-306). Berlin Heidelberg: Springer.

Author Information

Yasemin Bozkurt
Kutahya Dumlupinar University
Engineering Faculty, Computer Engineering Department,
Kutahya, Türkiye

Hasan Temurtas
Kutahya Dumlupinar University
Engineering Faculty, Computer Engineering Department,
Kutahya, Türkiye

Çigdem Bakir
Kutahya Dumlupinar University
Engineering Faculty, Software Engineering Department,
Kutahya, Türkiye
Contact e-mail: *cigdem.bakir@dpu.edu.tr*

To cite this article:

Bozkurt, Y., Temurtas, H., & Bakir, C. (2024). Machine learning approaches for bank customer churn analysis *The Eurasia Proceedings of Science, Technology, Engineering & Mathematics (EPSTEM), 32*, 208-229.

The Eurasia Proceedings of Science, Technology, Engineering & Mathematics (EPSTEM)
ISSN: 2602-3199

The Eurasia Proceedings of Science, Technology, Engineering & Mathematics (EPSTEM), 2024

Volume 32, Pages 230-237

IConTES 2024: International Conference on Technology, Engineering and Science

GraphQL: A Comprehensive Analysis of Its Advantages, Challenges, and Best Practices in Modern API Development

Ina Papadhopulli
Polytechnic University of Tirana

Hakik Paci
Polytechnic University of Tirana

Abstract: GraphQL, a query language and execution engine for application programming interfaces (APIs), has rapidly gained traction as a flexible and efficient alternative to traditional representational state transfer (REST) APIs. This paper aims to increase awareness of GraphQL by providing a comprehensive overview of its status in the industry, comparing its features and capabilities with those of REST, and addressing common concerns regarding security and performance. We explore the distinct advantages of GraphQL, such as its ability to allow clients to request precisely the data they need and its streamlined approach to data fetching and mutation. Additionally, we examine the inherent challenges and potential performance bottlenecks associated with GraphQL, offering best practices and solutions to mitigate these issues. The paper also delves into security considerations specific to GraphQL, emphasizing the importance of proper query validation, authorization, and rate limiting. Through detailed analysis, this paper seeks to elucidate the benefits and drawbacks of GraphQL, ultimately demonstrating why it is a powerful tool for modern API development and how it can be effectively implemented to enhance data interaction and overall application performance.

Keywords: GraphQL, APIs, REST, Performance, Security

Introduction

Representational State Transfer (REST) services are commonly employed for facilitating communication between web applications. REST services are utilized in scenarios such as mobile applications communicating with backend servers, web applications built with frameworks like React or Vue communicating with backend servers, or even when two backend servers interact. REST APIs provide access to server functionality through endpoints that clients can invoke. However, REST APIs have inherent limitations, including over-fetching, where more data than necessary is retrieved, and under-fetching, where insufficient data is retrieved for client needs.

Graph Query Language (GraphQL) was originally developed at Facebook in 2012 before they open-sourced it around 2016. It is a query language for APIs and a query runtime engine (The GraphQL Foundation). It acts as a middleware layer between frontend and backend data sources, including databases. Most people use it as a better API specification in their applications for their back-end systems (Doolittle, 2023). GraphQL enables clients to precisely specify the data they require in a single query, thereby mitigating issues related to over-fetching and under-fetching of data (Mukhiya et al., 2019). With GraphQL, a schema is defined that outlines how clients can query and mutate data. This schema does not replace the database schema but complements it. The database schema dictates how data is structured and stored, while the GraphQL schema specifies how clients interact with that data. When a GraphQL query is executed, the GraphQL server resolves the query by retrieving data from the database based on the query's specifications. This approach ensures optimal performance by fetching only necessary data.

- Selection and peer-review under responsibility of the Organizing Committee of the Conference

While GraphQL facilitates precise data retrieval, it still relies on a database for storing and retrieving data. GraphQL itself is not a database technology but rather a query language for APIs that enhances control over data fetching. In contrast to SQL queries, which require direct interaction with database tables and knowledge of the database schema, GraphQL queries are schema-agnostic. The GraphQL server handles query resolution and fetches data from appropriate data sources, which can include SQL databases, NoSQL databases, or other APIs. It achieves this through the use of resolvers, which are functions that map GraphQL queries to the underlying data sources. Resolvers ensure that the data requested by the client is efficiently retrieved and formatted according to the schema defined for the API. This abstraction allows clients to interact with a single GraphQL endpoint while the server manages the complexities of data retrieval from multiple sources (Microsoft, July 2024). GraphQL puts more control in the hands of the client, allowing front-end developers to fetch data in a way that suits their UI requirements more precisely, reducing the need for multiple endpoints or transformations.

GraphQL is compatible with various programming languages such as Java, Python, PHP, Ruby, JavaScript, etc., underscoring its versatility and adoption across different technology stacks. The rest of the paper is structured as follows: the next section provides a detailed description of GraphQL and compares it with other query languages and REST. The following two sections discuss the challenges associated with GraphQL and best practices for security and performance. The final two sections present the conclusions and recommendations for future work.

Graphql Comparison with Other Query Languages and Status

GraphQL

GraphQL is a query language for APIs and a runtime for executing those queries by using a type system you define for your data. To get/mutate data we need to define a schema. Schema provides flexibility to consumers regarding which attributes they want in the response. It is the contract between the consumer and provider on how to get and alter the data for the application. Query and Mutation are the root types in the schema representing read and write operations, respectively. Additionally, GraphQL supports the use of custom scalar types and enumerations, enabling developers to define precise data structures and enforce specific data formats.

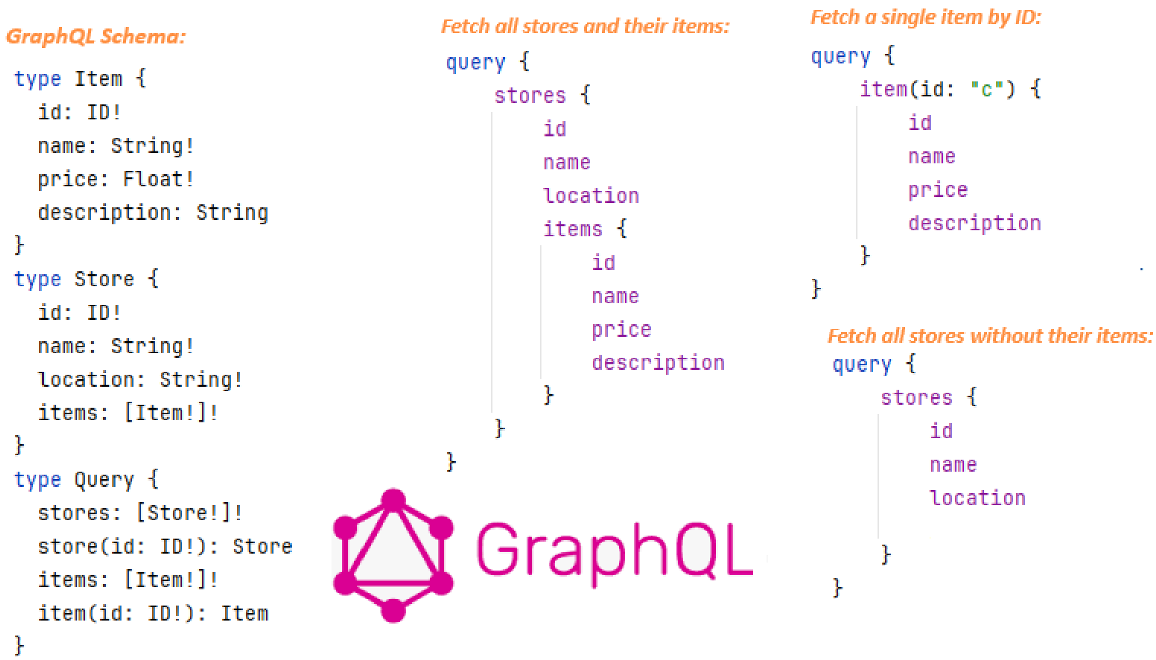

Figure 1. Example of GraphQL schema, queries for a store that has items

GraphQL offers the resolver mechanism that is a central concept that defines how to fetch the data for the fields in a query. Each field in a GraphQL schema is backed by a resolver function, which determines how that field's data should be obtained. Resolvers can be defined for queries, mutations, and individual fields within types. It is a powerful feature that enables precise, field-level data resolution. Allowing custom logic for individual fields provides flexibility and control over how data is fetched and processed, making it particularly suitable for complex and nested data structures. If this feature is used appropriately, it can reduce the load on the server and improve the overall performance of the API.

Suppose we don't need the items as shown in the request: '*Fetch all stores without their items'* (Figure 1). If a resolver is not used, the items will still be retrieved from the data source but will not be included in the response since the user has not specified them in the request. Using a resolver for the Store ensures that the items are not fetched from the data source at all, increasing code efficiency. While the same behavior can be achieved with REST APIs, it is not as straightforward as it is with the GraphQL resolver mechanism.

GraphQL: Current Status and Developments

Over the past decade, several query languages have emerged as alternatives for API data access, each with its own strengths and use cases. SPARQL, for instance, is designed for querying Resource Description Framework (RDF) data and is widely used in semantic web applications. Cypher, developed by Neo4j, excels in handling graph databases. Gremlin, part of the Apache TinkerPop framework, provides a versatile graph traversal language that can operate across various graph databases (Quina-Mera et al., 2023). Among these, GraphQL has emerged as the most successful and widely adopted query language in recent years (Seifer et al., 2019).

Initially released publicly in 2015, GraphQL has since garnered significant attention and adoption within the development community. It is an open-source technology supported by an active and expanding community (GraphQL.com, 2024), making it suitable for teams of all sizes. Major industry players such as Microsoft, IBM, AWS, and Atlassian leverage GraphQL extensively in their applications (The GraphQL Foundation, 2024).

Despite its growing acceptance and adoption as a powerful tool for API development, GraphQL currently lacks a widely established scientific community dedicated to its study and advancement. While there is a noticeable trend of publications in reputable venues, there remain notable gaps in the existing literature. Specifically, shortcomings persist in terms of the maturity of empirical evidence supporting GraphQL's efficacy, validation through realistic use cases, and the comprehensive evaluation of its diverse quality characteristics and underutilized features (Quina-Mera et al., 2023). Addressing these gaps is crucial for enhancing the understanding and maximizing the potential of GraphQL in real-world applications.

GraphQL vs REST

Despite the many types of APIs, debates about two major paradigms have dominated the conversation in recent years: REST and GraphQL. Both are popular approaches for designing APIs, each with its own advantages and ideal use cases. However, they differ significantly in how they manage data traffic (IBM, June 2024). REST has different HTTP methods and separate endpoints for each API. In GraphQL we have Query and Mutation and there is only one endpoint. All calls go to the same endpoint and are HTTP POST methods. REST does not need Schema, GraphQL does. The choice between GraphQL and REST depends on the project's specific requirements and the data interactions' complexity. Some projects even use both, utilizing GraphQL for complex queries and REST for simpler endpoints.

When to Use GraphQL?

- *Complex Queries*: Ideal for retrieving complex or nested data structures in a single request, reducing over-fetching and under-fetching.
- *Flexible Data Retrieval*: Beneficial when API consumers need the flexibility to dictate the structure of the response, allowing clients to request only the data they need.
- *Rapid Development*: Supports agile development environments and frequent API updates, allowing schema changes without impacting existing clients.
- *Multiple Data Sources*: Simplifies the process of aggregating data from multiple sources or services into a single endpoint.
- *Strongly Typed Schema*: Uses a schema to define data structure, beneficial for validating requests and ensuring client-server data contract understanding.

When to Use REST?

- *Simple and Standardized*: Well-understood by many developers and suitable for simple needs met with standard HTTP methods (GET, POST, PUT, DELETE).
- *Caching*: Effectively leverages HTTP caching mechanisms to improve performance.
- *Stateless Operations*: Inherently stateless, with each client request containing all necessary information, simplifying design and scaling.
- *Standard Methods*: Uses standard HTTP methods and status codes, making it easy to understand and use.
- *Simple Relationships*: Easier to implement and maintain if the data model is straightforward without deeply nested or complex relationships.

GraphQL Security Challenges and Best Practices

Security should be considered carefully when utilizing GraphQL. GraphQL itself does not inherently pose security risks; however, if we do not follow the design guidelines and best practices related to security, we might expose vulnerabilities and compromise data security. (Shrey, 2024).

Common Security Issues Associated with GraphQL

a) *Introspection Queries*: This is a special type of query that allows clients to query the schema itself for information about types, fields, and operations that are available in the GraphQL API. Usually, the schema is not supposed to be public. If introspection queries are enabled, it would lead to:

1) Exposure to internal structure
2) Discovery of hidden fields and endpoints
3) Facilitation of targeted attacks.

b) *Excessive Data Exposure*: Situations where more data than necessary is exposed through the API. This is often done unintentionally, and this can lead to various security and privacy issues. Causes of excessive data exposure:

i. Over-fetching: The client requests more data than needed. This can happen even though with GraphQL we can specify exactly what data we want.
ii. Unprotected fields: All fields can be accessed by the clients if not explicitly protected in the schema.

c) *SQL Injection*: This type of attack can happen when user inputs are directly used in SQL queries without proper validation and sanitization. GraphQL allows for complex queries with parameters. This gives the possibility to attackers to write malicious queries to manipulate the SQL queries executed by the server.

```
query {
    item(id: "'); DROP TABLE store; ") {
        id
        name
        price
        description
    }
}
```

The resolver could generate the following SQL query:

```
SELECT * FROM item WHERE id = ''); DROP TABLE store;
```

Figure 2. Example of a SQL injection for the schema defined in Figure 1

d) *Denial of Service (DoS) Attacks*: An attacker aims to make the GraphQL API unavailable to legitimate users by overwhelming the server with a large number of expensive or complex queries. This type of attack can be achieved through various methods, including:

i. Batched Queries and Resource Exhaustion: Attackers can send batched queries with multiple operations into a single request, causing significant resource consumption on the server.
ii. Aliases-based attack: By using the aliases feature, the attacker can circumvent rate-limiting measures that typically count the number of HTTP requests from an IP address.

iii. Deep Recursive Query Attack: Types can reference each other leading to potentially infinite recursion. This can crash the server due to excessive resource consumption.

Best Practices to Mitigate Security Risks

a) *Rate Limiting and Throttling*: Implement rate limits to prevent abuse and overuse of the API.
b) *Query Complexity Analysis*: Evaluate and limit the complexity of GraphQL queries to protect the API from resource exhaustion and DoS attacks.
c) *Introspection Control*: Disable introspection. If it is needed for development or debugging purposes, ensure it is disabled in production.
d) *Authentication and Authorization*: Define roles and specify the permissions for each role. Check permissions within resolvers to ensure users can only perform actions they are authorized for.
e) *Logging*: Log information to detect anomalous behavior, track API usage, and gather information about errors.
f) *Monitoring*: Enhance security through real-time alerts, user behavior analytics, resource utilization analysis, and more.
g) *Avoid SQL Injection*:

i. Always use parameterized queries
ii. Validate and sanitize inputs
iii. Use Object-Relational Mappers (ORMs) because they handle parameterization automatically.
iv. Apply least privilege principles

GraphQL Performance Challenges and Best Practices

GraphQL offers a powerful and flexible way to query and manipulate data, but with this power comes several performance challenges. This section explores these challenges, particularly when dealing with large graphs and high volumes of API requests, and outlines solutions to mitigate them.

Dealing with Large Graphs

Handling large graphs in GraphQL can lead to performance bottlenecks, especially when deep nesting or complex queries are involved. Some strategies to manage large graphs effectively include:

a) *Efficient Data Loading*: Utilize techniques like data loaders to batch and cache requests, reducing the number of database queries.
b) *Pagination and Filtering*: Implement pagination and filtering to limit the amount of data returned in a single query, thus avoiding over-fetching.
c) *Query Complexity Analysis*: Use tools to analyze and limit query complexity, preventing overly complex or expensive queries from degrading performance.

Maintaining GraphQL APIs

Maintaining a GraphQL API with a high volume of requests presents several challenges, including schema management, performance optimization, and ensuring high availability. Here are some key aspects and solutions:

Schema Visualization and Management

- *Schema Visualization*: Tools for visualizing the schema help understand how objects are connected and identify potential bottlenecks. Visualization aids in managing and optimizing the schema.
- *Checks and Insights*: Improved schema-checking tools, such as Apollo Studio, offer validation, change tracking, and usage analytics. These tools ensure that the schema remains well-defined, compatible, and error-free.

Architectural Approaches

There are two primary architectural approaches for implementing GraphQL: Monolith and Supergraph (Federated GraphQL) (Apollo Graph Inc., 2024). Understanding these architectural approaches is crucial for making informed decisions about how to implement GraphQL in a way that best suits the needs of a given application or organization. Each approach has its advantages and disadvantages:

Monolith Architecture:

- *Advantages:*

  - *Simplicity*: Easier to set up and manage with a single schema and resolver map.
  - *Performance*: Direct inter-resolver communication minimizes latency.
  - *Deployment*: Only one service to manage, reducing overhead.
  - *Consistency*: Uniform coding practices and schema design across the codebase.

- *Disadvantages:*

  - *Scalability*: Harder to scale as the application grows.
  - *Flexibility*: Riskier updates affecting the entire system.
  - *Team Collaboration*: Potential for conflicts in a single codebase.
  - *Resilience*: Failure in one part can impact the whole application.

Supergraph Architecture:

- *Advantages*:

  - *Scalability*: Independent scaling of subgraphs addresses specific performance bottlenecks.
  - *Flexibility*: Isolated changes to subgraphs without affecting the entire system.
  - *Team Collaboration*: Teams can work independently on different subgraphs.
  - *Resilience*: Failures in one subgraph do not affect the entire system.

- *Disadvantages*:

  - *Complexity*: More complex setup and management with additional infrastructure.
  - *Performance*: Potential latency from inter-subgraph communication.
  - *Deployment*: More challenging deployment coordination of multiple services.
  - *Consistency:* Requires robust schema management across subgraphs.

Query Batching

Modern applications often require several requests to render a single page. Not only does this cause a performance overhead (different components may be requesting the same data) but it can also cause a consistency issue. Query batching allows multiple operations to be combined into a single request, reducing network overhead and improving performance. This technique ensures efficient client-server communication by minimizing the number of network requests (Apollo Graph Inc, 2024).

Persisted Queries

Persisted Queries involve storing pre-defined queries on the server side, reducing the payload size and improving performance. Clients send unique identifiers instead of full query strings, which the server uses to retrieve and execute the stored queries. This approach also enhances security by preventing malicious queries and ensuring consistent authorization.

High Availability and Reliability

Ensuring high availability and reliability involves implementing redundant systems and failover mechanisms. It also includes setting up performance alerts and monitoring metrics to proactively address issues before they impact users.

Conclusion

GraphQL can be considered a flexible and efficient alternative to traditional REST APIs. Through this comprehensive analysis, we have explored the distinct advantages of GraphQL, including its ability to allow clients to request precisely the data they need and its streamlined approach to data fetching and mutation. We have also highlighted the inherent challenges and potential risks associated with GraphQL, providing best practices and solutions to mitigate these issues. Implementing robust security measures, such as query complexity analysis, rate limiting, and proper authentication and authorization, is crucial to safeguard against potential vulnerabilities like DoS attacks and SQL injection.

In addressing performance challenges, strategies such as efficient data loading, pagination, and query batching can be used especially when dealing with large graphs and high volumes of requests. Additionally, adopting appropriate architectural approaches, whether monolith or supergraph and leveraging tools for schema visualization and management can enhance the maintainability and scalability of GraphQL APIs. Organizations can effectively manage these challenges by adhering to best practices in security, performance optimization, and architectural design. GraphQL offers great potential, ensuring robust and efficient API implementations that meet the dynamic needs of today's applications.

Recommendations

While this analysis has provided a comprehensive overview of GraphQL's advantages, challenges, and best practices, several areas need further exploration. Future work could focus on developing more sophisticated tools for automated query complexity analysis and enhanced introspection control to strengthen GraphQL API security further. Additionally, empirical studies evaluating GraphQL's performance in large-scale, real-world applications would provide valuable insights into its scalability and efficiency. Investigating the integration of GraphQL with emerging technologies such as machine learning could also reveal new opportunities for innovation and optimization. Finally, establishing a more robust scientific community dedicated to the study and advancement of GraphQL will be crucial for driving its evolution and addressing any emerging challenges in the field.

Scientific Ethics Declaration

The authors declare that the scientific ethical and legal responsibility of this article published in EPSTEM Journal belongs to the authors.

Acknowledgments or Notes

* This article was presented as an oral presentation at the International Conference on Technology, Engineering and Science (www.icontes.net) held in Antalya/Turkey on November 14-17, 2024.

References

Apollo Graph Inc. (2024, June 25). *Query batching*. https://www.apollographql.com/docs/router/executing-operations/query-batching/

Shrey, A. (2024,). Hacking GraphQL APIs for fun & profit. *Toptal Global Talent Conference, 2024*

Doolittle, J. (2023). APIs with GraphQL. *IEEE Software*, *40*(2), 118-120.

Mukhiya, S., Rabbi, F., Ka I Pun, V., Rutla, A., & Lamo, Y. (2019). A GraphQL approach to healthcare information exchange with HL7 FHIR. *The 9th International Conference on Current and Future Trends of Information and Communication Technologies in Healthcare (ICTH 2019),* 4-7,

The GraphQL Foundation. (2024, June 21). *Introduction to GraphQL*. Retrieved from https://graphql.org/learn/

GraphQL.com. (2024, July 10). Community. Retrieved from https://graphql.com/community/

The GraphQL Foundation. (2024, June 25). *Who's using GraphQL*? Retrieved from https://graphql.org/users/

Apollo Graph Inc. (2024, July 07). Optimizing GraphQL APIs for operational success. Retrieved from https://www.apollographql.com/events

Seifer, P., Härtel, J., Leinberger, M., Lämmel, R., & Staab, S. (2019). Empirical study on the usage of graph query languages in open source Java projects. *Proceedings of the 12th ACM SIGPLAN International Conference on Software Language Engineering (SLE'19) ACM,* 152–166.

IBM (2024, June 01). *GraphQL vs. REST API: What's the difference?* Retrieved from: https://www.ibm.com/blog/graphql-vs-rest-api/

Microsoft. (2024, July 09). *Configure a GraphQL resolver*. Retrieved from https://learn.microsoft.com/en-us/azure/api-management/configure-graphql-resolver

Quiña-Mera, A., Fernandez, P., García, J. M., & Ruiz-Cortés, A. (2023). GraphQL: A systematic mapping study. *ACM Computing Surveys*, *55*(10), 1-35.

Author Information

Ina Papadhopulli
Polytechnic University of Tirana
"Mother Tereza" Square, Tirana, 1001, Albania
Contact e-mail: *ipapadhopulli@fti.edu.al*

Hakik Paci
Polytechnic University of Tirana
"Mother Tereza" Square, Tirana, 1001, Albania

To cite this article:

Papadhopulli, I., & Paci, H. (2024). GraphQL: A comprehensive analysis of its advantages, challenges, and best practices in modern API development. *The Eurasia Proceedings of Science, Technology, Engineering & Mathematics (EPSTEM), 32,* 230-237.

The Eurasia Proceedings of Science, Technology,
Engineering & Mathematics (EPSTEM)
ISSN: 2602-3199

The Eurasia Proceedings of Science, Technology, Engineering & Mathematics (EPSTEM), 2024

Volume 32, Pages 238-243

IConTES 2024: International Conference on Technology, Engineering and Science

Design, Analysis and Manufacturing of Plastic Parts Made from Bio-Added Polymers

Hasan Oktem
Kocaeli University

Halit Karasungur
Kocaeli University

Ali Oz
Mehmet Akif University

Abstract: Bio-reinforced materials are plastic parts that can be produced by adding general-purpose polymers in certain proportions, where their important contributions to human and environmental health are stored. This study covers the design, analysis and manufacturing processes of food product insertion compartments of tea and coffee machines, which are kitchen products, by plastic injection method. For this purpose, first of all, the plastic parts and mold design of the food compartments in tea and coffee machines were made in CAD (Computer Aided Design) software. The most appropriate injection parameters were determined, trial and error. Based on the results obtained, a series of plastic products were performed in the mold using two bio-added polymers such as Polypropylene (PP) and Acrylonitrile butadiene styrene (ABS) to check the accuracy and quality of the injected products. Finally, after injection a metallic plastic mold of bio-added polymers, selected errors are determined in advance with the help of CAD/CAM/CAE programs and are applied to minimize cost, durability and time. Additionally, the manufacturability of kitchen utensils with bio-added polymers was tested using the plastic injection method.

Keywords: Bio-added polymers, Plastic injection, Design and analysis, Coffee and tea machines, Plastic products

Introduction

In today's mold industry, many plastic materials are widely used in industrial and household appliances. For these purposes, general purpose engineering polymers are preferred (Akyuz, 2006; Atasimsek, 2006). Plastic products are highly preferred due to advantages such as low cost, high dimensional accuracy, lightness, ease of production and mass production (Beamunt et al., 2002). Polypropylene (PP) polymer and Acrylonitrile butadiene styrene (ABS) are polymers with two different properties close to these mentioned properties (Kayalı, 2022). PP is a crystalline thermoplastic consisting of a mixture of different polypropylene monomers. It is known for its durability and hardness. It is a versatile material with various applications due to its unique properties such as high strength, excellent chemical resistance and good thermal stability (Seyhan, 2023). ABS polymer is a hard, rigid and tough material at low temperatures. Additionally, it has good tensile, impact, dimensional stability, rigidity and chemical resistance properties. Since ABS is an amorphous polymer, the dimensional accuracy of printed plastic products is quite high (Bitirgic, 2010).

The use of plastic products is especially important in designs developed for home appliances. Polymers such as Polypropylene (PP) polymer and Acrylonitrile butadiene styrene (ABS) are used extensively in kitchen utensils. (Campo, 2008). By reinforcing glass fibers with engineering polymers such as PP and ABS, higher strength plastic products can be produced (Wyzgoski et al., 2004). In another study, authors stated that by reinforcing glass fiber to PP polymer material, they achieved an increase of at least 2-3 times in the mechanical properties of plastic parts (Fu et al., 2001). It can be stated that reinforcing glass fiber into harder materials such as concrete provides a significant increase in strength in concrete (Jan et al., 2022).

Important strategies are created for model design of plastic products, analysis of the model, mold design and manufacturing, and selection of injection parameters for injection of plastic product. In the design of a product to be injected in plastic injection, cold-hot runners, holes on the plastic part, ribs, wall thickness, slope and rounding of the part are important factors to be taken into consideration. All these factors are now realized with advanced computer-aided programs (Topcu, 2010). Before injection of plastic products, the polymer should be effectively planned and designed to enter the cold and hot runner while it is molten. If the flow length is short and the product volume is low, cold runners are preferred; if the flow length is long and the product volume is high, hot runners are generally preferred (Ozturk & Ozkan, 2015; Wang et al., 1996). Another group of researchers examined the effects of injection parameters on injected plastic products using the same type of polymer materials. It can be concluded that parameters such as temperature, pressure and injection speed are effective on both the strength and geometric change of the parts (Farotti &Natalini, 2017), (Oktem &Erzincanlı, 2012). In this study, Gonullleroglu (2015), examined the distortion analysis, experimental and theoretical results of the plastic product (refrigerator door profile part) after injection. The researcher tried to eliminate the defects of the plastic product by improving the design parameters based on flow analysis.

Plastic products used in household appliances are expected to have superior properties in terms of strength and will not have a negative impact on human health and the environment. In order to minimize these negative effects, it is necessary to develop plastic products with higher strength and better cosmetic appearance. For this reason, some researchers have examined the effect of process parameters during hot runner injection of plastic products such as garbage containers and bottles by adding bio-additives to Polyethylene Terephthalate (PET) polymer. They examined the effects of injection temperature, mold temperature, packing pressure and cooling time on volumetric shrinkage (Srikhumsuk et al., 2024).

This study focuses on examining the necessary design, manufacturing, analysis and dimensional accuracy control stages during the production of kitchen appliances using the plastic injection method. For this purpose, the product design and mold design of the coffee machine spoon and tea machine body handle cover model were made. Then, molds were manufactured and the plastic products of the models were injected on an injection machine. During injection, the dimensional accuracy of the plastic products was checked by a 3D optical scanner by making several attempts at three different temperature, pressure and injection speed parameters.

Materials and Method

In this study, coffee powder for the coffee spoon and tea fiber for the tea machine body handle cover were added to PP and ABS polymer materials as bio-additives. Coffee spoon and tea machine body handle cover samples from PP and ABS polymers were injected by injection molding method with three different injection parameters. Experiments have been carried out by adding certain proportions of glass fiber and bio-added materials to PP and ABS polymer materials.

Design and Manufacturing

The plastic product design of the coffee spoon and tea machine body handle cover was carried out in NX Siemens CAD program. The mold design required for printing both plastic products was made in the same program. Then, the designed molds were manufactured on the CNC machine. Using the manufactured molds, plastic products were injected on an injection machine. Figure 1 shows the coffee spoon used in the coffee machine. Figure 2 shows the design of the tea machine body handle cover. Figure 3 shows the female mold half required to inject the plastic product of the coffee spoon. Four coffee spoons can be pressed at a time in the mold half. In similar way, four tea machine body handle cover can be injected.

Figure 1. The design of coffee spoon model

Figure 2. The design of tea machine body handle cover model

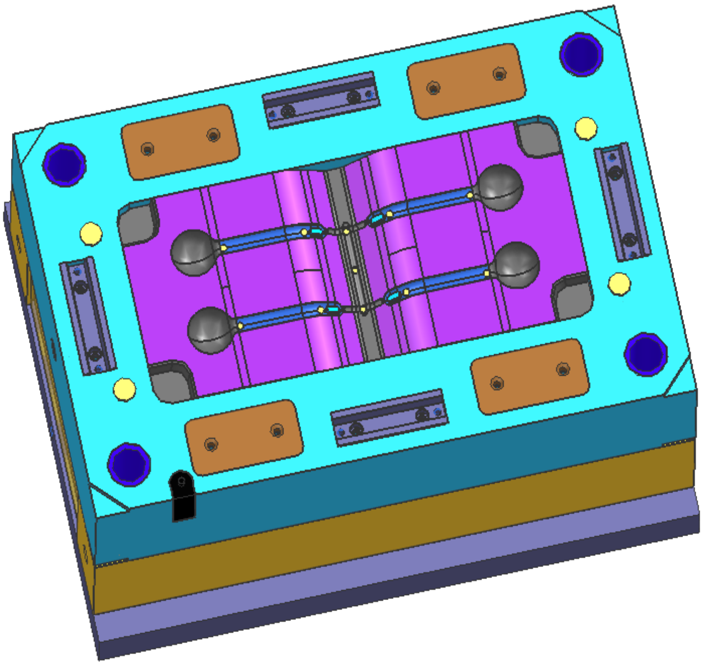

Figure 3. The design of coffee spoon model

Controlling of Dimensional Errors of Plastic Products

Figure 4. The check of dimensional accuracy of plastic products with 3D optical scanner

Figure 5. The injected of coffee spoon

A 3D optical scanning system was to check the dimensional accuracy of plastic products (coffee spoon and tea machine body handle cover) injected by combining glass fiber and bio-additives reinforced with PP and ABS polymers. Figure 4 shows the measurement process with the VYLO Rapotor3DX brand FOV 300 model three-dimensional scanning device. Figure 5 shows the plastic product model of the measured coffee spoon model.

Results and Discussion

In this section, CAD data and dimensional errors of the actual dimensions of the plastic products of the bio-added coffee spoon and tea machine handle cover made of PP and ABS polymers were determined. Figure 6 and 7, dimensional errros of coffee spoon and tea machine body handle cover. From Figure 6 is examined, it is seen that there is a maximum deviation of -1.88 mm at the bottom end of the handle of the coffee spoon and -0.22 mm at the top. From Figure 7, it is seen that there is a deviation of +0.15 mm near the bottom end of the tea machine body handle cover and -1.68 mm to the right edge of the bottom end.

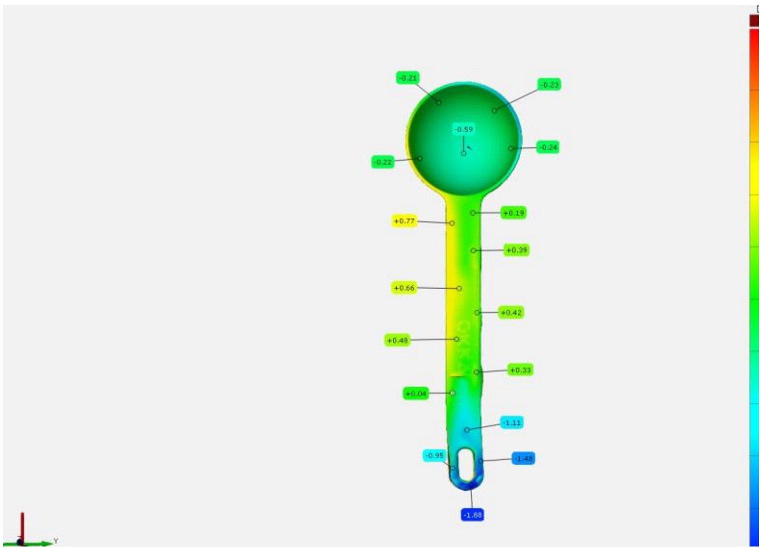

Figure 6. The control of coffee spoon

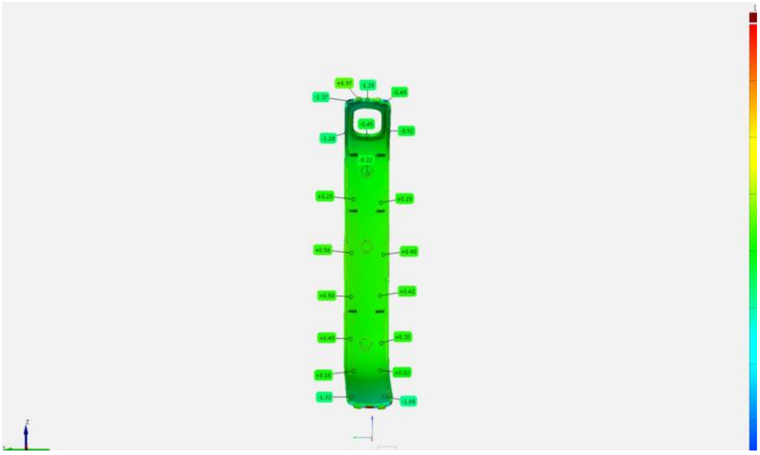
Figure 7. The control of tea machine body handle cover

Conclusions

In this study, glass fiber reinforced plastic products were produced by injection method by adding bio-added materials to PP and ABS polymers. A 3D optical scanner was used to check the dimensional accuracy of plastic products. Reverse engineering was performed by finding the difference between the CAD model of plastic products and the real model. It was observed that the measured error results were within tolerance values. As a result of this study, the negative effects on human health were tried to be eliminated by adding coffee powder and tea fiber to polymers such as PP and ABS. In addition, glass fiber reinforcement prevents the decrease in strength in plastic products that require weight under the influence of heat.

Recommendations

In future trends, plastic products will conduct mold flow analysis, mechanical properties and optical measurement.

Scientific Ethics Declaration

The authors declare that the scientific ethical and legal responsibility of this article published in EPSTEM journal belongs to the authors.

Acknowledgements or Notes

* This article was presented as an oral presentation at the International Conference on Technology, Engineering and Science (www.icontes.net) held in Antalya/Turkey on November 14-17, 2024.

* The authors would like thanks to Güneş Plastic Molding Industrial Company.

References

Akyuz, O. F. (2006). *Introduction of plastics and plastic technologies* (3rd ed.). Istanbul, Turkiye: PAGEV Publications.

Atasimsek, S. (2006). *Plastic and metal molding techniques* (2 nd. ed.). Istanbul, Turkiye: Birsen Publications.

Bitirgic, C. (2010). *Effect of ABS and glass fiber added to PP material in plastic injection molding on mechanical properties.* (Master's thesis, Gebze Institute Technology, Engineering and Natural Sciences).

Beaumont, J.P., Nagel, R., & Sherman, R. (2002). *Successful injection molding.* Cincinati, USA: Hanser/Gardner Publications Inc.

Campo, A. (2008). *Selection of polymeric materials.* Norwich, USA: William Andrew Publishing.

Gonulleroglu, T. (2015). *Comparison of warpage analysis, theoretical and experimental results during plastic injection process of the refrigerator door profile part* (Master's thesis, Dokuz Eylul University, Natural Science Institute).

Farotti, E., & Natalini, M. (2018). Injection molding. Influence of process parameters on mechanical properties of polypropylene polymer. A first study. *Procedia Structural Integrity, 8*, 256-264.

Fu, S. Y., Mai, Y. W., Lauke, B., & Yue, C. Y. (2002). Synergistic effect on the fracture toughness of hybrid short glass fiber and short carbon fiber reinforced polypropylene composites. *Materials Science and Engineering: A*, *323*(1-2), 326-335.

Jan, A., Pu, H., Khan K. A., Ahmad, I., & Khan, I. (2022). Effect of glass fibers on the mechanical behavior as well as energy absorption capacity and toughness indices of concrete bridge decks. *Silicon, 14,* 2283-2297.

Kayalı, O. (2022*). Examining the effect of plastic injection molding on mechanical behavior.* (Master's thesis, Istanbul Technical University Graduate School of Education).

Oktem, H., & Erzincanlı, F. (2012). Determination of optimal process parameters affecting shrinkage caused by plastic injection pressing of a DVD ROM front cover by Taguchi method. *III. National Design Manufacturing Analysis Conference*.

Ozturk, T., & Ozkan, A. (2015). Comparison of runner systems of cold and hot, *Journal of Duzce University Science and Technology*, *3*, 283-298.

Seyhan, H. (2023). *Effects of cooling system in plastic injection molds on the quality of produced.* (Master's thesis, Sakarya University, Natural Sciences Institute).

Topcu, E., (2010). Computer aided molding design. (Master's thesis, Namık Kemal University Natural Sciences Institute).

Srikhumsuk, P., Butdee, S., Nitnara, C. (2024). Effect of glass fibers on the mechanical behavior as well as energy absorption capacity and toughness indices of concrete bridge decks. *Materials Today: Proceedings, publish online,* 2024.

Wang, H., Prystay, M., Hétu, J. F., Cao, B., & Jen, C. K. (1996). Gap between mold and part and its effect on cooling of injection-molded plastics. In *Technical Papers of the Annual Technical Conference-Society of Plastics Engineers Incorporated* (pp. 1049-1053). Society of Plastics Engineers Inc.

Wyzgoski, M. G., Krohn, J. A., & Novak, G. E. (2004). Fatigue of glass fiber reinforced injection molded plastics. Tensile versus flexural loading. *Polymer Composites*, *25*, 569-576.

Author Information

Hasan Oktem
Professor
Kocaeli University, Hereke Asım Kocabıyık Vocational, Polymer Science and Technology, Natural Sciences Institute/Umuttepe Campus, Kocaeli, Türkiye
Contact e-mail: *hoktem@kocaeli.edu.tr*

Halit Karasungur
Msc. Student-
Reseach Department/ Guneş Plastic Trade Company, Türkiye
Kocaeli University /Umuttepe Campus, Natural Sciences Institute, Kocaeli, Türkiye

Ali Oz
Assoc. Prof. Dr.
Mehmet Akif University/Automotive Department
Mechanical Engineer/RD Department, Burdur, Türkiye

To cite this article:

Oktem, H., Karasungur, H., & Oz, A. (2024). Design, analysis and manufacturing of plastic parts made from bio-added polymers. *The Eurasia Proceedings of Science, Technology, Engineering & Mathematics (EPSTEM), 32*, 238-243.

The Eurasia Proceedings of Science, Technology, Engineering & Mathematics (EPSTEM)
ISSN: 2602-3199

The Eurasia Proceedings of Science, Technology, Engineering & Mathematics (EPSTEM), 2024

Volume 32, Pages 244-250

IConTES 2024: International Conference on Technology, Engineering and Science

Comparative Analysis of RTK and Net-RTK Accuracy in UAV-Based Photogrammetry

Oyku Alkan
Graduated Istanbul Technical University

Muntaha Kassim Alzubade
University of Technology

Mehmet Nurullah Alkan
Hitit University

Abstract: This study evaluates the positional accuracy of UAV photogrammetry using RTK and Network-based RTK (Net-RTK) methods. A two-story building was selected as the test site, and photogrammetric flights were conducted with consistent flight parameters for both RTK and Net-RTK systems. The 3D coordinates of characteristic points on the structure were digitized for both methods, with RTK-based data serving as the reference for comparison. Root Mean Square Error (RMSE) values were calculated to assess the accuracy, indicating minor random discrepancies in horizontal coordinates (Y and X) but a more notable and possible systematic error in the vertical component (H). Statistical analysis confirmed that while Y and X axis differences were random, height differences displayed a systematic trend, particularly evident in Net-RTK measurements. The results suggest that while RTK offers higher vertical accuracy suitable for precision applications, Net-RTK remains a viable alternative for general purposes, particularly in areas with reliable internet connectivity.

Keywords: GNSS, RTK, Net-RTK, UAV photogrammetry.

Introduction

The number of Unmanned Aerial Vehicles (UAVs) has significantly increased over the past decade and these devices are now actively used in a wide variety of applications. Initially developed for recreational purposes, UAVs have expanded their utility to sectors such as agriculture, mining, archaeology, construction, geology, and mapping through the acquisition and processing of digital data obtained from various mounted sensors, such as thermal cameras and LiDAR (Light Detection and Ranging). Photogrammetric flights and evaluations (Alkan et al.,2022; Alkan et al.,2023), used due to their production capabilities of 3D coordinates of objects or areas, have gained momentum due to these advancements (Vollgger & Cruden, 2016; Ozyurt & Celen, 2022; Aksoy et al., 2023; Pargiela, 2023).

Photogrammetry is defined as the science of deriving three-dimensional positional data of objects within a scene by evaluating two-dimensional images. Today, it is highly effective due to the rapid processing capabilities of digital imagery. Images derived by UAVs, with predefined forward and side overlap rates, can be analyzed through specialized software to reconstruct the region's 3D point cloud and model in digital environments. Autonomous flights with pre-set routes are typically preferred for such processes. The precision of these results varies depending on factors such as flight altitude, weather conditions, camera resolution, and type of connection to the terrestrial coordinate system. However, results with accuracies up to centimeter level are achievable. Furthermore, photogrammetric 3D digital terrain models offer numerous advantages, including rapid point cloud production, flexible autonomous flight planning, realistic evaluation of data under actual field conditions, various outputs tailored to the objective (such as orthophotos, ortho-mosaic images, digital terrain models) (Alkan&Alzubade,2022) , repeatable measurements on the model, and the elimination of potential damage to the target object (Dering et al., 2019; Choi et al., 2023; Lenda et al., 2023; Oliveira et al., 2023; Pargiela, 2023; Specht et al., 2023; Subramanian et al., 2024, URL-1).

To create a 3D model of an area using photogrammetric methods, a typical approach involves autonomous UAV flights at low altitudes (<120 m) with forward-side overlap, capturing numerous digital images of the target. Captured images can be collectively analyzed using automated procedures like Structure-from-Motion (SfM), which enables high-accuracy 3D model generation and association with local/regional/global terrestrial coordinate systems (Woodget et al., 2017; Kenako et al., 2023; Lenda et al., 2023; Mazza et al., 2023; Pargiela, 2023, URL-2).

Scaling and positioning of a photogrammetrically produced model relative to a known terrestrial reference system is called "georeferencing." This process requires points with known coordinates, both in the model and on the actual ground. The traditional approach involves establishing Ground Control Points (GCPs) within the target area that will remain visible across all photographs. Their coordinates are measured in 3D using methods, such as GNSS observations, and then manually entered the software during digital processing. A typical model is assumed to require around 5–8 GCPs for adequate alignment with real-world coordinates, thus enabling highly accurate, centimeter-level field measurements based on the 3D model, which can save both time and cost (Vollgger & Cruden, 2016; Dering et al., 2019; Lenda et al., 2023; Pargiela et al., 2023, URL-3).

An alternative approach for georeferencing involves measuring the coordinates of photo capture points in real-time during the flight, eliminating the need for GCPs. In this case, 3D coordinate data, also known as exterior orientation parameters, are automatically calculated, facilitating high-accuracy Digital Terrain Model (DTM) production using SfM. This method can be implemented in two different ways: Real-Time Kinematic (RTK) and Network Real-Time Kinematic (Net-RTK). In the first method, a stationary GNSS station is established on a pre-observed position and transmits correction vectors in real time to the UAV. In the latter, correction vectors are obtained by connecting to a regional network via Network Transport of RTCM via Internet Protocol (NTRIP), requiring an internet connection. In both methods, the camera position at the time of capture can be determined with high accuracy during autonomous flights (Kahveci, 2017; Mazza et al., 2023; Pargiela et al., 2023; Specht et al., 2023, URL-6).

In this study, two different photogrammetric flights were conducted over a test area using both RTK and Net-RTK principles, and the characteristic points of a structure in the field were calculated for each model using a photogrammetric software. Data obtained through the RTK method were used as reference, and statistical tests were performed to examine the significance of differences with the model produced by latter. Through these analyses, the performance of the Net-RTK method in UAV-based photogrammetric field studies was evaluated.

Method

Study Area and Methodology

In this study, a building located within the campus of the Faculty of Arts and Sciences at Hitit University in Çorum was selected as the flight zone (Figure 1). This two-story building is bordered by the campus parking lot to the south and a road to the north, separated from its surroundings by a series of walls. For photogrammetric flights, the DJI Mavic 3 Enterprise was chosen. This UAV provides high resolution (20 MP) and, due to its integrated RTK unit, can connect to a local ground station or the Continuously Operating Reference Stations (CORS-TR (TUSAGA-AKTİF)) system via NTRIP. The UAV offers theoretical accuracy of 1–1.5 cm + 1 ppm both horizontally and vertically (Figure 2, URL-4).

For autonomous flights conducted with both RTK and Net-RTK, the same flight plan and altitudes (40 m) were selected to minimize potential differences between the two models during the process. Prior to the RTK-based flight, a location for the fixed station within the field was chosen, and its coordinates were determined using a CORS-TR compatible GNSS receiver by observation of 100 epochs. The UAV’s remote-control device was then connected to the GNSS ground station via Wi-Fi, enabling the transmission of correction vectors. For the Net-RTK flight, the UAV’s remote controller was connected to the internet through a mobile hotspot on a smartphone, and correction vectors were transmitted using the necessary login credentials for a CORS-TR account.

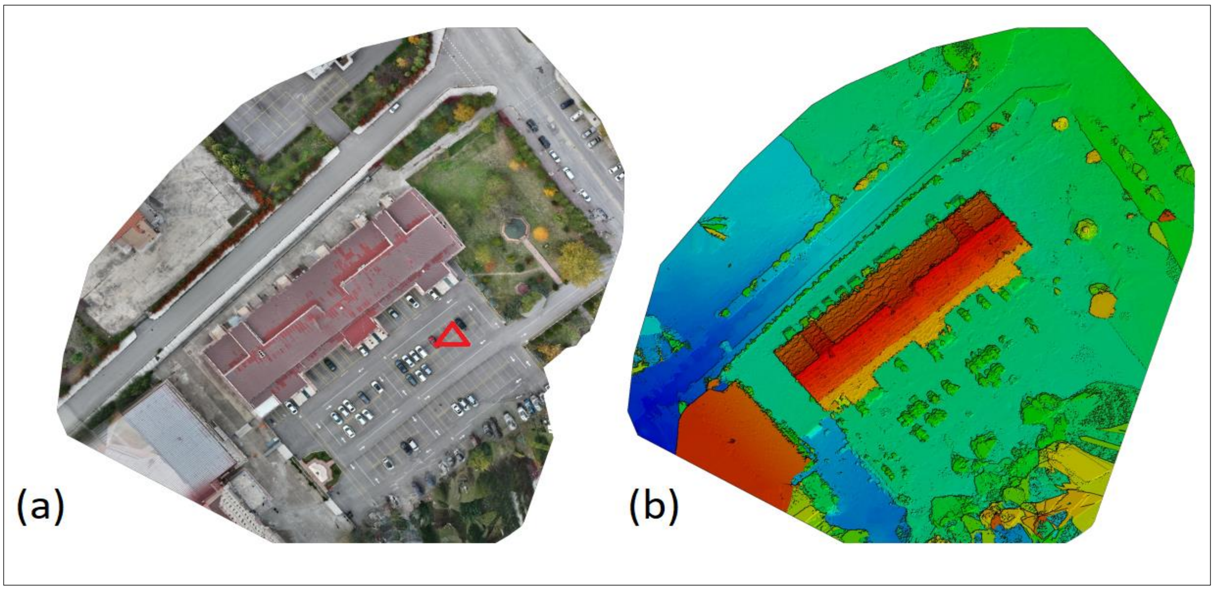

Figure 1. Study area. (a) Ortho-mosaic image, (b) Digital Terrain Model (DTM). The location of the fixed station established during the RTK-based flight is marked with a red triangle on the left (URL-5).

Figure 2. DJI Mavic 3 enterprise RTK (URL-7).
The cylindrical apparatus on top of the UAV functions as the RTK unit.

Pix4D Mapper software was chosen for photogrammetric processing in this study (URL-5). With this software, all photogrammetric images can be processed using Structure-from-Motion (SfM), generating ortho-mosaic images and point clouds via bundle block adjustment. Additionally, the software enables users to produce various outputs, such as orthophotos and DTM.

Results and Discussion

To examine the compatibility of 3D positional data, particularly for the characteristic points on the building, which are clearly observable in both models and appear in multiple digital images were selected (Figure 3). Considering the flight routes of both models, it can be stated that almost every corner of the structure, excluding the eaves, can be digitized from the model. In this study, the 3D coordinates of 10 points were compared (Figure 4). The Average Ground Sampling Distance (GSD) for both models was calculated as 1.1 cm, and the geolocation error for each of the three axes was measured to be under 0.01 m.

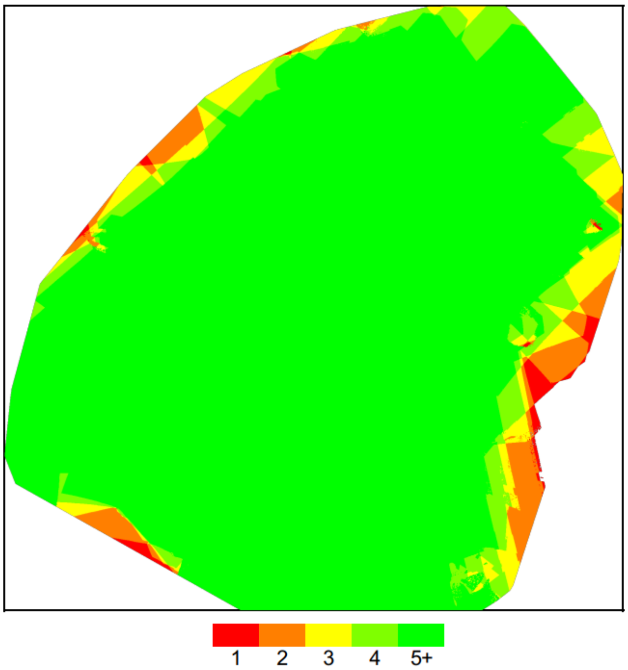

Figure 3. Number of overlapping images. Models through 1-2 images cannot be created and visualized. Main object (two-floored building) is in the green area.

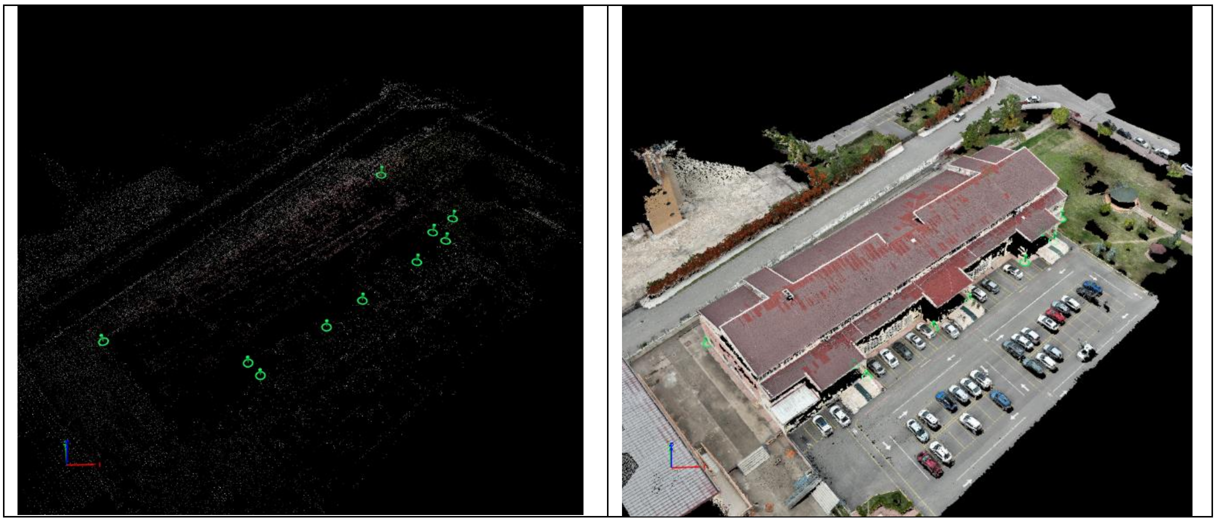

Figure 4. Selected points on the structure used for positional data comparison. On the left, building corner locations digitized through photogrammetric tie points are shown in green, while the point cloud used for digitization is displayed on the right.

Table 1. Coordinates of the characteristic points of the building.

#	Model based on RTK			Model based on NTRIP			Differences		
	Y	X	H	Y	X	H	ΔY (m)	ΔX (m)	ΔH (m)
1	409614.897	4492984.249	828.384	409614.907	4492984.244	828.308	-0.010	0.005	0.076
2	409676.809	4493036.333	828.460	409676.792	4493036.326	828.579	0.017	0.007	-0.119
3	409691.643	4493018.298	828.434	409691.629	4493018.283	828.509	0.014	0.015	-0.075
4	409685.870	4493013.479	828.495	409685.892	4493013.448	828.564	-0.022	0.031	-0.069
5	409688.286	4493010.496	828.488	409688.293	4493010.488	828.563	-0.007	0.008	-0.075
6	409680.404	4493003.783	828.528	409680.393	4493003.731	828.645	0.011	0.052	-0.117
7	409667.028	4492992.772	828.567	409667.021	4492992.782	828.687	0.007	-0.010	-0.120
8	409659.052	4492985.971	828.513	409659.032	4492985.960	828.608	0.020	0.011	-0.095
9	409645.861	4492974.808	828.528	409645.838	4492974.834	828.551	0.023	-0.026	-0.023
10	409643.509	4492977.713	828.601	409643.489	4492977.712	828.656	0.020	0.001	-0.055

Table 2. RMS and standart deviation for coordinate differences in all axes.

Metric	ΔY (m)	ΔX (m)	ΔH (m)
RMSE	0.016	0.022	0.088
Standart deviation	0.014	0.020	0.056

The point locations were initially measured using the RTK model. These 3D coordinates, considered as the reference, were then verified using the NTRIP-based model (Table 1). Root Mean Square Errors (RMSE) were also calculated for the coordinate differences in all axes (Table 2). According to Tables 1 and 2, errors in the Y and X coordinates appear to be random, while the differences in height show a systematic deviation. A graphical representation of these differences has also been provided (Figure 4).

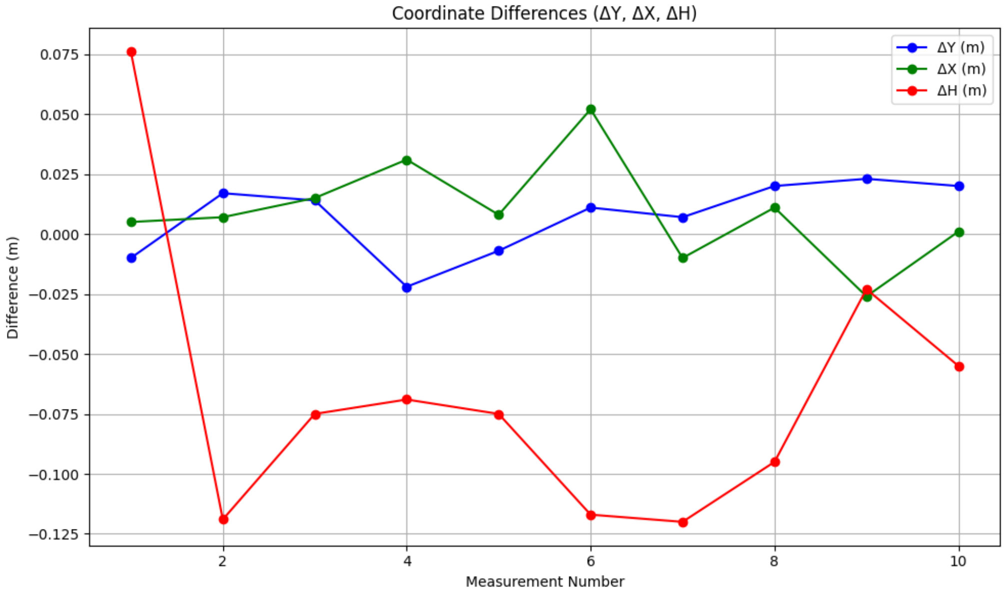

Figure 5. Coordinate differences for all axes.

In Figure 5, it can be observed that coordinate differences in the H axis almost entirely exhibit a systematic negative trend, whereas this trend appears random for the other axes. To identify this trend more clearly, statistical tests were used at this stage. In these kinds of analyses, one first should determine whether the dataset exhibits a normal distribution or not, followed by a parametric or non-parametric test to ascertain if the differences are systematic. In this study, the Shapiro-Wilk test was used to assess the distribution (Shapiro & Wilk, 1965). If the test p-value is greater than 0.05, the data is considered to fit a normal distribution for all axes (Table 3).

Table 3. Shapiro-Wilk test result for coordinate differences.

Metric	ΔY	ΔX	ΔH
Test Statistics	0.8799	0.9514	0.8190
p-value	0.1300	0.6849	0.0246
Result	Normal distribution	Normal distribution	Non-normal distribution

According to the results, the Paired t-test can be applied for coordinate differences in the Y and X axes, while the Wilcoxon, a non-parametric test, can be used for height differences (Gehan, 1965; Hedberg & Ayers, 2015). Based on these test results, it can be determined whether there is a systematic difference between the two measurement methods (Table 4). Table 4 suggests that differences in the Y and X axes are random, while height differences may contain a systematic error.

Tablo 4. Paired t-test (for ΔY and ΔX) and Wilcoxon (for ΔH) test results.

Metric	ΔY	ΔX	ΔH
Test Statistics	1.5170	1.4026	6.0000
p-value	0.1636	0.1943	0.0273
Result	Non-systematic	Non-systematic	Systematic

Conclusion

This study aimed to evaluate the positional accuracy of UAV-based photogrammetry by comparing RTK and Net-RTK methods in a controlled environment. The findings reveal that both methods yielded centimeter-level accuracies, consistent with previous research. For the coordinate differences of the 3D positional data, the horizontal coordinates (Y and X) reveal minimal random differences, with RMSE values of 0.016 m and 0.022 m, respectively. In contrast, the vertical component (H) exhibited a more significant discrepancy (RMSE = 0.088 m), suggesting a potential systematic error specific to height measurements.

Statistical analyses were used to clarify the observations. The Shapiro-Wilk test indicated that while the Y and X axes followed a normal distribution, and the H-axis data deviated from normality and requires to implement non-parametric testing. The Wilcoxon test results showed a statistically significant systematic difference in height between RTK and Net-RTK measurements ($p = 0.0273$). This aligns with recent studies that observed similar challenges in achieving consistent vertical accuracy due to the varying conditions of satellite-based correction signals in Net-RTK operations.

Results highlight the reliability of RTK for high-accuracy tasks requiring precise vertical positioning. However, for broader applications where minor vertical discrepancies are acceptable, Net-RTK remains a viable and efficient alternative, particularly in areas with robust internet connectivity. Future research could explore additional calibration techniques or hybrid methods that mitigate vertical inaccuracies in Net-RTK, especially for environments where local RTK ground stations are not feasible.

Scientific Ethics Declaration

The authors declare that the scientific ethical and legal responsibility of this article published in EPSTEM Journal belongs to the authors.

Acknowledgements or Notes

* This article was presented as an oral presentation at the International Conference on Technology, Engineering and Science (www.icontes.net) held in Antalya/Turkey on November 16-19, 2023.

References

Aksoy, B., Eylence, M., Yuksel, A.S., & Inan, S.A. (2023). Insansız hava araçları kullanılarak deforme olmuş karayolu cizgilerinin tespitinde yapay zekâ yöntemlerinin kullanılması. *Gazi Journal of Engineering Sciences*, *9*(4), 211-219.

Alkan, O., Alzubade, M.K., & Alkan, M.N. (2023) Assessing the effects of alluvial transport in the Kizilirmak river on dams with local, photogrammetric and remote sensing methods, *The Eurasia Proceedings of Science, Technology,Engineering and Mathematics*, *26*, 217-224

Alkan, O., Al-Zubade, M.K., Alkan,M.N.(2022) Detection of the mineral presence and ıts effects on different tree species using drone photogrammetry and remote sensing methods, *The Eurasia Proceedings of Science, Technology,Engineering and Mathematics*, *21*, 266-273.

Al-Zubade, M. K. H. & Alkan, O. (2022). The role of drone photogrammetry, remote sensing and GIS methods in the detection of ore areas and their surroundings. *The Eurasia Proceedings of Science Technology Engineering and Mathematics*, *21*, 380-387.

Choi, S. J., Lee, J. Y., Yoo, S. J., & Kim, S. H. (2023). 3D photogrammetry modeling for safety monitoring of fortress walls. *The International Archives of the Photogrammetry, Remote Sensing and Spatial Information Sciences*, *48*, 421-426.

Dering, G.M., Micklethwaite, S., Thiele, S.T., Vollgger, S.A., & Cruden, A.R. (2019). Review of drones, photogrammetry and emerging sensor technology for the study of dykes: Best practises and future potential. *Journal of Volcanology and Geothermal Research*, *373*, 148–166.

Djı Enterprise. (n.d.). Mavic-3-enterprise. Retrieved from https://enterprise.dji.com/mavic-3-enterprise/specs.

Gehan, E.A. (1965). A generalized Wilcoxon test for comparing arbitrarily singly-censored samples. *Biometrika*, *52*(1-2), 203–224.

Hedberg, E.C., & Ayers, S. (2015). The power of a paired t-test with a covariate. *Social Science Research, 50,* 277-291.

HKMO. (2008). *Acıklamalı örneklemeli buyuk olcekli harita ve harita bilgileri uretim yonetmenligi*. https://obs.hkmo.org.tr/show-media/resimler/ekler/7VST_ff3e350028d0cfc_ek.pdf.

Kaneko, K., Yokochi, M., Inoue, T., Kato, Y., & Fujita, H. (2023). Topographic conditions as governing factors of mire vegetation types analyzed from drone-based terrain model. *Journal of Vegetation Science, 35*(1), e13226.

Lenda, G., Borowiec, N., & Marmol, U. (2023). Study of the precise determination of pipeline geometries using uav scanning compared to terrestrial scanning, aerial scanning and uav photogrammetry. *Sensors*, *23*(19), 8257.

Mazza, D., Parente, L., Cifaldi, D., Meo, A., Senatore, M.R., Guadagno, F.M., & Revellino, P. (2023). Quick bathymetry mapping of a Roman archaeological site using RTK UAS-based photogrammetry. *Frontiers in Earth Science, 11*,1183982.

Oliveira, L.L., Andriolo, A., Cremer, M.J., & Zerbini, A.N. (2023). Aerial photogrammetry techniques using drones to estimate morphometric measurements and body condition in South American small cetaceans. *Marine Mammal Science*, *39*(3), 811-829.

Ozyurt, H.B., & Celen, I. H., (2022). Insansız hava araçları ile yapılan pestisit uygulamalarında farklı meme tiplerinin damla dagılımına etkisinin incelenmesi. *Tarım Makinaları Bilimi Dergisi*, *18*(3), 157-172.

Pargiela, K. (2023). Optimising UAV data acquisition and processing for photogrammetry: A review. *Geomatics and Environmental Engineering*, *17*(3), 29-59.

Pix4D. (n.d.). Product pix4d mapper photogrammetry software. Retrieved from https://www.pix4d.com

Pix4D. (n.d.). Retrieved from https://support.pix4d.com/hc/en-us/articles/202557489

Shapiro, S.S., & Wilk, M.B. (1965). An analysis of variance test for normality (complete samples). *Biometrika. 52*(3-4), 591-611.

SHM.(2020). *Insansız hava aracı sistemleri talimatı (SHT-IHA).* Retrieved from https://web.shgm.gov.tr/documents/sivilhavacilik/files/mevzuat/sektorel/talimatlar.pdf

Specht, M. Widzgowski, S., Stateczny, A., Specht, C., & Lewicka, O. (2023). Comparative analysis of unmanned aerial vehicles used in photogrammetric surveys. *The International Journal on Marine Navigation and Safety of Sea Transportation*, *17*(2), 433-443.

Subramanian, J.A., Asirvadam, V.S., Zulkifli, S.A.B.M., Singh, N.S.S., Shanti, N., Lagisetty, R.K., & Kadir, K.A. (2024). Integrating computer vision and photogrammetry for autonomous aerial vehicle landing in static environment. *IEEE Access*, *12*, 4532-4543.

U blox. (2024, February 1). *What is NTRIP*. Retrieved from https://www.u-blox.com/en/technologies/what-is-ntrip.

Vollgger, S.A., & Cruden, A.R. (2016). Mapping folds and fractures in basement and cover rocks using UAV photogrammetry, Cape Liptrap and Cape Paterson, Victoria, Australia. *Journal of Structural Geodesy, 85*, 168-187.

Woodget, A. S., Austrums, R., Maddock, I. P., & Habit, E. (2017). Drones and digital photogrammetry: from classifications to continuums for monitoring river habitat and hydromorphology. *Wiley Interdisciplinary Reviews: Water*, *4*(4), e1222.

Zhang, W., Peng, X., Cui, G., Wang, H., Takata, D., & Guo, W. (2023). Tree branch skeleton extraction from drone-based photogrammetric point cloud. *Drones*, *7*, 65.

Author Information

Oyku Alkan
Graduated Istanbul Technical University
İstanbul, Türkiye
Contact e-mail: *oyku*.alk*@gmail.com*

Muntaha Kassim Alzubade
University of Technology, Baghdad
Iraq

Mehmet Nurullah Alkan
Hitit University, Corum, Turkiye

To cite this article:

Alkan, O., Alzubade, M.K. & Alkan, M.N. (2024). Comparative analysis of RTK and Net-RTK accuracy in UAV-based photogrammetry. *The Eurasia Proceedings of Science, Technology, Engineering & Mathematics (EPSTEM), 32*, 244-250.

The Eurasia Proceedings of Science, Technology, Engineering & Mathematics (EPSTEM)
ISSN: 2602-3199

The Eurasia Proceedings of Science, Technology, Engineering & Mathematics (EPSTEM), 2024

Volume 32, Pages 251-256

IConTES 2024: International Conference on Technology, Engineering and Science

Mechanical Auto Booting on Production Lines

Kaan Pehlivan
Samsung Electronics

Okan Temizturk
Samsung Electronics

Abstract: Auto-booting is the process of automatically turning on an electronic card. The aim of this study is to transform the auto-booting process from a software to a mechanical process and to analyse and sample the benefits of this process. In this context, 5 samples were carried out in the Samsung Electronics phone production facility and the aim was to change the opening process of the phones to a mechanical process, various studies were carried out and trial productions were carried out. The ppm target and tact time were used as a reference to test the hypotheses. The results of the study showed that the mechanical opening of the phones reduced the tact time and minimised the possible errors.

Keywords: Electronic card, Tact time, Auto booting, Ppm

Introduction

In modern manufacturing and computing environments, efficiency and rapid response times are crucial. One method to achieve this automation is by utilizing AT commands to streamline the booting process.AT (Attention) commands are a set of instructions used for controlling modems and other devices. While traditionally employed in telecommunications, AT commands can be adapted for various devices including embedded systems, enabling users to manage tasks efficiently. These commands are especially useful for initiating boot processes in devices automatically. To implement auto booting through AT commands, the first step involves configuring the device firmware to recognize the commands. In today's fast-paced manufacturing landscape, optimizing production lines is crucial for maintaining competitiveness. One of the innovative solutions that have been gaining traction is the Mechanical Auto Push system. This technology significantly enhances production efficiency and decreases tact time, which is vital for meeting today's demanding market requirements.

Tact time is the time available to produce one unit of product in order to meet customer demand. In a world where speed and efficiency are paramount, minimizing tact time is essential. The Mechanical Auto Push technology is engineered to optimize this measurement by ensuring that every segment of the production line operates smoothly and according to rhythm. For instance, if a factory needs to produce 600 units in eight hours, the required tact time would be 48 seconds per unit. By implementing Mechanical Auto Push systems, manufacturers can automate repetitive tasks, allowing for a more consistent flow that meets or exceeds this pacing. This technological integration not only enhances output but also maintains quality control by reducing the chances of product mishandling.

Mechanical Auto Push refers to a system designed to automate the movement of items through production lines. It simplifies the process of transferring products between different stages of production without the need for manual labor. This reduces human error and increases speed, making it an integral component in both assembly and manufacturing environments.

- Selection and peer-review under responsibility of the Organizing Committee of the Conference

Auto Push

1. Increased Efficiency: The most immediate advantage of Mechanical Auto Push technology is its ability to speed up the entire production process. By automating the opening time of phones products, companies can reduce labor costs and increase throughput.
2. Consistency in Production:Machines operate with a predictable precision that humans cannot always match. Implementing a Mechanical Auto Push system ensures that products move through the production stages without delays or inaccuracies, thereby enhancing overall quality.
3. Reduced Labor Costs: While initial investment in automation may seem significant, the long-term savings are substantial. With machines handling the more mundane aspects of production, businesses can redirect human resources toward roles that require creativity and critical thinking.
4. Flexible Integration: Mechanical Auto Push systems are versatile and can be integrated into various types of production lines. Whether a factory is producing automotive parts, electronics, or consumer goods, these systems can be tailored to meet specific needs, enhancing overall productivity.

Takt Time

Cycle time was originally used to design the work content of operators (Monden, 1998). The term "Tachzeit" comes from the German word "takt" which refers to rhythm and meter in music. In manufacturing, it refers to the speed at which a product is produced.(International Automotive Manufacturing)(Cochran, 1999). Takt times can be as long as days. An aircraft manufacturer, for example, uses a takt time of 4 days (Chao, & Graves, 1992). Takt time represents the average pace of sales over a specific time period. It defines the time available to pro-duce one part (Shingo & Dillon, 1989). It is the overall availableproduction time in a chosen time interval divided by the overall forecasted customer demand for the time interval. The definition is as follows;

Takt Time = Time Available / Avarage Customer Demand per Time Period
Time Available = Total Time – (Maintenance Time + Time Allowances)

The following steps are necessary to calculate takt time:

1. Define the time interval, for which the takt time needs to be calculated
2. Determine the available time per shift
3. Define the customer(s), whose demand needs to be satisfied
4. Determine the demand forecast for the chosen time interval

AT Command

1. Firmware Configuration: Ensure that your device's firmware supports AT commands. This may involve loading a suitable firmware version or modifying existing firmware.
2. Create an Auto Boot Script: Develop a script composed of various AT commands that the device will execute during the boot-up phase. This could include commands for initializing hardware components, connecting to networks, or running diagnostics.
3. Test Commands Individually: Before automating, run each command independently to ensure they execute as expected without errors.
4. Combine Commands into a Sequence: Once verified, arrange the series of commands that you want to execute in the correct order. This sequence will be crucial for a smooth booting process.
5. Set Trigger for Boot: Identify a physical trigger (like a button press) or a timing mechanism (like a timer) that will initiate this sequence of AT commands automatically.

Implementing an auto boot process through AT commands provides several advantages:

- Reduced Tact Time: This is the total time taken from one production unit to the next. By automating booting, manufacturers can significantly decrease the time taken for devices to become operational, thus improving overall productivity.
- Enhanced Precision: Automated processes minimize the likelihood of human error. The use of AT commands ensures each device undergoes the necessary initialization steps every time it boots.

- Consistent Performance: Devices booting through an automated process maintain consistency across multiple cycles. This reliability is critical in production settings, where any inconsistency can lead to defects or inefficiencies.

PPM

Part Per Million (PPM) is a quality metric often employed to gauge defects or errors in processes. To calculate PPM in the context of booting, one must:

1. Define the Sample Size: Determine the number of devices booted in a specific timeframe.
2. Count Boot Errors: Log the number of devices that fail to boot correctly.
3. PPM Calculation: Use the formula:
   $$
   PPM = \left(\frac{\text{Number of Defective Units}}{\text{Total Units}} \right) \times 1,000,000
   $$

By tracking PPM closely, manufacturers can identify issues in the auto booting process and make necessary adjustments to minimize failures. PPM is an expression of one millionth of a whole, but technically the use of this acronym is incorrect. According to technical standards ISO 80000-1, Article 6.5.5 the correct expression is in powers of tenths. Calculation of this dimensionless number is used in manufacturing and other companies to monitor non-conforming parts, the quantity of nonconforming products from a single batch or in the monitored period divided by the total number of units in the same batch or during the monitoring period, and then multiplied by 10^6

PPM= (ND/NS)*1 000 000(Bebr et al.,2017)

Where: ND - number of defect units; NS - number of supplied units As can be seen from the above formula ppm is used as an indicator for comparing production efficiency, supplier performance, or to compare businesses, etc(Bebr et al.,2017)

Setting up an automated booting process using AT commands is a powerful way to enhance productivity, reduce tact time, and ensure consistent performance in any manufacturing environment. By leveraging these commands, businesses can create efficient, error-resilient systems that lead to better overall quality and performance metrics. Implementing these methods effectively can revolutionize operations, paving the way for a more automated and efficient future.

The Mechanical Auto Push technology represents a significant leap forward in manufacturing processes. By decreasing tact time and enhancing overall production efficiency, it addresses some of the most pressing challenges in modern manufacturing. As industries continue to innovate, the adaptation of such technologies will be paramount in achieving sustainable growth and productivity.

Method

Auto Booting with IF Pack

The AT command method is a system that enables commands to be sent to the PBA via the IF Pack, which then facilitates the phone's operation. The IF Pack is a transfer cable equipped with a USB-C connector. Once the phone is fully set up, booting is initiated by executing the AT command using the IF Pack during the initial testing process, allowing the phone to power on. Due to the lengthy process of opening the phone, this step was initially transitioned to the Auto Screw section.

The assembly process for the IF Pack Type C is accomplished by utilizing the auto screw method during pressing, thereby enabling the AT command procedure. Although this adjustment reduced the tact time during the initial attempt, it led to an increase in overall defects, with the IF Pack causing damage to the USB area. The defect rate was recorded at 35 per 1,000 pieces, equating to 35,000 parts per million (ppm) in Table 1.

Table 1. Samples of Samsung

Variables		Product	Defect Ppm
	1.	1000	35000(%3.5)
Group	2.	10000	0(%0)
	3.	10000	0(%0)
Model	Rear Back Cover	10000	0
	Auto Screw	10000	0
	Press AT Command	1000	35000

Results and Discussion

Mechanical Auto Boot on Auto Screw

5 phone models were tested for auto-boot processes. In PD chargers where the software boot process is applied using the AT command method, the phone boot process is performed using the IF Pack input. IF Pack input and output time: 1.6 s + AT command time: 0.4 s = 2 s is defined as the processing time. The average opening time of a phone is 43 seconds. The pressing time of the mechanical process is 4 s and 6 ports perform the same process; the pressing process is completed in 7,3 second on average. A similar process takes place with the Auto Screw process and the average screw time for models with full backs is between 40 and 50 seconds. The mechanical booting is that we added 1 button (Figure 3.) of the autoscrew fixture when close the autoscrew cover, a boot button and split power switch while this push on phone in turn presses. Not require any software operation at all but boots up by user interaction with both physical buttons.ones.

This has been tested on 10000 phones, without any error and failure rate has result as 0 ppm As Samsung uses 2 types of housings to make phones, Auto Screw is not well-supported. Because we needed a sustainable answer, so 2 types has to be separated and also need that why cases lives in dark areas. Full Set Rear model: With this model, the Full Set is attached to the phone and there is a power button on it. Auto screw process initiates and mechanical booting can be performed once full set is fitted. Top / Bottom Rear Antenna Model: There are 2 antennas and this models use a Rear Press Jig (Figure 1.) but since the power key is on the back cover for auto screw-on wiring it cannot be done in mechanical boot. To solve this, the button (Figure 2.) was planned to drive on, press taking advantage of a place for another botton in suitable location during back cover pressing action- and turn-on phone as experiment were conducted over failure rate causes detection & deformation. As a result of 10000 units of production, no error was found and the process was developed for all Samsung models.

1. Material Selection: The choice of materials for the button body and internal components plays a crucial role in durability and user experience. Common materials include plastic, metal, and composites. Each has its pros and cons regarding weight, cost, and resilience to wear and tear.
2. Ergonomics: The design should prioritize ease of use, ensuring that the button is intuitive and comfortable to press.
3. Sensitivity and Feedback: Mechanical push buttons must provide immediate feedback upon activation to reassure users that their action has been registered. This can be achieved through tactile and auditory cues, enhancing user satisfaction.
4. Environmental Factors: Consideration of where the push button will be used is essential. For example, buttons exposed to moisture or dust need to have protective seals to maintain functionality over time.

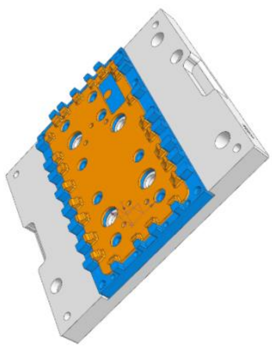

Figure 1. Without booting button

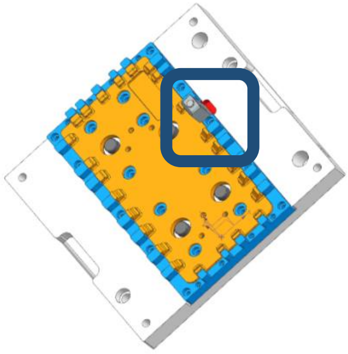

Figure 2. Implemented booting button

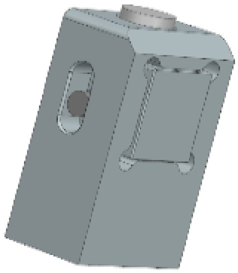

Figure 3. Booting button

More efficient results were obtained compared to the AT Command process and a total of 1 man-power/2 shift was gained during this process. Although the model classifications are very variable, mechanical booting was found to be more functional and effective in all areas.

Conclusion

When all the data was evaluated, the mechanical boot process was found to be suitable for lower error rates and longer use. It was found to be efficient and possible in terms of applicability to the existing production order and production lines. As a result of the visual and functional tests performed on 5 different phone models used in this study, the mechanical boot process can be preferred over other alternatives in phone production lines.

Recommendations

All production lines can be considered suitable for similar line developments and harmonization improvements, and similar ones can be tried in test productions. Their efficiency can be tested by evaluating them within the established takt time, ppm rate and LOB limits and, if appropriate, implemented. In production lines based on operating performance, it will be more effective to use mechanical booting with mechanical and durable material selection.

Scientific Ethics Declaration

The authors declare that the scientific ethical and legal responsibility of this article published in EPSTEM Journal belongs to the authors.

Acknowledgements or Notes

* This article was presented as an poster presentation at the International Conference on Technology, Engineering and Science (www.icontes.net) held in Antalya/Turkey on November 14-17, 2024.

References

Bebr, L., Bícová, K., & Zídková, H. (2017). Use of the ppm and its function in the production process. *Procedia Manufacturing*, *13*, 608-615.

Chao, J. S, & Graves, S. C. (1992), *Reducing flow time in aircraft industry*. MIT working paper. https://dspace.mit.edu/bitstream/handle/1721.1/2455/SWP-3539-28521185.pdf

Linck, J., & Cochran, D. S. (1999). *The importance of takt time in manufacturing system design* (No. 1999-01-1635). SAE Technical Paper.

Monden, Y. (1998). *Toyota production system: An ıntegrated approach to just*-in-*time (3rd Edition)*. Engineering & Management Press

Shingo, S. & Dillon, A.P. (1989). *A study of the toyota production system from an ındustrial engineering viewpoint*. Productivity Press

Author Information

Kaan Pehlivan
Samsung Electronics
Mimar Sinan Mahallesi, 103. Cadde No:72, 59500 Kapaklı/Tekirdağ, Türkiye
Contact e-mail: k.pehlivan@samsung.com

Okan Temiztürk
Samsung Electronics
Mimar Sinan Mahallesi, 103. Cadde No:72, 59500 Kapaklı/Tekirdag, Türkiye

To cite this article:

Pehlivan, K., & Temizturk, O. (2024). Mechanical auto booting on production lines. *The Eurasia Proceedings of Science, Technology, Engineering & Mathematics (EPSTEM), 32*, 251-256.

The Eurasia Proceedings of Science, Technology, Engineering & Mathematics (EPSTEM)
ISSN: 2602-3199

The Eurasia Proceedings of Science, Technology, Engineering & Mathematics (EPSTEM), 2024

Volume 32, Pages 257-265

IConTES 2024: International Conference on Technology, Engineering and Science

Green Supplier Selection with CoCoFISo-G

Halil Sen
Burdur Mehmet Akif Ersoy University

Mustafa Serdar Toksoy
Burdur Mehmet Akif Ersoy University

Abstract: Green supplier selection is the process of evaluating suppliers for environmental sustainability and efficient use of resources. In recent years, there has been a growing trend to work with suppliers that meet environmental sustainability standards. Green sourcing considers criteria such as the source of a product's raw materials and its impact on the environment. In the cosmetics industry, green supplier selection is a critical step in increasing the environmental and social sustainability of products. This process ensures that green and ethical practices are considered at every stage of the supply chain. Supplier selection is a multi-criteria decision problem. This study aims to solve the supplier selection problem in the supply of perfume bottles for a cosmetics company using the CoCoFISo-G method. The CoCoFISo-G method was created by extending the CoCoFISo (Combined Compromise for Ideal Solution) method with gray numbers. The CoCoFISo method is an extension of the CoCoSo method, and the purpose of the CoCoFISo method is to find an ideal compromise solution to improve the algorithm of the CoCoSo method. In this study, the developed CoCoFISo-G method is used for green supplier selection.

Keywords: Multi-criteria decision-making, Green supplier selection, Grey values, Combined compromise solution method, Combined compromise for ideal solution

Introduction

The environmental pollution caused by the conscious or unconscious production activities of businesses, the unconscious and excessive consumption of consumers, the risk of depletion of natural resources and global warming have made societies more conscious about the environment. While this awareness of consumers puts pressure on businesses, legal regulations have been established in many countries to protect the natural environment and many environmental protocols have been signed at both national and international levels. These developments have forced businesses to produce environmentally friendly products and have led them to make additional demands from their suppliers in this direction. The concept of green supply chain has emerged. It has emerged as a result of activities aimed at reducing or eliminating the negative effects of supply chain activities on the environment and increasing their positive effects. In this paper GSCM is defined as: Green Supply Chain Management (GSCM) = Green Purchasing + Green Manufacturing / Materials Management + Green Distribution / Marketing + Reverse Logistics (Hervani et al., 2005). Green purchasing is of key importance in terms of effective and successful management of the supply chain. It expresses environmental sensitivity in the selection, evaluation and development of suppliers and also covers the measures to be taken against possible environmental problems. Studies on green supplier selection are increasing.

Hashemi et al. (2015) proposed a comprehensive green supplier selection model using both economic and environmental criteria. They used ANP and an improved GRA to weight the criteria and rank the suppliers. They determined cost, quality, technology, resource consumption, pollution production, management commitment as criteria and presented a case study in the automotive industry. In the study of Yu and Hou

- Selection and peer-review under responsibility of the Organizing Committee of the Conference

(2016) proposed a modified multiplicative analytical hierarchy process method to solve the green supplier selection problem. They determined four main criteria: product performance, supplier criteria, cooperation and development potential, and green performance. Liao et al. (2016) combined the fuzzy analytic hierarchy process (FAHP), fuzzy additive ratio assessment method (ARAS-F) and multi-segment goal programming (MSGP) methods to solve green supplier selection problems and presented a solution proposal for the green supplier selection problem. They demonstrated this integrated model with an example from a watch company. The criteria used are purchasing cost, quality service, technology capability, environmental capability and delivery performance.

In the study of Keshavarz Ghorabaee et al. (2016) a new integrated approach based on the Weighted Total Product Assessment (WASPAS) method was proposed to address multi-criteria group decision-making problems with Interval type-2 fuzzy sets (IT2FS). They used the entropy method in calculating the criteria weights. The criteria used are; environmental pollution of production, resource consumption, ecological design, environmental management system, adherence of managers to GSCM, use of green technology, use of green materials. Qin et al. (2017) developed and implemented a new TODIM method in green supplier selection in their study. They used ten criteria: green product innovation; green image, use of environmentally friendly technology, resource consumption, green competencies, environment management, quality management, total product life cycle cost, pollution production, staff environmental training. Govindan et al. (2017) proposed a hybrid approach combining the revised Simos procedure, PROMETHEE methods, algorithms to generate a group consensus ranking, and robustness analysis, and used the cost, quality, delivery, environmental impacts, technology capability as criteria. Bakeshlou et al. (2017) developed a multi-objective fuzzy linear programming model for a GSS problem, including 17 criteria, formed into 5 clusters while a hybrid fuzzy multi objective decision making (MODM) is employed to solve it. Banaeian et al. (2018) compared three popular multi-criteria decision-making methods, TOPSIS, VIKOR and GRA, in the application of supplier selection method in a fuzzy environment. Wu et al., 2019). Presented an integrated methodology for addressing MCGDM problems in discrete type-2 fuzzy environment based on best-worst method (BWM) and VlseKriterijumska Optimizacija I Kompromisno Resenje (VIKOR) technique. Green product innovation, environmental regime, use of green technology, product quality management, total green product cost, resource consumption, environmental pollution of production were used as a criteria. In the study conducted by Rouyendegh et al. (2020) the hybrid method, which emerged by combining Intuitive Fuzzy Set and TOPSIS, was used to select which supplier is more suitable among the alternatives.

This study aims to solve the supplier selection problem in the supply of perfume bottles for a cosmetics company using the CoCoFISo-G method. The CoCoFISo-G method was created by extending the CoCoFISo (Combined Compromise for Ideal Solution) method with gray numbers. The CoCoFISo method is an extension of the CoCoSo method, and the purpose of the CoCoFISo method is to find an ideal compromise solution to improve the algorithm of the CoCoSo method.

The CoCoSo (Combined Compromise Solution) method developed by Yazdani et al. (2019) is based on the integration of simple additive weighting (SAW) and the exponentially weighted product model (MEP). The essence of this method lies in the combination of compromise perspectives that ultimately reconcile often conflicting evaluation criteria. The CoCoSo method provides an overview of possible compromise solutions available to the decision maker (Popović, 2021).

The research by Wen et al. (2019) extends the CoCoSo method to solve the multi-expert, multi-criteria decision making (MCDM) problem in selecting third-party logistics service providers (3PLs) in a hesitant fuzzy language environment. The research presents an innovative approach to evaluate and select 3PL service providers. Stanujkic et al. (2020) evaluated the progress of European Union countries towards achieving the 2030 Sustainable Development Goals (SDGs) using CoCoSo and Shannon Entropy methods. Torkayesh et al. (2021) evaluates the social sustainability performance of seven developed countries, including the G7 countries. The study analyzes social sustainability using an integrated data-driven weighting system and the CoCoSo model. Torkayesh et al. (2021) developed an integrated multi-criteria framework for evaluating health care sectors in Eastern Europe. The methods used include BWM (Best Worst Method), LBWA (Linear Best Worst Approach), and CoCoSo (Combined Compromise Solution). This framework emphasizes that the health sector is an important element of infrastructure. In their study, Peng and Luo (2021) propose a decision model for market bubble warning of Chinese stocks. This model facilitates decision making using image fuzzy information with a unified consensus solution (CoCoSo). The authors address comparability issues by developing an innovative image fuzzy score function and calculating target weights using Renyi entropy. The goal of the study is to demonstrate the applicability of the algorithm. Deveci et al. (2021) investigated a CoCoSo method based on the Fuzzy Power Heronian function to prioritize the benefits of autonomous vehicles in real-time traffic management. Ecer (2021) proposes an integrated multi-criteria decision making (MCDM) framework for the performance evaluation of battery electric vehicles (BEVs). In the study, ten BEVs are selected as alternatives. These vehicles are then ranked based on technical attributes such as acceleration, price, battery, range, and battery using SECA, MARCOS, MAIRCA, COCOSO, ARAS, and COPRAS multi-criteria techniques. Bagal et al. (2021) aimed to investigate the effect of welding variables (such as compression time, welding time and current) on resistance spot welding of different materials. Optimization was achieved and results were evaluated using CoCoSo, EDAS and WASPAS methods, which are advanced hybrid Taguchi methods.

Yazdani et al. (2019) aimed to measure the performance of supplier selection in construction management using CoCoSo-G, an improved unified consensus solution method with gray numbers. Gabriel -Rasoanaivo et al. (2024) introduced the CoCoFISo method, which is an improved version of the CoCoSo method. The authors tested and validated this method using real case studies and compared its performance with other multi-criteria decision-making methods such as PROMETHEE, WSM, and TOPSIS2. The results show that CoCoFISo can overcome the limitations of CoCoSo and provide stable results. In this study, we extended the COCOFISo method with gray numbers and used this method, which we named COCOFISO-G, in green supplier selection.

Methods

SWARA

Different methods such as AHP, Entropy and SWARA can be used to determine criterion weights. In this study, SWARA (Step-by-Step Weight Assessment Ratio Analysis Method) was used and the method follows these steps:

Step 1: Determination of criteria (C_j, j = 1,2,3, ... n) and decision makers (DM_D, D = 1,2, ... d).

Step 2: Sort the criteria from most important to insignificant according to their own knowledge and experience.

Step 3: In this step, each decision maker, starting from the second order criterion, specifies the relational significance (s_j^d) of C_{j-1} according to the C_j criterion for decision maker d. For example, how important is the first-order criterion compared to the second-order criterion.

Step 4: A criterion (k_j^d) is calculated for each criterion in the following equation.

$$k_j^d = \begin{cases} 1 & j = 0 \\ s_j^d + 1, & j > 1 \end{cases} \tag{1}$$

Step 5: The weight coefficients (q_j^d) are calculated for each criterion using the following equation.

$$q_j^d = \begin{cases} 1 & j = 0 \\ \frac{q_{j-1}^d}{k_j}, & j > 1 \end{cases} \tag{2}$$

Step 6: The relative weight (w_j^d) values of the criteria are calculated.

$$w_j^d = \frac{q_j^d}{\sum_{j=1}^{n} q_j^d} \tag{3}$$

Step 7: In case group decision making, it is received by the geometric mean of the calculated weight value, then the relative weight values of the found weight values are calculated and the final result is reached. It is indicated by Wj.

CoCoFISo-G

The CocoFISo method was developed by Yazdani et al. due to the problems encountered in the CoCoSo method in some special cases. One of these special cases is that when a criterion has the same value for all alternatives, the normalization process cannot be calculated. The other is that when an alternative has the worst element in all criteria, it is not possible to calculate the addition step in the algorithm. In this study, this developed algorithm was extended with gray numbers. The steps of the algorithm are as follows.

1. Step: The first stage is grey decision-making matrix (GDMM) forming. In the GMCDM of the discrete optimization problem any problem to be solved is represented by the following DMM of preferences for m reasonable alternatives (rows) rated on n criteria (columns): where m – number of alternatives, n – number of criteria describing each alternative, $\otimes x_{ij}$ – grey value representing the performance value of the i alternative in terms of the j criterion.

$$\tilde{X} = \begin{bmatrix} \otimes x_{11} & \cdots & \otimes x_{1j} & \cdots & \otimes x_{1n} \\ \vdots & \ddots & \cdots & \ddots & \vdots \\ \otimes x_{i1} & \cdots & \otimes x_{ij} & \cdots & \otimes x_{in} \\ \vdots & \ddots & \ddots & \ddots & \vdots \\ \otimes x_{m1} & \cdots & \otimes x_{mj} & \cdots & \otimes x_{mn} \end{bmatrix}$$

$$i = \overline{0,m}; j = \overline{1,n}. \tag{4}$$

2. Step: Normalization of the matrix. The second stage the initial values of all the criteria are normalized-defining values $\otimes \overline{X_{ij}}$ of normalized decision-making matrix $\otimes \bar{X}$:

$$\otimes \bar{X} = \begin{bmatrix} \otimes \bar{x}_{11} & \cdots & \otimes \vec{x}_{1j} & \cdots & \otimes \bar{x}_{1n} \\ \vdots & \ddots & \cdots & \ddots & \vdots \\ \otimes \bar{x}_{i1} & \cdots & \otimes \bar{x}_{ij} & \cdots & \otimes \bar{x}_{in} \\ \vdots & \ddots & \ddots & \ddots & \vdots \\ \otimes \bar{x}_{m1} & \cdots & \otimes \bar{x}_{mj} & \cdots & \otimes \vec{x}_{mn} \end{bmatrix}$$

$$i = \overline{0,m}; j = \overline{1,n}. \tag{5}$$

The following formula is used in the normalization process:

$$\otimes \bar{x}_{ij} = \frac{\otimes x_{ij}}{\sqrt{\sum_{i=0}^{m} (\otimes x_{ij})^2}} \tag{6}$$

3. Step: The third stage is defining normalized-weighted matrix – $\otimes \bar{\bar{X}}$. Only well-founded weights should be used because weights are always subjective and influence the solution. The values of weight w_j are usually determined by the expert evaluation method.

$$\sum_{j=1}^{n} w_j = 1, \tag{7}$$

$$\otimes \bar{\bar{x}}_{ij} = \otimes \bar{x}_{ij} \times w_j, \tag{8}$$

$$\otimes \bar{\bar{X}} = \begin{bmatrix} \otimes \bar{\bar{x}}_{11} & \cdots & \otimes \bar{\bar{x}}_{1j} & \cdots & \otimes \bar{\bar{x}}_{1n} \\ \vdots & \ddots & \cdots & \ddots & \vdots \\ \otimes \bar{\bar{x}}_{i1} & \cdots & \otimes \bar{\bar{x}}_{ij} & \cdots & \otimes \bar{\bar{x}}_{in} \\ \vdots & \ddots & \ddots & \ddots & \vdots \\ \otimes \bar{\bar{x}}_{m1} & \cdots & \otimes \bar{\bar{x}}_{mj} & \cdots & \otimes \bar{\bar{x}}_{mn} \end{bmatrix}$$

$$i = \overline{0,m}; j = \overline{1,n}. \tag{9}$$

4. Step: Obtaining the total of the weighted comparability series and the total power weight of the comparability series for each alternative as $\otimes S_i$ and $\otimes P_i$, respectively.

$$\otimes S_i = \sum_{j=1}^{n} \otimes \overline{\overline{x_{ij}}} \tag{10}$$

$$\otimes P_i = \sum_{j=1}^{n} \otimes \overline{x_{ij}}^{w_j} \tag{11}$$

5. Step: Ranking of considered alternatives. For ranking purposes, method uses a relative performance score $\otimes k_i$, which is calculated based on three aggregate estimated results $\otimes k_{ia}$, $\otimes k_{ib}$ and $\otimes k_{ic}$, as follows:

$$\otimes k_{ia} = \frac{(\otimes S_i + \otimes P_i)}{\sum_{i=1}^{m}(\otimes S_i + \otimes P_i)} \tag{12}$$

$$\otimes k_{ib} = \frac{(\otimes S_i + \otimes P_i)}{1+\left(\frac{\otimes S_i}{1+\otimes S_i}\right)+\left(\frac{\otimes P_i}{1+\otimes P_i}\right)} \tag{13}$$

$$\otimes k_{ic} = \frac{(\lambda \otimes S_i + (1-\lambda)\otimes P_i)}{(\lambda \max_i \otimes S_i + (1-\lambda)\max_i \otimes P_i)} \tag{14}$$

for $0 \leq \lambda \leq 1$.

In Eqn. (11), decision-makers chose λ (usually λ = 0.5).

$$\otimes k_i = (\otimes k_{ia} \otimes k_{ib} \otimes k_{ic})^{1/3} + \frac{(\otimes k_{ia} + \otimes k_{ib} + \otimes k_{ic})}{3} \tag{15}$$

6. Step: Calculation of K. K is the crisp value for the assumed grey number. The score obtained by Eqn. (16) is called the CoCoFISo-G score. The alternative with the highest score is the best.

$$\otimes k_i = [k^-, k^+]$$

$$Ki = k^- + ((k^+ - k^-)/2) \tag{16}$$

If the current method is developed for group decision making, the following equation can be used for the calculation of the utility degree Ki of an alternative i is given below:

$$K_i = \sqrt[D]{\prod_{d=1}^{D} K_i^d} \tag{17}$$

K_i^d : d is the decision maker d, i is the alternative i, D is the number of decision makers.

Results and Discussion

NaturaLux is one of the leading cosmetic companies in Turkey and exports 70% of its production to European Union countries and Russia. The increasing environmental awareness of its customers and the legal sanctions in these countries have led the company to green supply chain management practices. Choosing a green supplier not only contributes to the environment but is also critical to the long-term success and sustainability of businesses.

This study aims to solve the supplier selection problem in the supply of perfume bottles for NaturaLux by using the CoCoFISo-G method. For perfume bottles, suppliers were subjected to a preliminary evaluation and as a result of this preliminary evaluation, ten suppliers were included in this study. Our criteria for choosing a green supplier consist of;

- Delivery performance (C_1); covers features such as the deviation of the order from the specified date, the conformity of the ordered product to the specified conditions.
- Green product innovation(C_2); covers addressing environmental problems through product design and technical innovation.
- Green technology use(C_3); covers the use of technologies developed to protect the natural environment and resources and reduce the negative effects of human intervention.
- Cost (C_4); covers all cost items related to purchasing; product cost, logistics cost, insurance cost, etc. (The lower the cost, the higher the evaluation value.)
- Resource consumption (C_5); covers the effective and efficient consumption of natural resources, the less amount of harmful waste, and the less manufacturing waste. The lower the resource consumption, the higher the evaluation value.
- Quality Management (C_6); covers the effectiveness of the established quality management system, its reflection on the products, and the integration of quality and environmental management systems.

While determining these criteria, studies in the literature and the company's goals and objectives were taken into consideration. Our decision makers consist of the purchasing manager (DM_1), quality manager (DM_2), export manager (DM_3) and production manager (DM_4). Firstly, the weights of the criteria were calculated using the SWARA method. The criteria weight information of the decision makers was combined using the geometric mean and the data in Table 1 was obtained. After determining the criteria weights, as the first step of the CoCoFISo-G method, the initial decision matrix was created by taking the decision makers' opinions on the options based on the criteria. The evaluation scale in Table 2 was used while creating this. Table 3 shows the initial decision matrix of the purchasing manager (DM_1). As a second step, the initial decision matrices obtained were normalized (Table 4). Normalization was done using Eqn. (6).

Table 1. Criteria Weights

	Decision Makers					
Criteria	DM1	DM2	DM3	DM4	Geometric mean	Wi
C1	0,193225	0,204756	0,181536	0,184852	0,190885121	0,191104
C2	0,175659	0,16922	0,165033	0,168048	0,169445961	0,16964
C3	0,139412	0,153836	0,157174	0,145496	0,148815303	0,148986
C4	0,212548	0,186142	0,181536	0,203338	0,195488065	0,195712
C5	0,146383	0,146511	0,165033	0,152771	0,152490308	0,152665
C6	0,132773	0,139534	0,149689	0,145496	0,14172886	0,141892

Table 2. Criteria evaluation scale

Rating	Gray Number Correspondence
Very Low	(0.0,0.2)
Low	(0.2,0.4)
Medium	(0.4,0.6)
High	(0.6,0.8)
Very High	(0.8,1.0)

Table 3. Purchasing Manager's (DM_1) initial grey decision making matrix

	Resource consumption		Green product innovation		Green technology use		Cost		Delivery performance		Quality Management	
Supplier	C_1		C_2		C_3		C_4		C_5		C_6	
S_1	0,80	1,00	0,60	0,80	0,40	0,60	0,80	1,00	0,40	0,60	0,60	0,80
S_2	0,60	0,80	0,40	0,60	0,20	0,40	0,60	0,80	0,60	0,80	0,40	0,60
S_3	0,80	1,00	0,40	0,60	0,60	0,80	0,80	1,00	0,20	0,40	0,60	0,80
S_4	0,60	0,80	0,20	0,40	0,40	0,60	0,60	0,80	0,40	0,60	0,40	0,60
S_5	0,60	0,80	0,40	0,60	0,20	0,40	0,60	0,80	0,40	0,60	0,60	0,80
S_6	0,40	0,60	0,60	0,80	0,40	0,60	0,60	0,80	0,80	1,00	0,60	0,80
S_7	0,20	0,40	0,40	0,60	0,60	0,80	0,80	1,00	0,60	0,80	0,60	0,80
S_8	0,60	0,80	0,60	0,80	0,20	0,40	0,60	0,80	0,80	1,00	0,40	0,60
S_9	0,40	0,60	0,40	0,60	0,40	0,60	0,60	0,80	0,60	0,80	0,20	0,40
S_{10}	0,20	0,40	0,60	0,80	0,40	0,60	0,40	0,60	0,60	0,80	0,60	0,80

Table 4. Purchasing Manager's (DM_1) normalized decision-making matrix

	Resource consumption		Green product innovation		Green technology use		Cost		Delivery performance		Quality Management	
Supplier	C_1		C_2		C_3		C_4		C_5		C_6	
S_1	0,34	0,57	0,28	0,53	0,21	0,47	0,30	0,49	0,17	0,33	0,27	0,49
S_2	0,25	0,45	0,19	0,40	0,11	0,31	0,22	0,39	0,25	0,44	0,18	0,37
S_3	0,34	0,57	0,19	0,40	0,32	0,62	0,30	0,49	0,08	0,22	0,27	0,49
S_4	0,25	0,45	0,09	0,26	0,21	0,47	0,22	0,39	0,17	0,33	0,18	0,37
S_5	0,25	0,45	0,19	0,40	0,11	0,31	0,22	0,39	0,17	0,33	0,27	0,49
S_6	0,17	0,34	0,28	0,53	0,21	0,47	0,22	0,39	0,33	0,56	0,27	0,49
S_7	0,08	0,23	0,19	0,40	0,32	0,62	0,30	0,49	0,25	0,44	0,27	0,49
S_8	0,25	0,45	0,28	0,53	0,11	0,31	0,22	0,39	0,33	0,56	0,18	0,37
S_9	0,17	0,34	0,19	0,40	0,21	0,47	0,22	0,39	0,25	0,44	0,09	0,24
S_{10}	0,08	0,23	0,28	0,53	0,21	0,47	0,15	0,29	0,25	0,44	0,27	0,49

In the next step, the weighted normalized decision matrix (Table 5.) and normalized weighted power matrix (Table 6.) were created. These decision matrices were of course made separately for each decision maker.

Table 5. Purchasing Manager's (DM_1) weighted normalized decision matrix

Supplier	Resource consumption C_1		Green product innovation C_2		Green technology use C_3		Cost C_4		Delivery performance C_5		Quality Management C_6	
S_1	0,065	0,108	0,048	0,090	0,032	0,070	0,058	0,095	0,025	0,051	0,038	0,069
S_2	0,048	0,087	0,032	0,067	0,016	0,047	0,044	0,076	0,038	0,068	0,025	0,052
S_3	0,065	0,108	0,032	0,067	0,047	0,093	0,058	0,095	0,013	0,034	0,038	0,069
S_4	0,048	0,087	0,016	0,045	0,032	0,070	0,044	0,076	0,025	0,051	0,025	0,052
S_5	0,048	0,087	0,032	0,067	0,016	0,047	0,044	0,076	0,025	0,051	0,038	0,069
S_6	0,032	0,065	0,048	0,090	0,032	0,070	0,044	0,076	0,051	0,085	0,038	0,069
S_7	0,016	0,043	0,032	0,067	0,047	0,093	0,058	0,095	0,038	0,068	0,038	0,069
S_8	0,048	0,087	0,048	0,090	0,016	0,047	0,044	0,076	0,051	0,085	0,025	0,052
S_9	0,032	0,065	0,032	0,067	0,032	0,070	0,044	0,076	0,038	0,068	0,013	0,035
S_{10}	0,016	0,043	0,048	0,090	0,032	0,070	0,029	0,057	0,038	0,068	0,038	0,069

Table 6. Purchasing Manager's (DM_1) normalized weighted power matrix

Supplier	Resource consumption C_1		Green product innovation C_2		Green technology use C_3		Cost C_4		Delivery performance C_5		Quality Management C_6	
S_1	0,813	0,897	0,807	0,898	0,794	0,893	0,789	0,868	0,760	0,846	0,829	0,903
S_2	0,769	0,860	0,753	0,855	0,716	0,841	0,746	0,831	0,809	0,884	0,782	0,867
S_3	0,813	0,897	0,753	0,855	0,843	0,932	0,789	0,868	0,684	0,795	0,829	0,903
S_4	0,769	0,860	0,670	0,798	0,794	0,893	0,746	0,831	0,760	0,846	0,782	0,867
S_5	0,769	0,860	0,753	0,855	0,716	0,841	0,746	0,831	0,760	0,846	0,829	0,903
S_6	0,712	0,814	0,807	0,898	0,794	0,893	0,746	0,831	0,845	0,914	0,829	0,903
S_7	0,624	0,753	0,753	0,855	0,843	0,932	0,789	0,868	0,809	0,884	0,829	0,903
S_8	0,769	0,860	0,807	0,898	0,716	0,841	0,746	0,831	0,845	0,914	0,782	0,867
S_9	0,712	0,814	0,753	0,855	0,794	0,893	0,746	0,831	0,809	0,884	0,709	0,819
S_{10}	0,624	0,753	0,807	0,898	0,794	0,893	0,689	0,786	0,809	0,884	0,829	0,903

In the next step, $\otimes S_i$ and $\otimes P_i$ values were calculated by using Eqn. (10) and (11) (Table 7.).

Table 7. Purchasing Manager's (DM_1) $\otimes S_i$ and $\otimes P_i$ values

S_1	0,266	0,483	4,792	5,305
S_2	0,203	0,396	4,576	5,137
S_3	0,253	0,467	4,711	5,251
S_4	0,190	0,380	4,521	5,095
S_5	0,203	0,397	4,573	5,135
S_6	0,244	0,455	4,732	5,253
S_7	0,230	0,436	4,647	5,195
S_8	0,232	0,436	4,665	5,211
S_9	0,190	0,381	4,523	5,095
S_{10}	0,201	0,397	4,551	5,116

For ranking, a relative performance score $\otimes k_i$, was calculated using Eqn. (12), (13), (14), (15) and then The CoCoFISo-G score (K) calculated by Eqn. (16) (Table 8.)

Table 8. CoCoFISo-G Score for DM_1

Supplier	$\otimes \boldsymbol{k_{ia}}$		$\otimes \boldsymbol{k_{ib}}$		$\otimes \boldsymbol{k_{ic}}$		$\otimes \boldsymbol{k_i}$		**K**
S_1	0,0903	0,1193	2,201	2,985	0,873665311	1	1,613	2,077	1,8449
S_2	0,0853	0,1141	2,123	2,926	0,825572814	0,956016	1,542	2,016	1,7788
S_3	0,0886	0,1179	2,165	2,969	0,857529826	0,987808	1,585	2,060	1,8226
S_4	0,0841	0,1129	2,101	2,913	0,813983611	0,94589	1,524	2,001	1,7626
S_5	0,0853	0,1141	2,122	2,926	0,825175472	0,955764	1,541	2,015	1,7782
S_6	0,0888	0,1177	2,181	2,966	0,859721146	0,986127	1,593	2,057	1,8253
S_7	0,0870	0,1161	2,144	2,949	0,842434203	0,97289	1,564	2,039	1,8016
S_8	0,0874	0,1164	2,154	2,952	0,846059584	0,975506	1,571	2,043	1,8070
S_9	0,0841	0,1129	2,102	2,913	0,814216715	0,946028	1,524	2,002	1,7629
S_{10}	0,0848	0,1137	2,109	2,921	0,82085565	0,952544	1,533	2,010	1,7715

Since group decision making was used in this study, the last step was to combine the K values of the decision makers. For this, Eqn. (17) is used. The supplier with the highest CoCoFISo-G score was at the top of the ranking, which was supplier S_1.

Conclusion

Today, selecting green suppliers has become an important part of a company's sustainability and environmental efforts. Green suppliers are companies that minimize their environmental impact and adopt sustainable practices. This helps to conserve natural resources and reduce pollution. Many countries and regions have regulations and standards for environmental protection. By complying with these regulations, green suppliers help companies avoid criminal penalties and enhance their reputations. Sustainability enhances a company's brand value and reputation. Environmentally conscious consumers prefer companies that adopt sustainable practices and work with green suppliers. This increases customer loyalty and market competitiveness. Green suppliers also invest in innovative and sustainable technologies. These technologies help companies reduce their environmental impact and develop more sustainable business models.

Working with green suppliers is part of a company's corporate social responsibility. Environmentally responsible practices improve the overall well-being of society and enable companies to contribute to social responsibility projects. Adopting sustainable practices and working with green suppliers ensures long-term business success and sustainability. Environmental responsibility ensures future business success.

In this study, the CoCoFISo (Combined Compromise for Ideal Solution) method has been extended with gray numbers to create the CoCoFISo-G method. The CoCoFISo method is an extension of the CoCoSo method, and the purpose of the CoCoFISo method is to find an ideal compromise solution to improve the algorithm of the CoCoSo method. This extended method was used for green supplier selection. The supplier with the highest CoCoFISo-G score was identified as the best alternative. The method can be applied to many selection and ranking problems.

Scientific Ethics Declaration

The authors declare that the scientific ethical and legal responsibility of this article published in EPSTEM Journal belongs to the authors.

Acknowledgements or Notes

* This article was presented as an oral presentation at the International Conference on Technology, Engineering and Science (www.icontes.net) held in Antalya/Turkey on November 14-17, 2024.

References

Bagal, D. K., Giri, A., Pattanaik, A. K., Jeet, S., Barua, A., & Panda, S. N. (2021). MCDM optimization of characteristics in resistance spot welding for dissimilar materials utilizing advanced hybrid taguchi method-coupled CoCoSo, EDAS and WASPAS Method. *Springer Proceedings in Materials*, *9*, 475–490.

Bakeshlou, E. A., Khamseh, A. A., Asl, M. A. G., Sadeghi, J., & Abbaszadeh, M. (2017). Evaluating a green supplier selection problem using a hybrid MODM algorithm. *Journal of Intelligent Manufacturing*, *28*(4), 913–927.

Banaeian, N., Mobli, H., Fahimnia, B., Nielsen, I. E., & Omid, M. (2018). Green supplier selection using fuzzy group decision making methods. A case study from the agri-food industry. *Computers & Operations Research*, *89*, 337–347.

Deveci, M., Pamucar, D., & Gokasar, I. (2021). Fuzzy Power Heronian function based CoCoSo method for the advantage prioritization of autonomous vehicles in real-time traffic management. *Sustainable Cities and Society*, *69*, 102846.

Ecer, F. (2021). A consolidated MCDM framework for performance assessment of battery electric vehicles based on ranking strategies. *Renewable and Sustainable Energy Reviews*, *143*, 110916.

Gabriel- Rasoanaivo, R., Yazdani, M., Zaraté, P., & Fateh, A. (2024). Combined compromise for ideal solution (CoCoFISo). A multi-criteria decision-making based on the CoCoSo method algorithm. *Expert Systems with Applications*, *251*, 124079.

Govindan, K., Kadziński, M., & Sivakumar, R. (2017). Application of a novel PROMETHEE-based method for construction of a group compromise ranking to prioritization of green suppliers in food supply chain. *Omega*, *71*, 129–145.

Hashemi, S. H., Karimi, A., & Tavana, M. (2015). An integrated green supplier selection approach with analytic network process and improved grey relational analysis. *International Journal of Production Economics*, *159*, 178–191.

Hervani, A. A., Helms, M. M., & Sarkis, J. (2005). Performance measurement for green supply chain management. *Benchmarking*, *12*(4), 330–353.

Keshavarz- Ghorabaee, M., Zavadskas, E. K., Amiri, M., & Esmaeili, A. (2016). Multi-criteria evaluation of green suppliers using an extended WASPAS method with interval type-2 fuzzy sets. *Journal of Cleaner Production*, *137*, 213–229.

Liao, C. N., Fu, Y. K., & Wu, L. C. (2016). Integrated FAHP, ARAS-F and MSGP methods for green supplier evaluation and selection. *Technological and Economic Development of Economy*, *22*(5), 651–669.

Peng, X., & Luo, Z. (2021). Decision-making model for China's stock market bubble warning. the CoCoSo with picture fuzzy information. *Artificial Intelligence Review*, *54*(8), 5675–5697.

Popović, M. (2021). An Mcdm approach for personnel selection using the Cocoso method. *Journal of Process Management and New Technologies*, *9*(3–4), 78–88.

Qin, J., Liu, X., & Pedrycz, W. (2017). An extended TODIM multi-criteria group decision making method for green supplier selection in interval type-2 fuzzy environment. *European Journal of Operational Research*, *258*(2), 626–638.

Rouyendegh, B. D., Yildizbasi, A., & Ustunyer, P. (2020). Intuitionistic Fuzzy TOPSIS method for green supplier selection problem. *Soft Computing*, *24*(3), 2215–2228.

Stanujkic, D., Popovic, G., Zavadskas, E. K., Karabasevic, D., & Binkyte-Veliene, A. (2020). Assessment of progress towards achieving sustainable development goals of the agenda 2030 by using the CoCoSo and the shannon entropy methods. the case of the EU Countries. *Sustainability 2020, 12*(14), 5717.

Torkayesh, A. E., Ecer, F., Pamucar, D., & Karamasa, C. (2021). Comparative assessment of social sustainability performance. Integrated data-driven weighting system and CoCoSo model. *Sustainable Cities and Society*, *71*, 102975.

Torkayesh, A. E., Pamucar, D., Ecer, F., & Chatterjee, P. (2021). An integrated BWM-LBWA-CoCoSo framework for evaluation of healthcare sectors in Eastern Europe. *Socio-Economic Planning Sciences*, *78*, 101052.

Wen, Z., Liao, H., Kazimieras Zavadskas, E., & Al-Barakati, A. (2019). Selection third-party logistics service providers in supply chain finance by a hesitant fuzzy linguistic combined compromise solution method. *Economic Research-Ekonomska Istraživanja*, *32*(1), 4033–4058.

Wu, Q., Zhou, L., Chen, Y., & Chen, H. (2019). An integrated approach to green supplier selection based on the interval type-2 fuzzy best-worst and extended VIKOR methods. *Information Sciences*, *502*, 394–417.

Yazdani, M., Wen, Z., Liao, H., Banaitis, A., & Turskis, Z. (2019). A grey combined compromise solution (Cocoso-g) method for supplier selection in construction management. *Journal of Civil Engineering and Management*, *25*(8), 858–874.

Yazdani, M., Zarate, P., Zavadskas, E. K., & Turskis, Z. (2019). A combined compromise solution (CoCoSo) method for multi-criteria decision-making problems. *Management Decision*, *57*(9), 2501–2519.

Yu, Q., & Hou, F. (2016). An approach for green supplier selection in the automobile manufacturing industry. *Kybernetes*, *45*(4), 571–588.

Author Information

Halil Sen
Burdur Mehmet Akif Ersoy University,
Industrial Engineering Department,
Istiklal Kampus,15030, Burdur-Türkiye
Contact e-mail: *halilsen@mehmetakif.edu.tr*

Mustafa Serdar Toksoy
Burdur Mehmet Akif Ersoy University,
Industrial Engineering Department,
Istiklal Kampus,15030, Burdur-Türkiye

To cite this article:

Sen, H. & Toksoy, M.S. (2024). Green supplier selection with CoCoFISo-G. *The Eurasia Proceedings of Science, Technology, Engineering & Mathematics (EPSTEM), 32,* 257-265.

The Eurasia Proceedings of Science, Technology, Engineering & Mathematics (EPSTEM)
ISSN: 2602-3199

The Eurasia Proceedings of Science, Technology, Engineering & Mathematics (EPSTEM), 2024

Volume 32, Pages 266-274

IConTES 2024: International Conference on Technology, Engineering and Science

Application of Transparent Insulation Materials on the Roof of a Building: A Case Study in North Cyprus

Lida Ebrahimi-Vafaei
Near East University

Abstract: The reduction of energy consumption for heating and air conditioning and electric energy saving in illumination plants could be improved by innovative Transparent Insulating Materials (TIMs), which aim to optimize two opposite requirements: transparency and thermal insulation. Aerogel is one of the more promising for use in highly energy-efficient windows: in addition to the low thermal conductivity (0.010 W/(mK) in evacuated conditions), a high solar energy and daylight transmittance is achieved. Eight samples were manufactured, by assembling several types of glass with monolithic and granular aerogel in the interspace. Measurements of transmission and reflection properties were carried out and the energetic and luminous parameters (light transmittance (τv), solar factor (g) and thermal transmittance (U)) were calculated. U-values slightly higher than 1 W/m^2 K were obtained for all the samples. The monolithic aerogel introduces a better light transmittance (τv = 0.60) than granular one (τv = 0.27), while U-values are comparable in not evacuated conditions.

Keywords: Insulation, Heat transfer, Data logger

Introduction

The thermal efficiency of regular glazing systems is demonstrated by systems using polycarbonate as a type of transparent insulation material. This research focuses on the optical characterization of several polycarbonate panels for buildings based on different chamber numbers and geometries. To track the long-term solar properties of polycarbonate panels, the optical quality was evaluated using outdoor measurements to demonstrate the effect of year-round aspects on solar transmission. As well, the solar transmission is assessed for the different outdoor time scales for each hour, day month, and year round. The polycarbonate panels show that they can have some characteristics about the solar radiation that enters within their inner structure from the solar transmission perspective the solar transmission of polycarbonates, to which the outdoor conditions time scales react, can vary considerably. Overall, the differences between solar transmission in laboratories and outdoor tests are pretty clear; they are 10% different. The research gives full view about transparent insulating types and uses.

Transparent Insulation

Transparent Insulation is considered as the new modern technology which is being used now in most of the modern counties to save a big amount of energy and it was proved as a very useful way to save energy and heat for buildings old and new buildings as well. The Studies in Germany and Austria proved that about 250 KWh/m^2 which equals to 25 Liters of heating fuel can be saved for each square of the transparent insulating that is installed on the southern panels of those countries, even though these countries have a lack of the brightness of the sun in winter times. The transparent insulation is mostly made as a plastic or glass panels within (5-15 cm) and it contains a huge amount of cells in the form of contiguous microtubules within 3 cm diameter or even less and they are perpendicular to the panel.

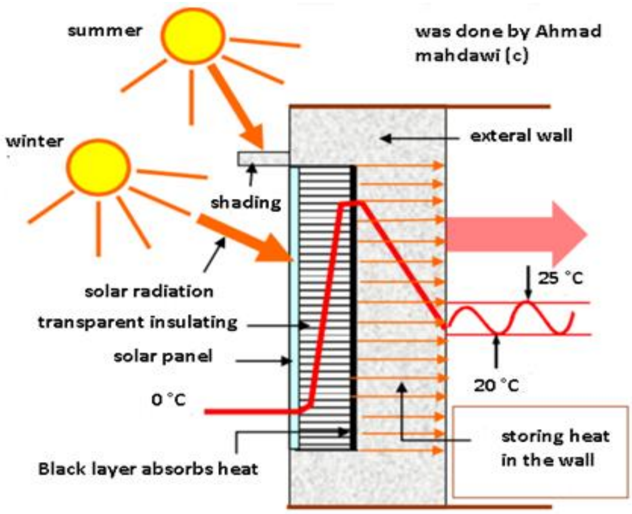

Figure1. Transparent insulation with glass on walls

Honeycomb Collector is a New Type of Solar Thermal Collector Targeting High Temperature Differential Applications

At the heart of the Honeycomb Collector is a polymer-made layer of transparent insulation (TI). The TI honeycomb substance is transparent to solar irradiation, allowing for energy to enter the collector and heat the absorber plate. However, it creates a layer of air that cannot circulate, thus dramatically reducing losses related to convection – the major reason for energy losses and lower efficiency of flat plate collectors at high temperature differentials. In addition, the polymer blocks back radiation in the infrared, further reducing energy losses. The principle of operation behind the Honeycomb Collector's transparent insulation modules can be visualized as follows.

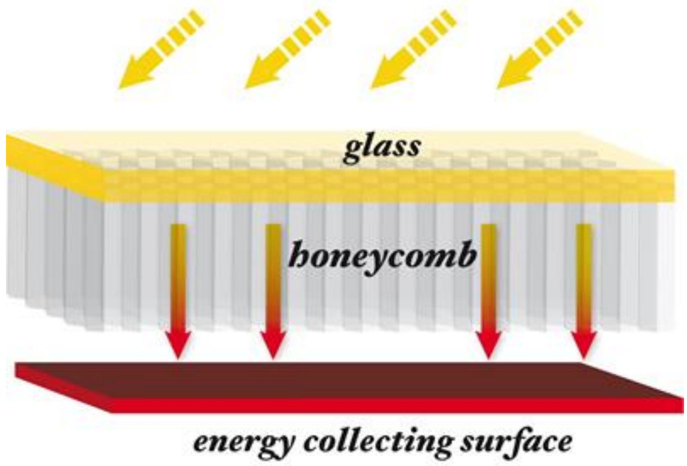

Figure 2. Sunlight passes through the transparent insulation, heating the energy collecting surface

The Transparent Insulation Layer Suppresses Convection Heat Losses

Solar energy, in the form of heat, is trapped and stored in a water tank and can be used later locally. In addition to the low energy losses, the Honeycomb Collector does not necessarily need direct sunlight in order to function and can generate energy from diffused light as well, as on hazy or cloudy days. This makes it a particularly attractive solution in the cold and temperate climates of the developed world, including much of Europe, North America and colder parts of Asia. If not taken care of, the Honeycomb Collector's high efficiency could result in overheating of the collector and system components under extreme conditions, including stagnation when heat transfer fluid flow is insufficient.

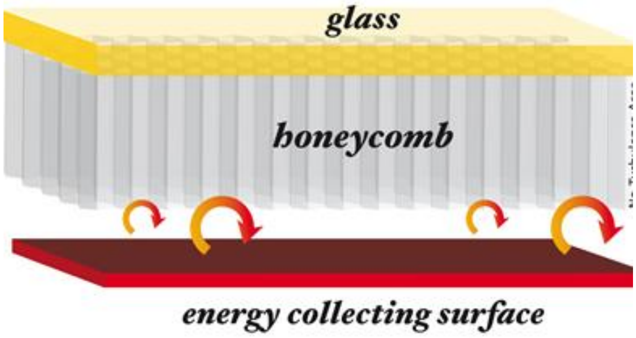

Figure 3. Radiation coming and pass through honeycomb and coming to energy collecting surface

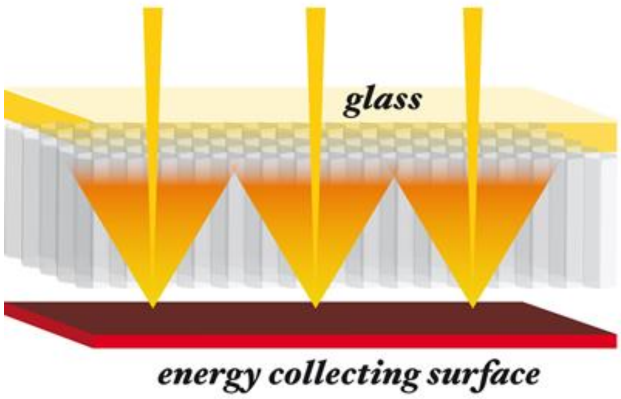

Figure 4. The transparent insulation layer provides high resistance to thermal back-radiation

The result is a system with very high energy-efficiency, allowing energy to enter freely but limiting energy losses to a minimum

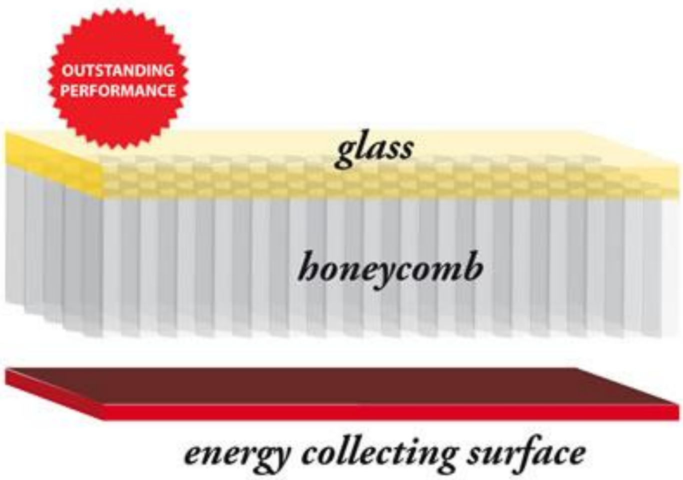

Figure 5. The result is a system with very high energy-efficiency, allowing energy to enter freely but limiting energy losses to a minimum

Infact, by using the passive solar energy through windows, it is possible to reduce the annual energy consumption for space-heating in cold climates, such as in the northern European Countries or in highlands. Aerogel is a highly porous light material with a number of exceptional and even unique physical properties: it attracts the attention of researchers in various areas of science and technology. The first aerogel specimens appeared eighty years ago. The production is localized in Europe (Sweden, Germany), USA, Japan and Russia. Aerogels are manufactured on the basis of silicon dioxide (SiO_2, amorphous quartz): they are constituted by approximately 96% of air and 4% open-pored structure of silica; such structure confers the characteristic of extreme lightness to the material (density is about 50-200 kg/m3). (Braun, Geotzberger , Schmid, & Stahl, 1992).

Applications of Transparent Insulation

Transparent Insulation in Roof Plate Solar Collectors

The most widely use of transparent insulation materials is in the flat roof collectors. This system is designed to heat air when irradiated by the sun. Basic components are a south directed transparent insulation material cover that transfers the solar energy while reducing the convection and the radiation losses to the atmosphere. The average working temperatures are between 40 and 80^0C . Also it's possible to achieve a High working temperatures up to 259^0C using glass, because the plastic covers would melt at temperatures above 120^0C.

Transparent Insulation in Passive Solar Walls

When directed to the south, external walls can be used to capture solar energy with transparent insulation materials with an air gap behind them. This energy can be used by emptying the warm air inside, and by allowing the heat to conduct passively through the wall. Transparent insulation materials can also provide a significant energy savings when retrofitted to residential and commercial opaque walls. As well for cold sunny days, there is no need for any additional heating but the control strategies are necessary in summer to reduce overheating (B.P. Jelle A. Hynd A. Gustavsen D. Arasteh H. Goudey R, 2012).

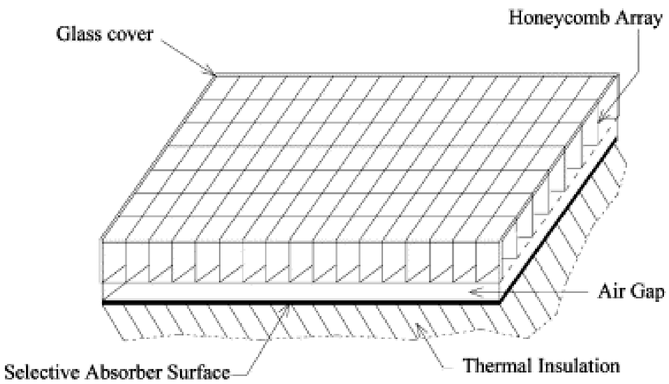

Figure 6. installation of honeycomb insulation

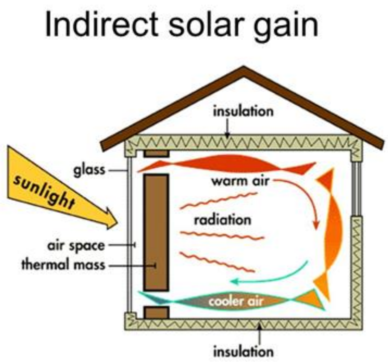

Figure 7. Wall transparent insulation

Materials and Methods for Transparent Insulations

Types of Transparent Insulation Materials

There are four types of transparent insulation:

1) Absorber Parallel Covers
2) Cavity Structures
3) Absorber Vertical Covers
4) Quasi-Homogeneous Structures

The absorber structures as honeycomb and capillary materials with different geometries, and structures in those structures as the incident light is mirrored and transmitted to the absorber by the walls, there are very low optical losses. Quasi-homogenous materials are distinguished by different optical properties, in this category the losses are big and it’s because of the pores that come with (10 to 50mm) so the light would scatter with the materials (Ghoneim, 2005).

Advantages of Transparent Insulation

1) Relative low thermal conductivity
2) Possible transparency
3) On-site use similar to traditional materials
4) Very low pristine thermal conductivity

Disadvantages of transparent insulation:

1) Uncertain long-term physical properties
2) Energy-extensive and expensive production process
3) Uncertain health risk
4) Aging and resulting increase of thermal conductivity
5) No adaptation on-site
6) Thermal bridging at panel edges

Pyranometer

A pyranometer is a type of acidometer used to measure broadband solar irradiance on a planar surface. In other words: a pyranometer is a sensor that is designed to measure the solar radiation flux density (in watts per meter square) from a field of view of 180 degrees.

Figure 8. Pyranometer

Picture of a pyrometer, clearly showing the instrument main components: glass dome, metal body, black sensor, level and cable. Dimensions: diameter of the dome is 20 mm. Photo shows model LP02 Courtesy Hukseflux Thermal Sensors. The name pyranometer stems from Greek, "pyr" meaning "fire" and "ano" meaning "sky". Pyranometers are frequently used in meteorology, climatology, solar energy studies and building physics. They can be seen in many meteorological stations - typically installed horizontally and next to solar panels - typically mounted with the sensor surface in the plane of the panel. Pyranometers are standardized according to the ISO 9060 standard that is also adopted by WMO, the World Meteorological Organization. This standard discriminates three classes. The best is (confusingly) called "secondary standard", the second best "first class" and the last one "second class"(https://en.wikipedia.org/wiki/Pyranometer).

Calibration of Thermocouples

Calibration is the process of comparing a reading on one piece of equipment or system, with another piece of equipment that has been calibrated and referenced to a known set of parameters

The goal of calibration is to minimize any measurement uncertainty by ensuring the accuracy of test equipment. Calibration quantifies and controls errors or uncertainties within measurement processes to an acceptable level. A Thermocouple is a sensor used to measure temperature. Thermocouples consist of two wire legs made from different metals. The wires legs are welded together at one end, creating a junction. This junction is where the temperature is measured. In our project we used Thermocouple type T. The Type T is a very stable thermocouple and is often used in extremely low temperature applications. First of all we connected the thermocouples to the PC through the data logger (UDL 100). Then, we started heating the water, thermocouples and thermometers. At the same time, we considered 6 different temperatures and compared them with the measured temperatures shown in our device (https://www.thermocoupleinfo.com). I would like to thanks to Ossma Radwan, Jaafar Khalife, Hasan Asad and Ahmad Mahdawı

Experiment Part

In our project we started by collecting the equipment and tools, the main equipment which is an insulation and two single glasses, we install them over each other on the roof that faced the south because we have maximum solar radiation and the angle is 36 for Cyprus, also we fixed the pyranometer and the three data loggers, thermocouples after we fixed all thermocouples for two identical roof one with insulation and glass, and the other one with just glass we started taking the data for 7 day’s as an input.

Installation of Thermocouples for the Roof with Insulation

Figure 9. Roof with transparent insulation

We applied four thermocouples for this first roof that contains the transparent insulation:

- On the glass
- Under the glass
- Under the insulation
- Under the roof

Installation of Thermocouples for the Roof without Insulation

Figure 10. Roof without transparent insulation

Also, we applied three thermocouples for the second roof that contains just glass without any insulation:

- On the glass
- Under the glass
- Under the roof

By addition to those two roofs we added one thermocouple to measure the outside temperature.

Figure 11. Data logger

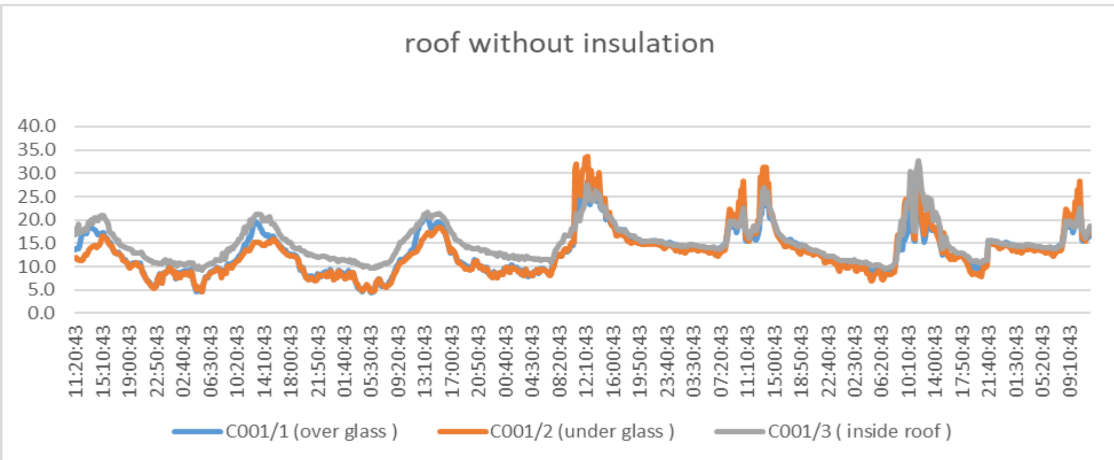

Figure 12. Roof without insulation

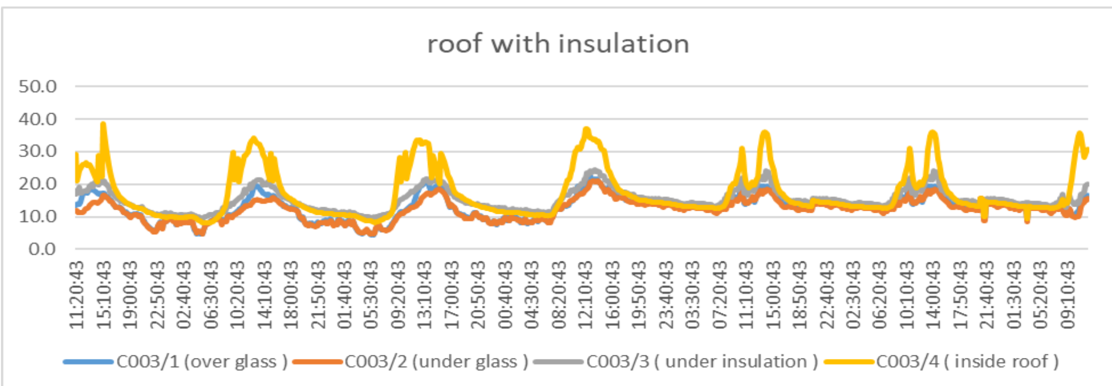

Figure 13. Graph of the results over seven days

As we can see in the figure above this is a graph for the results over seven days for both roofs on the left without the transparent insulation and on the right with the transparent insulation. We notice that from the thermocouples (C001/3) and (C003/4) that under the roofs that the thermocouple in (C003/4) the roof with insulation the reading temperature is higher by minimum 5 degrees from the reading of thermocouple (C001/3) that is under the roof that contains just glass without insulation.

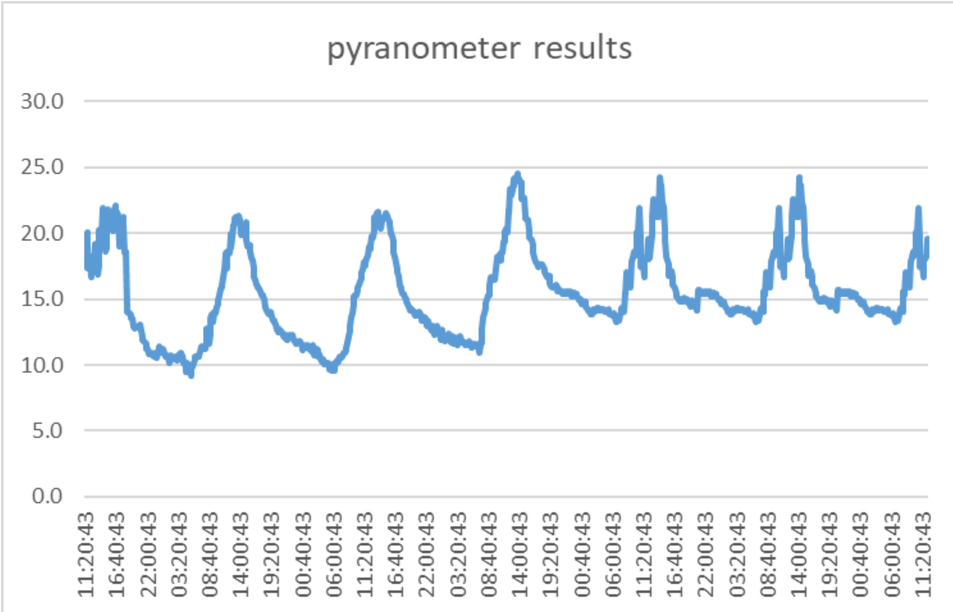

Figure 14. Pyranometer chart over seven days

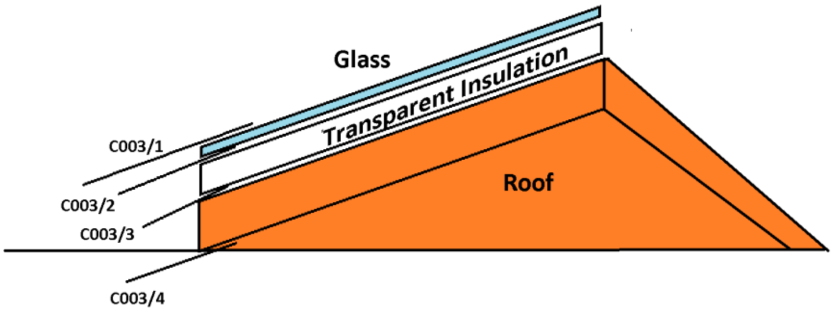

Figure.15 Sketch the connecting parts of thermocouples

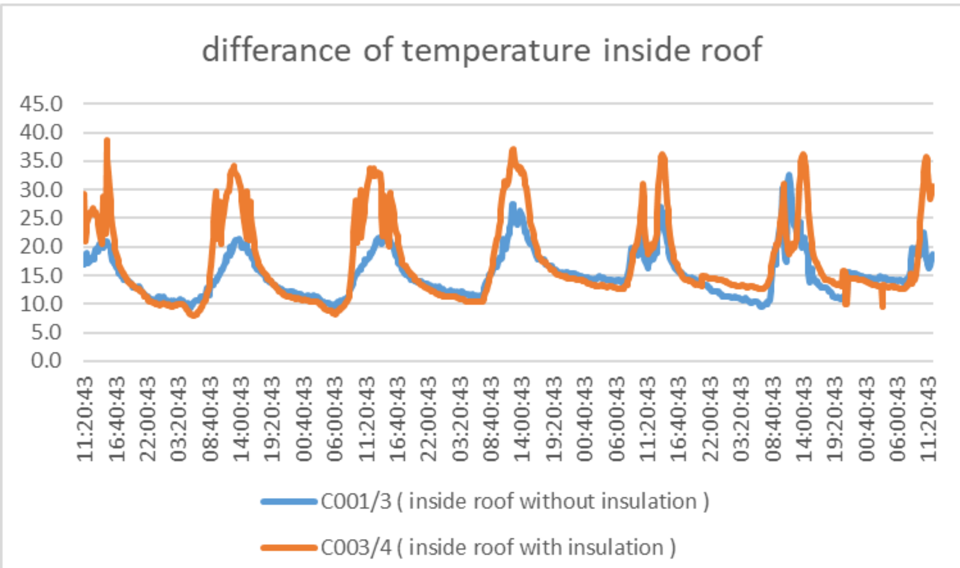

Figure 16. Comparing the inside roof with insulation and without insulation

Conclusion

This research shows the importance of the transparent insulating, as well it shows its applications, it can be used to heat buildings and water as well using the solar energy which is costless, so it has many advantages as its completely safe to be used, permanent heating source, it doesn't need any fuel to be used which proves how cheap it is. And the research describes its materials and describes their mechanism, in addition to that the research focused on the polycarbonate systems and described some samples of them and their performance.

In the end of this research, it's clear that transparent insulation is so important and that people should start using it for all the buildings in the whole world , even the in the cold countries since it can perform well in the cold summer weather. In the recent years there has been a growing interest in high insulation glazing systems, because of their important role in building envelope from thermal, acoustic and visual point of view. Among innovative transparent materials, aerogel is one of the more promising because of very low thermal conductivity and transparency. In order to evaluate the performance of this new material, some samples with monolithic and granular aerogel were investigated, thanks to optical parameters measurements carried out by the UV/VIS/NIS spectrophotometer Solid Spec 3700.

Scientific Ethics Declaration

The author declares that the scientific ethical and legal responsibility of this article published in EPSTEM Journal belongs to the author.

Acknowledgements or Notes

* This article was presented as an oral presentation at the International Conference on Technology, Engineering and Science (www.icontes.net) held in Antalya/Turkey on November 14-17, 2024.

References

Braun, P. O., Goetzberger, A., Schmid, J., & Stahl, W. (1992). Transparent insulation of building facades—Steps from research to commercial applications. *Solar Energy*, *49*(5), 413-427.

Ghoneim, A. (2005). Performance optimization of solar collector equipped with different arrangement of squarecelled honeycomb. *International Journal of Thermal Sciences*, *44*(1), 95-105.

Jelle, B. P., Hynd, A., Gustavsen, A., Arasteh, D., Goudey, H., & Hart, R. (2012). Fenestration of today and tomorrow: A state-of-the-art review and future research opportunities. *Solar Energy Materials and Solar Cells*, *96*, 1-28.

Pyrantomer. (n.d.). In *Wikipedia.* Retrieved from https://en.wikipedia.org/wiki/Pyranometer

Thermacoupleinfo. (n.d.). Retrieved from https://www.thermocoupleinfo.com/

Author Information

Lida Ebrahimi- Vafaei
Near East University
Near East Boulevard, ZIP: 99138Nicosia / TRNC Mersin 10,
Türkiye
Contact e-mail: *lida.ebrahimivefaei@neu.edu.tr*

To cite this article:

Ebrahimi-Vafaei, L. (2024). Application of transparent insulation materials on the roof of a building: A case study in North Cyprus. *The Eurasia Proceedings of Science, Technology, Engineering & Mathematics (EPSTEM)*, *32*, 266-274.

The Eurasia Proceedings of Science, Technology, Engineering & Mathematics (EPSTEM)
ISSN: 2602-3199

The Eurasia Proceedings of Science, Technology, Engineering & Mathematics (EPSTEM), 2024

Volume 32, Pages 275-280

IConTES 2024: International Conference on Technology, Engineering and Science

Prediction of Constituents of Concrete Mixtures Containing Fly Ash and Blast Furnace Slag Using Machine Learning Techniques

Mohammed Jaradat
Al-Zaytoonah University of Jordan

Mohammad Massoud
Al-Zaytoonah University of Jordan

Ahmad Manasrah
Al-Zaytoonah University of Jordan

Yousef Jaradat
Al-Zaytoonah University of Jordan

Abstract: The prediction of concrete mix proportions is of the utmost importance to civil engineers to complete the design process of structures. This process is usually done through a trial-and-error process which involves simple regression techniques and is usually done to achieve a specific strength at a specific age. The incorporation of supplementary cementitious materials into concrete mixtures for environmental purposes has deemed the prediction process more complex and created a need to come up with more advanced techniques. Furthermore, the ability to predict the constituents of concrete mixtures given multiple inputs is still limited. Hence, in this work several machine learning algorithms were utilized to make a prediction regarding mix proportions of concrete mixtures based on concrete compressive strength, concrete age, and density as inputs. Random forest, decision tree, and K-neighbors regressors were used to achieve this objective. Mean squared error as well as root squared error were used to measure the accuracy of the constructed models. Random Forest algorithm obtained the highest accuracy with 98.5%.

Keywords: Concrete, Compressive strength, Machine learning, Artificial intelligence, Supplementary cementitious materials.

Introduction

Concrete is a widely used construction material for infrastructure as it combines several beneficial characteristics such as strength, durability, and financial viability. The worldwide continuous growth in infrastructure means that concrete will remain in use for a long period of time. However, cement production, which is the main binder in concrete mixtures, is associated with negative impacts on the environment due to high carbon dioxide emissions (Lila et al., 2020; Schneider, 2019; Yang et al., 2015). This has led researchers to look for means to alleviate high CO_2 emissions through partially replacing cement with supplementary cementitious materials (SCMs) sourced from agricultural and industrial by-products (Abebaw et al., 2021; Berndt, 2009; Garcia-Lodeiro et al., 2016; Thomas et al., 2021). These materials are associated with pozzolanic activity which allows them to aid in the formation of CSH gel and, consequently, build-up compressive strength (Donatello et al., 2010). Therefore, this adds to the complexity of concrete mixtures which are usually made up of cement, water, aggregates, and admixtures. Thus, there is a continuous need to study this material to facilitate the design process and ensure its safety. One of the main performance indicators that is of great importance to design of infrastructure is the compressive strength of concrete. Therefore, the ability to predict mechanical properties of concrete is crucial to designers. However, it is a complicated task due to the heterogenous nature of this material which is increasingly becoming more complex with the addition of SCMs (Mohtasham- Moein et al., 2023). Therefore, the constituent materials of concrete can vary greatly from one mix to another in both types of material as well as the ratios of the materials used. The relationship between the constituent materials of concrete and its compressive strength development is most often a nonlinear one (Chou et al., 2011; Mohtasham- Moein et al., 2023). Furthermore, as the concrete ages, the strength development also varies. This time-dependent nature of concrete strength development is also nonlinear which adds to the complexity of compressive strength prediction.

Two main paradigms are typically followed by researchers to predict the compressive strength of concrete mixtures: empirical and computational (Li et al., 2022). The empirical models rely on linear and nonlinear regression models to predict concrete properties through the developed analytical models. These models depend on trial-and-error mixing and destructive testing of specimens at different ages of concrete to develop them. As a result, they are resources and time consuming to develop due to the trial-and-error nature of experiments (Ben Chaabene et al., 2020). Additionally, these models are considered sufficient for fairly simple concretes that are made up of cement, aggregates, and water. However, the rise in complexity of concrete materials necessitates the need for more practical and sophisticated models. Computational models, on the other hand, have been developed through using density-functional theory (DFT) and molecular dynamics simulations. These models require a deep understanding of the microstructural properties of the constituent materials of the concrete mixture. Moreover, the complex nature of cement hydration makes the generalization of models that can predict concrete properties a very challenging task. They are also computationally expensive and difficult to validate through experiments due to their small time and length scales (Li et al., 2022).

Recently, artificial intelligence (AI), machine learning (ML), and deep learning methods have been adopted to produce predictive models of concrete compressive strength. These models can make up for what the conventional regression models and the sophisticated computational models lack through their special algorithms. They can accommodate large amounts of data and learn from them to predict the mechanical properties of concrete. Researchers have utilized artificial neural networks (ANN), support vector machine (SVM), random forest (RF), and decision tree (DT) algorithms (Khambra & Shukla, 2023) among others, in concrete science for various reasons. The unique characteristics of machine learning aided researchers in not only predicting various properties of concrete, but also finding the influencing factors of these properties. Gucluer et al. (2021) developed a machine learning model using input data from nondestructive testing (NDT) techniques as well as physical properties of the hardened concrete to predict its compressive strength. Several ML algorithms were used; however, DT algorithm was able to provide the least amount of error. Sun et al. (2023) combined the use of machine learning algorithms with analytical hierarchy process (AHP) to optimize the design of ultra-high performance concrete (UHPC) mixtures. The optimized design was set to meet low carbon and low-cost requirements. Several machine learning algorithms were included in their work but XGBoost provided the best prediction performance in terms of compressive strength. Researchers have also worked on providing a machine learning based model to predict the compressive strength of concrete containing recycled aggregates. Shang et al. (2022). Found that AdaBoost regressor provides higher values of R^2 as opposed to decision tree algorithm. On the other hand, Salimbahrami et al. (2021) utilized multiple linear regression (MLR) as well as ANN and SVM. The results indicated the superiority of machine learning methods over MLR and concluded that SVM was able to provide a model with higher prediction accuracy than ANN. On the other hand, Deng et al. (2018). Proposed a predictive model based on convolutional neural network (CNN) and then the results were compared with a traditional neural network model. It was shown that CNN provides higher precision and efficiency as well as better generalization ability when compared to ANN. ML predictive models of the compressive strength of nano-modified concrete were also developed Nazar et al. (2022). The input variables were different nanomaterials in addition to the components on conventional concrete. The results showed that RF had a better performance than both DT and gene expression programming models.

Researchers have utilized various ML methods in their quest to develop a predictive model to estimate the compressive strength of concrete containing SCMs. For instance, Khursheed et al (2021) utilized several machine learning techniques to predict the 28-day compressive strength of concrete mixtures that contain fly ash. It was concluded that minimum probability machine regression (MPMR) provides the most accurate prediction. Moreover, Song et al. (2021) applied machine learning techniques to experimental data to predict the compressive strength of concrete mixtures with fly ash as an admixture. The bagging algorithm showed higher prediction accuracy than other machine learning techniques. Ahmad et al (2021) employed several supervised ML techniques such as bagging, AdaBoost, gene expression programming, and decision tree to predict the compressive strength of concrete containing fly ash and blast furnace slag. The input variables were the constituents of a concrete mix in addition to its age. The authors found that bagging algorithms were more effective in their prediction prowess than the other algorithms used. Furthermore, Qi et. al. (2022) proposed ML-based model that can estimate the compressive strength of concrete that contains BFS, FA, and superplasticizer (SP). RF algorithm was used in conjunction with principal component analysis (PCA) and particle swarm optimization to estimate the strength of concrete. It was concluded that RF algorithm can provide an excellent prediction of the compressive strength, however, PCA processing negatively impacts its predictive capability. Kocamaz et al. (2021) used the tree model M5P to predict both the compressive strength and ultrasonic pulse velocity of concrete that contains SF, FA, and BFS. The results of the study support the use of this tree model for concrete containing mineral admixtures. Jiang et al. (2022) proposed four machine learning algorithms to predict the compressive strength of fly ash containing concrete. Eight input variables, all pertaining to the concrete mix ratios and age, were used as inputs. The study showed that the use of a hybrid model that incorporates support vector regression and grid search optimization algorithm was the most successful. It was able to capture the correlations between the input variables as well as an accurate prediction of the compressive strength. In this work, the constituents of concrete mixtures containing fly ash and blast furnace slag, which are widely used industrial by-products with good pozzolanic activity, are predicted using several machine learning algorithms.

Method

To construct a machine learning model, a dataset is required to train and test the model. The dataset found in I-Cheng Yeh (1998) consists of nine different columns. The description of these columns is shown in Table 1

Table 1. Description of dataset

Material	Units	Description
Cement (C)	Kg/m^3	Output
Blast Furnace Slag (BFS)	Kg/m^3	Output
Fly Ash (F)	Kg/m^3	Output
Water (W)	Kg/m^3	Output
Superplasticizer (SP)	Kg/m^3	Output
Coarse Aggregate (CA)	Kg/m^3	Output
Fine Aggregate (FA)	Kg/m^3	Output
Density	Kg/m^3	Feature
Age	Days (1-365)	Feature
Compressive Strength (f'_c)	MPa	Feature

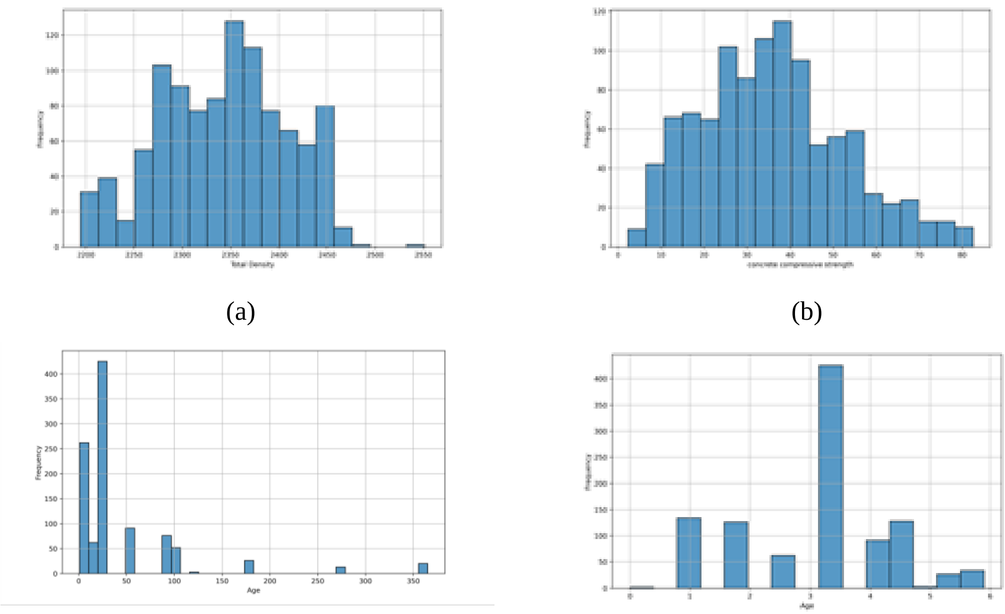

(a) (b) (c) (d)

Figure 1. Histogram statistics for feature variables: (a) total density, (b) compressive strength, (c) age, and (d) semi-normally distributed age

A new column has been added to the dataset, which is the total density. This column is the sum of the first seven columns. Unlike the models that have been trained in the related works, the proposed model predicts the components of the mixture and not its strength. This means that the strength, age and the total density are the input features of the proposed model, and the output results are the seven components of the mixtures. The dataset is 1030x10. Seven output columns and three features.The total density and the strength features are normally distributed as shown in Figures 1a and 1b, however, the age is not. Logarithmic transformation has been utilized to transfer these features into semi-normally distributed as shown in Figures 1c and 1d, respectively.

Figure 2 shows the correlation heatmap of the dataset. We can observe that the output columns have positive correlation with at least one of the input features utilized in the model. Finally, the dataset has been normalized to make all the values in the interval {-1, 1} by subtracting the mean and divide by the max value of each feature. The final dataset has been divided into 70% training, 15% for testing and 15% for validation.

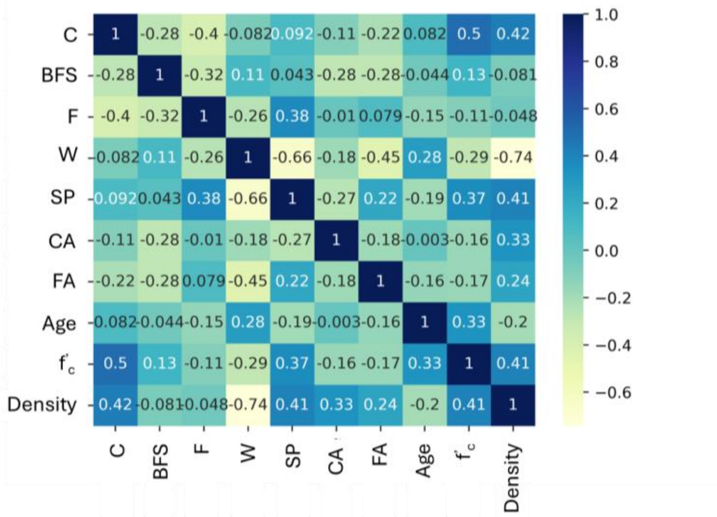

Figure 2. Correlation heatmap

Three different machine learning algorithms have been utilized in this work; random forest, decision tree and Knn. The regression version of these models have been leveraged since the prediction problem is continuous or a regression problem. Python has been used to train these models and to test their accuracy. Mean square error (MSE) and R^2 have been used to validate the accuracy of these models. The training process of the models have been repeated 30 times and the average accuracy of these iterations have been recorded.

Results and Discussion

Figure 3a shows the MSE value of the three models. We can observe that the random forest has the highest accuracy compared with the KNN and decision tree. However, we can observe that the accuracy of the three models is more than 97%. It is worth mentioning that KNN has the highest accuracy value before the logarithm conversion of the age feature and the decision tree has the lowest with 97.2% for KNN and 96.1% for decision tree. Figure 3b shows the R^2 value of these models. We can observe that the random forest model has the highest R^2 value among these models.

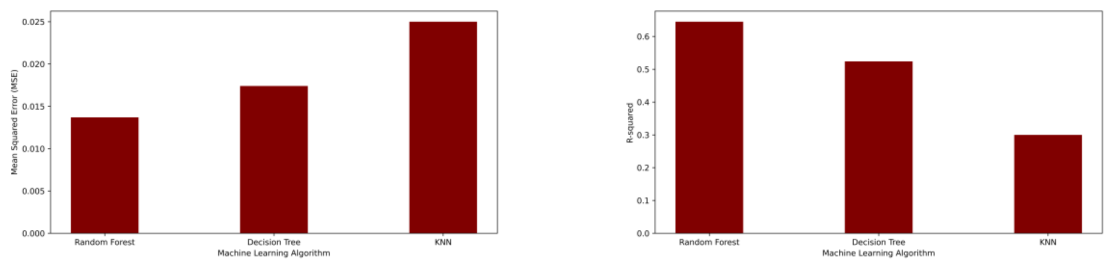

(a) (b)

Figure 3. Performance measures using (a) MSE and (b) R^2

Conclusion

This study showcases the exciting potential of machine learning to revolutionize concrete mix design—a crucial task for civil engineers. Moreover, this work addresses the growing need for sustainable construction practices by emphasizing on the incorporation of supplementary cementitious materials into concrete mixtures. By moving away from the traditional trial-and-error methods, we used various algorithms, with the Random Forest model standing out, achieving an impressive accuracy of 98.5%. This success highlights how machine learning models can simplify the complexities of predicting concrete mix proportions based on factors like compressive strength, concrete age, and density. Nevertheless, rheological factors such as workability were not considered in this work which limits the applicability of the developed predictive models. Furthermore, the size of the data set can be increased and include more supplementary cementitious materials to enhance the predictive accuracy of the developed models. Hence, there’s a lot of potential for further exploration. We can adapt these machine learning techniques to different concrete scenarios and conditions, making them even more useful for the industry.

Scientific Ethics Declaration

The authors declare that the scientific ethical and legal responsibility of this article published in EPSTEM Journal belongs to the authors.

Acknowledgements or Notes

* This article was presented as an oral presentation at the International Conference on Technology, Engineering and Science (www.icontes.net) held in Antalya/Turkey on November 14-17, 2024.

* I would like to acknowledge Al-Zaytoonah University of Jordan for their continuous support of this research.

References

Abebaw, G., Bewket, B., & Getahun, S. (2021). Experimental ınvestigation on effect of partial replacement of cement with bamboo leaf ash on concrete property. *Advances in Civil Engineering*, *2021*, e6468444.

Ahmad, W., Ahmad, A., Ostrowski, K. A., Aslam, F., Joyklad, P., & Zajdel, P. (2021). Application of advanced machine learning approaches to predict the compressive strength of concrete containing supplementary cementitious materials. *Materials*, *14*(19), 19.

Ben Chaabene, W., Flah, M., & Nehdi, M. L. (2020). Machine learning prediction of mechanical properties of concrete. Critical review. *Construction and Building Materials*, *260*, 119889.

Berndt, M. L. (2009). Properties of sustainable concrete containing fly ash, slag and recycled concrete aggregate. *Construction and Building Materials*, *23*(7), 2606–2613.

Chou, J.-S., Chiu, C.-K., Farfoura, M., & Al-Taharwa, I. (2011). Optimizing the prediction accuracy of concrete compressive strength based on a comparison of data-mining techniques. *Journal of Computing in Civil Engineering*, *25*(3), 242–253.

Deng, F., He, Y., Zhou, S., Yu, Y., Cheng, H., & Wu, X. (2018). Compressive strength prediction of recycled concrete based on deep learning. *Construction and Building Materials*, *175*, 562–569.

Donatello, S., Tyrer, M., & Cheeseman, C. R. (2010). Comparison of test methods to assess pozzolanic activity. *Cement and Concrete Composites*, *32*(2), 121–127.

Garcia-Lodeiro, I., Carcelen-Taboada, V., Fernández-Jiménez, A., & Palomo, A. (2016). Manufacture of hybrid cements with fly ash and bottom ash from a municipal solid waste incinerator. *Construction and Building Materials*, *105*, 218–226.

Gucluer, K., Ozbeyaz, A., Goymen, S., & Gunaydın, O. (2021). A comparative investigation using machine learning methods for concrete compressive strength estimation. *Materials Today Communications*, *27*, 102278.

Yeh, I. C. (2007). Concrete compressive strength. *UCI Machine Learning Repository*, *10*, C5PK67.

Jiang, Y., Li, H., & Zhou, Y. (2022). Compressive strength prediction of fly ash concrete using machine learning techniques. *Buildings*, *12*(5), 5.

Khambra, G., & Shukla, P. (2023). Novel machine learning applications on fly ash based concrete. An overview. *Materials Today. Proceedings*, *80*, 3411–3417.

Khursheed, S., Jagan, J., Samui, P., & Kumar, S. (2021). Compressive strength prediction of fly ash concrete by using machine learning techniques. *Innovative Infrastructure Solutions*, *6*(3), 149.

Kocamaz, A. F., Ayaz, Y., Karakoç, M. B., Türkmen, İ., & Demirboğa, R. (2021). Prediction of compressive strength and ultrasonic pulse velocity of admixtured concrete using tree model M5P. *Structural Concrete*, *22*(S1), E800–E814.

Li, Z., Yoon, J., Zhang, R., Rajabipour, F., Srubar III, W. V., Dabo, I., & Radlińska, A. (2022). Machine learning in concrete science. Applications, challenges, and best practices. *Npj Computational Materials*, *8*(1), 1–17.

Lila, K., Belaadi, S., Solimando, R., & Zirour, F. R. (2020). Valorisation of organic waste. Use of olive kernels and pomace for cement manufacture. *Journal of Cleaner Production*, *277*, 123703.

Mohtasham- Moein, M., Saradar, A., Rahmati, K., Ghasemzadeh Mousavinejad, S. H., Bristow, J., Aramali, V., & Karakouzian, M. (2023). Predictive models for concrete properties using machine learning and deep learning approaches. A review. *Journal of Building Engineering*, *63*, 105444.

Nazar, S., Yang, J., Ahmad, W., Javed, M. F., Alabduljabbar, H., & Deifalla, A. F. (2022). Development of the new prediction models for the compressive strength of nanomodified concrete using novel machine learning techniques. *Buildings*, *12*(12), 12.

Qi, C., Huang, B., Wu, M., Wang, K., Yang, S., & Li, G. (2022). Concrete strength prediction using different machine learning processes. Effect of slag, fly ash and superplasticizer. *Materials*, *15*(15), 15.

Salimbahrami, S. R., & Shakeri, R. (2021). Experimental investigation and comparative machine-learning prediction of compressive strength of recycled aggregate concrete. *Soft Computing*, *25*(2), 919–932.

Schneider, M. (2019). The cement industry on the way to a low-carbon future. *Cement and Concrete Research*, *124*, 105792.

Shang, M., Li, H., Ahmad, A., Ahmad, W., Ostrowski, K. A., Aslam, F., Joyklad, P., & Majka, T. M. (2022). Predicting the mechanical properties of rca-based concrete using supervised machine learning algorithms. *Materials*, *15*(2), 2.

Song, H., Ahmad, A., Farooq, F., Ostrowski, K. A., Maślak, M., Czarnecki, S., & Aslam, F. (2021). Predicting the compressive strength of concrete with fly ash admixture using machine learning algorithms. *Construction and Building Materials*, *308*, 125021.

Sun, C., Wang, K., Liu, Q., Wang, P., & Pan, F. (2023). Machine-learning-based comprehensive properties prediction and mixture design optimization of ultra-high-performance concrete. *Sustainability*, *15*(21), Article 21.

Thomas, B. S., Yang, J., Mo, K. H., Abdalla, J. A., Hawileh, R. A., & Ariyachandra, E. (2021). Biomass ashes from agricultural wastes as supplementary cementitious materials or aggregate replacement in cement/geopolymer concrete. A comprehensive review. *Journal of Building Engineering*, *40*(July 2020), 102332.

Yang, K. H., Jung, Y. B., Cho, M. S., & Tae, S. H. (2015). Effect of supplementary cementitious materials on reduction of CO2 emissions from concrete. *Journal of Cleaner Production*, *103*, 774–783.

Author Information

Mohammed Jaradat
Al-Zaytoonah University of Jordan
Amman 11733, Jordan
Contact e-mail: *m.jaradat@zuj.edu.jo*

Mohammad Massoud
Al-Zaytoonah University of Jordan
Amman 11733, Jordan

Ahmad Manasrah
Al-Zaytoonah University of Jordan
Amman 11733, Jordan

Yousef Jaradat
Al-Zaytoonah University of Jordan
Amman 11733, Jordan

To cite this article:

Jaradat, M., Massoud, M., Manasrah, A., & Jaradat, Y. (2024). Prediction of constituents of concrete mixtures containing fly ash and blast furnace slag using machine learning techniques. *The Eurasia Proceedings of Science, Technology, Engineering & Mathematics (EPSTEM), 32,* 275-280.

The Eurasia Proceedings of Science, Technology, Engineering & Mathematics (EPSTEM)
ISSN: 2602-3199

The Eurasia Proceedings of Science, Technology, Engineering & Mathematics (EPSTEM), 2024

Volume 32, Pages 281-287

IConTES 2024: International Conference on Technology, Engineering and Science

A Numerical Approach to Predict the Flexural Response of Simply Supported Nonhomogeneous and Non-Slender Graded Beams

Baya Allala
Mouloud Mammeri University of Tizi Ouzou

Abdelmadjid Si-Salem
Mouloud Mammeri University of Tizi Ouzou

Souad Ait-Taleb
Mouloud Mammeri University of Tizi Ouzou

Fatma Kheloui-Taouche
Mouloud Mammeri University of Tizi Ouzou

Soraya Ferhat
Mouloud Mammeri University of Tizi Ouzou

Abstract: In recent years, one promising avenue to optimize material design is the development of functionally graded materials (FGMs), which represent a new generation of composites with tailored mechanical properties. These properties vary continuously according to a function-law, allowing FGMs to mitigate issues like interfacial debonding and stress concentration. Accordingly, this study focuses on simulating the mechanical behavior of simply supported FGM non-slender beams under bending using finite element modeling (FEM). The numerical procedure and the loading setup as well as the implementation the power-law function which governs the stiffness distribution of the used metal and ceramic materials are explicitly presented. In addition, an optimal mesh size is determined for the modeled FGM beams. The numerical results show the effect of material exponent index and beam span ration on displacements and stresses distributions. The validated FEM-tool developed in this work provides a reliable means for estimating the elastic flexural response of non-slender graded beams under bending.

Keywords: Non-slender beams, Functionally graded materials, Three-point bending, Finite element approach, Mechanical properties.

Introduction

Functionally graded materials (FGMs) constitute a new category of nonhomogeneous composite materials made of different material components. Their microstructure and composition gradually and continuously vary to optimize the mechanical and thermal performance of the structures. Scientific research has focused on developing their mechanical and thermal properties (Ameryan et al., 2020). The concept of FGMs was invented in 1984 by Japanese scientists were looking for a material capable of withstanding high temperatures for space applications (Mahamood et al., 2017). FGMs possess a special structure, known for their lightweight, strength and durability, as well as their ability to combine contradictory thermomechanical properties in a single structure. By combining different materials, FGMs enhance both mechanical and thermal properties. Notably, FGMs exhibit two contrasting properties: conductivity and thermal insulation (Medjmadj et al., 2022; 2023).

- Selection and peer-review under responsibility of the Organizing Committee of the Conference

The scientific literature shows that the mechanical behavior of FGM beams has been extensively investigated and analytically solved the differential equation which governs the behavior of beams in bending (Ait Taleb, et al., 2017; 2020). In this connection, Ktili, Irwan and Katili (2020) presented a study which consists of determining the mechanical characteristics of an FGM beam. Vo et al. (2013) established a static analysis of an FGM beam using a refined shear deformation theory. In addition, Garg et al. (2020) made a comparative study of the bending of FGM sandwich beams composed of different materials variation laws using refined layer theory. The difficulty of implementing these materials, along with environmental and economic conditions, has prompted scientific researchers (Zhou et al., 2021; Li. et al.; 2021). To analytically investigate resolving mechanical problems associated with structures designed using FGM materials. Compared to analytical methods, numerical investigations are few. Therefore, simulation and numerical analysis were currently prioritized. These approaches play crucial role in studying complex mechanical behaviors (Djenad, et al,. 2022, 2023). Additionally, these simulations are more cost-effective than extensive laboratory testing with optimized number of trials.

To address these convergence issues, the objective of this study is to analyze the mechanical behavior of simply supported and non-slender FGM beams subjected to bending. We achieve this through a combination of analytical modeling and numerical simulation using the finite element method. The novelty of this approach lies in proposing a numerical solution that accounts for the differential equation governing the bending behavior of FGM beams while considering shear and warping effects. Specifically, 3D modeling using (Abaqus, 2014) were performed which is then validated against previous research. This validation demonstrates the model's effectiveness in predicting strength and deformability of the studied structures.

FEM Procedure

In this study, an analytically studied beam made of FGMs based on (Katili & Irwan Katili, 2020)'s research will be simulated. Indeed, a rectangular Timoshenko beam, with a width b = 1 (unit), length-to-height ratio, L/h = 4 is modeled to represent the performance in a simply supported ceramic-metal FGM beam subjected to a uniformly distributed load f_0. The composting materials consist of the metal at the bottom and ceramic on the upper surface of the beam. The lower surface of the beam has an elastic modulus E_m = 70 GPa, and a poisson's ratio υ_m = 0.3, while the upper ceramic surface has an elastic modulus E_c = 200 GPa, and a poisson's ratio υ_c = 0.3. The bouadary and loafing configutation of the simulated beam is given in Figure 1.

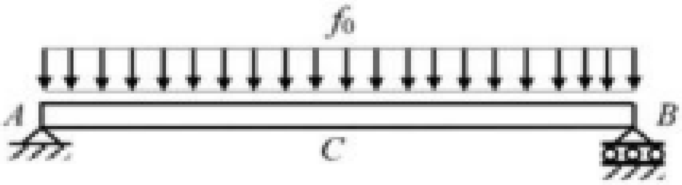

Figure 1. Boundary and loading conditions of the FGM beam.
A : Simple support ; **B** : Non-slender support

Model for FGM Beam Materials

A parametric study is carried out to study the effect of varying the number of layers using the power-law with different value of p and the exponent laws given by the following equation according to following equations. The parameters sought are the density and Young's modulus for each material.

$$E(z)_{p-FGM} = E_m e^{\beta(\frac{z+H}{2})} \tag{1}$$

$$\beta = \frac{1}{H}\ln(\frac{E_c}{E_m}) \tag{2}$$

Table 1. and Figure 2 show the variation of densities and the Young's modulus in the modeled beam according to the p values and the z/h position.

Table 1. Densities (D: kg/m3) and Young's modulus (E: Mpa) according z/h using the power-law function.

P/ z		**1**	**2**	**3**	**4**	**6**	**7**	**8**	**9**
0	**D**	3960	3960	3960	3960	3960	3960	3960	3960
	E	200	200	200	200	200	200	200	200
0.2	**D**	2702	3531.970	3655.385	3735.919	3847.134	3889.662	3926.848	3960
	E	70	155.768	168.521	176.844	188.337	192.731	196.574	200
0.5	**D**	2702	3146.77	3331	3472.364	3696.536	3791.456	3878.751	3960
	E	70	115.962	135	149.608	172.774	182.583	191.604	200
1	**E**	2702	2859.25	3016.5	3173.75	3488.25	3645.5	3802.75	3960
	D	70	86.25	102.5	118.75	151.25	167.5	183.75	200
2	**D**	2702	2721.656	2780.625	2878.906	3193.406	3409.625	3665.156	3960
	E	70	72.031	78.125	88.281	120.781	143.125	169.531	200
5	**D**	2702	2702.038	2703.228	2711.329	2821.972	3000.529	3347.239	3960
	E	70	70.004	70.127	70.964	82.398	100.850	136.678	200
10	**D**	2702	2702	2702.001	2702.069	2713.441	2772.842	3347.239	3960
	E	70	70	70	70.007	70.182	77.320	104.201	200
∞	**D**	2702	2702	2702	2702	2702	2702	2702	2702
	E	70	70	70	70	70	70	70	70

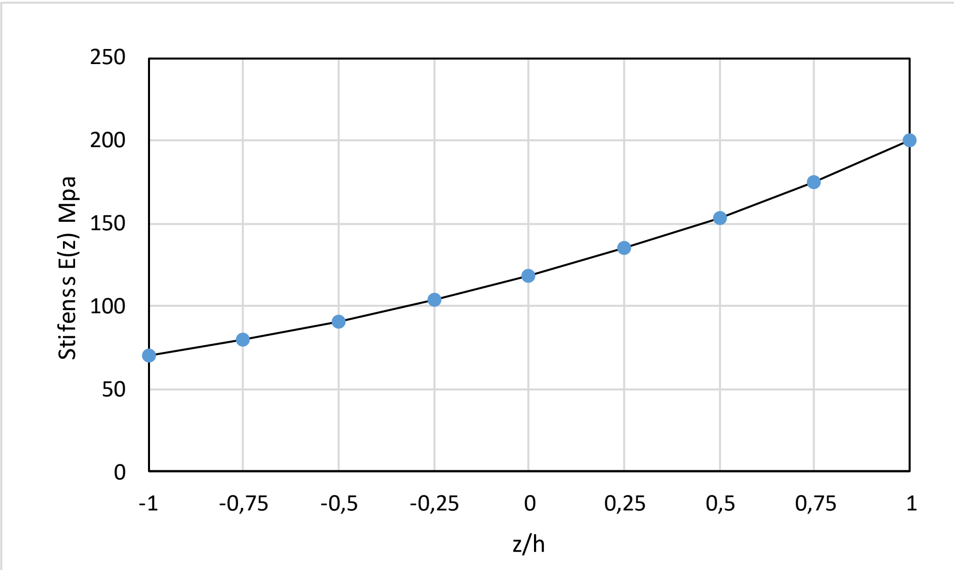

Figure 2. Stiffness variation in the FGM beam modeled using exponent-law function

Results and Discussion

In this section, a presentation and interpretation of the obtained results from numerical simulations are provided. The mechanical characteristics of the materials are mentioned in the numerical simulation section, the geometry variant considered is h *x* b *x* L corresponding to adimensional 2 *x* 1 *x* 8. Accordingly, all the obtained results in terms of displacements and stresses under mechanical loading are discussed and presented in the form of graphs and tables.

Calibration of the Numerical Model

The numerical procedure and the proposed finite element model are validated by a comparison with the experimental ones. A comparison between the test results and the theoretical model is deemed necessary to enhance the model. These results are presented in the Table 2. Based on the results, a good agreement emerges between the numerical and analytical outcomes regarding the overall behavior of beams subjected to bending loading. Indeed, the ultimate error rate between the adimensional mid-span displacement both approaches not exceed 0.23%. The displacement of the FGM beam increases linearly with the power-law exponent p. Additionally, the maximum error of the proposed model remains below 1% across all cases, thereby validating the accuracy of the numerical models used to predict the bending response of FGM beams.

Table 2. Comparison of numerical and theoretical adimensional mid-span displacement.

p-parameter value	**0**	**0,2**	**0,5**	**1**	**2**	**5**	**10**	∞
(Katili & Katili, 2020)	5,268	6,024	6,535	7,460	8,362	9,508	11,305	15,052
(Nguyen &Thai, 2013)	5,268	-	6.535	7,464	8,370	9,510	11,297	15,052
(Simsek 2009)	5,149	-	6.403	7,313	8,194	9,307	11,055	14,713
(Vo et al., 2014)	5,268	-	6,535	7,464	8,369	9,515	11,307	15,052
Present model	5,722	6,988	7,661	8,627	9,571	10,82	14,01	17,21
Error (%)	0.08	0.16	0.17	0.15	0.14	0.137	0.239	0.143

Displacements Distribution

Figure 4 illustrates the evolution of the displacements distribution of the FGM beam under mechanical bending load, with varying stiffness according to the law of rigidity variation and depicts the variation of deformations (displacements) as a function of x/L for P-FGM beams under different power-law exponent p. Indeed, when the value of p increases, the transition from the ceramic to metallic phase becomes rapid, resulting in low rigidity for the FGM beam and significant displacements. In order to validate the numerical results already obtained,

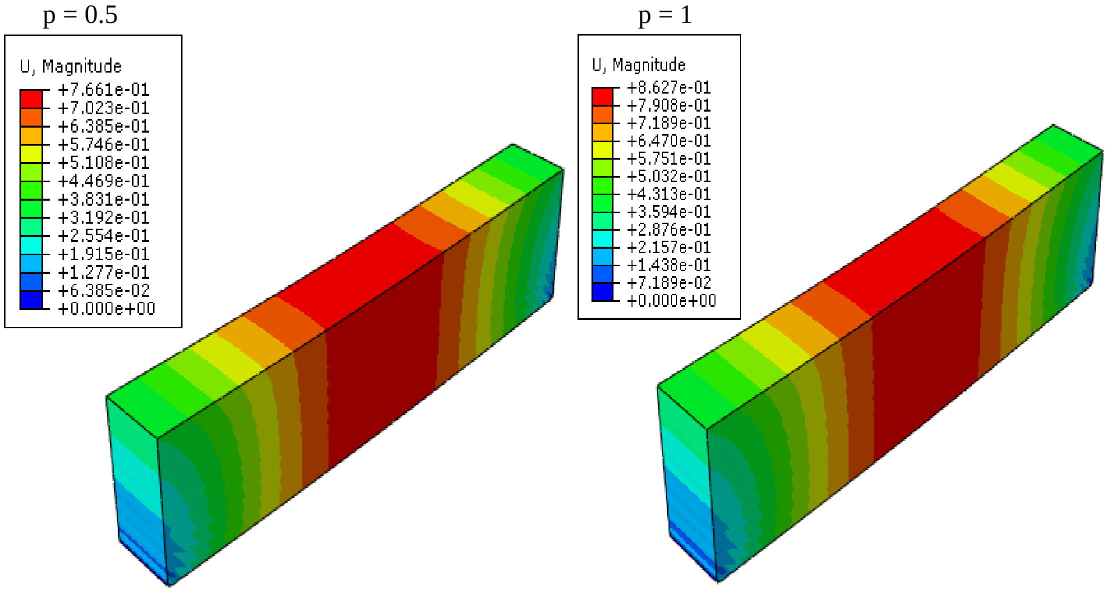

Figure 4. Cartography maps of displacements in longitudinal direction of non-slender FGM beam.

According to Figure 4, the maximum displacement for all variants appears in middle of the beam (at mid-span), then propagated respectively towards the supports, the value of the latter turns to zero at the supports. The displacement is greater for entirely ceramic beams which is equal to 17.21 mm, compared to the displacement of entirely metal beams which corresponds to 5.722 mm. This is due to the influence of the Young's modulus which is high for ceramic compared to that of metal. According to these results, which align with the analytical finding reported in scientific literature, this numerical model enables the prediction of the response of FGM beams subjected to bending.

Evolution of Normal Stresses

In this section, the variation of stresses according to the thickness of the FGM beam will be investigated. To achieve this, the same procedure as for displacement evolution will be employed, with the parameter p varying across the beam thickness. Figure 5, illustrates the evolution of the Von Mises stress distribution within the beam under mechanical loading for different parameter coefficients.

According to the evolution of normal stresses illustrated in Figure 5, the parameter p has a significant effect on the normal stresses. The stress ratio decreases as a function of p, reaching zero at the most tensile and compressive fibers. As p increases, the transition from the ceramic to the metallic phase becomes very rapid, resulting in reduced strength for the FGM beam and consequently lower stress levels.

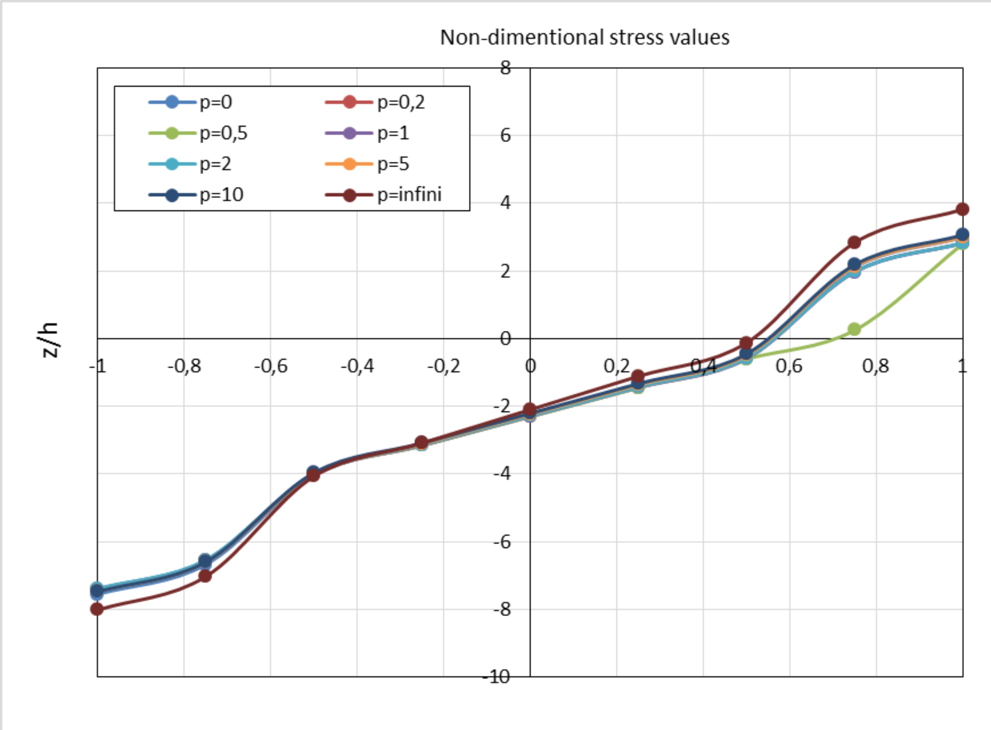

Figure 5. Evolution of normal stress according to the non-slender FGM beam thickness

The morphological distribution of the normal stresses in the FGM beams is represented using the cartography maps in the Figure 6. According to Figure 8, the maximum stress for all p variants appears at the supports of the beam and then propagated towards the beam's span; its value tends to diminish at the beam's mid-plane in the direction of its thickness. In the case of the FGM beams, the numerical displacements were marginally less than the analytical ones, this was caused by the geometric non-linearity conditions of loading application under the numerical procedure. as well as the convergence of the finite element model to the reliable solution.

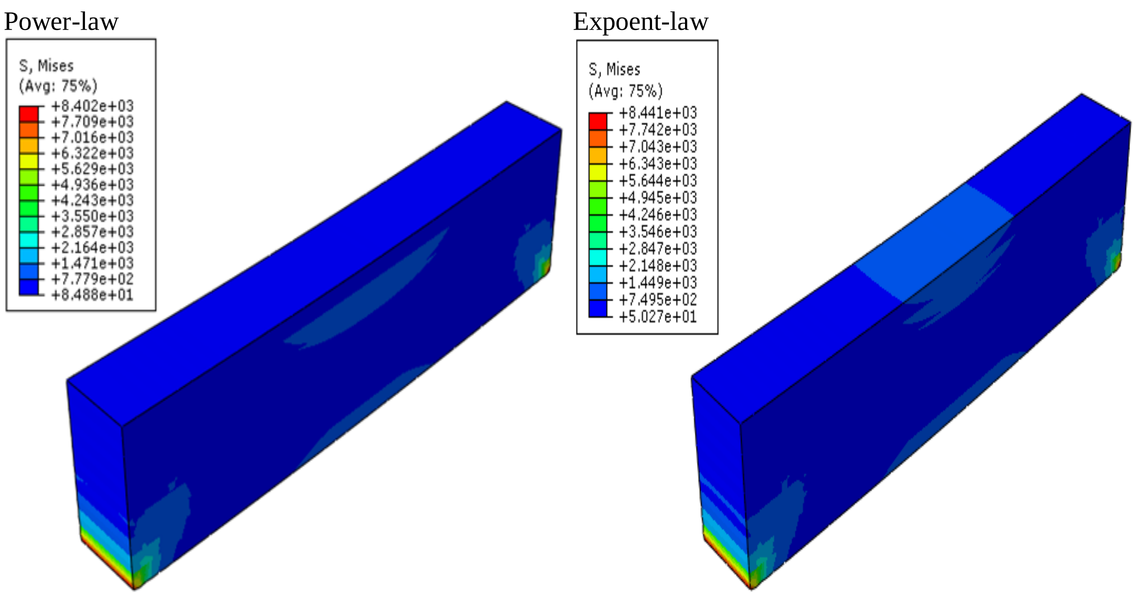

Figure 6. Cartography maps of normal stress according to the non-slender FGM beam thickness.

Conclusion

In this study, we conducted a numerical investigation using the ABAQUS code. Our focus was on the finite element method, aiming to propose and validate a model capable of analyzing the behavior of a functionally graded material (FGM) beam under bending. The key findings from our work are as follows:

- The established numerical model exhibited excellent agreement with analytical models from existing scientific literature when predicting mid-span displacements of the non-slender FGM beam.
- As the parameter p increases, the transition from the ceramic to metallic phase within the FGM beam occurs rapidly. Consequently, the beam exhibits low rigidity, resulting in significant displacements.
- Conversely, a good correlation between the results predicted by the proposed models when using power-law and exponential-law functions in terms of stresses values and arrangement.
- The normal stress values decrease proportionally to the p-parameter values. Nullity stress is observed on the center of gravity of the beam's transversal section. While, the stress achieves their ultimate values on the tensile and compressive zone;

Recommendations

In order to improve the findings of the present work, the authors advocate to introduce in the finite element simulations the real behavior of the constitutive materials namely: metal and ceramic to take into account the post-elastic phase. Consequently, predicting the failure and collapse mode of the studied non-slender FGM beams.

Scientific Ethics Declaration

The authors declare that the scientific ethical and legal responsibility of this article published in EPSTEM Journal belongs to the authors.

Acknowledgements or Notes

* This article was presented as a poster presentation at the International Conference on Technology, Engineering and Science (www.icontes.net) held in Antalya/Turkey on November 14-17, 2024.

References

Abaqus, C.A.E. (2018). *A general-purpose finite element software.* France : Dassault Systemes.

Ait Taleb, S., Si Salem, A., & Ait tahar, K. (2017). Behaviour of a new graded beam reinforced with externally bonded composite sheets: theoretical and experimental studies. *European Journal of Environmental and Civil Engineering 21*(9), 1171–85.

Ait Taleb, S., Si Salem, A., & Ait tahar, K. (2020). Experimental and theoretical modeling coupled to a reliability approach for flexural failure prediction in hybrid composite beams. *Asian Journal of Civil Engineering 21*(3), 495–504.

Ameryan, A., Ghalehnovi, M., & Rashki, M. (2020). Investigation of shear strength correlations and reliability assessments of sandwich structures by kriging method. *Composite Structures*, *253*, 112782.

Djenad, S., Taleb, S. A., Salem, A. S., & Bouzidi, M. A. (2022). NLFEA based design optimization of GFRP strips in partially confined concrete. *Procedia Structural Integrity*, *37*, 321-329.

Djenad, S., Ait Taleb, S., & Si Salem. A. (2023). Finite element modeling of partially-confined concrete and RC columns with embedded hexagonal-FRP strips under axial and horizontal loading. *Structures 54*, 369–85.

Garg, A., Chalak, H.D., & Chakrabarty,A. (2020). Comparative study on the bending of sandwich FGM beams made up of different material variation laws using refined layerwise theory. *Mechanics of Materials, 151*, 103634.

Katili, A.M., & Katili, I. (2020). A simplified UI element using third-order Hermitian displacement field for static and free vibration analysis of FGM beam. *Composite Structures 250* (2020), 112565.

Li. N et al. (2021). Optimal design and strength reliability analysis of pressure shell with grid sandwich structure. *Ocean Engineering, 223* (2021), 108657.

Mahamood, R. M., Akinlabi, E. T., Mahamood, R. M., & Akinlabi, E. T. (2017). *Types of functionally graded materials and their areas of application* (pp. 9-21). Springer International Publishing.

Medjmadj, S., Ait Taleb, S., & Si Salem, A. (2023). Analytical modeling of the bending behavior of plaster/cork functionally graded core sandwich beams: analysis and experimental validation. *Iranian Journal of Science and Technology - Transactions of Mechanical Engineering*, 48(3),1489-1507.

Medjmadj, S., Salem, A. S., & Taleb, S. A. (2022). Experimental behavior of plaster/cork functionally graded core sandwich panels with polymer skins. *Construction and Building Materials*, *344*, 128257.

Simsek, M. (2009). Static analysis of a functionally graded beam under a uniformly distributed load by Ritz method. *International Journal of Engineering and Applied Sciences, 1* (3), 1-11.

Simsek, M., & Kocaturk, T. (2009). Free and forced vibration of a functionally graded beam subjected to a concentrated moving harmonic load. *Composite Structures, 90*(4), (2009) 465-473.

Si Salem, A., Ait Taleb, S., & Ait tahar, K. (2017). A finite element approach for predicting the flexural response of light weight frp-concrete beams under cyclic loading. *5th Algerian Congress of Mechanics, CAM2015* (pp.*355*–363).Springer

Vo, T. P., Thai, H. T., Nguyen, T. K., & Inam, F. (2014). Static and vibration analysis of functionally graded beams using refined shear deformation theory. *Meccanica*, *49*, 155-168.

Zhou. C et al. (2021). Reliability and sensitivity analysis of composite structures by an adaptive Kriging based approach. *Composite Structures*, *278* (2021), 114682.

Author Information

Baya Allala
University Mouloud Mammeri of Tizi Ouzou
Tizi Ouzou, 15000, Algeria
Contact e-mail: *baya.allala@ummto.dz*

Abdelmadjid Si Salem
University Mouloud Mammeri of Tizi Ouzou
Tizi Ouzou, 15000, Algeria

Souad Ait Taleb
University Mouloud Mammeri of Tizi Ouzou
Tizi Ouzou, 15000, Algeria

Fatma Kheloui-Taouche
University Mouloud Mammeri of Tizi Ouzou
Tizi Ouzou, 15000, Algeria

Soraya Ferhat
University Mouloud Mammeri of Tizi Ouzou
Tizi Ouzou, 15000, Algeria

To cite this article:

Allala, B., Si-Salem, A., Ait-Taleb, S. Kheloui-Taouche, F & Ferhat, S. (2024). A numerical approach to predict the flexural response of simply supported nonhomogeneous and non-slender graded beams. *The Eurasia Proceedings of Science, Technology, Engineering & Mathematics (EPSTEM), 32*, 281-287.

The Eurasia Proceedings of Science, Technology, Engineering & Mathematics (EPSTEM)
ISSN: 2602-3199

The Eurasia Proceedings of Science, Technology, Engineering & Mathematics (EPSTEM), 2024

Volume 32, Pages 288-294

IConTES 2024: International Conference on Technology, Engineering and Science

Determining the Optimal Conditions for Dropping a Load from an Aircraft

Milen Atanasov
Georgi Benkovski Bulgarian Air Force Academy

Abstract: Optimum conditions for dropping a load from an aircraft are seen as conditions under which no collision with the aircraft is allowed, with stable flight of the load having a trajectory close to the calculated one. Depending on the aerodynamic characteristics, the weight of the load and the type of aircraft, it is necessary to determine the angle at which the load is attached to the aircraft, the initial angular velocity of the load at release, the forced vertical velocity of the load ejection, so that to prevent a collision with the aircraft. On the other hand, applying additional vertical speed to the load will reduce the detrimental effect of the disturbed air flow around the aircraft on its flight. All this is of great importance for ensuring the safe separation of the load from the aircraft and increases the accuracy of solving the targeting problem by a specific targeting system. Mathematical modelling of the flight of the load dropped by an aircraft with different initial vertical speeds of ejection was performed, for which the influence of the disturbed zone on the flight was investigated.

Keywords: Optimum conditions, Dropping, Aircraft, Load

Introduction

It is essential to ensure the safe release of loads from the aircraft during combat operations. For this purpose, it is necessary to know: the conditions for releasing the load (speed, altitude, orientation of the aircraft's axes in space), the aerodynamic characteristics of the aircraft, the dimensions of the disturbed zone around the aircraft in various flight modes, the coordinates of the load suspension point relative to the coordinate system associated with the aircraft, and the dimensions and aerodynamic characteristics of the load. Based on this information, it is necessary to preliminarily calculate the risk of collision between the load and the aircraft at the moment of release. If a collision condition exists, measures must be taken to prevent it. The measures that can be applied to prevent such a collision include:

- Providing additional vertical speed to the load using pyrotechnic devices;
- Releasing the load at an initial angle relative to the aircraft's axes;
- Applying initial rotary motion around the load's center of mass at the moment of separation;
- Limiting the conditions for releasing the load;
- Implementing measures to reduce the harmful effects of the disturbed zone at the moment of release (using additional fairings or mechanisms through which the load is released at the boundary of the disturbed zone).

Method

The conditions for preventing a collision during the release of load from an aircraft have been analytically determined, and it has been investigated what initial vertical speed needs to be applied to the load at the moment of release in order to avoid a collision. The relative distance between the load and the aircraft after release is determined using the following formulas:

$$\begin{aligned} \Delta x &= x - x_0; \\ \Delta y &= y - y_0; \\ \Delta z &= z - z_0, \end{aligned} \tag{1}$$

where x, y, z are the current coordinates of the load relative to the aircraft;

$-x_0$, y_0, z_0 are the coordinates of the load at the moment of separation.

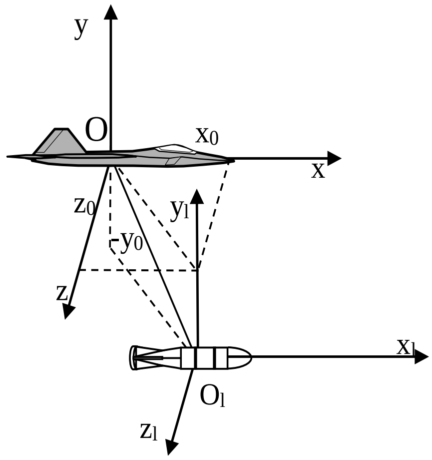

Figure 1. Determining the position of the load relative to the aircraft

The trajectory of the load is represented by a third-degree polynomial:
In general, the trajectory of the load at the moment of release is determined by solving the equations of motion for the center of mass (Bukhalev, 1966):

$$\dot{v} = \frac{1}{m}(P\cos\alpha\cos\beta - X - mg\sin\lambda);$$

$$\dot{\lambda} = \frac{1}{mv}[P(\cos\chi\sin\alpha + \sin\chi\sin\beta\cos\alpha) + \\ + Y\cos\chi - Z\sin\chi - mg\cos\lambda];$$

$$\dot{\varphi} = -\frac{1}{mv\cos\lambda}[P(\sin\chi\sin\alpha - \cos\chi\sin\beta\cos\alpha) + \\ + Y\sin\chi + Z\cos\chi]; \tag{2}$$

$$\begin{aligned} \dot{x} &= v\cos\lambda\cos\varphi; \\ \dot{y} &= v\sin\lambda; \\ \dot{z} &= -v\cos\lambda\sin\varphi; \end{aligned}$$

where P is the thrust force of the engine expressed as a function P(t);

X, Y, Z are the aerodynamic forces corresponding to drag, lift, and lateral forces, expressed by the following known formulas:

$$\begin{aligned} X &= \left(C_{x0} + B(C_y^\alpha)^2\alpha^2\right)\frac{S\rho v^2}{2}; \\ Y &= C_y^\alpha\alpha\frac{S\rho v^2}{2}; \\ Z &= C_z^\beta\beta_{пл}\frac{S\rho v^2}{2}, \end{aligned} \tag{3}$$

C_{x0}, B, C_y^{α}, C_z^{β} are aerodynamic coefficients determined through calculating or experimental methods.

ρ - is the density of the atmosphere, which depends on altitude. When performing calculations, the function ρ(H) is approximated with analytical relationships;

S - is the characteristic area (reference cross-section);

The motion of the load is considered in the vicinity of the aircraft, i.e., in the disturbed zone.

The system of equations (1) can be represented analytically as a third-degree polynomial (Bukhalev, 1966; Stoykov, 2021).

$$\begin{aligned} \Delta x &= a_{x1}t + a_{x2}t^2 + a_{x3}t^3; \\ \Delta y &= a_{y1}t + a_{y2}t^2 + a_{y3}t^3; \\ \Delta z &= a_{z1}t + a_{z2}t^2 + a_{z3}t^3, \end{aligned} \tag{4}$$

$a_{x1}=v_x$;
$a_{x2}=(1/2)\Delta J_x - (\omega_y v_z - \omega_z v_y)$;
$a_{x3}= - (1/6)\,[2(\omega_y \Delta J_z - \omega_z \Delta J_y)+\omega^2 v_x]$;

$$a_{y1}=v_y; \tag{5}$$

$a_{y2}=(1/2)\Delta J_y - (\omega_z v_x - \omega_x v_z)$;
$a_{y3}= - (1/6)\,[2(\omega_z \Delta J_x - \omega_x \Delta J_z)+\omega^2 v_y]$;
$a_{z1}=v_z$;
$a_{z2}=(1/2)\Delta J_z - (\omega_x v_y - \omega_y v_x)$;
$a_{z3}= - (1/6)\,[2(\omega_x \Delta J_y - \omega_y \Delta J_x)+\omega^2 v_z]$;

where ΔJ is the difference between the acceleration of the load and the aircraft - $\Delta J=J_l - J_a$;

ω - the acceleration of the aircraft;
v - the speed of the load.

It is assumed that for loads symmetric with respect to the longitudinal axis, the lateral velocity of the load v_z is very small, such that it can be neglected (vz=0v_z = 0vz=0). Accordingly, the coefficients $a_{z1}=a_{z2}=a_{z3}=0$.

The coefficients (5) take the form:

$a_{x1}=v_x$;
$a_{x2}=(1/2)\Delta J_x + \omega_z v_y$;
$a_{x3}= - (1/6)\,[2(\omega_y \Delta J_z - \omega_z \Delta J_y)+\omega^2 v_x]$;

$$a_{y1}=v_y \tag{6}$$

$a_{y2}=(1/2)\Delta J_y - \omega_z v_x$;
$a_{y3}= - (1/6)\,[2(\omega_z \Delta J_x - \omega_x \Delta J_z)+\omega^2 v_y]$.

When using overloads, the coefficients (6) take the form (Bukhalev, 1966):

$a_{x1}=v_x$;
$a_{x2}=(1/2)(n_{lx} - n_x)g + \omega_z v_y$;
$a_{x3}= - (1/6)[2g\omega_y (n_{lz} - n_z) - 2g\omega_z(n_{ly} - n_y)+\omega^2 v_x]$;

$$a_{y1}=v_y; \quad 7)$$

$a_{y2}=(1/2)(n_{ly} - n_{y;})g - \omega_z v_x$;
$a_{y3}= - (1/6)\,[2g\omega_x (n_{lx} - n_x) - 2g\omega_x(n_{lz} - n_z)+\omega^2 v_{y,}$

where $n_x = \frac{P - X}{G}; n_y = \frac{Y}{G}; n_z = \frac{Z}{G}$ are the overloads of the aircraft along its respective axes; $n_{xl} = \frac{P_l - X_l}{G_l}; n_{yl} = \frac{Y_l}{G_l}; n_{zl} = \frac{Z_l}{G_l}$ - the overloads of the load along its respective axes.

Using formula (7), the polynomial (4) describing the motion of the load in the vicinity of the aircraft takes the form:

$$\Delta x = v_x t + \left[\frac{1}{2}(n_{lx} - n_x)g + \omega_z v_y\right]t^2 - \frac{1}{6}\left[2g\omega_y(n_{lz} - n_z) - 2g\omega_z(n_{ly} - n_y) + \omega^2 v_x\right]t^3;$$
$$\Delta y = v_y t + \left[\frac{1}{2}(n_{ly} - n_y)g - \omega_z v_x\right]t^2 - \frac{1}{6}\left[2g\omega_z(n_{lx} - n_x) - 2g\omega_x(n_{lz} - n_z) + \omega^2 v_y\right]t^3. \quad 8)$$

To avoid a collision in the vertical plane between the aircraft and the released load, it is necessary to meet the condition:

$$\Delta y = y - y_0 = v_y t + \left[\frac{1}{2}(n_{ly} - n_y)g - \omega_z v_x\right]t^2 - \frac{1}{6}\left[2g\omega_z(n_{lx} - n_x) - 2g\omega_x(n_{lz} - n_z) + \omega^2 v_y\right]t^3 < 0 \quad (9)$$

Assuming that the load is released freely without applying vertical speed and the engine thrust P=0, (v_{ly}=v_{ly}=0), then $n_{lz} - n_z \cong 0$ and n_{lx} is significantly less than zero (Bukhalev, 1966; Stoykov, 2020). Accepting these assumptions, formula (8) takes the form:

$$\Delta x = \frac{1}{2}(n_{lx} - n_x)gt^2 + \frac{1}{3}\omega_z(n_{ly} - n_y)gt^3;$$
$$\Delta y = \frac{1}{2}(n_{ly} - n_y)gt^2 - \frac{1}{3}\omega_z(n_{lx} - n_x)gt^3. \quad (10)$$

In the case of free release of the load (formula 8), the condition for safe release (9) takes the form:

$$3(n_{ly} - n_y) < 2\omega_z(n_{lx} - n_x)t \quad (11)$$

In the case of horizontal flight, the angular velocity of the aircraft is $\omega_z \cong 0$, therefore:

$$n_y > n_{ly}, \text{ or} \quad (12)$$

$$\frac{C_y^\alpha \alpha S V^2}{m} > \frac{C_{yl} S_l v^2}{m_l} \quad (13)$$

For horizontal flight, it is necessary to meet the condition n_y=1, therefore it is necessary $\frac{C_{yl} S_l v^2}{m_l} < 1$. For high speeds of the aircraft and for loads that have a large mass (unguided bombs) and a small lift force approaching zero, the condition for safe release of the load is satisfied. For low speeds of the aircraft and for loads that have a small mass (containers) relative to their lift force, it is necessary to apply a forced vertical speed. Assuming we have a forced vertical speed v_y, the second equation of formula (10) takes the form:

$$\Delta y = y - y_0 = v_y t + \left[\frac{1}{2}(n_{ly} - n_y)g\right]t^2 - \frac{1}{6}\left[2g\omega_z(n_{lx} - n_x) + \omega^2 v_y\right]t^3 < 0 \quad (14)$$

From formula (14), the necessary vertical speed that must be applied to the load for it to safely separate from the aircraft is calculated:

$$v_y < \frac{2g\omega_z(n_{1x} - n_x)t^2 - 3(n_{1y} - n_y)gt}{6 - \omega^2 t^2} \tag{15}$$

he forced vertical speed v_y has a negative value, from which it follows that in absolute terms:

$$v_y > \frac{2g\omega_z(n_{1x} - n_x)t^2 - 3(n_{1y} - n_y)gt}{6 - \omega^2 t^2}\,. \tag{16}$$

For horizontal flight, condition (16) takes the form:

$$v_y > \frac{-(n_{1y} - 1)gt}{2}\,. \tag{17}$$

Results and Discussion

The relative distance Δy between the load and the aircraft after release has been calculated. The study is conducted for releases at speeds V ranging from 180 m/s to 300 m/s, from an altitude H=500 m, during horizontal flight and dive at an angle λ= -30^0. The release of two loads has been simulated:

1. The first load has a characteristic time Θ_1= 20.44 s, a diameter d_1=0.4 m, mass m_{l1}=520 kg
2. The second load has a characteristic time Θ_2= 21.39 s, a diameter d_2=0.203 m, mass m_{l2}=64 kg.

For this purpose, a simplified model of the aircraft's motion has been developed (Biliderov et al., 2024; Kambushev et al., 2020) using equations (1). From the aircraft model, the overloads on the aircraft and the loads under specific conditions are determined. Then, the relative distance Δy between the load and the aircraft is calculated, as well as the necessary vertical speed for the load's safe separation. When releasing the two loads from horizontal flight, the overload n_y on the aircraft is approximately 1 (from the condition for horizontal flight - n_y=1). The overload n_x is approximately 0.

The results obtained for the relative distance Δy for the two loads during horizontal flight are presented in Table 1. From Table 1, it can be seen that for the entire range of conditions for releasing the load from horizontal flight, the safety condition is met, i.e., Δy<0. As the release speed of both loads increases, Δy decreases in absolute value. This can be explained by the fact that with increasing release speed, the lift force of the load increases. It is observed that the load with a greater mass has a larger Δy in absolute terms during its passage through the disturbed zone of the aircraft (Table 1). This is due to the greater mass of the second load. Under the specified conditions for releasing from horizontal flight for both loads, it is evident that condition (12) is satisfied. The overload $n_{lx1,2}$ for both loads increase in absolute value due to the increase in release speed.

Table 1. The relative distance Δy between the load released from horizontal flight and the aircraft

Relative distance Δy			
	V=180 m/s	**240 m/s**	**300 m/s**
Δy_1, m	-2.0287	-1.7641	-1.4319
n_{lx1}	-0.5705	-1.0494	-2.3703
n_{ly1}	0.1463	0.2601	0.4063
Δy_2, m	-2.2048	-2.0770	-1.9147
n_{lx2}	-0.1383	-0.2544	-0.5746
n_{ly2}	0.0699	0.1243	0.1942

In Table 2, the relative distances Δy for the two loads released from a dive with negative overload - n_y= - 1 and very small values of overload n_x are presented. From the table, it can be seen that for the entire range of release speeds of both loads, the condition for safe separation from the aircraft is not met. Therefore, under these conditions, it is necessary to apply additional vertical speed to the load at the moment of separation. It is evident that forces are acting on both loads that prevent them from separating from the aircraft. For both loads, as the speed increases, $\Delta y_{1,2}$ also increase due to the increase in $n_{ly1,2}$ for both loads. Similarly, as with the release from horizontal flight, during the release from a dive, as the mass of the load increases, Δy_1 decreases.

Table 2. The relative distance Δy between the load and the aircraft released from a dive with $\lambda = -30^0$

Relative distance Δy			
	V=180 m/s	**240 m/s**	**300 m/s**
Δy_1, m	2.6835	2.9263	3.2014
Δy_2, m	2.5242	2.6483	2.7974

In Table 3, the minimum values of the vertical speed that must be applied to the loads to ensure safe separation are presented. The nature of the variation in $v_{y1,2}$ is the same as that of $\Delta y_{1,2}$.

Table 3. The calculated necessary vertical speed for the safe separation of the load released from a dive with $\lambda = -30^0$

Nessessary vertical speed v_y			
	V=180 m/s	**240 m/s**	**300 m/s**
v_{y1}, m/s	-3.8612	-4.2104	-4.6063
v_{y2} m/s	-3.6320	-3.8105	-4.0250

The release of two loads with approximately the same external dimensions but different characteristics has been simulated from horizontal flight at an altitude of H=500H = 500H=500 m and a speed of V=300V = 300V=300 m/s:

1. The first load has a characteristic time Θ_1= 21 s, C_{y1} = 0.23, d_1=0.4 m, mass m_{l1}=120 kg.
2. The second load has a characteristic time Θ= 20 s, C_y = 0.17, d_2=0.4 m, маса m_{l2}=520 kg.

Table 4. The relative distance Δy for loads with identical dimensions released from an aircraft in horizontal flight

Relative distance Δy	
	V=300 m/s
Δy_1 m	0.6699
n_{lx1}	-1.5922
n_{ly1}	1.2902
Δy_2, m	-2.0314
n_{lx2}	0.4030
n_{ly2}	0.1406
v_{y2} m/s	2.9228

From the table, it is evident that the first load, which has a smaller mass but a larger lift coefficient, does not meet the condition for safe release. For the first load, condition (12) is also not satisfied, $n_y > n_{ly}$. It is necessary to apply an initial vertical speed v_{y2} >2.9228 m/s to this load.

Conclusion

From the conducted study, the following conclusions can be drawn:

1. The derived analytical formulas for determining the safe conditions for the separation of loads from the aircraft and the minimum vertical speed to be applied to the load can be used for preliminary calculations for the release of specific load samples.
2. To ensure the safe separation of the load, the aircraft must be piloted in such a way that the overload on the aircraft n_y is greater than the overload n_{yl} on the load.
3. For the safe release of bulky loads with a small mass from an aircraft, mechanisms for applying an initial vertical speed upon separation must be used.

Recommendations

For each specific aircraft, it is essential to strictly adhere to the requirements for the safe separation of loads, ensuring that for loads with a large mass and a low lift coefficient, a solid piston should not be used to apply initial vertical speed to the load. This could lead to the breaking of the supporting levers of the locking mechanism. When releasing bulky loads with a small mass, mechanisms must be employed to apply initial vertical speed to ensure safe separation from the aircraft.

Scientific Ethics Declaration

The author declares that the scientific ethical and legal responsibility of this article published in EPSTEM Journal belongs to the author.

Acknowledgements or Notes

* This article was presented as an oral presentation at the International Conference on Technology, Engineering and Science (www.icontes.net) held in Antalya/Turkey on November 14-17, 2024.

* The research in this article was carried out in fulfilment of Task 1.1.2. "Analysis and assessment of disaster, accident, emergency and crisis management systems and development of science-based proposals for their improvement" from the National Scientific Program "Security and Defence", adopted by RMS No. 731 of 21.10.2021. and according to Agreement No. D01-74/19.05.2022.

References

Atanasov M., (2014). *Tochnost na reshavane na zadachata na pritselvane s neupravlyaemi aviatsionni bombi* Pleven: Monografiya.

Atanasov, M. (2020). Mathematical model and algorithm of operation of a system for release of load from airplane. *Aerospace Research in Bulgaria*, *32*, 64-74.

Atanasov, M. (2022). Mathematical model for operation of aviation systems for delivery of special means to air and earth objects. *Aerospace Research in Bulgaria*, *34*, 138-148.

Bukhalev, A.V. (1966). *Installations of rocket and bomber aviation weapons* (Part 1, pp.93-102) Moscow: VVIA.

Calovska, R., Genchev, A., & Biliderov, S. (2024). Synthesizing and study a fuzzy control system for the longitudinal motion of an unmanned aerial vehicle. In *AIP Conference Proceedings*, 3063, No. 1). AIP Publishing.

Kambushev, M., Chivarov, N., Marinov, A., & Dimitrova, R. (2020). Approbation of a mathematical model of a specialized mechatronic system. In *2020 XI National Conference with International Participation (ELECTRONICA)* (pp. 1-4). IEEE.

Stoykov O., & Atanasov M., (2009). *Aviatsionni pritselni sistemi – Pŭrva chast*. Dolna Mitropoliya: VGTS.

Stoykov S, (2020), Influence of the forced separation of aviation bombs on the accuracy of bombing, *Annual International Scientific Conference, Georgi Benkovski Bulgarian Air Force Academy, Aviation Faculty,* 122 – 130.

Stoykov S, (2021). Potential methods for forced release of aviation bombs. *Annual International Scientific Conference, Georgi Benkovski Bulgarian Air Force Academy, Aviation Faculty,*170 – 173.

Author Information

Milen Atanasov
Georgi Benkovski Bulgarian Air Force Academy
St. St. Ciril and Methodius 1, 5855, Dolna Mitropolia, Bulgaria
Contact e-mail: matanasov@af-acad.bg

To cite this article:

Atanasov, M. (2024). Determining the optimal conditions for dropping a load from an aircraft. *The Eurasia Proceedings of Science, Technology, Engineering & Mathematics (EPSTEM), 32,* 288-294.

The Eurasia Proceedings of Science, Technology, Engineering & Mathematics (EPSTEM)
ISSN: 2602-3199

The Eurasia Proceedings of Science, Technology, Engineering & Mathematics (EPSTEM), 2024

Volume 32, Pages 295-303

IConTES 2024: International Conference on Technology, Engineering and Science

Significant Improvement in License Plate Recognition through Image Deduplication

Djamel Berrabah
EEDIS, University Djillali Liabes

Yacine Gafour
LIM, University Ibn Khaldoun

Abstract The detection of license plates, or Automatic Number Plate Recognition (ANPR), is crucial for applications in parking management, vehicle tracking, and security. However, the efficiency of ANPR systems is often compromised by large datasets containing numerous similar or duplicate images, leading to increased storage costs and slowed processing times. This research proposes an innovative approach that combines perceptual hashing and locality-sensitive hashing (LSH) to enhance the detection of redundant images. Perceptual hashing generates unique visual fingerprints for images, facilitating efficient duplicate identification, while LSH groups similar images to reduce false positives. Additionally, Optical Character Recognition (OCR) is applied to the image pairs identified by LSH to extract license plates and verify vehicle identity. By integrating these techniques, the proposed method effectively mitigates redundancy, optimizing storage and improving the performance of ANPR systems for accurate real-world recognition.

Keywords: Automatic number plate recognition (ANPR), Perceptual hashing, Locality-sensitive hashing (LSH), Optical character recognition (OCR), Duplicate image detection.

Introduction

The application of ANPR (Automatic Number Plate Recognition) systems has gained significant traction in recent years, becoming integral to various domains such as traffic management, law enforcement, parking control, and toll collection. These systems rely on advanced image processing techniques to accurately recognize license plates from vehicles in real time. However, as the volume of data generated by ANPR systems increases, managing large datasets becomes more challenging. One critical issue is the presence of redundant images, which can result in increased storage requirements and slower image processing times, ultimately affecting both efficiency and accuracy.

Image deduplication techniques based on perceptual hashing (A-Hash, D-Hash, P-Hash, etc.) offer an effective solution. These algorithms generate a visual fingerprint for each image by simplifying its key characteristics, enabling rapid duplicate detection. In the ANPR context, these methods identify nearly identical license plate images, even under variations in lighting or viewing angle. For example, D-Hash is particularly effective for comparing differences between adjacent pixels, while P-Hash extracts global shapes and contrasts, detecting similar images even with slight visual modifications.

Recent research has focused on optimizing image databases in ANPR systems. For instance, hybrid techniques combining perceptual hashing and machine learning have been proposed to automatically detect and remove duplicates, improving dataset quality. Other studies explore specialized convolutional neural networks (CNNs) to classify images based on similarity, streamlining the filtering process. Additionally, wavelet-based methods have proven effective in extracting multi-resolution features, enabling detection of subtle variations in license

- Selection and peer-review under responsibility of the Organizing Committee of the Conference

plate images. These advanced techniques reduce redundancy, optimizing storage and computational resources while enhancing model performance.

In this context, our proposal involves applying perceptual hashing followed by locality-sensitive hashing (LSH) to improve duplicate filtering. LSH refines this process by grouping similar images more granularly, reducing false positives. Finally, an OCR (Optical Character Recognition) analysis is performed on image pairs identified by LSH to verify whether the vehicles' license plates correspond to the same car. By combining perceptual hashing, LSH, and OCR, this approach effectively ensures deduplication while maintaining accuracy, optimizing both storage and the performance of ANPR models for reliable real-world recognition.

State of the Art in Image Deduplication Techniques

Image deduplication plays a crucial role in various applications, particularly facilitating optimized storage management and efficient content retrieval. This section examines modern approaches to image deduplication and explores their potential to enhance the performance of Automatic Number Plate Recognition (ANPR).

Combination of Descriptors for Optimized Feature Extraction

Velmurugan and Baboo (2011) combined SURF features with color moments for content-based image retrieval (CBIR), demonstrating that using combined feature extraction techniques can increase the accuracy of image retrieval. Although this work targets general image retrieval, the approach could inspire a similar strategy for identifying nearly duplicate license plate images in an ANPR context. Li et al. (2014) proposes an enhancement of the classic SURF algorithm by combining it with the DAISY descriptor to strengthen its rotation invariance. This model, designed to overcome SURF's limitations in handling image rotations, offers a more robust matching. While Li does not directly address deduplication, his approach highlights the importance of solid feature extraction for reliable matches—a valuable asset for identifying similar license plate images under varying shooting conditions.

Fast Indexing for Nearly Duplicate Image Detection

Lei et al. (2014) present an innovative indexing structure, Uniform Randomized Tree Groups (URT), which enables rapid detection of nearly duplicate images. This technique is based on two main concepts: uniformity (grouping images with similar features in the same scale subsets) and the use of feature subspaces and random projections to enhance the flexibility and robustness of the indexing structure. While this approach specifically targets near-duplicates, the search space reduction and robustness it provides are directly applicable to deduplication needs in ANPR.

Locality-Sensitive Hashing and Part-Based Representations

Ke et al. (2004) explore the detection of nearly duplicate images through a part-based representation combined with locality-sensitive hashing (LSH). Although their work focuses on copyright infringement detection, their strategy of local feature representation aligns with the needs for robust feature extraction in the ANPR context. By adapting LSH to index these license plate-specific features, it is possible to efficiently manage nearly duplicate images, thereby enhancing ANPR system performance.

PCA and Clusturing

Berrabah and Gafour (2023) explore the combined use of Principal Component Analysis (PCA) and K-means clustering for dataset reduction, enhancing efficiency while maintaining data quality. PCA effectively reduces dimensionality, preserving essential information, while K-means organizes the dataset, minimizing redundancy. The choice of parameters and feature selection is crucial for achieving optimal results. The experiments demonstrate the potential for eliminating redundant data, though success may vary based on dataset characteristics and algorithms used. Additionally, the challenge of class imbalance is highlighted, as it can lead to biased model predictions. The study suggests that while K-means is effective for identifying duplicate images, alternative methods like perceptual hashing may also be appropriate, emphasizing the importance of selecting the right feature representation and similarity metrics for optimal results.

Visual Bag of Words Models and Clustering

Li and Feng (2013) developed a method for detecting nearly duplicate images that combines the visual bag of words (BoW) model with locality-sensitive hashing (LSH) for fast and robust image comparison. The BoW model, which groups local features extracted via SIFT descriptors, facilitates image comparison based on visual vocabulary rather than pixel values. This model, coupled with the K-means algorithm for clustering similar features, provides robustness against variations in conditions such as lighting changes or occlusions, which are common in license plate images.

Efficient and Memory-Friendly Deduplication

Nian et al. (2016) designed an approach for deduplicating nearly duplicate images called Local Binary Representation (LBR). This binary coding scheme reduces memory requirements and computational costs by representing local regions as binary vectors of statistical texture histograms. While this method primarily targets near-duplicates in the context of video and online multimedia, it could potentially be adapted to identify nearly duplicate license plate images within ANPR systems.

Method

Automatic Number Plate Recognition (ANPR) systems are essential in areas such as traffic surveillance and security. Their effectiveness relies on accurately detecting and recognizing license plates under various conditions; however, achieving high precision is often challenging due to factors such as lighting, weather conditions, and the complexity of plate designs. To ensure optimal performance, it is crucial to train these systems on datasets that faithfully reflect local plate characteristics.

This study aims to enhance the accuracy of license plate detection through data deduplication. We propose an approach that integrates a deduplication technique to eliminate redundant images while preserving data diversity. Indeed, removing duplicates can strengthen the quality of training data, which is vital for the effectiveness of machine learning models.

Our methodology relies on three algorithms: perceptual hashing, Locality Sensitive Hashing (LSH), and Optical Character Recognition (OCR). We begin by hashing the images using a perceptual hashing function, then employ LSH to efficiently identify duplicates. By extracting and comparing the license plates from similar image pairs, we can determine which images are indeed duplicates.

Perceptual Hashing

Perceptual hashing refers to techniques that generate a unique fingerprint (hash) for images based on their visual content, rather than their binary data (Hamadouch et al., 2021). These hashes are designed to ensure that two images that are visually similar produce hashes that are highly correlated, while images that are distinctly different yield uncorrelated hashes. An effective perceptual hashing technique can recognize that one image has been derived from another—such as through resizing, compression, or minor alterations—while still maintaining a perceptual resemblance. This property is particularly useful in applications such as image retrieval, copyright enforcement, and duplicate detection, where identifying similar images despite variations is essential. Common algorithms used in perceptual hashing include Average Hash (A-Hash), Difference Hash (D-Hash), and Discrete Cosine Transform Hash (P-Hash), each with its own method of capturing and comparing visual features (Hamadouch et al., 2021).

Steps in Generating Perceptual Hashes

Perceptual hashing algorithms leverage the visual characteristics of images to create unique hashes. The primary goal is to produce hashes that remain unchanged or only slightly altered when modifications preserving the content are made to the image. For two images X and Y, their corresponding perceptual hashes are defined as $h_X=H(X)$ and $h_Y=H(Y)$. A similarity metric $D(h_X,h_Y)$ is then employed, with a threshold t determined empirically. If $D(h_X,h_Y) < t$, this indicates that X and Y are copies of the same image, altered only minimally. The three main steps involved in perceptual hashing are: 1) Image Preprocessing, which prepares the image for analysis; 2) Extraction of Perceptual Features, where relevant visual characteristics are identified; and 3) Quantification or Compression, which generates the final hash string. Various algorithms, such as Average Hash (A-Hash), Difference Hash (D-Hash), and Discrete Cosine Transform Hash (P-Hash), differ in how they extract perceptual features from the image (Samanta, & Jain, 2021).

Image Preprocessing

The preprocessing phase in perceptual hashing algorithms prepares the image to facilitate feature extraction. This step reduces the amount of data to be processed, thereby speeding up the entire process. Various operations are typically carried out at this stage, such as resizing, color transformation, normalization, filtering, and histogram equalization. For instance, an image may be converted to a specific color model, such as YCbCr (luminance and chrominance), HSV (hue, saturation, value), or grayscale. Noise, often introduced by capture conditions, can be reduced through the application of Gaussian filters. Additionally, histogram equalization is sometimes used to enhance contrast by redistributing intensity values. Finally, images may be resized to a standard size, ensuring consistency in subsequent processing.(Samanta & Jain, 2021).

Extraction of Perceptual Features

Feature extraction is a crucial step in the perceptual hashing process, as it determines how effectively the algorithm can capture the essential visual characteristics of an image. The objective is to identify robust features that remain invariant to common image transformations such as resizing, rotation, and compression. Effective feature extraction can be achieved using two main types of techniques: (a) frequency domain transformations, such as Discrete Fourier Transform (DFT), Discrete Cosine Transform (DCT), Discrete Wavelet Transform (DWT), and Fourier-Mellin Transform, and (b) dimensionality reduction techniques, including Principal Component Analysis (PCA), Non-negative Matrix Factorization (NMF), and Singular Value Decomposition (SVD). (Samanta & Jain, 2021).

These features are then used to create a compact representation of the image, which serves as its perceptual hash. By focusing on the most significant aspects of the image, the hashing algorithm can produce hashes that are similar for visually similar images while remaining distinct for those that are different. This allows the system to recognize modified versions of an image effectively, even when the underlying content has been altered.

Quantification or Compression

The numerical values representing the features of an image can be quantified to generate a fixed-size hash, providing a compact and relatively unique representation of the image. This quantification process often relies on the statistical properties of the extracted features. For example, in algorithms utilizing the Discrete Cosine Transform (DCT), the DCT coefficients can be quantified by comparing each coefficient to references such as the median or mean of the coefficients. It is crucial for this quantification to be carefully calibrated to preserve essential visual information, ensuring that the hashes remain significant for similar images while remaining distinct for those that differ. This plays a central role in the effectiveness of perceptual hashing, facilitating the detection and recognition of modified images.

The perceptual hashing algorithm has consistently demonstrated its effectiveness in various applications, such as image retrieval and duplicate detection. However, it involves a sequential comparison of image features, which can become computationally expensive when dealing with large datasets. This increased processing time poses challenges in efficiently managing and analyzing extensive image collections. To address this issue, we propose applying the Locality Sensitive Hashing (LSH) algorithm instead of relying on sequential comparisons of image hashes. By leveraging LSH, we can efficiently group similar images together, thereby reducing the overall number of comparisons required. This approach not only mitigates the time cost associated with large datasets but also enhances the scalability of the perceptual hashing process.

Locality-Sensitive Hashing

After perceptual hashing is performed, locality-sensitive hashing (LSH) is applied to efficiently and scalably identify similar or nearly similar images. LSH techniques utilize specialized hashing functions that group similar images into the same compartments, increasing the likelihood that similar items will be found together. While LSH does not guarantee that all data in a compartment are similar, it significantly improves the chances of clustering similar items, making it a valuable approach for image retrieval, duplicate detection, and similar tasks.

Locality-sensitive hash functions are defined as follows: A family of functions H = {h : S → U} is an LSH family for any two points p, q ∈ S, if for any function h in H, the following conditions are satisfied:

If d(p, q) ≤ r1, then PrH (h(p) = h(q)) ≥ P1.

If d(p, q) ≥ r1, then PrH (h(p) = h(q)) ≤ P1.

Here d(p, q) denotes the distance between p and q, PrH () indicates the probability, r1 and r2 are constants for distribution. (r1 < r2), and P1 and P2 are constants for the probabilities (P1 > P2). A family H of functions satisfying the above conditions is called locality-sensitive with respect to (r1, r2, P1, P2).(Lee, 2012; Slaney & Casey, 2004)

The hashing functions by Indyk et al. are defined as follows: First, data points are encoded in binary codes within Hamming space. To define a hashing function $h()$, a fixed number of positions are randomly sampled with replacement from the set of positions, and the function value for a data point is constructed by concatenating the binary values at the selected positions. When the number of selected positions is d, the bucket size for a hashing function becomes 2^d. Several hashing functions H are constructed in the same way. Each data point in the database is hashed by hashing functions into buckets. When a query d_q is given, it is hashed by each hashing function h into the corresponding bucket. The data points from the buckets to which the hashing functions map the query become the candidates with which the query is compared to determine if they are neighbors.

How LSH Works in Practice

Preprocessing: From Image to Signature

In this preprocessing step, the goal is to compress images into signatures, making the task of finding duplicates easier. If two images are similar, their signatures should also be similar. For a given hashing function and for a given k, the generated signature is of length k2, For k=16, the generated signature looks like this:

$$
\begin{matrix}
1 & 1 & 1 & 0 & 1 & 1 & 1 & 0 & 1 & 1 & 0 & 0 & 0 & 0 & 0 & 0 \\
1 & 1 & 1 & 0 & 1 & 1 & 0 & 0 & 1 & 1 & 1 & 0 & 0 & 0 & 0 & 0 \\
1 & 1 & 1 & 1 & 1 & 0 & 0 & 0 & 0 & 1 & 1 & 0 & 0 & 0 & 0 & 0 \\
1 & 1 & 1 & 1 & 1 & 0 & 0 & 1 & 0 & 1 & 1 & 0 & 0 & 0 & 0 & 0 \\
1 & 1 & 1 & 1 & 1 & 1 & 0 & 1 & 0 & 0 & 1 & 0 & 0 & 0 & 0 & 0 \\
1 & 1 & 1 & 1 & 1 & 0 & 1 & 1 & 0 & 0 & 1 & 1 & 0 & 0 & 0 & 0 \\
1 & 1 & 0 & 1 & 1 & 0 & 1 & 1 & 0 & 1 & 1 & 1 & 0 & 0 & 0 & 0 \\
1 & 1 & 0 & 1 & 1 & 0 & 0 & 1 & 0 & 1 & 1 & 1 & 0 & 0 & 0 & 0 \\
1 & 0 & 1 & 1 & 1 & 0 & 1 & 1 & 0 & 0 & 0 & 1 & 1 & 0 & 0 & 0 \\
1 & 0 & 1 & 1 & 0 & 1 & 1 & 1 & 1 & 0 & 0 & 0 & 1 & 1 & 0 & 0 \\
1 & 0 & 1 & 0 & 0 & 1 & 1 & 1 & 1 & 0 & 0 & 1 & 1 & 1 & 1 & 1 \\
0 & 1 & 1 & 1 & 0 & 1 & 1 & 1 & 0 & 0 & 0 & 1 & 1 & 0 & 1 & 1 \\
1 & 0 & 1 & 0 & 0 & 1 & 1 & 1 & 0 & 0 & 0 & 1 & 0 & 1 & 0 & 1 \\
1 & 0 & 1 & 1 & 0 & 0 & 1 & 1 & 1 & 0 & 0 & 0 & 0 & 0 & 1 & 0 \\
0 & 0 & 1 & 1 & 0 & 1 & 1 & 0 & 1 & 1 & 0 & 1 & 0 & 0 & 1 & 0 \\
1 & 1 & 1 & 0 & 0 & 1 & 0 & 0 & 1 & 1 & 0 & 0 & 0 & 1 & 0 & 0
\end{matrix}
$$

Generating Candidate Pairs

Now, instead of comparing the signatures with each other, each signature is divided into b bands of r rows (bits). This means, of course, that b × r = k2 with k2 being the length of the signature. We will then apply b hashing functions 1 to each band to all substrings of signatures (pieces of r bits) from band b.

If any of these signature substrings end up in the same bucket for any of the hashing functions, we will consider these signatures and their associated files as candidate pairs (quasi-duplicates). We can influence the sensitivity of candidate pair detection by adjusting the parameters b and r. If we take fewer but wider bands, it becomes less "easy" for the signature substrings (bands) to hash into the same bucket, and vice versa (Lee, 2012).

Since this process is likely to create false positives, a post-processing step is necessary where we actually compare the signatures of our candidate pairs with each other. This allows us to check whether they are indeed quasi-duplicates and to what extent. We do this by calculating the Hamming distance between two signatures, that is, the number of bits where the two signatures differ. If this number divided by the signature length (Hamming Distance / k2) is less than a self-defined threshold t, we can consider them as quasi-duplicates. For example, one might choose t equal to 0.8 to consider images that are 80% similar as quasi-duplicates.

The problem lies in defining the threshold, which sometimes leads to the removal of images that have unique existence in the dataset, resulting in a loss of information regarding the vehicle's license plate in question. To remedy this issue, we thought about using OCR to ensure whether the pair of images represents the same vehicle or two different vehicles.

OCR (Optical Character Recognition)

Optical Character Recognition (OCR) is a technology that converts text images (such as scanned documents, photos of text, or PDFs) into editable digital text. It allows a computer to "read" printed, handwritten, or typed characters and convert them into digital data. The OCR process begins by capturing an image containing text, often using a scanner or camera. The image is converted into pixels, with each pixel containing information about color and shape. Next, the OCR software analyzes the image to detect characters and distinguish them from the background. This step may involve "cleaning" the image to remove visual noise like spots or shadows. The software identifies each character and word by using methods based on letter shapes. Modern OCR systems utilize neural networks or other machine learning algorithms, enhancing their accuracy, even for handwritten text or challenging fonts. Once characters have been identified, they are converted into digital text, which users can then edit, search, or use within other software.

Final Check; License Plate Comparison

In this phase, we review the near-duplicates found in the previous step, first extracting the license plate from each image and then comparing them. This step ensures that no essential data is lost, as the use of hashing may introduce some loss of precision.

Experimental Results

In this section, we outline the evaluation plan to demonstrate the effectiveness of our image deduplication technique in enhancing license plate recognition (LPR) systems. Our evaluation aims to determine whether removing nearly duplicate images from the dataset using image deduplication improves the performance of a YOLOv8 object detection model trained on a customized dataset for LPR.

Computational Environment Used for Experimentation

- Operating System: Ubuntu 22.04.4 LTS x86_64
- Hôte : 80XH Lenovo ideapad 320-15ISK
- Kernel : 6.5.0-35-generic
- Shell : bash 5.1.16
- CPU : Intel i3-6006U (4) @ 2.000GHz

- GPU : Intel HD Graphics 520
- Memoire : 11735MB
- Storage : SSD, 120 GB

Dataset

In the experimental phase, we utilized the CCPD dataset, which contains images of Chinese vehicles. This dataset is extensive, diverse, and meticulously annotated. The images in CCPD were collected from an urban parking management company in a provincial capital in China. For specific street locations, the company records parking fees by logging details such as the license plate number, cost, and parking duration, along with a front or rear photo of the vehicle as proof. Consequently, CCPD includes images captured under a variety of lighting conditions and weather environments. Since the only requirement for capturing these photos is to include the license plate, images vary in angles and positions and occasionally include slight motion blur. This results in a rich dataset with images taken from different perspectives and angles, sometimes with a bit of blur.

CCPD contain:

- train: 5769 images for the train
- test: 5006 images for the test
- Valid: 1001 images for the validation

YOLOv8 Object Detection Model

YOLOv8 is the latest version of YOLO by Ultralytics. As a state-of-the-art (SOTA) model, YOLOv8 builds on the success of previous versions by introducing new features and improvements for enhanced performance, flexibility, and efficiency. YOLOv8 supports a comprehensive range of AI vision tasks, including detection, segmentation, pose estimation, tracking, and classification. This versatility allows users to leverage the capabilities of YOLOv8 across various applications and domains.

Evaluation Metrics

We will use standard metrics (mAP50, mAP50-95, Precision, and Recall) commonly employed to evaluate object detection models to assess the impact of image deduplication on YOLOv8's performance in license plate recognition. These metrics consider the trade-off between the model's ability to correctly identify license plates and its capacity to find all license plates present in the images.

Evaluation Procedure

To evaluate the effectiveness of image deduplication on YOLOv8's performance in license plate recognition (LPR), we will follow a structured evaluation procedure. We will use a multi-step training approach to assess the impact of image deduplication on YOLOv8's performance in license plate recognition:

Training the Model without Deduplication:

Initially, we will train a baseline YOLOv8 model using the original dataset without applying any deduplication. This baseline model serves as a reference point for comparison with the results obtained using our deduplication technique (Table 1).

Table 1. Results without deduplication

Variables	Values
Precision	0.89902
Rappel	0.94274
mAP50	0.91463
mAP50-95	0.47924

Model Training with Deduplication

We will then explore the impact of different image deduplication parameters on model performance. This will involve multiple training runs, each with a distinct set of deduplication parameters. These parameters include: similarity threshold, hash size, and hash bands (Table 2)

Table 2. Results with deduplication

Variables	values			
Hash Signature Size	1024	4096	16384	65536
Hash Signature Bands	64	32	16	64
Threshold	0.9	0.8	0.9	0.9
Precision	0.94238	0.94238	0.94246	0.94238
Recall	0.92408	0.92408	0.90002	0.92408
mAP50	0.95009	0.95009	0.94672	0.95009
mAP50-95	0.48136	0.48136	0.48993	0.48136

Conclusion

In this paper, we explored the enhancement of Automatic Number Plate Recognition (ANPR) systems through the integration of image deduplication techniques. Our research found that established deduplication methods significantly contribute to the accuracy, efficiency, and robustness of ANPR systems by improving dataset quality.

Through evaluating various deduplication algorithms, we identified effective strategies for removing redundant images, refining the data used by ANPR models. Our experiments, conducted on the CCPD dataset in China, showed measurable improvements in recognition accuracy and reduced computational costs, validating the hypothesis that deduplication strengthens ANPR system performance.

This work fills a gap in current research, which has largely focused on recognition algorithms without considering the benefits of preprocessing with deduplication. We demonstrate the potential of deduplication for ANPR systems and open avenues for further optimization of preprocessing steps to advance smart city initiatives and traffic management capabilities.

Scientific Ethics Declaration

The authors declare that the scientific ethical and legal responsibility of this article published in EPSTEM Journal belongs to the authors.

Acknowledgements or Notes

* This article was presented as an poster presentation at the International Conference on Technology, Engineering and Science (www.icontes.net) held in Antalya/Turkey on November 14-17, 2024.

References

Berrabah, D., & Gafour, Y. (2023). Improve image classification using data optimization. *The Eurasia Proceedings of Science Technology Engineering and Mathematics,26*, 262-271.

Hamadouche, M., Zebbiche, K., Guerroumi, M., Tebbi, H., & Zafoune, Y. (2021). A comparative study of perceptual hashing algorithms: Application on fingerprint images. In *The 2nd International Conference on Computer Science's Complex Systems and their Applications*.

Ke, Y., Sukthankar, R., & Huston, L. (2004). An efficient parts-based nearduplicate and sub-image retrieval system. *Proceedings of the 12th Annual ACM International Conference on Multimedia*, 869–876.

Lee, K, M, (2012). Locality-sensitive hashing techniques for nearest neighbor search. *International Journal of Fuzzy Logic and Intelligent Systems*, *12*(4), 300– 307.

Lei, Y., Qiu, G., Zheng, L., & Huang, F. (2014). Nearduplicate image detection using uniform randomized trees. *ACM Transactions on Multimedia Computing, Communications, and Applications, 10*, 1–15.

Li, L., & Zic, J. (2014). Image matching algorithm based on feature-point and DAISY descriptor. *Journal of Multim.*, *9*(6), 829-834.

Li, Z., & Feng, X. (2013). Near duplicate image detecting algorithm based on bag of visual word model. *Journal of Multimedia, 8,* 557–564.

Nian, F., Li, T., Wu, X., Gao, Q., & Li, F. (2016). Efficient near-duplicate image detection with a local-based binary representation. *Multimedia Tools Applications, 75*(5), 2435–2452.

Samanta, P., & Jain, S. (2021). Analysis of perceptual hashing algorithms in image manipulation detection. *Procedia Computer Science*, *185*, 203-212.

Slaney, M., & Casey, M. (2008). Locality-sensitive hashing for finding nearest neighbors (lecture notes). *IEEE Signal Processing Magazine*, *25*(2), 128-131.

Velmurugan, K., & Baboo, L. D. S. S. (2011). Content-based image retrieval using SURF and colour moments. *Global Journal of Computer Science and Technology*, *11*(10), 1-4.

Author Information

Djamel Berrabah
EEDIS, University of Djillali Liabes
Sidi Bel Abbes, Algeria
Contact e-mail: *berrabdjamel@gmail.com*

Yacine Gafour
University Ibn Khaldoun
Tiaret, Algeria

To cite this article:

Berrabah, D., & Gafour, Y. (2024). Significant improvement in license plate recognition through image deduplication. *The Eurasia Proceedings of Science, Technology, Engineering & Mathematics (EPSTEM), 32,* 295-303.

The Eurasia Proceedings of Science, Technology, Engineering & Mathematics (EPSTEM)
ISSN: 2602-3199

The Eurasia Proceedings of Science, Technology, Engineering & Mathematics (EPSTEM), 2024

Volume 32, Pages 304-310

IConTES 2024: International Conference on Technology, Engineering and Science

Tackling FSO-WDM System Challenges with Artificial Neural Networks: A Comprehensive Analysis

Rima Kebaili
University of Djillali Liabes

Samia Driz
University of Djillali Liabes

Benattou Fassi
University of Djillali Liabes

Abstract: The integration of Free-Space Optical (FSO) communications with Wavelength Division Multiplexing (WDM) offers significant advancements in high-bandwidth, high-capacity systems. However, FSO-WDM systems face challenges due to atmospheric impairments and channel fading. Traditional mitigation techniques often struggle to address these complex and dynamic issues. Recently, Artificial Neural Networks (ANNs) have emerged as powerful tools for learning and adapting to system behaviors, providing novel solutions to enhance FSO-WDM performance. This study analyzes FSO-WDM systems, focusing on applying ANNs to predict channel attenuation accurately and enabling more stable transmission. An OptiSystem simulation was conducted across various transmission distances and climatic scenarios, with Q-Factor and Bit Error Rate (BER) as input features and channel attenuation as the target variable. Following preprocessing, the dataset was split into training, validation, and testing sets. The ANN model, implemented in MATLAB, consisted of an input layer, a hidden layer with 10 neurons, and an output layer. Performance was evaluated using Root Mean Square Error (RMSE) and R-squared (R^2) metrics. The trained ANN model demonstrated an optimal mean squared error of 0.23439 and strong correlation between predicted and actual attenuation, with R^2 values of 0.99907 for the training set and 0.99745 for the validation set. These results confirm the model's robustness in accurately predicting channel attenuation across varying conditions.

Keywords Free-space optic (FSO), Wavelength division multiplexing (WDM), Artificial neural networks (ANNs), Channel attenuation prediction, Root mean square error (RMSE), R-squared (R^2).

Introduction

Free-Space Optical (FSO) communication systems are a promising technology for high-speed wireless data transmission due to their ability to offer large bandwidths and immunity to electromagnetic interference. However, the performance of FSO systems is significantly affected by atmospheric conditions, particularly attenuation caused by various weather phenomena such as fog, rain, and snow (Moon et al., 2023). This attenuation can severely degrade the quality of the transmitted signal, leading to reduced system reliability and performance (Al-Gailani et al., 2020; Sangeetha et al., 2017; Hall et al., 2022).

In Wavelength Division Multiplexing (WDM)-FSO systems, accurate prediction of channel attenuation is essential for maintaining efficient and reliable operation. By anticipating the effects of atmospheric conditions on the communication link, network operators can implement adaptive techniques, such as modulation and coding schemes, power control, and other mitigation strategies, to ensure acceptable performance levels (Driz et al., 2020). Traditional attenuation prediction methods often rely on empirical models that are based on limited weather data, which may not fully capture the complex interactions between atmospheric parameters and the FSO link characteristics (Driz et al., 2024).

Recently, machine learning (ML) techniques have demonstrated significant potential in addressing the challenges associated with predicting complex phenomena like atmospheric attenuation (Lionis et al., 2023.). ML algorithms can analyse large datasets, identify hidden patterns, and make accurate predictions even in the presence of uncertainty and noise (Driz et al., 2024). In the context of FSO systems, ML has become an invaluable tool for predicting channel attenuation, as it can leverage historical data on atmospheric conditions and link performance to uncover complex relationships. Common ML approaches used in this domain include Support Vector Machines (SVM), regression models, neural networks, and ensemble methods (Sajid et al., 2024; Puspitasari et al., 2023; Song et al., 2021).

Among these methods, Artificial Neural Networks (ANNs) stand out for their ability to model nonlinear relationships and adapt to dynamic environments. ANNs, inspired by the structure and functioning of the human brain, consist of layers of interconnected neurons that process input data and learn from experience. This allows them to capture intricate patterns in data that might be overlooked by traditional models. In particular, ANNs are highly effective in scenarios where the relationship between input features and the target variable is not linear, making them suitable for predicting channel attenuation in WDM-FSO systems (Gao et al., 2020; Yu et al., 2019; Manuylovich et al., 2023).

Methodology

This study follows a structured methodology, begining with the design and simulation of WDM-FSO system, which serves as the basis for generating the dataset required for model training and evaluation. The steps involved in this process are outlined as follows:

System Design and Data Collection

The first step involves modeling the WDM-FSO system (Figure1) within the OptiSystem simulation environment. This system was designed to simulate real-world transmission scenarios under various atmospheric conditions, such as fog, rain, and haze. The setup includes three main components: transmitter, channel, and receiver, as described below (Vanderka et al., 2016).

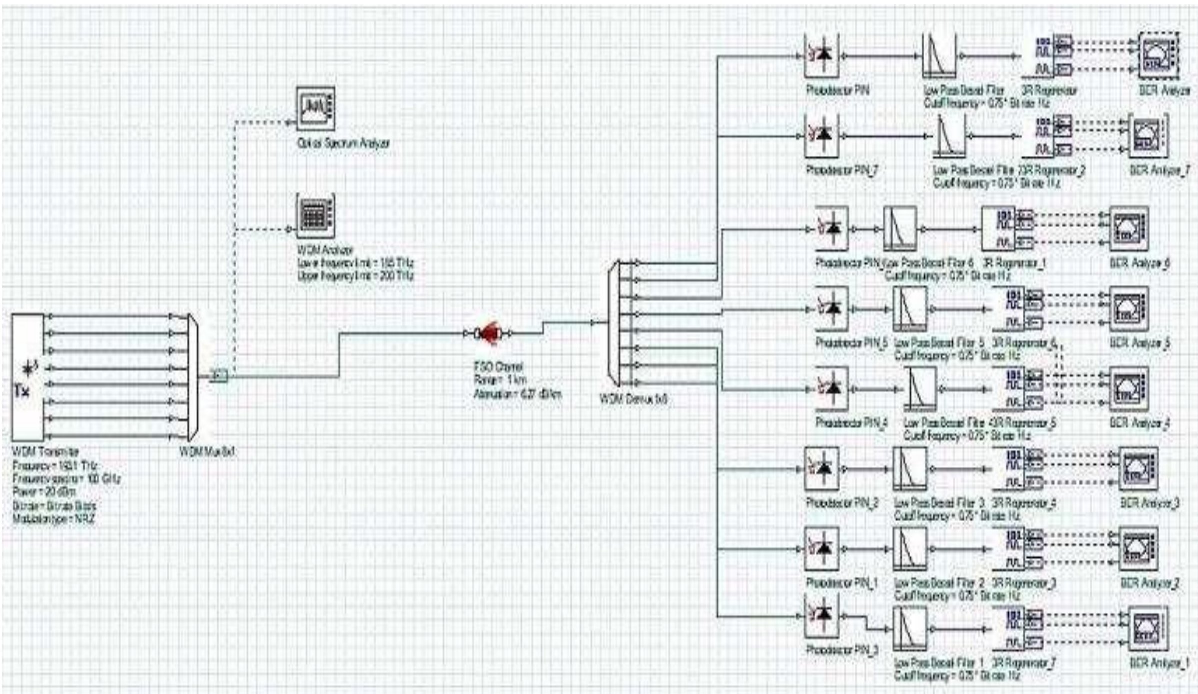

Figure 1. WDM-FSO design

Transmitter

The transmitter unit generates and modulates the optical signal for transmission. Components include a Pseudo-Random Bit Sequence (PRBS) generator to simulate real-world data, a Non-Return to Zero (NRZ) pulse generator to convert the digital bits into electrical pulses, CW lasers operating at different wavelengths (8 channels), Mach-Zehnder Modulators (MZMs) for signal modulation, and a WDM Multiplexer to combine the modulated signals.

Channel

The channel simulates the free-space optical link under various weather conditions, such as clear skies, fog, and rain, affecting signal attenuation. The attenuation values for different conditions are summarized in Table 1.

Table 1. Attenuation values under different weather conditions at a wavelength of 1550 nm. (Robinson & Jasmine, 2016)

Weather conditions	Attenuation(dB/Km)
Very Clear	0.065
Clear	0.233
Light Haze	0.55
Light Fog	15.5
Heavy Fog	25.5
Light Rain	6.27
Medium Rain	9.64
Heavy Rain	19.28
Dry Snow	6.2

Receiver

At the receiver side, the WDM De-multiplexer separates the incoming composite signal into individual wavelength channels, and a PIN Photodetector converts the optical signal back into an electrical signal. The parameters used in this simulation closely approximate real-world scenarios, including data rate, modulation format, channel spacing, and transmitter /receiver aperture sizes. The key system parameters are summarized in Table 2.

Table 2. Simulation parameters

Parameter	Value
Data rate	2.5 Gbps
Launch power	20 dBm
Frequency spacing	100 GHz
Transmitter aperture	5 Cm
Receiver aperture	20 Cm
Modulation type	NRZ
Electrical filter type	Bessel
PIN photodiode responsivity	1 A/W

Data Generation

To generate the dataset, the system was simulated across different weather conditions and transmission distances. For each scenario, the Q-Factor, Bit Error Rate (BER), and attenuation were recorded. The goal was to gather data that represents a wide range of operational conditions, allowing for the training of a machine learning model to predict channel attenuation accurately.

Preprocessing and Feature Selection

After collecting the data, preprocessing was carried out. Features like Q-Factor, BER, and distance were selected as input variables, while channel attenuation was the target output. The dataset was split into training, validation, and test sets.

Model Training

An Artificial Neural Network (ANN) was developed using MATLAB to predict channel attenuation. The network consisted of an input layer, a hidden layer with 10 neurons, and an output layer (Figure 2) .

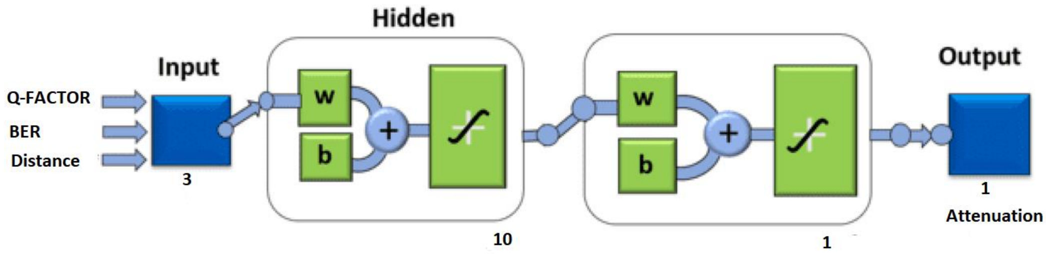

Figure 2. Schematic diagram of ANN model for attenuation prediction.

The model was trained on the training set and evaluated on the validation and testing sets using metrics such as:

Root Mean Square Error (RMSE)

RMSE is a commonly used metric that calculates the square root of the average of the squared differences between the predicted values ($\widehat{y}_i$) and the actual values (y_i). The formula is given by Chicco et al. (2021).

$$\text{RMSE} = \sqrt{\frac{1}{N}\sum_{i=1}^{n}(\widehat{y}_i - y_i)^2} \tag{1}$$

Where *n* represents the total number of samples.

This metric indicates how far, on average, the predicted values deviate from the actual values. A lower RMSE value means the model's predictions are closer to the actual values, indicating higher accuracy and better overall model performance .

R-squared (R^2)

R^2 is a measure that indicates how much of the variation in the actual data is accounted for by the model's predictions. The closer the R^2 value is to 1, the stronger the relationship between the predicted and actual values. It is calculated as follows (Gonenc et al., 2022)

$$R^2 = 1 - \frac{\sum_{i=1}^{n}(\widehat{y}_i - y_i)^2}{\sum_{i=1}^{n}(\widehat{y}_i - \overline{y}_i)^2} \tag{2}$$

Where $\overline{y}_i$ is the mean of the actual values.

R^2 provides insight into how well the model fits the data, with higher values indicating a better fit.

Results and Discussion

This section provides a detailed evaluation of the performance of ANN model in predicting channel attenuation, FSO systems integrated with WDM. The assessment is grounded in two key performance metrics: RMSE and (R^2), analyzed across training, validation, and testing datasets. The ANN model achieved impressive R^2 values of 0.9907, 0.99745, and 0.99926 for the training, validation, and testing sets, respectively, as illustrated in Figure 3. These values indicate a strong correlation between the predicted and actual channel attenuation, with the high validation R^2 underscoring the model's exceptional generalization capability. This consistency with training results suggests minimal overfitting, further supported by the model's performance on the test set, which indicates robust predictive accuracy with previously unseen data. Overall, the combined dataset yielded an R^2 of 0.99885, reflecting the model's stability and reliability in predicting channel attenuation across varying atmospheric conditions.

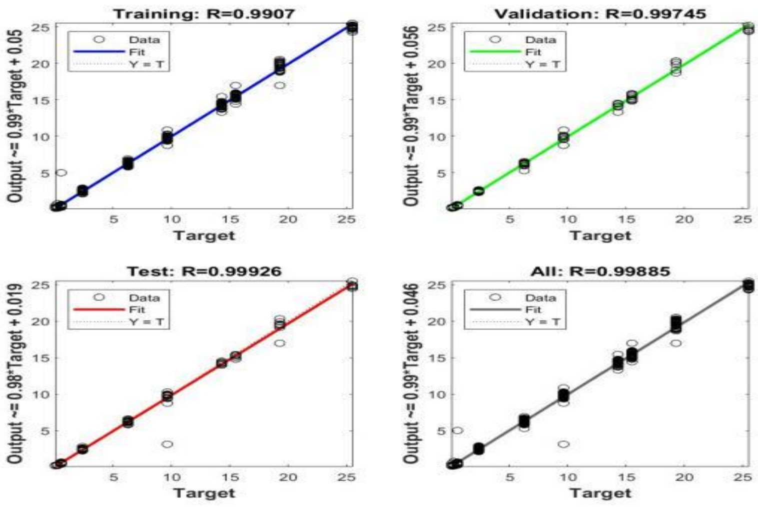

Figure 3. Regression fit plot of 10-neuron model

Notably, the model reached optimal performance early in the training process, achieving an MSE of 0.23439 at epoch 0. Subsequent epochs showed diminishing returns in performance improvement, as depicted in Figure 4. This rapid convergence highlights the model's efficiency in learning the underlying patterns of the dataset, suggesting that the chosen architecture and training parameters effectively capture the complexities inherent in FSO-WDM attenuation characteristics. The consistently low RMSE across all datasets further affirms the model's ability to accurately replicate actual attenuation values, an important factor for the implementation of adaptive control mechanisms in FSO-WDM systems.

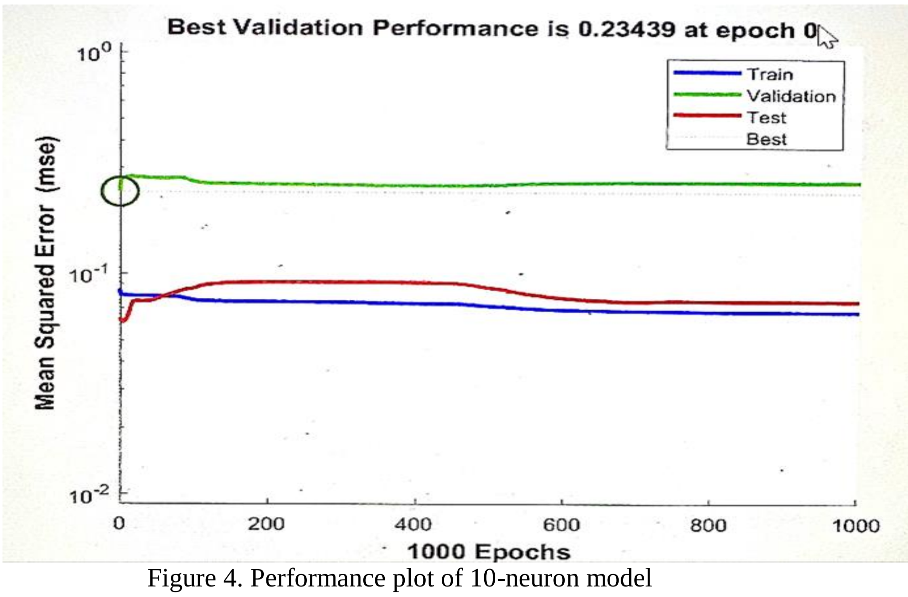

Figure 4. Performance plot of 10-neuron model

Conclusion

In this study, we presented a robust ANN model designed for predicting channel attenuation in FSO systems integrated with WDM. The evaluation metrics, including R-squared and RMSE, demonstrated the model's high accuracy and generalization capability across training, validation, and testing datasets. The achieved R^2 values indicate a strong correlation between predicted and actual attenuation values, while the consistently low RMSE confirms the model's reliability.

The model's rapid convergence during training highlights its efficiency in capturing the complex patterns inherent in FSO-WDM attenuation characteristics. Moreover, its robustness across various climatic conditions underscores its potential for real-time adaptive control mechanisms in FSO systems, facilitating proactive adjustments to maintain signal integrity.

Overall, this study lays a strong foundation for future applications of machine learning in WDM-FSO technology, suggesting avenues for further exploration, such as the integration of additional environmental factors and the enhancement of model architectures.

Recommendations

This research offers solutions for enhancing FSO-WDM systems by using ANN-based models to accurately predict channel attenuation under various atmospheric conditions. This approach provides a foundation for resilient optical communication infrastructure capable of maintaining performance despite environmental challenges.

Scientific Ethics Declaration

The authors declare that the scientific ethical and legal responsibility of this article published in EPSTEM Journal belongs to the authors.

Acknowledgements or Notes

This article was presented as an poster presentation at the International Conference on Technology, Engineering and Science (www.icontes.net) held in Antalya/Turkey on November 14-17, 2024.

References

Al-Gailani, S. A., Salleh, M. F. M., Salem, A. A., Shaddad, R. Q., Sheikh, U. U., Algeelani, N. A., & Almohamad, T. A. (2020). A survey of free space optics (FSO) communication systems, links, and networks. *IEEE Access, 9*, 7353-7373.

Amar, T., Benattou, F., Samia, D., & Iman, O. (2022). Investigation on different rain conditions over 40 Gbps DPSK-FSO link: Algeria climate. In *7th International Conference on Image and Signal Processing and Their Applications (ISPA)* (pp. 1-6). IEEE.

Anbarasi, K., Hemanth, C., & Sangeetha, R. G. (2017). A review on channel models in free space optical communication systems. *Optics & Laser Technology, 97*, 161–171.

Chicco, D., Warrens, M. J., & Jurman, G. (2021). The coefficient of determination R-squared is more informative than SMAPE, MAE, MAPE, MSE and RMSE in regression analysis evaluation. *PeerJ Computer Science, 7*, e623.

Freire, P., Manuylovich, E., Prilepsky, J. E., & Turitsyn, S. K. (2023). Artificial neural networks for photonic applications—from algorithms to implementation tutorial. *Advances in Optics and Photonics, 15*(3), 739-834.

Gao, Z., Yan, S., Zhang, J., Mascarenhas, M., Nejabati, R., Ji, Y., & Simeonidou, D. (2020). ANN-based multi-channel QoT-prediction over a 563.4-km field-trial testbed. *Journal of Lightwave Technology, 38*(9), 2646-2655.

Gonenc, A., Acar, E., Demir, I., & Yılmaz, M. (2022). Artificial ıntelligence based regression models for prediction of smart grid stability. In *2022 Global Energy Conference (GEC)* (pp. 374-378). IEEE.

Jahid, A., Alsharif, M. H., & Hall, T. J. (2022). A contemporary survey on free space optical communication potentials, technical challenges, recent advances and research direction. *Journal of Network and Computer Applications*, *200*, 1-59.

Jeon, H. B., Kim, S. M., Moon, H. J., Kwon, D. H., Lee, J. W., & Chung, J. M. (2023). Free-space optical communications for 6G wireless networks: Challenges, opportunities, and prototype validation. *IEEE Communications Magazine*, *61*(4), 116-121.

Khalid, H., Sajid, S. M., Nistazakis, H. E., & Ijaz, M. (2024). Survey on limitations, applications and challenges for machine learning aided hybrid FSO/RF systems under fog and smog influence. *Journal of Modern Optics*, *71*(4-6), 101-125.

Lionis, A., Sklavounos, A., Stassinakis, A., Cohn, K., Tsigopoulos, A., & Peppas, K. (2023). Experimental machine learning approach for optical turbulence and FSO outage performance modeling. *Electronics, 12*(3), 1-19.

Puspitasari, A. A., An, T. T., Alsharif, M. H., & Lee, B. M. (2023). Emerging technologies for 6G communication networks machine learning approaches. *Sensors, 23*(18), 1-40.

Rima, K., Samia, D., & Benattou, F. (2024). Supervised machine learning method based modulation formats classification for WDM systems. *8th International Conference on Image and Signal Processing and their Applications (ISPA)* (pp. 1-6). IEEE.

Robinson, S., & Jasmine, S. (2016). Performance analysis of hybrid WDM-FSO system under various weather conditions. *Frequenz, 70*(9-10), 433–441.

Song, S., Liu, Y., Xu, T., Liao, S., & Guo, L. (2021). Channel prediction for intelligent FSO transmission system. *Optics Express, 29*(17), 27882-27899.

Tou, A., Driz, S., Fassi, B., & Mahadjoubi, I. S. K. (2024). Harnessing polarization diversity for enhanced reliability in free space optical communications. *Progress in Electromagnetics Research C, 142*, 27-35.

Vanderka, A., Hajek, L., Bednarek, L., Latal, J., Vitasek, J., Hejduk, S., & Vasinek, V. (2016). Testing FSO WDM communication system in simulation software optiwave OptiSystem in different atmospheric environments. *In Laser Communication and Propagation through the Atmosphere and Oceans V*, 9979, 284-292.

Yu, J., Mo, W., Huang, Y. K., Ip, E., & Kilper, D. C. (2019). Model transfer of QoT prediction in optical networks based on artificial neural networks. *Journal of Optical Communications and Networking, 11*(10), C48-C57.

Author Information

Rima Kebaili
Telecommunications and Digital Signal Processing Laboratory, Faculty of Electrical Engineering, University of Djillali Liabes, Sidi Bel Abbes 22000, Algeria
Contact e-mail: rima.kebaili@univ-sba.dz

Samia Driz
Telecommunications and Digital Signal Processing Laboratory, Faculty of Electrical Engineering, University of Djillali Liabes, Sidi Bel Abbes 22000, Algeria

Benattou Fassi
Telecommunications and Digital Signal Processing Laboratory, Faculty of Electrical Engineering, University of Djillali Liabes, Sidi Bel Abbes 22000, Algeria

To cite this article:

Kebaili, R., Driz, S & Fassi, B. (2024). Tackling FSO-WDM system challenges with artificial neural networks: A comprehensive analysis. *The Eurasia Proceedings of Science, Technology, Engineering & Mathematics (EPSTEM), 32,* 304-310.

The Eurasia Proceedings of Science, Technology, Engineering & Mathematics (EPSTEM)
ISSN: 2602-3199

The Eurasia Proceedings of Science, Technology, Engineering & Mathematics (EPSTEM), 2024

Volume 32, Pages 311-319

IConTES 2024: International Conference on Technology, Engineering and Science

Parallel Machine Scheduling with Re-entrant Jobs with Consideration of Set up Times

Betul Kayisoglu
Abdullah Gul University

Seyma Bekli
Abdullah Gul University

Ayse Sena Sahin
Abdullah Gul University

Gamze Gul Akyurek
Abdullah Gul University

Ruveyda Aydinli
Abdullah Gul University

Sevda Nur Copur
Abdullah Gul University

Tugba Ekinci
Abdullah Gul University

Abstract: We study the identical parallel machine problem with re-entrant jobs. Re-entrant jobs require to pass through the processing line multiple times. In many real-life manufacturing systems with parallel machine environments, one of the scheduling problems that needs to be addressed is the order of jobs on each machine with re-entrant jobs. In addition, manufacturing systems may require periodic maintenance, systematic manufacturing equipment cleaning, or predetermined upper limits on the overtime. Therefore, machine availability may vary during the scheduling horizon. We propose an integer programming model to find the optimal sequence of the re-entrant jobs at parallel machines with consideration of machine availability. The model aims to reduce setup times and maximize capacity utilization by scheduling tasks with similar set up requirements consecutively. We tested the proposed model at a panel line manufacturing company located in Turkey. The order of the panels is scheduled optimally by the proposed model for 3 different instances on the identical parallel machines for the coating process. We also provided relevant information on the user interface we developed to make the proposed scheduling model usable to by the company. The proposed model and interphase offer a systematic approach to panel line planning and can also be implemented in other industries.

Keywords: Production scheduling, Re-entrant scheduling, Parallel machine scheduling, Sustainable manufacturing, Integer programming model.

Introduction

- Selection and peer-review under responsibility of the Organizing Committee of the Conference

In today's globalizing world, one of the key aspects for companies to survive and compete is efficiency. In manufacturing companies, production efficiency could be considered as the primary factor to success. Production efficiency can be defined as a metric of how well the companies are using their available resources to produce the goods/services they are providing. The production efficiency of a manufacturing company (or shop floor) can be found by comparing the actual production amount to the company’s (shop floor’s) theoretical maximum value. Therefore, understanding the maximum achievable value as the production capacity is important. Production efficiency depends heavily on effective scheduling, as optimized schedules allocate resources optimally, minimizing idle time and/or reducing the setup time between tasks.

The scheduling problem has been of interest to researchers since it was first introduced by (Johnson (1954). The literature on scheduling is quite extensive and covers process optimizations that have been developed over many years. Since the manufacturing process varies by product, different solution methods and algorithms have been created theoretically. Processes involving re-entrant jobs differ from standard machine scheduling operations and vary in this respect.

Re-entrant scheduling problems are characterized by the jobs entering a facility or a machine more than once. Many real-world manufacturing processes require products to be processed on the same machine more than once. Mirror manufacturing, dying process, printed circuit board production, tests done more than once in microbiological laboratories, and surgery schedules when patients need operations more than once could be given as re-entrant scheduling examples Chakhlevitch and Glass (2009), Choi and Kim (2008), Wang et al. (2021). Out of many re-entrant scheduling problems, motivated by a panel line manufacturing facility, we focus on an identical parallel machine scheduling problem with re-entrant jobs (IPMS_RJ). In real-world manufacturing environments, not all the machines are available throughout the given time horizon. Periodic maintenance or cleaning reduces the availability of the machines for a certain period.

Even though parallel machine literature is vast, scheduling re-entrant jobs in parallel machines has not been adequately addressed. To the best of our knowledge, no study has examined IPMS_RJ with the consideration of deterministic machine unavailability. To close this literature gap, we present a new integer programming model that optimizes the sequence of the jobs which may or may not require additional processing on parallel machines with deterministic unavailability.

The rest of this paper is organized as follows: first, we present a summary of related literature. Next, an integer programming model is introduced to optimally solve the IPMS_JS problem. We discuss the results in the Computational Experiments section using real-world data. We also give an interphase for solving the IPMS_JS problem. Finally, concluding remarks and future research directions are given.

Related Literature

In this section, we present a literature review on scheduling with a focus on re-entrant scheduling. For a detailed re-entrant scheduling literature review, readers are referred to Danping and Lee (2011). Re-entrant scheduling could be analyzed through the single-machine environment, flow-shop, and job-shop environments (Chen & Chao-Hsien Pan, 2006). Since we have a parallel machine environment in our problem, we focus on multi-machine environments (i.e. flow-shop and job-shop environments) in the related literature.

In the flow-shop environment, all the jobs require similar manufacturing techniques. This is why; the machine sequence of the jobs is similar. Minimizing makespan in a re-entrant flow-shop environment is proved to be at least binary NP-hard for even 2-machine case Wang et al. (1997) and Chen et al. (2008) investigate the use and performance of hybrid genetic algorithms while minimizing makespan for re-entrant flow-shop environments. The study shows that hybrid genetic algorithms work well in finding the near-optimal values. Choi and Kim (2007) also investigates similar problems of minimization makespan by using different types of heuristic algorithms such as lower bound-based, idle time-based, constructive heuristics, and simulated annealing algorithms. The computational experiments show that the suggested heuristics work well and provide good results in a short amount of time. Chamnanlor et al. (2017) considered minimizing makespan at a re-entrant flow-shop with time-window constraints. This study is representative of real-life manufacturing problems hard-disk drive sector where the product quality has to be monitored within certain time intervals. Genetic algorithms and ant colony algorithms are used together as a heuristic algorithm.

Since parallel machine environments can be considered a special type of flexible job-shop environment, we present literature on re-entrant scheduling in job-shop environments. In job-shop environments, each job follows its predetermined path. Low et al. (2005) investigated re-entrant scheduling in a job shop environment with the sequence-dependent set-up time consideration. Three optimization models are proposed for minimizing total job flow time, total tardiness, and machine idle. Since the optimization models related to job-shop scheduling with re-entrant jobs are computationally intractable, many of researchers have focused on heuristic algorithms to provide near-optimal solutions. Zoghby et al. (2005) addressed the re-entrant scheduling problem by incorporating sequence-dependent set-up times in a job-shop environment. They have investigated the feasibility conditions for constructing heuristic algorithms. Sun (2009) also studied a similar problem where set-up times are defined by the sequences of the machines. Two heuristic algorithms and a genetic algorithm have been developed as solution algorithms. The computational experiments show that the genetic algorithm is providing better quality solutions within a reasonable computational time. Mason et al. (2002) studied a re-entrant job-shop problem with the goal of minimizing total weighted tardiness. A modified shifting bottleneck-type heuristic is proposed as a solution algorithm. The proposed algorithm is tested using a semiconductor manufacturer's data. It is shown that the proposed heuristic algorithm works well in delivering the orders on time. Belkaid et al. (2016) studied the re-entrant parallel machine scheduling problem under the consideration of consumable resources. It is assumed that each job consumes a certain number of resources to be processed at the machines. An integer linear programming model and a genetic algorithm are proposed for solving the problem to minimize makespan. The focus of the research reported in this paper is on modelling the problem of optimal sequences of the jobs in parallel machines taking into account re-entrant jobs and changes in machine availability. This problem is intended to represent a real-world scheduling problem that is often encountered when using the identical parallel machines with jobs requiring more than one process at the machines such as coating of the panel lines. This study contributes to the current state of knowledge by introducing a new integer programming model that aims to find the optimal schedules of the jobs on parallel machines while considering the required time/shift between consecutive executions of the re-entrant jobs.

Problem Definition

We focus on scheduling of jobs on identical parallel machines with re-entrant jobs. By re-entrant, we mean that certain jobs are processed once, while others re-enter the system after a waiting period, such as for drying. We consider a scheduling horizon, which is a predetermined period, such as a day, week, or month, within which all jobs will be processed. This scheduling horizon is divided into shifts, represented by the set K. The jobs to be processed during this scheduling horizon are known in advance. These jobs are assigned to a group of identical parallel machines, meaning each job can be processed on any machine since they share the same capabilities. Let L represent the set of parallel machines available for processing. Each machine may be restricted to certain shifts; for example, some machines may be under maintenance and may not work on predetermined shifts. We define a parameter b_{kl} to specify the shifts that machine l will work within the scheduling horizon, b_{kl} gets the value 1 if machine l can work on shift k, 0 otherwise.

Let I represent the set of jobs with subsets I_1 for jobs processed once and I_2 for re-entrant jobs processed more than once. We define a parameter m_i to denote the number of times job $i \in I$ requires processing. Additionally, we create another subset I_3 for dummy jobs that are not actual jobs but are introduced for modeling purposes. Each parallel machine has a dummy starting job and a dummy ending job. Let n be the number of jobs. We assign job 0 as the starting dummy job and job n+1 as the ending dummy job for each parallel machine. Thus, $I=I_1 \cup I_2 \cup I_3$. Each job has processing time that we represent by the parameter p_i where $i \in I$. For dummy jobs in I_3 , we set $p_i = 0$. When a job enters the system, it requires a setup time before processing begins. If the preceding job is similar to the current job, the setup time may be reduced. Therefore, the setup time varies depending on the specific sequence of jobs. We define the parameter s_{ij} to represent the setup time required when job j is processed immediately after job i, where $i, j \in I$. The aim of IPMSP_RJ is to minimize total setup time.

Mathematical Model for IPMSP_RJ

In this study, a mathematical model was developed for IPMSP_RJ presented below.

Sets

I	$Set\ of\ jobs$
I_1	$Set\ of\ jobs\ processed\ once$
I_2	$Set\ of\ re-entrant\ jobs\ that\ are\ processed\ multiple\ times$

I_3	$Set\ of\ dummy\ jobs\ that\ are\ not\ actual\ jobs$
K	$Set\ of\ shifts$
L	$Set\ of\ identical\ machines$

Parameters

p_i	$Processing\ time\ of\ job\ i \in I$
s_{ij}	$Setup\ time\ required\ when\ job\ j\ is\ processed\ immediately\ after\ job\ i, where\ i, j \in I$
v_k	$Total\ working\ time\ of\ shift\ k \in K$
b_{kl}	$1\ if\ machine\ l \in L\ can\ work\ on\ shift\ k \in K, 0\ otherwise$
a	$Number\ of\ shifts\ re-entrant\ jobs\ must\ wait\ before\ reentering\ the\ system$
m_i	$Number\ of\ times\ job\ i\ \in I\ is\ processed$

Decision Variables

Y_{jlk}	1,	$if\ job\ j \in I\ is\ assigned\ to\ machine\ l\ \in L\ in\ shift\ k \in K;\ 0\ otherwise$
X_{kijl}	1,	$if\ job\ j \in I\ is\ assigned\ to\ machine\ l \in L$ just after job i $\in I\ in\ shift\ k \in K;$ $0, otherwise$
U_{ikl}		$Order\ of\ job\ i \in I\ on\ machine\ l \in L\ in\ shift\ k \in K$

With these definitions, the proposed model for IPMSP_RJ is given below:

$$Z = \text{Min} \sum_{i,j,l,k} s_{ij}\ X_{ijkl} \quad (1)$$

s.t.

$$\sum_{l,k} Y_{ilk} = 1 \qquad \forall i\ \in I_1 \quad (2)$$

$$\sum_{l,k} Y_{ilk} = m_i \qquad \forall i\ \in I_2 \quad (3)$$

$$Y_{ilk}\ \leq b_{lk} \qquad \forall i\ \in I, \forall k\ \in\ K, \forall l\ \in\ L \quad (4)$$

$$Y_{0,l,k} = 1 \qquad \forall k\ \in\ K, \forall l\ \in\ L \quad (5)$$

$$Y_{n+1,l,k} = 1 \qquad \forall k\ \in\ K, \forall l\ \in\ L \quad (6)$$

$$\sum_l \sum_{k+1}^{k+a} Y_{ilk}\ \leq 1 - \sum_l Y_{ilk} \qquad \forall i\ \in I_2,\ \forall k \in\ K \quad (7)$$

$$\sum_{i,j} s_{ij}\ X_{kijl} + \sum_j p_j\ Y_{jlk}\ \leq\ v_k \qquad \forall k\ \in\ K, \forall l\ \in\ L \quad (8)$$

$$\sum_j X_{kijl}\ =\ Y_{ilk} \qquad \forall k\ \in\ K,\ \forall l\ \in\ L,\ \forall i\ \in I_1 \cup I_2 \quad (9)$$

$$\sum_j X_{kjil}\ = Y_{ilk} \qquad \forall k\ \in\ K,\ \forall l\ \in\ L, \forall i\ \in I_1 \cup I_2 \quad (10)$$

$$\sum_j X_{k,j,0,l}\ = 0 \qquad \forall k\ \in\ K, \forall l\ \in\ L \quad (11)$$

$$\sum_j X_{k,n+1,j,l}\ = 0 \qquad \forall k\ \in\ K, \forall l\ \in\ L \quad (12)$$

$$\sum_j X_{k,0,j,l}\ = 1 \qquad \forall k\ \in\ K, \forall l\ \in\ L \quad (13)$$

$$\sum_j X_{k,j,n+1,l}\ = 1 \qquad \forall k\ \in\ K, \forall l\ \in\ L \quad (14)$$

$$U_{ikl} - U_{jkl} + (n+1)\ X_{kijl} \leq n \qquad \forall k\ \in\ K,\ \forall l\ \in\ L, \forall i, j\ \in I \quad (15)$$

$$X_{kijl}\ + X_{kjil}\ \leq 1 \qquad \forall k\ \in\ K,\ \forall l\ \in\ L, \forall i, j\ \in I \quad (16)$$

$$Y_{ilk} \in \{0,1\} \qquad \forall k\ \in\ K,\ \forall l\ \in\ L, \forall i\ \in I \quad (17)$$

$$X_{kijl} \in \{0,1\} \qquad \forall k\ \in\ K,\ \forall l\ \in\ L, \forall i, j\ \in I \quad (18)$$

$$U_{ikl} \geq 0 \qquad \forall k\ \in\ K,\ \forall l\ \in\ L, \forall i\ \in I \quad (19)$$

The model aims to minimize the total setup time required on all the machines during the scheduling horizon as defined in the objective function (1). Constraints (2) assign the jobs once that require only a single processing stage, while Constraints (3) assign each re-entrant jobs $i,\ m_i$ times to the machines. Constraints (4) ensure that assignments to machine l in shift k is possible if machine l can work during shift k; otherwise, assignments are not allowed. Constraints (5) and (6) ensure that dummy starting and ending jobs will be assigned to each machine in every shift. When a re-entrant job is processed, Constraints (7) ensure that it waits at least a shifts before re-entering the system. Constraints (8) impose that the total setup and production time of a machine in each shift should not exceed the total available working time for that machine in that shift. Constraints (9) and

(10) ensure that if a non-dummy job is assigned to a machine in a shift, a job must be scheduled before and after that job, respectively. Constraints (11) prevent any job from being scheduled before the starting job, while Constraints (12) prevent any job from being scheduled after the ending job in each shift on each machine. Similarly, Constraints (13) impose a job to be scheduled after the starting job, and Constraints (14) impose a job to be scheduled before the ending dummy job. Constraints (15) determine the job sequence of each machine at each shift. Constraints (16) ensure that job i is scheduled either before or after job j. Constraints (17), (18) and (19) define the domains of the variables.

Case Study: IPMSP_RJ in Panel Line Production

This study examines the identical parallel machine scheduling problem in the panel production section of a company that specializes in providing semi-finished wood-based panels used in furniture and interior decoration. The company is located in Turkey. The process involves applying coatings to the panels, which include glue and coating materials (bobbins). Product characteristics dictate the need for glue and bobbin changes, depending on order specifics. When transitioning between different product types, a bobbin change is required. Moreover, since the type of glue can vary depending on the product, there may be glue setup process that is more complex and time-consuming than the bobbin change. The glue change process begins with washing and drying the tank, adding new glue, and resuming production. The company knows in advance the setup times required for both bobbin and glue when transitioning between different product types. There are two identical parallel machines with same capabilities operating day and night shift in a day. The company creates a weekly production plan based on incoming orders, scheduling all products to be produced in two shifts each day: a day shift and a night shift, over five days, for a total of 10 shifts. During the day shifts, both machines operate simultaneously. However, on night shifts, only one machine is operating, as the other undergoes a scheduled maintenance in a rotating sequence each night. Certain products require double-sided surface coating. After coating the front side, the products are left in a designated area for one day before the backside can be coated. The production planning department knows the time required to coat each product and calculates the total coating time for each order based on the order quantity.

The aim of the company is to schedule the orders (jobs) in a way that minimizes total setup time. While the setup times required between each job are known in advance, sequencing jobs with lower setup times may seem like a viable solution. However, re-entrant jobs that enter the system the next time at least two shifts later can encounter significantly higher setup times. This highlights the need for precise scheduling in the production line. The lack of planning in sequencing can lead to job delays, increased lead times, and consequently, missed deadlines, ultimately resulting in customer dissatisfaction.

Computational Experiments with the Mathematical Model for IPMSP_RJ

We conduct computational experiments to verify and validate the proposed model developed for IPMSP_RJ. Also with these computational experiments we tested the performance of the proposed model. The company creates a weekly production plan based on incoming orders. For our analysis, we got three distinct weekly production plans from the company, referred to as Case 1, Case 2, and Case 3. These cases contain 74, 88, and 100 jobs, respectively. We used CPLEX to solve each case and obtained the optimal solutions. Moreover, we conducted a sensitivity analysis on the number of the shifts. The company is operating across 10 shifts per week, but we examined the impact of reducing the number of shifts. When we rerun our model with fewer shifts, we found that the same objective function value could be achieved with 8 shifts in all three cases, effectively reducing the whole schedule by one working day. When we tested the model with 7 shifts, we were unable to achieve a feasible solution. Based on these results, we continued our analysis using an 8-shift schedule.

Figure 1 presents the Gantt chart for the schedule obtained by the proposed model in Case 1. The left side of the chart represents Line 1, that operates on both day and night shifts, while the right side shows Line 2, that operates only during day shifts. Each section of the chart shows the job schedule in a single shift. Dark blue segments denote setup times, whereas light blue segments represent production times. In this schedule, all jobs have been allocated within the production plan. Case 1 includes six re-entrant jobs, which require re-processing after at least 2-shift long waiting period. For instance, Job 39, a re-entrant job, is firstly processed on Day 1 in the night shift on Machine 1 and afterwards processed on Day 3 in the day shift on Machine 2. This schedule meets the requirement of a minimum waiting period of two shifts between re-entries. Re-entrant jobs can return to any machine, as both machines are identical in function.

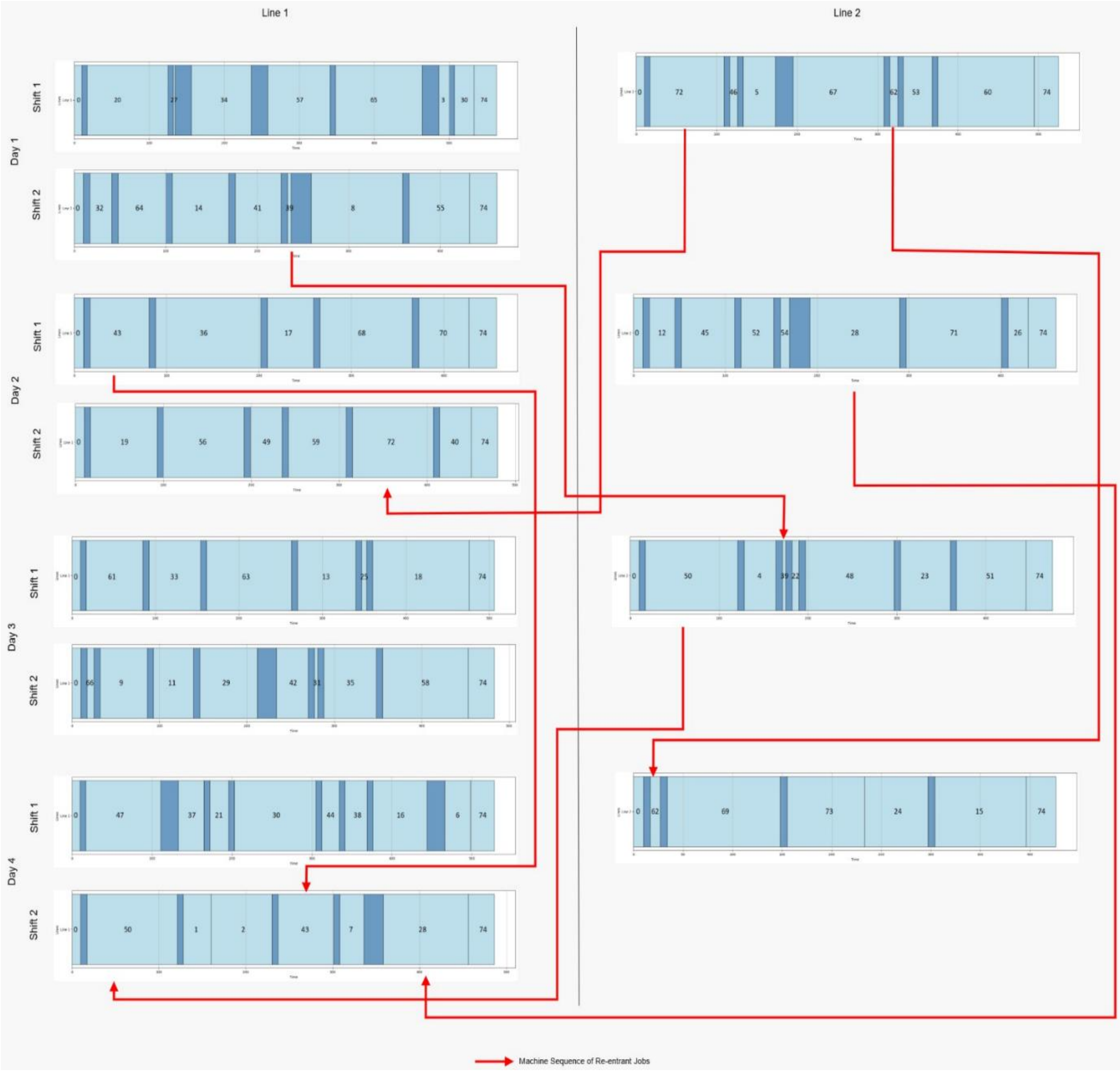

Figure 1. Gannt chart of the schedule obtained by the proposed model in Case 1

Figure 2 shows the percentage of total setup and production times for each case. In case 1, there is a higher proportion of similar jobs, resulting in a setup time percentage of 8%, while case 3 has jobs requiring longer setups, with the setup time percentage reaching 20%. The average setup time across all cases is 14%, resulting an average production time of 86%. This production percentage shows a worthy level of productivity, particularly when compared to the company’s current productivity rates.

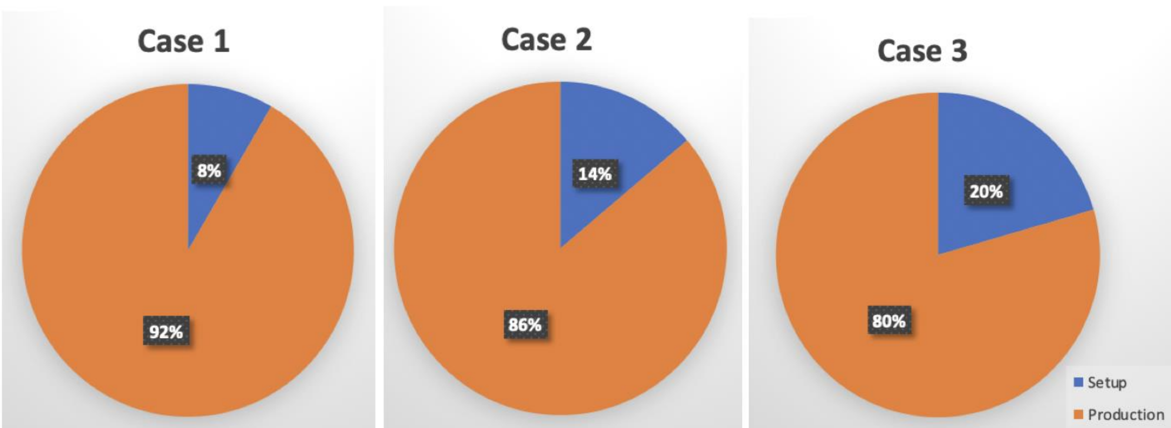

Figure 2. Percentage of setup and production times across three cases

Interface Developed for IPMSP_RJ.

In this study, we present a user-friendly Phyton-based interface developed for solving the proposed model for IPMSP_RJ in panel line production. This interface integrates the proposed model that operates in the background to schedule the jobs. The primary objective of the interface is to enhance accessibility for users, enabling them to input custom datasets and achieve scheduling of the jobs with minimum setup times. The interface design prioritizes usability, offering a step-by-step workflow for users from data input to solution visualization. After successful login, users upload a dataset formatted to system specifications. Once uploaded, the dataset is displayed for verification, enhancing data accuracy and transparency in the scheduling process.

Users define the scheduling duration by specifying the number of shifts in the “Shift Select” section. The “Make a Scheduling” function initiates the scheduling process, after which users can visualize the schedule through a Gantt chart. This chart displays the sequence of products assigned to each shift and production line, providing a clear representation of the production timeline and order distribution. Figure 3 shows an example for the Gantt charts for schedules obtained by the interface developed and Figure 4 gives the details of a Gantt chart. In summary, the interface efficiently guides users through dataset input, scheduling configuration, and solution visualization. This structured approach ensures a seamless experience while facilitating optimal scheduling in complex production environments.

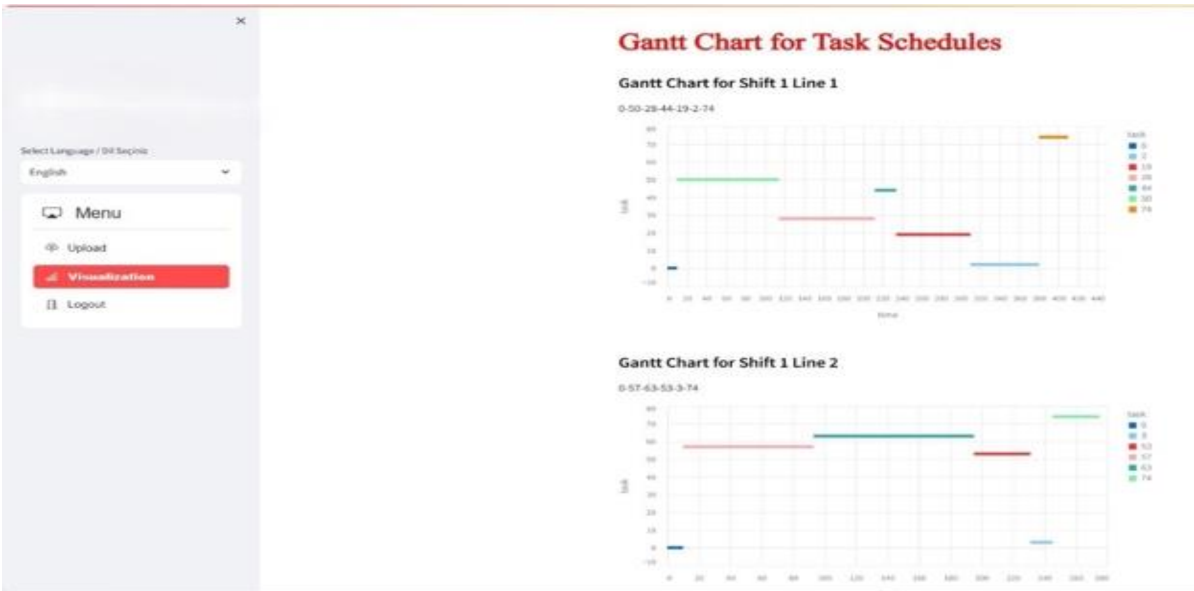

Figure 3. Gantt charts presented by the interface

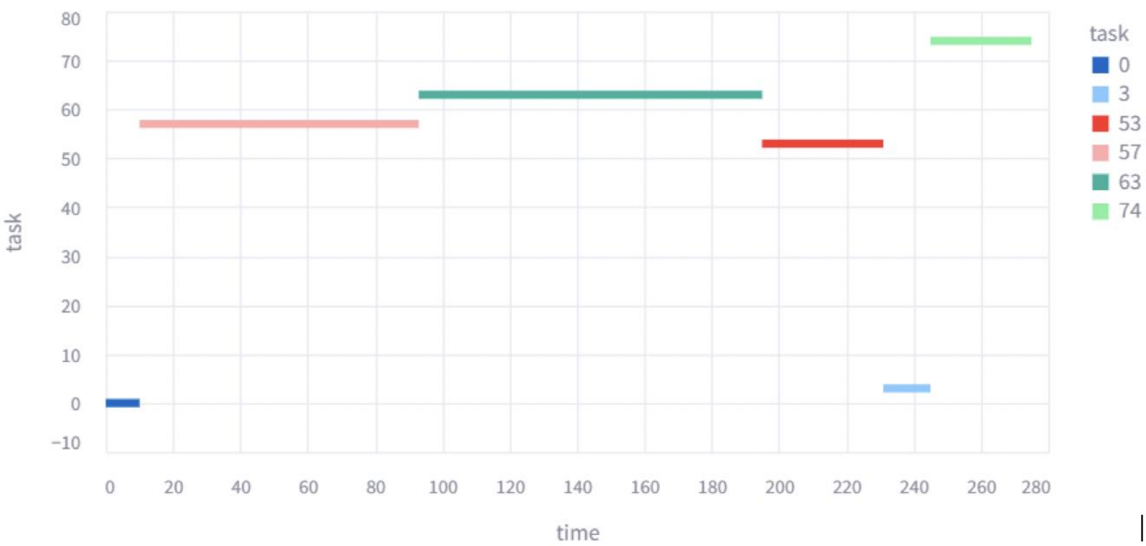

Figure 4. Details of a gantt chart presented by the interface

Concluding Remarks and Future Research Directions

This study addresses IPMSP_RJ, an identical parallel machine scheduling problem with re-entrant jobs that re-enter the system after a designated waiting period with the objective of minimizing the total setup time in the scheduling horizon. Minimizing setup time guarantees the production efficiency. In today's industrial environment, production efficiency is critical for companies to remain competitive.

An integer programming model is developed for IPMSP_RJ. This model takes into account re-entrant job requirements and deterministic machine unavailability, that is a realistic feature often seen in industrial settings. The model was tested on three distinct cases from the production facility, with the number of jobs 74, 88, and 100 respectively. We use CPLEX to obtain optimal solutions. When we investigate the solutions, we validated that the model represents the problem accurately, satisfying all specified requirements. To further understand the impact of number of shifts, a sensitivity analysis was conducted on it. While the company typically schedules over 10 shifts per week, we observe that same production outcomes can be achieved with only 8 shifts. This results in savings of one working day per week, improving resource utilization. Moreover, we developed a Python-based user interface to make the proposed scheduling model usable to production planners in the company. This interface allows users to input datasets, decide number of shifts, and visualize the optimal schedules via Gantt charts. The interface is designed to provide a valuable tool for the production planning personnel to generate production schedules without extensive technical knowledge of scheduling models.

In conclusion, by incorporating re-entrant job requirements and machine unavailability constraints into a parallel machine scheduling model, this study addresses an important gap in the literature. There is also a case study from real life showing the applicability of the proposed mathematical model. The analysis shows the potential for increased efficiency in complex production scheduling problems and provide a framework for further research on re-entrant scheduling problems. Future studies could extend this model by exploring stochastic machine availability, considering different objectives, e.g., minimizing makespan or/and number of shifts or integrating additional constraints based on more different industrial settings.

Scientific Ethics Declaration

The authors declare that the scientific ethical and legal responsibility of this article published in EPSTEM Journal belongs to the authors.

Acknowledgements or Notes

This article was presented as an poster presentation at the International Conference on Technology, Engineering and Science (www.icontes.net) held in Antalya/Turkey on November 14-17, 2024.

References

Belkaid, F., Yalaoui, F., & Sari, Z. (2016). An efficient approach for the reentrant parallel machines scheduling problem under consumable resources constraints. *International Journal of Information Systems and Supply Chain Management*, *9*(3), 1–25.

Chakhlevitch, K., & Glass, C. A. (2009). Scheduling reentrant jobs on parallel machines with a remote server. *Computers & Operations Research*, *36*(9), 2580–2589.

Chamnanlor, C., Sethanan, K., Gen, M., & Chien, C.-F. (2017). Embedding ant system in genetic algorithm for re-entrant hybrid flow shop scheduling problems with time window constraints. *Journal of Intelligent Manufacturing*, *28*(8), 1915–1931.

Chen, J. S., & Pan, C. H. J. (2006). Integer programming models for the re-entrant shop scheduling problems. *Engineering Optimization*, *38*(5), 577–592.

Chen, J. S., Pan, J. C.H., & Lin, C. M. (2008). A hybrid genetic algorithm for there-entrant flow-shop scheduling problem. *Expert Systems with Applications*, *34*(1), 570–577.

Choi, S.-W., & Kim, Y.-D. (2007). Minimizing makespan on a two-machine re-entrant flowshop. *Journal of the Operational Research Society*, *58*(7), 972–981.

Choi, S.-W., & Kim, Y.-D. (2008). Minimizing makespan on an -machine re-entrant flowshop. *Computers & Operations Research*, *35*(5), 1684–1696.

Danping, L., & Lee, C. K. M. (2011). A review of the research methodology for the re-entrant scheduling problem. *International Journal of Production Research*, *49*(8), 2221–2242.

Johnson, S. M. (1954). Optimal two- and three-stage production schedules with setup times included. *Naval Research Logistics Quarterly*, *1*(1), 61–68.

Low, C., Wu, T.-H., & Hsu, C.M. (2005). Mathematical modelling of multi-objective job shop scheduling with dependent setups and re-entrant operations. *The International Journal of Advanced Manufacturing Technology*, *27*(1–2), 181–189.

Mason, S. J., Fowler, J. W., & Matthew Carlyle, W. (2002). A modified shifting bottleneck heuristic for minimizing total weighted tardiness in complex job shops. *Journal of Scheduling*, *5*(3), 247–262.

Sun, J. U. (2009). A genetic algorithm for a re-entrant job-shop scheduling problem with sequence-dependent setup times. *Engineering Optimization*, *41*(6), 505–520.

Wang, K., Qin, H., Huang, Y., Luo, M., & Zhou, L. (2021). Surgery scheduling in outpatient procedure centre with re-entrant patient flow and fuzzy service times. *Omega*, *102*, 102350.

Wang, M. Y., Sethi, S. P., & van de Velde, S. L. (1997). Minimizing makespan in a class of reentrant shops. *Operations Research*, *45*(5), 702–712.

Zoghby, J., Wesley Barnes, J., & Hasenbein, J. J. (2005). Modeling the reentrant job shop scheduling problem with setups for metaheuristic searches. *European Journal of Operational Research*, *167*(2), 336–348.

Author Information

Betul Kayısoglu
Abdullah Gul University, Kayseri, Türkiye
Email: betul.kayisoglu@agu.edu.tr

Seyma Bekli
Abdullah Gul University, Kayseri, Türkiye

Ayse Sena Sahin
Abdullah Gul University, Kayseri, Türkiye

Gamze Gul Akyurek
Abdullah Gul University, Kayseri, Türkiye

Ruveyda Aydınlı
Abdullah Gul University, Kayseri, Türkiye

Sevda Nur Copur
Abdullah Gul University, Kayseri, Türkiye

Tugba Ekinci
Abdullah Gul University, Kayseri, Türkiye

To cite this article:

Kayısoglu, B., Bekli, S., Sahin, A. S., Akyurek, G. G., Aydınlı, R., Copur, S. N., & Ekinci, T. (2024). Parallel machine scheduling with re-entrant jobs with consideration of set up times. *The Eurasia Proceedings of Science, Technology, Engineering & Mathematics (EPSTEM), 32,* 311-319.

The Eurasia Proceedings of Science, Technology, Engineering & Mathematics (EPSTEM)
ISSN: 2602-3199

The Eurasia Proceedings of Science, Technology, Engineering & Mathematics (EPSTEM), 2024

Volume 32, Pages 320-328

IConTES 2024: International Conference on Technology, Engineering and Science

Generalized Predictive Control of Multi-Phase Induction Machine Supplied by Multi-Level Inverter

Bessaad Taieb
Hassiba Benbouali University

Khelifa Khelifi-Otmane
Blida University

Sahraoui Hamza
Hassiba Benbouali University

Lekhal Djamel
University of Science and Technology of Oran Mohamed Boudiaf

Abstract: With more than three phases, multi-phase induction machines provide an alluring substitute for lowering the strains placed on the machine's switches and windings. The management of overly produced current is one of the most important issues when making quick and significant adjustments to the speed control of a multi-phase induction motor. Thus, if the speed controller lacks an output amplitude limitation, it may cause harm to both the motor and the power electronics converter. The speed control loop and the two internal current control loops are the first two areas in which this research suggests using polynomial predictive controllers to solve the saturation phenomena of the speed regulator. Then, by convexly optimizing the Youla parameter while accounting for time and frequency constraints, the external predictive speed controller is readjusted. This ensures that the speed response to the reference stays in an imposed model with minimal current control during transient periods, while also preserving the closed-loop functionalities that the initial predictive controller had achieved. The results of the simulation demonstrate how well the suggested control system controls speed under different multi-phase induction machine operating situations.

Keywords: Five-phase, Induction motor, Vector control, Generalized predictive control, Multi-level inverter.

Introduction

In some applications, multiphase drives have emerged as a viable substitute for their three-phase counterparts because of their inherent benefits, which include fault tolerance and the ability to divide power among more than three phases (Guo, 2021). These benefits are especially intriguing for propulsion and safety-critical applications all-electric ship propulsion (Yin, 2013). Electrical and hybrid vehicles (Kumar,2020; Gang, 2019). And more-electric aircraft (Guo, 2021). Where the rotating field in the three-phase machine cannot be maintained if one of the phases is lost. When one or more phases are lost, on the other hand, multiphase drives can still function with the rotating field. This is because a multiphase machine always needs just two degrees of freedom to produce a spinning field, regardless of the actual number of stator phases. Therefore, even with some derating, post-fault operation with a rotating field is feasible. Additionally, in some of the previously described applications, the low inverter DC link voltage supplied by batteries necessitates large phase current needs; thus, multiphase drives are particularly appropriate since they reduce the current per phase for the specified power (Liu, 2020).

The five-phase machine is among the most intriguing multiphase devices for these uses (Yin, 2013). There are two distinct five-phase electrical machine architectures in the literature. A sinusoidal MMF distribution serves as the foundation for the first one. Because this multiphase drive only needs sinusoidal voltages, low order harmonics in the machine's input voltage are undesired. The stator windings in the second one are concentrated. In this instance, stator current low-order harmonic injection can be used to increase torque generation. This is especially true for the third harmonic, while evaluating reference voltage vectors places a heavy computational load on the real-time processing system (Qu, 2023). Although a five-phase machine with sinusoidal MMF distribution is used in this study as an example of a multiphase drive, the findings may be applied to a five-phase machine with concentrated windings.

Multiphase drives with high performance applications need particular control systems. Field Oriented Control (FOC) is the most widely used control structure. It is a cascaded method that has an outer speed control loop and an inner current control loop (Yin, 2013). A two-level multiphase voltage source inverter (MVSI) is usually controlled by switching signals produced by the inner control loop. A suitable carrier-based or space vector pulse width modulation approach (CPWM or SVPWM, respectively) is used to regulate the MVSI. Although CPWM techniques are easier to use, SVPWM provides a deeper understanding of the characteristics of multiphase drives and inverters.

An alternative to cascade PI control of electrical drives is Model Predictive Control (MPC), which is an optimization-based approach that computes the next control action by minimizing difference between the predicted output of a system and the specified reference. Many MPC design algorithms are available and, in general terms, can be categorized as: (i) transfer-function based, such as Generalized Predictive Control (GPC) (Clarke et al., 1987). (ii) step response model based, such as Dynamic Matrix Control (DMC) (Cutler & Ramaker, 1979). And (iii) state-space model based (Kerrigan, 2002).

Generalized Predictive Control (GPC)

Generalized predictive control (GPC) is one of the most popular predictive control algorithms developed by Clarke in 1987 (Ling, 2023; Feng, 2010). GPC retains the design flexibility and performance of GMV/PP technique. It also caters for offsets (since it uses integrated controlled auto regressive moving average (CARIMA) model), feed-forward signals, and multivariable plant without detailed prior knowledge of structural indices. The main difference between GPC and DMC is the model used to describe the plant and the formulation of the dynamic matrix. For satisfying the control objectives, it makes the use of a CARIMA model and various horizons. This model is more appropriate in industrial applications where disturbances are non-stationary. A CARIMA model is used to obtain good output predictions and optimize a sequence of future control signals to minimize a multistage cost function defined over a prediction horizon. The inclusion of disturbance is necessary to deduce the correct controller structure.

$$A(z^{-1})y(t) = B(z^{-1})u(t-1) + C(z^{-1})\,{}^{e(t)}\!/_{\Delta(z^{-1})} \tag{1}$$

In both cases (speed loop or current loops), the GPC control strategy uses for the prediction the CARIMA model (controlled autoregressive integrated moving average)

Whre *u(t-1)* is the control, *y(t)* is the process output, *e(t)* is the zero mean white noise, $\Delta(z^{-1}) = 1 - z^{-1}$, *A* and *B* are polynome in backward shift operator z^{-1} derived from (5). The predictive outputin the *j*-th prediction step over the costing horizons $N_1 \leq j \leq N_2$ is done by:

$$\underbrace{y(t+j) = F_j(z^{-1})y(t) + H_j(z^{-1})\Delta u(t-1)}_{Free\ response} \quad \underbrace{+\, G_j(z^{-1})\Delta u(t+j-1) + J_j(z^{-1})e(t+j)}_{Forced\ response} \tag{2}$$

F_j , G_j , H_j are polynomilas determined from soling intertively Diophantine equation. The GPC control law is obtained by minimizing the cost function given by:

To generate a set of predicted outputs $\hat{y}(t+j/t)$, the prediction model equation (2) is used. The value of $\hat{y}(t+j/t)$ for $j>t$ depent on future control signals $u(t+j)$. These control signals are used to achieve the objective in GPC by minimizing the cost function given as:

$$J(N_1,N_2,N_u)=\sum_{j=N_1}^{N_2}\delta(j)[\hat{y}(t+j/t)-w(t+j)]^2+\lambda\sum_{j=1}^{N_u}\lambda(j)[\Delta u(t+j-1)]^2 \quad (3)$$

$$\Delta u(t+1) = 0 \text{ for } j \geq N_u$$

GPC depends on the integration of assumption of a CARIMA plant model, use of LRPC, recursion of Diophantine equation, consideration of weighting of control increments in cost function and the choice of a control horizon (Nail, 2015; Clarke, 1987). GPC is applicable to non-minimum phase, open loop unstable and having variable dead time. It is capable of considering both constant and varying future set points. It is unaffected (unlike pole-placement strategies) if the plant model is over parameterized.

However, GPC has limitations with minimum phase processes for some of the most obvious choices of its design parameters (Duan, 1991). GPC shows better performance in cement mill, a spray-drying tower and compliant robot arms.

Mathematical Model for Five-Phase Induction Motor

The electric equation of a five-phase an asynchronous machine in the natural base is given by the following expression for each phase:

$$\begin{cases}[V_s]=[R_s].[I_s]+\dfrac{d[\phi_s]}{dt}\\[V_r]=[R_r].[I_r]+\dfrac{d[\phi_r]}{dt}\end{cases} \quad (4)$$

Where

$$[V_s] = [v_{sa}\ v_{sb}\ v_{sc}\ v_{sd}\ v_{se}];\ [I_s] = [i_{sa}\ i_{sb}\ i_{sc}\ i_{sd}\ i_{se}]\quad;\ [V_r] = [v_{ra}\ v_{rb}\ v_{rc}];\ [I_r] = [i_{ra}\ i_{rb}\ i_{rc}];$$

$$R_s = R_{sa} = R_{sb} = R_{sc} = R_{sd} = R_{se}\quad;\ R_r = R_{ra} = R_{rb} = R_{rc};$$

$$[\phi_s]=[\phi_{sa}\ \phi_{sb}\ \phi_{sc}\ \phi_{sd}\ \phi_{se}]\ ;\ [\phi_r]=[\phi_{ra}\ \phi_{rb}\ \phi_{rc}]$$

The model of five-phase an asynchronous machine is as follows after converting Phase variables into *d-q* variables:

$$\begin{cases}V_{sd}=[R_s].i_{sd}-\omega_s\phi_{sq}+\dfrac{d\phi_{sd}}{dt}\\V_{sq}=[R_s].i_{sq}+\omega_s\phi_{sd}+\dfrac{d\phi_{sq}}{dt}\\V_{rd}=[R_r].i_{rd}-(\omega_s-\omega_r)\phi_{rq}+\dfrac{d\phi_{rd}}{dt}\\V_{rq}=[R_r].i_{rq}+(\omega_s-\omega_r)\phi_{rd}+\dfrac{d\phi_{rq}}{dt}\end{cases} \quad (5)$$

The electromagnetic torque for asynchrounous machine is equal to:

$$T_e=\frac{5}{2}pL_m(\phi_{rd}.i_{sq}-\phi_{rq}.i_{sd}) \quad (6)$$

On the other hand, the mechanichal equation of the machine is:

$$J\frac{d\Omega_r}{dt} = T_e - T_r - f_m.\Omega_r \tag{7}$$

This set of equations allows characterizing the electromechanical behaviour of a five-phase PMSM machine.

Indirect Vector Control for Five-Phase Asynchronous Motor Drive

Vector control technique aims to make equivalence between the five-phase asynchronous motor drive and DC motor. This objective can be achieved by controlling the q-axis flux component to zero. Stator flux and rotor flux orientation are examples of field oriented control techniques for an asynchronous machine. The stator current space vector for an asynchronous machine has two components i_{sd} and i_{sq}.

The i_{ds} produces the rotor flux component and i_{qs} produces the torque-producing component in rotor flux orientation. The rotary flow direction control model is given by the following equation:

$$\begin{cases} i_{rq} = 0 \\ i_{rd}^* = \phi \end{cases} \tag{8}$$

The simplified model of the machine as follows:

$$\begin{cases} \sigma L_s \dfrac{di_{sd}}{dt} = -\left(R_s + \dfrac{L_m^2}{L_r^2}R_r\right)i_{sd} + \sigma L_s \omega_s i_{sq+} \dfrac{L_m}{L_r.T_r}\phi_r + V_{sd} \\ \sigma L_s \dfrac{di_{sq}}{dt} = -\left(R_s + \dfrac{L_m^2}{L_r^2}R_r\right)i_{sq} - \sigma L_s \omega_s i_{sd} - \dfrac{L_m}{L_r.T_r}\omega_r\phi_r + V_{sq} \\ \dfrac{d\phi_r}{dt} = \dfrac{L_m}{T_r}i_{sd} - \dfrac{1}{T_r}\phi_r \\ T_e = p\dfrac{L_m}{T_r}\phi_r i_{sq} \\ \omega_r = \dfrac{M}{T_r}.\dfrac{1}{\phi_r}.i_{sq} \\ J\dfrac{d\Omega_r}{dt} = T_e - L_r - f\Omega_r \end{cases} \tag{9}$$

With $T_s = L_s / R_s$: stator time constant ; $T_r = L_r / R_r$: rotor time constant ; σ = 1- $\dfrac{L_m^2}{L_r.L_s}$: Total leakage coefficient.

Dynamic Model of Flux and Torque

The rotor flux and the electromagnetic torque can be estimated from the currents i_{sd} and i_{sq} , stator quantities accessible from the measurement of real currents stator subject to the realization of the Park transformation.

$$\begin{cases} \hat{\phi}_r + T_r\dfrac{d}{dt}\hat{\phi}_r = L_m i_{sd} \\ \hat{T}_e = p\dfrac{L_m}{T_r}\hat{\phi}_r i_{sq} \\ \hat{\omega}_s - \omega_r = \dfrac{L_m}{T_r}.\dfrac{1}{\hat{\phi}_r}.i_{sq} \\ \hat{\theta}_s = \int \hat{\omega}_s dt \end{cases} \Rightarrow \begin{cases} \hat{\phi}_r = \dfrac{L_m}{1+T_r}i_{sd} \\ \hat{T}_e = p\dfrac{L_m}{T_r}\hat{\phi}_r i_{sq} \\ \hat{\omega}_s - \omega_r = \dfrac{L_m}{T_r}.\dfrac{1}{\hat{\phi}_r}.i_{sq} \\ \hat{\theta}_s = \int (p\Omega_r \dfrac{L_m}{T_r}.\dfrac{1}{\hat{\phi}_r}.i_{sq})dt \end{cases} \tag{10}$$

Decoupling by Compensation

The decoupling principle amounts to defining two new control variables v_{sd1} and v_{sq1} such as v_{sd1} only acts on i_{sd} and v_{sq1} on i_{sq}.

So, we can write the voltages v_{sd} and v_{sq} as a function of v_{sd1} and v_{sq1} as follows:

$$\begin{cases} v_{sd} = v_{sd1} - e_1 \\ v_{sq} = v_{sq1} - e_2 \end{cases} \tag{11}$$

With:

$$\begin{cases} e_1 = \sigma L_s \omega_s i_{sq} + \dfrac{L_m R_r}{L_r^2} \phi_r \\ e_2 = -\sigma L_s \omega_s i_{sd} - \dfrac{L_m}{L_r} \omega_s \phi_r \end{cases} \tag{12}$$

Defluxing

The defluxing block are written as follows

$$\phi_r^* = \begin{cases} \phi_{rn} & if \quad \Omega_r < \Omega_{rn} \\ \dfrac{\phi_{rn} \Omega_{rn}}{\Omega_r} & if \quad \Omega_r > \Omega_{rn} \end{cases} \tag{13}$$

A system illustration of the vector control of five-phase an asynchronous motor is given in figure 1.

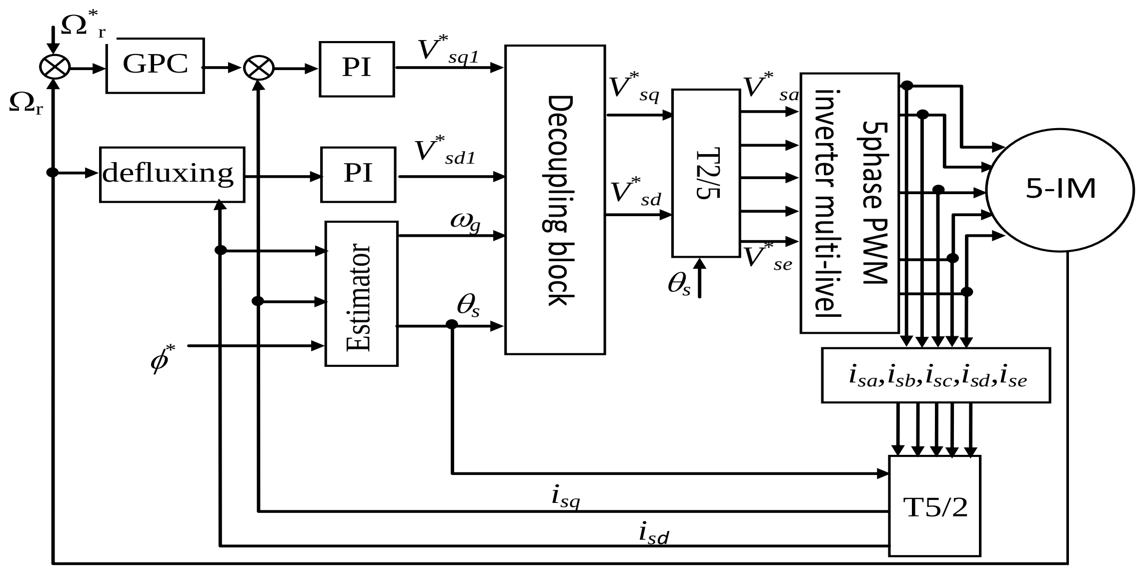

Figure 1. Vector control for a five-phase an asynchronous machine.

Results and Discussion

The simulations have been performed in a MATLAB envi-ronment writing the differential equations for the evolution of the five induction motor and load. Figures 2 and 3 illustrate respectively the rotor speed, rotor flux magnitude, components currents (i_{ds},i_{qs}), Flux and the real stator current i_{as} control by PI regulator. To illustrate the performance of the predictive control applied to the speed control, the five induction motor was simulated with a reference speed of 157 rad/s vacuum and then applying a nominal load of 10 N.m at t = 1s (Figure 4).

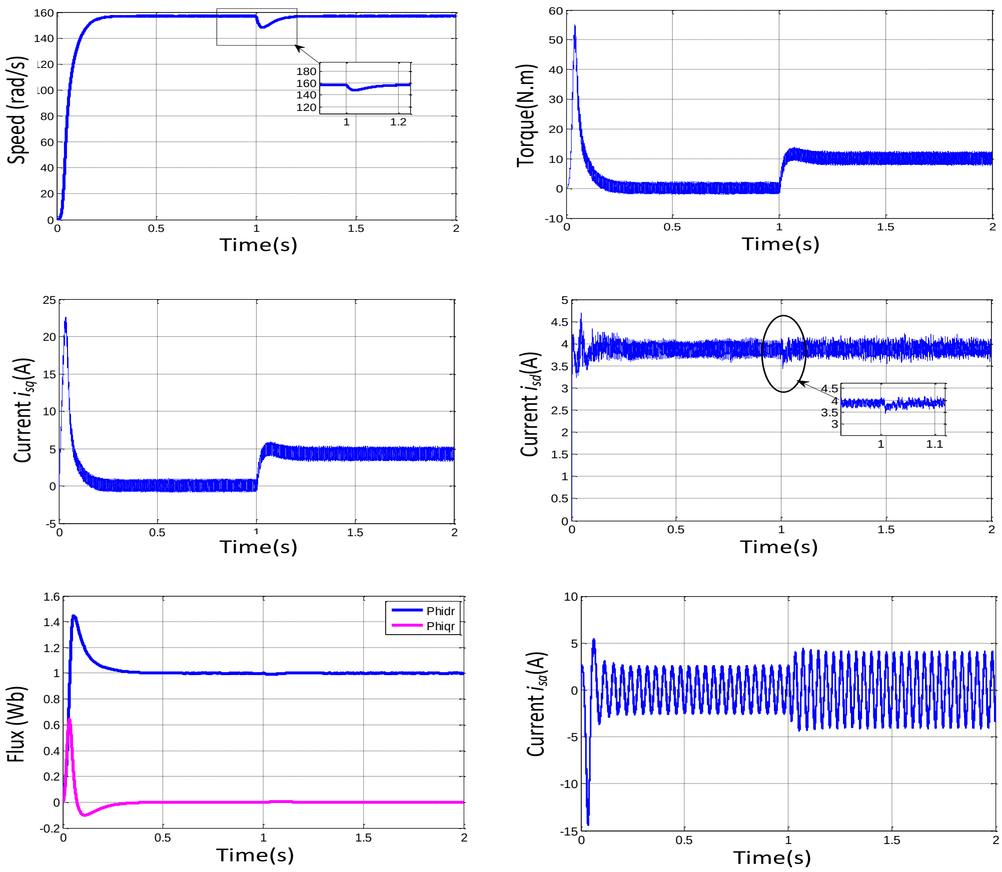

Figure 2. Indirect vector control performance of the five-phase IM with PI regulators.

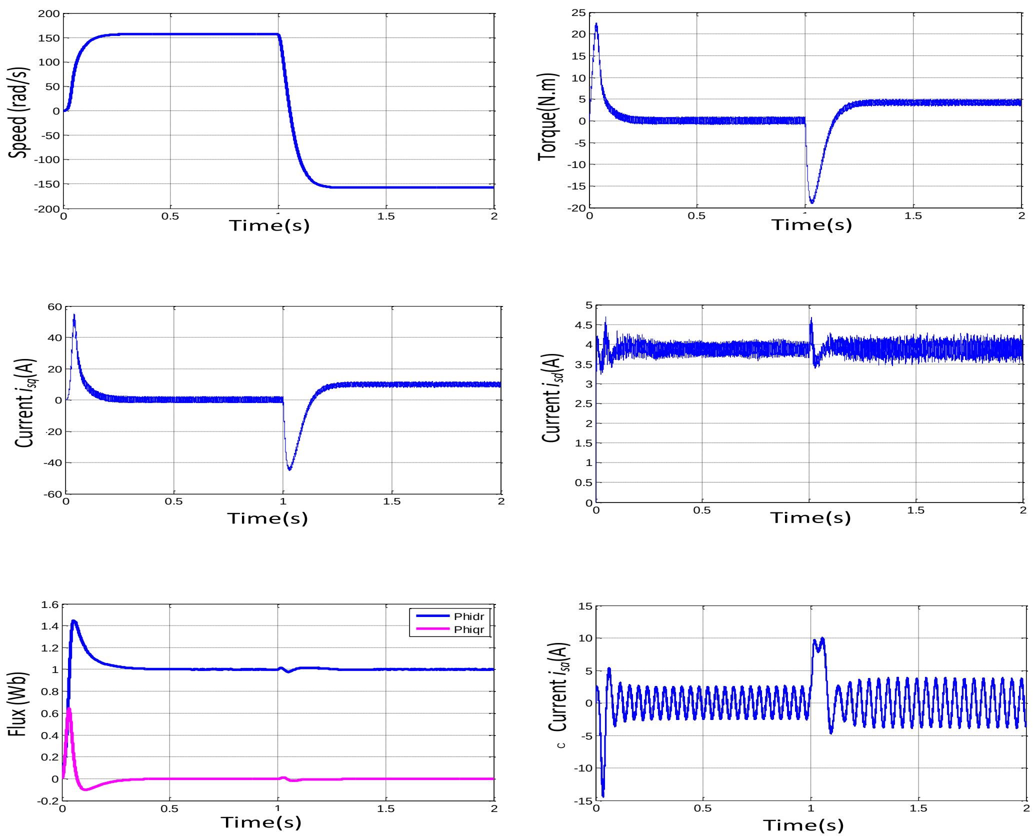

Figure 3. Indirect vector control performance of the five-phase IM with PI regulators in speed reversal

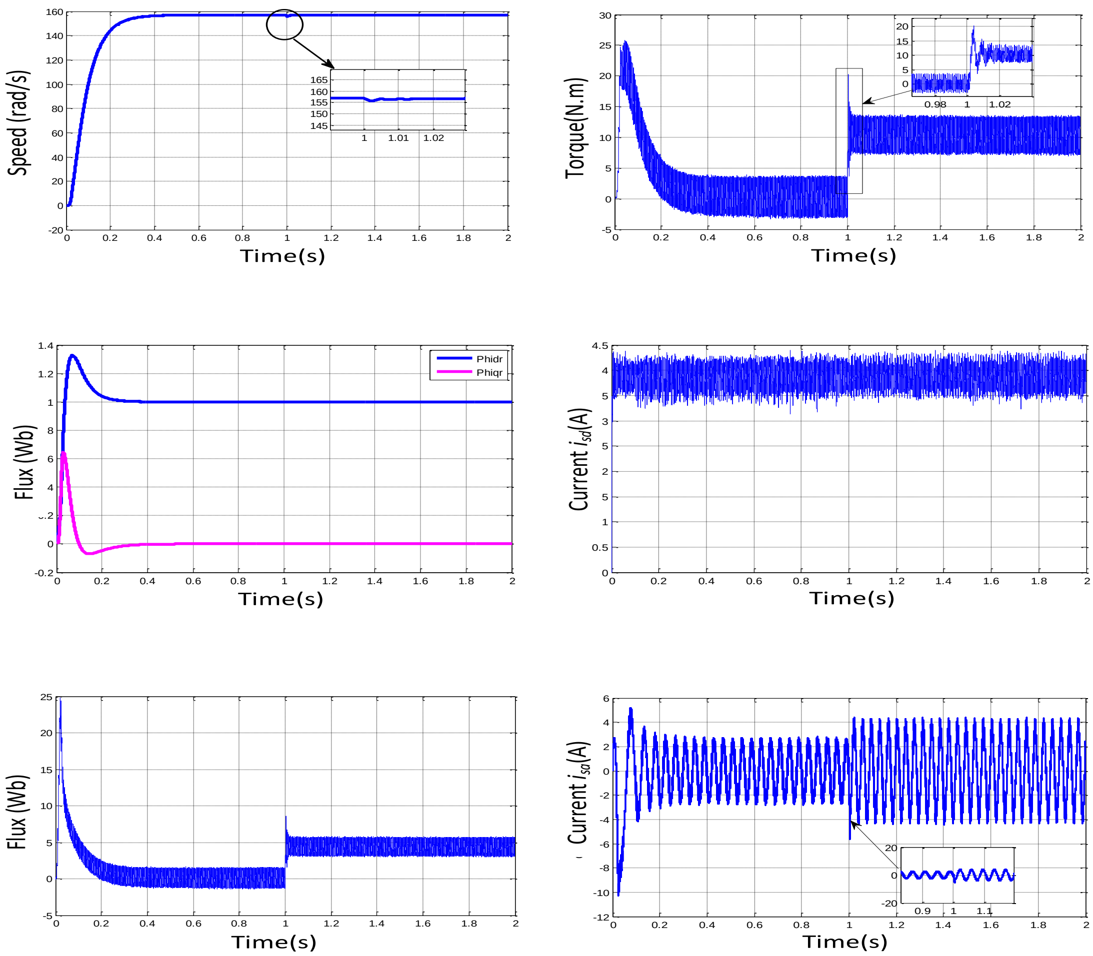

Figure 4. Indirect vector control performance of the five-phase IM with GPC regulators

System Robustness

Variation of Rotor Inertia J=200% Jn

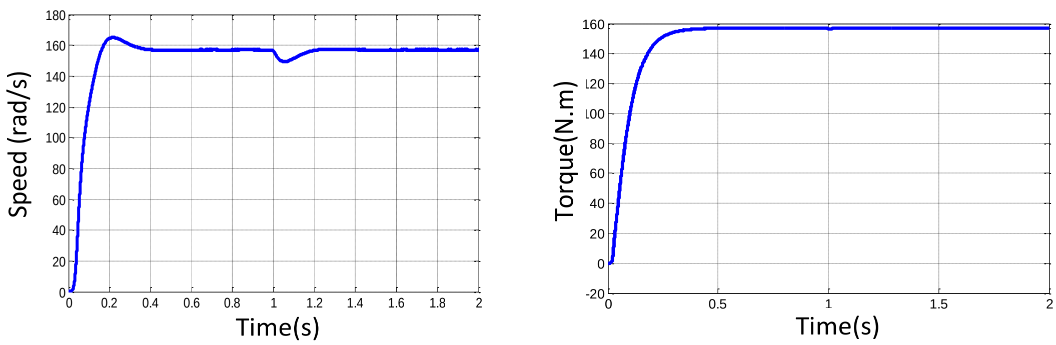

a) b)

Figure 5. Comparison between GPC and PI conventional - a) PI, b) GPC -

Figs. 5, the five-phase an asynchronous IM driver controlled by predictive control and conventional PI of the system under variation of the load and inertial moment (200% J_n). At the bottom of the Fig.5, it shows that with GPC, the process is less disturbed by an external disturbance than by compared to the conventional control (PI). In addition, it is noted that the GPC provides means to better control the transient error due to external disturbance. Finally, the speed response is without overshoot, without static error and with very fast disturbance rejection. Despite internal and external disturbances, the predictive control maintains the desired performance.

Conclusion

A novel approach to preventing five-phase induction motor speed controller saturation during transient periods which are brought on by rapid and significant step changes in the speed reference has been proposed in this study. The machine was then driven using the GPC approach in polynomial form, with an outer machine to regulate speed and two inner ones to regulate currents. The Youla parameterization has been used to fine-tune the outer GPC speed controller in the next stage. The resultant controller has two benefits and maintains the same RST form. In the transient regime without saturation, it may first decrease the current command. Secondly, it maintains the system's temporal response from before the alteration without altering the behavior of disturbance rejection. Simulations support these findings. Predictive control's effectiveness has been evaluated. The simulation's findings demonstrate how resilient GPC is to disruptions brought on by changes in the load and moment of inertia. Despite the disruptions, the speed response accurately adheres to the selected reference model.

Induction Motor Data

Rated power P_n= 3kW, nominal currant I_n= 3.6/6.2A, stator resistance R_s= 2.5Ω, rotor resistance R_r=1.9Ω, stator inductance L_s= 0.24H, rotor inductance L_r= 0.24H, mutual inductance L_m= 0.226H, rated phase stator voltage V_n = 380V, pole pair number P=2, rotor speed N = 1499tr/min, viscous friction coefficient K_f= 0.0006Nms/rad, Rotor inertia J= 0.031kg.m2.

Scientific Ethics Declaration

The authors declare that the scientific ethical and legal responsibility of this article published in EPSTEM Journal belongs to the authors.

Acknowledgements or Notes

* This article was presented as an oral he International Conference on Technology, Engineering and Science (www.icontes.net) held in Antalya/Turkey on November 14-17, 2024.

References

Clarke, D.W., Mohtadi, C., & Tuffs, P.S. (1987). Generalized predictive control—part ıı. extensions and ınterpretations. *Automatica*, *23*, 149-160.

Clarke, D.W., Mohtadi, C., & Tuffs, P. S. (1987). Generalized predictive control -part ı. *The Basic Algorithm. Automatica*, *23*(2), 137-148.

Clarke, D.W.. (1987). Generalized predictive control: a robust self-tuning algorithm. *American Control Conference*, *10*(12), 990-995.

Du, F., & Du, W. (2009). Wireless networked control systems with generalized predictive control and novel smith predictor. *2009 IITA International Conference on Control, Automation and Systems Engineering (case 2009)*, 640-643.

Du, F., Du, W., Du, Y., & Chen, B. (2010, May). Wireless networked control systems with GPC and new Smith predictor. *2010 Chinese Control and Decision Conference* (pp. 1920-1924). IEEE.

Duan, J., & Grimble, M. (1991, November). Design of long-range predictive control algorithms for industrial applications. In *IEE Colloquium on industrial applications of model based predictive control* (pp. 1-5).

Gang, Y., Yichang, G., Lidan, Z., Dongdong, L., & Xing, L. (2019). Multi-phase permanent magnet synchronous generator variable speed constant frequency offshore wind system based on modular multilevel converter. *2019 Innovative Smart Grid Technologies - Asia (ISGT Asia)*, 2127-2132.

Guo, R., Zhang, L., & Yang, Z. (2021). Multiphase ımage segmentation model based on clustering algorithm. *IEEE Asia-Pacific Conference on Image Processing, Electronics and Computers (IPEC)*, 1236-1239.

Kennel, R., Linder, A., & Linke, M. (2001). Generalized predictive control (GPC)-ready for use in drive applications? *32nd Annual Power Electronics Specialists conference (IEEE Cat. No. 01CH37230)*, *4*, 1839-1844.

Kerrigan, E. C., & Maciejowski, J. M. (2002, September). Designing model predictive controllers with prioritised constraints and objectives. In *Proceedings. IEEE International Symposium on Computer Aided Control System Design* (pp.33-38). IEEE.

Kumar, R. R., Saxena, A., Kumari, A., & Srivastava, R. K. (2020). Design and thermal ınvestigation of a dual rotor de-coupled stator multi-phase permanent magnet synchronous generator for wind power application. *2020 IEEE International Conference on Power Electronics, Drives and Energy Systems (PEDES)*, 1-6.

Ling, L., Huang, S. D. G., Cao, Z., and Qiu, H. (2023). Comparison analysis on control-ıncrement-based and control-quantity-based predictive controls of permanent magnet synchronous motors. *2023 IEEE International Conference on Predictive Control of Electrical Drives and Power Electronics (PRECEDE)*, , 1-6.

Liu, D., Song, X., Deng, F., & Dong, J. (2020). Investigation ınto multi-phase armature windings for high-temperature superconducting wind turbine generators. *IEEE Transactions on Applied Superconductivity*, *30* (4), 1-5, 5201005.

Nail, B., Bekhiti, B., Bdirina, K., Kouzou, A. and Hafaifa, A. (2015). Sliding mode control and optimal GPC algorithm for coupled tanks. *2015 3rd International Conference on Control, Engineering & Information Technology (CEIT)*, 1-6.

Ogunnaike, B. A., & Adewale, K. E. P. (1986). Dynamic matrix control for process systems with time varying parameters. *Chemical Engineering Communications*, *47*(4-6), 295-314.

Qu, Q., Zhang, Y., and Shi, Y. (2023). An ımproved power compensation based-on model-free predictive power control of vienna rectifiers under distorted power grid. *2023 IEEE International Conference on Predictive Control of Electrical Drives and Power Electronics (PRECEDE)*, 1-6.

Yin, S., and Shi, G. (2013). The design and implementation for oil-gas-water multiphase pipeline test system. *Proceedings of 2013 2nd International Conference on Measurement, Information and Control*, 98-102.

Author Information

Bessaad Taieb
Hassiba Benbouali University of Chlef
Hssania Chlef, Algeria
Contact e-mail: *t.bessaad@univ-chlef.dz*

Khelifa Khelifi Otmane
Department of Automatic and Electrotechnic, Blida University 1, Algeria

Sahraoui Hamza
Hassiba Benbouali University of Chlef
Hssania Chlef, Algeria

Lekhal Djamel
University of Science and Technology of Oran Mohamed Boudiaf, BP1505 El Mnaouer, Oran 31000, Alger

To cite this article:

Taieb, B., Khelifi Otmane, K., Hamza, S., & Djamel, L., (2024). Generalized predictive control of multi-phase induction machine supplied by multi-level inverter. *The Eurasia Proceedings of Science, Technology, Engineering & Mathematics (EPSTEM), 32,* 320-328.

The Eurasia Proceedings of Science, Technology, Engineering & Mathematics (EPSTEM)
ISSN: 2602-3199

The Eurasia Proceedings of Science, Technology, Engineering & Mathematics (EPSTEM), 2024

Volume 32, Pages 329-335

IConTES 2024: International Conference on Technology, Engineering and Science

Performance Evaluation of a Self-Compacting Mortar Altered with Dune Sand

Nacim Khelil
University Mouloud Mammeri of Tizi Ouzou

Said Boukais
University Mouloud Mammeri of Tizi Ouzou

Randa Makkeb
University Mouloud Mammeri of Tizi Ouzou

Karim Akkouche
University Mouloud Mammeri of Tizi Ouzou

Amar Kahil
University Mouloud Mammeri of Tizi Ouzou

Abstract: In this paper, a laboratory-performed study relating to the evaluation of a self-compacting mortar (SCM) made initially from crushed quarry aggregates and modified by the addition of fine dune sand (DS) is presented. The aim was to show the modification of the rheological, acoustic, and mechanical properties of the SCM brought about by this very fine aggregate, whose use is deemed to be unsuitable for the production of cementitious materials. Though, its valorization could save the overexploited natural resource that is crushed quarry sand (CS). For this purpose, different mortar mixtures made with DS rates of 0%, 25%, 50%, 75%, and 100% by volume of CS were prepared, and subjected to mini-cone flow, ultrasonic pulse velocity (UPV), and destructive compressive and flexural tensile strength tests. The results showed the improvement of several of the parameters studied after the addition of DS, as well as the possibility of using DS in the design of such kinds of mortars even at very high substitution rates. The study also concludes that DS could serve as a viable alternative to CS, in the sense that it could allow to manage in a more sustainable way the otherwise depleting and overexploited supply of quarry sand.

Keywords: Self-compacting mortar, Dune sand, Crushed sand, Ultrasonic pulse velocity, Sustainability

Introduction

Self-compacting mortar (SCM) is a specifically engineered type of mortar that has the ability to flow and consolidate in a confined volume without the need for any type of settlement aid. This remarkable property is a result of its high flowability (Turk et al., 2022; Yon et al., 2022). The concept of self-compacting mortar SCM derives from that of self-compacting concrete SCC which was introduced in the late 1990s, before raising widespread interest among researchers as concrete technology improved.

The primary focus when developing SCC has been to achieve the best possible workability performance - through the usage of high-range water-reducing agents - in addition to the high flowability required for excellent workability. To be in line with the viscosity requirements of such mixtures, mineral additions are often used in the form of inert or active supplementary cementitious materials such as limestone filler (inert), fly ash, silica fume,..etc (active). These materials incur in the SCM in addition to an improved cohesion and flowability at the

- Selection and peer-review under responsibility of the Organizing Committee of the Conference

fresh state, the formation of a denser matrix and denser ITZ (Khelil, 2020) At the hardened state. One way to achieve the required flowability, instead of mineral additions, could be the use of very fine sand particles in the likes of dune sand (DS). Indeed, research has shown that dune sand particles, thanks to their morphological properties (near-spherical shape, smooth surface texture), have a positive impact on the rheological properties of cementitious materials (Khelil et al., 2023).

The present paper shows the results of an experimental study exploring the possibility of using dune sand in substitution of crushed sand in SCMs, with the objective on the one hand, to improve their rheological properties, and on the other hand, to reduce the usage of regular crushed sand and hence diminish its environmental impact.

Materials and Procedures

Materials

In this study, a CEM II/A-L 42.5R cement with a specific gravity of 3.1 supplied by SPA Biskria and conforming to standard EN 197-1 (British Standards Institution, 2011). Was used. Two types of sands were used to prepare the mortars. The first one is a crushed sand (CS) sourced from a local quarry in the region of Tizi-Ouzou, whereas the second originates from the mid-southern region of Touggourt, in the Algerian desert. The particle size distribution of both sands is presented in (Figure 1). From the graph, a difference in fineness can be observed between the studied sands. DS is finer than CS to the extent where its fineness modulus is measured at 1.94 whereas that of CS is at 3.09. In terms of absolute density, both sands share a near-similar density of 2.66 and 2.65 for CS and DS respectively. To complete the mix, tap water as well as a high-range water-reducer supplied by Granitex under the commercial designation of Medaplast SP 40 was used.

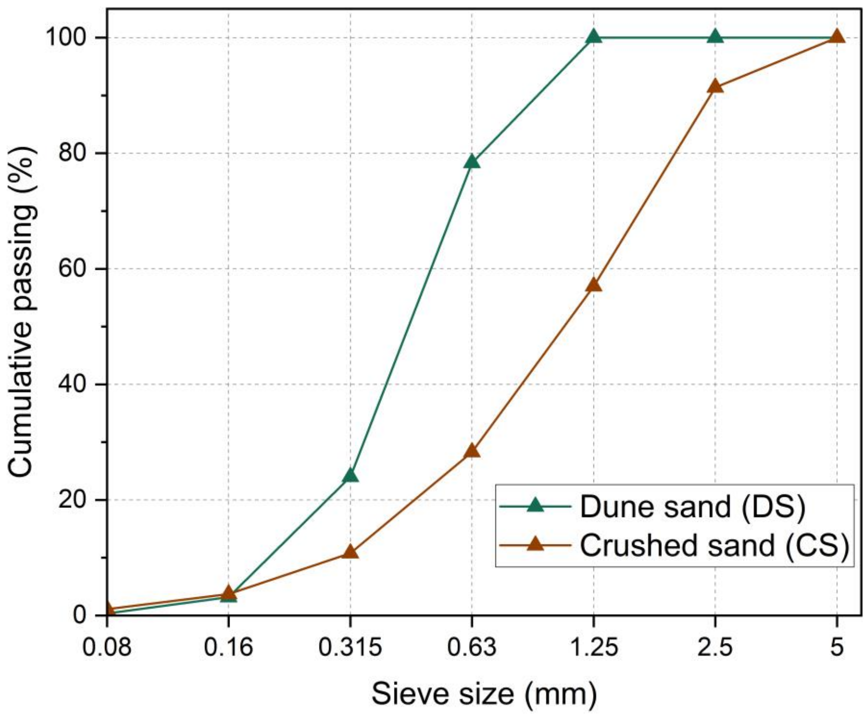

Figure 1. Particle size distribution of the tested sands

Mortars Mix Proportions

In total 5 SCM mixtures were prepared using the CEM II 42.5 R as the sole binding material. No supplementary material was included in the study. Playing the role of the supplementary material at least on the very fine and compaction-favoring aspect was the dune sand DS. Indeed, due to its fine particle size distribution along with its general near-spherical shape, DS could help achieve the rheological requirements of the SCM, while being quite cheap and easy to handle. The tested CS-DS sand blends in the mortars are presented in (Table 1). The mixing protocol is based on that of EN 196-1 (British Standards Institution, 2016). Dealing with regular mortar. It consisted of an overall mixing duration of 180s, comprising the following steps: Firstly, the water and cement are introduced into the mixing bowl, before the planetary mixer in switched on at a low speed for 30s. After that, the addition of the sand blend is performed during another 30s, right before switching to the higher speed for 30 more seconds. At this point, the mixer is paused for 30s to allow to scrape any material stuck to the bottom or the walls of the bowl. Lastly, mixing is resumed for 60s at high speed, before termination. After completion, the fresh SCM mixtures are tested for their flowability properties using a mini-slump cone. The mixtures are then introduced in 40 x 40 x 160 mm^3 prismatic molds for 24h at room temperature of around 25°C. After 24h, the specimens are demolded and allowed to age in a water tank at the same temperature for another 27d before further testing. For each SCM mixture, three prismatic specimens were cast, in order to be subjected to Ultrasonic Pulse Velocity testing (UPV), flexural tensile strength testing and finally compressive strength testing. The results displayed hereafter are the averaged values recorded on those three specimens.

Table 1. Mortars mix proportions

Mortar ID (%CS-%DS)	CS (g)	DS (g)	Cement (g)	water (g)	HRWR (%)	W/C
M0 (100CS-0DS)	1191.6	0	685.6	205.68	0.68	0.3
M1 (75CS-25DS)	893.7	299.24	685.6	205.68		
M2 (50CS-50DS)	595.8	598.49	685.6	205.68		
M3 (25CS-75DS)	297.9	897.74	685.6	205.68		
M4 (0CS-100DS)	0	1196.99	685.6	205.68		

Mini-Slump Testing

This is the most common test, as it is the easiest to implement. It allows to characterize mobility in an unconfined environment. This is a spreading test that is used to characterize the fluidity of the mortar. It is a variant of the slump test used for concrete but this time it is carried out on a truncated mini cone (mini slump test). It protocol consists in measuring on two perpendicular sides, the spreading diameter of the mortar pancake and comparing the results to the spreading values of an SCM that are usually set between 240 and 260 mm according to EFNARC (European Federation of Specialist Construction Chemicals and Concrete Systems) guidelines (2005). In detail, the test method consists in filling a mini-cone of base-diameter:100mm, top-diameter:70mm and height:60mm, in two steps, during which, the mortar is consolidated by performing 25 strokes using and tamping rod. The mini-cone is then lifted allowing for the fresh mixture to freely flow. The measurements are performed once the fresh SCM stops flowing and remains still, and no segregation and bleeding is observed.

Ultrasonic Pulse Velocity Testing

Ultrasonic Pulse Velocity Testing **(**UPV) is a non-destructive testing method used to determine the quality and integrity of materials, such as concrete or mortar. It works by transmitting high-frequency acoustic waves into the material and measuring the time it takes for these waves to travel through it, as described by BS EN 12504-4 (British Standards Institution, 2004). And ASTM C597-16 (American Society for Testing and Materials, 2016). The speed of the sound waves depends on the material's properties, such as its density, elasticity, and presence of cracks or voids. The testing of the mortar prismatic specimen was carried out using a UPV apparatus possessing two transducers, an emitting transducer and a receiving one. After setting the UPV frequency (150KHz) the specimen to be tested is placed between the transducers, before turning the apparatus on. For each mortar formulation, three specimens were tested, each one tested three times. The results shown in this paper are the averaged values of 9 tests.

Tensile and Compressive Strength Testing

The destructive tests were carried out using a computer-controlled hydraulic press. Each SCM specimen was initially subjected to a three-point flexural test at a constant loading rate of 50 ± 10 N/s, as outlined in EN 196-1

(British Standards Institution, 2016). This test determined the flexural tensile strength of the specimen. Subsequently, the two resulting half-prisms were crushed at a constant loading rate of 2400 ± 200 N/s following EN 196-1 prescriptions (British Standards Institution, 2016). Allowing for the measurement of compressive strength. The mechanical properties reported in this study represent the average values calculated from the three test specimens prepared for each mixture.

Results and Discussion

Mini-Slump Testing

The results of the mini-slump test carried out on the fresh mortars are presented in (Figure 2).

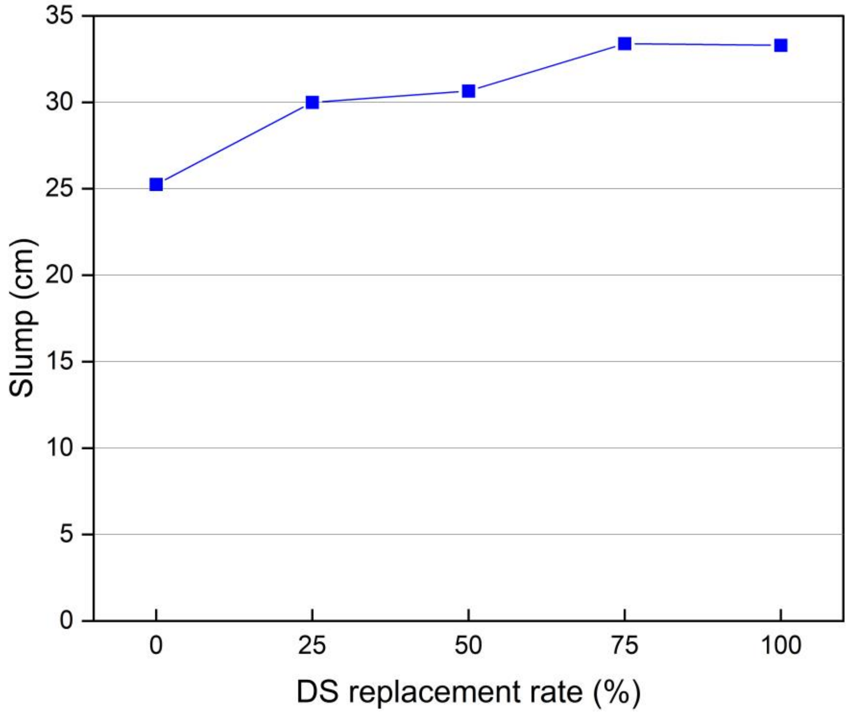

Figure 2. Slump values of the tested mortars

The data show the improvement of slump values as the amount of DS increases in the mortars. Indeed, slump values increase from 25.25 cm for the control specimen M0 to 30.0 cm, 30.65 cm, 33.4 cm and 33.3 cm for M1, M2, M3 and M4 respectively, representing an increase of 18.81%, 21.39%, 32.27%, 31.88%. These results show the positive effect of dune sand addition in amelioration the fresh mortar flowability performance. This improvement could be related as mentioned earlier, to the shape of DS particles, since they are mostly constituted of near-spherical particles. This particularity, makes it easier for the mortars constituents to flow under their own weight. DS particles in that case can be considered as playing the role of a lubricant, facilitating along with the HRWR, the motion of the cement and the CS particles at the fresh state, enabling their arrangement in a more compact configuration within the cementitious matrix.

Ultrasonic Pulse Velocity testing

The ultrasonic pulse velocity test results are shown in (Figure 3). It can be seen from the data that the presence of DS in the mortars in increasing proportions leads to the overall decrease of the acoustic velocity, transitioning from 5319m/s for M0 and M1 to 4990m/s, 4939m/s and 4799m/s for M2, M3 and M4 respectively. The decrease in the recorded data show the alteration of mortar properties brought about by DS particles, in the sense that, those particles seem to make the mortar somewhat less dense compared to the control. Indeed, as mentioned earlier, UPV testing is often used to assess the material compactness, and the higher the UPV recorded, the denser the material. This decreased compactness observed here could be indicative of a poorer material strength-wise and durability-wise, since those parameters are often correlated.

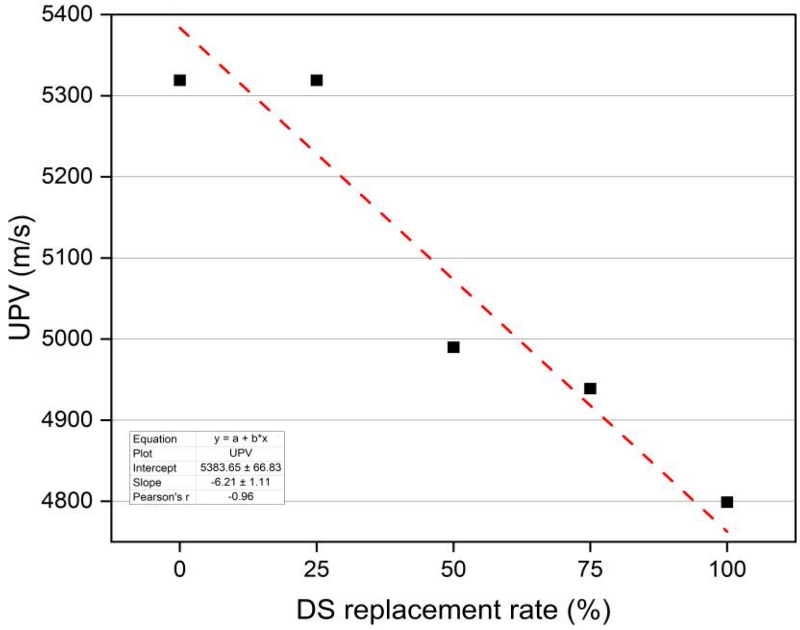

Figure 3. Ultrasonic pulse velocity test results at 28d

Tensile Strength Test Results

The following figure (Figure 4) presents the flexural tensile strength of the tested mortar specimens.

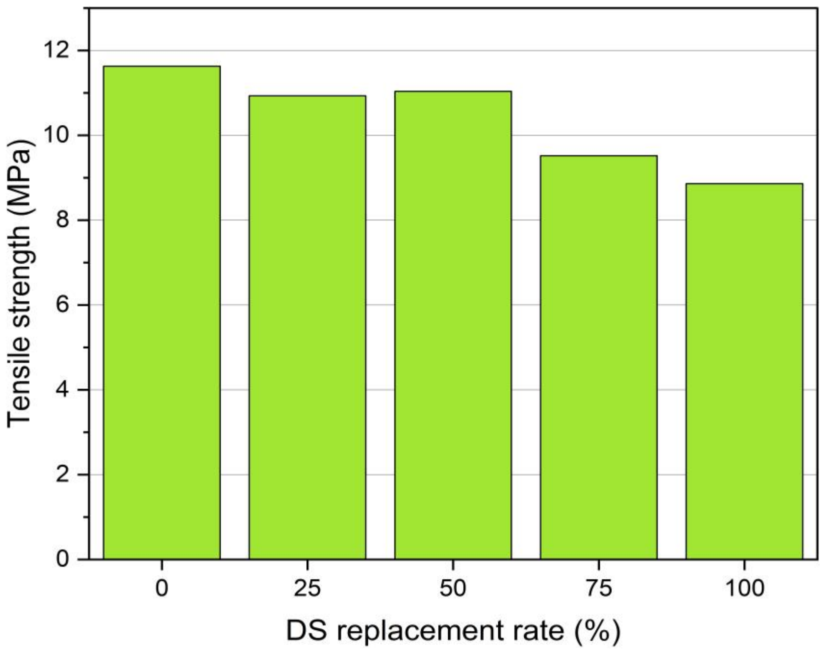

Figure 4. Tensile strength of the tested mortars at 28d

Globally, what is observed is a steady decrease of the tensile strength of the mortars as the amount of dune sand increases in the mixtures. From the control tensile strength value of 11.63MPa, the strength decreases down to 10.93MPa, 11.04MPa, 9.52MPa and 8.86MPa for M1, M2, M3 and M4 respectively, account for a decrease of 6.02%, 5.07%, 17.54% and 23.82%. These results seem to be accord with the UPV test results, which indicated that the mortar mixture becomes more porous with the increasing amount of dune sand. Indeed, it is well known that DS particles hold a spherical shape and a smooth surface texture (Khelil et al., 2023). This property as much as it allows to improve the mortars flowability and particles arrangement at the fresh state, at the hardened state however, it makes the particle bond to the cement matrix specifically at the porous ITZ weaker that its CS counterpart (Khelil, 2020). As a consequence, very little resistance to crack propagation during loading are observed on these mortars, making them less able to withstand loading compared to the control.

Compressive Strength Test Results

The compressive strengths of the tested mortars are presented in (Figure 5).

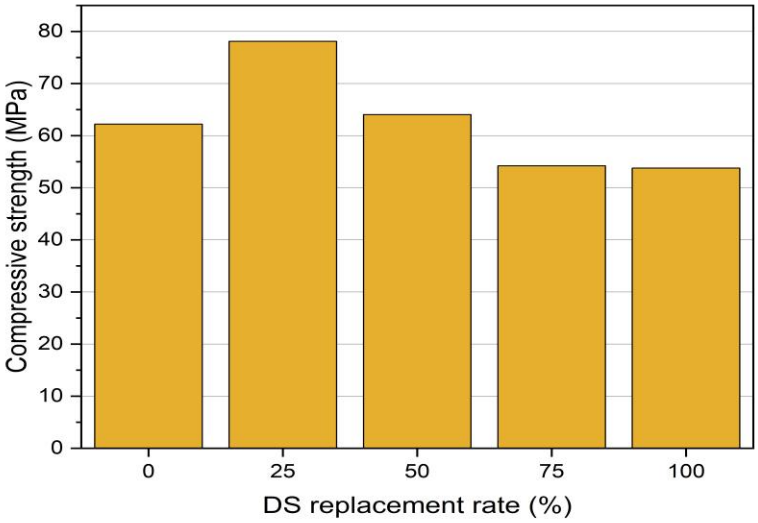

Figure 5. Compressive strength of the tested mortars at 28d

From the graph, one can note that the mortars containing DS particles exhibit two types of behaviors depending on the amount of DS in the mixtures. For mixtures M1 (25% DS) and M2 (50% DS), the compressive strengths are valued at 78MPa and 64.04MPa representing an increase of 25.51% and 2.92% compared to the control (62.22MPa). At higher DS amounts, namely M3 (75% DS) and M4 (100% DS), a decrease is recorded, valued at 15.78% and 13.56% at 54.2 and 53.75 MPa respectively. These results seem to indicate that there is a positive effect to adding DS to the SCMs up to a certain DS content valued at 50%. These observations are indicative of the improvement of the particles arrangement within the cementitious matrix during the mixing process and casting, making it possible to reduce inter-granular spacing and hence improve the granular phase interlocking. Beyond that value, lower strengths are observed. This could be explained by the high amounts of DS particles, which, exhibit a relatively easy debonding from the cement matric under loading and cracking, making the overall ability of the mortar less able to achieve high compressive strength. Nevertheless, it is noteworthy, that even though the high DS mortars are less performing, their strength remains significant enough (>50MPa), for them to be considered as appropriate building materials.

Conclusion

In light of the experimental data, the following conclusions may be inferred:

- DS addition improves the flowability of SCMs made of natural crushed sand particles, on all the DS-containing mixtures. The flow increases by up to 32.27% for Mixture M3 (75% DS).
- DS addition reduces the acoustic properties (UPV) of the SCMs, meaning that porosity of the cementitious matrix increases, and consequently so is the durability of the SCMs.
- Flexural tensile strength test results showed a slight decrease of resistance when DS content is lower or equal to 50%, whereas the decrease is steeper beyond.
- Compressive strength test results show that at low DS contents (below 50% DS), the SCMs behave better than the control, whereas beyond, poorer strengths are observed.

Overall, these findings show that dune sand DS could represent a viable alternative, capable of replacingordinary crushed sand in SCMs, while improving their properties provided that the replacement rate is low (around 25%).

Scientific Ethics Declaration

The authors declare that the scientific ethical and legal responsibility of this article published in EPSTEM Journal belongs to the authors.

Acknowledgements or Notes

* This article was presented as a poster presentation at the International Conference on Technology, Engineering and Science (www.icontes.net) held in Antalya/Turkey on November 14-17, 2024.

References

American Society for Testing and Materials. (2016). *Standard test method for pulse velocity through concrete. ASTM C597-16:2016*. Retrieved from https://www.astm.org/

British Standards Institution. (2004). *Testing concrete - part 4: Determination of ultrasonic pulse velocity. BS EN 12504-4:2004*. Retrieved from https://www.bsigroup.com/

British Standards Institution. (2011). *Cement–part 1: Composition, specifications and conformity criteria for common cements. BS EN 197-1:2011*. Retrieved from https://www.bsigroup.com/

British Standards Institution. (2016). *Methods of testing cement determination of strength. BS EN 196-1:2016*. Retrieved from https://www.bsigroup.com/

European Federation of Specialist Construction Chemicals and Concrete Systems. (2005). *The European guidelines for selfcompacting concrete: Specification, production and use*. Retrieved from https://efnarc.org/

Khelil, N. (2020). Silica fume-hydrated lime blended cements: Contribution of pre-blending to strength development in mortars. *Australian Journal of Civil Engineering*, *19*(1), 12–25.

Khelil, N., Ould Ouali, M., & Meziane, L. (2023). On the use of fine dune sand in reactive powder concrete: Effect on resistance, water absorption and UPV properties. *Construction and Building Materials*, *388*, 131684.

Turk, E., Karatas, M., & Dener, M. (2022). Rheological, mechanical and durability properties of self-compacting mortars containing basalt powder and silica fume. *Construction and Building Materials*, *356*, 129229.

Yon, M. S., Arslan, F., Karatas, M., & Benli, A. (2022). High-temperature and abrasion resistance of self-compacting mortars incorporating binary and ternary blends of silica fume and slag. *Construction and Building Materials*, *355*, 129244.

Author Information

Nacim Khelil
Mouloud Mammeri university of Tizi Ouzou
BP 17RP, 15000, Algeria.
Contact e-mail: *nacim.khelil@ummto.dz*

Said Boukais
Mouloud Mammeri university of Tizi Ouzou
BP 17RP, 15000, Algeria.

Randa Makkeb
Mouloud Mammeri university of Tizi Ouzou
BP 17RP, 15000, Algeria.

Karim Akkouche
Mouloud Mammeri university of Tizi Ouzou
BP 17RP, 15000, Algeria.

Amar Kahil
Mouloud Mammeri university of Tizi Ouzou
BP 17RP, 15000, Algeria.

To cite this article:

Khelil, N., Bouakis, S., Makkeb, R., Akkouche, K., & Kahil, A. (2024). Performance evaluation of a self-compacting mortar altered with dune sand. *The Eurasia Proceedings of Science, Technology, Engineering & Mathematics (EPSTEM), 32,* 329-335.

The Eurasia Proceedings of Science, Technology, Engineering & Mathematics (EPSTEM)
ISSN: 2602-3199

The Eurasia Proceedings of Science, Technology, Engineering & Mathematics (EPSTEM), 2024

Volume 32, Pages 336-341

IConTES 2024: International Conference on Technology, Engineering and Science

Automation of IMEI Label Attachment Process in Mobile Device Production

Okan Temizturk
Samsung Electronics Türkiye Production

Kaan Pehlivan
Samsung Electronics Türkiye Production

Abstract: The methods of sticking labels on products produced in mass production facilities can vary greatly depending on the type of product to which the label will be attached, the size of the label and the level of adhesion of the label. The suitability and performance of the label sticking method vary greatly depending on the size of the label and especially the level of adhesion of the label. In particular, the correct selection of the method of sticking labels with low adhesion to products in mass production lines significantly affects the accuracy of the sticking process, the quality and performance of the sticking process. Some mobile phone manufacturers deliver mobile phones to users with a label attached to the back of the device. This label contains IMEI number information and a QR code for the IMEI number. The code on this IMEI label is read by barcode scanners to manage production processes and applications in the production process. Depending on the country where the mobile phones will be sold, this label can be removed before the packaging process before being sent to the user, or it may be desired to send the user with the IMEI label attached to the mobile phone. In case this label is requested to be removed for various purposes, the label size is designed to be both very small and easy to remove by keeping the adhesive level low in some countries. The fact that the IMEI label is small and has a low adhesive level requires the most appropriate selection of the attachment method in mass production facilities. This article will discuss the most appropriate adhesive method for low-adhesive and small-sized IMEI labels.

Keywords: IMEI label, Label attachment, Label attachment automation,

Introduction

Each mobile phone has its own information, such as the manufacturer, model, IMEI code, S/N code, network access permission, etc., which are implanted in the mobile phone at the factory or pasted on the mobile phone cover, generally the position of the back cover. It is very important whether the information is accurately pasted to the designated location before leaving the factory, and whether the pasting quality meets the requirements. To meet these requirements, various bonding methods are applied in today's production processes. The choice of these application methods may vary due to factors such as the size of the label to be attached, the level of adhesion or the geometry of the bonding zone. As an application method, the methods of IMEI label adhesion process can be analyzed under the following three headings.

Label Attachment Methods

In today's industry, there are various methods of attaching low-adhesive labels to products. Labels can be attached to the desired areas of the products with different methods. These attaching methods can vary according to the size of the label, its level of adhesion and the level of production speed to meet the needs. Labels can be stuck manually in cases where the geometry of the product is complex, there is no need for an automated attaching process at current production speeds or the precision of the attaching position of the label is not required, or due to requests such as performing a fast and effective sticking process in accordance with the production speed to a certain shade of the product or completing the sticking process with better quality. Labeling methods can be examined under 3 headings.

Manual Label Application

Though it may seem outdated in an era of automation, manual label application is still prevalent, particularly in small-scale production settings or when dealing with complex products. Manual application allows for flexibility that mechanical methods cannot easily replicate. Workers can inspect each product for quality control, ensuring that labels are applied correctly and securely. However, this method can be labor-intensive and may hinder throughput. In industries where precision is of vital importance, manual labeling may not provide the expected precision, accuracy and quality to the desired extent, and in such cases, manual labeling is at a disadvantage when compared to other labeling methods.

Semi-Automatic Labelers

Semi-automatic labelers strike a balance between manual labor and full automation. Operating typically with an operator overseeing the process, these machines require some manual input but are designed to speed up the labeling process considerably. An example includes labeling machines that allow workers to place items on the conveyor and the machine applies the label. This method reduces the time taken for label application while still involving human oversight to ensure accuracy. This method can be used especially in cases where a fully automatic label attachment system cannot be installed but the label needs to be applied precisely to a specific area of the product.

Fully Automatic Labeling Systems

In mass production settings, fully automated labeling systems represent the cutting edge of efficiency. These systems are programmed to apply labels in a consistent manner at high speeds, which is essential for large-scale operations. Conveyor belts transport products through a series of automated stations where labels are printed, cut, and applied, all in a matter of seconds. Fully automatic systems are particularly beneficial for manufacturers expecting high volumes of products, ensuring that each item is labeled precisely while minimizing the risk of human error.

In mass production facilities, all three application techniques mentioned above can be used as an application. However, in terms of both production efficiency and accuracy and precision of the labeling process, the most suitable method in mass production facilities is the systems where the labeling process is carried out using a fully automatic system.

IMEI Number

IMEI (International Mobile Equipment Identity) is a unique 15-digit serial number given to every mobile phone which can then be used to check information such as the phone's Country of Origin, the Manufacturer and it's Model Number (Samsung, 2024). IMEI is a unique number to identify mobile phones and satellite phones over diversified network of GSM, Universal Mobile Telecommunications System (UMTS) and Long-Term Evolution (LTE) network (Roa, 2015). These IMEI numbers are stored in a database called the EIR (Equipment Identity Register), which contains information about all valid mobile phone equipment.

The IMEI number reveals details about a phone without having to physically have it, including the brand and model, year of release, and other specifications. Most phones have a very simple key-in method to retrieve IMEI/MEID numbers, enter a 5-digit string—*#06#—and the number will be displayed on phone(Sahni, 2014). It is also printed by laser on back cover or printed on the label which is attached on back cover of the mobile device’s to keep the IMEI number safe if it is needed. Another way to learn IMEI number is checking the package. The sticker with the IMEI code number is placed on the box with the phone (Davronbekov 2019).

Method

Attachment of Low Sticky Label in Automation Line

In mobile phone production facilities, there are many processes carried out with full automation systems during the production process. Many of the operations performed with these full automation systems need to be done precisely by targeting the correct position. One of the processes that must be done precisely in mobile phone production facilities is the process of sticking the IMEI label to the correct position on the phone fully automatically. This label also has an IMEI number QR code, which is read by scanners at many stages of the fully automated production process. In order for the barcode scanning of this label to be carried out accurately, the labels must be precisely attached to each phone in the correct position. The fully automatic equipment has been developed to fulfill the desired process accurately and precisely eliminates human error and performs the process of precisely sticking each label in the correct position. The fully automatic IMEI label sticking machine is able to meet all requirements accurately and with the same quality.

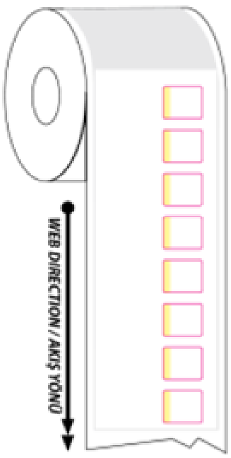

Figure 1. IMEI label Roll

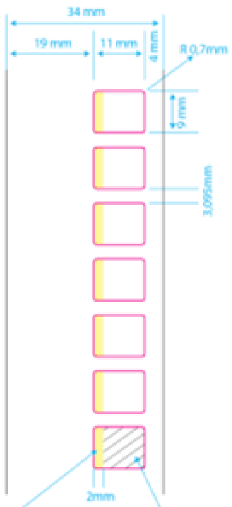

Figure 2. IMEI label dimensions

Figure 3. Actual IMEI label roll

In above picture (Figure 1) it is shown that IMEI label and the roll on which the IMEI label is wrapped in Samsung Electronics Turkiye Production Company. IMEI label dimensions (Figure 2) which (9mm x 11mm) is smaller than 1 cm2 area make it difficult to apply common sticky label attachment processes which are generally applied in industries. One of the most commonly using sticky label attachment process is taken place as peeling partially label from their roll and make contact between product and label which is partly peeled from its own roll (Figure 3). After this contact of the sticky label to product, the product continues to move along the conveyor belt and the label continues to attach to the product as it moves along the belt, and the attaching process is completed. However, this attaching method is quite difficult to apply for labels that are small in size and have low adhesive levels. This widely used attaching method makes things quite difficult, especially when labels need to be attached to a specific location on the product with high accuracy, such as in the attaching process of IMEI labels. For this reason, the peeling/vacuuming technique comes to the fore and gives better results in order to correctly stick small IMEI labels with low adhesive level onto the mobile phone.

In the peeling/vacuuming technique, in the first stage, labels are partially peeled off (Figure 4 & Figure 5) from the rolls they are wrapped in. Then, a vacuum head comes to the peeled part (Figure 6 & Figure 7) of this peeled IMEI label and starts vacuuming. Then, the IMEI label peeling process continues with the help of the peeling mechanism (Figure 8 & Figure 9) Thus, while the IMEI label is peeled off, it is held by vacuuming with the help of the vacuum head. Then, this vacuum head is directed towards the area where the IMEI label is desired to be attached with the help of pneumatic pistons (Figure 10 & Figure 11). When the phones moving on the conveyor belt reach the appropriate position for the IMEI label to be attached, the conveyor belt is stopped and the vacuum head holding the IMEI label moves towards the mobile phone and presses on the surface where the IMEI label is attached for at least one second (Figure: 12 & Figure 13), helping the adhesive to hold better on the label. In addition, during the pressure of the vacuum head on the mobile phone, the vacuum holding the IMEI label is disabled and air is blown through these vacuuming holes to ensure better adhesion of the label.

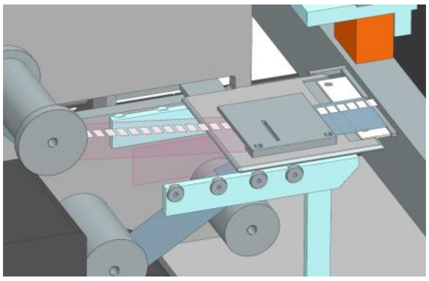

Figure 4. IMEI label partially peeling

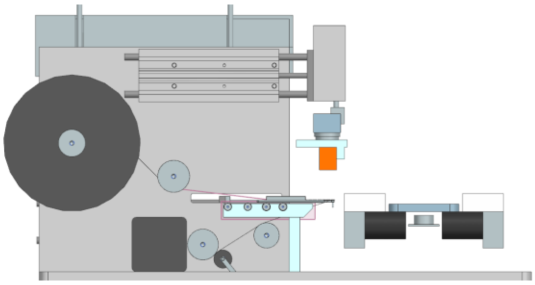

Figure 5. IMEI label partially peeling side view

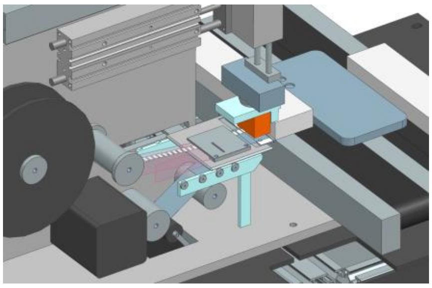

Figure 6. Vacuum head vacuum start position

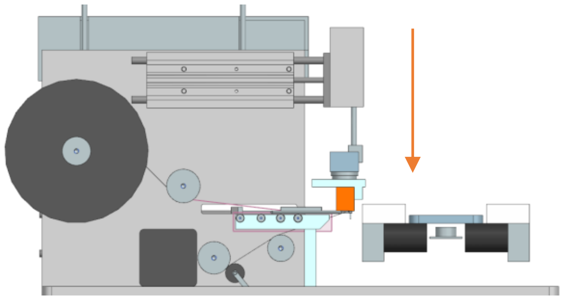

Figure 7. Vacuum head vacuum start position side view

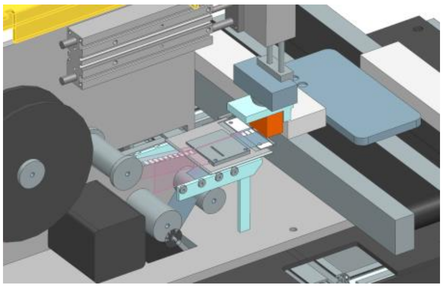

Figure 8. Label peeling mechanism move back

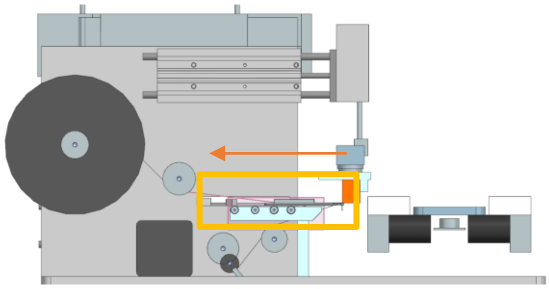

Figure 9. Label peeling mechanism move back side view

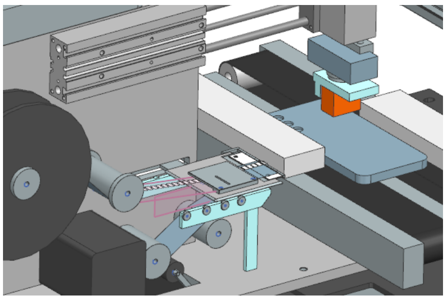

Figure 10. Label peeling mechanism moving back

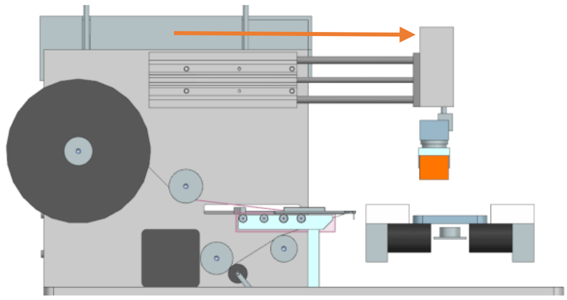

Figure 11**.** Label peeling mechanism motion side view

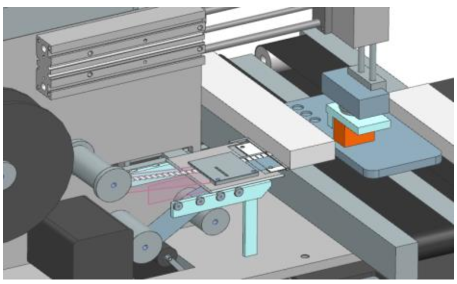

Figure 12. Label attachment position

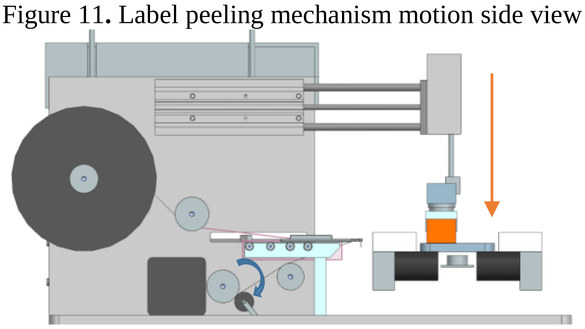

Figure 13. Label attachment position side view

Thanks to the 180-degree rotation feature of the piston to which the vacuuming head is connected, which vacuums the IMEI label, labels can be attached to the desired area in the desired direction and at the desired angle. At the same time, with the help of a barcode reader placed in the IMEI label sticking area (Figure 14), it is checked whether there is already a label on the existing mobile phone before the IMEI label sticking process in order to prevent label printing on top of each other. If the IMEI label is detected with the help of the barcode reader, the IMEI label is not printed on the mobile phone and the mobile phone is advanced on the conveyor belt for the next processes.

After the IMEI label is peeled with the help of the vacuum head that peels the label, it is compressed and pulled forward with the help of two cylinders so that the next IMEI label can be peeled by the vacuum head. If the sensor at the end of the label peeling mechanism detects a label during the label peeling process, the peeling process is stopped and thus the IMEI label is brought to the correct position for the next vacuuming process. The IMEI roll is compressed with the help of a cylinder connected to a stepper motor and a cylinder connected to a piston (Figure 15) and the label roll is pulled for the next process by the rotation of the cylinder of the stepper motor and the IMEI label is brought to the correct position for the vacuuming process. A fully automated equipment that can perform Peeling/Vacuuming functions at the correct timing can automatically perform the IMEI labeling process in mobile phone production facilities. (Figure 16)

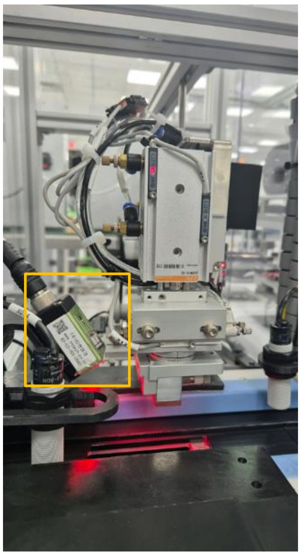

Figure 14. Barcode Scanner

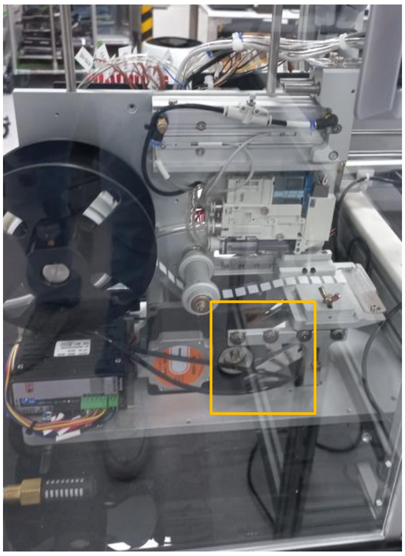

Figure 15. Pulling mechanism of roll

Figure 16. Automation Machine

Results and Discussion

By using the peeling/vacuuming technique, small-sized and low-adhesive IMEI labels can be correctly and safely attached to mobile phones. In addition, by using a barcode scanner, it is possible to check whether there is an IMEI label on existing mobile phones, thus preventing existing errors and the problem of attaching labels on top of each other. The most efficient way to properly attach the IMEI label to the correct location in mass production lines is the peeling/vacuuming method. This process is suitable for production lines with a tact time of more than 3 seconds. In lines with much faster tact times, methods that will provide faster sticking should be preferred.

Conclusion

There are many label attachment methods in mass production facilities. However, the current widely used label attaching methods do not provide the desired results for small-sized and low-adhesive labels such as IMEI labels. The most suitable method for these types of labels in mass production lines is the peeling/vacuuming method. Thanks to the Peel/Vacuum method, labels can be attached to the desired area of mobile phones in the most accurate way. Unlike other label attachment methods, the best and most efficient results were obtained with the peel/vacuum technique in the application of small labels with low adhesiveness, such as IMEI labels.

Recommendations

In the Peeling/Vacuuming method, it takes a certain amount of time to peel the label from the roll and move it between the axes with pneumatic pistons. In addition, in the IMEI label attaching process, the vacuum head applies pressure to the IMEI label for about one second to increase the strength of the bonding process. All of these processes take more than 3 seconds to complete. This method is not recommended for mass production lines with a tact time of less than 3 seconds.

Scientific Ethics Declaration

The authors declare that the scientific ethical and legal responsibility of this article published in EPSTEM Journal belongs to the authors.

Acknowledgements or Notes

This article was presented as an poster presentation at the International Conference on Technology, Engineering and Science (www.icontes.net) held in Antalya/Turkey on November 14-17, 2024.

References

Davronbekov, D. A., Isroilov, J. D. & Akhmedov, B. I. (2019). Principle of organizing database ıdentification on mobile devices by IMEİ. *International Conference on Information Science and Communications Technologies (ICISCT)*, Tashkent, Uzbekistan, pp. 1-5

Rao, S. P., Holtmanns, S. Oliver, I. & Aura, T. (2015). Unblocking stolen mobile devices using SS7-MAP vulnerabilities: exploiting the relationship between IMEI and IMSI for EIR Access. *IEEE Trustcom/BigDataSE/ISPA*, Helsinki, Finland, pp. 1171-1176.

Samsung. (n.d.). *Smart phone: How do I locate my phone IMEI number?* Samsung New Zealand. Retrieved October 31, 2024, from https://www.samsung.com/nz/support/mobile-devices/smart-phone-how-do-i-locate-my-phone-imei-number/?srsltid=AfmBOoq5WbpH7jplr3Q7pYwJz-4H-j_WVWgDBq9Vz-9LAFQwfVXNChwa

Sahni, M. (2014). Detectıng and automated reportıng of change in IMEI Number. *International Journal of Advancements in Research & Technology, 3(*5), 186-188.

Xibin, W., Junhong, W., Wenbin, C., Yuran, W., & Nan, W. (2020, November). Mobile phone label online detection system based on machine vision. In *2020 Chinese Automation Congress (CAC)* (pp. 1784-1787). IEEE.

Author Information

Okan Temizturk
Samsung Electronics Turkiye Production
Mimar Sinan mah. 103. Cad No:72
Kapaklı /Tekirdağ / Türkiye
Email: o.temizturk@samsung.com

Kaan Pehlivan
Samsung Electronics Turkiye Production
Mimar Sinan mah. 103. Cad No:72
Kapaklı /Tekirdağ / Türkiye

To cite this article:

Temiztürk, O. & Pehlivan, K. (2024). Automation of IMEI label attachment process in mobile device production. *The Eurasia Proceedings of Science, Technology, Engineering & Mathematics (EPSTEM), 32,* 336-341

The Eurasia Proceedings of Science, Technology, Engineering & Mathematics (EPSTEM)
ISSN: 2602-3199

The Eurasia Proceedings of Science, Technology, Engineering & Mathematics (EPSTEM), 2024

Volume 32, Pages 342-352

IConTES 2024: International Conference on Technology, Engineering and Science

Integrated Best-Worst Method and Gray Relational Analysis for Hospital Location Selection: The Case of Burdur Province

Mustafa Serdar Toksoy
Burdur Mehmet Akif Ersoy University

Abstract: The hospital location (site) selection problem involves determining the most suitable location for a healthcare facility. As a multi-criteria decision-making (MCDM) problem, it requires the evaluation of several factors, including strategic, economic, and social considerations, due to the direct impact hospital locations have on public health. To make an optimal decision, MCDM methods are typically employed to accurately assess the relevant criteria. These methods assist decision-makers in evaluating various factors and determining the best location for the hospital. This study focuses on selecting a site for a private hospital planned for Burdur Province, where no private hospital currently exists. In this context, three alternative locations were evaluated based on expert opinions from academicians, health managers, and urban planners. In the first phase of the study, the Best-Worst Method (BWM) was used to calculate the criteria weights, allowing for the subjective evaluation of multiple factors. Following this, the Gray Relational Analysis (GRA) method was applied to determine the most appropriate location by assessing the degree of similarity or dissimilarity between the alternatives. This combination of methods enabled the ranking of the alternatives, ultimately identifying the best site for the hospital.

Keywords: Hospital site selection, Multi-criteria decision-making, Best-worst method, Gray relational analysis

Introduction

Rapid changes in technology, the globalisation of the world and an increasingly competitive environment have made the decision-making processes of companies more crucial. In this context, the site selection is of vital importance for the success of a company. The basis of site selection studies is Weber's 'location theory'. Although location selection was initially based only on the purpose of reducing transport costs, subsequent studies have shown that site selection has an effect on service quality and thus its importance has increased (Aydın et al., 2009). Site selection for critical facilities such as hospitals is a complex process that requires consideration of many factors such as efficiency, accessibility, safety and cost. The consideration of natural, human and economic factors is of great importance for the efficiency, quality and equity of health services (Sahin et al., 2019). Therefore, hospital site selection is a strategic decision with long-term implications and requires an approach that has the potential for sustainability and prevention of future problems. Wrong site selection can lead to patient dissatisfaction and increased costs (Chatterjee, 2013). Hospital site selection is a critical decision process not only for health care managers, but also for government and health policy makers. This selection process involves evaluating criteria such as patient access to the hospital, environmental factors, proximity to other healthcare facilities and land costs. In this context, hospital site selection is usually analysed using MCDM techniques. MCDM techniques, which take more than one criterion into account, allow the advantages and disadvantages of each alternative to be systematically analysed and different factors to be effectively evaluated. In addition to MCDM, the carrying capacity model, Geographical Information Systems (GIS) or fuzzy models can also be used to solve this problem. One of the most preferred and widely used MCDM methods is Analytic Hierarchy Process (AHP). Other widely used methods include Analytic Network Process (ANP), Technique for Order of Preference by Similarity to Ideal Solution (TOPSIS), Vlsekriterijumska Optimizacija I Kompromisno Resenje (VIKOR), Elimination and Choice Expressing Reality (ELECTRE),

- Selection and peer-review under responsibility of the Organizing Committee of the Conference

Simple Additive Weighting (SAW), GRA, Evaluation Based on Distance from Average Solution (EDAS), Additive Ratio Assessment with Grey Relational Analysis (ARAS-G), Combined Distance-based Approach for Ranking Alternatives (CODAS), Criteria Importance Through Intercriteria Correlation (CRITIC), Entropy and fuzzy versions of these methods. Each stage of hospital site selection has its own specific MCDM method. This preference is due to the fact that the relevant stage of the problem is fully compatible with the method structure (Gul & Guneri, 2021).

This study presents a multi-criterion decision-making (MCDM) approach to determine the optimal site for a private hospital in Burdur, a province in Turkiye's Mediterranean region recognized for its agricultural, industrial, and tourism potential. Despite the fact that Burdur is a student hub and an important transport corridor, there is currently no private hospital in the city. To address this, a four-member decision-making team - comprising academics, health managers, health professionals and local government representatives – is assembled to evaluate three alternative sites. Based on a review of hospital site selection literature, seven criteria selected and a two-stage MCDM methodology is proposed. In the first stage, the selected criteria's are weighted using the linear BWM method; in the second stage, GRA is used to evaluate and rank the alternatives according to their scores. The remainder of the study is organised as follows: the second section is a literature review of hospital site selection methodologies. The third section describes in detail the MCDM methods used in this study, while the fourth section is dedicated to the application. The results are discussed in the conclusion and evaluation section.

Literature

Hospital site selection is a critical decision to improve the efficiency of health services and to meet the health needs of the community. This decision requires a MCDM process in which various factors are considered. The literature in this area shows that different methods and analyses have been used to optimise hospital site selection decisions. Lin et al. (2008) managed subjective judgements by using fuzzy AHP and sensitivity analysis for hospital site selection in Taiwan this approach was adapted by Aydın (2009) for Ankara, Türkiye, highlighting the flexibility of FAHP in dealing with uncertainty. Wu and Zhou (2012) obtained more reliable results by using GIS-based multi-criteria analysis method in Beijing et al. (2013) emphasised that the most important criteria are land cost and proximity to public transport with Fuzzy AHP in rural areas in India. Dehe and Bamford (2015) compared two different MCDM models for the NHS in the UK. Khaksefidi and Miri (2016) used MCDA methods considering multiple criteria in Iran. Kmail et al. (2017) combined GIS and AHP to identify the most suitable locations. Kumar et al. (2016) used ELECTRE approach in India. Celikbilek (2018) included the opinions of the board members in the decision-making process with the VIKOR method. Dell'Ovo et al. (2018) integrated MCDM and GIS for healthcare facilities in Milan. Mic and Antmen (2019) revealed the potential for improvement in site selection with fuzzy TOPSIS in Adana. Neisani Samani and Alesheikh (2019) increased citizen participation with Fuzzy-VIKOR. Rezayee (2020) used GIS-based multi ciriteria analysis to achieve balance by including environmental impacts and traffic flow. Nsaif et al. (2020) created a suitability map with GIS and remote sensing. Adalı and Tus (2021) determined market conditions with CRITIC method and ranked with TOPSIS, EDAS, and CODAS methods. Sutcuoglu and Yalcınkaya (2021) developed a decision support model including environmental and accessibility factors in Izmir.

Recently, Agac and Simsir (2022) evaluated risks and opportunities with AHP for pandemic hospitals. Hadi and Abdullah (2022) developed a web application with Cost-Effective-Impact Results Evaluation Model (MEREC) and modified TOPSIS for COVID-19 patients. Todorov and Todorova (2023) examined hospital site selection in terms of accessibility with GIS-based analysis in Bulgaria. Al Mohamed et al. (2023) integrated FAHP and Fuzzy TOPSIS methods for pandemic hospitals. Gazi et al. (2024) studied sustainable hospital site selection in Saudi Arabia using Spherical Entropy and Spherical VIKOR methods to meet the requirements of various diseases. Zandi et al. (2024) introduced a hybrid methodology combining GIS with MCDM methods for hospital site suitability in Tehran. The study used AHP, BWM, and Step-wise Weight Assessment Ratio Analysis (SWARA) to evaluate socio-environmental factors. For an in-depth literature review on the topic, the studies by Gul and Guneri (2021) and Ozkan et al. (2024) are recommended.

Method

In this study, a two-stage integrated integrated BWM and GRA method was applied for a private hospital selection problem. A review of the literature shows that these two methods are rarely used together, and the limited studies that do exist have not applied them to hospital site selection. Firstly, a decision-making team consisting of four experts working in Burdur province was formed. This decision-making team includes a doctor, a health manager, an engineer working in local government and an academician from the Industrial Engineering department. Afterwards, the main and sub-criteria to be used in the study are determined by reviewing the relevant literature, and the study is started.

In the first stage, the linear BWM method was used to determine the weights of the main criteria. While AHP is the most widely used method for this purpose, BWM, a newer approach, is less frequently applied. BWM's advantage is its reduced need for comparisons, as it only requires evaluating criteria against the best and worst options, enhancing consistency. In contrast, AHP uses pairwise comparisons for all criteria, offering more detail but requiring more effort. In the second stage, GRA was used for its strength in handling incomplete or uncertain data, making it effective even with limited information. This makes GRA suitable for real-world applications where data is restricted.

Best-Worst Method

The BWM method is one of the most recent methods developed by Rezaei (2015). As an MCDM method. In this method, the best (most important, most desirable) and worst (least important, least desirable) criteria are defined by the decision maker and a binary comparison vectors are used between best-others and worst-others to determine the weights of the criteria and the scores of the alternatives. By defining vector weight values for each alternative and criteria sets, final scores are determined and the best alternative is selected. The steps of the BWM as follows:

Step 1. Determination of decision criteria $(c_1, c_2, \dots, c_n)$ by experts.

Step 2. Determining the best and the worst criterion among the criteria. If the experts decide on two or more criteria as best or worst, the best and worst criteria are chosen arbitrarily. No comparison is made at this stage, where the decision maker determines the overall best and worst criteria.

Step 3. Determination of the preference for the best criterion over the other criteria using a number between 1 and 9. Here, 1 means that the criteria are equally important, while 9 means that the best criterion is much more important than the criterion in question. As a result, the best comparison vector $A_B = (a_{B1}, a_{B2}, \dots, a_{Bn})$ is obtained for the other criteria. Here, a_{Bj} denotes the preference of the best criterion (B) over criterion *j*. The value $a_{B_B} = 1$ signifies that the best criterion is compared to itself.

Step 4. Determination of the preference for the worst criterion relative to the other criteria using a number between 1 and 9. The worst comparison vector $A_W = (a_{1W}, a_{2W}, \dots, a_{nW})^T$ for other criteria is obtained: Here , a_{jW} denotes the preferability of criterion *j* with respect to the worst criterion (*W*). Also, since it is the same as the status of the best criterion, the value of the worst criterion compared to itself is equal to 1, $a_{W_W} = 1$. The benchmark comparison scale in Table 1 is used for the binary evaluations in Step 3 and 4.

Table 1. Benchmark comparision scale.

Scale	1	3	5	7	9	2,4,6,8
Definition of value	equal	medium	strong	very strong	absolute superiority	intermediat e values

Step 5. Finding the optimal weights of the criteria $(w_1^*, w_2^*, \dots, w_n^*)$. The most suitable weights for the criteria are given by each value pair of $\frac{w_B}{w_j} = a_{Bj}$ and $\frac{w_j}{w_w} = a_{jW}$, which are determined based on comparisons. To satisfy the conditions for all *j*, a solution must be found by minimizing the maximum absolute differences $\left|\frac{w_B}{w_j} - a_{Bj}\right|$ and $\left|\frac{w_j}{w_w} - a_{jW}\right|$ as shown in Equation (1). Considering the condition that the sum of weights equals one and that weights are non-negative, the following optimization problem is formulated:

$$\min maxS_j \left\{ \left|\frac{w_B}{w_j} - a_{Bj}\right|, \left|\frac{w_j}{w_w} - a_{jW}\right| \right\} \tag{1}$$

Under the following constraints

$$\sum_j w_j = 1, \quad w_j \geq \forall_j$$

The equation can be linearized as follows (Eq. (2)):

$$\text{Min } \mu \tag{2}$$

$$\left|\frac{w_B}{w_j} - a_{Bj}\right| \leq \mu, \qquad \left|\frac{w_j}{w_w} - a_{jW}\right| \leq \mu, \qquad \sum_j w_j = 1, \qquad w_j \geq \forall_j$$

Step 6. Determination of consistency ratios by using $\mu^*$and the consistency index value, as shown in Equation (3). To check the consistency of comparisons, the consistency index formula in Table 2 is applied. If the condition $a_{Bj}\ x\ a_{jW} = a_{BW}$ is met for all criteria *j*, the comparisons are fully consistent.

$$Consistency\ Ratio\ = \frac{\mu^*}{Consistency\ Index} \tag{3}$$

As the value approaches zero, consistency increases. Values below one are considered to have sufficient consistency (Arslanhan & Tosun, 2021).

Table 2. Consistency ındex values.

a_{BW}	1	2	3	4	5	6	7	8	9
Consistency index	0,00	0,44	1,00	1,63	2,30	3,00	3,73	4,47	5,23

Grey Relational Analysis

Deng Ju-Long introduced the Grey System Theory for the first time with his work ‘Control Problems of Grey System’ published in 1982. This theory aims to quantify uncertain information and detailed explanations of the structure of the theory were presented in the book ‘Introductions to Grey System’ published in 1989. In the Grey System, uncertain information is described as ‘black’, fully known information is described as ‘white’ and the data in between these two, which express partial information, is described as ‘grey’ (Lui & Lin, 2011). According to Lui and Lin (2011) grey systems are systems with uncertainty and these systems have two main characteristics:

Partial Information Status: Incomplete information, which is encountered in social, economic and scientific fields, includes incomplete information about parameters, structural elements, boundaries and behavioural characteristics of the system.

Data Inaccuracy: There are inherent errors in such uncertain systems and inaccuracies can be seen in conceptual, level and estimation types.

Grey numbers, which are the basic element of grey systems, are numbers whose exact value is unknown but are known to lie within a boundary range. In grey mathematics analyses, interval grey numbers with known upper and lower bounds are frequently used and are represented as ⊗a ∈ [a-,a+] (Aydemir et al., 2013). GRA is a method developed based on grey system theory and is used in relational rating, classification and decision making processes (Liu & Lin, 2006). Method aims to measure the relationship of each factor in a grey system with the reference factor and this relationship level is called ‘grey relational degree’. Used to determine the most appropriate option according to different criteria, GRA is a method that aims to select the best alternatives as a multi-criteria decision-making tool (Hinduja & Pandey, 2017; Fidan, 2018). The steps and formulation of the GRA method developed for group decision-making are as follows (Manzardo et al., 2012):

Step 1. Constructing the grey decision matrix in presence of *L* decision makers (Eq. (4)):

$$\otimes \mathrm{G}^{\mathrm{k}} = \begin{bmatrix} \otimes \mathrm{g}_{11}^{\mathrm{k}} & \cdots & \otimes \mathrm{g}_{1\mathrm{n}}^{\mathrm{k}} \\ \vdots & \ddots & \vdots \\ \otimes \mathrm{g}_{\mathrm{m}1}^{\mathrm{k}} & \cdots & \otimes \mathrm{g}_{\mathrm{mn}}^{\mathrm{k}} \end{bmatrix} \tag{4}$$

$\otimes \mathrm{g}_{\mathrm{ij}}^{\mathrm{k}} = [\mathrm{g_{ij}}^-, \mathrm{g_{ij}}^+]$, i= 1,2,3,….,m; j=1,2,……,n . $\otimes \mathrm{g}_{\mathrm{ij}}^{\mathrm{k}}$ represents the evaluation of the *i^th^* alternative by the *k^th^* decision-maker in terms of the *j^th^* criterion.

Step 2. Normalisation of the decision-making matrix. In this process, different calculation method is applied according to the criterion. If the larger value is better in the criterion, it can be called as benefit criterion (Eq. (5)), if the smaller value is better, it can be called as cost criterion and it is calculated using the relevant formula in Equation (6).

Benefit criteria: $$\otimes y_{ij}^{k} = \frac{\otimes g_{ij}^{k}}{\max_{i=1}^{m}\{\otimes g_{ij}^{k,+}\}}, \text{ i=1,2,3,….,m; j=1,2,……,n} \quad (5)$$

Non-benefit criteria: $$\otimes y_{ij}^{k} = \frac{\min_{i=1}^{m}\{\otimes g_{ij}^{k,-}\}}{\otimes g_{ij}^{k}}, \text{ i=1,2,3,….,m; j=1,2,……,n} \quad (6)$$

Step 3. Creation of standardised decision matrix and reference series. At this stage, a standardised decision matrix (Eq. (7)) is created using the values obtained in the previous step and a reference series is created from the largest values in each column of the decision matrix (Eq. (8) - (9)).

$$\otimes Y^{k} = \begin{bmatrix} \otimes y_{11}^{k} & \cdots & \otimes y_{1n}^{k} \\ \vdots & \ddots & \vdots \\ \otimes y_{m1}^{k} & \cdots & \otimes y_{mn}^{k} \end{bmatrix} \quad (7)$$

$$y^{k,0} = \{y_1^{k,0}, y_2^{k,0}, y_3^{k,0}, \ldots, y_n^{k,0}\} \quad (8)$$

$$\otimes y_j^{k,0} = \max_{i=1}^{m} y_{ij}^{k,+}, \; j = 1,2,3, \ldots\ldots, n \quad (9)$$

where $y_j^{k,0}$ is the reference value in relation to the j^{th} criterion

Step 4. Calculation of the difference between the alternatives and the reference alternative (Eq. (10), and construction of the difference matrix (Eq. (11)).

$$\otimes \Delta_{11}^{k} = \left[y_j^{k,0} - y_{ij}^{k,+}, y_j^{k,0} - y_{ij}^{k,-}\right], i = 1,2, \ldots\ldots, m; j = 1,2,3, \ldots., n \quad (10)$$

$$\otimes \Delta^{k} = \begin{bmatrix} \otimes \Delta_{11}^{k} & \cdots & \otimes \Delta_{1n}^{k} \\ \vdots & \ddots & \vdots \\ \otimes \Delta_{m1}^{k} & \cdots & \otimes \Delta_{mn}^{k} \end{bmatrix} \quad (11)$$

Step 5. Creation of the grey relationship coefficient by Equation (12), (13), and (14). Here, $\otimes \varepsilon_{ij}^{k}$ represents the grey relational coefficient. ρ is the distinguishing coefficient, which takes values between 0 and 1, and in this study, it is set to 0.5.

$$\otimes \varepsilon_{ij}^{k} = [\otimes \varepsilon_{ij}^{k,-}, \otimes \varepsilon_{ij}^{k,+}] \quad (12)$$

$$\otimes \varepsilon_{ij}^{k,-} = \frac{\min_{i=1}^{m}\min_{j=1}^{m}\otimes\Delta_{ij}^{k,-} + \rho\max_{i=1}^{m}\max_{j=1}^{m}\otimes\Delta_{ij}^{k,+}}{\otimes\Delta_{ij}^{k,+} + \rho\max_{i=1}^{m}\max_{j=1}^{m}\otimes\Delta_{ij}^{k,+}} \quad (13)$$

$$\otimes \varepsilon_{ij}^{k,+} = \frac{\min_{i=1}^{m}\min_{j=1}^{m}\otimes\Delta_{ij}^{k,-} + \rho\max_{i=1}^{m}\max_{j=1}^{m}\otimes\Delta_{ij}^{k,+}}{\otimes\Delta_{ij}^{k,-} + \rho\max_{i=1}^{m}\max_{j=1}^{m}\otimes\Delta_{ij}^{k,+}} \quad (14)$$

Step 6. Calculation of the grey relational degree: The grey relational coefficients are multiplied by the weight of the corresponding criterion and then summed for each alternative to obtain the grey relational degree (Eq. (15).

$$\otimes \gamma_i^{k} = \sum_{j=1}^{n} \otimes \varepsilon_{ij}^{k} \otimes \omega_j \quad (15)$$

Step 7. Clarification of the grey relational degree (Eq. (16)).

$$\otimes \gamma_i^{k} = [\gamma_i^{k,-}, \gamma_i^{k,+}], \quad \gamma_i^{k} = \frac{\gamma_i^{k,-} + \gamma_i^{k,+}}{2} \quad (16)$$

Step 8. Group decision making and sorting by Equation (17).

$$\gamma_i = \left(\prod_{k=1}^{L} \gamma_i^k\right)^{1/L} \tag{17}$$

Results and Discussion

A review of studies shows that the most frequently used criteria for hospital site selection are access, cost factors, population density and demographics, environmental factors, proximity to existing health services, government and policy influence, adequacy of infrastructure, presence of competition, risk and safety considerations, and community and urban factors - community support, land use compatibility and environmental effects. These criteria are important in terms of access to health services, cost-effectiveness and social-environmental harmony by addressing operational and strategic issues in hospital site selection decisions. The study considered criteria proposed by Gun and Guneri (2021). Which are thought to provide valuable insights for research in this field. These criteria and sub-criteria are listed below.

- c_1: Cost criteria (capital cost, demand cost, land use cost)
- c_2: Demand criteria (population quantity, population density, population age distribution)
- c_3: Location criteria (distance to arteries&main roads, distance to medical suppliers, distance to residential & social life)
- c_4: Firm strategy, structure&competitors (management objective, competitor hospitals, policy maker's attitude)
- c_5: Related and supporting sectors (medicine and pharmacy sector, health sector, hospital management sector)
- c_6: Govermental criteria (qualifications & regulations & tax, promotion of medical network, promulgating tasks)
- c_7: Chance (sharp change in demand, unusual fluctuations in production cost, financial changes & exchange rate)

In the evaluation made by the decision-makers, the cost and chance criteria were considered non-benefit, while the other criteria were evaluated as benefit criteria. Also, the location criterion is based on proximity, and the chance criterion, which can be viewed in a positive sense, was assumed as unexpected and undesirable situations. After determination of criteria, firstly, the best/worst criteria selected for linear BWM according to the benchmark comparison scale, along with the pairwise comparisons made by the decision makers, are shown in Table 3 and Table 4.

Table 3. Binary comparison between best criteria and other criteria.

Decision makers	best	c_1	c_2	c_3	c_4	c_5	c_6	c_7
DM_1	c_2	3	1	4	8	7	6	9
DM_2	c_1	1	3	4	7	6	4	9
DM_3	c_3	2	4	1	6	5	3	9
DM_4	c_2	2	1	3	5	7	6	9

Table 4. Binary comparison between worst criteria and other criteria.

criteria	DM_1 worst c_7	DM_2 worst c_7	DM_3 worst c_7	DM_4 worst c_7
c_1	7	9	7	7
c_2	9	7	8	9
c_3	6	6	9	6
c_4	2	4	5	5
c_5	4	5	5	4
c_6	3	3	3	3
c_7	1	1	1	1

In the evaluation made by the decision-makers, the cost and chance criteria are considered non-benefit, while the other criteria are evaluated as benefit criteria. Also, the location criterion was assumed to be proximity, and the chance criterion, which can be viewed in a positive sense, is assumed to be unexpected and undesirable situations.

Subsequently, the criteria weights, associated threshold, and input-based consistency ratios, calculated using Eq. (1), (2), and (3), are presented in Table 5, thus concluding the first stage in which linear BWM is applied. The BWM assesses criteria importance ratios but has some limitations: lack of immediate consistency feedback, ordinal consistency consideration, and reliability thresholds. Liang et al. (2020) introduced an input-based cardinal consistency for immediate feedback, along with an ordinal measure to align pairwise comparison order with results, providing balanced thresholds. This method was adopted to the study.

Table 5. Calculated weight and consistency ratios.

Decision makers	Criteria Weights							Associated Threshold	Input-Based CR
	w_1^*	w_2^*	w_3^*	w_4^*	w_5^*	w_6^*	w_7^*		
DM_1	0.17	0.43	0.13	0.07	0.07	0.09	0.04	0.35	0.26
DM_2	0.40	0.16	0.12	0.07	0.08	0.12	0.03	0.35	0.29
DM_3	0.22	0.11	0.34	0.07	0.09	0.15	0.03	0.35	0.32
DM_4	0.22	0.37	0.15	0.09	0.06	0.07	0.03	0.35	0.26
w_j^*/n	0.25	0.27	0.19	0.07	0.08	0.11	0.03		

In the initial step of the second GRA evaluation stage, decision-makers' opinions on the options are gathered using grey numbers (Table 6) for each criterion, creating the decision matrix ($\otimes \mathrm{G}^{\mathrm{k}}$) presented in Table 7. The reference series values are italicized according to the nature of the criteria.

Table 6. The scale of grey number for the assessment of the alternative.

Criteria	Abbreviation	Scale of grey number
Very low	VL	(1.5,3.0)
Low	L	(3.0,4.5)
Medium	M	(4.5,6.0)
High	H	(6.0,7.5)
Very high	VH	(7.5,9.0)

Table 7. Decision matrix.

$\otimes \mathrm{G}^{\mathrm{k}}$		c_1 Non beneficial	c_2 Beneficial	c_3 Beneficial	c_4 Beneficial	c_5 Beneficial	c_6 Beneficial	c_7 Non beneficial
	a_1	(7.5 , 9.0)	(7.5 , *9.0*)	(7.5 , *9.0*)	(6.0 , *7.5*)	(7.5 , *9.0*)	(7.5 , *9.0*)	(4.5 , 6.0)
DM_1	a_2	(4.5 , 6.0)	(3.0 , 4.5)	(4.5 , 6.0)	(4.5 , 6.0)	(1.5 , 3.0)	(6.0 , 7.5)	(*3.0* , 4.5)
	a_3	(*3.0* , 4.5)	(3.0 , 4.5)	(4.5 , 6.0)	(4.5 , 6.0)	(3.0 , 4.5)	(6.0 , 7.5)	(3.0 , 4.5)
	a_1	(7.5 , 9.0)	(7.5 , *9.0*)	(7.5 , *9.0*)	(6.0 , *7.5*)	(7.5 , *9.0*)	(6.0 , *7.5*)	(7.5 , 9.0)
DM_2	a_2	(*3.0* , 4.5)	(4.5 , 6.0)	(3.0 , 4.5)	(4.5 , 6.0)	(6.0 , 7.5)	(4.5 , 6.0)	(*4.5* , 6.0)
	a_3	(3.0 , 4.5)	(4.5 , 6.0)	(4.5 , 6.0)	(4.5 , 6.0)	(4.5 , 6.0)	(4.5 , 6.0)	(4.5 , 6.0)
	a_1	(7.5 , 9.0)	(7.5 , *9.0*)	(7.5 , *9.0*)	(6.0 , *7.5*)	(6.0 , 7.5)	(4.5 , 6.0)	(7.5 , 9.0)
DM_3	a_2	(4.5 , 6.0)	(6.0 , 7.5)	(3.0 , 4.5)	(4.5 , 6.0)	(3.0 , 4.5)	(1.5 , 3.0)	(*4.5* , 6.0)
	a_3	(*1.5* , 3.0)	(4.5 , 6.0)	(3.0 , 4.5)	(3.0 , 4.5)	(7.5 , *9.0*)	(6.0 , *7.5*)	(4.5 , 6.0)
	a_1	(7.5 , 9.0)	(7.5 , *9.0*)	(7.5 , *9.0*)	(6.0 , *7.5*)	(7.5 , *9.0*)	(6.0 , *7.5*)	(6.0 , 7.5)
DM_4	a_2	(6.0 , 7.5)	(4.5 , 6.0)	(6.0 , 7.5)	(3.0 , 4.5)	(1.5 , 3.0)	(4.5 , 6.0)	(*4.5* , 6.0)
	a_3	(*3.0* , 4.5)	(4.5 , 6.0)	(4.5 , 6.0)	(4.5 , 6.0)	(6.0 , 7.5)	(4.5 , 6.0)	(4.5 , 6.0)

In Step 2, the decision matrix was normalized, and in Step 3, the standardized decision matrix $\otimes \mathrm{Y}^{\mathrm{k}}$ and the reference series were created (Table 8).

Table 8. Standardized decision matrix.

$\otimes \mathrm{y}_{\mathrm{ij}}^{\mathrm{k}}$		c_1	c_2	c_3	c_4	c_5	c_6	c_7
$\mathbf{y}^{\mathbf{k,0}}$		1.00	1.00	1.00	1.00	1.00	1.00	1.00
	a_1	(0.33 , 0.40)	(0.83 , 1.00)	(0.83 , 1.00)	(0.80 , 1.00)	(0.83 , 1.00)	(0.83 , 1.00)	(0.50 , 0.67)
DM_1	a_2	(0.50 , 0.67)	(0.33 , 0.50)	(0.50 , 0.67)	(0.60 , 0.80)	(0.17 , 0.33)	(0.67 , 0.83)	(0.67 , 1.00)
	a_3	(0.67 , 1.00)	(0.33 , 0.50)	(0.50 , 0.67)	(0.60 , 0.80)	(0.33 , 0.50)	(0.67 , 0.83)	(0.67 , 1.00)
DM_2	a_1	(0.33 , 0.40)	(0.83 , 1.00)	(0.83 , 1.00)	(0.80 , 1.00)	(0.83 , 1.00)	(0.80 , 1.00)	(0.50 , 0.60)

	a_2	(0.67 , 1.00)	(0.50 , 0.67)	(0.33 , 0.50)	(0.60 , 0.80)	(0.67 , 0.83)	(0.60 , 0.80)	(0.75 , 1.00)
	a_3	(0.67 , 1.00)	(0.50 , 0.67)	(0.50 , 0.67)	(0.60 , 0.80)	(0.50 , 0.67)	(0.60 , 0.80)	(0.75 , 1.00)
	a_1	(0.17 , 0.20)	(0.83 , 1.00)	(0.83 , 1.00)	(0.80 , 1.00)	(0.67 , 0.83)	(0.60 , 0.80)	(0.50 , 0.60)
DM_3	a_2	(0.25 , 0.33)	(0.67 , 0.83)	(0.33 , 0.50)	(0.60 , 0.80)	(0.33 , 0.50)	(0.20 , 0.40)	(0.75 , 1.00)
	a_3	(0.50 , 1.00)	(0.50 , 0.67)	(0.33 , 0.50)	(0.40 , 0.60)	(0.83 , 1.00)	(0.80 , 1.00)	(0.75 , 1.00)
	a_1	(0.33 , 0.40)	(0.83 , 1.00)	(0.83 , 1.00)	(0.80 , 1.00)	(0.83 , 1.00)	(0.80 , 1.00)	(0.50 , 0.67)
DM_4	a_2	(0.40 , 0.50)	(0.50 , 0.67)	(0.67 , 0.83)	(0.40 , 0.60)	(0.17 , 0.33)	(0.60 , 0.80)	(0.75 , 1.00)
	a_3	(0.67 , 1.00)	(0.50 , 0.67)	(0.50 , 0.67)	(0.60 , 0.80)	(0.67 , 0.83)	(0.60 , 0.80)	(0.75 , 1.00)

In Step 4, the difference matrix ($\otimes\Delta^k$) was created with the weights of criterias in Table 9.

Table 9. Difference matrix.

$\otimes\Delta^k$		c_1	c_2	c_3	c_4	c_5	c_6	c_7
	a_1	(0.60 , 0.67)	(0.00 , 0.17)	(0.00 , 0.17)	(0.00 , 0.20)	(0.00 , 0.17)	(0.00 , 0.17)	(0.33 , 0.50)
DM_1	a_2	(0.33 , 0.50)	(0.50 , 0.67)	(0.33 , 0.50)	(0.20 , 0.40)	(0.67 , 0.83)	(0.17 , 0.33)	(0.00 , 0.33)
	a_3	(0.00 , 0.33)	(0.50 , 0.67)	(0.33 , 0.50)	(0.20 , 0.40)	(0.50 , 0.67)	(0.17 , 0.33)	(0.00 , 0.33)
	a_1	(0.60 , 0.67)	(0.00 , 0.17)	(0.00 , 0.17)	(0.00 , 0.20)	(0.00 , 0.17)	(0.00 , 0.20)	(0.40 , 0.50)
DM_2	a_2	(0.00 , 0.33)	(0.33 , 0.50)	(0.50 , 0.67)	(0.20 , 0.40)	(0.17 , 0.33)	(0.20 , 0.40)	(0.00 , 0.25)
	a_3	(0.00 , 0.33)	(0.33 , 0.50)	(0.33 , 0.50)	(0.20 , 0.40)	(0.33 , 0.50)	(0.20 , 0.40)	(0.00 , 0.25)
	a_1	(0.80 , 0.83)	(0.00 , 0.17)	(0.00 , 0.17)	(0.00 , 0.20)	(0.17 , 0.33)	(0.20 , 0.40)	(0.40 , 0.50)
DM_3	a_2	(0.67 , 0.75)	(0.17 , 0.33)	(0.50 , 0.67)	(0.20 , 0.40)	(0.50 , 0.67)	(0.60 , 0.80)	(0.00 , 0.25)
	a_3	(0.00 , 0.50)	(0.33 , 0.50)	(0.50 , 0.67)	(0.40 , 0.60)	(0.00 , 0.17)	(0.00 , 0.20)	(0.00 , 0.25)
	a_1	(0.60 , 0.67)	(0.00 , 0.17)	(0.00 , 0.17)	(0.00 , 0.20)	(0.00 , 0.17)	(0.00 , 0.20)	(0.33 , 0.50)
DM_4	a_2	(0.50 , 0.60)	(0.33 , 0.50)	(0.17 , 0.33)	(0.40 , 0.60)	(0.67 , 0.83)	(0.20 , 0.40)	(0.00 , 0.25)
	a_3	(0.00 , 0.33)	(0.33 , 0.50)	(0.33 , 0.50)	(0.20 , 0.40)	(0.17 , 0.33)	(0.20 , 0.40)	(0.00 , 0.25)

In Step 5, the grey relational coefficients were calculated by multiplying and summing the grey relation coefficients and the criterion weights obtained by the decision-makers using the BWM method, presented in Table 10.

Table 10. Grey relational coefficients.

w		c_1 0.25	c_2 0.27	c_3 0.19	c_4 0.07	c_5 0.08	c_6 0.11	c_7 0.03
	a_1	(0.38 , 0.41)	(0.71 , 1.00)	(0.71 , 1.00)	(0.67 , 1.00)	(0.71 , 1.00)	(0.71 , 1.00)	(0.45 , 0.56)
DM_1	a_2	(0.45 , 0.56)	(0.38 , 0.45)	(0.45 , 0.56)	(0.51 , 0.67)	(0.33 , 0.38)	(0.56 , 0.71)	(0.56 , 1.00)
	a_3	(0.56 , 1.00)	(0.38 , 0.45)	(0.45 , 0.56)	(0.51 , 0.67)	(0.38 , 0.45)	(0.56 , 0.71)	(0.56 , 1.00)
	a_1	(0.33 , 0.36)	(0.66 , 1.00)	(0.66 , 1.00)	(0.63 , 1.00)	(0.66 , 1.00)	(0.63 , 1.00)	(0.40 , 0.46)
DM_2	a_2	(0.50 , 1.00)	(0.40 , 0.50)	(0.33 , 0.40)	(0.46 , 0.63)	(0.50 , 0.66)	(0.46 , 0.63)	(0.57 , 1.00)
	a_3	(0.50 , 1.00)	(0.40 , 0.50)	(0.33 , 0.40)	(0.46 , 0.63)	(0.40 , 0.50)	(0.46 , 0.63)	(0.57 , 1.00)
	a_1	(0.33 , 0.34)	(0.71 , 1.00)	(0.71 , 1.00)	(0.67 , 1.00)	(0.56 , 0.71)	(0.51 , 0.67)	(0.45 , 0.51)
DM_3	a_2	(0.36 , 0.38)	(0.56 , 0.71)	(0.38 , 0.45)	(0.51 , 0.67)	(0.38 , 0.45)	(0.34 , 0.41)	(0.62 , 1.00)
	a_3	(0.45 , 1.00)	(0.45 , 0.56)	(0.38 , 0.45)	(0.41 , 0.51)	(0.71 , 1.00)	(0.67 , 1.00)	(0.62 , 1.00)
	a_1	(0.38 , 0.41)	(0.71 , 1.00)	(0.71 , 1.00)	(0.67 , 1.00)	(0.71 , 1.00)	(0.67 , 1.00)	(0.45 , 0.56)
DM_4	a_2	(0.41 , 0.45)	(0.45 , 0.56)	(0.56 , 0.71)	(0.41 , 0.51)	(0.33 , 0.38)	(0.51 , 0.67)	(0.62 , 1.00)
	a_3	(0.56 , 1.00)	(0.45 , 0.56)	(0.45 , 0.56)	(0.51 , 0.67)	(0.56 , 0.71)	(0.51 , 0.67)	(0.62 , 1.00)

The γ_i^k values were obtained by clarification in Step 6 - 7, as shown in Table 11.

Table 11. Clarification of the grey relational degree

		$\gamma_i^{k,-}$	$\gamma_i^{k,+}$	γ_i^{k}			$\gamma_i^{k,-}$	$\gamma_i^{k,+}$	γ_i^{k}
	a_1	0.6176	0.8389	0.7283		a_1	0.5663	0.8232	0.6948
DM_1	a_2	0.4431	0.5534	0.4983	DM_2	a_2	0.4371	0.6580	0.5476
	a_3	0.4729	0.6699	0.5714		a_3	0.4289	0.6453	0.5371
	a_1	0.5711	0.7616	0.6664		a_1	0.6138	0.8389	0.7263
DM_3	a_2	0.4347	0.5318	0.4832	DM_4	a_2	0.4605	0.5690	0.5148
	a_3	0.4868	0.7422	0.6145		a_3	0.5028	0.7145	0.6086

In the final step, the alternatives were scored, identifying Alternative $_3$ as the highest-ranking option (Table 12).

Table 12. Scores obtained for the alternatives.

Alternative $_1$	0.7035
Alternative $_2$	0.5104
Alternative $_3$	0.5821

Conclusion

Hospital site selection is critical for efficient delivery of healthcare services and accessible service provision to the community. Appropriate site selection not only improves patient access and comfort, but also affects operating costs, resource allocation and long-term sustainability of the service. Effective hospital site selection improves public health, shortens response times and ensures that services reach a wide segment of the population.

In this study, BWM and GRA MCDM methods were used to determine the most appropriate site for a private hospital in Burdur province. BWM is a simple and fast method that allows decision makers to determine weights by comparing only the best and worst criteria, and it provides more reliable results by reducing comparison errors. In addition, its flexibility allows it to be used effectively in various fields. GRA, on the other hand, provides an objective approach to comparing alternatives and determining the most appropriate option by providing robust results even when data are uncertain or incomplete. Both methods provide decision makers with a flexible, reliable and practical solution, making them the preferred tools in complex decision-making processes.

The decision-making group consisting of four experts in the field evaluated the alternative three sites in the light of seven criteria. In the first stage, the criteria were weighted with the linear BWM method, and then grey numbers were used in the evaluation of three alternatives. The results revealed that the most suitable site for a privata hospital according to the determined criteria is Alternative$_1$. It is obvious that such analyses are an effective decision support tool for the development of health infrastructure and will help health institutions to make more informed, data-driven decisions.

The proposed method, which have been used together in only a limited number of studies in the literature, are considered a promising alternative when applied in a hierarchical structure or combined with other methods, especially given the complexity of real-world MCDM problems.

Scientific Ethics Declaration

The author declares that the scientific ethical and legal responsibility of this article published in EPSTEM Journal belongs to the author.

Acknowledgements or Notes

* This article was presented as an oral presentation at the International Conference on Technology, Engineering and Science (www.icontes.net) held in Antalya/Turkey on November 14-17, 2024.

References

Adalı, E. A., & Tus, A. (2021). Hospital site selection with distance-based multi-criteria decision-making methods. *International Journal of Healthcare Management*, *14*(2), 534-544.

Agac, G., & Simsir, I. (2022). Optimal site selection of a pandemic hospital using multi-criteria decision-making approach. *International Journal of the Analytic Hierarchy Process*, *14*(1), 946.

Al Mohamed, A. A., Al Mohamed, S., & Zino, M. (2023). Application of fuzzy multicriteria decision-making model in selecting pandemic hospital site. *Future Business Journal*, *9*(1), 14.

Arslanhan, H., & Tosun, O. (2021). Ulastırma modu secimi probleminin bütünleşik en iyi-en kötü ve WASPAS yontemleriyle çözülmesi. *Pamukkale Universitesi Mühendislik Bilimleri Dergisi*, *27*(1), 13-23.

Aydemir, E., Yalcınkaya, A., & Tas, E. (2013). Grey system theory and its applications in decision making problems. *Academic Journal of Research in Social Science, 1*(1), 89-102.

Aydın, O. (2009). Hospital location selection for Ankara with Fuzzy AHP. *Journal of the Faculty of Economics and Administrative Sciences, Dokuz Eylul University*, *24*(2), 87-104.

Chatterjee, D., & Mukherjee, B. (2013). Potential hospital location selection using fuzzy-AHP: an empirical study in Rural India. *International Journal of Innovative Technology and Research*, *1*(4), 304-314.

Celikbilek, Y. (2018). Group decision making for hospital location selection using VIKOR under fuzzy environment. *Istanbul Gelisim University Journal of Health Sciences*, *(5),* 435-450.

Dehe, B., & Bamford, D. (2015). Development, test and comparison of two multiple criteria decision analysis (MCDA) models: A case of healthcare infrastructure location. *Expert Systems with Applications*, *42*(19), 6717-6727.

Dell'Ovo, M., Capolongo, S., & Oppio, A. (2018). Combining spatial analysis with MCDA for the siting of healthcare facilities. *Land use policy*, *76*, 634-644.

Fidan, H. (2018). E-ticaret musteri baglılıgı gri iliskisel kumeleme analizi. *AJIT-e: Academic Journal of Information Technology*, *9*(32), 163-182.

Gazi, K. H., Momena, A. F., Salahshour, S., Mondal, S. P., & Ghosh, A. (2024). Synergistic strategy of sustainable hospital site selection in Saudi Arabia using spherical fuzzy MCDM methodology. *Journal of Uncertain Systems*, 2450004.

Gul, M., & Guneri, A. F. (2021). Hospital location selection: A systematic literature review on methodologies and applications. *Mathematical Problems in Engineering*, *2021*(1), 6682958.

Hadi, A., & Abdullah, M. Z. (2022). Web and IoT-based hospital location determination with criteria weight analysis. *Bulletin of Electrical Engineering and Informatics*, *11*(1), 386-395.

Hinduja, A., & Pandey, M. (2017). Multicriteria recommender system for life insurance plans based on utility theory. *Indian Journal of Science and Technology*, *10*(14), 1-8.

Khaksefidi, M., & Miri, M. (2016). Hospital location in the Southern Fars province by using multi criteria decision making techniques. *European Online Journal of Natural and Social Sciences: Proceedings*, *4*(3 (s)), 638.

Kmail, A., Jubran, J., Sabbah, W., & Jenin, P. (2017). Coupling GIS-based MCA and AHP techniques for hospital site selection. *International Journal of Computer Science and Information Security (IJCSIS)*, *15*(12), 49-56.

Kumar, P., Singh, R. K., & Sinha, P. (2016). Optimal site selection for a hospital using a fuzzy extended ELECTRE approach. *Journal of Management Analytics*, *3*(2), 115-135.

Liang, F., Brunelli, M., & Rezaei, J. (2020). Consistency issues in the best worst method: Measurements and thresholds. *Omega*, *96*, 102175.

Lin, C. T., Wu, C. R., & Chen, H. C. (2008). The study of construct key success factors for the Taiwanese hospitals of location selection by using the fuzzy AHP and sensitivity analysis. *International journal of Information and Management Sciences*, *19*(1), 175-200.

Liu, S., & Lin, Y. (2006). *Grey prediction*. London: Springer.

Liu, S., & Lin, Y. (2011). Introduction to grey systems theory. In *Grey systems: Theory and applications* (Vol.8, pp.1-18).

Manzardo, A., Ren, J., Mazzi, A., & Scipioni, A. (2012). A grey-based group decision-making methodology for the selection of hydrogen technologies in life cycle sustainability perspective. *International Journal of Hydrogen Energy*, *37*(23), 17663-17670.

Mic, P., & Antmen, Z. F. (2019). A healthcare facility location selection problem with the Fuzzy TOPSIS method for a regional hospital. *European Journal of Science and Technology,* (16), 750–757.

Neisani Samani, Z., & Alesheikh, A. A. (2019). Uncertainty modelling of citizen-centered group decision making using fuzzy-vikor case study: Site selection of healthcare services. *The International Archives of the Photogrammetry, Remote Sensing and Spatial Information Sciences*, *42*, 809-814.

Nsaif, Q. A., Khaleel, S. M., & Khateeb, A. H. (2020). Integration of GIS and remote sensing technique for hospital site selection in Baquba district. *Journal of Engineering Science and Technology, 15*(3), 1492-1505.

Ozkan, B., Ozdemir, Y., Yıldırım, M., & Kavak, H. (2024). Hospital location selection: A literature review. *Journal of Engineering and Basic Sciences, 2*, 63-71.

Rezaei, J. (2015). Best-worst multi-criteria decision-making method. *Omega*, *53*, 49-57.

Rezayee, M. (2020). Hospital site selection in Iskandar Malaysia using GIS-multi criteria analysis. *Int J Basic Sci Appl Comput*, *2*(10), 8-15.

Sutcuoglu, G. G., & Yalcınkaya, S. (2021). AHP and GIS based multi-criteria site suitibility approach for hospitals in scope of sustainable environmental planning–case study Aliaga, Izmir. *JENAS Journal of Environmental and Natural Studies*, *3*(3), 258-270.

Sahin, T., Ocak, S., & Top, M. (2019). Analytic hierarchy process for hospital site selection. *Health Policy and Technology*, *8*(1), 42-50.

Todorov, L., & Todorova, E. (2023). GIS-based location analysis for hospital site selection: A case study on national children's hospital in Sofia, Bulgaria. *Journal of the Bulgarian Geographical Society*, *49*, 3-15.

Wu, J., & Zhou, L. (2012). *GIS-Based multi-criteria analysis for hospital selection in Haidian district of Beijing.* (Master's thesis, University of Gävle, Faculty of Engineering and Sustainable Development).

Zandi, I., Pahlavani, P., Bigdeli, B., Lotfata, A., Alesheikh, A. A., & Garau, C. (2024). GIS-enabled multi-criteria assessment for hospital site suitability: A case study of Tehran. *Sustainability*, *16*(5), 2079.

Author Information

Mustafa Serdar Toksoy
Burdur Mehmet Akif Ersoy University,
Industrial Engineering Department,
Istiklal Kampus,15030, Burdur-Türkiye
Contact e-mail: *mstoksoy@mehmetakif.edu.tr*

To cite this article:

Toksoy, M.S. (2024). Integrated best-worst method and gray relational analysis for hospital location selection: The case of Burdur province. *The Eurasia Proceedings of Science, Technology, Engineering & Mathematics (EPSTEM), 32*, 342-352.

The Eurasia Proceedings of Science, Technology, Engineering & Mathematics (EPSTEM)
ISSN: 2602-3199

The Eurasia Proceedings of Science, Technology, Engineering & Mathematics (EPSTEM), 2024

Volume 32, Pages 353-359

IConTES 2024: International Conference on Technology, Engineering and Science

Evaluation of Glutathione-Related Antioxidant Enzyme Activity in Patients with Polycystic Ovary Syndrome (PCOS) and Investigation of Clinical Correlations

Ali Hameed Mahmood Al-Qaysi
University of Cankiri Karatekin

Sevki Adem
University of Cankiri Karatekin

Omeed Akbar Ali-Ali
University of Tikrit

Abstract: The aim of this study was to illustrate the importance of glutathione-associated enzymes as vital markers of antioxidant/oxidant activity in PCOS disease. Our study comprised a cohort of forty patients, all of whom were above the age of 18 and had been diagnosed with Polycystic Ovary Syndrome (PCOS) according to the 2003 Rotterdam diagnostic criteria. In addition, we recruited forty healthy individuals who were free from any metabolic disorders. The Rotterdam diagnostic criteria for polycystic ovarian syndrome consist of three main factors: oligo-anovulation, clinical and/or biochemical hyperandrogenism, and ultrasonographic confirmation of polycystic ovaries. Individuals who satisfied at least two of the three criteria were categorized as having Polycystic Ovary Syndrome (PCOS). The levels of gamma-glutamyl transferase (GGT) and delta-glutamyl cysteine synthetase (γ-GCS) in serum samples from both patients and controls were measured using the enzyme-linked immunosorbent assay (ELISA) technique. The study examined the levels of essential enzymes involved in glutathione metabolism in patients with PCOS. The enzymes displayed significant differences between PCOS patients and control groups, indicating that glutathione metabolism plays a pivotal role in the progression of this disease. After conducting correlation analysis, it is clear that enzymes have a reciprocal impact on the progression of the disease. The analytical findings suggest that there was no statistically significant disparity in GGT levels between the PCOS group and the control group ($p>0.05$). The levels of γ-GCS were significantly higher in the PCOS group compared to the control group ($P< 0.05$). Considering the involvement of γ-GCS in the process of glutathione catalysis, it is postulated that its concentrations would increase in response to an elevation in glutathione levels. Our analysis of the available evidence leads us to conclude that glutathione will exert a substantial influence on the mechanism of PCOS. Polycystic ovarian syndrome (PCOS) is a notable medical illness that frequently affects women and has a substantial influence on their overall well-being.

Keywords: Polycystic ovary syndrome, Antioxidant, Gamma-glutamyl transferase, Gamma-glutamyl cysteine synthetase

Introduction

Polycystic ovary syndrome (PCOS) is a medical disorder characterized by ovarian dysfunction, elevated levels of male hormones (hyperandrogenism), and the presence of several cysts in the ovaries as observed through ultrasound imaging (multicyclic ovarian morphology) (Fathi, 2023). Although it is the most common hormonal problem among women of reproductive age, the precise origin of this disease remains incompletely understood

(Baqer et al., 2017). Nevertheless, it is hypothesized that the present expression of the illness arises in individuals with a susceptible genetic predisposition, which is altered by specific environmental factors (Trent & Gordon, 2020). Polycystic ovarian syndrome has a wide array of clinical symptoms that are diverse and varied. Elevated levels of androgens in the bloodstream are indicative of hyperandrogenism. In addition, it can present itself through dermatological symptoms such as hirsutism (abnormal hair growth), acne, and androgenic alopecia (male pattern hair loss). Ovarian failure commonly manifests as infrequent menstrual periods, known as oligomenorrhea, and can ultimately result in the inability to conceive, also known as infertility. Individuals with Polycystic Ovary Syndrome (PCOS) often encounter metabolic complications such as insulin resistance and obesity (Melkiyur et al., 2023). Studies have shown that women diagnosed with polycystic ovarian syndrome have an increased vulnerability to various mood and anxiety disorders, as well as problems associated to their endocrine and metabolic systems (Cunha & Póvoa, 2021 ; Buczinski et al.,2023) observed a correlation between the occurrence of acne and depression (Buczinski et al., 2020). In addition, a study carried out in Turkey showed hirsutism and monthly irregularity as notable risk factors for patients, as reported by Chen et al. (2020). In 1990, the National Institutes of Health (NIH) created specific guidelines for diagnosing polycystic ovarian syndrome (PCOS). The criteria for diagnosis include the presence of clinical/biochemical hyperandrogenism and recurrent irregular anovulatory menstrual cycles. However, it was later found that the two criteria set by the National Institutes of Health (NIH) may not be sufficient for diagnosing polycystic ovarian syndrome (PCOS) in later years. Research has discovered that individuals with less severe features, such as normal levels of androgens and regular ovulation, can also experience PCOS, as shown by ultrasonographic evidence. Following that, PCOS was categorized into four separate clinical phenotypes according to the Rotterdam criteria, which were published in 2003 by Esher and ASRM in 2004. Serum gamma-glutamyl transferase (GGT) and gamma-glutamyl cysteine synthetase (γ-GCS) play a role in the oxidant/antioxidant system of eukaryotes. The aim of this study was to enhance our comprehension of the progression of the disease by measuring the quantities of crucial enzymes involved in glutathione metabolism in women diagnosed with PCOS and healthy volunteers.

Materials and Methods

The study was conducted in accordance with the principles described in the World Medical Association Declaration of Helsinki, after obtaining approval from the ethics committee. The study was undertaken independently, without any financial support.

Patients' Inclusion Criteria

Our study involved a sample of forty adult patients who were diagnosed with polycystic ovarian syndrome (PCOS) based on the 2003 Rotterdam diagnostic criteria. In addition, we recruited forty healthy individuals who did not have any metabolic conditions to serve as a control group. The Rotterdam diagnostic criteria for polycystic ovarian syndrome consist of three main factors: oligo-anovulation, clinical and/or biochemical hyperandrogenism, and ultrasonographic confirmation of polycystic ovaries. Individuals who satisfied at least two of the three criteria were categorized as having Polycystic Ovary Syndrome (PCOS).

Studying Parameters

The quantification of GGT and γ-GCS was performed using the double sandwich ELISA technique. The enzyme-linked immunosorbent test (ELISA) is largely recognised as the most dependable technique for identifying disease-associated biomarkers in clinical laboratories worldwide. Neurological disorders, malignancies, and inflammatory diseases can be diagnosed with ELISA tests that are available for purchase. Subtle nuances in facial expression can facilitate the identification of many biomarkers linked to illness. The enzyme-linked immunosorbent assay (ELISA) was developed from a radioimmunoassay (RIA) created by Hoffman (1973). In a traditional ELISA, antibodies are used to fix antigens onto an ELISA plate, which acts as a rigid support composed of plastic. Afterwards, an enzyme is used to convert the substrate into a detectable signal. The level of the antigen is directly proportional to the strength of the signal (Klumpp Thomas et al., 2021). Thus, ELISA can be employed to detect the antigen and ascertain its quantity. The procedure entails the step-by-step introduction of ELISA components onto the test plate, followed by a period of incubation and subsequent analysis of the obtained results. An ELISA assay has several crucial elements, namely antigen, substrate, secondary antibody, enzyme-conjugated antibody, and primary antibody. During ELISA, various buffers are used to dilute the components, eliminate any surplus chemicals, occupy any vacant areas on the plate, and terminate the substrate reaction. Over the course of time, various iterations of ELISA have been created in order to enhance the assay's specificity, decrease interference, and enhance sensitivity. The five predominant types of these procedures comprise direct ELISA, indirect ELISA, sandwich ELISA, competitive ELISA, and ELISA utilising nanoparticles. The interaction between antigens and antibodies remains constant in all ELISA formats; however, the order and quantity of steps involved may vary (Williams et al., 2016).

Gamma-Glutamyl Transferase (GGT)

The samples, kit reagents, and microplate utilized in the investigation were allowed to equilibrate to room temperature. The concentration of human GGT in the samples was determined using the enzyme-linked immunosorbent assay (ELISA) technique, with the aid of a kit provided by Bioassay Technology Laboratory (Catalogue No: E6022Hu, China). This kit uses the biotinylated double sandwich method for measurement. This kit uses a microplate that has been pre-coated with a purified rat monoclonal GGT antibody. 50 µL of GGT standards (2400, 1200, 600, 300, and 150 ng/L) and 40 µL of samples were added to the wells. A volume of 10 microliters of biotinylated anti-GGT antibody was added to the samples. Subsequently, 50 µL of streptavidin-HRP was added to both the samples and standards. Subsequently, the mixture was transferred to a Sanyo Sterilizer incubator, a device manufactured in Japan, and kept at a constant temperature of 37 °C for a period of 1 hour. After the incubation period ended, the ELISA (Biotek ELx50, USA) was cleaned using a specialized washing apparatus. Afterwards, 50 µL of Chromogen A and Chromogen B solutions were added and placed in a light-restricted environment at a temperature of 37 ^{o}C for 15 minutes. The reaction was stopped by putting it to darkness to enhance color formation, and then introducing an acidic solution. The color intensity was quantified at a wavelength of 450 nm using an ELISA reader (Biotek ELx800, USA). The GGT levels were assessed using conventional graphical techniques (Gnawali et al., 2021).

Gamma-Glutamyl-Cysteine Synthetase (γ-GCS)

The samples, kit reagents, and microplate designated for the enquiry were allowed to equilibrate to the surrounding temperature. The amount of human γ-GCS (Bioassay Technology Laboratory, Catalogue No: E6022Hu, China) in the samples was measured using an Enzyme Linked Immunosorbent Assay (ELISA) kit. This kit uses the biotinylated double sandwich method for measurement. This kit employs a microplate that has been pre-coated with a highly pure rat monoclonal gamma-glutamyl cysteine synthetase (γ-GCS) antibody. 50 µL of gamma-glutamyl cysteine synthetase (γ-GCS) standards (2.5, 1.25, 0.625, 0.312, and 0.156 ng/L) and 40 µL of samples were added to the wells. The samples were exposed to 10 microliters of biotinylated anti-gamma-glutamyl cysteine synthetase (γ-GCS) antibody. Subsequently, 50 µL of streptavidin-HRP was added to both the samples and standards. Subsequently, the mixture was transferred to a Sanyo Sterilizer incubator, a device manufactured in Japan, and kept at a constant temperature of 37 °C for a period of 1 hour. After the incubation period, the ELISA (Biotek ELx50, USA) was washed using the washing equipment. Afterwards, 50 µL of Chromogen A and Chromogen B solutions were added and placed in a light-free environment at a temperature of 37 oC for 15 minutes. The reaction was stopped by putting it to darkness to enhance color formation, and then introducing an acidic solution. The color intensity was quantified at a wavelength of 450 nm using an ELISA reader (Biotek ELx800, USA). γ-GCS levels were measured using traditional graphical methods (Muraoka et al., 2022).

Statistical Analysis

The data collected from our enquiry was examined using the SPSS 22.0 statistical software. The data collected prior to analysis and evaluation was assessed for conformity to a normal distribution using the Kolmogorov-Smirnov test. The Kolmogorov-Smirnov test was employed to compare measurements acquired from numerous distinct groups that were not influenced by each other. If the analysis demonstrated statistical significance, a one-way analysis of variance (ANOVA) was employed. Subsequently, pairwise comparison approaches were utilized to ascertain the distinct group or groups that exhibited differences. If the assumptions necessary for parametric testing were not satisfied, the Kruskal-Wallis test was used to compare results from many groups, independent of the variable being measured. The Kruskal-Wallis test is employed to ascertain the statistical significance of a decision through analysis. The Man-Whitney U test is thereafter employed to pinpoint the particular group or groups accountable for the observed disparity. The Chi-square test is used to evaluate qualitative data obtained from a census. The researchers considered a significance threshold of $p<0.05$ to be acceptable for statistical analysis (Mohr et.al.,2021).

Results

This study included a total of 40 patients who received a diagnosis of Polycystic Ovary Syndrome (PCOS) and 40 healthy volunteers who were matched in terms of age. After evaluating the demographic data of both sick and healthy individuals, no statistically significant difference was seen in terms of age (p>0.05). Table 1.

Table 1. Demographic data in patients and controls

Variables	PCOS (n=40)	Control (n=40)	p
Age (Year's)	31,28 ± 5,43	30,38 ± 4,33	0,745
p<0,05 is statistically important value			

The study examines the levels of Serum GGT and γ-GCS in both PCOS patients and the control group, as presented in Table 4.2. The statistical analysis showed that the levels of GSS and γ-GCS were significantly higher in the PCOS group compared to the other groups (p<0.05). Table 2

Table 2. Comparison of biomarkers in groups

	PCOS (n=40) Mean ± SD	Control (n=40) Mean ± SD	p
GGT	49,53 ± 17,01	51,05 ± 18,30	0,702
γ-GCS	0,228 ± 0,192	0,122 ± 0,126	0,006*
p<0,05 is statistically important value			

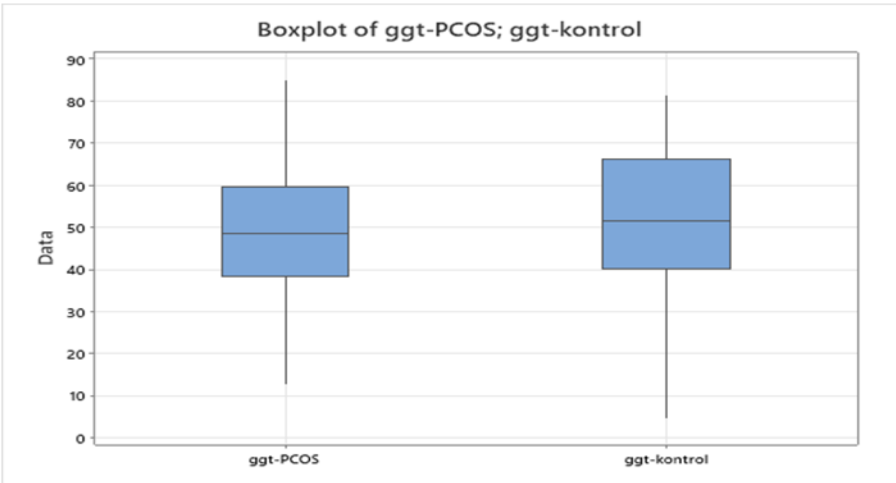

Figure 1. Boxplot graphic of GGT

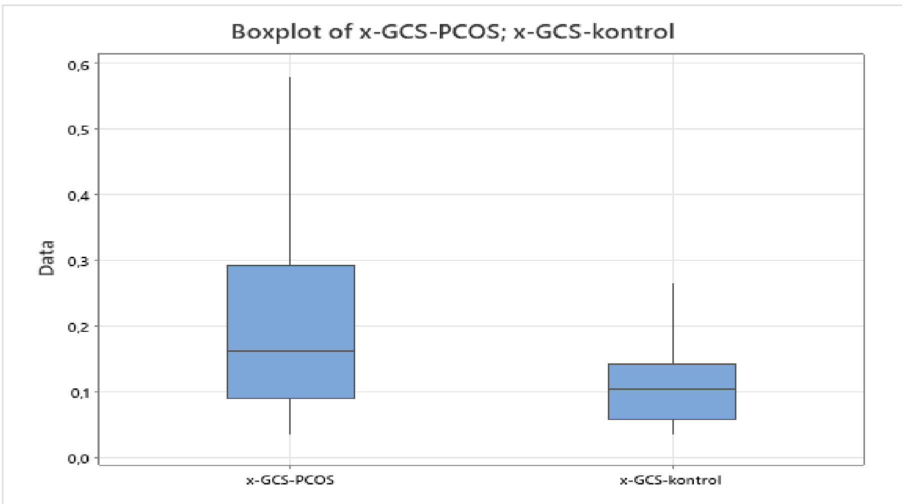

Figure 2. Boxplot graphic of GCS

Spearman's rho correlation analysis was performed to investigate the relationship between parameters in both the control and patient groups. Tables 3 and 4.

Table 3. Correlation analyzes for PCOS group

Spearman's rho		GGT	γ-GCS
GGT	r	1,000	0,226
	p		0,160
γ-GCS	r	0,226	1,000
	p	0,160	
$p<0{,}05$ is statistically important value			

A statistically significant and weak positive connection (p:0.160 and r:0.226) was identified between GGT and GCS in the group of individuals with PCOS.

Table 4. Correlation analyzes for control group

Spearman's rho		GGT	γ-GCS
GGT	r	1,000	0,724
	p		0,001*
γ-GCS	r	0,724	1,000
	p	0,001*	
$p<0{,}05$ is statistically important value			

A significant and strong positive correlation was observed between GGT and GCS in the control group. Polycystic ovarian syndrome is a medical illness that is defined by the presence of many physical characteristics and its effects on different body systems. The diagnosis is determined using a comprehensive set of 40 criteria that include clinical, biochemical, and imaging methods (Ramos et al., 2017). The study encompassed participants who were diagnosed with Polycystic Ovary Syndrome (PCOS) as well as persons who were in a state of excellent health. The individuals diagnosed with polycystic ovarian syndrome were identified based on the 2012 criteria established by the National Institutes of Health. The 2012 NIH standards adopted the 2003 Rotterdam diagnostic criteria as the official criteria for diagnosing PCOS. The diagnostic criteria for this disorder include oligo-anovulation, the presence of clinical and/or biochemical hyperandrogenism, and an ultrasonographic observation of polycystic ovary appearance (characterised by an ovarian volume greater than 10 cm^3 or the presence of more than 12 antral follicles) (Dybciak et al., 2022). In order to receive a diagnosis for this illness, an individual must meet a minimum of two out of these three criteria. The aim of our study was to measure the levels of key enzymes with antioxidant properties in persons diagnosed with PCOS, and to examine their influence on the development and advancement of the condition. To accomplish this goal, the levels of GGT and γ-GCS were measured using the ELISA technique in serum samples obtained from the subjects. After analysing the ages of both the patients and healthy volunteers, it was seen that there was no statistically significant difference. Enzyme levels and functions may vary depending on an individual's age. The absence of age gap between the groups indicates that our findings were not affected by age. After analysing our results, we found that the levels of γ-GCS were considerably higher in the PCOS group compared to the control group. Sonino et al. (1993) did a study which found that there was no notable disparity in GGT levels between the two groups (Sonino et al., 1993).

No studies have been undertaken to investigate the effects of glutathione-associated enzymes on the group with polycystic ovary syndrome (PCOS). Therefore, our study is important in clarifying the relationship between PCOS and the enzymes involved in the glutathione route. There is a significant amount of study in scientific literature that examines the relationship between Polycystic Ovary Syndrome (PCOS) and the interaction between antioxidants and oxidants. We examined the influence of glutathione-associated enzymes on the development of PCOS pathophysiology. Research has shown that levels of γ-GCS increase in patients with PCOS, possibly as a result of higher levels of oxidants. This may lead to an increase in antioxidants as a protective response (Tsiasioti & Tzanavaras, 2020).

Conclusion

We conducted a study to examine the levels of essential enzymes involved in glutathione metabolism in individuals diagnosed with polycystic ovarian syndrome (PCOS). The enzymes in individuals with polycystic ovary syndrome (PCOS) were significantly different from those in control groups, indicating that glutathione metabolism plays a vital role in the progression of this condition. After conducting correlation analysis, it is clear that enzymes have a reciprocal impact on the progression of the disease. Polycystic ovarian syndrome (PCOS) is a notable medical illness that frequently affects women and has a substantial influence on their overall well-being. Therefore, it is essential to better elucidate the fundamental factors contributing to the illness.

Scientific Ethics Declaration

* The authors declare that the scientific ethical and legal responsibility of this article published in EPSTEM Journal belongs to the authors.

* Permission was obtained from the Tikrit University Local Ethics Committee for this study (Date: 05.04.2021, No: 2021.03/73).

Acknowledgements or Notes

* This article was presented as an oral presentation at the International Conference on Technology, Engineering and Science (www.icontes.net) held in Antalya/Turkey on November 14-17, 2024.

References

Baqer, L., Ahmeid, M., & Al-Obaidi, A. (2017). Evaluatıon the effect of metformın on hormones serum levels in women wıth polycystic ovary syndrome. *Tikrit Journal of Pure Science, 22*(9).

Buczinski, S., Dubuc, J., Bourgeois, V., Baillargeon, P., Côté, N., & Fecteau, G. (2020). Validation of serum gamma-glutamyl transferase activity and body weight information for identifying dairy calves that are too young to be transported to auction markets in Canada. *Journal of Dairy Science, 103*(3), 2567-2577.

Chen, Y. (2020). Fluorescent probes for detection and bioimaging of leucine aminopeptidase. *Materials Today Chemistry, 15*, 100216.

Cunha, A., & Póvoa, A. M. (2021). Infertility management in women with polycystic ovary syndrome: a review. *Porto Biomed J, 6*(1), e116.

Dybciak, P., Humeniuk, E., Raczkiewicz, D., Krakowiak, J., Wdowiak, A., & Bojar, I. (2022). Anxiety and depression in women with polycystic ovary syndrome. *Medicina, 58*, 942.

Fathi, F. (2023). C-reactıve proteın and adıposıty ın women wıth polycystıc ovary syndrome. *Tikrit Journal of Pure Science, 23*, 47-51.

Gnawali, A., Patel, V., Cuello-Ramírez, A., Al Kaabi, A. S., Noor, A., Rashid, M. Y., . . .& Mostafa, J. A. (2021). Why are women with polycystic ovary syndrome at ıncreased risk of depression? exploring the etiological maze. *Cureus, 13*(2), e13489.

Hoffman, D. R. (1973). Estimation of serum IgE by an enzyme-linked immunosorbent assay (ELISA). *J Allergy Clin Immunol, 51*(5), 303-307.

Klumpp-Thomas, C., Kalish, H., Drew, M., Hunsberger, S., Snead, K., Fay, M. P., . . .& Sadtler, K. (2021). Standardization of ELISA protocols for serosurveys of the SARS-CoV-2 pandemic using clinical and at-home blood sampling. *Nat Commun, 12*(1), 113.

Melkiyur, I., Rathinam, Y., Kumar, P. S., Sankaiya, A., Pitchaiya, S., Ganesan, R., & Velauthapillai, D. (2023). A comprehensive review on novel quaternary metal oxide and sulphide electrode materials for supercapacitor: Origin, fundamentals, present perspectives and future aspects. *Renewable and Sustainable Energy Reviews, 173*, 113106.

Mohr, A., McEvoy, C., Sears, D., Arciero, P., & Sweazea, K. (2021). Impact of Intermittent fasting regimens on circulating markers of oxidative stress in overweight and obese humans: a systematic review of randomized controlled trials. *Advances in Redox Research, 3*, 100026.

Muraoka, M., Yoshida, S., Ohno, M., Matsuura, H., Nagano, K., Hirata, Y., . . .& Hirata, K. (2022). Reactivity of γ-glutamyl-cysteine with intracellular and extracellular glutathione metabolic enzymes. *FEBS Lett, 596*(2), 180-188.

Ramos, I., Magalhaes, L., Barreiros, L., Reis, S., Lima, J., & Segundo, M. (2017). Micro-bead injection spectroscopy for label-free automated determination of immunoglobulin G in human serum. *Analytical and Bioanalytical Chemistry, 410*(3), 981-988.

Sonino, N., Fava, G., Mani, E., Belluardo, P., & Md, M. (1993). Quality of life of hirsute women. *Postgraduate Medical Journal, 69*, 186-189.

Trent, M., & Gordon, C. M. (2020). Diagnosis and management of polycystic ovary syndrome in adolescents. *Pediatrics, 145*(2), 10-218.

Tsiasioti, A., & Tzanavaras, P. (2020). Determination of glutathione and glutathione disulfide using zone fluidics and fluorimetric detection. *Talanta, 222*, 121559.

Author Information

Ali Hameed Mahmood Al-Qaysi
Department of Chemistry, University of Cankiri Karatekin
University of Cankiri Karatekin, Cankiri, Turkiye
Contact e-mail: *aali1882@yahoo.com*

Sevki Adem
Department of Chemistry, University of Cankiri Karatekin
University of Cankiri Karatekin, Cankiri, Turkiye

Omeed Akbar Ali-Ali
Department of Biochemistry, College of Medicine,
University of Tikrit, Tikrit, Iraq

To cite this article:

Al-Qaysi, A.H.M., Adem S & Ali-Ali, O.A. (2024). Evaluation of glutathione-related antioxidant enzyme activity in patients with polycystic ovary syndrome (PCOS) and investigation of clinical correlations. *The Eurasia Proceedings of Science, Technology, Engineering & Mathematics (EPSTEM), 32*, 353-359.

The Eurasia Proceedings of Science, Technology, Engineering & Mathematics (EPSTEM)
ISSN: 2602-3199

The Eurasia Proceedings of Science, Technology, Engineering & Mathematics (EPSTEM), 2024

Volume 32, Pages 360-365

IConTES 2024: International Conference on Technology, Engineering and Science

Removal of Carcinogenic Direct Azo Dyes from Aqueous Solution Using a Functional Biopolymer

Lamia Moulahcene
University of Bouira

Fadila Oughlis-Hammache
University of Bouira

Ounissa Kebiche-Senhadji
University of Bejaia

Mohamed Skiba
University of Rouen Normandie

Abstract: In this study, a batch system was used to investigate the adsorption methyl violet from aqueous solution onto a β-cyclodextrin polymer synthesized with citric acid as a crosslinking agent. Several operational variables were tested. The results showed that increasing the amount of adsorbent improved the removal efficiency. Higher temperatures also enhanced dye adsorption, while ionic strength had no significant effect on the process. A slight decrease in removal efficiency was observed as pH values increased. FTIR spectra revealed the formation of a complex inclusion, which was identified as the dominant adsorption mechanism; this was further confirmed by the absence of the characteristic peaks of methyl violet in β-cyclodextrin polymer after adsorption.

Keywords: Cyclodextrin polymer, Textile dyes, Adsorption.

Introduction

The textile dyeing industry, in particular, is one of the largest polluters worldwide. It is estimated that this industry uses over five trillion liters of water annually, with effluents from textile processing and dyeing contributing to 20% of global water pollution. The toxic effects of dyes and their metabolites on living organisms, including humans, are well-documented. Azo dyes, such as methyl violet, eriochrom black T, and helianthin, are known for their harmful, long-lasting impact on ecosystems due to their persistence and xenobiotic properties. Although natural processes can remediate these contaminants, they do not always produce by-products that are non-toxic or less toxic, some environmental processes can even transform hazardous dyes into more toxic metabolites, including aromatic amines, diazonium ions, and hydrolyzed products. Moreover, microflora in the skin or intestinal ecosystems of mammals can convert certain non-toxic dyes into carcinogenic substances, which can have various toxic effects across different biological compartments.

The removal of dyes from wastewater has been a long-standing challenge. Several methods have been developed to address this issue, including membrane filtration (Raval et al., 2022). Photodegradation (Saeed et al., 2022). and adsorption (Salih et al., 2022). Among these, adsorption has proven to be the most effective and economically viable method for dye removal. Understanding adsorption equilibrium is crucial, as these data inform the selection of suitable adsorbents and the design of effective separation processes. There is a wide range of adsorbents available, with non-conventional materials such as (Oughlis-Hammache et al., 2010). Agricultural waste (Dubey et al., 2010; Ofomajas et al., 2011), and biomass receiving increasing attention. Biopolymers and natural molecules, such as cellulose (Musyoka et al., 2014). Chitosan (Huang et al., 2011). Starch, and cyclodextrins (Moulahcene et al., 2015). Have become popular for removing toxic pollutants from water. While adsorbents like activated carbon are highly effective, they can be difficult to regenerate. In contrast, cyclodextrin-based polymers are promising due to their ability to undergo multiple regeneration cycles, making them a more sustainable option (Oughlis-Hammache et al., 2024).

β-Cyclodextrin (β-CD) materials, which are natural, non-toxic, and inexpensive cyclic oligosaccharides derived from starch through enzymatic conversion, have shown significant potential for removing organic micropollutants from wastewater. Traditional β-CD-based polymers are chemically crosslinked with toxic agents like epichlorohydrin to improve their properties. However, these polymers tend to have limited nanoporous structures, which can restrict the adsorption capacity and efficiency. Recently, β-CD-based polymers crosslinked with citric acid have been developed, offering a larger surface area and mesoporous structure that enhances their ability to remove organic micropollutants. Insoluble cyclodextrin polymers are unconventional adsorbents, synthesized by using cyclodextrin (CD) as a complex molecule and a biopolyfunctional substance as a cross-linking agent. These adsorbents have been shown to be highly effective in removing dyes from wastewater, yielding excellent results.

This study investigates the use of cyclodextrin polymer; synthesized by combining β-cyclodextrin with citric acid as a cross-linking agent, for adsorbing methyl violet, in water treatment. The influence of several parameters, including contact time, adsorbent amount, initial pH, ionic strength and temperature, was evaluated.

Materials and Methods

Reagents

Methyl violet, was obtained from Sigma (Figure 1). The insoluble β-cyclodextrin polymer (P-β-CD) was sourced from In-Cyclo, a start-up company at the University of Rouen, France. Hydrochloric acid, sodium chloride, and sodium hydroxide were purchased from Chemi-nova, Labosi, and Merck KGaA, respectively.

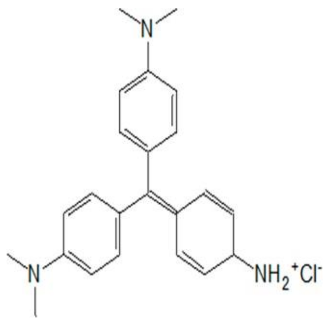

Figure 1. Chemical structure of methylviolet.

Apparatus

IR spectra were recorded using a Perkin-Elmer 4000 FTIR spectrometer, with a scanning range from 4000 cm^{-1} to 400 cm^{-1}. UV-Visible analysis was performed using a JASCO V-R30 spectrophotometer (Japan). For these measurements, a glass tank was used, and methyl violet solutions were prepared in deionized water. The absorbance was measured at 550 nm, the morphology of the polymer was analyzed using scanning electron microscopy (SEM) on a Cambridge Steroscan 360, operating in the LFD mode.

Adsorption Study

Adsorption experiments were conducted in a batch system. A 100 mL dye solution was placed in a glass bottle, and a known amount of cyclodextrin polymer was added and stirred. At specified time intervals, 3 mL of the solution was sampled. The dye solution was then separated from the adsorbent by centrifugation at 2000 rpm for 5 minutes and analyzed using a UV-Visible spectrophotometer.Stock solution of the dye ($2.5\ 10^{-5}$ $mol \cdot L^{-1}$) was prepared in deionized water. Experimental solutions with the desired dye concentrations were obtained by successively diluting the stock solution with deionized water. Calibration curve for the dye was created by measuring the absorbance of samples with known concentrations at 550 nm, using a UV/VIS spectrophotometer (JASCO V-R30, Japan).

Results and Discussion

Characterization of Cyclodextrin Polymer by SEM

As reported by Moulahcene et al. (2015). The β-cyclodextrin polymer exhibits a high swelling capacity due to its porous morphology, as confirmed by the SEM image (Figure 2). Additionally, this polymer has a relatively small surface area, suggesting that its adsorption mechanism differs from those of conventional adsorbents. Similar findings have been reported in the literature (Skiba & Lahiani-Skiba, 2013). The polymer also contains a relatively high number of acidic groups, which enables significant physical interactions within the polymer network, facilitating the adsorption of dyes.

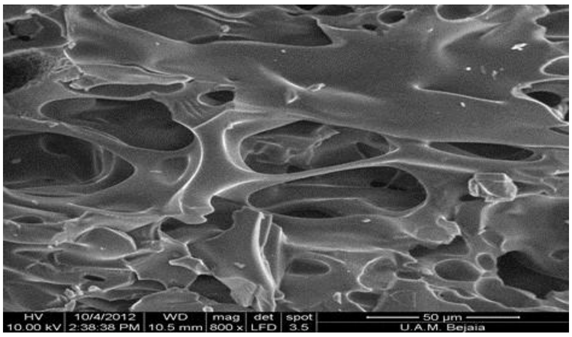

Figure 2. Feature (SEM) of ß-cyclodextrin polymer at 800×magnification.

Effect of Operators Variables on Methyl Violet Adsorption

Effect of pH and Ionic Strength

The effect of pH on methyl violet adsorption is illustrated in Figure 3b. Methyl violet does not remain undissociated under varying pH conditions. A slight decrease in adsorption is observed as pH increases. This behavior may be attributed to the substitution of chloride (Cl) by hydroxyl (-OH) groups, which reduces the ability of methyl violet to form inclusion complexes with cyclodextrins. Similar effects have been reported for other adsorbents, such as cellulose, where pH plays a significant role in methyl violet adsorption due to the positive charge on the dye (Musyoka et al., 2014). The effect of ionic strength was examined by varying the concentration of NaCl from 0 to 3 M. As shown in Figure 4a, ionic strength does not appear to influence methyl violet adsorption.

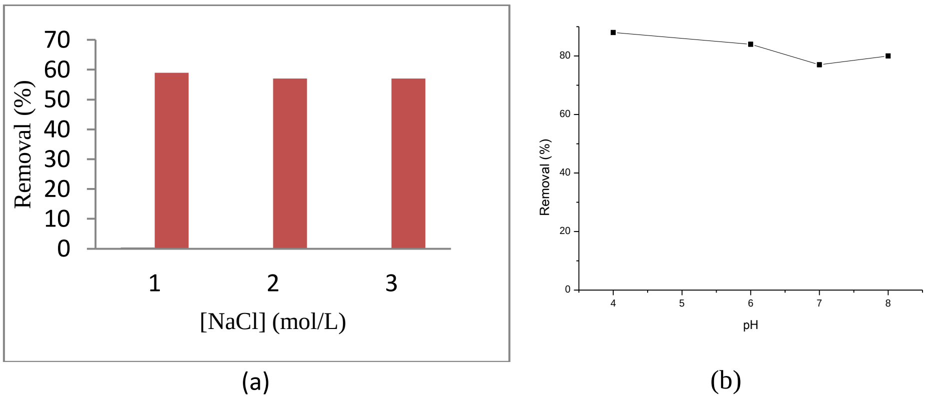

Figure 3. (a) ionic strength, (b) Effect of pH on methyl violet removal
by ß-cyclodextrin polymer, T= 30°C.

Effect of Adsorbent Amount

Effect of adsorbent amount on methyl violet adsorption is represented in the figure 4, the efficiently increases with increase of adsorbent amount and the equilibrium is attained at 1700 min.

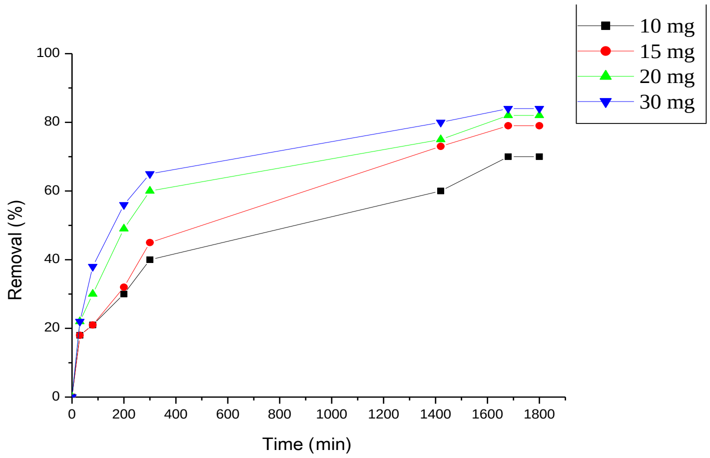

Figure 4. Effect of ß-cyclodextrin polymer amount on methyl violet removal, pH=4, T= 30 °C.

Effect of Temperature

Temperature plays a significant role in the adsorption of methyl violet onto ß-cyclodextrin polymer, as shown in Figure 5. The adsorption kinetics improve with an increase in temperature, which may be attributed to a higher rate of intraparticle diffusion or an expansion of the pore size (Moulahcene et al., 2015).

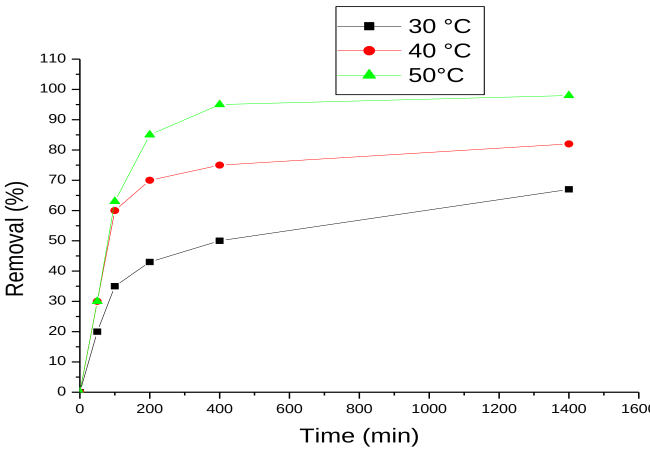

Figure 5. Effect of temperature (T) on methyl violet removal.

FTIR Characterization

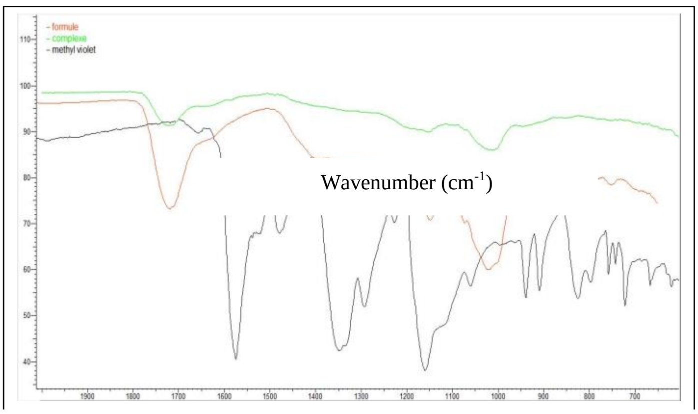

Figure 6. FTIR spectra of methyl violet and β-cyclodexrin polymers after and before adsorption, red (β-cyclodextrin polymer before adsorption), green (β-cyclodextrin polymer after adsorption) and black (methyl violet).

The FTIR spectra (400–4000 cm^{-1}) of methyl violet and β-cyclodextrin polymer, both before and after adsorption, are shown in Figure 6. The peaks at 1500 cm^{-1} and 1600 cm^{-1} correspond to the vibration of the aromatic C=C bond, while the peaks at 1200 cm^{-1} and 1300 cm^{-1} are attributed to the vibration of the aromatic amine bond in the methyl violet spectra. The absence of these characteristic peaks in the β-cyclodextrin polymer afteradsorption confirms the formation of an inclusion complex between β-cyclodextrin and methyl violet. This suggests that the adsorption process is governed by the formation of the inclusion complex rather than physical adsorption.

Conclusion

The synthesis of insoluble polymer using β-cyclodextrin as the base material and citric acid as the cross-linking agent was found to be a viable approach, producing a product that can serve as an effective and promising sorbent in the liquid-solid sorption process for removing azo dyes from wastewater effluents. The adsorption of methyl violet, onto the β-cyclodextrin polymer was investigated,various operational parameters were tested for this dye. Adsorption of methyl violet onto the β-cyclodextrin polymer increased with a higher amount of adsorbent, while pH had a slight effect. In contrast, ionic strength did not influence the adsorption process. The adsorption mechanism was primarily governed by the formation of an inclusion complex between methyl violet and β-cyclodextrin, as evidenced by the absence of characteristic peaks in the FTIR spectra of methyl violet within the β-cyclodextrin polymer after adsorption. These results suggest that the β-CD polymer could be a promising alternative for methyl violet removal, offering a more cost-effective solution compared to other adsorbents. Its advantages include good adsorption properties, ease of preparation, and relatively low cost. This β-CD polymer could help mitigate the environmental impact of dye effluents released into aquatic systems, while also lowering the costs associated with wastewater treatment, whether for disposal or reuse in industrial processes.

Scientific Ethics Declaration

The author declares that the scientific ethical and legal responsibility of this article published in EPSTEM Journal belongs to me.

Notes

This article was presented as an oral presentation at International Conference on Technology, Engineering and Science (www.icontes.net) held in Antalya/Turkey on November 14-17, 2024.

References

Dubey, S. P., Dwivedi, A. D., Sillanpää, M., & Gopal, K. (2010). Artemisia vulgaris-derived mesoporous honeycomb-shaped activated carbon for ibuprofen adsorption. *Chemical Engineering Journal*, *165*(2), 537-544.

Huang, X.Y., Bin, J.P., Bu, H. T., & Jiang, G. B.(2011). Removal of anionic dye from aqueous solution using ethylenediamine modified chitosane. *Carbohydrate Polymer*, *84*(4), 1350-1356.

Moulahcene, L., Skiba, M., Senhadji, O., N. Milon, N., Benamor, M., &Lahiani-Skiba, M. (2015).Inclusion and removal of pharmaceutical residues from aqueous solution using water-insoluble cyclodextrin polymers. *Chemical Engineering Research.and Design*, *97,* 145–158.

Musyoka, S. M., Mittal, H., Mishra, S.B., & Ngila, J.C.(2014).Effect of functionalization on the adsorption capacity of cellulose for the removal of methyl violet. *International Journal of Biological Macromolecules*, *65,* 389–397.

Raval, A. R., Kohli, H. P., & Mahadwad, O. M.(2022). Application of emulsion liquid membrane for removal of malachite green dye from aqueous solution. Extraction and stability studies. *Chemical Engineering Journal Advances*, *12,* 100398.

Saeed, M., Alwadi, N., Ben Ferhat, L., Baig, A., Nabgan, W., & Iqbal, M.(2022). Co_3O_4-Bi_2O_3 heterojunction . An effective photocatalyst for rhodamine B dye. *Arabian Journal of Chemistry*, *15*(4), 103732.

Skiba, M., &Lahiani-Skiba, M.(2013) Novel method for preparation of cyclodextrin polymers physico-chemical characterization and cytotoxicity. *Journal of Inclusion Phenomena and Macrocyclic Chemistry*, *75*, 341–34.

Salih, S. J., Abdul Kareem, A. S., & Anwer, S. S.(2022). Adsorption of anionic dye from textile wastewater raw corncob. *Hellyone*, *8*(8), e10092.

Ofomaja, A. E. Ukpebor, E. E., & Uzoekwe, S. A.(2011). Biosorption of methyl violet onto palm kernel fiber. Diffusion studies and multistage process design to minimize biosorbent mass and contact time. *Biomass and Bioenergy*, *35*(10), 411, 2-4123.

Oughlis-Hammache, F., Moulahcene, L., Senhadji-Kebiche, O., Moussi, N., Meziani, H., Benamor, M., Skiba, M., &Lahiani-Skiba, M.(2024). Modeling and optimization of the adsorption process of pharmaceutical residues in aqueous solution by the experimental design method. *Materials*, *17,* 3594.

Oughlis-Hammache, F., Hamaidi-Maouche, N., Aissani-Benissad, F., & Bourouina-Bacha, S. (2010). Central composite design for the modeling of the phenol adsorption process in a fixed-bed reactor. *Journal of Chemical & Engineering Data*, *55*(7), 2489-2494.

Author Information

Lamia Moulahcene
University of Bouira
Institute of Technology, Departement of Industriel Chimical Technology, Algeria.
Contact e-mail: *l.moulahcene@univ-bouira.dz*

Fadila Oughlıs-Hammache
University of Bouira
Faculty of Sciences and Applied Sciences, Departement of Process Engineering, Algeria.

Ounissa Kebiche-Senhadji
University of Bejaia
Faculty of Technology, Laboratory of Membrane Processes and of Separation and Recovery Techniques, Bejaia, Algeria.

Mohamed Skiba
Normandie Univ, UNIROUEN,
Galenic Pharmaceutical Laboratory, NorDIC Inserm U1239, UFR Medicine and Pharmacy, Rouen University, 22 Bd Gambetta, F-76183 Rouen, France.

To cite this article:

Moulahcene, L., Oughlis-Hammache, F., Kebiche-Senhadji, O., & Skiba, M. (2024). Removal of carcinogenic direct azo dyes from aqueous solution using a functional biopolymer. *The Eurasia Proceedings of Science, Technology, Engineering & Mathematics (EPSTEM), 32,* 360-365.

The Eurasia Proceedings of Science, Technology, Engineering & Mathematics (EPSTEM)
ISSN: 2602-3199

The Eurasia Proceedings of Science, Technology, Engineering & Mathematics (EPSTEM), 2024

Volume 32, Pages 366-372

IConTES 2024: International Conference on Technology, Engineering and Science

Impact Assessment of Structural and Non-Structural Components on the Vulnerability Level of Reinforced Concrete Buildings

Karim Akkouche
Mouloud Mammeri University of Tizi Ouzou

Aghiles Nekmouche
National Center of Applied Research in Earthquake Engineering Algiers

Nacim Khelil
Mouloud Mammeri University of Tizi Ouzou

Leyla Bouzid
Mouloud Mammeri University of Tizi Ouzou

Kahil Amar
Mouloud Mammeri University of Tizi Ouzou

Abstract: Over the past four decades, Algeria has suffered considerable losses, due to several large earthquakes that hit its various northern parts. These destructive effects are amplified by the large volume of buildings constructed using imprecise and unfinished codes (before the appearance of the Algerian paraseismic code RPA99/03). Indeed, the majority of cities have developed in total ignorance of seismic risks. Also, these heavy losses recorded are the consequence of the use of poor materials as well as poor control of implementation. Furthermore, reducing human and economic losses during a disaster requires raising awareness among the population at risk. In this context, a study on the seismic vulnerability of constructions built before 2003 is carried out in our laboratory. Knowing that the "IV" vulnerability index level to be considered for a structure threatened by an earthquake is a combination of several parameters. This document proposes an approach to quantify the "IV" index level of column-beam buildings, based on the design of experiments method (DEM). The DEM is a correlation established between this "IV" index level and certain parameters considered sources of danger by several researchers. Two types of factors are distinguished: those designated as internal to the construction, such as: the age "Ag", the symmetry in plane "Sy", the regularity in elevation "Re", the quality of the bracing "Qc", the quality of the resistant system "Qr", the state of conservation "Ec", the secondary elements "Es", the infrastructure "If" and the redundancy of the rows "Rf" and those designated as external, such as: collision "And" and the ground condition "So". The resulting formula from this correlation allows managers to classify vulnerable buildings with a better approximation.

Keywords: Buildings, Reinforced concrete, Earthquake, Vulnerability, Design of experiments.

Introduction

In recent decades, Algeria has experienced earthquakes causing considerable human and material losses. These disasters have called into question the development process, causing disorganization at the level of the urban fabric and the economic fabric as well as the societal structure (Akkouche et al., 2020). Thus, the Chlef earthquake of 1980 and that of Boumerdes in 2003, creating a disaster and total upheaval in these regions; it is therefore important to undertake a real reflection on prevention, before investing in development programs

- Selection and peer-review under responsibility of the Organizing Committee of the Conference

which could be wiped out by a natural disaster (Schlupp et al., 2001). In this context, a number of studies have been carried out and reported in the literature dealing with knowledge on:

- The perception of seismic risk and the desire to take measures to reduce this risk (Kanti et al., 2010; Tekeli-Yesil et al., 2010; Isabelle et al., 2012; Bouzid et al., 2020).;
- The development of a vulnerability index (Lang et al., 2002; Mebarki et al, 2004; AFPS, 2005; Belheouane et al., 2009; Gulay et al., 2011);
- The development of new means of assessing vulnerability (Hamizi et al., 2007; Olson et al., 2010; Lutman et al., 2014; Nekmouche et al., 2017; Akkouche et al., 2019);
- The production of seismic scenarios (Boukri et al., 2014).

Despite the differences between these methods, they are based on the basic principle, which is the identification and estimation of seismic consequences. According to Gulay (2011), the vulnerability of a population is dominated by the most vulnerable buildings, it is therefore important to first determine what these buildings are, their number as well as their importance in relation to existing buildings.

In this perspective, based on the failure modes observed in reinforced concrete frames, Mitcheletll et al. (2001) and Mazare (2002) give a list of parameters most likely to cause significant damage. However, with such data, it is generally not easy to quantitatively identify the seismic capacities of existing structures, knowing in fact that these methods remain more or less simple, as they relate to simple visual inspections. To this end, in what follows, all the parameters judged to be influential factors on column-beam structures are studied: age “Ag”, symmetry in plane “Sy”, regularity in elevation “Re”, quality of the bracing “Qc”, quality of the resistant system “Qr”, state of conservation “Ec”, secondary elements “Es”, infrastructure “If”, redundancy of rows “Rf”, collision “Et” and ground condition “So”.

This study is based on post-seismic data processing based on the theory of experimental designs (Goupy,2006). For this purpose, a database of 508 post-seismic evaluation sheets is processed. Finally, an orientation allowing property managers to identify and prioritize high-risk buildings is given, and this, to be able to find the appropriate decisions with the objective to perform repairs or rehabilitation.

Methodology

The processing of feedback data (evaluation sheets) made it possible to show that the vulnerability of buildings varies greatly depending on the parameters characterizing the initial structural conditions. In this perspective, we seek to determine the factors and their degrees which can influence the overall behavior of column-beam structures. The experimental design method is carried out according to the following approach:

Identification of all the factors likely to weaken column-beam structures under the influence of seismic loads. Eleven factors were selected from a database made up of 508 files (constructions) (Hamizi et al., 2006), application of the Koshal screening experimental design, in order to distinguish the most influential factors. Application of the full factorial optimization experiment to develop a model for assessing the vulnerability of self-stable reinforced concrete frame buildings. Before discussing the results, a presentation, in the following two paragraphs, of some data specific to the Koshal and full factorial designs is performed.

KOSHAL Experiment and Full Factorial Experiment

KOSHAL designs: Koshal screening experimental designs make it possible to estimate the main effects or "weights" of k factors on a given property (response) in order to distinguish the truly influential factors. These experimental designs only admit a single first-degree polynomial model without interaction. For this purpose, the experiment matrix used, represents the beginning of the matrix of a complete factorial design (Goupy, 2006).

The matrices of the KOSHAL experimental design with N lines make it possible to study a number of k factors (k = N-1), each taking two levels. The latter, designated by Ri (inf) and Ri (sup) in natural variables, take the values -1 (denoted –) and +1 (denoted +) respectively in coded variables [Telford J.K et al, 2007]. The experience matrices are obtained by a circular permutation of a series of levels – and + given in the form of lines (Table 1).

Table 1. KOSHAL experiment matrix.

Configuration	Factors (Xi)											Response
N°	X_1	X_2	X_3	X_4	X_5	X_6	X_7	X_8	X_9	X_{10}	X_{11}	
1	-1	-1	-1	-1	-1	-1	-1	-1	-1	-1	-1	1,128
2	+1	-1	-1	-1	-1	-1	-1	-1	-1	-1	-1	4,155
3	-1	+1	-1	-1	-1	-1	-1	-1	-1	-1	-1	4,319
4	-1	-1	+1	-1	-1	-1	-1	-1	-1	-1	-1	2,971
5	-1	-1	-1	+1	-1	-1	-1	-1	-1	-1	-1	3,741
6	-1	-1	-1	-1	+1	-1	-1	-1	-1	-1	-1	2
7	-1	-1	-1	-1	-1	+1	-1	-1	-1	-1	-1	3,624
8	-1	-1	-1	-1	-1	-1	+1	-1	-1	-1	-1	3,758
9	-1	-1	-1	-1	-1	-1	-1	+1	-1	-1	-1	1,882
10	-1	-1	-1	-1	-1	-1	-1	-1	+1	-1	-1	3,706
11	-1	-1	-1	-1	-1	-1	-1	-1	-1	+1	-1	3,802
12	-1	-1	-1	-1	-1	-1	-1	-1	-1	-1	+1	3,867

The student statistical test of significance (Goupy, 2009; Kamoun et al, 2011) is used to choose whether significant effects are taken into account. PFC Full Factorial Designs: Two-level full factorial designs allow all possible combinations to be studied with a minimum number of configurations. In other words, these plans make it possible to determine the effects of factors and all the interactions that may exist between them. In this case, the experiment matrix has a dimension of k columns (Factors) and 2k rows (configurations). This matrix takes two levels for each factor k: -1 and +1. The experiment matrix is thus obtained by a classic arrangement of the experimental points (Table 2).

Table 2: PFC experiment matrix.

Configuration	Factor (Xi)						
	X_1	X_2	X_3	X_4	.	.	X_N
1	-1	-1	-1	-1	.	.	-1
2	+1	-1	-1	-1	.	.	-1
3	-1	+1	-1	-1	.	.	-1
4	+1	+1	-1	-1	.	.	-1
5	-1	-1	+1	-1	.	.	-1
.	.	.	.	.	.	.	.
.	.	.	.	.	.	.	.
2^{N-1}	-1	+1	+1	+1	.	.	+1
2^N	+1	+1	+1	+1	.	.	+1

In the case where the factors are continuous, the mathematical model associated with the two-level Complete Factorial Experiment is of the additive polynomial type (of first or second degree and with interactions):

$$Y = a_0 + \sum_{i=1}^{N} a_i X_i + \sum_{i=1}^{N}\sum_{j=1}^{N} a_{ij} X_i X_j + \dots \dots + \sum_{i=1}^{N}\sum_{j=1}^{N}\sum_{k=1}^{N}\sum_{l=1}^{N} a_{ijkl} X_i X_j X_k X_l \qquad (1)$$

Where: Y: the response (damage state), X: the factor influencing the structure and a: the model coefficient.

Note: in the case where no factor appears in the structure (configuration No. 1: all factors are fixed at their lower level), assuming that the construction is healthy. For this purpose, the coefficient a_0=0.

Identification of Vulnerable Components

The identification of vulnerable components is established on a sample of structures assessed in the area affected by the 2003 Boumerdes earthquake, Algeria. Potential losses are quantified for each significant source of vulnerability. The classification of the sample of 508 structures is carried out by typologies, as indicated in Figure 1. The study is carried out on the typology representing more than 70% of residential use constructions, which are the structures made of reinforced concrete columns and beams. The degrees of damage relating to the 340 free-standing structures are given in the Figure 2.

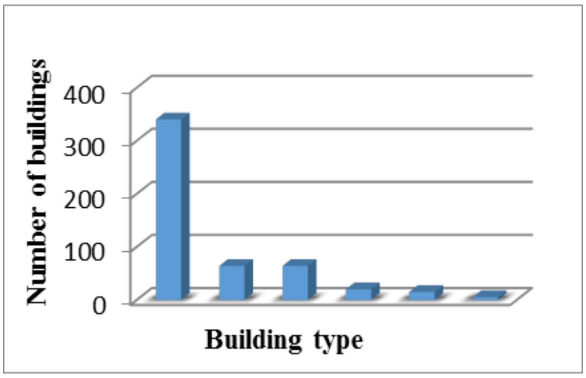

Figure 1. Classification according to the structures typology.

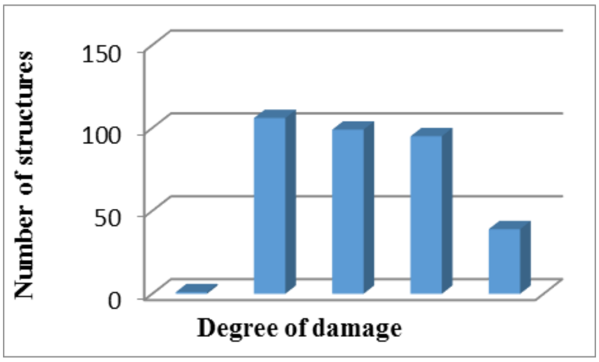

Figure 2. Classification of the 340 buildings according to the degree of damage

After inventorying the 340 column-beam buildings, the following process is carried out:

- Choice of 11 pathological factors for each structure (each survey sheet).
- Accounting for the factors having suffered damage, for each structure

Results

Application of the Koshal Experimental Design

The eleven factors likely to have a bad influence on the proper behavior of column-beam constructions as well as the levels assigned to them are given in Table 3. The lower and upper levels represent the two limits of the evaluation domain of the factors (as shown on the post-seismic evaluation sheet in the context of Algerian buildings).

Table 3. Factor levels following the Koshal experimental design.

Factors	Constructions classified in [D1-D2]		Constructions classified in [D3-D5]	
	Lower level		Higher level	
	Natural	coded	Natural	coded
Qr	D1	-1	D5	+1
Qc	D1	-1	D5	+1
Ag	After RPA 99	-1	Before RPA 99	+1
Ec	Good (D1)	-1	Bad (D5)	+1
Et	No	-1	Yes	+1
Es	D1	-1	D5	+1
So	D1	-1	D5	+1
If	D1	-1	D5	+1
Sy	Yes (D1)	-1	No (D5)	+1
Re	Yes (D1)	-1	No (D5)	+1
Rf	Yes (D1)	-1	No (D5)	+1

The overall damage levels are indicated in the last column of Table 3. Note that each of the 12 configurations were replicated several times. The values shown in Table 3 represent the test averages. The effects of the factors were estimated using the least squares method, as presented in Table 4.

Table 4. Estimated effects of Koshal experimental design factors.

Factor	Coefficient	Weight	Standard deviation	Significance test
Qr	a1	-0,72818	0,0033	***
Qc	a2	-0,63156	0,0033	*
Ag	a3	-0,6156	0,0033	NS
Ec	a4	-0,68772	0,0033	**
Et	a5	-0,62562	0,0033	NS
Es	a6	- 0,67839	0,0033	**
So	a7	-0,64934	0,0033	*
If	a8	-0,7331	0,0033	***
Sy	a9	-0,6231	0,0033	NS
Re	a10	-0,61 34	0,0033	NS
Rf	a11	-0,61039	0,0033	NS

With: NS: not significant; *: significant with a 95% confidence level; **: significant with a 99% confidence level; ***: significant with a confidence level of 99.9%

The results obtained made it possible to estimate the standard deviations of the coefficients [D. MATHIEU et al, 2000] and to distinguish, using the STUDENT test, the effects of statistically significant factors with a 95% confidence level (Table 4). Considering the confidence interval of the coefficient values, one can state that at most six factors can induce a vulnerable behavior in column-beam buildings. Those factors are: the quality of the resistant system (Qr), the quality of the bracing (Qc), the state of conservation (Ec), the secondary elements (Es), the ground conditions (So) and the infrastructure (If).

Note: We consider the two factors Qr and Qc to be comparable in a self-stable frame structure. Therefore, only the Qr factor is taken into account in this study.

Application of the Full Factorial Design

The two levels assigned to each of the five factors are the same as those indicated in Table 3. This is equivalent to considering a two-level system of five factors with 25 possible states (32 Configurations). Following the recommendations given in Goupy (2006), only the main effects and first-order interactions are taken into consideration. The results of the studied configurations are given in Table 5:

Table 5. Results of the different configurations

Configuration	1	2	3	4	5	6	7	9
Response	1,29	3,42	2,37	3,61	2,89	4,11	3,08	3,43
Configuration	10	11	12	17	18	19	20	21
Response	4,05	3,59	3,88	3,93	4,67	4,02	4,21	3,97

The analysis of the results is performed with the classic tools of experimental designs. Under these conditions, the model coefficients are estimated using the least squares method. The results obtained are illustrated in the Table 6.

Table 6**.** Importance of factors and interactions.

Main effects		Order interactions 1			
Effect	Weight	Interaction	Weight	Interaction	Weight
E1	-0,208	I12	0,0512	I24	0,0114
E2	-0,105	I13	0,0518	I25	-0,0265
E3	0,097	I14	-0,035	I34	0,0554
E4	-0,085	I15	0,0537	I35	0,0348
E5	-0,115	I23	0,0643	I45	0,0649

From the results presented above, a mathematical model making it possible to quantify the vulnerability of existing column-beam buildings was developed and given by the following formula:

$$V_{pp} = -0{,}208 * Q_R - 0{,}105 * E_C + 0{,}097 * E_S - 0{,}085 * S_O - 0{,}115 * I_F + 0{,}0512 * Q_R * E_C + 0{,}0518 Q_R * E_S - 0{,}035 Q_R * S_O + 0{,}0537 * Q_R * I_F + 0{,}064 * E_C * E_S + 0{,}0114 * E_C * S_O - 0{,}0265 * E_C * I_F + 0{,}0554 E_S * S_O + 0{,}0348 E_S * I_F + 0{,}0649 * S_O * I_F$$

Conclusions

The statistical procedure bringing together seismic vulnerability and structural characteristics, in the form of a mathematical model, offers a reliable possibility and capacity to provide real data on the structural state in the face of earthquakes. This is done by introducing data collected on site and taking into consideration the internal and external parameters of the construction.

The present work evaluates and quantifies the seismic vulnerability of a specific reinforced concrete structure, in this case: self-stable. The method of experimental designs, following the application of the Koshal design and the full factorial design, makes it possible to classify this typology of construction into two categories:

- Vulnerable when VPP= [3; 5]: encompassing structures that require intervention for reinforcement and rehabilitation. These are buildings with low earthquake resistance.
- Not vulnerable VPP= [0; 2]: encompassing healthy buildings, which do not require any intervention.

Therefore, this model can be used to translate a master plan on the vulnerability and fragility of the structures and buildings of the Algerian real estate stock.

References

Akkouche K., Hannachi N.E., Hamizi M., Khelil N., K., & Daoui M. (2019). Knowledge-based system for damage assessment after earthquake: Algerian buildings case. *Asian Journal of Civil Engineering, 20*(6), 769-784.

Akkouche, K., Hannachi, N. E., Hamizi, M., & Khelil, N. (2020). Development of a relation model for global and local damage categorization : The case of the Algerian building. *Bulletin of Earthquake Engineering*, *18*, 3057-3077.

Beck, E., André-Poyaud, I., Davoine, P. A., Chardonnel, S., & Lutoff, C. (2012). Risk perception and social vulnerability to earthquakes in Grenoble (French Alps). *Journal of Risk Research, 15*(10), 1245-1260.

Belheouane, F. I., & Bensaibi, M. (2009). Calcul de l’indice de vulnérabilité pour les constructions en béton armée. *9th Congrès de Mécanique.*

Boukri, M., Farsi, M. N., Mebarki, A., Belazougui, M., Amellal, O., Mezazigh, B., ... & Benhamouche, A. (2014). Seismic risk and damage prediction : Case of the buildings in Constantine city (Algeria). *Bulletin of Earthquake Engineering*, *12*, 2683-2704.

Bouzid, L., Hamizi, M., Hannachi, N. E., Nekmouche, A., & Akkouche, K. (2020). Plastic hinges mechano-reliability analysis in the beams of RC frames structures. *World Journal of Engineering*, *17*(5), 719-732.

Combescure, D., Guéguen, P., & Lebrun, B. (2005). Vulnérabilité sismique du bâti existant: approche d'ensemble. *Cahier Technique AFPS,* (25),121.

Goupy, J. (2000). Modélisation par les plans d'expériences. *Techniques de l'ingénieur. Mesures et contrôle*, (R275), R275-1.

Goupy, J., & Creighton, L. (2009). *Introduction aux plans d'expériences-3ème édition-Livre+ CD*-Rom (4th ed.). Dunod, Paris : Hachette.

Hamizi, M., Bouzid, L., Boukais, S., & Hannachi, N. E. (2010). Méthodologie de l'évaluation de la fonction de vulnérabilité et du risque sismique pour les structures en poteaux poutres étude de cas: Wilaya de boumerdès Algérie. *Annales du Bâtiment et des Travaux Publics*, *4*, 23.

Hamizi, M., Rassoul, I., & Hannachı, N.E. *Conception et réalisation d’un système d’aide à l’évaluation de la vulnérabilité du bâti existant*. Colloque National Pathologie des constructions, Université Mentouri Constantine, Algérie,

Kamoun, M., Chaabouni, M., & Ayedi, H. F. (2011). *Plans d’expériences et traitements de surface : Etude quantitative des effets et interactions*. Retrieved from https://www.techniques-ingenieur.fr/base-documentaire/materiaux-th11.

Lang, K. (2002). *Seismic vulnerability of existing building*. (Doctoral dissertation, Swiss Federal Institute of Technology).

Lutman, M., Sket-Motnikar, B., Weiss, P., Klemenc, I., … & Banovec P. Aspects of earthquake risk management in Slovenia. *Procedia Economics and Finance, 18,* 659-666.

Mathieu, D., Nony, J., & Phan-Tan-Luu, R. (2000). *New efficient methodology for research using optimal design (NEMRODW) software.* Aix-Marseille France : LPRAI.

Mazars, J. (2002). La vulnérabilité sismique des constructions, les produits de la recherche un atout pour avancer. *Risques Infos*, (13).

Mebarki A., &Valencia, N. (2004). *Informal masonry structures: Seismic vulnerability and GIS maps*. *Masonry International Journal, 17,* 18–25.

Nekmouche, A., Hamizi, M., Khelil, N., & Kezman, A. (2017). Simplified models to control plastic hinges in reinforced concrete frame structures. *Asian Journal of Civil Engineering*, *19*(105), 13-25.

Olson, D. L., & Wu, D. D. (2010). Earthquakes and risk management in China. *Human and Ecological Risk Assessment*, *16*(3), 478-493.

Paul, B. K., & Bhuiyan, R. H. (2010). Urban earthquake hazard : Perceived seismic risk and preparedness in Dhaka City, Bangladesh. *Disasters*, *34*(2), 337-359.

Saatcioglu, M., Mitchell, D., Tinawi, R., Gardner, N. J., Gillies, A. G., Ghobarah, A., ... & Lau, D. (2001). The August 17, 1999, Kocaeli (Turkey) earthquake damage to structures. *Canadian Journal of Civil Engineering*, *28*(4), 715-737.

Schlupp, A. Mendel V. Van-der-woerd K. & Sira C. (2011). *Évaluation statistique de la vulnérabilité sismique, au sens de l'EMS 98, des bâtiments en Alsace (Vol.1, p.128).* Rapport méthodologique. https://www.franceseisme.fr/donnees/rapport-methodo-DREAL-11-2011_f_sec.pdf

Tekeli-Yesil, S., Dedeoglu, N., Tanner, M., Braun-Fahrlaender, C., & Obrist, B. (2010). Individual preparedness and mitigation actions for a predicted earthquake in Istanbul. *Disasters*, *34*(4), 910-930.

Telford, J. K., & Breif, A. (2007). Introduction to design of experiments. *Johns Hopkins APL Technical Digest*, *27*(3), 224-232.

Tezcan, S. S., Bal, I. E., & Gulay, F. G. (2011). P25 scoring method for the collapse vulnerability assessment of R/C buildings. *Journal of the Chinese Institute of Engineers*, *34*(6), 769-781.

Author Information

Karim Akkouche
Civil engineering department, Mouloud Mammeri University of Tizi Ouzou, 15000, Algeria.
Contact e-mail*: karim.akkouche@ummto.dz*

Aghiles Nekmouche
National Center of Applied Research in Earthquake Engineering Algiers, 16000, Algeria.

Nacim Khelil
Civil engineering department, Mouloud Mammeri University of Tizi Ouzou, 15000, Algeria.

Leyla Bouzid
Civil engineering department, Mouloud Mammeri University of Tizi Ouzou, 15000, Algeria.

Kahil Amar
Civil engineering department, Mouloud Mammeri University of Tizi Ouzou, 15000, Algeria.

To cite this article:

Akkouche, K., Nekmouche, A., Khelil, N., Bouzid, L., & Amar, K., (2024). Impact assessment of structural and non-structural components on the vulnerability level of reinforced concrete buildings. *The Eurasia Proceedings of Science, Technology, Engineering & Mathematics (EPSTEM), 32,* 366-372.

The Eurasia Proceedings of Science, Technology, Engineering & Mathematics (EPSTEM)
ISSN: 2602-3199

The Eurasia Proceedings of Science, Technology, Engineering & Mathematics (EPSTEM), 2024

Volume 32, Pages 373-378

IConTES 2024: International Conference on Technology, Engineering and Science

Thermal Agitation Study on a 90° Surface of the Radius of Curvation of an Elbow

Sofiane Maachou
University Centre of Maghnia

Djezouli Moulai-Khatir
Abou Bekr Belkaid University

Abdeldjalil Benbakhti
University Centre of Maghnia

Mohamed Mokhtari
Ecole Nationale Polytechnique Maurice Audin

Abstract: The straight sections of steel pipes are subjected to accumulated loads over the course of their service life, which in most cases are highly damaging. Under ambient temperature conditions, the proposed reinforcement to improve the strength of these structures by thermal agitation in A510AP grade steel bends (used in the manufacture of LPG gas tanks and pipes) under mechanical behavior and different bending moment loads, opening and closing, was studied in this work by FEM, and by using the numerical calculation code ABAQUS as well as the XFEM technique with solid elements as structure, our objective is to evaluate the effect of loading mode, internal pressure level, thermal agitation surface and time of this agitation which is expressed by the graduation exponents of the HAZ in the tubular structure in a steel bend under mixed pressure and moment loading. Numerical damage results are presented in the form of moment-rotation curves. They illustrate the variation in damage as a function of these simultaneously acting effects.

Keywords: A510AP steel, HAZ, Thermal agitation, XFEM technique, Crack initiation

Introduction

The innovative idea in our work is to use the new UMM technique (Benzaama et al., 2023) to graduate the heat-affected zone in our tubular structure, in fact the heat-affected zone gives an additional resistance with a new behavior of the material, each zone in the structure has a certain resistance which is a function of the new properties issued by the heat effect in the structure, this heat-affected zone has two parameters; that of the surface previously selected for thermal agitation, and that also of the time of this thermal agitation (Constant et al. (1992), Pratap-Singh et al. (2018), Shimatsu et al. (2000) and Lawrence-Bragg (1934), which is expressed by the graduation exponent of the HAZ Tomerlin et al. (2023), Rui -Yan et al. (2023) and Shrivastava et al. (2023) in the tubular structure with its own base material.

The finite element method is implemented in the standard Abaqus calculation code (Dassault Systemes, 2014). On the basis of two materials, that of the heat-affected zone and the base material, the material failure parameters are scaled by volume fraction. The maximum principal stress is the strength value of the structure, based on the tensile test of the bar specimens tested, which yielded a value of 499MPa. The damage evolution criterion is the maximum tensile displacement (maximum crack opening of the steel is measured at 0.14 mm).

Damage is continuous in the structure, with crack propagation and subsequent stiffness degradation due to element separation. For this, it is necessary to plan methods for repairing cracks (Maachou et al., 2024).

Geometry Studied and Properties of the Material Used

The geometry studied is a structure of two straight parts on which our boundary condition is applied, such as the load and the structure's attachment, fastened by welding with a 90° elbow. The elbow element is connected to two straight pipes of length 960 mm (Figure 1). The length is sufficient to ensure that there is no stress interference in the region of the elbow due to loads applied to the ends of the linear parts.

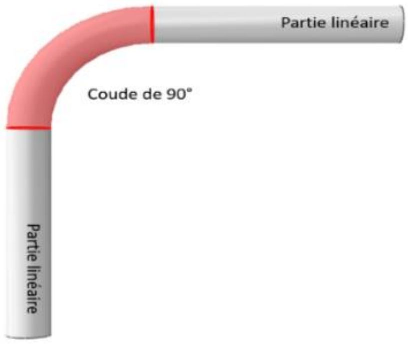

Figure 1. Studied geometry.

Table 1. Mechanical properties of the two zones of A510AP steel (Sliman, 2016)

Materials	Mechanical properties	
	Re [MPa]	Rm [MPa]
Basic metal (BM)	297	499
Heat-Affected Zone (HAZ)	480	631

Results and Discussion

Our study is based on three levels of graduation that express the thermal agitation time and are applied to the entire surface of the bend; in the upper surface and in the lower surface of the bend.

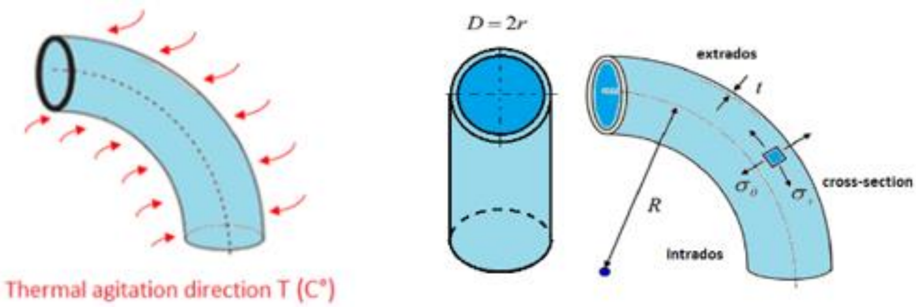

Figure 2. Schematics showing the thermal agitation surface

Fig. 3 and 5 show the structural response to bending mode and pressure damage for 90° surface thermal agitation and different graduation percentages of HAZ in the base material, chosen according to a graduation direction which is usually thickness and with a two-way graduation at the end of the surface thermal agitation. The graduation exponent 0,5 expresses a very low presence, for the graduation exponent 1 is for an identical presence of HAZ in the base metal, and finally 1,5 for a fairly high presence of HAZ in the base metal.

These captures are important to present; we are limited only to the case of the HAZ zone angle at 90° from the surface of the bend. These captures enable us to determine the crack initiation zone, which develops rapidly once it reaches its critical length. We can see that damage starts in the fixed side of the structure, otherwise it is favored at the bend without HAZ reinforcement.

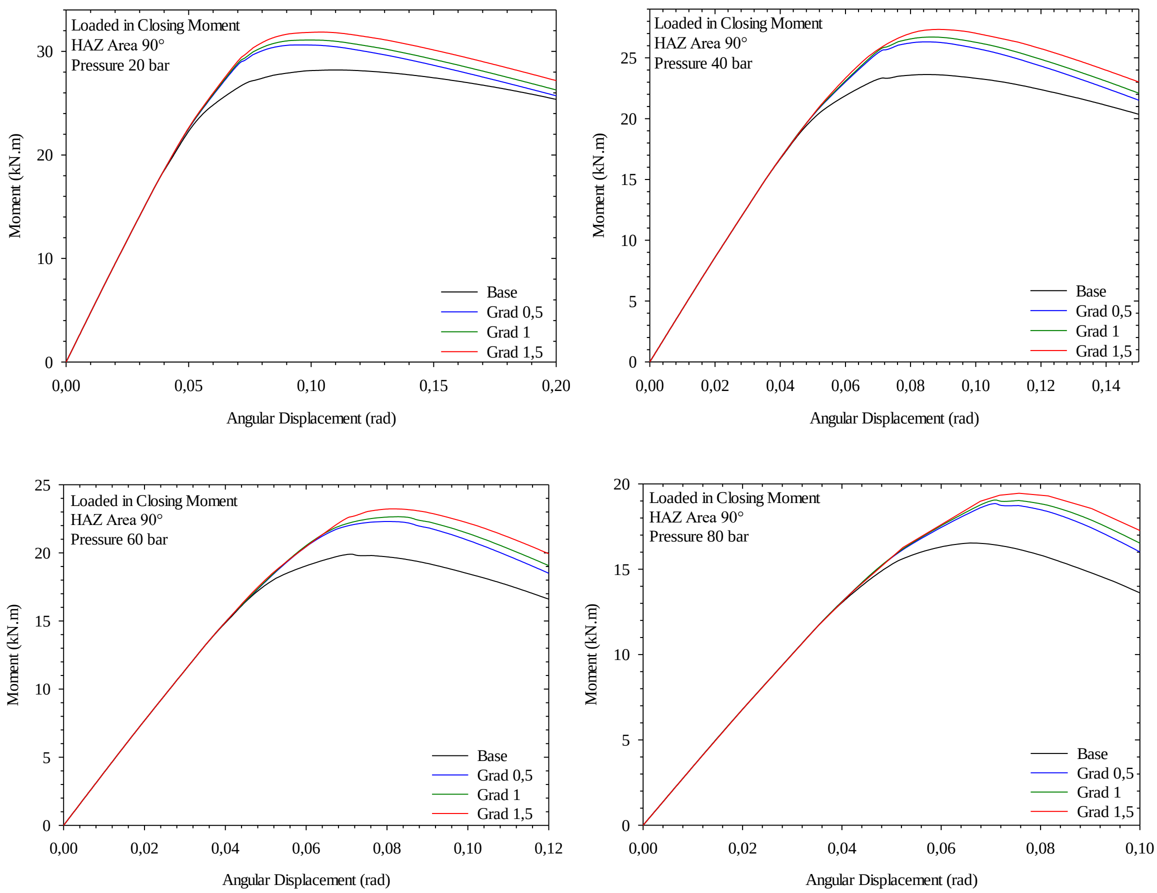

Figure 3. 90° closing graduation effect

In this Fig. 3 we have a bending moment in closure, we studied the effect of the graduation of the HAZ in the base metal at different pressure levels that of 20 bar 40 bar 60 bar and 80 bar, evaluating the response and structural damage helps us to properly identify the behavior under reinforcement of our structure analyze.,

In this bending moment mode (closure), the effect of HAZ scaling is significant, since the thermally affected surface area is large, the pressure effect becomes equally important, always regardless of the thermally-affected surface area, as the internal pressure increases there will always be a decrease in strength, most noticeable in its damage force value. The response of our structure is twofold: elasticity, which is identical due to the graduation effect, and plasticity, which is very different up to the point of damage. Reinforcement in this bending mode is very high, up to 4KNm.

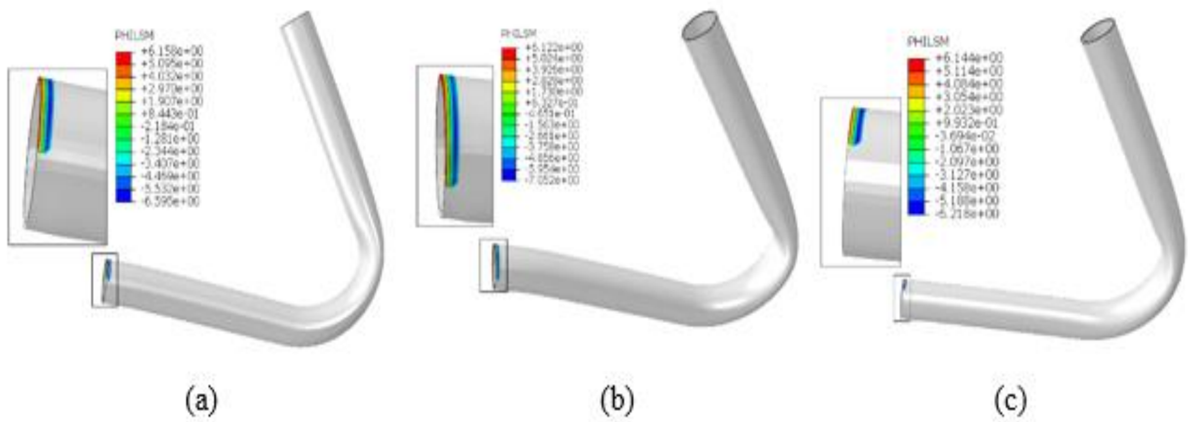

Figure 4. Representation of crack initiation at 80 bar pressure and pure fraction closure bending moment: (a) 1.5; (b) 1; (c) 0.5.

These captures are still the best way of presenting the crack location, but as in the previous presentation, they are limited to the case of the HAZ zone angle at 90° to the surface of the bend. In fact, any damage is rapidly triggered after a very slow crack propagation, but once it reaches its critical length, its propagation speed increases, and its propagation path differs according to the parameters studied in the previous sections. Damage always starts in the fixed side of the structure, otherwise it is favored at the bend without HAZ reinforcement.

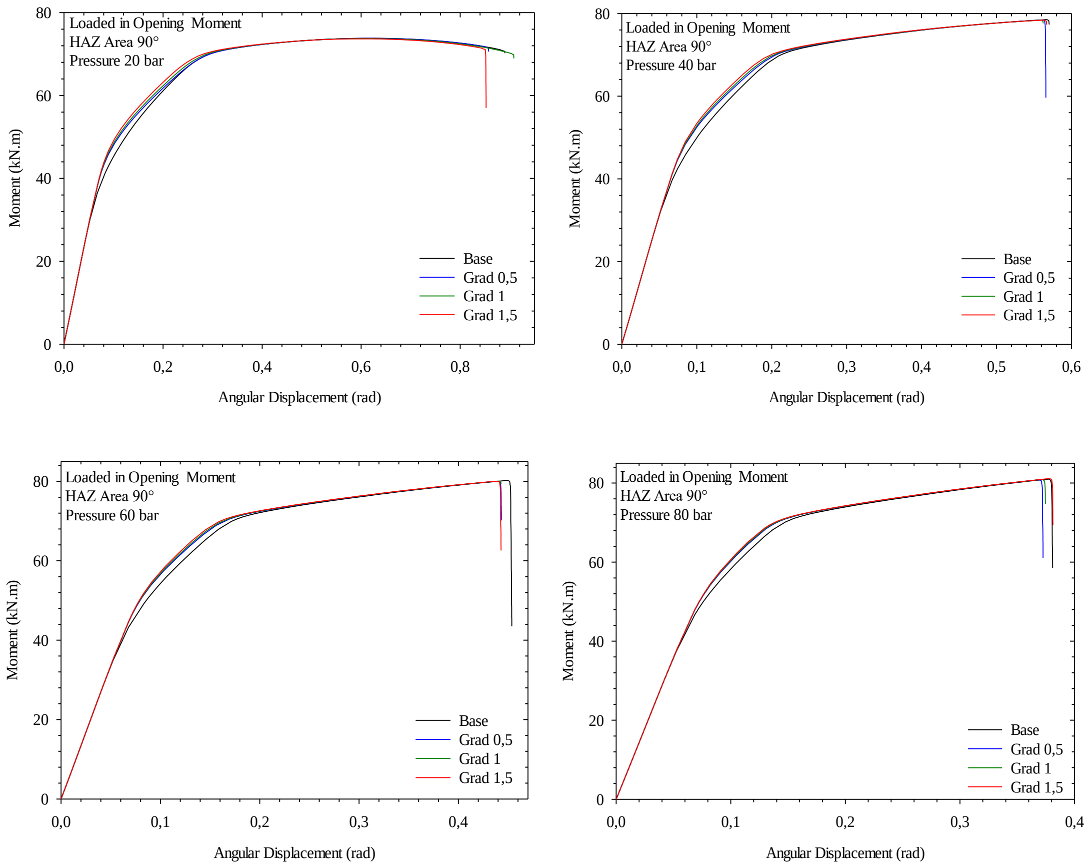

Figure 5. 90° opening graduation effect

In this part of the results presented in Fig. 5, we apply the HAZ graduation over a fairly large area, given by the angle of curvature of the bend, i.e. 90°. As in the previous analysis, we apply this HAZ area to the structure at each internal pressure value, from 20bar 40bar 60bar and 80 bar. In order to gain a broader understanding of the effect of the HAZ.

This figure shows and confirms the same results as above, such as the effect of HAT on the bending moment of the analyzed structure. For different levels of pressure, we still have the same observations: as pressure increases, the opening angle of the bend that corresponds to the damage decreases.

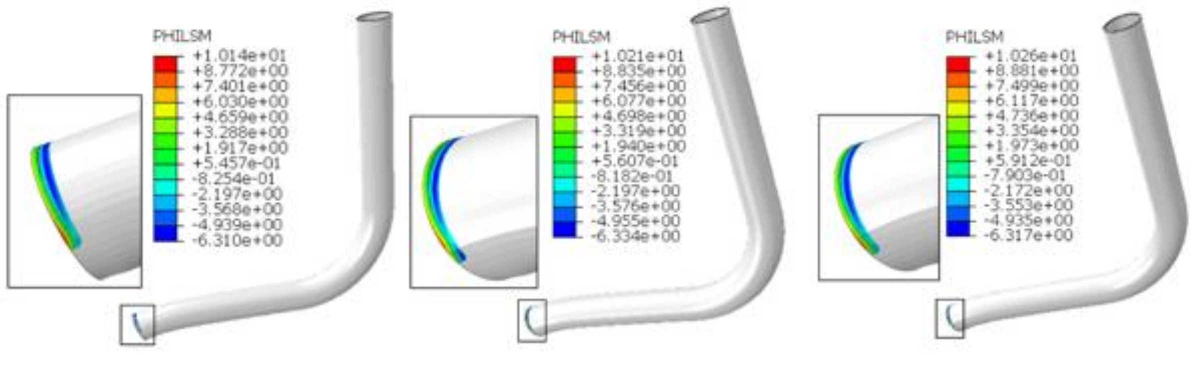

(a) (b) (c)

Figure 6. Crack initiation at 80 bar pressure and pure fraction opening bending moment: (a) 1.5; (b) 1; (c) 0.5.

Regardless of the bending mode, the crack location is always the same as that adjacent to the fixed part of our analyzed structure, even when internal pressure is quite high, which is the advantage of these captures. As previously presented, we remain limited to the case of the HAZ zone angle at 90° from the surface of the bend. The bend remains protected by the applied reinforcement of the heat-affected zone.

Conclusion

A new strengthening technique proposed in this work that can be applicable in tubular structures, these structures that work permanently under internal pressure, to properly present the advantage of our strengthening proposal, it is previously important to make a study on the mechanical behavior and that of the damage of these tubular structures, the conditions of these different structures is in stresses compound accumulated by other loading, our work is the subject of studying our structure with strengthening by surface heat treatment and localize, we have from the results obtained concluded the following:

- Numerical calculation with the new meshing technique eliminates any difficulties in calculation convergence, despite the introduction of several graded damage properties in the same structure, and also despite more complex loading conditions such as the bending moment in the presence of internal pressure and with more complex structure geometries, likewise when it comes to all mechanical behavior up to their damage.
- The XFEM (extend finite element method) technique used in the finite element method to predict damage in a graded structure is a method that proves its advantage in detecting critical values introduced into the graded structure with properties differing from one element to another.
- It can be seen that the closing bending moment is the most dangerous as an accumulated load in the presence of internal pressure.
- We can see that the presence of reinforcement in our analyzed structure considerably increases damage levels.
- In all the cases studied, reinforcement capacity depends largely on the surface area thermally affected and the presence of the HAZ in the structure.
- Using the XFEM method, which has the advantage of presenting the opening, we can locate the damage zone and predict the crack propagation path in the structure.

This numerical approach provides a broad view of mechanical behavior and the possibility of new reinforcement concepts for use in these types of structure to predict damage and improve strength.

Scientific Ethics Declaration

We, the authors, declare that the scientific, ethical and legal responsibility for this article published in EPSTEM Journal belongs to us.

Acknowledgements or Notes

* This article was presented as a poster presentation at the International Conference on Technology, Engineering and Science (www.icontes.net) held in Antalya/Turkey on November 14-17, 2024.

* I would like to thank the International Scientific Committee very sincerely for having done the honor of accepting our work, as well as the Organizing Committee and the Executive Committee, and all those who worked on the organization of this event.

References

Benzaama, A., Mokhtari, M., Ahmed-Bouziane, N. E. I., Abdelouahed, E., Habib, B., Ghermaoui, I. M. A., & Aliane, I. (2024). Using a UMM-XFEM technics to predict the damage in CFRP bi-graded with glass-epoxy materials of notched plate under quasi-static loading. *Mechanics of Advanced Materials and Structures*, *31*(25), 7367-7385.

Bragg, W. L., & James -Williams, E. J. (1934). The effect of thermal agitation on atomic arrangement in alloys. *Proceedings of the Royal Society of London. Series A, Containing Papers of a Mathematical and Physical Character, 145*(855), 699–730.

Constant, A., Henry, G., & Charbonnier, J.C. (1992). *Principes de base des traitements thermiques thermomécaniques et thermochimiques des aciers.* PYC (Ed.). https://esith.biblio.ma/opac_css/index.php?lvl=notice_display&id=9213

Dassault Systemes, D. (2014). *Abaqus Documentation*. Dassault Systemes, Providence, RI. http://62.108.178.35:2080/v6.14/index.html

Maachou, S., Mechab, B., Bachir Bouiadjra, B., & Salem, M. (2024). New predictıon of cracks propagatıon in repaired steel plate with bonded composite patch at cyclic loading. *Acta Mechanica et Automatica, 18*(4), 579-584.

Pratap-Singh, A., Pui-Li Yen, P., Ramaswamy, & H.S., Singh, A. (2018). Recent advances in agitation thermal processing. *Current Opinion in Food Science, 23*, 90-96.

Rui Yan, Hui Xie, Fei Yang, & Xiao-Ling Zhao. (2023). A macro prediction model for butt-welded (U)HSS connections with softened HAZ. *Journal of Constructional Steel Research, 211*, 108-153.

Shimatsu, T., Komagome, H., Muramatsu, K., & Nakamura, Y. (2000) Effect of thermal agitation on the magnetic properties of CoCrTa perpendicular recording media.. *Journal of the Magnetics Society of Japan, 24*(4−2), 239-242.

Shrivastava, R., Kumar, R. R., Santhoshkumar, R., Anoop, C. R., Cyriac, J., Chakravarthy, P., & Murty, S. N. (2024). Effect of grain size on the heat-affected zone (HAZ) cracking susceptibility in Ni base XH67 superalloy. *Metallurgical and Materials Transactions A*, *55*(1), 183-197.

Sliman, A. (2016). *Influence d’une hétérogénéité mécanique sur la déchirure d'une structure soudée*. Doctoral dissertation.

Tomerlin, D., Gubeljak, N., & Kozak, D. (2023). Gleeble simulation of HAZ in S690QL steel: Microstructural and mechanical properties. *Key Engineering Materials, 966*(4), 115-120.

Author Information

Sofiane Maachou
University Centre of Maghnia
PB 600, Maghnia, Tlemcen - Algeria
Contact e-mail: *sofianemaachou@gmail.com*

Djezouli Moulai-Khatir
Abou Bekr Belkaid University
PB 119, Tlemcen – Algeria

Abdeldjalil Benbakhti
University Centre of Maghnia
PB 600, Maghnia, Tlemcen - Algeria

Mohamed Mokhtari
Ecole Nationale Polytechnique Maurice Audin
PB 1523, Essenia, Oran - Algeria

To cite this article:

Maachou, S., MoulaI-Khatir D., Banbakhti, A., & Mokhtari, M. (2024). Thermal agitation study on a 90° surface of the radius of curvation of an Elbow. *The Eurasia Proceedings of Science, Technology, Engineering & Mathematics (EPSTEM), 32*, 373-378.

The Eurasia Proceedings of Science, Technology, Engineering & Mathematics (EPSTEM), 2024

Volume 32, Pages 379-388

IConTES 2024: International Conference on Technology, Engineering and Science

Experimental Study of Acoustical Properties of Recycled Rubber Panels

Yonka Ivanova
Sofia University "St. Kliment Ohridski"

Todor Partalin
Sofia University "St. Kliment Ohridski"

Abstract: This paper is focused on the characterization of multilayer acoustic panels made from recycled rubber waste produced by the Zebra factory in Bulgaria. The acoustical characteristics of rubber samples as well as three-layer panels were investigated to determine their applications as sound barriers or resilient flooring. The experiments to determine the sound absorption and sound reflection coefficients were carried out in laboratory conditions using the standing wave method in the frequency range from 100 to 2000 Hz. The potential of recycled materials to reduce airborne and impact noise was investigated and discussed. The sound insulation coefficients of recycled rubber panels were determined by the "two-chamber" method in the frequency range from 100 to 4000 Hz. For this purpose, small acoustic chambers were constructed and tested. The dynamic properties (dynamic stiffness and damping ratio) of the experimental materials were also investigated by an impact test. The obtained results have been discussed and analyzed with a view to evaluating the possibilities of application as acoustic barriers and flooring.

Keywords: Recycled rubber panel, Sound absorption, Sound insulation, Dynamic stiffness

Introduction

In recent years, the automotive industry has produced about 1.5 billion waste tires worldwide every year (Balmori et al., 2024; Presti et al., 2013; Martin et al., 2014; Valentini et al., 2022). Used tires accumulate and pollute the environment. An alternative solution to reduce used tires is to transform them through recycling and their subsequent application. Rubber granulate can be used for various applications in the production of elastomers, replacement of filler materials, panels with good sound and thermal insulation properties, resilient flooring and many other applications in civil construction (Balmori et al., 2024; Schiavoni et al., 2016; Kumar et al., 2020; Benkreira et al., 2011).

Recently, there has been a growing interest in the study of the properties of waste rubber materials and their appropriate application (Asdrubali et al., 2008; Medina et al., 2018; Nuzaimah et al., 2018; Balmori et al., 2024; Vilniškis et al., 2024). Despite the already published results about sound-absorbing and noise-insulating properties, the topic is relevant in view of the development of new materials from recycled rubber in the form of panels, partitions, elastic pads.

The aim of the present study is to investigate the properties such as sound absorption and reflection coefficient, sound insulation and dynamic stiffness of materials, made out of rubber crumbs.

Experimental Procedure

Materials

The object of investigation is the operational properties of recycled rubber products produced by the company Zebra AD, Sofia. The rubber panels are made from rubber granules of irregular shape and sizes from 2 to 5 mm, adhesive and a sheet of styrene butadiene rubber (SBR) with a thickness of 3 mm by pressing. Table 1 shows the materials from which five samples were made with the shape and dimensions required for the measurement. Comparative samples of Ethylene vinyl acetate (EVA)-Expanded Rubber with a density of 50 kg/m3 are also used in the research. The acoustic properties of double panels made of SBR rubber and two samples of rubber granules are also investigated.

Table 1. Materials

Material	Code	Density, kg/m3	Thickness, m
SBR+Rubber granules plate		1180	0.019
SBR+Rubber granules+SBR	SBR+M+SBR	1230	0.022

The methodology of experiments is consisted of the following steps:

Study of sound absorption and reflection coefficients;
Study of sound insulation and impact sound reduction by small-sized acoustic chambers;
Study of dynamic stiffness.

Sound Absorption Research Methodology

Investigation of the sound absorption and reflection properties of rubber panels was carried out in the impedance tube in laboratory conditions. The experimental setup consists of impedance tube with a diameter of 90 mm, a loudspeaker, a sound generator, PC based Real Time Analyzer and Sound Level Meter System, a microphone and Multi-Instrument Software. The testing equipment according to the standard EN ISO 10534-1 is presented in Figure 1.

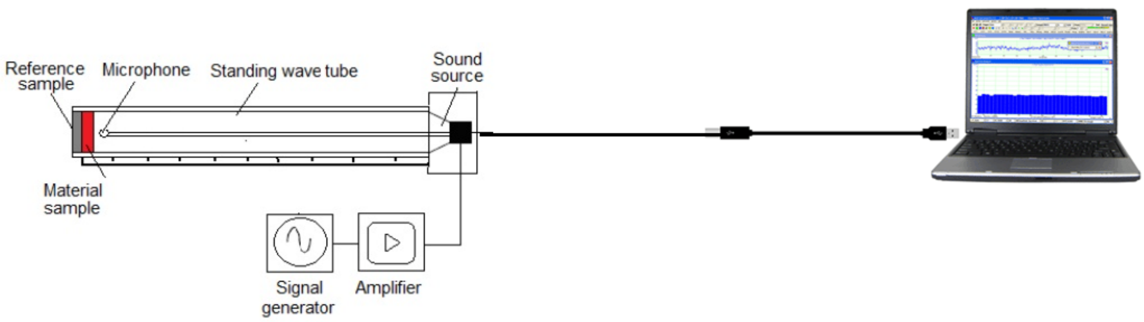

Figure 1. Schematic experimental setup of sound absorption and reflection measurement

The loudspeaker, which is located at one end of the tube, was induced by signal generator that generates sine waves in the frequency range from 100 to 2000 Hz. According to physical theory, the waves propagating in the tube to the other end and are reflected at the hard termination end cap made from brass material. The rubber samples are placed on the rigid end cap. The phase interference between the waves in the pipe which are incident upon and reflected from the test sample results in the formation of standing waves. The pressure amplitudes at nodes and antinodes are measured with a microphone probe which slides along a ruler. The ratio of the pressure maximum (antinode) to the pressure minimum (node) is called the standing wave ratio (SWR).

$$SWR = \frac{p_{rms,max}}{p_{rms,min}} \tag{1}$$

This ratio is used to determine the sample's reflection coefficient R and absorption coefficient α. Sound power reflection coefficient Rp can be expressed by

$$R_P = \beta = \left|\frac{SWR-1}{SWR+1}\right|^2 \tag{2}$$

The sound absorption coefficient α at a given resonance frequency is calculated by EN ISO 10534-1.

$$\alpha = 1 - R_p \tag{3}$$

$$\alpha = \frac{4SWR}{(SWR+1)^2} \tag{4}$$

Measurements in the frequency range were performed five times on each sample, which was glued and firmly attached to the pipe wall.

Methodology of Sound Insulation Measurement

Laboratory equipment for the evaluation of airborne and impact noise reduction must meet the requirements of the standards EN 16283, which requires the presence of a reverberation chamber with a volume of more than 10 m^3. For research purposes, many researchers have developed and used miniature acoustic boxes with a camera for the sound source and a camera to receive the transmitted sound (Godinho et al., 2010; Branco et al., 2010; Pleban et al., 2018; Kim et al., 2011:;Reddi et al.,2020; Wen et al., 2019). These non-standardized testing systems have been used to analyze and to compare the sound insulation of walls, partitions, and also initial evaluation of the impact noise of elastic layers (Rushforth et al., 2005).

To determine the sound insulation capacity of the experimental materials, the two-room method (Fahy, 2000; Isaac et al., 2020; Prato et al., 2013; ElSaeed et al., 2019). Has been applied. For the purpose of current investigation, a small acoustic box has been built especially for the tested materials. The use of small chambers does not follow the standards, but allows receiving the evaluation of sound insulation potential of the some materials. The testing in certain laboratory conditions can be reduced lateral sound transmissions from the test plate. Due to the small size, the system is expected to provide better results at mid and high frequencies.

The developed reduced acoustic box consists of two chambers. The chamber in which the sound source is located is a reverberation type and has dimensions of 700x600x600 mm. This chamber is built from the outside in from plasterboard, chipboard, mineral wool and glass panels. The glass walls on the inside form a five-sided box without parallel walls. Two full-range speakers with a frequency range of 20Hz to 20,000Hz are installed in the source chamber.

The receiving chamber is anechoic type with dimensions of 700x600x500 mm. It is made of chipboard, mineral wool and two insulation layers of foam and noise-absorbing pyramid-type foam. Between the two chambers there is a frame with an opening for mounting the examined specimens. Measurement microphones have a frequency range of 20Hz to 20,000Hz and are mounted in both cameras.

The differences in sound pressure levels of the sound waves in the source room and receiving room are recorded by a two-channel acoustic analyzer in real time by means of a special control and measurement software Multi Instrument 3.9 Proffessional. The sound transmission outside the experimental setup is minimized. Figure 2 shows a schematic of the small acoustic chambers used for sound insulation study.

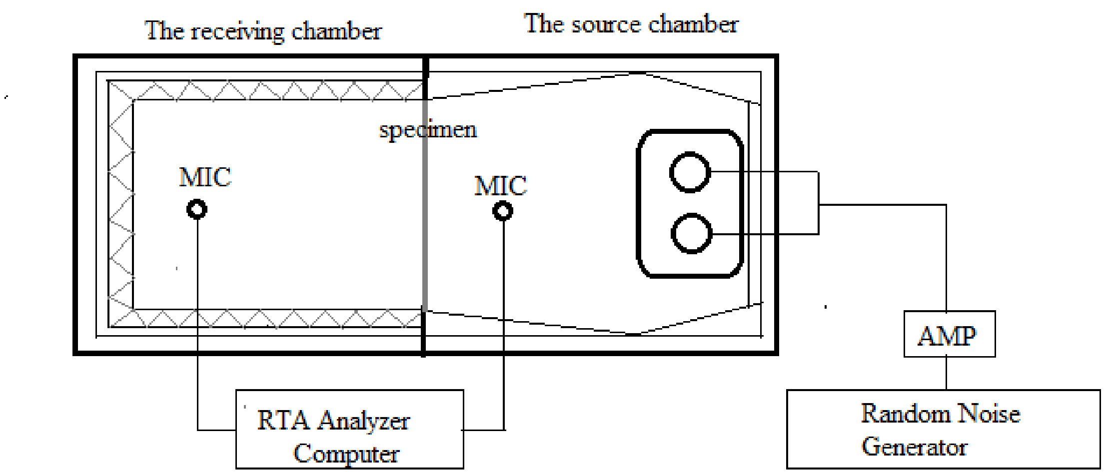

Figure 2. Schematic experimental setup of small-sized acoustic chambers.

Study of Dynamic Stiffness of Recycled Rubber Materials

The resilient materials such as recycled rubber are used in constructions called "floating floors". The effectiveness of the floating floors depends on the mechanical properties of the insulation layers (Belli et al.,2003; Schiavi et al., 2007; Schiavi et al., 2015). Dynamic stiffness is one of important properties impact sound insulation materials. The measurement method for the determination of dynamic stiffness is defined in EN 29052-1. A mass representative for typical floating floors is used to impose a static load on the tested specimen. The mass is excited by impact hammer and from the resonance frequency of this spring-mass system, the dynamic stiffness (s') is calculated with the relation:

$$s' = (2\pi f_r)^2 . m \tag{5}$$

Where *m* is the mass per unit area of the loading plate (200 kg/m^2), f_r is the resonance frequency in Hz. Another important property of elastic layers is internal damping. The resonant frequency curve carries this information. Using the half-power point method, it is possible to estimate the internal damping ratio δ and quality factor Q.

$$Q = \frac{f_o}{f_2 - f_1} = \frac{f_o}{\Delta f} = \frac{1}{2\delta} \tag{6}$$

Where the frequencies f_1 and f_2 are these frequency values, where the acceleration level has decreased by 3 dB.

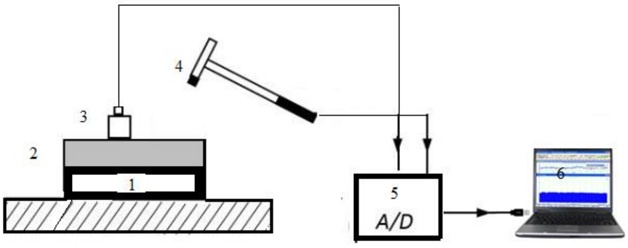

Figure 3. Schematic experimental setup for measuring the dynamic stiffness: 1) the rubber test specimen; 2) the upper steel plate; 3) the accelerometer (CA-YD-160); 4) the impact hammer (LC-01KE); 5) the data acquisition card (VT IEPE-2G05) and 6) the PC.

Results and Discussion

Results of Sound Absorption Measurement

Figure 4 shows the sound absorption and reflection coefficients vs. frequency for the tested materials. Figure 4a presents the test results of SBR+M sample, with the sound-reflecting surface being the smooth SBR rubber side. Figure 4 b gives results from the same specimen, with the sound-reflecting surface being the rough side of the recycled rubber granules plate. Figure 4c shows the sound absorption and reflection for a 22 mm thick SBR+rubber granule plate+ SBR panel. Figure 4d shows the results of an examination of a panel made of SBR, two plates of rubber granules and SBR with a total thickness of 28 mm.

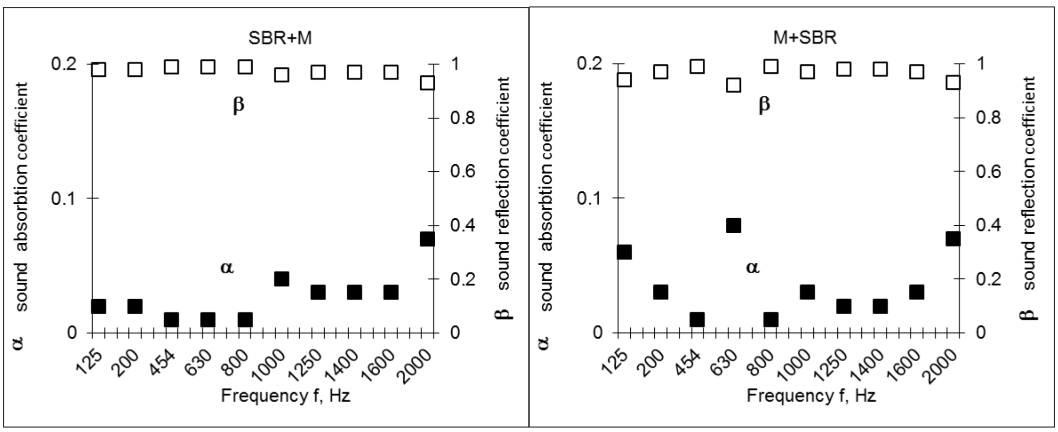

a) b)

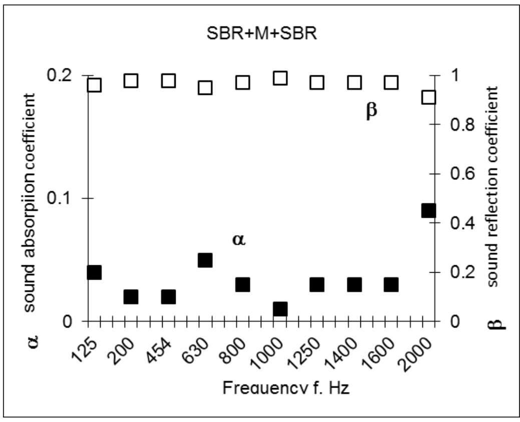

c)

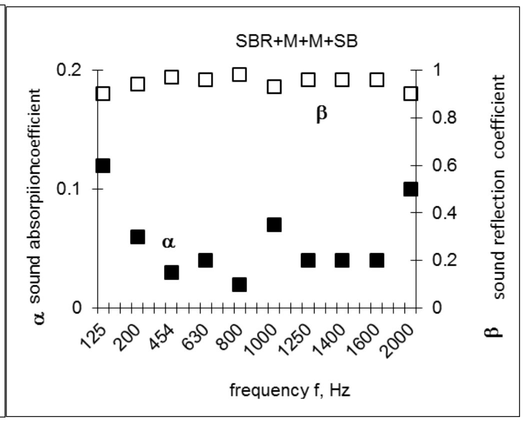

d)

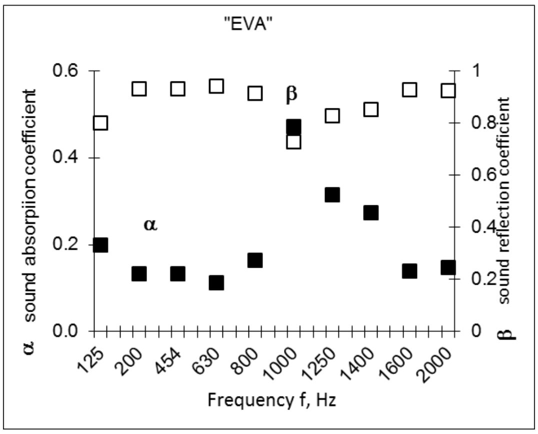

e)

Figure 4. Sound absorption and sound reflection for different waste materials:
a – SBR+M; b – M+SBR; c- SBR+M+SBR; d- SBR+M+M+SBR; e- EVA sample

It can be observed that the values of the sound absorption coefficients are low throughout the frequency range of the study, with average values below 0,1. The relatively high density and pore-free test samples show a high sound reflection coefficient of about 0,9. Figure 4 e) shows the results of a comparison sample type "EVA" with a thickness of 26 mm and a density of 50 kg/m^3. The average value of the sound absorption coefficient is about 0,4. It can be seen that at some frequencies the coefficient increases. The results can be explained by the closed cell surface structure with high sound impedance and high sound reflection. (Segura, et al., 2015).

Results of Sound Insulation Measurement

The sound insulation coefficient has been determined using the two small acoustics chambers between which a test specimen is placed. The test samples are recycled rubber plates with dimensions of 500x500 mm and different thicknesses. The mode of operation is stationary. The following conditions have been maintained during the measurements: the distance between the source and the microphone is greater than 0.5 m; the measurement time is greater than 120 s; white noise is used as a sound signal; the level of the emitted sound signal is 100 dB.

The determination of sound insulation coefficient of the experimental samples consists of making measurements of the sound pressure levels in the source chamber and in the receiving chamber, followed by a calculation of the difference between the two values. The emitted and received signals and their frequency characteristics have been monitored using an oscilloscope, and the analysis has been performed in one-third octave frequencies. The sound insulation coefficient R is calculated using the relationship:

$$R = Lp_1 - Lp_2 \tag{7}$$

Where Lp_1 is the average sound pressure level in the source chamber, Lp_2 is the average sound pressure level in the receiving chamber.

The results of the measurements carried out for the rubber plates are averaged and given in Figure 5. Figure 5a shows the results of the sound insulation coefficients when testing a rubber granules plate, and Figure 5b -the results of the meadurement of a SBR+M+SBR panel.

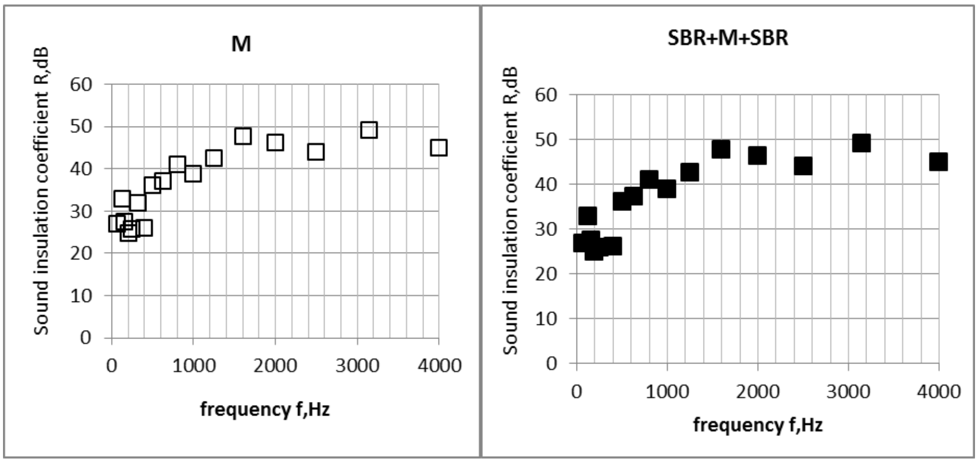

a) b)

Figure 5. Sound insulation coefficients vs. frequency

a) Recycled rubber granules specimen; b) Panel SBR+M+SBR

It can be noted that the average sound insulation coefficients for the studied recycled rubber samples (M), as well as for the panels made with the addition of rubber sheet (SBR+M+SBR), are about 38 dB in the studied frequency range up to 4000 Hz. The products could be used for soundproofing walls, ceilings and floors.

Results of Impact Sound Reduction

The measurements of the impact sound reduction have been performed in the described small-sized acoustic chambers. A metal ball weighing 0.5 kg was used as the impact source dropping from a height of 40 mm. The floor was not a concrete slab, but chipboard with a thickness of 20 mm. The impact sound pressure level resulting from the installation of a chipboard floor has been determined. A panel of recycled rubber is then added to the chipboard and the impact sound pressure level resulting from the placement of the tested flooring is measured. The defined characteristic is the improvement in impact sound insulation, ΔL, defined as the reduction in normalized impact sound pressure level resulting from the placement of the tested flooring.

$$\Delta L = L_{no} - L_n \qquad (8)$$

Where L_{n0} is the normalized sound pressure level when hitting a floor without a rubber coating and Ln is the normalized sound pressure level upon impact on the floor with rubber coating. The results of the ΔL, in decibels are given in the Figure 6. It can be seen that the impact noise reduction at frequencies from 1000 to 4000 Hz averages about 22-23 dB for the rubber crumbs plate and SBR+M+SBR panel.

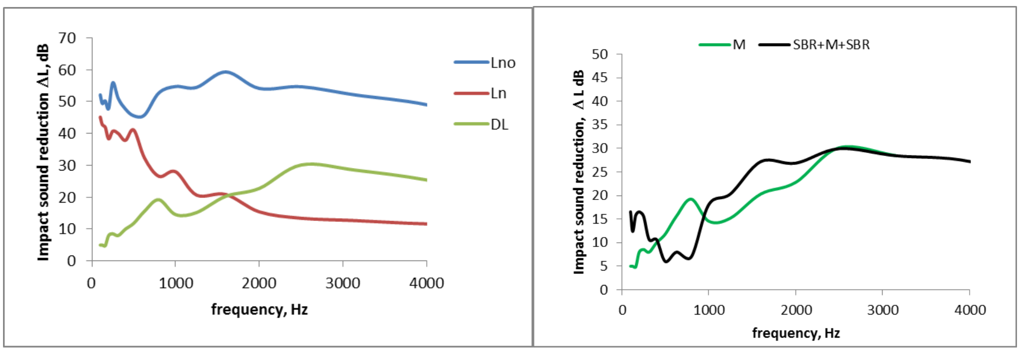

a) b)

Figure 6. Impact sound reduction vs. frequency

a) sound pressure levels without a rubber, with recycled rubber plate and impact sound reduction;

b) impact sound reduction for rubber crumbs plate M and panel SBR+M+SBR

Results of Dynamic Stiffness Measurement

The measurements of the dynamic hardness of the recycled rubber samples are performed by setup, shown in the Figure 3. The test specimens are cylindrical with the same diameter of 90 mm and different thicknesses as shown in Table 2. They are placed on a main solid steel plate weighing 30 kg. The loading steel plate weighs 1.2 kg, so the reduced loading mass is 200 kg/m^2.The accelerometer is glued in the center of the steel plate. Excitation is by an impact modal hammer with a stiff tip. A signal from the accelerometer is recorded after the excitation is applied. The chosen frequency resolution is $\Delta f = 0.2$ Hz.

The frequency analyzer allows us to identify the resonant frequency of the mass-spring system, consisting of the load plate and the elastic material. The widths of the resonance curve at a level 3 dB from the maximum of the resonance peak, necessary for the calculation of the quality factor and damping ratio, have been also determined. On each sample, 5 recordings were made for 20 seconds and the resonance curves have been obtained.

The results are averaged and shown in Table 2. Figure 7 present frequency resonance curves of tested samples: a- test sample SBR rubber sheet with a thickness of 3 mm; b- test sample recycled rubber from rubber crumbs and tightly glued rubber sheet SBR; 3- panel obtained from SBR+M+SBR; 4- SBR+M+M+SBR; 5- test specimen is EVA type porous rubber. The dynamic stiffness was calculated according to (5), and quality factor and damping ratio - according to (6).

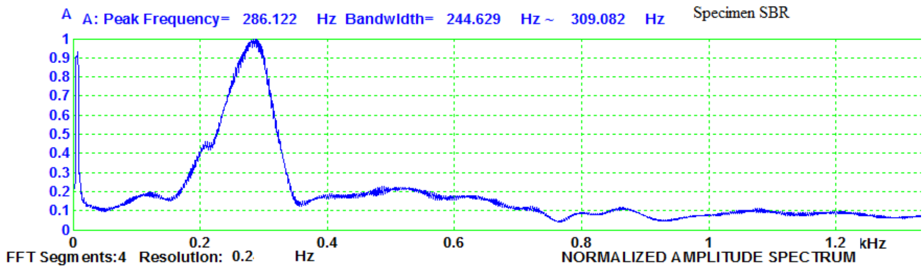

a)

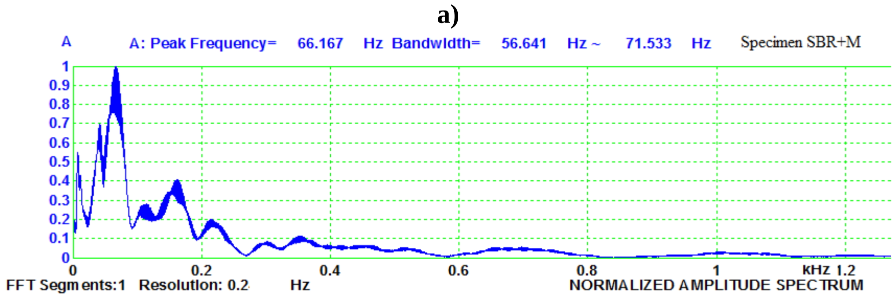

b)

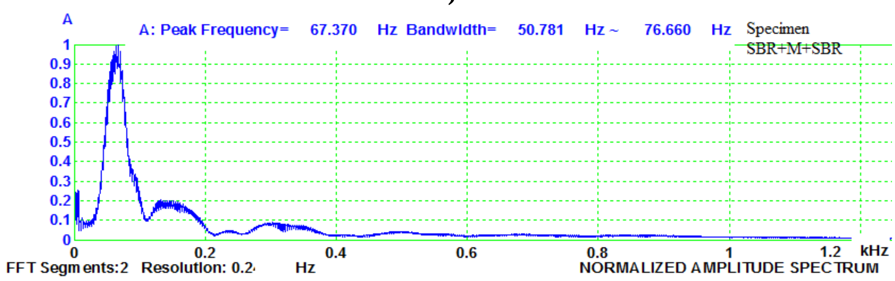

c)

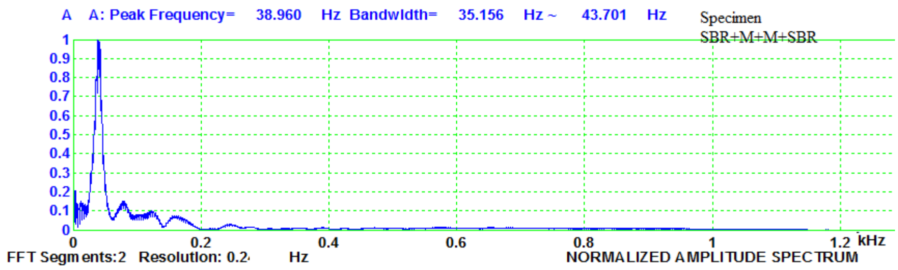

d)

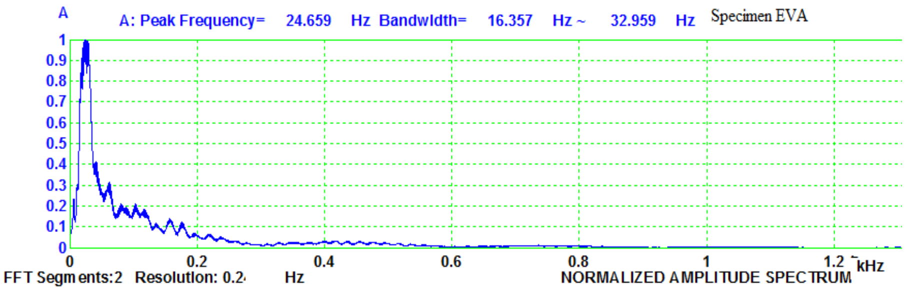

e)

Figure 7. Frequency resonance curves of tested materials:
a) Rubber sheet SBR; b) SBR+M ; c) SBR+M+SBR; d) SBR+M+M+SBR; e) EVA rubber

Table 2. Resonance frequencies, quality factor Q, damping ratio δ (%) and calculated dynamic stiffness

Ho	Specimens	Thickness, mm	Resonance Frequency, Hz	f1,Hz	f2,Hz	Quality factor	Damping, %	Dynamic stiffness, MN/m2
1	SBR	3	286.12	244.6	309.1	4,4	11,3	645,7
2	SBR+M	19	66.17	56.64	71.53	4,4	11,3	34,5
3	SBR+M+SBR	22	65.94	50.3	77.15	2,46	20,4	34,3
4	SBR+M+M+SBR	28	39.96	35.16	43.70	4,67	10,69	12,6
5	EVA	26	27.33	20.508	34.18	2,00	25,00	5,9

The value of the dynamic stiffness of the recycled materials SBR+M and SBR+M+SBR is about 34.5 MN/m^2. Increasing the thickness of the resilient layer to 38 mm leads to a decrease in the value of the dynamic stiffness and it is 12.5 MN/m^2. For comparison, the result of the EVA tire, where the dynamic stiffness is approximately 6 MN/m^2, is also given. However, insulation layers with a high elasticity coefficient, under load, deteriorate the acoustic properties. Harder insulating layers will retain their insulating properties longer (Belli et al.,2003).

In Baron et al. (2004) the dynamic stiffness is given for various polymers used as elastic materials, e.g. synthetic polystyrene or treated rubber material mixed with elastomeric elements and their values are lower than 30 MN/m^3. The lower the dynamic stiffness, the better is the impact noise isolation. According to Segura et al. (2015) the dynamic stiffness values of some commercial resilient layers for floor applications are below 20 MN/m^3. According to Belli et al. (2003), Schiavi et al. (2007), Schiavi et al. (2015) once the resonant frequency and the damping ratio are known, it is possible to estimate the impact sound reduction and predict the behavior of the floating floor insulation layers (Belli, et al.,2003).

Conclusion

The paper presents a study of the properties of recycled rubber sheets and panels. These rubber products have low sound absorption and are not suitable as sound absorbing materials. In addition, the sound insulation properties against airborne and impact noise were investigated using small acoustic chambers. The average values of the sound insulation coefficient are about 36-38 dB for both the rubber crumbs plate and the SBR+M+SBR panel. These recycled materials can be used for sound insulation of walls, floors and ceilings, etc. and have potential for vibration insulation. Some results were also obtained for the dynamic stiffness. As the thickness of the insulating rubber layers increases, the stiffness decreases. Knowing this characteristic enables an indirect assessment of impact noise reduction in the application of recycled rubber products as underlays for floating floors.

Recommendations

The presented research can provide new knowledge to students and engineers about evaluation of the acoustic properties of recycled rubber products.

Scientific Ethics Declaration

The author declares that the scientific ethical and legal responsibility of this article published in EPSTEM Journal belongs to the authors.

Acknowledgements or Notes

This article was presented as a poster presentation at the International Conference on Technology, Engineering and Science (www.icontes.net) held in Antalya/Turkey on November 14-17, 2024.

References

Abou-zeid, M., Elsaeed, A., & Ghaly, A. (2019). A proposed use of sound insulation systems. *CSCE Annual Conference, Canadian Society for Civil Engineering*, 1-7.

Asdrubali, F., D'Alessandro, F., & Schiavoni, S. (2008). Sound absorbing properties of materials made of rubber crumbs. *Journal of the Acoustical Society of America, 123*(5), 3037.

Balmori, J. A., Casado-Sanz, M., Machimbarrena, M., Quirós-Alpera, S., Mostaza, R., & Acuña, L. (2023). The use of waste tyre rubber recycled products in lightweight timber frame systems as acoustic ınsulation: A comparative analysis of acoustic performance. *Buildings*, *14*(1), 35.

Baron, N., Bonfiglio, P., & Fausti, P. (2004). Dynamic stiffness of materials used for reduction in impact noise: Comparison between different in measurement techniques. *Acoustica, Paper ID*, *66*, 1-8.

Belli, A. P., Russo, F., & Schiavi, A. (2003, May). Measurement of dynamic stiffness to estimate the reduction in impact sound pressure level. In *Proceedings of the 5th European Conference on Noise Control* ,19-21.

Benkreira, H., Khan, A., & Horoshenkov, K.V. (2011). Sustainable acoustic and thermal insulation materials from elastomeric waste residues. *Chemical Engineering Science*, *66*, 4157–4171.

Branco, F.G., Godinho, L., Pereira, A., & Masgalos, R. (2010). Analysis of impact sound reduction by floor coverings using a small-sized acoustic chamber, *Proceedings of Conference Internoise, 2010*(8),2805-2815.

Carbajo, J., Poveda, P., Segovia, E., Prieto, A., Río-Martín, L., Pastor, J.D., & Ramis, J. (2024). An alternative approach to determine the dynamic stiffness of resilient materials under low prestatic load. *Applied Sciences*. *14* (11), 4925.

ENISO, I. (2001). *10534-1, determination of sound absorption coefficient and ımpedance in ımpedance tubes part 1: Method using standing wave ratio*. British Standards Institution.

Fahy, F. (2000). *Foundations of engineering acoustics* (1st ed.). Elsevier.

Godinho, L., Masgalos, R., Pereira, A., & Branco, F. G. (2010). On the use of a small-sized acoustic chamber for the analysis of impact sound reduction by floor coverings. *Noise Control Engineering Journal*, *58*(6), 658-668.

Isaac, C.W., Pawelczyk, M., & Wrona, S. (2020). Comparative study of sound transmission losses of sandwich composite double panel walls. *Applied Sciences, 10* (4), 1543.

Kim, T. M., & Kim, J. T. (2011). Comparison study of sound transmission loss in high speed train, *IJR International Journal of Railway*, *4* (1),19-27.

Kumar, D., Alam, M., Zou, P.X.W., Sanjayan, J.G., & Memon, R.A.(2020). Comparative analysis of building insulation material properties and performance. *Renewable and Sustainable Energy Reviews*, *131*, 110038.

Martin, F. (2014). *Recycling and re-use of waste rubber.* Shawbury, UK: Smithers.

Medina, N.F., Garcia, R., Hajirasouliha, I., Pilakoutas, K., Guadagnini, M., & Raffoul, S. (2018). Composites with recycled rubber aggregates. Properties and opportunities in construction. *Construction and Building Materials, 88*(1–2), 884-897.

Nuzaimah, M., Sapuan, S.M., Nadlene, R., & Jawaid, M. (2018). Recycling of waste rubber as fillers: A review. *IOP Conference Series: Materials Science and Engineering*, *368*, 012016.

Pleban, D., & Mikulski , W.(2018). Methods of testing of sound insulation properties of barriers intended for high frequency noise and ultrasonic noise protection. *Journal of mechanical engineering – Strojnícky časopis*, *68*(4), 55 – 64.

Reddi, Chi, & Naidu B. (2020). Construction of small twin reverberation chamber for measurement of sound transmission loss, *Proceedings of 49th International Congress and Exposition on Noise Control Engineering "Internoise 2020",* 1-12.

Rushforth, I.M. , Horoshenkov, K.V., Miraftab, M., & Swift, M.J. (2005). Impact sound insulation and viscoelastic properties of underlay manufactured from recycled carpet waste. *Applied Acoustics*, *66*,731–749.

Schiavi, A., Pavoni -Belli A., Corallo, M., & Russo, F. (2007). Acoustical performance characterization of resilient materials used under floating floors in dwellings. *Acta Acustica United with Acustica, 93*(3), 477-485.

Schiavi, A., Prato, A., Barbaresi, L., & Semprini, G. (2015). The effect of damping in resilient materials used in floating floors on impact sound insulation. *Atti del Convegno ICSV22, Firenze*, 12-16.

Schiavoni, S., D'Alessandro, F., Bianchi, F., & Asdrubali, F. (2016). Insulation materials for the building sector. A review and comparative analysis. *Renewable and Sustainable Energy Reviews*, *62*, 988–1011.

Segura J. G., Julia, E., & Gadea, J. M. (2015). Impact acoustic isolation of ethylene vinyl acetate panels. *Annals of the Oradea Universit , Fascicle of Management and Technological Engineering*, *1*, 245-248.

Valentini, F., & Pegoretti, A. (2022). End-of-life options of tyres. *Advanced Industrial and Engineering Polymer Research, 5*, 203-213.

Vilniškis, T., & Januševicius T. (2024). Sound insulation properties of sound-reduction louvers with innovative devulcanized rubber. *Archives of Acoustics*, *49* (3), 359–368.

Wen, Z. H., Wang, D. W., & Ma, L. (2021). Sound transmission loss of sandwich panel with closed octahedral core. *Journal of Sandwich Structures & Materials*, *23*(1), 174-193.

Zebra-AD. (n.d.). *Products.* Retrieved from https://www.zebra-bg.com/en/products.

Author Information

Yonka Ivanova
Sofia University "St. Kliment Ohridski", Faculty of Physics, Bulgaria
Institute of Mechanics at Bulgarian Academy of Sciences, Sofia, 1113, Acad. G. Bontchev Str.,bl.4, Bulgaria
Contact e-mail: *yonivan@phys.uni-sofia*.

Todor Partalin
Sofia University "St. Kliment Ohridski",
Faculty of Mathematics and Informatics, 1164 Sofia, 5 James Bourchier Blvd. Sofia, Bulgaria.

To cite this article:

Ivanova Y., & Partalin, T. (2024). Experimental study of acoustical properties of recycled rubber panels. *The Eurasia Proceedings of Science, Technology, Engineering & Mathematics (EPSTEM), 32*, 379-388.

The Eurasia Proceedings of Science, Technology, Engineering & Mathematics (EPSTEM)
ISSN: 2602-3199

The Eurasia Proceedings of Science, Technology, Engineering & Mathematics (EPSTEM), 2024

Volume 32, Pages 389-399

IConTES 2024: International Conference on Technology, Engineering and Science

Simulation Study of Electronic Band Diagram Engineering and Electrical Parameters to Boost the Photovoltaic Performance of Novel Rb_2PtI_6 Double Perovskite Solar Cell

Souheyla Mamoun
Abou Bekr Belkaid University of Tlemcen

Abdelkrim El-Hasnaine Merad
Abou Bekr Belkaid University of Tlemcen

Amina Benmansour
Abou Bekr Belkaid University of Tlemcen

Abstract: It was shown recently that the double perovskite Rb_2PtI_6 exhibits excellent electronic and optical properties that are relevant for photovoltaic applications in particular. Herein, we report deep simulation results of a novel high-performance lead-free halide double perovskite solar cell (PSC) with the architecture FTO/ZnSe/Rb_2PtI_6/$MoSe_2$/C. The thicknesses of all layers such as: FTO, hole transport layer (HTL), Rb_2PtI_6 absorber and electron transport layer (ETL) for the device were optimized. The role of electronic band diagram engineering is demonstrated to be essential for the photovoltaic performance of the solar cell. Moreover, the effects of capacitance (C-V), Mott–Schottky (M-S) characteristics, generation and recombination rates, series resistance (R_s) and shunt resistance (R_{sh}) on the current-voltage characteristics (J-V), and quantum efficiency (QE) are analyzed. Our obtained results shows that this best proposed Rb_2PtI_6-based device can serve as a potential eco-friendly high efficiency solar cell candidate due to the chemical stability and non-toxicity of its active layer. The best obtained efficiency PCE reaches 20.54 %, with short circuit current density J_{SC} of 34.41 mA/cm^2, open circuit voltage V_{oc} of 0.79 V and fill factor FF of 75.8 % compared to the initial PCE of 12.94 %. To validate our results, we compared the simulation outcomes with other similar double PSC cells previously published. Good agreement is obtained with experimental and simulation studies.

Keywords: Lead-free halide double perovskite solar cells based on Rb_2PtI_6, band gap diagram, Generation and recombination rates, Series resistance (R_s), Shunt resistance (R_{sh}).

Introduction

In the purpose to enhance the power conversion efficiency (PCE) of photovoltaic (PV) solar cells (SC) in a hand and preserve the ecologic system for future generation from polluted materials in the other hand, several experimental and theoretical studies have been published. Thus, a scientific and ecologic race to search and use appropriate materials appeared. Recently, halide perovskites (HP) ABX_3 are in the top of this race due to their attractive properties such as tunable band gap (Huang et al., 2017). Strong light absorption (Yue et al., 2016). And high carrier mobilities (Sun et al., 2021**)**. To have more ideas about the whole perovskites' studies published we can refer to the following review papers: Jodlowski et al. (2018),Yin et al. (2019), Lu. et al. (2020), Zhao et al. (2021), Nair et al. (2022).

In some studies, the cation A (who was formed by the methylammonium $[CH_3NH_3]^+(MA^+)$ in the earlier studies of HP) was substituted partially or completely by another organic cation formamidinium $[HC(NH_2)_2]^+(FA^+)$ (Zhang et al., 2018; Zheng et al., 2022). And inorganic ones like cesium (Cs^+), Gallium (Ga), potassium (K^+) and rubidium (Rb^+) (Saliba et al., 2016;Park et al., 2017;Ono et al., 2017).

In others studies, the anion B (who was formed by the toxic element lead (Pb^{2+}) in the earlier studies of HP) has been also partially or completely replaced by other elements like: silver (Ag^{+}) (Abdi-Jalebi et al., 2016). Copper Cu^{+}(Shahbazi et al., 2017). Tin (Sn^{2+}) (Fujihara et al., 2017**)**. Germanium (Ge^{2+}) (Kanoun et al., 2019**)**. Antimony (Sb^{3+}) (Boopathi et al., 2017). Bismuth (Bi^{3+}) (Jin et al., 2020). It seems that this effect responds to this need but it affects negatively the stability: the mixed organic-inorganic cation (HP) structures formed are vulnerable to degradation upon exposure to light, high temperature and humidity (Wei et al., 2020).

However, in inorganic halide double perovskite structures (IHDP) A_2BX_6, and especially in the vacancy ordered ones, this main problem is taken off due to the strong covalency in the cluster $[BX_6]^{2-}$(Bartel et al., 2019). And especially in platinum (Pt) based ones (Suzuki et al., 2021). It is shown that the rotation angles θ of the PtX_6 octahedra are non-zero. For a given A-site cation, θ increases from Cl to Br to I while for a given halide anion, θ decreases from K to Rb to Cs. It is found that the band gap values increase when the halogen element X is varied from iodide I, to bromide Br to chloride Cl (Cai et al., 2017; Faizan et al., 2021). Also, it is proved that iodide based double perovskite are the most efficiency (Kumar et al., 2021**)**.

It was proven by ab initio calculation Cai et al. (2017), Zhao et al. (2021), (Suzuki et al., 2021) that the two vacancy ordered IHDP Cs_2PtI_6 and Rb_2PtI_6 are stables (formation enthalpy equal to -0,97 and - 0.92 eV/atom respectively), have suitable band gap (1.4 eV and 1.3 eV in the cubic structure respectively), their absorption coefficients are of the order of 10^4–10^5 cm^{-1}. Indeed, employing the spectroscopically limited maximum efficiency as a metric for quantifying the photovoltaic performance, these iodides compounds are found to be promising absorbers in solar cells.

Since recently, a new promising solar cell based on the vacancy ordered IHDP Cs_2PtI_6 has been synthetized and experimentally tested by Schwartz et al. (2020) it has an excellent stability and oxidation resistance, high absorption coefficient (4×10^5 cm^{-1} superior than $MAPbI_3$'one $10^5 cm^{-1}$) and long carrier life time (superior than 2μs as long as that of $MAPbI_3$). The PCE of their adopted structure FTO/CdS/Cs_2PtI_6(10-15 μm)/ElectroDAG440B/Cu is about 10.7% and can enhance to 13.88 % when ethylene diamine EDA (a chemical treatment) is added.

Using SCAPS-1D software **(**Burgelman et al., 2021). Cs_2PtI_6 was also theoretically studied by Shamna et al. (2022), AbdElaziz et al. (2022), and Amjad et al. (2023). They showed that the PCE of their optimized structure FTO/ZnO/Cs_2PtI_6/MoO_3/C, FTO/WS_2/Cs_2PtI_6(0.4 μm)/Cu_2O/C and FTO/SnO_2/Cs_2PtI_6(0.4 μm)/MoO_3/C can reach 20.45 %, 22.4 % and 23.52 % respectively.

Then, as Cs_2PtI_6, Rb_2PtI_6 can be also an effective candidate for lead-free photovoltaic materials whereas, to our best knowledge, it has not been used in any theoretical or experimental solar cell study. In this context, we aim to investigate numerically, for the first time, the photovoltaic performances of a novel solar cell architecture based on the vacancy ordered IHDP Rb_2PtI_6 as absorber using the SCAPS-1D code (Burgelman et al., 2021**)**.

In this study, we sandwich the IHDP Rb_2PtI_6 between ZnSe used as electron transport layer (ETL) and $MoSe_2$ used as hole transport layer (HTL) and we try to ameliorate the PV performance of this initial device by the optimization of the thicknesses of all layers. We extend the study to the analysis of the effects of capacitance (C-V), Mott–Schottky (M-S) characteristics, generation and recombination rates, series resistance (R_s) and shunt resistance (R_{sh}) on the current-voltage characteristics (J-V).

Method

We used SCAPS-1D code (Burgelman et al., 2021**)**. Which is based theoretically on the fundamental equations: Poisson's equation (1) and continuity equation for holes and electrons equation (2):

$$\frac{d^2\psi}{dx^2} = \frac{e}{\varepsilon_0\varepsilon_r}\left[p(x) - n(x) + N_D - N_A + \rho_p - \rho_n\right] \tag{1}$$

Where ψ is electrostatic potential, n and p are electron and hole concentrations, ε_0 is vacuum and ε_r is relative permittivity, N_D and N_A are donor and acceptor doping density, ρ_n, ρ_p are electrons and holes distribution,

$$\frac{dJ_p}{dx} = \frac{dJ_n}{dx} = G - R \tag{2}$$

Where G is generation rate and R is recombination rate, J_p and J_n are holes and electron current densities.

Carrier transport occurs according to the following drift and diffusion equations:

$$J_n = \mu_n n \frac{d\psi}{dx} + D_n \frac{dn}{dx} \quad (3)$$

$$J_p = \mu_p p \frac{d\psi}{dx} + D_p \frac{dp}{dx} \quad (4)$$

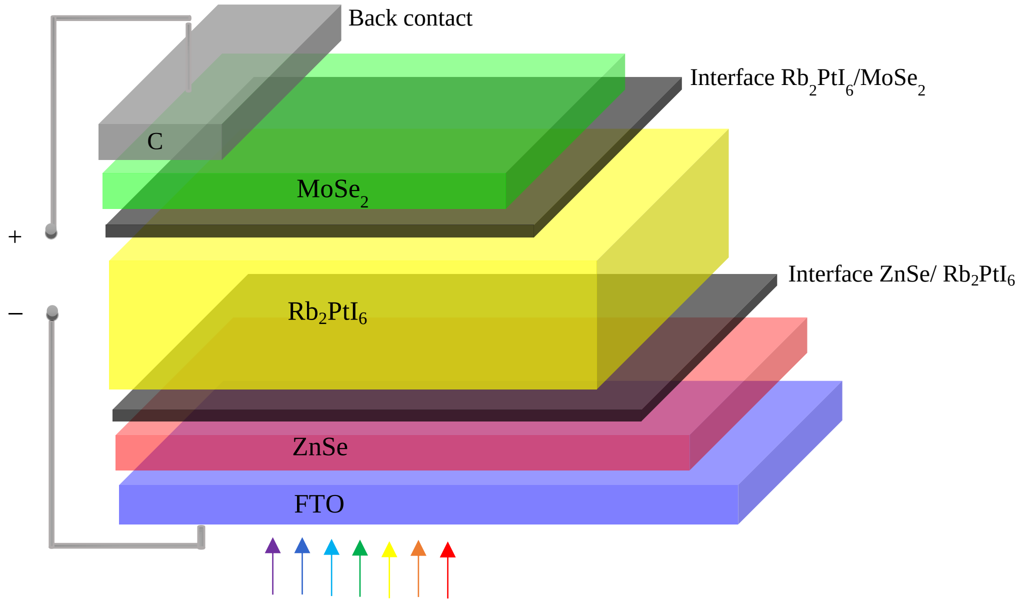

Figure 1. Architecture of the adopted device

The device architecture model FTO/ZnSe/Rb_2PtI_6/$MoSe_2$/C is depicted in (Figure1). The zinc selenide ZnSe is used as an electron transport layer (ETL). The absorber or active layer is formed by the double perovskite Rubidium (IV) platinum iodide Rb_2PtI_6 material. The Molybdenum diselenide $MoSe_2$ is used as a hole transport layer (HTL). The Fluorine-doped tin oxide (FTO) is use in the front side and the carbon C is used as contact in the back side.

Our studied device is a n-i-p type, for that, the n part is the ETL, the i part is the absorber and the p part is the HTL. To make our model more realistic, we have added the interface layers: interface (ETL/Rb_2PtI_6) and interface (Rb_2PtI_6/HTL), with a thickness of 5nm and keeping the same physical parameters as those of the perovskite.

We report in (Table 1**)** the input parameters for $MoSe_2$, Rb_2PtI_6, ZnSe and FTO derived from the literature and also, obtained with our calculations since some parameters of Rb_2PtI_6 are not yet available. For that, we have opted to the theoretical determination of such parameters based on the following equations:

$$N_t = \frac{1}{\sigma \tau V_{th}} \quad (5)$$

$$\mu_{n/p} = \frac{D_{n/p} q}{KT} \quad 6)$$

$$D_{n/p} = \frac{{l_{n/p}}^2}{\tau} \quad (7)$$

Where N_t is the defect density, $\mu_{n/p}$ is the electron/hole mobility, $D_{n/p}$ is the electron/hole diffusion coefficient, K is Boltzmann's constant, τ is the charge carrier lifetime, $l_{n/p}$ is the electron/hole diffusion length; σ is the capture cross-section of electron/hole and V_{th} is the thermal velocity of electron/hole. Also, the absorber layer effective conduction band density of states, N_c and effective valence band density of states, N_v are determined using the two following expressions:

$$N_c = 2\left(\frac{2\pi m_n^* KT}{h^2}\right)^{\frac{3}{2}} \text{ and } N_v = 2\left(\frac{2\pi m_p^* KT}{h^2}\right)^{\frac{3}{2}} \quad 8)$$

Where m_n^* and m_p^* are the effective masses of electrons and holes, respectively.

We notice that all initial layer's thicknesses are set to be 0.1μm and the simulation is done under the following physical conditions: solar illumination of $AM\ 1.5\ G$, with an intensity of $100\ mWcm^{-2}$, temperature of $300\ K$, and working frequency of $10^6 Hz$.

Table 1. The input parameters of the adopted device

Input parameter	$MoSe_2$	Rb_2PtI_6	ZnSe	FTO
Band gap, $E_g\ (eV)$	1.35 [a]	1.3 [b]	2.81[f]	3.5[g]
Affinity, $\chi\ (eV)$	4.05 [a]	4.43 [c]	4.09 [f]	4[g]
Relative Dielectric permittivity, ε_r	11.9 [a]	4.34 [d]	8.6 [f]	9[g]
CB effective density of states, N_c (cm^{-3})	2.8×10^{19} [a]	7.5×10^{18} [c]	2.2×10^{18} [f]	9.2×10^{18} [g]
VB effective density of states, $N_v\ (cm^{-3})$	2.65×10^{19} [a]	3.5×10^{19} [c]	1.8×10^{19} [f]	1.8×10^{19} [g]
Electron mobility, $\mu_n\ (cm^2V^{-1}s^{-1})$	1450 [a]	0.65 [e]	400 [f]	20[g]
hole mobility, $\mu_p\ (cm^2V^{-1}s^{-1})$	50 [a]	3.25 [e]	100 [f]	10[g]
Electron effective mass, m_n^*	-	0.45 [b]	-	-
hole effective mass, m_p^*	-	1.245 [b]	-	-
Density of n-type doping, $N_D\ (cm^{-3})$	0	0	10^{18} [f]	10^{19} [g]
Density of p-type doping, $N_A\ (cm^{-3})$	4×10^{18} [a]	10^{15} [c]	0	0
Density of defect, $N_t\ (cm^{-3})$	10^{14} [a]	3.5×10^{15} [c]	10^{15} [f]	10^{15} [g]

[a]data from Teyou- Ngoupo et al. (2022)
[b]data from Cai et al. (2017), [c] our calculations, [d] from Zhao et al.(2021),[e] from Yang (2019)
[f]data from (Owolabi J.A. et al. 2020)
[g]data from (Jahantigh et al. 2019)

Results and Discussion

Optimization of the Device Layers Thicknesses

Since the thickness of each layer of the device is critical to the overall photovoltaic performance of the device, the thicknesses of the FTO, HTL, absorber and ETL of the initial device were optimized. In this step, our strategy of optimization is started for FTO/ZnSe/Rb_2PtI_6/$MoSe_2$/C and is preceded in such the way: The optimization was done sequentially by varying the thickness of a particular layer while keeping the thickness of the remaining layers constant. In this manner, each layer was investigated in turn until a maximum PCE was achieved.

For instance, for the initial SC FTO($0.1\ \mu m$)/ZnSe($0.1\ \mu m$)/Rb_2PtI_6($0.1\ \mu m$)/$MoSe_2$($0.1\ \mu m$)/C) which has initially an $PCE = 12.94$ % for $R_s = 0\ \Omega$, the thickness optimization was carried out as follows: first, the absorber thickness was varied from 0.1 to 2 μm until a maximum PCE was obtained, while the thicknesses of the HTL, ETL, and FTO were kept constant at $0.1\ \mu m$. The best absorber thickness was determined to be 1.2 μm ($PCE = 20.54$ %), after which it was kept constant at this value. The ETL and FTO thicknesses were kept constant, while the thickness of the HTL was varied from 0.01 to 2 μm until an optimum value was attained at 0.04 μm ($PCE = 20.54$ %).

Likewise, the ETL thickness was varied from 0.01 to 2 μm, while the absorber, HTL and FTO thicknesses were kept constant. The optimum ETL thickness was found to be $0.06\ \mu m$ ($PCE = 20.54$ %). Finally, the FTO thickness was optimized by varying its value between 0.01 to 2 μm, and the optimum thickness was determined to be 0.01 μm ($PCE = 20.54$ %).

Then, the optimized SC is: FTO($0.01\ \mu m$)/ZnSe($0.06\ \mu m$)/Rb_2PtI_6($1.2\ \mu m$)/$MoSe_2$($0.04\ \mu m$)/C gives an PCE of 20.54 %. Figure 2 shows the PV performance and quantum efficiency (QE) comparison between the initial and obtimized simulated FTO/ZnSe/Rb_2PtI_6/$MoSe_2$/C structure. The initial solar cell (SC) provides PCE of 12.94 %, J_{SC} of 19.39 mA/cm^2, V_{oc} of 0.79 V, and FF of 87.54 % with QE near 360 nm 360, which is in the UV range. Upon optimizing the thicknesses of FTO, HTL, perovskite and ETL, we have obtained a higher performance: PCE of 20.54 %, J_{SC} of 34.41 mA/cm^2, V_{oc} of 0.79 V and FF of 75.8 % with about 98 % QE from 100 nm to 800 nm, which covers the UV and the visible range.

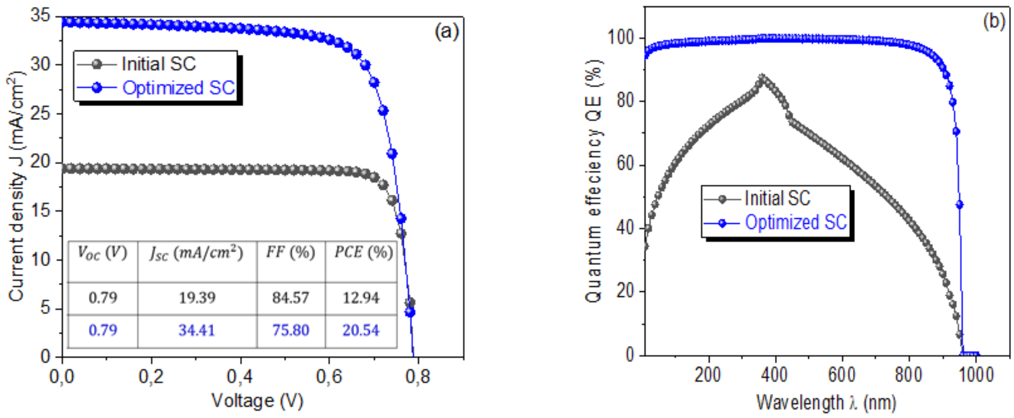

Figure 2. a) J-V characteristic and b) QE versus wavelength of FTO/ZnSe/Rb_2PtI_6/$MoSe_2$/C solar cell (SC).

Energy Band Diagram

In order to achieve a higher level of efficiency, the hole transport layer (HTL) and electron transport layer (ETL) must have band gap edges that correspond with the valence band maximum (VBM) and the conduction band minimum (CBM) of the active layers. (Figure 3.a) illustrate the band gap alignment of ZnSe, MoSe2 and Rb_2PtI_6, as well as the back and front device contacts. The lowest unoccupied molecular orbital (LUMO) of ZnSe (ETL) is in excellent alignment with the conduction band of Rb_2PtI_6. Likewise, the highest occupied molecular orbital (HOMO) of $MoSe_2$ (HTL) is well-aligned with the valence band level of an absorbing material

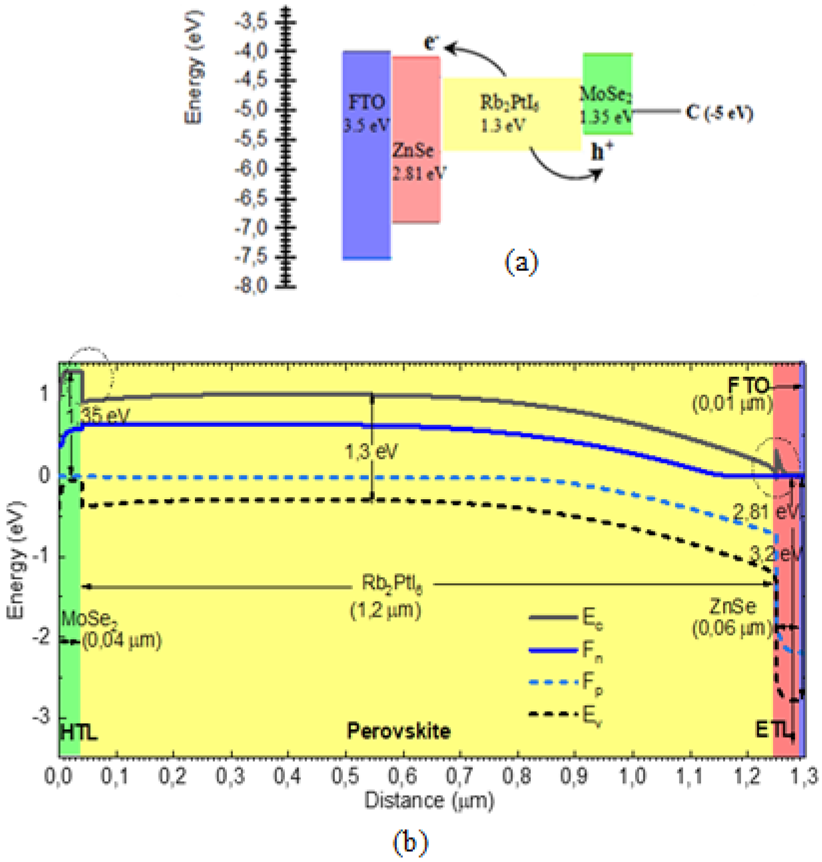

Figure 3. a) Energy level diagram b) conduction and valence energies of the optimized device.

The proper alignment of these energy levels is crucial for the photovoltaic performance of PSCs. Indeed, when light is absorbed, electrons are generated and injected into the conduction band of the ETL, while holes are simultaneously transported to the HTL. Then, electrons and holes are gathered at their corresponding front and back metal contacts. The energy band mismatch at the interfaces between ETL/Rb_2PtI_6 and Rb_2PtI_6/HTL has a significant impact on the device performance parameters. The characteristics of these interfaces exert control over the consequences of interfacial recombination (Sabbah et al., 2022). Therefore, it is necessary to perform precise tuning of the electronic characteristics of ETL and HTL materials. (Sabbah et al., 2022)

According to Ravidas et al. (Ravidas et a 2023). When the valence band offset (VBO) is positive, the spike is established at the absorber/HTL interface. Conversely, when the VBO is negative, a cliff is created at the absorber/HTL interface as shown in (Figure 3.b). The cliff does not obstruct photo-generated hole flow toward a back metal contact (C). However, the activation energy (E_a) for carrier recombination becomes lower than band gap of the absorber E_g (Rb_2PtI_6) and E_a is expressed by E_g (Rb_2PtI_6) - |VBO|. Consequently, a decrease in E_a due to the negative VBO elevates the interface recombination (Ravidas et al. 2023). The VBO at the $MoSe_2/Rb_2PtI_6$ interface is -0.37 eV which is sufficiently small to allow the holes to travel smoothly towards electrodes. When the CBO is positive, the spike is created at the ETL/ absorber interface and when the CBO is negative, the cliff is established at the ETL/ absorber interface (Agha et al., 2022). As illustrated in the inset of (Figure 3.b). The CBO at the Rb_2PtI_6/ZnSe interface is positive; it is about 0.31 eV.

Effect of Generation and Recombination Rate

Carrier generation describes the processes by which electrons gain energy and move from the valence band to the conduction band, producing two mobile carriers (creation); while recombination describes the processes by which an electron in the conduction band loses energy and reoccupies the energy state of an electron hole in the valence band.

Figure 4 illustrates the carrier generation and recombination rates in our model cell at different depths, ranging from 0.0 to 1.3 µm. According to the results, the generation rate of the device reached the peak of 1.447×10^{22} cm^3.s at 1.25 µm. This peak value is considered very higher compared to other solar devices such as ITO/C60/$CsSnBr_3$/Cu_2O/Au structure which demonstrated the highest generation rate of 0.7×10^{22} cm^3.s in its class (Dar et al. 2024).

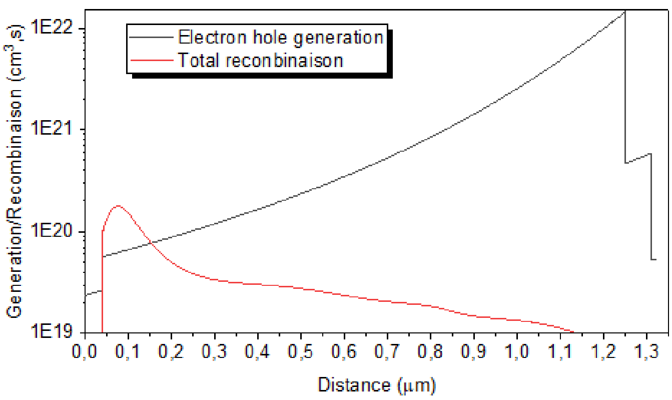

Figure 4. Effect of generation and recombination rate

Effect of Capacitance and Mott-Schotteky

Figure 5 illustrates the variation of the capacitance characteristics as a function of a voltage between -0.8 and 0.8 V. The numerical calculations were performed at a fixed frequency of 1 MHz. The capacitance increases nonlinearly as the voltage increases up to the value of 0.6 V. Beyond this value, the capacitance undergoes an exponential expansion. Normally, we would expect the capacitance to eventually reach its saturation point. It is well known in semiconductor device physics that the Mott-Schotteky (M-S) plot describes the inverse square of the capacitance, given in (Figure 6), versus the potential. The relationship between the capacitance (C), the built-in potential V_{bi} and the doping density (N_D) of the semiconductor is expressed by the following equation:

$$\frac{1}{C^2} = \frac{2\left(V - V_{bi} - \frac{KT}{q}\right)}{q\epsilon_r\epsilon_0 N_D} \tag{9}$$

Where V is the applied voltage and C is the capacitance per unit area.

This equation is used for the calculation of the doping density (N_D) of the semiconductor, while the extrapolation of the intercept can be used to derive the built-in potential (V_{bi}) (Otoufi et al., 2020). The V_{bi} obtained for the considered structure is equal to 1 V as shown in (Figure 6).

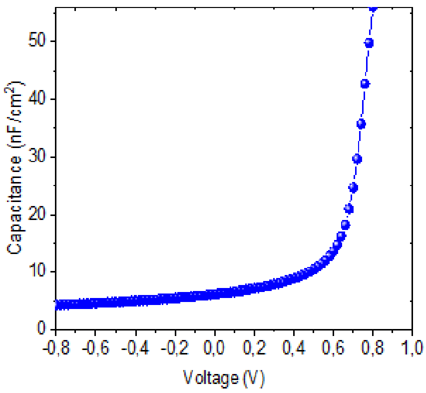

Figure 5. Effect of capacitance

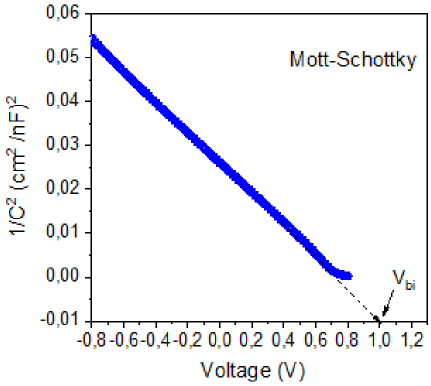

Figure 6. Effect of Mott-Schotteky

Effect of Series and Shunt Resistances

Series resistance (R_s) is due to factors such as ohmic contacts, metallic contacts, ITO sheet resistance, contact resistance inside the cell, and manufacturing imperfections. While, shunt resistance (R_{sh}) results from factors such as crystallographic defects, pinholes in the absorber layer, grain boundaries and the preparation process. R_{sh} is created due to alternating current paths for photogenerated charge carriers, which are provided by various charge recombination pathways in PSCs. The Shockley equation illustrates the relationship between the J-V characteristics of the cell and the resistances.

- For R_s, the Shockley equation is defined as follows:

$$J = J_{ph} - J_0 exp\left[\frac{q(V+IR_s)}{\eta KT}\right] \tag{10}$$

- For R_{sh}, the Shockley equation is defined as follows:

$$J = J_{ph} - J_0 exp\left[\frac{qV}{\eta KT}\right] - \frac{V}{R_{sh}} \tag{11}$$

Where J_{ph} is the photocurrent density, J_0 is reverse saturation current density, V is the output voltage and η is diode ideality factor.Figure 7 shows the contour plot of the variation of the photovoltaic parameters with resistances R_s and R_{sh}. As illustrated, the increase of R_s leads to the decrease of PCE, while the increase of R_{sh} leads to the increase of PCE. Therefore, R_s has a negative effect of the solar cell performance, while R_{sh} has a positive effect. The PCE reaches the maximum value of 20.60 % for very low R_s and very high R_{sh}.

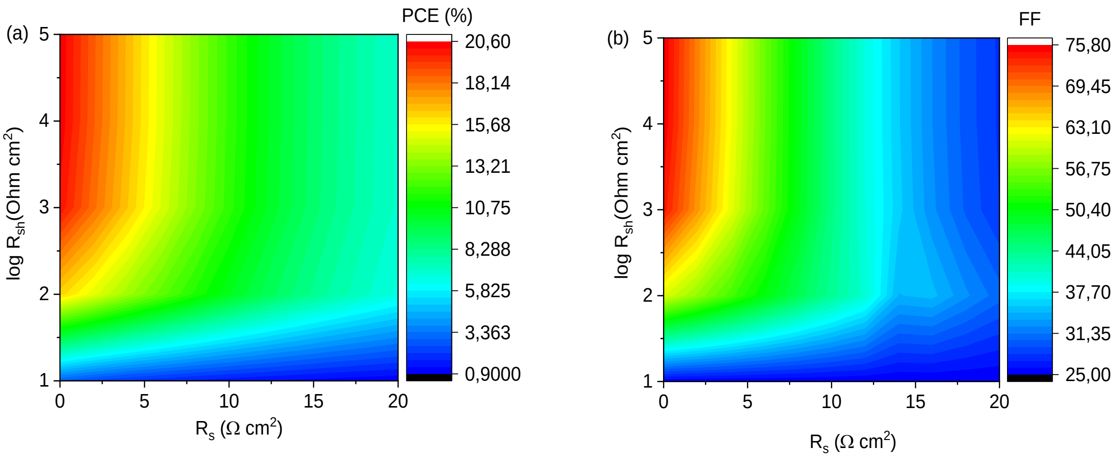

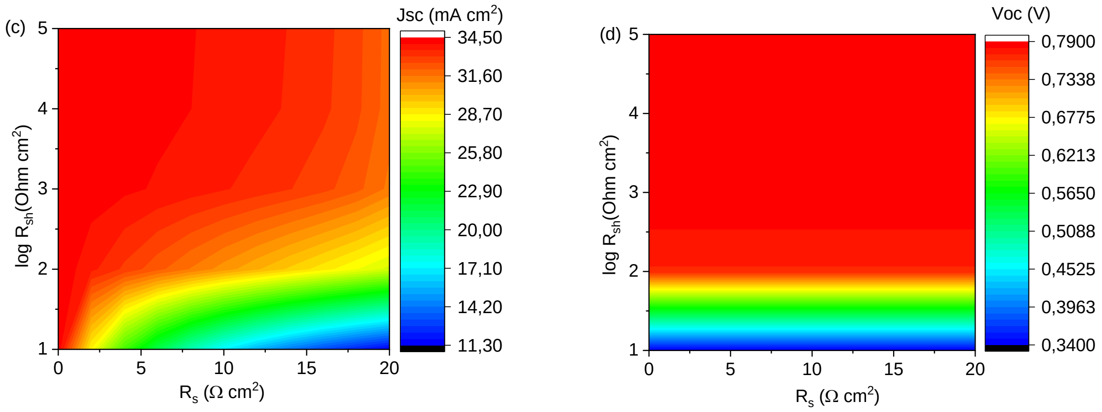

Figure 7. Contour plot of the effect of series and shunt resistances on the PV parameters of the solar cell: a) PCE, b)PCE, c) J_{SC} and d) V_{oc}

Comparison of Our PV Parameters and Others Studies

Since the active layer of our studied device Rb_2PtI_6 is from the same IHDP family as Cs_2PtI_6, we compare the photovoltaic (PV) characteristics of our predicted solar cell based on Rb_2PtI_6 to other ones based on Cs_2PtI_6 where experimental and numerical data are available. We summarized the finding results in (Table 2).

Table 2. PV characteristics of our optimized solar cell compared with other IHDP solar cells. The values between parenthesis are the layers' thicknesses given in ($\boldsymbol{\mu m}$).

Structure	V_{oc} (V)	J_{sc} (mA/cm^2)	FF (%)	PCE (%)	R_s $(\Omega\ cm^2)$	R_{sh} $(\Omega\ cm^2)$	Used Method
FTO (0.01)/ ZnSe(0.06)/ Rb_2PtI_6 (1.2)/$MoSe_2$(0.04)/C [a]	0.79 [a]	34.41 [a]	75.80 [a]	20.54 [a]	0	0	SCAPS-1D
	0.79 [a]	34.41 [a]	75.75 [a]	20.53 [a]	0.01	10^5	
	0.79 [a]	34.41 [a]	75.62 [a]	20.49 [a]	0.01	10^4	
	0.79 [a]	34.38 [a]	71.02 [a]	19.49 [a]	1	4.2×10^3	
	0.79 [a]	15.15 [a]	25.17 [a]	03.01 [a]	50	10^4	
	0.79 [a]	33.47 [a]	35.71 [a]	09.42 [a]	14	10^4	
FTO/CdS (0.08-0.1)/ Cs_2PtI_6 (10-15)/ElectroDAG 440B/Cu [b]	0.90 [b]	19.83 [b]	59.85 [b]	10.70 [b]	14	-	Exp
FTO/CdS (0.08-0.1)/ Cs_2PtI_6 (10-15)/ElectroDAG 440B/Cu with EDA traitment [b]	1.07 [b]	19.84 [b]	65.03 [b]	13.88 [b]			
FTO (0.5)/WS_2/ Cs_2PtI_6 (0.4)/Cu_2O /C [c]	1.3 [c]	28.15 [c]	61.00 [c]	22.4 [c]	14	-	SCAPS-1D
FTO (0.5)/SnO_2(0.01)/ Cs_2PtI_6 (0.4)/MoO_3(0.024)/C [d]	1.11 [d]	26.95 [d]	79.90 [d]	24.10 [d]	0.01	10^4	SCAPS-1D
	1.11 [d]	26.95 [d]	78.07 [d]	23.52 [d]	1	4.2×10^3	
	1.11 [d]	21.06 [d]	25.57 [d]	06.03 [d]	50	10^4	
FTO/ZnO / Cs_2PtI_6 /MoO_3 /C [e]	1.40 [e]	16.11 [e]	90.01 [e]	20.45 [e]	0	0	SCAPS-1D

[a] our optimized SC based on Rb_2PtI_6
[b] experimental SC based on Cs_2PtI_6 (Schwartz et al., 2020)
[c] simulated SC based on Cs_2PtI_6 (AbdElAziz et al., 2022)
[d] simulated SC based on Cs_2PtI_6 (Amjad et al., 2023)
[e] simulated SC based on Cs_2PtI_6 (Shamna et al., 2022)

The PCE ranges from 6.03 % (FTO/ZnO/Cs_2PtI_6/MoO_3/C) to 24.1 % (FTO/SnO_2/Cs_2PtI_6/MoO_3/C) with Cs_2PtI_6 perovskite. We can see that the negative effect of the series resistance R_s is remarkable in this case because it drastically decreases the PCE of the solar cell. Compared to these similar solar cells, our results for FTO/SnO_2/Rb_2PtI_6/$MoSe_2$/C show good agreement with the PCE of 20.54 %. We notice that SCAPS-1D PV results reported in the references given in Table 2, the authors performed their obtained devices with the study of the effect of acceptor density N_A and defect density N_t of the active layer. We expect, then, a clear improvement in PCE of our predicted device if we also take into account these later effects.

Conclusion

This paper provided deep simulation results of a novel high-performance solar cell based on the double perovskite: Rubidium (IV) platinum iodide Rb_2PtI_6. Our adopted architecture is FTO/ZnSe/Rb_2PtI_6/$MoSe_2$/C. The optimal performance of our proposed cell was achieved by varying the thicknesses of all layers such as: FTO, hole transport layer (HTL), Rb_2PtI_6 absorber and electron transport layer (ETL). We have presented a valuable insight on how the electronic band diagram engineering is fundamental for the photovoltaic performance of the solar cell. Moreover, the effects of capacitance (C-V), Mott–Schottky (M-S) characteristics, generation and recombination rates, series resistance (R_s) and shunt resistance (R_{sh}) are analyzed. The best obtained efficiency PCE reaches 20.54 % and we expect, even more improvement in PCE if we investigate the effect of acceptor density, and defct concentration of the absorber layer.

The QE of our redicted devive is 98 % from $100\ nm$ to $800\ nm$, which covers the UV and the visible range. Our findings shows that our proposed Rb_2PtI_6-based device can serve as a potential eco-friendly high efficiency solar cell candidate due to the chemical stability and non-toxicity of its active layer. Good agreement is obtained with available experimental and simulation studies for similar solar cells.

Scientific Ethics Declaration

The authors declare that the scientific ethical and legal responsibility of this article published in EPSTEM Journal belongs to the authors.

Acknowledgements

The authors are thankful to Professor Marc Burgelman and his coworkers at the University of Ghent, Belgium, for providing the SCAPS-1D software used in this study.

Notes

* This article was presented as an oral presentation at the International Conference on Technology, Engineering and Science (www.icontes.net) held in Antalya/Turkey on November 14-17, 2024.

References

AbdElAziz, H. H., Taha, M., El Rouby, W.M.A., Khedr, M.H., & Saad, L. (2022). Evaluating the performance of $Cs_2PtI_{6-x}Br_x$ for photovoltaic and photocatalytic applications using first-principles study and SCAPS-1D simulation. *Heliyon*, *8*(10), e10808.

Agha, D.N.Q., & Algwari Q.Th. (2022). The influence of the conduction band engineering on the perovskite solar cell performance. *Results in Optics*, *9*(15), 100291.

Amjad, A., Qamar, S., Zhao, C., Fatima, K., Sultan, M., & Akhter, Z. (2023). Numerical simulation of lead-free vacancy ordered Cs_2PtI_6 based perovskite solar cell using SCAPS-1D. *RSC Advances,13*(33), 23211–23222.

Bartel, C.J., Sutton, C., Goldsmith, B.R., Runhai, O., Musgrave, C.B., Ghiringhelli, L.M., & Scheffler, M. (2019). New tolerance factor to predict the stability of perovskite oxides and halides. *Science Advances, 5(2)*, eaav0693.

Boopathi, K.M., Karuppuswamy, P., Singh, A., Hanmandlu, C., Lin, L., Abbas, S. A., Chang, C.C, Wang, P.C., Li, G. & Chu, C. W. (2017). Solution-processable antimony-based light-absorbing materials beyond lead halide perovskites. *Journal of Materials Chemistry A, 5*(39), 20843-20850.

Burgelman, M., Decock, K., Niemegeers, A., Verschraegen, J., & Degrave, S. J. F. (2021). *SCAPS manual.* Retrieved from https://scaps.elis.ugent.be/SCAPS%20manual%20most%20recent.pdf

Cai, Y., Xie, W., Ding, H., Chen, Y., Thirumal, K., Wong, L.H., Mathews, N., Mhaisalkar, S.G., Sherburne, M., & Asta, M. (2017). Computational study of halide perovskite-derived a_2bx_6 inorganic compounds: chemical trends in electronic structure and structural stability. *Chemistry of Materials*, *29*(18), 7740−7749.

Dar S.A., & Sengar, B. S. (2024). Analysis of lead free $CsSnBr_3$ based perovskite solar cells utilizing numerical modeling. *Physica Scripta, 99*(6), 065013.

Faizan, M., Bhamu, K. C., Khan, S. H., Murtaza, G., & He, X., (2020). Computational study of defect variant perovskites a_2bx_6 for photovoltaic applications. *arXiv:2002*, 07543.

Fujihara, T., Terakawa, S., Matsushima, T., Qin, C., Yahiro, M., & Adachi, C. (2017). Fabrication of high coverage MASnI 3 perovskite films for stable, planar heterojunction solar cells. *Journal of Materials Chemistry C*, *5*(5), 1121-1127.

Huang, H., Raith, J., Kershaw, S. V., Kalytchuk, S., Tomanec, O., Jing, L., ... & Rogach, A. L. (2017). Growth mechanism of strongly emitting CH3NH3PbBr3 perovskite nanocrystals with a tunable bandgap. *Nature Communications*, *8*(1), 996.

Jahantigh, F., & Safikhani, M. J. (2019). The effect of HTM on the performance of solid-state dye-sanitized solar cells (SDSSCs): A SCAPS-1D simulation study. *Applied Physics A*, *125*(4), 276.

Jin, Z., Zhang, Z., Xiu, J., Song, H., Gatti, T., & He, Z. (2020). A critical review on bismuth and antimony halide based perovskites and their derivatives for photovoltaic applications: recent advances and challenges. *Journal of Materials Chemistry A*, *8*(32), 16166-16188.

Jodlowski, A., Rodríguez-Padrón, D., Luque, R., & de Miguel, G. (2018). Alternative perovskites for photovoltaics. *Advanced Energy Materials*, *8*(21), 1703120.

Kanoun, A.A., Kanoun, M.B., Merad, A.E. & Goumri-Said, S., (2019). Toward development of high-performance perovskite solar cells based on $CH_3NH_3GeI_3$ using computational approach. *Solar Energy 182*, 237-244.

Kumar, N., Rani, J. & Kurchania, R. (2021). A review on power conversion efficiency of lead iodide perovskite-based solar cells. *Materials Today: Proceedings 46*, 5570-5574.

Lu, L., Pan, X., Luo, J., & Sun, Z. (2020). Recent advances and optoelectronic applications of lead-free halide double perovskites. *Chemistry–A European Journal*, *26*(71), 16975-16984.

Nair, S.S., Krishina, L., Trukhanov, A., Thakur, P., & Thakur, A. (2022). Prospect of double perovskite over conventional perovskite in photovoltaic applications. *Ceramics International*, *48*(3), 34128-34147.

Otoufi, M.K., Ranjbar, M., Kermanpur, A., Taghavinia, N., Minbashi, M., Forouzandeh, M., & Ebadi F. (2020). Enhanced performance of planar perovskite solar cells using TiO_2/SnO_2 and TiO_2/WO_3 bilayer structures Roles of the interfacial layers. *Solar Energy*, *208*, 697–707.

Ono, L. K., Juarez-Perez, E. J., & Qi, Y. (2017). Progress on perovskite materials and solar cells with mixed cations and halide anions. *ACS Applied Materials & Interfaces*, *9*(36), 30197-30246.

Owolabi, J.A., Onimisi, M.Y., Ukwenya, J.A., Bature, A.B., & Ushiekpan, U.R. (2020). Investigating the effect of ZnSe (ETM) and Cu_2O (HTM) on absorber layer on the performance of pervoskite solar cell using SCAPS-1D. *American Journal of Physics and Applications 8*, 8-18.

Park, Y. H., Jeong, I., Bae, S., Son, H. J., Lee, P., Lee, J., ... & Ko, M. J. (2017). Inorganic rubidium cation as an enhancer for photovoltaic performance and moisture stability of HC (NH2) 2PbI3 perovskite solar cells. *Advanced Functional Materials*, *27*(16), 1605988.

Ravidas, B. K., Roy, M.K. & Samajdar, D.P. (2023). Investigation of photovoltaic performance of lead-free CsSnI3-based perovskite solar cell with different hole transport layers, first principle calculations and SCAPS-1D analysis. *Solar Energy*, *249*, 163–173.

Sabbah, H., Arayro, J.& Mezher, R. (2022). Numerical simulation and optimization of highly stable and efficient lead-free perovskite $FA_{1-x}Cs_xSnI_3$-based solar cells using SCAPS. *Materials 15*(14), 4761.

Saliba, M., Matsui, T., Seo, J. Y., Domanski, K., Correa-Baena, J. P., Nazeeruddin, M. K., ... & Grätzel, M. (2016). Cesium-containing triple cation perovskite solar cells: improved stability, reproducibility and high efficiency. *Energy & Environmental Science*, *9*(6), 1989-1997.

Schwartz, D., Murshed, R., Larson, H., Usprung, B., Soltanmohamad, S., Pandey, R., Barnard, E.S., Rockett, A., Hartmann, T., Castelli, I.E., & Bansal S. (2020). Air stable, high-efficiency, pt-based halide perovskite solar cells with long carrier lifetimes. *Physica Statu Solidi*, *14*, 2000182.

Shahbazi, S., Tsai, C. M., Narra, S., Wang, C. Y., Shiu, H. S., Afshar, S., ... & Diau, E. W. G. (2017). Ag doping of organometal lead halide perovskites: morphology modification and p-type character. *The Journal of Physical Chemistry C*, *121*(7), 3673-3679.

Shamna, M.S., & Sudheer, K.S. (2022). Device modeling of Cs_2PtI_6-based perovskite solar cell with diverse transport materials and contact metal electrodes: A comprehensive simulation study using solar cell capacitance simulator. *Journal of Photonics for Energy*, *12*(3), 032211.

Sun, P.P., Kripalani, D.R., Chi, W., Snyder, S.A., & Zhou, K. (2021). High carrier mobility and remarkable photovoltaic performance of two-dimensional Ruddlesden–Popper organic–inorganic metal halides $(PA)_2(MA)_2M_3I_{10}$ for perovskite solar cell applications. *Materials Today, 47,* 45-52.

Suzuki, S., & Tsuyama, M., (2021). Structural, electronic, and optical properties of Pt-based vacancy-ordered double perovskites A_2PtX_6 (A = K, Rb, Cs; X = Cl, Br, I) in tetragonal P4/mnc polymorph. *Optical Materials 119,* 111323.

Teyou Ngoupo, A. & Ndjaka, J.M.B. (2022). Performance enhancement of Sb_2Se_3 -based solar cell with hybrid buffer layer and $MoSe_2$ as a hole transport material using simulator device. *Discover Mechanical Engineering*, *1*(1), 5.

Wei, H., Chen, S., Zhao, J., Yu, Z., & Huang, J. (2020). Is formamidinium always more stable than methylammonium?. *Chemistry of Materials*, *32*(6), 2501-2507.

Yang, Z., Yu, Z., Wei, H., Xiao, X., Ni, Z., Chen, B., ... & Huang, J. (2019). Enhancing electron diffusion length in narrow-bandgap perovskites for efficient monolithic perovskite tandem solar cells. *Nature Communications*, *10*(1), 4498.

Yin, H., Xian, Y., Zhang, Y., Li, W., & Fan, J. (2019). Structurally stabilizing and environment friendly triggers: Double-metallic lead-free perovskites. *Solar Rrl*, *3*(9), 1900148.

Yu, Y., Zhao, D., Grice, C. R., Meng, W., Wang, C., Liao, W., ... & Yan, Y. (2016). Thermally evaporated methylammonium tin triiodide thin films for lead-free perovskite solar cell fabrication. *RSC Advances*, *6*(93), 90248-90254.

Zhao, S., Cai, W., Wang, H., Zang, Z., & Chen, J. (2021). All-inorganic lead-free perovskite (-like) single crystals: Synthesis, properties, and applications. *Small Methods*, *5*(5), 2001308.

Zhao, X. H., Wei, X. N., Tang, T. Y., Gao, L. K., Xie, Q., Lu, L. M., & Tang, Y. L. (2021). First-principles study on the structural, electronic and optical properties of vacancy-ordered double perovskites Cs2PtI6 and Rb2PtI6. *Optical Materials*, *114*, 110952.

Zheng, Z., Wang, S., Hu, Y., Rong, Y., Mei, A., & Han, H. (2022). Development of formamidinium lead iodide-based perovskite solar cells: Efficiency and stability. *Chemical Science*, *13*(8), 2167-2183.

Author Information

Souheyla Mamoun
Solid State Physics Team, Theoretical Physics Laboratory, Faculty of Sciences, A Belkaid University, Box 119, 13000, Tlemcen, Algeria
Contact e-mail*: souhila.mamoun@univ-tlemcen.dz*

Abdelkrim El-Hasnaine Merad
Solid State Physics Team, Theoretical Physics Laboratory, Faculty of Sciences, A Belkaid University, Box 119, 13000, Tlemcen, Algeria

Amina Benmansour
Solid State Physics Team, Theoretical Physics Laboratory, Faculty of Sciences, A Belkaid University, Box 119, 13000, Tlemcen, Algeria

To cite this article:

Mamoun, S., Merad, A.E., & Benmansour, A. (2024). Simulation study of electronic band diagram engineering and electrical parameters to boost the photovoltaic performance of novel Rb_2PtI_6 double perovskite solar cell. *The Eurasia Proceedings of Science, Technology, Engineering & Mathematics (EPSTEM), 32,* 389-399.

The Eurasia Proceedings of Science, Technology, Engineering & Mathematics (EPSTEM)
ISSN: 2602-3199

The Eurasia Proceedings of Science, Technology, Engineering & Mathematics (EPSTEM), 2024

Volume 32, Pages 400-405

IConTES 2024: International Conference on Technology, Engineering and Science

Magnetic Behavior and Structural Properties of $Fe_{10}Al_{40}(ZnO)_{50}$ and $Fe_{10}Al_{50}(ZnO)_{40}$ Nanocomposites

Rachid Amraoui
Research Centre in Industrial Technologies (CRTI)

Abderrahmane Younes
Research Centre in Industrial Technologies (CRTI)

Abderahim Abada
University of Blida 1

Djilali Allou
Research Centre in Industrial Technologies (CRTI)

Abstract: Nanocomposite materials comprising $Fe_{10}Al_{40}(ZnO)_{50}$ and $Fe_{10}Al_{50}(ZnO)_{40}$ were synthesized using the powder metallurgy technique. The investigation of their structural, morphological, and magnetic properties at various synthesis stages was carried out utilizing advanced characterization methods, including Scanning Electron Microscopy (SEM), Energy Dispersive Spectroscopy (EDS), X-ray Diffraction (XRD), and Vibrating Sample Magnetometer (VSM). In the $Fe_{10}Al_{40}(ZnO)_{50}$ nanocomposite, the crystallite size was determined to be at its minimum, measuring 27.30 ± 5.82 nm, with the lattice strain (ε) reaching its maximum value of $0.155 \pm 0.008\%$. Similarly, $Fe_{10}Al_{50}(ZnO)_{40}$ nanocomposite exhibited analogous trends in its structural and magnetic properties. Furthermore, the alteration in the mass ratio of aluminum and zinc oxide in the FeAlZnO nanocomposite influenced magnetic properties such as coercivity (Hc), magnetization saturation (Ms), magnetization remanence (Mr), and squareness (MR/MS). These findings indicate the potential of the FeAlZnO nanocomposite system as a high-frequency soft magnetic material.

Keyword: $Fe_{10}Al_{40}(ZnO)_{50}$ and $Fe_{10}Al_{50}(ZnO)_{40}$ Nanocomposites, Magnetic behavior, Structural properties, Morphology.

Introduction

In recent years, nanocomposite metal oxides have attracted a great deal of attention because of their amazing properties and great potential for a wide range of applications. Zinc oxide, one of the most popular semiconductor materials, comes in two basic crystalline forms: cubic zinc blende and hexagonal wurtzite. The zinc oxide displays antiferromagnetic behavior at room temperature; however, it can sometimes show ferromagnetic characteristics because of the existence of zinc or oxygen vacancies in the wurtzite crystal structure (Gur et al., 2022; Pushpalatha et al., 2022; Jiang et al., 2023; Chahal et al., 2023). Zinc oxide can be synthesized in a number of forms, including single crystals, sintered pellets, thick and thin films, as well as heterojunctions, enabling a large field of applications (Zonta et al., 2020; Benrezgua et al., 2022; Nguyen et al., 2020; Kumar et al., 2020; Guo et al., 2021). Incorporating iron and aluminum into zinc oxide gives hysteresis loops a sigmoidal shape, while retaining ferromagnetic properties at room temperature (Kuru et al., 2022; Ahmed et al., 2021). In contrast to other manufacturing procedures, mechanical alloying represents a very important and uncomplicated process. It has many advantages for growing nanostructured materials, enabling uniform distribution and homogeneity of particle components in accurate control (Suryanarayana, 2022; Sharath et al., 2024; Suryanarayana et al., 2022; Moravcik

- Selection and peer-review under responsibility of the Organizing Committee of the Conference

et al., 2020). Various types of characterization methods are employed in order to assess the structural, morphological and magnetic properties of milled powder, such as scanning electron microscopy (SEM), X-ray diffraction (XRD) and vibrating sample magnetometry (VSM).

In this research, the main aim is to investigate the impact of changing the chemical content of FeAl(ZnO) nanocomposites, in particularly by varying the quantities of Al and ZnO, on the structural and magnetic properties during mechanical alloying at room temperature. Additionally, this research aims to determine the optimal composition of the nanocomposite.

Materials and Experimental Procedure

Basic powders of Fe, Al and ZnO, having particle sizes of 70 µm, 60 µm and 60 µm and in purities of 99.3%, 99.15% and 99.22%, respectively, were milled in a high-energy PM400 planetary mill by the use of zirconium balls within argon atmosphere to obtain FeAl(ZnO) nanocomposites with changing concentrations. The weight ratio of powder to ball was around 1:10, and the milling speed was fixed at 280 rpm. The mixture of powders was milled in 20-minute cycles and then paused for 10 minutes.

The morphology and crystal structure of the samples were analyzed using a Gemini SEM 300 scanning electron microscope (SEM) equipped with an energy dispersive X-ray spectroscopy (EDS) analyzer. The X-ray diffraction (XRD) analysis was carried out by means of a PANalytical XPERT-PRO diffractometer with Co-Kα radiation. The magnetic properties were determined using a vibrating sample magnetometer (VSM) under a maximum applied field of 15 kOe.

Results and Discussion

SEM Examination

The morphology and elemental distribution of FeAl(ZnO) nanocomposites at various compositions are depicted in Figure 1. Figure 1(a) displays $Fe_{10}Al_{40}(ZnO)_{50}$ nanocomposites, whereas Figure.1(b) indicates $Fe_{10}Al_{50}(ZnO)_{40}$ nanocomposites. Scanning electron microscope (SEM) images show a diversity of particle sizes, which could be due to the aggregation of smaller particles and the varying compositions of ZnO and Al within the nanocomposites.

The EDS spectra affirm the presence of Zn, O, Al and Fe, with each detected element at compositions matching their respective proportions in the various nanocomposite formulations. This coherence in the elemental composition of the samples demonstrates the perfect integration of ZnO and Al in the Fe matrix.

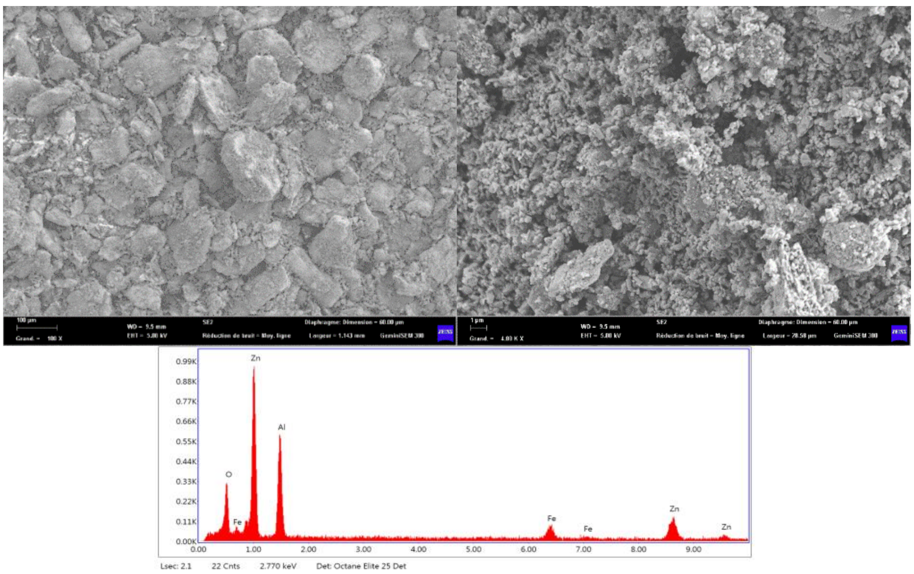

Figure 1.a. Morphology of $Fe_{10}Al_{40}(ZnO)_{50}$ nanocomposite

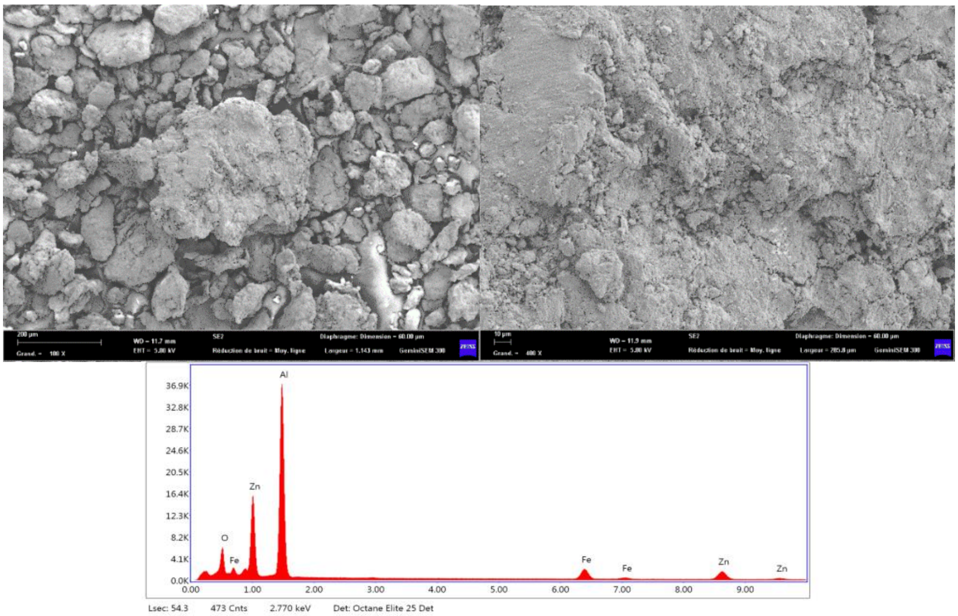

Figure 1.b. Morphology of $Fe_{10}Al_{50}(ZnO)_{40}$ nanocomposite

The variations in particle morphology observed in the SEM images indicate that the higher concentration of ZnO in the $Fe_{10}Al_{40}(ZnO)_{50}$ sample (Figure 1a) results in more pronounced aggregation, in comparison with the $Fe_{10}Al_{50}(ZnO)_{40}$ sample (Figure 1b). This difference could affect the total structural as well as the magnetic properties of the nanocomposites. Early reports (Rosowska et al., 2020; Tian et al., 2021) indicated that nanoparticle aggregation can have a significant effect on the physical characteristics of nanocomposites, potentially affecting their performance in different applications.

Structural Analysis

Figure. 2 displays X-ray diffraction patterns of FeAl(ZnO) nanocomposites at various compositions. All peaks match the hexagonal phases of the wurtzite structure of ZnO, the face-centered cubic crystal structure of aluminum, the iron-centered cubic phases and the new phases of the B2 structure of FeAl. The difference between both nanocomposites is the intensity and broadening of most peaks. The irregularity of the majority of peaks affirms the good crystallinity of the mechanically milled alloy (Peng et al., 2021). The X-ray diffraction (XRD) patterns of FeAl(ZnO) nanocomposites at various compositions are given in Figure 2. All the peaks observed match the hexagonal phases of the wurtzite structure of ZnO, the face-centered cubic (FCC) crystal structure of aluminum, the body-centered cubic (BCC) phases of iron and the new B2 phases of the FeAl alloy. The difference between the two nanocomposites lies in the intensity and broadening of most of the peaks.

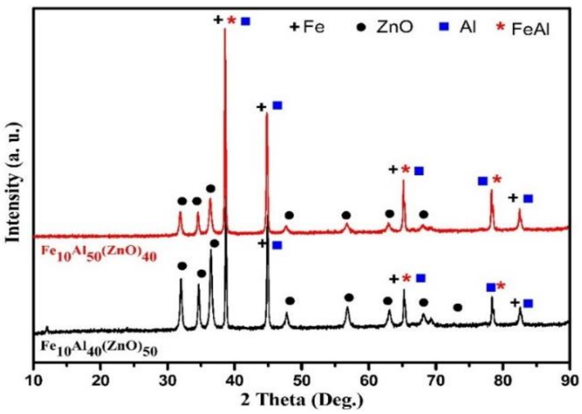

Figure 2. XRD patterns of FeAl(ZnO) nanocomposite with different concentration

The intensity variation and broadening of the peaks reveal differences in crystallite size and internal deformation within the nanocomposites. The pronounced sharpness of the majority of peaks confirms the good crystallinity of the mechanically milled alloy. In addition, the presence of broad peaks suggests a reduction in crystallite size and an increase in microstrain, which are typical results of high-energy ball milling (Peng et al., 2021). The strong crystallinity found in the XRD patterns is a testament to the efficiency of the mechanical alloying process in producing well-ordered nanocomposites. XRD analysis also shows that the composition of ZnO and Al strongly influences the structural characteristics of the nanocomposites, as shown by the different peak profiles in the diffraction patterns. Figure.3 presents the evolution of crystallite size and lattice strain in FeAl(ZnO) nanocomposites. These parameters were calculated using the Williamson-Hall method (Imtiaz et al., 2024), based on the maximum width at half maximum (FWHM) of the X-ray diffraction peaks.

The observed variation in crystallite size and increase in lattice strain could be attributed to severe plastic deformation induced during the mechanical alloying process. In addition, variation in chemical composition contributes to lattice distortions, resulting in high dislocation density. The severe plastic deformation splits the larger crystallites into smaller ones, increasing the number of grain boundaries and defects. In the meanwhile, the introduction of ZnO and Al into the Fe matrix causes lattice distortions due to differences in atom size and bonding characteristics, further increasing lattice strain. In summary, the combination of mechanical milling and compositional variations results in reduced crystallite sizes and increased lattice strain in the FeAl(ZnO) nanocomposites, as evidenced by the Williamson-Hall analysis.

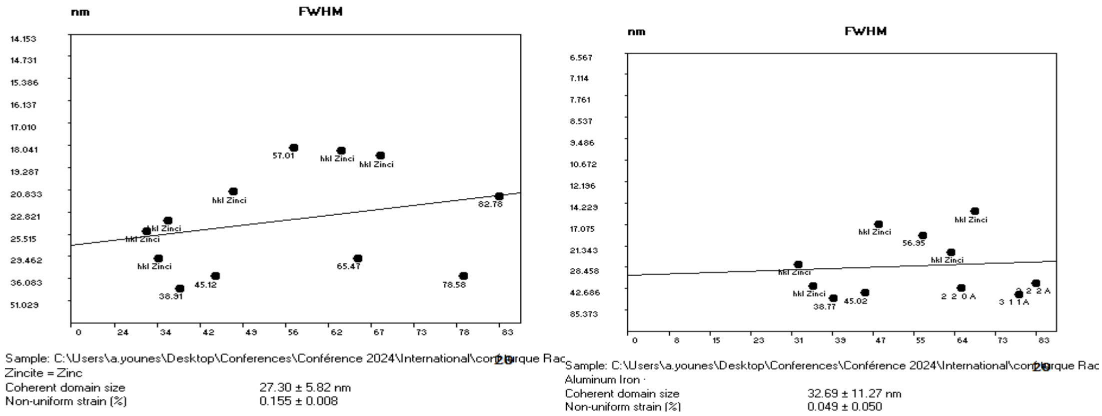

Figure 3. Crystallite size and lattice strain of FeAl(ZnO) nanocomposite with different concentration

Magnetic Characterization

In Figure 4, the hysteresis curves of $Fe_{10}Al_{40}(ZnO)_{50}$ and $Fe_{10}Al_{50}(ZnO)_{40}$ nanocomposites are plotted, at room temperature, by means of a vibrating sample magnetometer (VSM). The goal of this magnetic investigation is to assess the effect of different chemical compositions on the magnetic behavior of these nanocomposites.

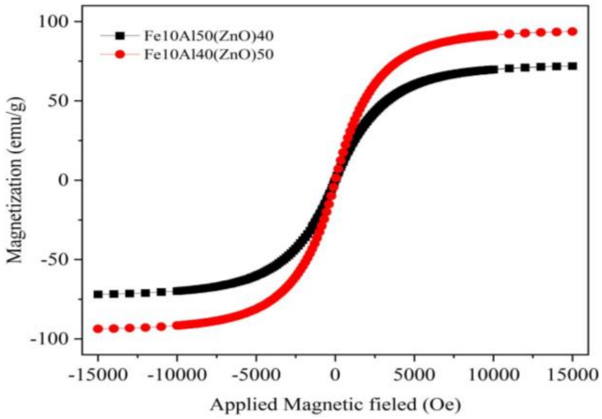

Figure 4. Hysreresis curve of $Fe_{10}Al_{40}(ZnO)_{50}$ and $Fe_{10}Al_{50}(ZnO)_{40}$ nanocomposites

Table 1 shows the magnetic parameters. Based on hysteresis curves, the magnetic properties of $Fe_{10}Al_{40}(ZnO)_{50}$ and $Fe_{10}Al_{50}(ZnO)_{40}$ nanocomposites differ significantly as a function of changes in their chemical composition. More specifically, variations in Al and ZnO compositions affect the saturation magnetization, coercivity and remanence of the nanocomposites. These differences can be attributed to the influence of Al and ZnO on the magnetic domain structure and interactions within the Fe matrix.

Table 1. The magnetic parameters of $Fe_{10}Al_{50}(ZnO)_{40}$ and $Fe_{10}Al_{40}(ZnO)_{50}$

$Fe_{10}Al_{50}(ZnO)_{40}$			$Fe_{10}Al_{40}(ZnO)_{50}$		
Hc (Oe)	Mr (emu/g)	Ms (emu/g)	Hc (Oe)	Mr (emu/g)	Ms (emu/g)
12,39	0,31	71,95	12,74	0,49	93,67

The results demonstrate that the $Fe_{10}Al_{40}(ZnO)_{50}$ nanocomposite exhibits different magnetic characteristics compared to the $Fe_{10}Al_{50}(ZnO)_{40}$ nanocomposite, highlighting the importance of chemical composition in tailoring the magnetic properties of FeAl(ZnO) nanocomposites. These findings are crucial for optimizing the magnetic performance of such materials for various applications (Khalid et al., 2019; Vijayakumar et al., 2020).

Conclusion

The study of FeAl(ZnO) nanocomposites has enabled us to gain a better understanding of the way in which variations in chemical composition can affect their structural and magnetic properties. X-ray diffraction analysis has shown that incorporating different concentrations of Al and ZnO leads to different changes in crystallite size and lattice strain, mainly due to significant plastic deformation and lattice distortions induced during mechanical alloying. Morphological analysis by SEM and EDS confirmed the successful incorporation of the elements Zn, O, Al and Fe into the nanocomposites, with variations in particle size attributed to aggregation phenomena and compositional differences. XRD diagrams also confirmed the formation of a well-crystallized nanocomposite with characteristic phases matching the wurtzite structure of ZnO, aluminum FCC, iron BCC and B2 FeAl phases. Magnetic characterization by hysteresis curve analysis confirmed that the magnetic properties of nanocomposites are extremely dependent on chemical composition. Variations in Al and ZnO compositions strongly influenced saturation magnetization, coercivity and remanence, indicating that magnetic behavior can be tailored by adjusting elemental proportions. In conclusion, the results highlight the critical role of chemical composition in determining the structural and magnetic properties of FeAl(ZnO) nanocomposites. This insight is essential for optimizing these materials for specific applications, which could enhance their performance in various technological fields.

Scientific Ethics Declaration

The authors declares that the scientific ethical and legal responsibility of this article published in EPSTEM Journal belongs to the authors.

Acknowledgements or Notes

* This article was presented as an poster presentation at the International Conference on Technology, Engineering and Science (www.icontes.net) held in Antalya/Turkey on November 14-17, 2024.

References

Ahmed, S. K., Mahmood, M. F., Arifuzzaman, M., & Hossen, M. B. (2021). Enhancement of electrical and magnetic properties of Al3+ substituted CuZn nano ferrites with structural Rietveld refinement. *Results in Physics, 30*, 104833.

Benrezgua, E., Deghfel, B., Zoukel, A., Basirun, W. J., Amari, R., Boukhari, A., & Mohamad, A. A. (2022). Synthesis and properties of copper doped zinc oxide thin films by sol-gel, spin coating and dipping: A characterization review. *Journal of Molecular Structure*, *1267*, 133639.

Chahal, S., Kumar, S., Kumar, A., Duhan, S., & Kumar, P. (2023). Magnetism in zinc oxide (ZnO). In *Defect-induced magnetism in oxide semiconductors* (pp. 547-561). Woodhead Publishing.

Guo, Z., Huo, W., Cao, T., Liu, X., Ren, S., Yang, J., & Zhang, Y. (2021). Heterojunction interface of zinc oxide and zinc sulfide promoting reactive molecules activation and carrier separation toward efficient photocatalysis. *Journal of Colloid and Interface Science*, *588*, 826-837.

Gur, T., Meydan, I., Seckin, H., Bekmezci, M., & Sen, F. (2022). Green synthesis, characterization and bioactivity of biogenic zinc oxide nanoparticles. *Environmental Research*, *204*, 111897.

Imtiaz, M., Alotaibi, B.M., Gassoumi, A., Alrowaily, A.W., Alyousef, H.A., Alotiby, M.F., & Henaish, A.M.A .(2024). Synthèse simple de matériau d'électrode FeAl2O4@ZnO pour application de supercondensateur. Journal of Physics and Chemistry of Solids, 188, 111941.

Jiang, Z., Liu, B., Yu, L., Tong, Y., Yan, M., Zhang, R., & Li, W. (2023). Research progresses in preparation methods and applications of zinc oxide nanoparticles. *Journal of Alloys and Compounds, 956,* 170316.

Khalid, NR, Hammad, A., Tahir, MB, Rafique, M., Iqbal, T., Nabi, G., & Hussain, MK (2019). Activité photocatalytique améliorée des nanobâtonnets de ZnO co-dopés Al et Fe pour la dégradation du bleu de méthylène. *Ceramics International, 45* (17), 21430-21435.

Kumar, S., Kumar, A., Kumar, A., & Krishnan, V. (2020). Nanoscale zinc oxide based heterojunctions as visible light active photocatalysts for hydrogen energy and environmental remediation. *Catalysis Reviews, 62*(3), 346-405.

Kuru, M., Kılıç Dokan, F., & Şaşmaz Kuru, T. (2022). Structural, electrical and magnetic characterization of Al3+ substituted Mg–Zn ferrites. *Applied Physics A*, *128*(4), 286.

Moravcik, I., Kubicek, A., Moravcikova-Gouvea, L., Adam, O., Kana, V., Pouchly, V., & Dlouhy, I. (2020). The origins of high-entropy alloy contamination induced by mechanical alloying and sintering. *Metals*, *10*(9), 1186.

Nguyen, T., Adjeroud, N., Guennou, M., Guillot, J., Fleming, Y., Papon, A. M., & Polesel-Maris, J. (2020). Controlling electrical and optical properties of zinc oxide thin films grown by thermal atomic layer deposition with oxygen gas. *Results in Materials, 6,* 100088.

Peng, Z., Li, Y., Wang, W., Li, X., Lv, X., Chen, X., & Zhou, S. (2021). Synthèse simple de nanocomposites magnétiques Fe@Al-ZnO pour l'inactivation bactérienne photocatalytique sous irradiation à la lumière visible. *Science Des Matériaux Dans Le Traitement Des Semi-Conducteurs, 123*, 105560.

Pushpalatha, C., Suresh, J., Gayathri, V. S., Sowmya, S. V., Augustine, D., Alamoudi, A., & Patil, S. (2022). Zinc oxide nanoparticles: a review on its applications in dentistry. *Frontiers in Bioengineering and Biotechnology*, *10*, 917990.

Rosowska, J., Kaszewski, J., Witkowski, B., Kuryliszyn-Kudelska, I., & Godlewski, M. (2020). L'effet de la teneur en fer sur les propriétés des nanoparticules de ZnO préparées par la méthode hydrothermale par micro-ondes. *Matériaux Optiques, 109,* 110089.

Sharath, B. N., & Rao, R. (2024). Comparative study of mechanical alloying and other conventional powder metallurgical methods. In Mechanical Alloying of Ferrous and Non-Ferrous Alloys (pp. 83-118). Elsevier.

Suryanarayana, C. (2022). Mechanical alloying: a critical review. *Materials Research Letters, 10(*10), 619-647.

Suryanarayana, C., Al-Joubori, A. A., & Wang, Z. (2022). Nanostructured materials and nanocomposites by mechanical alloying: an overview. *Metals and Materials International, 28(*1), 41-53.

Tian, W., Li, J., Liu, Y., Ali, R., Guo, Y., Deng, L., & Jian, X. (2021). Dépôt couche par couche à l'échelle atomique d'hybride FeSiAl@ ZnO@ Al2O3 avec des propriétés anti-corrosion à seuil et d'absorption micro-ondes ultra-élevée dans les bandes basse fréquence. *Lettres Nano-Micro, 13* (1), 161.

Vijayakumar, Y., Nagaraju, P., Yaragani, V., Parne, S.R., Awwad, N.S., & Reddy, M.R. (2020). Films minces nanostructurés en ZnO co-dopés Al et Fe pour une détection améliorée de l'ammoniac. *Physica B: Condensed Matter, 581*, 411976.

Zonta, G., Astolfi, M., Casotti, D., Cruciani, G., Fabbri, B., Gaiardo, A., & Malagù, C. (2020). Reproducibility tests with zinc oxide thick-film sensors. *Ceramics International, 46*(5), 6847-6855.

Author Information

Rachid Amraoui
Research Center in Industrial Technologies (CRTI)
P.O Box 64, Cheraga 16014 Algiers, Algeria
Contact e-mail: *amrachid21@gmail.com*

Abderrahmane Younes
Research Centre in Industrial Technologies (CRTI)
P.O Box 64, Cheraga 16014 Algiers, Algeria

Abderahim Abada
Aeronautic Institute, University of Blida 1
BP 270 road Soumâa -Blida-, Algeria

Djilali Allou
Research Centre in Industrial Technologies (CRTI)
P.O Box 64, Cheraga 16014 Algiers, Algeria

To cite this article:

Amraoui, R., Younes, A., Abada, A., & Allou, D. (2024). Magnetic behavior and structural properties of $Fe_{10}Al_{40}(ZnO)_{50}$ and $Fe_{10}Al_{50}(ZnO)_{40}$ nanocomposites. *The Eurasia Proceedings of Science, Technology, Engineering & Mathematics (EPSTEM), 32,* 400-405.

The Eurasia Proceedings of Science, Technology, Engineering & Mathematics (EPSTEM)
ISSN: 2602-3199

The Eurasia Proceedings of Science, Technology, Engineering & Mathematics (EPSTEM), 2024

Volume 32, Pages 406-416

IConTES 2024: International Conference on Technology, Engineering and Science

Phases Unlocked: The Crucial Role of Qubit Phases in Quantum Computing

Yousef Jaradat
Al-Zaytoonah University of Jordan

Mohammad Masoud
Al-Zaytoonah University of Jordan

Ahmad Mansrah
Al-Zaytoonah University of Jordan

Ismael Jannoud
Al-Zaytoonah University of Jordan

Mohammad Alia
Al-Zaytoonah University of Jordan

Abstract: Quantum computing applies quantum physics ideas to problems that traditional computers cannot address. The qubit, or quantum equivalent of the classical bit, is fundamental to this paradigm shift. Unlike its classical equivalent, a qubit can exist in a superposition of states, representing both 0 and 1. This superposition is defined not only by magnitudes, but also by important phase variables. These phases have a significant impact on qubit behavior and quantum computation outputs. This work conducts a thorough investigation of qubit phases, exploring their tremendous impact on the efficacy and capabilities of quantum algorithms. We investigate how constructive and destructive interference caused by phase interactions provides the foundation of quantum algorithms. Furthermore, we look into the intricate role of phases in establishing and managing entanglement, a unique quantum phenomenon that allows tremendous interactions between qubits. Our investigation includes the effects of numerous quantum operations on qubit phases. We present a thorough mathematical framework for describing how typical quantum gates, such as Hadamard, Pauli, and phase-shift gates, change the phase and thus the overall state of a qubit. We show these concepts through actual implementations of the Qiskit library. Finally, we discuss the intrinsic difficulty of managing and monitoring qubit phases, particularly the negative impacts of decoherence, which disrupts the delicate phase relationships. We describe tactics for mitigating these obstacles and investigate techniques for extracting phase information indirectly, such as quantum state tomography and interferometry. This comprehensive study seeks to provide a better understanding of the critical role phases play in quantum computing, paving the way for advances in algorithm design, quantum control, and the development of fault-tolerant quantum computers.

Keywords: Qubit, Relative phase, Global phase, Quantum algorithm, Qiskit

Introduction

Quantum computing is a field interested in performing computational tasks using the principles of quantum mechanics. At its core, quantum computing seeks to solve complex problems significantly faster than possible on classical computers. Classical computers are engineered using electrical devices, which employ the principles of classical mechanics to perform calculations. Quantum computing, on the other hand, is based on quantum mechanics, where nature is described using completely different rules than those for macroscopic objects. The adoption of these quantum mechanics principles into computing enables performing calculations and operations that remain otherwise impossible using classical methods. Quantum computers store, process, and transfer information using quantum bits, also known as qubits. The states of qubits provide information about a system. In quantum computing, qubits are the minimal units of quantum information processing (Bravyi et al., 2022; Uehara et al., 2021).

One notable characteristic of qubits is their ability to exist in multiple states simultaneously, a phenomenon known as superposition. This occurs because qubits function on a scale that is far more fragile than that of classical bits, leading to behaviors that are not typically observed in the classical realm. Additionally, quantum computers leverage a fundamental connection between qubits known as entanglement, which enhances operational efficiency by distributing tasks among the states of multiple qubits. In practical applications, simulated qubits are represented as physical qubits positioned on computer chips. The potential applications of quantum computing are vast, encompassing fields such as cryptography and information security (Ajala et al., 2024). Drug development and medical diagnostics (Blunt et al., 2022). Traffic management, and financial risk assessment (Ajagekar et al., 2020; Harwood et al., 2021). However, significant challenges remain due to the complexities of quantum mechanics. For a quantum computer to be effective, it must manipulate each qubit with high precision and at rapid computational speeds (Mohamed et al., 2022, Deutsch, 2020).

The two main types of quantum computers currently being developed are gate-based quantum computers and adiabatic quantum computers (Hegade et al., 2021; Jaradat et al., 2023). Gate-based quantum computers- which are the most common type of quantum computers- work by using quantum gates to manipulate qubits, while adiabatic quantum computers find the lowest energy state of a quantum system through a process called adiabatic evolution.

Quantum computers utilize qubits, which can exist in superposition and entangled states, offering tenfold greater processing capacity than classical bits. A fundamental principle of quantum mechanics that differentiates quantum computing from classical computing is the notion of phase. In contrast to classical computing, which represents bits as binary values 0 and 1, quantum states employ complex amplitudes. The amplitudes possess both magnitude and phase, with the phase governing interference patterns and determining the evolution of qubits under transformations.

A qubit's state is represented as:

$$|\psi >= \alpha|0> +\beta|1> \tag{1}$$

where α and β are complex amplitudes, and satisfies the normalization condition $|\alpha|^2 + |\beta|^2 = 1$. While $|\alpha|^2$ and $|\beta|^2$ dictate the probabilities of measuring 0 or 1, the phase difference between α and β is critical for quantum computation.

In quantum computing, two principal types of phases significantly influence the behavior of qubits and quantum computation and algorithms: global phase and relative phase. These phases stem from the intricate characteristics of quantum states and influence the interference and evolution of qubits during computation. The two types of phases are significant for the following reasons (Gill et al., 2022; Bhat et al., 2022):

- Global Phase: The overall phase of a qubit state that does not impact measurement probabilities but affects interference.
- Relative Phase: The phase difference between components of a superposition state, essential for algorithms such as Grover's and Shor's.

This work aims to examine and emphasize the significant importance of qubit phases, particularly global and relative phases, in quantum computing. This study seeks to deliver a comprehensive assessment of the impact of these phases on quantum state evolution, interference patterns, and the efficacy of quantum algorithms. This study aims to further our comprehension of phase manipulation as an essential tool in quantum computation by analyzing the impacts of different quantum gates on qubit phases. Moreover, through simulations of Qiskit, the study seeks to provide practical insights into how phase control might enhance the execution of quantum algorithms, thereby contributing to the development and deployment of more efficient quantum computing systems.

The rest of the paper is organized as follows. Section II provides an analysis of the quantum phases. Phase gates and their effect are provided in section III. Section IV provides simulation results of the role of relative phase in quantum interference and algorithms. Finally, section V concludes the paper.

Quantum Phase Analysis

Equation (1) represents a general formula for the representation of the quantum state, where α and β are complex amplitudes. Equation (1) can be re-written in vector form as:

$$|\psi >= \begin{bmatrix} \alpha \\ \beta \end{bmatrix} \tag{2}$$

The complex numbers α and β can be represented as:

- $\alpha = r_1 e^{j\theta_1}$
- $\beta = r_2 e^{j\theta_2}$

r_1,*r2* being the magnitudes of the coefficients, and θ_1,θ_2 being the phases associated with each state. Then equation (2) becomes:

$$|\psi >= \begin{bmatrix} r_1 e^{j\theta_1} \\ r_2 e^{j\theta_2} \end{bmatrix} \tag{3}$$

Global Phase

The global phase is a common phase factor applied uniformly to all components of a quantum state. This can be done by multiplying the entire state by a phase factor $e^{j\gamma}$ where γ is a real number, this gives:

$$|\psi' >= e^{j\gamma}\big|\psi > = e^{j\gamma}(\ \alpha\big|0 > +\beta|1 >) \tag{4}$$

This phase γ represents the global phase. Mathematically, it changes the phase of the entire state by the same amount. The global phase affects neither physical observables nor measurement probabilities because it is shared by both terms. Only the relative phases between the components of a superposition can be observed using quantum mechanics. The reason for this can be seen from the fact that measurement probabilities depend on the squared magnitudes of the state components, and for any complex number $z = re^{j\phi}$, $|z|^2 = r^2$, which is independent of the phase ϕ. Thus, the global phase γ drops out in measurement probabilities, leaving the physical state unaffected.

Relative Phase

In contrast to global phase, relative phase refers to the phase difference between the superposition state's components. The phase difference is important because it influences the interference patterns that can be measured. Utilizing quations (1) and (2), the relative phase can be given by:

$$\Delta\theta = \theta_1 - \theta_2 \tag{5}$$

To figure out what this relative phase means, let's rewrite the state in terms of the coefficients' magnitude and phase:

$$\big|\psi > = r_1 e^{j\theta_1}\big|0 > + r_2 e^{j\theta_2}|1 > \tag{6}$$

Factoring out a global phase $e^{j\theta_1}$ from both terms, we get:

$$\big|\psi > = e^{j\theta_1}(r_1\big|0 > + r_2 e^{j(\theta_2 - \theta_2)}|1 >) \ = e^{j\theta_1}(r_1\big|0 > + r_2 e^{j\Delta\theta}\big|1 >) \tag{7}$$

Here θ_1, is the global phase (which can be ignored in terms of measurement outcomes), and $\Delta\theta=\theta2-\theta1$ is the relative phase. The relative phase directly affects the interference between $|0\rangle$ and $|1\rangle$, as it controls how the superposition state evolves under quantum gates.

Bloch Sphere Representation

Bloch spheres are a way to show the qubit state in three dimensions using geometric shapes. We rewrite the amplitudes α and β in terms of spherical coordinates to show a qubit state on the Bloch sphere. Using equation (7) define new parameters θ and ϕ to describe the state on the Bloch sphere. These angles describe the state in spherical coordinates:

$$\left|\psi > = \cos(\frac{\theta}{2})\right| 0 > + e^{j\phi} \sin(\frac{\theta}{2}) |1 > \tag{8}$$

Where θ is the polar angle (latitude) on the Bloch sphere and determines the ratio of $|0\rangle$ to $|1\rangle$, and ϕ is the azimuthal angle (longitude) and represents the relative phase between $|0\rangle$ and $|1\rangle$. Fig. (1) shows an example of the impact of the global phase on the state of a single qubit. In this example The global phase multiplies the entire quantum state by a constant phase factor $e^{j\phi}$. In our case, $\phi=\pi/2$. Global phase factors do not influence measurement results. In quantum physics, they remain unobservable since all physical probabilities rely on the modulus squared of the amplitudes, resulting in the cancellation of the global phase.

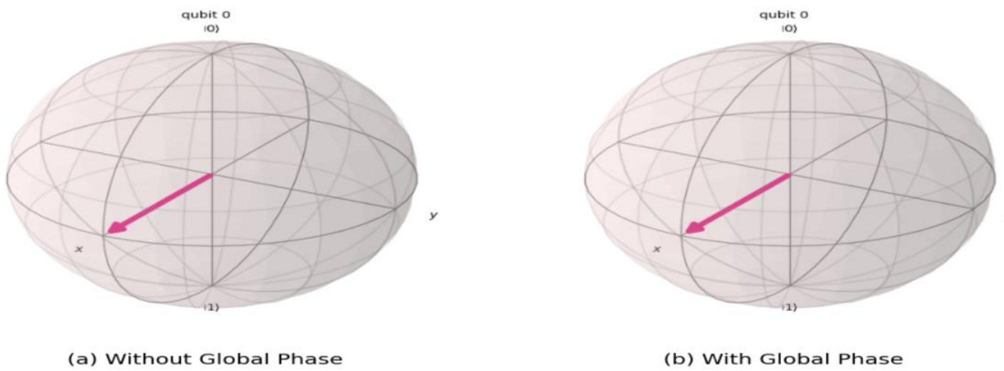

Figure 1. Global phase impact on the state vector of a single qubit

We show below how solve the above example numerically by showing the quantum state vector before and after applying the global phase.

- **No global phase**

$$|\psi_{no-global} >= \frac{1}{\sqrt{2}}(|0 > +|1 >) = \frac{1}{\sqrt{2}}\begin{bmatrix}1\\1\end{bmatrix} = \begin{bmatrix}0.7071 + 0j\\0.7071 + 0j\end{bmatrix}$$

- **With global phase**

A global phase of *π/2* is applied:

$$|\psi_{with-global} >= e^{j\frac{\pi}{2}}\frac{1}{\sqrt{2}}(|0 > +|1 >) = \frac{j}{\sqrt{2}}\begin{bmatrix}1\\1\end{bmatrix} = j\begin{bmatrix}0.7071 + 0j\\0.7071 + 0j\end{bmatrix} = \begin{bmatrix}0 + j0.7071\\0 + j0.7071\end{bmatrix}$$

From the above example we notice these essential Insights:

a. The experiment validates that global phases lack physical significance and do not modify the qubit's representation on the Bloch sphere.
b. The state vectors exhibit a numerical difference characterized by a phase factor $e^{j\frac{\pi}{2}}$, which is seen in the imaginary components of the amplitudes in the "With Global Phase" scenario.
c. Upon measuring these qubits, both would produce identical probability for $|0\rangle$ and $|1\rangle$.

Fig. 2 shows a demonstration of the impact of a relative phase on a qubit's state. We'll create two quantum circuits:

- **Without Relative Phase**: A qubit in a superposition state created by a Hadamard gate.

$$|\psi_{no-relative}>= \frac{1}{\sqrt{2}}(|0>+|1>) = \frac{1}{\sqrt{2}}\begin{bmatrix}1\\1\end{bmatrix} = \begin{bmatrix}0.7071+0j\\0.7071+0j\end{bmatrix}$$

- **With Relative Phase**: The same superposition state with an added relative phase using a phase gate.

A phase ϕ can be introduced utilizing the phase gate $P(\Phi)$.

$$P(\Phi) = \begin{bmatrix}1 & 0\\0 & e^{j\phi}\end{bmatrix} \tag{9}$$

$$|\psi_{with-relative}>= P(\frac{\pi}{2})\frac{1}{\sqrt{2}}(|0>+|1>) = \begin{bmatrix}1 & 0\\0 & j\end{bmatrix}\frac{1}{\sqrt{2}}\begin{bmatrix}1\\1\end{bmatrix} = \begin{bmatrix}0.7071+0j\\0+0.7071j\end{bmatrix}$$

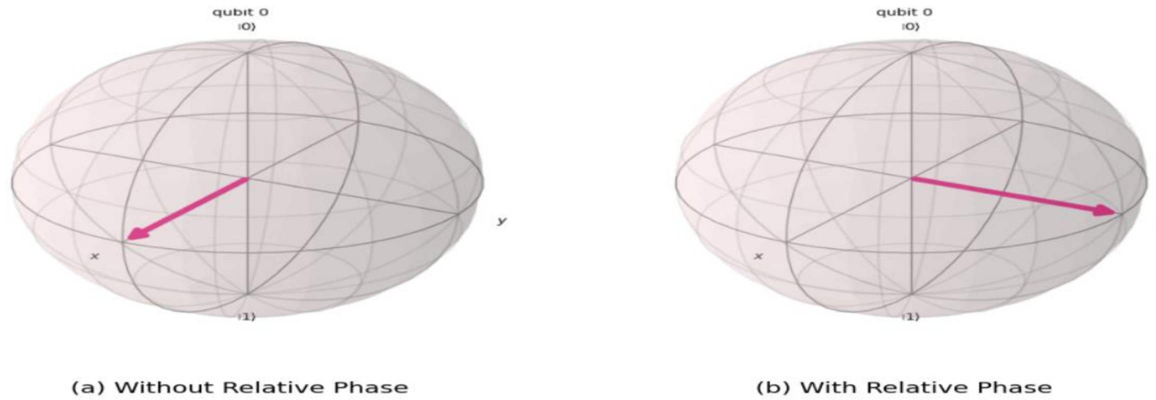

Figure 2. Relative phase impact on the state vector of a single qubit

It is clearly obvious that the relative phase has rotate the qubit's state vector around the Z-axis. The angle of rotation is equal to the relative phase ϕ which is π/2 in this example.

Phase Gates and Their Effect on the State Vector of a Qubit

In quantum computing, phase gates are single-qubit operations that apply a phase shift to the quantum state. They are vital for manipulating the relative phases among quantum states, which is critical for quantum interference and entanglement. This section examines the prevalent phase gates, their mathematical formulations, and their impact on qubit states (Hill et al.,2021 Feng et al., 2021). Phase gates induce a phase shift in the |1⟩ component of a qubit's state. The generic phase gate is represented as $P(\Phi)$ and is characterized by equation (9). When applied to a qubit in a superposition state, phase gates alter the relative phase between the |0⟩ and |1⟩ components, affecting how the qubit interferes with other qubits or itself.

Table 1 shows the different types of relative phase gates applied to a qubit in superposition state after applying the Hadamard gate. When a qubit is in a superposition stateas shown in equation (1), applying a phase gate modifies the phase of the |1⟩ component while leaving the |0⟩ component unchanged.

- The Z gate introduces a phase shift of π, effectively multiplying the |1⟩ coefficient by −1. This reflects the state vector across the X-axis on the Bloch sphere, turning |+⟩ into |−⟩.
- The S gate, with a phase shift of π/2, multiplies the |1⟩ component by j. This rotates the state vector by 90∘ around the Z-axis, moving it from the positive X-axis to the positive Y-axis on the Bloch sphere.
- The T gate applies a phase shift of π/4, multiplying the |1⟩ component by $e^{j\frac{\pi}{4}}$. This results in a 45∘ rotation around the Z-axis, positioning the state vector between the positive X and Y axes.

- The general phase gate $P(\Phi)$ allows for an arbitrary phase shift , offering precise control over the qubit's relative phase. Applying $P(\Phi)$ rotates the state vector by Φ around the Z-axis on the Bloch sphere.

By altering the relative phases, these gates change how qubit states interfere with each other, which is crucial for quantum algorithms and operations that rely on quantum interference and entanglement.

Table 1. Relative phase gates

	Gate name	Gate relative phase	Gate matrix	Gate Bloch sphere
1.	Hadamard	None	$\frac{1}{\sqrt{2}}\begin{bmatrix}1 & 1\\ 01 & -1\end{bmatrix}$	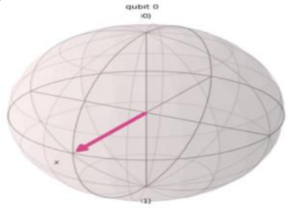
2.	Z	$\phi=\pi$	$\begin{bmatrix}1 & 0\\ 0 & -1\end{bmatrix}$	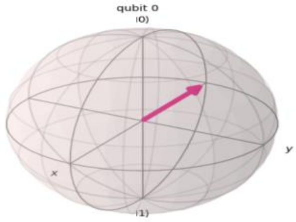
3.	S	$\phi=\pi/2$	$\begin{bmatrix}1 & 0\\ 0 & j\end{bmatrix}$	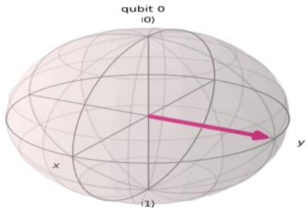
4.	T	$\phi=\pi/4$	$\begin{bmatrix}1 & 0\\ 0 & e^{j\frac{\pi}{4}}\end{bmatrix}$	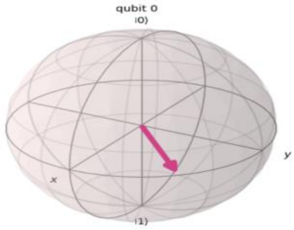
5.	P	ϕ any other phase Choose $\phi=\pi/3$	$\begin{bmatrix}1 & 0\\ 0 & e^{j\frac{\pi}{3}}\end{bmatrix}$	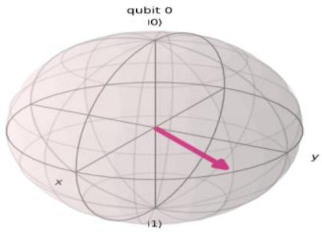

Relative Phase Role in Quantum Interference and Algorithms

Quantum interference arises when the probability amplitudes of distinct quantum states combine, resulting in a cumulative probability that may exceed (constructive interference) or diminish (destructive interference) the sum of the individual probabilities. In contrast to classical probabilities, quantum probability amplitudes are complex numbers, and their phases are essential for interference phenomena.

Consider a quantum system that can be in states $|\psi 1\rangle$ and $|\psi 2\rangle$. The system's state can be a superposition:

$$|\Psi> = \alpha|\psi_1> + \beta|\psi_2> \quad (10)$$

where α and β are complex probability amplitudes. The probability of measuring a particular outcome is given by the modulus squared of the total amplitude:

$$P = |\alpha + \beta|^2 = |\alpha|^2 + |\beta|^2 + 2Re(\alpha^*\beta) = |\alpha|^2 + |\beta|^2 + 2\,|\alpha||\beta|\cos(\phi_\beta - \phi_\alpha) \quad (11)$$

The cross term $2Re(\alpha^*\beta)$ represents the interference effect, which depends on the relative phase between α and β. A constructive Interference, ($\cos(\phi_\beta - \phi_\alpha) = 1$), occurs when the relative phase between amplitudes leads to an increased probability of an outcome. On the other hand, a destructive Interference, ($\cos(\phi_\beta - \phi_\alpha) = -1$) , occurs when the relative phase causes the amplitudes to cancel out, decreasing the probability. This shows the importance and the necessity of having relative phase as quantum interference inherently depends on relative phases between quantum states. Without relative phases, the interference terms vanish, and quantum systems behave classically in terms of probability distributions.

Quantum interference and relative phase are an essential assets in quantum computing, allowing quantum algorithms to surpass classical algorithms. They permit:

- Parallelism: Quantum superposition facilitates concurrent computation across various states.
- Algorithmic Speedup: Algorithms such as Shor's factoring algorithm and Grover's search algorithm utilize interference to achieve solutions more rapidly than conventional algorithms.
- Quantum Simulations: Interference is crucial for simulating quantum systems, as phase relationships dictate physical features.

Some examples of quantum algorithms that utilize relative phase and quantum interference include: Grover's algorithm which uses interference to amplify the probability amplitude of the desired solution while suppressing others; Quantum phase estimation (QPE) which relies on interference patterns to estimate eigenvalues of unitary operators; and quantum Fourier transform (QFT) which transforms quantum states into a superposition where interference encodes frequency components.

Figure 3. shows a quantum circuit that is comprised of a single qubit initiated in the state $|0\rangle$. Initially, it employs a Hadamard gate to establish an equal superposition of the states $|0\rangle$ and $|1\rangle$. Subsequently, it creates a relative phase shift by employing a phase gate, which adds a certain phase angle Φ to the $|1\rangle$ component of the superposition. Subsequently, a second Hadamard gate is applied, resulting in the interference of the probability amplitudes of the qubit's states. The relative phase Φ dictates the combination of these amplitudes, resulting in constructive or destructive interference, which directly influences the probability of measuring the qubit in either state $|0\rangle$ or $|1\rangle$. The qubit is ultimately measured. This circuit illustrates the essential function of relative phase in quantum interference and how its manipulation can influence the results of quantum measurements.

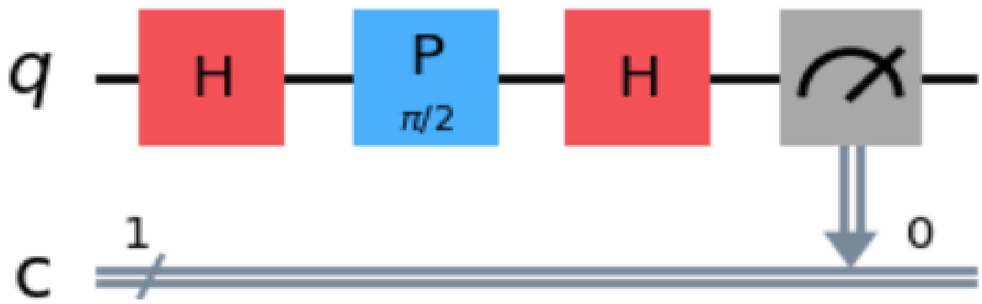

Figure 3. Quantum circuit to demonstrate the effect of relative phase on interference

Fig. 4 depicts how the probabilities of measuring the qubit in states $|0\rangle$ and $|1\rangle$ fluctuate when the relative phase Φ alters. It demonstrates that when Φ varies from 0 to 2π, the probabilities P(0) and P(1) fluctuate sinusoidally between 0 and 1. This oscillation illustrates the constructive and destructive interference effects resulting from the relative phase introduced by the phase gate. At specific phase values (e.g., Φ =0 or 2π), the probability P(0) attains its maximum, signifying constructive interference for the $|0\rangle$ state. Conversely, for Φ =π, P(1) attains its maximum due to constructive interference for the $|1\rangle$ state. The figure clearly illustrates the significant influence of relative phase on quantum interference and emphasizes that manipulating this phase can govern the results of quantum experiments.

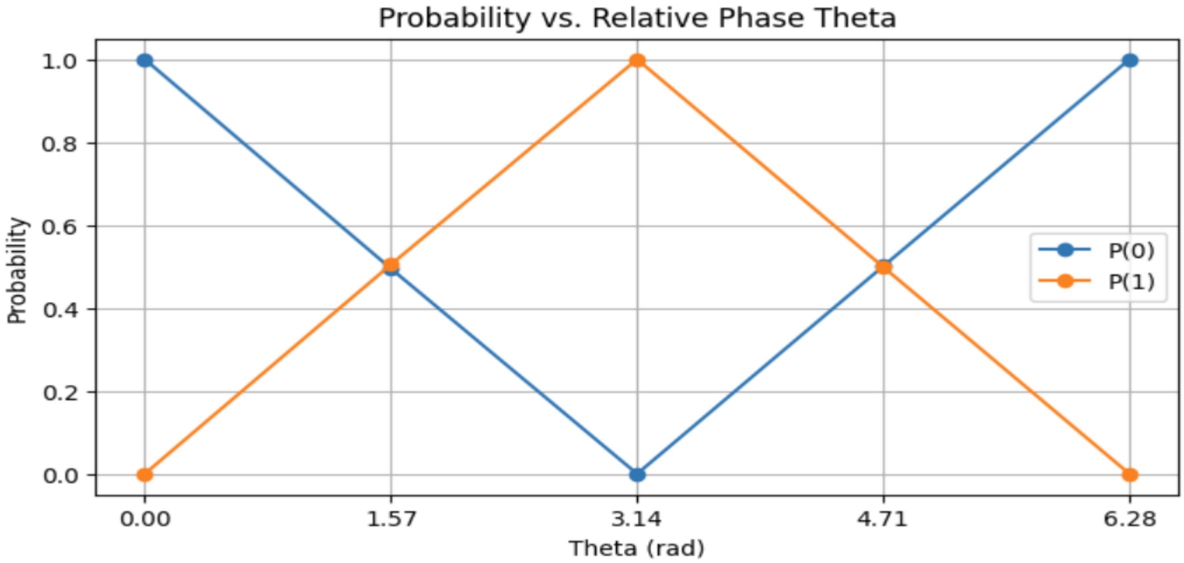

Figure 4. Probability vs relative phase (rad)

Fig. 5 shows a quantum circuit introduces with Hadamard gates applied to both qubits immediately before the measurement step. These additional Hadamard gates effectively change the measurement basis from the standard computational basis to the Hadamard (or X) basis. The circuit begins by creating an entangled Bell state between the two qubits, and a relative phase shift is introduced to one qubit using a phase gate. By applying the Hadamard gates before measurement, the circuit allows the relative phase to influence the measurement outcomes. This modification makes the impact of the phase shift observable, as it causes the probability amplitudes of the qubit states to interfere differently, depending on the value of the phase. The circuit demonstrates how changing the measurement basis can reveal subtle effects of quantum phases on entangled states.

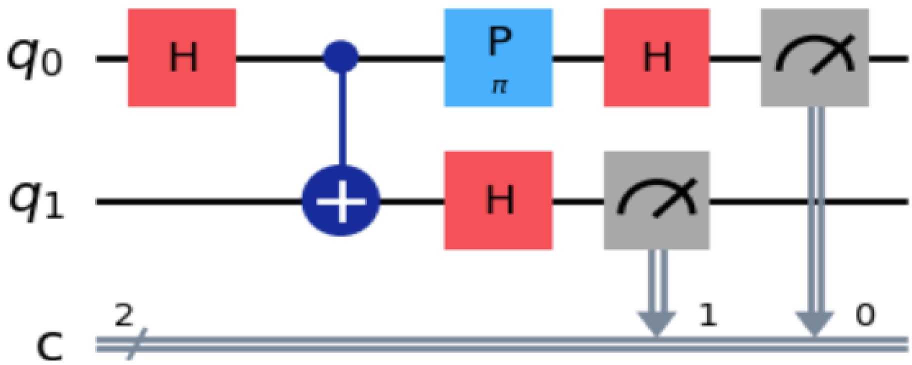

Figure 5. Entangled circuit with relative phase

Figure 6. shows the resulting histograms of the probability for each potential two-qubit outcome assessed in the computational basis following the use of Hadamard gates. The data indicate that the probability of detecting particular outcomes fluctuate considerably with varying values of the phase angle Φ. For example, when the relative phase (Φ is 0, π or 2π) the computational basis '00' and '11' are only have non-zero probabilities. While when the relative phase (Φ is $\pi/2$ or $3\pi/2$) all of the computational bases have non-zero probabilities. This variant demonstrates that the previously introduced relative phase in the circuit influences the interference patterns when the measurement basis is modified. The histograms demonstrate how constructive and destructive interference, affected by the phase shift, result in varying probabilities for each scenario. This demonstrates the crucial role of relative phases and measurement bases in quantum mechanics, as they directly impact the observable properties of quantum systems.

One final note to point out that drastically affects the relative phase and quantum interference is the decoherence problem. Decoherence, which can be defined as the loss of quantum coherence due to interactions with the environment, disrupts the delicate phase relationships between qubits. This interference can cause errors in computations and loss of information, posing a significant challenge to building reliable quantum computers. To overcome these obstacles, researchers are developing solutions such as quantum error correction codes, which can detect and fix errors without directly measuring the qubits. Other approaches include isolating qubits from environmental noise using sophisticated shielding techniques, employing decoherence-free subspaces where qubits are less susceptible to interference, and implementing dynamic decoupling methods to counteract decoherence effects. These strategies aim to preserve the integrity of qubit phases, allowing quantum computers to perform complex calculations accurately (Abdelmagid et al., 2023; Salmanogli & Sirat, 2024).

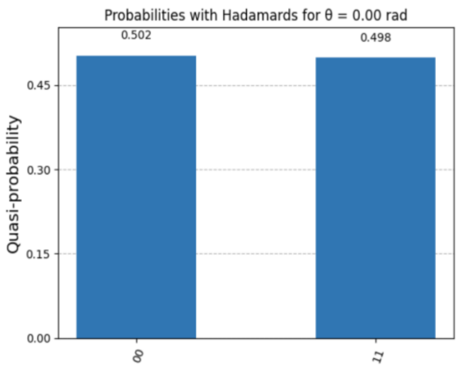

(a)

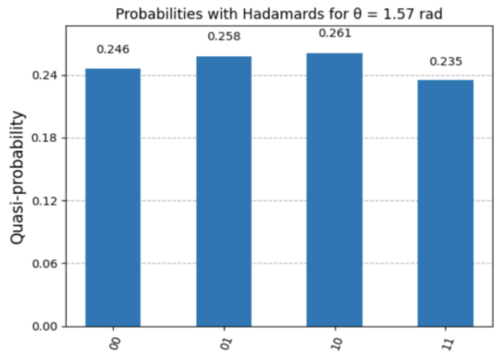

(b)

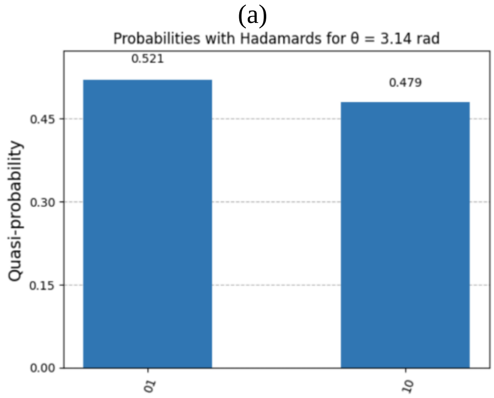

(c)

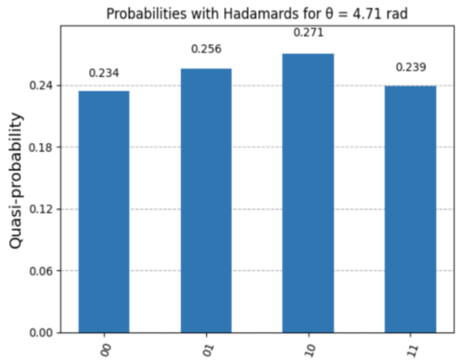

(d)

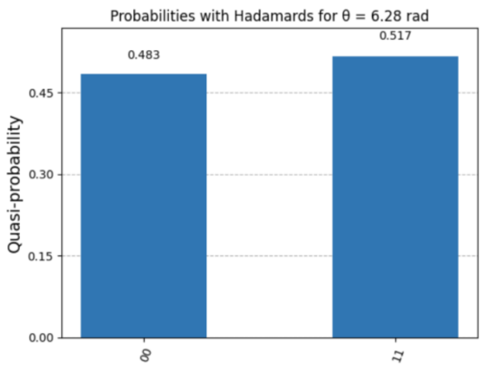

(e)

Figure 6. Probabilities for Entangled state with different relative phases

Conclusion

This paper explores the essential value of relative phases and quantum interference in quantum computing. We examined the impact of quantum gates, including the Z, S, T, and general phase gates, on the relative phases of qubits in superposition through comprehensive explanations and realistic Qiskit simulation. These gates alter the phase of quantum states, resulting in constructive or destructive interference patterns crucial for the operation of quantum algorithms. Through the analysis of particular quantum circuits, we illustrated how modifications to the relative phase affect measurement results. In the interference circuit with a single qubit, we demonstrated that altering the relative phase θ directly influences the probabilities of measuring the qubit in either the $|0\rangle$ or $|1\rangle$ state. This highlights how quantum interference, influenced by relative phases, can be utilized to manipulate quantum systems. We also examined the influence of relative phases in entangled systems. The application of phase gates to a single qubit inside an entangled pair demonstrated that the relative phase can affect the joint state and measurement probabilities, particularly when measurements are conducted in different bases. This underscores the complex interplay of entanglement, relative phases, and measurement results.

Moreover, the research examined the significance of relative phases in other quantum algorithms, including the Quantum Fourier Transform (QFT), Quantum Phase Estimation (QPE), Grover's Algorithm, among others. These algorithms utilize the manipulation of relative phases to generate interference patterns that amplify desired computational outcomes while diminishing undesired ones.

In summary, the precise control and understanding of relative phases are crucial for the advancement of quantum computing. Quantum interference, facilitated by these phases, is a key resource that enables quantum algorithms to outperform classical counterparts. Mastery over phase manipulation not only aids in the development of more efficient quantum algorithms but also deepens our comprehension of quantum mechanics and its applications in technology.

Scientific Ethics Declaration

The authors declare that the scientific ethical and legal responsibility of this article published in EPSTEM Journal belongs to the authors.

Acknowledgements or Notes

* This article was presented as an oral presentation at the International Conference on Technology, Engineering and Science (www.icontes.net) held in Antalya/Turkey on November 14-17, 2024.

* The authors would like to thank the Deanship of scientific research and Innovation at Al-Zaytoonah University of Jordan (ZUJ) for Funding this work.

References

Abdelmagid, R., Alshehhi, K., & Sadiek, G. (2023). entanglement degradation in two interacting qubits coupled to dephasing environments. *Entropy, 25*(10),1458,

Ajala, O. A., Arinze, C. A., Ofodile, O. C., Okoye, C. C., & Daraojimba, A. I. (2024). Exploring and reviewing the potential of quantum computing in enhancing cybersecurity encryption methods. *Magna Scientia Advanced Research and Reviews, 10*(1),321-329.

Ajagekar, A., Humble, T., & You, F. (2020). Quantum computing based hybrid solution strategies for large-scale discrete-continuous optimization problems. *Computers & Chemical Engineering,132,* 106630.

Bhat, H. A., Khanday, F. A., Kaushik, B. K., Bashir, F., & Shah, K. A. (2022). Quantum computing: fundamentals, implementations and applications. *IEEE Open Journal of Nanotechnology, 3,* 61-77.

Blunt, N. S., Camps, J., Crawford, O., Izsák, R., Leontica, S., Mirani, A., ... & Holzmann, N. (2022). Perspective on the current state-of-the-art of quantum computing for drug discovery applications. *Journal of Chemical Theory and Computation, 18*(12), 7001-7023.

Bravyi, S., Dial, O., Gambetta, J. M., Gil, D., & Nazario, Z. (2022). The future of quantum computing with superconducting qubits. *Journal of Applied Physics, 132*(16),160902.

Deutsch, I. H. (2020). Harnessing the power of the second quantum revolution. *PRX Quantum, 1*(2),020101.

Feng, T., Ren, C., & Zhou, X. (2021). Direct measurement of density-matrix elements using a phase-shifting technique. *Physical Review A, 104*(4),042403.

Gill, S. S., Kumar, A., Singh, H., Singh, M., Kaur, K., Usman, M., & Buyya, R. (2022). Quantum computing: A taxonomy, systematic review and future directions. *Software Practice and Experience, 52*(1), 66-114.

Harwood, S., Gambella, C., Trenev, D., Simonetto, A., Bernal, D., & Greenberg, D. (2021). Formulating and solving routing problems on quantum computers. *IEEE Transactions on Quantum Engineering, 2,* 1-17.

Hegade, N. N., Paul, K., Ding, Y., Sanz, M., Albarrán-Arriagada, F., Solano, E., & Chen, X. (2021). Shortcuts to adiabaticity in digitized adiabatic quantum computing. *Physical Review Applied, 15*(2), 024038.

Hill, A. D., Hodson, M. J., Didier, N., & Reagor, M. J. (2021). Realization of arbitrary doubly-controlled quantum phase gates. *arXiv preprint arXiv:2108*, 01652.

Jaradat, Y., Alıa, M., Masoud, M., Mansrah, A., Jannoud, I., & Alheyasat, O. (2023). Roadmap for simulating quantum circuits utilising ıbm's qiskit library: Programming approach. *The Eurasia Proceedings of Science Technology Engineering and Mathematics, 26*, 624–632.

Mohamed, A. B. A., Rahman, A. U., & Eleuch, H. (2022). Measurement uncertainty, purity, and entanglement dynamics of maximally entangled two qubits interacting spatially with isolated cavities, intrinsic decoherence effect. *Entropy*,*24*(4),545.

Salmanogli, A. & Sirat, V. S. (2024). Engineering qubit coupling to reservoir mode: optimizing circuitry to extend coherence time. *Chinese Journal of Physics*,*90*,1005-1014.

Uehara, G. S., Spanias, A., & Clark, W. (2021, July). Quantum information processing algorithms with emphasis on machine learning. In *2021 12th International Conference on Information, Intelligence, Systems & Applications (IISA)* (pp. 1-11). IEEE.

Author Information

Yousef Jaradat
Al-Zaytoonah University of Jordan
Amman - Jordan
Contact e-mail: *y.jaradat@zuj.edu.jo*

Mohammad Masoud
Al-Zaytoonah University of Jordan
Amman - Jordan

Ahmad Mansrah
Al-Zaytoonah University of Jordan
Amman - Jordan

Ismael Janooud
Al-Zaytoonah University of Jordan
Amman - Jordan

Mohammad Alia
Al-Zaytoonah University of Jordan
Amman - Jordan

To cite this article:

Jaradat, Y., Masoud, M., Mansrah, A., Jannoud, I., & Alia, M. (2024). Phases unlocked: The crucial role of Qubit phases in quantum computing. *The Eurasia Proceedings of Science, Technology, Engineering & Mathematics (EPSTEM), 32*, 406-416.

The Eurasia Proceedings of Science, Technology, Engineering & Mathematics (EPSTEM), 2024

Volume 32, Pages 417-425

IConTES 2024: International Conference on Technology, Engineering and Science

Development and Characterization of a Biodegradable Composite Based on PLA Matrix and Date Kernels Powder

Abdelouahab Ait-Kaci
MouloudMammeri University of Tizi-Ouzou

Manel Hannachi
MouloudMammeri University of Tizi-Ouzou

Mustapha Nechiche
MouloudMammeri University of Tizi-Ouzou

Abstract: In the present study, a biodegradable composite material based on polylactic acid (PLA) and date kernels (DK) is developed by hot pressing. In first, all the raw materials were processed into powders. Then, PLA-50% date kernels (DK) (% vol.) mixtures were hot-pressed at 180°C under 10 MPa pressure during 5 minutes. Microstructural characterization of the obtained composites was performed using Scanning electron microscopy (SEM), Fourier Transform InfraRed spectroscopy (FTIR), and Differential Scanning Calorimetry (DSC) analyzes. The mechanical behavior was evaluated through tribological tests and mass loss measurements were also taken. The results show that the developed composite material exhibits a homogeneous microstructure, with a continuous (polylactic acid) PLA- (date pits) DP interface and chemical bonds of PLA and plant fiber interactions. The tribological tests revealed a low coefficient of friction for this material.

Keywords: Biodegradable composite, Date kernels, PLA, Friction coefficient.

Introduction

Nowadays sustainable development becomes highly important, so researchers and industries are focusing on replacing nonrenewable and fossil based materials with environmentally friendly materials **(**Dicker et al., 2014). Composites with biodegradable matrices reinforced by natural and especially plant-based reinforcements present an interesting alternative to fossil based materials, they have also been introduced in automotive, building and other industries. This has been the focus on different research subjects recently (Fazita et al., 2016)**.** Polylactic acid (PLA) is a biodegradable polymer derived from renewable resources, making it a good replacement to petroleum-based plastics and PLA-based composites are well known for their ecological benefits. PLA polymers offer good thermal stability and high resistance, which makes its applicability wider (Wang et al., 2014)**.** Despite all these advantages, they also have some disadvantages such as their high costs compared to their lower mechanical properties than other polymer-based composites. Advancements in material science and manufacturing techniques are overcoming these limitations, by adding other different reinforcements to the polymer which can allow better properties.

In Algeria where the palm trees are very widespread, the exploitation of its fruit wastes (date kernels) is a very interesting. In order to valorize these date wastes, we used them as natural reinforcements in biodegradable polymer based composite materials (Rahmoune, 2017) They can possibly improve their characteristics. (Nagarjun et al., 2021). Developed biodegradable composites using poly-lactic acid (PLA). The composites were manufactured through compression molding technique. Their tensile results showed that the date seed filler reinforcement has significantly improved the tensile strength of PLA matrix. Moreover, the obtained composites showed 34.68% improvement in micro hardness when compared with neat PLA. The authors revealed that the

- Selection and peer-review under responsibility of the Organizing Committee of the Conference

composition wt.% of fillers has a mojor role in deciding the properties of the PLA composites. Different studies have investigated the wear and friction properties of polymer matrix composites reinforced with vegetal fibers and it is deduced that the incorporation of reinforcements can either improve or decrease the tribological performance of the polymer matrix.

The aim of this work is to develop a fully biodegradable composite material based on PLA matrix and date kernels (DK) powder reinforcement. Thus, the raw materials have been reduced into powders and hot-compacted. Microstructural characterization using Scanning electron microscopy (SEM) was carried out in addition to Differential scanning calorimetry (DSC) and Fourier transform infrared spectroscopy (FTIR) analysis. The materials mechanical behavior was evaluated through tribological tests in which coefficients of friction were deduced.

Experimental

Processing of Raw Materials into Powders and Sample Preparation

The PLA powder was obtained by grinding pellets in a grinder-chopper. In order to allow a better yield of this process, the PLA pelletswere previously brought to a temperature of -10 °C, what fragilizes them and facilitates their fragmentation. The powder thus obtained is then sieved to select the particles having upper 200 µm of size. Date kernels was washed and roasted in an oven at 180°C for 2 hours and then processed into powder with the same grinder-chopper. PLA-DK mixtures at the proportion 50% (% vol.) was prepared and homogenized in Turbula® to be compacted at 180°C under 10 MPa during 5 mn.

Samples were characterized by SEM to highlight their microstructure and by Fourier Transform InfraRed Spectroscopy (FTIR) to reveal the possible formation of new chemical bonds between PLA and DK reinforcement. DSC analysis was used to follow the evolution of the structural transformations in the PLA and in the DK of the developed composite. Also, the friction coefficients of the composite were determined by tribological tests.

Results and Discussion

SEM Observations of Raw Materials

Figure 1and Figure 2 show the SEM micrographs of the developed PLA-DK composite. The figure 1, obtained in secondary electron mode reveals a microporous appearance of the sample (pores of sizes less than 2 µmwith illuminated edges; circled in yellow, points 1 and 2) as well as particles presenting a more contrasting dark color but without luminous edges (points 3 and 4) suggesting that these are date kernel particles.

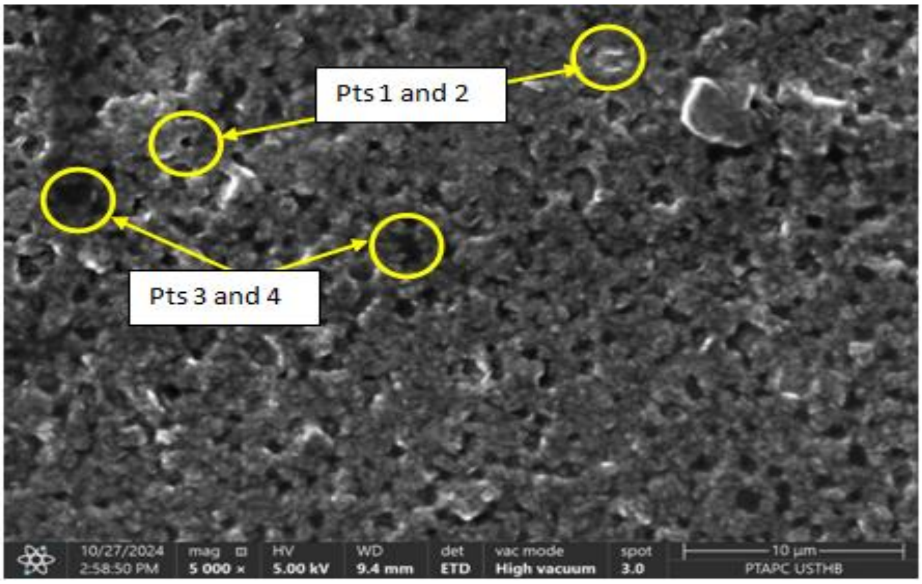

Figure 1.SEM image obtained in secondary electron mode.

Figure 2 represents SEM micrograph in backscattered electrons (CBS) of composite. Compared to that obtained in secondary electrons (Fig. 1), it clearly shows the significant contrast color of a phase contrast. Indeed, the PLA; of chemical formula $(C_3H_4O_2)_n$ has an average atomic number greater than that of the molecules constituting the date kernels (also for cellulose, lignin, etc.). We also notice a difference in the contrast between the particles (in light gray) and the pores (in dark) that we have located (points 1 and 2 in Figure 1).

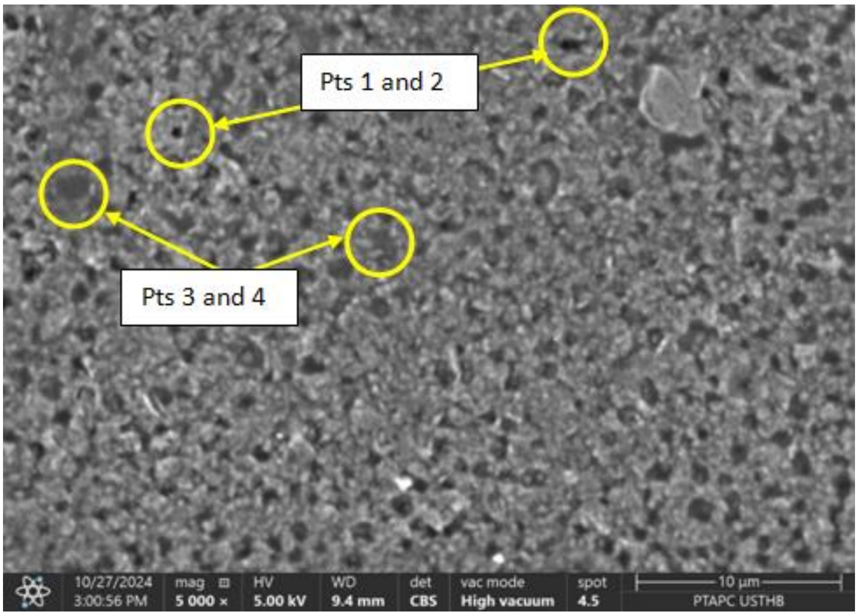

Figure 2. The SEM image obtained in backscattered electrons

Differential Scanning Calorimetry DSC Analysis

To understand PLA behaviour during heating and the influence of the addition of date pits reinforcements on the structural transformations of the obtained composite material, DSC analyzes were carried out starting from the ambient temperature to 400°C under N_2/50%/air atmosphere. The figure below (Fig. 3) shows the obtained curves. For virgin PLA, we observe a peak at 176.1 °C (minima value) which corresponds to the total melting of the PLA powder. At 307°C, the curve shows a significant endothermic peak from the onset of PLA evaporation which ends at 355.3°C. Another endothermic peak appears at 385.8°C which corresponds to the evaporation of residual substances produced by PLA transformations. The evaporation temperature of the composite was determined to start at 299°C. The decrease of PLA's evaporation and melting temperature is due to the chemical bonds formed between PLA and DK components.

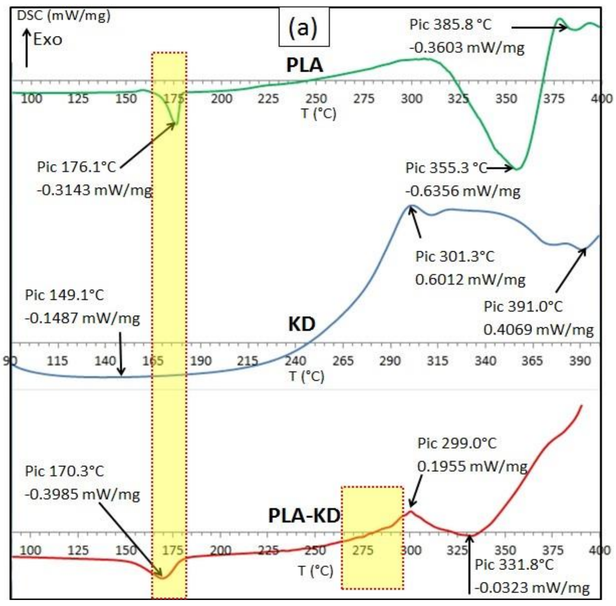

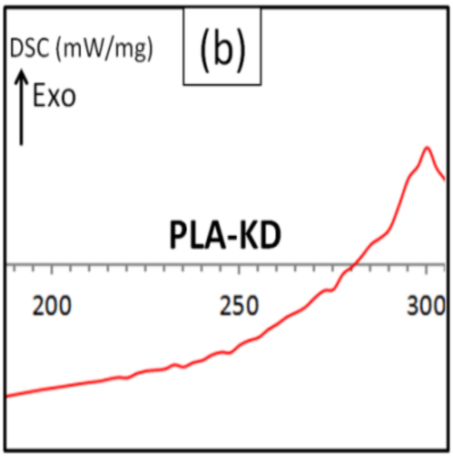

Figure 3 . DSC curves

FTIR Analysis

The FTIR spectra of the obtained PLA-DK composite sample is shown in Figure 4.A, comparison with the obtained result and the FTIR analysis previously carried out on PLA alone is done. For high wave numbers values (up to 3500 cm^{-1}), low-intensity elongation vibrations are observed, which are explained by the presence of alcohols and phenols in the date kernels.

The peaks of 2951 cm^{-1}wavenumbers value (and those in the vicinity) are due to the C-H and C = CH groups of PLA. Peaks around 2340-2360 cm^{-1} corresponding to C≡N nitriles appear with high intensities translating a high probability of formation of chemical bonds between PLA and date kernels compounds. They are less intense in the case of PLA alone. The peak at 1730 cm^{-1}corresponds to the aliphatic aldehydes of PLA, whereas those at 1650-1684 $cm^{-1}$are due to the aromatic aldehydes, alkenes and ketones. The peaks between 1241 and 1149 cm^{-1} correspond to PLA (different alcohols). For values between 1092 and 843 cm^{-1}, these ones occur in the case of date kernels (presence of ethers). At low wavenumbers values, peaks corresponding to the C-C and C = O bonds occur and instead reflect the presence of date kernels.

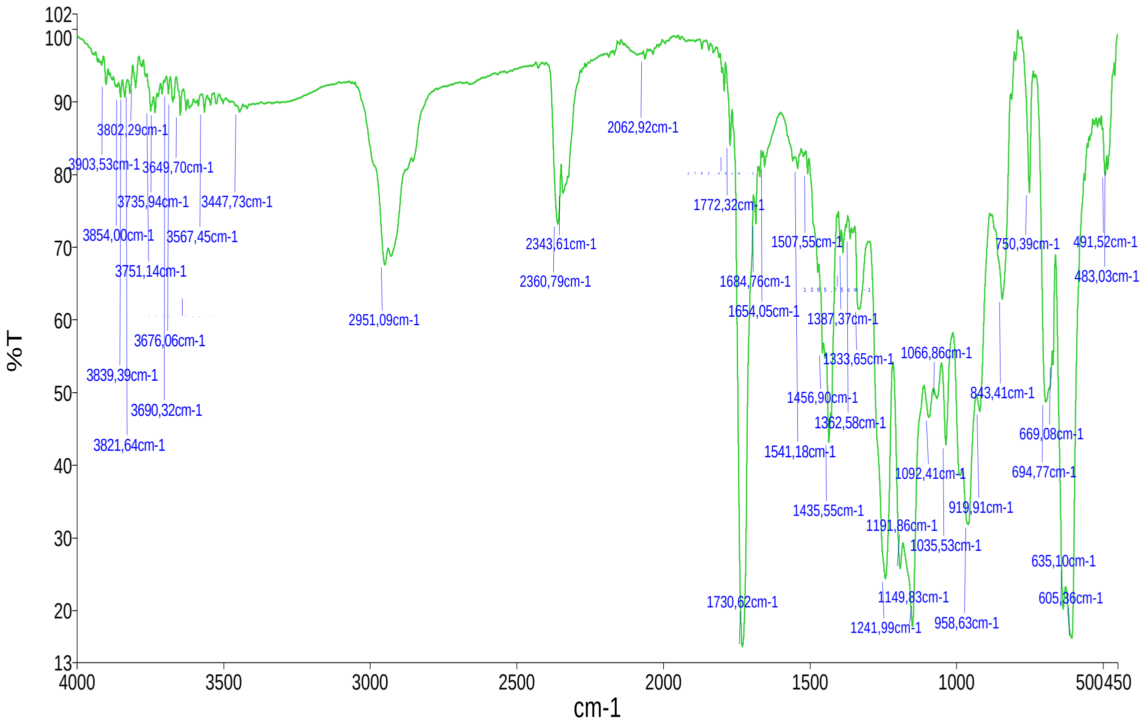

Figure 4.A. Fourier transform infrared spectra of PLA-DK sample

Tribological Tests

PLA alone and PLA-DK samples in the form of thick disks were tribologically tested using a CSM tribometer (Figure 5). The different results are recorded using a data logger with a frequency of 40 Hz.

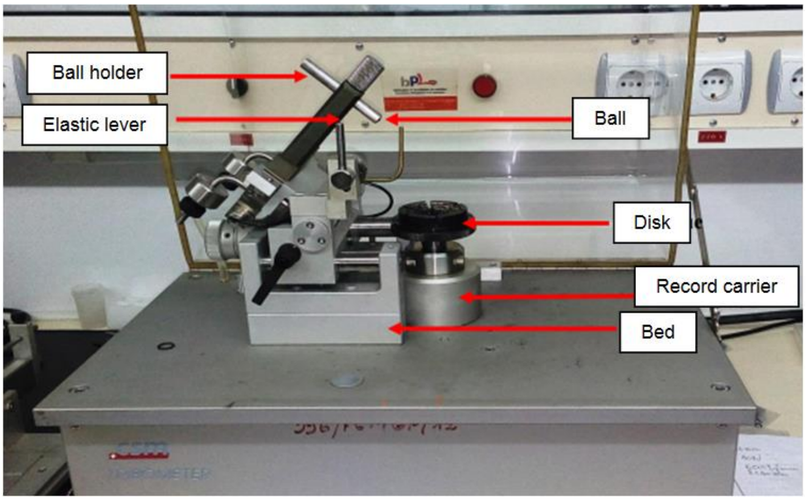

Figure 5. Overview of the tribometer and its instrumentation

A ball of stainless steel 6 mm in diameter rubs on the rotating sample with a distance of 200 m traveled with a speed of 10 cm / s, 20 cm/s and 30 cm/s.The tests are carried out at ambient temperature, under loads of 3, 5,7 and 10 N. They make it possible to determine the variation of the coefficient of friction of the material, and to estimate the rate of wear.Its principle is to apply a vertical load on a stationary ball in contact with the horizontal surface of the sample placed on a rotating disk as shown in Figure 6.

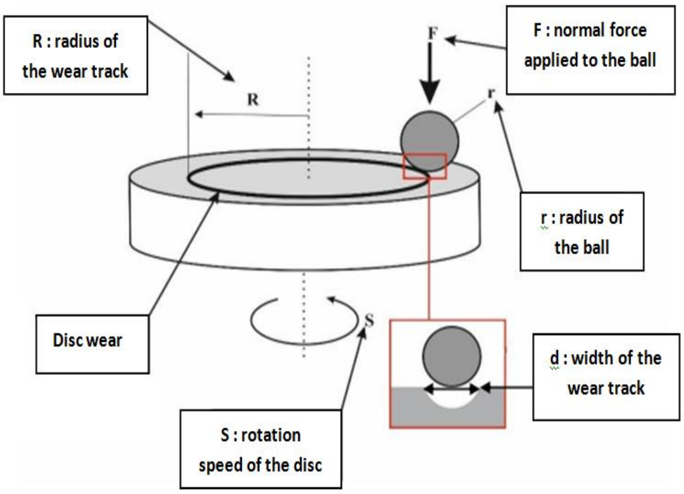

Figure 6. Schematic diagram of the tribometer

Measurement of Friction Coefficient

The contact of two bodies during a rotary movement causes a friction force which opposes the sliding. The coefficient of friction μ is given as a ratio ofthe tangential force (F_t) on the normal force (F_n)

$$\mu = \frac{F_t}{F_n}$$

The tangential force causes a lateral displacement of the resilient arm that supports the ball rod.The elastic deformation of the arm is sensed by an inductive sensor, which allows to deduce the value of F_t.Since the normal force is known (the applied force), the coefficient of friction, μ, is calculated by the data acquisition and processing software. This value is recorded according to the number of revolutions.

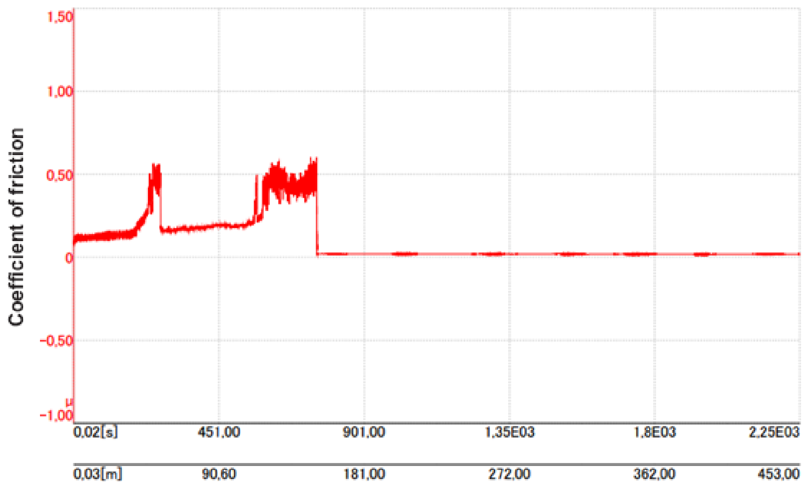

Figure 7. Evolution of the coefficient of friction of PLA alone

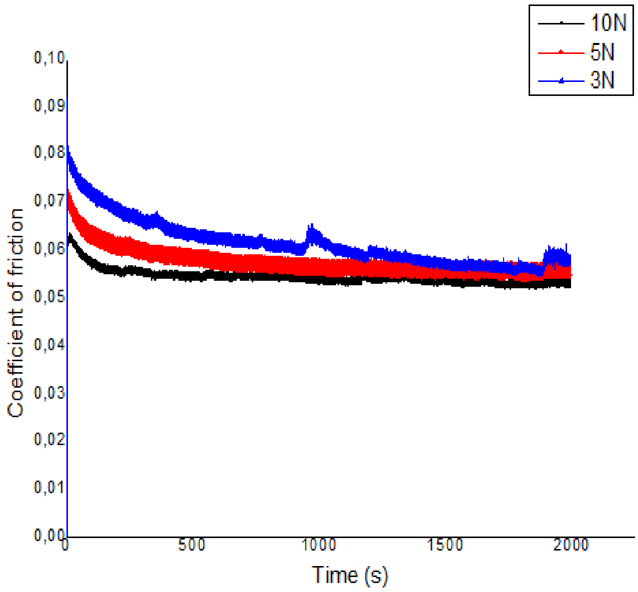

Figure 8. Evolution of the coefficient of friction of PLA –DK composite sample for a linear rotation speed of 10 cm/s

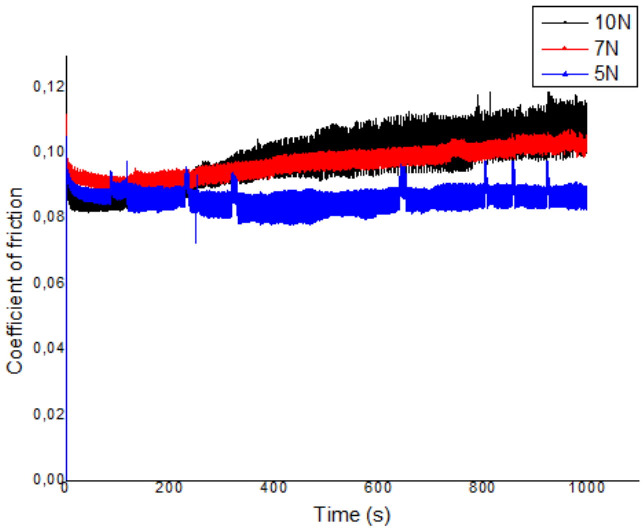

Figure 9. Evolution of the coefficient of friction of PLA –DK composite sample for a linear rotation speed of 20 cm/s

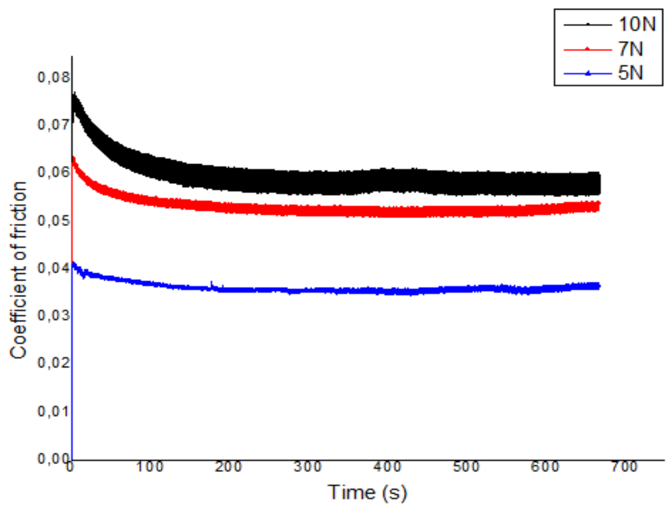

Figure 10. Evolution of the coefficient of friction of PLA –DK composite sample for a linear rotation speed of 30 cm/s

The friction coefficient was recorded periodically during the tribological test for PLA and PLA-DK composite sample. The experimental work was carried out for the composite on the tribometer shown in figure 5, under a normal load of 3,5,7 and 10N and a linear rotation speed of 10, 20 and 30cm/s. We observe a consequent decrease of the coefficient of friction for PLA-DK sample due to the addition of DK particles to the PLA matrix. The possible mechanism behind reduction in friction coefficient is the release of fatty substances contained in the micro-pores of DK particles. Mass loss measurements were also carried out, and the results are summurazied in the table 1,2 and 3.

Table 1. Mass loss measurementsfor a linear rotation speed of 10cm/s

Speed (cm/s)	Load (N)	Mass (g)	M_0 (g)
	3	9.4535	
10	5	9.4534	9.4536
	10	9.4528	

Table2. Mass loss measurementsfor a linear rotation speed of 20cm/s

Speed (cm/s)	Load (N)	Mass (g)	M_0 (g)
	5	9.4692	
20	7	9.4685	9.4697
	10	9.4665	

Table 3. Mass loss measurements for a linear rotation speed of 30cm/s

Speed (cm/s)	Load (N)	Mass (g)	M_0 (g)
	5	9.2413	
30	7	9.2409	9.2417
	10	9.2402	

Figure 11. Overview of the helium pycnometer and its instrumentation

Density Measurements

After carrying analyzes using helium pycnometer for the sample PLA –DK composite and DK alone we obtained density values 1.3317 g/cm^3 and1.4405 g/cm^3 respectively.

Conclusion

A fully biodegradable composite material has been developed from PLA and OK particles using hot-compaction process. SEM observations of this material showed continuous interfaces and particles well embedded in the matrix with a significantly different contrast from a phase contrast. DSC analyses show significant changes in transformation points as well as in the energies characterizing them, indicating the presence of new chemical compounds different from those present in the PLA and in the OK particles alone. The FTIR spectrum of the composite (compared to those obtained for the starting compounds separately) shows some differences. These notably include characteristic peaks of various phenolic compounds and certain ketones, which may be attributed to the formation of new chemical bonds at the PLA-DK interfaces which is consistent with the formation of new interfaces, during hot compaction, consisting of phases formed by the reaction between PLA and DK macromolecules. Tribological tests show that this biodegradable material exhibits sufficiently satisfactory characteristics given the nature of the starting constituents, namely PLA and DK. The interesting values of the coefficients of friction and the low mass losses indicate good tribological performance.

Scientific Ethics Declaration

The authors declare that the scientific ethical and legal responsibility of this article published in EPSTEM Journal belongs to the authors.

Acknowledgements or Notes

* This article was presented as an oral presentation at the International Conference on Technology, Engineering and Science (www.icontes.net) held in Antalya/Turkey on November 14-17, 2024.

References

Al-Mosawi, A. I., Abdulsada, S. A., & Hashim, A. A. (2018). Sustainable procedure for using waste of date seeds as a reinforcement material for polymeric composites. *Open Access Library Journal*, *5*(3), 1-9.

Benarab, A., Blázquez-Blázquez, E., Krache, R., & Benavente R., (2021). Composites of a polypropylene random copolymer and date stone flour. crystalline details and mechanical response. *Polymers, 13*(17), 2957.

Chandra, R., & Rustgi ,R. (1998). Biodegradablepolymers. *Progress in Polymer Science*, *23*(7), 1273-1335.

Dicker, M. P., Duckworth, P. F., Baker, A. B., Francois, G., Hazzard, M. K., & Weaver, P. M. (2014). Green composites: A review of material attributes and complementary applications. *Composites Part A: Applied Science and Manufacturing*, *56*, 280-289.

El-Tayeb, N. S. M., Yousif, B. F., & Yap, T. C. (2006). Tribological studies of polyester reinforced with CSM 450-R-glass fiber sliding against smooth stainless steel counterface. *Wear*, *261*(3-4), 443-452.

Fikry, M., Yusof, Y. A., Al-Awaadh, A. M., Rahman, R. A., Chin, N. L., Mousa, E., & Chang, L. S. (2019). Effect of the roasting conditions on the physicochemical, quality and sensory attributes of coffee-like powder and brew from defatted palm date seeds. *Foods*, *8*(2), 61.

Kalia, S. (2016). *Biodegradable and green composite.* John Wiley and Sons.

Kasuga, T., Ota, Y., Nogami, M., & Abe, Y. (2000). Preparation and mechanical properties of polylactic acid composites containing hydroxyapatite fibers. *Biomaterials, 22*(1), 19-23.

Khali, M., Boussena, Z., & Boutekrabt, L. (2015). Effet de l'incorporation de noyaux de dattes sur les caractéristiques technologiques et fonctionnelles de la farine de blé tendre . *Nature & Technology*, *12,* 15.

Koutsomitopoulou, A. F., Bénézet, J. C., Bergeret, A., & Papanicolaou, G. C. (2014). Preparation and characterization of olive pit powder as a filler to PLA-matrix bio-composites. *Powder Technology, 255,* 10-16.

Kumar Bajpai, P., Singh I., & Madaan J. (2013). Tribological behavior of natural fiberre in forced PLA composites. *Wear*, *297*,829-840.

La Mantia, F. P., & Morreale M. (2011). Green composites. A brief review, compos. *Part A Appl. Sci. Manuf. 42*, 579–588.

Mittal, V., Luckachan, G. E., Chernev, B., & Matsko, N. B. (2015). Bio-polyester–date seed powder composites: Morphology and component migration. *Polymer Engineering & Science*, *55*(4), 877-888.

Nagarjun, J., Kanchana, J., RajeshKumar, G., Manimaran, S., & Krishnaprakash, M. (2022). Enhancement of mechanical behavior of PLA matrix using tamarind and date seed micro fillers. *Journal of Natural Fibers*, *19*(12), 4662-4674.

Nurul-Fazita, M. R., Jayaraman, K., Bhattacharyya, D., Mohamad Haafiz, M. K., Saurabh, C. K., Hussin, M. H., & Hps, A. K. (2016). Green composites made of bamboo fabric and poly (lactic) acid for packaging applications—A review. *Materials*, *9*(6), 435.

Oksman, K., Skrifvars, M., & Selin, J. F. (2003). Natural fibres as reinforcement in polylactic acid (PLA) composites. *Composites Science and Technology*, *63*(9), 1317-1324.

Orue, A., Corcuera, M. A., Peña, C., Eceiza, A., & Arbelaiz, A. (2016). Bionanocomposites based on thermoplastic starch and cellulose nanofibers. *Journal of Thermoplastic Composite Materials*, *29*(6), 817-832.

Rahmoune, M. (2017). *Etude des propriétés physico-chimiques et thermomécaniques d'un nouveau matériau composite à base de fibres végétales et de déchets de PVC*. Doctoral dissertation.

Samouh, Z., Molnár, K., Hajba, S., Boussu, F., Cherkaoui, O., & El Moznine, R. (2021). Elaboration and characterization of biocomposite based on polylactic acid and Moroccan sisal fiber as reinforcement. *Polymer Composites*, *42*(8), 3812-3826.

Touati, Z., Hoyos-Martinez, P. L, &. Belhaneche-Bensemra, N. (2021). Influence of different diss fiber treatments over the properties of poly propylene/recycled and regenerated low density polyethylene based biocomposites. *Journal of Polymers and the Environment, 29*(1), 291-303.

Tsuji, H. (2016). Poly (lactic acid) stereocomplexes: A decade of progress. *Advanced Drug Delivery Reviews*, *107*, 97-135.

Wang, Y., Weng, Y., & Wang, L. (2014). Characterization of interfacial compatibility of polylactic acid and bamboo flour (PLA-BF) in biocomposites. *Polymer Testing*, *36*, 119-125.

Wu, Y., Gao, X., Wu, J., Zhou, T., Nguyen, T. T., & Wang, Y.(2023). Biodegradable polylactic acid and its composites. Characteristics, processing, and sustainable applications in sports. *Polymers*, *15*(14), 3096.

Author Information

Abdelouahab Ait Kaci
LEMM Laboratory, Mouloud Mammeri University, Tizi-Ouzou,15000, Algeria
Contact e-mail. *wahab_ait@outlook.fr*

Manel Hannachi
LEMM Laboratory, Mouloud Mammeri University, Tizi-Ouzou,15000, Algeria

Mustapha Nechiche
Mechanical Engineering Department, Mouloud Mammeri University, Tizi-Ouzou,15000, Algeria

To cite this article.

Ait-Kaci, A .Hannachi, M. & Nechiche, M..(2024). Development and characterization of a biodegradable composite based on PLA matrix and date kernels powder**.** *The Eurasia Proceedings of Science, Technology,Engineering & Mathematics (EPSTEM), 32*, 417-425.

The Eurasia Proceedings of Science, Technology, Engineering & Mathematics (EPSTEM)
ISSN: 2602-3199

The Eurasia Proceedings of Science, Technology, Engineering & Mathematics (EPSTEM), 2024

Volume 32, Pages 426-432

IConTES 2024: International Conference on Technology, Engineering and Science

Numerical Study of Tungsten Cathode Characteristics During TIG Welding

Sayah Merazi
Research Centre in Industrial Technologies -CRTI

Leila Belgacem
Research Centre in Industrial Technologies -CRTI-

Samira Benharat
Research Centre in Industrial Technologies -CRTI-

Houria Kaddour
University of Science and Technology Houari Boumediene-USTHB-

Mounir Sakmeche
University of Adrar

Abstract: Tungsten Inert Gas (TIG) is widely utilized across various industries. The understanding of tungsten electrode behavior, key component in this process, is vital for optimizing processes and enhancing weld quality. The shape of the electrode tip, influenced by its operational characteristics, significantly impacts the behavior of the electric arc and, consequently, the quality of the welded assembly. This study aims to analyze the influence of current intensity on the thermal and electrical characteristics of the cathode tip during TIG welding, using numerical simulations conducted with Comsol software. The analyses are carried out by applying Direct Current (DC) welding on an aluminum alloy sheet. The results show a similar evolution in the operational characteristics of the electrode as its tip angle varies. In contrast, the current intensity affects only the temperature, which increases with a higher tip angle, while the current density depends solely on the geometry of the electrode tip. The appropriate selection of welding parameters is imperative to preserve the electrode shape and ensure an efficient welding process.

Keywords: Cathode, TIG welding, Operating characteristics, Current density

Introduction

Electric arc welding has long been a cornerstone of industrial processes, continuously evolving and advancing over the decades. Despite its widespread application and technological progress, a thorough understanding of the underlying mechanisms and the development of predictive simulation models remain vital. Such models are essential for improving process efficiency, optimizing outcomes, and minimizing the costs associated with experimental trials. In the specific context of Gas Tungsten Arc Welding (GTAW), also known as TIG welding, the properties and performance of refractory cathodes are critical to the welding process (Sun et al., 2017; Liao et al., 2018; Chen et al., 2017; Botticher & Botticher, 2000). These cathodes are instrumental in maintaining arc stability, regulating heat distribution, and influencing overall weld quality. However, the complex interplay between factory-controlled welding parameters and the operational characteristics of these cathodes hasnot been fully explored.

The advent of modern high-speed computing has made it possible to predict the properties of electric arcs in detail, based on the fundamental properties of materials, particularly for those using thermionically emitting cathodes. Nevertheless, most previous studies have relied on assumptions regarding cathode conditions, especially current density, as input parameters (Benilov et al., 2016; Baeva, 2017; Lowke et al., 1995; Uhrlandth et al., 2015; Askri & Minoo, 2008). The calculated maximum arc temperature varies depending on the initially assumed current density.

This study addresses this gap by using predictive numerical simulations to establish a direct correlation between welding parameters and the operational characteristics of the refractory cathode. By employing finite element analysis (FEA), this research aims to clarify the effect of the electrode tip shape and input current intensity on the evolution of current density and temperature distribution. A comprehensive understanding of these relationships is crucial for optimizing welding conditions, extending cathode lifespan, and ultimately enhancing the reliability and efficiency of GTAW operations in industrial environments. This paper presents the methodology employed for numerical simulations, outlines the expected contributions to the field, and discusses the implications for future research and industrial applications.

Physical Phenomena and Mathematical Formulation in TIG Welding

The arc plasma flow is modeled under an axi-symmetrical assumption at atmospheric pressure. The 2D geometry used in our model is illustrated in Figure 1. The cathode is considered to be made of pure tungsten with a diameter of 3.2 mm. The distance between the frontal tip of the cathode and the anode surface is 5 mm. Pure argon is used as the shielding gas.

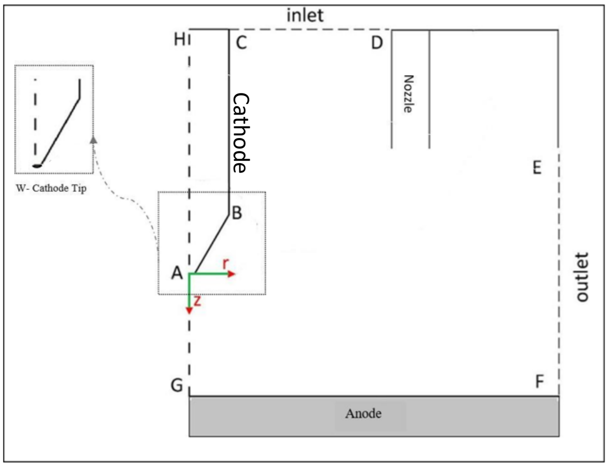

Figure 1. Geometric configuration of the computational area

In TIG welding, the temperature distribution and current density at the cathode are governed by several interrelated physical phenomena

1- Joule Heating: When current passes through the cathode, it generates heat due to the resistance of the material, described by Joule's law. It can be expressed as:

$$Q = J^2 \rho \qquad (1)$$

Where:

- J: Current density;
- ρ: Electrical resistivity of tungsten.

2- Thermal Conduction: Heat generated at the cathode is conducted away through the material. The temperature distribution is influenced by the thermal conductivity of the cathode.

For steady-state conditions, it is given by:

$$\rho c_p \frac{\partial T}{\partial t} = \nabla\cdot(k\nabla T) + Q \qquad (2)$$

Where:

- ρ: Density of the cathode material (kg/m³);
- c_p: Specific heat capacity (J/kg·K);
- T: Temperature (K);
- k: Thermal conductivity (W/m·K);
- Q: Volumetric heat generation rate (W/m³), which includes Joule heating and other heat sources.

For steady-state conditions ($\frac{\partial T}{\partial t} = 0$), the equation simplifies to:

$$\nabla \cdot (k\nabla T) + Q = 0 \tag{3}$$

Where:

- k: Thermal conductivity of tungsten;
- T: Temperature;
- Q: Volumetric heat generation term (including Joule heating and other heat sources).

3- Current density: The total current density at the surface of the cathode, is given by:

$$J_s = J_i + J_{bd} - J_{em} \tag{4}$$

Where:

- J_{em} denotes the current density resulting from thermionic emission,
- J_i signifies the current density caused by ion collisions,
- J_{bd} represents the current density due to the back-diffusion of plasma electrons. The detailed formulas for each component of the current density are provided in [10].

The dominant component of current density, J_{em}, is calculated using the Richardson–Schottky formula and is expressed as follows:

$$j_{em} = e\, A_j\, T_{ca}^2 \exp\left(-\frac{A - \Delta A}{k_B\ T_{ca}}\right) \tag{5}$$

Where:

- e: Electron;
- A_j: Richardson constan;
- T_{ca} : Cathode Temperature;
- A : Work function of the electrode material;
- ΔA: Schottky correction to work function;
- k_B : Boltzmann's constant.

To streamline the mathematical modeling, an axisymmetric coordinate system was employed, as shown in figure. Boundary conditions were established to simulate the current density and temperature distribution at the electrode tip interface during the TIG welding process.

Numerical Results

The figures below present the results for various cathode tip shapes and input currents. These include electrode tips with truncation angles of 30° and 60°, and input currents of 80 A and 110 A.

Temperature Distribution

In TIG welding, understanding temperature distribution is crucial for analyzing the thermal behavior of the tungsten cathode. The high welding temperatures lead to significant heat transfer through the cathode, impacting its lifespan and performance. Figures 2 to 5 show numerical results for two variables studied: tip angle and current intensity. The temperature distribution at the cathode tip is not uniform. The maximum temperature is typically found at the tip's extremity, and it decreases gradually from this point, with a more pronounced reduction along the vertical axis (the body) compared to the periphery. This variation is influenced by the thermal diffusion of tungsten.

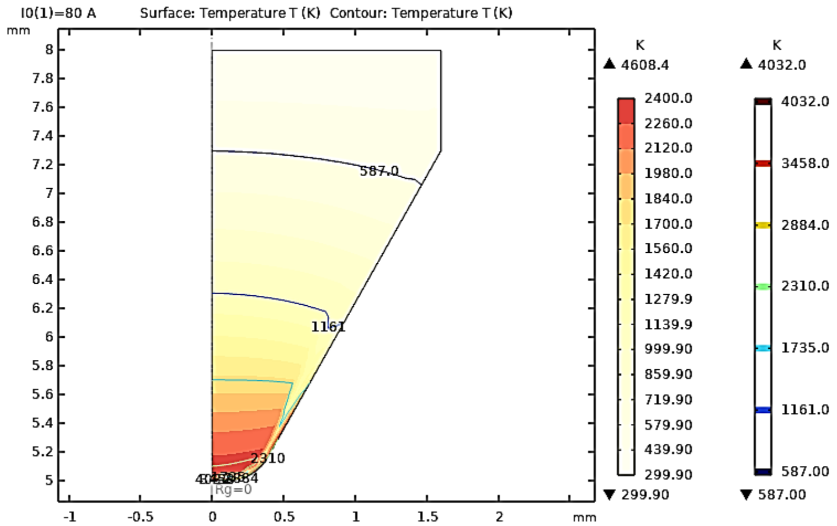

Figure 2. Temperature distribution at cathode tip

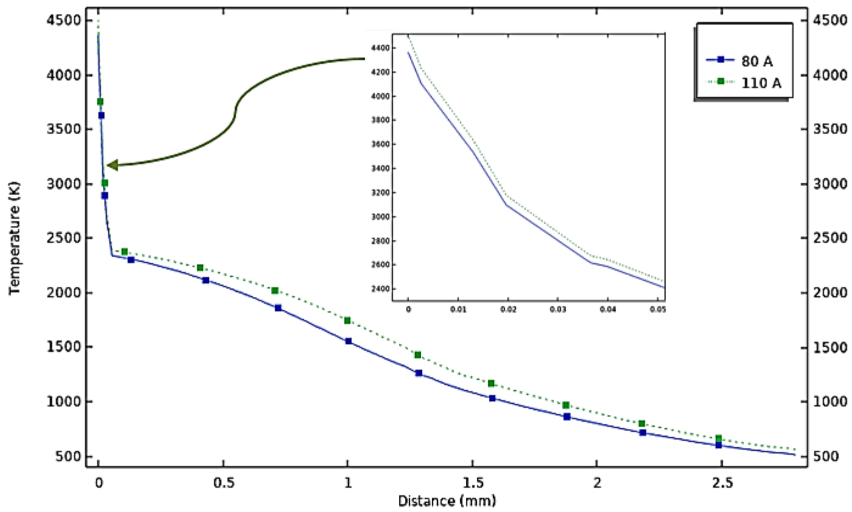

Figure 3. Temperature distribution along the electrode tip from its end for two different current intensities

Figure 4 presents a close-up view of the electrode tip, highlighting the specific areas where peak temperatures are reached with an applied current intensity of 80 A. This comparison examines two electrode angles, 30° and 60°, to emphasize the differences in thermal distribution associated with each angle. Figure 5 illustrates the maximum temperatures for the various cases studied, thereby enhancing our understanding of how electrode geometry impacts temperature behavior during the TIG welding process.

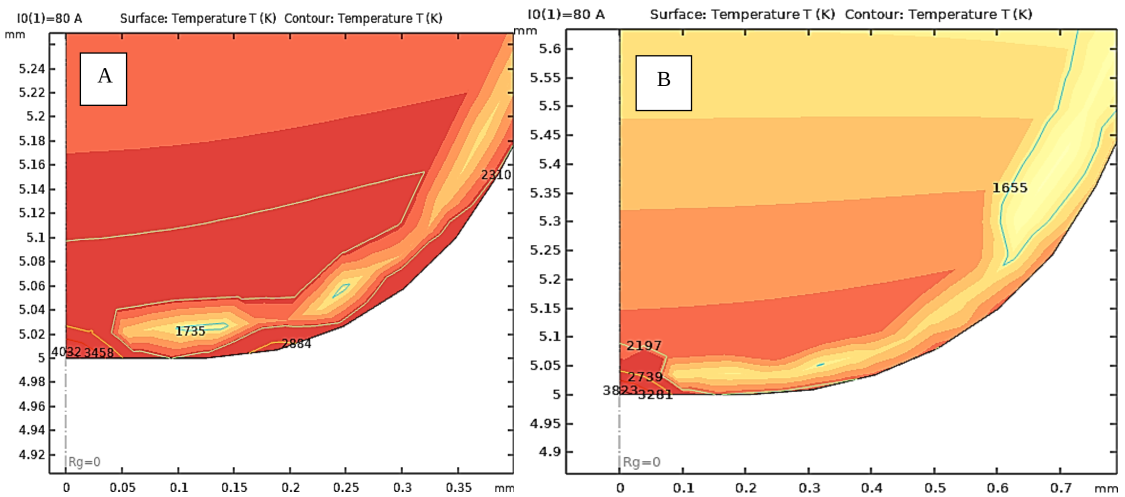

Figure 4. Zoom on the temperature distribution at the cathode tip under a current of 80 A: (A) 30°; (B) 60°

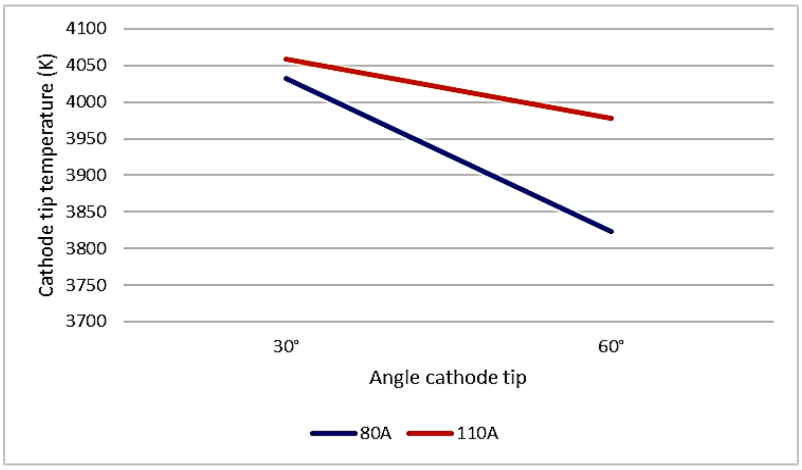

Figure 5. Effect of tip angle on cathode temperature for 80 A and 110 A currents

Current Density Distribution

The distribution of current density in the tungsten cathode is another essential aspect (see Figure 6), influencing the stability of the welding arc and the overall quality of the weld. Current density is affected by the electrode geometry and, to a lesser extent, by the applied current, as illustrated in figure 6 &figure 7.

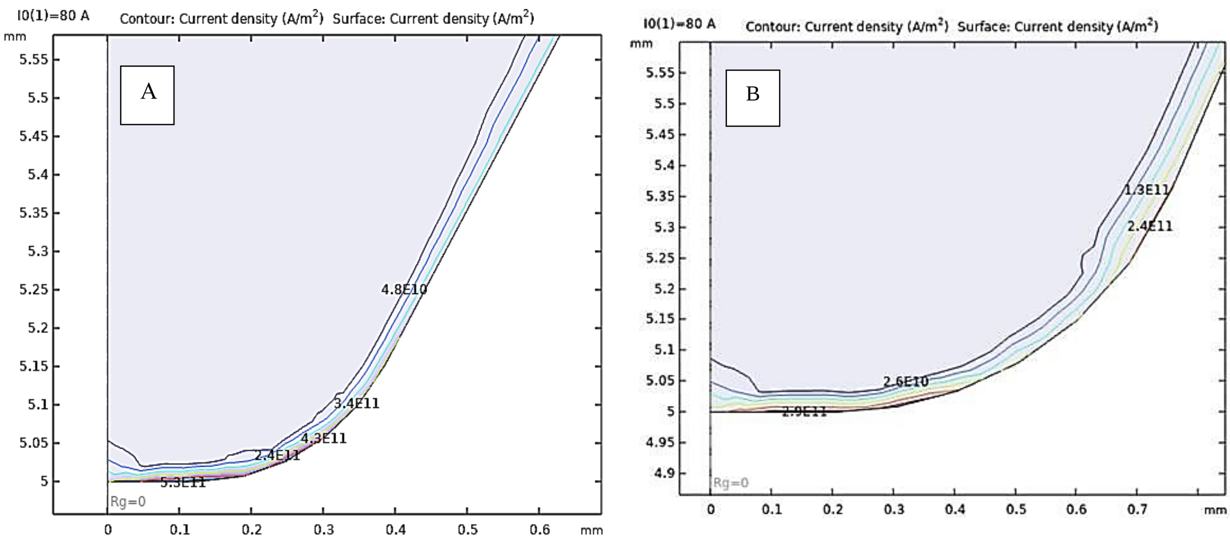

Figure 6. Current density distribution at the cathode tip under a current of 80 A: (A) 30°; (B) 60°

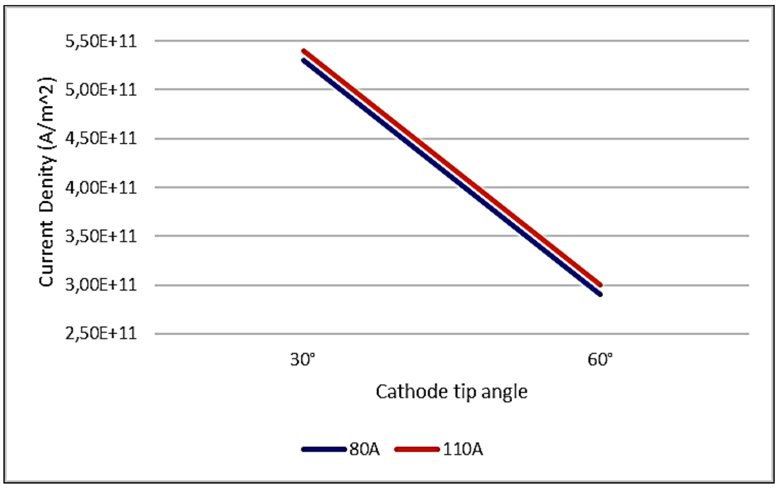

Figure 7. Evolution of current density as function of angle tip cathode and intensity

Discussion

Influence of Angle Tip of the Electrode

An electrode tip with a sharp angle means that the contact surface of the tip is smaller. When electrical current passes through this tip, the current density (current per unit area) becomes higher due to the small surface. The increased current density leads to a greater concentration of heat at the tip. This concentrated heat can cause a significant rise in the local temperature. Conversely, if the angle of the electrode tip is more obtuse, the contact surface is larger. The same amount of current will then be spread over a larger surface, thereby reducing the current density and, consequently, the concentration of heat. The local temperature at the electrode tip will therefore be lower compared to a sharper tip.

Influence of Current Intensity

When the current intensity increases, the total amount of heat generated by the Joule effect (thermal dissipation due to electrical resistance) also increases. In the case of a sharp tip, this increased heat is even more concentrated due to the small surface area, which can lead to extremely high temperatures, potentially reaching the melting point of the electrode material. While, a tip with a more obtuse angle, although also experiencing a temperature rise with the increase in current, spreads this heat over a larger surface area, thereby mitigating the local temperature increase.

Practical Consequences

A higher temperature at the tip can be desirable for operations requiring high precision or deep penetration, such as in certain welding processes where localized melting is necessary. However, this can also lead to faster electrode wear or uncontrolled melting risks. A wider angle is useful for operations that require uniform heat distribution, such as heating larger surfaces or preventing rapid electrode wear. This allows for better thermal management, reducing the risk of premature electrode degradation. From figure 8, it can be observed that the temperature is simultaneously affected by both the shape of the electrode tip and the current intensity, whereas the current density is governed solely by the shape of the tip.

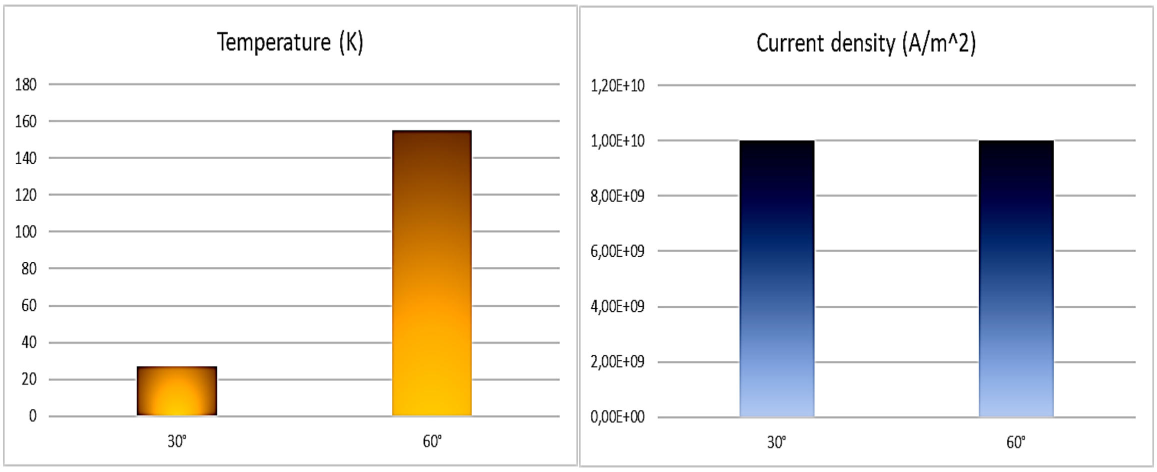

Figure 8. Differences in temperature and current density between measurements at 80 A and 110 A

Conclusion

The angle of the electrode tip plays a crucial role in how heat is distributed, as it directly influences the current density. A sharp angle increases the current density, concentrating the heat and raising the local temperature. In contrast, a blunt angle reduces the current density, spreading the heat over a larger surface and thereby lowering the local temperature. These effects become particularly pronounced at high current intensities, where effective thermal management is essential for the performance and durability of the ongoing process.

Scientific Ethics Declaration

The authors declare that the scientific ethical and legal responsibility of this article published in EPSTEM Journal belongs to the authors..

Acknowledgements or Notes

* This article was presented as a poster presentation at the International Conference on Technology, Engineering and Science (www.icontes.net) held in Antalya/Turkey on November 14-17, 2024.

References

Askari, S., & Minoo, H. (2008). Analytical expression for the electric potential in the plasma sheath near an arc-cathode. *Physics of Plasmas, 15*(4), 043503.

Baeva, M. (2017). Non-equilibrium modeling of tungsten-inert gas arcs. *Journal of Plasma Chemistry and Plasma Processing, 37*(2), 341-370.

Benilov, M.S., Almeida, N.A., Baeva, M., Cunha, M.D., Benilova, L.G., & Uhrlandt, D. (2016). Account of near-cathode sheath in numerical models of high-pressure arc discharges. *Journal of Physics D: Applied Physics, 49* (21), 215201.

Botticher, R., and Botticher, W. (2000). Numerical modelling of arc attachment to cathodes of high intensity discharge lamps. *Journal of Physics D: Applied Physics, 33*(4), 367-374.

Chen, T., Wang, C., Zhang, X.N., Zhang, H., & Xia, W.D. (2017). Thermal and electrical influences from bulk plasma in cathode heating modeling. *Plasma Sources Science and Technology, 26*(2), 025002.

Choquet, I. (2018). Gas tungsten arc models including the physics of the cathode layer: Remaining issues. *Weld World, 62,* 177–196.

Liao, M.R., Chen, T., & Lv. W.J. (2020). Heating of the cathode with a conical tip by atmospheric pressure arc plasma. *International Journal of Numerical Methods for Heat & Fluid Flow, 30*(5), 2379-2395.

Lowke, J.J., Kovitya1, P., & Schmidt, H.P. (1995). Theory of free-burning arc columns including the influence of the cathode. *Journal of Physics D Applied Physics, 25*(11), 1600.

Sun, Q., Wang, C., Chen, T., & Xia, W.D. (2017). Comparison of thermal and electric characteristic for free-burning arc using coupled and decoupled sheath models. *Journal of Physics D: Applied Physics, 50* (42), 1-19.

Uhrlandt, D., Baeva, M., Pipa, A., Kozakov, V. R. & Gott, G. (2015). Cathode fall voltage of TIG arcs from a non-equilibrium arc mode. *Weld World, 59*(1), 127–135.

Author Information

Sayah Merazi
Research Centre in Industrial Technologies -CRTI-
Echahid Mohammed ABASSI Cheraga, Algiers, Algeria

Leila Belgacem
Research Centre in Industrial Technologies -CRTI-
Echahid Mohammed ABASSI Cheraga, Algiers, Algeria
Contact e-mail: *belgacem.leila27@gmail.com*

Samira Benharat
Research Centre In Industrial Technologies -CRTI-
Echahid Mohammed ABASSI Cheraga, Algiers, Algeria

Houria Kaddour
Laboratory of Materials Sciences, Faculty of Chemistry, University of Science and Technology Houari Boumediene , Bab Ezzouar, Algiers, Algeria

Mounir Sakmeche
Laboratory of Catalytic Materials and Industrial Processes (LMPCI), Department of hydrocarbons and renewable energies, Faculty of Science and Technology. University of Adrar, National High way No. 06. Adrar 01000, Algeria

To cite this article:

Merazi, S, Belgacem. L, Benharat, S, Kaddour, H & Sakmeche, M. (2024). Numerical study of tungsten cathode characteristics during TIG welding. *The Eurasia Proceedings of Science, Technology, Engineering & Mathematics (EPSTEM), 32*, 426-432.

The Eurasia Proceedings of Science, Technology, Engineering & Mathematics (EPSTEM)
ISSN: 2602-3199

The Eurasia Proceedings of Science, Technology, Engineering & Mathematics (EPSTEM), 2024

Volume 32, Pages 433-438

IConTES 2024: International Conference on Technology, Engineering and Science

Autopilot and Operator Assistance Systems for Wheel Loaders

Mustafa Karahan
Hidromek

Abstract: In recent years, employing personnel for construction machinery operators has become challenging, requiring a lot of effort and experience. Meanwhile, personnel costs are increasing in Europe, Turkey, and other developed countries. The autopilot system facilitates the bucket loading and unloading process, among the most basic functions of wheel loader machines. It reduces the need for experienced operators and operator errors, increases the operational efficiency and productivity of the vehicle, and reduces fuel consumption and exhaust emissions to the environment. This study is about autopilot and operator assist systems and their benefits and advantages. It explains the working systematics, skid detection and prevention systems, mapping the earth, detecting people and objects, developments to increase vehicle efficiency and productivity, improving operator comfort level, etc. Even though some of the functions are carried out automatically, the vehicle still runs under the control and supervision of the operator in the cabin or a remote-control station.

Keywords: Autonomous construction machinery, Driving assistance for wheel loaders, Smart machines, Automated functions.

Introduction

Increasing fuel prices, global climate change, and the development of environmental awareness make the need for smart machines and systems operating at high efficiency indispensable. Similar and parallel to the automotive industry, intelligent and autonomous systems are developed and applied to machines in the construction machinery sector. Electronic control has been implemented for the systems and components of conventional construction machines, such as the powertrain, engine, hydraulic, steering, brake, etc. Meanwhile, due to the developments in GSM and Wi-Fi networks, large data transfers like video images have become possible. Therefore, automation and teleoperation of the machines have been applicable. Compared to autonomous passenger vehicles traveling on roads open to vehicle traffic and pedestrians, automation of construction machines can be easier and safer due to the restricted and defined working fields and less human density. Especially in teleoperated machines, operators are not in the cabin; thus, they cannot feel the machine and its operations. Therefore, machines can unnecessarily overload, productivity decreases, and tires wear out. If the main functions like loading and unloading run automatically, these kinds of failures and losses can be avoided. Operators' effort and fatigue are reduced drastically when the machine is controlled remotely. The exterior and interior view of Hidromek Opera, the remote-control station, is shown in Figure 1. & 2.

Overall System Layout

Conventional wheel loaders consist of the powertrain, work equipment, brake and steering systems, and machine control unit. Several devices, such as lidars, radars, thermal cameras, a touch screen, high-performance industrial computer and RTK GNSS antennas, have been added to the machine for these automated functions. The radars and lidars scan and detect the earth, gravel, obstacles, humans, and the environment. Thermal cameras detect the environment and distinguish between living things and objects. Even though there are omnidirectional cameras, thermal cameras significantly contribute to increasing safety levels for remote

- Selection and peer-review under responsibility of the Organizing Committee of the Conference

operations. The industrial computer processes the images from lidars, radars, and thermal cameras and matches them. Also, it sends commands to control and drive the machine automatically. The GNSS antennas detect the machine's position on the ground precisely. The touch screen shows the mapped earth, gravel, etc., provided by the industrial computer. The overall system layout is shown in Figure 3.

Figure 1. & Figure 2. The exterior and interior view of Hidromek opera, remote-control station.

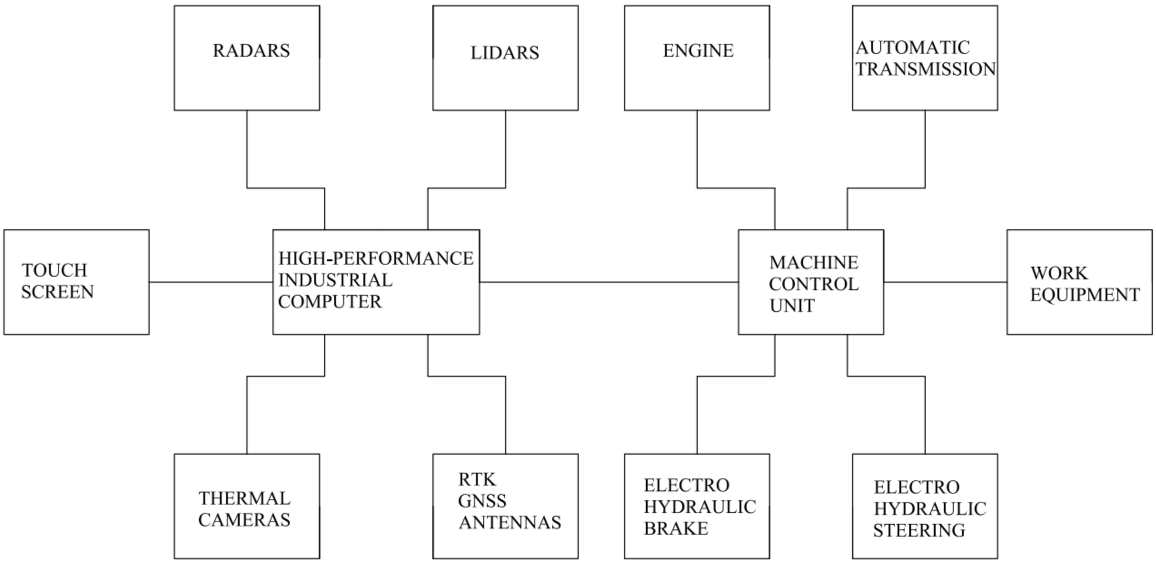

Figure 3. Overall system layout

Working Systematics

The working system consists of the preparation and implementation phases. At the preparation phase, the vehicle gets ready for the implementation phases such as loading and unloading the bucket. Firstly, the load and bucket types are determined by operators to obtain higher efficiency and productivity. Then, the driving assistance is activated. The preparation phase is shown in Figure 4. In the implementation phase, the machine loads the bucket automatically. The implementation phase is shown in Figure 5.

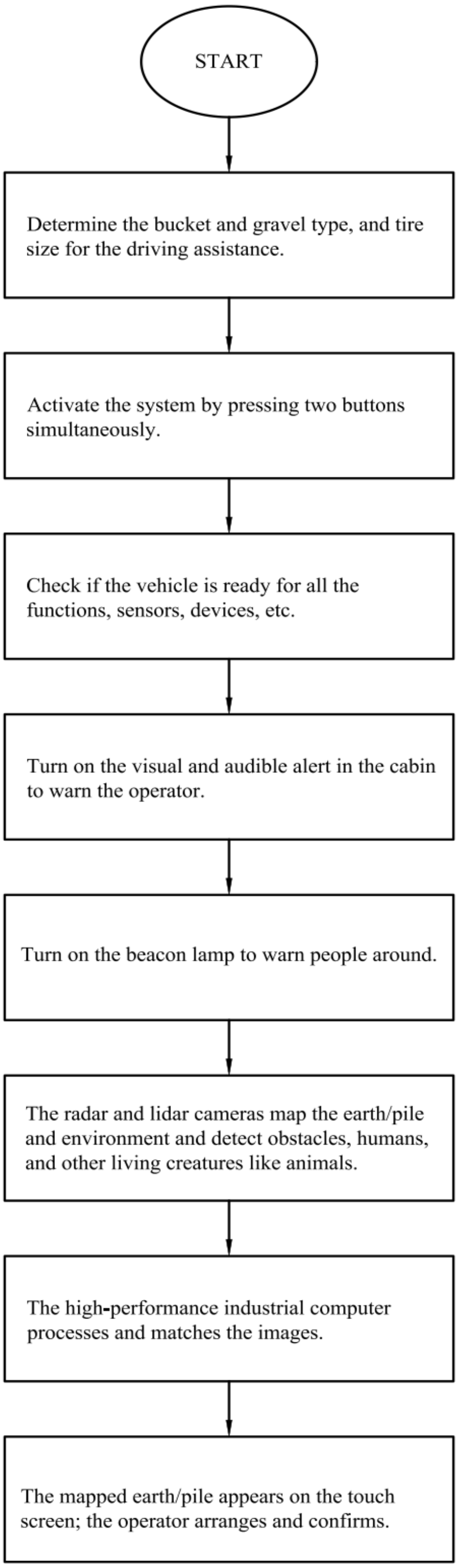

Figure 4. Preparation phase

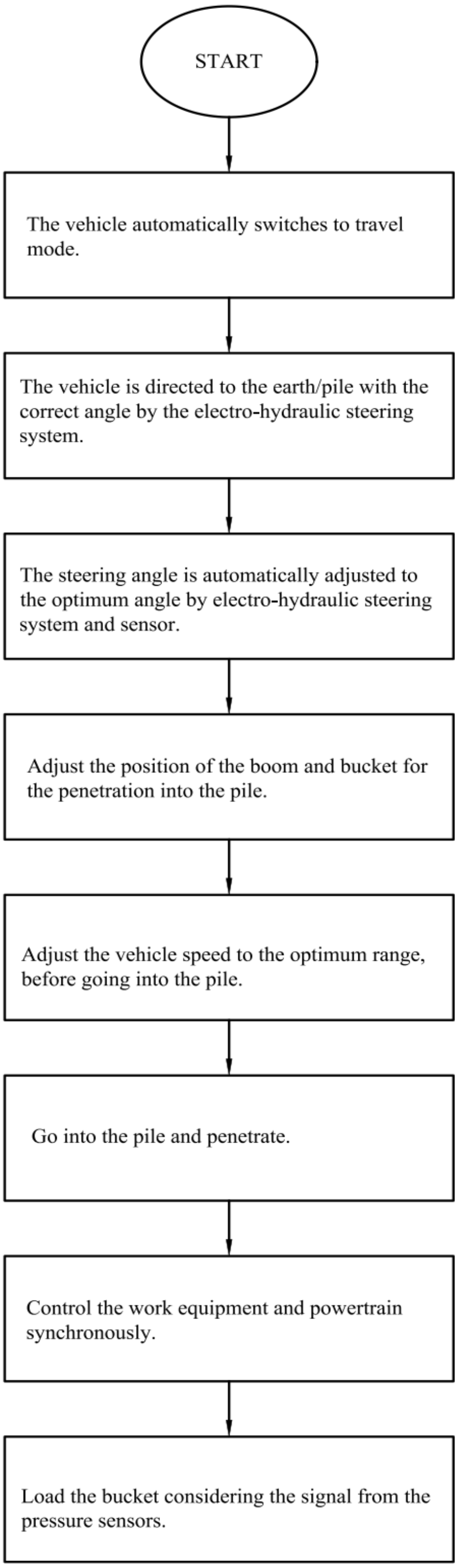

Figure 5. Implementation phase

Loading the buckets of wheel loaders is provided by the perfect harmony between the powertrain and work equipment. Both systems must work together synchronously. In order to load the bucket efficiently and fully, the vehicle must work without skidding and engine stall. When the machine skids, the energy of the engine converts into heat in the torque converter instead of the useful work. Skidding the wheels increases fuel consumption, damages the powertrain, heats up the transmission oil, and causes tire wear and operator fatigue due to the high vibrations. In this study, automatic loading and unloading systems, which is the state of the art, is explained.

The radars and GNSS RTK antennas determine the vehicle ground speed precisely. The lidar, GNSS antennas, radar, and thermal camera are shown in Figure 6. & 7. In closed areas, when the GNSS antennas cannot provide data, the speed data is ensured by the radars. Meanwhile, the wheel speed is determined by measuring the transmission output speed. Then, both data are compared to detect whether the wheels skid or not. If the system detects any wheels' skid, the engine speed and work equipment are controlled to prevent the skidding. Therefore, the bucket penetrates the excavation, pile, earth, etc. The skidding is not prevented by means of the differential lock or limited slip differential. It is carried out by running the powertrain and work equipment synchronously and simultaneously, which is provided by the system algorithms. The system controls the traction, bucket and boom cylinders together. The pressure sensors installed on the hydraulic lines of work equipment detect the load and send signals to submit status of the load percentage. When the loading is completed, the system warns with visual and audible alerts.

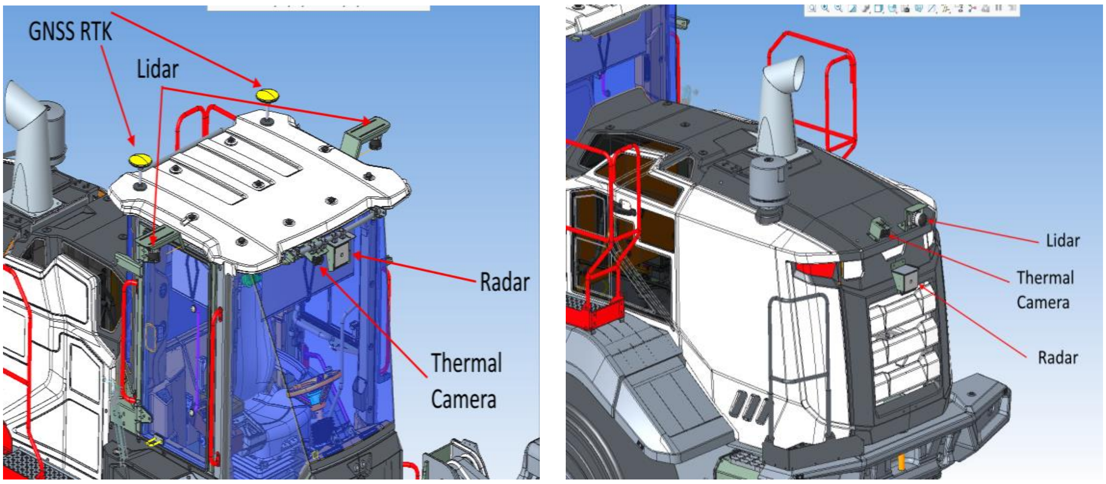

Figure 6. & Figure 7. GNSS RTK antennas, lidars, radars, and thermal cameras

The system algorithms are designed for the engine, torques converter and pumps to run in the efficient ranges by considering the machine's requirements. The engine and vehicle speed are controlled by automatically. Besides, the engine is driven at the stabile speed to increase the efficiency. Diesel engines have different efficiency characteristic in different speed range and load conditions. The fuel map of the engine is shown in Figure 8.

After loading the bucket, the bucket is positioned to the carry condition. The machine is driven to a truck or anyplace manually. When the boom raises and the bucket dumps, since the hydraulic cylinders reach the end of the stroke, the shock loads occur on the machine and cause fatigue on machine and as well as operators. The automatic bucket unloading system provides the boom raising in a controlled manner by angle sensors preventing from shock movements at end of the stroke. Meanwhile, the transmission clutch cut-off system activates automatically to provide more power to the work equipment and increase the efficiency of the operation. When the machine switched to the driving mode, it disactivates automatically as well. While dumping, the system shakes the bucket to make bucket fully unload without shocking the machine by controlling the hydraulic system automatically.

For dumping the bucket, how much the bucket is empty designates the efficiency of the operation. After dumping, the boom and bucket reach the carry position automatically. In the conventional machines, lowering the boom can cause shock loads and vibrations on the machine and operators, which can also cause damages on the machine and fatigue of the operator. In the automatic mode, the shock loads are prevented and the smooth movements are provided. In the meantime, as lowering, the gravity provides the sufficient force, therefore, the engine throttle is reduced to minimum level to increase the efficiency.

Mapping of Earth

4D radar and ultra-wide view high-resolution lidar cameras are used to map the earth, pile, excavation, etc. The images from the radar and lidar are matched and processed in the industrial computer to increase accuracy and precision. Lidar has higher resolution and can provide accurate, consistent results. However, it cannot measure long distances, and its performance reduces depending on the weather and ambient conditions, such as in rain or dusty environments. Radar can identify things in long-range, adverse weather and ambient conditions.

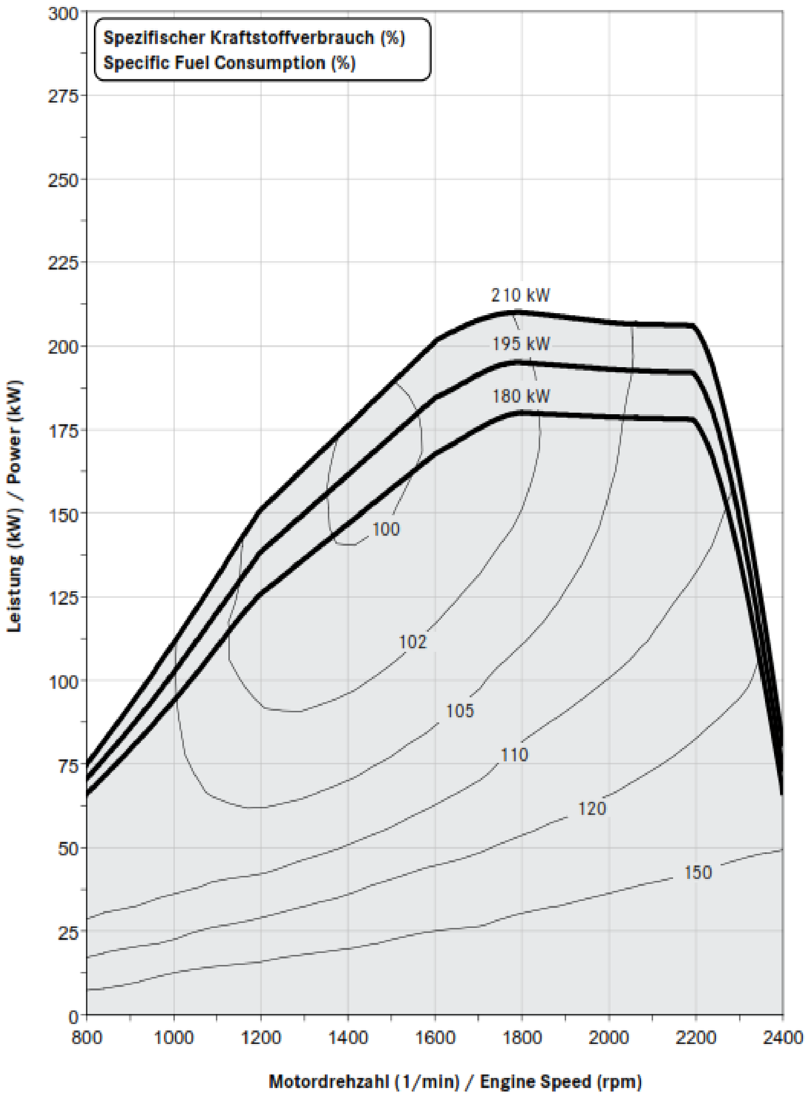

Figure 8. Fuel map of the engine

Conclusions and Recommendations

In this study, a commercially viable semi-autonomous system is explained where operator presence and control are still present. This study provides a valuable approach to next-generation fully autonomous construction machinery. Switching from conventional machines to semi-autonomous ones can be safer and more economical than switching to fully autonomous. However, we might see construction machines with artificial intelligence and machine learning capabilities in the near future. It is recommended to switch to automated machines gradually to avoid safety issues and the rise of the unemployment rate in the construction sector. One of the handicaps of fully autonomous construction machines is the high initial investment cost. Processing and matching the images necessitates high technology and deep know-how and, therefore, is quite expensive. Cloud-based machine learning can reduce overall costs and drastically speed up and improve AI learning. It can use the data from other machines with similar working fields and conditions. Thus, machines can gain experience faster and increase efficiency and productivity.

The operator's experience and feelings come to the fore in conventional machines controlled inside the cabin. In remote-control machines, since the operator's feelings cannot constitute or can stay at low levels, the operators' adaptation or synchronization is not at the desired level. The autopilot and driving assistance systems eliminate these kinds of deficiencies and not only raise the overall efficiency, productivity, and functional safety but also extend the lifespan of the machines and reduce operator fatigue, fuel consumption, and carbon emissions.

Scientific Ethics Declaration

The authors declare that the scientific ethical and legal responsibility of this article published in EPSTEM Journal belongs to the authors.

Acknowledgements or Notes

* This article was presented as an oral presentation at the International Conference on Technology, Engineering and Science (www.icontes.net) held in Antalya/Turkey on November 14-17, 2024.

References

Charroud, A., El Moutaouakil, K., Palade, V., Yahyaouy, A., Onyekpe, U., & Eyo, E. U. (2024). Localization and mapping for self-driving vehicles: A survey. *Machines*, *12*(2), 118.

Dubizzle. (n.d.).*Lıdar systems in self-driving cars*. Retrieved from https://www.dubizzle.com/blog/cars/lidar-autonomous-driving/

FlyGuys.(n.d.). *Advantages and disadvantages of Lidar technology*. Retrieved from https://flyguys.com/advantages-disadvantages-lidar-technology/

Jin S., Kang L., Peng Y., Song Z., Qian L., & Zhang L. (2023). Autonomous excavator system for construction Earth moving. *ICRA 2023 Future of Construction Workshop Papers*, 24-27.

Ran, B. (2024). Impact of AI large models and computing on CCAM. *ERF Conference.*

YellowScan.(2020, May 20). *Lidar vs radar*. Retrieved from https://www.yellowscan.com/knowledge/lidar-vs-radar/

Author Information

Mustafa Karahan
Head of Wheel Loader Engineering
Hidromek
Osmanlı Cad. No: 1, Sincan / Ankara /Turkiye
Contact e-mail:mustafa.karahan@hidromek.com.tr

To cite this article:

Karahan, M. (2024). Autopilot and operator assistance systems for wheel loaders. *The Eurasia Proceedings of Science, Technology, Engineering & Mathematics (EPSTEM),* 32, 433-438.

The Eurasia Proceedings of Science, Technology, Engineering & Mathematics (EPSTEM)
ISSN: 2602-3199

The Eurasia Proceedings of Science, Technology, Engineering & Mathematics (EPSTEM), 2024

Volume 32, Pages 439-448

IConTES 2024: International Conference on Technology, Engineering and Science

Design and Numerical Investigation of Highly Photovoltaic Efficiency of Novel Non-Toxic Double Perovskite Solar Cell with Igzo as Electron Transport Layer

Abdelkrim El-Hasnaine Merad
Abou Bekr Belkaid University of Tlemcen

Souheyla Mamoun
Abou Bekr Belkaid University of Tlemcen

Abd-El-Illah Abbaci
Abou Bekr Belkaid University of Tlemcen

Abstract: The development of lead-free perovskite solar cells, is indeed a promising solution to the toxicity issue associated with traditional lead-based perovskites. These lead-free alternatives aim to maintain high efficiency while being environmentally friendly. In this context, we aim to propose a novel lead-free double perovskite solar cell with IGZO as electron transport layer (ETL). It has been demonstrated recently that this inorganic halide double perovskite with the structure A_2BX_6 is more stable compared to the lead-free perovskite with the structure ABX_3. We design our solar cell with the planar architecture where the perovskite layer is sandwiched between an electron transport layer IGZO and a hole transport layer $MoSe_2$. This contributes to efficient charge separation and collection, which is crucial for the performance of the solar cell. Our work focuses on the optimization and analysis of various key parameters governing perovskite solar cell performance, including the thicknesses of all layers, the acceptors N_A and defects N_t charge carrier densities, parasitic series resistance R_S and the working temperature T. The current-voltage characteristics (J-V), and quantum efficiency (QE) are analyzed via these key parameters. Our final optimal results, gives an impressive Power Conversion Efficiency (PCE) up to 25%. These findings represent a significant advancement and proposes the perovskite as a potential photoactive material in the renewable energy technology.

Keywords: Lead-free halide double perovskite solar cell, SCAPS simulation, IGZO, Acceptors density N_A, Defect density N_t, Series resistance R_S, Working temperature T.

Introduction

Recently, researchers have turned their attention to investigating the ABX_3 perovskite alternative structure known as inorganic halide double perovskites (IHDP) A_2BX_6 (A= K^+, Rb^+, Cs^+, B= Sn^{2+}, Pd^{2+}, Pt^{2+}, X= Cl^-, Br^-, I^-) (Tranka et al., 2018; Bartel et al., 2019). These IHDP structures are being studied for their strong covalency within the $[BX_6]^{2-}$ cluster, offering a potential solution to the stability challenges faced by conventional Pb-based perovskites (Nair et al., 2022). In fact, in addition to the toxicity problem, $APbX_3$ perovskites suffers from long-term instability caused by degradation after exposure to light, oxygen, moisture or heat, attributed to polymorphic transformation, hydration or decomposition. Both of these problems hamper their development and commercialization. (Ji et al., 2023).

Recently, Schwartz et al. (2020) synthesized a promising solar cell based on the IHDP Cs_2PtI_6 with excellent stability and oxidation resistance, high absorption coefficient ($4 \times 10^5\ cm^{-1}$ superior than $MAPbI_3$'one $10^5\ cm^{-1}$) and long carrier life time (superior than $2\ \mu s$ as long as that of $MAPbI_3$). The power conversion efficiency (PCE) of their adopted structure FTO/CdS/Cs_2PtI_6 ($10-15\ \mu m$)/ElectroDAG440B/Cu is about $10.7\ \%$ and can enhance to $13.88\ \%$ when ethylene diamine EDA (a chemical treatment) is added. This result makes Cs_2PtI_6 one of the most promising photovoltaic (PV) materials for such a first attempt. Furthermore, Yang et al. (2020) have confirmed the stability (experimentally and using ab initio calculation) of their synthesized IHDP Cs_2PtI_6 even when exposed to extreme condition such high humidity, high temperature and UV-light irradiation.

Using the one-dimensional solar cell simulator capacitance software SCAPS-1D (Burgelman et al., 2021). Cs_2PtI_6 was also theoretically studied by Shamna et al. (2022), AbdElaziz et al. (2022), Amjad et al. (2023). They showed that the PCE of their optimized structure FTO/ZnO/Cs_2PtI_6/MoO_3/C, FTO/WS_2/Cs_2PtI_6($0.4\ \mu m$)/Cu_2O/C and FTO/SnO_2/Cs_2PtI_6($0.4\ \mu m$)/MoO_3/C can reach $20.45\ \%$, $22.4\ \%$ and $23.52\ \%$ respectively.

In the ab initio papers of Cai et al. (2017) and Zhao et al. (2021). The co-workers have investigated the structural, electronic and optical properties of Cs_2PtI_6 and Rb_2PtI_6. Their results affirmed that Rb_2PtI_6 is stable (formation enthalpy equal to $-0.92\ eV/atom$), has suitable indirect band gap ($1.3\ eV$ **(**Cai et al., 2017). And $1.15\ eV$ (Zhao et al., 2021). In the cubic structure) and high absorption in the photon energy range from 0 to $12\ eV$. Then, as Cs_2PtI_6, Rb_2PtI_6 can be highly desirable candidate, as lead-free double perovskite for photovoltaic (PV) applications.

In this context, we aim to investigate numerically, the photovoltaic (PV) performance of a new solar cell (SC) based on the IHDP Rb_2PtI_6. At the first step of our study, we try to constitute the experimental solar cell of Schwartz et al. (2020) based on Cs_2PtI_6 . We adopted their same architecture FTO/CdS/Cs_2PtI_6/Spiro-OMeTAD/C in the same conditions (at $T = 300K$, $f = 1\ MHz$, $R_s = 14\ \Omega\ cm^2$). Since we are arrived to reproduce their experimental PV performance, we are encouraged to study this SC replacing the cadmium sulfite CdS by another nontoxic ETL like Indium Gallium Zinc Oxyde IGZO and replacing the Spiro-OMeTAD by another non degradable inorganic ETL like molybdenum diselenide $MoSe_2$.

In order to enhance the power conversion efficiency of our novel Rb_2PtI_6 based solar cell (FTO/IGZO /Rb_2PtI_6/$MoSe_2$/C), we studied the effect of the absorber thickness, of its acceptors density N_A, of its defect density N_t, of series resistance (Rs), and of working Temperature T.

Devices Modeling and Simulation Parameters

We used SCAPS-1D code (Burgelman et al., 2021). Which is based theoretically on the fundamental equations: Poisson's equation (1) and continuity equation for holes and electrons equation (2):

$$\frac{d^2\psi}{dx^2} = \frac{e}{\varepsilon_0 \varepsilon_r}\left[p(x) - n(x) + N_D - N_A + \rho_p - \rho_n\right] \tag{1}$$

Where ψ is electrostatic potential, n and p are electron and hole concentrations, ε_0 is vacuum and ε_r is relative permittivity, N_D and N_A are donor and acceptor doping density, ρ_n, ρ_p are electrons and holes distribution,

$$\frac{dJ_p}{dx} = \frac{dJ_n}{dx} = G - R \tag{2}$$

Where G is generation rate and R is recombination rate, J_p and J_n are holes and electron current densities.

Carrier transport occurs according to the following drift and diffusion equations:

$$J_n = \mu_n n \frac{d\varphi}{dx} + D_n \frac{dn}{dx} \tag{3}$$

$$J_p = \mu_p p \frac{d\varphi}{dx} + D_p \frac{dp}{dx} \tag{4}$$

The initial device architecture model FTO/ETL/A_2PtI_6/HTL/C is depicted in (Figure1.a). The cadmium sulfite CdS is used as an electron transport layer (ETL). The absorber or active layer is formed by the vacancy ordered double perovskite A_2PtI_6 material (where A=Cs/Rb). The 2,2'7,7'-tetrakis (N, N-di-p-methoxyphenyl-amin)-9,9'-spirobifluorene (Spiro-OMeTAD) is used as a hole transport layer (HTL). The Fluorine-doped tin oxide FTO is use in the front side and the carbon C is used as contact in the back side.

Our studied devices are a n-i-p type, for that, the n part is the ETL, the i part is the absorber A_2PtI_6 and the p part is the HTL. In order to make our model more realistic, we have considered the interface layers: interface 1 (ETL/A_2PtI_6) and interface 2 (A_2PtI_6/HTL), with a thickness of 5nm and keeping the same physical parameters as those of the perovskite.

Figure 1(c) illustrates the band gap alignment of HTL, ETL, and A_2PtI_6 with A=Cs/Rb, as well as the back and front device contacts of the initial and the alternative novel devices. The lowest unoccupied molecular orbital (LUMO) of IGZO (ETL) is in excellent alignment with the conduction band of Rb_2PtI_6. Likewise, the highest occupied molecular orbital (HOMO) of $MoSe_2$ (HTL) is well-aligned with the valence band level of an absorbing material.

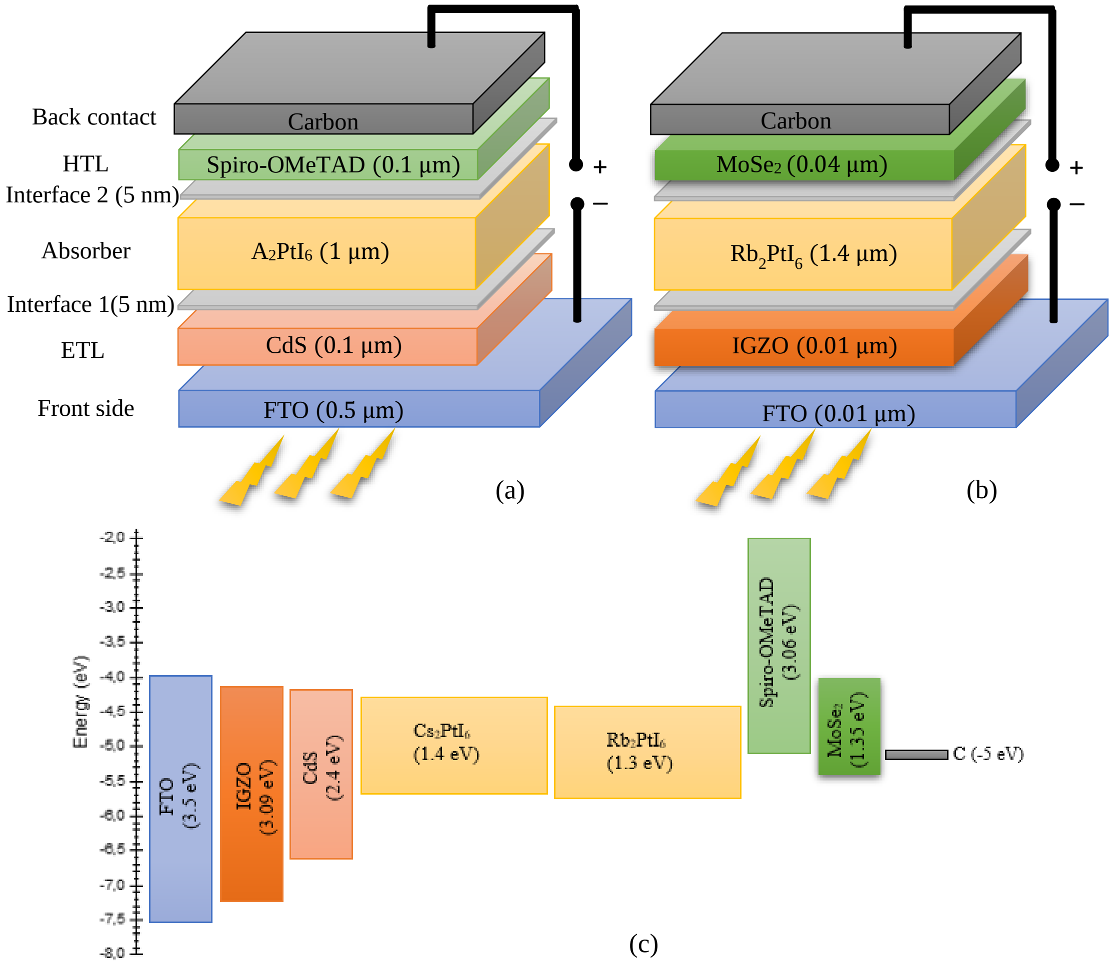

Figure 1. Architecture of (a) initial devices and (b) optimized device based on the platinum iodide perovskite where A=Cs/Rb. (c) Energy level diagram

To assess how the performance of PSCs is affected by operating temperature, we conducted simulations at approximately 300 K in an environment with an incoming power density of 100 mW/cm^2 and a frequency of 1 MHz. These simulations were conducted under the AM 1.5 G solar spectrum. We report in (Table 1**)** the input parameters for all HTL, ETL, A_2PtI_6 and FTO adopted for this study. Some of these parameters are derived from the literature and the others are obtained with our calculations since some parameters are not yet available in the literature for Rb_2PtI_6. For that, we have opted to the theoretical determination of such parameters based on the following equations:

$$N_t = \frac{1}{\sigma \tau V_{th}} \tag{5}$$

$$\mu_{n/p} = \frac{D_{n/p} q}{KT} \tag{6}$$

$$D_{n/p} = \frac{{l_{n/p}}^2}{\tau} \tag{7}$$

Where N_t is the defect density, μ is the electron and hole mobility, D is the diffusion coefficient, K is Boltzmann's constant, τ is the charge carrier lifetime, $l_{n/p}$ is the electron/hole diffusion length; σ is the capture cross-section of electron/hole and V_{th} is the thermal velocity of electron/hole. Also, the absorber layer effective conduction band density of states, N_c and effective valence band density of states, N_v are determined using the two following expressions:

$$\mathrm{N_c} = 2\left(\frac{2\pi \mathrm{m_n^*KT}}{\mathrm{h}^2}\right)^{\frac{3}{2}} \quad \text{and} \quad N_v = 2\left(\frac{2\pi m_p^* KT}{h^2}\right)^{\frac{3}{2}} \tag{8}$$

Where m_n^* and m_p^* are the effective masses of electrons and holes, respectively.

Table 1. The input parameters of the adopted devices collected from our calculation and available data

	HTL		Absorber		ETL		Front side
Input parameter	Spiro-OMeTAD	$MoSe_2$	Cs_2PtI_6	Rb_2PtI_6	CdS	IGZO	FTO
Band gap, E_g (eV)	3.06 [a]	1.35 [b]	1.4 [c]	1.3 [f]	2.4 [i]	3.05 [b]	3.5 [a]
Affinity, χ (eV)	2.05 [a]	4.05 [b]	4.44 [d]	4.43 [d]	4.2 [i]	4.16 [b]	4 [a]
Relative Dielectric permittivity, ε_r	3 [a]	11.9 [b]	4.8 [e]	4.34 [g]	10 [i]	10 [b]	9 [a]
CB effective density of states, N_c (cm^{-3})	2.8×10^{19} [a]	2.8×10^{19} [b]	9×10^{18} [d]	7.5×10^{18} [d]	2.2×10^{18} [i]	5×10^{18} [b]	9.2×10^{18} [a]
VB effective density of states, N_v (cm^{-3})	10^{19} [a]	2.65×10^{19} [b]	4×10^{19} [d]	3.5×10^{19} [d]	1.8×10^{19} [i]	5×10^{19} [b]	1.8×10^{19} [a]
Electron mobility, $\mu_n (cm^2V^{-1}s^{-1})$	10^{-4} [a]	1450 [b]	0.19 [d]	0.65 [h]	100 [i]	15 [b]	20 [a]
hole mobility, $\mu_p (cm^2V^{-1}s^{-1})$	2×10^{-4} [a]	50 [b]	62.6 [c]	3.25 [h]	25 [i]	0.1 [b]	10 [a]
Electron effective mass, m_n^*	-	-	0.51 [f]	0.45 [f]	-	-	-
hole effective mass, m_p^*	-	-	1.45 [f]	1.245 [f]	-	-	-
Density of n-type doping, N_D (cm^{-3})	0	0	0	0	10^{18} [i]	10^{18} [b]	10^{19} [a]
Density of p-type doping, $N_A (cm^{-3})$	10^{18} [a]	4×10^{18} [b]	10^{15} [d]	10^{15} [d]	0	0	0
Density of defect, $N_t (cm^{-3})$	10^{14} [a]	10^{14} [b]	2.5×10^{12} [d]	3.5×10^{13} [d]	10^{19} [i]	10^{15} [b]	10^{15} [a]

[a] data from Jahantigh et al. (2019)
[b] data from Teyou Ngoupo et al. (2022)
[c] experimental data from Schwartz et al. (2020)
[d] our calculation
[e] experimental data from Yang et al. (2020)
[f] ab initio data from Cai et al. (2017)
[g] ab initio data from Zhao et al. (2021)
[h] from Yang et al. (2019)
[i] from Nykyry et al. (2019)

Results and Discussion

Verification of the Devices Model

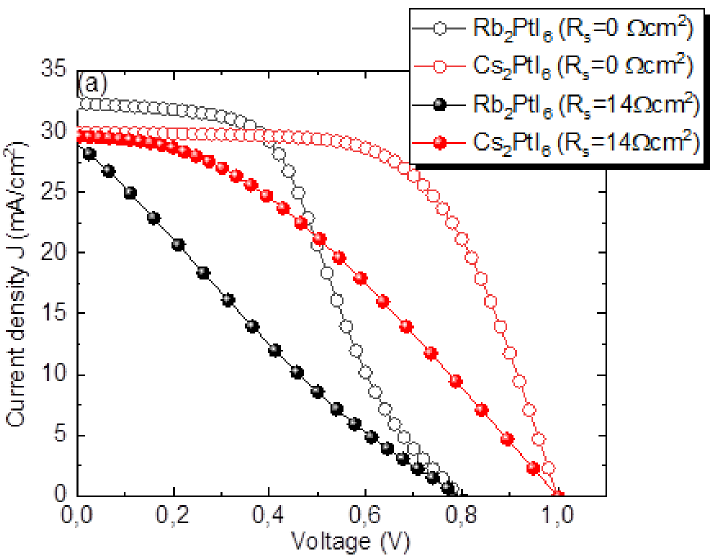

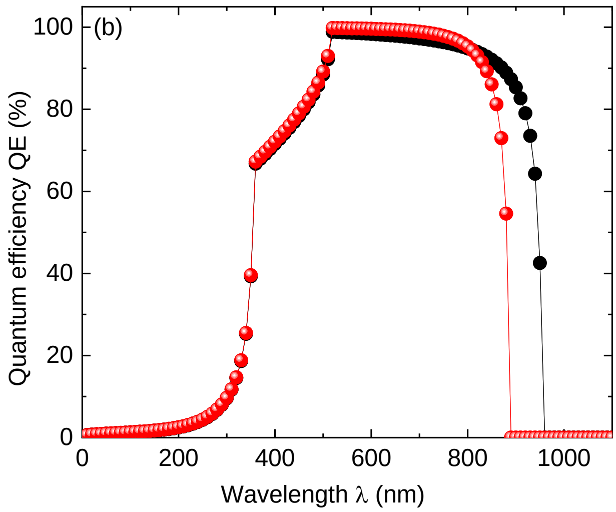

Figure 2. Initial PV simulation results of Cs_2PtI_6 and Rb_2PtI_6 based solar cells for ($R_s = 0$ and $R_s = 14\ \Omega\ cm^2$) (a) J-V curves (b) QE versus wavelength

The initial PV simulation of FTO/CdS/A_2PtI_6/Spiro-OmeTAD/C with A=Cs/Rb based solar cells is conducted for ($R_s = 0$ and $R_s = 14\ \Omega\ cm^2$). Figure 2 illustrates the photovoltaic characteristics, such as the current density curves (J-V curves) and the quantum efficiency (QE). Our obtained PV values of FTO/CdS/Cs_2PtI_6/Spiro-OmeTAD/C solar cell (Figure 1.a) align with experimental outcomes reported by (Schwartz et al., 2020). (Table 2) thereby reinforcing the integrity of the numerical simulation. As a result, the chosen material parameters for the device model are justified. As a second step, we have taken our novel solar cell model (FTO/IGZO/Rb_2PtI_6/$MoSe_2$/C) and proceeded our optimization by varying the thicknesses of all constructing layers. The optimized solar cell based on the platinum iodide perovskite with the optimal thicknesses is depicted in Figure 1.b.

Table 2. J-V characteristic of initial Rb_2PtI_6 and Cs_2PtI_6 based solar cells compared with other simulation and experimental available results for ($\boldsymbol{R_s = 0}$ **and** $\boldsymbol{R_s = 14\ \Omega\ cm^2}$)

Structure	R_s ($\Omega\ cm^2$)	V_{oc} (V)	J_{sc} (mA/cm^2)	FF (%)	PCE (%)
FTO (0.5μm)/CdS (0.1μm)/ Rb_2PtI_6 (1μm)/Spiro-OmeTAD (0.1μm)/C	0	0.79	32.33	46.15	11.83
FTO (0.5μm)/CdS (0.1μm)/ Rb_2PtI_6 (1μm)/Spiro-OmeTAD (0.1μm)/C	14	0.79	28.95	22.23	5.10
FTO (0.5μm)/CdS (0.1μm)/ Cs_2PtI_6 (1μm)/Spiro-OmeTAD (0.1μm)/C	0	0.99	29.95	61.69	18.45
FTO (0.5μm)/CdS (0.1μm)/ Cs_2PtI_6 (1μm)/Spiro-OmeTAD (0.1μm)/C	14	0.99	29.60	36.19	10.70
FTO/CdS (0.08-0.1μm)/ Cs_2PtI_6 (10-15μm)/ElectroDAG 440B/Cu	14	0.9 [a]	19.83 [a]	59.85 [a]	10.70 [a]
FTO/CdS/ Cs_2PtI_6/Spiro-OmeTAD/C	14	1.12 [b]	20.1 [b]	44 [b]	10.16 [b]

[a]: Experimental results from Schwartz et al. (2020)
[b]: SCAPS-1D simulation results (Abdelaziz et al. 2023)

Absorber Acceptor Density N_A Effect

The enhancement of the photovoltaic performance of a solar cell depends crucially on the optimization of the absorber layer thickness as well as the acceptor doping density N_A. To illustrate this effect, we have shown in (Figure 3) the contour plot of the photovoltaic parameters as function of absorber thickness and N_A of our simulation for absorber thickness varying from 0.2 to 1.4 μm and N_A varying from 10^{15} to 10^{20} cm^{-3}. The figure reveals that the highest PCE value is 23.75% for high thickness and high N_A. it is evident that lower absorber thickness leads to lower PCE. This is because for thin absorber layers, most incident photons are transmitted through the material, leading to reduced generation of electron-hole (e-h) pairs and consequently, lower PCE. However, increasing the absorber thickness leads to an increase in optical absorption and generation of (e-h) pairs, which results in an improvement in PCE.

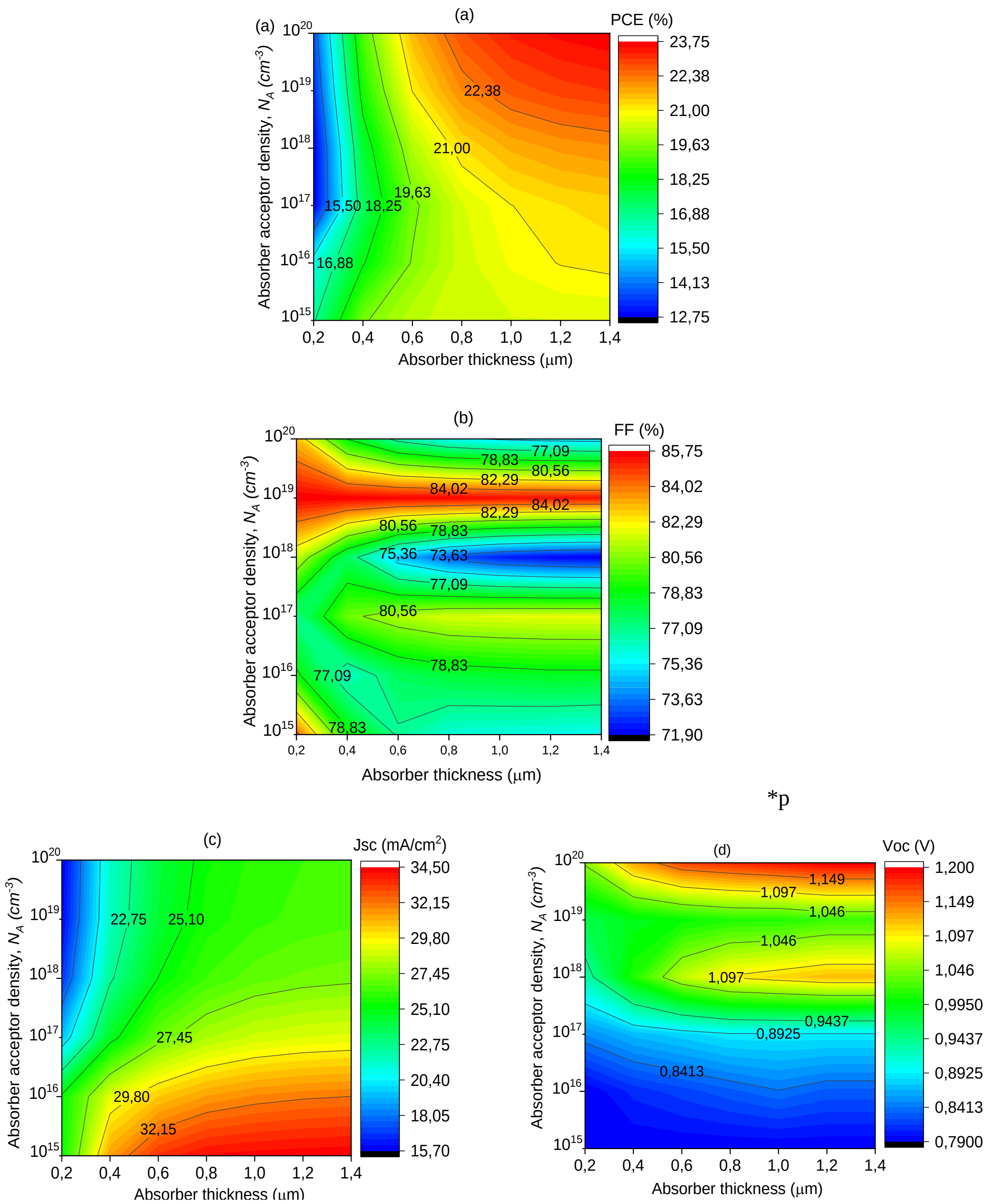

Figure 3. Contour plot of photovoltaic parameters as function of absorber thickness and N_A.

Absorber Defect Density N_t Effect

The impact of the absorber defect density on the photovoltaic parameters of the PSC is illustrated in (Figure 4) by a contour plot. As the defect density (or trap density) increases in the absorber material for higher thickness, Jsc remains constant between 10^{10} cm^{-3} and 10^{11} cm^{-3} and after that, it shows a gradual decrease up to 10^{14} cm^{-3}. This decrease occurs because the traps tend to trap charge carriers, preventing them from participating in the current flow in the solar cell. The Voc decreases as the defect density increases. This phenomenon occurs because the defects in the perovskite material serve as sites where electrons and holes recombine. This recombination process decreases the amount of charge carriers available for collection by the solar cell, thus reducing both the voltage and output current. The increased defect density facilitates the recombination of electrons and holes, hampering their ability to generate current efficiently and leading to a decrease in Voc.

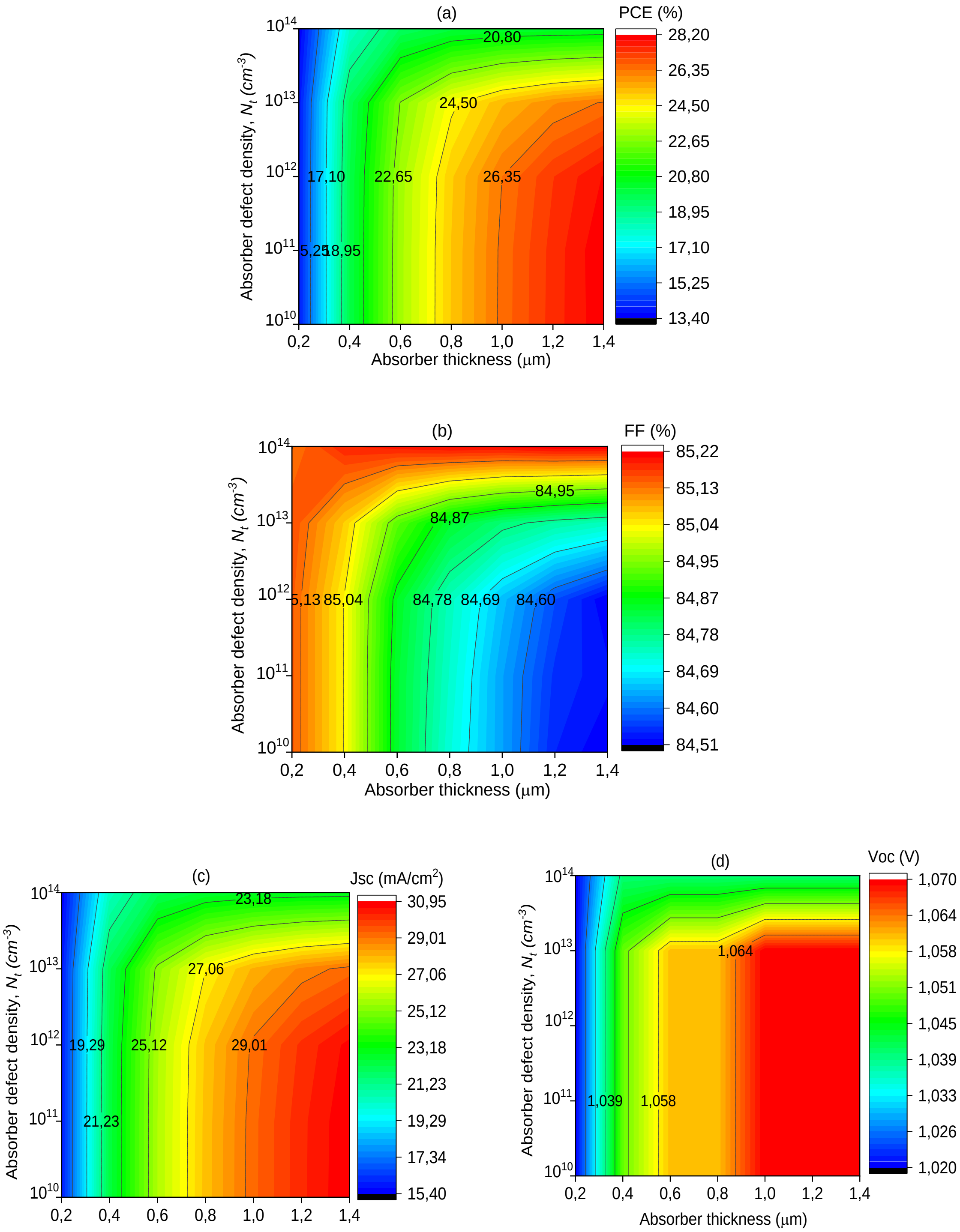

Figure 4. Contour plot of photovoltaic parameters as function of absorber thickness and N_t.

Series Resistance R_S Effect

The optimum performance of a solar cell corresponds to the ideal value of R_S which is equal to zero, but in practical reality, this is not the case for R_S. In fact, the series resistance is due to factors such as ohmic contacts, metallic contacts, ITO sheet resistance, contact resistance inside the cell and manufacturing imperfections. Figure 5 shows the impact of R_S on various photovoltaic parameters of PSC including PCE, Voc, Jsc and FF. As R_S increases, PCE decreases significantly, from 28.14% to 16.7%, while the Voc and Jsc parameters remain practically constant.

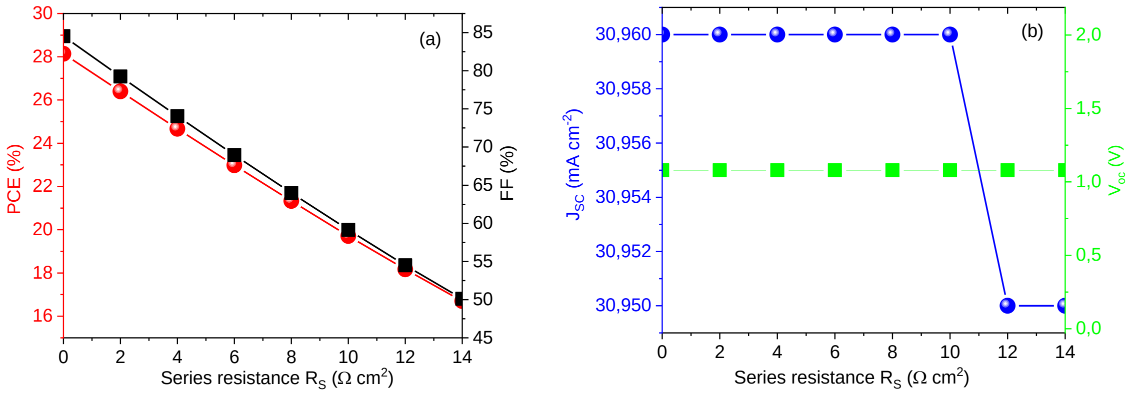

Figure 5. Series resistance effect on the photovoltaic parameters.

Working Temperature Effect

One of major problems for PSCs is their degradation over time under exposure to high temperatures due to the chemical and structural changes of perovskite materials at elevated temperatures. This can negatively impact their performance. Indeed, the interfaces between different layers in the solar cell can be affected by temperature, leading to increased recombination and reduced charge transport. Hence, to examine the behavior of PSCs in a real-world setting, a performance study across a temperature range spanning from 270 K to 370 K is conducted.

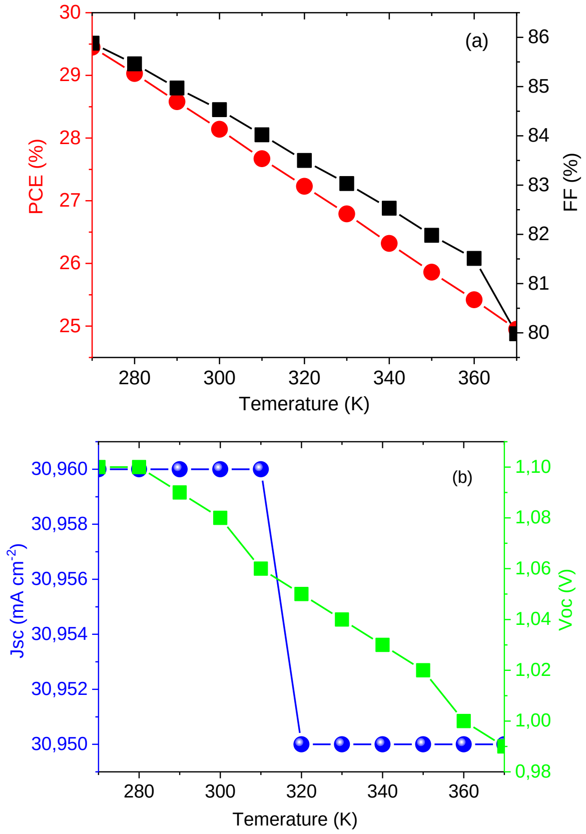

Figure 6. Temperature effect on the photovoltaic parameters.

Figure 6 illustrates this effect. A constant decrease in PCE, Voc and FF values as the temperature increases, while the Jsc remains stable up to 310 K and shows a smaller decrease up to 320 K and after that it continues its stability up to 370 K.

Conclusion

This work provides a valuable design of the planar architecture of the solar cell where the double perovskite layer is sandwiched between an electron transport layer IGZO and a hole transport layer $MoSe_2$. We have optimized and analyzed of various fundamental parameters governing perovskite solar cell performance, including the thicknesses of all layers, the acceptors N_A and defects N_t charge carrier densities, parasitic series resistance Rs and the working temperature T. The current-voltage characteristics (J-V), and quantum efficiency (QE) are analyzed via these key parameters. Our final optimal results, gives an impressive power conversion efficiency (PCE) up to 28.14% for $N_A=10^{20}$ cm^{-3} and $N_t=10^{10}$ cm^{-3}. These predictive findings propose our novel lead-free double perovskite solar cell as a potential candidate for non-toxic an environmentally friendly solar cell applications.

Scientific Ethics Declaration

The authors declare that the scientific ethical and legal responsibility of this article published in EPSTEM Journal belongs to the authors.

Acknowledgements

The authors are thankful to Professor Marc Burgelman and his coworkers at the University of Ghent, Belgium, for providing the SCAPS-1D software used in this study.

Notes

* This article was presented as an oral presentation at the International Conference on Technology, Engineering and Science (www.icontes.net) held in Antalya/Turkey on November 14-17, 2024.

References

AbdElAziz, H. H., Taha, M., El Rouby, W.M.A., Khedr, M.H., & Saad, L. (2022). Evaluating the performance of $Cs_2PtI_{6-x}Br_x$ for photovoltaic and photocatalytic applications using first-principles study and SCAPS-1D simulation. *Heliyon, 8*(10), e10808.

Amjad, A., Qamar, S., Zhao, C., Fatima, K., Sultan, M., & Akhter, Z. (2023). Numerical simulation of lead-free vacancy ordered Cs_2PtI_6 based perovskite solar cell using SCAPS-1D. *RSC Advances,13*(33), 23211–23222.

Bartel, C.J., Sutton, C., Goldsmith, B.R., Runhai, O., Musgrave, C.B., Ghiringhelli, L.M., & Scheffler, M. (2019). New tolerance factor to predict the stability of perovskite oxides and halides. *Science Advances, 5(2)*, eaav0693.

Burgelman, M., Decock, K., Niemegeers, A., Verschraegen, J., & Degrave, S. J. F. (2021). *SCAPS manual.* Retrieved from https://scaps.elis.ugent.be/SCAPS%20manual%20most%20recent.pdf

Cai, Y., Xie, W., Ding, H., Chen, Y., Thirumal, K., Wong, L.H., Mathews, N., Mhaisalkar, S.G., Sherburne, M., & Asta, M. (2017). Computational study of halide perovskite-derived a_2bx_6 inorganic compounds: chemical trends in electronic structure and structural stability. *Chemistry of Materials, 29*(18), 7740−7749.

Jahantigh, F., & Safikhani, M. J. (2019). The effect of HTM on the performance of solid-state dye-sanitized solar cells (SDSSCs): A SCAPS-1D simulation study. *Applied Physics A*, *125*(4), 276.

Ji, F., Boschloo, G., Wang, F., & Gao, F. (2023). Challenges and progress in lead-free halide double perovskite solar cells. *Solar RRL*, *7*(6), 2201112.

Nair, S. S., Krishnia, L., Trukhanov, A., Thakur P., & Thakur A. (2022). Prospect of double perovskite over conventional perovskite in photovoltaic applications. *Ceramics International*, *48*(23), 34128.

Nykyruy, L.I., Yavorskyi, R.S., Zapukhlyak, Z.R., Wisz, G., & Potera, P. (2019). Evaluation of CdS/CdTe thin film solar cells: SCAPS thickness simulation and analysis of optical properties. *Optical Materials* 92, 319-329.

Schwartz, D., Murshed, R., Larson, H., Usprung, B., Soltanmohamad, S., Pandey, R., Barnard, E.S., Rockett, A., Hartmann, T., Castelli, I.E., & Bansal S. (2020). Air stable, high-efficiency, pt-based halide perovskite solar cells with long carrier lifetimes. *Physica Statu Solidi*, *14*, 2000182.

Shamna, M.S. & Sudheer, K.S. (2022). Device modeling of Cs_2PtI_6-based perovskite solar cell with diverse transport materials and contact metal electrodes: A comprehensive simulation study using solar cell capacitance simulator. *Journal of Photonics for Energy*, *12*, 032211.

Tanaka, H., Oku, T., & Ueoka, N. (2018). Structural stabilities of organic–inorganic perovskite crystals. *Japanese Journal of Applied Physics*, *57*(8S3), 08RE12.

Teyou- Ngoupo, A., & Ndjaka, J.M.B. (2022). Performance enhancement of Sb_2Se_3 -based solar cell with hybrid buffer layer and $MoSe_2$ as a hole transport material using simulator device. *Discover Mechanical Engineering*, *1*(1), 5.

Yang, S., Wang, L., Zhao, S., Liu, A., Zhou, Y., Han, Q., Yu, F., Gao, L., Zhang, C., & Ma, T. (2020). A novel lead-free material Cs_2PtI_6 with narrow bandgap and ultra-stable for its photovoltaic application. *ACS Appl. Mater. Interfaces*, *12*(40), 44700–44709.

Yang, Z., Yu, Z., Wei, H., Xiao, X., Ni, Z., Chen, B., ... & Huang, J. (2019). Enhancing electron diffusion length in narrow-bandgap perovskites for efficient monolithic perovskite tandem solar cells. *Nature Communications*, *10*(1), 4498.

Zhao, X.H., Wei, X.N., Tang, T.Y., Gao, L.K., Xie, Q., Lu, L.M. & Tang, Y.L. (2021). First-principles study on the structural, electronic and optical properties of vacancy-ordered double perovskites Cs_2PtI_6 and Rb_2PtI_6. *Optical Materials 114*, 110952.

Author Information

Abdelkrim El-Hasnaine Merad
Solid State Physics Team, Theoretical Physics Laboratory, Faculty of Sciences, A Belkaid University, Box 119, 13000, Tlemcen, Algeria
Contact e-mail: abdelkrim.merad@univ-tlemcen.dz

Souheyla Mamoun
Solid State Physics Team, Theoretical Physics Laboratory, Faculty of Sciences, A Belkaid University, Box 119, 13000, Tlemcen, Algeria

Abd-El-Illah Abbaci
Solid State Physics Team, Theoretical Physics Laboratory, Faculty of Sciences, A Belkaid University, Box 119, 13000, Tlemcen, Algeria

To cite this article:

Merad, A.E., Mamoun, S., & Abbaci A.E. (2024). Design and numerical investigation of highly photovoltaic efficiency of novel non-toxic double perovskite solar cell with IGZO as electron transport layer. *The Eurasia Proceedings of Science, Technology, Engineering & Mathematics (EPSTEM), 32,* 439-448.

The Eurasia Proceedings of Science, Technology, Engineering & Mathematics (EPSTEM)
ISSN: 2602-3199

The Eurasia Proceedings of Science, Technology, Engineering & Mathematics (EPSTEM), 2024

Volume 32, Pages 449-454

IConTES 2024: International Conference on Technology, Engineering and Science

Beyond One-Sided Solar Unlocking Efficiency and Space with Bifacial Photovoltaic Systems

Ahmad Manasrah
Al-Zaytoonah University of Jordan

Yousef Jaradat
Al-Zaytoonah University of Jordan

Mohammad Masoud
Al-Zaytoonah University of Jordan

Mohammad Jaradat
Al-Zaytoonah University of Jordan

Abstract: Bifacial photovoltaic systems (bPVs) have become increasingly popular in the past decade due to their ability to generate electricity from both sides of the module, resulting in improved efficiency through the utilization of scattered and reflected light. Typically, while bPVs tend to be more expensive than traditional monofacial photovoltaic panels, this is offset by their higher energy output on less land space. An economic analysis is conducted in this study to swap out a 2.4 MW single-sided solar panel system with bifacial ones on the rooftops of a university campus in Jordan. The additional space generated will be used to enhance the system's capability. The findings indicated that the new double-sided system could reduce the required area by over 27% if its capacity matched the current system. The findings indicated that expanding the area significantly augmented the current capacity by 47%. The return on investment (ROI) for the replacement procedure is 5.43% with a payback period of 8.2 years over a lifespan of 20 years.

Keywords: Photovoltaics, Bifacials, Return on investment, Payback period.

Introduction

Clean and sustainable energy sources are now one of the essential necessities in today's world. Renewable energy systems are classified as clean and viable sources (Sayed et.al., 2023). Normally, there are six sources of renewable energy: solar, wind, geothermal, hydropower, biomass, and hydrogen. Solar energy is the most prevalent option because of its dependability, affordability, and ease of use (Jordan et.al., 2020). Solar photovoltaics is a form of solar energy systems. These systems are in such high demand that their projected total capacity worldwide is expected to exceed 1.5 TW (Manasrah et.al., 2024). A standard solar photovoltaic module is comprised of two layers made of p-type and n-type silicon as well as other semiconductors. Sunlight energy enables electrons to move between these layers, generating current (Manasrah et.al., 2021). Despite the positivity surrounding solar photovoltaics, they require large amounts of land for installation, particularly with larger systems, leading to higher capital costs (Tawalbeh, et.al., 2021). There will be difficulties in expanding the current systems due to restrictions on space, particularly when they are mounted on rooftops.

Bi-facial solar panels (bPVs) are a potential solution to this issue. In contrast to traditional mono-facial modules, these modules are able to produce electricity from both sides by utilizing reflected and scattered sunlight (Jang & Lee, 2020; Manasrah et.al., 2023). Stated that bPVs can generate approximately 30% additional energy

- Selection and peer-review under responsibility of the Organizing Committee of the Conference

during certain times of the day compared to conventional mono-facial modules of similar size and capacity. Nonetheless, these solar photovoltaics are typically pricier than conventional mono-facial ones. Nevertheless, researchers have been studying the techno-economic characteristics of building-integrated PVs as substitutes for current solar PV farms and systems. For example, a study compared a traditional single-sided solar farm to a comparable double-sided one using a SWOT analysis. The results revealed that the bPV farm had a net present value that was more than 12% higher based on the assumptions provided (Kumbaroglu et.al., 2023).

This study involves conducting an economic analysis on substituting the modules in a 2.4 MW mono-facial system with bifacial ones. The existing system is situated on the rooftops of Al-Zaytoonah University of Jordan's buildings, which are in Amman, Jordan. The extra space created will be utilized to expand the capacity of the new system while using the existing rooftop areas. The goal of this research is to determine the expense of replacing, and to assess the payback and return on investment of the newly improved system using the equipment and labor costs in the local market. This research will offer an analysis on the economic viability of upgrading outdated photovoltaic systems with building-integrated photovoltaics (bPVs).

Background

Bifacial photovoltaics (bPVs) have been present in the worldwide market starting from the 1980s (Eguren, 2022). Numerous improvements and enhancements have been implemented since that time. Nonetheless, it wasn't until there was a notable decrease in the cost of silicon wafers that they began to attract attention (Kopecek & Libal, 2021). Subsequent to that, numerous studies have been carried out centering on the advantages of using bPVs as a substitute for traditional mono-facial solar panels. For instance, a particular study examined various characteristics of mono-facial and bifacial photovoltaic systems (Rodríguez-Gallegos et.al., 2018). The findings indicated that bifacial photovoltaic panels were a more economical choice than single-sided panels at latitudes higher than 40 degrees for installations with "any module orientation." Nonetheless, latitudes below 40 degrees experienced the opposite results due to low albedo values. In the same way, another research demonstrated that bPVs could lower the levelized cost of energy LCOE for solar photovoltaic systems at specific latitudes and module tilt angles (Patel et.al., 2019). Even in solar farms built on the ground.

Researching efficiency comparisons between monofacials and newer bPVs has also been a popular theme in literature. A recent research conducted in Poland by Olczak and colleagues (2021) compared the two types in terms of power gain and reduction of CO2 emissions. The research demonstrated that bifacial photovoltaic systems generated about 10% to 28% higher electrical power compared to mono-facial systems. Additionally, the research revealed that the reduction in CO2 emissions is 16% greater in bifacial photovoltaic systems compared to monofacial systems. A different experiment carried out in Fiji yielded comparable findings regarding economic impact and reduced CO2 emissions (Prasad & Prasad, 2023). The research found that bPVs are a better choice than mono-facials on smaller land sizes. The research conducted in this study examines if it is possible to replace the modules of a functioning 2.4 MW traditional single-sided system with new bifacial modules. The new units will offer additional room for the growth of the existing system situated on the roofs of Al-Zaytoonah University of Jordan. The research will allow for the exploration of various upgrade options for comparable systems in the Middle East area.

Location

Figure 1. The campus of ZUJ, located in Amman, Jordan.

Table 1. Estimated current PV capacities for each building.

Building	Estimated PV capacity [KW]	Approximate utilized area [m^2]
School of Pharmacy	150	1,400
Schools of Business	340	3,300
Library	260	2,500
Schools of Engineering and Architecture	300	2,800
Schools of Science and Nursing	320	3,000
School of Literature	190	1,800
Deanship of Scientific Research	60	560
Deanship of Student Affairs	60	600
Main Cafeteria	55	550
Center of Consultations and Services	25	240
Sports Center	230	2,200
Workshops and Warehouse building	170	1,700
University's Nursery	50	450
University's mosque	40	400
Bus parking lot	180	1,700
Total	**2,430**	**23,200**

ZUJ is situated in the southern part of Amman, Jordan. The campus covers about 300,000 square meters, as depicted in Figure 1. Since 2011, major campus buildings have had a 2.4 MW mono-facial photovoltaic system installed on their rooftops. At the moment, there are 14 structures equipped with rooftop solar panels, along with the bus parking lot roofs. Table 1 illustrates the current distribution of photovoltaics on buildings, including the size of their rooftop areas based on Google Earth phootage and measurements.

Slight variances in PV capacity can be observed among buildings with comparable rooftop sizes. This results from variations in the kinds and formations of the modules as the system underwent installations at various times, along with numerous replacements and upgrades. The PV capacities were estimated based on location sitings, utilized areas, and inverter capacities. The typical power output of the modules in place is approximately 305 W per module, with an average efficiency of 16% and measurements of 1690 x 990 mm. All modules face south with a tilt angle of approximately 23 degrees over different installation heights.

Methodology

To assess the necessary space for installation of the new bPV modules, a specific type of bPV will be utilized for this analysis. Table 2 displays the features of the updated bPV module in use. The selected bPV module has an average power output of 385 W, and can achieve a power gain of up to 30% when installed at heights ranging from 1.2 to 1.5 meters. The new module has a slightly bigger surface area, requiring more rooftop space. Nevertheless, increased capacity and power increase will compensate for the discrepancy.

Table 2. Electrical and physical characteristics of the bi-facial module.

Open circuit voltage [V]	49.58
Short circuit current [Amp]	9.87
Maximum power voltage [V]	40.88
Maximum power current [Amp]	9.42
Maximum power - Pmax [W]	385
Module efficiency [%]	19.8
Dimensions [mm]	1968 x 990 x 40

Labor, exchanging, and setup expenses will be determined by the typical prices found in the local Jordanian market. Normally, quotes and proposals are bundled together, so breaking down costs will be estimated based on the total price. Local market quotes and offers will be used to conduct an economic assessment, in order to estimate the levelized cost of energy (LCOE), payback period, and return on investment (ROI). This evaluation will take into account expenses and revenues associated with dismantling old modules and building taller steel structures where necessary. The revised system is linked to the grid but does not include battery pack choices. Based on that, the average cost of bPV solar energy is around $700 per KW. This includes the costs of the modules, tall structures and inverters. However, to calculate the levelized cost of energy LCOE, Equation 1 can be used (Emblemsvåg, 2021).

$$LCOE = \{\frac{Capital\ Cost * Recovery\ factor + fixed\ O\&M}{8760 * Capacity\ factor}\} + \{fuel\ cost * heatrate\} + \{variable\ O\&M\}$$

In this system, heat rate and fuel costs do not apply because there is no heat storage or solar-thermal subsystems. The analysis relied on a 20-year operational timeframe, a 20% capacity factor common for solar PV systems (i.e., the ratio of the annual energy the system produces as opposed to full capacity), and set costs of $25 per KW fixed and $0.2 per KW variable. The campus was classified as non-residential so electricity rates were set at $0.18 per KWh. Moreover, the return on the investment and payback period are calculated using the follwing equations (Benli & Gurturk, 2021).

$$ROI = \frac{Gain\ from\ investment - Cost\ of\ investment}{Cost\ of\ investment}$$

$$Payback\ period = \frac{Initial\ investment}{Cash\ flow\ per\ year}$$

Results and Discussion

With a cost of $700 per KW, a 2.4 MW bPV system would have an estimated price of approximately $1,700,00.00, equivalent to the capacity of the previous mono-facial system. Nevertheless, the new system requires only 6.5m^2 for each 1KW while the current system needs 9m^2 according to Table 1. This results in a decrease in size of over 27% by utilizing the bPV capacity and dimensions listed in Table 2. We can determine the capacities of the subsystems for every building on campus, as demonstrated in Table 3. The findings indicated that a 3573 KW (equal to 3.57 MW) setup could potentially be placed on the same allotted space, allowing for approximately 47% more capacity than the existing system.

Table 3. Estimated new bPVs capacities for same building areas.

Building	Estimated bPV capacity [KW]	Approximate utilized area [m^2]
School of Pharmacy	215.6	1,400
Schools of Business	508.2	3,300
Library	385.0	2,500
Schools of Engineering and Architecture	431.2	2,800
Schools of Science and Nursing	462.0	3,000
School of Literature	277.2	1,800
Deanship of Scientific Research	86.24	560
Deanship of Student Affairs	92.40	600
Main Cafeteria	84.70	550
Center of Consultations and Services	36.96	240
Sports Center	338.8	2,200
Workshops and Warehouse building	261.8	1,700
University’s Nursery	69.30	450
University’s mosque	61.60	400
Bus parking lot	261.8	1,700
Total	**3,573**	**23,200**

According to the prices in the local market, a 3.57 MW bifacial photovoltaic system is priced at $2,500,960.00. The new system will encompass the total space currently used by the existing system on campus. The price encompasses the expenses of elevating the steel structures as necessary and the earnings from selling the previous mono-facial system as scrap. Additionally, the ROI can be determined using the equation that was previously mentioned. Figure 2 displays profits and expenses for investments throughout a 20-year period, representing the system's lifespan. The new system has an annualized ROI of 5.43%.

The payback period was determined using the previously mentioned equation. In this estimate, a reduction of 5% in cash flow was taken into account, along with a 10% discount rate, over a span of 20 years. Figure 3 depicts the payback period for the recent bPV system at 8.2 years and an annual cash flow return rate of 8.36%.

Furthermore, the levelized cost of energy, LCOE, for the new modules was calculated between \$0.04~\$0.06 per KWh compared to the utility rate at \$0.18 per KWh.

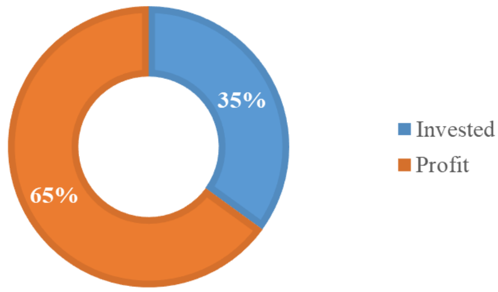

Figure 2. Profits and expenses of the investment over 20 years.

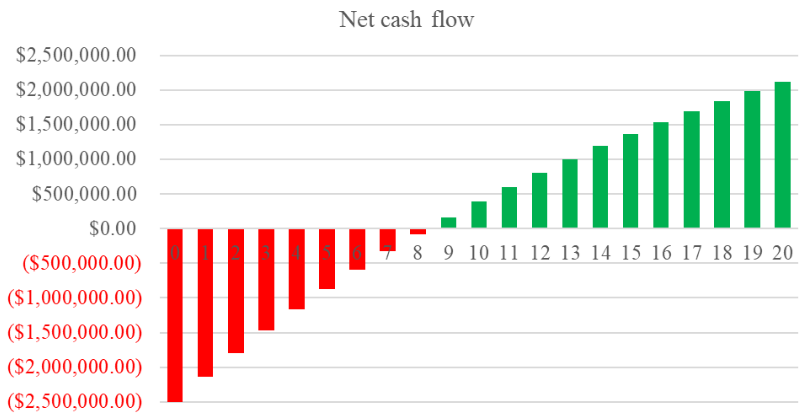

Figure 3. Net cashflow and payback period of the investment.

Conclusion

An economic analysis was carried out in this research to assess the viability of installing new bifacial modules instead of traditional mono-facial modules in a 2.4MW system. The installation took place on the rooftops of the buildings situated on a university campus. This theoretically will conserve space for future system expansions. Replacing a 2.4MW system would cost \$1,700,000.00. Using the new bPV modules would mean assigning 6.5m^2 per kilowatt instead of the current 9m^2, resulting in a 27% reduction in space utilization. Nonetheless, it is possible to install a 3.57MW bPV system that will use up all available space and result in a 47% boost in electrical capacity compared to the current system. According to the findings, the recently proposed 3.57MW system would have a price tag of \$2,500,960.00. The new bPV system is projected to generate a yearly ROI of 5.43% throughout its 20-year lifespan. The system had a payback period of 8.2 years, annual cash flow return rate of 8.36%, and LCOE ranging from \$0.04 to \$0.06 per KWh.

Scientific Ethics Declaration

The authors declare that the scientific ethical and legal responsibility of this article published in EPSTEM Journal belongs to the authors.

Acknowledgements or Notes

* This article was presented as an oral presentation at the International Conference on Technology, Engineering and Science (www.icontes.net) held in Antalya/Turkey on November 14-17, 2024.

* Authors would like to acknowledge Al-Zaytoonah University of Jordan for financially supporting this study.

References

Benli, H., & Gurturk, M. (2021). Investigation of the effect of pv panel efficiency parameter on ınvestment payback period. *International Journal of Innovative Engineering Applications*, *5*(2), 88-92.

Eguren, J., Martínez-Moreno, F., Merodio, P., & Lorenzo, E. (2022). First bifacial PV modules early 1983. *Solar Energy, 243*, 327-335.

Emblemsvåg, J. (2021). On the levelised cost of energy of solar photovoltaics. *International Journal of Sustainable Energy*, *40*(8), 755-780.

Jang, J., & Lee, K. (2020). Practical performance analysis of a bifacial PV module and system. *Energies*, *13*(17), 4389.

Jordan, D. C., Marion, B., Deline, C., Barnes, T., & Bolinger, M. (2020). PV field reliability status—Analysis of 100 000 solar systems. *Progress in Photovoltaics: Research and Applications*, *28*(8), 739-754.

Kopecek, R., & Libal, J. (2021). Bifacial photovoltaics 2021 status, opportunities and challenges. *Energies*, *14*(8), 2076.

Kumbaroğlu, G. S., Camlibel, M. E., & Avcı, C. (2021). Techno-economic comparison of bifacial vs monofacial solar panels. *Engineering Structures and Technologies*, *13*(1), 7-18.

Manasrah, A., Al Zyoud, A., & Abdelhafez, E. (2021). Effect of color and nano film filters on the performance of solar photovoltaic module. *Energy Sources, Part A: Recovery, Utilization, and Environmental Effects*, *43*(6), 705-715.

Manasrah, A., Masoud, M., Jaradat, Y., & Jannoud, I. (2024). Advancements in bifacial photovoltaics: A review of machine learning techniques for enhanced performance. *The Eurasia Proceedings of Science, Technology, Engineering & Mathematics (EPSTEM)*, *27*, 239-245.

Manasrah, A., Masoud, M., Jaradat, Y., Alia, M., Almanasra, S., & Suwais, K. (2023). Shading anomaly detection framework for bi-facial photovoltaic modules. *Energy Sources, Part A: Recovery, Utilization, and Environmental Effects*, *45*(4), 12955-12972.

Olczak, P., Olek, M., Matuszewska, D., Dyczko, A., & Mania, T. (2021). Monofacial and bifacial micro PV installation as element of energy transition—The case of Poland. *Energies*, *14*(2), 499.

Patel, M. T., Khan, M. R., Sun, X., & Alam, M. A. (2019). A worldwide cost-based design and optimization of tilted bifacial solar farms. *Applied Energy*, *247*, 467-479.

Prasad, M., & Prasad, R. (2023). Bifacial vs monofacial grid-connected solar photovoltaic for small islands: A case study of Fiji. *Renewable Energy*, *203*, 686-702.

Rodríguez-Gallegos, C. D., Bieri, M., Gandhi, O., Singh, J. P., Reindl, T., & Panda, S. K. (2018). Monofacial vs bifacial Si-based PV modules: Which one is more cost-effective?. *Solar Energy, 176*, 412-438.

Sayed, E. T., Olabi, A. G., Alami, A. H., Radwan, A., Mdallal, A., Rezk, A., & Abdelkareem, M. A. (2023). Renewable energy and energy storage systems. *Energies*, *16*(3), 1415.

Tawalbeh, M., Al-Othman, A., Kafiah, F., Abdelsalam, E., Almomani, F., & Alkasrawi, M. (2021). Environmental impacts of solar photovoltaic systems: A critical review of recent progress and future outlook. *Science of the Total Environment, 759*, 143528.

Author Information

Ahmad Manasrah
Al-Zaytoonah University of Jordan
Amman, Jordan
Contact e-mail: *ahmad.mansrah@zuj.edu.jo*

Yousef Jaradat
Al-Zaytoonah University of Jordan
Amman, Jordan

Mohammad Masoud
Al-Zaytoonah University of Jordan
Amman, Jordan

Mohammad Jaradat
Al-Zaytoonah University of Jordan
Amman, Jordan

To cite this article:

Manasrah, A., Jaradat, Y., Masoud, M., & Jaradat, M. (2024). Beyond one-sided solar unlocking efficiency and space with bifacial photovoltaic systems. *The Eurasia Proceedings of Science, Technology, Engineering & Mathematics (EPSTEM), 32,* 449-454.

The Eurasia Proceedings of Science, Technology, Engineering & Mathematics (EPSTEM)
ISSN: 2602-3199

The Eurasia Proceedings of Science, Technology, Engineering & Mathematics (EPSTEM), 2024

Volume 32, Pages 455-462

IConTES 2024: International Conference on Technology, Engineering and Science

Effect of Porosity on the Nonlinear Thermal Stability of Functionally Graded Material Beams under Various Boundary Conditions

Hichem Bellifa
University Djillali Liabes of Sidi Bel Abbes

Abdelmoumen Anis Bousahla
University Djillali Liabes of Sidi Bel Abbes

Abdeldjalil Benbakhti
University Centre of Maghnia

Abstract: In this project work, the impact of porosity on the nonlinear thermal buckling response of power law functionally graded beam with various boundary conditions is investigated; the derivation of equations is based on the Euler–Bernoulli beam theory where the distribution of material properties is imitated polynomial function. Using the nonlinear strain–displacement relations, equilibrium equations and stability equations of beam are derived. The beam is assumed under thermal loading, namely: Nonlinear temperature distribution through the thickness. Various types of boundary conditions are assumed for the beam with combination of roller, clamped and simply-supported edges equations for these types of structures. The effects of the porosity parameter, slenderness ratio and power law index on the thermal buckling of P-FG beam are discussed.

Keywords: Euler beam theory, Functionally graded material, Porosity parameter, Thermal buckling

Introduction

During last two decades, the need to design the high per Functionally graded materials (FGMs) are composite materials composed of two or more constituent phases with a continuously variable variation by gradually changing the volume fraction. These materials type have been proposed, developed and successfully employed in industrial application since 1980s (Koizumi, 1993). FGMs were designed as a thermal barrier coating in aerospace application, such as ceramic-metal composite structure.

Nowadays, FGMs are alternative materials widely employed in aerospace, civil, mechanical, nuclear, optical, electronic, chemical, shipbuilding, and biomechanical industries (Akavci, 2016; Kar & Panda, 2015, 2016;Eltaher et al., 2014; Belkorissat et al., 2015; Ait Atmane et al.,.2015; Akbas, 2015; Arefi 2015a,2015b;Arefi & Allam, 2015b; Celebi et al.,2016; Darabi & Vosoughi, 2016; Turan et al., 2016; Ebrahimi & Shafiei, 2016; Mouaici al.2016, Mouffoki et al.,2017; Zidi et al., 2017, Bellifa et al.,2017; Karami et al., 2018a, 2019a; Bennai et al., 2019; Bouamoud et al., 2019; Bellifa et al., 2017, 2021; Batou et al., 2019; Chaabane et al., 2019; Alwabli et al., 2021; Benbakhti et al., 2023 , 2024; Benfrid et al., 2023; Maachou et al., 2024; Semmah et al., 2024).

The problem of buckling of the porous materials with varying properties has been discussed by many authors. The buckling analysis of thin functionally graded (FG) rectangular plates based on the classical or first order shear deformation theory (FSDT) under various loads were discussed by Mohammadi et al. (2010). Jabbari et al. (2013, 2014) examined porosity distribution influence on buckling characteristics of plates. Buckling of metal foam porous beams using a shear deformation beam model was studied by Chen et al. (2015). In a recent study, Bellifa et al. (2016) analyzed the wave propagation of an infinite FG plate having porosities by using various simple higher-order shear deformation theories. Ebrahimi et al. (2016) considered the thermal effects on linear free vibration of functionally graded Euler-Bernoulli beams with porosities for pinned-pinned and clamped pinned edges.

To conclude, we have noticed through our reading in the literature that studies on the effect of porosity across the thickness of the FG beam are rare. For this, the aim of this paper first is to extend the Euler–Bernoulli beam theory proposed by Eslami and Kiani (2010) and Bellifa et al. (2017) to porous functionally graded (FG) beams, then to study the critical buckling temperature for FG beams with porosity for different types of boundary conditions and thermal loadings which are assumed to be non-linear distribution through the thickness. Material properties were assumed to be temperature dependent, and graded in the thickness direction according to a simple power law distribution. Finally, the results based on the Euler-Bernoulli beam theory and the effects of thermal loading, porosity, and other parameters on FG beam buckling thermo mechanical behaviour are investigated.

Theoretical Formulations

Kinematics

The classic beam theory is applied throughout the work. Based on the Euler-Bernoulli assumption, the following displacement field can be obtained, (Kiani & Eslami 2010; Belbachir et al., 2024).

$$\begin{aligned} u(x,z) &= u_0(x) - z\frac{\partial w_0}{\partial x} \\ v(x,z) &= 0 \\ w(x,z) &= w_0(x) \end{aligned} \tag{1}$$

Where $u_0(x,y)$, $w_0(x,y)$ are the two unknown displacement functions of middle surface of the beam in the *x* and *z* directions. The Von-Karman-type of geometric non-linearity is taken into consideration in the strain–displacement relations which are as follows

$$\varepsilon_x = \varepsilon_x^0 + z\,k_x \tag{2}$$

Where ε_x^0 and k_x are, respectively, the nonlinear longitudinal strain and curvature defined as (Bellifa and al. 2017)

$$\varepsilon_x^0 = \frac{du_0}{dx} + \frac{1}{2}\left(\frac{d\,w_0}{dx}\right)^2 \text{ and } k_x = -\frac{d^2 w_0}{dx^2} \tag{3}$$

Constitutive Relations

Consider a FG rectangular beam with thickness h, length a and width b The Cartesian coordinate system is established so that $0 \le \mathrm{x} \le 1$, and $-\frac{h}{2} \le \mathrm{z} \le +\frac{h}{2}$.

Functionally graded materials (FGMs) are composed of two kinds of materials: one is a metal and the other is ceramic. Here, Young's modulus E (z) varies continuously through the beams thickness by a polynomial material law. We will consider a non-homogeneity material with a porosity volume function, $\xi \ (0 \le \xi \le 1)$. In such a way, the efficient material properties, as Young's modulus E, the coefficient of thermal expansion α and thermal conductivity K at a point are usually assumed to be given by the rule of mixture (Ait Atmane and al. 2017)

$$\mathrm{E(z)} = \mathrm{E_m} + (E_c - E_m)\left(\frac{h+2z}{2h}\right)^p - (E_c + E_m)\frac{\xi}{2}$$
$$\alpha(\mathrm{z}) = \alpha_m + (\alpha_c - \alpha_m)\left(\frac{h+2z}{2h}\right)^p - (\alpha_c + \alpha_m)\frac{\xi}{2} \quad (4)$$
$$K(\mathrm{z}) = K_m + (K_c - K_m)\left(\frac{h+2z}{2h}\right)^p - (K_c + K_m)\frac{\xi}{2} \tag{4}$$

Where p is the volume fraction exponent. The value of p equal to zero represents a fully ceramic beam, whereas infinite p indicates a fully metallic beam. The distribution of the combination of ceramic and metal is linear for $p=1$.

The constitutive relation of a FG beam under thermal and mechanical conditions using thermo-elasticity can be expressed as

$$\sigma_x = E(\varepsilon_x - \alpha(T - T_r)) \tag{5}$$

Where σ_x, T and T_r are, respectively, the axial stress, the temperature distribution through the thickness and the reference temperature. The axial force N , the bending moment M caused by thermal stress, respectively are written as

$$(\mathrm{N}, M) = \int_{-\frac{h}{2}}^{\frac{h}{2}} \sigma_x (1, z) dz \tag{6}$$

By substituting Eq. (4) and Eq. (5) into Eq. (6) we obtain

$$N = \overline{A}\left(\frac{du_0}{dx} + \frac{1}{2}\left(\frac{d\ w_0}{dx}\right)^2\right) - \overline{B}\frac{d^2 w_0}{dx^2} - N_T$$
$$M = \overline{B}\left(\frac{du_0}{dx} + \frac{1}{2}\left(\frac{d\ w_0}{dx}\right)^2\right) - \overline{C}\frac{d^2 w_0}{dx^2} - M_T \tag{7}$$

Total potential energy of the FGM beam may be expressed as follows

$$\delta U = \int_0^l \int_A \left(\sigma_x\left(\varepsilon_x - \alpha(T - T_r)\right)\right) dA dx \tag{8}$$

Substituting Eq.(3) and Eq.(5) into Eq.(8) and integrating with respect to z and y, The total potential energy of the beam is given by

$$\delta U = \frac{b}{2}\left[\int_0^l \begin{pmatrix} \overline{A}\left(\frac{du_0}{dx} + \frac{1}{2}\left(\frac{d\ w_0}{dx}\right)^2\right)^2 - 2\overline{B}\frac{d^2 w_0}{dx^2}\left(\frac{du_0}{dx} + \frac{1}{2}\left(\frac{d\ w_0}{dx}\right)^2\right) \\ + \overline{C}\left(\frac{d^2 w_0}{dx^2}\right)^2 - 2N_T\left(\frac{du_0}{dx} + \frac{1}{2}\left(\frac{d\ w_0}{dx}\right)^2\right) + 2M_T\left(\frac{d^2 w_0}{dx^2}\right) \end{pmatrix} dx + \int_0^l \int_{-\frac{h}{2}}^{\frac{h}{2}} \left[E(z)\alpha(z)(T - T_r)\right] dx\right] \tag{9}$$

The stability equations of the beam may be derived by the adjacent equilibrium criterion. Assume that the equilibrium state of the FGM beam under thermal loads is defined in terms of the displacement components $(u_0^0, u_0^1, w_0^0, w_0^1)$. The displacement components of a neighboring stable state differ by (u_1, u_2, w_1, w_2) with respect to the equilibrium position. Thus, the total displacements of a neighboring state are

$$
\begin{aligned}
u_0 &= u_0^0 + u_0^1 \\
w_0 &= w_0^0 + w_0^1
\end{aligned}
\tag{10}
$$

The stability equation of an FGM beam under thermal loading is assumed to be given by eliminating (u_0^1) as

$$\frac{d^4 w_0^1}{dx^4} + \lambda^2 \frac{d^2 w_0^1}{dx^2} = 0 \tag{11}$$

Where

$$\lambda^2 = \frac{\overline{A} N_T}{\overline{A}\,\overline{C} - \overline{B}^2} \tag{12}$$

The parameter λ is a constant and the Eq. (11) is a linear homogeneous equation whose general solution is

$$w_0^1(x) = D_1 \sin(\lambda x) + D_2 \cos(\lambda x) + D_3 x + D_4 \tag{13}$$

Where D_1, D_2, D_3 and D_4 are undetermined constants calculated via the boundary conditions.

$$
\begin{aligned}
w_0^1(x) &= D_1 \sin(\lambda x) + D_2 \cos(\lambda x) + D_3 x + D_4 \\
u_0^1(x) &= \frac{\overline{B}}{\overline{A}} \lambda D_1 \cos(\lambda x) - \frac{\overline{B}}{\overline{A}} \lambda D_2 \sin(\lambda x) + D_5 x + D_6 \\
M_0^1(x) &= \frac{\overline{A}\,\overline{C} - \overline{B}^2}{\overline{A}} \lambda^2 D_1 \sin(\lambda x) + \frac{\overline{A}\,\overline{C} - \overline{B}^2}{\overline{A}} \lambda^2 D_2 \cos(\lambda x) + \overline{B} D_5 \\
N_0^1(x) &= \overline{A} D_5
\end{aligned}
\tag{14}
$$

(13)

The following boundary conditions are imposed at the edges for FGM beam

$$u_0^1(0) = w_0^1(0) = \frac{dw_0^1}{dx}(0) = u_0^1(l) = w_0^1(l) = \frac{dw_0^1}{dx}(l) = 0 \tag{15}$$

(14)

Finally, the critical thermal force of the beam, N_{Tcr} for all cases of boundary conditions, can be expressed as follows

$$N_{Tcr} = D \frac{\overline{A}\,\overline{C} - \overline{B}^2}{\overline{A}(l)^2} \tag{16}$$

Where D is a constant and depends on the type of boundary conditions (clamped-clamped, simply supported-simply supported, clamped-roller edges, simply supported-roller edges, clamped-simply supported).

Thermal Buckling Solution

Buckling of FGM Beams Under Non-Linear Temperature Across the Thickness

The FGM beams are subjected to transversely non-linear temperature rise, and the increments of temperature on top surface and bottom surface are T_t and T_b, respectively. Four sides of the beam are adiabatic with environment. Due to the increments of transversely temperature inside FGM beams are assumed to be the function of thickness coordinate z, the increments $T = T(z)$ satisfy the following one-dimensional thermal conduction equation

$$\frac{d}{dz}\left[\left(K(z)\frac{dT}{dz}\right)\right] = 0 \tag{17}$$

This model ignores the time of heat conduction, and the change of temperature due to work produced by the deformations is also neglected. However, the non-linear temperature fields can be obtained easily by using the boundary conditions as

$$T(z) = T_t + \left(\frac{\Delta T}{\Omega}\right)\left[\sum_{i=0}^{5}\frac{(-1)^i}{(ip+1)}\left(\frac{(K_c - K_m)}{K_m}\right)^i\left(\frac{h+2z}{2h}\right)^{(ip+1)}\right] \tag{18}$$

with

$$\Omega = \sum_{i=0}^{5}\frac{(-1)^i}{(ip+1)}\left(\frac{(K_c - K_m)}{K_m}\right)^i \tag{19}$$

Numerical Results and Discussion

In this study, various numerical examples are presented and discussed for verifying the accuracy and efficiency of the present theory in predicting buckling stability of FG beams with various boundary conditions under mechanical nonlinear thermal loadings through the thickness. For the verification purpose, the results obtained by the present theory are compared with the existing data in the literature. It is assumed that the functionally graded beam is made of a mixture of aluminum and alumina. The Young modulus and coefficient of thermal expansion for aluminum are $E_m = 70$ GPa, $\alpha_m = 23\times10^{-6}$ /°C and $K_m = 204$ W/m˚K and for alumina are $E_c = 380$ GPa, $\alpha_c = 7{,}4\times10^{-6}$ /°C and $K_c = 10{,}4$ W/m˚K, respectively. It is assumed that the temperature difference between the metal-rich surface of the FGM and reference temperature is $T_m - T_r = 5°C$.

Table 1 present the comparisons of the critical buckling temperature for a CR FG beam under non-linear temperature rise with results of Kiani and Eslami (2015) for different values power law index *p*. It can be concluded that the results obtained by the present model and those obtained by Kiani and Eslami (2015) are identical for all considered values of power law index *p*. As we can see, our results are in excellent agreement with those published. It can be concluded that the present theory is efficient for the prediction of critical thermal buckling loads.

Table 1. Critical buckling temperature for a CR FG beam non-linear temperature rise for different values of power law index *p* with porosity coefficient $\xi = 0$, $(l/h = 8)$

Temperature load	Theory	p p=0.2	p=1	p=2	p=4	p=5	p=6	p=10
Non linaire	Kiani(2010)	1542.24	965.23	745.45	541.15	325.70	245.12	141.52
	Present	1542.24	965.23	745.45	541.15	325.70	245.12	141.52

Critical buckling temperature of FG beam under linear and non-linear temperature rise for different values of power law index *p*, porosity coefficient ξ and thickness ratio l/h is illustrated in table 2. For nonlinear temperature distribution across the thickness, the buckling temperature decreases with the increase of the power law index *p*. It can be conclude that the critical buckling temperature difference decreases as the thickness ratio and power law index increases and that the maximum critical buckling temperature is obtained with a porosity coefficient equal to $\xi = 0.2$.

Table 2 Critical buckling temperature for a SS FG beam under non-linear temperature rise for different values of power law index *p*, porosity coefficient ξ and thickness ratio l/h

l/h	$\xi = 0$				$\xi = 0.15$				$\xi = 0.2$			
	p=0.2	p=1	p=3	p=8	p=0.2	p=1	p=3	p=8	p=0.2	p=1	p=3	p=8
5	7882.6064	5363.8274	4153.6144	4010.3236	9245.1247	5843.2816	4199.4816	605.1055	11961.7043	6386.9652	3764.3410	3859.2009
15	864.9335	584.4105	451.3542	436.3786	956.2357	637.7606	458.3493	309.4740	1317.6582	698.2690	409.1272	420.8147
25	303.5197	202.0572	155.17341	150.4630	302.4521	221.3189	159.0587	151.2763	466.1345	243.1733	140.7101	145.7438
35	148.8445	96.7149	73.5726	71.6903	120.2457	106.5850	76.6011	151.2763	231.5311	117.7898	66.7585	69.9590
45	85.1921	53.3642	39.9920	39.2736	94.3254	59.3694	42.6679	37.8191	134.9864	66.1916	36.3257	38.7718

Conclusion

This article deals with thermo-mechanical analysis of nonlinear thermal buckling behaviour of porous FG beams with various combinations of boundary conditions under non-linear thermal loadings distribution through the thickness based on Euler–Bernoulli beam theory. Comparison studies are presented out for a large number of beams with different values of thickness ratio, power law index and various combinations of boundary conditions. It can be conclude that the critical buckling temperature difference decreases as the thickness ratio and power law index increases. From the results and the comparisons between the different porosity distributions, it was found that the different distributions give values that are more at least close with the exception of . Finally, some new results critical thermal buckling loads of FG beams with porosity are reported in tabular form for a wide range of thickness ratio and power law index. This new results can be used for comparison with other beam models developed in the future.

Scientific Ethics Declaration

The authors declare that the scientific ethical and legal responsibility of this article published in EPSTEM journal belongs to the authors.

Acknowledgements or Notes

* This article was presented as a poster presentation at the International Conference on Technology, Engineering and Science (www.icontes.net) held in Antalya/Turkey on November 14-17, 2024.

References

Akavci, S.S. (2016). Mechanical behavior of functionally graded sandwich plates on elastic foundation. *Composites Part B: Engineering*, *96*, 136-152.

Akbas, S. D. (2015). Wave propagation of a functionally graded beam in thermal environments. *Steel and Composite Structures*, *19*(6), 1421-1447.

Alwabli, A. , Kaci, A., , Bellifa, H., Bousahla A, A., & Tounsi, A. (2021). The nano scale buckling properties of isolated protein microtubules based on modified strain gradient theory and a new single variable trigonometric beam theory. *Advances in Nano Research*, *10*(1) 15-24.

Arefi, M. (2015a). Elastic solution of a curved beam made of functionally graded materials with different cross sections. *Steel Composite Structures*, *18*(3), 659-672.

Arefi, M. (2015b). Nonlinear electromechanical analysis of a functionally graded square plate integrated with smart layers resting on Winkler-Pasternak foundation. *Smart Structure Systems*, *16*(1), 195-211.

Abdeldjalil, B., Abdelmoutalib, B., Mohamed, C., Rabie, H. Z., & Mohamed, B. B. (2023). Validation of the Ruees-Voight homogenisation model for glass powder-based eco-concretes. *The Eurasia Proceedings of Science Technology Engineering and Mathematics*, *26*, 93-99.

Belbachir, A., Belbachir, N., Bahar, S., Benbakhti, A., Louhibi, Z. S., & Amziane, S. (2024). Unlocking resilience: examining the influence of fluid viscous dampers on seismic performance of reinforced-concrete structures in earthquake-prone regions. *Periodica Polytechnica Civil Engineering*, *68*(4), 1393-1404.

Bellifa, H., Benrahou, K. H., Hadji, L., Houari, M. S. A., & Tounsi, A. (2016). Bending and free vibration analysis of functionally graded plates using a simple shear deformation theory and the concept the neutral surface position. *Journal of the Brazilian Society of Mechanical Sciences and Engineering*, *38,* 265-275.

Bellifa, H., Tounsi, A., Benbakhti, A., Abdelkader, F., & Benrahou, K. (2017). A new first shear deformation plate theory for dynamic stability analysis of S-FGM plates based on physical neutral surface. In *CFM 2017-23ème Congrès Français de Mécanique*.

Bellifa, H., Benrahou, K.H., Bousahla, A.A., Tounsi, A., & Mahmoud, S.R. (2017). Nonlocal zerothorder shear deformation theory for nonlinear postbuckling of nanobeams, *Structural Engineering and Mechanics, 62*(6) 695-702.

Bellifa H., , Bousahla, A., , Chikh, A., Bourada, F., Tounsi, A. (2021). Influence of porosity on thermal buckling behavior of functionally graded beams. *Smart Structures and Systems, 27*(4), 719-728.

Benbakhti, A., Benfrid, A., Harrat, Z. R., Chatbi, M., Bouiadjra, M. B., & Krour, B. (2024). An analytical analysis of the hydrostatic bending to design a wastewater treatment plant by a new advanced composite material. *Journal of Composite & Advanced Materials/Revue des Composites et des Matériaux Avancés*, *34*(2),177-188.

Benfrid, A., Benbakhti, A., Harrat, Z. R., Chatbi, M., Krour, B., & Bouiadjra, M. B. (2023). Thermomechanical analysis of glass powder based eco-concrete panels: Limitations and performance evaluation. *Periodica Polytechnica Civil Engineering*, *67*(4), 1284-1297.

Chaabane, L. A. (2019). Analytical study of bending and free vibration responses of functionally graded beams resting on elastic foundation. *Structural Engineering and Mechanics, An Int'l Journal*, *71*(2), 185-196.

Chen, D., Yang, J., & Kitipornchai, S. (2015). Elastic buckling and static bending of shear deformable functionally graded porous beam. *Composite Structures*, *133*, 54-61.

Darabi, A., & Vosoughi, A. R. (2016). A hybrid inverse method for small scale parameter estimation of FG nanobeams. *Steel and Composite Structures*, *20*(5), 1119-1131.

Ebrahimi, F. , & Barati, M. R. (2016). Thermal buckling analysis of size-dependent FG nanobeams based on the third-order shear deformation beam theory. *Acta Mechanica Solida Sinica, 29* (5), 547–554.

Eltaher, M. A., Khairy, A., Sadoun, A. M., & Omar, F. A. (2014). Static and buckling analysis of functionally graded Timoshenko nanobeams. *Applied Mathematics and Computation*, *229*, 283-295.

Feldman, E., & Aboudi, J. (1997). Buckling analysis of functionally graded plates subjected to uniaxial loading. *Composite Structures*, *38*(1-4), 29-36.

Jabbari, M., Mojahedin, A., Khorshidvand, A. R., & Eslami, M. R. (2014). Buckling analysis of a functionally graded thin circular plate made of saturated porous materials. *Journal of Engineering Mechanics*, *140*(2), 287-295.

Jabbari, M., Hashemitaheri, M., Mojahedin, A., & Eslami, M. R. (2014). Thermal buckling analysis of functionally graded thin circular plate made of saturated porous materials. *Journal of Thermal Stresses*, *37*(2), 202-220.

Javaheri, R., & Eslami, M. (2002). Thermal buckling of functionally graded plates. *AIAA Journal*, *40*(1), 162-169.

Karami, B., Shahsavari, D., & Janghorban, M. (2018). Wave propagation analysis in functionally graded (FG) nanoplates under in-plane magnetic field based on nonlocal strain gradient theory and four variable refined plate theory. *Mechanics of Advanced Materials and Structures*, *25*(12), 1047-1057.

Kiani, Y. & Eslami, M. R. (2010). Thermal buckling analysis of functionally graded material beams. *International Journal of Mechanics and Materials in Design, 6* (3), 229–238.

Maachou, S., Benbakhti, A., & Moulgada, A. (2024). Comparative study of mechanical behavior between an adhesive made from date palm waste and FM-73 adhesive. In *Materials Science Forum* (Vol. 1125, pp. 65-69). Trans Tech Publications Ltd.

Najafizadeh, M. M., & Heydari, H. R. (2004). Thermal buckling of functionally graded circular plates based on higher order shear deformation plate theory. *European Journal of Mechanics-A/Solids*, *23*(6), 1085-1100.

Semmah, A., Bellifa, H., Bourada, F., Bousahla, A. A., Tounsi, A., Mohamed, S. M., & Selim, M. M. (2024). Exploring the effect of axial magnetic fields on the thermal stability of SWBNNTs resting on elastic medium using the N-TBT. *The European Physical Journal Plus*, *139*(6), 504.

Simsek, M. (2010). Fundamental frequency analysis of functionally graded beams by using different higher-order beam theories. *Nuclear Engineering and Design*, *240*(4), 697-705.

Tounsi, A., Houari, M. S. A., & Benyoucef, S. (2013). A refined trigonometric shear deformation theory for thermoelastic bending of functionally graded sandwich plates. *Aerospace Science and Technology*, *24*(1), 209-220.

Author Information

Hichem Bellifa
University Djillali Liabes of Sidi Bel Abbes, Materials and Hydrology laboratory, Algeria
Contact e-mail: bellifa.hichem@gmail.com

Abdelmoumen Anis Bousahla
University Djillali Liabes of Sidi Bel Abbes, Materials and Hydrology laboratory, Algeria

Abdeldjalil Benbakhti
University Centre of Maghnia, Algeria

To cite this article:

Bellifa, H., Bousahla, A. A., & Benbakhti, A. (2024). Effect of porosity on the nonlinear thermal stability of functionally graded material beams under various boundary conditions. *The Eurasia Proceedings of Science, Technology, Engineering & Mathematics (EPSTEM), 32,* 455-462.

The Eurasia Proceedings of Science, Technology, Engineering & Mathematics (EPSTEM)
ISSN: 2602-3199

The Eurasia Proceedings of Science, Technology, Engineering & Mathematics (EPSTEM), 2024

Volume 32, Pages 463-475

IConTES 2024: International Conference on Technology, Engineering and Science

Study of the Mechanical Properties and the Durability of Concrete Based on Recycled Wastes Aggregates

Youcef Ghernouti
University M'Hamed Bougara of Boumerdes

Bahia Rabehi
University M'Hamed Bougara of Boumerdes

Sabria Malika Mansour
University M'Hamed Bougara of Boumerdes

Abstract: This work focuses on the valorization and recycling of waste materials of brick aggregates (BA) and demolition concrete aggregates (DCA) for the formulation and mechanical characterization as well as the study of the durability of concrete.Five (05) concrete formulations; a control concrete based on natural aggregates and four concrete formulations based on recycled aggregates by volume substitution of natural aggregates with rates of 25% and 50% brick waste and 50%, 75% demolition concrete waste, were studies in the fresh state to estimate the workability and the density and in the hardened state to estimate the mechanical properties and the durability of concretes: Compressive and flexural strengths, impermeability to water and the diffusion of chloride ions.The results of this experimental study show that the increase in the rate of demolition or brick aggregates wastes in substitution of natural aggregates causes a decrease in the mechanical characteristics and the durability of the concrete. Nevertheless, concrete mixes containing 50% of recycled aggregates have good mechanical resistance and good durability which are close to that of concrete based on natural aggregates. Therefore, the results obtained suggest a possible use of brick and demolition concrete wastes, as aggregates in the formulation of structural concretes.

Keywords: Waste, Brick, Demolition concrete, Recycled aggregates, Durability

Introduction

Aggregate is one of the main ingredients in producing concrete. It covers 75% of the total for any concrete mix. The strength of the concrete produced is dependent on the properties of aggregates used. However, the construction industry is increasingly making higher demands of this material and is feared to accommodate the many requests at one time. Hence need for an alternative coarse aggregate arises (Sivakumar et al., 2014).

The use of recycled aggregates from construction and demolition wastes is showing prospective application in construction as alternative to primary (natural) aggregates. Research on the usage of waste construction materials is very important since the materials waste is gradually increasing with the increase of population and increasing of urban development. The reasons that many investigations and analysis had been made on recycled aggregate are because recycled aggregate is easy to obtain and the cost is cheaper than virgin aggregate (Saadani, 2006).

Faced with the ever-increasing needs for material resources and the requirements and conditions for preserving the environment in a vision of sustainable development, it has become necessary and relevant to prospect and

- Selection and peer-review under responsibility of the Organizing Committee of the Conference

study all the possibilities and opportunities for reusing and recovering waste and industrial by-products, particularly in the field of civil engineering and public works (Hobnob & Belachia, 2011).

In Algeria, an abusive use of a non-renewable resource of natural aggregates is observed even for the production of simple elements such as sidewalks. For this use, demolition materials can be an ‘economic and ecological’ alternative. The production of recycled aggregates developed in the early 80s, it meets the need for another source of aggregates and the reduction of waste volumes (Saadani, 2006). In this context, the use of recycled products takes on its full meaning. The right approach is to use the 'right product', for the 'right use', under the 'right conditions'.

This waste has been the subject of work using, for example, marble as aggregates in concrete (Saadani, 2006), ceramics (Shruthi et al., 2016; Anderson et al., 2016; Abadou et al., 2016; Al Bakri et al., 2013; Rabehi et al., 2017), tires (Fedroff et al, 1996; Segre & Joekes, 2000), glass (Tung et al, 2012; Kou & Poon, 2009, Topcu et al, 2008), but also waste from brick demolitions (Debieb & Kenai, 2008; Poon & Chan, 2006; Bhanbhro et al., 2014; Khalaf, 2006; Ghernouti et al., 2016) and crushed concrete (Berredjem et al, 2015; Silva et al ,2015; Gomez, 2002; Tu et al., 2006). Some studies have shown the benefit of combining bricks and demolition waste in the manufacture of hydraulic concrete (Meftah & Arabi, 2011; Bourmatte, 2017; Kenai & Debieb, 2011). Other work focuses on the recovery and recycling of plastic waste for the formulation and characterization of concrete based on this waste (Guendouz et al., 2015; Rebeiz, 2007; Siddique et al., 2008; Ghernouti et al., 2012; Ghernouti et al., 2014; Boucedra et al., 2020).

In this study, natural aggregates were replaced by waste materials of brick aggregates and demolition concrete aggregates to produce concrete. Then, the fresh and hardened states properties of the concrete: workability, compressive and flexural strengths, impermeability to water and the diffusion of chloride ions of the recycled waste concretes were examined by conducting physic- mechanical and durability tests.

Experimental program

Materials Used

Cement

All concrete mixtures investigated in this work were prepared with Ordinary Portland cement (OPC) CEMII/A42.5.

Water

The water used for mixing concrete is drinking water.

Super Plasticizer

As super plasticizer, a new generation super-plasticizer high range water reducer, named Master Glenium 26, based on polycarboxylate with solid contend of 30% and specific gravity of 1.08 was used to achieve the required workability of all mixtures.

Aggregates

In this work, we used three types of aggregates for making concrete: natural aggregates recycled concrete demolition waste aggregates and recycled brick waste aggregates.

- The natural aggregates used are natural sand (NS), with a maximum particle size of 3 mm and two natural crushed limestone gravel with particle size between 3/8 and 8/15 (Fig 1)
- The recycled concrete demolition waste aggregates used in this work come from local sources resulting from the crushing of demolition concrete waste to different grain sizes: sand 0/3 and gravels (3/8 and 8/15) (Fig 2)
- The recycled brick waste aggregates used come from local sources resulting from the crushing of brick waste to different grain sizes: sand 0/3 and gravels (3/8 and 8/15) (Fig 2)

The physical properties of the aggregates used are given in tables 1 and 2.

Table 1. Physical properties of fines aggregates

	Natural sand	Recycled brick waste sand	Recycled demolition concrete sand
Apparent density, (g/cm^3)	1.56	1.26	1.24
Specific gravity, (g/cm^3)	2.64	2.22	2.3
Visual sand equivalent, VES (%)	81	26.52	73.45
Fineness modulus	3	2.3	3.4
Water absorption (%)	3	19	8

Table 2. Physical properties of coarse aggregates

	Natural coarse aggregates (3/8 and 8/15)	Recycled brick coarse aggregates (3/8 and 8/15)	Recycled demolition concrete coarse aggregates (3/8 and 8/15)
Apparent density, (g/cm^3)	1.20	1.02	1.19
Specific gravity, (g/cm^3)	2.38	2.27	2.4
Los Angeles (%)	28.5	24.7	28.5
Micro-Deval (%)	27.5	26.4	27.2

Figure 1. Natural aggregates

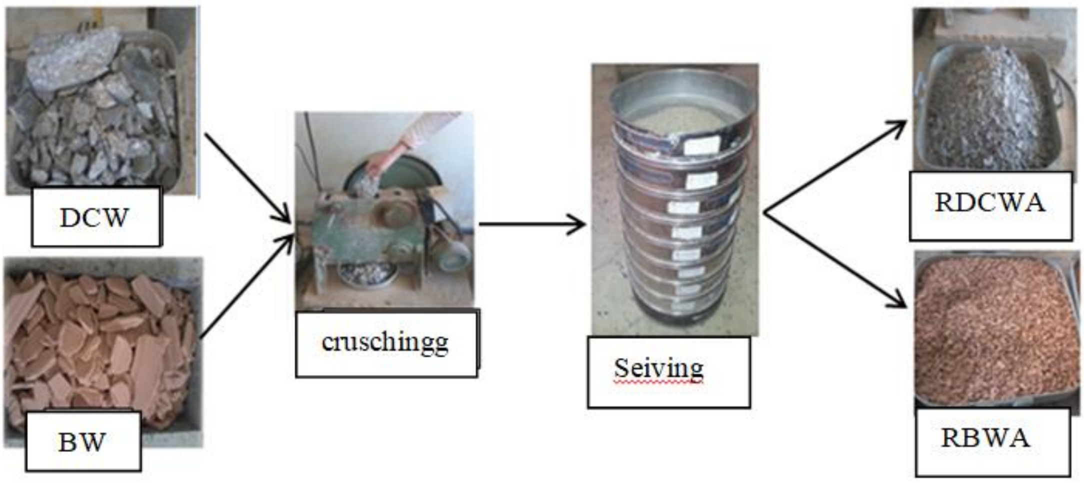

Figure 2. Preparation of recycled aggregates

Mixtures Proportion

The concrete formulation method used, is the "Dreux Gorisse" method (Dreux & Festa, 1998). Five (05) concrete formulations were studied; a control concrete based on natural aggregates (C-NA) and four (4) mixtures based on recycled aggregates by volume substitution of natural aggregates with rates of 25% and 50% recycled brick waste (C-25BW, C-50BW) and 50%, 75% Recycled demolition concrete waste (C-50DCW,C-75DCW). All mixtures concretes were made with a constant W/C ratio (0.46) and cement amount of 400 kg/m^3, respectively.

Fresh State Tests

Two tests were carried out in the fresh state of all concretes mixtures, the first is the Abrams cone slump test according to the specification of EN 12350-2 to measure workability. The other is the fresh bulk density determination test according to the recommendations of EN 12350- 6.

Figure 3. Fresh state tests: Slump test and bulk density.

Hardened State Tests

Bulk Density and Mechanical Strengths Tests

The bulk density of hardened SCC concretes cured 28days was measured according to the standard NF EN 12390-7; it was calculated by dividing the dry weight of each sample by its overall volume. The tests performed to determine the mechanicals strengths were compressive and flexural strengths at the age of 28 days. The compressive strength carried out on cubic specimens (10x10x10) cm according to standard NF EN 12390-3 and the flexural strength on prismatic specimens (7x7x28) cm, according to standard NF EN 12390-5. The test results were reported as the average of three tested specimens

Durability Tests

This study evaluated the three following durability indicators: Water absorption and porosity, water permeability test and Diffusion of chloride ions test.

Water Absorption and Porosity:

Water absorption and porosity tests of all concretes were carried out on specimen discs of (11x5) cm at the age of 28 days. The porosity was determined by the knowledge of the saturated and oven-dried mass of samples. The dried mass was obtained after drying saturated in an oven at 60°C until constant weight. The method used is a variant of water porosity by hydrostatic weighing. It gives the value of the total porosity but does not allow the pore distribution to be determined.

The water absorption test was carried out on the same samples which were served for the determination of porosity according to ASTM C642-13. The dry mass of each sample was recorded and then they were totally immersed in water at 20°C until they achieved a constant mass. The constant mass was taken as the saturated mass of sample after 24h. The absorption percentage was then obtained by the ratio of the amount of water absorbed to oven-dried mass.

Water Permeability Test

The water permeability test is a method of determining the depth of penetration of water under pressure into hardened concrete. Water permeability measurements were carried out according to standard NF EN 12390-8. (28). Cube specimens with dimensions of 150x150x150 mm were casted, demoulded 24 hours after casting and conditioned for 28 days in a moisture chamber. The specimens were then placed into a water permeability measurement apparatus, and a sealing ring with an inner diameter of 100 mm was placed on top. A constant water pressure of 500 kPa was exerted on the specimens for 72 hours. At the end of this period the specimens were split, and the maximum depth of penetration was measured to assess the extent of water permeation.

Diffusion of Chloride Ions Test

The resistance to penetration of chloride ions in concretes is one of the most important questions about the durability of concrete structures. When the chloride concentration exceeds a certain threshold, a depassivation steel occurs and there is a beginning of corrosion of reinforcing steel (Thomas, 1996; Alonso et al., 2000). Consequently, the development of protection materials with resistance to penetration of chlorides is required for concrete structures. For this test we used cylindrical specimens (11x22) cm which are sawn to obtain 5 cm discs, whose hardening was in drinking water for up to 28 days. The samples are introduced into a concentrated solution of 10% NaCl, to evaluate the durability of all concretes to the penetration of chloride ions; we followed the evolution of the depth of penetration of chloride ions at 28. The solutions were changed every 7 days until the age of 28 days. Each test specimen is divided into two parts and then solution of silver nitrate $AgNO_3$ was poured on each section according to UNI 79287 (1978). A whitish color appeared on the specimen surface, using a caliper measuring the depth of penetration of chloride ions.

Figure 4. Compressive and flexural strength tests

Figure 5. Water absorption and porosity tests

Figure 6. Water permeability test

Figure 7. Diffusion of chlorine ions test

Results and Discussion

Workability

The results of slump tests of all mixtures concrete studied are shown in figure 8. The obtained results show that the increase in the rate of demolition concrete or brick waste aggregates reduces the slump value but these decrease is more remarkably by the use of brick waste, in fact the recycled brick waste aggregates is more porous than natural aggregates, leads the mixture to a high water absorption resulting in a decrease in workability. The concretes based on 25% and 50% of recycled brick waste aggregates have very low slump 4 and 0 cm, which corresponds to a firm concrete. However, it was necessary to vary the water content, due to their absorption, to obtain the required consistency that guarantees the S2 class of flowability.

For recycled demolition concrete waste aggregates, the phenomenon is less remarkable because they have similar characteristics of natural aggregates. The mixtures containing 50% and 75% of recycled demolition concrete waste aggregates exhibited satisfactory slump flows in the range of 15 and17cm respectively, which is an indication of a good fluidity of these concretes. The same findings were reported by (Khalaf & DeVenny, 2005) that in case of using crushed brick aggregate in concrete, it will be less workable than concrete containing natural aggregates.

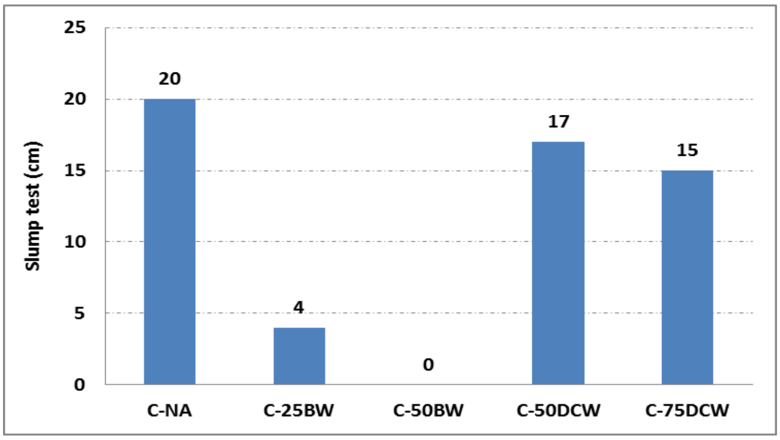

Figure 8. Slump test of all mixtures

Fresh Bulk Density

Figure 9, show the fresh bulk density test results of all mixtures concretes. It was clearly observed according these results, that increasing the rate of brick or demolition concrete waste aggregates by substitution of naturel aggregates, decreases the bulk density of all mixtures. The low density of the recycled aggregates used compared to the natural aggregates is the probable cause of this difference.

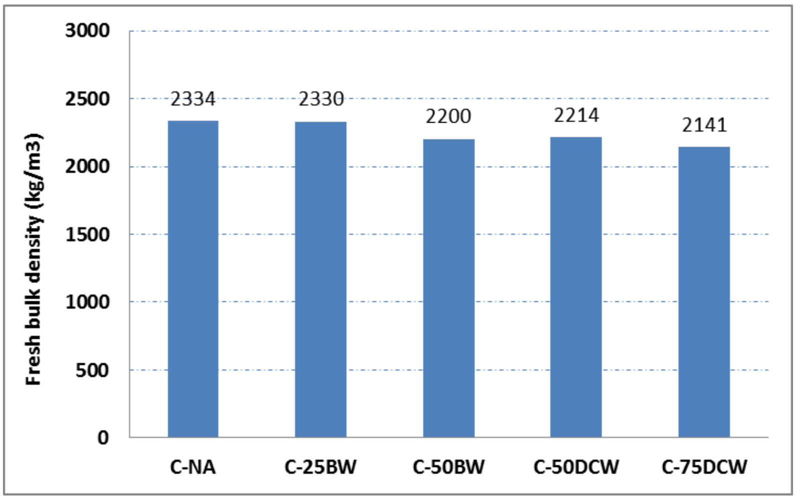

Figure 9. Fresh bulk density of all mixtures

Dry Bulk Density

The Dry bulk density values in kg/m3 for the all concretes mixes at 28 days curing time as a function of the substitution percentage of natural aggregates are shown Figure 10. Density values ranges from 2141 to 2214 kg/m^3 for concrete containing DCW aggregates and 2200 to 2330 kg/m^3 for concrete containing BW aggregates, while the control mixture exhibit the largest dry bulk density in the order to 2325 kg/m^3. A decrease in bulk density of concretes can be observed as the percentage of recycled aggregate content increases.

The hardened bulk density for 50% replacement of BW aggregates had dropped around 8.94%. Even up to 50% replacement by DCW aggregates, the Hardened bulk density gets reduced only to a maximum of 5.3% with respect to that of control concrete. There is a drop of 9 % bulk density for the 75% DCW aggregates.

The reduced dry bulk density of the concretes based on recycled aggregates is due to the reduced unit weight of recycled aggregates compared to natural aggregates. These results are similar to those obtained by Sadek (2012). The decreasing of hardned bulk density of concrete by increasing the recycled aggregate ratio was found by several authors (Hansen, 1992; Sanchez de Juan, 2004)

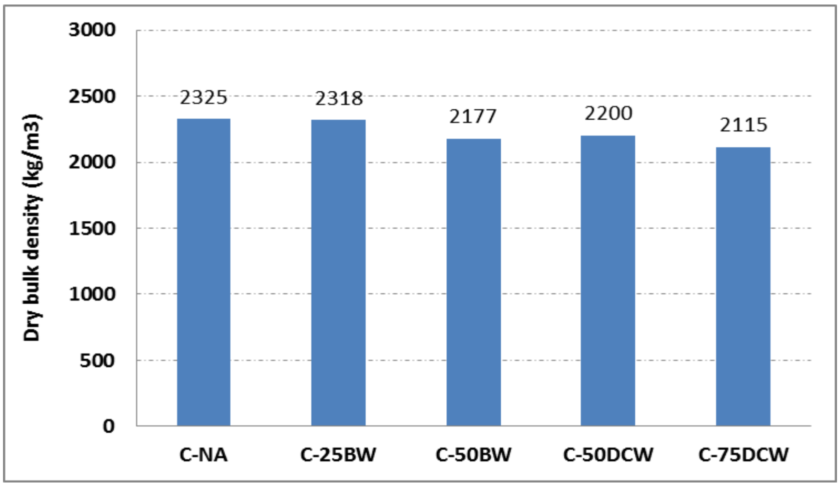

Figure 10. Dry bulk density of all concretes

Compressive and Flexural Strength

Figures 11 and 12 illustrate the mechanical strengths evolution of all mixtures concretes. It can be observed that all concrete samples based on natural aggregates or recycled wastes aggregates, have a compressive strength higher then 29MPa at the age of 28 days, so we can classify them as structural concretes. A decrease in the compressive and flexural strength for all concrete compositions based on recycled brick and demolition concrete wastes aggregates, compared to the control concrete based on natural aggregates is recorded. This decrease in mechanical strengths can be explained by the decrease in the compactness of the granular mixture which causes an increase in porosity and a decrease in resistance, as well as the low hardness of the recycled aggregates wastes used compared to natural aggregates.

We note that for a rate of 25% and 50% of recycled brick waste aggregates (C25-BW and C50-BW), the loss of compressive strength reaches 12.94% and 16.42% respectively compared to the control concrete. For the flexural strength, we noticed the same trend. Indeed, by increasing the rate of recycled waste aggregates substitution, the flexural strength decreases.

The concretes based on recycled demolition waste aggregates (C50-DCW and C75-DCW) also presents a decrease in mechanical strengths according to the rate of substitutions, or we recorded a loss of compressive strength in the order of 16.17% with 50% of the recycled demolition concrete aggregates waste compared to the control concrete, this loss increases in the case of 75% of these aggregates and reaches 27.87%. Differences between compressive and flexural strengths of concrete based on BW and DCW are negligible for the same rate of substitution.

On the basis of the results presented figure 11 and 12, it was concluded that compressive and flexural strength of concrete decreases when the recycled aggregate ratio increases, This conclusion is similar to results of other authors (Yang et al., 2008; Xiao et al., 2005; Poon et al., 2004), who found that compressive strength decreases with increasing quantity of recycled aggregates in concrete with the same effective water-cement ratio. However, in these experiments, recycled aggregate was obtained from demolished concrete structures of unknown compressive strength. Hansen (1992) find out that substitution of natural aggregate with recycled concrete aggregate up to 30% has no significant influence on concrete compressive strength. On the other hand Mirjana et al. 2(010) concluded that differences between measured compressive strengths of concrete made entirely with natural aggregate (R0) as a control concrete and two types of concrete made with natural fine and recycled coarse aggregate (50% and 100% replacement of coarse recycled aggregate) are insignificant (all results belong to the same set of results). This conclusion led to the fact that coarse aggregate type didn't influence the concrete compressive strength value in this experimental research. These results confirm the statement that compressive strength of RAC depends more on the quality of recycled aggregate than on the quantity.

Results of previous work on recycled aggregate concrete vary in wide limits, sometimes are even opposite, but general conclusions about the properties of concrete with recycled coarse aggregate compared to concrete with natural aggregate are decreased compressive strength up to 25% (Hansen, 1992; Rahal, 2007; Yang et al., 2008, Ajdukiewicz & Kliszczewicz, 2002) and decreased flexural strength up to 10% (Hansen, 1992; Yang et al., 2008; Ajdukiewicz & Kliszczewicz, 2002).

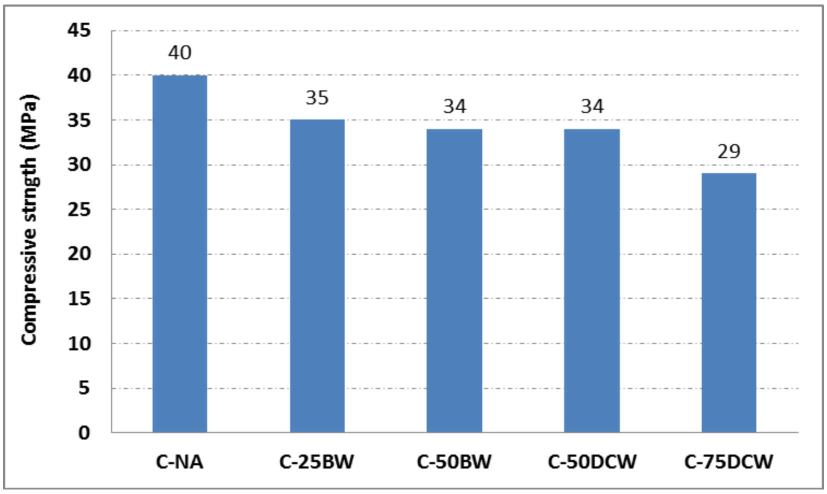

Figure 11. Compressive strength evolution of all concretes

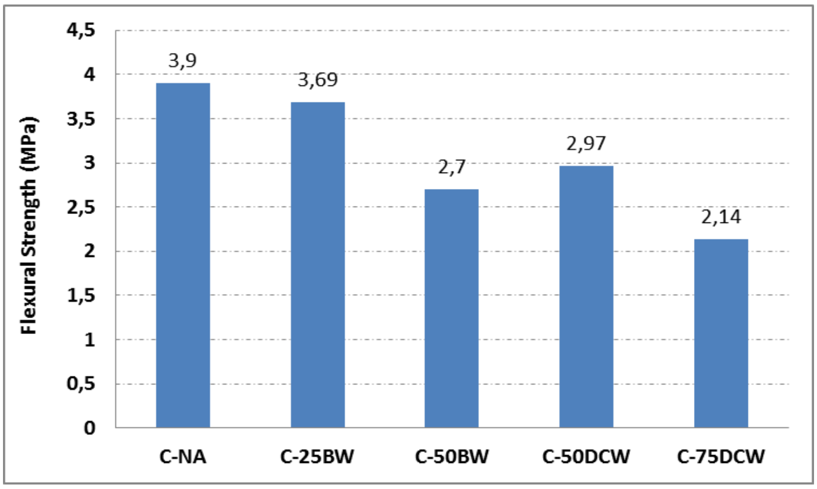

Figure12. Flexural strength evolution of all concretes

Water Absorption and Porosity

The main agents of deterioration require the presence and movement of water within the material itself. The presence of water can cause freeze-thaw damage to the product. Furthermore, water can carry chlorides and sulfates as well as other harmful ions. Hence, the absorption of the product has a great effect on its durability

(Dina M. Sadek, 2012). The Water absorption and porosity of all concretes studied are given in figure 13, according to the results obtained, it can be seen that the incorporation of the waste used (brick and demolition waste aggregates) in the concrete causes an increase in the porosity, probably due to the geometric shape of the recycled aggregates which are flattened compared to the natural aggregates, this leads the mixture to a high absorption of water.

Water absorption of recycled brick aggregate was from 19% and 8% for recycled demolition concrete aggregates. Water absorption of aggregate reflects to water absorption of concrete. That is reason why water absorption of concrete with recycled aggregate was significantly increases compared to concrete with natural aggregates. The water absorption for 50% replacement of brick waste aggregates (BW) had increased around 215.38%. Even up to 50% replacement by Demolition concrete waste aggregates (DCW), water absorption gets increased only to a maximum of 88.46% with respect to that of control concrete. There is an increase of 276.92 % water absorption for the 75% DCW aggregates.

The main problem of using the recycled brick as an aggregate for concrete is its high water absorption. The water absorption of recycled crushed brick aggregate concrete is significantly greater than the one of the natural aggregate concrete (Debieb & Kenai, 2008). The evolution porosity of all concretes varies with the same trend as the water absorption.

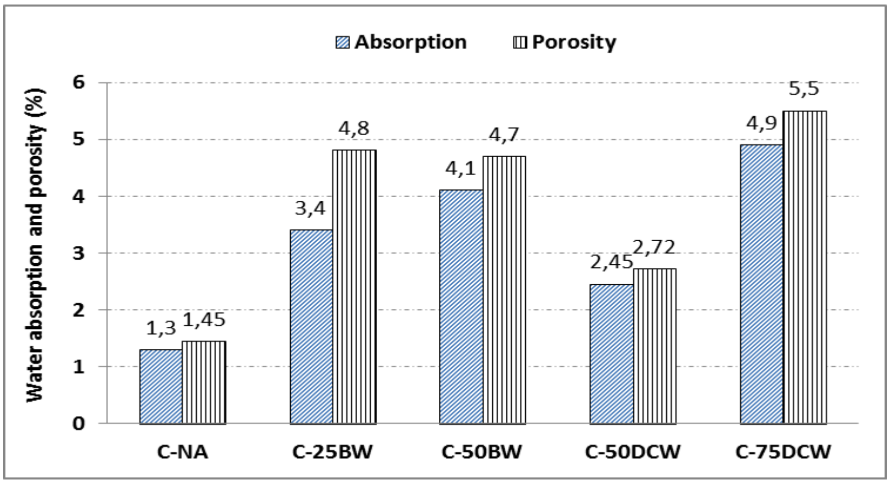

Figure 13. Evolution of water absorption and porosity of all concretes

Water Permeability

Figure 14 shows the water penetration depth values for the different concrete compositions.

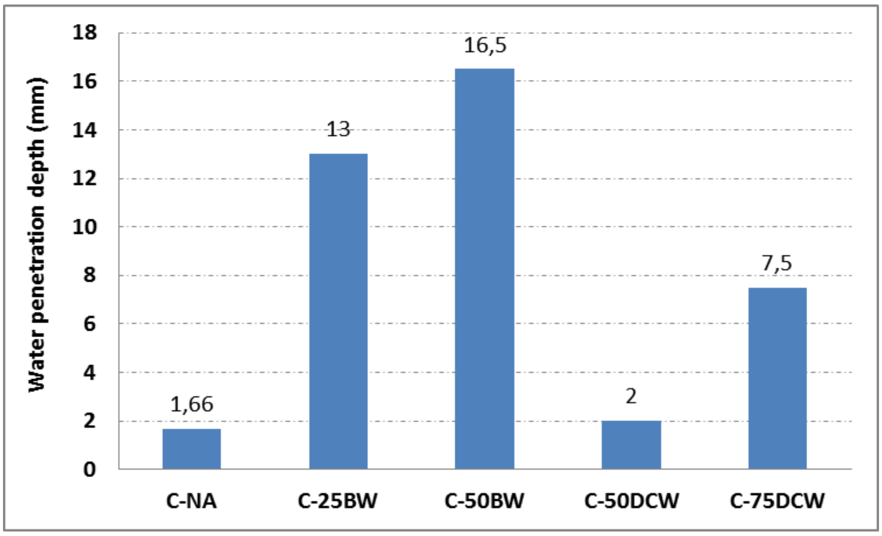

Figure 14. Water penetration depth of all concrete

The obtained results indicate that the substitution of natural aggregates by the brick or demolition concrete aggregates causes an increases of the depth of water penetration and when the rates of substitution increase, the water penetration depth values increased, and it is more remarkably by the substitution of brick waste. For demolition waste, the phenomenon is less remarkable. This increase in water penetration depth is probably due to the height porosity of the concretes based on recycled aggregates compared to the control concrete based on natural aggregates.

The maximum value of water penetration depth recorded is that of the concrete based on 50% brick waste aggregates (C-50BW) it is in the order of 16.5 mm, while in the control concrete based on natural aggregates (C-NA) the value is 1.66mm. In all tested concretes, the average water penetration depth is smaller than 50 mm and so the tested concretes according to DIN 1045 are considered watertight.

Diffusion of Chloride Ions

Figure 15 chows the depth chloride ion penetration in the all concrete compositions, an increase in the depth of chloride ion penetration of all concrete compositions based on recycled brick and demolition concrete wastes aggregates is recorded compared to the control concrete based on natural aggregates (figure 17). This increase can be explained by the decrease in the compactness of the granular recycled wastes mixtures, which causes an increase in the porosity and a decrease in the penetration resistance of the concrete. Two variants concrete, the control concrete based on natural aggregates (C-NA) and the concrete based on 50% demolition concrete aggregates (C-50DCW), showed better resistance to the penetration of chloride ions. The penetration depth of the chloride ions of the two variants (C-NA) and (C-50DCW) is of the order of 9 mm and 1.05 mm respectively. The test method followed in the present investigation to determine the depth of chloride ions penetration is reliable and accurate, and has also been recommended by other researchers (Erhan & Kasım, 2007; Wee et al, 2000; Otsuki et al, 1992; Wee et al, 1999; Meck & Sirivivatnanon, 2003).

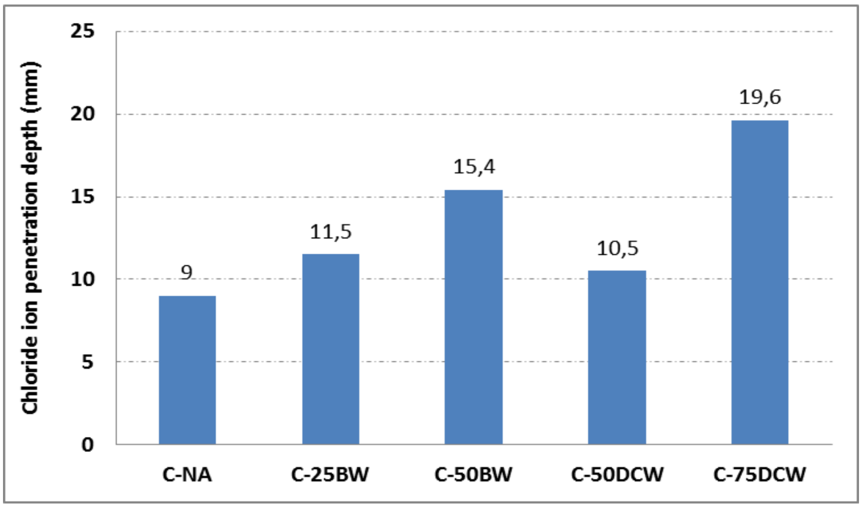

Figure 15. Chloride ion penetration depth in the all concretes

Conclusion

In this study, the effects of brick and demolition concrete wastes aggregates on the physic-mechanical properties and the durability study of concrete are presented. Based on the above results, the following conclusions can be drawn:

- The increase in the rate of demolition concrete or brick waste aggregates reduces the slump value of concrete but this decrease is more remarkably by the use of brick waste. The concretes based on 25% and 50% of recycled brick waste aggregates have very low slump 4 and 0 cm, which corresponds to a firm concretes. The mixtures containing 50% and 75% of recycled demolition concrete waste aggregates exhibited satisfactory slump flows in the range of 15 and17cm respectively, which is an indication of a good fluidity of these concretes.

- A decrease in bulk density of concretes is recorded when the percentage of recycled aggregates content increases. The hardened bulk density for 50% replacement of BW aggregates had dropped around 8.94%. Even up to 50% replacement by DCW aggregates, the Hardened bulk density gets reduced only to a maximum of 5.3% with respect to that of control concrete. There is a drop of 9 % bulk density for the 75% DCW aggregates.
- A decrease in the compressive and flexural strength for all concrete based on recycled brick and demolition concrete wastes aggregates, compared to the control concrete based on natural aggregates is recorded, and when the recycled aggregate ratio increases, the compressive and flexural strengths decreased.
  All concrete samples based on natural aggregates or recycled wastes aggregates, have a compressive strengths higher then 29MPa at the age of 28 days, so we can classify them as structural concretes.
- The substitution of natural aggregates by brick and demolition concrete waste aggregates in the concrete causes an increase in the porosity; this leads the mixture to a high absorption of water.
- The substitution of natural aggregates by the brick or demolition concrete aggregates causes increases of the water penetration depth, and when the rates of substitution increase, the water penetration depth values increased, and it is more remarkably by the substitution of brick waste.
  In all tested concretes, the average water penetration depth is smaller than 50 mm and so the tested concretes according to DIN 1045 are considered watertight.
- An increase in the depth of chloride ion penetration of all concrete based on recycled brick and demolition concrete wastes aggregates is recorded compared to the control concrete based on natural aggregates. The depth of chloride ion penetration of the control concrete based on natural aggregates (C-NA) and the concrete based on 50% demolition concrete aggregates (C-50DCW) is in the order of 0.9 mm and 1.05 mm respectively, consequently these variants showed better resistance to the penetration of chloride ions.

Finally we we concluded that the increase in the rate of recycled demolition concrete or brick wastes aggregates in substitution of natural aggregates causes a decrease in the physic-mechanical characteristics and the durability of the concrete. Nevertheless, concrete mixes containing 50% of recycled wastes aggregates have good mechanical properties and good durability which are close to that of concrete based on natural aggregates. Therefore, the results obtained suggest a possible use of brick and demolition concrete waste as aggregates in the formulation of structural concretes.

Scientific Ethics Declaration

The authors declare that the scientific ethical and legal responsibility of this article published in EPSTEM Journal belongs to the authors.

Acknowledgements or Notes

* This article was presented as an oral presentation at the International Conference on Technology, Engineering and Science (www.icontes.net) held in Antalya/Turkey on November 14-17, 2024.

References

Abadou, Y., Mitiche-Kettab, R., & Ghrieb, A. (2016). Ceramic waste influence on dune sand mortar performance. *Construction and Building Materials*, *125*, 703-713.

Ajdukiewicz, A., & Kliszczewicz, A. (2002). Influence of recycled aggregates on mechanical properties of HS/HPC. *Cement and Concrete Composites*, *24*(2), 269-279.

Alonso, C., Andrade, C., Castellote, M., & Castro, P. (2000). Chloride threshold values to depassivate reinforcing bars embedded in a standardized OPC mortar. *Cement and Concrete Research, 30*(7), 1047–1055.

Anderson, D. J., Smith, S. T., & Au, F. T. (2016). Mechanical properties of concrete utilising waste ceramic as coarse aggregate. *Construction and Building Materials*, *117*, 20-28.

Berredjem, L., Arabi, N., Molez, L., & Jauberthie, R. (2015). Propriétés mécaniques et durabilité des bétons à base de graviers et sables recyclés issus de béton de démolition. In *Deuxième Conférence Internationale Francophone Nouveaux Matériaux et Durabilité.*

Bhanbhro, R., Memon, I., Ansari, A., Shah, A., & Memon, B. A. (2014). Properties evaluation of concrete using local used bricks as coarse aggregate. *Engineering*, *6*(5), 211-216.

Boucedra, A., Bedrina. M., & Ghernouti, Y., (2020). Study of the acoustical and thermo-mechanical properties of dune and river sand concretes containing recycled plastic aggregates. *Construction and Building Materials*, 256, 119447.

Bourmatte, N., & Houari, H. (2017). *Granulats recyclés de substitution pour bétons hydrauliques* (Doctoral dissertation, Université Frères Mentouri-Constantine 1).

Debieb, F., & Kenai, S. (2008). The use of coarse and fine crushed bricks as aggregate in concrete. *Construction and Building Materials*, *22*(5), 886-893.

Dreux G., & Festa. J. (1998). *New guide of concrete and its constituents*. Paris, France: Eyrolles.

Erhan, G., & Kasım, M. (2007). Comparative study on strength, sorptivity, and chloride ingress characteristics of air-cured and water-cured concretes modified with metakaolin. *Materials and Structures*, *40*, 1161–1171.

Fedroff, D., Ahmad, S., & Savas, B. Z. (1996). Mechanical properties of concrete with ground waste tire rubber. *Transportation Research Record*, *1532*(1), 66-72.

Ghernouti, Y., & Rabehi, B. (2012). Strength and durability of mortar made with plastics bag waste (MPBW). *International Journal of Concrete Structures and Materials*, *6*(3), 145-153.

Ghernouti, Y., & Rabehi, B. (2012). Strength and durability of mortar made with plastics bag waste (MPBW). *International Journal of Concrete Structures and Materials*, *6*, 145-153.

Ghernouti, Y., Rabehi, B., Bouziani, T., & Chaid., R. (2016). Valorization of brick wastes in the fabrication of concrete blocks. *Materialials and Technology*, *50*(6), 911-916.

Gómez-Soberón, J. M. (2002). Porosity of recycled concrete with substitution of recycled concrete aggregate: An experimental study. *Cement and Concrete Research*, *32*(8), 1301-1311.

Guendouz, M., & Debieb, F. (2015). Formulation et caractérisation d'un béton de sable à base de déchets plastiques. In *Rencontres Universitaires de Génie Civil*.

Gutiérrez, A. (2004). Influence of recycled aggregate quality on concrete properties. In *International RILEM Conference on the Use of Recycled Materials in Building and Structures* (pp. 545-553). RILEM Publications SARL.

Hansen, T.C., (1992). *Recycling of demolished concrete and masonry* (p.316). Oxfordshire, UK: Taylor and Francis.

Hebhoub, H., & Belachia, M. (2011). Introduction de sable de déchet de marbre dans le béton hydraulique. *Nature & Technology*, (4), 41-46.

Kenai, S., & Debieb, F. (2011). Caractérisation de la durabilité des bétons recyclés abase de gros et fins granulats de briques et de béton concassés Characterization of the durability of recycled concretes using coarse and fine crushed bricks and concrete aggregates. *Materials and Structures*, *44*, 815-824.

Khalaf, F. M. (2006). Using crushed clay brick as coarse aggregate in concrete. *Journal of Materials in Civil Engineering*, *18*(4), 518-526.

Khalaf, F. M., & DeVenny, A. S. (2005). Properties of new and recycled clay brick aggregates for use in concrete. *Journal of Materials in Civil Engineering*, *17*(4), 456-464.

Kou, S.C., & Poon, C.S. (2009). Properties of self-compacting concrete prepared with recycled glass aggregate. *Cement and Concrete Composites, 31*(2), 107–13.

Meck, E., & Sirivivatnanon, V. (2003). Field indicator of chloride penetration depth. *Cement and Concrete Research*, *33,* 1113–1117.

Meftah. H., & Arabi. N, (2011) 'Les granulats recyclés humidifies: Comportements des bétons frais et durcis' *XXIX éme Rencontres Universitaires de Génie Civil*, *2,* 401-410

Mirjana. M., Vlastimir. R., & Snežana., M., (2010). Recycled concrete as aggregate for structural concrete production. *Sustainability, 2,* 1204-1225.

Otsuki, N., Nagataki, S., Nakashita, K. (1992). Evaluation of AgNO3 nitrate solution spray method for measurement of chloride penetration into the hardened cementitious matrix materials. *ACI Materials Journal, 89*(6), 587–592.

Poon, C.S., Shui, Z.H., Lam, C.S., Fok, H., Kou, S.C. (2004). Influence of moisture states of natural and recycled aggregates on the slump and compressive strength of concrete. *Cement and Concrete Research*, *34*, 31-36.

Poon. C.S., & Chan. D, (2006). Paving blocks made with recycled concrete aggregate and crushed clay brick. *Construction and Building Materials*, *20* (8), 569-577.

Rabehi, B., Ghernouti, Y., Boumchedda, K., & Zermout, S. (2017). Recycling of waste from the ceramic industry as an active cementitious addition. *3rd International Porous and Powder Materials Symposium and Exhibition PPM*, 12-15.

Rahal, K. (2007). Mechanical properties of concrete with recycled coarse aggregate. *Build. Environ. 1*, 407-415.

Rebeiz, K.S. (2007). Time-temperature properties of polymer concrete using recycled PET. *Cement and Concrete Composites*, *17,* 603–608.

Saadani, S., & Houari, H. (2000). *Comportement des bétons à base de granulats recyclés* (Doctoral dissertation, Université Frères Mentouri-Constantine 1).

Sadek D.M., (2012). Physico-mechanical properties of solid cement bricks containing recycled aggregates. *Journal of Advanced Research 3,* 253–260

Segre, N., & Joekes, I. (2000). Use of tire rubber particles as addition to cement paste. *Cement and Concrete Research*, *30*(9), 1421-1425.

Shruthi. H. G., Prasad. G. M. E., Taj. S., & Pasha. R. S. (2016). Reuse of ceramic waste as aggregate in concrete. *International Research Journal of Engineering and Technology (IRJET), 3*(7), 115–119.

Siddique, R., Khatib, J., & Kaur, I. (2008). Use of recycled plastic in concrete: A review. *Waste Manage, 28,* 1835–1852.

Silva, R. V., Brito, J. D., Neves, R., & Dhir, R. (2015). Prediction of chloride ion penetration of recycled aggregate concrete. *Materials Research*, *18*(2), 427-440.

Sivakumar, N., Muthukumar, S., Sivakumar, V., Gowtham, D., & Muthuraj, V. (2014). Experimental studies on high strength concrete by using recycled coarse aggregate. *International Journal of Engineering and Science*, *4*(1), 27-36.

Thomas, M. (1996). Chloride thresholds in marine concrete. *Cement and Concrete Research*, *26*(4), 513-519.

Topcu, I. B., Boga, A. R., & Bilir, T. (2008). Alkali–silica reactions of mortars produced by using waste glass as fine aggregate and admixtures such as fly ash and Li2CO3. *Waste Management*, *28*(5), 878-884.

Tu, T. Y., Chen, Y. Y., & Hwang, C. L. (2006). Properties of HPC with recycled aggregates. *Cement and Concrete Research*, *36*(5), 943-950.

Tung-Chai. L., Chi-Sun. P., Shi-Cong. K, (2012) 'Influence of recycled glass content and curing conditions on the proper+ties of self-compacting concrete after exposure to elevated temperatures. *Cement and Concrete Composites, 34* (2), 265-272.

Wee, T. H., Suryavanshi, A. K., & Tin, S. S. (1999). Influence of aggregate fraction in the mix on the reliability of the rapid chloride permeability test. *Cement and Concrete Composites, 21,* 59–72.

Wee, T. H., Suryavanshi, A. K., & Tin, S. S. (2000). Evaluation of rapid chloride permeability test (RCPT) results for concrete containing mineral admixtures. *ACI Materials Journal, 97*(2), 221–232.

Xiao, J., Li, J., & Zhang, C. (2005). Mechanical properties of recycled aggregate concrete under uniaxial loading. *Cement and Concrete Research*, *35*(6), 1187-1194.

Yang, K.H., Chung, H.S., & Ashour, A. (2008). Influence of type and replacement level of recycled aggregates on concrete properties. *ACI Materials Journals, 105*(3), 289-296.

Author Information

Youcef Ghernouti
University M'Hamed Bougara of Boumerdes
Independence Avenue, 35000 Boumerdes, Algeria
Contact e-mail: y.ghernouti@*univ-boumerdes.dz*

Bahia Rabehi
University M'Hamed Bougara of Boumerdes
Independence Avenue, 35000 Boumerdes, Algeria

Sabria Malika Mansour
University M'Hamed Bougara of Boumerdes
Independence Avenue, 35000 Boumerdes, Algeria

To cite this article:

Ghernouti, Y., Rahebi, B., & Mansour, S.M. (2024). Study of the mechanical properties and the durability of concrete based on recycled wastes aggregates. *The Eurasia Proceedings of Science, Technology, Engineering & Mathematics (EPSTEM), 32,* 463-475.

The Eurasia Proceedings of Science, Technology,
Engineering & Mathematics (EPSTEM)
ISSN: 2602-3199

The Eurasia Proceedings of Science, Technology, Engineering & Mathematics (EPSTEM), 2024

Volume 32, Pages 476-482

IConTES 2024: International Conference on Technology, Engineering and Science

Assessment of Fatigue and Corrosion Effects on Coating from the SMAW Process

Djilali Allou
Research Center in Industrial Technologies (CRTI)

Sarra Djemmah
Research Center in Industrial Technologies (CRTI)
University of Mons

Youcef Faci
Research Center in Industrial Technologies (CRTI)

Rachid Amraoui
Research Center in Industrial Technologies (CRTI)

Abstract: This study examines how wear impacts the mechanical properties of the interface between weld overlay Inconel 182 and a 25CD4 substrate when using the SMAW process. The microstructure at the interface of the Inconel 182 /25CD4 substrate mainly featured columnar Ni-γ, with a gradient of Ni ;Cr and Fe, elements diffusing from the melting limits to the type II boundary close to the interface. A scratch resistance test was carried out on the interface to evaluate the adhesion and wear resistance of the Inconel 182 overlay and the 25CD4 substrate. The test was performed under a constant load of approximately 100 N, with a spherical indenter of 0.6 mm radius, creating a (5 mm) scratch length over a period of 50 s at a scratch speed (0.1 mm/s). There are two zones. A reloading zone (Inconel 182) with totally Viscoplastic contact another zone which is that of the substrate presenting elastic deformations at the same time. The variation of the coefficient of friction over time across the substrate/recharge interface reveals three distinct zones. The coefficient of friction increases rapidly until it reaches a maximum of 0.63, corresponding to a zone of high roughness (inter-diffusion zone). The electrochemical characteristics of the Inconel 182 overlay and the 25CD4 substrate in a 3.5% NaCl solution revealed evidence of galvanic corrosion.

Keywords: 25CD4, Corrosion, Wear, SMAW process, Inconel 182 weld overlay

Introduction

The oil industry relies on blowout preventers (BOPs) as part of well control equipment to shut down the well in case of a blowout (Han et al., 2015; Specification API, 2010). Xindu et al. has shown that both hard and soft shut-ins are viable options, but hard shut-ins are the fastest and safest method for closing the well (Han et al., 2013; Metals, 2000). During drilling operations, it is essential to regularly test the BOPs every 21 days to ensure they are functioning properly as safety devices, in compliance with (API 16A R and SP53), the American Petroleum Institute Code (Lyon et al., 2024; Specification API, 2010).

In the environment of drilling, the walls of the Blowout Preventer (BOP) are subordinated to specific service conditions, including dynamic stresses and climate. The walls of the Blowout Preventer (BOP) are exposed to colorful cyclic lading conditions during drilling. The pressure of the drilling fluid, climate, and shocks, the movement of the font, as well as contraction and bending forces are some of the main conditions they face (Su

- Selection and peer-review under responsibility of the Organizing Committee of the Conference

et al., 2018). The pressure of the fluid pumped into the well fluctuates at high pressure, causing repeated stress on the BOP's walls. The drill bit encountering different creates climate and shocks, generating cyclic tension cycles. also, the weight of the drilling outfit and rods exerts contraction and bending forces, applying cyclic stresses on the walls. (Jianhong et al., 2012).

Inconel 182 is a chromium, nickel, and iron-based alloy that is highly resistant to corrosion in harsh environments. It has excellent mechanical properties at high temperatures, making it suitable for use in the chemical and petrochemical industries for manufacturing heat exchangers and reactors. Steel 25CD4, on the other hand, is a chrome-molybdenum alloy steel with high mechanical strength, toughness, and hardness. It is known for its resistance to wear, fatigue, and stress corrosion cracking, and is widely used in the manufacturing of parts that are subjected to dynamic loads, such as transmission shafts and gears, as well as for equipment requiring high strength. This study examines the impact of wear and electrochemical behavior on the mechanical properties of the interface between a weld overlay of Inconel 182 and a 25CD4 substrate, using the SMAW process in a drilling environment.

Materials and Experimental Procedures

The weld overlaid used used in this work is Inconel 182, which is provided in the form of 3.2 mm diameter electrode and coated on the surface of 25CD4 substrate using arc welding (SMAW) process. The chemical compositions of the materials used in this study are shown in Table 1.For the deposition process, the Inconel 182 electrode was connected to the positive terminal (EP), while the workpiece (25CD4 substrate) was connected to the negative terminal. The welding process was performed in two passes, working at similar speeds, with the first pass using 170 A direct current (DC) mode at 33 V and the second pass using 220 A and 34 V. The microstructure evolution was analyzed and examined by ZEISS optical microscope. Scratch measurements were conducted to evaluate the mechanical properties across the Inconel 182 /steel substrate interface. The scratch obtained at the level of the substrate interface 25CD4/ recharged by Inconel 182 in the case of the SMAW process with a typical constant load scratching ~ 100 N, in contact with spherical indentor, of a radius of 06 mm, a scratcher length of 5 mm corresponding to 50s and a scraping speed of 0.1mm/s.

Table 1. Chemical composition of the substrate and the filler metal (wt.%)

Elements / Wt%	25CD4	Inconel 182
C	0.3	0.1
Ni	0.12	61
Cr	1.04	15
Mo	0.23	-------
Mn	0.56	8
Si	0.28	0.4
Cu	0.15	0.5
P	0.01	0.3
S	0.02	0.15
Fe	bal	bal

Electrochemical impedance spectroscopy (EIS) and potentiodynamic polarization curve measurements were performed using a PGSTAT302N potentiostat and an Autolab electrochemical analyzer from Metrohm using NOVA software. The potentiodynamic polarization curves were measured at a scan rate of 0.01 V/s. The curves provide information about the corrosion behavior and enable the determination of corrosion current and potential. The EIS measurements were performed in the frequency range of 100 kHz to 100 MHz with an amplitude of 0.01 V. EIS is a powerful technique for analyzing electrochemical processes occurring at metal-electrolyte interfaces.

Results and Discussion

Microstructural Evolution

Figure 1-a) shows a cross section of a weld with a layer thickness of 6 mm. Two distinct regions can be seen: the 25CD4 base material (dark area) and the Inconel 182 layer associated with the weld (white area). The slow cooling rate during deposition promotes the transformation of austenite in the 25CD4 matrix into pearlite (dark) and fine ferrite grains (white), resulting in a unique microstructure as shown in Figure 1-b).

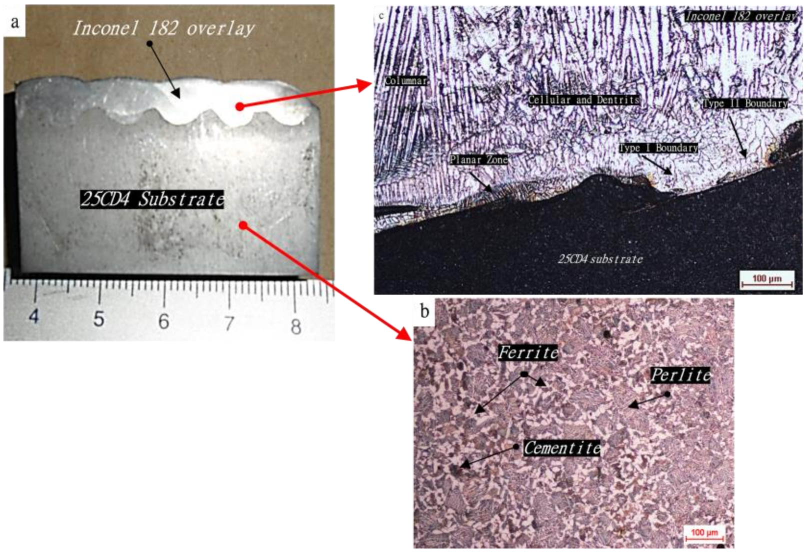

Figure 1. (**a**), Macrograph of weld overlaid Inconel 182 overlay/25CD4 substrate and optical Micrograph of different regions at the interface, fusion boundary zone: (**b**) 25CD4, (**c**) interface

Figure 1c shows the microstructure at the interface between the base material and the Inconel 182 coating. It is clear that the welded state exhibits a fine-grained structure, which is due to the high temperatures reached during welding. The microstructure of the Inconel 182 coating near the interface is shown in Figure 1c, showing the solidification morphology growing epitaxially from the steel-based interface towards the weld axis. This epitaxial growth corresponds to the planar region, which is characterized by the mixing of the chemical composition of the steel base with the Inconel elements, forming a thinning zone. This observation is consistent with previous studies (Allou et al.,2020; Bao et al.,2009; Tandon et al.,2020). The Inconel 182 overlay shows the creation of a Type I boundary, which follows the cooling direction and is aligned with the γ-structure (Shariatpanahi & Farhangi, 2010). As depicted in Figure 1c, the structure shifts from parallel to perpendicular to the line interface, forming a Type II boundary. Further away from the interface, a typical cellular-dendritic microstructure of Inconel 182 is visible.

Scratch Behavior

Figure 2 shows the MEB micrography of the scratch obtained at the level of the substrate interface 25CD4/ recharged by Inconel 182 in the case of the SMAW process with a typical constant load scratching ~ 100 N, in contact with spherical indentor, of a radius of 06 mm, a scratcher length of 5 mm corresponding to 50s and a scraping speed of 0.1mm/s.

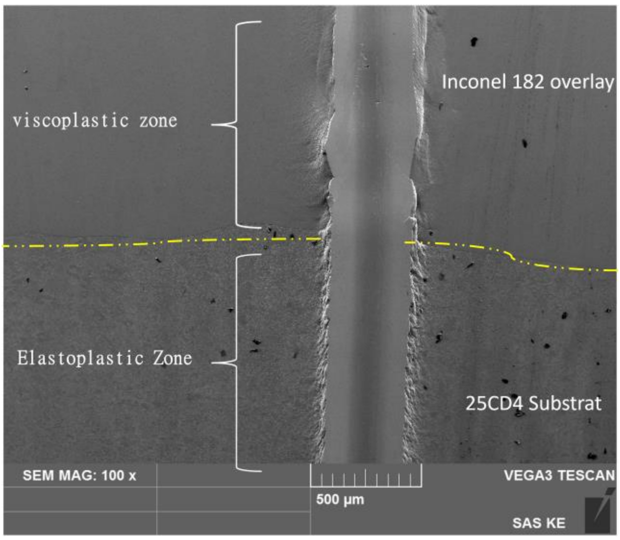

Figure 2. MEB micrography of the scratch obtained at the interface 25CD4/ recharged by Inconel 182 in the case of the SMAW process

Through this figure we can see the existence of two zones. A recharge area (Inconel 182) with a fully Viscoplastic contact with a very visible strip whose trajectory does not appear to be a perfect straight a separate non-symmetrical surface (half-circle) and another area that is that of the substrate with elastic deformations at the same time This type of contact, called plastic elastos, is caused by the appearance of fairly uniform side blades. The appearance of the secondary electron scratch at the level of the 25CD4/ interface for the SMAW process in strong magnification (Figure 2), the indenter footprint shows heterogeneous damage (different bottles) between the substrate and the recharge.

The flow of the material from both sides of the indentor takes place from the top to the bottom of the contact. Modes of deformation of the material, such as viscosity, plasticity, and friction, are involved, thus inducing an upward-down disymmetry of the contact and hence the formation of a residual rod because the material (fitting) is not elastic. We are in the presence of a plowing phenomenon; micro abrasion mechanisms appear. The upper part of the recharge is usually the most exposed to external aggression. We notice the presence of material pulling under a charge of 100 N (Figure 3).

The overlapping of the graphs of the variation of the friction coefficient depending on the time of the SMAW recharge through the substrate/recharge interface with the tangential forces (Fz(N)) are represented by figures 4. These graphs indicate the limit where the charge becomes constant and reaches 100 N. This configuration will allow us to delimit the end of zone 1. The graph of the variation of the coefficient of friction as a function of time across the substrate/load interface is shown in Figure 5, the curve presents three distinct zones.

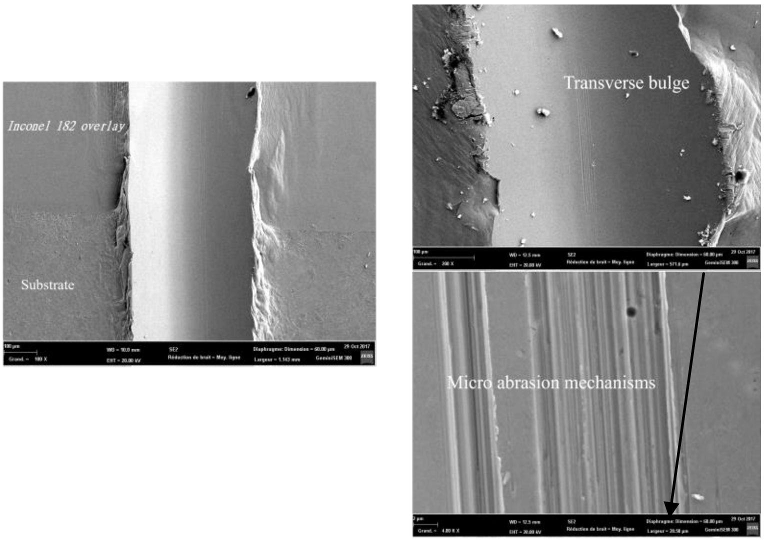

Figure 3. Appearance of the strip in e-secondary showing the emergence of the buffer, at the level of the interface

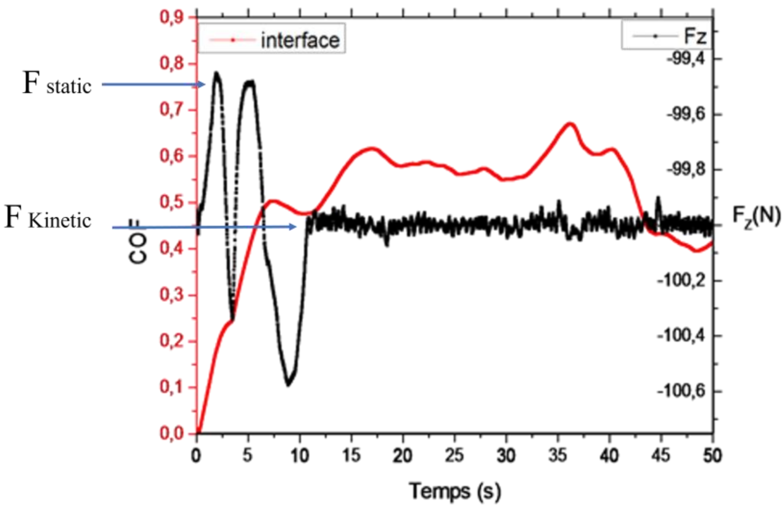

Figure 4. Superposition of the friction coefficient curves at the Substrate/ interface and the tangential force as a function of time (SMAW process)

Zone 1: Corresponds to the application of the load, where the coefficient of friction changes very rapidly. This increase is due to the presence of oxide and impurities, causing the indentor to undergo a frictional force during penetration, gradually reaching the depth of the scratch, with a coefficient of friction of 0.52 in 11 s.

Zone 2: represents the part of the substrate where the coefficient is fairly stable and constant, at around 0.55.

Zone 3: this is the resurfacing part; the coefficient of friction increases rapidly until it reaches a maximum of 0.63. This corresponds to a zone of high roughness (inter-diffusion zone). In adhesive mode, the curve falls gradually and stabilises at around 0.4. Referring to Figure 4, this value represents the upper part of the hardfacing. We note that in this zone, the curve takes on a downward trend, which seems to correspond to a sliding of the indentor without tearing of the material. In the specific case of our hardfacing, the coefficient of friction follows the trend of the hardness allocated to this hardfacing.

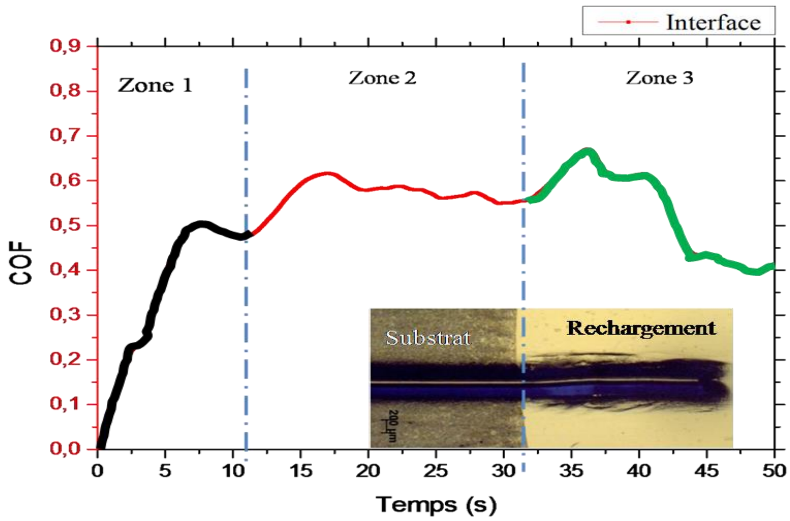

Figure 5. Curve of the coefficient of friction at the interface

Corrosion Behavior

Figure 6 shows the stacked polarisation curves for the system (substrate, interface and recharge) in a 3.5% NaCl-based electrolyte. They correspond to scan intervals between -1 and 0.1 V. The Ag/AgCl reference electrode was used for scan intervals between -0.6 and 0.4 V. We used a scan rate of 1mV/s from cathode to anode. Table 2 summarises the results of the polarisation curve in Figure 6 and shows the corrosion potential (E_{corr}), corrosion current density (i_{corr}) and corrosion rate.

Table 2. Electrochemical parameters of potentiodynamic tests

Eléments	Substrat	Interface Inconel 182 /25CD4	Reload
E_{corr} (MV)	-668	-626	-235
Icorr (µa/cm^2)	18,53	5,37	1,137
Corrosion rate (mm/year)	0,143	0,115	0,012

We observed a corrosion potential of -668 mV Ag/AgCl for the substrate and -235 mV Ag/AgCl for the Inconel 182 hard coating. The corrosion potential of the Inconel 182 interface/ substrate corresponds to an average value of -626 mV Ag/AgCl. This value is the point where the anode branch of the substrate intersects with the cathode branch of the hard facing.

Comparison of the average corrosion rates reinforces the choice of the hardfacing grade selected, as the corrosion rate of the base material (0.143 mm/yr) is higher than that of the Inconel182/base material interface (0.115 mm/yr) and the hardfacing (0.012 mm/yr). Galvanic corrosion, defined as corrosion between two materials with different potentials, follows the principle of a galvanic cell. The base material has a base potential (-668mV), while the overlay has the higher potential (-235mV), resulting in an increase in current flow. The average potential fluctuations (ΔEcorr) between base/recharge and base/interface are -433mV and -42mV respectively, with a ratio of one tenth.

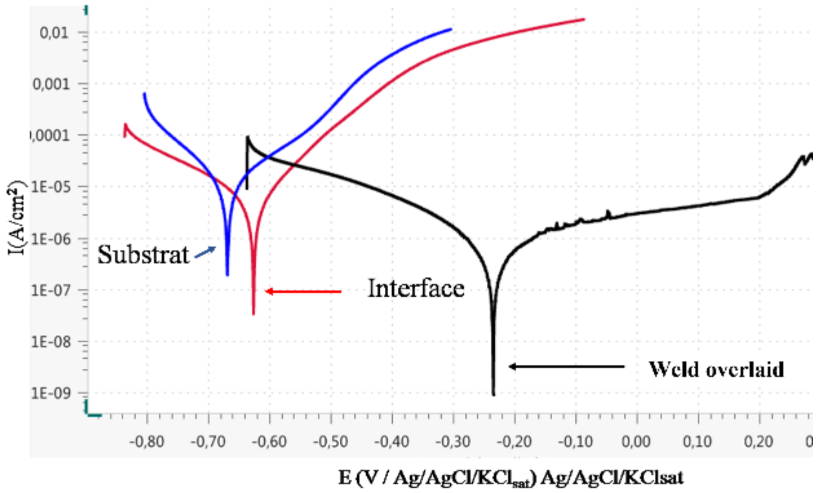

Figure 6**.** Superposition of the potentiodynamic curves

This indicates increased corrosion in a very hostile environment (3.5% NaCl).The dissimilar materials, 25CD4 substrate and Inconel 182 hardfacing, have different electrochemical potentials, which accelerates galvanic corrosion. The substrate acts as a sacrificial anode, causing it to degrade more rapidly than the hardfacing. Once the substrate degrades, the interface will be impacted. To prevent corrosion, including microscopic corrosion sites on the anode's surface, the metal couple requires a cathodic bias.

Conclusion

The effect of the impact of wear and electrochemical behavior on the mechanical properties of the interface between a weld overlay of Inconel 182 and a 25CD4 steel substrate is evaluated. The following conclusions can be drawn:

- Cross section of weld overlaid with a 6 mm layer thickness. Two distinct regions can be observed, the 25CD4 substrate (dark region) and the Inconel 182 layer referred to the weld overlay (white region).
- The friction coefficient depending on the time of the SMAW recharge through the substrate/recharge interface with the tangential forces (Fz(N))
- The scratch obtained at the level of the substrate interface 25CD4/ recharged by Inconel 182 in the case of the SMAW process. we can see the existence of two zones. A recharge area (Inconel 182) with a fully Viscoplastic contact and another area that is that of the substrate with elastic deformations at the same time This type of contact, called plastic elastos, is caused by the appearance of fairly uniform side blades
- The Inconel 182/substrate interface has a corrosion potential of around -626 millivolts, which is the point where the substrate's anode and the hardfacing's cathode meet. The existence of this galvanic cell at the interface speeds up the corrosion of the samples.

Scientific Ethics Declaration

The authors declare that the scientific ethical and legal responsibility of this article published in EPSTEM Journal belongs to the authors.

Acknowledgements or Notes

* This article was presented as a poster presentation at the International Conference on Technology, Engineering and Science (www.icontes.net) held in Antalya/Turkey on November 14-17, 2024.

* Thanks the Research Institute for Materials Science and Engineering

References

Allou, D., Miroud, D., Ouadah, M., Cheniti, B., & Bouyegh, S. (2020). Criterion for cathodic protection of 25CD4/Inconel 182 system. *Applied Surface Science*, *502*, 144100.

Bao, G., Yamamoto, M., & Shinozaki, K. (2009). Precipitation and Cr depletion profiles of Inconel 182 during heat treatments and laser surface melting. *Journal of Materials Processing Technology*, *209*(1), 416-425.

Han, C., & Zhang, J. (2013). Study on well hard shut-in experiment based on similarity principle and erosion of ram rubber. *Engineering Failure Analysis*, *32*, 202-208.

Han, C., Yang, X., Zhang, J., & Huang, X. (2015). Study of the damage and failure of the shear ram of the blowout preventer in the shearing process. *Engineering Failure Analysis*, *58*, 83-95.

Jianhong, F., Kexiong, S., Zhi, Z., Dezhi, Z., Fei, L., Xin, X., & Xin, Z. (2012). Stress analysis on drilling string vibration in gas drilling. *Energy Procedia*, *16*, 1264–1268.

Lyons, W. C., & Plisga, G. J. (2004). *Standard handbook of petroleum and natural gas engineering* (2nd ed.). Elsevier.

Metals, S. (2000). High-performance alloys for resistance to aqueous corrosion. *SM Aqueous Corrosion Book*, *28*, 68.

Shariatpanahi A, M., & Farhangi, H. (2010). Microstructure and mechanical properties of dissimilar ferritic and austenitic steel joints with an intermediate Inconel-182 buttering layer. *Advanced Materials Research*, *6*, 449–456,

Specification API. (2010). Specification for wellhead and christmas tree equipment. *API 6A*, *552*(3), 10.

Su, K., Butt, S., Yang, J., & Qiu, H. (2018). Coupled dynamic analysis for the riser-conductor of deepwater Surface BOP Drilling System. *Shock and Vibration*, *2018*(1), 6568537.

Tandon, V., Thombre, M. A., Patil, A. P., Taiwade, R. V., & Vashishtha, H. (2020). Effect of heat input on the microstructural, mechanical, and corrosion properties of dissimilar weldment of conventional austenitic stainless steel and low-nickel stainless steel. *Metallography, Microstructure, and Analysis*, *9*, 668-677.

Author Information

Djilali Allou
Research Center in Industrial Technologies (CRTI), PB 64, Chéraga, Algiers, Algeria.
Contact e-mail : djilallou@yahoo.fr

Sarra Djemmah
Research Center in Industrial Technologies (CRTI), PB 64, Chéraga, Algiers, Algeria.

Youcef Faci
Research Center in Industrial Technologies (CRTI), PB 64, Chéraga, Algiers, Algeria.

Rachid Amraoui
Research Center in Industrial Technologies (CRTI), PB 64, Chéraga, Algiers, Algeria.

To cite this article:

Allou, D., Djemmah, S., Faci, Y., & Amraoui, R. (2024). Assessment of fatigue and corrosion effects on coating from the SMAW process. *The Eurasia Proceedings of Science, Technology, Engineering & Mathematics (EPSTEM), 32,* 476-482.

The Eurasia Proceedings of Science, Technology, Engineering & Mathematics (EPSTEM)
ISSN: 2602-3199

The Eurasia Proceedings of Science, Technology, Engineering & Mathematics (EPSTEM), 2024

Volume 32, Pages 483-487

IConTES 2024: International Conference on Technology, Engineering and Science

Magnetic Control of Phase Evolution in Titanium-Based Alloys Synthesized by Ball Milling

Abderahim Abada
University of Saad Dahleb Blida

Abderrahmane Younes
Research Centre in Industrial Technologies (CRTI) Cheraga

Rachid Amraoui
Research Centre in Industrial Technologies (CRTI) Cheraga

Abstract: Nanostructured TiAlV alloys were synthesized from pure titanium, aluminum, and vanadium powders using the mechanical alloying technique in a high-energy planetary ball mill. The magnetic behavior, morphology, and microstructural properties were examined using a Vibrating Sample Magnetometer (VSM), Scanning Electron Microscope (SEM), and X-ray Diffraction (XRD), respectively. The crystallite size decreased from 48.73 nm to 9.38 nm, while lattice strain increased from 0.15% to about 0.81% after 60 hours of grinding. X-ray diffraction confirmed the formation of new phases during the grinding process. Magnetic non-destructive testing revealed that the nanocrystalline TiAlV alloy contains magnetic particles whose properties vary over time periods, attributed to the reduction in crystallite size of these particles due to collisions with the milling balls. NDT by magnetic measurement confirmed that the state of the nanocrystalline alloy can be controlled using a vibrating sample magnetometer.

Keyword: Nanostructured Tialv Alloys, Mechanical Alloying, NDT, Magnetic Measurement.

Introduction

Nanocrystalline alloys, synthesized through various methods including powder metallurgy, offer significant advantages in engineering applications. Non-destructive techniques play a crucial role in controlling nanocrystalline materials for industrial use, as they provide insights into performance evaluation without damaging the material (Abada et al., 2020; Yang et al., 2016). Titanium alloys, known for their exceptional properties, are extensively used in aerospace manufacturing despite being non-magnetic and exhibiting poor tribological behavior. Among these, TiAlV alloys are prominent, comprising α and β phases that are stable at low temperatures. However, limited research exists on the production of nanocrystalline titanium alloys via mechanical milling, a technique capable of producing nanometric structures (Metidji et al., 2020;Ter Haar et al., 2018; Daswa et al., 2018). In this study, nanocrystalline TiAlV alloy was synthesized using mechanical milling, which relies on welding and fracture phenomena caused by mechanical impacts between powder particles, grinding balls, and the jar wall.

The research aims to evaluate the alloy using magnetic non-destructive testing to identify impurities generated during grinding and their effects on different properties. The approach involves using a vibrating sample magnetometer for magnetic measurements to monitor the progression of the nanocrystalline alloy and detect defects introduced during mechanical grinding.

- Selection and peer-review under responsibility of the Organizing Committee of the Conference

Materials and Experimental Procedure

High-purity Ti, Al, and V powders were used as starting materials, with elemental compositions of 99.9%, 99.7%, and 99.9%, respectively. These powders were subjected to grinding in a high-energy planetary ball mill at room temperature and under a controlled atmosphere, using hardened Cr steel balls (20 mm diameter) at a speed of 300 rpm. A ball-to-powder weight ratio of 12:1 was employed, and the grinding time ranged from 0 to 60 hours. This process aims to produce TiAlV alloys and reduce grain sizes through severe plastic deformation. The magnetic non-destructive testing was conducted using vibrating sample magnetometers (EV9). Morphological analysis of the powders was carried out using a scanning electron microscope (Gemini SEM 300) equipped with an energy-dispersive X-ray analyzer (EDS).

Results and Discussion

Magnetic Measurements

Figure 1 depicts the relationship between magnetization and magnetic field strength at room temperature for the nanocrystalline TiAlV alloy, illustrating the impact of ball collisions during milling. Initially, the elemental powder is non-magnetic. However, after undergoing ball milling, the samples exhibit a significant increase in coercivity (Hc) and a reduction in saturation magnetization. This change in magnetic behavior indicates a transformation in the alloy's microstructure. The increase in coercivity suggests an enhancement in the material's resistance to demagnetization, which can be attributed to the refinement of grain sizes and the introduction of defects induced by the milling process. The decrease in saturation magnetization indicates a reduction in the alignment of magnetic moments within the material, possibly due to the disruption of the crystalline structure caused by severe plastic deformation during milling. These findings highlight the role of mechanical grinding in altering the magnetic properties of the nanocrystalline TiAlV alloy (Zhao et al., 2010; López-Dominguez et al., 2001; Getzlaff et al., 2008; Foner et al.,1996).

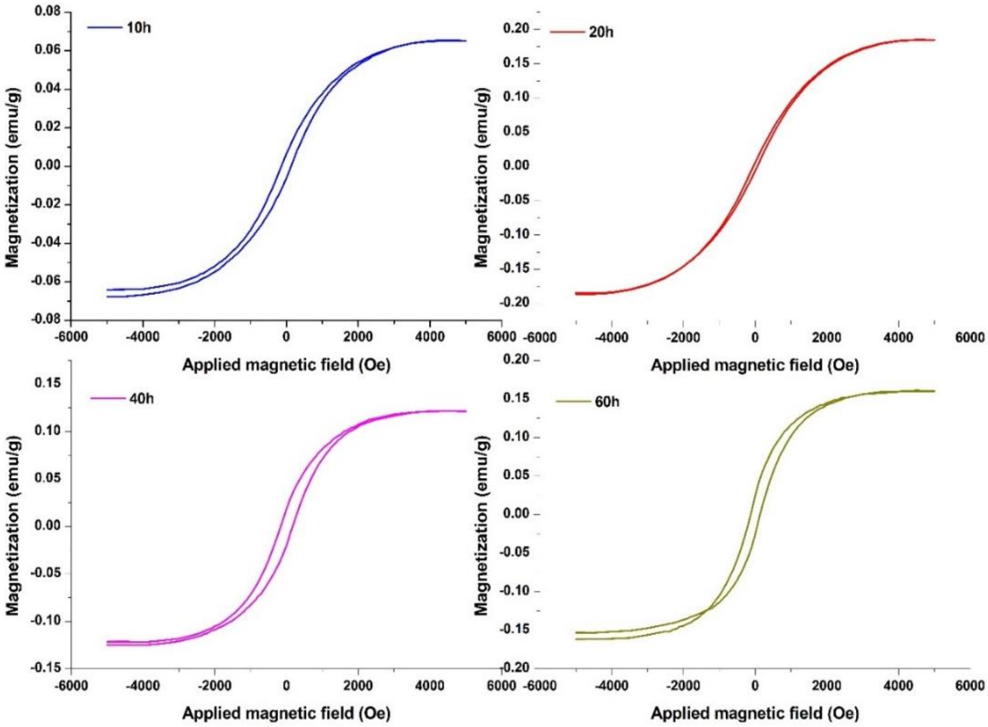

Figure 1. Hysteresis curve of nanostructured TiAlV alloy grinded for different durations

Figure 2 illustrates the variation in various magnetic parameters during mechanical alloying. The coercivity shows significant variation throughout the milling process, attributed to the reduction in crystallite size of iron particles worn off from the milling balls due to repeated ball collisions. The Ms is a key characteristic of magnetic materials, influenced by the chemical composition of the local atomic environment and their electronic structures. The presence of iron particles from the milling balls, mixed with Ti(Al) and Ti(Al,V) during milling, results in a non-saturating magnetic behavior.

This behavior suggests that the introduction of iron from the milling balls alters the local magnetic environment, affecting the alignment of magnetic moments within the material. This alteration is likely due to the introduction of defects and changes in the alloy's microstructure caused by the milling process (El-Alaily et al., 2015; Babu et al., 2020).

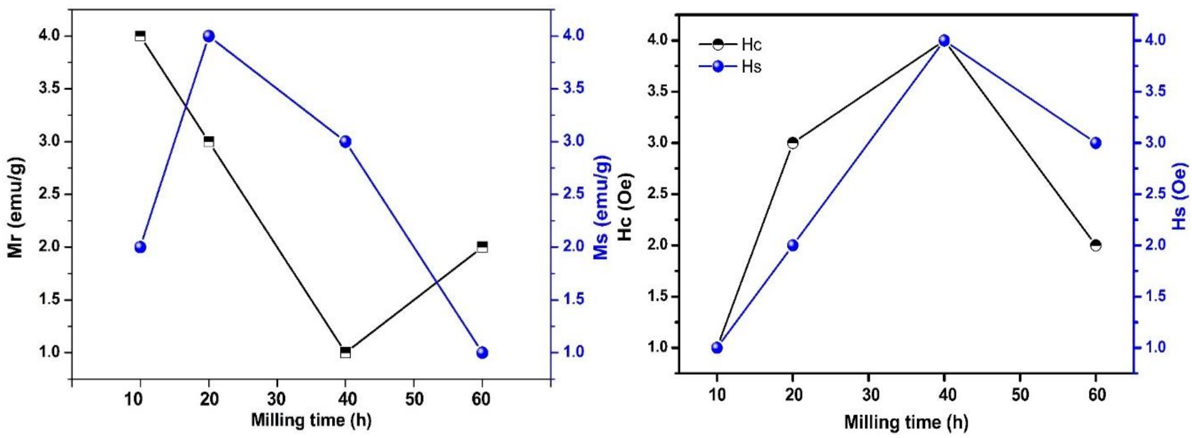

Figure 2. Different magnetic parameters as function of milling time

Morphology

Figure 3 illustrates the morphological changes in nanocrystalline TiAlV alloy at different grinding times (0, 20, and 40 hours), indicating significant variations in particle size, shape, and nature with increasing grinding time. Initially, Ti, Al, and V particles exhibit irregular shapes and sizes.

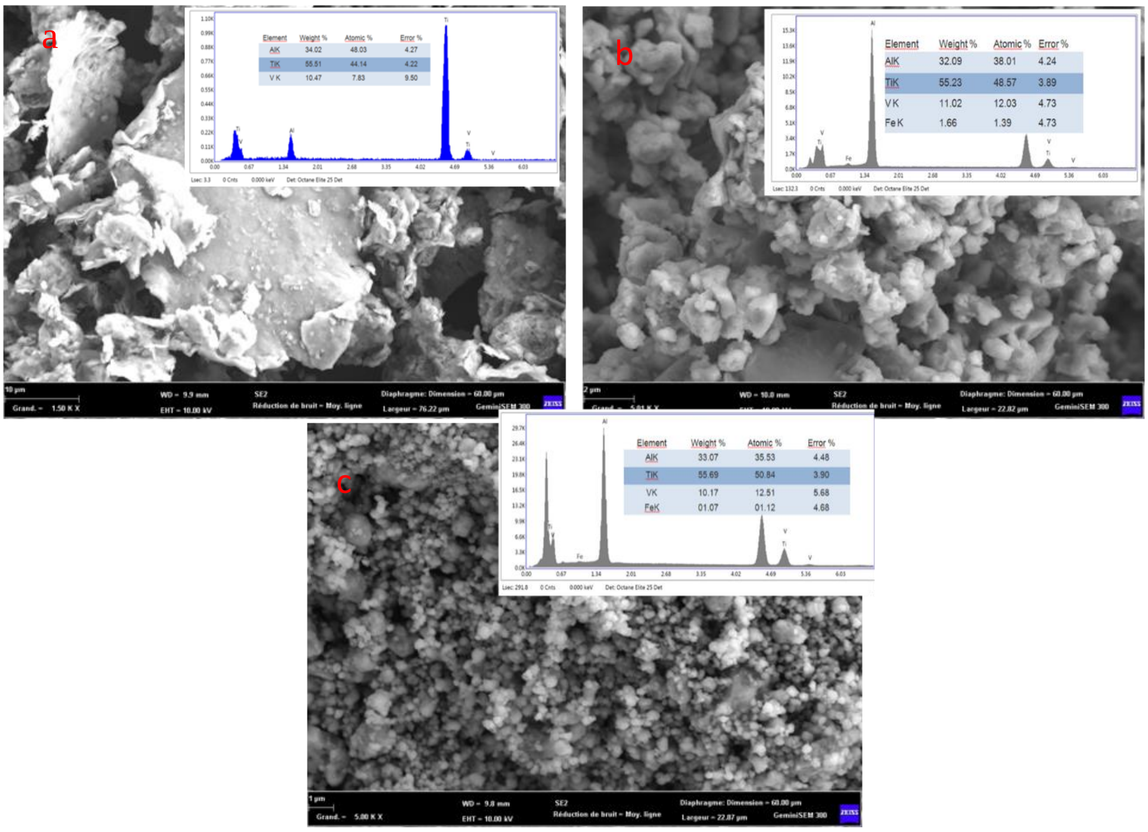

Figure 3. SEM micrographs and EDS analysis of nanostructured TiAlV alloys grinded for different duration: (a) 0 h, (b) 20 h, and (f) 40 h.

After 20 hours, particles become spherical and irregularly shaped, with an average size of 5-10 μm, attributed to repeated welding and fracturing during mechanical alloying. Further grinding reduces particle size, reaching a more homogeneous distribution after 40 hours, where fracturing and cold welding processes are in equilibrium. EDS micrographs reveal that before grinding, Ti, Al, and V elements are not homogeneously dispersed, with no contamination. During grinding, the element distribution becomes uniform, with some iron contamination from worn grinding balls, indicating the formation of TiAlV alloy powder. After 40 hours, particles show homogeneous dispersion, with some iron residue from grinding ball collisions (Dilmi et al., 2020; Younes et al., 2021; Shah et al., 2016; Mahboubi et al., 2012).

Conclusion

The synthesis of nanocrystalline TiAlV alloy through high-energy ball grinding for varying durations has been successfully achieved, revealing several stages in its formation. Initially, the elemental powders are non-magnetic. However, during milling, the coercivity varies, primarily attributed to the reduction in crystallite size of iron particles worn off from the milling balls due to repeated ball collisions. EDS analysis of the nanocrystalline TiAlV alloy after mechanical grinding indicates the presence of iron contamination from the grinding balls, confirming the magnetic behavior observed in the magnetic measurement results. This contamination corroborates the impact of ball collision on the alloy's magnetic properties. The study highlights the effectiveness of high-energy ball grinding in synthesizing nanocrystalline TiAlV alloy and underscores the importance of understanding the role of milling parameters in tailoring the alloy's properties.

Recommendations

Future research should focus on optimizing milling parameters, such as duration and ball material, to better control crystallite size and minimize iron contamination, which affects the TiAlV alloy’s magnetic properties. Using alternative grinding media or protective coatings on milling balls could further reduce contamination, allowing for more accurate magnetic measurements. Advanced characterization techniques would deepen understanding of milling effects, while testing the alloy’s magnetic behavior in varied conditions would help evaluate its suitability for targeted applications, enhancing its potential as a tailored nanocrystalline material for industrial use.

Scientific Ethics Declaration

The authors declare that the scientific ethical and legal responsibility of this article published in EPSTEM Journal belongs to the authors.

Acknowledgements or Notes

* This article was presented as a poster presentation at the International Conference on Technology, Engineering and Science (www.icontes.net) held in Antalya/Turkey on November 14-17, 2024.

References

Abada, A., Bergheul, S., & Younes, A. (2020). Mechanical and structural behaviour of TiAlV nanocrystalline elaborated by mechanical milling technique. *Micro and Nano Letters*, *15*(14), 1023–1027.

Daswa, P., Gxowa, Z., Monareng, M. J., & Mutombo, K. (2018, September). Effect of milling speed on the formation of Ti-6Al-4V via mechanical alloying. In *IOP Conference Series: Materials Science and Engineering*, *430*(1), 012030.

Dilmi, N., Bacha, N. E., & Younes, A. (2020). Structural and magnetic properties of Fe60–x Ni x (ZnO) 40 nanocomposites produced by mechanical milling and coated by thermal spraying on a steel substrate. *Powder Metallurgy and Metal Ceramics*, *59*(1), 35-45.

El-Alaily, T. M., El-Nimr, M. K., Saafan, S. A., Kamel, M. M., Meaz, T. M., & Assar, S. T. (2015). Construction and calibration of a low cost and fully automated vibrating sample magnetometer. *Journal of Magnetism and Magnetic Materials*, *386*, 25-30.

Foner, S. (1996). The vibrating sample magnetometer: Experiences of a volunteer. *Journal of Applied Physics*, *79*(8), 4740-4745.

Getzlaff, M. (2007). *Fundamentals of magnetism*. Springer Science & Business Media.

Lopez-Dominguez, V., Quesada, A., Guzmán-Mínguez, J. C., Moreno, L., Lere, M., Spottorno, J., ... & García, M. A. (2018). A simple vibrating sample magnetometer for macroscopic samples. *Review of Scientific Instruments*, *89*(3), 034707.

Metidji, N., Bacha, N. E., Younes, A., & Saidi, D. (2020). The effect of Ti addition on microstructure and magnetic properties of nanocrystalline FeAl 40 alloy powders prepared by mechanical alloying. *Powder Metallurgy and Metal Ceramics*, *59*, 160-170.

Sankhi, B. R., & Turgut, E. (2020). A low-cost vibrating sample magnetometry based on audio components. *Journal of Magnetism and Magnetic Materials*, *502*, 166560.

Shah, F. A., Trobos, M., Thomsen, P., & Palmquist, A. (2016). Commercially pure titanium (cp-Ti) versus titanium alloy (Ti6Al4V) materials as bone anchored implants—Is one truly better than the other?. *Materials Science and Engineering: C*, *62*, 960-966.

Soufiani, A. M., Karimzadeh, F., & Enayati, M. H. (2012). Formation mechanism and characterization of nanostructured Ti6Al4V alloy prepared by mechanical alloying. *Materials & Design*, *37*, 152-160.

Ter Haar, G. M., & Becker, T. H. (2018). Selective laser melting produced Ti-6Al-4V: Post-process heat treatments to achieve superior tensile properties. *Materials*, *11*(1), 146.

Yang, J., Yu, H., Yin, J., Gao, M., Wang, Z., & Zeng, X. (2016). Formation and control of martensite in Ti-6Al-4V alloy produced by selective laser melting. *Materials & Design*, *108*, 308-318.

Younes, A., Kherrouba, N., & Bouamer, A. (2021). Magnetic, optical, structural and thermal properties of copper ferrite nanostructured synthesized by mechanical alloying. *Micro & Nano Letters*, *16*(4), 251-256.

Zhao, J., Ding, H., Zhong, Y., & Lee, C. S. (2010). Effect of thermo hydrogen treatment on lattice defects and microstructure refinement of Ti6Al4V alloy. *International Journal of Hydrogen Energy*, *35*(12), 6448-6454.

Author Information

Abderahim Abada
Laboratory of Aeronautic Science, Aeronautic Institute,
University of Saad Dahleb Blida 1, Blida, Algeria
Contact e-mail: abada_75@yahoo.fr

Abderrahmane Younes
Research Centre in Industrial Technologies (CRTI)
P.OBox 64, Cheraga 16014 Algiers, Algeria

Rachid Amraoui
Research Center in Industrial Technologies (CRTI)
P.OBox 64, Cheraga 16014 Algiers, Algeria

To cite this article:

Abada, A., Younes, A., & Amraoui, R., (2024). Magnetic control of phase evolution in titanium-based alloys synthesized by ball milling. *The Eurasia Proceedings of Science, Technology, Engineering & Mathematics (EPSTEM), 32,* 483-487.

The Eurasia Proceedings of Science, Technology, Engineering & Mathematics (EPSTEM)
ISSN: 2602-3199

The Eurasia Proceedings of Science, Technology, Engineering & Mathematics (EPSTEM), 2024

Volume 32, Pages 488-514

IConTES 2024: International Conference on Technology, Engineering and Science

The Determinant of Cubic-Matrix of Order 2 and Order 3, Some Basic Properties and Algorithms

Armend Salihu
Universum International College

Orgest Zaka
Agricultural University of Tirana

Abstract: Based on geometric intuition, in this paper we are trying to give an idea and visualize the meaning of the determinants for the cubic-matrix. In this paper we have analysed the possibilities of developing the concept of determinant of matrices with three indexed 3D Matrices. We define the concept of determinant for cubic-matrix of order 2 and order 3, study and prove some basic properties for calculations of determinants of cubic-matrix of order 2 and 3. Furthermore we have also tested several square determinant properties and noted that these properties also are applicable on this concept of 3D Determinants.

Keywords: 3D determinants, Determinant properties, Computer algorithm, Time complexity.

Introduction and Preliminaries

Based on the determinant of 2D square matrices (Salihu et al., 2021b; Artin, 1991; Bretscher, 2005; Salihu, 2018; Schneide et al., 1973; Salihu et al., 2019; Lang, 1987). As well as determinant of rectangular matrices (Radić, 1966; Salihu et al., 2022b, Salihu et al., 2023; Radić, 2005; Salihu et al., 2022a; Salihu et al., 2022c; Salihu et al., 2021a; Amiri et al., 2010; Makarewicz et al., 2014). We have come to the idea of developing the concept of determinant of 3D cubic matrices, our concept is based on permutation expansion method. Encouraged by geometric intuition, in this paper we are trying to give an idea and visualize the meaning of the determinants for the cubic-matrix. Our early research mainly lies between geometry, algebra, matrix theory, etc., (see Peters-Zaka, 2023; Zaka, 2019a; Zaka-Filipi, 2016; Filipi et al., 2019; Zaka, 2017b; Zaka, 2018; Zaka, 2016; Zaka-Peters, 2020; Zaka-Peters, 2021; Zaka et al., 2020a; Zaka et al., 2020b; Zaka-Peters, 2024a; Zaka-Peters, 2024b; Deda-Zaka, 2024). This paper is continuation of the ideas that arise based on previous researches of 3D matrix ring with element from any whatever field F see (Zaka, 2017a). But here we study the case when the field F is the field of real numbers R. In the paper (Salihu-Zaka, 2023; Zaka-Salihu, 2024).

We have made progress in our research, related to cubic-matrix determinants, we have studied some basic properties related to determinants of cubic matrix, we have also tried how the Laplace expansion method works in the calculation of cubic-matrix determinants for cubic-matrix of order 2 and 3. In this paper we follow a different method from the calculation of determinants of 3D matrix, which is studied in (Zaka, 2019b). In contrast to the meaning of the determinant as a multi-scalar studied in (Zaka, 2019b). İn this paper we give a new definition, for the determinant of the 3D-cubic-matrix, which is a real-number. In the papers (Zaka, 2017a; Zaka, 2019b). Have been studied in detail, properties for 3D-matrix, therefore, those studied properties are also valid for 3D-cubic-Matrix. Our point in this paper is to provide a concept of determinant of 3D matrices. Our concept is based on Milne-Thomson (see Milne-Thomson, 1941). Or permutation method used in regular square matrices.

The following is definition of 3D matrices provided by Zaka in 2017, see (Zaka, 2017a; Zaka, 2019b).

- Selection and peer-review under responsibility of the Organizing Committee of the Conference

Definition 1 *3-dimensional $m \times n \times p$ matrix will call, a matrix which has: m-horizontal layers (analogous to m-rows), n-vertical page (analogue with n- columns in the usual matrices) and p-vertical layers (p-1 of which are hidden).*

The set of these matrix's the write how:

$$M_{m\times n\times p}(\mathrm{F}) = \{a_{i,j,k} | a_{i,j,k} \in F - field\ \forall i = \overline{1,m}; \quad j = \overline{1,n}; \quad k = \overline{1,p}\}. \tag{1}$$

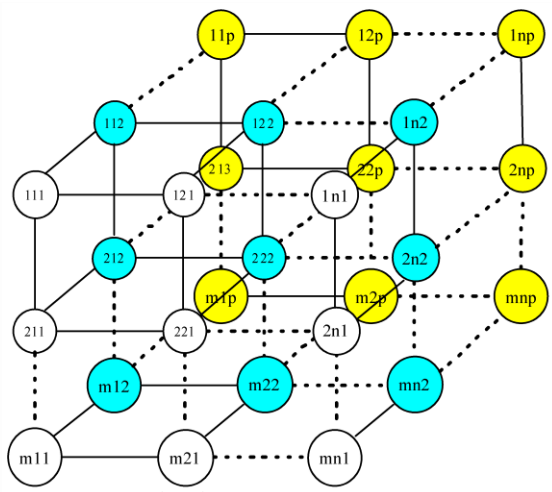

Figure 1. 3D-*Matrix view.*

In the following is presented the determinant of 3D-cubic matrices, as well several properties which are adopted from 2D square determinants.

Cubic-Matrix of Order 2 and 3 and Their Determinants

A 3-dimensional-matrix $A_{n\times n\times n}$ for $n = 2,3, \ldots$, called "cubic-matrix of order n". For $n = 1$ we have that the cubic-matrix of order 1 is an element of F.

Let us now consider the set of cubic-matrix of order n, for $n = 2$ or $n = 3$, with elements from a field F (so when cubic-matrix of order n, there are: n −vertical pages, n −horizontal layers and n −vertical layers). From (Zaka, 2017a; Zaka, 2019b). We have that, the addition of 3D-matrix stands also for cubic-matrix of order 2 and 3. Also, the set of cubic-matrix of order 2 and 3 forms an commutative group (Abelian Group) related to 3Dmatrix addition.

Determinants of Cubic-Matrix of Order 2 and 3

In paper (Salihu-Zaka, 2023). We have defined and described the meaning of the determinants of cubic-matrix of order 2 and order 3, with elements from a field F. Recall that a cubic-matrix $A_{n\times n\times n}$ for $n = 2,3, \ldots$, called "cubic-matrix of order n".

For $n = 1$ we have that the cubic-matrix of order 1 is an element of F.

Let us now consider the set of cubic-matrix of order n, with elements from a field F (so when cubic-matrix of order n, there are: n −vertical pages, n −horizontal layers and n −vertical layers),

$$\mathcal{M}_n(F) = \{A_{n\times n\times n} = (a_{ijk})_{n\times n\times n} | a_{ijk} \in F,\ \forall i = \overline{1,n}; j = \overline{1,n}; k = \overline{1,n}\}.$$

In this paper, we define the *determinant of cubic-matrix* as a element from this field, so the map,

$$\begin{aligned} \det: \mathcal{M}_n(F) &\to F \\ \forall A \in \mathcal{M}_n(F) &\mapsto \det(A) \in F. \end{aligned}$$

Below we give two definitions, how we will calculate the determinant of the cubic-matrix of orders 2 and 3.

Definition 2 *Let $A \in \mathcal{M}_2(F)$ be a $2 \times 2 \times 2$, with elements from a field F.*

$$A_{2\times2\times2} = \left(\begin{matrix} a_{111} & a_{121} \\ a_{211} & a_{221} \end{matrix}\middle|\begin{matrix} a_{112} & a_{122} \\ a_{212} & a_{222} \end{matrix}\right).$$

Determinant of this cubic-matrix, we called,

$$\det[A_{2\times2\times2}] = \det\left(\begin{matrix} a_{111} & a_{121} \\ a_{211} & a_{221} \end{matrix}\middle|\begin{matrix} a_{112} & a_{122} \\ a_{212} & a_{222} \end{matrix}\right) = a_{111}\cdot a_{222} - a_{112}\cdot a_{221} - a_{121}\cdot a_{212} + a_{122}\cdot a_{211}.$$

The follow example is case where cubic-matrix, is with elements from the number field $\mathbb{R}$.

Example 1 *Let's have the cubic-matrix, with element in number field $\mathbb{R}$,*

$$\det[A_{2\times2\times2}] = \det\left(\begin{matrix} 4 & -3 \\ -1 & 5 \end{matrix}\middle|\begin{matrix} -2 & 4 \\ -7 & 3 \end{matrix}\right).$$

then according to the definition 2, we calculate the Determinant of this cubic-matrix, and have,

$$\det[A_{2\times2\times2}] = \det\left(\begin{matrix} 4 & -3 \\ -1 & 5 \end{matrix}\middle|\begin{matrix} -2 & 4 \\ -7 & 3 \end{matrix}\right) = 4\cdot3 - (-2)\cdot5 - (-3)\cdot(-7) + 4\cdot(-1)$$

$$\det[A_{2\times2\times2}] = 12 - (-10) - 21 + (-4) = 12 + 10 - 21 - 4 = -3.$$

We are trying to expand the meaning of the determinant of cubic-matrix, for order 3 (so when cubic-matrix, there are: 3-vertical pages, 3-horizontal layers and 3-vertical layers).

Definition 3 *Let $A \in \mathcal{M}_3(F)$ be a $3\times3\times3$ cubic-matrix with element from a field F,*

$$A_{3\times3\times3} = \left(\begin{matrix} a_{111} & a_{121} & a_{131} \\ a_{211} & a_{221} & a_{231} \\ a_{311} & a_{321} & a_{331} \end{matrix}\middle|\begin{matrix} a_{112} & a_{122} & a_{132} \\ a_{212} & a_{222} & a_{232} \\ a_{312} & a_{322} & a_{332} \end{matrix}\middle|\begin{matrix} a_{113} & a_{123} & a_{133} \\ a_{213} & a_{223} & a_{233} \\ a_{313} & a_{323} & a_{333} \end{matrix}\right).$$

Determinant of this cubic-matrix, we called,

$$\det[A_{3\times3\times3}] = \det\left(\begin{matrix} a_{111} & a_{121} & a_{131} \\ a_{211} & a_{221} & a_{231} \\ a_{311} & a_{321} & a_{331} \end{matrix}\middle|\begin{matrix} a_{112} & a_{122} & a_{132} \\ a_{212} & a_{222} & a_{232} \\ a_{312} & a_{322} & a_{332} \end{matrix}\middle|\begin{matrix} a_{113} & a_{123} & a_{133} \\ a_{213} & a_{223} & a_{233} \\ a_{313} & a_{323} & a_{333} \end{matrix}\right). \tag{2}$$

$$\det[A_{3\times3\times3}] = a_{111}\cdot a_{222}\cdot a_{333} - a_{111}\cdot a_{232}\cdot a_{323} - a_{111}\cdot a_{223}\cdot a_{332}$$

$$+a_{111}\cdot a_{233}\cdot a_{322} - a_{112}\cdot a_{221}\cdot a_{333} + a_{112}\cdot a_{223}\cdot a_{331}$$

$$+a_{112}\cdot a_{231}\cdot a_{323} - a_{112}\cdot a_{233}\cdot a_{321} + a_{113}\cdot a_{221}\cdot a_{332}$$

$$-a_{113}\cdot a_{222}\cdot a_{331} - a_{113}\cdot a_{231}\cdot a_{322} + a_{113}\cdot a_{232}\cdot a_{321}$$

$$-a_{121}\cdot a_{212}\cdot a_{333} + a_{121}\cdot a_{213}\cdot a_{332} + a_{121}\cdot a_{232}\cdot a_{313}$$

$$-a_{121}\cdot a_{233}\cdot a_{312} + a_{122}\cdot a_{211}\cdot a_{333} - a_{122}\cdot a_{213}\cdot a_{331}$$

$$-a_{122}\cdot a_{231}\cdot a_{313} + a_{122}\cdot a_{233}\cdot a_{311} - a_{123}\cdot a_{211}\cdot a_{332}$$

$$+a_{123}\cdot a_{212}\cdot a_{331}+a_{123}\cdot a_{231}\cdot a_{312}-a_{123}\cdot a_{232}\cdot a_{311}$$

$$+a_{131}\cdot a_{212}\cdot a_{323}-a_{131}\cdot a_{213}\cdot a_{322}-a_{131}\cdot a_{222}\cdot a_{313}$$

$$+a_{131}\cdot a_{223}\cdot a_{312}-a_{132}\cdot a_{211}\cdot a_{323}+a_{132}\cdot a_{213}\cdot a_{321}$$

$$+a_{132}\cdot a_{221}\cdot a_{313}-a_{132}\cdot a_{223}\cdot a_{311}+a_{133}\cdot a_{211}\cdot a_{322}$$

$$-a_{133}\cdot a_{212}\cdot a_{321}-a_{133}\cdot a_{221}\cdot a_{312}+a_{133}\cdot a_{222}\cdot a_{311}.$$

The follow example is case where cubic-matrix, is with elements from the number field $\mathbb{R}$.

Example 2 *Let's have the cubic-matrix of order 3, with element from number field (field of real numbers)* $\mathbb{R}$,

$$\det[A_{3\times3\times3}]=\det\left(\begin{array}{ccc|ccc|ccc}3&0&-4&-2&4&0&5&1&0\\2&5&-1&-3&0&3&3&1&2\\0&3&-2&-3&2&5&0&4&3\end{array}\right).$$

Then, we calculate the Determinant of this cubic-matrix following the Definition 3, and have that,

$$\det[A_{3\times3\times3}]=\det\left(\begin{array}{ccc|ccc|ccc}3&0&-4&-2&4&0&5&1&0\\2&5&-1&-3&0&3&3&1&2\\0&3&-2&-3&2&5&0&4&3\end{array}\right)$$

$$\begin{gathered}=3\cdot0\cdot3-3\cdot3\cdot4-3\cdot1\cdot5+3\cdot2\cdot2-(-2)5\cdot3+(-2)1(-2)+(-2)(-1)\cdot4-(-2)2\cdot3\\+5\cdot5\cdot5-5\cdot0\cdot(-2)-5\cdot(-1)\cdot2+5\cdot3\cdot3-0\cdot(-3)\cdot3+0\cdot3\cdot5+0\cdot3\cdot0-0\cdot2\cdot(-3)\\+4\cdot2\cdot3-4\cdot3\cdot(-2)-4\cdot(-1)\cdot0+4\cdot2\cdot0-1\cdot2\cdot5+1\cdot(-3)\cdot(-2)+1\cdot(-1)\cdot(-3)-1\cdot3\cdot0\\+(-4)(-3)\cdot4-(-4)3\cdot2-(-4)0\cdot0+(-4)1(-3)-0\cdot2\cdot4+0\cdot3\cdot3+0\cdot5\cdot0-0\cdot1\cdot0+\end{gathered}$$

$$+0\cdot2\cdot2-0\cdot(-3)\cdot3-0\cdot5\cdot(-3)+0\cdot0\cdot0$$

so,

$$\begin{aligned}\det[A_{3\times3\times3}]&=0-36-15+12+30+4+8+12+125+0+10+45+0+0+0+0+24+24+0\\&\quad+0-10+6+3-0+48+24+0+12-0+0+0-0+0+0+0+0=326.\end{aligned}$$

Hence,

$$\det\left(\begin{array}{ccc|ccc|ccc}3&0&-4&-2&4&0&5&1&0\\2&5&-1&-3&0&3&3&1&2\\0&3&-2&-3&2&5&0&4&3\end{array}\right)=326.$$

Some Basic Properties of Determinants for Cubic-Matrix of Order 2 and Order 3

Definition 4 *We will call* I_n, *a unit-3D-cubic-matrix of order 2 or 3, with elements* e_{ijk}, *which are:*

$$e_{ijk}=\begin{cases}0 & for,\quad i\neq j\neq k\\1 & for,\quad i=j=k\end{cases}$$

Proposition 1 *For every unit-cubic-matrix of order 2 or 3, with element from number field* $\mathbb{R}$, *we have that* $det(I_n)=1$.

Let's have the unit cubic-matrix of order 2,

$$I_2=\left(\begin{array}{cc|cc}1&0&0&0\\0&0&0&1\end{array}\right)$$

then, this determinant is,

$$\det(I_2) = \det\left(\begin{matrix}1 & 0\\ 0 & 0\end{matrix}\middle|\begin{matrix}0 & 0\\ 0 & 1\end{matrix}\right) = 1 \cdot 1 = 1.$$

Now lets have the unit-cubic matrix of order 3,

$$I_3 = \left(\begin{matrix}1 & 0 & 0\\ 0 & 0 & 0\\ 0 & 0 & 0\end{matrix}\middle|\begin{matrix}0 & 0 & 0\\ 0 & 1 & 0\\ 0 & 0 & 0\end{matrix}\middle|\begin{matrix}0 & 0 & 0\\ 0 & 0 & 0\\ 0 & 0 & 1\end{matrix}\right)$$

then this determinant is,

$$\det(I_3) = \det[I_{3\times3\times3}] = \det\left(\begin{matrix}1 & 0 & 0\\ 0 & 0 & 0\\ 0 & 0 & 0\end{matrix}\middle|\begin{matrix}0 & 0 & 0\\ 0 & 1 & 0\\ 0 & 0 & 0\end{matrix}\middle|\begin{matrix}0 & 0 & 0\\ 0 & 0 & 0\\ 0 & 0 & 1\end{matrix}\right) = 1 \cdot 1 \cdot 1 = 1$$

Theorem 1 *Suppose that A is a cubic-matrix of order 2 or 3, with a plan where every entry is zero then its determinant is 'zero', so $\det(A) = 0$.*

Proof. We are discussing the following cases:

1. For plan $i = 1$: Let A be cubic-matrix of order 2, where all elements on the plan $i = 1$ are equal to zero, then based on definition 2:

$$\det[A_{2\times2\times2}] = \det\left(\begin{matrix}0 & 0\\ a_{211} & a_{221}\end{matrix}\middle|\begin{matrix}0 & 0\\ a_{212} & a_{222}\end{matrix}\right) = 0 \cdot a_{222} - 0 \cdot a_{221} - 0 \cdot a_{212} + 0 \cdot a_{211} = 0.$$

2. For plan $i = 2$: Let A be cubic-matrix of order 2, where all elements on the plan $i = 2$ are equal to zero, then based on definition 2:

$$A_{2\times2\times2} = \left(\begin{matrix}a_{111} & a_{121}\\ 0 & 0\end{matrix}\middle|\begin{matrix}a_{112} & a_{122}\\ 0 & 0\end{matrix}\right) = a_{111} \cdot 0 - a_{112} \cdot 0 - a_{121} \cdot 0 + a_{122} \cdot 0 = 0.$$

3. For plan $j = 1$: Let A be cubic-matrix of order 2, where all elements on the plan $j = 1$ are equal to zero, then based on definition 2:

$$\det[A_{2\times2\times2}] = \det\left(\begin{matrix}0 & a_{121}\\ 0 & a_{221}\end{matrix}\middle|\begin{matrix}0 & a_{122}\\ 0 & a_{222}\end{matrix}\right) = 0 \cdot a_{222} - 0 \cdot a_{221} - a_{121} \cdot 0 + a_{122} \cdot 0 = 0.$$

4. For plan $j = 2$: Let A be cubic-matrix of order 2, where all elements on the plan $j = 2$ are equal to zero, then based on definition 2:

$$\det[A_{2\times2\times2}] = \det\left(\begin{matrix}a_{111} & 0\\ a_{211} & 0\end{matrix}\middle|\begin{matrix}a_{112} & 0\\ a_{212} & 0\end{matrix}\right) = a_{111} \cdot 0 - a_{112} \cdot 0 - 0 \cdot a_{212} + 0 \cdot a_{211} = 0.$$

5. For plan $k = 1$: Let A be cubic-matrix of order 2, where all elements on the plan $k = 1$ are equal to zero, then based on definition 2:

$$\det[A_{2\times2\times2}] = \det\left(\begin{matrix}0 & 0\\ 0 & 0\end{matrix}\middle|\begin{matrix}a_{112} & a_{122}\\ a_{212} & a_{222}\end{matrix}\right) = 0 \cdot a_{222} - a_{112} \cdot 0 - 0 \cdot a_{212} + a_{122} \cdot 0 = 0.$$

6. For plan $k = 2$: Let A be cubic-matrix of order 2, where all elements on the plan $k = 2$ are equal to zero, then based on definition 2:

$$\det[A_{2\times2\times2}] = \det\left(\begin{matrix}a_{111} & a_{121}\\ a_{211} & a_{221}\end{matrix}\middle|\begin{matrix}0 & 0\\ 0 & 0\end{matrix}\right) = a_{111} \cdot 0 - 0 \cdot a_{221} - a_{121} \cdot 0 + 0 \cdot a_{211} = 0.$$

Now we will consider for ***third order*** cubic-matrix, as following.

1. For plan $i = 1$: Let A be cubic-matrix of order 3, where all elements on the plan $i = 1$ are equal to zero, then based on definition 3:

$$\det[A_{3\times3\times3}] = \det\left(\begin{matrix} 0 & 0 & 0 \\ a_{211} & a_{221} & a_{231} \\ a_{311} & a_{321} & a_{331} \end{matrix}\middle| \begin{matrix} 0 & 0 & 0 \\ a_{212} & a_{222} & a_{232} \\ a_{312} & a_{322} & a_{332} \end{matrix}\middle| \begin{matrix} 0 & 0 & 0 \\ a_{213} & a_{223} & a_{233} \\ a_{313} & a_{323} & a_{333} \end{matrix}\right)$$

$$= 0\cdot a_{222}\cdot a_{333} - 0\cdot a_{232}\cdot a_{323} - 0\cdot a_{223}\cdot a_{332} + 0\cdot a_{233}\cdot a_{322}$$

$$-0\cdot a_{221}\cdot a_{333} + 0\cdot a_{223}\cdot a_{331} + 0\cdot a_{231}\cdot a_{323} - 0\cdot a_{233}\cdot a_{321}$$

$$+0\cdot a_{221}\cdot a_{332} - 0\cdot a_{222}\cdot a_{331} - 0\cdot a_{231}\cdot a_{322} + 0\cdot a_{232}\cdot a_{321}$$

$$-0\cdot a_{212}\cdot a_{333} + 0\cdot a_{213}\cdot a_{332} + 0\cdot a_{232}\cdot a_{313} - 0\cdot a_{233}\cdot a_{312}$$

$$+0\cdot a_{211}\cdot a_{333} - 0\cdot a_{213}\cdot a_{331} - 0\cdot a_{231}\cdot a_{313} + 0\cdot a_{233}\cdot a_{311}$$

$$-0\cdot a_{211}\cdot a_{332} + 0\cdot a_{212}\cdot a_{331} + 0\cdot a_{231}\cdot a_{312} - 0\cdot a_{232}\cdot a_{311}$$

$$+0\cdot a_{212}\cdot a_{323} - 0\cdot a_{213}\cdot a_{322} - 0\cdot a_{222}\cdot a_{313} + 0\cdot a_{223}\cdot a_{312}$$

$$-0\cdot a_{211}\cdot a_{323} + 0\cdot a_{213}\cdot a_{321} + 0\cdot a_{221}\cdot a_{313} - 0\cdot a_{223}\cdot a_{311}$$

$$+0\cdot a_{211}\cdot a_{322} - 0\cdot a_{212}\cdot a_{321} - 0\cdot a_{221}\cdot a_{312} + 0\cdot a_{222}\cdot a_{311} = 0.$$

2. For plan $i = 2$: Let A be cubic-matrix of order 3, where all elements on the plan $i = 2$ are equal to zero, then based on definition 3:

$$\det[A_{3\times3\times3}] = \det\left(\begin{matrix} a_{111} & a_{121} & a_{131} \\ 0 & 0 & 0 \\ a_{311} & a_{321} & a_{331} \end{matrix}\middle| \begin{matrix} a_{112} & a_{122} & a_{132} \\ 0 & 0 & 0 \\ a_{312} & a_{322} & a_{332} \end{matrix}\middle| \begin{matrix} a_{113} & a_{123} & a_{133} \\ 0 & 0 & 0 \\ a_{313} & a_{323} & a_{333} \end{matrix}\right)$$

$$= a_{111}\cdot 0\cdot a_{333} - a_{111}\cdot 0\cdot a_{323} - a_{111}\cdot 0\cdot a_{332} + a_{111}\cdot 0\cdot a_{322}$$

$$-a_{112}\cdot 0\cdot a_{333} + a_{112}\cdot 0\cdot a_{331} + a_{112}\cdot 0\cdot a_{323} - a_{112}\cdot 0\cdot a_{321}$$

$$+a_{113}\cdot 0\cdot a_{332} - a_{113}\cdot 0\cdot a_{331} - a_{113}\cdot 0\cdot a_{322} + a_{113}\cdot 0\cdot a_{321}$$

$$-a_{121}\cdot 0\cdot a_{333} + a_{121}\cdot 0\cdot a_{332} + a_{121}\cdot 0\cdot a_{313} - a_{121}\cdot 0\cdot a_{312}$$

$$+a_{122}\cdot 0\cdot a_{333} - a_{122}\cdot 0\cdot a_{331} - a_{122}\cdot 0\cdot a_{313} + a_{122}\cdot 0\cdot a_{311}$$

$$-a_{123}\cdot 0\cdot a_{332} + a_{123}\cdot 0\cdot a_{331} + a_{123}\cdot 0\cdot a_{312} - a_{123}\cdot 0\cdot a_{311}$$

$$+a_{131}\cdot 0\cdot a_{323} - a_{131}\cdot 0\cdot a_{322} - a_{131}\cdot 0\cdot a_{313} + a_{131}\cdot 0\cdot a_{312}$$

$$-a_{132}\cdot 0\cdot a_{323} + a_{132}\cdot 0\cdot a_{321} + a_{132}\cdot 0\cdot a_{313} - a_{132}\cdot 0\cdot a_{311}$$

$$+a_{133}\cdot 0\cdot a_{322} - a_{133}\cdot 0\cdot a_{321} - a_{133}\cdot 0\cdot a_{312} + a_{133}\cdot 0\cdot a_{311} = 0.$$

3. For plan $i = 3$: Let A be cubic-matrix of order 3, where all elements on the plan $i = 3$ are equal to zero, then based on definition 3:

$$\det[A_{3\times3\times3}] = \det\left(\begin{matrix} a_{111} & a_{121} & a_{131} \\ a_{211} & a_{221} & a_{231} \\ 0 & 0 & 0 \end{matrix}\middle| \begin{matrix} a_{112} & a_{122} & a_{132} \\ a_{212} & a_{222} & a_{232} \\ 0 & 0 & 0 \end{matrix}\middle| \begin{matrix} a_{113} & a_{123} & a_{133} \\ a_{213} & a_{223} & a_{233} \\ 0 & 0 & 0 \end{matrix}\right)$$

$$= a_{111} \cdot a_{222} \cdot 0 - a_{111} \cdot a_{232} \cdot 0 - a_{111} \cdot a_{223} \cdot 0 + a_{111} \cdot a_{233} \cdot 0$$

$$-a_{112} \cdot a_{221} \cdot 0 + a_{112} \cdot a_{223} \cdot 0 + a_{112} \cdot a_{231} \cdot 0 - a_{112} \cdot a_{233} \cdot 0$$

$$+a_{113} \cdot a_{221} \cdot 0 - a_{113} \cdot a_{222} \cdot 0 - a_{113} \cdot a_{231} \cdot 0 + a_{113} \cdot a_{232} \cdot 0$$

$$-a_{121} \cdot a_{212} \cdot 0 + a_{121} \cdot a_{213} \cdot 0 + a_{121} \cdot a_{232} \cdot 0 - a_{121} \cdot a_{233} \cdot 0$$

$$+a_{122} \cdot a_{211} \cdot 0 - a_{122} \cdot a_{213} \cdot 0 - a_{122} \cdot a_{231} \cdot 0 + a_{122} \cdot a_{233} \cdot 0$$

$$-a_{123} \cdot a_{211} \cdot 0 + a_{123} \cdot a_{212} \cdot 0 + a_{123} \cdot a_{231} \cdot 0 - a_{123} \cdot a_{232} \cdot 0$$

$$+a_{131} \cdot a_{212} \cdot 0 - a_{131} \cdot a_{213} \cdot 0 - a_{131} \cdot a_{222} \cdot 0 + a_{131} \cdot a_{223} \cdot 0$$

$$-a_{132} \cdot a_{211} \cdot 0 + a_{132} \cdot a_{213} \cdot 0 + a_{132} \cdot a_{221} \cdot 0 - a_{132} \cdot a_{223} \cdot 0$$

$$+a_{133} \cdot a_{211} \cdot 0 - a_{133} \cdot a_{212} \cdot 0 - a_{133} \cdot a_{221} \cdot 0 + a_{133} \cdot a_{222} \cdot 0 = 0.$$

4. For plan $j = 1$: Let A be cubic-matrix of order 3, where all elements on the plan $j = 1$ are equal to zero, then based on definition 3:

$$\det[A_{3\times3\times3}] = \det\left(\begin{array}{ccc|ccc|ccc} 0 & a_{121} & a_{131} & 0 & a_{122} & a_{132} & 0 & a_{123} & a_{133} \\ 0 & a_{221} & a_{231} & 0 & a_{222} & a_{232} & 0 & a_{223} & a_{233} \\ 0 & a_{321} & a_{331} & 0 & a_{322} & a_{332} & 0 & a_{323} & a_{333} \end{array}\right)$$

$$= 0 \cdot a_{222} \cdot a_{333} - 0 \cdot a_{232} \cdot a_{323} - 0 \cdot a_{223} \cdot a_{332} + 0 \cdot a_{233} \cdot a_{322}$$

$$-0 \cdot a_{221} \cdot a_{333} + 0 \cdot a_{223} \cdot a_{331} + 0 \cdot a_{231} \cdot a_{323} - 0 \cdot a_{233} \cdot a_{321}$$

$$+0 \cdot a_{221} \cdot a_{332} - 0 \cdot a_{222} \cdot a_{331} - 0 \cdot a_{231} \cdot a_{322} + 0 \cdot a_{232} \cdot a_{321}$$

$$-a_{121} \cdot 0 \cdot a_{333} + a_{121} \cdot 0 \cdot a_{332} + a_{121} \cdot a_{232} \cdot 0 - a_{121} \cdot a_{233} \cdot 0$$

$$+a_{122} \cdot 0 \cdot a_{333} - a_{122} \cdot 0 \cdot a_{331} - a_{122} \cdot a_{231} \cdot 0 + a_{122} \cdot a_{233} \cdot 0$$

$$-a_{123} \cdot 0 \cdot a_{332} + a_{123} \cdot 0 \cdot a_{331} + a_{123} \cdot a_{231} \cdot 0 - a_{123} \cdot a_{232} \cdot 0$$

$$+a_{131} \cdot 0 \cdot a_{323} - a_{131} \cdot 0 \cdot a_{322} - a_{131} \cdot a_{222} \cdot 0 + a_{131} \cdot a_{223} \cdot 0$$

$$-a_{132} \cdot 0 \cdot a_{323} + a_{132} \cdot 0 \cdot a_{321} + a_{132} \cdot a_{221} \cdot 0 - a_{132} \cdot a_{223} \cdot 0$$

$$+a_{133} \cdot 0 \cdot a_{322} - a_{133} \cdot 0 \cdot a_{321} - a_{133} \cdot a_{221} \cdot 0 + a_{133} \cdot a_{222} \cdot 0 = 0.$$

5. For plan $j = 2$: Let A be cubic-matrix of order 3, where all elements on the plan $j = 2$ are equal to zero, then based on definition 3:

$$\det[A_{3\times3\times3}] = \det\left(\begin{array}{ccc|ccc|ccc} a_{111} & 0 & a_{131} & a_{112} & 0 & a_{132} & a_{113} & 0 & a_{133} \\ a_{211} & 0 & a_{231} & a_{212} & 0 & a_{232} & a_{213} & 0 & a_{233} \\ a_{311} & 0 & a_{331} & a_{312} & 0 & a_{332} & a_{313} & 0 & a_{333} \end{array}\right)$$

$$= a_{111} \cdot 0 \cdot a_{333} - a_{111} \cdot a_{232} \cdot 0 - a_{111} \cdot 0 \cdot a_{332} + a_{111} \cdot a_{233} \cdot 0$$

$$-a_{112} \cdot 0 \cdot a_{333} + a_{112} \cdot 0 \cdot a_{331} + a_{112} \cdot a_{231} \cdot 0 - a_{112} \cdot a_{233} \cdot 0$$

$$+a_{113} \cdot 0 \cdot a_{332} - a_{113} \cdot 0 \cdot a_{331} - a_{113} \cdot a_{231} \cdot 0 + a_{113} \cdot a_{232} \cdot 0$$

$$-0 \cdot a_{212} \cdot a_{333} + 0 \cdot a_{213} \cdot a_{332} + 0 \cdot a_{232} \cdot a_{313} - 0 \cdot a_{233} \cdot a_{312}$$

$$+0 \cdot a_{211} \cdot a_{333} - 0 \cdot a_{213} \cdot a_{331} - 0 \cdot a_{231} \cdot a_{313} + 0 \cdot a_{233} \cdot a_{311}$$

$$-0 \cdot a_{211} \cdot a_{332} + 0 \cdot a_{212} \cdot a_{331} + 0 \cdot a_{231} \cdot a_{312} - 0 \cdot a_{232} \cdot a_{311}$$

$$+a_{131} \cdot a_{212} \cdot 0 - a_{131} \cdot a_{213} \cdot 0 - a_{131} \cdot 0 \cdot a_{313} + a_{131} \cdot 0 \cdot a_{312}$$

$$-a_{132} \cdot a_{211} \cdot 0 + a_{132} \cdot a_{213} \cdot 0 + a_{132} \cdot 0 \cdot a_{313} - a_{132} \cdot 0 \cdot a_{311}$$

$$+a_{133} \cdot a_{211} \cdot 0 - a_{133} \cdot a_{212} \cdot 0 - a_{133} \cdot 0 \cdot a_{312} + a_{133} \cdot 0 \cdot a_{311} = 0.$$

6. For plan $j = 3$: Let A be cubic-matrix of order 3, where all elements on the plan $j = 3$ are equal to zero, then based on definition 3:

$$\det[A_{3\times3\times3}] = \det\begin{pmatrix} a_{111} & a_{121} & 0 & a_{112} & a_{122} & 0 & a_{113} & a_{123} & 0 \\ a_{211} & a_{221} & 0 & a_{212} & a_{222} & 0 & a_{213} & a_{223} & 0 \\ a_{311} & a_{321} & 0 & a_{312} & a_{322} & 0 & a_{313} & a_{323} & 0 \end{pmatrix}$$

$$= a_{111} \cdot a_{222} \cdot 0 - a_{111} \cdot 0 \cdot a_{323} - a_{111} \cdot a_{223} \cdot 0 + a_{111} \cdot 0 \cdot a_{322}$$

$$-a_{112} \cdot a_{221} \cdot 0 + a_{112} \cdot a_{223} \cdot 0 + a_{112} \cdot 0 \cdot a_{323} - a_{112} \cdot 0 \cdot a_{321}$$

$$+a_{113} \cdot a_{221} \cdot 0 - a_{113} \cdot a_{222} \cdot 0 - a_{113} \cdot 0 \cdot a_{322} + a_{113} \cdot 0 \cdot a_{321}$$

$$-a_{121} \cdot a_{212} \cdot 0 + a_{121} \cdot a_{213} \cdot 0 + a_{121} \cdot 0 \cdot a_{313} - a_{121} \cdot 0 \cdot a_{312}$$

$$+a_{122} \cdot a_{211} \cdot 0 - a_{122} \cdot a_{213} \cdot 0 - a_{122} \cdot 0 \cdot a_{313} + a_{122} \cdot 0 \cdot a_{311}$$

$$-a_{123} \cdot a_{211} \cdot 0 + a_{123} \cdot a_{212} \cdot 0 + a_{123} \cdot 0 \cdot a_{312} - a_{123} \cdot 0 \cdot a_{311}$$

$$+0 \cdot a_{212} \cdot a_{323} - 0 \cdot a_{213} \cdot a_{322} - 0 \cdot a_{222} \cdot a_{313} + 0 \cdot a_{223} \cdot a_{312}$$

$$-0 \cdot a_{211} \cdot a_{323} + 0 \cdot a_{213} \cdot a_{321} + 0 \cdot a_{221} \cdot a_{313} - 0 \cdot a_{223} \cdot a_{311}$$

$$+0 \cdot a_{211} \cdot a_{322} - 0 \cdot a_{212} \cdot a_{321} - 0 \cdot a_{221} \cdot a_{312} + 0 \cdot a_{222} \cdot a_{311} = 0.$$

7. For plan $k = 1$: Let A be cubic-matrix of order 3, where all elements on the plan $k = 1$ are equal to zero, then based on definition 3:

$$\det[A_{3\times3\times3}] = \det\begin{pmatrix} 0 & 0 & 0 & a_{112} & a_{122} & a_{132} & a_{113} & a_{123} & a_{133} \\ 0 & 0 & 0 & a_{212} & a_{222} & a_{232} & a_{213} & a_{223} & a_{233} \\ 0 & 0 & 0 & a_{312} & a_{322} & a_{332} & a_{313} & a_{323} & a_{333} \end{pmatrix}$$

$$= 0 \cdot a_{222} \cdot a_{333} - 0 \cdot a_{232} \cdot a_{323} - 0 \cdot a_{223} \cdot a_{332} + 0 \cdot a_{233} \cdot a_{322}$$

$$-a_{112} \cdot 0 \cdot a_{333} + a_{112} \cdot a_{223} \cdot 0 + a_{112} \cdot 0 \cdot a_{323} - a_{112} \cdot a_{233} \cdot 0$$

$$+a_{113} \cdot 0 \cdot a_{332} - a_{113} \cdot a_{222} \cdot 0 - a_{113} \cdot 0 \cdot a_{322} + a_{113} \cdot a_{232} \cdot 0$$

$$-0 \cdot a_{212} \cdot a_{333} + 0 \cdot a_{213} \cdot a_{332} + 0 \cdot a_{232} \cdot a_{313} - 0 \cdot a_{233} \cdot a_{312}$$

$$+a_{122} \cdot 0 \cdot a_{333} - a_{122} \cdot a_{213} \cdot 0 - a_{122} \cdot 0 \cdot a_{313} + a_{122} \cdot a_{233} \cdot 0$$

$$-a_{123} \cdot 0 \cdot a_{332} + a_{123} \cdot a_{212} \cdot 0 + a_{123} \cdot 0 \cdot a_{312} - a_{123} \cdot a_{232} \cdot 0$$

$$+0\cdot a_{212}\cdot a_{323}-0\cdot a_{213}\cdot a_{322}-0\cdot a_{222}\cdot a_{313}+0\cdot a_{223}\cdot a_{312}$$

$$-a_{132}\cdot 0\cdot a_{323}+a_{132}\cdot a_{213}\cdot 0+a_{132}\cdot 0\cdot a_{313}-a_{132}\cdot a_{223}\cdot 0$$

$$+a_{133}\cdot 0\cdot a_{322}-a_{133}\cdot a_{212}\cdot 0-a_{133}\cdot 0\cdot a_{312}+a_{133}\cdot a_{222}\cdot 0=0.$$

8. For plan $k=2$: Let A be cubic-matrix of order 3, where all elements on the plan $k=2$ are equal to zero, then based on definition 3:

$$\det[A_{3\times3\times3}]=\det\left(\begin{array}{ccc|ccc|ccc} a_{111} & a_{121} & a_{131} & 0 & 0 & 0 & a_{113} & a_{123} & a_{133}\\ a_{211} & a_{221} & a_{231} & 0 & 0 & 0 & a_{213} & a_{223} & a_{233}\\ a_{311} & a_{321} & a_{331} & 0 & 0 & 0 & a_{313} & a_{323} & a_{333}\end{array}\right)$$

$$=a_{111}\cdot 0\cdot a_{333}-a_{111}\cdot 0\cdot a_{323}-a_{111}\cdot a_{223}\cdot 0+a_{111}\cdot a_{233}\cdot 0$$

$$-0\cdot a_{221}\cdot a_{333}+0\cdot a_{223}\cdot a_{331}+0\cdot a_{231}\cdot a_{323}-0\cdot a_{233}\cdot a_{321}$$

$$+a_{113}\cdot a_{221}\cdot 0-a_{113}\cdot 0\cdot a_{331}-a_{113}\cdot a_{231}\cdot 0+a_{113}\cdot 0\cdot a_{321}$$

$$-a_{121}\cdot 0\cdot a_{333}+a_{121}\cdot a_{213}\cdot 0+a_{121}\cdot 0\cdot a_{313}-a_{121}\cdot a_{233}\cdot 0$$

$$+0\cdot a_{211}\cdot a_{333}-0\cdot a_{213}\cdot a_{331}-0\cdot a_{231}\cdot a_{313}+0\cdot a_{233}\cdot a_{311}$$

$$-a_{123}\cdot a_{211}\cdot 0+a_{123}\cdot 0\cdot a_{331}+a_{123}\cdot a_{231}\cdot 0-a_{123}\cdot 0\cdot a_{311}$$

$$+a_{131}\cdot 0\cdot a_{323}-a_{131}\cdot a_{213}\cdot 0-a_{131}\cdot 0\cdot a_{313}+a_{131}\cdot a_{223}\cdot 0$$

$$-0\cdot a_{211}\cdot a_{323}+0\cdot a_{213}\cdot a_{321}+0\cdot a_{221}\cdot a_{313}-0\cdot a_{223}\cdot a_{311}$$

$$+a_{133}\cdot a_{211}\cdot 0-a_{133}\cdot 0\cdot a_{321}-a_{133}\cdot a_{221}\cdot 0+a_{133}\cdot 0\cdot a_{311}=0.$$

9. For plan $k=3$: Let A be cubic-matrix of order 3, where all elements on the plan $k=3$ are equal to zero, then based on definition 3:

$$\det[A_{3\times3\times3}]=\det\left(\begin{array}{ccc|ccc|ccc} a_{111} & a_{121} & a_{131} & a_{112} & a_{122} & a_{132} & 0 & 0 & 0\\ a_{211} & a_{221} & a_{231} & a_{212} & a_{222} & a_{232} & 0 & 0 & 0\\ a_{311} & a_{321} & a_{331} & a_{312} & a_{322} & a_{332} & 0 & 0 & 0\end{array}\right)$$

$$=a_{111}\cdot a_{222}\cdot 0-a_{111}\cdot a_{232}\cdot 0-a_{111}\cdot 0\cdot a_{332}+a_{111}\cdot 0\cdot a_{322}$$

$$-a_{112}\cdot a_{221}\cdot 0+a_{112}\cdot 0\cdot a_{331}+a_{112}\cdot a_{231}\cdot 0-a_{112}\cdot 0\cdot a_{321}$$

$$+0\cdot a_{221}\cdot a_{332}-0\cdot a_{222}\cdot a_{331}-0\cdot a_{231}\cdot a_{322}+0\cdot a_{232}\cdot a_{321}$$

$$-a_{121}\cdot a_{212}\cdot 0+a_{121}\cdot 0\cdot a_{332}+a_{121}\cdot a_{232}\cdot 0-a_{121}\cdot 0\cdot a_{312}$$

$$+a_{122}\cdot a_{211}\cdot 0-a_{122}\cdot 0\cdot a_{331}-a_{122}\cdot a_{231}\cdot 0+a_{122}\cdot 0\cdot a_{311}$$

$$-0\cdot a_{211}\cdot a_{332}+0\cdot a_{212}\cdot a_{331}+0\cdot a_{231}\cdot a_{312}-0\cdot a_{232}\cdot a_{311}$$

$$+a_{131}\cdot a_{212}\cdot 0-a_{131}\cdot 0\cdot a_{322}-a_{131}\cdot a_{222}\cdot 0+a_{131}\cdot 0\cdot a_{312}$$

$$-a_{132}\cdot a_{211}\cdot 0+a_{132}\cdot 0\cdot a_{321}+a_{132}\cdot a_{221}\cdot 0-a_{132}\cdot 0\cdot a_{311}$$

$$+0\cdot a_{211}\cdot a_{322}-0\cdot a_{212}\cdot a_{321}-0\cdot a_{221}\cdot a_{312}+0\cdot a_{222}\cdot a_{311}=0.$$

Based on definition 2 and definition 3, we can see that each term is multiplied with elements of each plan once, hence the proof can be easily seen, as presented above.

Proposition 2 *Suppose that A is cubic-matrix of order 2 or 3, and let's be B the cubic-matrix of same order with A, which obtained from A by multiplying any single: "horizontal layer" or "vertical page" or "vertical layer" with scalar α. Then $det(B) = \alpha \cdot det(A)$, if $\alpha \neq 0$.*

Proof. We are discussing the following cases for cubic matrix of order 2 and cases for cubic matrix of order 3:

Case 1. The cubic-matrix A of order 2, (and B has order 2), we will proof the case 1 for each "horizontal layer", "vertical page" and "vertical layer", as following:

1. For plan $i = 1$: Let A be cubic-matrix of order 2, where all elements on the plan $i = 1$ are equal to zero, then based on definition 2:

$$\det[B_{2\times2\times2}] = \det\left(\begin{matrix} \alpha\cdot a_{111} & \alpha\cdot a_{121} \\ a_{211} & a_{221} \end{matrix}\middle| \begin{matrix} \alpha\cdot a_{112} & \alpha\cdot a_{122} \\ a_{212} & a_{222} \end{matrix}\right)$$

$$= \alpha\cdot a_{111}\cdot a_{222} - \alpha\cdot a_{112}\cdot a_{221} - \alpha\cdot a_{121}\cdot a_{212} + \alpha\cdot a_{122}\cdot a_{211} = \alpha\cdot\det[A_{2\times2\times2}]$$

2. For plan $i = 2$: Let A be cubic-matrix of order 2, where all elements on the plan $i = 2$ are equal to zero, then based on definition 2:

$$\det[B_{2\times2\times2}] = \det\left(\begin{matrix} a_{111} & a_{121} \\ \alpha\cdot a_{211} & \alpha\cdot a_{221} \end{matrix}\middle| \begin{matrix} a_{112} & a_{122} \\ \alpha\cdot a_{212} & \alpha\cdot a_{222} \end{matrix}\right)$$

$$= a_{111}\cdot\alpha\cdot a_{222} - a_{112}\cdot\alpha\cdot a_{221} - a_{121}\cdot\alpha\cdot a_{212} + a_{122}\cdot\alpha\cdot a_{211} = \alpha\cdot\det[A_{2\times2\times2}]$$

3. For plan $j = 1$: Let A be cubic-matrix of order 2, where all elements on the plan $j = 1$ are equal to zero, then based on definition 2:

$$\det[B_{2\times2\times2}] = \det\left(\begin{matrix} \alpha\cdot a_{111} & a_{121} \\ \alpha\cdot a_{211} & a_{221} \end{matrix}\middle| \begin{matrix} \alpha\cdot a_{112} & a_{122} \\ \alpha\cdot a_{212} & a_{222} \end{matrix}\right)$$

$$= \alpha\cdot a_{111}\cdot a_{222} - \alpha\cdot a_{112}\cdot a_{221} - a_{121}\cdot\alpha\cdot a_{212} + a_{122}\cdot\alpha\cdot a_{211} = \alpha\cdot\det[A_{2\times2\times2}]$$

4. For plan $j = 2$: Let A be cubic-matrix of order 2, where all elements on the plan $j = 2$ are equal to zero, then based on definition 2:

$$\det[B_{2\times2\times2}] = \det\left(\begin{matrix} a_{111} & \alpha\cdot a_{121} \\ a_{211} & \alpha\cdot a_{221} \end{matrix}\middle| \begin{matrix} a_{112} & \alpha\cdot a_{122} \\ a_{212} & \alpha\cdot a_{222} \end{matrix}\right)$$

$$= a_{111}\cdot\alpha\cdot a_{222} - a_{112}\cdot\alpha\cdot a_{221} - \alpha\cdot a_{121}\cdot a_{212} + \alpha\cdot a_{122}\cdot a_{211} = \alpha\cdot\det[A_{2\times2\times2}]$$

5. For plan $k = 1$: Let A be cubic-matrix of order 2, where all elements on the plan $k = 1$ are equal to zero, then based on definition 2:

$$\det[B_{2\times2\times2}] = \det\left(\begin{matrix} \alpha\cdot a_{111} & \alpha\cdot a_{121} \\ \alpha\cdot a_{211} & \alpha\cdot a_{221} \end{matrix}\middle| \begin{matrix} a_{112} & a_{122} \\ a_{212} & a_{222} \end{matrix}\right)$$

$$= \alpha\cdot a_{a_{111}}\cdot a_{222} - a_{112}\cdot\alpha\cdot a_{221} - \alpha\cdot a_{121}\cdot a_{212} + a_{122}\cdot\alpha\cdot a_{211} = \alpha\cdot\det[A_{2\times2\times2}]$$

6. For plan $k = 2$: Let A be cubic-matrix of order 2, where all elements on the plan $k = 2$ are equal to zero, then based on definition 2:

$$\det[B_{2\times2\times2}] = \det\left(\begin{matrix} a_{111} & a_{121} \\ a_{211} & a_{221} \end{matrix}\middle| \begin{matrix} \alpha\cdot a_{112} & \alpha\cdot a_{122} \\ \alpha\cdot a_{212} & \alpha\cdot a_{222} \end{matrix}\right)$$

$$= a_{111} \cdot \alpha \cdot a_{222} - \alpha \cdot a_{112} \cdot a_{221} - a_{121} \cdot \alpha \cdot a_{212} + \alpha \cdot a_{122} \cdot a_{211} = \alpha \cdot \det[A_{2\times2\times2}]$$

Case 2. The cubic-matrix A of order 3, (and B has order 3)

1. For plan $i = 1$: Let A be cubic-matrix of order 2, where all elements on the plan $i = 1$ are equal to zero, then based on definition 3:

$$\det[B_{3\times3\times3}] = \det\left(\begin{array}{ccc|ccc|ccc} \alpha\cdot a_{111} & \alpha\cdot a_{121} & \alpha\cdot a_{131} & \alpha\cdot a_{112} & \alpha\cdot a_{122} & \alpha\cdot a_{132} & \alpha\cdot a_{113} & \alpha\cdot a_{123} & \alpha\cdot a_{133} \\ a_{211} & a_{221} & a_{231} & a_{212} & a_{222} & a_{232} & a_{213} & a_{223} & a_{233} \\ a_{311} & a_{321} & a_{331} & a_{312} & a_{322} & a_{332} & a_{313} & a_{323} & a_{333} \end{array}\right)$$

$$= \alpha \cdot a_{111} \cdot a_{222} \cdot a_{333} - \alpha \cdot a_{111} \cdot a_{232} \cdot a_{323} - \alpha \cdot a_{111} \cdot a_{223} \cdot a_{332} + \alpha \cdot a_{111} \cdot a_{233} \cdot a_{322}$$

$$-\alpha \cdot a_{112} \cdot a_{221} \cdot a_{333} + \alpha \cdot a_{112} \cdot a_{223} \cdot a_{331} + \alpha \cdot a_{112} \cdot a_{231} \cdot a_{323} - \alpha \cdot a_{112} \cdot a_{233} \cdot a_{321}$$

$$+\alpha \cdot a_{113} \cdot a_{221} \cdot a_{332} - \alpha \cdot a_{113} \cdot a_{222} \cdot a_{331} - \alpha \cdot a_{113} \cdot a_{231} \cdot a_{322} + \alpha \cdot a_{113} \cdot a_{232} \cdot a_{321}$$

$$-\alpha \cdot a_{121} \cdot a_{212} \cdot a_{333} + \alpha \cdot a_{121} \cdot a_{213} \cdot a_{332} + \alpha \cdot a_{121} \cdot a_{232} \cdot a_{313} - \alpha \cdot a_{121} \cdot a_{233} \cdot a_{312}$$

$$+\alpha \cdot a_{122} \cdot a_{211} \cdot a_{333} - \alpha \cdot a_{122} \cdot a_{213} \cdot a_{331} - \alpha \cdot a_{122} \cdot a_{231} \cdot a_{313} + \alpha \cdot a_{122} \cdot a_{233} \cdot a_{311}$$

$$-\alpha \cdot a_{123} \cdot a_{211} \cdot a_{332} + \alpha \cdot a_{123} \cdot a_{212} \cdot a_{331} + \alpha \cdot a_{123} \cdot a_{231} \cdot a_{312} - \alpha \cdot a_{123} \cdot a_{232} \cdot a_{311}$$

$$+\alpha \cdot a_{131} \cdot a_{212} \cdot a_{323} - \alpha \cdot a_{131} \cdot a_{213} \cdot a_{322} - \alpha \cdot a_{131} \cdot a_{222} \cdot a_{313} + \alpha \cdot a_{131} \cdot a_{223} \cdot a_{312}$$

$$-\alpha \cdot a_{132} \cdot a_{211} \cdot a_{323} + \alpha \cdot a_{132} \cdot a_{213} \cdot a_{321} + \alpha \cdot a_{132} \cdot a_{221} \cdot a_{313} - \alpha \cdot a_{132} \cdot a_{223} \cdot a_{311}$$

$$+\alpha \cdot a_{133} \cdot a_{211} \cdot a_{322} - \alpha \cdot a_{133} \cdot a_{212} \cdot a_{321} - \alpha \cdot a_{133} \cdot a_{221} \cdot a_{312} + \alpha \cdot a_{133} \cdot a_{222} \cdot a_{311} = \alpha \cdot \det[A_{3\times3\times3}]$$

2. For plan $i = 2$: Let A be cubic-matrix of order 2, where all elements on the plan $i = 2$ are equal to zero, then based on definition 3:

$$\det[B_{3\times3\times3}] = \det\left(\begin{array}{ccc|ccc|ccc} a_{111} & a_{121} & a_{131} & a_{112} & a_{122} & a_{132} & a_{113} & a_{123} & a_{133} \\ \alpha\cdot a_{211} & \alpha\cdot a_{221} & \alpha\cdot a_{231} & \alpha\cdot a_{212} & \alpha\cdot a_{222} & \alpha\cdot a_{232} & \alpha\cdot a_{213} & \alpha\cdot a_{223} & \alpha\cdot a_{233} \\ a_{311} & a_{321} & a_{331} & a_{312} & a_{322} & a_{332} & a_{313} & a_{323} & a_{333} \end{array}\right)$$

$$= a_{111} \cdot \alpha \cdot a_{222} \cdot a_{333} - a_{111} \cdot \alpha \cdot a_{232} \cdot a_{323} - a_{111} \cdot \alpha \cdot a_{223} \cdot a_{332} + a_{111} \cdot \alpha \cdot a_{233} \cdot a_{322}$$

$$-a_{112} \cdot \alpha \cdot a_{221} \cdot a_{333} + a_{112} \cdot \alpha \cdot a_{223} \cdot a_{331} + a_{112} \cdot \alpha \cdot a_{231} \cdot a_{323} - a_{112} \cdot \alpha \cdot a_{233} \cdot a_{321}$$

$$+a_{113} \cdot \alpha \cdot a_{221} \cdot a_{332} - a_{113} \cdot \alpha \cdot a_{222} \cdot a_{331} - a_{113} \cdot \alpha \cdot a_{231} \cdot a_{322} + a_{113} \cdot \alpha \cdot a_{232} \cdot a_{321}$$

$$-a_{121} \cdot \alpha \cdot a_{212} \cdot a_{333} + a_{121} \cdot \alpha \cdot a_{213} \cdot a_{332} + a_{121} \cdot \alpha \cdot a_{232} \cdot a_{313} - a_{121} \cdot \alpha \cdot a_{233} \cdot a_{312}$$

$$+a_{122} \cdot \alpha \cdot a_{211} \cdot a_{333} - a_{122} \cdot \alpha \cdot a_{213} \cdot a_{331} - a_{122} \cdot \alpha \cdot a_{231} \cdot a_{313} + a_{122} \cdot \alpha \cdot a_{233} \cdot a_{311}$$

$$-a_{123} \cdot \alpha \cdot a_{211} \cdot a_{332} + a_{123} \cdot \alpha \cdot a_{212} \cdot a_{331} + a_{123} \cdot \alpha \cdot a_{231} \cdot a_{312} - a_{123} \cdot \alpha \cdot a_{232} \cdot a_{311}$$

$$+a_{131} \cdot \alpha \cdot a_{212} \cdot a_{323} - a_{131} \cdot \alpha \cdot a_{213} \cdot a_{322} - a_{131} \cdot \alpha \cdot a_{222} \cdot a_{313} + a_{131} \cdot \alpha \cdot a_{223} \cdot a_{312}$$

$$-a_{132} \cdot \alpha \cdot a_{211} \cdot a_{323} + a_{132} \cdot \alpha \cdot a_{213} \cdot a_{321} + a_{132} \cdot \alpha \cdot a_{221} \cdot a_{313} - a_{132} \cdot \alpha \cdot a_{223} \cdot a_{311}$$

$$+a_{133} \cdot \alpha \cdot a_{211} \cdot a_{322} - a_{133} \cdot \alpha \cdot a_{212} \cdot a_{321} - a_{133} \cdot \alpha \cdot a_{221} \cdot a_{312} + a_{133} \cdot \alpha \cdot a_{222} \cdot a_{311} = \alpha \cdot \det[A_{3\times3\times3}]$$

3. For plan $i = 3$: Let A be cubic-matrix of order 2, where all elements on the plan $i = 3$ are equal to zero, then based on definition 3:

$$\det[B_{3\times3\times3}] = \det\left(\begin{array}{ccc|ccc|ccc} a_{111} & a_{121} & a_{131} & a_{112} & a_{122} & a_{132} & a_{113} & a_{123} & a_{133} \\ a_{211} & a_{221} & a_{231} & a_{212} & a_{222} & a_{232} & a_{213} & a_{223} & a_{233} \\ \alpha\cdot a_{311} & \alpha\cdot a_{321} & \alpha\cdot a_{331} & \alpha\cdot a_{312} & \alpha\cdot a_{322} & \alpha\cdot a_{332} & \alpha\cdot a_{313} & \alpha\cdot a_{323} & \alpha\cdot a_{333} \end{array}\right)$$

$$= a_{111}\cdot a_{222}\cdot\alpha\cdot a_{333} - a_{111}\cdot a_{232}\cdot\alpha\cdot a_{323} - a_{111}\cdot a_{223}\cdot\alpha\cdot a_{332} + a_{111}\cdot a_{233}\cdot\alpha\cdot a_{322}$$

$$-a_{112}\cdot a_{221}\cdot\alpha\cdot a_{333} + a_{112}\cdot a_{223}\cdot\alpha\cdot a_{331} + a_{112}\cdot a_{231}\cdot\alpha\cdot a_{323} - a_{112}\cdot a_{233}\cdot\alpha\cdot a_{321}$$

$$+a_{113}\cdot a_{221}\cdot\alpha\cdot a_{332} - a_{113}\cdot a_{222}\cdot\alpha\cdot a_{331} - a_{113}\cdot a_{231}\cdot\alpha\cdot a_{322} + a_{113}\cdot a_{232}\cdot\alpha\cdot a_{321}$$

$$-a_{121}\cdot a_{212}\cdot\alpha\cdot a_{333} + a_{121}\cdot a_{213}\cdot\alpha\cdot a_{332} + a_{121}\cdot a_{232}\cdot\alpha\cdot a_{313} - a_{121}\cdot a_{233}\cdot\alpha\cdot a_{312}$$

$$+a_{122}\cdot a_{211}\cdot\alpha\cdot a_{333} - a_{122}\cdot a_{213}\cdot\alpha\cdot a_{331} - a_{122}\cdot a_{231}\cdot\alpha\cdot a_{313} + a_{122}\cdot a_{233}\cdot\alpha\cdot a_{311}$$

$$-a_{123}\cdot a_{211}\cdot\alpha\cdot a_{332} + a_{123}\cdot a_{212}\cdot\alpha\cdot a_{331} + a_{123}\cdot a_{231}\cdot\alpha\cdot a_{312} - a_{123}\cdot a_{232}\cdot\alpha\cdot a_{311}$$

$$+a_{131}\cdot a_{212}\cdot\alpha\cdot a_{323} - a_{131}\cdot a_{213}\cdot\alpha\cdot a_{322} - a_{131}\cdot a_{222}\cdot\alpha\cdot a_{313} + a_{131}\cdot a_{223}\cdot\alpha\cdot a_{312}$$

$$-a_{132}\cdot a_{211}\cdot\alpha\cdot a_{323} + a_{132}\cdot a_{213}\cdot\alpha\cdot a_{321} + a_{132}\cdot a_{221}\cdot\alpha\cdot a_{313} - a_{132}\cdot a_{223}\cdot\alpha\cdot a_{311}$$

$$+a_{133}\cdot a_{211}\cdot\alpha\cdot a_{322} - a_{133}\cdot a_{212}\cdot\alpha\cdot a_{321} - a_{133}\cdot a_{221}\cdot\alpha\cdot a_{312} + a_{133}\cdot a_{222}\cdot\alpha\cdot a_{311} = \alpha\cdot\det[A_{3\times3\times3}]$$

4. For plan $j = 1$: Let A be cubic-matrix of order 2, where all elements on the plan $i = 1$ are equal to zero, then based on definition 3:

$$\det[B_{3\times3\times3}] = \det\left(\begin{array}{ccc|ccc|ccc} \alpha\cdot a_{111} & a_{121} & a_{131} & \alpha\cdot a_{112} & a_{122} & a_{132} & \alpha\cdot a_{113} & a_{123} & a_{133} \\ \alpha\cdot a_{211} & a_{221} & a_{231} & \alpha\cdot a_{212} & a_{222} & a_{232} & \alpha\cdot a_{213} & a_{223} & a_{233} \\ \alpha\cdot a_{311} & a_{321} & a_{331} & \alpha\cdot a_{312} & a_{322} & a_{332} & \alpha\cdot a_{313} & a_{323} & a_{333} \end{array}\right)$$

$$= \alpha\cdot a_{111}\cdot a_{222}\cdot a_{333} - \alpha\cdot a_{111}\cdot a_{232}\cdot a_{323} - \alpha\cdot a_{111}\cdot a_{223}\cdot a_{332} + \alpha\cdot a_{111}\cdot a_{233}\cdot a_{322}$$

$$-\alpha\cdot a_{112}\cdot a_{221}\cdot a_{333} + \alpha\cdot a_{112}\cdot a_{223}\cdot a_{331} + \alpha\cdot a_{112}\cdot a_{231}\cdot a_{323} - \alpha\cdot a_{112}\cdot a_{233}\cdot a_{321}$$

$$+\alpha\cdot a_{113}\cdot a_{221}\cdot a_{332} - \alpha\cdot a_{113}\cdot a_{222}\cdot a_{331} - \alpha\cdot a_{113}\cdot a_{231}\cdot a_{322} + \alpha\cdot a_{113}\cdot a_{232}\cdot a_{321}$$

$$-a_{121}\cdot\alpha\cdot a_{212}\cdot a_{333} + a_{121}\cdot\alpha\cdot a_{213}\cdot a_{332} + a_{121}\cdot a_{232}\cdot\alpha\cdot a_{313} - a_{121}\cdot a_{233}\cdot\alpha\cdot a_{312}$$

$$+a_{122}\cdot\alpha\cdot a_{211}\cdot a_{333} - a_{122}\cdot\alpha\cdot a_{213}\cdot a_{331} - a_{122}\cdot a_{231}\cdot\alpha\cdot a_{313} + a_{122}\cdot a_{233}\cdot\alpha\cdot a_{311}$$

$$-a_{123}\cdot\alpha\cdot a_{211}\cdot a_{332} + a_{123}\cdot\alpha\cdot a_{212}\cdot a_{331} + a_{123}\cdot a_{231}\cdot\alpha\cdot a_{312} - a_{123}\cdot a_{232}\cdot\alpha\cdot a_{311}$$

$$+a_{131}\cdot\alpha\cdot a_{212}\cdot a_{323} - a_{131}\cdot\alpha\cdot a_{213}\cdot a_{322} - a_{131}\cdot a_{222}\cdot\alpha\cdot a_{313} + a_{131}\cdot a_{223}\cdot\alpha\cdot a_{312}$$

$$-a_{132}\cdot\alpha\cdot a_{211}\cdot a_{323} + a_{132}\cdot\alpha\cdot a_{213}\cdot a_{321} + a_{132}\cdot a_{221}\cdot\alpha\cdot a_{313} - a_{132}\cdot a_{223}\cdot\alpha\cdot a_{311}$$

$$+a_{133}\cdot\alpha\cdot a_{211}\cdot a_{322}\, a_{133}\cdot\alpha\cdot a_{212}\cdot a_{321} - a_{133}\cdot a_{221}\cdot\alpha\cdot a_{312} + a_{133}\cdot a_{222}\cdot\alpha\cdot a_{311} = \alpha\cdot\det[A_{3\times3\times3}]$$

5. For plan $j = 2$: Let A be cubic-matrix of order 2, where all elements on the plan $i = 2$ are equal to zero, then based on definition 3:

$$\det[B_{3\times3\times3}] = \det\left(\begin{array}{ccc|ccc|ccc} a_{111} & \alpha\cdot a_{121} & a_{131} & a_{112} & \alpha\cdot a_{122} & a_{132} & a_{113} & \alpha\cdot a_{123} & a_{133} \\ a_{211} & \alpha\cdot a_{221} & a_{231} & a_{212} & \alpha\cdot a_{222} & a_{232} & a_{213} & \alpha\cdot a_{223} & a_{233} \\ a_{311} & \alpha\cdot a_{321} & a_{331} & a_{312} & \alpha\cdot a_{322} & a_{332} & a_{313} & \alpha\cdot a_{323} & a_{333} \end{array}\right)$$

$$= a_{111}\cdot\alpha\cdot a_{222}\cdot a_{333} - a_{111}\cdot a_{232}\cdot\alpha\cdot a_{323} - a_{111}\cdot\alpha\cdot a_{223}\cdot a_{332} + a_{111}\cdot a_{233}\cdot\alpha\cdot a_{322}$$

$$-a_{112}\cdot\alpha\cdot a_{221}\cdot a_{333}+a_{112}\cdot\alpha\cdot a_{223}\cdot a_{331}+a_{112}\cdot a_{231}\cdot\alpha\cdot a_{323}-a_{112}\cdot a_{233}\cdot\alpha\cdot a_{321}$$

$$+a_{113}\cdot\alpha\cdot a_{221}\cdot a_{332}-a_{113}\cdot\alpha\cdot a_{222}\cdot a_{331}-a_{113}\cdot a_{231}\cdot\alpha\cdot a_{322}+a_{113}\cdot a_{232}\cdot\alpha\cdot a_{321}$$

$$-\alpha\cdot a_{121}\cdot a_{212}\cdot a_{333}+\alpha\cdot a_{121}\cdot a_{213}\cdot a_{332}+\alpha\cdot a_{121}\cdot a_{232}\cdot a_{313}-\alpha\cdot a_{121}\cdot a_{233}\cdot a_{312}$$

$$+\alpha\cdot a_{122}\cdot a_{211}\cdot a_{333}-\alpha\cdot a_{122}\cdot a_{213}\cdot a_{331}-\alpha\cdot a_{122}\cdot a_{231}\cdot a_{313}+\alpha\cdot a_{122}\cdot a_{233}\cdot a_{311}$$

$$-\alpha\cdot a_{123}\cdot a_{211}\cdot a_{332}+\alpha\cdot a_{123}\cdot a_{212}\cdot a_{331}+\alpha\cdot a_{123}\cdot a_{231}\cdot a_{312}-\alpha\cdot a_{123}\cdot a_{232}\cdot a_{311}$$

$$+a_{131}\cdot a_{212}\cdot\alpha\cdot a_{323}-a_{131}\cdot a_{213}\cdot\alpha\cdot a_{322}-a_{131}\cdot\alpha\cdot a_{222}\cdot a_{313}+a_{131}\cdot\alpha\cdot a_{223}\cdot a_{312}$$

$$-a_{132}\cdot a_{211}\cdot\alpha\cdot a_{323}+a_{132}\cdot a_{213}\cdot\alpha\cdot a_{321}+a_{132}\cdot\alpha\cdot a_{221}\cdot a_{313}-a_{132}\cdot\alpha\cdot a_{223}\cdot a_{311}$$

$$+a_{133}\cdot a_{211}\cdot\alpha\cdot a_{322}-a_{133}\cdot a_{212}\cdot\alpha\cdot a_{321}-a_{133}\cdot\alpha\cdot a_{221}\cdot a_{312}+a_{133}\cdot\alpha\cdot a_{222}\cdot a_{311}=\alpha\cdot\det[A_{3\times3\times3}]$$

6. For plan $j=3$: Let A be cubic-matrix of order 2, where all elements on the plan $i=3$ are equal to zero, then based on definition 3:

$$\det[B_{3\times3\times3}]=\det\left(\begin{array}{ccc|ccc|ccc} a_{111} & a_{121} & \alpha\cdot a_{131} & a_{112} & a_{122} & \alpha\cdot a_{132} & a_{113} & a_{123} & \alpha\cdot a_{133}\\ a_{211} & a_{221} & \alpha\cdot a_{231} & a_{212} & a_{222} & \alpha\cdot a_{232} & a_{213} & a_{223} & \alpha\cdot a_{233}\\ a_{311} & a_{321} & \alpha\cdot a_{331} & a_{312} & a_{322} & \alpha\cdot a_{332} & a_{313} & a_{323} & \alpha\cdot a_{333}\end{array}\right)$$

$$=a_{111}\cdot a_{222}\cdot\alpha\cdot a_{333}-a_{111}\cdot\alpha\cdot a_{232}\cdot a_{323}-a_{111}\cdot a_{223}\cdot\alpha\cdot a_{332}+a_{111}\cdot\alpha\cdot a_{233}\cdot a_{322}$$

$$-a_{112}\cdot a_{221}\cdot\alpha\cdot a_{333}+a_{112}\cdot a_{223}\cdot\alpha\cdot a_{331}+a_{112}\cdot\alpha\cdot a_{231}\cdot a_{323}-a_{112}\cdot\alpha\cdot a_{233}\cdot a_{321}$$

$$+a_{113}\cdot a_{221}\cdot\alpha\cdot a_{332}-a_{113}\cdot a_{222}\cdot\alpha\cdot a_{331}-a_{113}\cdot\alpha\cdot a_{231}\cdot a_{322}+a_{113}\cdot\alpha\cdot a_{232}\cdot a_{321}$$

$$-a_{121}\cdot a_{212}\cdot\alpha\cdot a_{333}+a_{121}\cdot a_{213}\cdot\alpha\cdot a_{332}+a_{121}\cdot\alpha\cdot a_{232}\cdot a_{313}-a_{121}\cdot\alpha\cdot a_{233}\cdot a_{312}$$

$$+a_{122}\cdot a_{211}\cdot\alpha\cdot a_{333}-a_{122}\cdot a_{213}\cdot\alpha\cdot a_{331}-a_{122}\cdot\alpha\cdot a_{231}\cdot a_{313}+a_{122}\cdot\alpha\cdot a_{233}\cdot a_{311}$$

$$-a_{123}\cdot a_{211}\cdot\alpha\cdot a_{332}+a_{123}\cdot a_{212}\cdot\alpha\cdot a_{331}+a_{123}\cdot\alpha\cdot a_{231}\cdot a_{312}-a_{123}\cdot\alpha\cdot a_{232}\cdot a_{311}$$

$$+\alpha\cdot a_{131}\cdot a_{212}\cdot a_{323}-\alpha\cdot a_{131}\cdot a_{213}\cdot a_{322}-\alpha\cdot a_{131}\cdot a_{222}\cdot a_{313}+\alpha\cdot a_{131}\cdot a_{223}\cdot a_{312}$$

$$-\alpha\cdot a_{132}\cdot a_{211}\cdot a_{323}+\alpha\cdot a_{132}\cdot a_{213}\cdot a_{321}+\alpha\cdot a_{132}\cdot a_{221}\cdot a_{313}-\alpha\cdot a_{132}\cdot a_{223}\cdot a_{311}$$

$$+\alpha\cdot a_{133}\cdot a_{211}\cdot a_{322}-\alpha\cdot a_{133}\cdot a_{212}\cdot a_{321}-\alpha\cdot a_{133}\cdot a_{221}\cdot a_{312}+\alpha\cdot a_{133}\cdot a_{222}\cdot a_{311}=\alpha\cdot\det[A_{3\times3\times3}]$$

7. For plan $k=1$: Let A be cubic-matrix of order 2, where all elements on the plan $k=1$ are equal to zero, then based on definition 3:

$$\det[B_{3\times3\times3}]=\det\left(\begin{array}{ccc|ccc|ccc} \alpha\cdot a_{111} & \alpha\cdot a_{121} & \alpha\cdot a_{131} & a_{112} & a_{122} & a_{132} & a_{113} & a_{123} & a_{133}\\ \alpha\cdot a_{211} & \alpha\cdot a_{221} & \alpha\cdot a_{231} & a_{212} & a_{222} & a_{232} & a_{213} & a_{223} & a_{233}\\ \alpha\cdot a_{311} & \alpha\cdot a_{321} & \alpha\cdot a_{331} & a_{312} & a_{322} & a_{332} & a_{313} & a_{323} & a_{333}\end{array}\right)$$

$$=\alpha\cdot a_{111}\cdot a_{222}\cdot a_{333}-\alpha\cdot a_{111}\cdot a_{232}\cdot a_{323}-\alpha\cdot a_{111}\cdot a_{223}\cdot a_{332}+\alpha\cdot a_{111}\cdot a_{233}\cdot a_{322}$$

$$-a_{112}\cdot\alpha\cdot a_{221}\cdot a_{333}+a_{112}\cdot a_{223}\cdot\alpha\cdot a_{331}+a_{112}\cdot\alpha\cdot a_{231}\cdot a_{323}-a_{112}\cdot a_{233}\cdot\alpha\cdot a_{321}$$

$$+a_{113}\cdot\alpha\cdot a_{221}\cdot a_{332}-a_{113}\cdot a_{222}\cdot\alpha\cdot a_{331}-a_{113}\cdot\alpha\cdot a_{231}\cdot a_{322}+a_{113}\cdot a_{232}\cdot\alpha\cdot a_{321}$$

$$-\alpha\cdot a_{121}\cdot a_{212}\cdot a_{333}+\alpha\cdot a_{121}\cdot a_{213}\cdot a_{332}+\alpha\cdot a_{121}\cdot a_{232}\cdot a_{313}-\alpha\cdot a_{121}\cdot a_{233}\cdot a_{312}$$

$$+a_{122}\cdot\alpha\cdot a_{211}\cdot a_{333}-a_{122}\cdot a_{213}\cdot\alpha\cdot a_{331}-a_{122}\cdot\alpha\cdot a_{231}\cdot a_{313}+a_{122}\cdot a_{233}\cdot\alpha\cdot a_{311}$$

$$-a_{123}\cdot\alpha\cdot a_{211}\cdot a_{332}+a_{123}\cdot a_{212}\cdot\alpha\cdot a_{331}+a_{123}\cdot\alpha\cdot a_{231}\cdot a_{312}-a_{123}\cdot a_{232}\cdot\alpha\cdot a_{311}$$

$$+\alpha\cdot a_{131}\cdot a_{212}\cdot a_{323}-\alpha\cdot a_{131}\cdot a_{213}\cdot a_{322}-\alpha\cdot a_{131}\cdot a_{222}\cdot a_{313}+\alpha\cdot a_{131}\cdot a_{223}\cdot a_{312}$$

$$-a_{132}\cdot\alpha\cdot a_{211}\cdot a_{323}+a_{132}\cdot a_{213}\cdot\alpha\cdot a_{321}+a_{132}\cdot\alpha\cdot a_{221}\cdot a_{313}-a_{132}\cdot a_{223}\cdot\alpha\cdot a_{311}$$

$$a_{133}\cdot\alpha\cdot a_{211}\cdot a_{322}-a_{133}\cdot a_{212}\cdot\alpha\cdot a_{321}-a_{133}\cdot\alpha\cdot a_{221}\cdot a_{312}+a_{133}\cdot a_{222}\cdot\alpha\cdot a_{311}=\alpha\cdot\det[A_{3\times3\times3}]$$

8. For plan $k=2$: Let A be cubic-matrix of order 2, where all elements on the plan $k=2$ are equal to zero, then based on definition 3:

$$\det[B_{3\times3\times3}]=\det\left(\begin{array}{ccc|ccc|ccc} a_{111} & a_{121} & a_{131} & \alpha\cdot a_{112} & \alpha\cdot a_{122} & \alpha\cdot a_{132} & a_{113} & a_{123} & a_{133} \\ a_{211} & a_{221} & a_{231} & \alpha\cdot a_{212} & \alpha\cdot a_{222} & \alpha\cdot a_{232} & a_{213} & a_{223} & a_{233} \\ a_{311} & a_{321} & a_{331} & \alpha\cdot a_{312} & \alpha\cdot a_{322} & \alpha\cdot a_{332} & a_{313} & a_{323} & a_{333} \end{array}\right)$$

$$=a_{111}\cdot\alpha\cdot a_{222}\cdot a_{333}-a_{111}\cdot\alpha\cdot a_{232}\cdot a_{323}-a_{111}\cdot a_{223}\cdot\alpha\cdot a_{332}+a_{111}\cdot a_{233}\cdot\alpha\cdot a_{322}$$

$$-\alpha\cdot a_{112}\cdot a_{221}\cdot a_{333}+\alpha\cdot a_{112}\cdot a_{223}\cdot a_{331}+\alpha\cdot a_{112}\cdot a_{231}\cdot a_{323}-\alpha\cdot a_{112}\cdot a_{233}\cdot a_{321}$$

$$+a_{113}\cdot a_{221}\cdot\alpha\cdot a_{332}-a_{113}\cdot\alpha\cdot a_{222}\cdot a_{331}-a_{113}\cdot a_{231}\cdot\alpha\cdot a_{322}+a_{113}\cdot\alpha\cdot a_{232}\cdot a_{321}$$

$$-a_{121}\cdot\alpha\cdot a_{212}\cdot a_{333}+a_{121}\cdot a_{213}\cdot\alpha\cdot a_{332}+a_{121}\cdot\alpha\cdot a_{232}\cdot a_{313}-a_{121}\cdot a_{233}\cdot\alpha\cdot a_{312}$$

$$+\alpha\cdot a_{122}\cdot a_{211}\cdot a_{333}-\alpha\cdot a_{122}\cdot a_{213}\cdot a_{331}-\alpha\cdot a_{122}\cdot a_{231}\cdot a_{313}+\alpha\cdot a_{122}\cdot a_{233}\cdot a_{311}$$

$$-a_{123}\cdot a_{211}\cdot\alpha\cdot a_{332}+a_{123}\cdot\alpha\cdot a_{212}\cdot a_{331}+a_{123}\cdot a_{231}\cdot\alpha\cdot a_{312}-a_{123}\cdot\alpha\cdot a_{232}\cdot a_{311}$$

$$+a_{131}\cdot\alpha\cdot a_{212}\cdot a_{323}-a_{131}\cdot a_{213}\cdot\alpha\cdot a_{322}-a_{131}\cdot\alpha\cdot a_{222}\cdot a_{313}+a_{131}\cdot a_{223}\cdot\alpha\cdot a_{312}$$

$$-\alpha\cdot a_{132}\cdot a_{211}\cdot a_{323}+\alpha\cdot a_{132}\cdot a_{213}\cdot a_{321}+\alpha\cdot a_{132}\cdot a_{221}\cdot a_{313}-\alpha\cdot a_{132}\cdot a_{223}\cdot a_{311}$$

$$+a_{133}\cdot a_{211}\cdot\alpha\cdot a_{322}-a_{133}\cdot\alpha\cdot a_{212}\cdot a_{321}-a_{133}\cdot a_{221}\cdot\alpha\cdot a_{312}+a_{133}\cdot\alpha\cdot a_{222}\cdot a_{311}=\alpha\cdot\det[A_{3\times3\times3}]$$

9. For plan $k=3$: Let A be cubic-matrix of order 2, where all elements on the plan $k=3$ are equal to zero, then based on definition 3:

$$\det[B_{3\times3\times3}]=\det\left(\begin{array}{ccc|ccc|ccc} a_{111} & a_{121} & a_{131} & a_{112} & a_{122} & a_{132} & \alpha\cdot a_{113} & \alpha\cdot a_{123} & \alpha\cdot a_{133} \\ a_{211} & a_{221} & a_{231} & a_{212} & a_{222} & a_{232} & \alpha\cdot a_{213} & \alpha\cdot a_{223} & \alpha\cdot a_{233} \\ a_{311} & a_{321} & a_{331} & a_{312} & a_{322} & a_{332} & \alpha\cdot a_{313} & \alpha\cdot a_{323} & \alpha\cdot a_{333} \end{array}\right)$$

$$=a_{111}\cdot a_{222}\cdot\alpha\cdot a_{333}-a_{111}\cdot a_{232}\cdot\alpha\cdot a_{323}-a_{111}\cdot\alpha\cdot a_{223}\cdot a_{332}+a_{111}\cdot\alpha\cdot a_{233}\cdot a_{322}$$

$$-a_{112}\cdot a_{221}\cdot\alpha\cdot a_{333}+a_{112}\cdot\alpha\cdot a_{223}\cdot a_{331}+a_{112}\cdot a_{231}\cdot\alpha\cdot a_{323}-a_{112}\cdot\alpha\cdot a_{233}\cdot a_{321}$$

$$+\alpha\cdot a_{113}\cdot a_{221}\cdot a_{332}-\alpha\cdot a_{113}\cdot a_{222}\cdot a_{331}-\alpha\cdot a_{113}\cdot a_{231}\cdot a_{322}+\alpha\cdot a_{113}\cdot a_{232}\cdot a_{321}$$

$$-a_{121}\cdot a_{212}\cdot\alpha\cdot a_{333}+a_{121}\cdot\alpha\cdot a_{213}\cdot a_{332}+a_{121}\cdot a_{232}\cdot\alpha\cdot a_{313}-a_{121}\cdot\alpha\cdot a_{233}\cdot a_{312}$$

$$+a_{122}\cdot a_{211}\cdot\alpha\cdot a_{333}-a_{122}\cdot\alpha\cdot a_{213}\cdot a_{331}-a_{122}\cdot a_{231}\cdot\alpha\cdot a_{313}+a_{122}\cdot\alpha\cdot a_{233}\cdot a_{311}$$

$$-\alpha\cdot a_{123}\cdot a_{211}\cdot a_{332}+\alpha\cdot a_{123}\cdot a_{212}\cdot a_{331}+\alpha\cdot a_{123}\cdot a_{231}\cdot a_{312}-\alpha\cdot a_{123}\cdot a_{232}\cdot a_{311}$$

$$+a_{131}\cdot a_{212}\cdot\alpha\cdot a_{323}-a_{131}\cdot\alpha\cdot a_{213}\cdot a_{322}-a_{131}\cdot a_{222}\cdot\alpha\cdot a_{313}+a_{131}\cdot\alpha\cdot a_{223}\cdot a_{312}$$

$$-a_{132} \cdot a_{211} \cdot \alpha \cdot a_{323} + a_{132} \cdot \alpha \cdot a_{213} \cdot a_{321} + a_{132} \cdot a_{221} \cdot \alpha \cdot a_{313} - a_{132} \cdot \alpha \cdot a_{223} \cdot a_{311}$$

$$+\alpha \cdot a_{133} \cdot a_{211} \cdot a_{322} - \alpha \cdot a_{133} \cdot a_{212} \cdot a_{321} - \alpha \cdot a_{133} \cdot a_{221} \cdot a_{312} + \alpha \cdot a_{133} \cdot a_{222} \cdot a_{311} = \alpha \cdot \det[A_{3\times3\times3}]$$

Example 3 *Let's be A a cubic matrix with order 2 then we will obtain determinant a cubic-matrix B from A by multiplying any plan $i = 1$ with scalar 3 and have,*

$$\det[B_{2\times2\times2}] = \det\left(\begin{matrix} 3\cdot2 & 3\cdot1 \\ 3 & 5 \end{matrix}\middle|\begin{matrix} 3\cdot4 & 3\cdot7 \\ 3 & 2 \end{matrix}\right) = 3\cdot2\cdot2 - 3\cdot4\cdot5 - 3\cdot1\cdot3 + 3\cdot7\cdot3 = 6.$$

If we compare with example 2, we can see that $|A| = 3 \cdot |B|$.

Theorem 2 *Let's be A a cubic-matrix of order 2 or order 3, and B be another cubic-matrix, which obtained from A by interchanging the location of two consecutive "horizontal layer" in i-index, then $det(A) = det(B)$.*

Proof. We try the cases in order for cubic matrix of order 2 and cases for cubic matrix of order 3:

Case 1. Let B be cubic-matrix of order 2, where we have interchanged to "horizontal layer", then based on definition 2: Let B be cubic-matrix of order 2, where we have interchanged two "horizontal layer", then based on definition 2:

$$\det[B_{2\times2\times2}] = \det\left(\begin{matrix} a_{211} & a_{221} \\ a_{111} & a_{121} \end{matrix}\middle|\begin{matrix} a_{212} & a_{222} \\ a_{112} & a_{122} \end{matrix}\right)$$

$$= a_{211} \cdot a_{122} - a_{212} \cdot a_{121} - a_{221} \cdot a_{112} + a_{222} \cdot a_{111} = \det[A_{2\times2\times2}]$$

Case 2. Let B be cubic-matrix of order 3, where we have interchanged to "horizontal layer", then based on definition 2:

1. Let B be cubic-matrix of order 3, where we have interchanged two "horizontal layer" (first layer with the second layer), then based on definition 3:

$$\det[B_{3\times3\times3}] = \det\left(\begin{matrix} a_{211} & a_{221} & a_{231} \\ a_{111} & a_{121} & a_{131} \\ a_{311} & a_{321} & a_{331} \end{matrix}\middle|\begin{matrix} a_{212} & a_{222} & a_{232} \\ a_{112} & a_{122} & a_{132} \\ a_{312} & a_{322} & a_{332} \end{matrix}\middle|\begin{matrix} a_{213} & a_{223} & a_{233} \\ a_{113} & a_{123} & a_{133} \\ a_{313} & a_{323} & a_{333} \end{matrix}\right)$$

$$= a_{211} \cdot a_{122} \cdot a_{333} - a_{211} \cdot a_{132} \cdot a_{323} - a_{211} \cdot a_{123} \cdot a_{332} + a_{211} \cdot a_{133} \cdot a_{322}$$

$$-a_{212} \cdot a_{121} \cdot a_{333} + a_{212} \cdot a_{123} \cdot a_{331} + a_{212} \cdot a_{131} \cdot a_{323} - a_{212} \cdot a_{133} \cdot a_{321}$$

$$+a_{213} \cdot a_{121} \cdot a_{332} - a_{213} \cdot a_{122} \cdot a_{331} - a_{213} \cdot a_{131} \cdot a_{322} + a_{213} \cdot a_{132} \cdot a_{321}$$

$$-a_{221} \cdot a_{112} \cdot a_{333} + a_{221} \cdot a_{113} \cdot a_{332} + a_{221} \cdot a_{132} \cdot a_{313} - a_{221} \cdot a_{133} \cdot a_{312}$$

$$+a_{222} \cdot a_{111} \cdot a_{333} - a_{222} \cdot a_{113} \cdot a_{331} - a_{222} \cdot a_{131} \cdot a_{313} + a_{222} \cdot a_{133} \cdot a_{311}$$

$$-a_{223} \cdot a_{111} \cdot a_{332} + a_{223} \cdot a_{112} \cdot a_{331} + a_{223} \cdot a_{131} \cdot a_{312} - a_{223} \cdot a_{132} \cdot a_{311}$$

$$+a_{231} \cdot a_{112} \cdot a_{323} - a_{231} \cdot a_{113} \cdot a_{322} - a_{231} \cdot a_{122} \cdot a_{313} + a_{231} \cdot a_{123} \cdot a_{312}$$

$$-a_{232} \cdot a_{111} \cdot a_{323} + a_{232} \cdot a_{113} \cdot a_{321} + a_{232} \cdot a_{121} \cdot a_{313} - a_{232} \cdot a_{123} \cdot a_{311}$$

$$+a_{233} \cdot a_{111} \cdot a_{322} - a_{233} \cdot a_{112} \cdot a_{311} - a_{233} \cdot a_{121} \cdot a_{312} + a_{233} \cdot a_{122} \cdot a_{311}$$

$$= a_{111} \cdot a_{222} \cdot a_{333} - a_{111} \cdot a_{232} \cdot a_{323} - a_{111} \cdot a_{223} \cdot a_{332} + a_{111} \cdot a_{233} \cdot a_{322}$$

$$-a_{112}\cdot a_{221}\cdot a_{333}+a_{112}\cdot a_{223}\cdot a_{331}+a_{112}\cdot a_{231}\cdot a_{323}-a_{112}\cdot a_{233}\cdot a_{321}$$

$$+a_{113}\cdot a_{221}\cdot a_{332}-a_{113}\cdot a_{222}\cdot a_{331}-a_{113}\cdot a_{231}\cdot a_{322}+a_{113}\cdot a_{232}\cdot a_{321}$$

$$-a_{121}\cdot a_{212}\cdot a_{333}+a_{121}\cdot a_{213}\cdot a_{332}+a_{121}\cdot a_{232}\cdot a_{313}-a_{121}\cdot a_{233}\cdot a_{312}$$

$$+a_{122}\cdot a_{211}\cdot a_{333}-a_{122}\cdot a_{213}\cdot a_{331}-a_{122}\cdot a_{231}\cdot a_{313}+a_{122}\cdot a_{233}\cdot a_{311}$$

$$-a_{123}\cdot a_{211}\cdot a_{332}+a_{123}\cdot a_{212}\cdot a_{331}+a_{123}\cdot a_{231}\cdot a_{312}-a_{123}\cdot a_{232}\cdot a_{311}$$

$$+a_{131}\cdot a_{212}\cdot a_{323}-a_{131}\cdot a_{213}\cdot a_{322}-a_{131}\cdot a_{222}\cdot a_{313}+a_{131}\cdot a_{223}\cdot a_{312}$$

$$-a_{132}\cdot a_{211}\cdot a_{323}+a_{132}\cdot a_{213}\cdot a_{321}+a_{132}\cdot a_{221}\cdot a_{313}-a_{132}\cdot a_{223}\cdot a_{311}$$

$$+a_{133}\cdot a_{211}\cdot a_{322}-a_{133}\cdot a_{212}\cdot a_{321}-a_{133}\cdot a_{221}\cdot a_{312}+a_{133}\cdot a_{222}\cdot a_{311}=\det[A_{3\times3\times3}]$$

2. Let B be cubic-matrix of order 3, where we have interchanged two "horizontal layer" (second layer with the third layer), then based on definition 3:

$$\det[B_{3\times3\times3}]=\det\left(\begin{array}{ccc|ccc|ccc} a_{111} & a_{121} & a_{131} & a_{112} & a_{122} & a_{132} & a_{113} & a_{123} & a_{133}\\ a_{311} & a_{321} & a_{331} & a_{312} & a_{322} & a_{332} & a_{313} & a_{323} & a_{333}\\ a_{211} & a_{221} & a_{231} & a_{212} & a_{222} & a_{232} & a_{213} & a_{223} & a_{233}\end{array}\right)$$

$$=a_{111}\cdot a_{322}\cdot a_{233}-a_{111}\cdot a_{332}\cdot a_{223}-a_{111}\cdot a_{323}\cdot a_{232}+a_{111}\cdot a_{333}\cdot a_{222}$$

$$-a_{112}\cdot a_{321}\cdot a_{233}+a_{112}\cdot a_{323}\cdot a_{231}+a_{112}\cdot a_{331}\cdot a_{223}-a_{112}\cdot a_{333}\cdot a_{221}$$

$$+a_{113}\cdot a_{321}\cdot a_{232}-a_{113}\cdot a_{322}\cdot a_{231}-a_{113}\cdot a_{331}\cdot a_{222}+a_{113}\cdot a_{332}\cdot a_{221}$$

$$-a_{121}\cdot a_{312}\cdot a_{233}+a_{121}\cdot a_{313}\cdot a_{232}+a_{121}\cdot a_{332}\cdot a_{213}-a_{121}\cdot a_{333}\cdot a_{212}$$

$$+a_{122}\cdot a_{311}\cdot a_{233}-a_{122}\cdot a_{313}\cdot a_{231}-a_{122}\cdot a_{331}\cdot a_{213}+a_{122}\cdot a_{333}\cdot a_{211}$$

$$-a_{123}\cdot a_{311}\cdot a_{232}+a_{123}\cdot a_{312}\cdot a_{231}+a_{123}\cdot a_{331}\cdot a_{212}-a_{123}\cdot a_{332}\cdot a_{211}$$

$$+a_{131}\cdot a_{312}\cdot a_{223}-a_{131}\cdot a_{313}\cdot a_{222}-a_{131}\cdot a_{322}\cdot a_{213}+a_{131}\cdot a_{323}\cdot a_{212}$$

$$-a_{132}\cdot a_{311}\cdot a_{223}+a_{132}\cdot a_{313}\cdot a_{221}+a_{132}\cdot a_{321}\cdot a_{213}-a_{132}\cdot a_{323}\cdot a_{211}$$

$$+a_{133}\cdot a_{311}\cdot a_{222}-a_{133}\cdot a_{312}\cdot a_{221}-a_{133}\cdot a_{321}\cdot a_{212}+a_{133}\cdot a_{322}\cdot a_{211}$$

$$=a_{111}\cdot a_{222}\cdot a_{333}-a_{111}\cdot a_{232}\cdot a_{323}-a_{111}\cdot a_{223}\cdot a_{332}+a_{111}\cdot a_{233}\cdot a_{322}$$

$$-a_{112}\cdot a_{221}\cdot a_{333}+a_{112}\cdot a_{223}\cdot a_{331}+a_{112}\cdot a_{231}\cdot a_{323}-a_{112}\cdot a_{233}\cdot a_{321}$$

$$+a_{113}\cdot a_{221}\cdot a_{332}-a_{113}\cdot a_{222}\cdot a_{331}-a_{113}\cdot a_{231}\cdot a_{322}+a_{113}\cdot a_{232}\cdot a_{321}$$

$$-a_{121}\cdot a_{212}\cdot a_{333}+a_{121}\cdot a_{213}\cdot a_{332}+a_{121}\cdot a_{232}\cdot a_{313}-a_{121}\cdot a_{233}\cdot a_{312}$$

$$+a_{122}\cdot a_{211}\cdot a_{333}-a_{122}\cdot a_{213}\cdot a_{331}-a_{122}\cdot a_{231}\cdot a_{313}+a_{122}\cdot a_{233}\cdot a_{311}$$

$$-a_{123}\cdot a_{211}\cdot a_{332}+a_{123}\cdot a_{212}\cdot a_{331}+a_{123}\cdot a_{231}\cdot a_{312}-a_{123}\cdot a_{232}\cdot a_{311}$$

$$+a_{131}\cdot a_{212}\cdot a_{323}-a_{131}\cdot a_{213}\cdot a_{322}-a_{131}\cdot a_{222}\cdot a_{313}+a_{131}\cdot a_{223}\cdot a_{312}$$

$$-a_{132}\cdot a_{211}\cdot a_{323}+a_{132}\cdot a_{213}\cdot a_{321}+a_{132}\cdot a_{221}\cdot a_{313}-a_{132}\cdot a_{223}\cdot a_{311}$$

$$+a_{133}\cdot a_{211}\cdot a_{322}-a_{133}\cdot a_{212}\cdot a_{321}-a_{133}\cdot a_{221}\cdot a_{312}+a_{133}\cdot a_{222}\cdot a_{311}=\det[A_{3\times3\times3}]$$

Example 4 *Let A be $2\times2\times2$ 3D determinant than we will obtain determinant B from A by interchanging location of two horizontal layer in i index:*

$$\det[A_{2\times2\times2}]=\det\left(\begin{matrix}2 & 1\\3 & 5\end{matrix}\middle|\begin{matrix}4 & 7\\3 & 2\end{matrix}\right)=2\cdot2-4\cdot5-1\cdot3+7\cdot3=2.$$

Then:

$$\det[A_{2\times2\times2}]=\det\left(\begin{matrix}3 & 5\\2 & 1\end{matrix}\middle|\begin{matrix}3 & 2\\4 & 7\end{matrix}\right)=3\cdot7-3\cdot1-5\cdot4+2\cdot2=2.$$

If we compare results with example 2, we can see that we have the same result.

Example 5 *Let A be a $3\times3\times3$ 3D determinant than we will obtain determinant B from A by interchanging location of two horizontal layer in i index:*

$$\det[A_{3\times3\times3}]=\det\left(\begin{matrix}1 & 4 & 2\\2 & 0 & 0\\0 & 4 & 2\end{matrix}\middle|\begin{matrix}3 & 1 & 3\\5 & 1 & 3\\3 & 2 & 0\end{matrix}\middle|\begin{matrix}2 & 1 & 0\\0 & 1 & 0\\2 & 1 & 0\end{matrix}\right)=-3+6-4+24+24+10+10-4+6-6=63$$

Then:

$$\det[B_{3\times3\times3}]=\det\left(\begin{matrix}2 & 0 & 0\\1 & 4 & 2\\0 & 4 & 2\end{matrix}\middle|\begin{matrix}5 & 1 & 3\\3 & 1 & 3\\3 & 2 & 0\end{matrix}\middle|\begin{matrix}0 & 1 & 0\\2 & 1 & 0\\2 & 1 & 0\end{matrix}\right)=6-4+10+10-4-3+24+24-6+6=63$$

If we compare results with example 2, we can see that we have the same result.

Theorem 3 *Let's be A a cubic-matrix of order 2 or order 3, and B be another cubic-matrix, which obtained from A by interchanging the location of two consecutive: "vertical page" in j-index or "vertical layer" in k-index, then $det(A)=-det(B)$.*

Proof. We discuss the cases in order for cubic matrix of order 2 and order 3:

Case 1. The cubic-matrix A of order 2, (and B has order 2), we will proof the case 1 for each "vertical page" and "vertical layer", as following:

1. For interchanging the location of two consecutive "vertical page": Let B be cubic-matrix of order 2, where we have interchanged two "vertical page", then based on definition 2:

$$\det[B_{2\times2\times2}]=\det\left(\begin{matrix}a_{121} & a_{111}\\a_{221} & a_{211}\end{matrix}\middle|\begin{matrix}a_{122} & a_{112}\\a_{222} & a_{212}\end{matrix}\right)$$

$$=a_{121}\cdot a_{212}-a_{122}\cdot a_{211}-a_{111}\cdot a_{222}+a_{112}\cdot a_{221}=-\det[A_{2\times2\times2}]$$

2. For interchanging the location of two consecutive "vertical layer": Let B be cubic-matrix of order 2, where we have interchanged two "vertical layer", then based on definition 2:

$$\det[B_{2\times2\times2}]=\det\left(\begin{matrix}a_{112} & a_{122}\\a_{212} & a_{222}\end{matrix}\middle|\begin{matrix}a_{111} & a_{121}\\a_{211} & a_{221}\end{matrix}\right)$$

$$=a_{112}\cdot a_{221}-a_{111}\cdot a_{222}-a_{122}\cdot a_{211}+a_{121}\cdot a_{212}=-\det[A_{2\times2\times2}]$$

Case 2. The cubic-matrix A of order 3, (and B has order 3), we will proof the case 2 for each "vertical page" and "vertical layer", as following:

1. For interchanging the location of two consecutive "vertical page": Let B be cubic-matrix of order 3, where we have interchanged two consecutive "vertical page" (First page with second page), then based on definition 3:

$$\det[B_{3\times3\times3}] = \det\left(\begin{array}{ccc|ccc|ccc} a_{121} & a_{111} & a_{131} & a_{122} & a_{112} & a_{132} & a_{123} & a_{113} & a_{133} \\ a_{221} & a_{211} & a_{231} & a_{222} & a_{212} & a_{232} & a_{223} & a_{213} & a_{233} \\ a_{321} & a_{311} & a_{331} & a_{322} & a_{312} & a_{332} & a_{323} & a_{313} & a_{333} \end{array}\right)$$

$$= a_{121}\cdot a_{212}\cdot a_{333} - a_{121}\cdot a_{232}\cdot a_{313} - a_{121}\cdot a_{213}\cdot a_{332} + a_{121}\cdot a_{233}\cdot a_{312}$$

$$-a_{122}\cdot a_{211}\cdot a_{333} + a_{122}\cdot a_{213}\cdot a_{331} + a_{122}\cdot a_{231}\cdot a_{313} - a_{122}\cdot a_{233}\cdot a_{311}$$

$$+a_{123}\cdot a_{211}\cdot a_{332} - a_{123}\cdot a_{212}\cdot a_{331} - a_{123}\cdot a_{231}\cdot a_{312} + a_{123}\cdot a_{232}\cdot a_{311}$$

$$-a_{111}\cdot a_{222}\cdot a_{333} + a_{111}\cdot a_{223}\cdot a_{332} + a_{111}\cdot a_{232}\cdot a_{323} - a_{111}\cdot a_{233}\cdot a_{322}$$

$$+a_{112}\cdot a_{221}\cdot a_{333} - a_{112}\cdot a_{223}\cdot a_{331} - a_{112}\cdot a_{231}\cdot a_{323} + a_{112}\cdot a_{233}\cdot a_{321}$$

$$-a_{113}\cdot a_{221}\cdot a_{332} + a_{113}\cdot a_{222}\cdot a_{331} + a_{113}\cdot a_{231}\cdot a_{322} - a_{113}\cdot a_{232}\cdot a_{321}$$

$$+a_{131}\cdot a_{222}\cdot a_{313} - a_{131}\cdot a_{223}\cdot a_{312} - a_{131}\cdot a_{212}\cdot a_{323} + a_{131}\cdot a_{213}\cdot a_{322}$$

$$-a_{132}\cdot a_{221}\cdot a_{313} + a_{132}\cdot a_{223}\cdot a_{311} + a_{132}\cdot a_{211}\cdot a_{323} - a_{132}\cdot a_{213}\cdot a_{321}$$

$$+a_{133}\cdot a_{221}\cdot a_{312} - a_{133}\cdot a_{222}\cdot a_{311} - a_{133}\cdot a_{211}\cdot a_{322} + a_{133}\cdot a_{212}\cdot a_{321}$$

$$= -a_{111}\cdot a_{222}\cdot a_{333} + a_{111}\cdot a_{232}\cdot a_{323} + a_{111}\cdot a_{223}\cdot a_{332} - a_{111}\cdot a_{233}\cdot a_{322}$$

$$+a_{112}\cdot a_{221}\cdot a_{333} - a_{112}\cdot a_{223}\cdot a_{331} - a_{112}\cdot a_{231}\cdot a_{323} + a_{112}\cdot a_{233}\cdot a_{321}$$

$$-a_{113}\cdot a_{221}\cdot a_{332} + a_{113}\cdot a_{222}\cdot a_{331} + a_{113}\cdot a_{231}\cdot a_{322} - a_{113}\cdot a_{232}\cdot a_{321}$$

$$+a_{121}\cdot a_{212}\cdot a_{333} - a_{121}\cdot a_{213}\cdot a_{332} - a_{121}\cdot a_{232}\cdot a_{313} + a_{121}\cdot a_{233}\cdot a_{312}$$

$$-a_{122}\cdot a_{211}\cdot a_{333} + a_{122}\cdot a_{213}\cdot a_{331} + a_{122}\cdot a_{231}\cdot a_{313} - a_{122}\cdot a_{233}\cdot a_{311}$$

$$+a_{123}\cdot a_{211}\cdot a_{332} - a_{123}\cdot a_{212}\cdot a_{331} - a_{123}\cdot a_{231}\cdot a_{312} + a_{123}\cdot a_{232}\cdot a_{311}$$

$$-a_{131}\cdot a_{212}\cdot a_{323} + a_{131}\cdot a_{213}\cdot a_{322} + a_{131}\cdot a_{222}\cdot a_{313} - a_{131}\cdot a_{223}\cdot a_{312}$$

$$+a_{132}\cdot a_{211}\cdot a_{323} - a_{132}\cdot a_{213}\cdot a_{321} - a_{132}\cdot a_{221}\cdot a_{313} + a_{132}\cdot a_{223}\cdot a_{311}$$

$$-a_{133}\cdot a_{211}\cdot a_{322} + a_{133}\cdot a_{212}\cdot a_{321} + a_{133}\cdot a_{221}\cdot a_{312} - a_{133}\cdot a_{222}\cdot a_{311}$$

$$= -(a_{111}\cdot a_{222}\cdot a_{333} - a_{111}\cdot a_{232}\cdot a_{323} - a_{111}\cdot a_{223}\cdot a_{332} + a_{111}\cdot a_{233}\cdot a_{322}$$

$$-a_{112}\cdot a_{221}\cdot a_{333} + a_{112}\cdot a_{223}\cdot a_{331} + a_{112}\cdot a_{231}\cdot a_{323} - a_{112}\cdot a_{233}\cdot a_{321}$$

$$+a_{113}\cdot a_{221}\cdot a_{332} - a_{113}\cdot a_{222}\cdot a_{331} - a_{113}\cdot a_{231}\cdot a_{322} + a_{113}\cdot a_{232}\cdot a_{321}$$

$$-a_{121}\cdot a_{212}\cdot a_{333} + a_{121}\cdot a_{213}\cdot a_{332} + a_{121}\cdot a_{232}\cdot a_{313} - a_{121}\cdot a_{233}\cdot a_{312}$$

$$+a_{122}\cdot a_{211}\cdot a_{333} - a_{122}\cdot a_{213}\cdot a_{331} - a_{122}\cdot a_{231}\cdot a_{313} + a_{122}\cdot a_{233}\cdot a_{311}$$

$$-a_{123}\cdot a_{211}\cdot a_{332} + a_{123}\cdot a_{212}\cdot a_{331} + a_{123}\cdot a_{231}\cdot a_{312} - a_{123}\cdot a_{232}\cdot a_{311}$$

$$+a_{131}\cdot a_{212}\cdot a_{323}-a_{131}\cdot a_{213}\cdot a_{322}-a_{131}\cdot a_{222}\cdot a_{313}+a_{131}\cdot a_{223}\cdot a_{312}$$

$$-a_{132}\cdot a_{211}\cdot a_{323}+a_{132}\cdot a_{213}\cdot a_{321}+a_{132}\cdot a_{221}\cdot a_{313}-a_{132}\cdot a_{223}\cdot a_{311}$$

$$+a_{133}\cdot a_{211}\cdot a_{322}-a_{133}\cdot a_{212}\cdot a_{321}-a_{133}\cdot a_{221}\cdot a_{312}+a_{133}\cdot a_{222}\cdot a_{311})=-\det[A_{3\times3\times3}]$$

2. For interchanging the location of two consecutive "vertical page": Let B be cubic-matrix of order 3, where we have interchanged two consecutive "vertical page" (Second page with third page), then based on definition 3:

$$\det[B_{3\times3\times3}]=\det\left(\begin{array}{ccc|ccc|ccc} a_{111} & a_{131} & a_{121} & a_{112} & a_{132} & a_{122} & a_{113} & a_{133} & a_{123}\\ a_{211} & a_{231} & a_{221} & a_{212} & a_{232} & a_{222} & a_{213} & a_{233} & a_{223}\\ a_{311} & a_{331} & a_{321} & a_{312} & a_{332} & a_{322} & a_{313} & a_{333} & a_{323}\end{array}\right)$$

$$=a_{111}\cdot a_{232}\cdot a_{323}-a_{111}\cdot a_{222}\cdot a_{333}-a_{111}\cdot a_{233}\cdot a_{322}+a_{111}\cdot a_{223}\cdot a_{332}$$

$$-a_{112}\cdot a_{231}\cdot a_{323}+a_{112}\cdot a_{233}\cdot a_{321}+a_{112}\cdot a_{221}\cdot a_{333}-a_{112}\cdot a_{223}\cdot a_{331}$$

$$+a_{113}\cdot a_{231}\cdot a_{322}-a_{113}\cdot a_{232}\cdot a_{321}-a_{113}\cdot a_{221}\cdot a_{332}+a_{113}\cdot a_{222}\cdot a_{331}$$

$$-a_{131}\cdot a_{212}\cdot a_{323}+a_{131}\cdot a_{213}\cdot a_{322}+a_{131}\cdot a_{222}\cdot a_{313}-a_{131}\cdot a_{223}\cdot a_{312}$$

$$+a_{132}\cdot a_{211}\cdot a_{323}-a_{132}\cdot a_{213}\cdot a_{321}-a_{132}\cdot a_{221}\cdot a_{313}+a_{132}\cdot a_{223}\cdot a_{311}$$

$$-a_{133}\cdot a_{211}\cdot a_{322}+a_{133}\cdot a_{212}\cdot a_{321}+a_{133}\cdot a_{221}\cdot a_{312}-a_{133}\cdot a_{222}\cdot a_{311}$$

$$+a_{121}\cdot a_{212}\cdot a_{333}-a_{121}\cdot a_{213}\cdot a_{332}-a_{121}\cdot a_{232}\cdot a_{313}+a_{121}\cdot a_{233}\cdot a_{312}$$

$$-a_{122}\cdot a_{211}\cdot a_{333}+a_{122}\cdot a_{213}\cdot a_{331}+a_{122}\cdot a_{231}\cdot a_{313}-a_{122}\cdot a_{233}\cdot a_{311}$$

$$+a_{123}\cdot a_{211}\cdot a_{332}-a_{123}\cdot a_{212}\cdot a_{331}-a_{123}\cdot a_{231}\cdot a_{312}+a_{123}\cdot a_{232}\cdot a_{311}$$

$$=-a_{111}\cdot a_{222}\cdot a_{333}+a_{111}\cdot a_{232}\cdot a_{323}+a_{111}\cdot a_{223}\cdot a_{332}-a_{111}\cdot a_{233}\cdot a_{322}$$

$$+a_{112}\cdot a_{221}\cdot a_{333}-a_{112}\cdot a_{223}\cdot a_{331}-a_{112}\cdot a_{231}\cdot a_{323}+a_{112}\cdot a_{233}\cdot a_{321}$$

$$-a_{113}\cdot a_{221}\cdot a_{332}+a_{113}\cdot a_{222}\cdot a_{331}+a_{113}\cdot a_{231}\cdot a_{322}-a_{113}\cdot a_{232}\cdot a_{321}$$

$$+a_{121}\cdot a_{212}\cdot a_{333}-a_{121}\cdot a_{213}\cdot a_{332}-a_{121}\cdot a_{232}\cdot a_{313}+a_{121}\cdot a_{233}\cdot a_{312}$$

$$-a_{122}\cdot a_{211}\cdot a_{333}+a_{122}\cdot a_{213}\cdot a_{331}+a_{122}\cdot a_{231}\cdot a_{313}-a_{122}\cdot a_{233}\cdot a_{311}$$

$$+a_{123}\cdot a_{211}\cdot a_{332}-a_{123}\cdot a_{212}\cdot a_{331}-a_{123}\cdot a_{231}\cdot a_{312}+a_{123}\cdot a_{232}\cdot a_{311}$$

$$-a_{131}\cdot a_{212}\cdot a_{323}+a_{131}\cdot a_{213}\cdot a_{322}+a_{131}\cdot a_{222}\cdot a_{313}-a_{131}\cdot a_{223}\cdot a_{312}$$

$$+a_{132}\cdot a_{211}\cdot a_{323}-a_{132}\cdot a_{213}\cdot a_{321}-a_{132}\cdot a_{221}\cdot a_{313}+a_{132}\cdot a_{223}\cdot a_{311}$$

$$-a_{133}\cdot a_{211}\cdot a_{322}+a_{133}\cdot a_{212}\cdot a_{321}+a_{133}\cdot a_{221}\cdot a_{312}-a_{133}\cdot a_{222}\cdot a_{311}$$

$$=-(a_{111}\cdot a_{222}\cdot a_{333}-a_{111}\cdot a_{232}\cdot a_{323}-a_{111}\cdot a_{223}\cdot a_{332}+a_{111}\cdot a_{233}\cdot a_{322}$$

$$-a_{112}\cdot a_{221}\cdot a_{333}+a_{112}\cdot a_{223}\cdot a_{331}+a_{112}\cdot a_{231}\cdot a_{323}-a_{112}\cdot a_{233}\cdot a_{321}$$

$$+a_{113}\cdot a_{221}\cdot a_{332}-a_{113}\cdot a_{222}\cdot a_{331}-a_{113}\cdot a_{231}\cdot a_{322}+a_{113}\cdot a_{232}\cdot a_{321}$$

$$-a_{121}\cdot a_{212}\cdot a_{333}+a_{121}\cdot a_{213}\cdot a_{332}+a_{121}\cdot a_{232}\cdot a_{313}-a_{121}\cdot a_{233}\cdot a_{312}$$
$$+a_{122}\cdot a_{211}\cdot a_{333}-a_{122}\cdot a_{213}\cdot a_{331}-a_{122}\cdot a_{231}\cdot a_{313}+a_{122}\cdot a_{233}\cdot a_{311}$$
$$-a_{123}\cdot a_{211}\cdot a_{332}+a_{123}\cdot a_{212}\cdot a_{331}+a_{123}\cdot a_{231}\cdot a_{312}-a_{123}\cdot a_{232}\cdot a_{311}$$
$$+a_{131}\cdot a_{212}\cdot a_{323}-a_{131}\cdot a_{213}\cdot a_{322}-a_{131}\cdot a_{222}\cdot a_{313}+a_{131}\cdot a_{223}\cdot a_{312}$$
$$-a_{132}\cdot a_{211}\cdot a_{323}+a_{132}\cdot a_{213}\cdot a_{321}+a_{132}\cdot a_{221}\cdot a_{313}-a_{132}\cdot a_{223}\cdot a_{311}$$
$$+a_{133}\cdot a_{211}\cdot a_{322}-a_{133}\cdot a_{212}\cdot a_{321}-a_{133}\cdot a_{221}\cdot a_{312}+a_{133}\cdot a_{222}\cdot a_{311})=-\det[A_{3\times3\times3}]$$

3. For interchanging the location of two consecutive "vertical layers": Let B be cubic-matrix of order 3, where we have interchanged 2-consecutive "vertical layers" (First layer with second layer), then based on definition 3:

$$\det[B_{3\times3\times3}]=\det\left(\begin{array}{ccc|ccc|ccc} a_{112} & a_{122} & a_{132} & a_{111} & a_{121} & a_{131} & a_{113} & a_{123} & a_{133}\\ a_{212} & a_{222} & a_{232} & a_{211} & a_{221} & a_{231} & a_{213} & a_{223} & a_{233}\\ a_{312} & a_{322} & a_{332} & a_{311} & a_{321} & a_{331} & a_{313} & a_{323} & a_{333}\end{array}\right)$$
$$=a_{112}\cdot a_{221}\cdot a_{333}-a_{112}\cdot a_{231}\cdot a_{323}-a_{112}\cdot a_{223}\cdot a_{331}+a_{112}\cdot a_{233}\cdot a_{321}$$
$$-a_{111}\cdot a_{222}\cdot a_{333}+a_{111}\cdot a_{223}\cdot a_{332}+a_{111}\cdot a_{232}\cdot a_{323}-a_{111}\cdot a_{233}\cdot a_{322}$$
$$+a_{113}\cdot a_{222}\cdot a_{331}-a_{113}\cdot a_{221}\cdot a_{332}-a_{113}\cdot a_{232}\cdot a_{321}+a_{113}\cdot a_{231}\cdot a_{322}$$
$$-a_{122}\cdot a_{211}\cdot a_{333}+a_{122}\cdot a_{213}\cdot a_{331}+a_{122}\cdot a_{231}\cdot a_{313}-a_{122}\cdot a_{233}\cdot a_{311}$$
$$+a_{121}\cdot a_{212}\cdot a_{333}-a_{121}\cdot a_{213}\cdot a_{332}-a_{121}\cdot a_{232}\cdot a_{313}+a_{121}\cdot a_{233}\cdot a_{312}$$
$$-a_{123}\cdot a_{212}\cdot a_{331}+a_{123}\cdot a_{211}\cdot a_{332}+a_{123}\cdot a_{232}\cdot a_{311}-a_{123}\cdot a_{231}\cdot a_{312}$$
$$+a_{132}\cdot a_{211}\cdot a_{323}-a_{132}\cdot a_{213}\cdot a_{321}-a_{132}\cdot a_{221}\cdot a_{313}+a_{132}\cdot a_{223}\cdot a_{311}$$
$$-a_{131}\cdot a_{212}\cdot a_{323}+a_{131}\cdot a_{213}\cdot a_{322}+a_{131}\cdot a_{222}\cdot a_{313}-a_{131}\cdot a_{223}\cdot a_{312}$$
$$+a_{133}\cdot a_{212}\cdot a_{321}-a_{133}\cdot a_{211}\cdot a_{322}-a_{133}\cdot a_{222}\cdot a_{311}+a_{133}\cdot a_{221}\cdot a_{312}$$
$$=-a_{111}\cdot a_{222}\cdot a_{333}+a_{111}\cdot a_{232}\cdot a_{323}+a_{111}\cdot a_{223}\cdot a_{332}-a_{111}\cdot a_{233}\cdot a_{322}$$
$$+a_{112}\cdot a_{221}\cdot a_{333}-a_{112}\cdot a_{223}\cdot a_{331}-a_{112}\cdot a_{231}\cdot a_{323}+a_{112}\cdot a_{233}\cdot a_{321}$$
$$-a_{113}\cdot a_{221}\cdot a_{332}+a_{113}\cdot a_{222}\cdot a_{331}+a_{113}\cdot a_{231}\cdot a_{322}-a_{113}\cdot a_{232}\cdot a_{321}$$
$$+a_{121}\cdot a_{212}\cdot a_{333}-a_{121}\cdot a_{213}\cdot a_{332}-a_{121}\cdot a_{232}\cdot a_{313}+a_{121}\cdot a_{233}\cdot a_{312}$$
$$-a_{122}\cdot a_{211}\cdot a_{333}+a_{122}\cdot a_{213}\cdot a_{331}+a_{122}\cdot a_{231}\cdot a_{313}-a_{122}\cdot a_{233}\cdot a_{311}$$
$$+a_{123}\cdot a_{211}\cdot a_{332}-a_{123}\cdot a_{212}\cdot a_{331}-a_{123}\cdot a_{231}\cdot a_{312}+a_{123}\cdot a_{232}\cdot a_{311}$$
$$-a_{131}\cdot a_{212}\cdot a_{323}+a_{131}\cdot a_{213}\cdot a_{322}+a_{131}\cdot a_{222}\cdot a_{313}-a_{131}\cdot a_{223}\cdot a_{312}$$
$$+a_{132}\cdot a_{211}\cdot a_{323}-a_{132}\cdot a_{213}\cdot a_{321}-a_{132}\cdot a_{221}\cdot a_{313}+a_{132}\cdot a_{223}\cdot a_{311}$$
$$-a_{133}\cdot a_{211}\cdot a_{322}+a_{133}\cdot a_{212}\cdot a_{321}+a_{133}\cdot a_{221}\cdot a_{312}-a_{133}\cdot a_{222}\cdot a_{311}$$

$$= -(a_{111} \cdot a_{222} \cdot a_{333} - a_{111} \cdot a_{232} \cdot a_{323} - a_{111} \cdot a_{223} \cdot a_{332} + a_{111} \cdot a_{233} \cdot a_{322}$$

$$-a_{112} \cdot a_{221} \cdot a_{333} + a_{112} \cdot a_{223} \cdot a_{331} + a_{112} \cdot a_{231} \cdot a_{323} - a_{112} \cdot a_{233} \cdot a_{321}$$

$$+a_{113} \cdot a_{221} \cdot a_{332} - a_{113} \cdot a_{222} \cdot a_{331} - a_{113} \cdot a_{231} \cdot a_{322} + a_{113} \cdot a_{232} \cdot a_{321}$$

$$-a_{121} \cdot a_{212} \cdot a_{333} + a_{121} \cdot a_{213} \cdot a_{332} + a_{121} \cdot a_{232} \cdot a_{313} - a_{121} \cdot a_{233} \cdot a_{312}$$

$$+a_{122} \cdot a_{211} \cdot a_{333} - a_{122} \cdot a_{213} \cdot a_{331} - a_{122} \cdot a_{231} \cdot a_{313} + a_{122} \cdot a_{233} \cdot a_{311}$$

$$-a_{123} \cdot a_{211} \cdot a_{332} + a_{123} \cdot a_{212} \cdot a_{331} + a_{123} \cdot a_{231} \cdot a_{312} - a_{123} \cdot a_{232} \cdot a_{311}$$

$$+a_{131} \cdot a_{212} \cdot a_{323} - a_{131} \cdot a_{213} \cdot a_{322} - a_{131} \cdot a_{222} \cdot a_{313} + a_{131} \cdot a_{223} \cdot a_{312}$$

$$-a_{132} \cdot a_{211} \cdot a_{323} + a_{132} \cdot a_{213} \cdot a_{321} + a_{132} \cdot a_{221} \cdot a_{313} - a_{132} \cdot a_{223} \cdot a_{311}$$

$$+a_{133} \cdot a_{211} \cdot a_{322} - a_{133} \cdot a_{212} \cdot a_{321} - a_{133} \cdot a_{221} \cdot a_{312} + a_{133} \cdot a_{222} \cdot a_{311}) = -\det[A_{3\times3\times3}]$$

4. For interchanging the location of two consecutive "vertical layers": Let B be cubic-matrix of order 3, where we have interchanged 2-consecutive "vertical layers" (Second layer with third layer), then based on definition 3:

$$\det[B_{3\times3\times3}] = \det\left(\begin{array}{ccc|ccc|ccc} a_{111} & a_{121} & a_{131} & a_{113} & a_{123} & a_{133} & a_{112} & a_{122} & a_{132} \\ a_{211} & a_{221} & a_{231} & a_{213} & a_{223} & a_{233} & a_{212} & a_{222} & a_{232} \\ a_{311} & a_{321} & a_{331} & a_{313} & a_{323} & a_{333} & a_{312} & a_{322} & a_{332} \end{array}\right)$$

$$= a_{111} \cdot a_{223} \cdot a_{332} - a_{111} \cdot a_{233} \cdot a_{322} - a_{111} \cdot a_{222} \cdot a_{333} + a_{111} \cdot a_{232} \cdot a_{323}$$

$$-a_{113} \cdot a_{221} \cdot a_{332} + a_{113} \cdot a_{222} \cdot a_{331} + a_{113} \cdot a_{231} \cdot a_{322} - a_{113} \cdot a_{232} \cdot a_{321}$$

$$+a_{112} \cdot a_{221} \cdot a_{333} - a_{112} \cdot a_{223} \cdot a_{331} - a_{112} \cdot a_{231} \cdot a_{323} + a_{112} \cdot a_{233} \cdot a_{321}$$

$$-a_{121} \cdot a_{213} \cdot a_{332} + a_{121} \cdot a_{212} \cdot a_{333} + a_{121} \cdot a_{233} \cdot a_{312} - a_{121} \cdot a_{232} \cdot a_{313}$$

$$+a_{123} \cdot a_{211} \cdot a_{332} - a_{123} \cdot a_{212} \cdot a_{331} - a_{123} \cdot a_{231} \cdot a_{312} + a_{123} \cdot a_{232} \cdot a_{311}$$

$$-a_{122} \cdot a_{211} \cdot a_{333} + a_{122} \cdot a_{213} \cdot a_{331} + a_{122} \cdot a_{231} \cdot a_{313} - a_{122} \cdot a_{233} \cdot a_{311}$$

$$+a_{131} \cdot a_{213} \cdot a_{322} - a_{131} \cdot a_{212} \cdot a_{323} - a_{131} \cdot a_{223} \cdot a_{312} + a_{131} \cdot a_{222} \cdot a_{313}$$

$$-a_{133} \cdot a_{211} \cdot a_{322} + a_{133} \cdot a_{212} \cdot a_{321} + a_{133} \cdot a_{221} \cdot a_{312} - a_{133} \cdot a_{222} \cdot a_{311}$$

$$+a_{132} \cdot a_{211} \cdot a_{323} - a_{132} \cdot a_{213} \cdot a_{321} - a_{132} \cdot a_{221} \cdot a_{313} + a_{132} \cdot a_{223} \cdot a_{311}$$

$$= -a_{111} \cdot a_{222} \cdot a_{333} + a_{111} \cdot a_{232} \cdot a_{323} + a_{111} \cdot a_{223} \cdot a_{332} - a_{111} \cdot a_{233} \cdot a_{322}$$

$$+a_{112} \cdot a_{221} \cdot a_{333} - a_{112} \cdot a_{223} \cdot a_{331} - a_{112} \cdot a_{231} \cdot a_{323} + a_{112} \cdot a_{233} \cdot a_{321}$$

$$-a_{113} \cdot a_{221} \cdot a_{332} + a_{113} \cdot a_{222} \cdot a_{331} + a_{113} \cdot a_{231} \cdot a_{322} - a_{113} \cdot a_{232} \cdot a_{321}$$

$$+a_{121} \cdot a_{212} \cdot a_{333} - a_{121} \cdot a_{213} \cdot a_{332} - a_{121} \cdot a_{232} \cdot a_{313} + a_{121} \cdot a_{233} \cdot a_{312}$$

$$-a_{122} \cdot a_{211} \cdot a_{333} + a_{122} \cdot a_{213} \cdot a_{331} + a_{122} \cdot a_{231} \cdot a_{313} - a_{122} \cdot a_{233} \cdot a_{311}$$

$$+a_{123} \cdot a_{211} \cdot a_{332} - a_{123} \cdot a_{212} \cdot a_{331} - a_{123} \cdot a_{231} \cdot a_{312} + a_{123} \cdot a_{232} \cdot a_{311}$$

$$-a_{131}\cdot a_{212}\cdot a_{323}+a_{131}\cdot a_{213}\cdot a_{322}+a_{131}\cdot a_{222}\cdot a_{313}-a_{131}\cdot a_{223}\cdot a_{312}$$

$$+a_{132}\cdot a_{211}\cdot a_{323}-a_{132}\cdot a_{213}\cdot a_{321}-a_{132}\cdot a_{221}\cdot a_{313}+a_{132}\cdot a_{223}\cdot a_{311}$$

$$-a_{133}\cdot a_{211}\cdot a_{322}+a_{133}\cdot a_{212}\cdot a_{321}+a_{133}\cdot a_{221}\cdot a_{312}-a_{133}\cdot a_{222}\cdot a_{311}$$

$$=-(a_{111}\cdot a_{222}\cdot a_{333}-a_{111}\cdot a_{232}\cdot a_{323}-a_{111}\cdot a_{223}\cdot a_{332}+a_{111}\cdot a_{233}\cdot a_{322}$$

$$-a_{112}\cdot a_{221}\cdot a_{333}+a_{112}\cdot a_{223}\cdot a_{331}+a_{112}\cdot a_{231}\cdot a_{323}-a_{112}\cdot a_{233}\cdot a_{321}$$

$$+a_{113}\cdot a_{221}\cdot a_{332}-a_{113}\cdot a_{222}\cdot a_{331}-a_{113}\cdot a_{231}\cdot a_{322}+a_{113}\cdot a_{232}\cdot a_{321}$$

$$-a_{121}\cdot a_{212}\cdot a_{333}+a_{121}\cdot a_{213}\cdot a_{332}+a_{121}\cdot a_{232}\cdot a_{313}-a_{121}\cdot a_{233}\cdot a_{312}$$

$$+a_{122}\cdot a_{211}\cdot a_{333}-a_{122}\cdot a_{213}\cdot a_{331}-a_{122}\cdot a_{231}\cdot a_{313}+a_{122}\cdot a_{233}\cdot a_{311}$$

$$-a_{123}\cdot a_{211}\cdot a_{332}+a_{123}\cdot a_{212}\cdot a_{331}+a_{123}\cdot a_{231}\cdot a_{312}-a_{123}\cdot a_{232}\cdot a_{311}$$

$$+a_{131}\cdot a_{212}\cdot a_{323}-a_{131}\cdot a_{213}\cdot a_{322}-a_{131}\cdot a_{222}\cdot a_{313}+a_{131}\cdot a_{223}\cdot a_{312}$$

$$-a_{132}\cdot a_{211}\cdot a_{323}+a_{132}\cdot a_{213}\cdot a_{321}+a_{132}\cdot a_{221}\cdot a_{313}-a_{132}\cdot a_{223}\cdot a_{311}$$

$$+a_{133}\cdot a_{211}\cdot a_{322}-a_{133}\cdot a_{212}\cdot a_{321}-a_{133}\cdot a_{221}\cdot a_{312}+a_{133}\cdot a_{222}\cdot a_{311})=-\det[A_{3\times3\times3}]$$

Example 6 *Let A be $2\times2\times2$ 3D determinant than we will obtain determinant B from A by interchanging location of two plans in j index:*

$$\det[A_{2\times2\times2}]=\det\left(\begin{matrix}2&1\\3&5\end{matrix}\middle|\begin{matrix}4&7\\3&2\end{matrix}\right)=2\cdot2-4\cdot5-1\cdot3+7\cdot3=2.$$

Then:

$$\det[B_{2\times2\times2}]=\det\left(\begin{matrix}1&2\\5&3\end{matrix}\middle|\begin{matrix}7&4\\2&3\end{matrix}\right)=1\cdot3-7\cdot3-2\cdot2+4\cdot5=-2.$$

Example 7 *Let A be a $3\times3\times3$ 3D determinant than we will obtain determinant B from A by interchanging location of two plans in j index:*

$$\det[A_{3\times3\times3}]=\det\left(\begin{matrix}1&4&2\\2&0&0\\0&4&2\end{matrix}\middle|\begin{matrix}3&1&3\\5&1&3\\3&2&0\end{matrix}\middle|\begin{matrix}2&1&0\\0&1&0\\2&1&0\end{matrix}\right)=-3+6-4+24+24+10+10-4+6-6=63$$

Then:

$$\det[A_{3\times3\times3}]=\det\left(\begin{matrix}4&1&2\\0&2&0\\4&0&2\end{matrix}\middle|\begin{matrix}1&3&3\\1&5&3\\2&3&0\end{matrix}\middle|\begin{matrix}1&2&0\\1&0&0\\1&2&0\end{matrix}\right)=-24-10-6+3-6-24+4+4+6-10=-63$$

If we compare results with example 2, we can see that $|A|=-|B|$

Example 8 *Let A be $2\times2\times2$ 3D determinant than we will obtain determinant B from A by interchanging location of two plans in k index:*

$$\det[A_{2\times2\times2}]=\det\left(\begin{matrix}2&1\\3&5\end{matrix}\middle|\begin{matrix}4&7\\3&2\end{matrix}\right)=2\cdot2-4\cdot5-1\cdot3+7\cdot3=2.$$

Then:

$$\det[B_{2\times2\times2}] = \det\begin{pmatrix} 4 & 7 & 2 & 1 \\ 3 & 2 & 3 & 5 \end{pmatrix} = 4\cdot5 - 2\cdot2 - 7\cdot3 + 1\cdot3 = -2.$$

If we compare results with example 2, we can see that $|A| = -|B|$.

Example 9 *Let A be a $3\times3\times3$ 3D determinant than we will obtain determinant B from A by interchanging location of two plans in k index:*

$$\det[A_{3\times3\times3}] = \det\left(\begin{array}{ccc|ccc|ccc} 1 & 4 & 2 & 3 & 1 & 3 & 2 & 1 & 0 \\ 2 & 0 & 0 & 5 & 1 & 3 & 0 & 1 & 0 \\ 0 & 4 & 2 & 3 & 2 & 0 & 2 & 1 & 0 \end{array}\right) = -3 + 6 - 4 + 24 + 24 + 10 + 10 - 4 + 6 - 6 = 63$$

Then:

$$\det[B_{3\times3\times3}] = \det\left(\begin{array}{ccc|ccc|ccc} 3 & 1 & 3 & 1 & 4 & 2 & 2 & 1 & 0 \\ 5 & 1 & 3 & 2 & 0 & 0 & 0 & 1 & 0 \\ 3 & 2 & 0 & 0 & 4 & 2 & 2 & 1 & 0 \end{array}\right) = -6 + 3 - 24 - 24 - 10 - 6 + 6 - 10 - 4 - 4 = -63$$

If we compare results with example 3, we can see that $|A| = -|B|$.

Algorithms Implementation of Determinants for Cubic-Matrix of Order 2 and 3

Computer Algorithm for Calculating Determinant of Cubic Matrices of Order 2 and Order 3

In the following we have presented the pseudocode of algorithm for calculating the determinant of cubic matrices of order 2 and order 3based on the Definition 2 and Definition 3.

tw]

P 1: Determinant calculation of cubic matrices of second and third order

tw]

Step 1: Determine the order of determinant:
$[m, n, o] = size(A);$

Step 2: Checking if 3D matrix is cubic:
if $m \sim n; m \sim= o; n \sim= o;$
disp('A is not square, cannot calculate the determinant')
$d = 0;$
Return
end

Step 3: Checking if 3D matrix is higher than the 3rd order:
if $m > 3;$
disp('A is higher than the third order, hence can not be calculated.')
$d = 0;$
return
end

Step 4: Initialize $d = 0;$

Step 5: Handling base case.
if $m == 1$
$d = A;$

return
end

Step 6: Check if A is of second order.
$d = A(1,1,1) * A(2,2,2) - A(1,1,2) * A(2,2,1) - A(1,2,1) * A(2,1,2) + A(1,2,2) * A(2,1,1)$

Step 7: Check if A is of third order.
$d =$

$$
\begin{aligned}
&= A(1,1,1) * A(2,2,2) * A(3,3,3) - A(1,1,1) * A(2,3,2) * A(3,2,3) - A(1,1,1) * A(2,2,3) * A(3,3,2) \\
&+A(1,1,1) * A(2,3,3) * A(3,2,2) - A(1,1,2) * A(2,2,1) * A(3,3,3) + A(1,1,2) * A(2,2,3) * A(3,3,1) \\
&+A(1,1,2) * A(2,3,1) * A(3,2,3) - A(1,1,2) * A(2,3,3) * A(3,2,1) + A(1,1,3) * A(2,2,1) * A(3,3,2) \\
&-A(1,1,3) * A(2,2,2) * A(3,3,1) - A(1,1,3) * A(2,3,1) * A(3,2,2) + A(1,1,3) * A(2,3,2) * A(3,2,1) \\
&-A(1,2,1) * A(2,1,2) * A(3,3,3) + A(1,2,1) * A(2,1,3) * A(3,3,2) + A(1,2,1) * A(2,3,2) * A(3,1,3) \\
&-A(1,2,1) * A(2,3,3) * A(3,1,2) + A(1,2,2) * A(2,1,1) * A(3,3,3) - A(1,2,2) * A(2,1,3) * A(3,3,1) \\
&-A(1,2,2) * A(2,3,1) * A(3,1,3) + A(1,2,2) * A(2,3,3) * A(3,1,1) - A(1,2,3) * A(2,1,1) * A(3,3,2) \\
&+A(1,2,3) * A(2,1,2) * A(3,3,1) + A(1,2,3) * A(2,3,1) * A(3,1,2) - A(1,2,3) * A(2,3,2) * A(3,1,1) \\
&+A(1,3,1) * A(2,1,2) * A(3,2,3) - A(1,3,1) * A(2,1,3) * A(3,2,2) - A(1,3,1) * A(2,2,2) * A(3,1,3) \\
&+A(1,3,1) * A(2,2,3) * A(3,1,2) - A(1,3,2) * A(2,1,1) * A(3,2,3) + A(1,3,2) * A(2,1,3) * A(3,2,1) \\
&+A(1,3,2) * A(2,2,1) * A(3,1,3) - A(1,3,2) * A(2,2,3) * A(3,1,1) + A(1,3,3) * A(2,1,1) * A(3,2,2) \\
&-A(1,3,3) * A(2,1,2) * A(3,2,1) - A(1,3,3) * A(2,2,1) * A(3,1,2) + A(1,3,3) * A(2,2,2) * A(3,1,1)
\end{aligned}
$$

Step 8: Return the result of 3D determinant.
tw]

Optimized Version of Computer Algorithm

The above-mention algorithm is hard-coded exactly as it is prescribed in the Definition 2 and Definition 3, it can be optimized further with nested-loop. Hence, in the following we have presented another optimized version of above algorithm which gives the same result.

tw]

P 2: Optimized algorithm for determinant calculation of cubic matrices of second and third order

tw]

Step 1: Determine the order of determinant:
$[m, n, o] = size(A);$

Step 2: Checking if 3D matrix is cubic:
if $m \sim n; m \sim= o; n \sim= o;$
disp('A is not square, cannot calculate the determinant')
$d = 0;$
return

end

Step 3: Checking if 3D matrix is higher than the 3rd order:
if $m > 3$;
disp('A is higher than the third order, hence can not be calculated.')
$d = 0$;
return
end

Step 4: Initialize $d = 0$;

Step 5: Handling base case.
if $m == 1$
$d = A$;
return
end

Step 6: Check if A is of second order.
Create loop for j from 1 to 2
Create loop for k from 1 to 2
Calculate determinant:

$$d = d + (-1)^\wedge(2 + j + k) * A(1, j, k) * det\_3D(A(2, [1{:}j - 1j + 1{:}2], [1{:}k - 1k + 1{:}2]));$$

end
end

Step 7: Check if A is of third order.
Create loop for j from 1 to 3
Create loop for k from 1 to 3
Calculate determinant:

$$d = d + (-1)^\wedge(2 + j + k) * A(1, j, k) * det\_3D(A(2{:}3, [1{:}j - 1j + 1{:}3], [1{:}k - 1k + 1{:}3]));$$

end
end

Step 8: Return the result of 3D determinant.
tw]

Scientific Ethics Declaration

The authors declare that the scientific ethical and legal responsibility of this article published in EPSTEM journal belongs to the authors.

Acknowledgements or Notes

* This article was presented as an oral presentation at the International Conference on Technology, Engineering and Science (www.icontes.net) held in Antalya/Turkey on November 14-17, 2024.

References

Amiri, M., Fathy, M., & Bayat, M. (2010). Generalization of some determinantal identities for non-square matrices based on Radic's definition. *TWMS J. Pure Appl. Math, 1*(2), 163–175.

Artin, M. (1991). *Algebra*. Upper Saddle River: Prentice Hall.

Bretscher, O. (2005). *Linear algebra with applications*(3rd ed.). Upper Saddle River: Prentice Hall.

Deda, G., & Zaka, O. (2024). A way to internet collects data. 'Related to a specific subject', the special case: for Albanian agritourism users'data. Retrieved from https://www.preprints.org/manuscript/202404.1470/v1

Filipi, K., Zaka, O., Jusufi, A. (2019). The construction of a corp in the set of points in a line of desargues affine plane. *Matematicki Bilten, 43*, 1-23.

Lang, S. (1987). *Linear algebra.* Springer-verlag.Berlin, New York.

Makarewicz, A., Pikuta, P., & Szałkowski, D. (2014). Properties of the determinant of a rectangular matrix. annales universitatis mariae curie-sklodowska. *Sectio A. Mathematica, 68*(1), 31-41.

Milne-Thomson, L. M. (1941). Determinant expansions. *The Mathematical Gazette, 25*(265), 130–135.

Peters, J. F., & Zaka, O. (2023). Dyck fundamental group on arcwise-connected polygon cycles. *Afrika Matematika, 34*(2), 31.

Radić, M. (1966). A definition of determinant of rectangular matrix. *Glasnik Mate-Maticki, 1*(21), 17-22.

Radić, M. (2005). About a determinant of rectangular 2 × n matrix and its geometric interpretation. *Beitr Age Algebra Geometrie, 46*(2), 321–349.

Salihu, A., & Zaka, O. (2023). Some 3D-determinant properties for calculating of cubic-matrix of order 2 and order 3. *The Eurasia Proceedings of Science Technology Engineering and Mathematics, 26*, 554-577.

Salihu, A. (2018). A modern modification of Gjonbalaj-Salihu cornice determinant, transformation to semi-diagonal determinant. *International Journal of Mathematics and Computer Science, 13*, 133–138.

Salihu, A., & Marevci, F. (2021a). Chio's-like method for calculating the rectangular (non-square) determinants. Computer algorithm interpretation and comparison. *European Journal of Pure and Applied Mathematics, 14(*2), 431–450.

Salihu, A., & Marevci, F. (2021b). Determinants order decrease/ıncrease for k orders, ınterpretation with computer algorithms and comparison. *International Journal of Mathematics and Computer Science, 14*(2), 501–518.

Salihu, A., Jusufi, A., & Salihu, F. (2019). Comparison of computer execution time of cornice determinant calculation. *International Journal of Mathematics and Computer Science, 14*, 9–16.

Salihu, A., Snopce, H., Ajdari, J., & Luma, A. (2022a). Generalization of Dodgson's condensation method for calculating determinant of rectangular matrices. *2022 International Conference on Electrical, Computer and Energy Technologies (ICECET). Presented at the 2022 International Conference on Electrical, Computer and Energy Technologies (ICECET), Prague, Czech Republic*.

Salihu, A., Snopce, H., Luma, A., & Ajdari, J. (2022b). Optimization of Dodgson's condensation method for rectangular determinant calculations. *Advanced Mathematical Models & Applications, 7* (3), 264-274.

Salihu, A., Snopce, H., Luma, A., & Ajdari, J. (2022c). Time complexity analysis for cullis/radic and Dodgson's generalized/modified method for rectangular determinants calculations. *International Journal of Computers and Their Applications, 29*(4), 236–246.

Salihu, A., Snopce, H., Luma, A., & Ajdari, J. (2023, February 10). Comparison of time complexity growth for different methods/algorithms for rectangular determinant calculations. *2023 International Conference on Recent Trends in Electronics and Communication (ICRTEC)*, 1–6.

Schneide, H., & Barker, G.P. (1973). *Matrices and linear algebra (dover books on mathematics)* (2nd ed.).

Zaka, O. (2016). *Contribution to reports of some algebraic structures with affine plane geometry and applications*. (Doctoral dissertation, University of Tirana, Albania).

Zaka, O. (2017a). 3D matrix ring with a "common" multiplication. *OAlib, 4*(5), 1–11.

Zaka, O. (2017b). A description of collineations-groups of an affine plane. *Libertas Mathematica,37*(2), 81–96.

Zaka, O. (2018). Three vertex and parallelograms in the aff+ine plane: Similarity and addition abelian groups of similarly n-vertexes in the desargues affine plane. *Mathematical Modelling and Applications, 3*(1), 9-15.

Zaka, O. (2019a). Dilations of line in itself as the automorphism of the skew-field constructed over in the same line in desargues affine plane. *Applied Mathematical Sciences, 13*(5), 231–237.

Zaka, O. (2019b). The general linear group of degree for 3D matrices. *Libertas Mathematica, New Series. Lib. Math. (N.S.), 39*(1), 13–30.

Zaka, O., & Filipi, K. (2016). The transform of a line of desargues affine plane in an additive group of its points. *Int. J. Of Current Research. 8*, 34983-34990.

Zaka, O., & Mohammed, M. A. (2020a). Skew-field of trace-preserving endomorphisms, of translation group in affine plane. Proyecciones. *Journal of Mathematics, 39*(4), 835–850.

Zaka, O., & Mohammed, M. A. (2020b). The endomorphisms algebra of translations group and associative unitary ring of trace-preserving endomorphisms in affine plane. Proyecciones. *Journal of Mathematics, 39*(4), 821–834.

Zaka, O., & Peters, J. F. (2020). Isomorphic-dilations of the skew-fields constructed over parallel lines in the Desargues affine plane. *Balkan Journal of Geometry and Applications, 25*, 141-157.

Zaka, O., & Peters, J. F. (2021). Ordered line and skew-fields in the desargues affine plane. *Balkan Journal of Geometry and Applications, 26*, 141-156.

Zaka, O., & Peters, J. F. (2024a). İnvariant and preserving transforms for cross ratio of 4-points in a line on desargues affine plane. *Journal of Prime Research in Mathematics. 20*(2), 48 – 63.

Zaka, O., & Peters, J. F. (2024b). Dyck free group presentation of polygon cycles in the ratio of collinear points in the desargues affine plane. *Journal of Mathematical Sciences, 280*(4), 605–630.

Zaka, O., & Salihu, A. (2024). Laplace method for calculate the determinant of cubic-matrix of order 2 and order 3. *The Eurasia Proceedings of Science Technology Engineering and Mathematics, 29*, 192-209.

Author Information

Armend Salihu	Orgest Zaka
Universum International College	Agricultural University of Tirana
Department of Computer Science	Faculty of Economy and Agribusiness
Str. Hasan Prishtina 1,1, Konjuh, Lipjan, 14000, Kosovo	Department of Mathematics-Informatics
Contact e-mail: *ar.salihu@gmail.com*	1025 Paisi Vodica Street, Tirana, Albania

To cite this article:

Salihu, A., & Zaka, O. (2024). The determinant of cubic-matrix of order 2 and order 3, some basic properties and algorithms. *The Eurasia Proceedings of Science, Technology, Engineering & Mathematics (EPSTEM), 32,* 488-514.

TheEurasiaProceedings of Science, Technology, Engineering&Mathematics (EPSTEM)
ISSN: 2602-3199

The Eurasia Proceedings of Science, Technology, Engineering & Mathematics (EPSTEM), 2024

Volume 32, Pages 515-519

IConTES 2024: International Conference on Technology, Engineering and Science

Spectrum Estimation of Spatial Velocity Component Pulsations

Alexander Kusyumov
Kazan National Research Technical University named after A. N.

Sergey Kusyumov
Kazan National Research Technical University named after A. N.

Abstract: One of the objectives in the study of turbulent flows is to determine the spectral features of flow parameters. Typically, the longitudinal and transverse components of the velocity vector are parameters for which spectral analysis is carried out. In the present study, the spectrum of pulsations of a turbulent velocity sampled in the spatial domain is considered. An application with the Reynolds number of 3900 is being examined for a turbulent flow past a 3D cylindrical surface. Numerical simulation is performed using ANSYS Fluent commercial code and based on the Navier-Stokes equations. The spatial signal is sampled on the centerline downstream of the flow. The energy of the transversal component of the velocity vector is analyzed using Fourier transforms of a signal sampled in the spatial domain. Two approaches are considered to study the spectral properties of the signal. The traditional Energy Signal Density (ESD) estimation is analyzed using Parseval's theorem. The alternative Energy Signal Spectra (ESS) estimation approach is based on the local signal energy definition. The energy spectra performances are compared to the "–5/3" law of A.N. Kolmogorov.

Keywords: Cylinder, Navier-Stokes equations, Turbulence, Spatial spectrum.

Introduction

Typically, the longitudinal and transverse components of the velocity vector of the turbulent flow are parameters for which spectral analysis is carried out. The spectral characteristics of the flow depend on the Reynolds number and the object geometry. For low Reynolds numbers (about 10^3), it is possible to use the Direct Numerical Simulation (DNS) based on solution of the Navier-Stokes equations (without involving turbulence models). A 3D cylindrical surface is a canonical object for numerical simulation. The potential to replicate different physical aspects of the flow, such as wake vortex generation, separation of the laminar boundary layer, and the creation of shear layers (including the Karman vortex street), explains the interest in this task. The results of the numerical simulation for Re =3900 can be found, for example, in Wissink and Rodi (2008). For the given value of the Reynolds number, some studies are also based on the Reynolds-averaged Navier-Stokes equations (Parnaudeau et al., 2008). To describe the Energy Spectral Density (ESD) of isotropic turbulent flow, one can use the "-5/3" law of Kolmogorov (1991). It should be noted that the "-5/3" law was obtained for the spatial spectrum of the longitudinal and transverse components of the velocity vector. In most studies, the "-5/3" law is also used to estimate the spectrum of a signal sampled in the temporal domain.

This paper presents an alternative approach for estimating the energy signal spectrum. As an illustration, estimates of the energy spectrum of the transverse velocity vector component are given for the flow near a 3D circular cylinder at the Reynolds number of 3900. Analysis of spectral characteristics is carried out for data obtained as a result of numerical modeling of the flow in the ANSYS Fluent package based on the Navier-Stokes equations without involving turbulence models. The spectral characteristics of the flow are estimated in the MATLAB code using the discrete Fourier transform of the signal sampled in the spatial domain.

Methodology for Evaluating of Spectral Characteristics

For a continuous spatial real signal $u(x)$, the signal energy is defined by the expression

$$E_\infty = \int_{-\infty}^{\infty} U(x)\,dx, \tag{1}$$

where $U(x) = u^2(x)$. Spectral analysis for a spatial-limited signal (in the range $-X/2 \le x \le X/2$) is carried out using the Fourier transform (Lathi & Ding, 2010):

$$\hat{u}(k) = \int_{-X/2}^{X/2} u(x)\, e^{-2\pi ixk} dx,$$

Where k is the wave number.

Using Parseval's theorem (Prandoni & Vetterli, 2008). Allows for the determination of the signal ESD (Lathi & Ding, 2010):

$$E_D(k) = |\hat{u}(k)|^2. \tag{2}$$

In references are also used the signal PSD estimation (Lathi & Ding, 2010):

$$P_D(k) = \frac{1}{X}|\hat{u}(k)|^2. \tag{3}$$

From expressions (2) and (3) it is follows that the ESD and PSD characteristics of the signal have the similar spectrum distributions and differ only in the amplitude. From (1), it follows that the signal energy E is evaluated by the integral of $U(x)$. Along with expressions (2) and (3), the Energy Signal Spectra (ESS) estimation was introduced in Kusyumov et al. (2023). To evaluate the energy characteristics of the time-sampled signal:

$$E_S(f) = \left|\widehat{U}(f)\right|, \tag{4}$$

Where

$$\widehat{U}(f) = \int_{-T/2}^{T/2} u^2(t)\, e^{-2\pi itf} dt. \tag{5}$$

From the analysis of expressions for ESD, PSD, ESS it follows that these characteristics are obtained using Fourier transforms of the function $u^m(x)$: $m = 1$ for ESD and PSD, whereas $m = 2$ for ESS. Note that to determine the spatial spectrum, one can introduce the Fourier transform for the spatial distribution of a spatial signal $u(x)$ (in the range $-X/2 \le x \le X/2$):

$$E_S(k) = \left|\widehat{U}(k)\right|. \tag{6}$$

Here $U(x) = u^2(x)$. The function $\widehat{U}(k)$ is defined by the spatial Fourier transform

$$\widehat{U}(k) = \int_{-X/2}^{X/2} U(x)\, e^{-2\pi ixk} dx. \tag{7}$$

Traditionally, the spectral characteristics of the ESD and PSD signals are aimed at analyzing the spectrum of velocity fluctuations. The obtained spectrum is usually compared with the spectral distribution determined by the K41 law of Kolmogorov. The K41 law was formulated by Kolmogorov (1991) within the framework of the statistical theory of turbulence. Based on this theory, Kolmogorov (1991) obtained the reference law "-5/3" for the spatial energy spectrum (in the inertial range of the spectrum):

$$EI_{ij}(k) \sim \alpha_{ij}\epsilon^{2/3}k^{-5/3}, \tag{8}$$

where ϵ is the turbulence energy dissipation rate. For isotropic flows $\alpha_{ij} = \alpha_i\delta_{ij}$, where δ_{ij} is the Kronecker symbol, $\alpha_1 = \alpha_2 = \alpha_3 = \alpha \approx 0.5$. Note that the dimension of the $EI_{ij}(k)$ coincides with the dimension of the function $E_S(k)$. Therefore, the spatial spectrum $E_S(k)$ can be compared with the K41 law.

From the K41 law, it follows that the reference spatial spectrum $EI_{ij}(k)$ of the signal energy is determined by the energy dissipation rate ϵ and the wave number k. Hence the resulting dimension of the reference estimation $EI_{ij}(k)$ is

$$[EI_{ij}(k)] = \frac{m^3}{s^2}.$$

One can determine also dimension of the $E_D(k)$ and $E_S(k)$ signal performances:

$$[E_D(k)] = \frac{m^4}{s^2}, \quad [E_S(k)] = \frac{m^3}{s^2}. \tag{9}$$

The $E_S(k)$ and $E_D(k)$ signal performances are used below to analyze turbulent flow properties obtained as a result of modeling the flow around a section of a circular cylinder.

Numerical Simulation Results

Numerical modeling was carried out for the Reynolds number $\mathrm{Re} = V_\infty d/\nu = 3900$, where V_∞ is the free stream velocity, d is the cylinder diameter, and ν is the kinematic viscosity coefficient. When carrying out calculations in the ANSYS Fluent code, the unsteady incompressible Navier-Stokes equations were used. Navier-Stokes equations were solved with second order discretization in space and first order in time. Longitudinal and transversal coordinates are denoted as x, y, and z. The distance from the inlet face to the cylinder axis was $5d$. The transversal dimension $l_z = \pi d$ was chosen in accordance with the recommendations of (Kravchenko & Moin, 2000; Maet al., 2000). At the inlet boundary, a uniform flow field was set with the velocity vector $(u, v, w)^T = (1,0,0)^T V_\infty$. On the sides of the computational domain (orthogonal to z coordinate), "symmetry" conditions were applied. The computational grid was built in the commercial ANSYS ICEM generator.

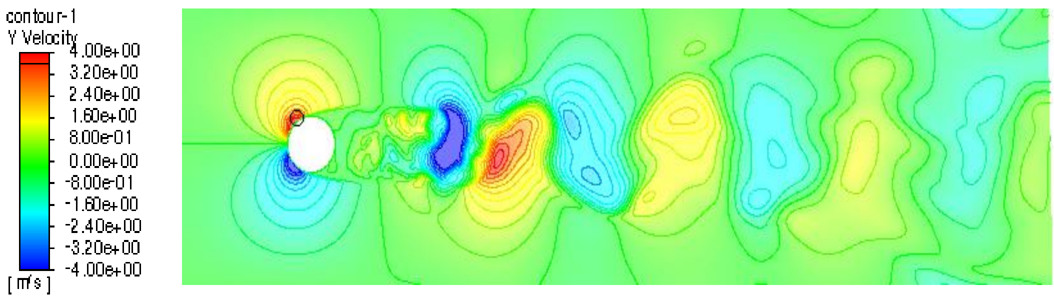

Figure 1. Instant field of the transversal velocity v in the symmetry plane.

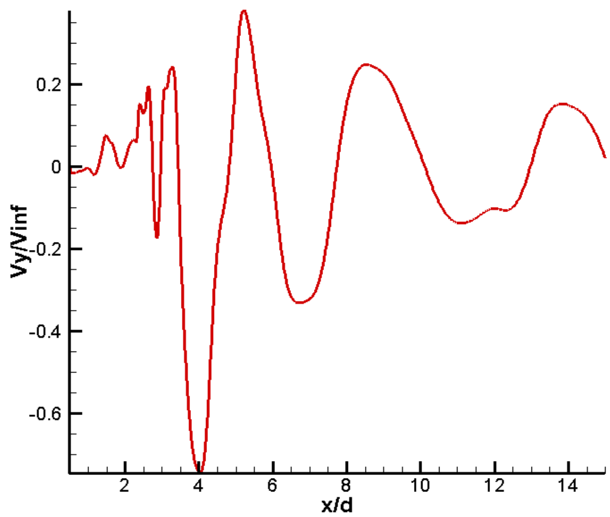

Figure 2. Instant distribution of the transversal velocity v in the symmetry plane.

The computational hexa-grid consisting of $16{\cdot}10^6$ elements was created. To resolve the boundary layer, the computational mesh was refined near the cylinder surface: the size of the first cell normal to the surface is about $10^{-3}d$. The time-step used in the simulation is $\Delta t = 0.0565\, d/V_\infty$. The period of integration corresponded to 100 cycles of vortex generation ($T \approx 500d/V_\infty$). Some other details of the simulation are presented in (Kusyumov et al., 2023). Figure 1 presents the distribution of the transverse component$v$of the velocity vector in the symmetry plane. From Figure1, it follows the inhomogeneities inside and outside of the recirculation zone. Figure 2 shows the spatial signal sampled at the center line (in the symmetry plane) downstream of the flow. The spatial distribution of the transversal velocity component in Figures 1 and 2 shows that small vortex structures are localized close to the cylinder surface ($x/d > 1$). Increasing the vortex structures dimension far from the cylinder surface is determined by the grow of the computational grid cells size and the dissipation of the turbulent energy process. Figure 3 shows the distribution of normalized functions $E_S(k)$ (ESS) and $E_D(k)$ (ESD) compared to the "-5/3" law.

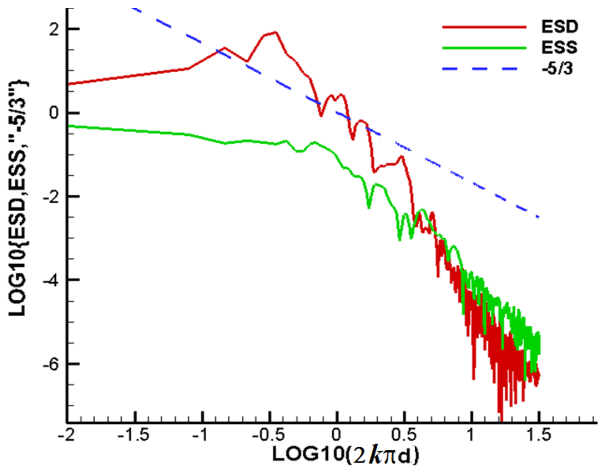

Figure 3. Spatial spectrum of the transversal velocity v.

In the inertial subrange, there are regions where the slope of both functions $E_S(k)$ (ESS) and $E_D(k)$ (ESD) curves corresponds to the "-5/3" law. Wherein, the gradient of the $E_S(k)$ curve in the inertial subrange is in better agreement with the "-5/3" law in comparison with the $E_D(k)$ gradient.

Conclusion

Three-dimensional flow around a section of a circular cylinder at Re = 3900 is studied numerically based on the unsteady incompressible Navier-Stokes equations using the Fluent commercial code. The main attention is paid to the spectrum of transverse flow velocity downstream of the cylinder. An alternate formulation (Energy Signal Spectrum) estimates the signal energy spectrum based on the square of the spatial signal function, in addition to the Energy Spectral Density (in the widely known formulation).The signal energy spectrum is compared with the "-5/3" law of Kolmogorov. Analysis of the numerical simulation results shows that the gradient of the Energy Signal Spectrum curve in the inertial subrange is in better agreement with the "-5/3" law in comparison with the Energy Spectral Density.

Scientific Ethics Declaration

The authors declare that the scientific ethical and legal responsibility of this article published in EPSTEM journal belongs to the authors.

Acknowledgements or Notes

* This article was presented as an oral presentation at the International Conference on Technology, Engineering and Science (www.icontes.net) held in Antalya/Turkey on November 14-17, 2024.

* This work was supported by the grant "FZSU-2023-0005" (No. 123030100016-5) of the Ministry of Education and Science of the Russian Federation.

References

Kolmogorov, A.N. (1991). The local structure of turbulence in ıncompressible viscous fluid for very large Reynolds numbers. *Mathematical and Physical Sciences*, *434* (1890), 9–13.

Kravchenko, A. G., & Moin, P. (2000). Numerical studies of flow over a circular cylinder at ReD= 3900. *Physics of Fluids*, *12* (2), 403–417.

Kusyumov, S.A., Kusyumov, A.N., & Romanova, E.V. (2023). Spectral characteristics of three-dimensional flow around a circular cylinder. *Russian Aeronautics*, *66* (2), 276–282.

Lathi, B. P., & Ding, Z. (2010). *Modern digital and analog communication systems* (4th ed.). New York, NY: Oxford University Press.

Ma, X., Karamanos, G. S., & Karniadakis, G. E. (2000). Dynamics andlow-dimensionality of a turbulent near wake. *Journal of Fluid Mechanics*, *410*, 29–65.

Parnaudeau, P.,Carlier, J., Heitz, D., & Lamballais, E. (2008). Experimental and numerical studies of the flow over a circular cylinder at Reynolds number 3900. *Physics of Fluids*, *20* (8).

Prandoni, P., & Vetterli, M. (2008). *Signal processing for communications* (1st ed.). New York, NY: EPFL Press.

Wissink, J. G., & Rodi, W. (2008). Numerical study of the near wake of a circular cylinder. *International Journal of Heat and Fluid Flow*, *29* (4), 1060–1070.

Authors Information

Alexander Kusyumov
Kazan National Research Technical University named after A. N. Tupolev - KAI, 10 Karl Marx Str., Kazan, Republic of Tatarstan, Russian Federation
Contact e-mail: *postbox7@mail.ru*

Sergey Kusyumov
Kazan National Research Technical University named after A. N. Tupolev - KAI, 10 Karl Marx Str., Kazan, Republic of Tatarstan, Russian Federation

To cite this article:

Kusyumov, A., & Kusyumov, S. (2024). Spectrum estimation of spatial velocity component pulsations. *The Eurasia Proceedings of Science, Technology, Engineering & Mathematics (EPSTEM), 32,* 515-519.

The Eurasia Proceedings of Science, Technology, Engineering & Mathematics (EPSTEM)
ISSN: 2602-3199

The Eurasia Proceedings of Science, Technology, Engineering & Mathematics (EPSTEM), 2024

Volume 32, Pages 520-531

IConTES 2024: International Conference on Technology, Engineering and Science

The Effect of Recovery Fibers and the Sand/Gravel Ratio on the Direct Tensile Behavior of Concrete

Atlaoui Djamal
University 'Mouloud Mammeri' of Tizi Ouzou

Ghouilem Kamel
University of Mouloud Mammeri, Tizi Ouzou

Bouafia Youcef
University 'Mouloud Mammeri' of Tizi Ouzou

Abstract: The purpose of this research is the experimental analysis of the mechanical behavior of steel chip reinforced concrete. The fibers used are obtained from metal chips recovered in steel machining workshops in Algeria (SNVI), where they are obtained in the form of cylindrical rolls. Once stretched, these rolls take the form of a coil, which is then cut to produce fibers of small lengths. This helical configuration ensures better anchoring in the concrete and prevents the formation of cylindrical voids that could weaken the matrix. The fibers were subjected to tests to assess their mechanical strength and pull-out resistance capacity. Direct tensile tests were conducted on gypsum samples of square section [100x100] mm², requiring the design and fabrication of a special fixing device on the tensile machine. Four percentages of fibers were selected for this study (W=0.3%, W=0.5%, W=0.8%, and W=1%), where W represents the volumetric fraction of added fibers. In order to determine the optimal composition of fiber-reinforced concrete in terms of workability, three concrete mixes with different sand/gravel ratios (S/G=0.642, S/G=0.8, and S/G=1) were made, all with a fixed water/cement ratio E/C = 0.543 for each fiber percentage. Compression tests were carried out on cylinders with a diameter of Ø16 cm and a height of H32 cm, using a computer-controlled hydraulic press. The analysis of the results reveals that the behavior of fiber-reinforced concrete is divided into two distinct phases: an initial linear phase, corresponding to elasticity, followed by a post-cracking phase where the fibers continue to provide resistance. The fibers provide significant ductility to the material after concrete cracking (post-rupture), while limiting cracks and improving strength and stiffness for certain percentages of fibers and specific sand/gravel ratios (S/G).

Keywords: Concrete, Recovered fibers, Direct tensile, Workability, Experimentation

Introduction

Concrete is universally recognized as a composite material, composed of aggregates of various sizes, sand, and cement paste. Its versatility makes it an essential component in all sectors of construction, whether it be industrial or residential buildings, retaining walls, infrastructure such as bridges, tunnels, and dams, or even for sidewalks or airport runways.

Fiber-reinforced concrete has been widely used for many years, primarily in specific applications such as jointless industrial floor slabs, shotcrete, auger-cast piles in seismic zones, as well as beams and floors. However, studies on this subject reveal divergences regarding the objectives of fiber reinforcement. According to some sources, such as Markovic et al. (2003), the main objective is to enhance the tensile strength and ductility of concrete. Conversely, other studies, like Kawamata et al. (2003), suggest that the introduction of

- Selection and peer-review under responsibility of the Organizing Committee of the Conference

fibers aims to control cracking and modify the behavior of the cracked material by bridging the cracks. Under tensile stress, cracks form in the concrete matrix, and fibers can link them, thereby reinforcing resistance to crack opening and delaying their propagation.

Experimental research has been conducted to explore the possibility of replacing traditional reinforcements in reinforced concrete with fibers, thereby offering improved tensile, flexural, and shear strength. (Djebal et al., 2011; Noghabai, 2000; Kwak et al., 2002; Slater et al., 2012; Majdzadeh et al., 2006; Dinh et al., 2010; Cucchiara et al., 2004; Meda et al., 2005; Ding et al., 2011; Statford & Burgoyne, 2003; Cho & Kim, 2003; Chalioris & Sfiri, 2011; Mirsayah & Banthia, 2002; Barragán et al., 2006; Fariborz et al., 2011; Lim & Oh, 1999; Barragán, 2002; Johnston, 1996). Initially, researchers attempted to enhance the mechanical properties of concrete, such as compressive and flexural strength, by adding fibers, but the results were limited (Sukontasukkul, 2004). It became evident that fibers primarily play two roles in a cementitious material:

1. Controlling the propagation of cracks in a service material by reducing their opening.
2. Transforming the brittle behavior of the material into a ductile one, thereby increasing safety during ultimate loads.

Direct tensile testing is typically recommended to characterize the behavior of a material under longitudinal stress. However, the complexity of conducting this test on concrete specimens often leads to its replacement with a splitting or flexural tensile test.

In our study, we focus on analyzing the behavior of concrete reinforced with chip fibers when subjected to tension. Our main objective is to examine how these fibers, derived from steel machining waste, influence the mechanical properties of concrete. We aim to find an optimal compromise between the workability of concrete and its ability to withstand tension. To this end, we conducted a series of experiments on square-shaped concrete samples (100x100 mm²), varying the percentages of fibers (W%) and the S/G ratios (sand/gravel) (S/G=0.642, S/G=0.8, and S/G=1) in the concrete mix, as well as the fixed E/C ratio (water/cement).

Materials and methods

Materials

Fiber Characterization

The tests involve conducting direct tensile tests with controlled deformation. Subsequently, we present the characteristic value of the rupture stress along with the obtained curve, as well as the comparisons made.

Fiber Geometry and Anchoring System

The fibers used are sourced from machining waste of steel parts, obtained from the National Company of Industrial Vehicles in Algeria (SNVI). Their spiral-shaped geometric form provides optimal anchoring within the cementitious matrix. Figure 1 depicts a view of these chips. Their dimensions are as follows: length (l) = 3 mm, diameter (d) = [missing], thickness (e) = 0.48 mm. During the tensile test on the fiber itself, both ends are coated with a fiberglass resin in a special mold to enhance their fixation in the clamping jaws of the hydraulic press.

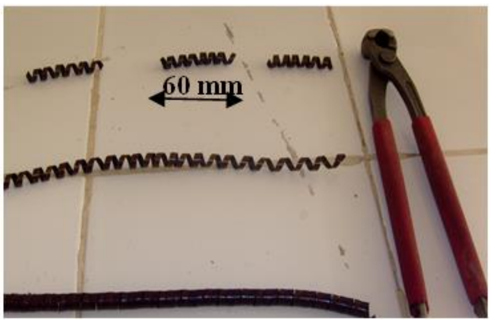

Figure 1. View of fibers in chips

Specimen Composition

Characterization of Aggregates and Cement

Test specimens are made of fiber chips embedded in a concrete matrix. The concrete composition for 1 cubic meter is established according to the Dreux-Gorisse experimental method, as indicated in Table 1. Four volumetric fractions (W) are considered: W=0.3%, W=0.5%, W=0.8%, and W=1%. The aggregates, sourced from the Tizi-Ouzou region, are quarry rocks with a crushed shape. The particle size classes used are 0/3mm, 3/8mm, and 8/15mm, respectively. The particle size distribution curves for each type of aggregate are shown in Figure 2. The cement used in our study is CPJ-CEMII/B 42.5 R NA 442, of class 42.5, sourced from Lafarge Cement in the M'sila region, Algeria.

Table 1. Composition optimized for 1m^3 of concrete

Constituents of concrete for a volume of 1m^3	
Sand 0/3 (kg)	701.35
Gravel 3/8 (kg)	116.61
Gravel 8/15 (kg)	97.,45
Cement CPJ CEMII/A 42.5(C) (kg)	380.00
Watter (E) (kg)	206.52

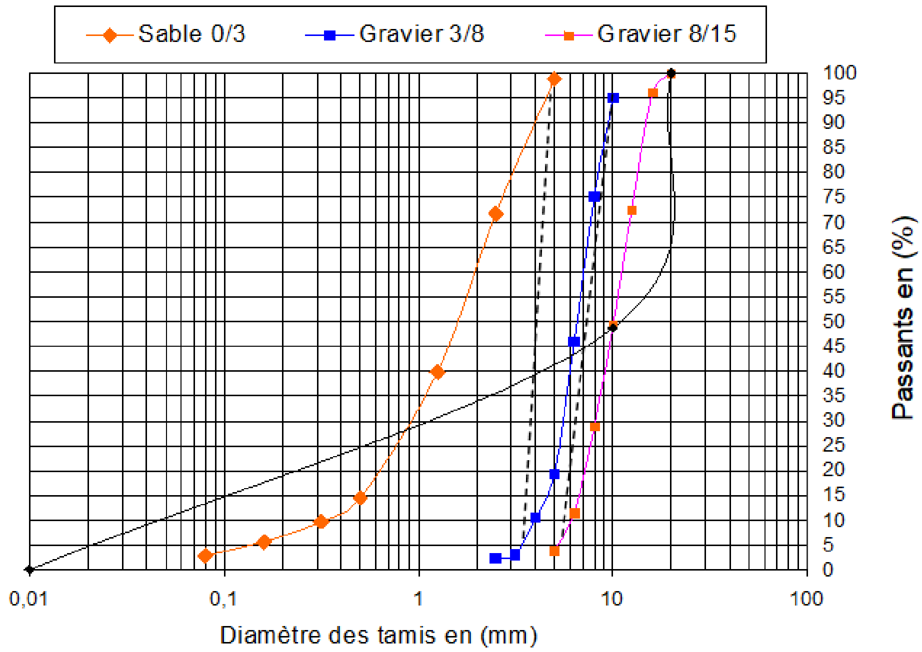

Figure 2. Grading curve

The mass of the different volume fractions for 1m^3 of concrete is indicated in table 2.

Table 2. Mass of the different fiber contents for 1m^3 of concrete

Fractions volumiques des fibres W (%)	0.3%	0.5%	0.8%	1%
Masses en (kg)	17.45	29.09	46.54	58.18

Optimization of Fiber Concrete

We used the L.C.L. maneuverability meter, developed within the Central Laboratory of Bridges and Roads (L.C.P.C), to assess the maneuverability of fiber concrete. This device allows testing a volume of 30 liters of concrete, as illustrated in Figure 3. To examine the maneuverability of fiber concrete, we conducted three separate mixes for each fiber percentage (W=0.3%, W=0.5%, W=0.8%, and W=1%), with varying sand/gravel (S/G) ratios (S/G=0.642, S/G=0.8, S/G=1), and a fixed water/cement (E/C) ratio of 0.543. The masses of the various components for a volume of 30 liters of concrete are shown in Table 3 below.

Figure 3. LCPC handling meter

Table 3. Masses of the different constituents for a mix of 30 liters of concrete

Constituents of concrete for a volume of 30 liters	S/G=0.642	S/G=0.8	S/G=1
Sand 0/3 (kg)	21.04	23.91	26.9
Gravel 3/8 (kg)	3.498	3.19	2.87
Gravel 8/15 (kg)	29.26	26.70	24.03
Cement CPJ CEMII/A 42.5(C) (kg)	11.40	11.40	11.40
Watter (E) (kg)	6.20	6.20	6.20

The mass of the different volumetric fractions for a batch of 30 liters of concrete is indicated in Table 4.

Table 4. Mass of the different fiber contents for 30liters of concrete

Volume fractions of fibers W(%)	0.3%	0.5%	0.8%	1%
Weights en (kg)	0.524	0.873	1.397	1.746

Methods

Fiber Characterization Tests

The tests are conducted on a controlled deformation hydraulic press at the Laboratory of Materials and Civil Engineering Structures Modeling at M.M. University of Tizi-Ouzou in Algeria. This press is equipped with a digital control and acquisition system, as illustrated in the view provided in Figure 4. Geometric characteristics are automatically inputted, with a useful fiber length of 100 mm. The loading speed is 20 mm/min. Chips are cut into three different lengths (30, 50, and 60 mm), and for each length, the number of undulations, or rather spirals, is 3, 5, and 7. Three tests are performed for each combination (length and number of spirals).

Figure 4. Test device view

Compression Tests

To assess the compressive strength of the concrete used, compression tests are carried out on cylinders with a diameter of 16 cm and a height of 32 cm, as illustrated in Figure 5. These tests are conducted using a computer-controlled hydraulic press, with a maximum capacity of 2000 kN (see Figure 6). The press is programmed for compression tests, accommodating different specimen dimensions (cylindrical or prismatic).

Figure 5. Cylindrical specimen (16x32)

Figure 6. Strengh press (2000KN)

Specimen Fixation Device

We have designed a special fixture (see Figure 7) to secure the specimens (see Figure 8) onto the jaws of the tensile testing machine. This design was developed using the value analysis method. . This fixture has been adapted to the 'IBERTEST' 200 KN tensile testing machine. It consists of two identical parts that attach to the upper and lower jaws of the tensile testing machine using fixed jaws. The specimens are positioned inside the fixture on corner supports. An adjustment screw allows for the positioning of the sliding jaws to accommodate specimens of different dimensions. The alignment of the specimen axis with that of the machine is ensured by stops. Since the fixture is attached to the jaws of the tensile testing machine, there is no need to install a ball joint. Vertical force is applied gradually at a controlled loading rate (0.005 MPa/second). The Wintest32 software, specially programmed for this press, records the vertical force value and corresponding deformation at each loading step, as well as stress versus deformation.

Figure 7. Vieu of speecimen claamping device

Figure 8. Tensile test device

Geometry and Composition of Specimens

Specimen Geometry

The specimens used are dumbbell-shaped specimens, with a cross-sectional area of 100x100 mm² (see Figure 9). They feature a U-shaped notch, measuring 5 mm deep by 5 mm wide, with a slight inclination on the sides to facilitate demolding of the specimen.

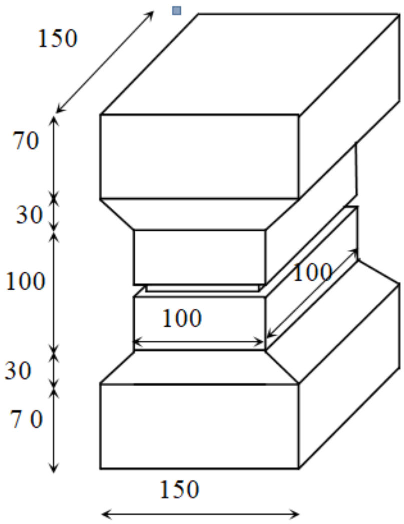

Figure 9. Fiber concrete specimen

Fiber Concrete Optimization

To optimize the composition of fiber-reinforced concrete, ensuring proper encapsulation of fibers by a matrix enriched with fine elements, we conducted a study on the workability of concrete considering the addition of fibers. In this part of our research, we utilized the experimental optimization method developed by the Central Laboratory of Bridges and Highways (LCPC), based on the Baron Lesage method (Rossi, 2002; Casanova, 1995). This approach involves fixing the water/cement ratio (W/C) and varying the sand/gravel ratio (S/G) from the composition of the control concrete, then measuring the flow time to determine the optimum. Thus, for each percentage of fibers (W = 0.3%, W = 0.5%, W = 0.8%, and W = 1%), we conducted four concrete mixes with different S/G ratios (S/G = 0.642, S/G = 0.8, S/G = 1), while maintaining a constant W/C ratio fixed at 0.543.

Results and Discussions

Fiber Tensile Characterization Tests

Figure 10 presents the "average of three tests" curve of the tensile stress as a function of strain σ = f(ε) for the fiber that exhibited the highest tensile strength.

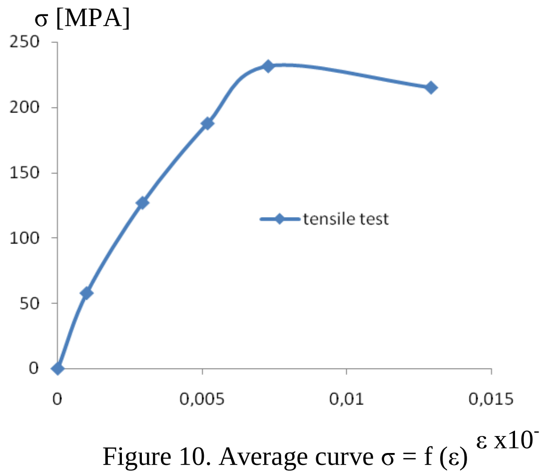

Figure 10. Average curve σ = f (ε)

During the test, it is observed that the ripples of the fiber gradually open until the fiber flattens out. Beyond this point, a ductile rupture of the steel is observed. It is noteworthy that the tensile strength increases with the number of ripples: it reaches Rm = 232 MPa for a length L = 60 mm and a number of ripples n = 5.

Compression Tests

The stress-strain curves obtained for the different compression tests after 28 days are presented in Figure 11.

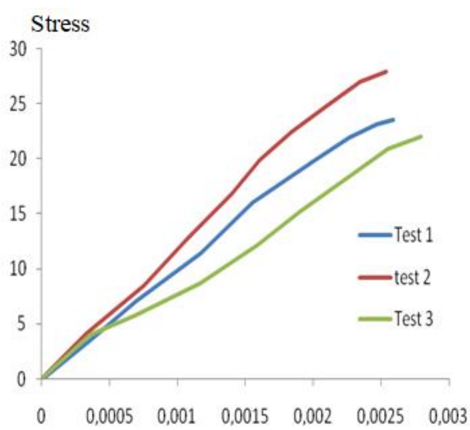

Figure 11. Superposition of stress-strain curves in compression

The maximum stresses for each test, as well as the measured mechanical characteristics, are provided in Table 5.

Table 5. Measured mechanical characteristics

Tests	Compressive stress σ [MPa]	Young's modulus E [MPa]
Test 1	23.48	30934
Test 2	27.73	29305
Test 3	22.02	33932
Average	24,41	31390.33

The results of the workability test are illustrated in the graph (see Figure 12), which shows the variation of flow time as a function of the S/G ratio.

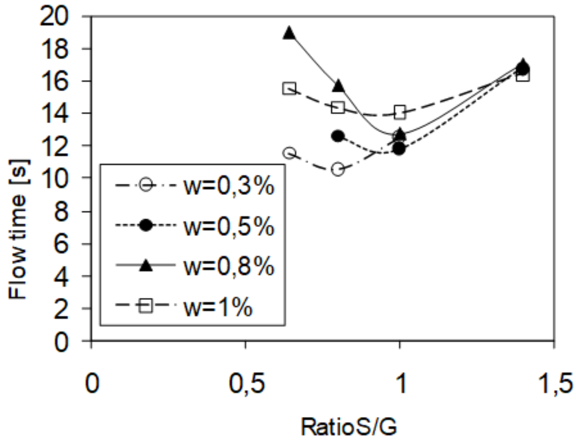

Figure 12. Evolution of the flow time as a function of the S/G ratio for each percentage of fibers W(%)

We observe that the optimal S/G ratio is 0.8 for a fiber percentage of 0.3%, and 1 for the other percentages. The flow times corresponding to these optima are between 10 and 15 seconds. These minimum times fall within the recommended optimum range by the LCPC. It should be noted that the optimal S/G ratio increases with the increase in fiber content. This increase can be explained by the behavior of the fibers, which act as large elements due to their shape and dimensions. Thus, increasing the volume of large elements (gravel + fibers) following the incorporation of higher fiber quantities requires an increase in the volume of sand.

Direct Tensile Tests of Fiber-Reinforced Concrete

After subjecting the fiber-reinforced concrete specimens to compression using the "IBERTEST" tensile machine, for various fiber contents (0.3%, 0.5%, 0.8%, and 1%) and different numbers of undulations, as well as for different sand/gravel ratios (S/G = 0.642, S/G = 0.8, and S/G = 1), the stress-strain curves are provided respectively in Figures 13, 14, 15, and 16.

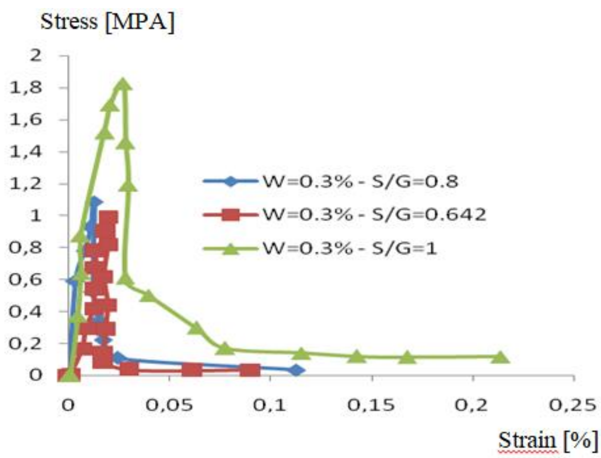

Figure 13. Stress-Strain curves for W=0.3% and S/G=0.642,0.8 and 1

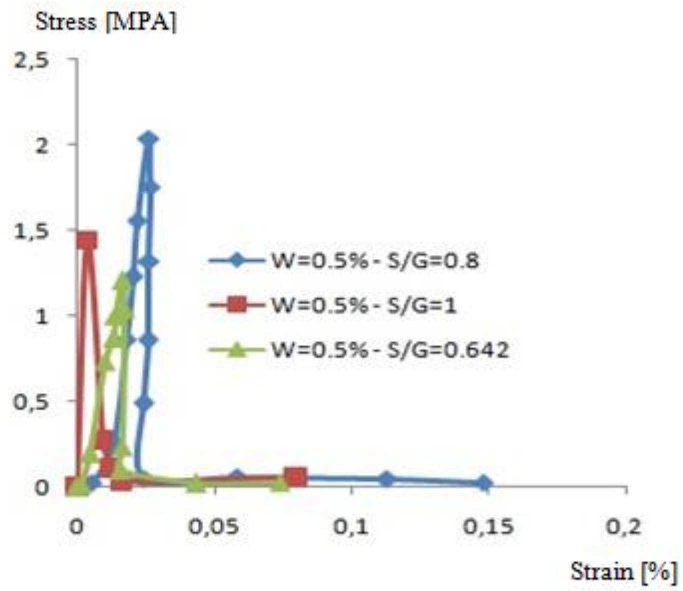

Fig.ure 14. Stress-Strain curves for W=0.5% and S/G=0.642, 0.8 and 1

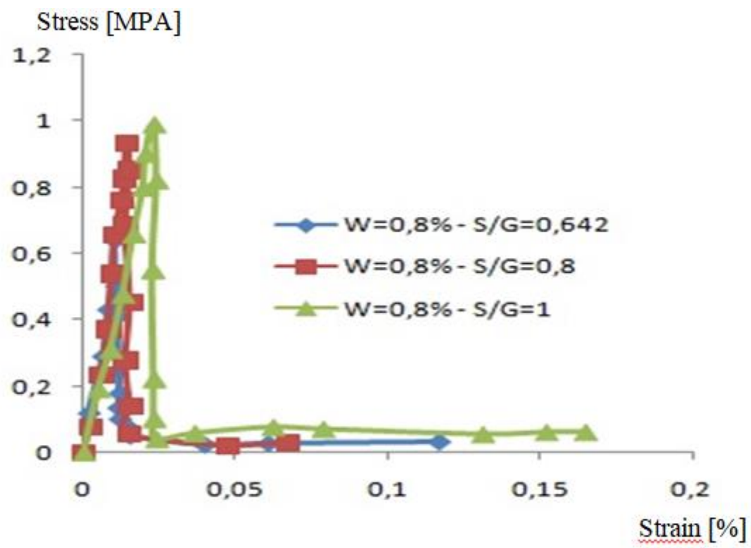

Figure 15. Stress-Strain curves for W=0.8% and S/G=0.642,0.8 and 1

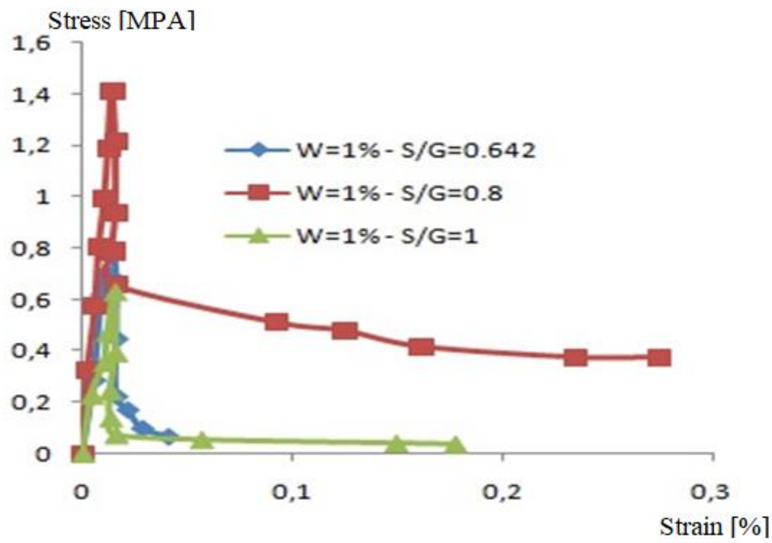

Figure 16. Stress-Strain curves for W=1% and S/G=0.642, 0.8 and 1

Figure 17 presents the overlay of stress-strain curves for different fiber contents (0.3%, 0.5%, 0.8%, and 1%), as well as for different sand/gravel ratios (S/G = 0.642, S/G = 0.8, and S/G = 1).

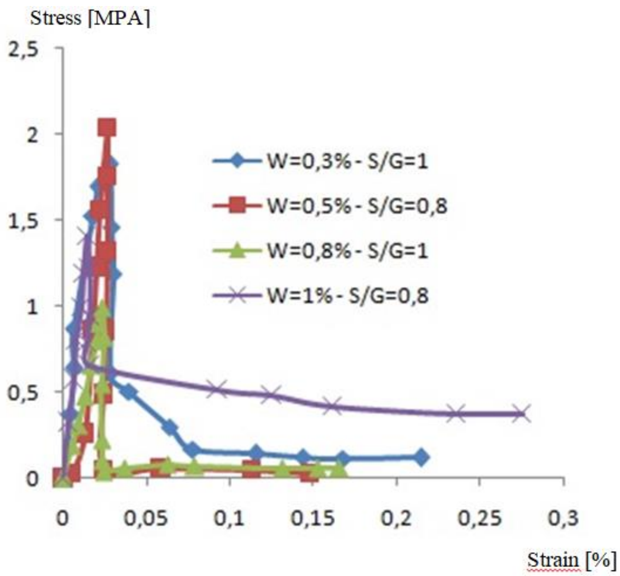

Figure 17. Superposition of the maximum stress-strain curves for the different w and S/G

The results from Figures 13, 14, 15, and 16 indicate that fiber-reinforced concrete is characterized by two distinct phases. The first phase is linear, corresponding to a quasi-elastic behavior of the material, marking the pre-cracking of the concrete. This phase ends with the appearance of a macro-crack. The second phase is characterized by a sudden drop, without abrupt rupture of the specimen, in the load-carrying capacity of the material, representing post-cracking. In this phase, the concrete matrix breaks while the fibers bridge the edges of the crack (see Figure 18), thus avoiding abrupt failure. The results also reveal that the addition of fibers imparts significant ductility to the material for different fiber percentages (W = 0.3%, W = 0.5%, W = 0.8%, and W = 1%), and this holds true for different sand/gravel ratios (S/G = 0.642, S/G = 0.8, and S/G = 1). Figure 17 shows that the maximum tensile stress of the fiber concrete is achieved for a fiber content of W = 0.5%, corresponding to a Sand/Gravel ratio (S/G = 0.8). This maximum stress is 2.04 MPa. It is interesting to note that adding fibers at low percentages leads to an increase in strength, as observed for a fiber percentage of W = 0.5% corresponding to S/G = 0.8. However, with an increase in fiber volume, this strength tends to decrease. This decrease could be attributed to the reduction in material compactness, which weakens it. This result is consistent with the observations of (Rossi, 1991).

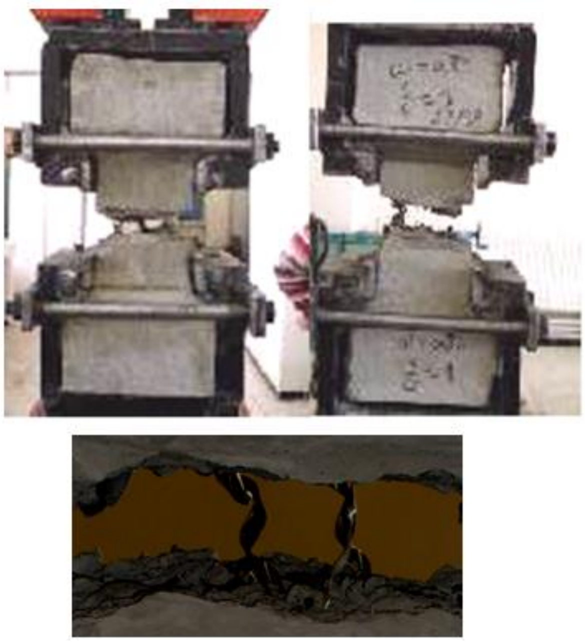

Figure 18. Failure mode of fibers in tension

Conclusion

This study revealed the impact of fiber length and the number of undulations on their tensile strength. The results indicate that the best strength is achieved with a fiber length of 60 mm and 5 undulations. During the tensile tests, the undulations tend to flatten out before the fiber steel elongates. The workability test helped determine the concrete composition with different sand/gravel ratios (S/G = 0.642, S/G = 0.8, and S/G = 1) and different fiber contents (0.3%, 0.5%, 0.8%, and 1%), thus ensuring good bond between fiber-reinforced concretes to enhance their stiffness and tensile strength. Analysis of the curves from this experimental study reveals that fiber-reinforced concrete exhibits two distinct phases. The first phase is linear, corresponding to quasi-elastic behavior of the material, while the second phase is characterized by a sudden drop in load-carrying capacity, without abrupt specimen failure. This experimental study enabled us to track the behavior of recycled fiber-reinforced concrete under tensile stress and determine the optimal fiber content and sand/gravel ratio (S/G) that yielded the highest peak stress, which was approximately 2.04 MPA for (S/G = 0.8).

In conclusion, we can state that the apparatus designed and implemented for conducting direct tensile tests has been successfully proven, and machining waste (chips) can be effectively utilized by incorporating them into fiber concrete preparation for industrial flooring and shotcrete applications, particularly in tunnels and the repair of large-diameter pipelines (Casanova, 1995; Rossi, 1991; Bouafia et al., 2002; Rossi et al., 1989; Lim et al., 1987) Furthermore, this concrete can be employed to enhance the fire resistance of reinforced concrete, as the fibers would restrict crack openings and shield traditional reinforcements from thermal radiation. In perspective, it would be interesting to carry out tests on test specimens of real large dimensions, to carry out tests with flat fibers instead of wavy ones in order to reduce the voids (cavities) in the cement paste, and also to associate these fibers to traditional reinforcements. Looking to the future, it would be intriguing to conduct tests on large-scale specimens to better simulate real-world conditions. Additionally, experimenting with flat fibers instead of wavy fibers could help minimize voids and cavities in the cement paste. Furthermore, exploring the combination of these fibers with traditional frameworks could provide valuable information on the synergistic effects of their interaction.

Scientific Ethics Declaration

The authors declare that the scientific ethical and legal responsibility of this article published in EPSTEM Journal belongs to the authors.

Acknowledgements or Notes

* This article was presented as a poster presentation at the International Conference on Technology, Engineering and Science (www.icontes.net) held in Antalya/Turkey on November 14-17, 2024.

References

Barragán, B. (2002). *Failure and toughness of steel fibre reinforced concrete under tension and shear* (Doctoral dissertation, Universitat Politecnica de Catalunya).

Barragan, B., Gettu, R., Agullo, L., & Zerbino, R. (2006). Shear failure of steel fiber-reinforced concrete based on push-off tests. *ACI Materials Journal*, *103*(4), 251.

Bouafia, Y., & Adjrad, A. (1997). Utilisation des fibres locales pour renforcement du beton. *Séminaire National de Génie Civil, M'sila (Algérie),* 16 et 17 novembre.

Bouafia, Y., Kachi, M. S & Fouré, P. (2002). Relation contrainte déformation en traction du béton armé de bres d'acier. *Annales de l'ITB*, 3.

Casanova, P., Rossi, P., & Schaller, I. (1995). Les fibres d'acier peuvent-elles remplacer les armatures transversales dans les poutres en béton armé, *Bulletin de liaison, LCPC*, 195.

Chalioris, C. E., & Sfiri, E. F. (2011). Shear performance of steel fibrous concrete beams. *Procedia Engineering*, *14*, 2064-2068.

Cho, S. H., & Kim, Y. I. (2003). Effects of steel fibers on short beams loaded in shear. *Structural Journal*, *100*(6), 765-774.

Cucchiara, C., La Mendola, L., & Papia, M. (2004). Effectiveness of stirrups and steel fibres as shear reinforcement. *Cement and Concrete Composites*, *26*(7), 777-786.

Ding, Y., Liu, H., Pacheco-Torgal, F., & Jalali, S. (2011). Experimental investigation on the mechanical behaviour of the fiber reinforced high-performance concrete tunnel segment. *Composite Structures*, *93*(4), 1284-1289.

Dinh, H. H., Parra-Montesios, G. J., & Wight, J.K. (2010). Shear behaviour of steel fibre reinforced concrete beams without stirrup reinforcement. *ACI Structural Journal*, 107(5), 597–606.

Djebali, S., Bouafia, Y., Atlaoui, D., & Bilek, A. (2011). Study of mechanical behavior of chips reinforced concrete. *Advanced Materials Research*, *324*, 360-363.

Kawamata, A., Mihashi, H., & Fukuyama, H. (2003). Properties of hybrid fiber reinforced cement-based composites. *Journal of Advanced Concrete Technology*, *1*(3), 283-290.

Kwak, Y., Eberhard, M. O., & Kim, J. (2002). Shear strength of steel fibre-reinforced concrete beams without stirrups. *ACI Structural Journal*, 99(4), 530–805.

Lim, D. H., & Oh, B. H. (1999). Experimental and theoretical investigation on the shear of steel fibre reinforced concrete beams. *Engineering Structures*, *21*(10), 937-944.

Lim, T. Y., Paramasivam, P., & Lee, S. L. (1987). Analytical model for tensile behavior of steel-fiber concrete. *Materials Journal*, *84*(4), 286-298.

Majdzadeh, F., Soleimani, S. M., & Banthia, N. (2006). Shear strength of reinforced concrete beams with a fiber concrete matrix. *Canadian Journal of Civil Engineering*, *33*(6), 726-734.

Majdzadeh, F., Soleimani, S. M., & Banthia, N. (2006). Shear strength of reinforced concrete beams with a fiber concrete matrix. *Canadian Journal of Civil Engineering*, *33*(6), 726-734.

Markovic, I., Walraven, J. C., & Van, M. J. (2003). Self compacting hybrid fiber concrete-mix design, workability and mechanical properties. In *Proceedings 3rd International Symposium on Self-Compacting Concrete*,763-775.

Meda, A., Minelli, F., Plizzari, G. A., & Riva, P. (2005). Shear behaviour of steel fibre reinforced concrete beams. *Materials and Structures*, *38*(4), 343-351.

Mirsayah, A. A., & Banthia, N. (2002). Shear strength of steel fiber-reinforced concrete. *Materials Journal*, *99*(5), 473-479.

Noghabai, K. (2000). Beams of fibrous concrete in shear and bending: experiment and model. *Journal of Structural Engineering*, *126*(2), 243-251.

Rossi, P. (1991). Formulation et comportement mécanique des bétons de fibres métalliques. *Annales del'ITBTP*, 492, 90-101.

Rossi, P. (2002). *Le développement industriel des bétons de fibres métalliques – Conclusions et recommandations*. Presses de l'École Nationale des Ponts et Chaussées.

Rossi, P., Harrouche, N., & Belloc, A. (1989). Méthode de composition des béton de fibres métalliques» *Annales de L'ITBTP*,° 475.

Slater, E., Moni, M., & Alam, M. S. (2012). Predicting the shear strength of steel fiber reinforced concrete beams. *Construction and Building Materials*, *26*(1), 423-436.

Stratford, T., & Burgoyne, C. (2003). Shear analysis of concrete with brittle reinforcement. *Journal of Composites for Construction*, *7*(4), 323-330.

Sukontasukkul, P. (2004). Toughness evaluation of steel and polypropylene fibre reinforced concrete beams under bending. *Thammasat International Journal of Science and Technology*, *9*(3), 35-41.

Author Information

Atlaoui Djamal
Department of Civil Engineering, Laboratory of Modeling of and Structures in Civil Engineering (L2MSGC), University 'Mouloud Mammeri' of Tizi Ouzou, 15000, Algeria.
Contact e-mail: *djamal.atlaoui@ummto.dz*

Ghouilem Kamel
Department of Civil Engineering, Faculty of Construction Engineering Laboratory of Geomaterial, Environment and Amenagement (LGEA), University of Mouloud Mammeri, Tizi Ouzou, Algeria.

Bouafia Youcef
Department of Civil Engineering, Laboratory of Modeling of Materials and Structures in Civil Engineering (L2MSGC), University 'Mouloud Mammeri' of Tizi Ouzou, 15000, Algeria.

To cite this article:

Atlaoui, D. Ghouilem, K & Bouafia, Y. (2024). The effect of recovery fibers and the sand/gravel ratio on the direct tensile behavior of concrete. *The Eurasia Proceedings of Science, Technology, Engineering & Mathematics (EPSTEM), 32*, 520-531.

The Eurasia Proceedings of Science, Technology, Engineering & Mathematics (EPSTEM)
ISSN: 2602-3199

The Eurasia Proceedings of Science, Technology, Engineering & Mathematics (EPSTEM), 2024

Volume 32, Pages 532-536

IConTES 2024: International Conference on Technology, Engineering and Science

Investigation of the Effect of Combined Thermomechanical Processing on the Microstructure Evolution of CuZn23Mn7Fe4 Brass

Sergey Lezhnev
Rudny Industrial University

Andrey Tolkushkin
Rudny Industrial University

Pavel Tsyba
Rudny Industrial University

Abdrakhman Naizabekov
Innovative University of Eurasia

Irina Volokitina
Karaganda Industrial University

Alexandr Arbuz
AEO Nazarbayev University

Abstract: The article investigates the effect of combined thermomechanical processing, including pre-heat treatment and radial-shear rolling on the microstructure evolution of CuZn23Mn7Fe4 brass. The conducted studies have shown that the most optimal pre-heat treatment for CuZn23Mn7Fe4 brass before deformation on a radial-shear rolling mill is annealing at a temperature of 500°C. As a result of subsequent deformation of workpieces with an initial diameter of 30 mm, subjected to pre-annealing at a temperature of 500°C, a gradient ultrafine structure was formed in this brass alloy on a radial-shear rolling mill up to a diameter of 18 and 12 mm. Thus, in the surface layer of the deformed rod, a structure with an average grain size of 7 μm was obtained when rolling it to a diameter of 18 mm, and 3 μm when rolling it to a diameter of 12 mm. In the central layer of the bars, a structure with a grain size of 31 μm and 17 μm was obtained when rolling the bar to a diameter of 18 mm and 12 mm, respectively.

Keywords: Pre-heat treatment, Annealing, Quenching, Radial-shear rolling, Brass, Microstructure

Introduction

For more than a decade, scientists around the world have been paying great attention to the development of various combined thermomechanical treatments, both ferrous and non-ferrous metals and alloys, including various types of heat treatment and various methods of processing these materials by pressure in a hot or cold state. Special attention is paid to pressure treatment methods that allow the implementation of severe plastic deformation (SPD) in ferrous and non-ferrous metals and alloys, as described by Bogatov and Leshchev (2012), Valiev et al. (2022), Galkin et al. (2009) revealed that one of the promising such methods is radial shear rolling (RSR). Due to the design features implemented in the working cage of mini radial-shear rolling mills (feed angle 18-20 °, rolling angle 0-12 °) and unique trajectory and deformation conditions, as described by Galkin et al. (2014), Iskhakov et al. (2020), Galkin et al. (2021), when deforming bars from various ferrous and non-

- Selection and peer-review under responsibility of the Organizing Committee of the Conference

ferrous metals on these mills, the possibility of obtaining a gradient ultrafine structure is realized, that was proved by Galkin et al. (2022), Akopyan et al. (2020), Mishin et al. (2020), Gamin et al. (2022). It has also long been proven that one of the promising ways to obtain a pre-regulated microcrystalline structure in various metals and alloys is pre-heat treatment. For example, Naizabekov et al. (2022), Naizabekov et al. (2023), Naizabekov et al. (2024) described the effects of combined thermomechanical processing, including pre-heat treatment and radial-shear rolling, on the microstructure evolution of M1 copper and CuZn36 brass. This work is devoted to the study of the effect of combined thermomechanical processing, including pre-heat treatment and radial-shear rolling, on the microstructure evolution of CuZn23Mn7Fe4 brass.

Method

The choice of CuZn23Mn7Fe4 brass as the starting material is justified by its wide application in various industries, including medicine, mechanical engineering, instrumentation, cable industry, etc. Due to the fine-grained structure caused by the presence of iron in the alloy, this brand of brass has high strength and increased viscosity. To achieve this goal, a physical experiment was conducted using a chamber furnace of resistance RCF 12/1400 and a radial-shear rolling mill RSR 10-30 (Figure 1). And as the initial blanks for the laboratory experiment, blanks with dimensions D × L = 30 × 200 mm were prepared.

Figure 1. Radial-shear rolling mill RSR 10-30

The laboratory experiment consisted of two stages. At the first stage of the research, the task was to determine the optimal mode of pre-heat treatment of CuZn23Mn7Fe4 brass, which ensures both the production of a fine-grained structure and the possibility of further workability on a radial-shear rolling mill without destruction. To solve this problem, based on the Cu-Zn state diagram, the following types of pre-heat treatment were selected and implemented:

- quenching at a temperature of 400 °C;
- quenching at a temperature of 500 °C;
- quenching at a temperature of 800 °C;
- annealing at a temperature of 500 °C;
- annealing at a temperature of 800 °C.

After all types of pre-heat treatment were carried out, templets were cut from the obtained blanks to prepare micro-grinders. The operation of cutting templets from the workpiece is performed using the Labotom-3 cutting machine, which is a high-precision cutting machine. The preparation of micro-grinders was carried out on the Tegra Pol – Tegra Force grinding and polishing machine by Struers. For etching the CuZn23Mn7Fe4 brass, a solution of ferric chloride with hydrochloric acid $FeCl_3$, HCl, H_2O mixed from a ratio of 1:20:100 was selected. The microslips were etched in the resulting solution at the beginning by wiping, and then by immersion from 30 seconds to 1-2 minutes, depending on the degree of deformation. Metallographic studies were carried out using a Leica optical microscope.

Results and Discussion

The analysis of the microstructure of CuZn23Mn7Fe4 brass obtained after quenching and annealing from various temperatures is shown in Figure 2. The analysis of the obtained data showed that annealing of

CuZn23Mn7Fe4 brass forms an almost equal-grained structure in it. The microstructure has two phases α and β. At the same time, an increase in the annealing temperature to 800 °C leads to grain growth. For example, at a temperature of 500 °C, a grain of 60 μm was obtained (Figure 2a), and at a temperature of 800 °C, a grain of 80 μm was obtained (Figure 2b). After quenching at temperatures of 400 °C, 500 °C and 800 °C, we also obtained a two-phase structure (Figures 2 c, d, e), only the grain size is different. Thus, quenching from 400 °C due to rapid cooling ensured the production of a homogeneous martensitic-type structure from α-phase crystals and β-phase residues (Figure 2c). When quenching from 800 °C, a structure consisting of residues of the initial α-phase and sections of a two-phase structure is observed, which includes crystals of a metastable β-phase with dispersed alpha-phase secretions in the middle of these sections (Figure 2e).

Since the β-phase embrittles the brass alloy, it is undesirable for further deformation of the samples. But in this alloy, a two-phase structure was obtained after all the pre-heat treatments. Therefore, based on the results [11], annealing at a temperature of 500 °C is applicable for further deformation of workpieces on a radial-shear rolling mill, as for CuZn36 brass.

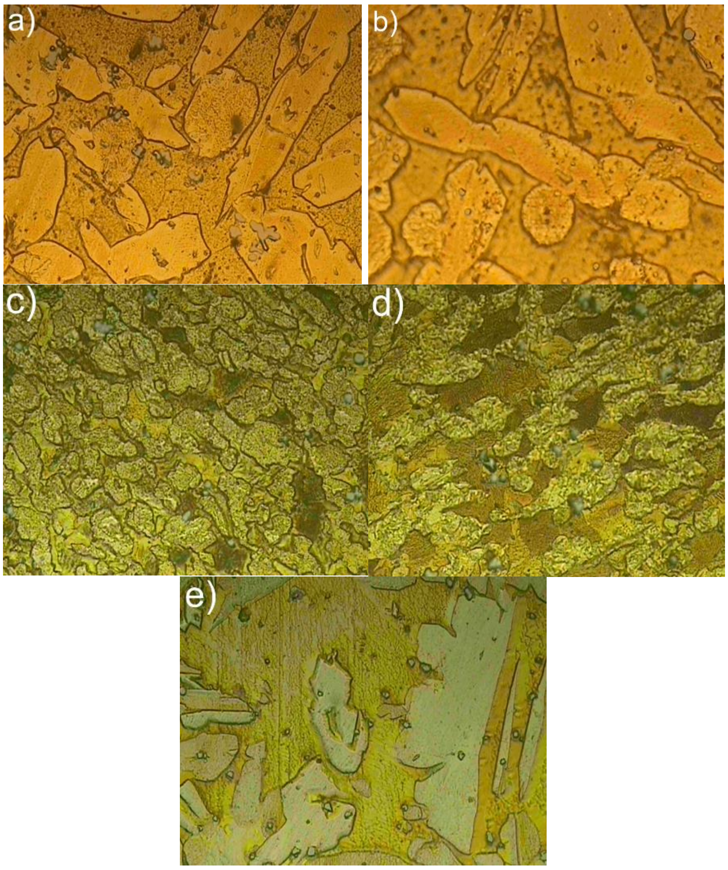

Figure 2. Microstructure of CuZn23Mn7Fe4 brass after preliminary heat treatment: a – annealing 500 °C; b – annealing 800 °C; c – quenching 400 °C; d – quenching 500 °C; d – quenching 800 °C

At the next stage of the research, the task was to identify the effect of radial-shear rolling on the microstructure evolution of CuZn23Mn7Fe4 brass subjected to the annealing at a temperature of 500 °C as the most optimal heat treatment. To solve this problem, a laboratory experiment was conducted on the deformation of brass samples subjected to annealing at a temperature of 500 °C at a radial-shear rolling mill RSR 10-30. This experiment was as follows. The initial workpieces with dimensions D × L = 30 × 200 mm were preheated to a temperature of 500 °C with exposure in a resistance furnace before deformation. After that, these samples were deformed at the RSR 10-30 mill with an absolute compression step of 3.0 mm in diameter until bars with diameters of 18 and 12 mm were obtained.

Metallographic analysis of RSR 10-30 CuZn23Mn7Fe4 brass rods obtained after deformation at the RSR mill showed that the microstructure of the surface layer of the rod differs significantly from the microstructure of the central zone of the rod (Figure 3), as well as in the cases of M1 copper [13] and CuZn36 brass [11]. Thus, in bars with a diameter of 18 mm in the surface layer, a structure with an average grain size of 7 μm was obtained, and in the center of the bar a multi-grained structure with an average grain size of 31 μm. After the RSR to a diameter of 12 mm, a fine–grained, equal-grained structure of 3 μm was obtained in the surface layer, and 17 μm in the center. The presence of such an alloying component as iron in CuZn23Mn7Fe4 brass, which inhibits grain growth during recrystallization, made it possible to achieve more intensive refinement of the initial grain size than during a similar combined thermomechanical processing of CuZn36 brass. As can be seen from Figure 3, dynamic softening processes do not lead to complete softening of the deformed metal, since they retain excessive dislocation density. Due to the short time of hot deformation, the hardening and softening processes lead to an unstable and heterogeneous structural state of the material. The heterogeneity of the grain structure in terms of volume and cross-section of the rod is manifested in the form of general zonal grain diversity, zones with abnormally large grains, line or island grain diversity.

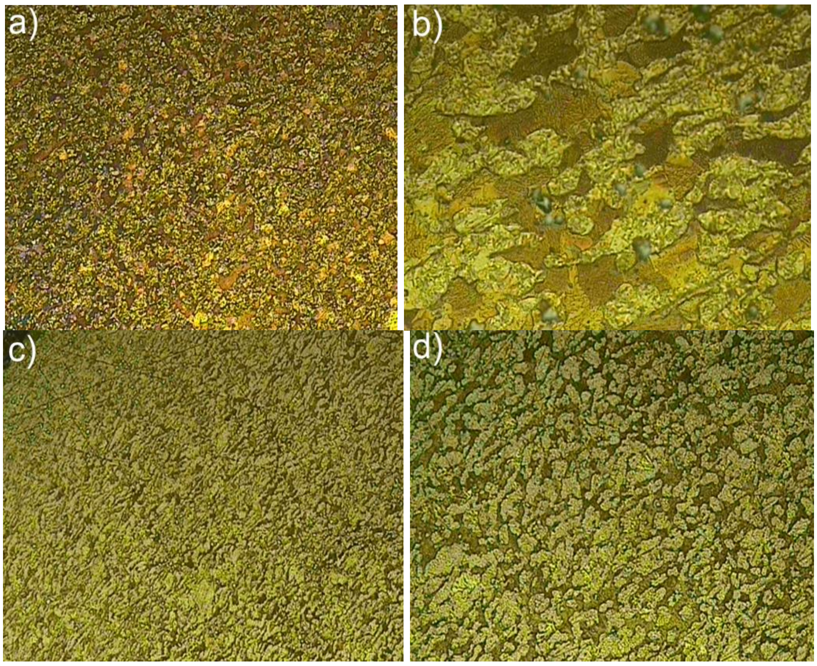

Figure 3 Microstructure of CuZn23Mn7Fe4 brass deformed at 500 °C (cross section): a – diameter of 18 mm (edge); b – diameter of 18 mm (center); c – diameter of 12 mm (edge); d – diameter of 12 mm (center)

Conclusion

Based on the results obtained, it can be concluded that combined thermomechanical processing, including pre-heat treatment and radial-shear rolling, makes it possible to obtain a gradient fine-grained structure in CuZn23Mn7Fe4 brass. At the same time, it was proved that the most suitable pre-heat treatment for CuZn23Mn7Fe4 brass is annealing at a temperature of 500 °C, since in this case both the most complete transition of the β-phase to the α-phase and the production of a uniform fine-grained structure is ensured.

Scientific Ethics Declaration

The authors declare that the scientific ethical and legal responsibility of this article published in EPSTEM Journal belongs to the authors.

Acknowledgements

* This article was presented as a poster presentation at the International Conference on Technology, Engineering and Science (www.icontes.net) held in Antalya/Turkey on November 14-17, 2024.

* This research was funded by the Science Committee of the Ministry of Science and Higher Education of the Republic of Kazakhstan (Grant № AP14869128).

References

Akopyan, T. K., Gamin, Y. V., Galkin, S. P., Prosviryakov, A. S., Aleshchenko, A. S., Noshin, M. A., Koshmin, A. N., & Fomin, A. V. (2020). Radial-shear rolling of high-strength aluminum alloys: Finite element simulation and analysis of microstructure and mechanical properties, *Materials Science and Engineering A, 768*, 139424.

Bogatov, A. A., & Leshchev, I. V. (2012). On intensive plastic deformation and metal pressure treatment processes. *Proceedings of the I International interactive Scientific and practical Conference*, 13-19.

Galkin, S. P., Kharitonov, E. A., & Romanenko, V. P. (2009). *Radial-shear rolling as a new highly efficient method of metal forming*. Moscow: IRIAS.

Galkin, S. P., Romantsev, B. A., & Kharitonov, E. A. (2014). Putting into practice innovative potential in the universal radial-shear rolling process. *CIS Iron and Steel Review*, *2014*(9), 35-39.

Galkin, S. P., Gamin, Y. V., Aleshchenko, A. S., & Romantsev, B. A. (2021). Modern development of elements of theory, technology and mini-mills of radial-shear rolling. *Chernye Metally*, *12*, 51-58.

Galkin, S. P., Aleshchenko, A. S., & Gamin, Y. V. (2022). Development and experimental testing of the technology for producing deformed bars of alloy D16T from continuously casting billets of small diameter with low elongation ratios. *Russ. J. Non-ferrous Metals, 63*, 328-335.

Gamin, Y. V., Korotitskiy, A. V., Kin, T. Y., Galkin, S. P. Kostin, S. A., & Tikhomirov, E. O. (2022). Development of temperature-rate modes of hot deformation of the Co–28Cr–6Mo alloy based on processing maps. *Steel in Translation*, *52*, 1027-1036.

Iskhakov, R., Gamin, Y., Kadach, M., & Budnikov, A. (2020). Development of radial-shear rolling mill special stands for continuous cast billets deformation. *IOP Conference Series: Materials Science and Engineering, 966*, 012074.

Mishin, I. P., Naydenkin, E. V., Ratochka, I. V., Lykova, O. N., Vinokurov, V. A., & Manisheva A. I. (2020). Effect of radial shear rolling and aging on the structure and mechanical properties of titanium alloy VT35, *AIP Conference Proceedings, 2310*(1), 020206.

Naizabekov, A. B., Volokitina, I. E., Panin, E. A., & Volokitin, A. V. (2022). Studies of the effect of pre-heat treatment on the microstructure evolution of copper during deformation, *Proceedings of the International Scientific and Practical Conference "Promising Engineering Technologies"*, 285-291.

Naizabekov, A., Volokitina, I., Panin, E., Rubanik, V., & Tsarenko, Yu. (2023). Role of pre-heat treatment in the formation of a favorable finegrained structure in copper and brass for further deformation, *Journal of Chemical Technology and Metallurgy, 58*, 783-787.

Naizabekov, A., Lezhnev, S., Volokitina, I., Panin, E., Tolkushkin, A., Belsky, S., & Pishchov, M. (2024). Investigation of the effect of combined thermomechanical processing on the brass microstructure evolution and the microhardness change. *Metalurgija, 63*, 283-286.

Valiev, R. Z., Straumal, B., & Langdon, T. G. (2022). Using severe plastic deformation to produce nanos tructured materials with superior properties. *Annual Review of Materials Research*, *52*(1), 357-382.

Author Information

Sergey Lezhnev
Rudny Industrial University
38 50 let Oktyabrya str., Rudny, Kazakhstan
Contact e-mail: *sergey_legnev@mail.ru*

Andrey Tolkushkin
Rudny Industrial University
38 50 let Oktyabrya str., Rudny, Kazakhstan

Pavel Tsyba
Rudny Industrial University
38 50 let Oktyabrya str., Rudny, Kazakhstan

Abdrakhman Naizabekov
Innovative University of Eurasia
Lomova 45 str., Pavlodar, Kazakhstan

Irina Volokitina
Karaganda Industrial University
Republic 30, Temirtau, Kazakhstan

Alexandr Arbuz
AEO Nazarbayev University
Kabanbai batyr, 53, Astana, Kazakhstan

To cite this article:

Lezhnev, S., Tolkushkin, A., Tsyba, P., Naizabekov, A., Volokitina, I., & Arbuz, A. (2024). Investigation of the effect of combined thermomechanical processing on the microstructure evolution of CuZn23Mn7Fe4 brass. *The Eurasia Proceedings of Science, Technology, Engineering & Mathematics (EPSTEM), 32,* 532-536.

The Eurasia Proceedings of Science, Technology, Engineering & Mathematics (EPSTEM)
ISSN: 2602-3199

The Eurasia Proceedings of Science, Technology, Engineering & Mathematics (EPSTEM), 2024

Volume 32, Pages 537-545

IConTES 2024: International Conference on Technology, Engineering and Science

Aspects of Influencing Factors in the Polishing of Plastic Optical Fibers

Brindus Comanescu
Optoelectronica Romania

Paul Schiopu
National University for Science and Technology Polytechnica Bucharest

Marian Vladescu
National University for Science and Technology Polytechnica Bucharest

Abstract: The interaction between the X-ray beam and the scintillating core of the optical fiber creates photons. The generated photons propagate through the fiber until the fiber end where they are captured by a solid state photon sensitive detector. This very sensitive detector converts generated photons into a low-level electronic signal that is amplified for later processing. For industrial, medical domains or for detection of contraband objects in custom control, flexible detectors can be built using 1 mm plastic scintillating optical fiber. The paper presents aspects related to the influencing factors of the optical fiber polishing process. Experiments related to the influencing factors of optical fiber polishing were performed. The results related to the influencing factors for cutting the optical fiber are presented. A proposal for plastic fiber cutting tool was given. The results related to factor of influence for polishing of plastic scintillating fiber were presented. In conclusion a possible technology for plastic scintillating fiber with 1 mm diameter is described.

Keywords: Fiber optics, Plastic fiber optics, Polish, Technology

Introduction

Fiber optic are used from many years in communication in order to send signals over the fiber length. The purpose of replacing copper wire in telecom is due to the following advantages: lower weight, lower power consumption, higher bandwidth. Fiber optic made from plastic or glass are used to transmit video, data, audio over long distances with reduced losses and distorsion. Fiber optics are flexible and durable. Plastic fiber with scintillating material in core is used from many years in scientific experiments, medical imaging, industrial application and other applications. The scope of paper is to present the results of researches related to low cost polishing technology developed. Based on a polishing model, we develop a polishing technology for plastic fibers, we make experiments and we get results. For experiments we use plastic scintillating fibers, SCSF 78 made by Kuraray (n.d.). Fibers used in experiments are produced with core from polystyrene and cladding from PMMA and has 1 mm diameter, We define the optimum process for polishing fibers used to make a flexible detector described by Panagopoulos et al. (2023).

Our investigations in literature related to modelling the polishing plastic scintillating fibers published papers found just few papers. In a technical document company describe how they make a trial to polish plastic scintillating fiber. (Kuraray, n.d.) There is a general method to polish plastic fiber produced by Kuraray, considered as starting point to perform polishing, without full details of operations.

Few methods for polishing plastic scintillating fiber are described by Hanlet et al. (1999). In that paper there is a comparison between 3 methods for polishing plastic fibers: first method uses a teflon block, second method uses an ice block and third one uses a FiberFin III polishing machine. Fibers polished were HFBR-RUS500 from Avago Optoelectronics with 1 mm core diameter and 2.2 mm outer diameter. Fibers were used in Muon Scintillator Counters (MSC) and in the InterCryostat Detector (ICD). Such detectors uses a large number of fibers so an industrial polishing method is necessary and reccomended over manual method. Other papers present polishing of plastic fibers for industrial or telecommunication application.

Process Modelling

For our researches we use polystyrene core and PMMA cladding fibers with 1 mm diameter fully described in Kuraray (n.d.). catalogues Plastic Scintillating Plastic lens used in industrial, medical or scientific applications are manufactured from polymer materials like: polycarbonate, TPU, PET or other materials. Those materials has similar characteristics and we consider appropriate to use same modeling process. For plastic scintillating fiber material removal modelling process, it is considered appropriate to use, Preston hypothesis as is described in Kaufmann (2017).

$$\frac{dz}{dt} = C_p * \frac{F}{A} * \frac{ds}{dx} \qquad (1)$$

Were: z - material removal [mm];

t - polishing time [s];
C_p - Preston coefficient;
F - polishing force [N];
A - polishing tool footprint size [mm^2];
s - oscillation length [mm].

In our case, of polishing plastic fiber, process parameters are followings: polishing tools (pad, flat surface), polishing solution, temperature, dilution, raw material, time, etc. Material removal thickness are influenced by pressure and speed because of polymer materials viscoelasticity behavior. A factor of influence of the tool positioned on the fiber is footprint size. In our experiments we check force distributed over the probe to verify if the value is constant.

During the polishing process of fibers we notice that we have no chemical reaction between abrasive grain and fiber surface. From this reason we may make a consider polishing plastic fiber a process similar with plastic lens lapping process. Kaufmann (2017) consider that is posible to compute material removal thickness if Preston coefficient is know and process parameters are also known. In fig. 1 we have the case of static load for penetration depth calculation. Penetration depth is a parameter of stock removal process.

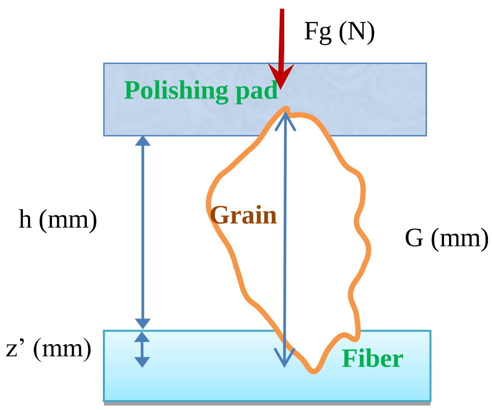

Figure 1. Polishing gap between tool and fiber with abrasive polishing grain (Kaufmann, 2017)

Based on the fig. 1, we may wrote following formula:

$$z' = \frac{Fg * S * G}{H * h} \qquad (2)$$

Were: z´ - penetration depth of the polishing grain [mm];

F_g - force per polishing grain;
S - shape of the polishing grain;
G - grain size [mm];
H - Young´s modulus of the fiber material [$N*mm^{-2}$];
h - thickness of the fluid layer between tool and fiber [mm].

Kaufmann (2017) verify the influence of the abrasive grain and he conclude that when increase the size of abrasive grain, increase the pressure applied on the material and the results is the increasing of thickness of material removal. He claim that when slurry density increase, the force per grain decrease because force is applied on increased number of grains. As consequence, the quantity of material removed, is reduced. When number of grains increase, the quantity of material removed is increased. Pad used for polishing purposes has a natural porosity were grain are kept. Using a pad with higher porosity, number of grains increase and decrease the force per grain because the area is not modified. He perform a penetration test and understand that geometry of the grain influence mechanical behavior of the penetrated material. As consequence a higher grain size increase the penetration depth.

The Young´s Modulus influence is not easy to be understood due to the viscoelastic behavior of most of the polymer materials. Young´Modulus depends on the load level and loading rate. Also, he claim that pressure applied during the polishing process is important because of the elastic and plastic deformation. Thickness of the abrasive film depends on the viscosity, the polishing pad roughness, the fiber end face roughness, the relative speed between tool and fiber and the pressure applied.

A particular interest is the viscosity, and the influence of grain number in the slurry and pH. Less agglomeration in slurry mean less sedimentation and this is important factor for lifespan. Number of grains in the polishing gap is important factor of stock removal process. pH-value is important for the amount of water in the polymer surface because can change the hardness of the fiber end face surface.

Experiments

Plastic Scintillating Fiber Polish Technology

A principle for polishing plastic fiber was described in Kuraray (n.d.) but they do not provided fiber diameter and other details. (Hanlet et al., 1999). Present also by comparison 3 methods for polishing plastic fiber: teflon block, ice polishing and FiberFin III. First two methods are manual methods, recommended for prototypes and a reduced number of fibers. Third method uses an industrial machine recommended for large number of fibers. For experiments were used as fiber HFBR-RUS500 from Avago Optoelectronics, with 1 mm diameter core and 2.2 mm diameter clad. In an manual related to connectorization of fibers produced by Thorlabs (2020) it is present principle for manual glass fiber polishing: tools, consumables, materials, etc. According with Hanlet et al. (1999) and manual for connectorization (Thorlab,2020), polishing fiber has few steps: coarse, medium and fine.

We start experiments by cutting fiber using FiberFin inc razor blade (figure 2). Cutting tool is composed by a metallic block provided with a number of holes with different diameters. Metallic block has a channel used to guide blade with purpose to avoid cutting errors. Fiber diameter is verified, inserted in proper hole and then blade is pressed.

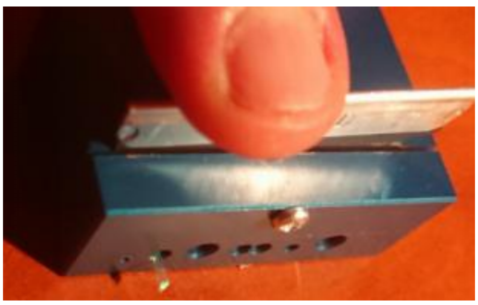

Figure 2. Fiberfin fiber razor blade (POF razor cutter multiple size fibers)

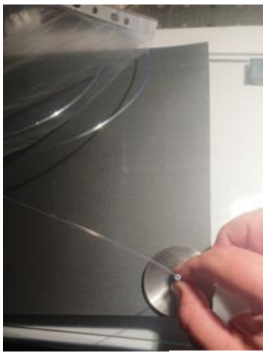

Figure 3. Glass plate (Thorlabs,2020)

For experiments we place on glass plate (figure 3) sandpaper fixed with few DI water drops. In the Guide (Thorlabs,2020) for manual polishing fiber, a movement of fiber in shape of number 8 it is reccomended (fig. 4a). Fiber is pressed gently fiber on abrasive surface. We experiments also complex movement from figure 4b . This a complex movement used especially in industrial polishing machines. We will compare results obtained using both movements.

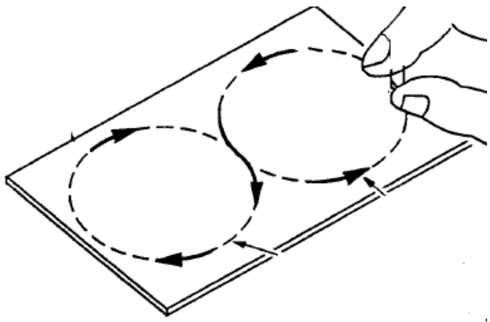

Figure 4a. Manual polishing pattern (Thorlabs, 2020)

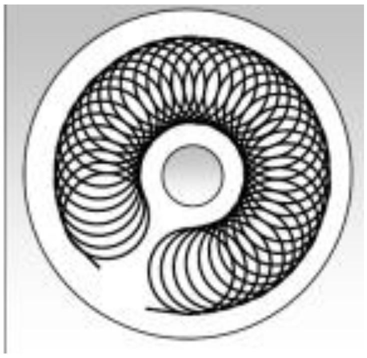

Figure 4b. Orbital pattern (Rubin, 2017)

We use a tool as in figure 5 to polish fibers. Tool is a 5 mm stainless steel circular plate with a central hole were fiber connector is fixed. Contact surface has anular channels (figure 5b) used to accumulated abrasive and plastic particle.

Figure 5a. Stainless steel tool back side

Figure 5b. Stainless steel tool front side

For coarse polishing we press gently fiber over flat surface with P800 sandpaper and tool is moved 3 times. Fiber endface is cleaned using pure air, DI water and non abrasive optical tissue. Sandpaper is changed from P800 to P1500 and as consequence abrasive grain size is reduced from 20 to 12 microns. Tool is pressed gently over sandpaper using 5 times movement. Fiber endface is cleaned. For medium polishing we change sandpaper from P1500 with P3000 and as consequence grain size is now 5 microns. Tool is pressed gently and 7 times movement is applied. Endface is cleaned.

For fine polish we use Buehler micropolish alumina solution with abrasive grain size of 0.3 microns. Solution is spread a non abrasive tissue fixed on flat surface (figure 6). Tool is press gently over abrasive surface and is rotated 10 times. Endface is cleaned and inspected. In next step it is used 0.02 microns abrasive particle size and a number of 15 complex rotation are applied.

Figure. 6. Abrasive suspension placed on non abrasive tissue

We investigate followings during our experiments: influence of abrasive particles: size, concentration in solution, influence of pressure in polishing, influence of gap between fiber and hole diameter in razor block, influence of tool pressure, influence of complex rotation. For investigations we use 2 tools: a stand described by Comanescu et al. (2023) and an optical microscope (videomicroscope n.d.) recommended by Fiber Optic Association. In figure 7a is a 30x portable magnification microscope, a flexible tool used especially for investigation of fiber cutting and coarse polishing. In figure 7b there is a video microscope from Edmund Optics, modified to work horizontally. This tool has 100x magnification and main advantage is screen visualization.

Figure 7a) Optical microscope used for fiber optic polishing quality investigation (video microscope n.d)

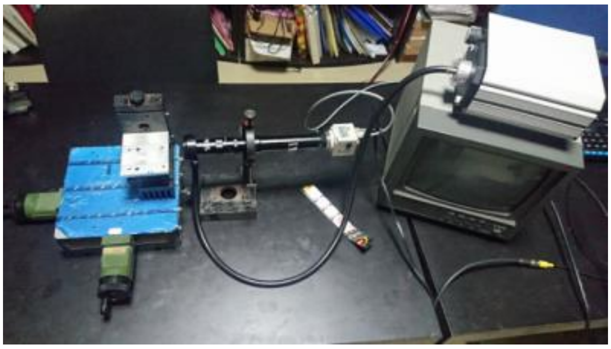

Figure 7b. Video microscope

Results and Discussion

We use as comparison for our experiments the cutting results from a fiber optic cutting and polishing operation from presentation New Termination Techniques for POF (Mulligan, 2009).

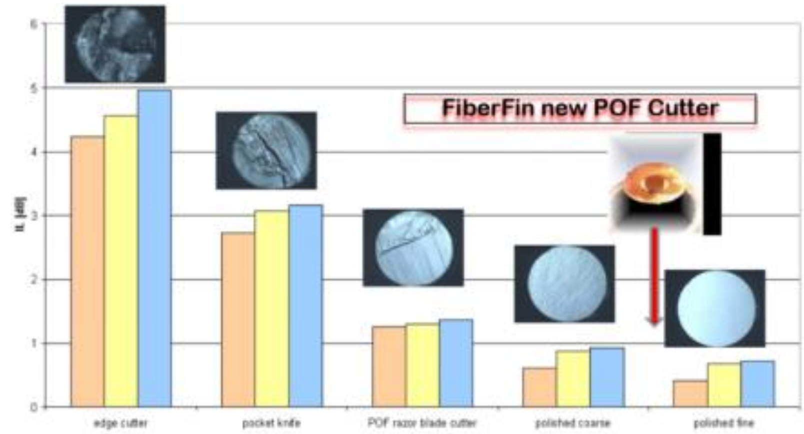

a) b) c) d) e)

Figure 8 Plastic fiber cutting (Mulligan, 2009)

According with Fiberfin presentation, New Termination Techniques for POF (Mulligan, 2009) for razor blade cutting plastic fiber, they offer the ability to cut fiber without the need to polish fiber or to have reduced polishing manpower resource consumption. In figure 8a is presented the results of fiber cutting using a scissor. In the figure 8b is presented another cutting process of plastic fiber. Figure 8c present the result of razor blade plastic fiber cutting. Comparing the fiber cutting using all processes we noticed that razor blade is a good tool for plastic fiber cutting compared with other types of cutters. In figure 8d is the image of fiber polished after cutting. Analising image based on roughness criteria that it is need to continue to polish. In the figure 8e is the results of fine fiber polishing after continuu the process analised in image 8d.

We cut 10 pieces from a Kuraray 1 mm plastic fiber using FiberFin razor blade and the results are presented in figure 9a,b. The endface is partial cut and it is need to be polished. In figure 9c we present a graphic for 10 cutting. On the vertical axis is the percentage of cutting endface and on the orizontal axis is number of cuttings. Based on our results presented also in figure 9 a, b, c we claim that cutting of endface is between 40 to 60%in the most of cases. There is also a reduced number of case when cutting of endface is full.

Figure 9a. Cutting a fiber well fixed in tool

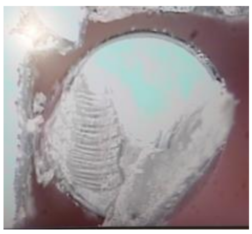

Figure 9b. Cutting a fiber not well fixed in tool

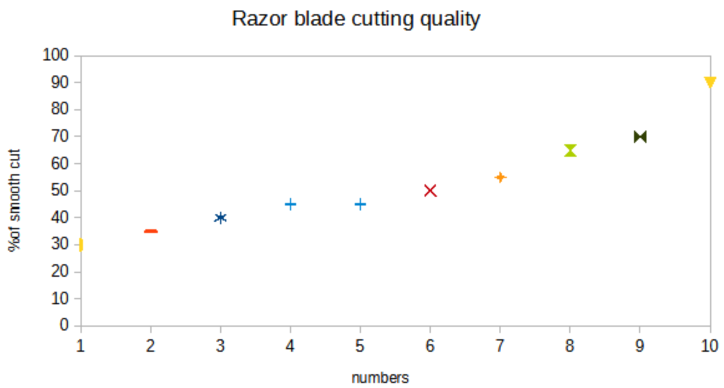

Figure 9c. Cutting quality

After (coarse) polishing using P800 sandpaper , the endface roughness is modified , traces of abrasive grains and dirty points are present as in figure 10a. We continue to polish using P3000. Depth of abrasive grains trace decrease and number of dirty points increase as in figure 10b.


Figure 10a. Coarse polishing Figure 10b. Medium polishing

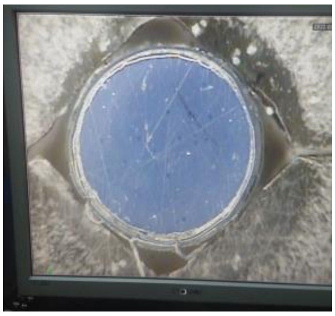


Figure 10c. Fine polishing Figure 10d. Final result for polishing

For fine polish we change sandpaper with liquid polishing solution. The results of polish using 0.3 microns abrasive grains is presented in figure 10c. The number of abrasive grain trace and dirty points decrease, also the depth of abrasive grain trace decrease. In figure 10d is the results of the fine polishing after using 0.02 microns abrasive liquid solution. There is a single abrasive grain line and no dirty points.

In fig. 13a,b is the results of fine polishing stage after we use 0,02 microns abrasive grain size solution. We obtain a face with almost no inclusions and reduced number of scratches. In order to analyse the influence of abrasive particle we use sandpaper with different grain size. When we increase the grain size, grain traces became deeper and material removal rate increase (figure 10a). When we decrease the grain size, grain traces are smaller and material removal rate decrease (figure 10b,c). We analyse the influence of the grain concentration in abrasive solution. When the grain concentration increase, the material removal rate increases. When the grain concentration decreases the material removal rate decreases. We analyse the influence of distance between fiber and abrasive surface. When the gap increases the material removal rate decreases and when the gap decreases the material removal rate increases. In order to analyse tool pressure influence we increase pressure and as results the material removal rate increase. When the pressure decreases the material removal rate decreases.

We analyse the influence of the fiber probe movement by comparison of "8 shape" and orbital. When we use the "8 shape" rotation we noticed that material removal is homogeneous and is possible to be used to polish the fiber, but the movement is dependent of the operator expertise. When we use the orbital movement due to complex rotation for a non-experienced operator were more easy to polish (figure 10c, d). We use the method for measurement of light at output of plastic fiber a stand as were described by. Comanescu et al. (2023). We obtain for output signal chart from figure 11.

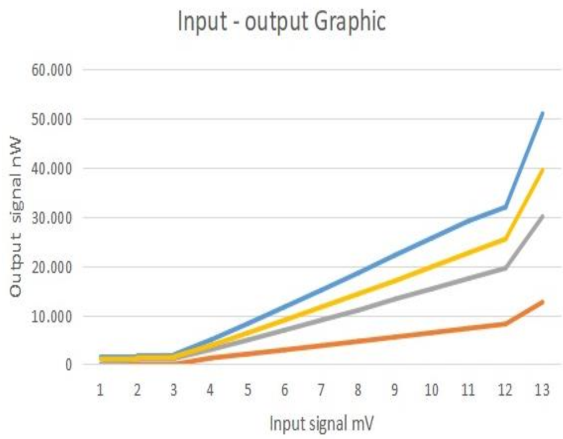

Figure 11. Output signal of polished fiber

When the LED input current increases, the LED light power that is pumped into fiber polished fiber increases, the output signal read by a detector increases as in figure 11. The output signal is measured using few fibers and we see that trend is similar.

Conclusion

Paper present the results after our research concerning the polishing of plastic scintillating fiber with 1 mm diameter. Our investigations related to a possible theory that can be used we found that can be applied for processing. We make two types of experiments: One type is related to fiber cutting and second one is related to fiber polishing.

Our experiments related to fiber cutting bring to us to following conclusions: is not possible to eliminate fiber polishing and a razor blade tool is a good tool to cut plastic fiber. The investigation of influence of abrasive particle shows direct correspondence between abrasive granule size and material removal rate. The investigation of the correspondence between concentation of abrasive grains and material removal rate shows direct correspondence.

The investigations related to influence of distance between fibers on material removal rate demonstrate a direct relation. The investigations related to the influence of the gap between fiber and abrasive surface conclude that there is a direct correlation. Our conclusions related to the using of a stand for measurement the signal through the fiber demonstrate that fibers are well polished.

Scientific Ethics Declaration

The authors declare that the scientific ethical and legal responsibility of this article published in EPSTEM Journal belongs to the authors.

Aknowledgments

* This article was presented as an oral presentation at the International Conference on Technology, Engineering and Science (www.icontes.net) held in Antalya/Turkey on November 14-17, 2024.

* This research was completed as part of the FleX-RAY project that has received funding from the European Union's Horizon 2020 research and innovation programme under grant agreement No 899634

References

Comanescu, B., Schiopu, P., Vladescu, M., & Vlad, M. (2023). Plastic fiber low light measurement method. *The Eurasia Proceedings of Science Technology Engineering and Mathematics*, *26*, 641-647.

Fiberfin. (n.d.). *POF razor cutter multiple size fibers*. Retrieved from https://fiberfin.com/product/pof-razor-cutter-multiple-size-fibers

Hanlet, P., Marcus, M., & Gallas, E. Comparison of fiber polishing techniques. *Fermilab-TM-2068*,1-12. Retrieved from https://inspirehep.net/files/7b95abd387515752105c5168e442da5b

Kaufmann.(2017, September 29). *An approach to stock removal for soft-tool polishing of freeform polymer lenses*. Retrieved from https://www.ak-hohenahr-consulting.com/single-post/2017/09/29/an-approach-to-stock-removal-for-soft-tool-polishing-of-freeform-polymer-lenses

Kuraray. (n.d). *How to polish*. Retrieved from https://www.kuraray.com/products/psf

Kuraray. (n.d.). *Plastic scintillating fibers*. Retrieved from https://www.kuraray.com/products/psf

Mulligan, P. M. (2009). *New termination techniques for POF*. Retrieved from http://www.pofto.org/home/downloads/member/2009.pofsymposium/1445_Mulligan_FIBERFIN.pdf

Octapart. (n. d.). *HFBR-RUS500 Avago optoelectronics datasheet.* Retrieved from https://octopart.com/datasheet/hfbr-rus500-avago-923772

Panagopoulos, N., Asfis, G., J. Koch, J., & Wilbur, S.(2023). Development of a silicon photo multiplier - based detector for spatial detection of X-ray photons impacting on a scintillating fibre grid. *Quantum Optics and Photon Counting 2023 Conference*,12570.

Rubin, R.(2017). *Mechanical fiber polishing*. Retrieved from https://www.prometoptics.com

Thorlabs. (2000, Jun 8). *CTG913 glass polishing plate*. Retrieved from https://www.thorlabs.com/thorproduct.cfm?partnumber=CTG913

Thorlabs. (n.d.). *Guide to connectorization and polishing optical fibers*. Retrieved from https://www.thorlabs.com/thorproduct.cfm?partnumber=FN96A

Author Information

Brindus Comanescu
Optoelectronica 2001 S.A.
35 Lacului st., 077125 Măgurele, Ilfov county, |Romania
Contact e-mail: *brindus_comanescu@yahoo.com*

Paul Schiopu
National University for Science and Technology Politechnica Bucharest, 313 Splaiul Independenţei st., 060042 Bucharest, sector 6, Romania

Marian Vladescu
National University for Science and Technology Politechnica Bucharest, 313 Splaiul Independenţei st., 060042 Bucharest, sector 6, Romania

To cite this article:

Comanescu, B., Schiopu, P., & Vladescu, M. (2024). Aspects of influencing factors in the polishing of plastic optical fibers. *The Eurasia Proceedings of Science, Technology, Engineering & Mathematics (EPSTEM), 32,* 537-545.

The Eurasia Proceedings of Science, Technology, Engineering & Mathematics (EPSTEM)
ISSN: 2602-3199

The Eurasia Proceedings of Science, Technology, Engineering & Mathematics (EPSTEM), 2024

Volume 32, Pages 546-559

IConTES 2024: International Conference on Technology, Engineering and Science

Temperature Effect on the Creep Behavior of the Upstream Bituminous Concrete Masks of the Bouhnifia Dam

Ghouilem Kamel
University Mouloud Mammeri of Tizi – Ouzou

Atlaoui Djamal
University Mouloud Mammeri of Tizi – Ouzou

Merakeb Seddik
University Mouloud Mammeri of Tizi – Ouzou

Mehaddene Rachid
University Mouloud Mammeri of Tizi – Ouzou

Abstract: This paper, presents creep behavior of the concrete bituminous and it evolution under three different temperatures (17°C, 32°C, and 40°C) and their effect on the stress curves evolution at the upstream mask in the bouhnifia dam (Algeria), who is considered a rock fill dam of 55m high sealed by an upstream sealing mask in bituminous coating 20 cm thick. Creep is a time-dependent deformation resulting from constant load who is characterized by a nonlinear behavior of the materials, in which the material continues to become deform under a constant load. In this study, we have applied the Finite Element Method based on a model called (Time Hardening Model) using the computer code ANSYS 17.0 in order to simulate a creep behavior of the upstream mask during 20000 hours of loading and the evolution stress curves under three different temperatures (17°C, 32°C, and 40°C) successively. First, we simulate the temperature distribution in transient conditions during a day of sunshine on the facing, and then we evaluate the creep behavior of the mask under different temperatures mentioned above.

Keywords: Concrete bituminous, Finite element method, Creep, Ansys, Temperatures

Introduction

The performance of bitumen in terms of waterproofing has been known since Antiquity. Today we see hydraulic structures based on bitumen 3000 years old, such as the dikes of the Tigris, in Assur, in Mesopotamia still in good condtion (Djemili & Chiblak, 2007; Chebbah 2020). Bituminous coatings are waterproof, durable, insensitive to water, resistant to most common chemical agents and micro-organisms, they have a great ability to solve many hydraulic problems; the flexibility of bituminous waterproofing allows them to adapt to the settlement of their support without cracking or losing their properties (Lombari, 2005; Djemili et al., 2012).

Asphalt concrete provides waterproofing for dams, and it can be use on any inclination of the embankment dam, where it has the capacity to take the movement of the foundation without any loss of waterproofing, due to its sufficient flexibility. Asphalt concrete layers have enough durability due to the low air content in the compacted layers, which reduces the effect of climate on these layers (Fadel, 2005). The ambient temperatures air influence directly the structure temperatures, while atmospheric conditions (solar radiation, UV radiation, clouds, etc.) can accentuate these phenomena (Rychen, 2013; Chebbah, 2021). The mechanical properties of asphalt concrete change significantly with temperature. Surface heat transfer produces high stress gradients near the mask surface, diurnal temperature cycles can induce fatigue cracking and reeze-thaw cycles can cause cracks (Mauduit et al., 2013; Chebbah, 2021). In this study we consider a rock fill dam of 55m high sealed by an upstream sealing mask in bituminous coating 20 cm thick see Figure 1. First, we simulate the temperature distribution in transient conditions during a day of sunshine on the facing, and then we evaluate the creep behavior of the mask under different temperatures mentioned above.

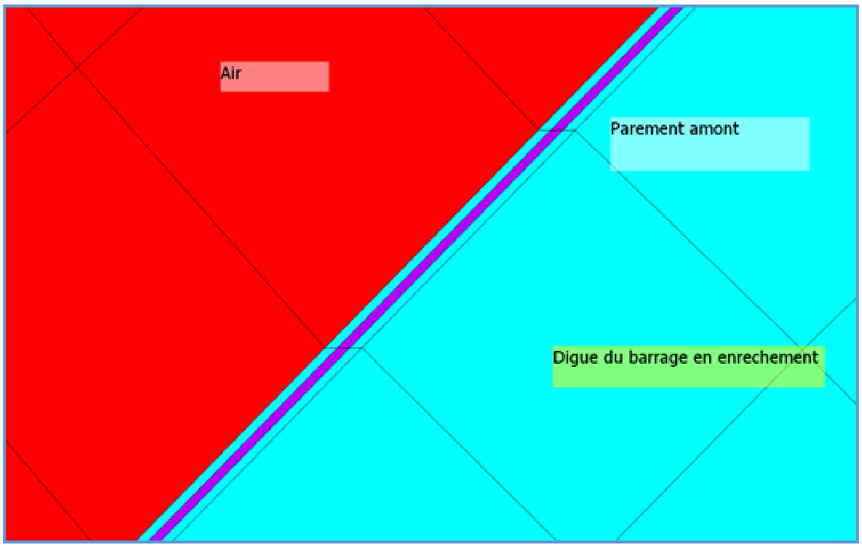

Figure 1. Upstream mask modeling

Materials and Method

Based on the existing documentation at the level of the National Agency for Dams and Transfer (ANBT), the data collection is summarized as follows: The waterproof mask is composed of a support layer (binder) 10 cm thick on which are applied one or two layers of 10 cm thick each of waterproof bituminous concrete (bitumen content: 7 to 9%, index of empty < 3%. The upstream mask includes the important details, such as :

- Climatic sun protection "mastic",
- 10 cm of waterproof asphalt concrete,
- 8 cm de bituminous drain,
- 10 cm of waterproof asphalt concrete,
- Binding layer,

Case Study

Figure 2, illustrate an dam overview which constitutes a basic model of the case study. The Bouhanifia dam located in western Algeria, at 02°35’9 37’’E of longitude and 36°9' 19.06"N of latitude. The dam structure is made by a secured rock embankment on which an upstream sealing mask of bituminous concrete is placed. It is a rock fill dam with an upstream bituminous concrete mask, inspired dy the Ghrib dam. Built between 1930 and 1941, the Bouhnifia dam is among the first rock-fill structures made with an upstream bituminous concrete mask (Djemili, 2006; Ghouilem, 2014). The study site is characterized by a semi-arid climate. The dam watershed has an area of 7,850 km^2 and the average annual flow reached 110.106 m^3. The structure dam is characterized by:

- Peak length : 464 m,
- Height above the talweg : 55 m,
- Crown width : 5 m,
- Fruit of the slope variable upstream: 0,8/1 à 1/2,
- Fruit of the slope downstream : 1,25/1,
- Base massif width: 137 m,
- Dam capacity: 72.106m^3.

Figure 2. Overview of the Bouhnifia dam

Structural Discretization

The finite element Analysis (FEA) method is a powerful computational technique for approximate solutions. Several software programs adopt it, in particular the Anysy calculated code. The graphical user interface (GUI) allows us to model the finite element structure, as shown in figure 4. Elements PLANE 55 are used to discretize the upstream mask. They are designe for heat transfert problems. The structure dam is modeled by the elements PLANE 183 with eight nodes, see figure 3. Figure 4 illustrat the structure discretization by the elements PLANE 183.

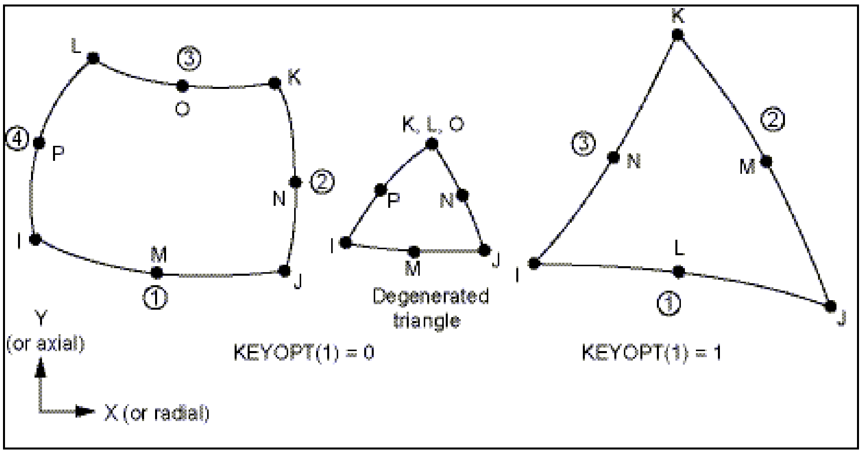

Figure 3. Elements PLANE183 (ANSYS Element Reference)

Temperature Evolution on the Mask Surface

The upstream mask structure is made up of layers of different nature and different thermal characteristics (see figure 2 above). In the study, we assume the following conditions:

- The structure temperature is not influenced by the heat input from the bituminous coating layer at a 1m of depth,
- The different structure layers are considered isotropic and homogeneous,
- The wind speed is constant over the entire period.
- There is conservation of flow at every massif point,
- The solar radiation acts only on the surface. It therefore does not constitute an internal source of heat

In reality, the upstream mask surface is subjects to the acts of solar radiation and convection of the surrounding atmosphere. They will be considered as boundary conditions. The heat quantity emitted or absorbed by the radiation thermal between the surface and the surrounding environment is given by the following equation (1) (Incropera et al., 2002).

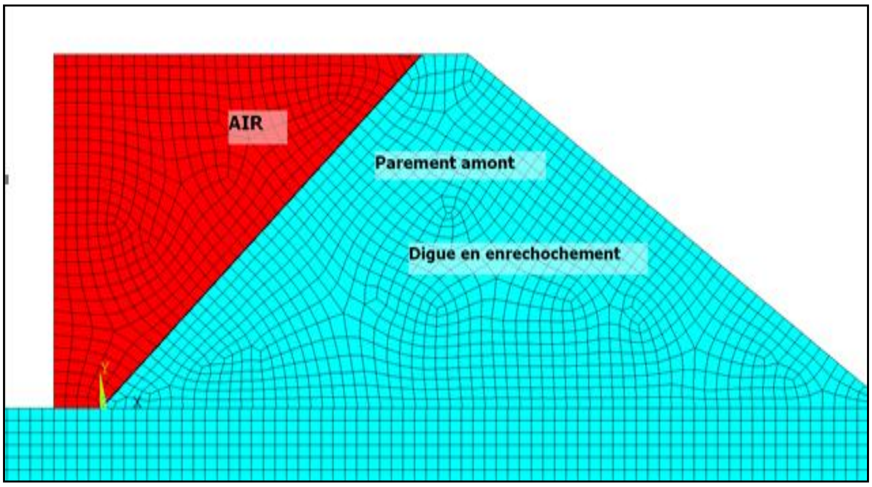

Figure 4. Structure discretization by the elements PLANE 183

$$q_{rad} = \varepsilon_s C_s (T_s^4 - T_{air}^4) \qquad (1)$$

With: $\boldsymbol{qrad}$ is Radiation heat flux (W/m²), $\boldsymbol{\varepsilon_s}$ is the emission surface coefficient (εs =1 for a black body, and 0.85< εs < 0.95 for a bituminous concrete), **Cs** is the stephan-Boltzmann constant (Cs=5.67 .10−8 w ⁄m 2 °C^4), **Ts** represent the mask surface temperature (°C) and $\boldsymbol{Tair}$ is the air temperature (°C). The modeling evolution of temperature for each layers mask is given by the following thermal field equation:

$$\frac{\partial^2 T_i}{\partial X^2} - \frac{1}{a_i}\frac{\partial T_i}{\partial t} = 0 \qquad (2)$$

with: ***a*** **= λ/ρ.c** is the thermal diffusivity (propagation coefficient heat), **λ** : Conductivity heat coefficient (w/m.k), **ρ** : Density (kg/m^3),and **c** is the specific heat (j/kg.°C). The following empirical equation (3) giving by (George KP & Husain S, 1986), estimate the surface temperature evolution (Ts) of the coating depending on the ambient air temperature.

$$T_s = T_{air}\left(1 + \frac{76.2}{h_1 + 304.8}\right) - \frac{84.7}{h_1 + 304.8} + 3.3 \quad (3)$$

With: $\mathbf{T_s}$ is the surface coating temperature, $\mathbf{T_{air}}$: Air temperature, $\mathbf{h_1}$: bituminous layer thickness in cm. The following Table 1 illustrates the temperature (Ts) maximal results achieved on the surface of upstream mask using equation (3) above:

Table 1. Temperature evaluation (Ts) on the mask surface

Temperature Air (Tair)	17°C	32°C	40°C
Ts	27°C	43°C	54°C

The following Figures 5 bellow, illustrates the daily variation temperature (17°C, 32°C and 40°C) as a function of time (t) on the mask surface. For the ambient temperature air of 17°C, we note that the maximal temperature reached at the upstream mask surface is 31°C during 6h30’ of exposure to the radiation solar. The evolution temperature of 32°C over time reached a pic of 60°C after 4h of exposure to solar radiation. Finally a maximal temperature of 65°C is reached on the surface upstream mask for the transient evolution of the temperature 40°C after 3h of exposure to the radiation solar. We note that from these results, the maximum temperatures reached on the surface mask are inversely proportional to the solar radiation time exposure. Figures 6, illustrates the variation daily temperature (17°C, 32°C andt 40°C) depending on the mask depth. These curves are obtained by the Fourier law (d^2T/dx^2= $dTi/a_i.dt$). Table 2 bellow illustrates the surface temperature evolution.(Ts) as a function of the mask depth according to equation (3) and the temperature obtained by Ansys simulation. Through the results obtained concerning the surface temperature (Ts), that there is a significant difference between the Ansys simulation and the empirical equation (3). This can allow us to conclude that this equation does not take into account time of exposure to solar radiation.

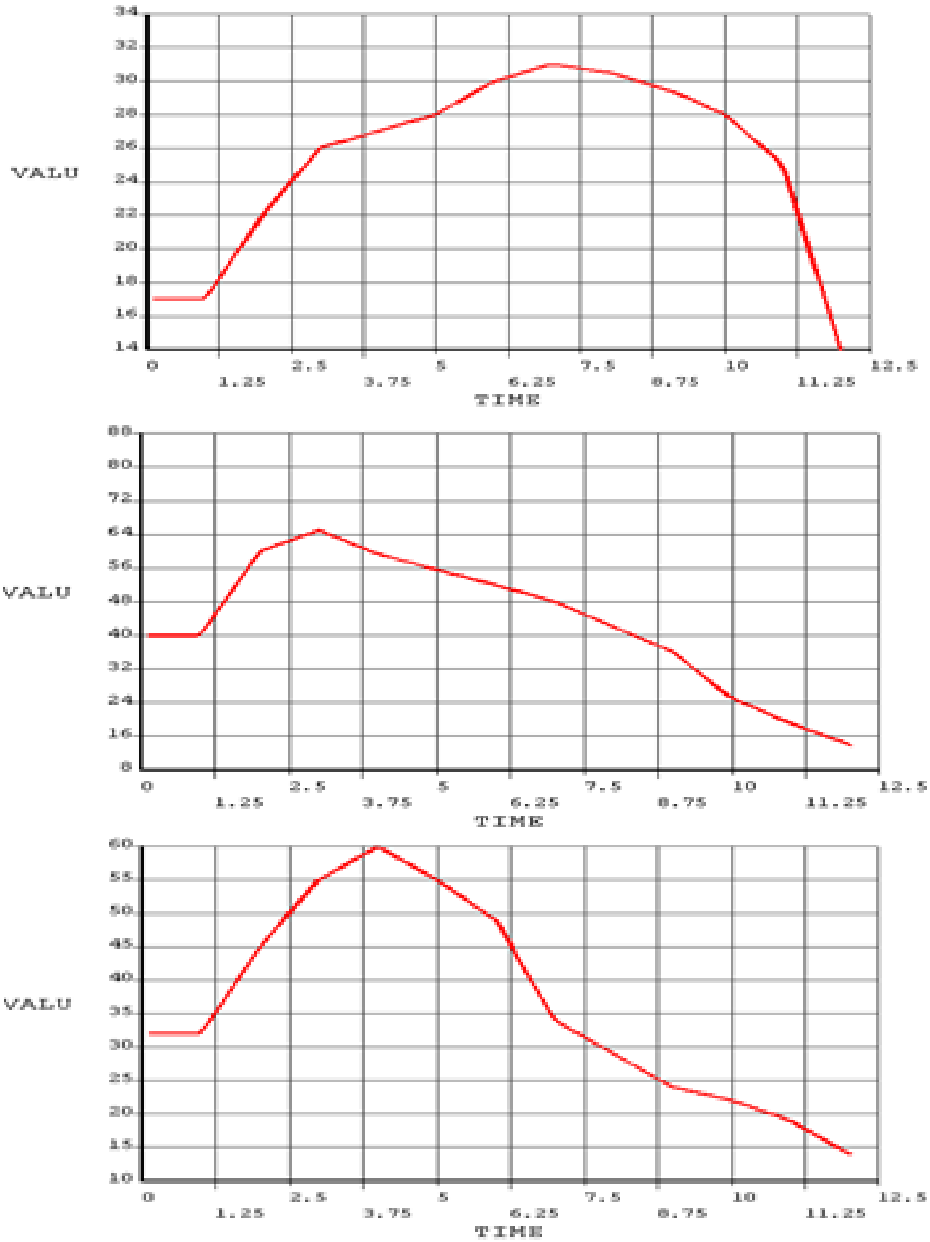

Figure 5. Temperatures evolution on the upstream ask

Creep Modeling Procedure by Ansys

Implicit creep is the most used method in the Ansys program for the reasons of efficiency. The command TB with Lab = CREEP allows us to programme this method and choose the corresponding equation creep by specifying the number of the model that it corresponding by using the TBOPT command, see example below.

TB, CREEP, 1,1,4,2

TBTEMP, 100

TBDATA,1, C1,C2,C3,C4

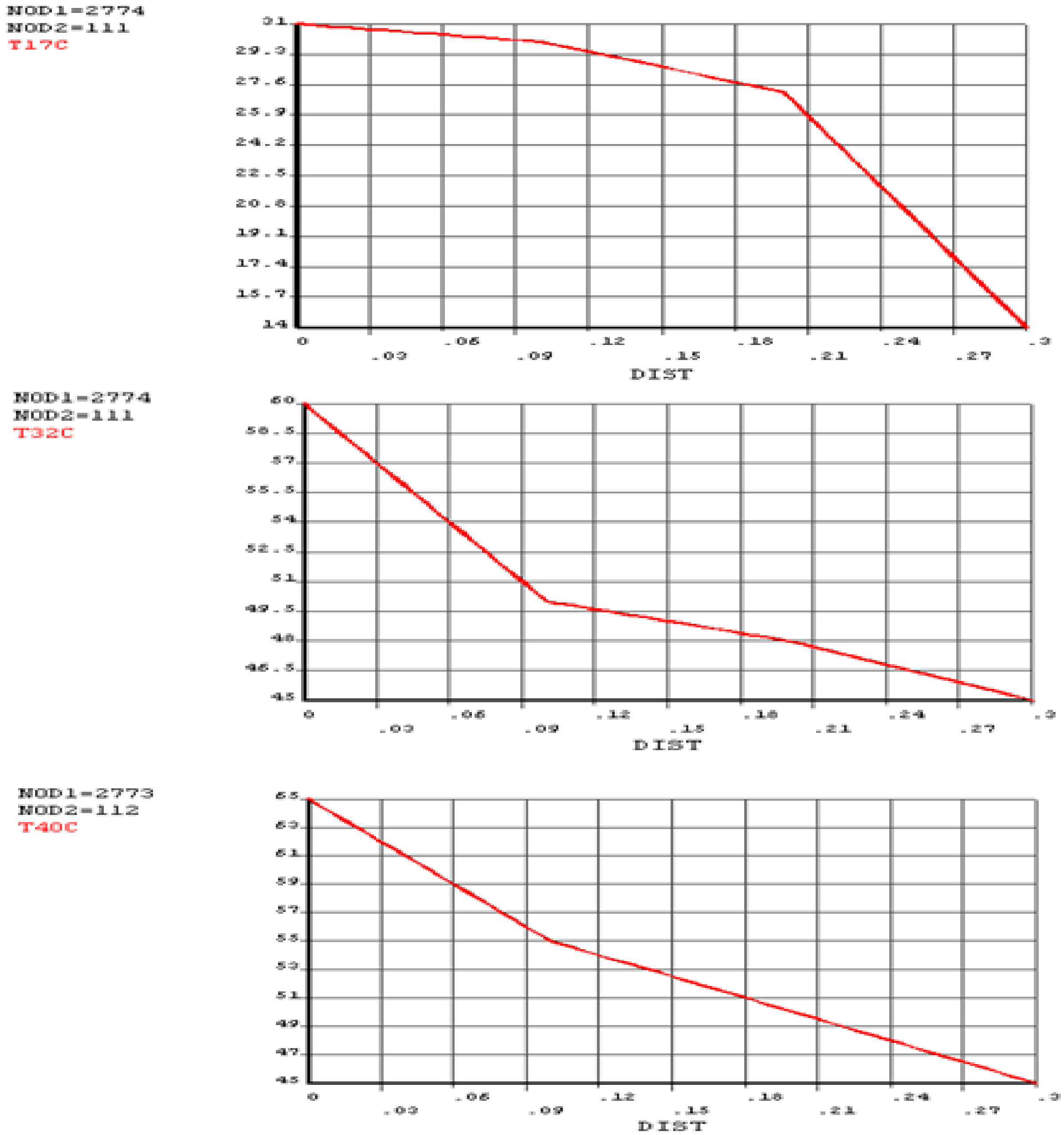

Figure 6. Variation des températures surfaciques en fonction de la profondeur du masque

TBOPT = 2 : Specifies the behavior law of model 2 namely (time hardening). This equation described the strain creep $(\dot{\varepsilon}_{cr})$ variation according to several parameters (C1, C2, C3, C4), such as the creep constants associated with the equation (4) bellow. Figure 7, illustrate the introduction of law creep procedure in the Ansys interface. In order to modeling the creep, the model used in our study is the model given in equation (4):

$$\varepsilon_{cr} = C_1 \sigma^{C_2} t^{C_3} e^{-C_4/T} \qquad (4)$$

With : ε_{cr} is the Creep strain, σ is the Equivalent stress, t represent the loading time, and C1, C2, C3, C4 : Creep parameters, giving as follows: C1 = 41.10-8 1/s, C2 = 1.48, C3 = -0.63, finally Tis the Medium temperature in Kelvin. Material is considered isotropic, and the basic solution method used is that of Newton-Raphson. This behavioral law is defined in ANSYS as “Time Hardening model”

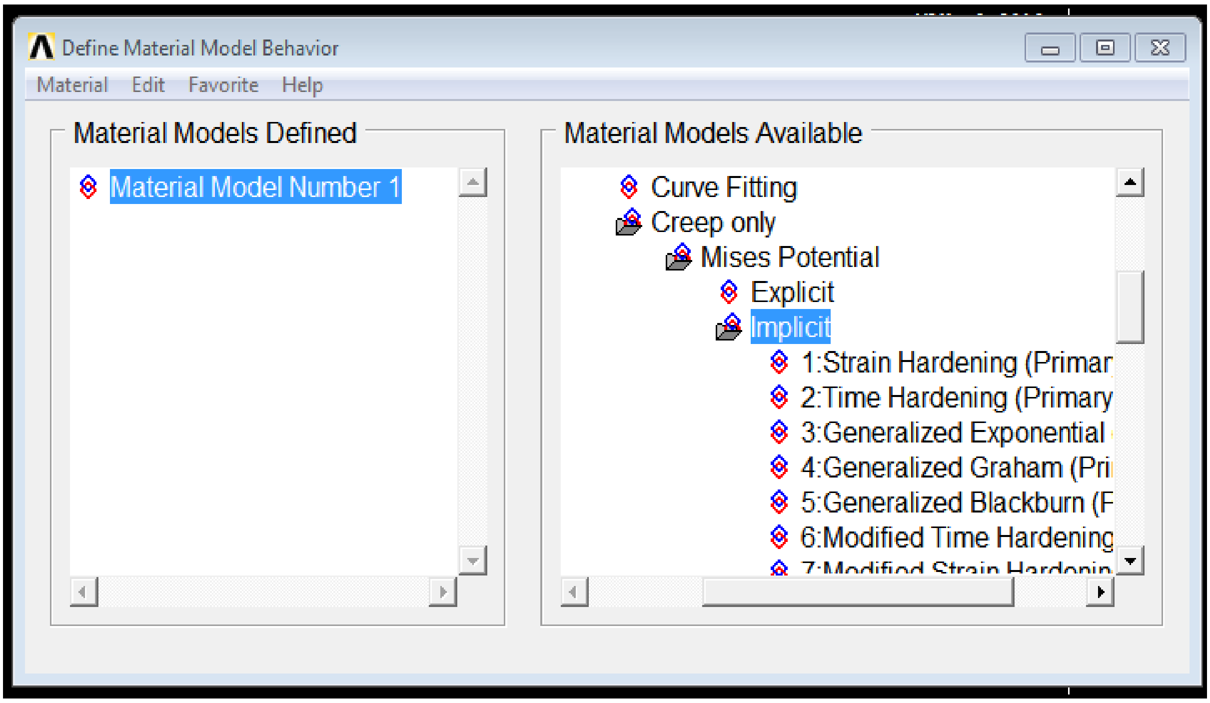

Figure 7. Interface introduction of the law creep model

Table 2. Surface mask temperature (Ts) and in the mask depth

Air temperature **(Ta)**	**17°C**		**32°C**		**40°C**	
	Eq (3)	Ansys	Eq (3)	Ansys	Eq (3)	Ansys
Ts at the mask surface	27°C	31°C	43°C	60°C	54°C	65°C
T° at 10cm of mask depth		29,5°C		50°C		55°C
T° at 20cm of mask depth		27.3°C		48°C		50°C
T° at 30cm of mask depth		14°C		45°C		47°C

Creep Phases

Under constant stress, the creep strain delayed is proportional to the load stress. It can therefore be classified as a "linear viscoelastic" material. Figure 8 bellow a curve typic of creep strain. We note thought the curve, three phases of creep, namely:

- Primary creep: represent the transient phase, during which the creep decreases with time, which corresponding to the material increase resistance.
- Secondary creep: corresponding to the phase stationary, or even quasi –viscous, during which the strain rate is constant over the time.
- Tertiary creep: in this phase, the strain rate grows until rupture.

From this figure, we see that the variation of "ε" and $\dot{\varepsilon}$ can be given by the following equation (5).

$$\varepsilon_{cr} = \varepsilon_0 + \varepsilon_1 + \varepsilon_2 + \varepsilon_3 + \varepsilon_4 \qquad (5)$$

With: ε_0: instantaneous deformation corresponding to the putting load, $\varepsilon_1 = At^x$: Primary creep with x < 1, ε_2 is the secondary creep wich is a linear function. $\varepsilon_3 = At^y$: Tertiary creep with y > 1

The function ε_2, ε_3 et ε_4, there are very large number of equations. The functions ε which describe the creep curves are the sum of power function with a linear and a logarithmic function.

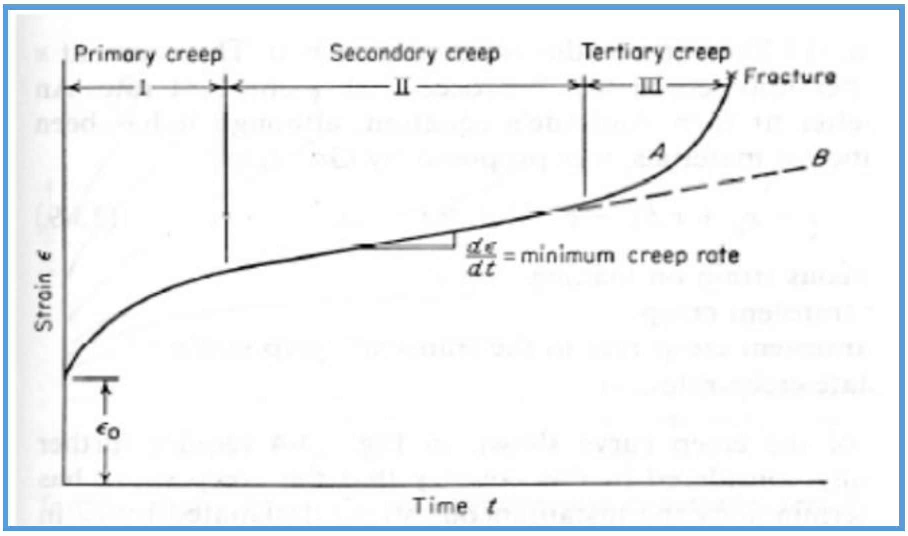

Figure 8. Creep curve typic under moderate load (1) and intense loading (2) (Dieter, 1988, Ashby & Jones, 1991)

Primary Creep

Primary creep is commonly described as transient phase, where the creep rate decreases; Andrade's law models it as follows:

$$\varepsilon_{cr} = \varepsilon_0 + At^{1/q} \quad (6)$$

With: ε_0 represents instantaneous creep , A.t1/q Andrad's coefficient and q is a dimensionless constant (Andrade, 1910 and Andrade, 1914). (Nabarro, 1997) formulated a primary creep equation given as follow :

$$\varepsilon_{cr} = A\sigma^n t^m \quad (7)$$

With : σ (MPa) is the applied loading, A (MPa–nhr-m), n et m are temperature dependent constants (Pantelakis, 1983).7

Secondary Creep

The Norton's Power Law (Norton, 1929) describes the classical approach to the secondary creep model:

$$\dot{\varepsilon}_{cr} = A\sigma_{eq}^n \quad (8)$$

With: A et n are a creep secondary constants.

During the secondary creep, the strain creep continues to grow under constant stress, it does so at constant speed. Thus, it is identical to viscous flow and is usually referred to as viscous creep.

Tertiary Creep

Microstructural damage mechanism occurring during creep can be manifested in a number of ways, such as micro cracks, cavities, voids, etc. in increased scale. Typically, creep damage is classed into two forms: trans granular (ductile) damage and intergranular (brittle) damage. Trans granular (ductile) damage arises were slip bands of plasticity forming under high stress and low temperature. Intergranular (brittle) damage is a micro cracking process at grain boundaries under high temperature and low stress (Skrzypek, and Ganczarski, 1999). Damage is an all-inclusive non-recoverable accumulation that exhibits the same dependences as creep deformation: material behavior (i.e., creep constants), temperature, time, and stress. Generally, damage is considered to be in continuum, (i.e., homogenous thought a body) thereby the expression continuum damage mechanics (CDM) is used. The damage phenomenon is closely aligned with the creep cracking and has been used to in local and nonlocal CDM approaches to predict creep crack growth. Many comprehensive lists of creep damage CDM-based formulations are available in literature (Skrzypek & Ganczarski, 1999; Lemaitre,1986). Early work in the characterization of creep damage by Kachanov (1967) and Rabotnov (1969), introduced the concept of scalar-valued damage evolution expressed as $\dot{\omega} = f(\sigma, \omega)$ where σ is uniaxial stress, is the current state damage. Damage is coupled within the creep strain rate via current damage and is expressed as $\dot{\varepsilon}_{cr} = f(\sigma, \omega)$. Within the creep strain equation, arises a net/effective stress which relates the physical space of damage where the presence of micro cracks and voids reduces creep strength, to an effective space, where microstructural creep damage is replaced with an effective increase in the applied stress

Results and Discussion

Figures 9, 10 and figure 11 illustrates the contour plot of creep strain $\boldsymbol{\varepsilon}_{\mathbf{cr}}^{\mathbf{Y}}$ and $\boldsymbol{\varepsilon}_{\mathbf{cr}}^{\mathbf{X}}$ and stress and stress of Von Mises in the structure dam and the upstream mask. The creep deformation results show that the creep curves are very spread in the plastic phase. The following equation allowed us to calculate the maximal plastic deformations$(\boldsymbol{\varepsilon}_x^p, \boldsymbol{\varepsilon}_y^p)$

$$\varepsilon_{cr} = \varepsilon_{el} + \varepsilon_{pl} \Rightarrow \varepsilon_{pl} = \varepsilon_{cr} - \varepsilon_{el}$$

Therefore, we will have as results:

$$\varepsilon_x^p = \varepsilon_x^{cr} - \varepsilon_x^{el} = 5.6207 - 0.1975 = 5.42355 \text{ mm/m}$$

$$\boldsymbol{\varepsilon_y^p = \varepsilon_y^{cr} - \varepsilon_y^{el} = 80.058 - 0.167 = 79.8913 \text{ mm/m}}$$

Through the results, we see that the elastic deformation values $\varepsilon_x^{el}, \varepsilon_y^{el}$, remain low compared to the plastic deformations. Furthermore, the plastic deformations are macroscopically homogeneous. In other words, they reflect the fact that the upstream mask is uniformly deformed, we can conclude this:

- During the primary creep, there is mainly creation and propagation of dislocations. In general, these dislocations do not form particular cellular structures, they are entangled. We observe dislocations formed by sliding, deformation bands and slip lines more or less spaced depending on the applied loading (stress and temperature) and the creep time.
- During the secondary creep, the dislocations assemble to form a more or less clear cellular structure. These cells are less formed when the temperature is low.. They often show an elongation depending on the type of sliding activated. The dislocation density remains stable during this stage. The substructure is constantly being formed and destroyed: there is a equilibrium between the formation processes and annihilation of dislocations. In contrast, the disorientation between sub grains increases with time.

Temperature Effect on the Creep

The variation of creep strain (ε_{cr}) increases with temperature, it is thermally activated. it is follows an Arrhenius equation type:

$$\varepsilon_{cr} = Ae^{-\frac{Q}{RT}} \qquad (9)$$

whith: ε_{cr}: Creep strain during the secondary creep, A : Sinzing parameter, Q (J.Mol-1) : Activation energy, R : Gas Constant molar (8.314 $J.mol^{-1}.K^{-1}$), T is Temperature in Kelvin, Figure 12 and 13 illustrates the creep strain curves under threes temperatures of 17°C, 32°C and 40°C respectively.

Effect of Temperature on Stresses

The following figures 14, 15 and figure 16 illustrates the temperature effect on the stress evolution over time, we constat that the stress evolution is carried in three phases:
The first phase speared over
a time interval of (0 < t < 1000h) were we note a stress maximal values of (σy), and a low values of elastic deformations. In this phase the upstream mask and the dam structure resist to the applied loads.

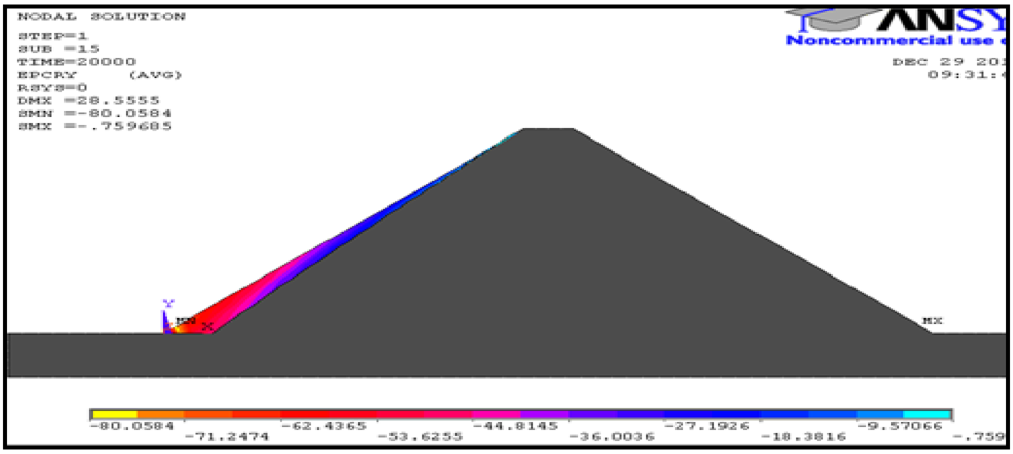

Figure 9. Creep strain contour plot (ε_{cr}^{y})

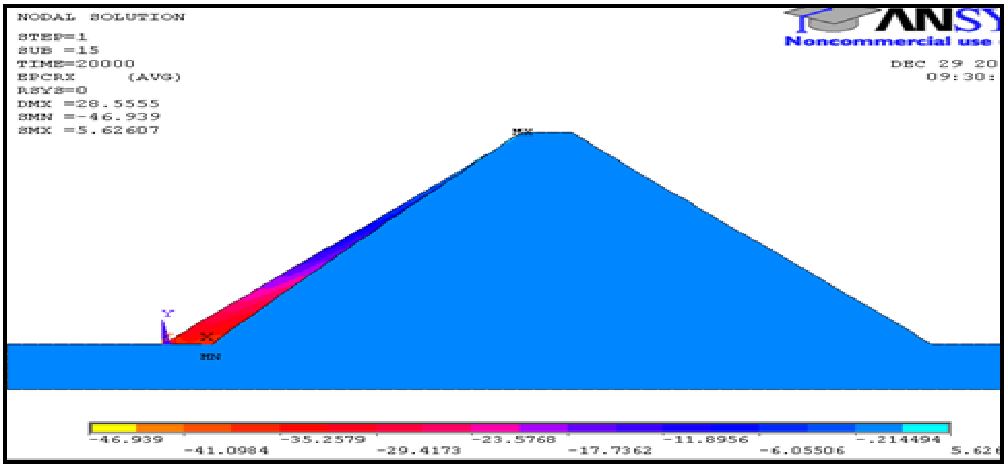

Figure10. Creep strain contour plot (ε_{cr}^{x})

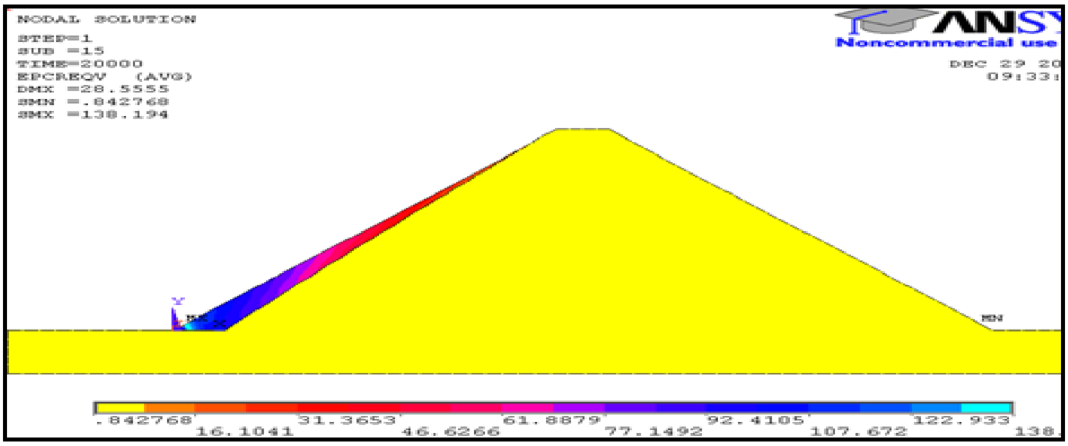

Figure.11. Von Mises creep stress contour plot

In the second phase, the stress decreases slightly to remain constant over a time interval (1000h < t < 2500h), this is the start process of thermal activation. At the end phase, the stress decrease suddenly. The third stage, characterized by a progressive increase in the stress up to a value of 2000Pa. This phase corresponds to the phase of secondary creep or the speed of deformation remains constant and the material hardened (work hardening). At the time of this phase, dislocations are assembled to form cellular at least clear, that corresponds to a polygonization of the slip. The density of dislocations remains stable during this stage, on the other hand, confusion between under grains increases with time.

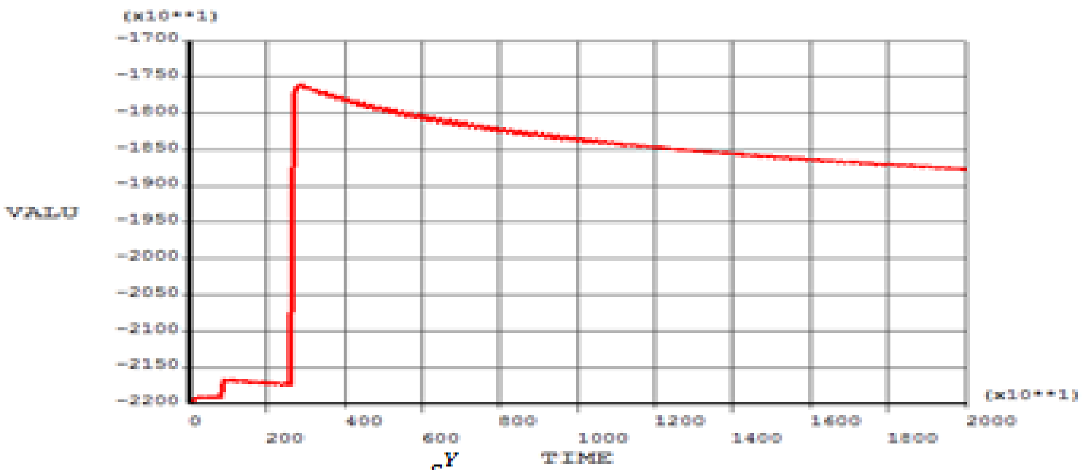

Figure.12.. Creep strain curve (ε_{cr}^{Y}) under three temperature 17°C, 32°C & 40°C

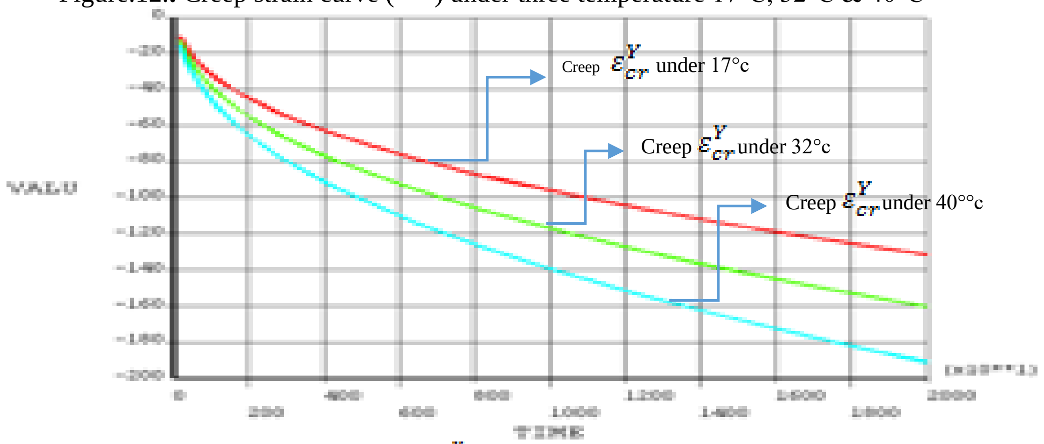

Figure13. Creep strain curve (ε_{cr}^{X}) under three temperature 17°C, 32°C & 40°C

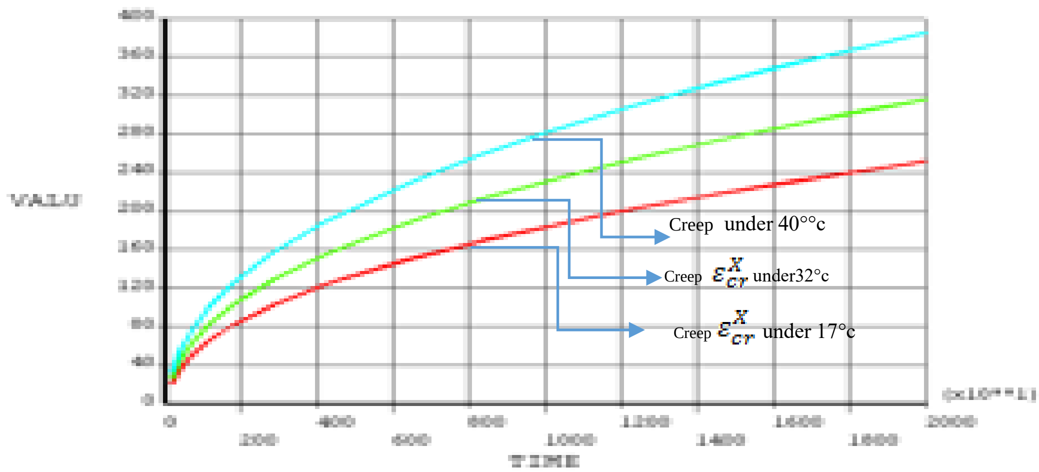

Figure 14. σ_Y stress evolution under temperature of 17°C

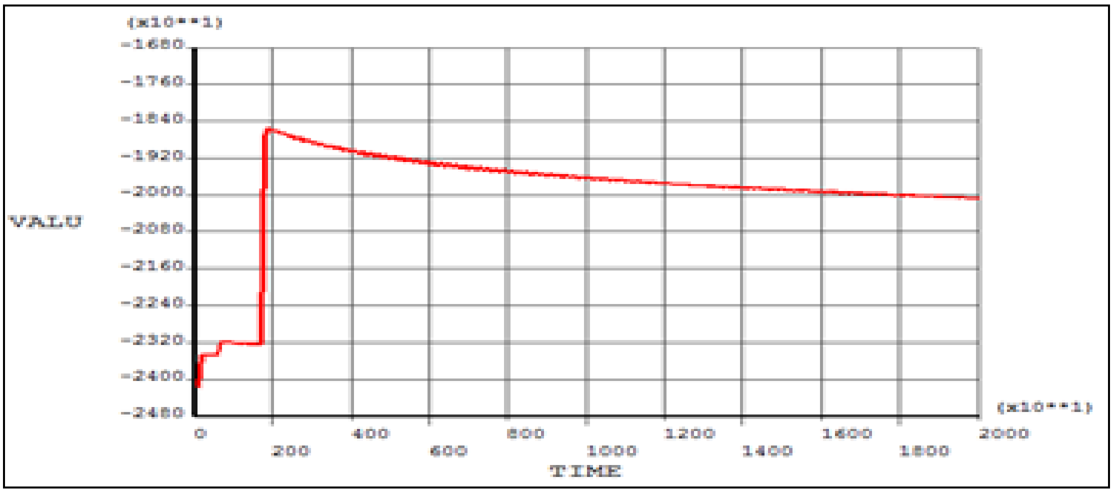

Figure 15. σ_Y stress evolution under temperature of 32°C

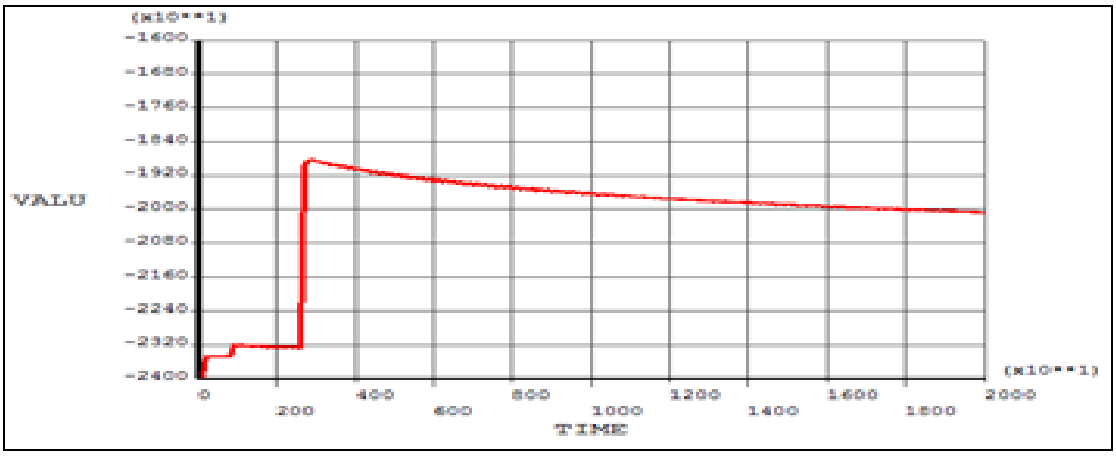

Figure 16. σ_Y stress evolution under temperature of 40°C

Conclusion

On a constaté à travers les résultats obtenus que le taux de déformations au fluage (ε_{cr}) atteint pratiquement 30% des déformations au bout d'un mois et 59% au bout de 6mois pour les différentes températures et chargement considérés. A 20000h du chargement constant, ces déformations atteignent une moyenne de 6.65 fois les déformations instantanées (ε_{el})

The objective of this study was to evaluate the stability of the bituminous concrete upstream mask in the rock-fill dams and to determine if it is possible to continue to build this type of mask upstream out of concrete the bituminous one on deposits of granular alluvia of average compactness in regions arid and semi-arid wine the temperature can reach the 60°C. The results obtained allowed to demonstrate the influence of temperature on the creep strain rate, and stress evolution applying the model of equation (4). It was found that the temperature increases the creep deformations, and the slope of the creep curve increases with the increase under temperature and we note through the results obtained that the rate of creep strain reached practically 30% of the deformations after one month and 59% after 6 months for the different temperatures and loading considered. At 20,000 hours of constant loading, these deformations reach an average of 6.65 times the instantaneous deformations.

The creep study, shows that the values of final creep are very important with high temperatures. The temperature of asphalt mixture has a great effect on deformation resistance ability, the higher the temperature, the more quickly the deformation resistance decrease. The total average deformations of creep reach 8,7 and 6 times the instantaneous strains for the temperatures of 17°c, 32°c and of 40°c respectively. Speeds of creep increase at the beginning of the loading and decrease then during time. The rate of viscous flow increases with the increase in viscosity λ and consequently the deformability of the binder increases. The increase in the temperature has an impact on the parameters intrinsic of the asphaltic concrete, because they increase viscosity λ and decrease rigidity E.

Scientific Ethics Declaration

The authors declare that the scientific ethical and legal responsibility of this article published in EPSTEM Journal belongs to the authors.

Notes

This article was presented as a poster presentation at the International Conference on Technology, Engineering and Science (www.icontes.net) held in Antalya/Turkey on November 14-17, 2024.

References

Adam, K., Říha, J., & Špano, M. (2016). Investigation on the temperature of the asphalt-concrete facing of embankment dams. *International Journal of Pavement Research and Technology*, *9*(1), 73-81.

Andrade, E. N. D. C. (1910). On the viscous flow in metals, and allied phenomena. *Proceedings of the Royal Society of London. Series A, Containing Papers of a Mathematical and Physical Character*, *84*(567), 1-12.

Andrade, E. N. D. C. (1914). The flow in metals under large constant stresses. *Proceedings of the Royal Society of London. Series A, Containing Papers of a Mathematical and Physical Character*, *90*(619), 329-342.

ANSYS. (n.d.). *Element reference, general element features, 2.5. data tables-implicit analysis, 2.5.8 creep equations, ANSYS release 17.0 documentation*. Retrieved from https://www.ansys.com.

Ashby, M. F., Jones, D. R. H., & Bréchet, Y. (1996). *Matériaux: Propriétés et applications*. Paris: Dunod.

Betten, J. (2002). *Creep mechanics*. Springer.

Chebbah, L., Djemili, L., Bouziane, M. T., & Chiblak, M. (2020). Modélisation d'un masque en béton bitumineux (brut et protégé) sous sollicitations thermiques en régime transitoire. cas du masque de barrage Ghrib (Ain Defla, Algérie). *La Houille Blanche*, *106*(1), 42-49.

Chebbah, L. (2020). *L'Utilisation du béton bitumineux dans les travaux hydrauliques : Etanchéité des barrages en remblai* (p.175). Doctoral dissertation, Université de Biskra.

Dieter, G. E. (1988). *Mechanical metallurgy*. McGraw-Hill Book Company.

Djemili, L. (2006). *Critères de choix de projet des barrages en terre « étanchéité par le masque en béton bitumineux.* Doctoral dissertation, Université de Batna.

Djemili, L., & Chiblak, M. (2007). Study of the temperature distribution in the bituminous concrete facing used in fill dams in the region of west Algeria. *Journal of Engineering and Applied Science*, *2*(3), 576–579.

Djemili, L., Behim, M., & Chiblak, M. (2012). Comportement du masque d'étanchéité du barrage Ghrib (Algérie) en absence de la protection thermique. *Courier du Savoir*, *13*, 21–25.

Dougherty, D. J. (1996). Thermoplastic creep analysis using resin manufacturer's creep modulus data for thermoplastic joints. *ANSYS International Conference Proceedings*, 1359-1370.

Fadel, I. (2005). Asphalt mixture-designing basics in dams sealing–Designing of impermeable asphalt shell used in AL-Sorani dam. *Tishreen University Journal –Engineering Science Series*, *27* (2), 23-38.

Garofalo, F. (1965). *Fundamentals of creep and creep-rupture in metals.* New York, NY: Macmillan.

George, K.P., & Husain, S. (1986). Thickness design for flexible pavement: A probablistic approach.' *Transportation Research Record*, *1095*, 27-36.

Ghouilem, K. (2014). *Impact du fluage et de température sur les organes de lutte contre les infiltrations dans les barrages* (p.166). Doctoral dissertation, Université Mouloud Mammeri Tizi Ouzzou.

Kachanov, L. M. (1967). *The theory of creep, National Lending Library for Science and Technology Boston Spa, England*. Chaps. IX, X Boston Spa, England, Chaps. IX, X

Kraus, H. (1980). *Creep analysis*. NewYork, NY: John Wiley & Sons, Inc.

Nabarro, F. R. N. (1997). Thermal activation and andrade creep. *Philosophical Magazine Letters*, *74*(4), pp 227-233.

Norton, F. H. (1929). *The creep of steel at high temperatures*. London: McGraw-Hill.

Odquist, F., & Hult, J. (1962). *Kriechfestigkeit metallischer Werkstoffe*, Springer Berlin.

Pantelakis, S. (1983). *Kriechverhalten metallischer werkstoffe bei zeitveranderlicher spannung*. Doctoral dissertation, RWTH Aachen University.

Rabotnov, Y. N. (1969). *Creep problems in structural members*, North Holland, Amsterdam

Skrzypek, J., & Ganczarski, A. (1999). *Modeling of material damage and failure of structures* (pp.69-78). Springer.

Trantina, G.G. (1986). *Creep analysis of polymer structures. Polymer Engineering and Science*, *26*(11), 776-780.

Uzarowski, L. (2007). *The development of asphalt mix creep parameters and finite element modelling of asphalt rutting*. Doctoral dissertation, University of Waterloo.

Skrzypek, J., & Ganczarski, A. (1999). *Modeling of material damage and failure of structures* (pp.69-78). Springer.

Lemaitre, J. (1986). Local approach of fracture. *Engineering Fracture Mechanics*, *25*(5-6), 523-537.

Mauduit, V., Mauduit, C., Greullet, N. V., Coulon, N., Hammoum, F., Hamon, D., ... & Chabot, A. (2013). Dégradation subite des enrobés bitumineux par période de gel/dégel: Analyse de cas de terrain et recherche exploratoire en laboratoire. *BLPC-Bulletin des Laboratoires des Ponts et Chaussées*, (279), 47.

National Agency of Dams and Transfers (ANBT). (2013). Execution study and monitoring of Souk N'Tleta dams construction in the wilaya of Tizi – Ouzou.

Lombari, L. (2005). *Bitume info manager, construire et innover* (p.36). Numéro Spécial Édition.

Rychen, R. (2013). *Impact du changement climatique sur les infrastructures routières – Analyse de risque et mesures d'adaptation*. Doctoral dissertation, EFPL

Incropera, FP., & DE WITT DP. (2002). *Introduction to heat transfer* (4th ed., pp.817-843). Wiley.

Author Information

Ghouilem Kamel
University Mouloud MAMMERI of Tizi - Ouzou
Ummto, BP 17 RP, Tizi-Ouzou 15000, Algeria
Contact e-mail: *kamel.ghouilem@ummto.dz*

Atlaoui Djamal
University Mouloud MAMMERI of Tizi - Ouzou
Ummto, BP 17 RP, Tizi-Ouzou 15000, Algeria

Merakeb Seddik
University Mouloud MAMMERI of Tizi - Ouzou
Ummto, BP 17 RP, Tizi-Ouzou 15000, Algeria

Mehaddene Rachid
University Mouloud MAMMERI of Tizi - Ouzou
Ummto, BP 17 RP, Tizi-Ouzou 15000, Algeria

To cite this article:

Kamel, G., Djamal, A., Seddik, M. & Rachid, M. (2024). Temperature effect on the creep behavior of the upstream bituminous concrete masks of the Bouhnifia dam. *The Eurasia Proceedings of Science, Technology, Engineering & Mathematics (EPSTEM), 32,* 546-559.

The Eurasia Proceedings of Science, Technology, Engineering & Mathematics (EPSTEM)
ISSN: 2602-3199

The Eurasia Proceedings of Science, Technology, Engineering & Mathematics (EPSTEM), 2024

Volume 32, Pages 560-567

IConTES 2024: International Conference on Technology, Engineering and Science

Clay Mineralogy of the Khabour and Akkas Formations, Akkas Field, Western Iraq: Implications for Reservoir Characterization and Paleoclimatic Conditions

Rahma S. Al-Auqadi
University of Mosul

Mohammad Aswad Al-Jeboury
University of Mosul

Ali I. Al-Juboury
Al-Kitab University

Abstract: Clastic sedimentation dominates the early Paleozoic succession in subsurface section from the Akkas-1 well, west Iraq. Mineralogical investigation has revealed that the main clay components include, illite, chlorite, kaolinite and mixed layer illite/smectite, whereas, the non-clay fractions include quartz, feldspar and calcite. The clay minerals exist in both detrital and authigenic forms and in different morphologies either as scattered or filling fractures and cavities in both sandstones and shale units which may impact on reservoir characteristics of the studied rocks. Presence of these clay minerals also reflects an arid-humid paleoclimatic conditions during which these minerals were formed in addition to effect of post depositional diagenetic processes.

Keywords: Clay minerals, Paleoclimate, Reservoir characters, Paleozoic, Mining engineering

Introduction

Because clay minerals are highly sensitive to changes in structure, temperature, and pH in the weathering regime, they are frequently utilized as evidence of changes in paleoenvironmental conditions (Chamley, 1989). The clay minerals found in oil and gas exploration target rocks, such as kaolinite, smectite, illite, and chlorite, are widely distributed (Jiang, 2012). Authigenic clay minerals influence reservoir quality such as presence of chlorite (in particular) that generally enhances reservoir quality (Xi et al., 2015), whereas, illite/smectite mixed layers commonly destroy porosity and permeability (Worden & Morad, 2003).

Iraq's Paleozoic hydrocarbon systems include the Silurian Akkas Formation and the Ordovician Khabour Formation (Al-Juboury & Mazeel, 2018). The Akkas field represents the main Paleozoic hydrocarbon reserve found in Iraq to far, a lot of research has been done on it (Al-Juboury et al., 2019). One of Iraq's two confirmed Paleozoic hydrocarbon systems, the Akkas Formation has "hot shale" source rocks with sandstones that serve as reservoir rocks between intra-formational shale. The other one is the sandstone of the Khabour Formation (Aqrawi et al., 2010; Al-Juboury et al., 2021).

In the present work, alternated sandstone and shale from both the Paleozoic Khabour and Silurian Akkas formations from the Akkas-1 well, west of Iraq have been conducted for mineralogical investigations using X-ray diffraction (XRD) and scanning electron microscopic (SEM) aiming to reveal the distribution of clay minerals and discuss their impact on reservoir characteristics on the sandstone and shale in one of promising oilfields in western Iraq and to show their paleoenvironmental conditions of deposition.

Geologic History

The Arabian Plate bordered the Paleo-Tethys Ocean and comprised a part of the northern margin of Gondwana during the Paleozoic (Beydoun, 1991). Iraq is located in the upper southern latitudes of the northeastern region of the Arabian Plate, where clastic sedimentation predominates (Husseini, 1992). Western Iraq was on the stable shelf of Iraq (Figure 1). In Iraq, clastic deposition of alternating sandstones and shales dominated during the early Paleozoic (Ordovician and Silurian). These clastic units, which were deposited in shallow marine epeiric seas (Al-Sharhan & Nairn, 1997; Al-Juboury & Al-Hadidy, 2009).

As the Paleozoic era progressed, the seas' areal extent altered in response to eustatic restrictions (Beydoun, 1991). Variable bed thicknesses and lithotype associations resulted from the regress and transgression of these epicontinental shallow epeiric seas over a broad area during the Paleozoic (Konert et al., 2001). The Paleozoic successions in western Iraq have thicknesses ranging from 3 to 4 km. During the Infracambrian and Paleozoic, north-south oriented graben formations predominated in some regions, which led to heavier deposition in these grabens. Although all of these grabens were abandoned and never became fully formed rifts, they do show evidence of an extensional tectonic regime (Sharland et al., 2001).

In the studied formations, the alternating marine shales and sandstones (Figure 1) are more than 2775 meters thick (Aqrawi, 1998). The Silurian hot shales are overmature in deeper parts of SW Iraq whereas in other shallower western sections, they may still be immature. An intense "Hercynian-age" horst-graben tectonic episode exacerbated the maturation distribution differential between the shallower and deeper Silurian hot shales (Al-Ameri, 2010).

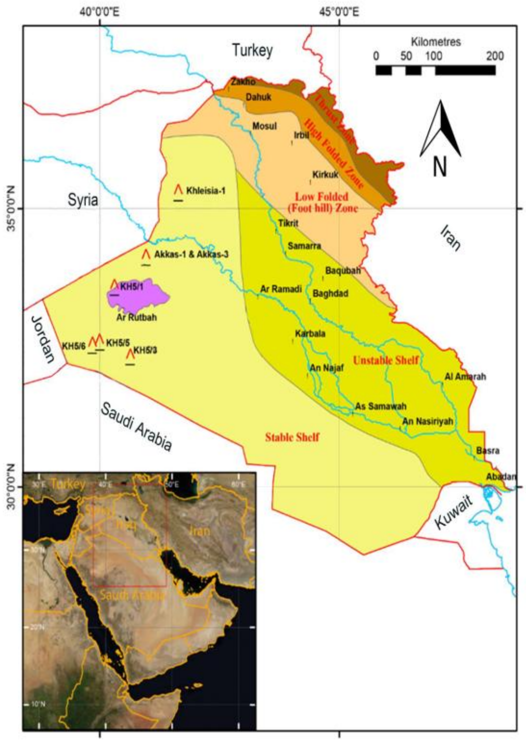

Figure 1. Structural divisions of Iraq (Buday & Jassim 1987) with the location of the studied well (B) Inset map showing countries neighboring Iraq.

Method

The X-ray diffractometer (Philips PW3710) was used to perform X-ray diffraction (XRD). The PDF/ICCD database was used to enable peak identification, and Siroquant, a commercial program from Siemens Australia, was used for Rietveld analysis and quantification. A Hitachi S-3000N scanning electron microscope was used for the analysis of the data using scanning electron microscopy (SEM) at Royal Holloway, University of London, UK.

Results and Discussion

The main clay minerals constituent of the Silurian samples includes; illite, chlorite, kaolinite and little of mixed layers of illite/smectite (Figure 2), in addition to quartz, feldspars, and carbonates (calcite and dolomite). XRD analysis for the Khabour clastics revealed that the clay minerals include; illite, mixed-layer, kaolinite, and chlorite.

The distribution of these clay minerals in the studied section (Figure 3) showed that, in the underlying Ordovician Khabour Formation, an increase in illite crystallinity is typically accompanied by an increase in illite, chlorite, and mixed-layer illite. On the other hand, the Silurian Akkas Formation shows a decrease in kaolinite clay minerals and a rise in illite and chlorite.

As burial depth and temperature rise, smectite frequently undergoes this gradual conversion into mixed-layer I-S and mica in shale deposits in sinking basins (Eberl, 1984). I-S layers are initially dispersed randomly in this reaction, and as depth grows, they progressively order. Dickite, chlorite, and the dissolution of potassium feldspars are present in conjunction with these layers (Hower et al., 1976).

Scanning electron microscopic study has revealed that several clay minerals and non-clay minerals are observed in the studied rocks including disc-shaped chlorite, fibrous illite and honey-comb illite/smectite, hexagonal kaolinite booklets, micro-quartz in detrital and with secondary overgrowth forms and calcite, mica (biotite) and pores (Figure 4 & 5).

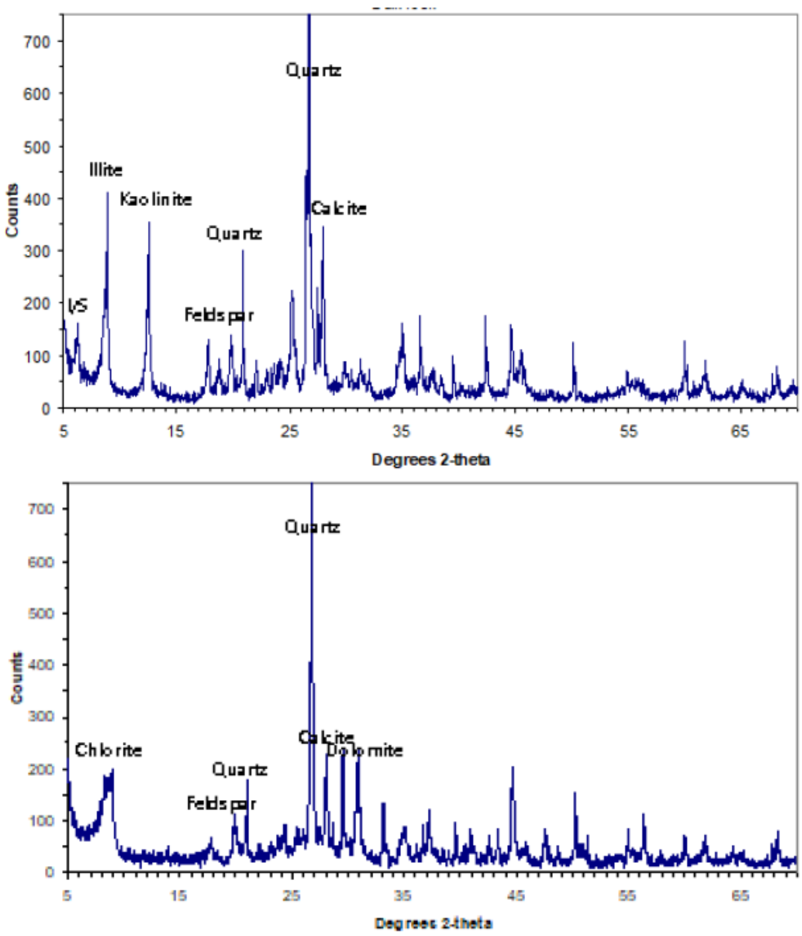

Figure 2. X-ray diffractograms of the Khabour sandstone (upper) and the Akkas shale (lower)

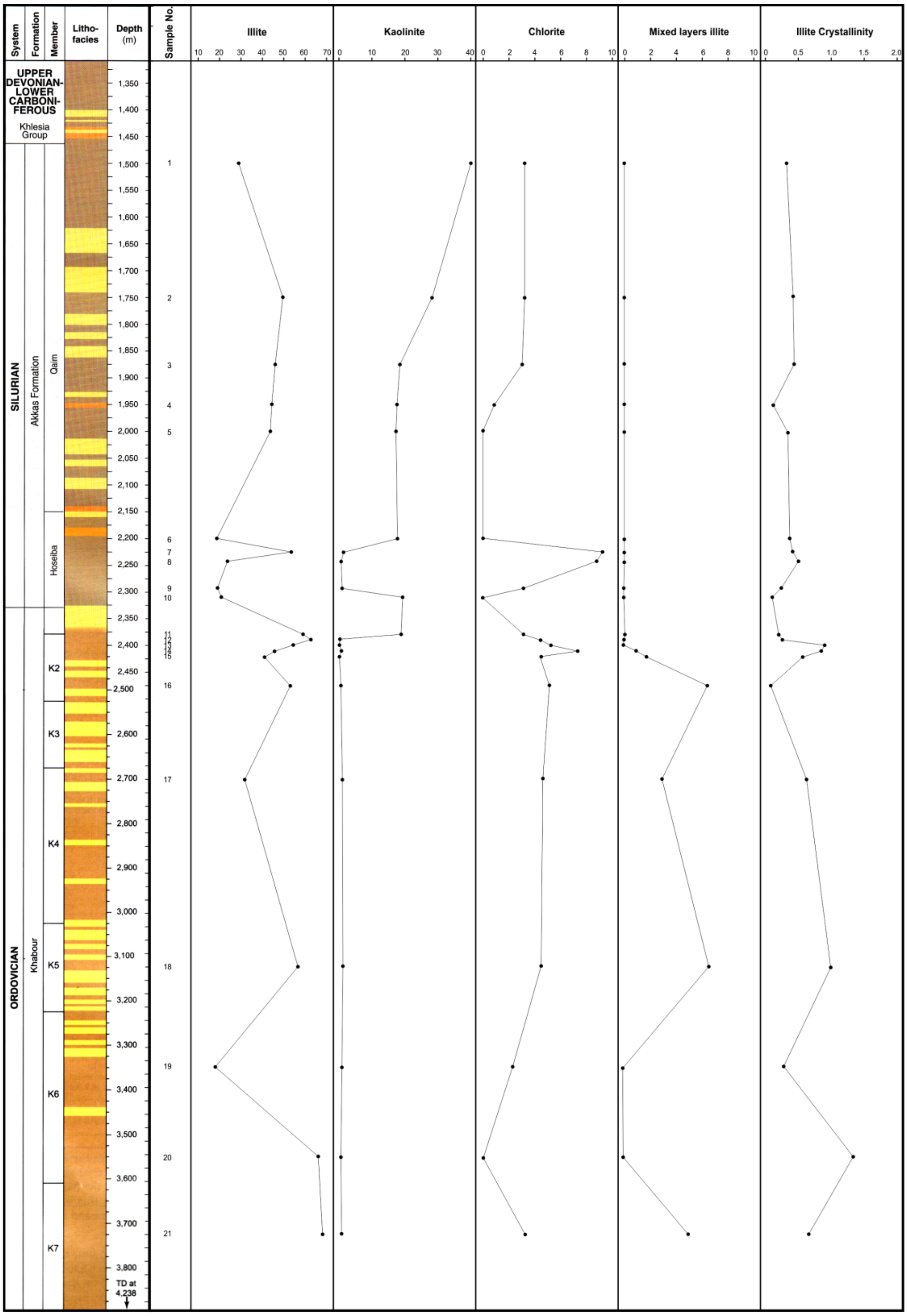

Figure 3. Distribution of the clay minerals along the lithological section in the studied formations from Akkas-1 well.

While illite and mixed-layer clays are byproducts of warm, humid climates, the presence of kaolinite is a good predictor of a humid climate (Chamley, 1989). Since chlorite typically cannot exist in cool, humid climates, its presence in sediments is a reliable indicator of a cool, dry climate (Chamley, 1989). The coexistence of illite and chlorite suggests arid climatic conditions. The SEM pictures clearly show the different morphologies of clay minerals (Figure 4).

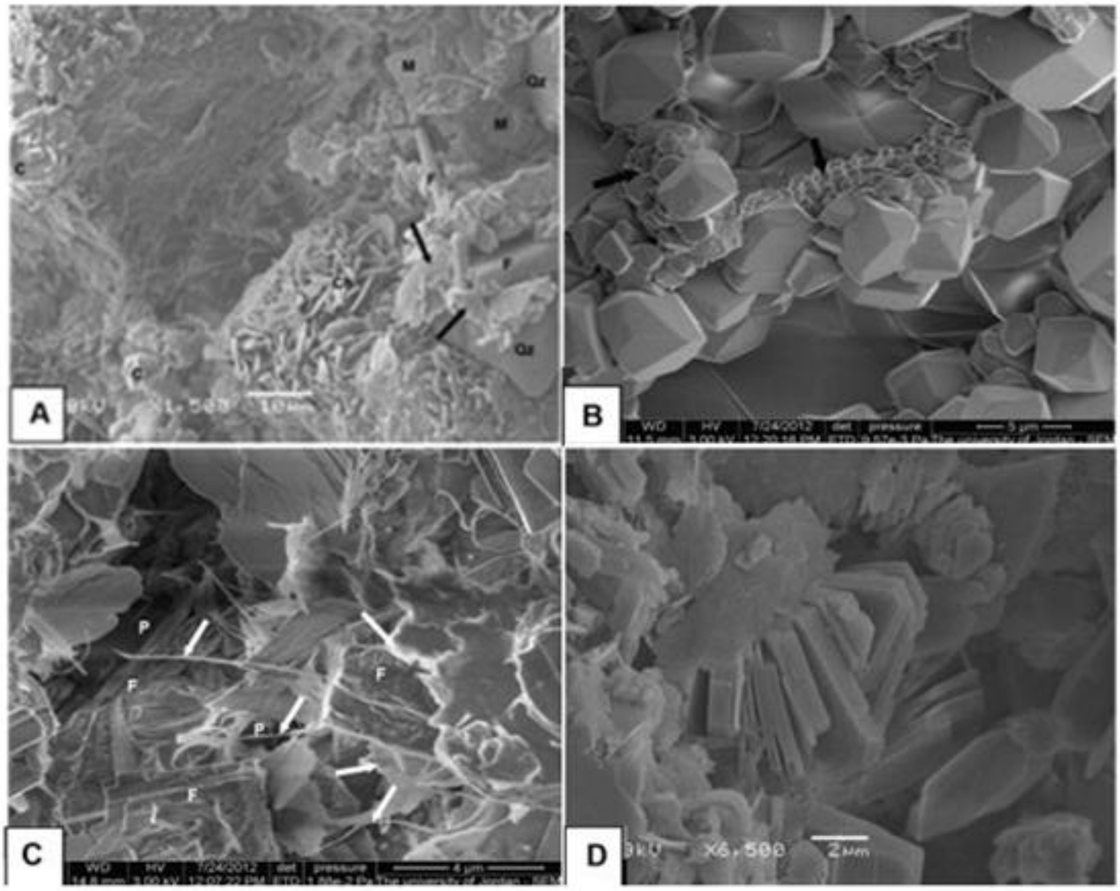

Figure 4. SEM micro images showing; A- chlorite (Ch) in a disc-shaped, carbonates (c), mica (M), feldspar (F) and, micro-quartz (Qz), B- fine to coarse carbonates (calcite) filling veins, C- fibrous illite and feldspars partly filling pores (P) D- kaolinite booklets. Samples from Khabour sandstones.

The detrital origin of the clay mineral may be indicated by the presence of kaolinite in booklets, pseudohexagonal shapes, and partially transformed hexagonal shapes into illite. Though the wispy overgrowth of illite fibers over platy detrital illite may indicate their authigenic genesis, the widespread disc-like shape of chlorite and the common flaky and fiber-like forms of illite are indicative of their detrital origin.

The sandstones from the Khabour Formation under study frequently have pore binding and pore-throat fibrous illite-smectite (I-S). Scattered carbonates and authigenic calcite and quartz also are observed. Presence of various clay and non-clay minerals filling pores or cavities has destructive effect on the porosity and permeability of the studied rocks.

The reservoir characteristics such as porosity and permeability are mostly preserved by microquartz coatings, which slow down the overgrowth of quartz by retrograding after burial. However, depending on the amount of fibrous illite present, the permeability-preserving function of microquartz is either eliminated or greatly diminished when it precipitates (Weibel et al., 2020). The authors also highlighted that the permeability is decreased when microquartz is coupled with fibrous illite, although coatings containing microquartz may assist maintain porosity and permeability.

A major factor in defining the reservoir quality of siliciclastic rocks is chlorite minerals, which are primarily found as clay coatings. They have the potential to improve reservoir quality by maintaining porosity during deep burial, but they also have the potential to worsen the situation by decreasing permeability through pore filling (Azzam et al., 2024).

Deeply buried sandstone reservoirs (>3500 m) in many sedimentary basins are regarded as high-risk prospects for geological exploration operations, such as CO_2 storage, hydrocarbon exploration, and geothermal activity. It is anticipated that quartz cementation will significantly diminish the reservoir characteristics at such burial depths (Giles et al., 1992). However, a number of investigations conducted in recent years have found that deeply buried clastic reservoirs with well-preserved reservoir quality have chlorite coats surrounding the detrital grains (Azzam et al., 2022).

By preventing quartz overgrowth, chlorite coatings can maintain porosity (Saïag et al., 2016). Therefore, estimating the quality of deeply buried reservoirs requires an understanding of the characteristics that govern chlorite coatings in sedimentary basins. In the current study, chlorite is identified in either coating of grains or in well preserved disc shaped chlorite (Figures 4 & 5).

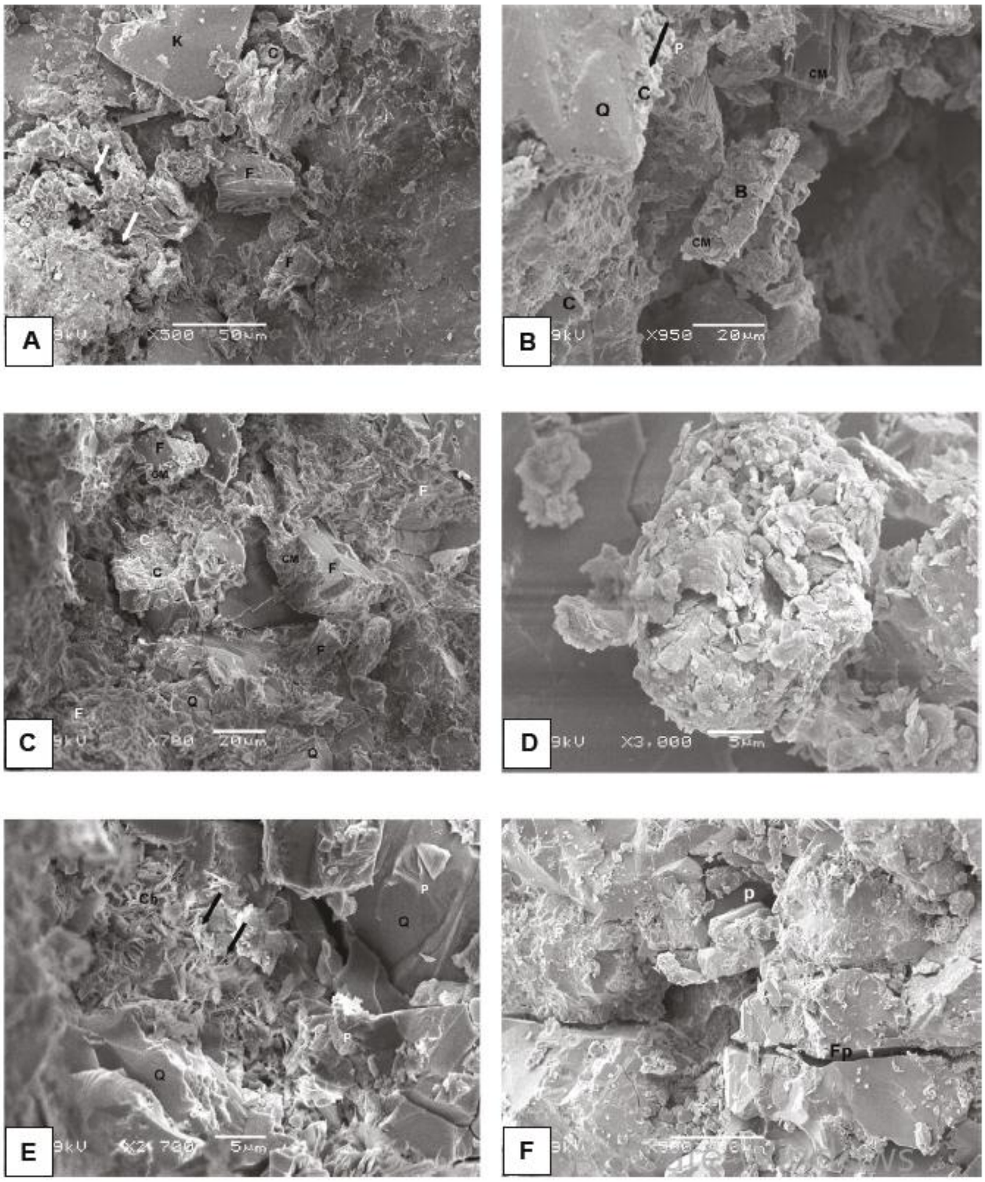

Figure 5. SEM micro-images of the Akkas sandstone displaying kaolinite (K) with dispersed calcite (C), altered feldspars (F), and common micropores (arrows). B: Quartz (Q), Mica (biotite) (B) grains dissolve, and are replaced by carbonates and clay minerals (arrows C, C, and CM, respectively). C. In carbonate cement (C), feldspar grains (F) and detrital quartz grains (Q) change into clay minerals (CM). D. A piece of corroded carbonate rock covered in clay minerals. E. Between detrital quartz grains (Q), there are illite laths (arrows) and chlorite (Ch); note the secondary quartz overgrowth. F. Microporosity (P) and fracture (Fp).

Conclusion

Evidence from clay minerals points to a changing environment during the Paleozoic succession's deposition, alternating between humid and arid climates. In general, there is a possible destructive nature on the porosity and permeability of the studied sandstone since most of clay minerals occluding pores and fractures. Several forms of clay and non-clay minerals are observed throughout the SEM current study, the presence of microquartz coupled with fibrous illite and chlorite may assist maintain porosity and permeability.

Scientific Ethics Declaration

The authors declare that the scientific ethical and legal responsibility of this article published in EPSTEM Journal belongs to the authors.

Acknowledgements or Notes

* This article was presented as a poster presentation at the International Conference on Technology, Engineering and Science (www.icontes.net) held in Antalya/Turkey on November 14-17, 2024.

References

Al-Ameri, Th. K. (2010). Palynostratigraphy and the assessment of gas and oil generation and accumulations in the Lower Paleozoic, western Iraq. *Arabian Journal of Geosciences*, *3*,155-179.

Al-Juboury, A., Howard, J.P., Vincent, S.J., & Nichols, G. (2021). Petrography, diagenesis and geochemistry of the Cambro-Ordovician Khabour sandstones, Western Iraq: Implications for reservoir quality and the impact of the Hirnantian glaciation. *Marine and Petroleum Geology*, *123*,104733

Al-Juboury, A.I. Howard, J. P., Nichols, G., Vincent, S., Manning, C., & Vautravers, B.P. (2019). Sedimentology, geochemistry and reservoir potential of sandstones in the silurian Akkas formation, Western Iraq. *Journal of Petroleum Geology*, *42*, 261-280.

Al-Juboury, A.I., & Al-Hadidy, A.H. (2009). Petrology and depositional evolution of the Paleozoic rocks of Iraq. *Marine and Petroleum Geology*, *26*, 208-231.

Al-Juboury, A.I., & Mazeel , M.A.Th. (2018). Silurian gas-rich “Hot Shale” from Akkas gas field, Western Iraq: Geological importance and updated hydrocarbon potential and reservoir development estimations of the field. In Al-Juboury A.I. (Ed.). *Shale gas- new aspects and technologies*. London: InTech Open.

Al-Sharhan, A.S., & Nairn, A.E.M. (1997). *Sedimentary basins and petroleum geology of the Middle East*. Amsterdam : Elsevier.

Aqrawi, A.A.M. (1998). Paleozoic stratigraphy and petroleum systems of the western and southwestern deserts of Iraq. *GeoArabia*, *3*, 229-248.

Azzam, F., Blaise, T., Patrier, P., Abd-Elmola, A., Beaufort, D., Portier, E., Brigaud, B., Barbar&, J., & Clerc, S. (2022). Diagenesis and reservoir quality evolution of the lower cretaceous turbidite sandstones of the agat formation (Norwegian North Sea): Impact of clay grain coating and carbonate cement. *Marine and Petroleum Geology*, *142*, 105768.

Azzam, F., Blaise, T., Patrier, P., Beaufort, D., Barbarand, J., Abd Elmola, A., Brigaud, B., Portier, E., & Clerc, S. (2024). Impact of sediment provenance and depositional setting on chlorite content in Cretaceous turbiditic sandstones, Norway. *Basin Research*, *36*(3), e12867.

Beydoun, Z.R. (1991). *Arabian plate hydrocarbon, geology and potential: A plate tectonic approach* (Vol.3). AAPG Studies in Geology.

Buday, T., & Jassim, S.Z. (1987). *The regional geology of Iraq: tectonism, magmatism and metamorphism*. State Organization for Minerals, Directorate General for Geological Survey and Mineral Investigations.

Chamley, H. (Ed.). (1989). *Clay sedimentology*. Springer.

Eberl, D.D. (1984). Clay mineral formation and transformation in rocks and soil. *Phil. Trans. R. Soc. London, A31*, 241-257.

Giles, M. R., Stevenson, S., Martin, S. V., Cannon, S. J. C., Hamilton, P. J., Marshall, J. D., & Samways, G. M. (1992). The reservoir properties and diagenesis of the Brent group: A regional perspective. *Geological Society, London, Special Publications*, *61*, 289-327.

Hower, J., Eslinger, E.V., Hower, M.E., & Perry, E.A. (1976). Mechanism of burial metamorphism of argillaceous sediments. Mineralogical and chemical evidence. *Bull. Geol. Soc. America*, *87*, 725-737.

Husseini, M.I. (1992). Upper Paleozoic tectono-sedimentary evolution of the Arabian and adjoining plates. *Journal of the Geological Society, London*, *149*, 419-429.

Jiang, S. (Ed.). (2012). *Clay minerals in nature – their characterization, modification and application*. Croatia: InTech Open.

Konert, G., Al-Afifi, A.M., Al-Hajri, S.A., & Droste, H.J. (2001). Paleozoic stratigraphy and hydrocarbon habitat of the Arabian plate. *GeoArabia*, *6*, 407-442.

Saiag, J., Brigaud, B., Portier, É., Desaubliaux, G., Bucherie, A., Miska, S., & Pagel, M. (2016). Sedimentological control on the diagenesis and reservoir quality of tidal sandstones of the upper Cape Hay Formation (Permian, Bonaparte Basin, Australia). *Marine and Petroleum Geology*, *77*, 597-624.

Sharl&, P. R., Archer, R., Casey, D. M., Davies, R. B., Hall, S., Heward, A. P., Horbury, A. D., & Simmons, M. D. (2001). *Arabian Plate Sequence Stratigraphy*, Manama, Bahrain: Gulf Petrolink

Weibel, R., Nielsen, M.T. Therkelsen,J., Jakobsen, F.C.,Bjerager, M., Mørk , F., Mathiesen, A., Hovikoski, J., Pedersen, S.S., Johannessen, P.N., & Dybkjær, K. (2020). Illite distribution and morphology explaining basinal variations in reservoir properties of Upper Jurassic sandstones, Danish North Sea. *Marine and Petroleum Geology*, *116*, 104290

Worden, R.H., & Morad, S. (2003). *Clay minerals in sandstones: Controls on formation, distribution and Evolution*. International Association of Sedimentologists, Special Publication

Author Information

Rahma S. Al-Auqadi
College of Petroleum and Mining Engineering, University of Mosul, Mosul, Iraq

Mohammad Aswad Al-Joboury
College of Petroleum and Mining Engineering, University of Mosul, Mosul, Iraq

Ali I. Al-Juboury
Al-Kitab University, Kirkuk, 36015, Iraq
Contact e-mail: *alialjubory@yahoo.com*

To cite this article:

Al-Auqadi, R. S., Al-Joboury, M. A., & Al-Juboury, A. I. (2024). Clay mineralogy of the Khabour and Akkas formations, Akkas field, Western Iraq: Implications for reservoir characterization and paleoclimatic conditions. *The Eurasia Proceedings of Science, Technology, Engineering & Mathematics (EPSTEM), 32,* 560-567.

The Eurasia Proceedings of Science, Technology, Engineering & Mathematics (EPSTEM)
ISSN: 2602-3199

The Eurasia Proceedings of Science, Technology, Engineering & Mathematics (EPSTEM), 2024

Volume 32, Pages 568-574

IConTES 2024: International Conference on Technology, Engineering and Science

From Concept to Reality: How 3D Printing Transforms Architectural Model-Making

Bushra Zalloom
Zarqa University

Abstract: Integrating technology in architectural model-making, particularly 3D printers, has transformed the design process, enhancing precision, efficiency, and creative potential. 3D printing allows architects to rapidly produce complex physical models with high levels of detail that traditional handcrafting methods often struggle to achieve. This technology supports the design processes, enabling faster prototyping and experimentation with various forms and structures. It also promotes sustainability by reducing material waste and encouraging the use of eco-friendly materials. Furthermore, digital fabrication tools such as 3D printers facilitate collaboration and communication by providing clear, tangible representations of architectural concepts. As a result, it has become an essential tool in contemporary model-making, enhancing creativity, precision, and innovation in both educational and professional settings. Using advanced technology in model-making reshapes architectural education and practice, drives innovation, and improves workflow efficiency. This paper presents the model-making process for the Zarqa University campus in Jordan, and the challenges it faces throughout the work, it also highlights the pluses and minuses of using this technology.

Keywords: Model-making, Digital fabrication, 3D printing

Introduction

Traditional techniques of model-making needs a significant number of manual labor and produces a considerable material waste unlike the modern process of additive manufacturing that builds materials layer by layer. The modern technology in model-making using 3D printing decreases mistakes, increases accuracy, and enhances sustainability. This technology is considered as an environmentally friendly process since it reduces waste and uses only the required materials (Duarte, 2020). By using 3D printing technology precise physical models are produced from digital plans, and concepts are tested to enable architects to make fast modification and develop their design (INJ Architects, 2024). Moreover, models that are created using this technology enables architects to include detailed features that are hard to be made with traditional techniques. Architects may use 3D printing to build unique and complicated forms that were previously hard to produce, they may create models with intricate curves, geometries, and overhangs that are difficult to create by hand. They can save money because 3D printing reduces the need for expensive molds and equipment. This gives a great option for professionals to produce models rapidly without losing quality, and cut expenses without sacrificing presentation and design requirements (INJ Architects, 2024; Khalil & Matar, 2021).

The traditional handcrafting of models, even with advanced tools, involves significant labor and can be limited in terms of the detail and complexity achievable. The automation of this process ensures that the models match the original design specifications exactly, reducing the chances of human error and making it easier to visualize design concepts in full (Lim & Shakir, 2020). In complex projects, this level of detail can also help in identifying potential issues before actual construction begins, improving the efficiency of the planning and building phases.

In general, 3D printing has transformed architectural model-making by improving precision, speeding up the design process, lowering costs, enhancing creative possibilities, and supporting sustainability, giving architects more flexibility and efficiency in their workflows. 3D printing provides architects with the creative freedom to push the boundaries of traditional model-making, enabling them to explore designs that are more visually compelling and technically accurate.

From Concept to Reality

Figure 1. The model transformation from concept to reality

The concept of model-making in this study is to represent the Zarqa University campus on a suitable scale, 1:350 is selected, for visitors to get general information about the campus contents, main faculties, available services, recreation areas, and green outdoor spaces. Figure 1 shows the transformation from the initial stage where pavements, streets, lighting, and some printed buildings to a detailed model. While 3D printing revolutionizes the speed and precision of architectural model-making, careful attention must be paid at every step—from design and slicing to post-processing—to ensure the model meets aesthetic and structural expectations. Creating the architectural model using 3D printing involves a detailed workflow from concept to final output, this process includes:

Design Phase (Creating a 3D Model)

- *Digital Modelling:* The first step is to create a digital 3D model using architectural design software like AutoCAD, Rhino, Sketch-Up, or Revit. Architecture Students at Zarqa University develop detailed digital models for all buildings on the campus using Revit, these models reflect the intended structure, with all necessary elements like walls, floors, windows, and other features.
- *Optimization for 3D Printing*: The model must be optimized for 3D printing by ensuring that all parts are watertight (no gaps or holes) and suitable for the printer's specifications. Elements like wall thicknesses sometimes need to be adjusted to ensure they can be accurately printed. Ensuring that the digital model is properly optimized for printing can be challenging, as not all design elements may be suitable for 3D printing.
- *File Conversion:* Once the digital model is complete, it is converted into a format that the 3D printer can read. STL (stereo lithography) is used to create the university Campus and represent the geometry of the model.

Slicing the Model

- *Slicing Software:* The STL file is then processed using slicing software (such as Cura or PrusaSlicer). The software divides the 3D model into thin layers and generates the corresponding G-code, which provides instructions for the 3D printer on how to print each layer.
- *Setting Parameters:* The slicing process allows users to set specific parameters such as layer height, infill percentage, print speed, and support structures (for overhangs or complex shapes). The IT engineers at Zarqa University help the architects in setting these parameters.

Preparing the 3D Printer

- **Selecting Materials**: Architects can choose from various materials, including PLA (Polylactic Acid), ABS (Acrylonitrile Butadiene Styrene), resin, or even more advanced materials like concrete for large-scale models. Material selection depends on the project's requirements for durability, detail, and finish. Accordingly, the PLA 1.75mm material was selected, mainly snow white colour, for the walls and grey for the ceilings, Figure 2. Choosing the right material for strength, detail, and aesthetic requirements is crucial and can impact both the cost and outcome.

Figure 2. Material and color selection

- **Calibrating the Printer**: Before printing, the 3D printer, Figure 3, is calibrated to ensure accuracy. This involves leveling the print bed and checking the nozzle alignment to avoid any printing errors. The IT engineers at Zarqa University also help the architects in Calibrating the Printer.

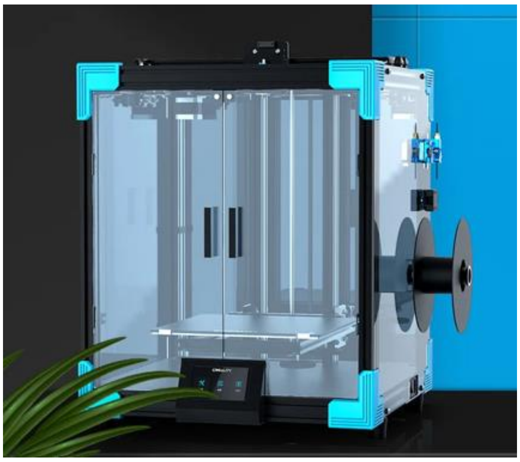

Figure 3. The 3D printer used in model making

Printing the Model

- *Layer-by-Layer Printing*: The printer then begins the process of building the model layer by layer, following the instructions in the G-code. The time required for printing depends on the model's complexity, size, and print speed. In general, each building takes about one working day, and each ceiling about 14 hours, Figure 4.

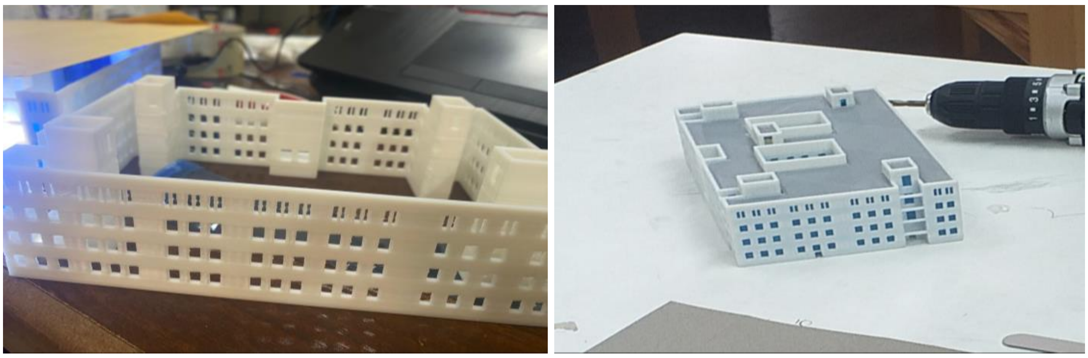

Figure 4. Printed buildings before and after fixing the ceilings

- *Monitoring the Process*: During printing, it is important to monitor the process to ensure everything is proceeding correctly. Adjustments can be made if issues like filament jams or warping occur.

Post-Processing

- *Removing Support Structures*: After printing, support structures, that are temporarily used, are carefully removed from the model without damaging the delicate features.
- *Sanding and Smoothing*: Depending on the material used, sanding or smoothing is required to remove visible layer lines and achieve a clean finish. This work takes extra time but improves the quality of finishing.
- *Painting and Finishing*: For presentation purposes, some parts of the model are painted or treated with different coatings to enhance its appearance or realism.

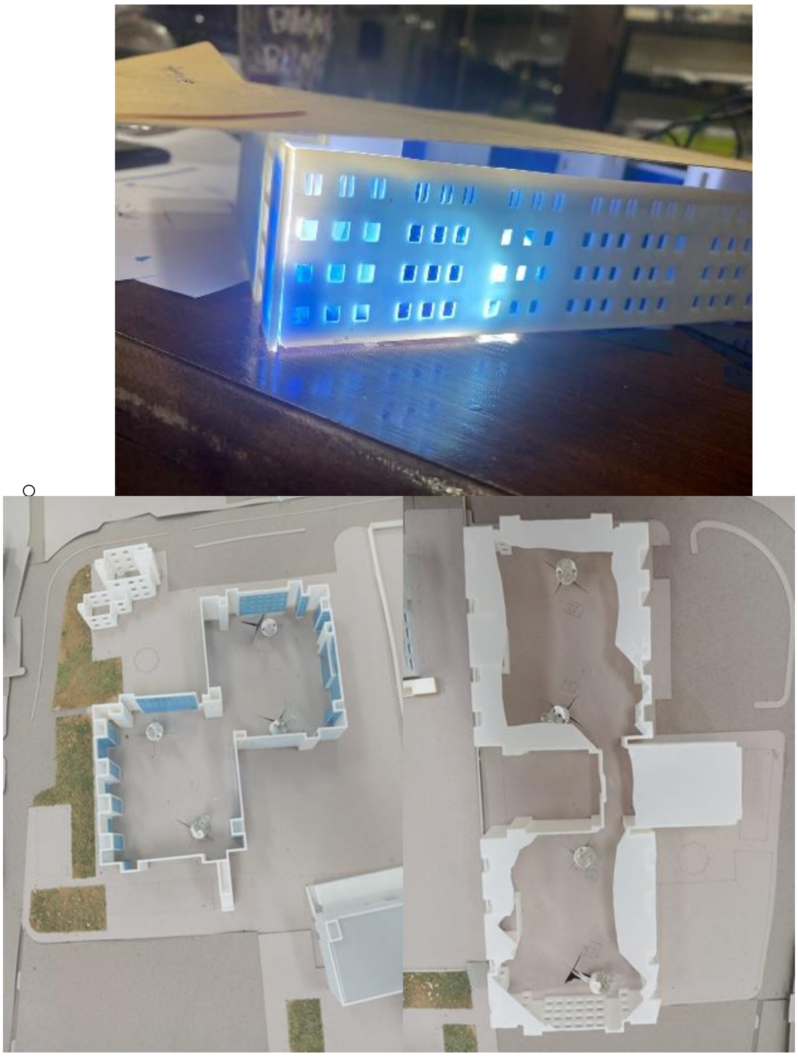

Figure 5. The post-processing phase

- *Lighting:* In parallel, the electrical engineers work on lighting the model as requested by the architects. Figure 5 shows the post-processing phase of lighting and removing support structures.

Assembling Components

- *Model Assembly*: Some buildings in the architectural model were printed in multiple parts (due to printer size constraints or design requirements), these components are assembled and glued together to form the complete model.

Presentation:

- *Display and Use:* The final 3D-printed model is used for client presentations, providing a tangible and detailed representation of the architectural concept. Therefore, after finishing the work, the model is located at the main hall of the university presidency to be accessible and seen by all visitors, Figure 6.

Figure 6. The campus model at the presidency hall at Zarqa University

Results and Discussion: Pluses of Using 3D Printing for Model-Making

Using 3D printing in architectural model-making offers numerous advantages, but it also poses challenges that practitioners and educators must navigate. While technology brings about innovation and efficiency, certain technical, material, and process-related hurdles need to be addressed. Here's a breakdown of the pluses and minuses of using 3D printing in model-making:

Speed and Efficiency:

- Rapid Prototyping: 3D printing allows for faster production of models compared to traditional handcrafting. Designers can quickly convert digital files into tangible objects, adjusting designs and printing new versions within hours or days rather than weeks (Perez & Gonzalez, 2020; INJ Architects, 2024).

1. Time-Intensive for Large or Detailed Models:

- Slow Printing Times: While 3D printing offers efficiency in terms of workflow, the actual printing process can be time-consuming, particularly for large or highly detailed models. It may take several hours or even days to print a single complex model.
- Post-Processing: Once printed, models often require post-processing, such as cleaning, sanding, or assembling, which can add time and effort to the workflow (Montero, 2019).

2. Material and Design Limitations:

- Material Constraints: While 3D printing offers a variety of materials, each type of material comes with its own limitations in terms of strength, texture, or appearance. Some materials may not capture the intended aesthetic, or they may not be suitable for certain architectural elements (INJ Architects, 2024).
- Scale Restrictions: Depending on the size of the printer, there are limitations on how large a single model can be printed. For larger projects, models may need to be printed in sections and then assembled, which can introduce seams or require more effort in post-processing (Perez & Gonzalez, 2020).

3. Technical Challenges:

- Learning Curve: 3D printing requires knowledge of both digital design software and the printing process itself. Architects and students must invest time in learning the technology to fully leverage its capabilities (Khalil & Matar, 2021).
- Printer Malfunctions: Like any advanced technology, 3D printers can experience technical issues such as jams, misalignments, or software errors, which can disrupt workflows and delay projects (INJ Architects, 2024; Khalil & Matar, 2021).

4. Environmental Concerns

- Plastic Waste: While 3D printing can reduce overall material waste, many printers use plastic filaments, which can contribute to environmental concerns if not properly managed.

Conclusion

Technology may be a strong instrument in contemporary architectural practice since its benefits frequently exceed its drawbacks. The 3D printing technology has improved efficiency, originality, and accuracy in the field of architectural model-making. Still, there are various disadvantages such as expenses, time consuming, and technological restrictions. Architects as well as students gain from increased creativity in creating novel ideas, and improved workflows when cutting-edge technology is included into the model-making process. Using 3D printing, models may be produced with extreme details. These technologies are prompting how architecture develops in the future by developing the model-making process for use in both professional and educational settings.

This study recommends the incorporation of 3D printing technology into architectural education and practice. This would enable architects to design and implement complicated forms and structures that are challenging to create, while also providing them with innovative tools to practice with. The practical exposure increases creativity, problem-solving skills, and design ideas that connected to digital manufacturing. A more dynamic and comprehensive experience is produced when architects are able to quickly prototype models, test their concepts, and collaborate with other disciplines to produce the final product.

Scientific Ethics Declaration

The author declares that the scientific ethical and legal responsibility of this article published in EPSTEM Journal belongs to the author.

Acknowledgments or Notes

* This article was presented as an oral presentation at the International Conference on Technology, Engineering, and Science (www.icontes.net) held in Antalya/Turkey on November 14-17, 2024.

* The author acknowledges the Deanship of Research at Zarqa University for funding this project

References

Baker, A. (2017). 3D printing in architecture. The promise and the challenges. *Journal of Architectural Technology*.

Duarte, S. (2020). The role of 3D printing in architecture: A design perspective. *Design Studies, 66*, 145-162.

INJ Architects. (2024). *Exploring traditional construction and 3D printing.* Retrieved from https://injarch.com/exploring-traditional-construction-and-3d-printing/

Jiang, H., & Hu, Y. (2022). Exploring the potential of 3d printing in sustainable architecture. *Sustainability, 14*(3), 1248.

Khalil, A., & Matar, S. (2021). Digital fabrication and the future of architectural design: Opportunities and challenges. *International Journal of Architectural Computing, 19*(1), 3-12.

Lim, S., & Shakir, M. (2020). 3D printing in architecture. current trends and future directions. *Design Studies, 68*, 100-120.

Montero, L. (2019). 3D Printing as a tool for architectural representation and model-making. *Journal of Architectural Education, 73*(4), 502-513.

Pérez, R., & González, M. (2020). Challenges of 3D printing in architecture: A review. *Journal of Building Engineering, 30*, 101292.

Tafuri, A. (2018). 3D printing in architecture from vision to reality. *Architectural Design, 88*(4), 78-85.

Wang, X., & Wang, D. (2019). 3D printing current and future directions in Architecture. *Architecture Research, 9*(2), 53-60.

Zalloom, B. (2022). Smart cities using GIS technology in urban infrastructure development at migration areas. *The Eurasia Proceedings of Science, Technology, Engineering & Mathematics (EPSTEM), 18*, 64-71

Author Information

Bushra Zalloom
Zarqa University
Zarqa, Jordan
Contact e-mail: *bzalloom@zu.edu.jo*

To cite this article:

Zalloom, B. (2024). From concept to reality: How 3D printing transform architectural model-making. *The Eurasia Proceedings of Science, Technology, Engineering & Mathematics (EPSTEM), 32,* 568-574.

The Eurasia Proceedings of Science, Technology, Engineering & Mathematics (EPSTEM)
ISSN: 2602-3199

The Eurasia Proceedings of Science, Technology, Engineering & Mathematics (EPSTEM), 2024

Volume 32, Pages 575-590

IConTES 2024: International Conference on Technology, Engineering and Science

The Effect of High Temperatures on the Compression and Flexural Characteristics of Recycled Fiber-Reinforced Concrete

Atlaoui Djamal
University 'Mouloud Mammeri' of Tizi Ouzou

Bouafia Youcef
University of 'Mouloud Mammeri' of Tizi Ouzou

Ghouilem Kamel
University of Mouloud Mammeri, Tizi Ouzou

Abstract: The objective of this experimental study is to examine the behavior of concrete reinforced with metallic fibers (CMF) and polypropylene fibers (CPPF) subjected to high temperatures, as well as the effect of temperature variations on their mechanical properties, by evaluating the residual mass loss as well as the residual compressive and flexural strength. Two optimal fiber contents were selected for this study: W = 0.2% in compression and W = 0.8% in flexure, while a control concrete (W=0%) of the same composition serves as a reference. The fibers are characterized by their mechanical strength and pull-out resistance. The concrete composition is determined using the experimental method known as the "Dreux-Gorisse" method. Compression tests are carried out on cylinders with a diameter of Ø16 cm and a height of H32 cm, while flexural tests are performed on prismatic specimens with dimensions [10x10x40] cm³. Fiber-reinforced concretes are subjected to different heating-cooling cycles, reaching maximum temperatures of 600°C and 800°C at 28 days of age. This study revealed that the residual compressive and flexural strength of fiber-reinforced concretes exposed to very high temperatures of 600°C and 800°C decreases compared to concretes not exposed to such temperatures (20°C). For all temperatures studied, concrete reinforced with metallic fibers (CMF) showed significantly higher strength than concrete reinforced with polypropylene fibers (CPPF). At 800°C, both metallic fiber concretes and polypropylene fiber concretes exhibited networks of microcracks, but no spalling occurred.

Keywords: Concrete, Flexion, Metal fibers, High temperature, Compression

Introduction

Recent incidents involving fires in concrete structures highlight the detrimental effects of high temperatures on the material's integrity. Various examples, whether it be tunnels or buildings, demonstrate significant damages, such as concrete spalling or structural collapses, caused by fires. Ensuring the safety of people, structures, and the environment in the face of such fire events requires particular attention during the design of constructions. Due to the complex composition of concrete, understanding the phenomena that occur during fires is essential for accurately assessing the fire resistance of structures (post-fire). Experimental studies have been conducted to replace the reinforcement in reinforced concrete with fibers capable of providing the concrete with good resistance to tension, bending, compression, and shear (Atlaoui & Gouilem, 2023; Atlaoui & Bouafia, 2017; Djebali et al., 2011; Atlaoui & Bouafia, 2008; Bouafia et al., 2012; Djebali et al., 2011; Tadepalli et al., 2013; Sorensen et al., 2014; Wang & Wang, 2013; Serbescu et al., 2015; Djebali et al., 2011; Atlaoui et al., 2023). Numerous research studies have focused on managing high temperatures to assess the residual performance of concrete under such conditions. The results suggest that incorporating fibers into the cement mix can improve various properties of concrete, such as tensile and flexural strength, as well as other physical characteristics.

According to the literature, the addition of polypropylene fibers is particularly effective in enhancing the behavior of concrete exposed to high temperatures (Hager, 2004; Noumowe, 2005; Pliya, 2010). Researchers have also noted that the use of steel or polypropylene fibers can enhance the resistance of reinforced concrete structures to high temperatures, with a preference for polypropylene fibers due to their ability to improve concrete strength and behavior in case of fire. Although the addition of steel fibers also offers advantages over traditional concrete, it is noted that polypropylene fibers generally outperform the achieved performances. The incorporation of these fibers has been recommended by several studies (Hager, 2004; Serrano et al., 2016; Yermak et al., 2017) to enhance both the initial and residual strength of concrete, while reducing the risk of spalling at high temperatures. Numerous research studies have been conducted on the behavior of fiber-reinforced concrete when exposed to fire. (Mohamed, 2007). In one study, the mechanical characteristics of fiber-reinforced concrete samples were examined after subjecting them to high temperatures up to 800°C. Tai et al., 2011) The results revealed that after heating, the residual compressive strength of fiber-reinforced concrete increased between 200 and 300°C, then experienced a significant decrease when the samples were exposed to temperatures higher than 300°C up to 800°C.

The impact of high temperatures (Sana & Abdul, 2013) on the mechanical characteristics of fiber-reinforced concrete, according to another study, was primarily observed in terms of compressive strength, flexural strength, and cracking tensile strength. Overall, the results demonstrated that beyond 400°C, the decrease in these strengths became more pronounced. At 600°C, the compressive strength, flexural strength, and cracking tensile strength were affected.

The heating rate plays a crucial role in the thermal stability of concrete. The higher the heating rate, the greater the risk of spallage. Characterization tests conducted by Coke and Venstermans (1977) on concrete samples subjected to heating-cooling cycles at a rate of 1°C/min resulted in spalling of the samples, while those heated at a rate of 0.1°C/min did not spall. A slower temperature rise rate limits the formation of saturated zones and reduces temperature gradients. Rapid heating of the concrete surface creates high thermal gradients, thus inducing thermal stresses. These stresses, whether in compression or tension, can lead to concrete spalling.

Characterizing concrete involves considering compressive strength, which generally decreases with increasing temperatures. A recent study reference Hager (2004) conducted hot compression tests on various concrete samples, including different formulations with water-to-cement (W/C) ratios of 0.3, 0.4, and 0.5. Data analysis revealed three distinct phases in the evolution of strength as a function of temperature. The first phase, ranging from ambient temperature to 100°C, showed a relative reduction in compressive strength of 20% to 30%. The second phase, between 100°C and 250°C, exhibited an increase in strength compared to 100°C, although this increase was observed only for high-performance concretes up to 400°C. This delayed increase, supported by other studies references (Castillo & Durrani, 1990; Pimienta, 2000 ; Tshimanga, 1992), can be attributed to the low permeability of high-performance concretes, which delays water release. Finally, the last phase, beyond 400°C for high-performance concretes and 250°C for other concretes, showed a continuous decrease in strength, accompanied by the appearance of initial cracks due to differential deformation between the aggregates and the paste.

Residual compression tests have also reported a similar trend for concrete. Other researchers (references (Diederichs & Jumppanen, 1992; Phan, 2002) have examined the evolution of compressive strength as a function of temperature and divided it into two ranges. The first range, from ambient temperature to 250-400°C, showed a slight decrease, stability, or even an increase in strength. In the second range, from the intermediate limit up to 600°C, a constant decrease in compressive strength was observed. Both hot and post-cooling tests revealed a decrease in compressive strength between 100°C and 200°C.

Since compression failure is due to surpassing shear stresses, the decrease in bonds between hydrates can create micro defects favoring sliding. An increase in compressive strength has been observed between temperatures of 250°C and 350°C (or even 400°C). This phenomenon could result from the loss of water from the material, possibly followed by a re-increase in bonding forces between hydrates and an increase in surface energies (Dias et al., 1990). These mechanisms overall contribute to an increase in compressive strength. Beyond 350°C (or 400°C), the strength gradually decreases. From this temperature threshold, the behavior of concrete is influenced by the hydroxylation of portlandite and by the differential thermal expansion between the cement paste (shrinkage) and the aggregates (expansion).

Our research aims to address these questions by focusing on the study of the compression and flexural behavior of steel fiber-reinforced concrete (CMF) and polypropylene fiber-reinforced concrete (CPPF). The objective of this experimental study is to analyze and gain a better understanding of the behavior of fiber-reinforced concretes at high temperatures (600°C and 800°C) and the impact of temperature evolution on their mechanical properties. We assess these changes by measuring the residual mass loss as well as residual compressive and flexural strength. In the scope of this study, we use two optimal fiber contents for compression tests (W=0.2%) and flexural tests (W=0.8%), as well as a control concrete BT (W=0%) serving as a reference without fibers (W=0%). The steel fiber-reinforced concrete, polypropylene fiber-reinforced concrete, and fiber-free concrete (W=0%) undergo various heating-cooling cycles up to maximum temperatures of 600°C and 800°C at the age of 28 days.

Materials and Methods

Materials

Characteristics of the Fibers Used in the Study

The metallic fibers (MF) and polypropylene fibers (PPF) used in the study are locally sourced fibers derived from recycling. The metallic fibers are in the form of metal chips (waste from machining steel parts) collected from the National Company of Industrial Vehicles (SNVI) in Algeria. They have a somewhat wavy geometric shape, which promotes their anchoring in concrete. Three fiber lengths were used (4, 5, and 6 cm) with 3, 5, and 6 undulations (spirals). Three tests for each type of combination were conducted. The anchoring of the ends of the metallic fibers in the grips of the hydraulic press is enhanced by a glass fiber resin. The appearance of the fibers used, the anchoring of the ends of the metallic fibers, and the mechanical and geometric properties of the fibers used are illustrated respectively in Figure 1, Figure 2, and Table 1.

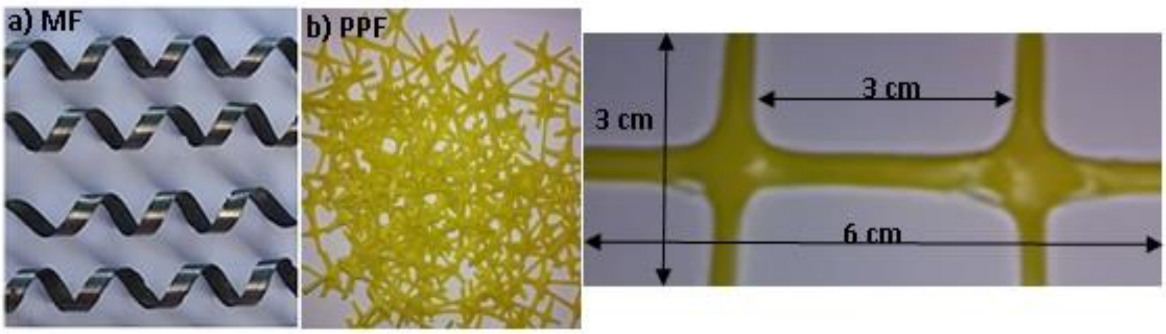

Figure 1. View of the fibers: a) metallic fibers; b) polypropylene fibers; c) dimensions of polypropylene fibers

Figure 2. Anchorage system

Table 1. Characteristics of mechanical properties of fibers under the study

Types of fibers	L (cm)	l (cm)	e_p (cm)	Φ (cm)	σ_e (MPa)	γ (g /cm^3)
Metal fibers	6	0.02	0.06	0.8275	7.87	
Polypropylene fibers	6	0. 3	0.3	/	16.92	0.95

Mass of different fiber contents for 1m3 concrete are given by Table 2.

Table 2. Mass different contents of fibers for concrete 1m^3

Fiber volume fractions W (%)	Metal fibers	Polypropylene fibers
Weights for 1m^3 of concrete) (kg)	7 870	950

Procedure for the Preparation of Test Specimens and Mixing Procedure

The concrete used in this study includes CPJ-CEMII/B 42.5 R NA 442 type cement, class 42.5, sourced from the Lafarge region in Msila, Algeria, in accordance with standard NF EN 196-6 (AFNOR, 2018). The aggregates used are from the Tizi Ouzou region, specifically quarry rocks. These aggregates are crushed, and the particle size classes used are 0/3 mm, 3/8 mm, and 8/15 mm, all washed and oven-dried. Particle size analysis by sieving was conducted according to standard NF P18-560, using a sieve with an adjustable frequency of 50 Hz. The concrete composition per cubic meter was formulated using the Dreux-Gorisse method (Dreux & Festa, 2007). Figure 3 presents the particle size distribution curves for each type of aggregate. The mixing process was carried out using a vertical-axis mixer with a capacity of 65 L. Table 3 provides a summary of the mixing proportions for 1 m^3 of concrete for all batches used in this test program. The concrete mixing was done in a rotary mixer, strictly following the following mixing procedure:

- Introduction of sand, aggregates, and cement, mixed for 60 seconds.
- Introduction of water, mixed for 40 seconds.
- Introduction of the water reducer, mixed for 30 seconds.
- For concrete mixes with fibers, they are introduced last, in small quantities, with a 20-second mix after each addition.

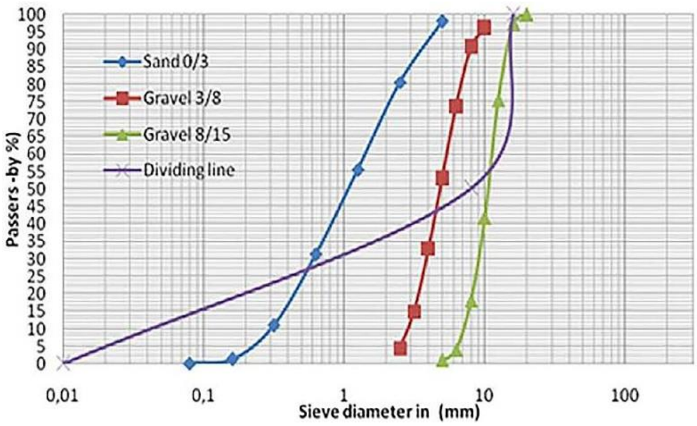

Figure 3. Particle size curve

Table 3. Proportions of the concrete mix used for 1m^3

Ingredient	Amount (kg/m^3)
coarse aggregate (8/15) (kg)	895.00
Medium aggregate (3/8) (kg)	171.00
Sand (0/3) (kg)	753.00
Water (W) (kg)	207.00
Cement CPJ CEMII/A 42.5 (C) (kg)	380.00
Superplasticizer (0.5% of cement weight) (ml)	190.00

Methods

Fiber Characterization Tests

To determine the mechanical characteristics of the fibers used (metallic and polypropylene), direct tensile tests were conducted. The tests were performed on an "Ibertest" hydraulic press with controlled deformation at the Laboratory of Materials and Structures Modeling of Civil Engineering at the Mouloud Mammeri University of Tizi Ouzou in Algeria. The press is equipped with numerical control (as shown in the view provided in Figure 4). Geometric characteristics are input automatically, and the effective length of the fiber is 100 mm. The loading speed is set at 20 mm/min.

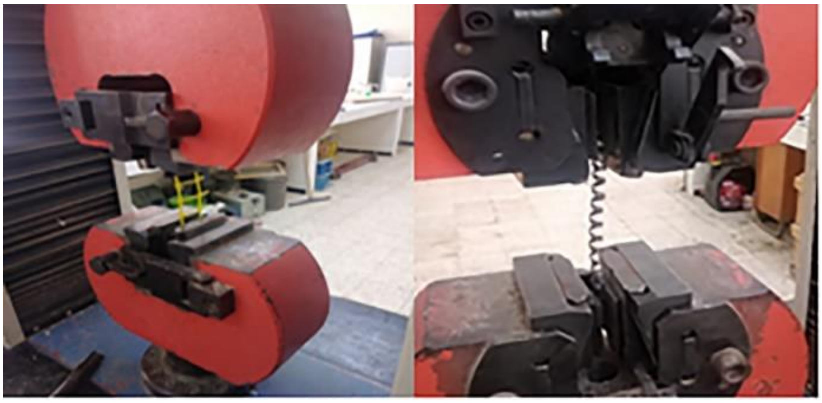

Figure 4. Test device view

Calculation of Mass Losses

For determining the mass loss as a function of the heating-cooling cycle, specimens are weighed before and after each heating-cooling cycle. The specimens from heating are weighed directly to avoid any rehydration phenomenon with the surrounding environment. The test aims to determine the material (or mass) loss experienced by the specimens during heating compared to their initial state (before heating). The mass loss expressed as a percentage is obtained using the following formula (1):

$$\text{mass loss} = \frac{\mathrm{M_0} - \mathrm{M_t}}{\mathrm{M_0}} \mathrm{x}100\% \ldots\ldots\ldots\ldots\ldots\ldots\ldots..(1)$$

Thermal Tests

Each cycle (heating-cooling) consists of three phases (Figure 5). The first phase involves a temperature ramp-up at a rate of 1°C.min-1. The second phase is a constant temperature plateau within the furnace to homogenize the temperature within the specimens. It lasts for four hours. The final phase is a temperature decrease until reaching ambient value at an average speed of -1°C.min-1. This cooling phase of the specimens is not controlled. It occurs naturally depending on the temperature inside the furnace, which is kept closed. Indeed, the aim is to ensure that the damage induced in the concrete results solely from the effect of temperature.

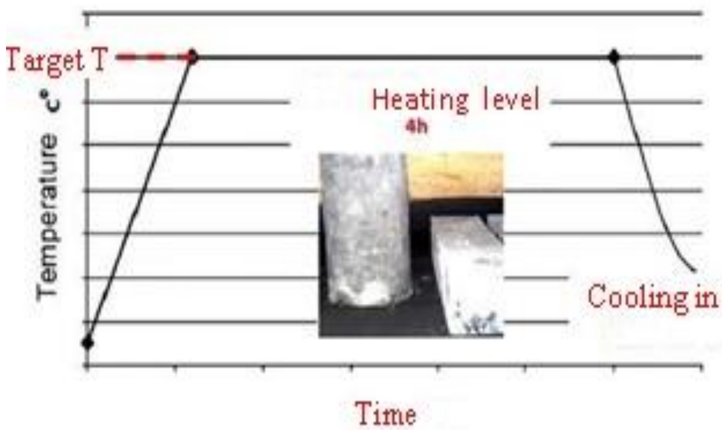

Figure 5. Heating – cooling cycles imposed on the specimens

The specimens are arranged within the furnace in such a way that heat is distributed evenly. This heat distribution is achieved through the furnace's ventilation system. The furnace control is carried out using a programmable controller connected to thermocouples. Figure 6 illustrates the arrangement of the specimens inside the furnace.

Figure 6. Arrangement of the test pieces inside the oven

Compression Tests

The compression tests are performed on an AUTOTEST hydraulic press with a maximum capacity of 2000 kN (Figure 7a), using cylindrical specimens with a diameter of 16 cm and a height of 32 cm (according to the NF EN12390-4 standard), as depicted in Figure 7b.

Figure 7a. Cylindrical test tubes

Figure 7b. With hydraulic press

Bending Tests (3-Point Bending)

Bending tests were conducted on prismatic specimens [10x10x40] cm^3 using the 'Ibertest' machine to investigate the mechanical behavior of concrete reinforced with metallic fibers (MF) and polypropylene fibers (PPF) at elevated temperatures (600°C and 800°C), with a fiber volume fraction (W) of 0.8%, as well as plain concrete

(BT) without fibers (W=0%). In total, 27 beams were tested. Figure 8 illustrates the static diagram of the three-point bending test.

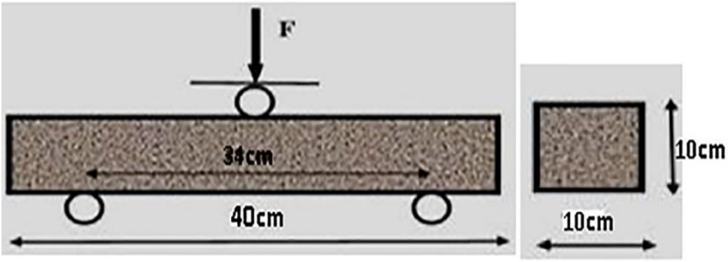

Figure 8. Static schema of the three-points bending test

Geometry and Composition of the Specimens

The specimens used for conducting three-point bending tests are prismatic specimens with dimensions [10x10x40] cm³, with a width (l) of 10 cm, a height (h) of 10 cm, and a length (L) of 40 cm. The prismatic molds used are shown in Figure 9. The metallic fibers (MF) and polypropylene fibers (PPF) are randomly dispersed within the cementitious matrix. A vibrated mixture was used during casting.

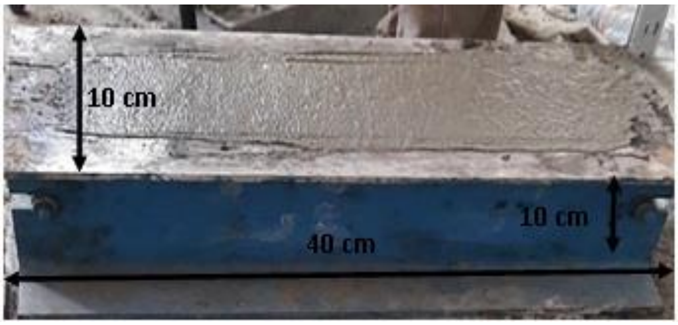

Figure 9. Prismatic molds used

Principle of the Test

After the heating-cooling cycle, the specimens of dimensions [10x10x40] cm³ are subjected to flexural failure by applying a bending moment using an upper roller and two lower rollers. The specimens are carefully placed on the two lower support rollers and centered so that the longitudinal axis of the rollers (upper and lower) is orthogonal to the axis of the specimen (see Figure 10). In accordance with the NF EN ISO 527-2 standard [Afnor, 2001], loading is performed at a speed of 0.25 mm/min until failure. The maximum load as well as the force-deformation curve is recorded during the test.

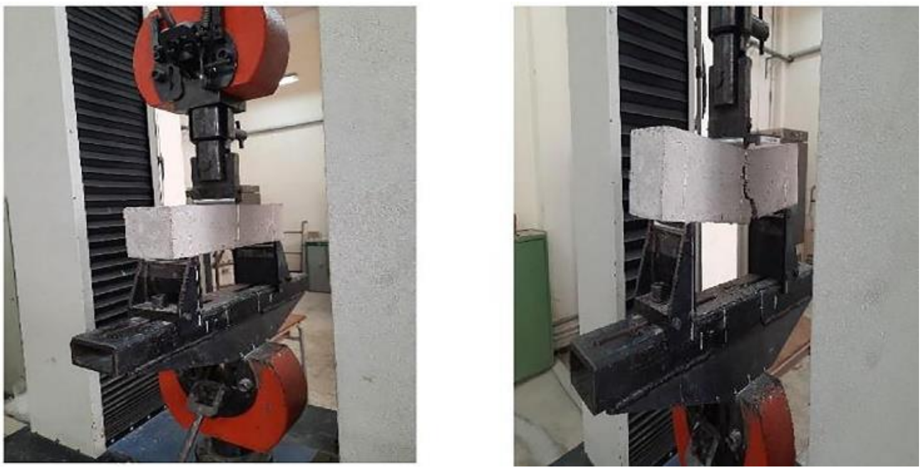

Figure 10. The setup of the three-point bending test

Results and Discussions

Characterization Trials of Fibers under Tension

The tension stress-strain curves for three lengths of fibers (4 cm, 5 cm, and 6 cm) containing six undulations along the length are demonstrated in Figure 11. During the test, it is observed that the undulations of the fiber gradually open up until the fiber flattens. Beyond that, a ductile fracture of the steel is observed. The tensile strength increases as a function of the number of undulations: it reaches R_m =281 MPa for a length L= 6 cm with 6 undulations shown in Figure 12.

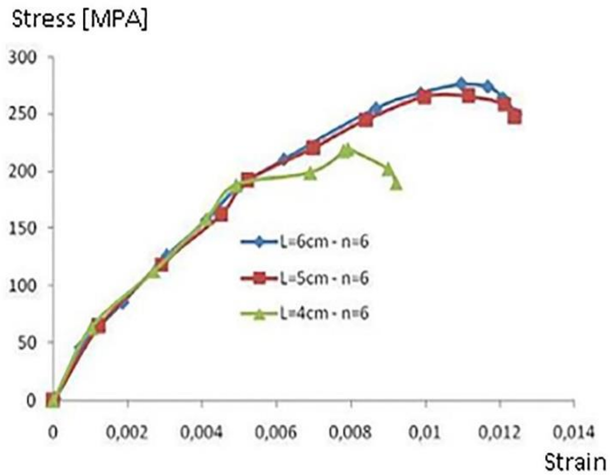

Figure 11. Average curve Stress-Strain

Figure 12. Fibers used L=6 cm with 6 undulations

Figure 13 shows the mean value of three stress-strain curves as a function of deformation σ = f (ε). This study allowed us to determine the tensile strength of the polypropylene grid fibers used. It appears that the average resistance R_m = 16.92 MPa.

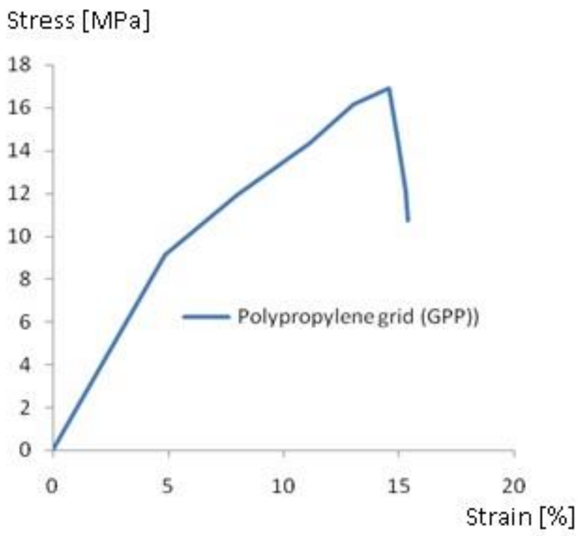

Figure 13. Average stress-strain curve of polypropylene fibers

Compression Tests

Mass Losses in Compression

Figure 14 illustrates the mass loss histogram under compression obtained by averaging three tests conducted on cylindrical specimens.

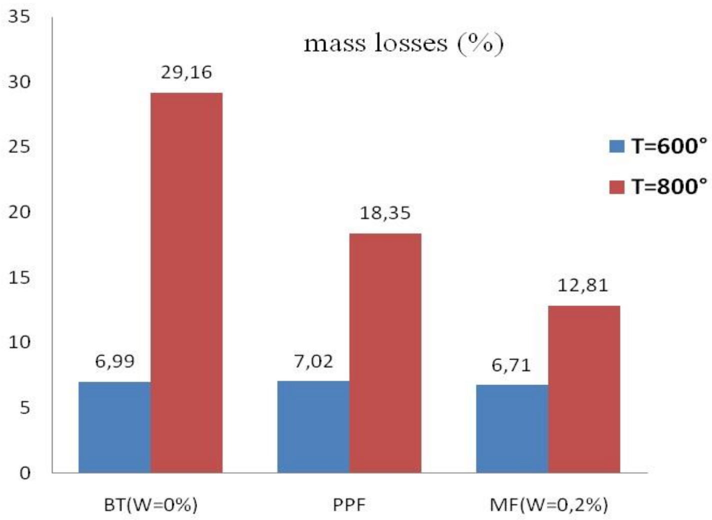

Figure 14. Mass losses of the different concretes studied

According to the histogram in Figure 14, it can be observed that as the temperature increases, the mass loss also increases. At 600°C, the various fiber-reinforced concretes (BT, CPPF and CMF) exhibited almost the same magnitude of mass loss, while at 800°C, the control concrete (BT with W=0%) and the polypropylene fiber-reinforced concrete (CPPF) showed a significant mass loss.

Compression Resistance

Figures 15, 16, and 17 illustrate the appearance of cylindrical specimens in plain concrete (BT), polypropylene fiber-reinforced concrete (CPPF), and metallic fiber-reinforced concrete (CMF) after being exposed to temperatures of 600°C and 800°C upon exiting the furnace.

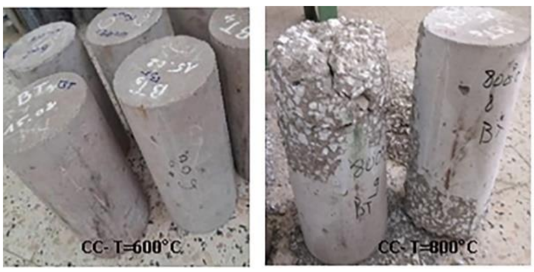

Figure 15. The appearance of the cylindrical specimens of the control concrete (BT) at the exit from the oven

Figure 16. The appearance of polypropylene fiber concrete specimens (CPPF) at the exit of the oven

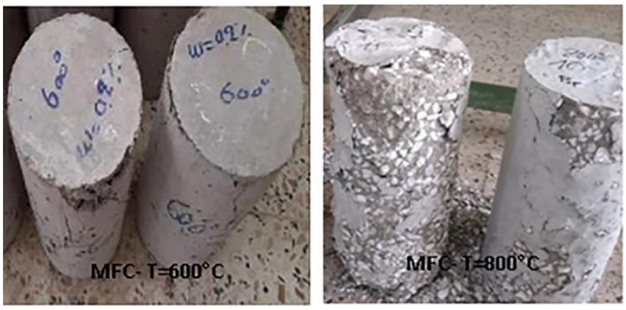

Figure 17. The appearance of fiber concrete specimen metallic (CMF) at the exit of the oven

Upon observing the appearance of the specimens upon exiting the furnace, we notice the occurrence of cracking in the form of crazing in the cases of metallic fiber-reinforced concrete (CMF), polypropylene fiber-reinforced concrete (CPPF), as well as in the case of plain concrete (CC). Furthermore, the polypropylene fiber-reinforced concrete (CFPP) subjected to a temperature of 800°C exhibited material detachment on half of the lateral surface of the cylinders. Figures 18, 19, and 20 respectively depict the overlay of average stress-strain curves under compression for plain concrete (BT), polypropylene fiber-reinforced concrete (CPPF), and metallic fiber-reinforced concrete (CMF) at temperatures of 20°C, 600°C, and 800°C.

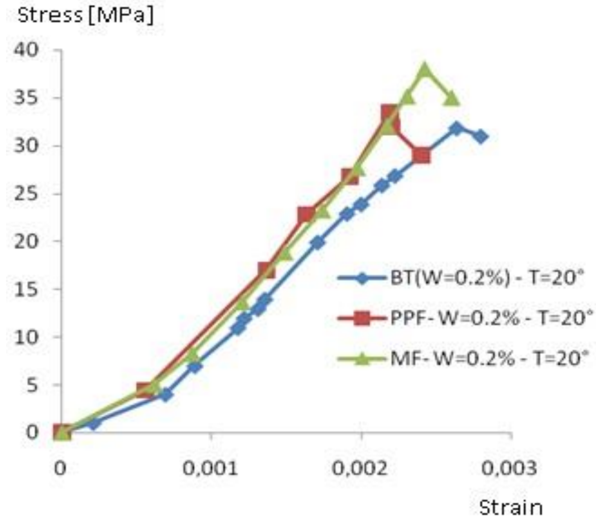

Figure 18. Stress-strain curves of concrete studied at T=20°C

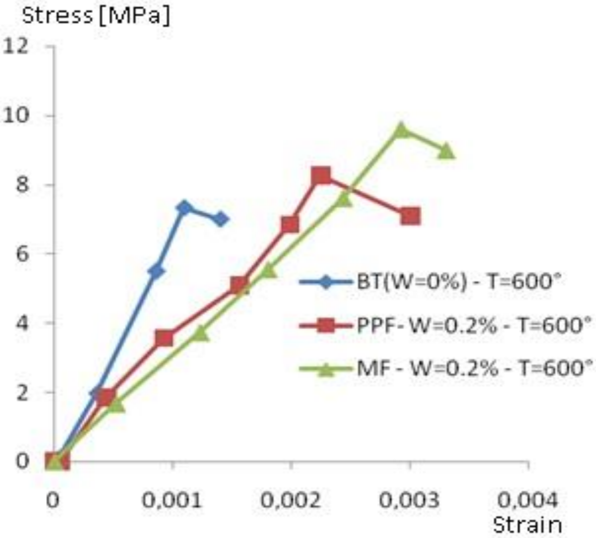

Figure 19. Stress-strain curves of concrete studied at T=600°C

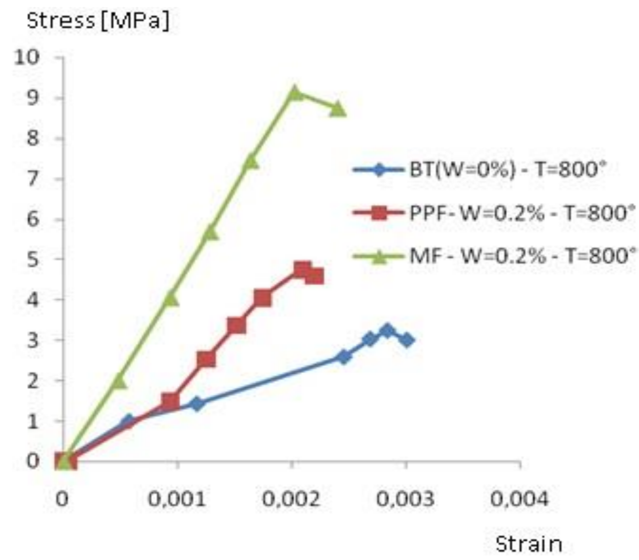

Figure 20. Stress-strain curves of concrete studied at T=800°C

According to the curves in Figures 18, 19, and 20 presenting stress-strain behavior under compression, for all types of concrete studied (BT, CPPF and CMF) subjected to temperatures of 20°C, 600°C, and 800°C, it was observed that concretes subjected to heating-cooling cycles at temperatures of 600°C and 800°C exhibited lower strengths as well as a decrease in the slope of the stress-strain curves compared to concretes that were not subjected to such heating-cooling cycles. As for steel fiber-reinforced concrete (CMF) and polypropylene fiber-reinforced concrete (CPPF), an improvement in deformability was observed. Figure 21 illustrates the histogram of compressive strength of the different concrete types studied (BT, CMF and CPPF) subjected to temperatures of 20°C, 600°C, and 800°C.

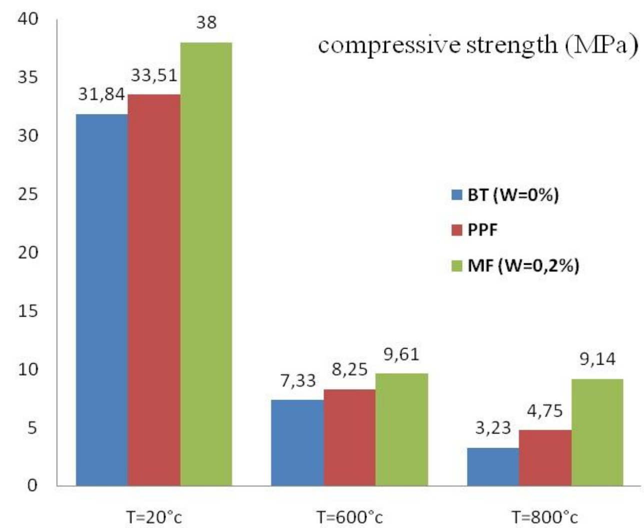

Figure 21. Compressive strength of the different concretes studied

According to Figure 20, for all temperatures, it is observed that steel fiber-reinforced concrete (CMF) exhibits higher compressive strength compared to polypropylene fiber-reinforced concrete (CPPF) and the control concrete BT (without fibers). At 800°C, there is a significant drop in the strength of the concretes (CMF and CPPF) compared to those at 20°C. This drop is approximately 76% for steel fiber-reinforced concrete (CMF) and 86% for polypropylene fiber-reinforced concrete (CPPF).

Bending Tests (3-Point Bending)

Figures 22, 23, and 24 illustrate examples of the failure mode of the beams tested in control concrete BT (W=0%), polypropylene fiber-reinforced concrete (CPPF), and steel fiber-reinforced concrete (CMF) after being exposed to temperatures of 20°C, 600°C, and 800°C.

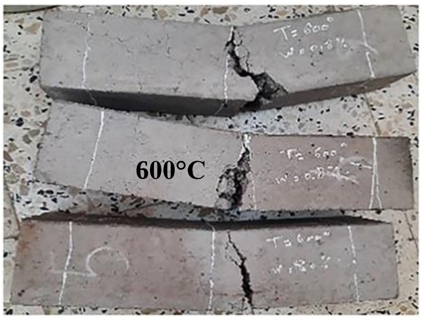

Figure 23. Exemple des poutres testées à

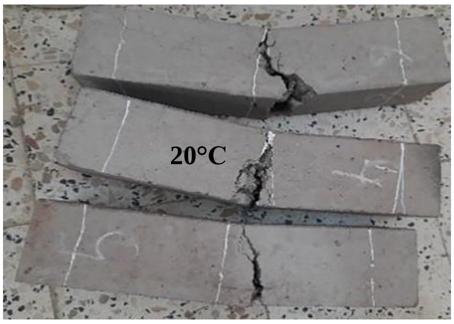

Figure 22. Exemple des poutres testées à 20°C

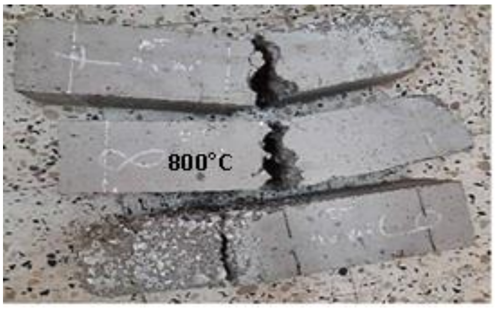

Figure 24. Exemple des poutres testées à 800°C

Loss of Mass in Flexure

Figure 25 illustrates the histogram of loss of mass in flexure obtained by averaging three tests conducted on the prismatic beams.

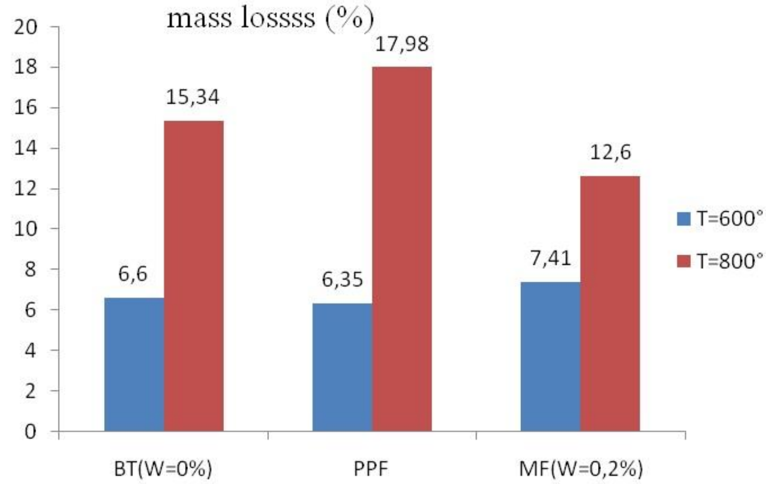

Figure 25. Mass losses of the different concretes studied

According to the histogram in Figure 25, it is observed that the loss of mass increases proportionally with the rise in temperature. At 600°C, the various fiber-reinforced concretes (BT (W=0%), CPPF and CMF) recorded similar mass losses, while at 800°C, the control concrete BT (without fibers) and polypropylene fiber-reinforced concrete (CPPF) experienced significant mass losses.

Bending Resistance

The Figures 26, 27, and 28 respectively present the superimposition of the average force-deformation curves in flexure for the control concrete BT (W=0%), polypropylene fiber-reinforced concrete (CPPF), and steel fiber-reinforced concrete (CMF) at temperatures of 20°C, 600°C, and 800°C.

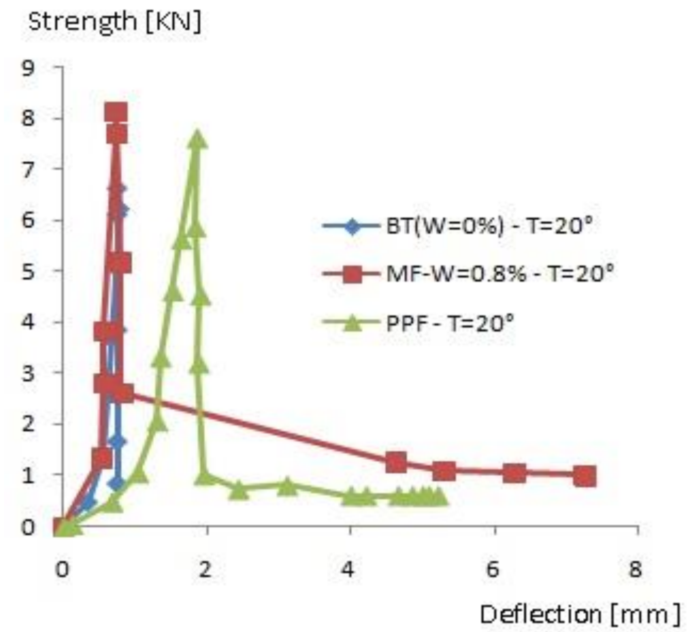

Figure 26. Superposition of the average strength-deflection curves of the beams tested at 20°C

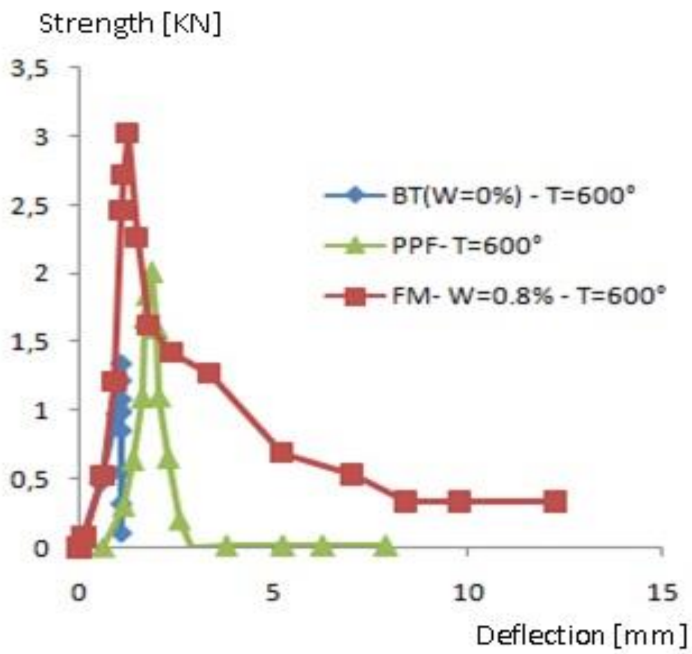

Figure 27. Superposition of the average strength-deflection curves of the beams tested at 600°C

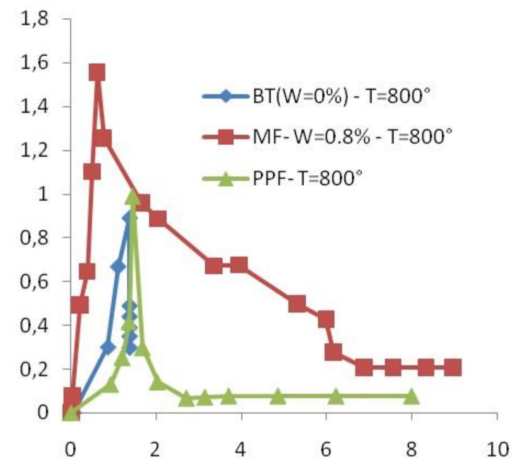

Figure 28. Superposition of the average strength-deflection curves of the beams tested at 800°C

Figures 26, 27, and 28 illustrate the relationship between force and deformation (deflection) during the flexural behavior of fiber-reinforced concretes. They reveal that the behavior of fiber-reinforced concretes can be divided into two distinct phases: an initial linear phase corresponding to elasticity, followed by a post-cracking phase where the fibers continue to provide resistance. These graphs demonstrate that steel fiber-reinforced concrete (CMF) exhibits better flexural performance at all studied temperatures. Particularly, its behavior after the peak strength is superior to that of plain concrete (BT, W=0%) and polypropylene fiber-reinforced concrete (CPPF). Additionally, a significant drop in strength is observed for all types of concretes (BT, CPPF and CMF) at a temperature of 800°C. Figure 29 illustrates the histogram of compressive strength of the different concrete types studied (BT, CMF, CPPF) subjected to temperatures of 20°C, 600°C, and 800°C.

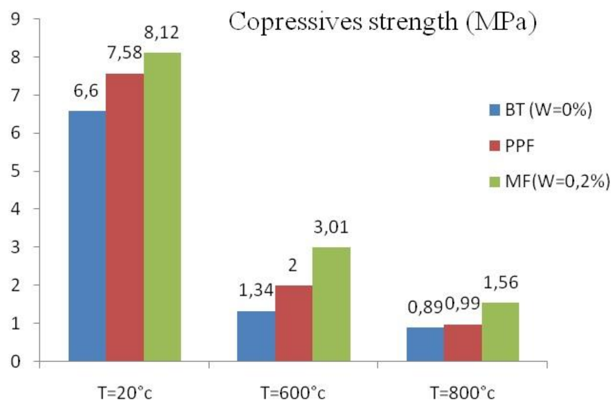

Figure 29. Compressive strength of the different concretes studied

According to the data from Figure 29, it is notable that metallic fiber reinforced concrete (CMF) exhibits higher flexural strength compared to polypropylene fiber reinforced concrete (CPPF) and unreinforced concrete (BT). At a temperature of 800°C, a significant decrease in strength is observed for the concretes (CMF and CPPF) compared to that at 20°C. This decrease represents approximately 81% for metallic fiber reinforced concrete (CMF) and 87% for polypropylene fiber reinforced concrete (CPPF).

Conclusion

The objective of this experimental study is to contribute to a better understanding of the behavior of recycled fiber-reinforced concrete exposed to high temperatures of 600°C and 800°C, as well as the influence of steel fibers (MF) and polypropylene fibers (PPF) on this behavior in compression and flexure. Concrete samples, whether containing fibers or not, were manufactured for testing purposes. The results of this experimental study have allowed us to draw the following conclusions:

The results obtained are very encouraging. Indeed, they indicate an increase in the tensile strength of steel fibers (MF) correlated with the fiber length and the number of spirals. The best performance is observed with fibers measuring 6 cm in length and having 6 spirals.The loss of mass in compression and flexure calculated for steel fiber-reinforced concrete (CMF), polypropylene fiber-reinforced concrete (CPPF), and plain concrete (BT, W=0%) allowed us to observe that as the temperature increases, the loss of mass also increases. At 600°C, the different fiber-reinforced concretes (BT, CMF and CPPF) exhibited almost the same magnitude of mass loss; this significant mass loss corresponds to the departure of chemically bound water. Whereas at 800°C, it was the polypropylene fiber-reinforced concrete (CPPF) that experienced significant mass loss, along with the control concrete BT (without fibers), caused by the degradation of the cementitious matrix. During the examination of compression tests on cylindrical specimens after removal from the furnace, cracking in the form of crazing was observed in the case of steel fiber-reinforced concrete CMF), polypropylene fiber-reinforced concrete (CPPF), as well as in the case of plain concrete BT (W=0%). Additionally, the plain concrete subjected to a temperature of 800°C exhibited material spalling on half of the lateral surface of the specimens. For all temperatures, it is noted that steel fiber-reinforced concrete (CMF) exhibited higher compressive and flexural strengths compared to polypropylene fiber-reinforced concrete (CPPF) as well as the plain concrete BT (without fibers). At 800°C, there is a significant drop in both compressive and flexural strength for all types of concrete, compared to the strengths at 20°C.

Finally, based on the results obtained, it can be concluded that the use of steel fibers (machining chips from steel parts) increases the fire resistance of concrete. Indeed, the chip fibers limit the opening of cracks, thus providing effective protection to traditional reinforcements against thermal radiation. From a broader perspective, it would be interesting to conduct tests on real large-scale specimens, to use flat chip fibers instead of corrugated fibers to reduce voids (cavities) in the cement paste, and also to combine these fibers with traditional reinforcement.

Scientific Ethics Declaration

The authors declare that the scientific ethical and legal responsibility of this article published in EPSTEM. Journal belongs to the authors.

Acknowledgements or Notes

* This article was presented as a poster presentation at the International Conference on Technology, Engineering and Science (www.icontes.net) held in Antalya/Turkey on November 14-17, 2024.

* The team from our Laboratory of Materials and Structures Modeling in Civil Engineering (L2MSGC) thanks you for giving us the opportunity to participate in the ICONTES 2024 conference and to contribute to our research together. We also express our gratitude to the reviewers for examining this work with the aim of improving it.

References

Atlaoui, D., & Bouafia, Y. (2017). Experimental characterization of concrete beams elements reinforced by long fiber chips. *Journal of Adhesion Science and Technology*, *31*(8), 844-857.

Atlaoui, D., & Ghouilem, K. (2023). Effect of chipped fiber languor on the bending behavior of concrete beam elements. *Journal of Applied Engineering Sciences*, *13*(2), 155-162.

Atlaoui, D., Adjrad, A., & Bouafia, Y. (2023). Effect of recovered fibers on the behavior of concrete in tension. *Slovak Journal of Civil Engineering*, *31*(4), 26-33.

Bouafia, Y., Kachı, M. S., Atlaoui, D., & Djebali, S. (2012). Study of mechanical behavior of concrete in direct tensile fiber chips. *Applied Mechanics and Materials*, *146*, 64-73.

Castillo, C., & Durrani, A. J. (1990). *Effect of transient high temperature on high-strength concrete* (pp.47-53). Rice University.

Coke, F., & Venstermans,J. (1977). Béton renforcéde fibresd'acier. *CSTCMagazine(Bruxelles), (3)*,2-19.

Dias, W .P. S., Khoury,G.A., &Sullivan, P.J.E.(1990). Mechanical properties of hardened cement paste exposed to temperature up to700°C. *ACIMaterials Journal*, *87*(2),160-166.

Diederichs, U., & Jumppanen,U. M.(1992).High temperature properties and spalling behavior of high-strength concrete In *Verlog fürarchitektur und techn.wissencheften* (pp.191-197).Ernst&schn.

Djebali, S., Atlaoui, D., & Bouafia, Y. (2011). Caractérisation en traction directe du béton de fibres métalliques. *Matériaux & Techniques*, *99*(3), 327-338.

Djebali, S., Bouafia, Y., Atlaoui, D., & Bilek, A. (2011). Study of mechanical behavior of chips reinforced concrete. *Advanced Materials Research*, *324*, 360-363.
Djebali, S., Bouafia, Y., Atlaoui, D., & Bilek, A. (2011). Study of mechanical behavior of chips reinforced concrete. *Advanced Materials Research*, *324*, 360-363.
Dreux, G.,& Festa,J. (2007).*Nouve auguide du bétonet deses constituants*. Huitième (Ed.).

Hager, I. (2004). *Comportementàhaute températuredes beton sàhaute performance-évolutiondes principales propriétés mécaniques*. Doctoral dissertation.

Noumowe, A. (2005). Mechanical properties and microstructure of high strength concrete containing polypropylene fibres exposed to temperatures up to 200 C. *Cement and Concrete Research*, *35*(11), 2192-2198.

Phan, L. T. (2002).High-strength concrete at high temperature-an overview, national institute of standards and technology. *High Performance Concrete 6th International Symposium Proceeding*, 1.

Pimienta, P.(2000).Le comportement aufeudes BHP, synthèse destravauxdu projet national surles bétons ahautes performances In *Pressesdel'ecole nationale des pontset chaussées* (pp.77-124*).*BHB.

Pliya, B. (2010). *Contribution des fibres de polypropylène et métalliques à l'amélioration du comportement du béton soumis à une température élevée*. Doctoral dissertation, Cergy-Pontoise).

Sana, T., &Abdul, H.(2013).Effect of elevated temperatures on compressive and tensile strengths of reactive powder concrete. *Journal of Engineering and Development*, *17*(4), 259-278.

Serbescu, A., Guadagnini, M.,& Pilakoutas, K. (2013). Mechanical characterization of basalt FRPR ebars and long-term strength predictivemodel. *Journal of Composites for Construction*, *19*(2), 04014037.

Serrano, R., Cobo, A., Prieto, M. I., & de las Nieves González, M. (2016). Analysis of fire resistance of concrete with polypropylene or steel fibers. *Construction and Building Materials*, *122*, 302-309.

Shallal, M. A., & Al-Owaisy, S. R. (2007). Strength and elasticity of steel fiber reinforced concrete at high temperatures. *Journal of Engineering and Sustainable Development*, *11*(2), 125-133.

Sorensen, C., Berge, E., & Nikolaisen, E. B. (2014). Investigation of fiber distribution in concrete batches discharged from ready-mix truck. *International Journal of Concrete Structures and Materials*, *8*(4), 279-287.

Tadepalli, P.R., Mo, Y., & Hsu, T.T.(2013). Mechanical properties of steel fiber concrete. *Magazine of Concrete Research*, 65(8), 462–474.

Tai, Y. S., Pan, H. H., & Kung, Y. N. (2011). Mechanical properties of steel fiber reinforced reactive powder concrete following exposure to high temperature reaching 800 C. *Nuclear Engineering and Design*, *241*(7), 2416-2424.

Tshimanga, M. K. (2007). *Influence des paramètres de formulation sur le comportement à haute température des bétons*. Doctoral dissertation, Cergy-Pontoise.

Wang, H. T., & Wang, L. C. (2013). Experimental study on static and dynamic mechanical properties of steel fiber reinforced lightweight aggregate concrete. *Construction and Building Materials*, *38*, 1146-1151.

Yermak, N., Pliya, P., Beaucour, A. L., Simon, A., & Noumowé, A. (2017). Influence of steel and/or polypropylene fibres on the behaviour of concrete at high temperature: Spalling, transfer and mechanical properties. *Construction and Building Materials*, *132*, 240-250.

Author Information

Atlaoui Djamal
Department of Civil Engineering, Laboratory of Modeling of and Structures in Civil Engineering (L2MSGC), University 'Mouloud Mammeri' of Tizi Ouzou, 15000, Algeria.
Contact e-mail: djamal.atlaoui@ummto.dz

Bouafia Youcef
Department of Civil Engineering, Laboratory of Modeling of Materials and Structures in Civil Engineering (L2MSGC), University 'Mouloud Mammeri' of Tizi Ouzou, 15000, Algeria.

Ghouilem Kamel
Department of Civil Engineering, Faculty of Construction Engineering Laboratory of Geomaterial, Environment and Amenagement (LGEA), University of Mouloud Mammeri, Tizi Ouzou, Algeria.

To cite this article:

Djamal, A., Youcef, B. & Kamel, G. (2024). The effect of high temperatures on the compression and flexural characteristics of recycled fiber-reinforced concrete. *The Eurasia Proceedings of Science, Technology, Engineering & Mathematics (EPSTEM), 32,* 575-590.

The Eurasia Proceedings of Science, Technology, Engineering & Mathematics (EPSTEM)
ISSN: 2602-3199

The Eurasia Proceedings of Science, Technology, Engineering & Mathematics (EPSTEM), 2024

Volume 32, Pages 591-603

IConTES 2024: International Conference on Technology, Engineering and Science

Load Insertion Influence on the Hysteresis Loop of a Single-Phase Transformer under Transients

Abdelghani Yahiou
University of Bouira

Souhila Abdoun
University of Bouira

Amar Maafa
University of Bouira

Hacene Mellah
University of Bouira

Badreddine Babes
Research Center in Industrial Technologies - CRTI

Hamza Sahraoui
University of Chlef

Hocine Terrab
General Electric Power

Abdelhafid Bayadi
University of Setif

Abstract: The hysteresis cycle is one of the main parameters that define the characteristics of materials used in the design of transformer. This parameter is strongly influenced by the transient regime of the transformer which has a great influence on the operating point of the transformer. The idea of this paper is original and represents an initiation to a research project aimed at visualizing the effect of load insertion on the characteristics (hysteresis loop) of the iron core. The main objective of this article is to address the influence of this load on the hysteresis loop of a single-phase transformer in transient mode, i.e. in inrush current, in terms of position, surface or size. First, a general study of the electromagnetic characteristics of the transformer iron core will be presented. Then, using the ATP_EMTP program, the simulation is performed to visualize the relationship between the hysteresis loop and the load insertion on the secondary side of the transformer in transient mode. Finally, the results show the decrease in the surface of the hysteresis loop and their shift from the origin of the axes following the increase in the load.

Keywords: Transformer, Inrush current, Transient regime, Hysteresis loop, Load, ATP_EMTP

Introduction

The hysteresis cycle is one of the main parameters that define the characteristics of materials used in the design of transformer. This parameter is strongly influenced by the transient regime of the transformer which has a great influence on the operating point of the transformer. Transformer transient phenomenon are caused by the saturation of a power transformer due to variations in the magnetization voltage (Yahiou, 2012; Yahiou et al., 2018a). When an unloaded transformer is energized, a transient phenomenon called inrush current may appear in the excited circuit side. Therefore, all necessary studies and investigations must be carried out in order to anticipate a suitable protecting system for the transformer.

There are many works in the literature that fall into this framework, such as those studied by the authors in Bertagnolli (1996), Specht (1951), Holcomb (1961). Where many numerical and analytical tools have been developed. Furthermore, the majority of studies on the field of transformer transient study are in the context of finding effective and inexpensive techniques to reduce this inrush current. Among these methods, the technique proposed in Cano-González et al. (2015, 2017). Where four different methods to reduce the inrush current are compared; The obtained result from the four techniques is to collect the ability to use the circuit breakers with an independent pole, as well as the ability to deem the residual flux in the iron core of the transformer. The measurement and simulation studies performed in Brunke et al. (2001a, 2001b) is one of the pioneering works, simulation and measurements, in the area of reducing the inrush current in three and single phase transformer. Taking into account the residual flux values, the authors propose three schemes in this technique, by closing the circuit breakers in a synchronous, quick, and delayed manner. In Cheng et al. (2004) the authors utilize the technique of making a modification in the transformer bobbin. This is intended to decrease the inrush current peaks by increasing the transient inductance value. Taking into account the phase shift between the three phases of the transformer during its energization, the authors introduce in the work presented in Arand (2013); Abdulsalam et al. (2017); Abdelsalam et al. (2015); Cui et al. (2005), a resistance between the ground and the transformer neutral. The authors in Xu et al. (2005) with taking into account the switching moment, are used the reversed flux technique for investigating the reduction of the inrush current using an existed photovoltaic generator.

In Schramm et al. (2011), the authors present several methods to protect and reduce the various interactions of transformer relays as well as the introduction and removal of the load in a random or studied manner by the circuit breakers in Rudez et al. (2016) have depended on differential equations and formal methods for solving them, based on the equivalent circuit represented using the state space equation. Pontt et al. (2007) have raised the resistance value of the transformer winding, using the transformer tap changer to reduce the effect of the inrush current power system as well as mitigating its peak value. The main contribution of paper Yahiou et al. (2018d) is to apply the technique proposed by the same authors of Yahiou et al. (2019) in the laboratory using a real-time measurement setup to eliminate the sympathetic inrush current, the latter results from the interaction of two transformers, one is energized and the second is already supplied. Moreover, there is a comparison of the results (measurement and simulation) to prove the efficacy of the proposed technique found in Yahiou et al. (2019). To mitigate also this sympathetic inrush current. Abdelsalam et al. (2016) presented an important technique in the field of inrush current mitigation, especially by using renewable energies (photovoltaic (PV)), where the reverse flux is applied. The authors in Danikas et al. (2020) presented a review of some factors which affect the resistance during breakdown of transformer oil. In (Le & Vu, 2019), the authors have exposed a generator differential protection relay system, its disadvantages and its advantages. This system is dual slope from Areva P343, ABB REG670, SEL300G and GE G60. The authors in Fan et al. (2016) a real power transformer is used in experiments, also the authors built a UHF-PD detection system.

Because the supply of the transformer primary, under its nominal voltage is accompanied by a transient regime during which the intensity of the inrush current can take values much higher than those of the nominal intensity, depending on the instant of appreciation of the voltage and the induction remanence of the magnetic circuit. Hence, the need to predetermine through the study of the transient regime, the approximate value of this inrush current which may be greater than or equal to several times the current of the transformer (Sahoo et al., 2019). Holcomb (1961) is considered among the first who raised the idea of the inrush current calculation, but without going far, where the author have studied only a method to compute the peak inrush current for the first and any succeeding cycle, without considering its effect on hysteresis loop.

In reference Faiz and Saffari (2010) the authors used a developed model to estimate the inrush current and hysteresis loop. However, the authors did not make a comparison between the relationships of the position of the hysteresis loop wave according to the corresponding inrush current. Even in (Abdulsalam et al., 2005b; Oyanagı et al., 2018). It is the same weakness observed in this works, where the authors estimate the saturation curve from the inrush current waveform. This major drawback of this previous works has been studied and accomplished in the present work, where the comparison has been made between different effects of transformer energization on the nature of iron core.The authors in Altun et al. (2021). Have exploited a real model of a transformer to study different phenomena such as the application of the nonlinear load. However, the authors have not totally studied the load influence in all operational modes. In other words, the authors limit their study to the load effects on the steady-state regime.

The study presented in this article is a continuation of the study presented in the articles (Yahiou, 2022a; Yahiou et al., 2022b). The main objective of this work is to study the influence of the load on the hysteresis cycle of a single-phase 2 kVA transformer. This study will carried out using a no-load and load simulation circuit under the software ATP/EMTP (Alternative Transient Program). Firstly, using measurement setup with a data acquisition system, the parameters of the transformer and the characteristics of the magnetizing branch (inductance and resistance) will identified. After a simulation will be carried out to arrive at a specific study of the influence of the load on the surface and the position of the hysteresis cycle of a single-phase transformer using the software ATPDraw. In order to observe the changes in the shape and location of the hysteresis loop caused by different values of the resistive load (R), for the transformer under transient inrush current.

Transformer Parameters Identification and Iron Core Characteristic

The Figure 1 shows real transformer used in the simulation this transformer.

Figure 1. Real used transformer

Table 1 shows the characteristics of the used transformer.

Table 1. Nameplate data of the transformer

Power	Frequency	Phase	Voltage Ration	Turn	current Ration	Class (isol)
2000 VA	50 Hz	01	0.22/0.25 kV	0330/0037 tr	9.10/080A	E

The calculated parameters of equivalent circuit for the transformer of figure 1 are presented in the following Table 2.

Table 2. Equivalent circuit parameters

Parameter	Value
Magnetizing resistance R_m	2847,05 Ω
Magnetizing reactance X_m	609,72 Ω
Series resistance $R_{éq}$	3,48 Ω
Series reactance $X_{éq}$	2,69 Ω

The study of any transformer transient regime such as inrush current requires careful modeling of the iron core nonlinearities.

Iron Core Nonlinearities

The dynamic behavior of a transformer can be characterized in different ways. Taking into account the saturation of the core, and therefore the non-linearity, implies that the functions to be solved will be more complicated in comparison with linear models. Figure 2 presents the magnetizing curve $\lambda = f(i_l)$ which presents the iron core inductance. Figure 3 shows the resistance characteristic $v = f(i_{lr})$. These figures are used as data in the realized work found in (Yahiou et al., 2018d).

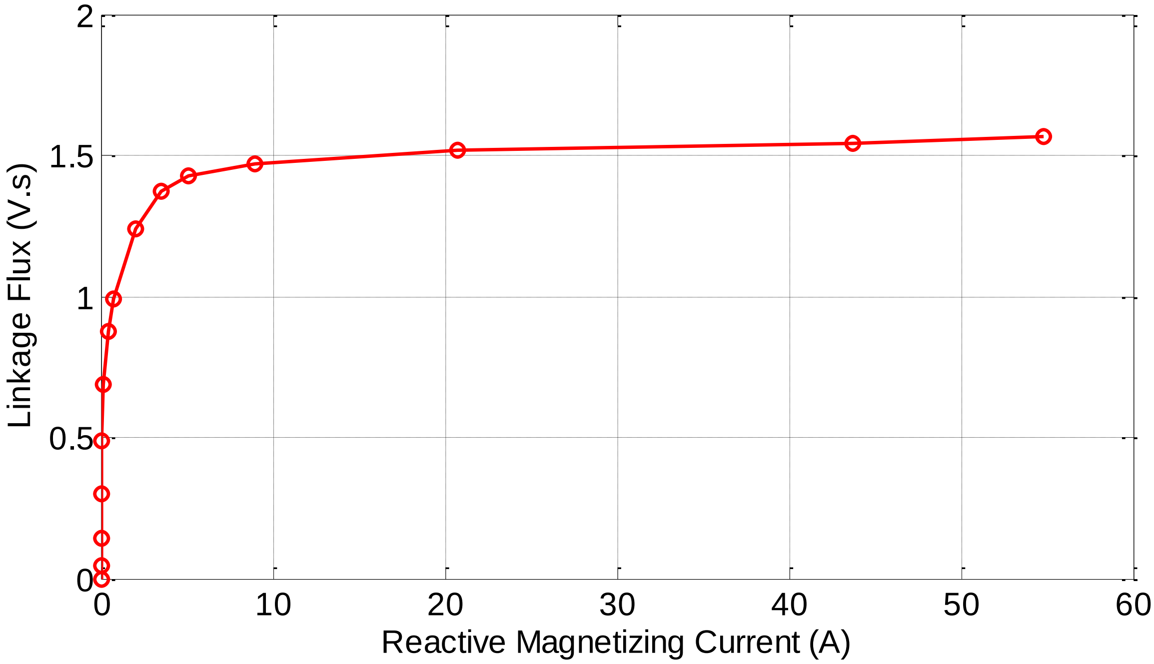

Figure 2. Saturation curve (nonlineair inductance) $\lambda = f(i_l)$ (Yahiou et al., 2018d).

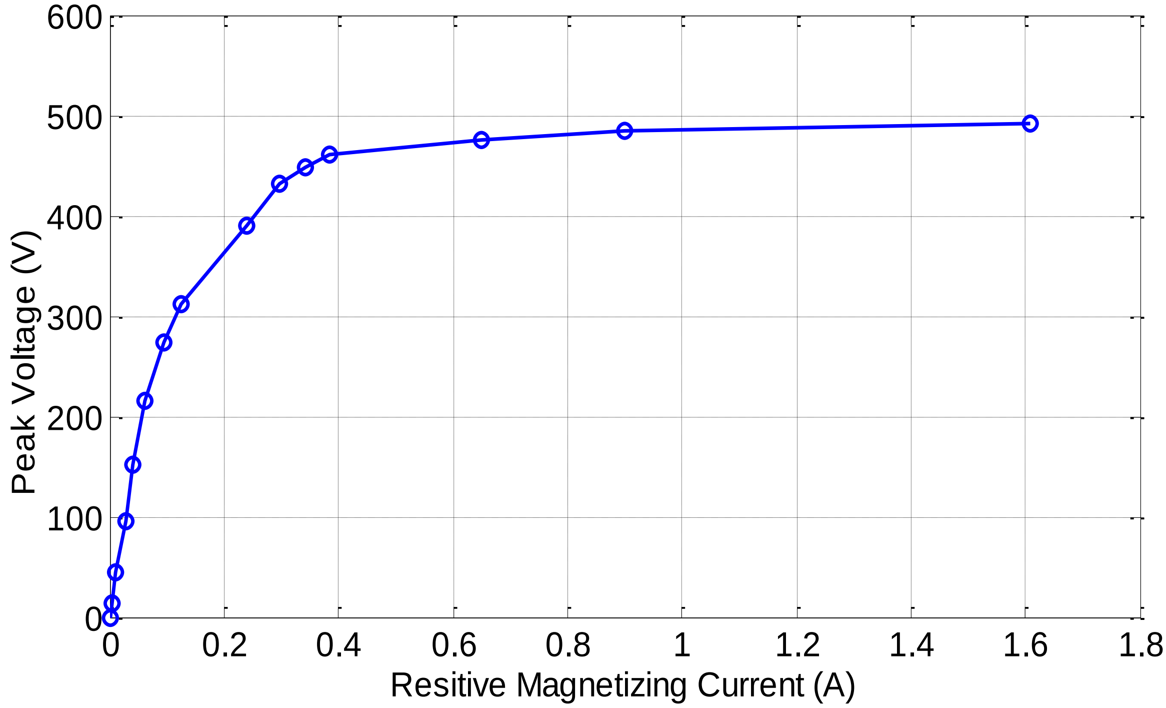

Figure 3. Resistance characteristic $\lambda = f(i_r)$ (Yahiou et al., 2018d)

The data found in Figures 2 and 3 are calculated by the improved technique presented by the authors in (Yahiou et al., 2019; Yahiou & Bayadi, 2012). And they have been inserted in the saturable transformer found in ATP-EMTP program to simulate the ferroresonance under different conditions.

Experimental Setup and dSPACE Interface

Figure 4 shows a measurement setup photo used to extract the parameters of the used single-phase transformer, as well as for measure the data used to estimate the saturation curve and the curve representing the nonlinear resistance.

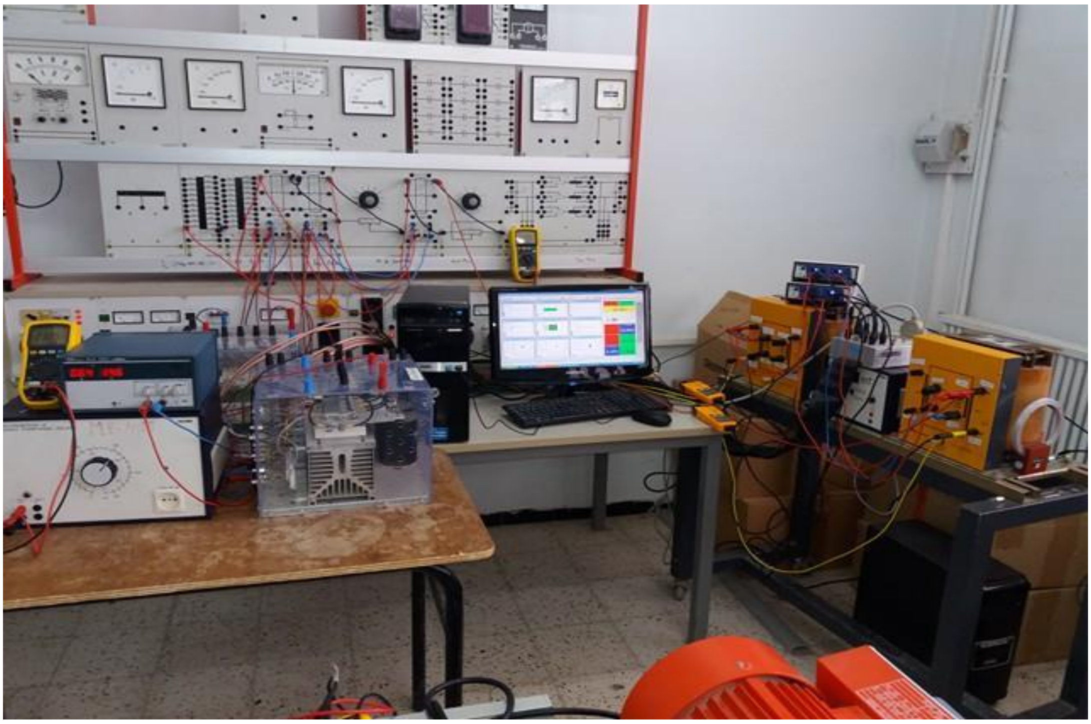

Figure 4. Laboratory setup for data measurement.

To visualize the different signals and acquisition values, an interface is created in the PC as shown in figure 5.

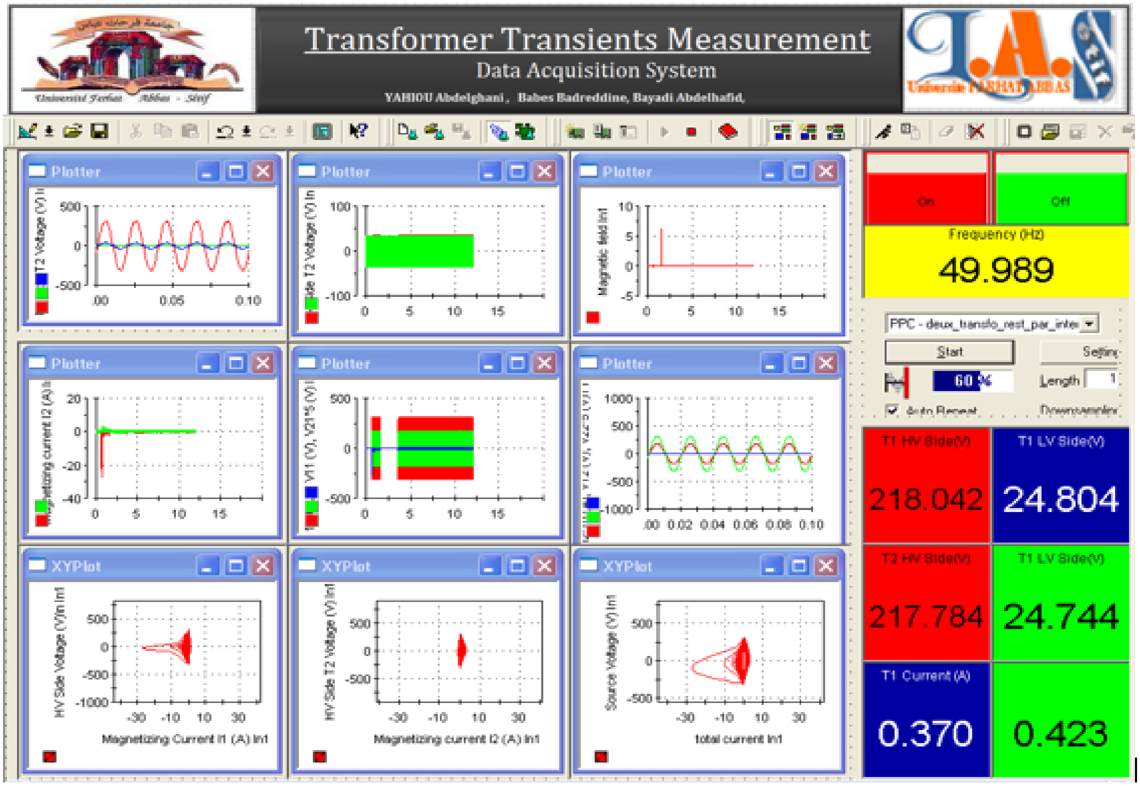

Figure 5. Data acquisition interface.

Simulation of Load Influences on Hysteresis Loop

The study of this paper consists of carrying out numerical simulations for a 2 kVA transformer, i.e. nonlinear phenomenon, which is supplied with a voltage of 220V, as shown in figure 6. The elaborated model in an electrical circuit to observe the behaviour of the transformer is implemented for both next cases:

First Case: Unloaded Transformer

The goal is to visualize the hysteresis cycle of a 2 kVA transformer without load (no-load) and its waveform for transient and steady state. Figure 6 shows the simulation block under ATPDraw software, which contains a sinusoidal power supply, a transformer, the magnetizing branch which includes a nonlinear inductance and resistance (its characteristics are those of Figure 2 and 3 respectively) and the series elements of the transformer.

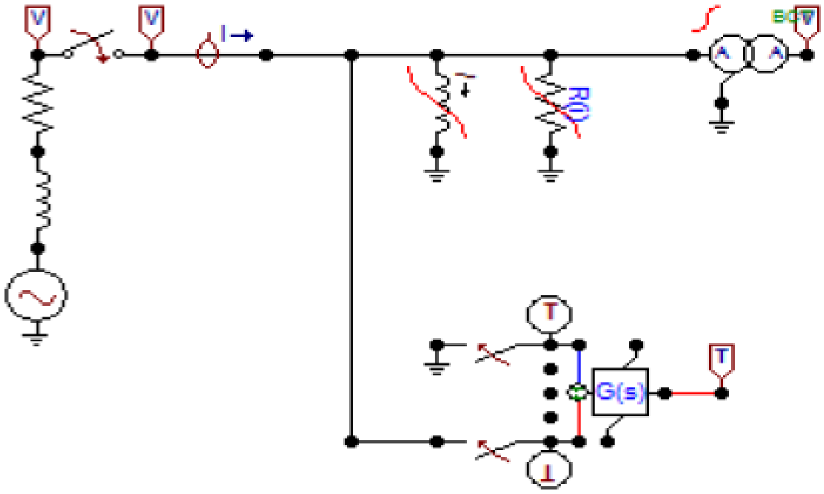

Figure 6. ATPDraw simulation diagram for unloaded transformer.

In steady state, when using a voltage source at the primary of the test transformer with the secondary in open circuit, we obtain the magnetizing current waveform presented in Figure 7.

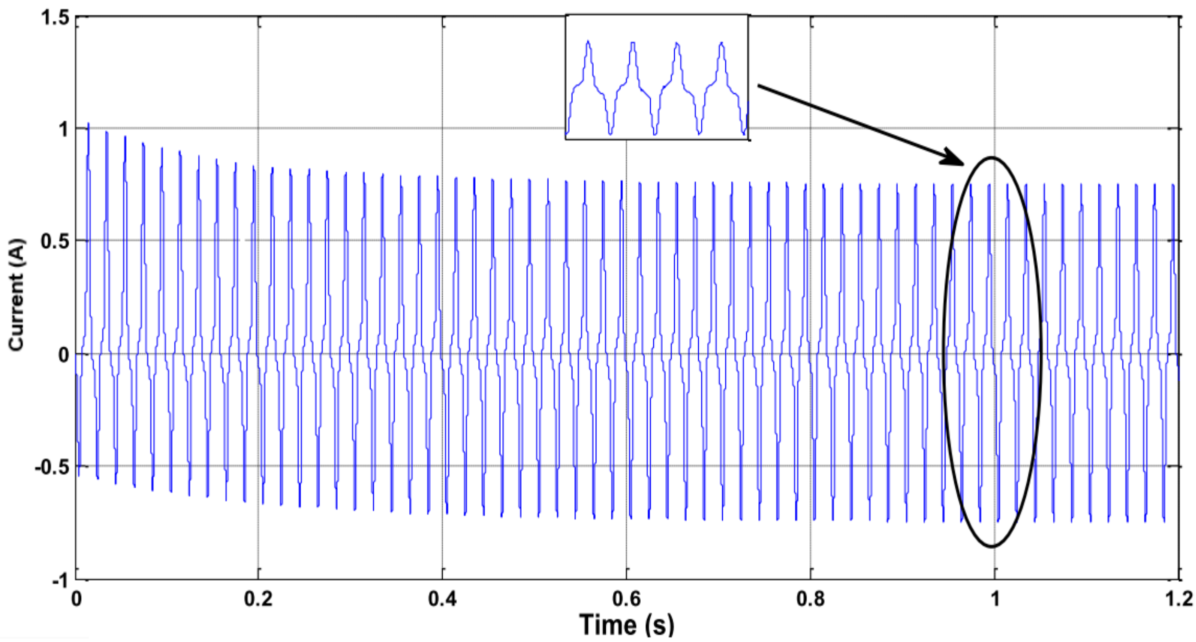

Figure 7. Magnetizing current for steady state with unloaded transformer.

Noting that the current waveform in the no-load steady state is non-sinusoidal distorted due to harmonics caused by the transformer core nonlinearity. In transient regime (using the circuit breaker), when using a voltage source at the primary of the test transformer with the secondary in open circuit, we obtain the simulated transient inrush current waveform presented in Figure 8.

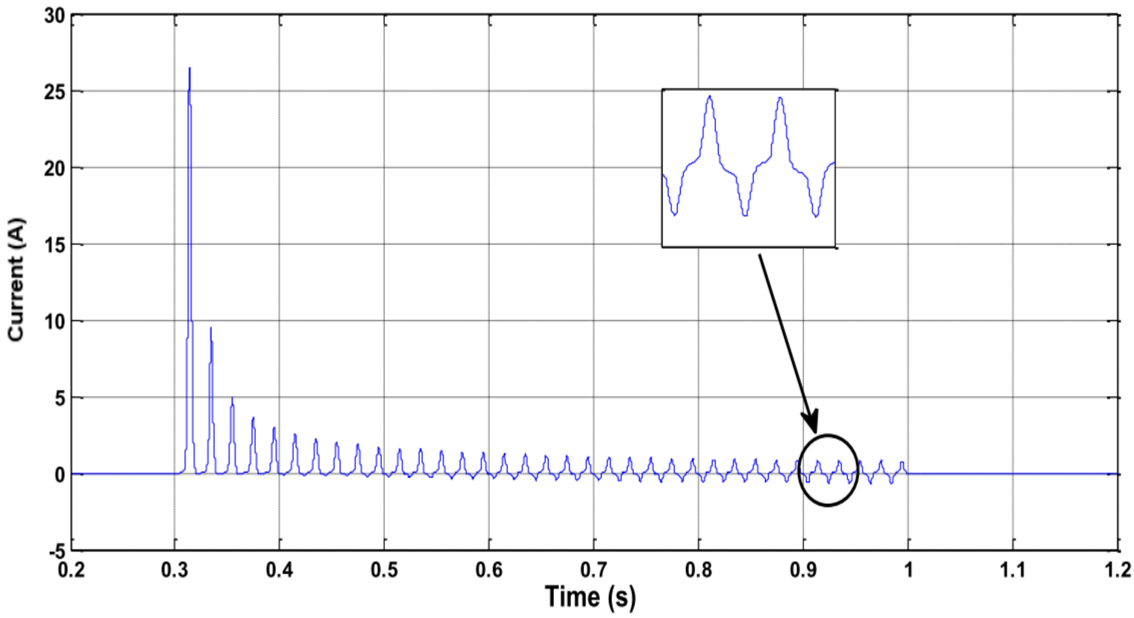

Figure 8. Transient inrush current for unloaded transformer

An important observation is that the inrush current during the transient regime has much higher peaks compared to the magnetizing current in the steady state. These simulations highlight the non-sinusoidal waveforms of the currents during the transient regime, as well as during the steady state for the unloaded transformer, due to the presence of harmonics. These harmonics are the result of the non-linear behavior of the transformer magnetic circuit. Figure 09 shows the hysteresis loop in steady state for a 2 kVA unloaded transformer, this cycle is the variation of the flux as a function of the magnetizing current.

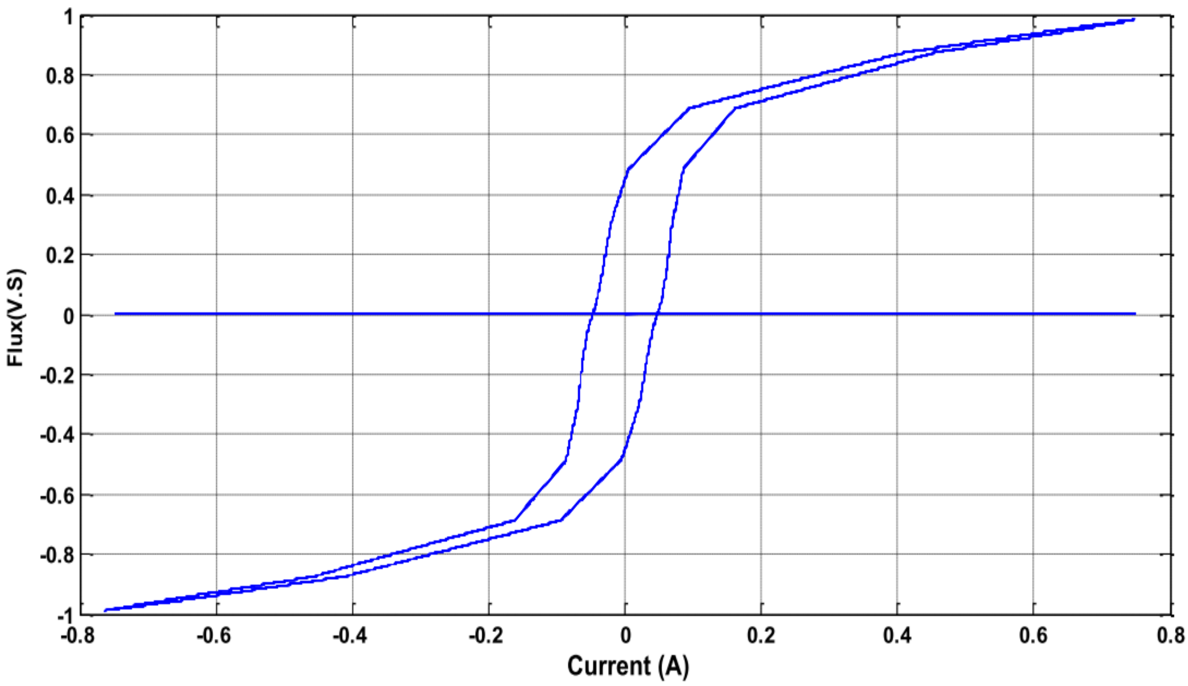

Figure 9. Hysteresis loop in steady state for unload transformer.

Figure 10 shows the hysteresis loop in transient regime for a 2 kVA unloaded transformer, this cycle is the variation of the flux as a function of the magnetizing current.

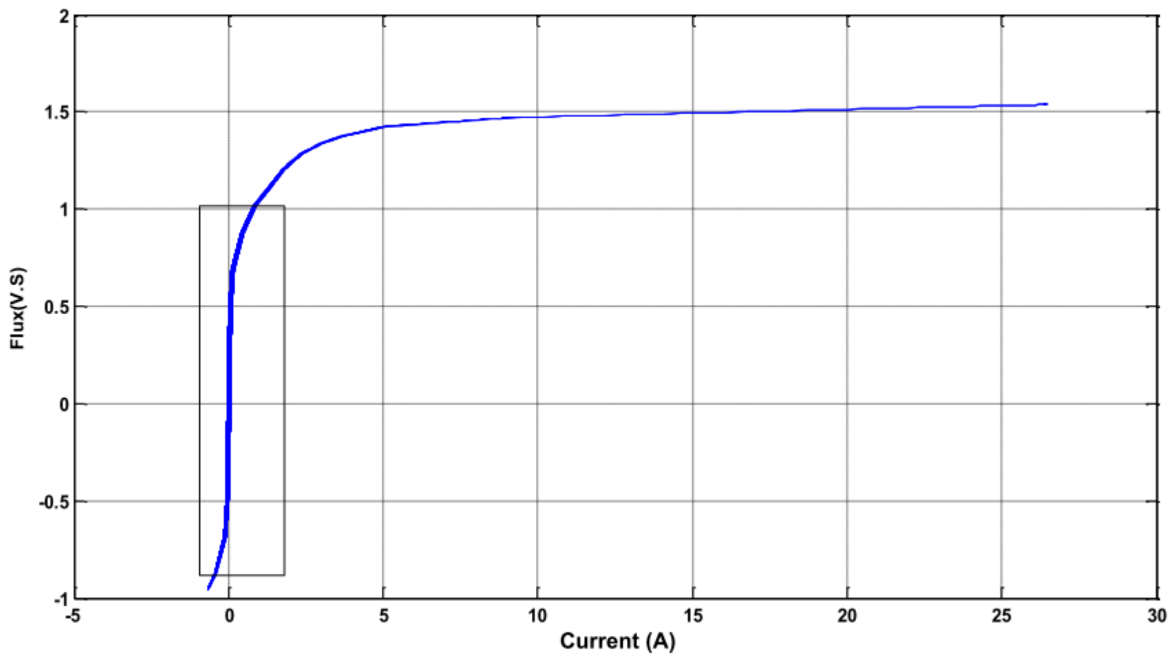

(a)

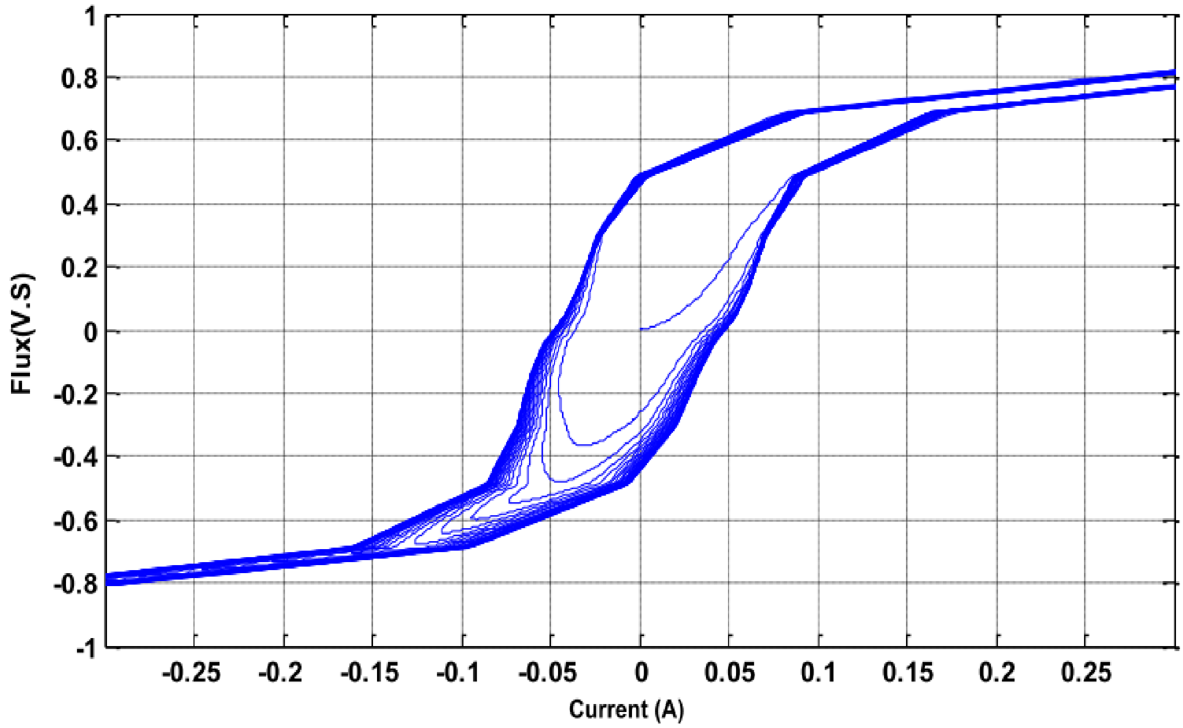

(b)

Figure 9. Hysteresis loop in transient regime for unload transformer.
(a) Total hysteresis loop (b) Zoom for hysteresis loop

Second Case: Loaded transformer

The aim is to apply different loads with different values to observe the influence of this variation on the transformer hysteresis loop in transient regime. Figure 10 shows the simulation block under ATPDraw software, which contains a sinusoidal power supply, a transformer, the magnetizing branch which includes a nonlinear inductance and resistance (its characteristics are those of Figure 2 and 3 respectively) and the series elements of the transformer. Here the resistive load is added to the secondary of the transformer.

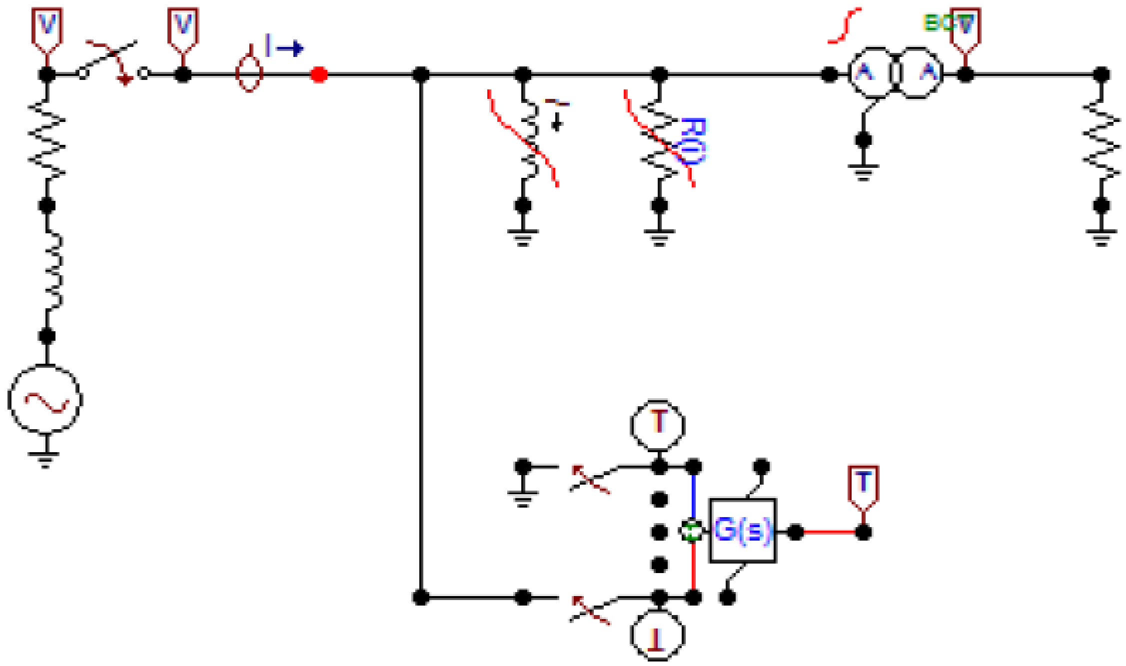

Figure 10. ATPDraw simulation diagram for loaded (resitiance) transformer.

Figure 11 shows a comparison between the current waveforms and their values in the transient and steady state after applying a resistive load with different values (the nominal load multiplied by 0.5, 0.8 and 1.2).

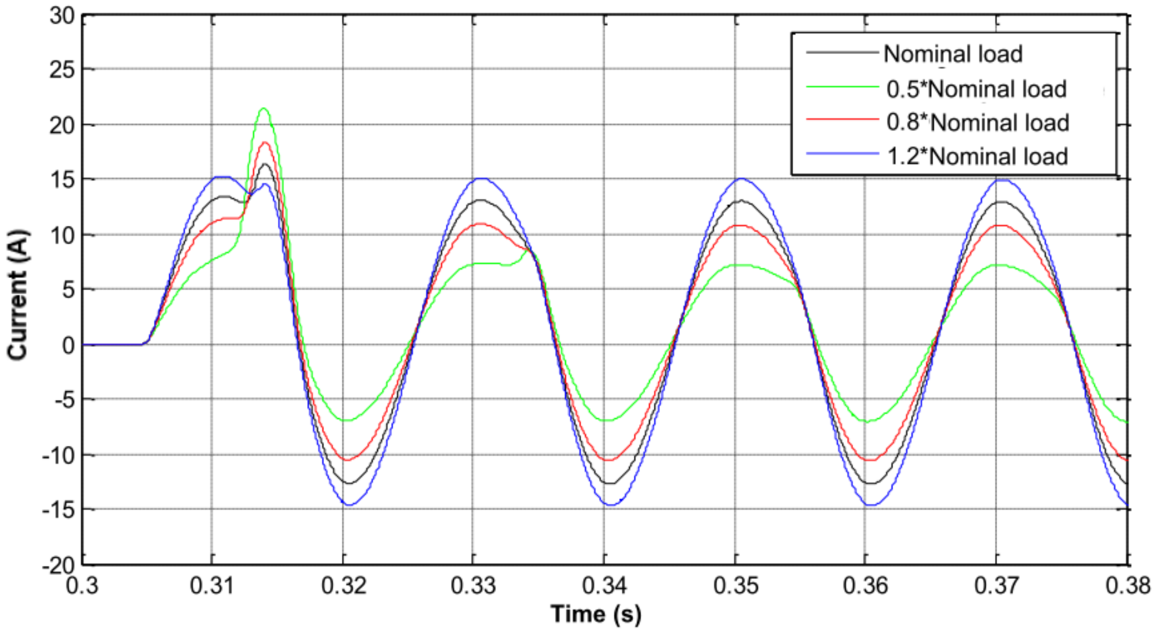

Figure 11. Primary current waveform with a resistive load.

- If the load is at nominal value, the peak inrush current in transient state is 16.37 A, and 12.87 A in steady state.
- If the load is 50 % of the nominal load value, the peak current in transient state equal to 21.39 A, and 7.128 A in steady state.
- If the load is 80 % of the nominal load value, the peak current in transient state equal to 18.35 A, and 10.72 A in steady state.
- If the load is 120 % of the nominal load value, the peak current in transient state equal to 15.25 A, and 14.86 A in steady state.

Figure 12 shows the hysteresis loop waveform for purely resistive load in transient operation.

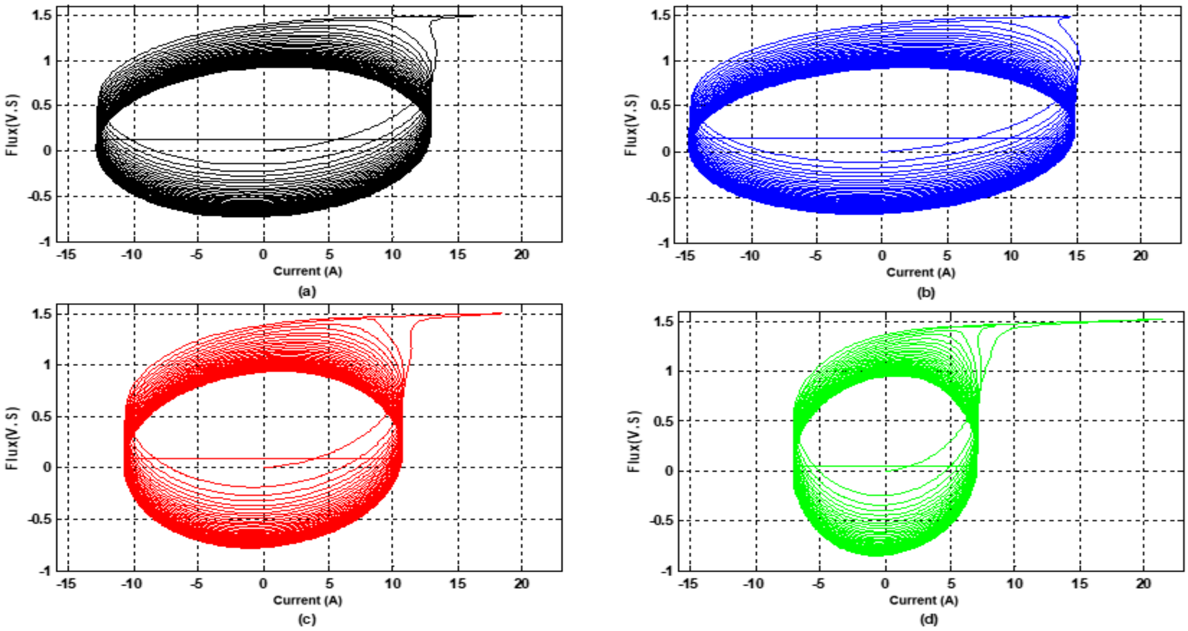

Figure 12. Hysteresis loop of 2 kVA transformer for resistive load.
(a) Nominal load value. (b) 120 % of the nominal load value.
(b) 80 % of the nominal load value. (d) 50 % of the nominal load value.

Since the aim is to observe the hysteresis loop during the appearance of transient inrush current, it was sufficient to show only three cycles of hysteresis loop (Figure 13).

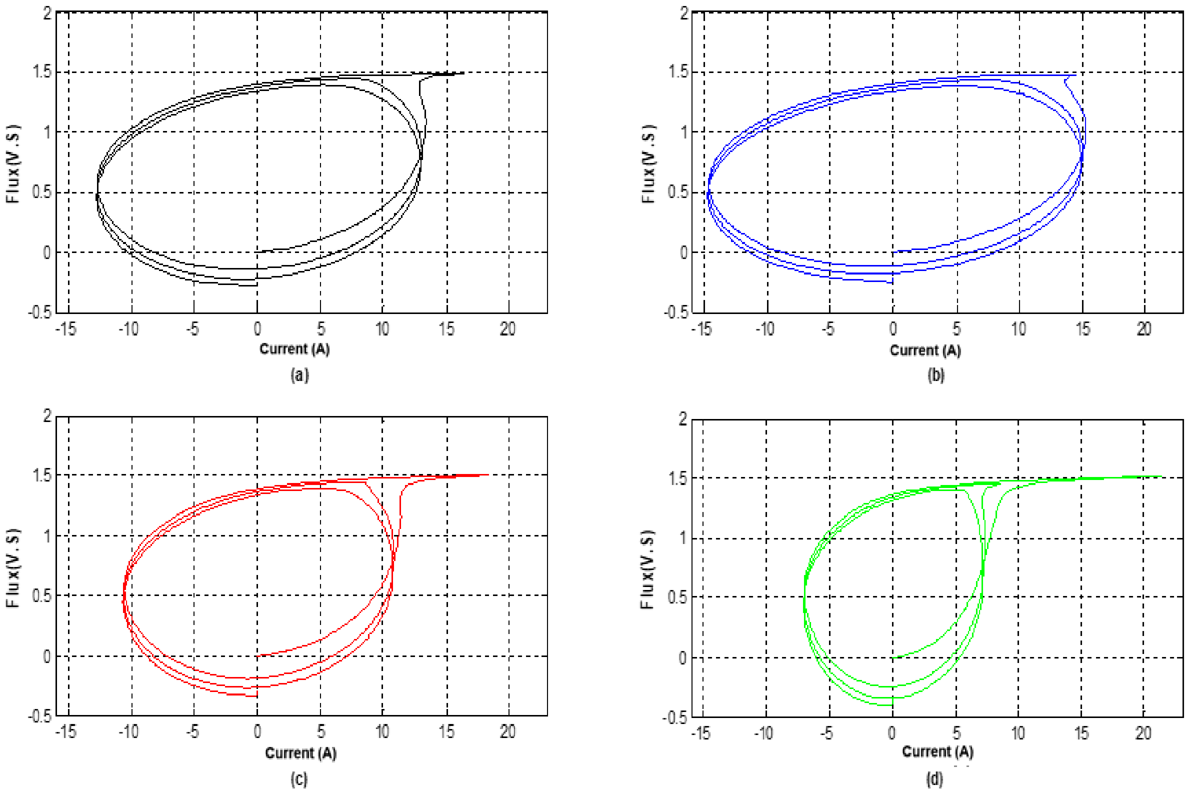

Figure 13. Hysteresis loop of 2 kVA transformer for resistive load (three cycles).
(a) Nominal load value. (b) 120 % of the nominal load value.
(c) 80 % of the nominal load value. (d) 50 % of the nominal load value.

1. Nominal load

The distorted hysteresis cycle with a positive saturation phase follows the inrush current peak (16.37A) corresponding to a flux value (1.49 V.s)

2. 120% of the Nominal load value

The distorted hysteresis cycle with a positive saturation phase follows the inrush current peak (15.25A) corresponding to a flux value (1.4851 V.s)

3. 80% of the Nominal load value

The distorted hysteresis cycle with a positive saturation phase follows the inrush current peak (18.35A) corresponding to a flux value (1.5044 V.s)

4. 50% of the Nominal load value

The distorted hysteresis cycle with a positive saturation phase follows the inrush current peak (21.39A) corresponding to a flux value (1.5173 V.s)

By applying different values of the resistive load (100%, 120%, 80% and 50%), it is clear that each time the load value is reduced, the transient regime increases, resulting in a decrease in the cycle area. The simulation results show that the value of the resistive load has an influence on the surface and the positioning of the hysteresis cycle according to the origin. This suggests that the transformer load has a direct influence on the hysteresis cycle waveform.

Conclusion

The work presented in this article makes a study on the influence of the load on the hysteresis loop of a 2 kVA transformer. To visualize this influence it is necessary to identify the transformer parameters and determine the iron core characteristics. Using the ATPDraw program, the simulations results are extracted with adding the resistive load at their nominal value, and for some percentage (120%, 80% and 50%). The results show that it is clear that the load directly affects the hysteresis cycle, and this is explained by the restriction and the shift of the hysteresis cycle caused by the load, this relationship results in a decrease in the surface and a displacement of the hysteresis cycle following the decrease in the load. The results of these simulations show that the value of the load driven has an influence on the surface and the positioning of the hysteresis cycle. The results of the simulation carried out in this styudy show that each time the value of the load is increased there is a decrease in the surface of the hysteresis cycle. This study can complement by the following perspectives:

- It would be interesting to apply the results of this study in a laboratory environment in order to perform experiments and compare the simulation results with the experimental results. This would allow to validate the models and methods used, as well as to identify possible differences or errors.
- The obtained results could have extrapolated and applied to larger power transformers, which would be of great interest in the field of large-scale power system engineering.

Scientific Ethics Declaration

The authors declare that the scientific ethical and legal responsibility of this article published in EPSTEM Journal belongs to the authors.

Acknowledgements or Notes

* This article was presented as an oral presentation at the International Conference on Technology, Engineering and Science (www.icontes.net) held in Antalya/Turkey on November 14-17, 2024.

References

Abdelsalam, H. A., & Abdelaziz, A. Y. (2015). A new strategy for selection of switching instant to reduce transformer inrush current in a single-phase grid-connected photovoltaic system. *Electric Power Components and Systems*, *43*(11), 1297–1306.

Abdelsalam, H. A., Ahmed, A., & Abdelaziz, A. Y. (2016). Mitigation of transformer inrush current using PV energy. *Recent Advances in Communications and Networking Technology, 4*(2), 95–102.

Abdulsalam, S. G., & Xu, W. (2007). A sequential phase energization method for transformer inrush current reduction andamp; mdash; transient performance & practical considerations. *IEEE Transactions on Power Delivery*, *22*(1), 208–216.

Abdulsalam, S., Xu, W., Neves, W., & Liu, X. (2005b). Estimation of transformer saturation characteristics from inrush current waveforms. *IEEE Transactions on Power Delivery, 21*(1), 170–177.

Altun, H., Sunter, S., & Aydogmus, O. (2021). Modeling and analysis of a single-phase core-type transformer under inrush current and nonlinear load conditions. *Electrical Engineering, 103*(6), 2961–2972.

Arand, S. J. (2013). Transformer inrush current mitigation using controlled switching and magnetic flux shunts. *International Journal of Energy and Power Engineering*, *2*(2), 46–53.

Bertagnolli, G. (1996). *Short-circuit duty of power transformers: The ABB approach*. Golinelli.

Brunke, J. H., & Frohlich, K. J. (2001a). Elimination of transformer inrush currents by controlled switching. I. theoretical considerations. *IEEE Transactions on Power Delivery*, *16*(2), 276–280.

Brunke, J. H., & Frohlich, K. J. (2001b). Elimination of transformer inrush currents by controlled switching. II. application and performance considerations. *IEEE Transactions on Power Delivery*, *16*(2), 281–285.

Cano-González, R., Bachiller-Soler, A., Rosendo-Macías, J. A., & Álvarez-Cordero, G. (2017). Controlled switching strategies for transformer inrush current reduction: A comparative study. *Electric Power Systems Research*, *145*, 12–18.

Cano-González, R., Bachiller-Soler, A., Rosendo-Macías, J. A., & Álvarez-Cordero, G. (2015). Inrush current mitigation in three-phase transformers with isolated neutral. *Electric Power Systems Research*, *121,* 14–19.

Cheng, C.-K., Liang, T.-J., Chen, J.-F., Chen, S.-D., & Yang, W.-H. (2004). Novel approach to reducing the inrush current of a power transformer. *IEE Proceedings - Electric Power Applications*, *151*(3), 289–295.

Cui, Y., Abdulsalam, S. G., Chen, S., & Xu, W. (2005). A sequential phase Energization technique for transformer inrush current reduction— part I: Simulation and experimental results. *IEEE Transactions on Power Delivery, 20*(2*)*, 943–949.

Danikas, M., Sarathi, R., Morsalin S. (2020). A short review of some of the factors affecting the breakdown strength of ınsulating oil for power transformers. *Engineering, Technology and Applied Science Research*, *10* (3), 5742–5747.

Faiz, J., & Saffari, S. (2010). Inrush current modeling in a single-phase transformer. *IEEE Transactions on Magnetics*, *46*(2), 578–581

Fan, H., Hu, J., Liu, H., Yin, Y., & Danikas, M. (2016). UHF PD experiments on real power transformer and its frequency characteristics results. *Engineering Technology and Applied Science Research, 6*(1), 906–912.

Holcomb, J. E. (1961). Distribution transformer magnetizing inrush current. *Transactions of the American Institute of Electrical Engineers. Part III: Power Apparatus and Systems*, *80*(3), 697–702.

Le, K. H., & Vu, P. H. (2019). Performance evaluation of a generator differential protection function for a numerical relay. *Engineering Technology and Applied Science Research*, *9*(4), 4342–4348.

Oyanagi, R., Noda, T., & Ichikawa, M. (2018). A method for estimating the current–flux curve of a single-phase transformer for electromagnetic transient simulations of inrush currents. *Electrical Engineering in Japan, 204*(2), 13–24.

Pontt, J., Rodriguez, J., San Martin, J., & Aguilera, R. (2007). Mitigation of sympathetic interaction between power transformers fed by long overhead lines caused by inrush transient currents. *2007 IEEE Industry Applications Annual Meeting* (pp.1360-1363). IEEE.

Rudez, U., & Mihalic, R. (2016). Sympathetic inrush current phenomenon with loaded transformers. *Electric Power Systems Research*, *138,* 3–10.

Sahoo, S., Abeywickrama, N., Bengtsson, T., & Saers, R. (2019). Understanding the sympathetic ınrush phenomenon in the power network using transformer explorer.*2019. IEEE 4th International Conference on Condition Assessment Techniques in Electrical Systems (CATCON), 352,* 1–5.

Schramm, S., Sihler, C., Rosado S., (2011). Limiting sympathetic interaction between transformers caused by inrush transients. *International Conference on Power Systems Transients IPST*, 11IPST053.

Specht, T. R. (1951). Transformer magnetizing inrush current. *Transactions of the American Institute of Electrical Engineers*, *70*(1), 323–328.

Xu, W., Abdulsalam, S. G., Cui, Y., & Liu, X. (2005). A sequential phase energization technique for transformer inrush current reduction—part II: Theoretical analysis and design guide. *IEEE Transactions on Power Delivery*, *20*(2*),* 950–957.

Yahiou, A., & Bayadi, A. (2012). investigation of magnetizing inrush current in single-phase power transformer. *7th International Conference on Electrical Engineering (CEE'12),* 8-10.

Yahiou, A., Adi, A. B., Mellah, H., Abid, M., R'gueyeg, M. S., & Merabet, A. O. (2022b). Inrush current influence on the hysteresis loop of a single-phase transformer. *19th International Multi-Conference on Systems, Signals and Amp; Devices (SSD)* (pp.18171-18179). IEEE.

Yahiou, A., Bayadi, A., & Babes, B. (2018a). Point on voltage wave switching for sympathetic inrush current reduction. *2018 International Conference on Applied Smart Systems (ICASS)*.

Yahiou, A., Bayadi, A., & Babes, B. (2018d). Mitigation of sympathetic inrush current in transformer using the technique of point on voltage wave control switching. *International Conference on Communications & Electrical Engineering (ICCEE), 20,* 1–6.

Yahiou, A., Bayadi, A., & Babes, B. (2019). Modified method for transformer magnetizing characteristic computation and point-on-wave control switching for inrush current mitigation. *International Journal of Circuit Theory and Applications*, *47*(10), 1664–1679.

Yahiou, A., (2012). Contribution to the study and analysis of transformers transient : case of inrush current, M.Sc thesis, University of Sétif, Sétif, Algeria,.

Yahiou, A., Mellah, H., Bayadi, A., & Abid, M. (2022a). Effects of inrush current on the hysteresis loop and load influences on the transient current of a single-phase transformer. *Engineering Technology and Applied Science Research, 12*(5), 9258–9264.

Author Information

Abdelghani Yahiou
Department of Electrical Engineering, University of Bouira, Algeria.
Contact e-mail: *abdelghani.yahiou@univ-bouira.dz*

Souhila Abdoun
Department of Electrical Engineering, University of Bouira, Algeria.

Amar Maafa
Department of Electrical Engineering, University of Bouira, Algeria.

Hacene Mellah
Department of Electrical Engineering, University of Bouira, Algeria.

Badreddine Babes
Research Center in Industrial Technologies - CRTI P.O.Box 64, Cheraga 16014, Algiers, Algeria

Hamza Sahraoui
Department of Electrical Engineering, University of Chlef, Algeria.

Hocine Terrab
General Electric Power, Algeria

Abdelhafid Bayadi
Automatic Laboratory of Setif (LAS), University of Setif-1-, Algeria.

To cite this article:

Yahiou, A., Abdoune, S., Maafa, A., Mellah H., Babes B., Sahraoui H., Terrab H., Bayadi, A., (2024). Load insertion influence on the hysteresis loop of a single-phase transformer under transients. *The Eurasia Proceedings of Science, Technology, Engineering & Mathematics (EPSTEM), 32,* 591-603.

The Eurasia Proceedings of Science, Technology, Engineering & Mathematics (EPSTEM)
ISSN: 2602-3199

The Eurasia Proceedings of Science, Technology, Engineering & Mathematics (EPSTEM), 2024

Volume 32, Pages 604-610

IConTES 2024: International Conference on Technology, Engineering and Science

Analysis of Delamination in Statically Indeterminate Steric Frames Subjected to Fixed Support Rotation

Victor Rizov
University of Architecture, Civil Engineering and Geodesy

Abstract: The paper is devoted to the problem of delamination in multilayered steric frames. The attention is focussed on statically indeterminate load-bearing frame structures that are under fixed support rotation. External mechanical loading is not applied on the frames under consideration. Only the stresses and strains induced by the fixed support rotation causes delamination. The layers of the frame are made of structural materials that continuously inhomogeneous in longitudinal direction. Thus, the elastic properties of the layers vary smoothly along the length of the frame portions. Due to steric geometry of the frame, the fixed support rotation generates torsion and bending in the frame portions. Therefore, in this paper we analyze delamination behaviour under combined action of bending and torsion moments. First, the mechanical behaviour of the frame portions is studied by using the equations of equilibrium. Then the strain energy release rate (SERR) is determined by analyzing the frame compliance.

Keywords: Steric frame, Multilayered material, Delamination, Fixed support rotation

Introduction

Steric frames are used as load-bearing engineering structures in various applications in construction, machine-building, shipbuilding, car industry, etc. Multilayered materials are potential candidates for application in various structures (Finot & Suresh, 1996; Rzhanitsyn, 1986; Sy-Ngoc Nguyen et al., 2020; Tokova et al., 2016). When steric frames are made of multilayered engineering materials, delamination fracture behaviour becomes one of the most important issues with great influence on the safety and reliability of structures. For example, in multilayered steric frame structures, the delamination is a frequent cause of a variety of uncertainties like reducing the load-bearing ability, worsening the stability performance, increasing deformations, reducing the life of structures, etc. The rapid growth of a delamination crack under certain conditions even may cause sudden collapse of the entire frame structure. The studies of delamination in pane load-bearing structures (mainly beams) are well documented in the scientific literature (Dolgov, 2005; Hutchinson & Suo, 1992; Rizov, 2018a, Rizov, 2018; Rizov, 2019). However, this is not the case with delamination in steric frames. There are many issues that need exploration when dealing with delamination problem in steric frames.

In this paper, we analyze delamination in a steric multilayered frame structure that is statically indeterminate. The frame layers are with continuous material inhomogeneity along the length. It should be noted here that continuous inhomogeneity is considered since the use of continuously inhomogeneous materials grows fast in many areas of engineering (Gandra et al., 2011; Udupa et al., 2014). The frame is under rotation of the fixed support. Since the frame is statically indeterminate, the fixed support rotation induces stressed and strained state in the frame. Besides, since the frame is steric, the fixed support rotation generates bending, and bending and torsion in the different members of the frame structure. The SERR in the frame is determined by the compliance method. Analysis of the SERR is performed with purpose to evaluate the influence of the fixed support rotation, frame geometry and layer inhomogeneity.

Model of a Steric Frame with Delamination

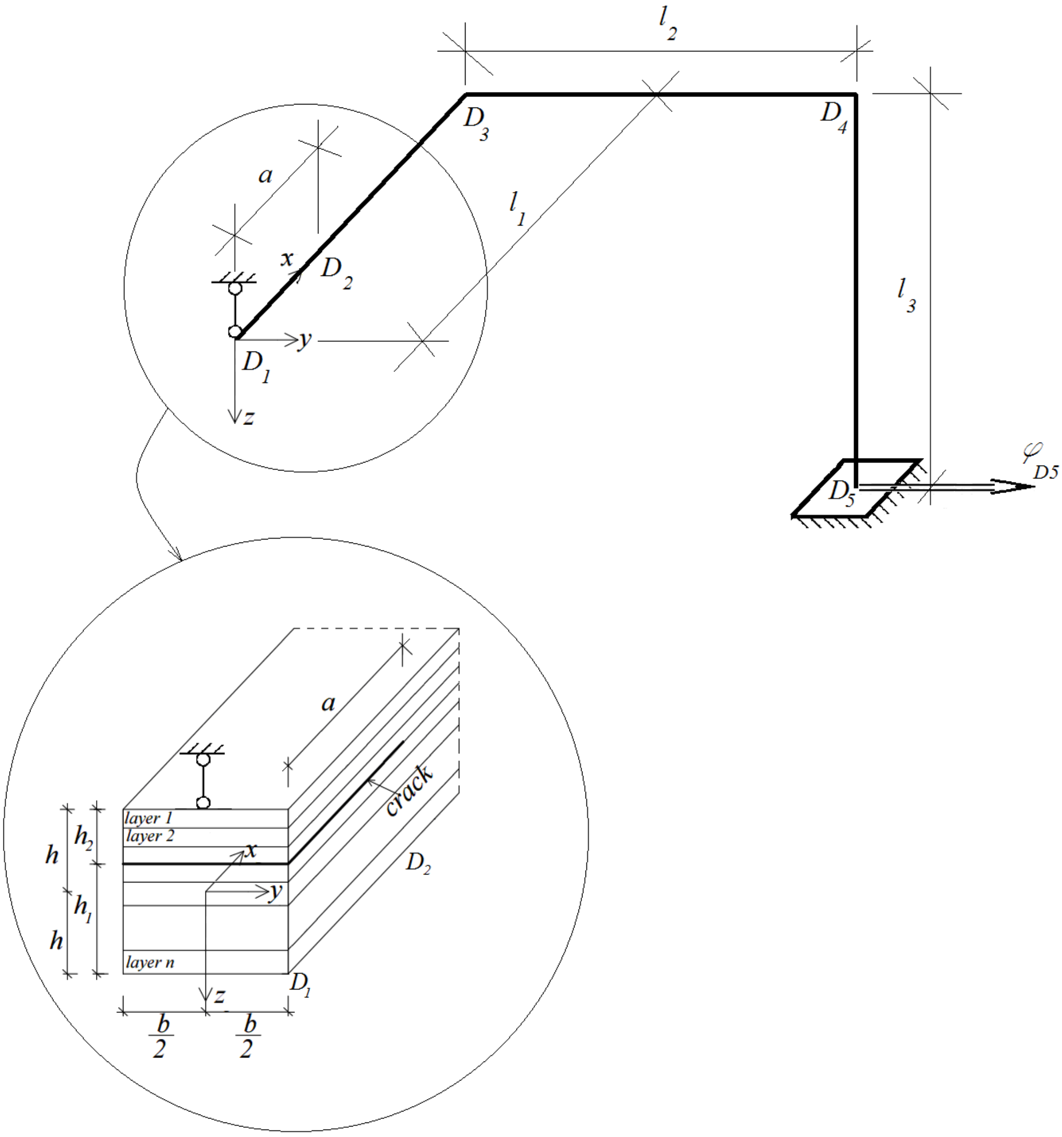

Figure 1. Steric frame under the fixed support rotation.

The steric frame structure in Fig. 1 is built-up by three members (two horizontal members, D_1D_3 and D_3D_4, and a vertical member, D_4D_5). The end, D_1 , of the member, D_1D_3, is supported by a vertical link, the lower end of the vertical member is fixed. Therefore, the frame represents a structure with one degree of static indeterminacy. The fixed support is under angle of rotation, φ_{D5}, as shown in Fig. 1. The delamination crack in portions, D_1D_2, of the frame has length of a. The SERR, G, for the delamination crack is obtained by formula (1) derived through the compliance method.

$$G = \frac{1}{2b}\left(M_{D5y4}^{2}\frac{dC_{MD5}}{da} \right) \tag{1}$$

where b is the beam width, M_{D5y4} is the bending moment in the fixed support along the rotation, C_{MD5} is the frame compliance. The latter is defined by formula (2).

$$C_{MD5} = \frac{\varphi_{D5}}{M_{D5y4}} \tag{2}$$

In order to apply formula (1), the static indeterminacy has to be considered first. This is done through the following equations. The angle of rotation, φ_{D5}, is written as

$$\varphi_{D5} = \int_0^a \kappa_{D1D2} \frac{1}{l_1} x dx + \int_0^{l_1} \kappa_{D2D3} \frac{1}{l_1}(a + x_2) dx_2 + \int_0^{l_2} \frac{T}{S} dx_3 + \int_0^{l_2} \kappa_{D3D4} \frac{1}{l_1} x_3 dx_3 + \int_0^{l_3} \kappa_{D4D5} dx_4 + \int_0^{l_3} \kappa_{D4D5} \frac{1}{l_1} l_2 dx_4 \tag{3}$$

where

κ_{D1D2}, κ_{D2D3}, κ_{D3D4} and κ_{D4D5} are the curvatures of the frame portions, l_1, l_2 and l_3 are the lengths (Fig. 1), T is the torsion moment in member, D_3D_4, of the frame, S is the stiffness in torsion (one can find the method for determination of S in Chobanian 1997). Formula (3) is obtained by the integrals of Maxwell-Mohr.

The stress, σ_j, in the layers of portion, D_1D_2, of the frame is

$$\sigma_j = E_j \varepsilon \tag{4}$$

where E_j is the modulus of elasticity, ε is the strain. The layers are inhomogeneous along the length. The distribution of the modulus of elasticity along the length is

$$E_j = E_{Lj} + \frac{E_{Qj} - E_{Lj}}{l_1^p} x^p \tag{5}$$

where E_{Qj} and E_{Lj} are the values of E_j in the points, D_1 and D_3, in portion, D_1D_3, of the frame, p is a parameter of the distribution, the axis, x, is shown in Fig. 1. The equilibrium of the elementary forces in the cross-sections of the frame portions is considered to formulate the following equations.

$$N_{D1D2} = \sum_{j=1}^{j=n_1} \iint_{(A_j)} \sigma_j dA, \tag{6}$$

$$M_{D1D2} = \sum_{j=1}^{j=n_1} \iint_{(A_j)} \sigma_j z dA, \tag{7}$$

$$N_{D2D3} = \sum_{j=1}^{j=n} \iint_{(A_j)} \sigma_{D2D3j} dA, \tag{8}$$

$$M_{D2D3} = \sum_{j=1}^{j=n} \iint_{(A_j)} \sigma_{D2D3j} z_2 dA, \tag{9}$$

$$N_{D3D4} = \sum_{j=1}^{j=n} \iint_{(A_j)} \sigma_{D3D4j} dA, \tag{10}$$

$$M_{D3D4} = \sum_{j=1}^{j=n} \iint_{(A_j)} \sigma_{D3D4j} z_3 dA, \tag{11}$$

$$N_{D4D5} = \sum_{j=1}^{j=n} \iint_{(A_j)} \sigma_{D4D5j} dA, \tag{12}$$

$$M_{D4D5y4} = \sum_{j=1}^{j=n} \iint_{(A_j)} \sigma_{D4D5j} z_4 dA, \tag{13}$$

$$M_{D4D5z4} = \sum_{j=1}^{j=n} \iint_{(A_j)} \sigma_{D4D5j} y_4 dA, \tag{14}$$

where n_1 and n are the number of layers in upper delamination arm and in the frame. The quantities, N_{D1D2}, N_{D2D3}, N_{D3D4} and N_{D4D5}, are the axial forces, M_{D1D2}, M_{D2D3}, M_{D3D4}, M_{D4D5y4} and M_{D4D5z4} are the bending moments in the frame portions. These quantities are

$$N_{D1D2} = 0 , \tag{15}$$

$$N_{D2D3} = 0 , \tag{16}$$

$$N_{D3D4} = 0 , \tag{17}$$

$$N_{D4D5} = R_{D1} , \tag{18}$$

$$M_{D1D2} = R_{D1} x , \tag{19}$$

$$M_{D2D3} = R_{D1}(a + x_2) , \tag{20}$$

$$M_{D3D4} = R_{D1} x_3 , \tag{21}$$

$$M_{D4D5y4} = R_{D1} l_1 , \tag{22}$$

$$M_{D4D5z4} = R_{D1} l_2 , \tag{23}$$

where R_{D1} is the support reaction in the vertical link. Equations (3), (6) – (14) are used to determine the curvatures and the neutral axis coordinates in the frame portions, the strain in the centre of cross-section of portion, D_4D_5, of the frame, and the support reaction in the vertical link by the MatLab. Then the SERR is obtained by using formula (2).

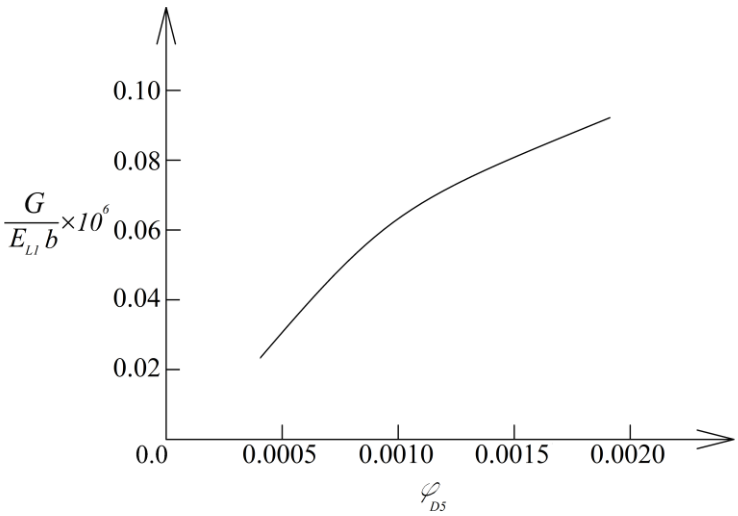

Figure 2. The non-dimensional SERR - φ_{D5} curve.

The SERR is checked-up by formula (24).

$$G = \frac{dU}{bda}, \tag{24}$$

where U is the strain energy in the frame.

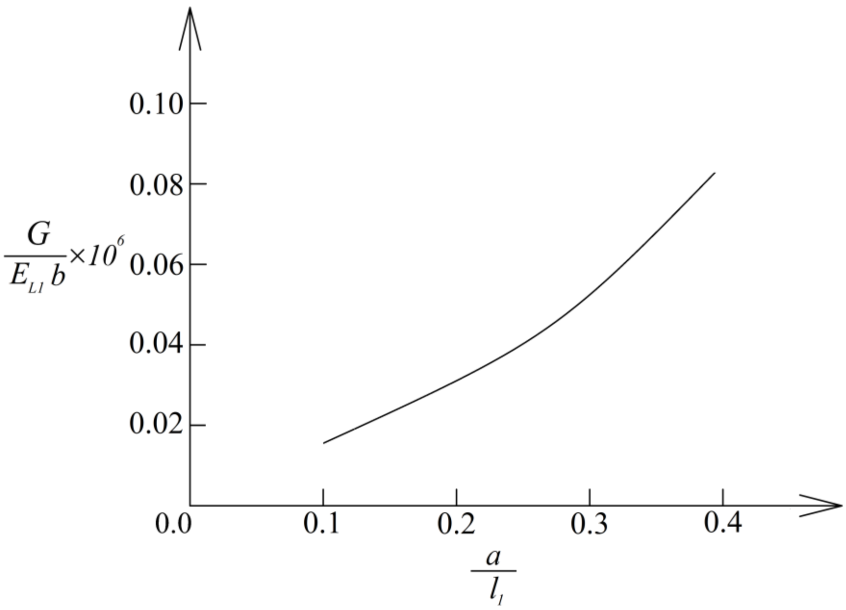

Figure 3. The non-dimensional SERR - a / l_1 curve.

Numerical Results

Numerical results are obtained and used to plot the curves shown in the next figures. These curves illustrate how the SERR changes when the basic parameters of the model vary. The data used for obtaining the SERR are $a = 0.120$ m, $b = 0.012$ m, $h = 0.008$ m, $l_1 = 0.300$ m, $l_2 = 0.400$ m, $l_3 = 0.500$ m, $n_2 = 2$, $n = 4$ and $p = 0.2$.

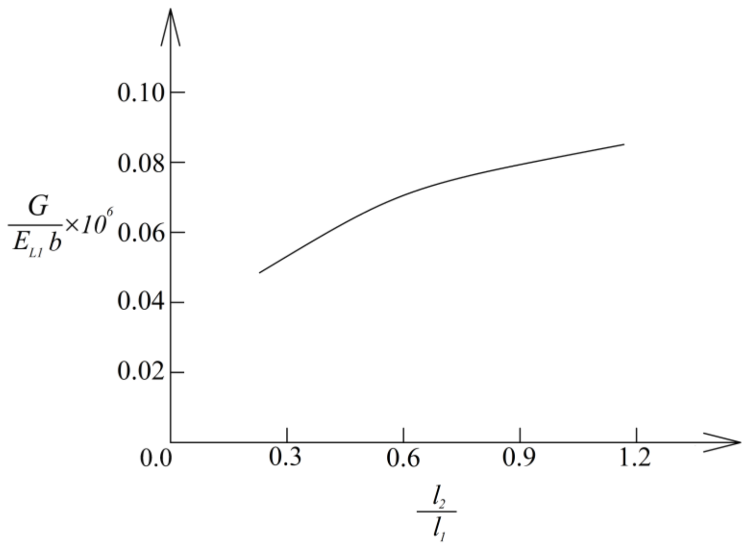

Figure 4. The non-dimensional SERR - l_2 / l_1 curve.

The influence of the value of the angle of rotation, φ_{D5}, on the SERR is shown in Fig. 2. The strong sensitivity of the SERR with respect to φ_{D5} indicates that the fixed support rotation has to be considered in delamination analyses of the statically indeterminate frames.

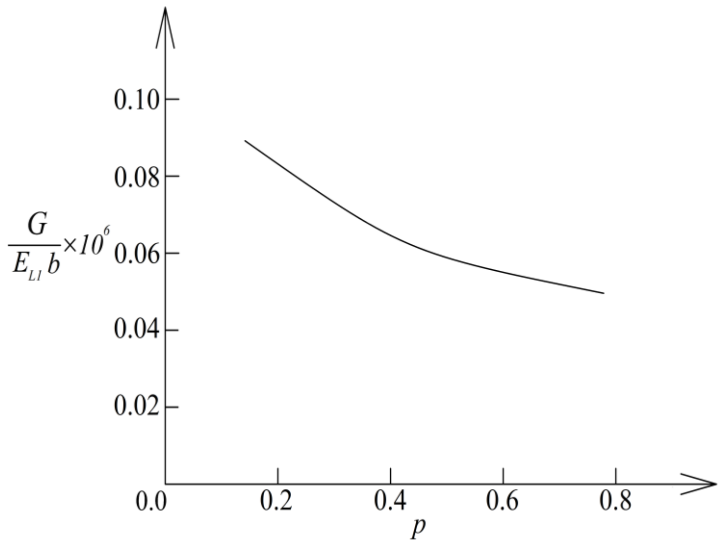

Figure 5. The non-dimensional SERR - p curve.

Other parameters whose influence on the SERR is studied are the non-dimensional delamination length, a / l_1, the ratio, l_2 / l_1, and the parameter of the distribution, p. The corresponding curves are shown in Fig. 3, Fig. 4 and Fig. 5, respectively. The sensitivity of the SERR with respect to these factors is also significant as can be seen in Fig. 3, Fig. 4 and Fig. 5.

Conclusion

Delamination in statically indeterminate steric multilayered frames under fixed support rotation is analyzed. In particular, a frame with three members (two horizontal members and a vertical member) is studied in detail. The lower end of the vertical member is fixed. Besides, the left end of the frame is supported by a vertical link. The SERR is derived. The influence of basic parameters of the model of the steric frame on the SERR is investigated. The significant sensitivity of the SERR with respect to parameters, φ_{D5}, a / l_1, l_2 / l_1 and p, detected by the investigation shows that the fixed support rotation has to be considered when analyzing delamination behaviour of statically indeterminate steric multilayered frames.

Recommendations

The analysis can be applied in design of streic statically indeterminate frames with considering the delamination behaviour under fixed support rotation.

Scientific Ethics Declaration

The author declares that the scientific ethical and legal responsibility of this article published in EPSTEM Journal belongs to the author.

Acknowledgements or Notes

* This article was presented as an oral presentation at the International Conference on Technology, Engineering and Science (www.icontes.net) held in Antalya/Turkey on November 14-17, 2024.

References

Chobanian, K.S. (1997). *Stresses in combined elastic solids*. Science.

Dolgov, N. (2005). Determination of stresses in a two-layer coating. *Strength of Materials, 37*(4), 422-431.

Finot, M., & Suresh, S. (1996). Small and large deformation of thick and thin-film multilayers: Effect of layer geometry and compositonal gradients. *Journal of Mechanics and Physic of Solids, 44*(5), 683-721.

Gandra, J., Mir&a, R., Vilaca, P., Velhinho, A., & Teixeira, J.P. (2011). Functionally graded materials produced by friction stir processing. *Journal of Materials Processing Technology, 211*(2011), 1659-1668.

Hutchinson, J. W., & Suo, Z. (1992). Mixed mode cracking in layered materials. *Advanced in Applied Mechanics, 64,* 804 – 810.

Nguyen, S. N., Lee, J., Han, J.W., & Cho, M. (2020). A coupled hygrothermo-mechanical viscoelastic analysis of multilayered composite plates for long-term creep behaviors. *Composite Structures, 242*, 112030.

Rizov, V. I. (2018). Non-linear delamination in two-dimensional functionally graded multilayered beam. *International Journal of Structural Integrity, 9,* 646-663.

Rizov, V.I. (2018). Analysis of cylindrical delamination cracks in multilayered functionally graded non-linear elastic circular shafts under combined loads. *Frattura ed Integrità Strutturale, 46*, 158-17.

Rizov, V.I. (2019). Influence of material inhomogeneity and non-linear mechanical behaviour of the material on delamination in multilayered beams. *Frattura ed Integrità Strutturale*, *47*, 468-481.

Rzhanitsyn, A.R. (1986). *Built-up bars and plates*. Stroyiizdat.

Tokova, L., Yasinskyy, A., & Ma, C.-C. (2016). Effect of the layer inhomogeneity on the distribution of stresses and displacements in an elastic multilayer cylinder. *Acta Mechanica*, *228*(8),2865-2877.

Udupa, G., Rao, S. S, & Gangadharan, K. V. (2014). Functionally graded composite materials: An overview. *Procedia Materals Science, 5*, 1291-1299.

Author Information

Victor Rizov
Department of Technical Mechanics, University of Architecture,
Civil Engineering and Geodesy, 1 Chr. Smirnensky blvd.
1046 – Sofia, Bulgaria
Contact e-mail: *V_RIZOV_FHE@UACG.BG*

To cite this article:

Rizov, V. (2024). Analysis of delamination in statically ındeterminate steric frames subjected to fixed support rotation. *The Eurasia Proceedings of Science, Technology, Engineering & Mathematics (EPSTEM), 32,* 604-610.

The Eurasia Proceedings of Science, Technology, Engineering & Mathematics (EPSTEM), 2024

Volume 32, Pages 611-618

IConTES 2024: International Conference on Technology, Engineering and Science

Numerical Computation of Turbulent Flow in a Square-Sectioned 90° Bend Using Open Foam

Bouabdellah Abed
University of Sciences and Technology M.B

Mohammed Hamel
University of Sciences and Technology M.B

Abiddine DebaB
University of Sciences and Technology M.B

Abstract: This study presents the results of Computational Fluid Dynamics (CFD) simulations using the open-source software OpenFOAM to evaluate the Reynolds-averaged Navier-Stokes steady (RANS) by reproducing the fluid flow in a 90° square-section curved pipe. The simulations were carried out using three turbulence models: the standard k-ε model, the RNG k-ε model and SST k-ω model. The results were compared to previously published experimental results. The objective was to investigate the performance of RANS models in turbulent flow in a curved pipe with a 90° square section at a Reynolds number of 40000. The velocity distribution and pressure drop across the entire computational domain were analyzed, with particular attention to regions within and after the bend where secondary vortex structures were illustrated. Flows at the elbow are characterized by the presence of counter-rotating cells responsible for disrupting the flow. Analysis of the numerical results obtained from all turbulence models found good agreement with the experimental data, but there are differences between the models.

Keywords: CFD analysis, OpenFOAM, Turbulent flow, 90° Square-section bend.

Introduction

Over the years, the turbulent flow mechanism in such curved conduits has been the subject of extensive research, both numerical and experimental, due to its academic interest and industrial importance. The three-dimensional characteristics of flow occurring in square-curved pipes pose challenges for computational fluid dynamics (CFD) simulations and serve as an effective benchmark for evaluating turbulence models. Square curved pipes are frequently used in the installation of energy and electrical systems, including fuel lines, exhaust systems, and various other applications. In the case of flow in straight and rectangular pipes, the pressure distributions over different sections tend to be relatively uniform. Conversely, when dealing with flow in installed pipes and curved conduits, the velocity and pressure fields become considerably complex. Inertial forces, particularly at the elbows, generate significant pressure gradients from the inner wall to the outer wall. The vortical zones that develop immediately before and after the bend contribute to the phenomenon of secondary flows within the curvature zone, leading to additional pressure losses. Various experimental and numerical studies have been carried out to analyze and characterize these complex flow behaviors.

Lyne (1971) is one of the first to address the phenomenon of flow induced by pulsation within a curved pipe. Researchers such as Humphrey et al. (1986), Enayet et al. (1982), Azzola et al. 1(986), Cheah et al. (1996). Employed Doppler Anemometry laser techniques to assess the velocity field and visualize flow within a 90° elbow of square cross-section. Iacovides et al. (1996) utilized hot-wire anemometry to conduct measurements in curved conduits. Additionally, Sudo et al. (2001) performed experimental investigations on turbulent flow in a 90° section of a curved square duct at a Reynolds number of 40000 using a hot-wire anemometer. Munch and Métais (2004) investigated the impact of the section's aspect ratio on compressible and three-dimensional turbulent flows through Large Scale Simulation, specifically in curved conduits with a rectangular cross-section. Sugiyama and Mukai (2008) employed the Reynolds algebraic constraint model (ARSM) to examine three-dimensional turbulent flow within a 180° bend. Additionally, Yang et al. (2005), Chu et al. (2010), Ono et al. (2011) conducted both experimental and numerical studies on the flow characteristics in curved rectangular micro-channels. The exploration of turbulent flows in curved conduits continues to be a significant challenge, presenting critical technological implications and remaining a compelling area of research within fluid mechanics.

The present study aims to evaluate the performance of different turbulence closure models on fluid flow through a square-section curved pipe with a 90° elbow. The numerical simulations were conducted using OpenFOAM v2212, an open-source computational fluid dynamics (CFD) software. The time-averaged velocity components and pressure fields flow through the square-sectioned pipe with a bend were calculated numerically. The results obtained underwent rigorous validation by comparing them with the relevant experimental data provided by (Sudo et al., 2001).

Method

Description of the Study Case

The problem considered in this study is the turbulent flow of air through a square-sectioned 90° bend pipe. To carry out the numerical computations, the modeled geometry shown in Fig. 1 is built. The computational domain is composed of a square-sectioned duct a × a = 80 × 80 (mm) with an installed 90-degree bend with a mean radius of curvature Rm = 160 (mm). The computational domain section length of the upstream and downstream pipes of the bend is taken as 50 Dh (Dh = 80 mm).

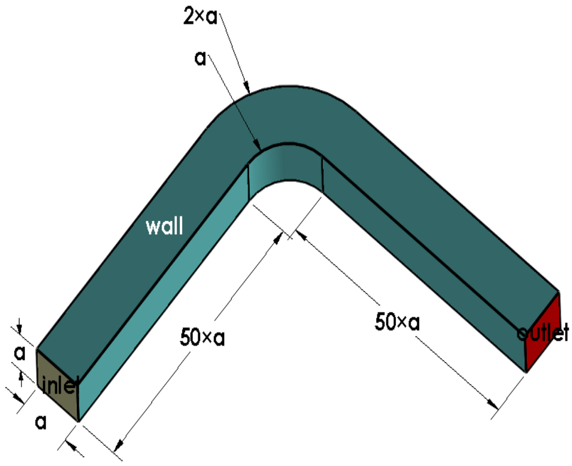

Figure 1. Geometry dimensions

Table 1. Dimensions

Dimensions	Length (mm)
Hydraulic diameter, Dh, a	80
Before elbow, L inlet	50×a
Bend curvature Radius, Rm	2×a
after the elbow, L outlet	50×a

The turbulent flow through the curved pipe is considered an incompressible isothermal flow. The numerical simulations are performed using OpenFOAM v2012 code. The CFD code uses the finite-volume method to solve governing equations for the incompressible turbulent. In this study, the numerical model solves the 3D steady incompressible Navier-Stokes and continuity equations in conjunction with two transport equation turbulence models: the k-epsilon model, the RNG model, and the k-omega model SST.

Mesh Generation

Mesh generation is an essential aspect of CFD analysis and has a significant influence on computation performance and accuracy. The computational mesh utilized in this work is generated using the blockMesh utility, a meshing tool in the open-source software OpenFOAM. A 3D multi-block structure of hexahedral meshes with inflation near the walls is used for the numerical domain considered, as shown in Fig. 2. Several meshes (Table 1) are evaluated to ensure that the solution is not mesh-dependent. As a result, a grid of one million cells will be used to illustrate the numerical results.

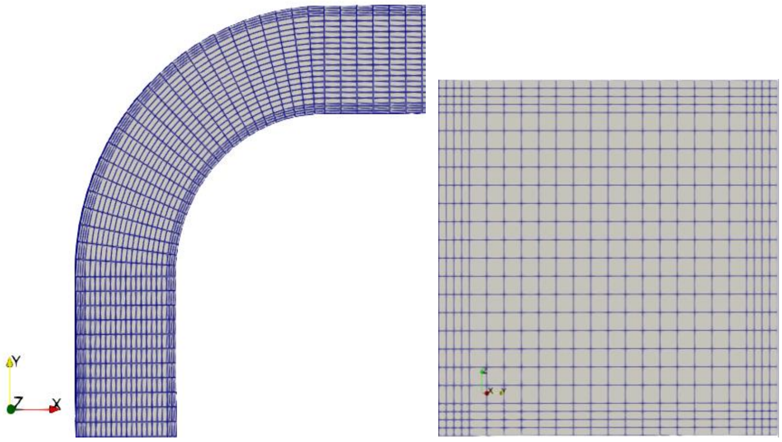

Figure 2. Computational grid (Mesh 1)

Table 2. Mesh Information

Mesh	Cells
Mesh 1	301824
Mesh 2	694656
Mesh3	1155336

Boundary Conditions

The resolution of the governing equations is achieved by utilizing the defined boundary conditions as follows: At the inlet boundary, the flow rate is determined by the Reynolds number (40000), and the flow direction is normal to the inlet surface. The velocities are zero in the remaining two directions. The pressure at this boundary is defined as a zero normal gradient. At the outlet, the velocity is established with a zero normal gradient, while the pressure is specified to be zero. For pipe walls, no-slip wall conditions are applied

(u = v = w = 0), and the wall surfaces are treated as smooth. At the pipe walls, the pressure is set with a zero normal gradient. The values of the turbulent kinetic energy and its specific dissipation rate are calculated from the inlet turbulence intensity and pipe diameter (Dutta et al., 2016).

Numerical Solution Procedure

The runs are performed using the linear upwind gradient (U) scheme as demonstrated in Beam and Warming (1976). To discretize the convective term in the momentum equation and the linear interpolation scheme for diffusion terms, while the upwind scheme as shown by Launder et al. (1983) is chosen for the divergence related to turbulence. For the gradient and divergence operators, the Gauss linear scheme is applied. The Gauss linear scheme is used for the Laplacian operator. Additionally, the interpolation scheme is set to linear. The pressure-velocity coupling is resolved using the SIMPLEC algorithm. The linear solvers used for each variable are defined as follows: The GAMG solver (Generalized Geometric-Algebraic Multigrid) (Wesseling & Oosterlee, 2001). For the pressure equation with a Gauss-Seidel type smoother and PbiCGStab (stabilized Preconditioned bi-conjugate gradient (Van der Vorst, 1992) solver for the velocity and equations with DILU preconditioner, which is a simplified diagonal-based incomplete LU preconditioner for asymmetric matrices. Tolerance values of all solvers are set to 10^{-6}.

Dependence of the Flow Solution on Grid Resolution

The dependence of the flow solution on grid resolution is investigated using three meshes. The number of grid points is multiplied by 2 in the xyz directions upstream, inside, and downstream of the elbow. The differences between results computed using different meshes are shown in Fig. 3. At U/Vc, longitudinal velocity components averaged in cross section profiles at locations y/Dh=-1 and x/Dh=1 computed using three mesh resolutions are depicted along with experimental data (Sudo et al., 2001). It seems that the differences between results calculated using different grids are very small, and henceforth, the grid with 694656 cells is used to analyze the numerical results.

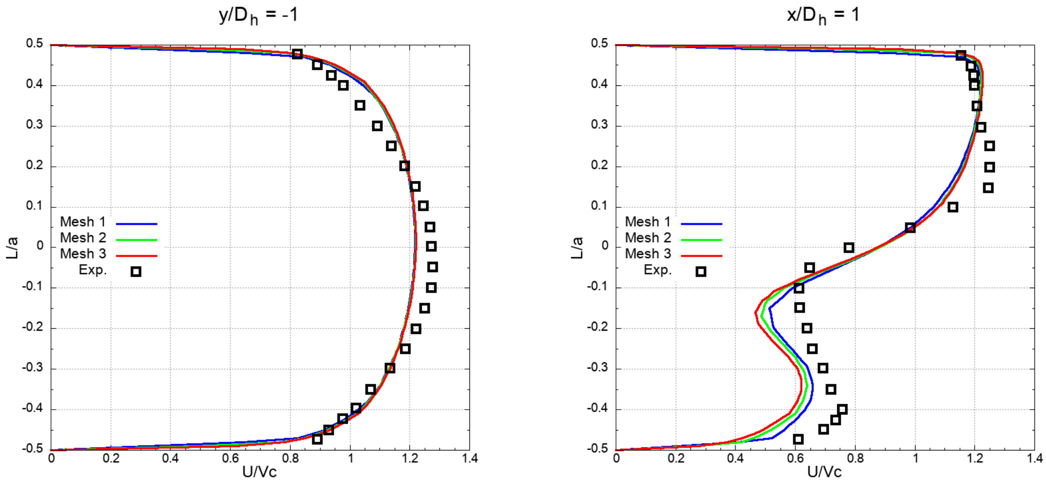

Figure 3. Comparison of the velocity profiles computed using different grids at y/Dh = -1.0 and x/Dh = 1.0 with k-ε turbulence model.

Results and Discussion

This study involves conducting a three-dimensional numerical simulation using the open-source computational fluid dynamics software, OpenFOAM version 2212, to investigate turbulent flow through a square-section curved pipe with a 90° elbow. The Reynolds number for the flow was Re = 40000, and the corresponding value of the Dean number was 20000 (Sudo et al., 2001). The Dean number is a dimensionless quantity that is used to analyze flows through curved pipes and represents the ratio of the inertial and centripetal forces to the viscous forces. The simulations were carried out using three turbulence models: the standard k-ε model, the RNG k-ε model, and the k-ω SST model. Figures 1 through 6 present a comparison between the calculated values and the measurements obtained from five stations along the streamwise direction at y/Dh = -1, φ = 30°, 60°, x/Dh = 1 and x/Dh = 10. Firstly, and in order to verify the numerical methods applied, a comparison between the numerical method utilized and the experimental results from Sudo et al. (2001) has been performed. This section presents the results of the velocity component profiles normalized with inlet velocity along the different positions in the central symmetry plane. The results indicate a significant quantitative consistency with the experimental results.

The data illustrated in Figures 4-a through 4-e indicates that there is no discernible discrepancy between this calculation and (Sudo et al., 2001). At the stations φ = 30 ° and 60 ° in the elbow, the agreement between code calculations and experimental results is very good. But at the outlet of the elbow at x/Dh = 1, computational results show no good agreement with the experiment. This difference can be produced by a deficiency of a turbulence model to predict well the flow fluctuation induced by the movement separation region and the acceleration of flow velocity.

According to Fig. 4-a, at y/Dh=-1, the flow is not yet influenced by the bend and is slightly accelerated near the inner wall and decelerated near the outer wall. At φ = 30° and φ = 60°, the flow is accelerated near the inner wall and decelerated near the outer wall. The maximum velocity occurs both near the inner wall of the bend and caused by the unfavorable pressure gradient. At the bends exit, at x/Dh = 1, the velocity profile value becomes more complex, and the fluid is further accelerated and moved near the outer wall due to the secondary flow formed in the presence of the elbow. Further downstream, z/Dh = 10, the flow has leaning to exhibit a velocity profile of a turbulent, developed flow.

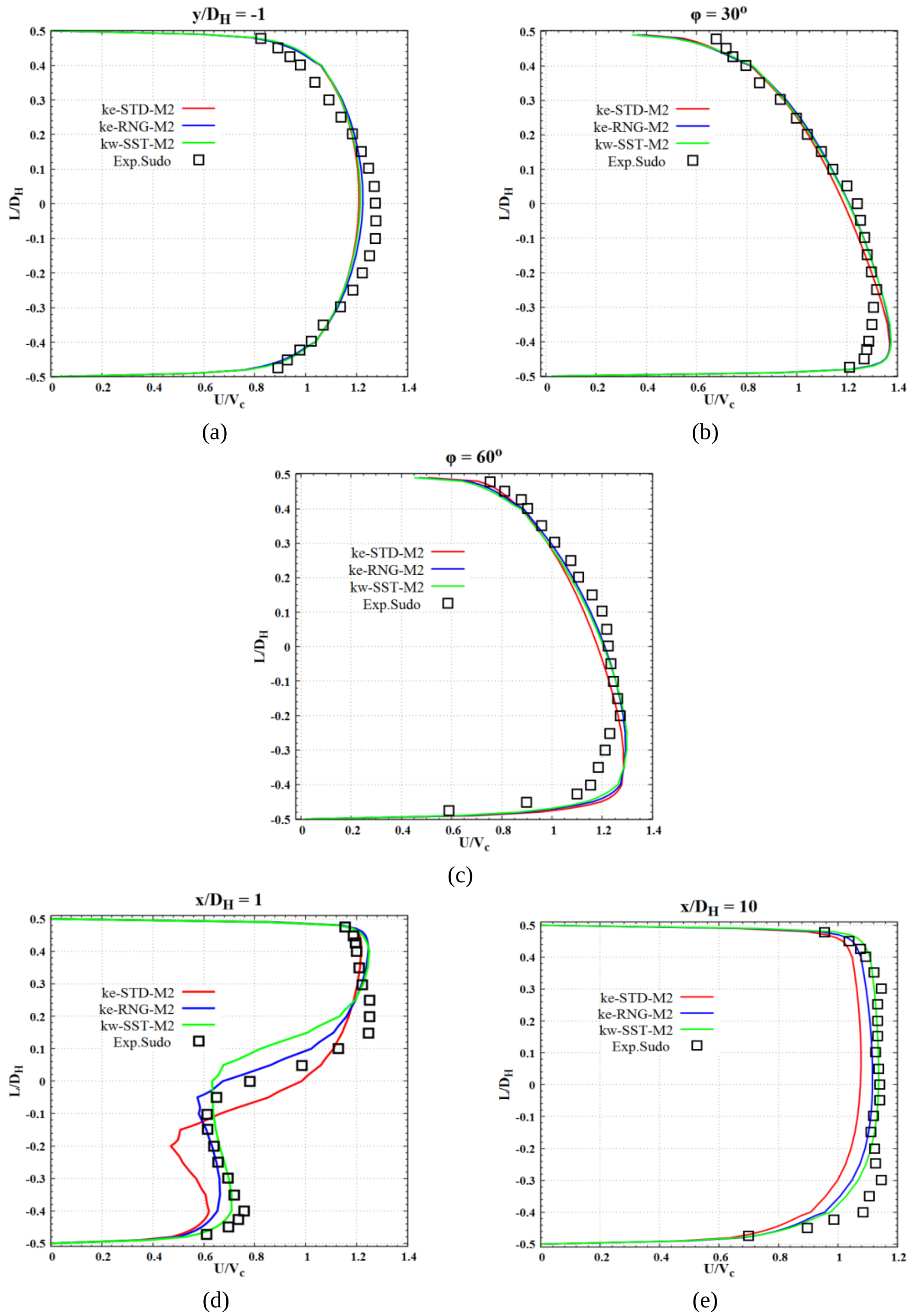

Figure 4. Normalized velocity profiles at different positions obtained with Standard k − ε, k − ε RNG and k − ω SST models and compared with experimental results of Sudo et al. (2001)

Visualizing streamlines contours provides key information on the flow field characteristics. Figure 5 illustrates the simulation results through the surface streamlines collected at various streamwise stations over curved pipe and also at 1 Dh upstream of the bend enter and at 10 Dh downstream of the bend exit. At 30°, 45°, and 60° sections in the bend, the secondary flow peculiar to the curved duct flow appears in the cross-section, and it forms two counter-rotating vortices that circulate outwards in the central part of the duct and inwards near the upper and lower walls (the formation of the counter-rotating vortices of Dean). The fluid crossing the elbow is decelerated near the outer wall and accelerated near the inner wall caused by the unfavorable pressure gradient. After the bend exit at x/Dh=1, owing to the centrifugal force, the velocity contours are more distorted. The fluid moves further toward the outer wall due to the strong secondary flow and produces distorted velocity contours, which concave outwards in the central region near the inner wall.

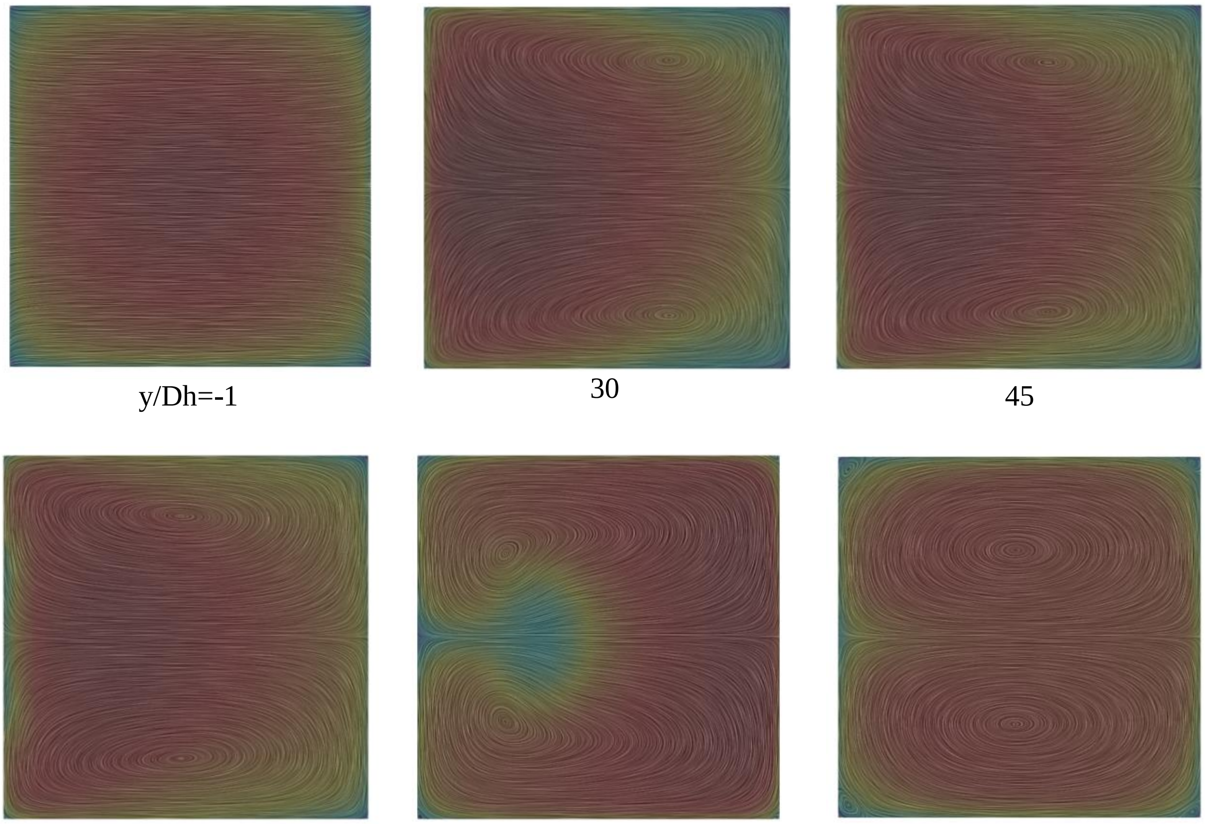

Figure 5. Surface streamlines in 90° curved pipe (k-ε turbulence model).

Figure 6 illustrates the variations in the pressure coefficient Cp along the outer and inner walls of the pipe with normalized bend cross-sectional length and for different angles α. The curves present results of numerical calculations by using different closure models. The reference pressure p_{ref} is the pressure located at the outer bend at the cross-section *y/D=-17.6* from the inlet of the bend. The pressure coefficient is defined as $Cp = \left(p - p_{ref}\right) / \left(\rho V_C^2 / 2\right)$, where V_C represents the mean velocity (m/s). From Fig. 6, it can be seen that the maximum pressure coefficient is observed on the outer wall of the bend (at the angle of 60°) and the minimum near the inner wall of the bend (at the angle of 30°), as expected due to the presence of centrifugal force.

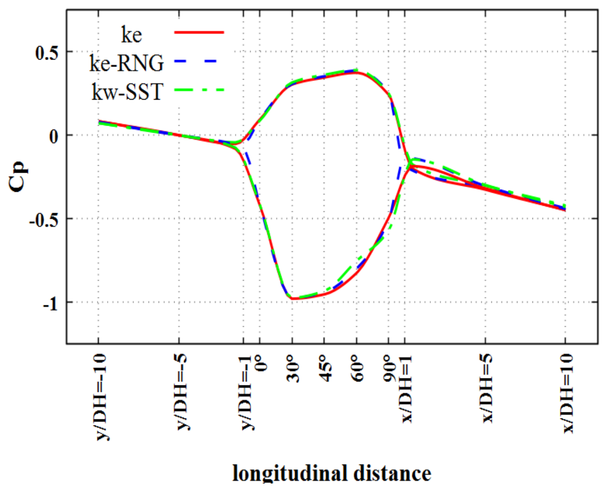

Figure 6. Pressure coefficient along the inner and outer walls in mid-plane.

Furthermore, it can be clearly observed that the Cp increases in the direction of the flow at the inner wall of the bend, by which the adverse pressure gradient occurs. Additionally, all turbulence models (the standard k-ε model, the RNG k-ε model, and the SST k-ω model) produce very similar Cp values along the inner and outer walls.

Conclusion

The current study, CFD modeling of a turbulent air flow through a square pipe with a 90 ° elbow at a Reynolds number of 40000, was performed using the open-source CFD code OpenFOAM. The study uses RANS-based CFD models to capture the main features of the turbulent 90° bent pipe with three turbulence models embedded in the code, namely, the standard k-ε model, the RNG k-ε model, and the SST k-ω model. The problem geometry and the mesh were generated by the blockMesh Dictionary tool of OpenFOAM v2212. The SIMPLEC algorithm was used for the treatment of the pressure-velocity coupling, and the PDEs conservation equations were solved using the finite volume method with a convergence criterion set to 10−6 for all variables.

Results curves of the numerical model showed a good agreement with the experimental data given by (Sudo et al., 2001). The results presented by streamlines at different stations show that the geometry of the bend induces a pair of counter-rotating vortices in the streamwise direction of the flow. The driving force of the secondary flows is a result of the centrifugal force-radial pressure gradient imbalance, which acts on the moving fluid along the side walls of the bend and downstream. As one of the main conclusions of this work, the open-source OpenFOAM CFD code and the numerical model adopted sufficiently captured the flow field and can be used to study fluid fluids over square curved pipes.

Scientific Ethics Declaration

The authors declare that the scientific ethical and legal responsibility of this article published in EPSTEM Journal belongs to the authors.

Acknowledgements or Notes

* This article was presented as an oral presentation at the International Conference on Technology, Engineering and Science (www.icontes.net) held in Antalya/Turkey on November 14-17, 2024.

* The authors are very thankful to the Laboratory of Applied Mechanics; Department of Mechanical Engineering; University of Sciences and Technology “Mohamed Boudiaf” Oran, Algeria.

References

Azzola, J., Humphrey, J. A. C., Iacovides, H., & Launder, B. E. (1986). Developing turbulent flow in a U-bend of circular cross-section: Measurement and computation. *Journals of Fluids Engineering, 108*(2), 214-221.

Beam, R. M., & Warming, R. F. (1976). An implicit finite-difference algorithm for hyperbolic systems in conservation-law form. *Journal of Computational Physics*, *22*(1), 87-110.

Cheah, S. C., Iacovides, H., Jackson, D. C., Ji, H., & Launder, B. E. (1996). LDA investigation of the flow development through rotating U-ducts. *Journal of Turbo Machinery, 118*(3), 590-596.

Chu, J. C., Teng, J. T., & Greif, R. (2010). Experimental and numerical study on the flow characteristics in curved rectangular microchannels. *Applied Thermal Engineering*, *30*(13), 1558-1566.

Dutta, P., Saha, S. K., Nandi, N., & Pal, N. (2016). Numerical study on flow separation in 90° pipe bend under high Reynolds number by k-ε modelling. *Engineering Science and Technology, an International Journal*, *19*(2), 904-910.

Enayet, M. M., Gibson, M. M., Taylor, A. M. K. P., & Yianneskis, M. (1982). Laser-Doppler measurements of laminar and turbulent flow in a pipe bend. *International Journal of Heat and Fluid Flow*, *3*(4), 213-219.

Humphrey, J. A. C., Whitelaw, J. H., & Yee, G. (1981). Turbulent flow in a square duct with strong curvature. *Journal of Fluid Mechanics*, *103*, 443-463.

Lyne, W. H. (1971). Unsteady viscous flow in a curved pipe. *Journal of Fluid Mechanics*, *45*(1), 13-31.
Lacovides, H., Launder, B. E., Loizou, P. A., & Zhao, H. H. (1990). Turbulent boundary-layer development around a square-sectioned U-bend: Measurements and computation. *Journal of Fluids Engineering, 112*(4), 409-415.
Launder, B. E., & Sharma, B. I. (1974). Application of the energy-dissipation model of turbulence to the calculation of flow near a spinning disc. *Letters in Heat and Mass Transfer*, *1*(2), 131-137.
Launder, B. E., & Spalding, D. B. (1983). The numerical computation of turbulent flows. In *Numerical prediction of flow, heat transfer, turbulence and combustion* (pp.96-116). Pergamon.
Menter, F. R. (1994). Two-equation eddy-viscosity turbulence models for engineering applications. *AIAA Journal*, *32*(8), 1598-1605.
Münch, C., Hébrard, J., & Métais, O. (2004). Large Eddy Simulations of turbulent flow in curved and s-shape ducts. *Direct and Large-Eddy Simulation V: Proceedings of the Fifth International ERCOFTAC Workshop* (pp.527-536). Netherlands: Springer.
Ono, A., Kimura, N., Kamide, H., & Tobita, A. (2011). Influence of elbow curvature on flow structure at elbow outlet under high Reynolds number condition. *Nuclear Engineering and Design*, *241*(11), 4409-4419.
Sudo, K., Sumida, M., & Hibara, H. (2001). Experimental investigation on turbulent flow in a square-sectioned 90-degree bend. *Experiments in Fluids*, *30*(3), 246-252.
Sugiyama, H., Tanaka, T., & Mukai, H. (2008). Numerical analysis of turbulent flow separation in a rectangular duct with a sharp 180-degree turn by algebraic Reynolds stress model. *International Journal for Numerical Methods in Fluids*, *56*(12), 2207-2228.
Van der Vorst, H. A. (1992). Bi-CGSTAB: A fast and smoothly converging variant of Bi-CG for the solution of nonsymmetric linear systems. SIAM *Journal on scientific and Statistical Computing*, *13*(2), 631-644.
Wesseling, P., & Oosterlee, C. W. (2001). Geometric multigrid with applications to computational fluid dynamics. *Journal of Computational and Applied Mathematics*, *128*(1-2), 311-334.
Yakhot, V. S. A. S. T. B. C. G., Orszag, S. A., Thangam, S., Gatski, T. B., & Speziale, C. (1992). Development of turbulence models for shear flows by a double expansion technique. *Physics of Fluids A: Fluid Dynamics*, *4*(7), 1510-1520.
Yang, W. H., Zhang, J. Z., & Cheng, H. E. (2005). The study of flow characteristics of curved microchannel. *Applied Thermal Engineering*, *25*(13), 1894-1907.
Zhang, J., Wang, D., Wang, W., & Zhu, Z. (2022). Numerical investigation and optimization of the flow characteristics of bend pipe with different bending angles. *Processes*, *10*(8), 1510.

Author Information

Bouabdellah Abed
University of Sciences and Technology M.B
Oran, Algeria
Contact e-mail : bouabdellah.abed@univ-usto.dz

Mohamed Hamel
University of Sciences and Technology M.B
Oran, Algeria

Abiddine Debab
University of Sciences and Technology M.B
Oran, Algeria

To cite this article:

Abed, B., Hamel, M., & Debab, A. (2024). Numerical computation of turbulent flow in a square-sectioned 90° bend using OpenFOAM. *The Eurasia Proceedings of Science, Technology, Engineering & Mathematics (EPSTEM), 32,* 611-618.

The Eurasia Proceedings of Science, Technology, Engineering & Mathematics (EPSTEM)
ISSN: 2602-3199

The Eurasia Proceedings of Science, Technology, Engineering & Mathematics (EPSTEM), 2024

Volume 32, pages 619-633

IConTES 2024: International Conference on Technology, Engineering and Science

Multi-Beat Digital Stethoscope

Rebecca Dib
Lebanese German University

Daniel Al-Boutros
Lebanese German University

Lama Bou-Farah
Lebanese German University

Abstract: Digital medical instruments are essential in today's world to make fast and precise diagnoses. By combining several features into a single device, healthcare can be provided more affordably and with greater patient care and medical efficiency. This project describes the development of a cost-effective digital stethoscope featuring an integrated oximeter sensor and a sound transducer. The stethoscope facilitates the simultaneous monitoring of spO2 (Saturation of Peripheral Oxygen) levels and heart activity. The sound transducer converts cardiac sounds into electrical signals, enabling the detection of anomalies in heart function. Real-time data on these vital signs is transmitted to a web-application that will be deployed on the doctors' phone, providing them with immediate access to patient information. This innovative device offers a two in one solution that is both efficient and affordable for both patients and medical practitioners.

Keywords: Stethoscope, SpO2, Heart function, Web-application, Monitoring.

Introduction

Monitoring and listening to the heart and lungs activities are crucial for identifying any abnormality or the beginning of any disease linked to both organs listed previously (American Lung Association, n.d.). In the rapidly evolving medical field, the need of multifunctional and especially low-cost devices has been increasing. The development of a digital stethoscope with integrated oximeter features is a significant advancement in this sector.

The proposed Multi-Beat digital stethoscope not only simplifies the process of monitoring the spO2 and heart activity levels but it also enhances the speed and reliability of diagnosis with a very affordable cost. Linking this device to a mobile web-application which ca be accessed on a doctor’s smartphone or PC(Personal computer), will smooth any abnormality visual recognition relying on real-time graph and values with high precision in case of inconspicuous sounds heard via the stethoscope.

Objectives

The goal of this project is to create a digital stethoscope with integrated oximeter capabilities, which will improve patient monitoring and diagnosis. The project aims to simplify vital sign evaluation by integrating these essential tasks into a single, affordable gadget. This would enable healthcare practitioners to identify and treat medical issues more efficiently. The cutting-edge tool will offer real-time data that can be accessed via a mobile application, facilitating speedier and better-informed medical choices to enhance patient care.

Literature Review

The literature analysis highlights the evolution of electronic stethoscopes from traditional acoustic models to more advanced models with digital recording capabilities and improved sound amplification. The challenge with these improvements is having reliable results with the lowest cost possible which is the main purpose of this project.

Stethoscope's Evolution

The initial purpose of stethoscopes was to listen to a patient's chest sounds, assess the respiratory and cardiovascular systems, and gauge how effectively the trachea and bronchial tree were working as an airway (Sarkar et al., 2015a). During chest auscultation, medical personnel must pay close attention to the patient's interior sounds, particularly during the vesicular breath sound intervals (J. I. Gupta & Shea, 2023).

Multifunctional devices with quick processing rates have been greatly enhanced by technological developments in the healthcare industry. Wearable digital stethoscopes provide cordless, continuous, real-time auscultation for a range of illnesses (Bishop, 1980). Applications for smartphones may be coupled with these devices to provide continuous auscultation monitoring. The improvements to classic auscultation procedures in clinical and instructional contexts are intended for healthcare practitioners. Figure 1 illustrates the major milestones in the evolution of stethoscopes from analog to electronic, and ultimately digital.

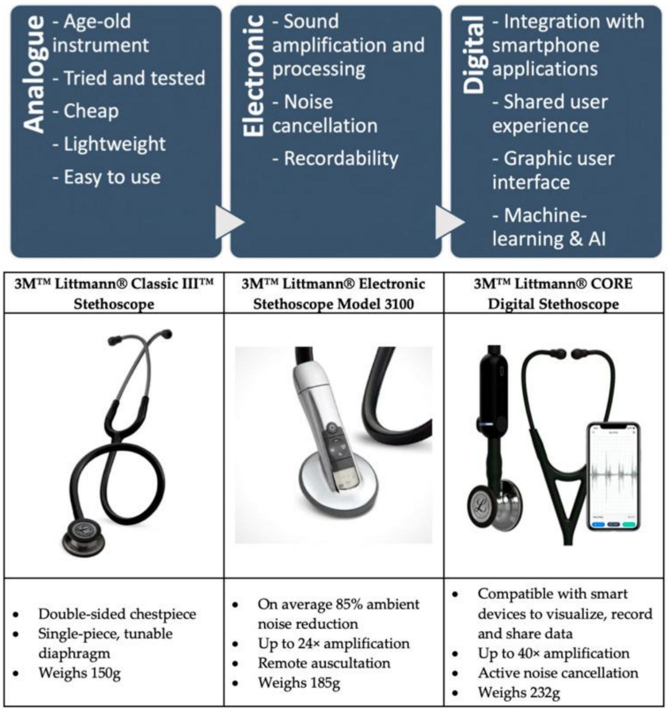

Figure 1. Evolution of stethoscopes over the year (Bishop, 1980)

Starting with the Analogue stethoscope, also known as "the traditional stethoscope", is used in order to amplify chest sounds during auscultations. It is mainly composed of a chest piece, a binaural earpiece, with the bell and diaphragm taking up lower and higher frequency (Bishop, 1980). Its ease of use and widespread availability make it a good choice for healthcare professionals.

Going to the Electronic stethoscope, which is considered an innovative method compared to the analogue one, has helped with higher clinical practice. Through it, chest sounds are amplified via electronic intervention providing audio feedback, sound level manipulation, audio data recording, and playback (Bishop, 1980). The conversion of chest sounds from analogue sound waves can be done via a microphone or a piezoelectric sensor, which will result in the amplification and processing of the sound waves' transduction into an electrical by passing through bandpass filters that are responsible of reducing unwanted noise that can corrupt the sound signal (Landge et al., 2018).

Now, concerning the digital stethoscope, it pushes the limits of chest auscultation techniques with the use of smartphone applications and connected data processing. Designed similarly to the electronic stethoscope, it incorporates a digital filter to eliminate interference from the electrical signal and extract the desired signal from the designated frequency range. The obtained heart and breath sounds are normalized to a particular scale and segmented into cycles thereby assisting in the identification and separation of the components of the pulse and breath (Bishop, 1980).

Motivation

As listed previously, digital stethoscopes are available in the healthcare market, or, the Multi-beat digital stethoscope encloses many sophisticated and trailblazing specifications that differentiate from any other normal digital stethoscopes. With its additional oximeter allowing the doctor the real-time tracking of the SpO2 value via the mobile application, the pulse sensor allowing the continuous bpm (Beats-Per-Minute) display, the conversion of sound to waves, as well as the reasonable low cost compared to any monotask digital stethoscopes, this multitask task stethoscope has significant advantages.

Lungs and heart function continuous wireless tracking is remarkably important for the doctors as well as any patient, allowing the avoidance of the direct turn to specialized and kind of complex medical tests like ECG (Electrocardiography) for heart activity, or the Spirometry for lungs activity. So, the visual and direct results added to the stethoscope's audible effects are very useful features that would help with making the diagnosis more accurate, improve clinical decision making, along with comfort provision for the patients.

Methodology

The Multi-Beat digital stethoscope contains an embedded network of various sensors and modules working together in order to give the user a very good accuracy and facilitate abnormalities diagnosis, using the stethoscope for a basic patient's examination will surely always available even with no power on. As soon as the batteries are connected to the MCU (Microcontroller Unit) of the device, heart sounds heard by the stethoscope will be directly transformed to electrical waves by the use of the microphone transducer which is responsible of converting sound energy into an electrical one. Moreover, the pulse sensor and the oximeter will also be automatically turned on allowing the continuous monitoring of spO2 and bpm levels.

The perpetual tracking will be done using a web-application (which will be accessible on the doctor's cell phone or PC), linked wirelessly to the MCU allowing real-time data transfer helping out the doctor to not only achieve multiple tests, but also having more reliable audible and visual results. Noting that all the data displayed on the web-app will be previously saved on the main database of this apparatus which is Google Firebase allowing each user (doctor) to create his own account along with data encryption as well as specific archive folders each for one patient. This resourceful innovation has a lot of potential usage in comfort technology and healthcare.

Components

Figure 2. Stethoscope

Medically wise, a stethoscope is used in order to listen to the internal sounds generated by the heart, lungs, and intestinal tract. In this project, the aim is to connect the stethoscope's internal circuit to an external circuit that will participate in converting the heart sounds to electrical waves, helping the doctor with a better diagnostic. This medical device represented in the (Figure 2) is used for acoustic auscultation and usually consists of flexible tubing, earpieces, and a chest piece with a bell, diaphragm, or both. The bell is more suited for low-frequency noises, whereas the diaphragm excels in picking up high-frequency sounds (Grenier et al., 1998).

Heart sound, a mechanical vibration that occurs during the cardiac cycle, is caused by the contraction of the heart muscle and the shock of blood flow to the ventricular wall during diastole. It creates a mild vibration signal as it goes around the chest wall (Swarup & Makaryus, 2018). By mimicking the features of an organism's life and organizational structure, medical bionics analyzes the structure, function, and functioning principles of living things and applies these concepts to medical technology.

The MEMS (Micro-Electro-Mechanical-System) heart sound sensor, which is composed of beams and cilia, primarily imitates the structural pickup mechanism of 3D fiber bundles seen in human otic hair cells which are represented in the (Figure 3 (a)). A cilium and very accurate cantilever beams make up the novel bionic MEMS microstructure, which combines the bionic principle, piezoresistive effect, and MEMS technology (Li et al., 2021).

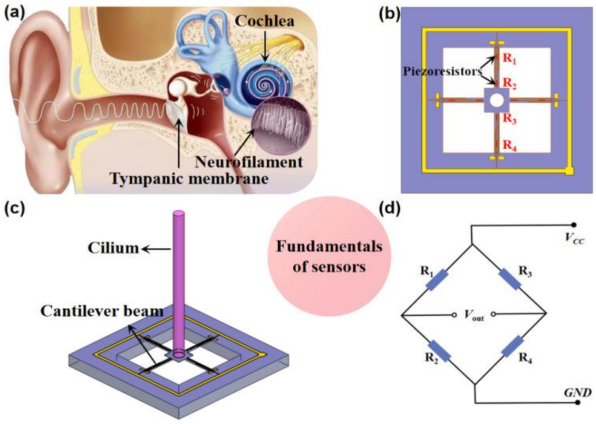

Figure 3. Principle of bionic microsensors (Yang et al., 2022)

A Wheatstone bridge is created when varistors with the same resistance are positioned underneath the greatest stress zone of cantilever beams. The bottom of the cilium is placed at the central connection of the beam members like shown in (Figure 3 (b)), (Figure 3 (c)) and (Figure 3 (d)) where V_{CC} means the input voltage of the bridge and V_{out} suggests the output voltage. When sound waves are applied to the biomimetic cilium, it oscillates and deforms the cantilever beams. Finally, the deformation of the cantilever alters the resistance of the varistor placed on its surface. The mechanical deformation is converted into electrical output via the Wheatstone bridge (Yang et al., 2022).

R_1, R_2, R_3 and R_4 form a set of Wheatstone bridge as shown in (Figure 3 (d)). At this time, the output voltage of the Wheatstone bridge is shown in [1]:

$$V_{out} = \frac{(R_1 + \Delta R_1)(R_4 + \Delta R_4) - (R_2 - \Delta R_2)(R_3 - \Delta R_3)}{(R_1 + \Delta R_1 + R_2 - \Delta R_2)(R_4 + \Delta R_4 + R_3 - \Delta R_3)} V_{cc} \qquad [1]$$

In formula [1], the output of the sensor's circuit is V_{out}, its input is V_{cc} and ΔR is the resistance change (Yang et al., 2022). Where R_1=R_2=R_3=R_4=R, the above formula can be simplified as shown in [2]:

$$V_{out} = \frac{\Delta R}{R} V_{cc} \qquad [2]$$

The resistance change is related to the stress on the cantilever beams, which is shown in [3]:

$$\frac{\Delta R}{R} = \pi_1 \sigma_1 \qquad [3]$$

In formula [3], σ_1 is the longitudinal stress component, and π_1 is their longitudinal piezoresistive coefficient (Yang et al., 2022). The sensor output must be set as high as achievable in order to increase the sensor's sensitivity. Placing the varistor in the maximum linear stress region of the cantilever beams can effectively improve the sensitivity of the sensor (Yang et al., 2022).

The schematic diagram of acoustic auscultation with bionic heart sound sensor is represented in (Figure 4). The transmitted acoustic energy decreases with the increasing impedance difference when sound is input over the border between two different mediums, but the reflection coefficient rises. The stethoscope and skin have a considerable reflection when they come into contact, which causes more attenuation and less transmitted acoustic energy. Consequently, after passing through human tissues and exhibiting increasing attenuation, the heart sounds were sent to the MEMS-based bionic sensor in order to get the maximal sound signal. Furthermore, because medical silicone oil (20cst) satisfies the unique acoustic impedance criteria of human soft tissue, it was chosen as the encapsulating material (Yang et al., 2022).

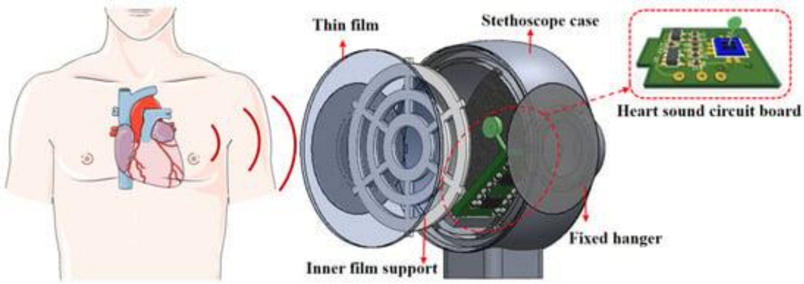

Figure 4. Diagram of auscultation with bionic heart sound sensor (Yang et al., 2022)

Moving to the next component of the Multi-Beat digital stethoscope which is the transducer which is an electrical device called a transducer is used to change the form of energy. One of the common examples is the microphone used in this project, which is a sound transducer. Thus, microphone is a transducer which converts variations of sound pressure into variations of electrical current (GeeksforGeeks, 2024). The sound detection sensor module shown in the (Figure 5) is the component that will be used in order to achieve this conversion process.

Figure 5. Microphone AMP MAX9814

Scientifically speaking, more than 2 types of microphones are available:

Carbon Microphone: Utilizes carbon granules whose resistance varies in response to differences in sound waves' pressure (Teja, 2024).

Moving Iron Microphone: This type of microphone moves an iron diaphragm in a magnetic field to produce a fluctuating electrical signal (Teja, 2024).

A moving coil microphone, also known as a dynamic microphone: uses a coil moving inside a magnetic field to convert sound waves into an electrical signal (Teja, 2024).

Ribbon Microphone: This device generates voltage by vibrating a narrow metal ribbon between two magnetic poles (Teja, 2024).

Piezoelectric Microphone: Utilizing materials that produce voltage when under mechanical stress, this device transforms sound into an electrical signal (Teja, 2024).

Capacitor Microphone: which encloses as an example, the High Sensitivity Sound Detection Sensor Module used in this project. It has two surfaces: a backplate and a conductive diaphragm. There is a fixed electric charge between the two surfaces. The diaphragm vibrates in response to the sound wave, changing the capacitance.

Given the constant charge, a voltage wave is produced by the fluctuation in capacitance. The distance between the plates determines the output. The output increases with decreasing surface spacing for a given sound level. The microphone capacitor operates under pressure. A voltage source is required in order to deliver the set charge. We refer to this voltage as polarizing voltage (Teja, 2024). Capacitor microphones offer excellent audio signals and linearity in their functioning. An electret is used to prevent polarizing voltage. An insulating substance that is permanently charged is called an electret. It is a magnet's electrostatic equivalent. A diaphragm and an electret slab make up one of the capacitor plates in electret capacitor microphones. There is no requirement for a voltage source because the electret offers a constant charge (Teja, 2024). The structure of the capacitor microphone is represented in the (Figure 6).

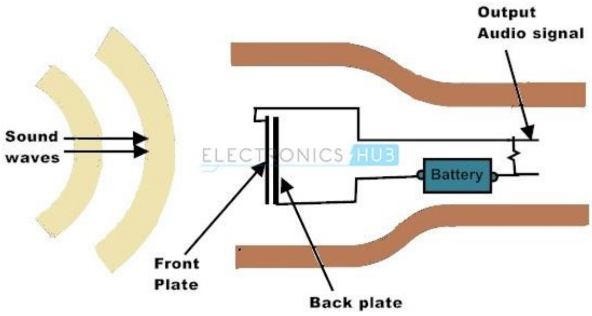

Figure 6. Capacitor microphone’s structure (Teja, 2024)

In this project, the MAX9814 (Figure 5) will be used due to its low cost and high sensitivity in detecting sounds. Or, knowing that the typical frequencies of normal heart sounds fall between 20 and 150 Hz makes it hard to hear these sounds on a naked ear, and that is why auscultation tools are needed (Alanazi et al., 2020). In order to amplify these sounds before detecting it with the microphone, a 3D printed connector (stethoscope to mic) is designed in order to amplify the sounds detected by the stethoscope before the microphone receives it for more reliability, as well as isolating noises coming from the stethoscope’s external environment (Figure 7).

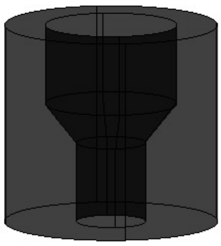

Figure 7. Customized 3D printed connector

This specific configuration of the connector placed on one end of the stethoscope’s ear tube instead of the standard ear piece and on the other hand on the microphone, will allow the execution of the previously listed functions. Moreover, a pulse oximeter and heart rate monitor will be implemented in the Multi-Beat digital stethoscope in order to measure and monitor the lungs (spO2) and heart (bpm) functions. The component is shown in the Figure 8.

Figure 8. MAX30100 IC

The pulse and blood oxygen levels are measured with a pulse oximeter. Certain medical issues may cause the person to have low oxygen saturation. The reading may also be impacted by skin tones. A non-invasive test called pulse oximetry gauges the blood's oxygen saturation level and the heart's pulse, which is expressed in beats per minute. It can quickly identify even minute variations in oxygen concentrations. These values demonstrate how well blood travels to the parts of the body that are farthest from the heart, such as the limbs and legs, to provide oxygen (How2Electronics, n.d.).

This component will be connected to the Multi-Beat device through wiring independent from the circuit composed of the MEMS heart sound sensor and the transducer in order to be able to achieve a parallel monitoring of the patient's bpm and spO2 as well as a continuous, non-stop display of the waves representing the heart's function carried through the stethoscope's use. Noting that these 2 independent circuitries will be connected to the same MCU(Microcontroller Unit) in the aim of establishing real-time multi-records of more than 1 organ. This sensor will be put in a direct contact with the patient's finger or can be even used on his earlobe. Its work will be divided into 2 parts: HR (Heart Rate) measurement in bpm and pulse oximetry (measuring the oxygen level of the blood).

Internal LEDs, optical components, photodetectors, low-noise circuitry, and ambient light rejection are all included. In order to adjust LED pulses for SpO2 and HR measurements, the MAX30102 includes Red and IR LED drivers. With the correct supply voltage, the LED current may be controlled between 0 and 50 mA. The LED pulse width may be adjusted between 69µs and 411µs, enabling the algorithm to maximize power consumption, accuracy of SpO2 and HR, and other factors based on use scenarios (How2Electronics, n.d.). Moving to the working principle of the MAX30100 (noting that the module being used in this project has the MAX30102 as its photodetector), it operates by beaming both lights onto the earlobe or finger (allowing both lights to readily penetrate the tissue), and then using a photodetector to measure the quantity of light that is reflected. This method of pulse detection through light is called Photoplethysmogram (How2Electronics, n.d.). One property of arterial blood's oxygenated hemoglobin (HbO2) is its ability to absorb infrared light. Further absorption of infrared light occurs in proportion to blood redness, or hemoglobin content. Shown in the (Figure 9) is a blood vessel existing in the finger. The amount of reflected light varies as the blood is pumped through the finger with each heartbeat, causing the photodetector's output waveform to shift. A heart-beat (HR) pulse reading soon appears as you keep shining light and collecting photodetector signals (How2Electronics, n.d.).

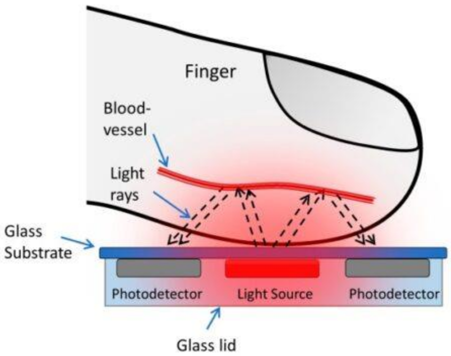

Figure 9. Working of the pulse oximeter sensor (How2Electronics, n.d.)

Concerning the pulse oximetry, it works on the theory that the quantity of oxygen in your blood affects how much RED and IR light is absorbed (How2Electronics, n.d.). The interval of Red light and infrared (IR) light shown in (Figure 10) shows the specific wavelengths that can be absorbed by the oxyhemoglobin (HbO2) in arterial blood.

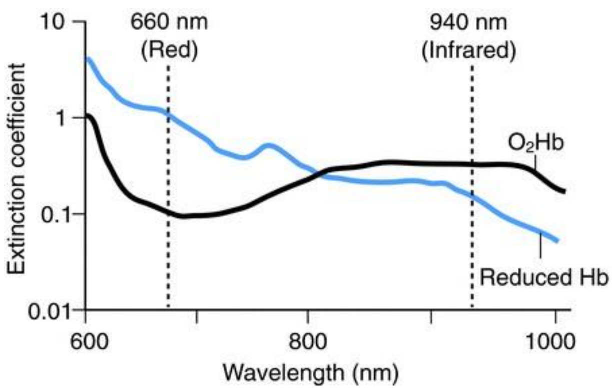

Figure 10. Pulse oximetry graph (How2Electronics, n.d.)

Moving to the main electronic component implemented in this innovation which is the Arduino UNO. It is a microcontroller-based device with 14 digital pins used for various purposes (Krelja-Kurelovic, 2023) shown in Figure 11. It can be used for almost every task. It can also be used for prototyping and developing new applications. This component is considered as the main brain of our device as well as its responsibility in monitoring and synchronizing all the components of the system.

Figure 11. Arduino UNO module

A mobile web-application will be connected wirelessly to this MCU via the use of the ESP8266 12-E NodeMCU shown in (Figure 12) which is a Wi-Fi module that is used in the development of Internet of Things (IoT) devices. It is based on the ESP8266 system-on-chip which integrates a microcontroller unit and a Wi-Fi radio. Using this unit allows interfacing with external sensors, actuators, and other devices, as well as the main database of this innovation: Google Firebase, where all the real-time data of each patient will be saved securily (Hanna & Rosencrance, 2023).

Figure 12. The ESP8266 12-E NodeMCU module

Results and Discussion

Once all signals are met, real-time monitoring of the heart-function waves, bpm, and spO2 will be done via a mobile web-app. With the help of Google Firebase which is a set of cloud-based development tools that helps mobile app developers build, deploy, and scale their apps, viewing and monitoring a continuous wave graph of the patient's heartbeat will be done on the groundbreaking web-app developed by the multi-beat digital stethoscope team, as well as displaying in real-time the collected bpm and spO2 values on it

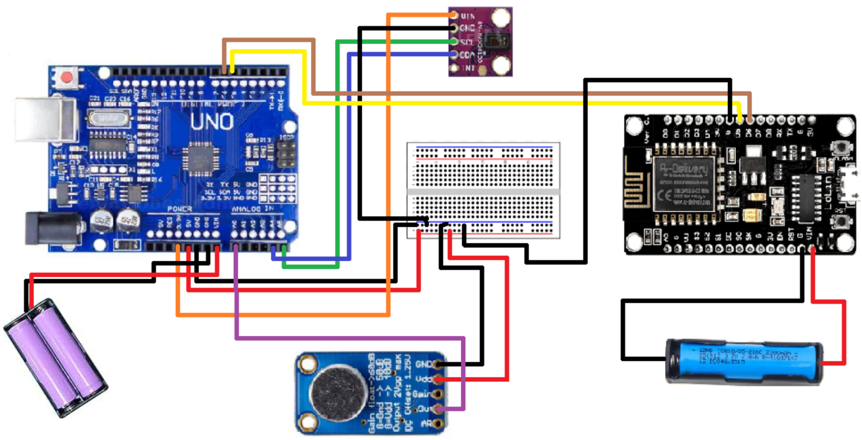

Figure 13. Design of the system

Figure 13 shows the interrelationship among these modules. The block diagram emphasizes the processes of the Multi-Beat Digital Stethoscope and is described in (Figure 14). The system's flowchart is showed in (Figure 15).

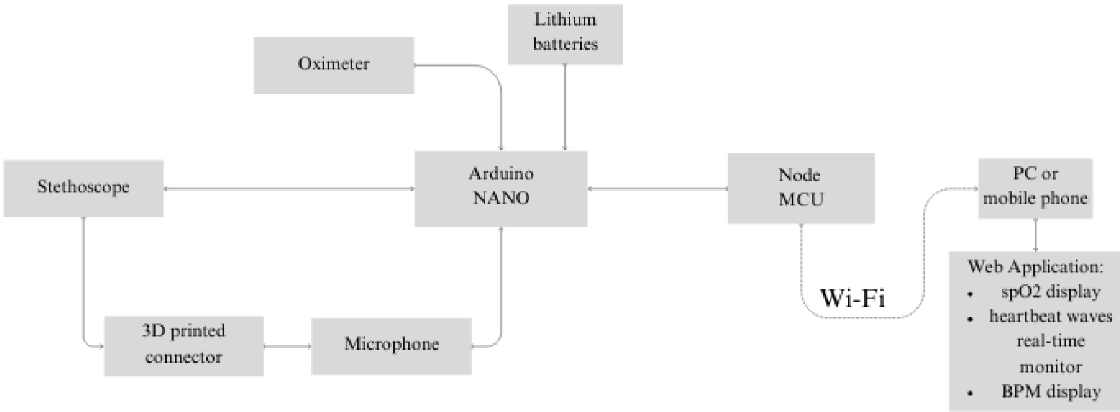

Figure 14. Block diagram of the system

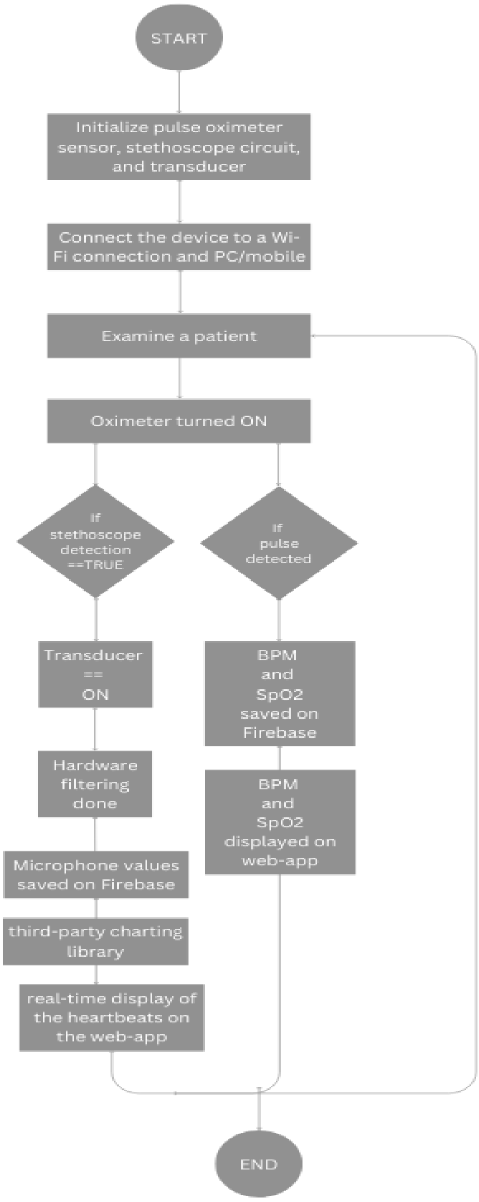

Figure 15. System's flowchart

Web Application Evaluation

After connecting all the components together, turning on the device, and start the patient's examination the stethoscope will be receiving the heartbeats' sounds that will be converted via the transducer to electronic waves. But even when using a high sensitivity sensor, incorporating filters to remove noise is mandatory. Knowing that high sensitivity detectors capture more details concerning the heart sounds, they are able to also pick up ambient noise and some unnecessary signals.

The heart sounds, typically, fall within the frequency range of 20 Hz to 500 Hz, so filtering out the frequencies falling outside this range is crucial; this process will be done using a band-pass filter to isolate the desired frequency interval (20 Hz to 500 Hz) what will enhance and improve the clarity of the signal. Providentially, the spO2 and bpm levels will be displayed on the same web dashboard after placing the patient's finger directly on the sensor which will be placed in a specialized case for it as well as placing the stethoscope's chest piece on the patient's chest. (Figure 16), (Figure 17), (Figure 18) and (Figure 19) show respectively the display and monitoring results on each of the Arduino and NodeMCU serial monitors, as well as each of Firebase and the web-app dashboards.

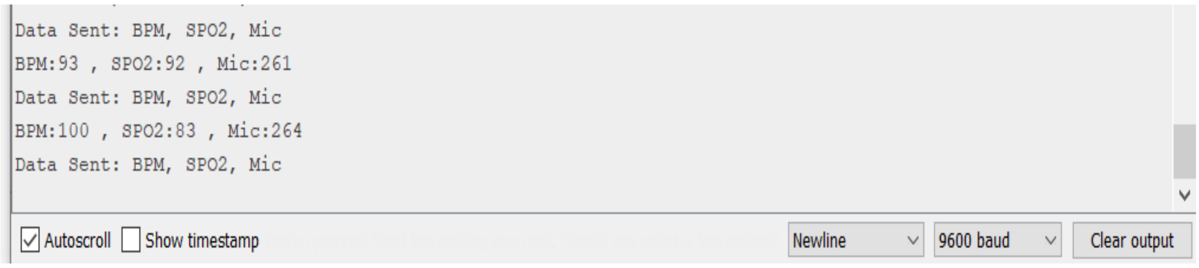

Figure 16. Arduino UNO serial monitor

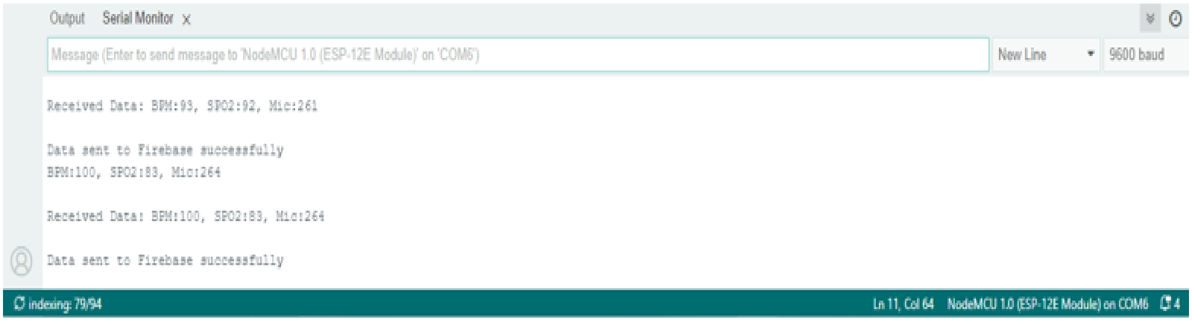

Figure 17. NodeMCU serial monitor

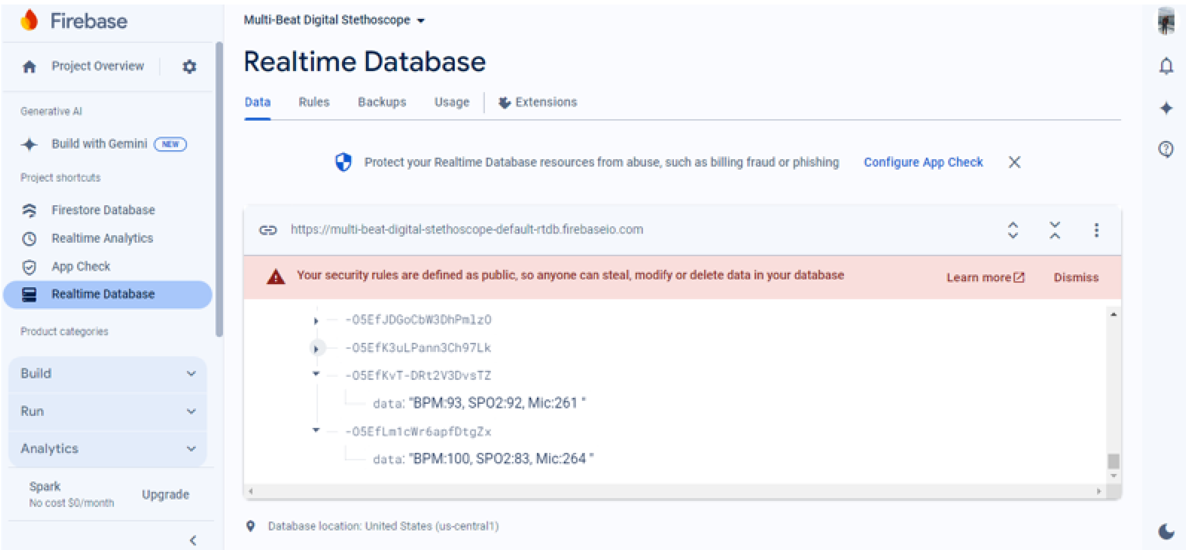

Figure 18. Firebase dashboard

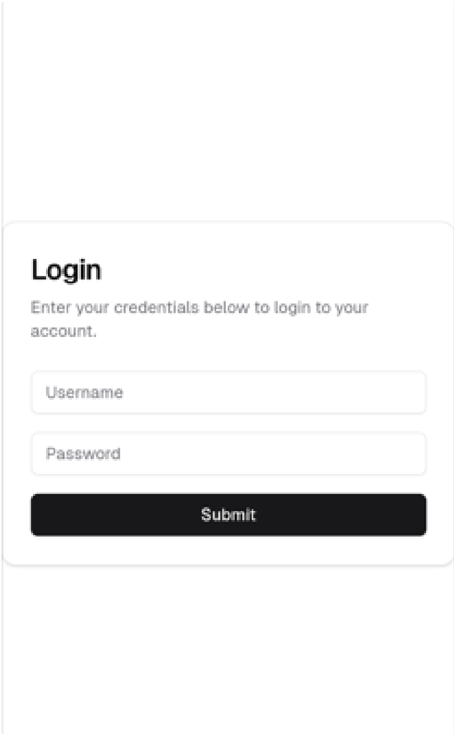

Figure 19. web-app first page

Figure 20. Web-app dashboard

Results Assessment

In order to discuss the results shown in the previous figures, the development of this innovation will be broken down extensively. First and foremost, the components are connected to the main brain of this machine as seen in the (Figure 13). Afterwards, the connection of this MCU to the NodeMCU is done. This microcontroller is responsible for transferring all the sensors' data collected in real-time from the Arduino to the Google Firebase via Wi-Fi. An analysis was done for the data received by the Arduino from the GY-MAX30100 and is shown in (Figure 21).

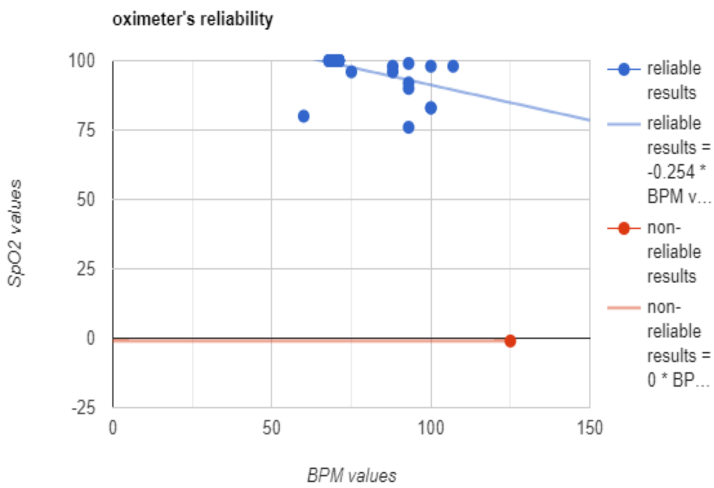

Figure 21. Scatter plot for Oximeter accuracy analysis

The scatter plot shown in (Figure 21) represents the variation of the sensor's reliability by focusing and analyzing the relationship between the BPM and SpO2 values.

$$Reliability = \frac{a-1}{a} \times 100 \qquad [4]$$

Referring to these 31 values received continuously from the GY-MAX30100 oximeter sensor, where the ranges of the BPM and SpO2 values are varying respectively from 60 to 107 and from 76 to 100, the reliability calculation can be done using formula [4] where 'a' represents the number of values which is 11 in this case. And since referring to the scatter plot out of 31 values only 1 of them is in the non-reliable range, the '-1' is used in the formula. In these circumstances, Reliability = 96.77 % which falls in the range of "high-reliability" sensors.

Subsequent to receiving the data from the sensors, the communication between the Arduino UNO and the ESP8266 is established via the serial communication where the pins used in the Arduino to achieve it are the pins 5 and 6 in addition to the NodeMCU pins used: D5 and D6. Eventually, the ESP8266 operates like a modem for Wi-Fi communication so, using the AT command set which is a set of instructions allowing the Arduino UNO to send and receive data from servers or even help with the connection of the NodeMCU to a Wi-Fi connection. In the Multi-beat digital stethoscope project case, AT commands are not needed since Arduino IDE is equipped with libraries such as "FirebaseESP8266" and "WiFiClientSecure" employed in this project abstract away the need of using this command set and applying it manually (Mobizt, n.d.). Accordingly, sensors' continuous data is sent to the NodeMCU where it is displayed on the serial monitor as shown in (Figure 17) to make sure that the serial connection is working successfully.

Afterwards, the ESP8266 starts a communication with Firebase, which occurs over HTTP requests sent from the NodeMCU to Firebase surely after the connection of the ESP8266 to the Wi-Fi connection via "WiFi.h" library. These requests are the REST API calls (Representational State Transfer Application Programming Interface), which allows the communication between different systems on the internet, like the sensors' values sending by using POST and PUT methods used respectively to create new resources on the server and update an existing resource on this server which is in this project the Firebase (L. Gupta, 2023), where a database will be created to saved GY-MAX30100 and MAX9814 values and then continuously updated each time ESP8266 receives new values since Firebase is known to offer real-time synchronization. Noting that these values are saved as JSON objects in order to allow structured storage. Providentially, the use of ESP8266 is shown to be advantageous in this case, not only because of its low cost or the previously listed working process, but also because of the authentication feature available in the data sending to the server where it securely sends data to Firebase by including authentication token in the HTTP headers which is an API (Application Programming Interface) key to validate the identity and ensure authorized access to the service. Therefore, the data will be saved in a real-time database and displayed on Firebase's dashboard of the specific account linked to the ESP8266, as shown in (Figure 18), noting that only in the testing procedure, the security rules of the account were declared as public.

For the live display of MIC values in the application, a combination of modern web technologies is utilized. Firebase Realtime Database is used along with backend services to create a responsive and real-time monitoring system. The key frameworks and technologies used include React.js, Recharts, Firebase Realtime Database, shadcn for UI components, and a Node.js backend with TypeScript for user authentication and data storage in MongoDB. Regarding the Fronted Framework (Shadcn, n.d.), React.js is used as the core front-end framework. React's component-based architecture allows to efficiently manage the UI state and handle real-time updates. Moving on with the MIC's live Data Visualization which is done using Recharts, a React-based charting library that integrates smoothly with the component architecture (Salimi-My, n.d.). The LineChart component is utilized to represent MIC data over time, with time on the X-axis and MIC values on the Y-axis. The chart is configured to update every 200 milliseconds, displaying the last 10 seconds of MIC data. For performance reasons, chart animations have been disabled to ensure smooth transitions during live data updates.

Providentially, We are using Firebase Realtime Database to fetch and sync live MIC, BPM, and SPO2 data. As mentioned earlier, Firebase is a cloud-hosted NoSQL database that provides real-time synchronization, making it ideal for this specific application (Hanna & Rosencrance, 2023). Using Firebase's JavaScript SDK (Software Development Kit), we establish listeners to monitor changes in the database for the MIC, BPM, and SPO2 values. Thus, Firebase SDK allows to set up a connection between the front-end and Firebase Realtime Database (SDKs and Client Libraries | Firestore | Firebase, n.d.). Using the onValue method, subscription to data changes is done. Each time a new MIC, BPM, or SPO2 value is pushed to Firebase, the listener is triggered, and the front-end is automatically updated with the new data. Over and above that, real-time data fetching is done where the new data is stored in React's state and triggers a re-render of the chart and cards displaying the live MIC, BPM, and SPO2 values. As new data is fetched, the state updates in real time, ensuring that the user always sees the latest data for all three metrics. Now, for the Backend Services, a Node.js application with TypeScript is employed. The backend is responsible for user authentication and securely managing the user's data. Also, the Node.js backend handles authentication, using JWT (JSON Web Tokens) to securely authenticate users.

The tokens are used to ensure that only authorized users can access the application and interact with the live data. User data, including authentication details and historical MIC data, is securely stored in a MongoDB database. MongoDB is a document-oriented NoSQL database that scales well with real-time applications like this (*W3Schools.com*, n.d.). The Node.js backend ensures secure storage, retrieval, and management of the data in the MongoDB database, ensuring data consistency and security. Furthermore, the UI (User Interface) is styled and structured using shadcn, a UI component library for React. shadcn provides reusable and customizable UI components that adhere to modern design principles. This allows in building a clean and consistent UI with minimal effort while ensuring that the UI remains highly responsive and visually appealing across all device sizes. Regarding the data flow, it will be divided to 4 subtitles for ease of understanding:

Backend Authentication: The user logs in to the system via the Node.js backend, which authenticates the user using TypeScript and stores user details in MongoDB.

Firebase Realtime Database: Once authenticated, the application subscribes to the Firebase Realtime Database, fetching live MIC, BPM, and SPO2 values. Firebase's real-time synchronization allows the app to receive updated data continuously as shown in (Figure 20).

Real-time Data Rendering: The fetched data is displayed using Recharts in a LineChart component for MIC and dynamically updated UI cards for BPM and SPO2 values (Figure 20). The chart and cards are updated every 200 milliseconds to show the latest data in real time. This data will be displayed on the web's dashboard after the user assign his login credentials on the login page that appears right after opening the web-app as shown in (Figure 19).

UI Components: The live data and additional metrics (such as BPM and SPO2 values) are displayed within UI cards built using shadcn components.

Last but not least, the domain name of this web-app is a free domain provided by vercel. So, in other words, the website is deployed on vercel. Eventually, during the process of the innovation's development, advantages and limitations were discovered. This apparatus is defined as very low-cost compared to other comparable devices, high accuracy referring to the calculated reliability as well as user friendly whether it is for the doctor or the patient due to its ease of use. Fortunately, few limitations were shown where this system lacks a two-factor authentication security.

Conclusion

To sum up, the Multi-Beat digital stethoscope, which incorporates integrated oximeter capabilities, represents a noteworthy progression in the medical domain. It remains lower costs than the closely resembling products in the medical market while improving diagnostic speed and reliability by simplifying the monitoring of cardiac activity and SpO2. Real-time data visualization is made possible by the device's link to a web-application that may be accessed on a doctor's PC or smartphone. This facilitates the early identification of anomalies even in the case of faint or subtle noises.

The Multi-Beat digital stethoscope serves as an example of how technology may improve conventional medical procedures by lowering the cost and increasing the accessibility of sophisticated diagnostic equipment. This gadget meets the demands of the healthcare sector today and establishes a benchmark for upcoming developments that prioritize affordability and usefulness. Essentially, it increases diagnostic precision, simplifies patient monitoring, and promotes the effectiveness of healthcare delivery, all of which lead to improved patient outcomes and a more robust healthcare system.

As a future work, the first thing that is being worked on is developing a two-factor authentication system allowing a high security website. Moreover, the ability to choose between a user-oriented system or admin-oriented one will be available as well as the capacity for each medical health staff especially doctors to create their own account enclosing all patients archive. At long last, collaborations with medical companies will be carried out in order to implement the whole circuit in a specialized traditional stethoscope.

Scientific Ethics Declaration

The authors, Rebecca Dib, Daniel Al Boutros and Lama Bou Farah, declare that they bear the scientific, ethical, and legal responsibility for this article published in the EPSTEM journal.

Acknowledgements or Notes

* This article was presented as an oral presentation at the International Conference on Technology, Engineering and Science (www.icontes.net) held in Antalya/Turkey on November 14-17, 2024.

References

Alanazi, A., Atcherson, S., Franklin, C., & Bryan, M. (2020). Frequency responses of conventional and amplified stethoscopes for measuring heart sounds. *Saudi Journal of Medicine and Medical Sciences, 8*(2), 112.

American Lung Association. (n.d.). *Your heart and lungs: the ultimate relationship*. Retrieved from https://www.lung.org/blog/heart-lung-relationship

Bishop, P. J. (1980). Evolution of the stethoscope. *Journal of the Royal Society of Medicine*, *73*(6), 448–456.

GeeksforGeeks. (2024, September 27). *Difference between sensor and transducer*. Geeks for Geeks. Retrieved from https://www.geeksforgeeks.org/difference-between-sensor-and-transducer.

Grenier, M., Gagnon, K., Genest, J., Durand, J., & Durand, L. (1998). Clinical comparison of acoustic and electronic stethoscopes and design of a new electronic stethoscope. *The American Journal of Cardiology*, *81*(5), 653–656.

Gupta, J. I., & Shea, M. J. (2023, March 8). *Cardiac auscultation*. MSD manual professional edition. Retrieved from https://www.msdmanuals.com/professional/cardiovascular-disorders/approach-to-the-cardiac.

Gupta, L. (2023, November 5). *Difference between PUT and POST in REST API*. REST API Tutorial. Retrieved from https://restfulapi.net/rest-put-vs-post/

Hanna, K. T., & Rosencrance, L. (2023, May 19). *Google firebase*. Mobile computing. https://www.techtarget.com/searchmobilecomputing/definition/Google-Firebase

How2Electronics. (n.d.). *MAX30102 with Arduino: Heart rate and blood oxygen monitoring.* Retrieved from https://how2electronics.com/max30102-arduino-heart-rate-blood-oxygen-monitoring/

Krelja-Kurelovic, E. (2023). Challenges of blended versus online learning with arduino for teachers and students. *The Eurasia Proceedings of Educational and Social Sciences (EPESS), 33,* 70-75.

Landge, K., Kidambi, B., Singhal, A., & Basha, A. (2018). Electronic stethoscopes: Brief review of clinical utility, evidence, and future implications. *Journal of the Practice of Cardiovascular Sciences*, *4*(2), 65.

Li, Y., Shi, P., Yang, Y., Cui, J., Zhang, G., & Duan, S. (2021). Design and verification of magnetic-induction electronic stethoscope based on MEMS technology. *Sensors and Actuators a Physical*, *331*, 112951.

Mobizt. (n.d.). *Firebase RTDB Arduino library for ESP8266 and RP2040 Pico. The complete, fast, secured and reliable Firebase Arduino client library that supports CRUD (create, read, update, delete) and Stream operations.* GitHub. https://github.com/mobizt/Firebase-ESP8266

Salimi-My. (n.d.). *GitHub - salimi-my/shadcn-ui-sidebar: A stunning, functional and responsive retractable sidebar for Next.js built on top of shadcn/ui.* GitHub. https://github.com/salimi-my/shadcn-ui-sidebar

Sarkar, M., Madabhavi, I., Niranjan, N., & Dogra, M. (2015b). Auscultation of the respiratory system. *Annals of Thoracic Medicine*, *10*(3), 158.

Firestore /Firebase (n.d.). *SDKs and client libraries* Firebase. Retrieved from https://firebase.google.com/docs/firestore/client/libraries

Shadcn. (n.d.). *Installation*. Shadcn/Ui. Retrieved from https://ui.shadcn.com/docs/installation

Swarup, S., & Makaryus, A. (2018). Digital stethoscope: Technology update. *Medical Devices Evidence and Research*, *11*, 29–36.

Teja, R. (2024, March 30). *An introduction to sound transducers*. ElectronicsHub. Retrieved from https://www.electronicshub.org/sound-transducer

W3Schools.com. (n.d.). https://www.w3schools.com/mongodb/

Yang, Y., Wang, B., Cui, J., Zhang, G., Wang, R., Zhang, W., He, C., Li, Y., Shi, P., & Wang, S. (2022). Design and realization of mems heart sound sensor with concave, racket-shaped cilium. *Biosensors*, *12*(7), 534.

Author Information

Rebecca Dib
Lebanese German University
Biomedical technologies department
Main, Sahel Alma, Lebanon
Contact e-mail: *rebeccadib2003@gmail.com*

Daniel Al-Boutros
Lebanese German University
Biomedical technologies department
Main, Sahel Alma, Lebanon

Lama Bou-Farah
Lebanese German University
Biomedical technologies department
Main, Sahel Alma, Lebanon

To cite this article:

Dib, R., Al-Boutros, D., & Bou-Farah, L. (2024). Multi-beat digital stethoscope. *The Eurasia Proceedings of Science, Technology, Engineering & Mathematics (EPSTEM), 32,* 619-633.

The Eurasia Proceedings of Science, Technology, Engineering & Mathematics (EPSTEM)
ISSN: 2602-3199

The Eurasia Proceedings of Science, Technology, Engineering & Mathematics (EPSTEM), 2024

Volume 32, Pages 634-641

IConTES 2024: International Conference on Technology, Engineering and Science

A Novel Approach to Visible Light Communication: Combining OFDM and $SrLa_2Al_2O_7:Er^{3+}$ LED

Halima Chahed
University of Djillali Liabes

Benattou Fassi
University of Djillali Liabes

Samia Driz
University of Djillali Liabes

Abstract: Visible Light Communication (VLC) presents a promising technology for future wireless communication systems, offering a high-speed and secure alternative to traditional radio frequency (RF) based wireless systems. To enhance VLC performance, the Orthogonal Frequency Division Multiplexing (OFDM) technique has been employed. OFDM's high spectral efficiency and robustness to multipath interference make it well-suited for mitigating inter-symbol interference (ISI) and maximizing spectral efficiency. This study explores the OFDM-VLC system under OptiSystem software, utilizing a high-efficiency Perovskite-based Light-Emitting Diode (LED). Specifically, the investigation emphasizes the $SrLa_2Al_2O_7:Er^{3+}$ LED, which exhibits high luminescence efficiency with a Quantum Efficiency (QE) of approximately 68.33%. The impact of the number of OFDM subcarriers and the $SrLa_2Al_2O_7:Er^{3+}$ LED's characteristics on system performance are thoroughly analyzed over various channel ranges and bit rates. To evaluate the system's efficacy, the performance of the proposed OFDM-VLC system was rigorously assessed using rigorous performance metrics, including Bit-Error Rate (BER) and constellation diagrams. The findings unequivocally demonstrate the substantial enhancement in communication reliability and efficiency achieved by the proposed OFDM-VLC system based on $SrLa_2Al_2O_7:Er^{3+}$ LED.

Keywords: Visible light communication (VLC), Orthogonal frequency division multiplexing (OFDM), $SrLa_2Al_2O_7:Er^{3+}$ LED, Quantum efficiency (QE), Bit-error rate (BER).

Introduction

Visible Light Communication (VLC) has emerged as a promising technology in the quest for high-speed, efficient wireless communication solutions. By modulating visible light emitted from LEDs, VLC serves a dual function, acting as both an energy-efficient lighting source and a high-bandwidth data transmission medium. This dual capability makes VLC particularly appealing for indoor wireless communication, where data transmission can seamlessly integrate into existing LED lighting infrastructure. However, despite these advantages, VLC faces challenges, particularly in maintaining signal quality over longer distances and managing high error rates under demanding conditions (Loureiro et al., 2023; Geng et al., 2022; He et al., 2023; Shi et al., 2022; Chi et al., 2018).

To overcome these limitations and make VLC more robust and capable of handling higher bit rates, researchers are exploring advanced LED materials that can better sustain signal integrity over extended distances. One of the key techniques for enhancing VLC systems is Orthogonal Frequency Division Multiplexing (OFDM), a modulation method known for its capacity to handle high data rates and its resilience to inter-symbol interference (ISI). By dividing a high-speed data stream into multiple lower-speed sub-streams, OFDM enables the VLC system to manage multipath distortion and interference more effectively, resulting in improved signal quality over various distances and bit rates (Shen et al., 2023; Fassi et al., 2022; Selvendran et al., 2019; Pradhan et al., 2021; Pradhan et al., 2023).

This study implements an OFDM-based VLC system to examine the performance of a standard LED compared with an LED that uses Strontium Lanthanum Aluminate doped with Erbium ions ($SrLa_2Al_2O_7$: Er^{3+}), a material noted for its enhanced optical characteristics and stability. $SrLa_2Al_2O_7$: Er^{3+}, a perovskite-type phosphor, is particularly promising for VLC applications due to its distinctive luminescence properties. With a structure similar to traditional perovskites (general formula ABX_3), its crystalline arrangement enhances luminescence efficiency, making it suitable for high-performance lighting and display applications. Doped with erbium ions, $SrLa_2Al_2O_7$: Er^{3+} emits a greenish light with a prominent peak at 548 nm. At an optimized Er^{3+} concentration of 2.0 mol%, it achieves a quantum efficiency of 68.33% and a radiative lifetime of 0.546 ms, making it a strong, stable light source capable of supporting high-bandwidth applications. Additionally, its nano phosphors display favorable color coordinates of (0.2657, 0.6031), supporting balanced white light generation. When paired with RGB phosphor chips, the $SrLa_2Al_2O_7$: Er^{3+} LED can emit warm white light with excellent color rendering, broadening its application potential for efficient VLC systems (Song et al., 2019a; Sehrawat et al., 2020; Zeng et al., 2022; Chen et al., 2023; Devi et al., 2019).

This study delves into the performance of an OFDM-VLC system, employing both a standard LED and an advanced $SrLa_2Al_2O_7$: Er^{3+} LED. To conduct a comprehensive analysis of the impact of varying transmission distances, bitrates ranging from 1 to 25 Gbps, and the number of subcarriers, OptiSystem software version 21.0.0 is used to simulate real-world indoor VLC scenarios. This paper is structured as follows: the *Methodology* section outlines the detailed simulation setup in OptiSystem used to evaluate VLC system performance. Subsequently, the *Results and Discussion* section presents an in-depth analysis, including a comparative examination of Bit Error Rate (BER), constellation diagrams, and Optical Signal-to-Noise Ratio (OSNR) between the two LED types. Finally, *Conclusion* section provides valuable findings on the potential benefits of utilizing $SrLa_2Al_2O_7$: Er^{3+} for advanced VLC applications and proposes directions for future research. This comparative analysis serves as a foundational step toward further exploration of advanced LED materials and their integration within VLC systems, ultimately contributing to the advancement of this innovative communication technology.

Methodology

This research rigorously evaluates the performance of a standard LED and a $SrLa_2Al_2O_7$: Er^{3+} enhanced LED within an OFDM-based VLC system, as illustrated in Figure 1. The simulation is configured to emulate indoor VLC conditions within a typical room of 5m x 5m x 3m, incorporating varying transmission distances from 1 to 5 meters and bit rates ranging from 1 to 25 Gbps to reflect realistic usage scenarios. Key performance indicators, including BER and OSNR, are assessed to evaluate the effectiveness of each LED type under identical conditions.

The data taransmission process begins with a Quadrature Amplitude Modulation (QAM) encoder, which converts binary data into a QAM signal at a symbol rate of 4 bits per symbol. This modulated data is then fed into an Orthogonal Frequency Division multiplexing OFDM Modulator. The OFDM modulator divides the signal into numerous orthogonal subcarriers, each carrying a portion of the modulated data. By employing a Fast Fourier Transform (FFT), the OFDM system transforms the time-domain signal into the frequency domain, enabling efficient transmission over wireless channels. This frequency-domain transmission significantly mitigates the effects of Inter-Symbol Interference (ISI), a common challenge in wireless communication, allowing for robust and high-speed data transmission (Selvendran et al., 2019).

The modulated signal undergoes amplification via an Electrical Amplifier, followed by filtration through a Low Pass Cosine Roll-Off Filter, which serves to restrict bandwidth and enhance signal integrity. The refined signal is then transmitted through one of the two light sources: either a standard LED operating at 550 nm with a quantum efficiency (QE) of 65% or a $SrLa_2Al_2O_7$: Er^{3+} LED emitting at 548 nm with an improved QE of 68.33%. The $SrLa_2Al_2O_7$: Er^{3+} LED is anticipated to demonstrate superior performance in comparison to the standard LED, owing to its optimized signal-emitting characteristics and advanced perovskite-based structure that enhances luminescence efficiency (Sehrawat et al., 2020).

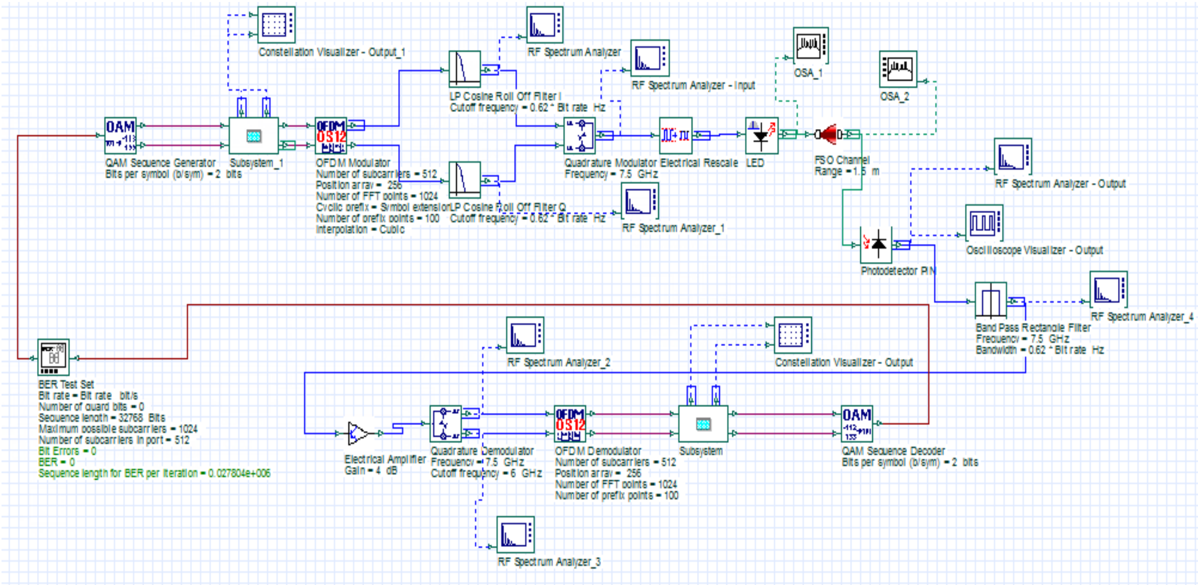

Figure 1. OFDM-VLC system model

The modulated light signal is transmitted through a Free Space Optical (FSO) Channel, set to a range of up to 5 meters, representing typical room-scale VLC applications. At the receiver end, a Photodetector PIN detects the transmitted light, which is then filtered and processed through a QAM Sequence Decoder to retrieve the original data. Various tools, such as RF Spectrum Analyzers, Constellation Visualizers, and an Oscilloscope Visualizer, are utilized to assess performance. The key metrics include BER, measured across different distances and bit rates using BER Test Set to gauge the reliability and accuracy of data transmission, and OSNR, calculated to assess the clarity of the transmitted signal, especially under high bit rate conditions.

Simulation Setup

To assess the performance of both the standard LED and $SrLa_2Al_2O_7$: Er^{3+}-enhanced LED in an OFDM-based VLC system, several simulation parameters were established to ensure accurate and comparable results. These parameters were configured to reflect typical indoor VLC conditions and are summarized in Table 1.

Table 1. Simulation parameters

LED parameters	Values
Frequency	550 nm (Standard LED); 548 nm ($SrLa_2Al_2O_7$: Er^{3+}LED)
Electron life Time	0.1 x10^{-9} s
RC constant	0.1 x10^{-9} s
Quantum Efficiency	65% (Standard LED), 68.33% ($SrLa_2Al_2O_7$: Er^{3+}LED)
OFDM parameters	Values
Numbers of Subcarriers	512 , 1024
Position array	256 , 512
Numbers of FFT points	1024 , 2048
PIN photodetector parameters	Values
Responsivity Type	Si
Dark current	10 nA
Shot noise distribution	Gaussian
FSO channel parameters	Values
Range	From 1m to 5m
Transmitter aperture diameter	7 cm
Receiver aperture diameter	1.5 cm
Layout parameters	Values
Bit Rate	From 1Gbps to 25 Gbps
Sequence Length	32768
Samples per bit	128
Number of samples	4194304

Results and Discussion

This analysis evaluates the performance of an OFDM-VLC system under two different configurations. The first configuration employs 512 subcarriers and a 1024-point FFT, while the second configuration utilizes 1024 subcarriers and a 2048-point FFT. This assessment employs the BER and OSNR as primary metrics to compare the performance of both the Standard LED and the $SrLa_2Al_2O_7$: Er^{3+} LED under varying conditions. Simulations were conducted over transmission distances ranging from 1 to 5 meters, with bit rates varying from 1 to 25 Gbps, allowing for an in-depth examination of the impact of subcarriers number on system performance (Selvendran et al., 2019).

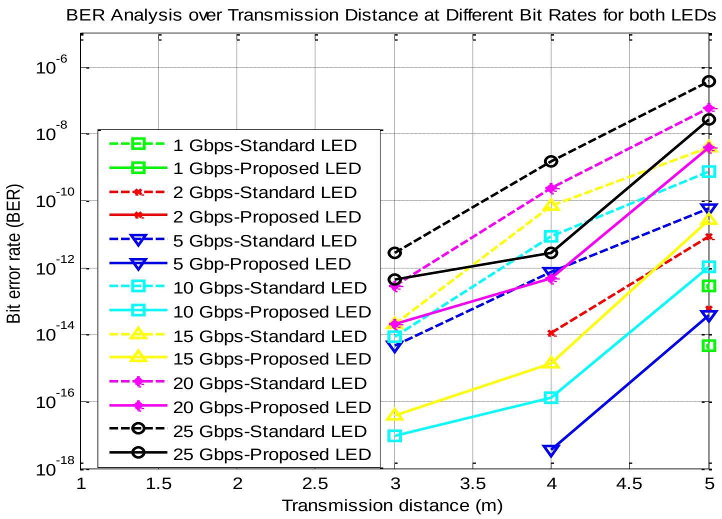

Figure 2. BER curves for both LEDs

Analysis for 512 Subcarriers: The analysis of BER for the Standard LED and $SrLa_2Al_2O_7$: Er^{3+} LED across various data rates and different transmission distance with 512 subcarriers reveals significant performance differences. For the Standard LED, the minimum BER values exhibit a general increase with rising data rates and transmission distances, particularly evident at higher rates (10 to 25 Gbps), where the BER reaches values as high as $3.65132e^{-7}$ at transmission of 5 meters and 25 Gbps. This trend aligns with the observed decrease in OSNR, suggesting that as noise levels rise with increasing of transmission range and data rate, the likelihood of error in signal transmission increases, indicating poor noise resistance.

In stark contrast, the $SrLa_2Al_2O_7$: Er^{3+} LED demonstrates a markedly lower BER, achieving values down to $4.01889e^{-9}$ at 20 Gbps and transmission range up to 5 meters . The improved OSNR values for this LED type correlate with its superior performance, showing that it can maintain signal integrity even under higher bitrates conditions. Overall, the $SrLa_2Al_2O_7$: Er^{3+} LED clearly outperforms the Standard LED, evidencing its effectiveness for high-speed optical communication, as detailed in Table 2, 3, and 4. This enhanced performance highlights the $SrLa_2Al_2O_7$: Er^{3+} LED's suitability for applications requiring high data rates, as it better preserves data integrity under increased bit rate and distance conditions. Figure. 2 illustrates the BER performance curves for both the standard LED and the $SrLa_2Al_2O_7$: Er^{3+} LED across various bit rates and transmission distances. The BER curves for the $SrLa_2Al_2O_7$: Er^{3+} LED consistently lies below that of the standard LED, indicating superior performance with lower BER values. In the plotted graphs, the BER for the $SrLa_2Al_2O_7$: Er^{3+} LED approaches zero, particularly at shorter distances and lower bit rates, which underscores its enhanced ability to maintain data integrity compared to the standard LED. This trend highlights the $SrLa_2Al_2O_7$: Er^{3+} LED's robustness in high-speed VLC applications.

Analysis for 1024 Subcarriers: For the 1024 subcarrier configuration, the differences in BER between the two LED types become even more pronounced. The Standard LED exhibits increasing BER values as the data rate escalates, with maximum values of $1.93751e^{-8}$ at 5 meters range and 25 Gbps, emphasizing its limitations in handling higher transmission ranges and data rates. This deterioration in performance aligns with the significant reduction in OSNR, which indicates a compromised signal-to-noise ratio detrimental to reliable data transmission. Conversely, the $SrLa_2Al_2O_7$: Er^{3+} LED continues to showcase minimal BER values, as low as $5.1556e^{-15}$ at 25 Gbps over a distance of 3 meters, and maintaining a BER of approximately $8.01504e^{-9}$ at a distance of 5 meters.

The consistently higher OSNR values indicate its robust performance against noise, allowing it to sustain a higher quality signal across a broader range of operating conditions. This stark contrast highlights the $SrLa_2Al_2O_7$: Er^{3+} LED as a superior choice for applications demanding high data rates, emphasizing its potential to enhance communication reliability and efficiency in demanding environments. as illustrated in Table 2 and 3. These results, coupled with higher OSNR values than the standard LED, illustrate the $SrLa_2Al_2O_7$: Er^{3+} LED's superior noise resistance and ability to maintain clear signal transmission over extended ranges and bit rates Table 5.

Table 2. Bit Error Rate (BER) values for Standard LED

	Min BER									
	512 Subcarriers					**1024 Subcarriers**				
Range / **Bitrate**	**1**	**2**	**3**	**4**	**5**	**1**	**2**	**3**	**4**	**5**
1	0	0	0	0	2.7536e^{-13}	0	0	0	0	3.27523e^{-17}
2	0	0	0	1.09591e-^{14}	8.32005e^{-12}	0	0	0	2.53843e^{-16}	2.7531e^{-14}
5	0	0	4.67661e^{-15}	7.24786e-^{13}	6.15734e^{-11}	0	0	2.34785e^{-18}	4.84125e^{-15}	1.32731e^{-13}
10	0	0	8.76182e^{-15}	8.78343e-^{12}	7.34375e^{-10}	0	0	4.57896e^{-17}	6.30251e^{-14}	5.78352e^{-12}
15	0	0	2.04984e-^{14}	6.98369e-^{11}	3.9465e^{-9}	0	0	8.94865e^{-17}	4.97035e^{-13}	1.2563e^{-11}
20	0	0	2.92168e^{-13}	2.51339e^{-10}	5.8137e^{-8}	0	0	1.23001e^{-16}	2.86695e^{-12}	4.97022e^{-10}
25	0	0	2.70977e^{-12}	1.52373e^{-9}	3.65132e^{-7}	0	0	7.61384e^{-14}	6.73365e^{-11}	1.93751e^{-8}

Table 3. Bit Error Rate (BER) values for SrLa2Al2O7:Er3+ LED

	Min BER									
	512 Subcarriers					**1024 Subcarriers**				
Range / **Bitrate**	**1**	**2**	**3**	**4**	**5**	**1**	**2**	**3**	**4**	**5**
1	0	0	0	0	4.72023e^{-15}	0	0	0	0	0
2	0	0	0	0	5.91018e^{-14}	0	0	0	0	0
5	0	0	0	3.713e^{-18}	3.9722e^{-14}	0	0	0	0	0
10	0	0	9.24549e^{-18}	1.27669e^{-16}	1.05681e^{-12}	0	0	0	0	0
15	0	0	3.72734e^{-17}	1.32878e^{-15}	2.603e^{-11}	0	0	2.674e-^{19}	3.51097e^{-17}	3.4062e^{-12}
20	0	0	2.08095e^{-14}	4.89778e^{-13}	4.01889e^{-9}	0	0	1.76282e^{-17}	8.16007e^{-14}	2.7346e^{-11}
25	0	0	4.56338e^{-13}	2.68356e^{-12}	2.6975e^{-8}	0	0	5.1556e^{-15}	7.3955e^{-13}	8.01504e^{-9}

Table 4. OSNR for both LEDs for 512 subcarriers

	OSNR (dB) for 512 Subcarriers									
	Standard LED					**$SrLa_2Al_2O_7$:Er^{3+} LED**				
Range / **Bitrate**	**1**	**2**	**3**	**4**	**5**	**1**	**2**	**3**	**4**	**5**
1	85.823	74.452	69.527	63.453	59.678	93.302	83.594	69. 883	67.374	60.412
2	82.318	71.583	65.114	59.427	55.861	90.604	79.982	67. 654	63.525	58.258
5	78.974	64.632	62.612	57. 826	53. 718	87.837	77.734	66. 672	62.041	56.623
10	74.415	62.336	59.393	54.668	49.914	85.308	75.637	63. 297	58.116	51.092
15	72.479	60.025	57.713	52.926	47.981	82.582	73.392	62. 142	55.784	48.615
20	71.614	58.214	53.688	48.894	45.085	80.584	70.014	59.017	52.182	46.126
25	70.683	56.418	50.135	47.929	44.576	77.723	69.415	57.121	49.651	45.984

Table 5. OSNR for both LEDs for 1024 subcarriers

	OSNR (dB) for 1024 Subcarriers									
	Standard LED					**$SrLa_2Al_2O_7$:Er^{3+} LED**				
Range / **Bitrate**	**1**	**2**	**3**	**4**	**5**	**1**	**2**	**3**	**4**	**5**
20	78.245	70.135	60.679	51.866	48.963	84.149	79.349	68.330	60.425	49.764
25	74.385	66.714	56.226	48.507	46.387	80.762	75.173	65.915	52.682	47.118

In Table 5, the OSNR was specifically evaluated at 20 Gbps and 25 Gbps with 1024 subcarriers, as increasing the subcarrier count mainly benefits systems operating at higher data rates. With 1024 subcarriers instead of 512, the system can manage complex, high-throughput data transmissions more effectively, allowing bit rates up to 25 Gbps while maintaining acceptable BER levels. Lower bit rates, such as 10 Gbps, were likely not tested with 1024 subcarriers because these rates could be supported within the desired link range using just 512 subcarriers. Therefore, the use of 1024 subcarriers was focused on the higher, more demanding bit rates to assess the system's capacity at the upper limits of its throughput.

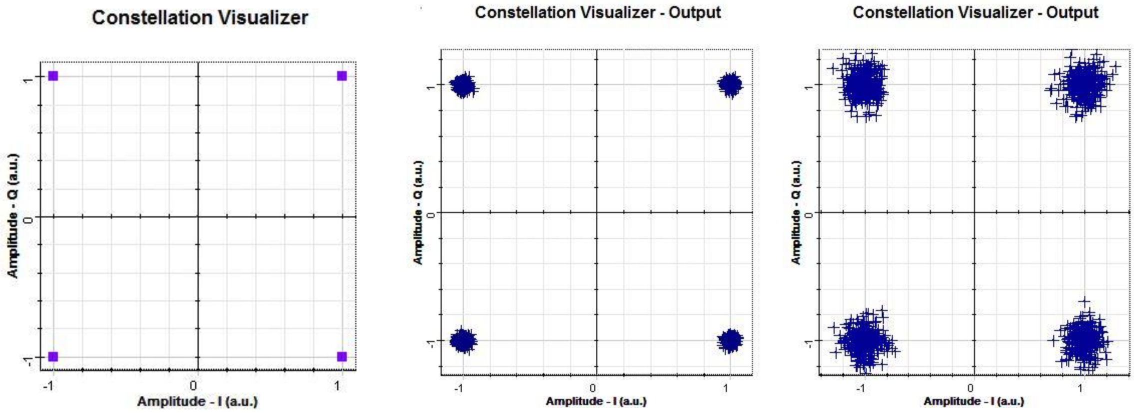

(a) (b) (c)

Figure 3. Constellation Diagrams. a. transmitted signal Constellation. b. Received signal Constellation for $SrLa_2Al_2O_7{:}Er^{3+}$ LED. c. received signal Constellation for standard LED

The constellation diagrams, shown in Figures 3a, 3b, and 3c, illustrate the constellation before and after transmission for both LEDs at 10 Gbps over a 3 meters range, revealing essential distinctions in performance. The $SrLa_2Al_2O_7$: Er^{3+} LED exhibits a well-organized and tightly clustered constellation with minimal distortion, indicating lower BER and enhanced signal integrity.

In comparison, the standard LED constellation displays a broader scatter in the data points, indicating a higher susceptibility to errors. This contrast in clustering suggests that the $SrLa_2Al_2O_7$: Er^{3+} LED provides superior stability and clarity in the transmitted signal, particularly at high bit rates and extended distances. Figure 4a and 4b displays the transmitted and received sequences when using the $SrLa_2Al_2O_7{:}Er^{3+}$ LED at 10 Gbps over 3 meters with configuration of 1024 subcarriers, showing an identical match. This close alignment indicates high signal integrity with minimal distortion, reflecting the LED's effectiveness in maintaining clear, stable transmission even at elevated data rates. The consistency suggests efficient ISI mitigation and noise suppression, underscoring the $SrLa_2Al_2O_7{:}Er^{3+}$ LED's reliability for high-speed VLC applications.

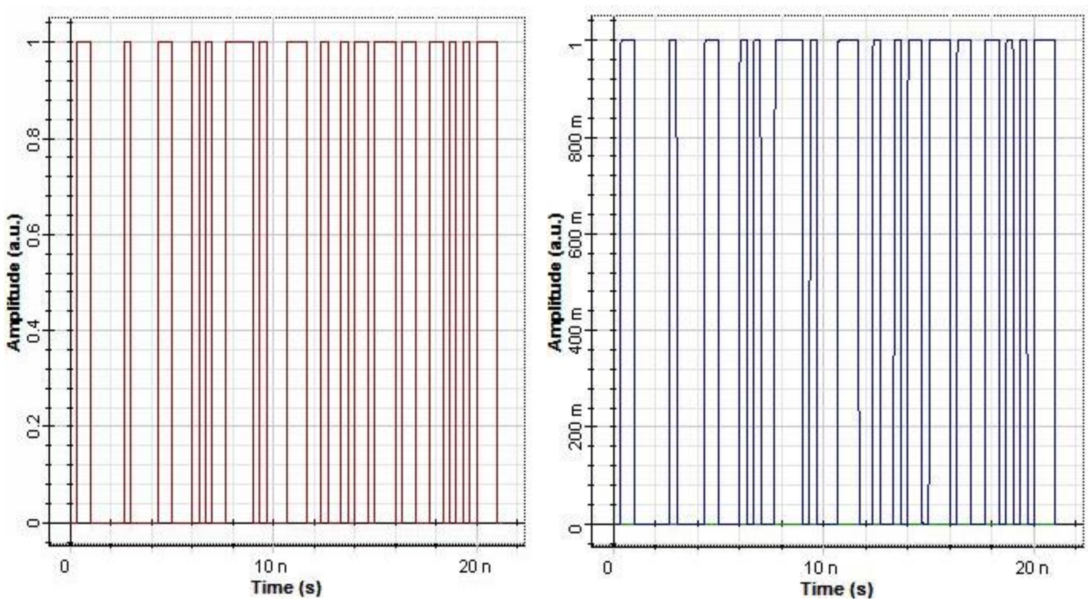

(a) (b)

Figure 4. Transmitted and received Sequence

Conclusion

In conclusion, this study demonstrates that $SrLa_2Al_2O_7$: Er^{3+} LEDs are a promising advancement for VLC systems, outperforming standard LEDs in important performance metrics such as BER and OSNR at various transmission distances and bit rates. Simulations in OptiSystem revealed that these LEDs achieved lower BER and better signal integrity, particularly at data rates of up to 25 Gbps and longer ranges. Their capability to produce clear constellation diagrams and closely match transmitted and received sequences highlights their potential for high-throughput VLC applications, with minimized inter-symbol interference and effective noise reduction. The findings indicate that $SrLa_2Al_2O_7:Er^{3+}$ LEDs greatly improve signal quality and stability, making them suitable for advanced VLC systems for reliable, high-speed indoor communication. This research deepens the understanding of LED materials in VLC performance and sets the stage for integrating phosphor-based LEDs into high-speed optical networks. Future studies should optimize parameters, explore real-world applications, and investigate the role of new phosphor materials in VLC technology development.

Scientific Ethics Declaration

The authors declare that the scientific ethical and legal responsibility of this article published in EPSTEM Journal belongs to the authors.

Acknowledgements or Notes

* This article was presented as a poster presentation at the International Conference on Technology, Engineering and Science (www.icontes.net) held in Antalya/Turkey on November 14-17, 2024.

References

Chen, X., Xiang, H., Wang, R., Wang, Y., Wang, Y., & Zeng, H. (2023). Perovskite-Organic coupling WLED Progress and perspective. *Advanced Functional Materials, 33*(46), 2304750.

Chi, N. (2018). *Visible light communication technology development trend. signals and communication technology* (pp.233–245). Springer.

Devi, S., Taxak, V. B., Chahar, S., Dalal, M., Dalal, J., Hooda, A., Khatkar, A., Malik, R. K., & Khatkar, S. P. (2019). Crystal chemistry and optical analysis of a novel perovskite type SRLA2AL2O7sm3+ nanophosphor for white leds. *Ceramics International, 45*(12), 15571–15579.

Fassi, B., Driz, S., Al-Douri, Y., Ameri, M., & Abd El-Rehim, A. F. (2022). Optical investigations of Cu2CdSnS4 quaternary alloy nanostructure for indoor optical wireless communications. *Optics Communications, 517*, 128351.

Geng, Z., Khan, F. N., Guan, X., & Dong, Y. (2022). Advances in visible light communication technologies and applications. *Photonics, 9*(12), 893.

He, C., & Chen, C. (2023). A review of advanced transceiver technologies in *Visible Light Communications. Photonics, 10*(6), 648.

Li, B., Shi, J., & Feng, S. (2022). Reconstructed hybrid optical OFDM-Noma for multiuser VLC Systems. *Photonics, 9*(11), 857.

Loureiro, P. A., Guiomar, F. P., & Monteiro, P. P. (2023, August 30). Visible light communications A survey on recent high-capacity demonstrations and digital modulation techniques. *Photonics. 10*(9), 993

Pradhan, J., Holey, P., Kappala, V. K., & Das, S. K. (2021). Performance analysis of ACO-OFDM Noma for VLC communication. *Optical and Quantum Electronics, 54*(8), 531

Pradhan, J., Kiran, K. V., & Das, S. K. (2023). Performance analysis of MIMO ACO OFDM VLC system under ambient noise. *International Conference for Advancement in Technology (ICONAT)*, 1–5.

Sehrawat, P., Khatkar, A., Devi, S., Kumar, R., Malik, R. K., Khatkar, S. P., & Taxak, V. B. (2020). Crystal structure and photophysical features of greenish perovskite type srla2al2O7er3+ nanocrystals for down conversion white leds. *Materials Research Express, 6*(12), 126213.

Selvendran, S., Sivanantha Raja, A., Esakki Muthu, K., & Lakshmi, A. (2019). Certain investigation on visible light communication with OFDM modulated white led using Optisystem simulation. *Wireless Personal Communications, 109*(2), 1377–1394.

Shen, P., & Lu, L. (2023). Reconfigurable intelligent surface enabled spatial modulation for visible light communications. IEEE *Photonics Journal, 15*(5), 1–12.

Shi, J., Niu, W., Ha, Y., Xu, Z., Li, Z., Yu, S., & Chi, N. (2022). AI-enabled Intelligent visible light communications Challenges, progress, and future. *Photonics, 9*(8), 529.

Song, Z., Zhao, J., & Liu, Q. (2019a, August 19). Luminescent Perovskites Recent advances in theory and experiments. *Inorganic Chemistry Frontiers. 6*(11), 2969-3011

Wang, G., Shao, Y., Chen, L.-K., & Zhao, J. (2021). Improved joint subcarrier and power allocation to enhance the throughputs and user fairness in indoor OFDM-Noma VLC Systems. Optics *Express, 29*(18), 29242.

Zeng, X., Yu, L., Peng, K., & Yu, Y. (2022). Enhancing the stability of perovskite quantum dots CSPBBR3 by encapsulation in kaolin nanosheets for WLED applications. SSRN *Electronic Journal 4265570*.

Author Information

Halima Chahed
Telecommunications and Digital Signal Processing Laboratory, Faculty of Electrical Engineering,
University of Djillali Liabes
Sidi Bel Abbes 22000, Algeria
Contact e-mail: halima.chahed@univ-sba.dz

Benattou Fassi
Telecommunications and Digital Signal Processing Laboratory, Faculty of Electrical Engineering,
University of Djillali Liabes
Sidi Bel Abbes 22000, Algeria

Samia Driz
Telecommunications and Digital Signal Processing Laboratory, Faculty of Electrical Engineering,
University of Djillali Liabes
Sidi Bel Abbes 22000, Algeria

To cite this article:

Chahed, H., Fassi, B., & Driz, S. (2024). A novel approach to visible light communication: Combining OFDM and $SrLa_2Al_2O_7:Er^{3+}$ LED. *The Eurasia Proceedings of Science, Technology, Engineering & Mathematics (EPSTEM), 32,* 634-641.